

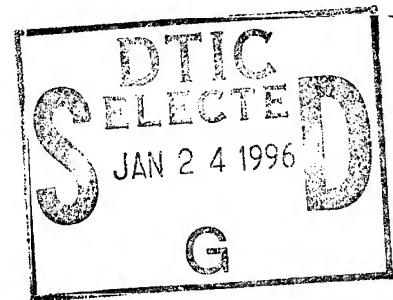
AIAA / ASME / ASCE / AHS

25th STRUCTURES, STRUCTURAL DYNAMICS AND MATERIALS CONFERENCE

Palm Springs, California
May 14-16, 1984

SPONSORED BY

AMERICAN INSTITUTE OF AERONAUTICS AND ASTRONAUTICS (AIAA)
AMERICAN SOCIETY OF MECHANICAL ENGINEERS (ASME)
AMERICAN SOCIETY OF CIVIL ENGINEERS (ASCE)
AMERICAN HELICOPTER SOCIETY (AHS)



AND

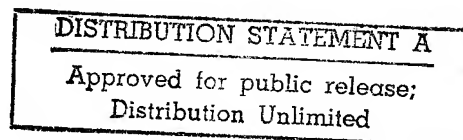
19960125 006

AIAA DYNAMICS SPECIALISTS CONFERENCE

Palm Springs, California
May 17-18, 1984

A COLLECTION OF TECHNICAL PAPERS

PART 2



DEPARTMENT OF DEFENSE
PERFORMING TECHNICAL EVALUATION CENTER
AFRADCOR, DOVER, N. J. 07801

DTIC QUALITY ASSURANCE

PLASTEC
4/18/84
4/18/84

*MSG 114 DROLS PROCESSING-LAST INPUT IGNORED

-- 3 OF 28

ITEM DOES NOT HAVE THIS ITEM

-- 1 - AD NUMBER: D409287
-- 5 - CORPORATE AUTHOR: AMERICAN INST OF AERONAUTICS AND ASTRONAUTICS
-- NEW YORK
-- 6 - UNCLASSIFIED TITLE: AIAA/ASME/ASCE/AHS 25TH STRUCTURES,
STRUCTURAL DYNAMICS AND MATERIALS CONFERENCE PART 2.
--11 - REPORT DATE: May 14, 1984
--12 - PAGINATION: 651P
--20 - REPORT CLASSIFICATION: UNCLASSIFIED
--21 - SUPPLEMENTARY NOTE: PROCEEDINGS: AIAA/ASME/ASCE/AHS 25TH
STRUCTURES, STRUCTURAL DYNAMICS AND MATERIALS CONFERENCE PART 2, 14-
16 MAY 84, PALM SPRINGS, CA. SPONSORED BY AMERICAN INSTITUTE OF
-- AERONAUTICS AND ASTRONAUTICS. (SEE PL-47858 - PL-47859).
--22 - LIMITATIONS (ALPHA): APPROVED FOR PUBLIC RELEASE; DISTRIBUTION
-- UNLIMITED. AVAILABILITY: PROCEEDINGS ONLY AVAILABLE FROM AIAA, 1630
-- BROADWAY, NEW YORK, N.Y. 10019. ATTN: MARKETING DEPT.
--33 - LIMITATION CODES: 1 24

-- END Y FOR NEXT ACCESSION ENO

Alt-Z FOR HELP3 ANSI 3 BOX 3 3 LOG CLOSED 2 PRINT OFF 2 PASTY

SPONSORED BY

AMERICAN INSTITUTE OF AERONAUTICS AND ASTRONAUTICS (AIAA)
AMERICAN SOCIETY OF MECHANICAL ENGINEERS (ASME)
AMERICAN SOCIETY OF CIVIL ENGINEERS (ASCE)
AMERICAN HELICOPTER SOCIETY (AHS)

**A COLLECTION
OF
TECHNICAL PAPERS**

PART 2

Accession For	
NTIS	CRA&I <input checked="" type="checkbox"/>
DTIC	TAB <input type="checkbox"/>
Unannounced	<input type="checkbox"/>
Justification	
By	
Distribution /	
Availability Codes	
Dist	Avail and/or Special
A-1	

**Includes: Structural Dynamics
(Sessions # 7, 14, 15, 19, 20, 24, 25, 31, 34, 35,
36 and 37 from SDM Conference
and All Papers from Dynamics Specialists Conference)**

**AIAA/ASME/ASCE/AHS
25th STRUCTURES, STRUCTURAL DYNAMICS
& MATERIALS CONFERENCE**

May 14-16, 1984/Palm Springs, California

AND

AIAA DYNAMICS SPECIALISTS CONFERENCE

May 17-18, 1984/Palm Springs, California

AIAA/ASME/ASCE/AHS 25th Structures, Structural Dynamics and Materials Conference Committee

General Chairman (AIAA)

LARRY D. PINSON
NASA Langley Research Center

General Co-Chairman (ASME)

FRANK W. CROSSMAN
Lockheed Palo Alto Research Labs

General Co-Chairman (ASCE)

CHARLES L. BLACKBURN
Kentron International

Technical Program Chairman

ANTHONY K. AMOS
Air Force Office of Scientific Research

Administrative Chairman

HASSEL SCHJELDERUP

Poster Session Chairman

JEROME PEARSON
Flight Dynamics Lab.

Chairman Work-In-Progress

SHELDON RUBIN
The Aerospace Corp.

Co-Chairman Anniversary Functions

HOLT ASHLEY
Stanford Univ.

Co-Chairman Student Papers

JERRY H. GRIFFIN
Carnegie-Mellon Univ.

Technical Program Committee

AIAA Design Committee

TOM GRIFFITH
Boeing Vertol Co.

AIAA Materials Committee

DONALD PETERSEN
Vought Advanced Technology Center

AIAA Structures Committee

EDWARD E. SPIER
General Dynamics Corp.

AIAA Structural Dynamics Committee

SAMUEL VENERRI
NASA Headquarters

AIAA Deputy Director for Structures and Materials

BRYAN NOTON
Batelle Columbus Labs

ASCE Aerospace Division

ROBERT HACKETT
Univ. of Alabama/Huntsville

ASCE Engineering Mechanics Division

STUART SWARTZ
Kansas State Univ.

ASCE Structures Division

VAN B. VENKAYYA
Flight Dynamics Lab.

AHS Representative

ROBERT BLACKWELL
Sikorsky Aircraft

ASME Representative

ROBERT L. SIERAKOWSKI
Univ. of Florida

AIAA Dynamics Specialists Conference Committee

General Chairman

BEN K. WADA
Jet Propulsion Lab.

Technical Program Chairman

KETO SOOSAAR
The Charles Stark Draper Lab., Inc.

Guidance and Control Invited

Session Coordinator

JERRY LOCKENOUR
Northrop Corp.

TABLE OF CONTENTS

AIAA NO.		PAGE NO.
84-0870	Effects of Viscosity and Modes on Transonic Aerodynamic and Aeroelastic Characteristics of Wings - J.W. MARSTILLER, G.P. GURUSWAMY, H.T.Y. YANG and P.M. GOORJIAN	1
0872	An Efficient Coordinate Transformation Technique for Unsteady, Transonic Aerodynamic Analysis of Low Aspect-Ratio Wings - G.P. GURUSWAMY and P.M. GOORJIAN	17
0874	Separated Flow Unsteady Aerodynamics for Propfan Applications - R.M. CHI	27
0875	Modeling of Unsteady Small Disturbance Transonic Flow Using Parametric Differentiation, Psuedospectral Analysis and Finite-Differencing - M. BROWN and W.L. HARRIS	38
0899	Design Oriented Identification of Critical Times in Transient Response - R.V. GRANDHI, R.T. HAFTKA and L.T. WATSON	46
0901	A Hybrid Frequency-Time Domain Solution Scheme for Nonlinear Transient Dynamic Response - J.D. KAWAMOTO	60
0904	Evaluation of Flutter Impact for Repaired T-38 Stabilizers - H.C. BRIGGS	67
0906	A Unified Flutter Analysis for Composite Aircraft Wings - G.A. OYIBO	73
0919	A Finite Element Method for Nonlinear Forced Vibrations of Rectangular Plates - C. MEI and K. DECHA-UMPHAI	81
0921	New Interface Models of Dynamic Friction Effects in Nonlinear Structural Dynamics - J.T. ODEN and J.A.C. MARTINS	90
0922	Dynamics of Protective Layers - S. GINSBURG	97
0923	Limit Cycle Oscillations of a Nonlinear Rotorcraft Model - B. TONGUE	102
0926	System Identification of Analytical Models of Damped Structures - J-S. FUH, S-Y. CHEN and A. BERMAN	112
0928	A Modal Identification Algorithm for Higher Accuracy Requirements - S.R. IBRAHIM	117
0929	System Identification of Structural Dynamic Models - Theoretical and Practical Bounds - A. BERMAN	123
0930	Identification of Structural Properties of a Continuous Longeron Space Mast - Y. SOUCY and F.R. VIGNERON	130
0941	Combined Experimental/Analytical Modeling Using Component Mode Synthesis - D.R. MARTINEZ, T.G. CARNE, D.L. GREGORY and A.K. MILLER	140
0943	Component Mode Synthesis Methods for Test-Based, Rigidly Connected, Flexible Components - M. BAKER	153
0944	A Substructure Coupling Procedure Applicable to General Linear Time-Invariant Dynamic Systems - T.G. HOWSMAN and R.R. CRAIG JR.	164
0947	The Space Shuttle Payload Transient Loads Analysis by the Flex-Base Drive Method - K. KUBOMURA	172
0948	Simulating the Dynamic Separation of Launch Vehicles from their Support Structures - D.J. OLBERDING	180
0969	Thermal and Electromagnetic Damping Analysis and its Application - U. LEE	183
0970	Active Control of Decoupled Underdamped Systems - C.K. NG and D.J. INMAN	192
0977	Dynamic Analysis of Laminated Plates Using a Higher-Order Theory - J.N. REDDY and N.D. PHAN	201

1.

2

AIAA NO.		PAGE NO.
84-0979	Vibration and Buckling of General Periodic Lattice Structures - M.S. ANDERSON and F.W. WILLIAMS	206
0980	A New Theory for the Dynamics of Shear-Deformable Rings - C.W. BERT and T.G. GARDNER	214
0981	Dynamic Analysis of Multiple Support Structures Using the Impulse Function Approach - S. RAMAMURTHY, D. BHARGAVA, B. NIYOGI and N.A. MUNI	221
0985	Control of Aeroelastic Instabilities Through Elastic Cross-Coupling - T.A. WEISSHAAR and R.J. RYAN	226
0986	Equations of Motion of an Elastic Flight Vehicle Utilizing Static Aeroelastic Characteristics of the Restrained Vehicle - W.P. RODDEN and J.R. LOVE	236
0987	Aeromechanical Stability Analysis of a Multirotor Vehicle Model Representing a Hybrid Heavy Lift Airship (HHLA) - C. VENKATESAN and P.P. FRIEDMANN	251
0988	Unsteady Aerodynamics in Time and Frequency Domains for Finite Time Arbitrary Motion of Rotary Wings in Hover and Forward Flight - M.A.H. DINYAVARI and P.P. FRIEDMANN	266
0993	Identification of Structural Dynamic Systems with Nonproportional Damping - S. HANAGUD, M. MEYYAPPA, Y.P. CHENG and J.I. CRAIG	283
0995	Analytical Determination of Real Normal Modes from Measured Complex Responses - N. NIEDBAL	292
0997	Structural Modifications to Reduce the LOS-Error in Large Space Structures - N.S. KHOT, V.B. VENKAYYA and F.E. EASTEP	296
1018	Modal-Space Active Damping of a Plane Grid: Experiment and Theory - W.L. HALLAUER JR., G.R. SKIDMORE and R.N. GEHLING	306
1020	Experimental Research on Flexible Beam Modal Control - B. SCHAFER and H. HOLZACH	317
1024	Dynamics of Flexible Bodies in Tree Topology - A Computer Oriented Approach - R.P. SINGH, R.J. VANDERVOORT and P.W. LIKINS	327
1025	Requirements and Issues for the Control of Flexible Space Structures - J.F. GARIBOTTI	338
1027	Active Control of Space Structures (ACOSS): A Status Report - R.R. STRUNCE JR. and R.W. CARMAN	348
1029	Exact Nonlinear Control of Spacecraft Slewing Maneuvers with Internal Momentum Transfer - T.A.W. DWYER, III	357
1031	Feedback Control of Spacecraft Large-Angle Maneuvers Using Reaction Wheels and On-Off Thrusters - S.R. VADALI	368
1032	Quaternion Feedback for Spacecraft Large Angle Maneuvers - B. WIE and P.M. BARBA	373
1033	Comparison of Various Controller-Reduction Methods: Suboptimal Versus Optimal Projection - D.C. HYLAND	381
1034	Decoupled Large Space Structure Control - R.A. CALICO JR.	390
1035	The Optimal Projection Equations for Fixed-Order Dynamic Compensation of Distributed-Parameter Systems - D.S. BERNSTEIN and D.C. HYLAND	396
1036	Enhanced Vibration Controllability by Minor Structural Modifications - R.T. HAFTKA, Z.N. MARTINOVIC and W.L. HALLAUER JR. 41851	401
1041	Optimal Design for Single Axis Rotational Maneuvers of a Flexible Structure - R.J. LISOWSKI and A.L. HALE	411
1043	Dynamics and Control of Lattice Beams Using Complex and Simplified Finite Element Models - D.T. BERRY, T.Y. YANG and R.E. SKELTON	422

AIAA NO.		PAGE NO.
84-1044	Frequency Control and the Effect on the Dynamic Response of Flexible Structures - V.B. VENKAYYA and V.A. TISCHLER	431
1045	Frequency Domain Analysis of a Plate with Discrete Elements Attached - M. OMRANI and D.J. INMAN	442
1046	An Optimal Single-Sensor Feedback Control Law for Flexible Dynamic Systems - S.B. SKAAR and L. TANG	445
1047	Closed-Form Solutions for a Class of Optimal Quadratic Regulator Problems with Terminal Constraints - J-N. JUANG, J.D. TURNER and H.M. CHUN	449
1049	A Perturbation Technique for Gyroscopic Systems with Small Internal and External Damping - L. MEIROVITCH and G. RYLAND	457
1050	A Generalized Multiple-Input, Multiple-Output Modal Parameter Estimation Algorithm - R.R. CRAIG JR. and M.A. BLAIR	469
1051	Spacecraft Structural System Identification by Modal Test - J-C. CHEN, L.F. PERETTI and J.A. GARBA	478
1052	Identification of Linear Time-Invariant Systems by the Method of Poisson Moment Functionals - L.A. BERGMAN, A.L. HALE and J.C. GOODDING	490
1053	Damping Synthesis for a Spacecraft Using Substructure and Component Data - K.W. LIPS and F.R. VIGNERON	497
1058	An Automated Tuning and Data Collection System for Sine Dwell Modal Testing - D.L. HUNT, J. MATTHEWS and R. WILLIAMS	507
1060	A Rapid Method for Obtaining Frequency-Response Functions from Multiple Input Photogrammetric Data - M.L. KROEN and J.S. TRIPP	510
1066	Assessment of Galileo Modal Test Results for Mathematical Model Verification - M. TRUBERT	528
1067	Some Measurement and Analysis Methods Used in the Galileo Spacecraft Modal Survey - R.C. STROUD, M.R. PAMIDI and H.P. BAUSCH	542
1068	Optimal Selection of Excitation Methods for Enhanced Modal Testing - D.L. HUNT, H. VOLD, E.L. PETERSON and R. WILLIAMS	549
1069	Application of Multiple Input Random and Polyreference Analysis Techniques to the Galileo Spacecraft Modal Test - J.C. CHEN and D.L. HUNT	554
1071	Evaluation of Modal Testing Methods - J-C. CHEN	561
1077	Dynamic Characterization and Microprocessor Control of the NASA/UVA Proof Mass Actuator - D.C. ZIMMERMAN, D.J. INMAN and G.C. HORNER	573

LATE PAPERS

84-0873	Transonic Calculation of Airfoil Stability and Response with Active Controls - J.T. BATINA and T.Y. YANG	578
0903	Aeroelastic Behavior of Straight and Forward Swept Graphite/Epoxy Wings - B.J. LANDSBERGER and J. DUGUNDJI	589
0996	Selection and Evaluation of Optimum Exciter Locations for Modal Testing Via Automated Acceleration Transfer Function Analysis - D.N. KOPEC and P. GIROLAMO	599
1022	Geometric Methods for Multibody Dynamics - M. EL-BARAKA and P.S. KRISHNAPRASAD	607
1023	Convected Transient Analysis for Large Space Structures Maneuver and Deployment - J. HOUSNER	616
1070	Galileo Spacecraft Modal Identification Using an Eigensystem Realization Algorithm - R.S. PAPPAS and J-N. JUANG	630

John W. Marstiller*
Purdue University, West Lafayette, Indiana

Guru P. Guruswamy†
Informatics General Corporation, Palo Alto, California

Henry T. Y. Yang‡
Purdue University, West Lafayette, Indiana

Peter M. Goorjian§
NASA Ames Research Center, Moffett Field, California

Abstract

The research reported in this paper is concerned with aerodynamic and aeroelastic computations in the transonic regime. The aerodynamic computations were made using small-disturbance, unsteady, transonic theory with viscous corrections. New areas of investigation included studying the effects of viscous corrections on the aerodynamics about wings and the effect of including higher structural modes in addition to the fundamental bending and torsion modes in transonic aeroelastic analyses. Two wings were studied, a rectangular wing, with a NACA 64A010 airfoil section, and a swept wing, with an MBB-A3 supercritical airfoil section. Viscous effects on both wings were analyzed by employing the viscous-wedge and lag-entrainment methods. Aeroelastic analyses were performed and the effects of including the first two bending and torsion modes into the analysis are shown. Also discussed are the practical aspects of generating unsteady, transonic aerodynamic coefficients. Results from this work show that the inclusion of viscous effects increases the flutter speed for the two wings studied. For the rectangular wing, the fundamental modes were sufficient to determine the flutter speed, but the second torsion mode was required for an accurate aeroelastic analysis of the swept wing. These studies can aid aeroelasticians in selecting viscous methods and also structural modes to conduct aeroelastic analyses in the transonic regime.

Nomenclature

b = semichord of wing
 c = full chord of wing
 C_{l_h} = sectional lift coefficient due to plunging mode
 C_{l_α} = sectional lift coefficient due to pitching mode
 C_{m_h} = sectional moment coefficient due to plunging mode

*Graduate Student. Member AIAA.
†Principal Analyst. Member AIAA.
‡Professor and Head, School of Aeronautics and Astronautics. Associate Fellow AIAA.
§Research Scientist. Member AIAA.

C_{m_α} = sectional moment coefficient due to pitching mode
 d = assumed bending deflection function of the wing
 $e.a.$ = position of elastic axis, measured in semichords, aft of the midchord
 f_R = displacement due to viscous ramp slope
 g = artificial damping
 h = bending deflection of the elastic axis
 I_α = polar moment of inertia about the elastic axis of the wing section
 k_b = reduced frequency based on semichord
 k_c = reduced frequency based on chord
 K_h = bending-spring stiffness
 K_α = pitch-spring stiffness
 l = semispan of the wing
 m = mass per unit length of the wing
 M_∞ = free-stream Mach number
 Q_h = generalized force due to bending
 Q_α = generalized force due to pitch
 r_α = radius of gyration about the elastic axis of the wing section
 S_α = sectional moment about the elastic axis
 U_F = dimensional flutter speed
 U_F^* = nondimensional flutter speed
 x_α = sectional distance, measured in semichords, from the elastic axis to the mass center
 α = pitch displacement of the elastic axis of the wing section
 δ = plunge displacement of the wing section, h/c
 λ = flutter eigenvalue
 μ = wing-section-to-air-mass density ratio

- ξ = nondimensional displacement of the wing due to bending
- ρ = free-stream air density
- ϕ = disturbance velocity potential
- ω_α = pitching natural frequency
- ω_h = bending natural frequency
- ω_r = reference frequency

Introduction

Extensive research in the area of two-dimensional, unsteady, transonic aerodynamics, as well as advancements in computer storage and efficiency, have recently allowed the practical computation of three-dimensional, unsteady, transonic airloads. Several methods have been considered for these computations. Traci et al.¹ developed the codes TDSTRN and TDUTRN to compute steady and unsteady transonic airloads, using the harmonic method. Borland et al.² developed a three-dimensional, unsteady, small-disturbance, transonic code, XTRAN3S, which is based on a time-integration method. This code is being evaluated by several groups and is used to calculate the aerodynamics in this study. Only limited aeroelastic analyses have been made using XTRAN3S. Borland and Rizzetta³ determined the flutter speed versus Mach number for an unswept rectangular wing using the time-response method contained in XTRAN3S. Guruswamy and Goorjian⁴ found the transonic flutter speed for an unswept rectangular wing, and Myers et al.⁵ determined the flutter speed for a transport wing. In Refs. 4 and 5, XTRAN3S was used to compute the airloads in a three-dimensional, inviscid flow field. To date, no three-dimensional aeroelastic analyses have been performed that have included the effects of flow viscosity.

Viscosity can play an important role in both the aerodynamic and aeroelastic characteristics of wings, as indicated by Guruswamy and Goorjian⁶ who used the two-dimensional code, LTRAN2 (viscous), to study airfoils. In transonic flow, viscous effects can alter the shock location and strength. These changes in the pressure distribution along the chord, will also influence the aeroelastic characteristics of the wing. The XTRAN3S code has been upgraded, to include the effects of flow viscosity, by Rizzetta and Borland.⁷ Two models are used to account for the viscous effects in XTRAN3S-Ames. The viscous wedge is an empirical method and the lag-entrainment method is based on a set of integral boundary-layer equations. Computing time would increase considerably if more exact equations, such as the Navier-Stokes equations, were used to calculate the three-dimensional viscous effects. These methods are the same as those first incorporated into LTRAN2 (viscous).⁸ The same viscous equations used in two dimensions are applied stripwise along the span to yield a three-dimensional correction. In this work, studies were made to determine the influence of viscous effects on the aerodynamic and aeroelastic characteristics of wings in transonic flow, using both methods.

It is important to study the structural modes to determine which are significant to the aeroelastic analysis. The deflection of an oscillating wing is exactly described by a combination of an infinite number of structural modes. For practical considerations, only a limited number of modes can be considered. All modes that contribute significantly to the dynamic motion of the wing should be included in the analysis. The modal participation not only depends on the geometry and physical properties of the wing, but also on the flight conditions. The contributing modes for a wing operating in transonic flow can be entirely different from those for the same wing in subsonic flow. Flutter analyses that compare well with experiment in subsonic flow can deviate substantially as the flow becomes transonic. This was demonstrated in Ref. 4, in which a study of a rectangular wing is reported. Only the fundamental structural modes were considered and inviscid aerodynamics were used. The neglect of viscosity and higher structural modes may have been the cause of the deviation. In this work, effects of modes on flutter speeds were studied in the transonic regime.

To illustrate the effects of viscosity and structural modes on flutter speeds, two wings were studied. The first was an unswept, rectangular wing with a full-span aspect ratio of 4 and an NACA 64A010 airfoil section. This wing has been accepted by AGARD⁹ as a standard wing for aerodynamic and aeroelastic research. Also, a typical transport wing with a sweep angle of 25°, taper ratio of 0.4, and an MBB-A3 supercritical airfoil was studied. Steady and unsteady aerodynamic results for the rectangular wing were obtained at $M = 0.7, 0.80, 0.85$, and 0.90 for the inviscid calculations; at $M = 0.80, 0.85$, and 0.90 for the viscous-wedge calculations; and at $M = 0.80$ and 0.85 for the lag-entrainment calculations. Studies were made at $M = 0.85$ for the swept wing. In this analysis, all the aerodynamic computations were made using the recently improved version of the code XTRAN3S-Ames.⁹ The version of the code has better coordinate transformations and viscous correction methods. A three-dimensional, assumed mode flutter analysis was used to determine flutter boundaries. The equations of motion were solved using the U-g method.¹⁰⁻¹²

Unsteady Transonic Aerodynamic Equations of Motion

The inviscid, three-dimensional, unsteady, transonic, small-disturbance potential equation as described in Ref. 7 is

$$\frac{\partial}{\partial t} (A\phi_t + B\phi_x) = \frac{\partial}{\partial x} (E\phi_x + F\phi_x^2 + G\phi_y^2) + \frac{\partial}{\partial y} (\phi_y + H\phi_x\phi_y) + \frac{\partial}{\partial z} (\phi_z) \quad (1)$$

where

ϕ is the perturbation velocity potential function and

$$A = M_\infty^2 k_c^2$$

$$B = 2M_{\infty} k_c$$

$$E = 1 - M_{\infty}^2$$

$$F = -(1/2)(\gamma + 1)M_{\infty}^2$$

$$G = (1/2)(\gamma - 3)M_{\infty}^2$$

$$H = -(\gamma - 1)M_{\infty}^2$$

For inviscid calculations the flow-tangency condition is

$$\phi_z = f_x^+ + k_c f_t \quad (2)$$

where f is the airfoil ordinate, and k_c is the reduced frequency. The jump across the trailing edge vortex is

$$[\phi_z] = 0 \quad \text{and} \quad [\phi_x + k\phi_t] = 0 \quad (3)$$

The $[\]$ indicate a jump in the parameter across the wake. These are the boundary conditions which are modified to include the viscous effects. Transformation equations to map a swept-tapered planform in the physical domain into a rectangle in the Cartesian domain are given in detail in Ref. 9.

When performing transonic aerodynamic calculations, viscous effects often play an important role. Besides altering the shock strength and location, boundary-layer displacements cause camber modifications to the airfoil surface and displacement and camber effects near the wake. The first, and simplest, of the two viscous techniques used in XTRAN3S is the viscous wedge method. Previous studies have shown that the shock-boundary-layer interaction can be modeled by placing a wedge-nosed ramp on the airfoil surface just downstream of the shock found from the inviscid calculations. The viscous wedge simulates the displacement effect of the shock-boundary-sonic point by predetermined lengths called the precursor and offset. The ramp slope and height depend on the shock strength and are calculated for each time step. The change in the surface geometry is described by the modified small-disturbance tangency condition,

$$\phi_z^+ = f_x^+ + k_c f_t^+ + f_{Rx} \quad \text{on } z = 0^+ \text{ for } x_{LE} \leq x \leq x_{TE} \quad (4)$$

This viscous-wedge method is two dimensional and is applied to the wing at each spanwise coordinate. Details of computing the ramp slope f_R can be found in Ref. 7. A two-dimensional shock profile was used to determine the placement of the wedge in this study, as opposed to the three-dimensional shock profile discussed in Ref. 7. This change was made to help reduce oscillations in the pressures obtained when using the viscous methods.

For some calculations, the wedge model alone is sufficient for accurate determination of the unsteady viscous pressure distributions. For other calculations, however, a more exact analysis is required to model the viscous effects. To do this, the wedge correction is used along with a set of integral boundary-layer equations, called

the lag-entrainment equations,⁷ to perform viscous calculations downstream of the shock wave, including the downstream wake. These equations are governed by three first-order ordinary differential equations.⁷ This method assumes that viscous regions are small relative to the wing or wake thickness. The modification to the small-disturbance surface tangency condition for the lag-entrainment method is

$$\phi_z^+ = f_x^+ + k_c f_t^+ + (F_1 + F_2 \phi_{xx})^+ \quad \text{on } z = 0^+ \text{ for } x_{LE} \leq x \leq x_{TE} \quad (5)$$

The downstream wake conditions are defined by

$$[\phi_z] = [F_1 + F_2 \phi_{xx}] \quad \text{on } z = 0 \text{ for } x > x_{TE} \quad (6)$$

and F_1 and F_2 are obtained by solving the lag-entrainment equations.⁷ Note that this method requires the solution of three ordinary differential equations, thus, 3 times more computational time was used than for the wedge correction. The time step must be sufficiently small to insure that the method is stable, as has been demonstrated in two dimensions.⁶ These viscous methods were derived for steady-state computations and incorporated into the unsteady equations of motion in a quasi-steady fashion. The viscous corrections, F_1 and F_2 , are determined at time-level t^n and are applied at time level t^{n+1} .

To solve the governing equations numerically, the flow field is discretized in the computational domain by using a three-dimensional Cartesian grid.² The grid used for both wings in this study contained 64 points in the streamwise direction, 20 points in the spanwise direction, and 40 points in the vertical direction. The wing was discretized into 39 points in the streamwise direction and 13 points in the spanwise direction. The displacement of each grid point on the wing was prescribed for each mode. The analysis was uncoupled, requiring one run of the transonic code for each mode of motion of the wing.

Aeroelastic Equations of Motion

In this study, the aeroelastic equations of motion for a cantilever wing were formulated using an assumed mode method.^{11,12} The superposition of the bending and torsion natural modes is used to describe the deflections shape of the wing at flutter. It was assumed that the amplitude of oscillation is small; this was done so that the transonic aerodynamics from each mode of motion could be superposed.¹³

Let the plunging and pitching of the wing at spanwise coordinate x , y and time t be denoted by $h(y,t)$ and $\alpha(y,t)$, respectively. A complete set of generalized coordinates is required to describe the motion as follows:

$$h(y,t) = \bar{h}_1(t)d_1(y) + \bar{h}_2(t)d_2(y) + \bar{h}_3(t)d_3(y) + \dots \quad (7a)$$

$$\alpha(y,t) = \bar{\alpha}_1(t)\theta_1(y) + \bar{\alpha}_2(t)\theta_2(y) + \bar{\alpha}_3(t)\theta_3(y) + \dots \quad (7b)$$

where $d_i(y)$ and $\theta_i(y)$ are the assumed bending and torsion mode shapes, respectively, and $h(t)$ and $\alpha(t)$ are generalized coordinates which represent the contribution of each of the assumed modes. For this analysis the modes were only a function of span.

Considering the kinetic energy and the strain energy of the wing through the use of Lagrange's equations, the equations of motion are

$$Q_{h_i} = \sum_{j=1}^n \bar{m}_{ij} \ddot{h}_j + \sum_{j=1}^n \bar{s}_{\alpha ij} \ddot{\alpha}_j + \sum_{j=1}^n K_{hij} \bar{h}_j \quad i = 1, 2, 3, \dots, n \quad (8a)$$

$$Q_{\alpha_i} = \sum_{j=1}^n \bar{I}_{\alpha ij} \ddot{\alpha}_j + \sum_{j=1}^n \bar{s}_{\alpha ij} \ddot{h}_j + \sum_{j=1}^n K_{\alpha ij} \bar{\alpha}_j \quad i = 1, 2, 3, \dots, m \quad (8b)$$

where the generalized mass is

$$\bar{m}_{ij} = \int_0^{\ell} m(y) d_i(y) d_j(y) dy \quad (9a)$$

the generalized mass moment of inertia is

$$\bar{I}_{\alpha ij} = \int_0^{\ell} I_{\alpha}(y) \theta_i(y) \theta_j(y) dy \quad (9b)$$

and the generalized static moment about the elastic axis is

$$\bar{s}_{\alpha ij} = \int_0^{\ell} S_{\alpha}(y) d_i(y) \theta_j(y) dy \quad (9c)$$

The $m(y)$, $I_{\alpha}(y)$, and $S_{\alpha}(y)$ terms are the sectional properties of the wing. The generalized forces Q_h and Q_{α} are functions of the lift and moment of the wing. The following relations require that the principle of linear superposition of airloads is valid. This assumption allows the aerodynamic lift and moment to be defined as (for first bending and torsion modes)

$$L = -qc(\bar{c}_{\ell h} \bar{h}_1 + \bar{c}_{\ell \alpha} \bar{\alpha}_1) \quad (10a)$$

$$M = qc^2(\bar{c}_{mh} \bar{h}_1 + \bar{c}_{m\alpha} \bar{\alpha}_1) \quad (10b)$$

where

$$\bar{c}_{\ell h} = \int_0^{\ell} C_{\ell h} d_1^2(y) dy, \quad \bar{c}_{mh} = \int_0^{\ell} C_{mh} d_1(y) \theta_1(y) dy \quad (11a)$$

$$\bar{c}_{\ell \alpha} = \int_0^{\ell} C_{\ell \alpha} d_1(y) \theta_1(y) dy, \quad \bar{c}_{m\alpha} = \int_0^{\ell} C_{m\alpha} \theta_1^2(y) dy \quad (11b)$$

The generalized lift and moments follow from these definitions:

$$Q_{h_i} = -qc \sum_{j=1}^n \int_0^{\ell} C_{\ell h_j} \bar{h}_j(t) d_i(y) d_j(y) dy - qc \sum_{j=1}^n \int_0^{\ell} C_{\ell \alpha_j} \bar{\alpha}_j(t) d_i(y) \bar{\theta}_j(y) dy \quad i = 1, 2, 3, \dots, n \quad (12a)$$

$$Q_{\alpha_i} = qc^2 \sum_{j=1}^n \int_0^{\ell} C_{mh_j} \bar{h}_j(t) d_j(y) \theta_i(y) dy + qc^2 \sum_{j=1}^n \int_0^{\ell} C_{m\alpha_j} \bar{\alpha}_j(t) \theta_j(y) \theta_i(y) dy \quad i = 1, 2, 3, \dots, m \quad (12b)$$

For the analyses in this study, $m = 2$ and $n = 2$. By assuming simple harmonic motion and nondimensionalizing, the equations of motion are written as the following eigenvalue problem:

$$\bar{h}_i(t) = h_{i0} e^{i\omega t}$$

$$\bar{\alpha}_i(t) = \alpha_{i0} e^{i\omega t}$$

$$\{\bar{\mu} K_b^2 [M] - [A]\} \begin{Bmatrix} \xi_1 \\ \xi_2 \\ \alpha_1 \\ \alpha_2 \end{Bmatrix} = \lambda [K] \begin{Bmatrix} \xi_1 \\ \xi_2 \\ \alpha_1 \\ \alpha_2 \end{Bmatrix} \quad (13)$$

where

$$\bar{\mu} = \frac{\bar{m}}{\pi \rho b^2 \ell^2}, \quad \xi_i = \frac{h_{i0}}{b}, \quad k_b = \frac{\omega b}{U_f}$$

The eigenvalue λ is defined as $\lambda = (1 + ig)(\omega_r^2 b^2 / U_f^2)$. Here g is an artificial structural damping coefficient obtained by replacing ω_{α} by $\omega_{\alpha}(1 + ig_{\alpha})$, replacing ω_h by $\omega_h(1 + ig_h)$, and letting g_{α} and g_h be small and of the same order so that $g_{\alpha} = g_h = g$. The mass matrix $[M]$ and stiffness matrix $[K]$ are assembled from parameters that describe the geometry and mass properties of the wing being studied. The generalized mass properties are obtained by multiplying the two-dimensional mass properties for a particular span station by the displacement owing to the chosen mode shape and integrating the product across the span as in Eqs. (9). The stiffness matrix is diagonal because the equations of motion are formulated about the elastic axis. The diagonal terms consist of the natural frequency of the corresponding natural mode shape:

$$[M] = \begin{bmatrix} \bar{a}_{ij} & \bar{x}_{\alpha ij} \\ \bar{x}_{\alpha ij} & \bar{r}_{\alpha ij}^2 \end{bmatrix}; \quad [K] = \begin{bmatrix} \bar{a}_{ii} \left(\frac{\omega_{h_i}}{\omega_r} \right)^2 & 0 \\ 0 & r_{\alpha ii}^2 \left(\frac{\omega_{\alpha_i}}{\omega_r} \right)^2 \end{bmatrix};$$

$$[A] = \begin{bmatrix} \bar{c}_{\ell \delta ij} / 2 & \bar{c}_{\ell \alpha ij} \\ -\bar{c}_{m \delta ij} & -2\bar{c}_{m \alpha ij} \end{bmatrix} \quad (14)$$

where

$$\bar{a}_{ij} = \bar{m}_{ij} / \bar{m}_{11}, \quad \bar{r}_{\alpha ij}^2 = \bar{I}_{\alpha ij} / m_{11} b^2, \quad \bar{x}_{\alpha ij} = \bar{s}_{\alpha ij} / \bar{m}_{ij} b^2,$$

$$\delta = h/c$$

and

$$\omega_r = \omega_{\alpha_1}$$

The U-g method is used to obtain the flutter boundaries from Eq. (11).

Procedure

The generation of the aerodynamic data is performed separately from the aeroelastic analysis. First, XTRAN3S is used to generate the steady and unsteady aerodynamic data by prescribing the wing motion. These data are then input into the aeroelastic equations of motion to solve for the flutter speed. An alternative procedure would be to solve both sets of equations in a coupled manner. This procedure is also possible with XTRAN3S, and an example calculation is described in Ref. 3. Using the former method, the unsteady solutions were obtained by forcing the wing to oscillate sinusoidally as the aerodynamic equation of motion was integrated in time. To obtain a steady solution, the amplitude of motion was set to zero. The unsteady viscous calculations were restarted from corresponding steady state solutions. For unsteady calculations, three cycles of motion were sufficient for the transients to die out and for a periodic solution to be obtained. For most inviscid calculations, 360 time steps per cycle were used. However, for a Mach number of 0.70 and a reduced frequency of 0.1, 720 time steps per cycle were required. Viscous calculations typically required 720 time steps per cycle for the wedge calculations and 2160 time steps per cycle for the lag-entrainment calculations. Figure 1 shows the unsteady lift versus the time step size for the second torsion mode at $M = 0.85$ and using the lag-entrainment method. The magnitude of the lift and phase is almost constant after 2000 time steps per cycle. Unsteady aerodynamic coefficients, based on the third cycle, were used to compute flutter boundaries for inviscid and viscous calculations.

Solutions obtained using the original viscous corrections incorporated into XTRAN3S contained high frequency oscillations in the unsteady airloads. An investigation into this problem determined that the shock sweep angles computed for the viscous-wedge⁷ corrections did not change smoothly across the span, but instead jittered in some span regions, as well as with time step, at some span locations. Also, it was determined that the use of these shock sweep angles to determine the shock location was not consistent with the method of locating the shock wave for use in the type-dependent differencing that is employed in the inviscid calculations. To correct this inconsistency, the shock location at each span station was determined by only using flow field values along that span station. This new method of determining the shock location was then used to place the viscous wedge on that span section. Figure 2 shows the unsteady upper-surface pressure across the chord at the 60% semispan station for both the original method and the new method used in this study. The four curves shown represent the pressures for four consecutive time steps in the third cycle of motion. The large fluctuations in the pressure profile at the shock location are eliminated when the new method is used. Even with this improvement, however, high-frequency oscillations in the lift still remain when the viscous corrections are used. Most of

these oscillations can be eliminated by using 2880 time steps per cycle. It is known that oscillations are also induced by the shock crossing a mesh point. The use of a finer mesh and other possible solutions are currently under investigation.

A three-dimensional U-g type flutter analysis has been employed to solve Eq. (14) and obtain the flutter boundaries. A Rayleigh-Ritz procedure was used in which a finite number of bending and torsion mode shapes were assumed to describe the modal motion of the wing at flutter. For this analysis, the first two bending and first two torsion modes were considered. The unsteady aerodynamic forces generated by the deflection of the wing have to be computed separately for each structural mode of motion. Thus, the cost of determining flutter boundaries is a direct multiple of the number of structural modes considered in the analysis. Because of the cost of computing three-dimensional, unsteady, transonic aerodynamic coefficients it is not practical to experiment with a large number of structural modes to determine which ones will play a significant role. The geometry of the structure and the boundary conditions applicable to the problem should be carefully considered. Using only the modes significant to the problem will greatly reduce the cost and time required to obtain a solution. In this study, the first two bending and torsion modes were chosen to describe the motion of the low-aspect-ratio, rectangular, cantilever wing. Previous studies have shown that the fundamental modes are sufficient to determine the flutter speed of a rectangular wing in subsonic flow. For comparison, the first two bending and torsion modes were also used for the swept wing. It may be, however, that even higher modes would be significant for this wing owing to its more complex geometry. The deflections caused by the natural mode shapes of the wing were calculated at 39 streamwise points, for each of the 13 span stations, and input into XTRAN3S. The code was run for three complete cycles of motion, and the Fourier coefficients from the third cycle were used to perform the aeroelastic calculations. For the rectangular wing, unsteady calculations were made for four modes at four different Mach numbers and from three to six reduced frequencies for each Mach number. Also the inviscid and the two viscous methods were considered, requiring 168 separate runs of the transonic code. Although only limited results were computed for the swept wing, another 36 runs of the code were required. The inviscid calculations required 500 sec of computing time on the Cray X-MP. The wedge and lag-entrainment methods required 1100 and 3300 sec, respectively. The U-g method of determining flutter boundaries is a proven method which has been accurately used for years for both two-dimensional and three-dimensional aeroelastic analyses.

Results

Rectangular Wing with NACA 64A010 Airfoil

One of the two wings considered in this study was the AGARD rectangular wing with an aspect ratio of 4 and a NACA 64A010 airfoil cross section. Aerodynamic and flutter results were

computed for the rectangular wing at $M = 0.8$ and at zero angle of attack, which is one of the AGARD suggested flow conditions.⁸ In addition, calculations for the same wing were made at $M = 0.70$, $M = 0.85$, and $M = 0.90$ to determine the effects of Mach number on three-dimensional aeroelastic calculations. First, steady state pressure distributions were obtained for the inviscid, wedge, and lag-entrainment methods. The steady wedge calculations were restarted from the steady inviscid solution and the steady lag-entrainment calculations were restarted from the steady wedge solution, following the procedure given in Ref. 7. The steady flow became fully developed in 1000 time steps. Figure 3 shows the steady pressure distribution for the three methods at the 60% semispan station and at three Mach numbers. The code diverged when the lag-entrainment method was used at $M = 0.90$, so no results were obtained for those conditions. The forward displacement of the shock and reduction in strength are characteristic of viscous flow. These trends are consistent with those shown in two dimensions for the same airfoil. It can be seen that the lag-entrainment method shows no deviation from the wedge for this particular wing.

The first and second bending and first and second torsion natural modes, shown in Fig. 4, were selected to accurately model the motion of the wing to obtain unsteady aerodynamic coefficients. Calculations were made at reduced frequencies, based on full chord, from 0.1 to 0.6. The maximum deflections were 3.44° for the torsion modes and 10% of the chord for the bending modes. The wing was constrained to pitch about the midchord. Figure 5 shows the magnitude of the unsteady local lift coefficient and the corresponding phase angle versus span for the rectangular wing at three Mach numbers. Results are shown for inviscid and for both the wedge and lag-entrainment viscous correction methods for the first torsion mode at a reduced frequency of 0.4. As expected from two-dimensional studies,⁶ the lift coefficients obtained by the viscous methods are lower than those calculated using the inviscid method; however, the magnitude of the lift using the wedge correction, shows little change over the inviscid method. The phase angles show a significant change for both viscous methods.

As mentioned earlier, the flutter boundaries were determined using a three-dimensional U-g method. Of primary interest in this study were the aeroelastic characteristics of the rectangular wing related to the effects of the structural modes and flow viscosity. Four combinations of the first two pure bending and torsion modes were considered. First, only the first bending and first torsion modes were included. Then the second modes of each type were added individually. Finally, all four modes, namely first bending, second bending, first torsion, and second torsion, were all included in the solution. For the modal analysis, the wing was configured so that the elastic axis and center of mass were located at 45% and 60% of the chord, respectively, aft of the leading edge. All other aeroelastic parameters were set to represent a typical wing. For the rectangular wing, the first bending and torsion modes were sufficient to determine the flutter speed (Table 1). The flutter frequency in all cases is very close to the first bending

frequency, which explains the dominance of the first bending mode. Figure 6 shows the deflection of the wing at flutter. It closely resembles the first bending mode. Many of the aeroelastic parameters were varied to see if any effect of the higher modes could be obtained; little to no effect was seen. Only when very unrealistic values were used was an appreciable effect of modes noticed. At all Mach numbers, the first bending and torsion modes are all that are required for an aeroelastic analysis of a small aspect ratio, unswept, rectangular wing in subsonic or transonic flow.

The effect of flow viscosity is an important factor to consider when computing the flutter boundaries of a wing in transonic flow. Viscosity can have a noticeable effect on the aerodynamic forces acting on the wing and, hence, on the flutter boundaries. Previously, only inviscid calculations had been made on wings. Viscous calculations were made at three Mach numbers, $M = 0.80$, $M = 0.85$, and $M = 0.90$. For each Mach number, aerodynamic coefficients were calculated over a range of reduced frequencies from 0.1 to 0.6 and for the same four structural modes discussed earlier. The wedge and lag-entrainment viscous methods were used. At $M = 0.85$, the flow is transonic and the shock is well defined. Figure 7 shows the sectional magnitude and corresponding phase angle of the lift coefficient versus the reduced frequency for the inviscid method and for two viscous methods. Sectional parameters are shown for span station 8, at the 60% semispan location. This figure shows that the lift coefficients calculated with viscous corrections included are slightly below the inviscid calculations. This is the trend that was anticipated because it corresponds to trends shown for two-dimensional airfoils. This small reduction in force, coupled with significant changes in the phase angles, contributes to the higher flutter speeds shown for the viscous methods in Fig. 8 and Table 1. A well-defined transonic dip can be seen in Fig. 8 with the lowest flutter speed occurring between $M = 0.85$ and $M = 0.90$. Inclusion of the viscous corrections resulted in about a 10% increase in flutter speed. The increase in flutter speed is a direct result of the viscous corrections causing a reduction in the magnitude of the lift coefficient. A higher flutter speed does not always follow from a reduction in magnitude of the lift because the change in phase angle must also be considered when one is trying to anticipate flutter trends. The wedge correction required little more computational effort than the inviscid method, but yielded an increase in flutter speed, as is depicted in Fig. 8. The lag-entrainment method on the other hand, required 6 to 8 times the computing time to obtain a converged, stabilized solution. The results obtained using the lag-entrainment method were about the same as the wedge correction provided. It is noted that the wedge calculations were performed at 720 time steps per cycle, and the lag-entrainment calculations were performed at 2160 time steps per cycle. Both of these are substantially less than for earlier, two-dimensional calculations. In Ref. 6, Guruswamy and Goorjian required 2160 time steps per cycle and 8640 time steps per cycle for the wedge and lag-entrainment calculations, respectively.

The rectangular wing was also used to study the effects of various aeroelastic parameters on

the aeroelastic behavior of wings at $M = 0.85$. In Fig. 9, flutter speed and corresponding reduced frequency are plotted versus wing-air-mass-density ratio by using both inviscid and viscous unsteady coefficients obtained for the two fundamental modes. Flutter speeds increase with an increase in wing-to-air-mass-density ratio. Flutter speeds obtained by using viscous coefficients are higher than those obtained using inviscid coefficients. The plot of flutter speed versus the center-of-mass position is shown in Fig. 10. The flutter speed increases as it moves forward. Also the rate of increase gets larger as the mass center approaches the elastic axis. The flutter speed increases, approximately linearly with increasing frequency ratio, as shown in Fig. 11. All trends are similar to those shown in Ref. 10 for the NACA 64006 and the NACA 64A010 airfoils. The viscous methods do not change any trends but merely increase the flutter speeds slightly from the inviscid calculations, for this wing.

Swept Wing with MBB-A3 Airfoil

This swept wing was chosen to represent a typical transport type wing. It has a full-span aspect ratio of 8, a taper ratio of 0.4, a leading-edge sweep angle of 25, and an MBB-A3 supercritical airfoil section. Because of the complex geometry, the computing time required per case was twice that required for similar calculations on the rectangular wing. Aerodynamic and flutter calculations were made inviscidly, as well as by using the wedge and lag-entrainment viscous corrections at a Mach number of $M = 0.85$. As was done for the rectangular wing, steady state data were computed, and then the unsteady runs were restarted from the corresponding steady-state data files.

The first bending, first torsion, second bending, and second torsion modes were incorporated into the flutter analysis of the swept wing (Fig. 12). Again the deflections of the wing were computed for each mode at 507 wing locations to describe the deflection shapes in the transonic code. It can be seen that the modes, despite the sweep and taper, are very similar to the corresponding modes for a cantilever beam. To obtain a converged inviscid solution, 720 time steps per cycle were required; 1440 and 2880 time steps per cycle were required for the viscous wedge and lag-entrainment methods, respectively. Calculations were made at $k = 0.4, 0.5, 0.6$, and 0.7 for all three methods. The steady pressure across the chord, at the 60% semispan location is shown in Fig. 13 for all three methods and for both the upper and lower surfaces. The viscous wedge shows a shock which has moved forward of the inviscid shock and is much weaker in strength. The lag-entrainment correction causes the shock to move still farther forward. For this wing and airfoil section, the lag-entrainment method does show a significant change from the viscous wedge method.

Figure 14 shows the magnitude and corresponding phase angle of the lift coefficient plotted versus reduced frequency. The same trend is shown here as was shown for the rectangular wing. The magnitude of the inviscid lift is greater than the viscous wedge lift, although

only slightly, which is even greater than the lift calculated using the viscous lag-entrainment method.

Flutter calculations were performed on this wing at $M = 0.85$; the results are shown in Table 2. Here again, the primary modes dominate the flutter solution. For this wing, however, the second torsion mode does cause a noticeable change in the flutter speed. When the second bending mode was added to the primary modes, only an insignificant change in the flutter speed was noted, but when the second torsion mode was added the flutter speed decreased by about 5%. It was expected that the torsion modes would play an important role in this analysis because of the sweep of the wing. The first two torsion modes can be seen along with the first bending mode in Fig. 15.

A 26% increase in flutter speed was observed when the viscous-wedge method was used. On the other hand, when aerodynamics that included the lag-entrainment method were input into the equations of motion, the flutter speed showed only a slight increase over that of the inviscid flutter solution. It can be seen in Fig. 14 that the change in phase angle from the inviscid solution is much greater for the wedge calculations than for the lag-entrainment calculations.

Conclusions

This study was performed to aid in the verification of the three-dimensional, unsteady, transonic, aerodynamic computer code XTRAN3S-Ames. Several three-dimensional computations were made and trends were compared to those previously determined for two-dimensional airfoils. Viscous calculations were made using the viscous-wedge and lag-entrainment viscous correction methods. Flutter analyses were performed on two wings and the effects of viscosity and modes were studied. From this work several conclusions may be drawn.

The results discussed in this paper indicate that two-dimensional viscous methods may be applied to three-dimensional flows over wings. Studies on the rectangular wing showed about a 10% increase in the flutter speed when the viscous effects were included in the analysis. For this wing, with a symmetric NACA 64A010 airfoil section, the Greens lag-entrainment method did not show much change over the viscous wedge method. The analysis performed on the swept wing, with an MBB-A3 airfoil section, yielded about a 25% increase in the flutter speed when the viscous wedge method was used. The lag-entrainment method did not cause as large of an increase over the flutter speeds calculated using inviscid aerodynamics. The current viscous methods tend to induce oscillations into the solution that do not occur in inviscid calculations. The implementation of a two-dimensional shock profile, used to place the wedge, helped to reduce these oscillations. Further research is required to improve the implementation of the viscous correction methods into XTRAN3S, as well as other inviscid codes. For the rectangular wing, the lag-entrainment method required 3 times as much computational time as the wedge method, but the two solutions deviated only slightly.

It is important to know which structural modes play a contributing role in a transonic flutter solution. Computing costs are directly proportional to the number of modes considered. For the rectangular wing with a low aspect ratio, the primary modes proved sufficient to accurately determine the flutter speed. For swept tapered wings, higher bending modes may not be as significant as higher torsion modes. At least the first two torsion modes must be considered when performing an aeroelastic analysis on a swept wing.

References

¹Traci, R. M., Albano, E. D., and Farr, J. L., "Small Disturbance Transonic Flows about Oscillating Airfoils and Planar Wings," AFFDL-TR-75-100, Air Force Flight Dynamics Laboratory, June 1975.

²Borland, C. J., Rizzetta, D. P., and Yoshihara, H., "Numerical Solution of Three Dimensional Unsteady Transonic Flow over Swept Wings," AIAA Paper 80-1369, Snowmass, Colo., July 1980.

³Borland, C. J. and Rizzetta, D. P., "Nonlinear Transonic Flutter Analysis," AIAA Journal, Vol. 20, Nov. 1982, pp. 1606-1615.

⁴Guruswamy, P. and Goorjian, P. M., "Comparison between Computational and Experimental Data in Unsteady Three Dimensional Transonic Aerodynamics, Including Aeroelastic Applications," AIAA/ASCE/ASME/AHS Structures, Structural Dynamics, and Materials Conference, New Orleans, La., May 1982.

⁵Myers, M. R., Guruswamy, P., and Goorjian, P. M., "Flutter Analysis of a Transport Wing Using XTRAN3S," AIAA/ASCE/ASME/AHS Structures, Structural Dynamics, and Materials Conference, Lake Tahoe, Nev., May 1983.

⁶Guruswamy, P. and Goorjian, P. M., "Effects of Viscosity on Transonic Aerodynamics and Aeroelastic Characteristics of Oscillating Airfoils," AIAA/ASCE/ASME/AHS Structures, Structural Dynamics, and Materials Conference, Lake Tahoe, Nev., May 1983.

⁷Rizzetta, D. P. and Borland, C. J., "Numerical Solution of Three Dimensional Unsteady Transonic Flow over Wings Including Inviscid/Viscous Interaction," AIAA 20th Aerospace Sciences Meeting, Orlando, Fla., Jan. 1982.

⁸Bland, S. R., "AGARD Three Dimensional Aeroelastic Configurations," NASA Langley Research Center, Hampton, Va., AGARD-AR-167, March 1982.

⁹Guruswamy, P. and Goorjian, P. M., "Development and Application of XTRAN3S - AMES," To be presented at the Computational Fluid Dynamics Users Workshop, University of Tennessee Space Institute, Tullahoma, Tenn., Mar. 1984.

¹⁰Yang, T. Y., Guruswamy, P., Stritz, A. G., and Olsen, J. J., "Flutter Analysis of a NACA 64A006 Airfoil in Small Disturbance Transonic Flow," Journal of Aircraft, Vol. 17, No. 4, Apr. 1980, pp. 225-232.

¹¹Bisplinghoff, R. L., Ashley, H., and Halfman, R. L., Aeroelasticity, Addison-Wesley Publishing Company, Menlo Park, Calif., 1957.

¹²Fung, Y. C., Theory of Aeroelasticity, Dover Publications, Inc., New York, 1969.

¹³Guruswamy, P. and Yang, T. Y., "Aeroelastic Time Response Analysis of Thin Airfoils by Transonic Code LTRAN2," Computers and Fluids, Vol. 9, No. 4., 1981, pp. 409-425.

Table 1 Flutter speeds for various modal combinations: rectangular wing

Modes	M = 0.70	M = 0.80			M = 0.85			M = 0.90	
	Inviscid	Inviscid	Wedge	Lag entrain- ment	Inviscid	Wedge	Lag entrain- ment	Inviscid	Wedge
First bending, first torsion	3.2511	1.8810	1.9556	1.990	1.0503	1.1542	1.1283	1.1934	1.2956
First and second bending first torsion	3.2910	1.8810	1.9557	1.991	1.0503	1.1541	1.1282	1.1933	1.2956
First bending, first and second torsion	3.2524	1.8816	1.9561	1.995	1.0504	1.1546	1.1283	1.1942	1.2962
First and second bending, first and second torsion	3.2897	1.8816	1.9562	1.995	1.0506	1.1549	1.1285	1.1941	1.2964

Table 2 Flutter speeds for various modal combinations: swept wing, M = 0.85

Modes	Inviscid	Wedge	Lag entrain- ment
First bending, first torsion	2.1237	2.8507	2.2066
First and second bending, first torsion	2.1240	2.8504	2.2057
First bending, first and second torsion	2.0666	2.9511	2.1856
First and second bending, first and second torsion	2.0670	2.9502	2.1850

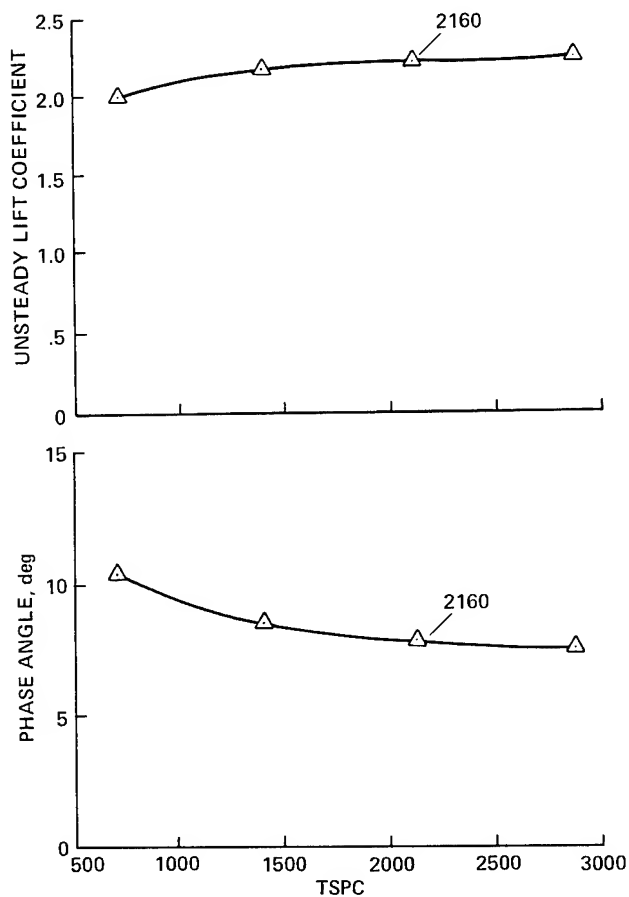


Fig. 1 Unsteady lift versus number of time steps per cycle for the lag-entrainment method.

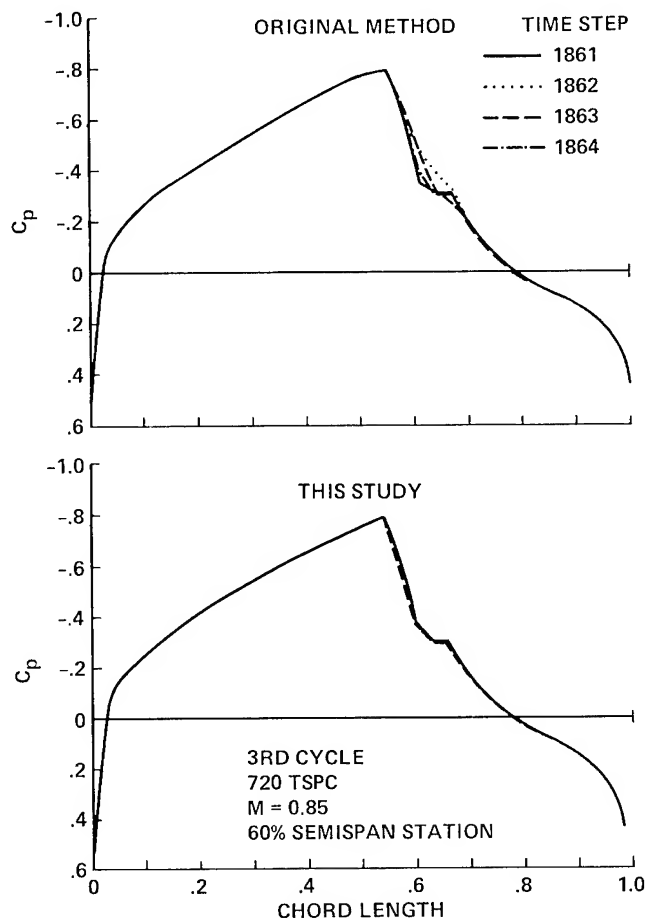


Fig. 2 Comparison of the original viscous wedge method using shock sweep angles and the method used in this study.

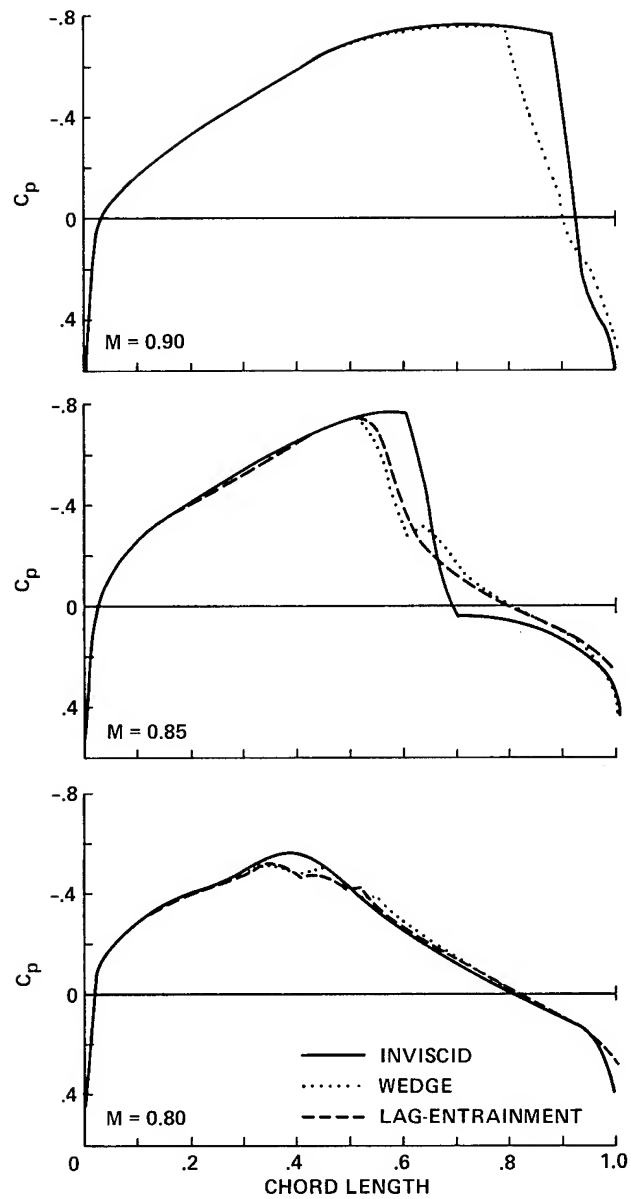
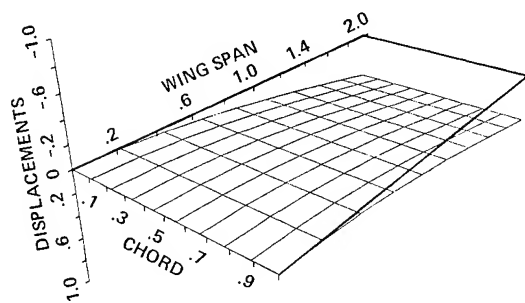
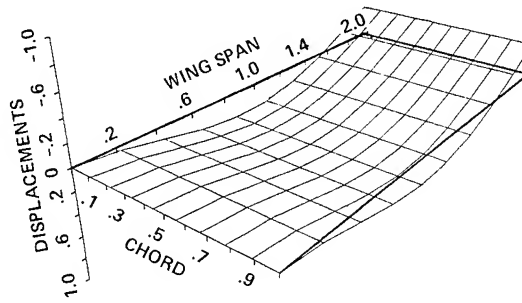


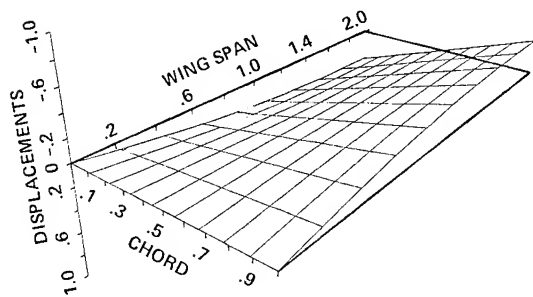
Fig. 3 Rectangular wing steady pressure shown for three Mach numbers and the inviscid and viscous methods at 60% semispan station and $\alpha = 0$.



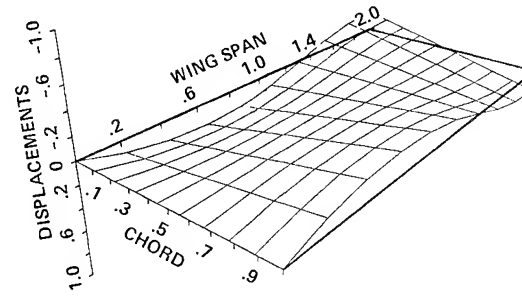
FIRST BENDING



SECOND BENDING



FIRST TORSION



SECOND TORSION

Fig. 4 Rectangular wing natural mode shapes.

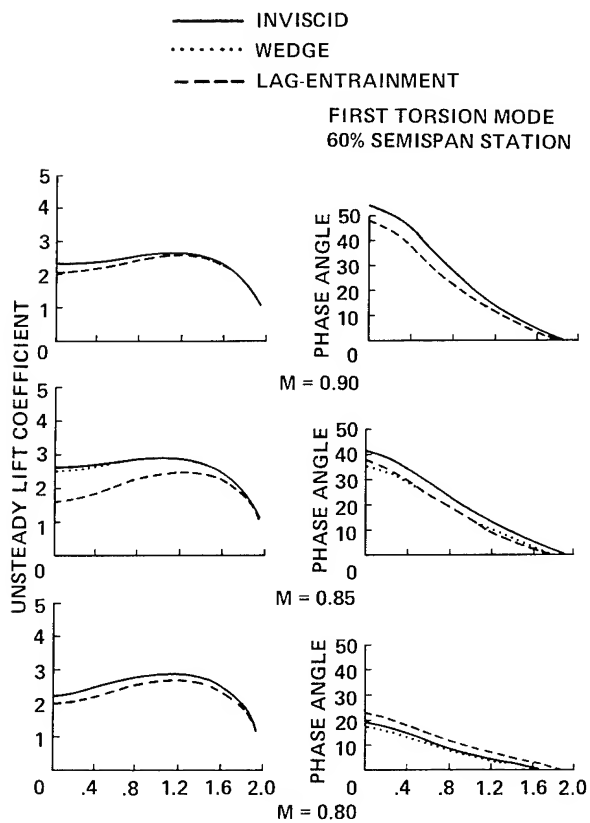


Fig. 5 Magnitude of unsteady lift and corresponding phase angle versus span for the inviscid and viscous methods.

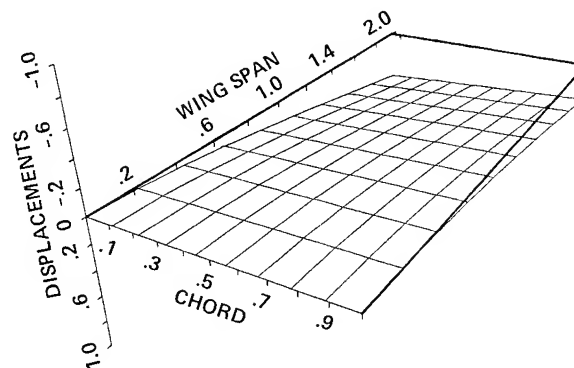


Fig. 6 The shape of the rectangular wing at flutter is composed of the first bending and torsion modes.

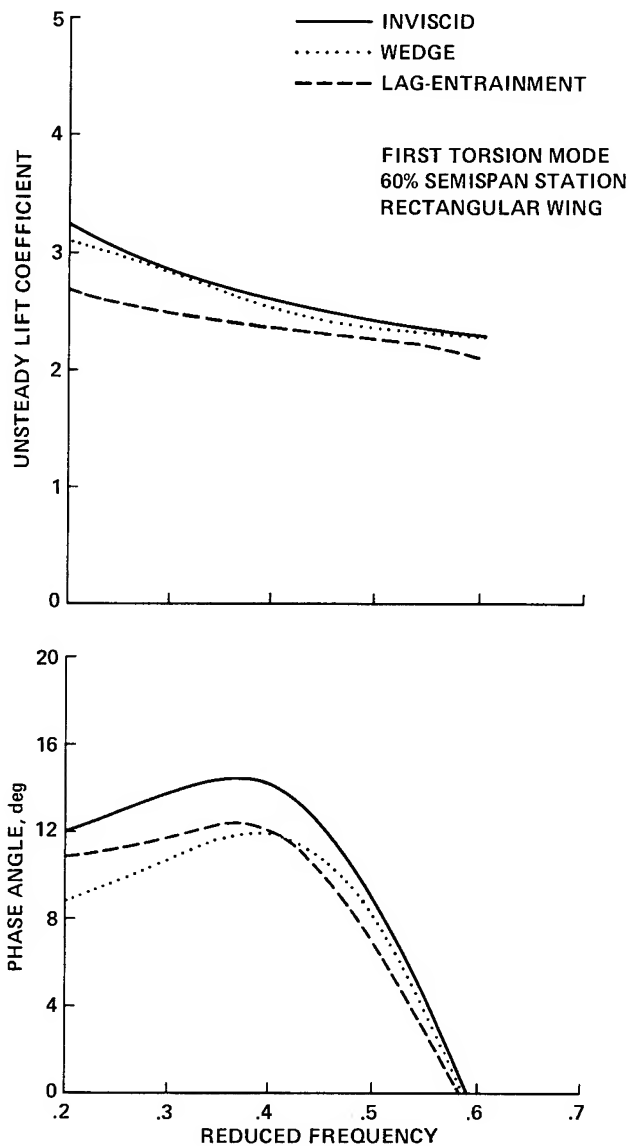


Fig. 7 Magnitude of unsteady lift and corresponding phase angle versus reduced frequency for the inviscid and viscous methods.

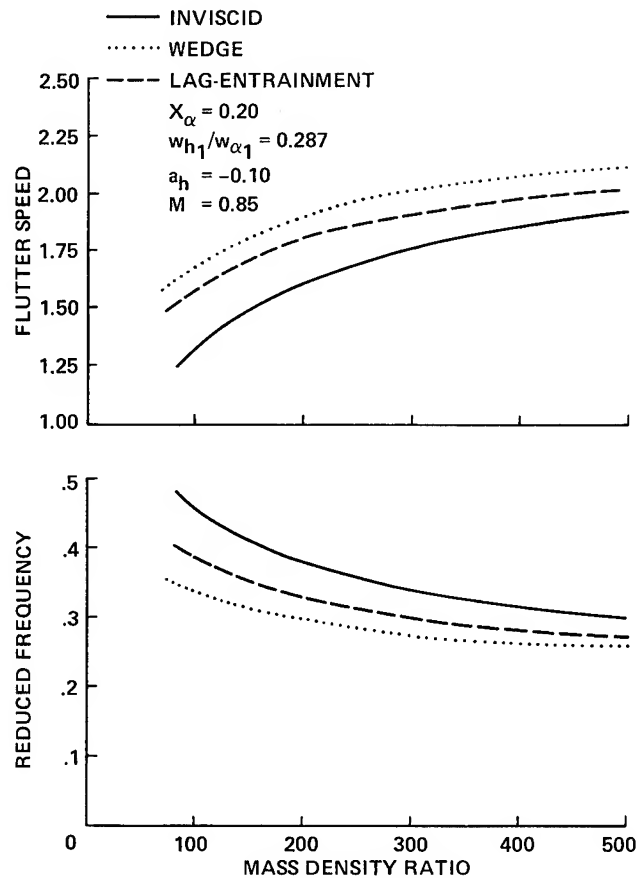


Fig. 8 Effect of Mach number and viscosity on flutter speed.

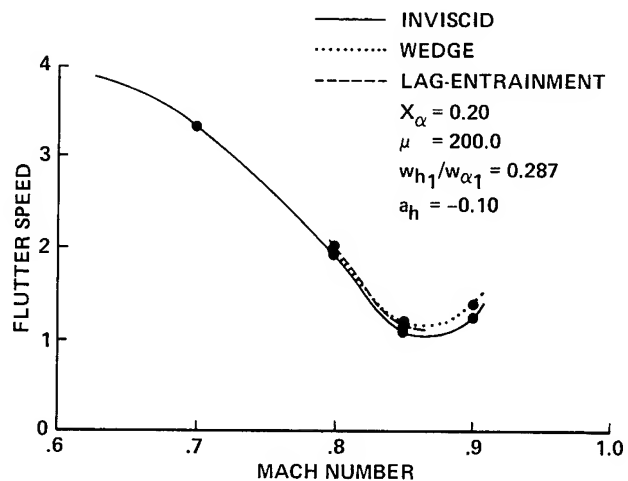


Fig. 9 Effect of wing to air mass density ratio and viscosity on flutter speed.

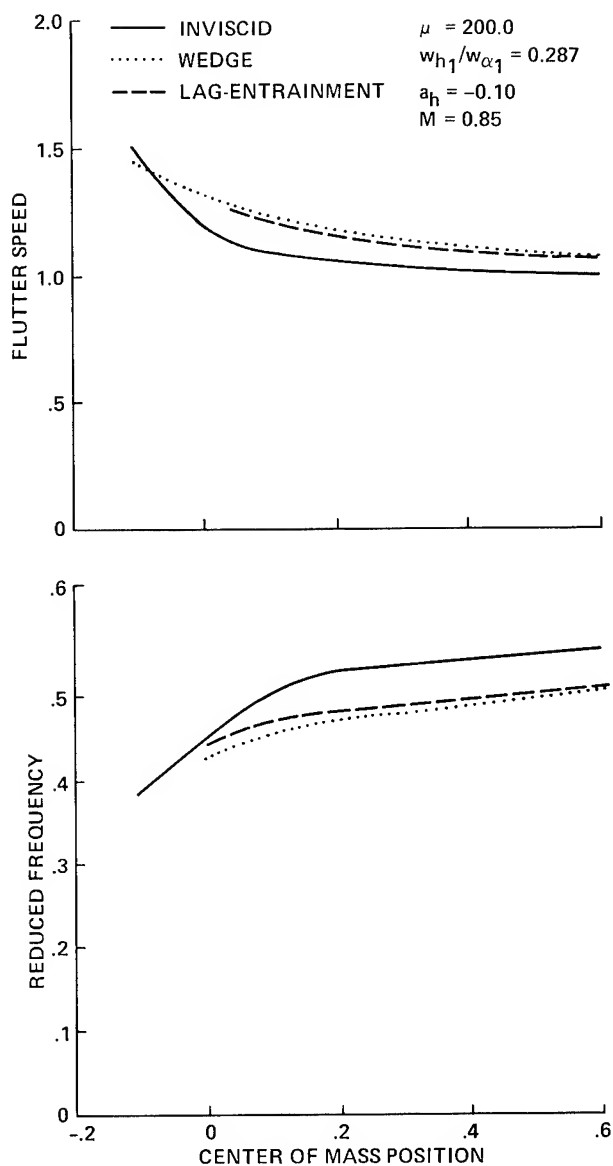


Fig. 10 Effect of wing center of mass position and viscosity on flutter speed.

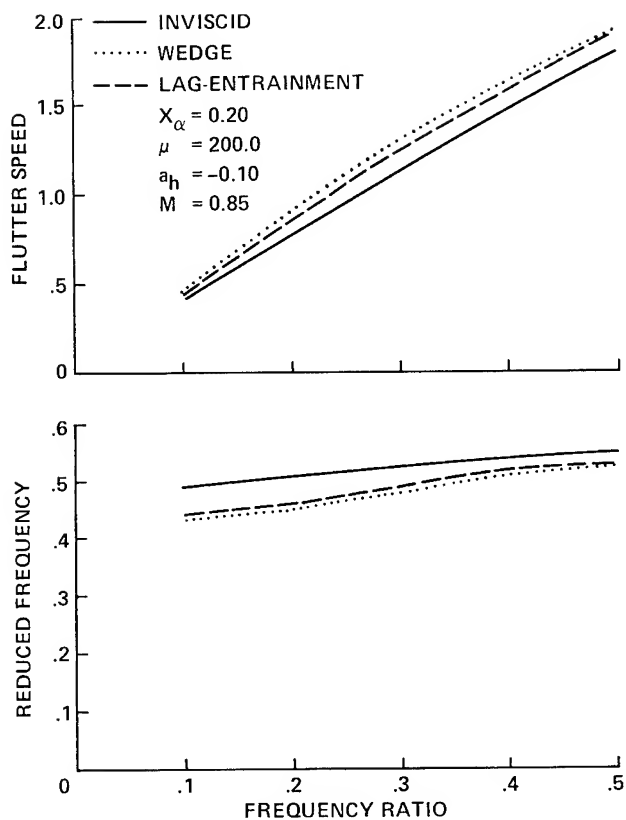


Fig. 11 Effect of frequency ratio and viscosity on the flutter speed.

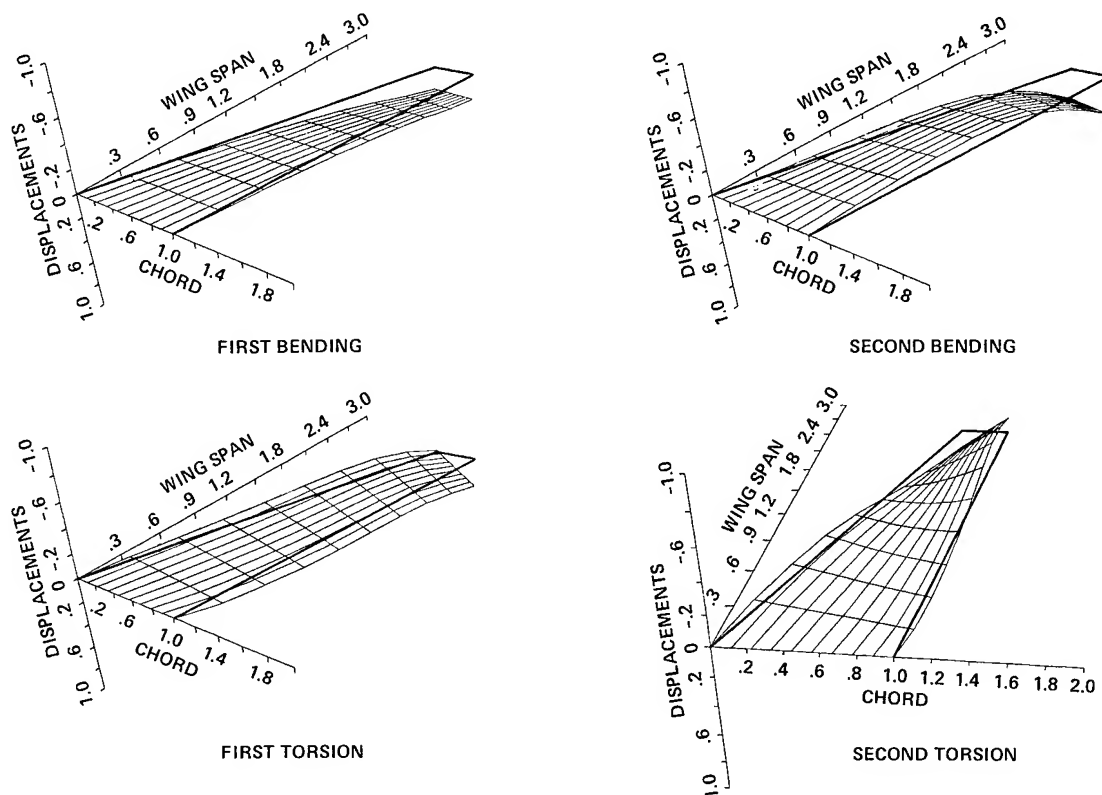


Fig. 12 Swept wing natural mode shapes.

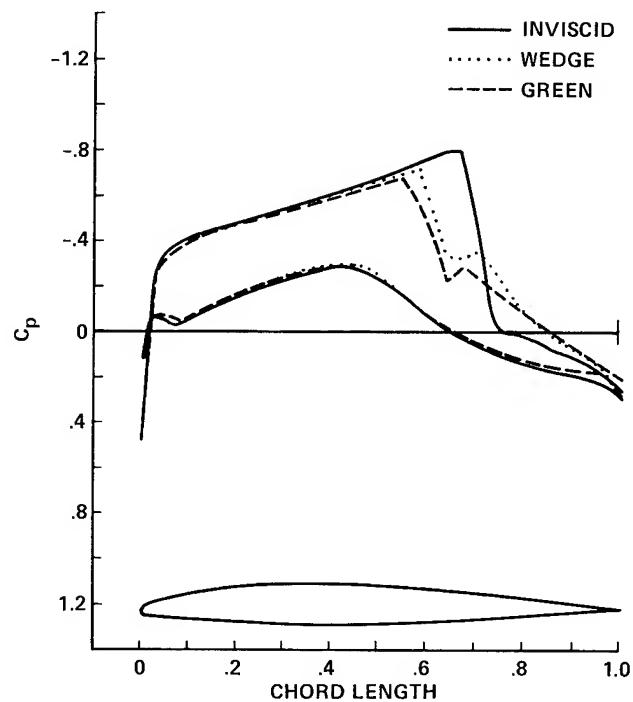


Fig. 13 Swept wing steady pressure for the inviscid and viscous methods at 60% semispan and $\alpha = 0$.

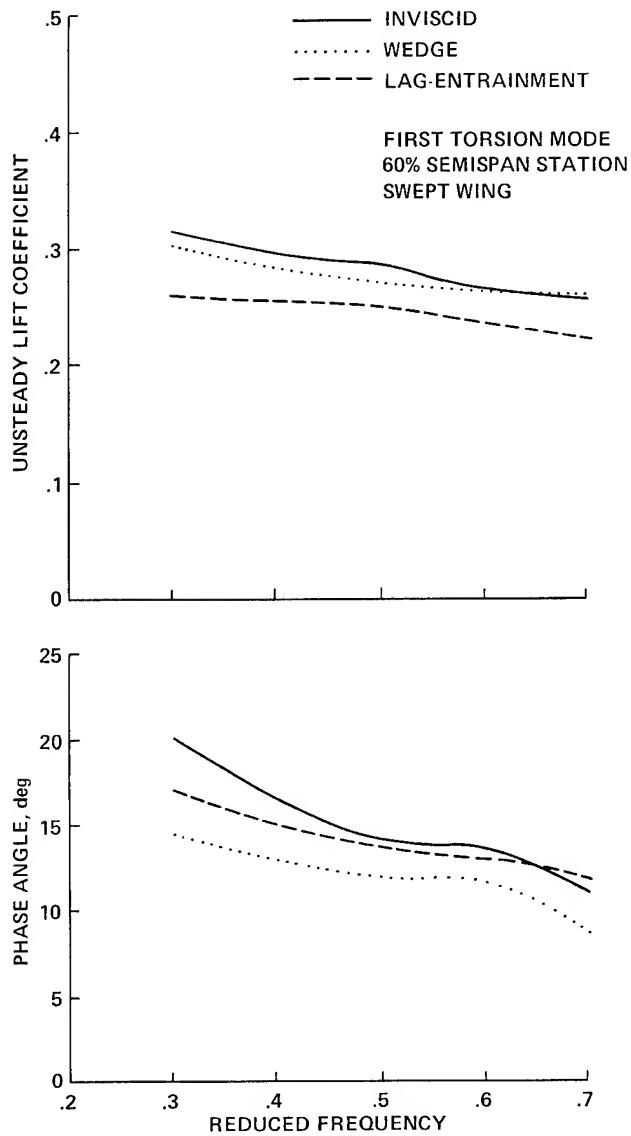


Fig. 14 Magnitude of the unsteady lift and corresponding phase angle versus reduced frequency for the inviscid and viscous methods.

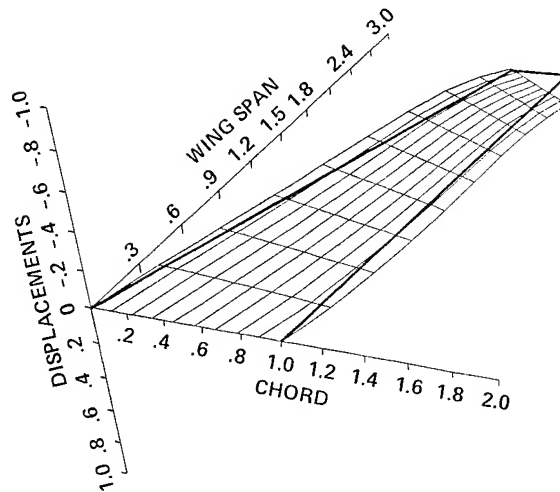


Fig. 15 The shape of the swept wing at flutter is composed of the first bending and the first and second torsion modes.

Guru P. Guruswamy*
Informatics General Corporation, Palo Alto, California

and

Peter M. Goorjian*
NASA Ames Research Center, Moffett Field, California

Abstract

An efficient coordinate transformation technique is presented for constructing grids for unsteady, transonic aerodynamic computations for delta-type wings. The original shearing transformation yielded computations that were numerically unstable and this paper discusses the sources of those instabilities. The new shearing transformation yields computations that are stable, fast, and accurate. Comparisons of those two methods are shown for the flow over the F5 wing that demonstrate the new stability. Also, comparisons are made with experimental data that demonstrate the accuracy of the new method. The computations were made by using a time-accurate, finite-difference, alternating-direction-implicit (ADI) algorithm for the transonic small-disturbance potential equation.

Introduction

There is a need both by aerodynamicists and aeroelasticians for efficient computational methods in the area of three-dimensional unsteady transonic aerodynamics for the design of aircraft in the transonic regime. Such methods are being developed in the area of computational fluid dynamics (CFD).¹ Methods based on the small disturbance theory have already led to the development of successful production codes that are in use for aeroelastic applications.^{2,3} Methods based on other theories, such as the full potential theory, are still in the early stages of development⁴ for three-dimensional calculations. Among small disturbance codes, XTRAN3S² is being actively used for aerodynamic and aeroelastic applications.^{2,5-8}

XTRAN3S is a three-dimensional, unsteady, transonic small-disturbance potential code based on a time-accurate, finite-difference method using an alternating-direction implicit (ADI) scheme. This code can analyze general wing configurations and has the capability of conducting static and dynamic aeroelastic computations by simultaneously integrating the aerodynamic and structural equations of motion. So far, XTRAN3S has been successfully applied to the aerodynamic and aeroelastic analysis of wings with high-aspect ratios, large-taper ratios and small sweep angles, e.g., rectangular or transport-type wings.^{2,5-8} From these studies, it has been observed^{6,7} that XTRAN3S requires from 360 to 1200 time steps per cycle for rectangular and transport-type wings, respectively, to give stable, accurate, unsteady results. With a decrease in the aspect ratio and the taper ratio and

increase in the sweep angle, the number of time steps required per cycle increases.

Preliminary computations diverged when an attempt was made to obtain steady results for the F5 wing⁹ which has an aspect ratio of 2.98, a taper ratio of 0.31, and a leading edge sweep of 32°. ¹⁰ The code was unstable at feasible time-step sizes such as $\Delta t = 0.01$, and it was still unstable at a very small time-step size of $\Delta t = 0.001$. At this smaller time-step size, unsteady computations (if stable) would have required about 30,000 time steps per cycle at a reduced frequency of 0.2. These facts have imposed severe limitations on the practical applications of XTRAN3S. (Similar failures have been reported by other investigators.⁸)

The main objective of this work was to investigate in detail, the sources of numerical instabilities in the procedures used in XTRAN3S, and to develop new, stable procedures. From studies conducted on the basic procedures employed in the code, it was found that the shearing coordinate transformation used in XTRAN3S was a major source for instability. As a result, an alternate, modified-shearing coordinate transformation has been developed. This new transformation gives stable and accurate results for cases that failed with the old transformation technique. These results were obtained at a time-step size that is ten times larger than the size at which the old method was unstable.

With the modified, shearing transformation procedure, steady and unsteady computations were made at $M = 0.80$, $M = 0.90$, and $M = 0.95$, and they were compared with wind-tunnel experiments.⁹

Sources of Instability

XTRAN3S uses a modified small-disturbance equation¹¹

$$A\phi_{tt} + B\phi_{xt} = (E\phi_x + F\phi_x^2 + G\phi_y^2)_x + (\phi_y + H\phi_x\phi_y)_y + (\phi_z)_z \quad (1)$$

where $A = M_\infty^2$; $B = 2M_\infty^2$; $E = (1 - M_\infty^2)$; $F = -(1/2)(\gamma + 1)M_\infty^2$; $G = (1/2)(\gamma - 3)M_\infty^2$; and $H = -(\gamma - 1)M_\infty^2$.

Equation (1), which is ideal for rectangular wings, can pose problems for swept tapered wings. The dependence of the solution on the wing leading edge mesh spacing poses a problem when applied to swept tapered wings. Because of the large number of points required, it is impractical to maintain a sufficiently fine mesh spacing along the leading edge of a swept wing in a Cartesian coordinate system. An alternative approach was developed by

*Research Scientist. Member AIAA.

This paper is declared a work of the U.S. Government and therefore is in the public domain.

Ballhaus and Bailey¹² who used a shearing transformation to map a trapezoidal planform wing in the physical plane into a rectangle in the computational plane as shown in Fig. 1, where

$$\xi(x,y) = \frac{x - x_{LE}(y)}{x_{TE}(y) - x_{LE}(y)} ; \quad \eta(y) = y ; \quad \zeta(z) = z \quad (2)$$

Use of this shearing transformation permits a more efficient distribution of mesh points. The leading and trailing edges lie on the coordinate lines $\xi = 0$ and 1, respectively, and each span station ($\eta = \text{constant}$) has the same number of chordwise mesh points on the wing surface. Thus, the complicating effect of geometry has been transferred from the boundary conditions to the governing equation. This shearing transformation was used in XTRAN3S throughout the flow field.

The conventional shearing transformation Eq. (2) is simple and adequate for wings with high-aspect ratios, small sweeps, and large taper ratios.^{2,6-8} However, for wings with low-aspect ratios, high sweeps, and small taper ratios (such as delta wings), use of this shearing transformation produces unstable calculations. Since the transformation Eq. (2) is only a function of local chord, computational flow regions obtained by its use depend on the planform. For delta-type wings, Eq. (2) yields highly skewed flow regions and thus large discontinuous values for the metrics, ξ_y , near the upstream- and downstream-flow boundaries. The metric, ξ_y , appears as a coefficient of the cross derivatives in the governing equation [as seen later in Eq. (3)] after applying the transformation Eq. (2) to Eq. (1). Far field grid boundaries are not aligned to the flow directions. Also in XTRAN3S, the cross derivatives have been differenced explicitly. These combined factors can make flow computations unstable (see the F5 wing).

Figure 2 shows the planform of the F5 wing which has an aspect ratio of 2.98, a taper ratio of 0.31, and a leading edge sweep angle of 31.92°. The computational flow region that was obtained by using the shearing transformation Eq. (2) is shown in Fig. 3. From this figure, the large skewness of the grid lines that causes large gradients for the metrics near the flow boundaries, can be observed. In fact, the scale in Fig. 3 is stretched 10 to 1 in the y (or vertical) direction. So the actual skewness is ten times worse than shown. Also the kink (i.e., discontinuity) in the upstream boundary grid line is ten times worse than shown. Figure 4a shows a plot of the metric value, ξ_y , versus chord for the root station for this shearing transformation. Figure 4b shows a corresponding plot of the metric value versus span along a grid line starting at a distance 15.6 chords from the leading edge of the root section. The downstream boundary is located 25 chords downstream at the root span station. From Fig. 4a, it is seen that ξ_y has a large value at the downstream boundary, and from Fig. 4b, ξ_y also changes value at the tip span location in a large discontinuous way. It is precisely at that location (the downstream boundary at the wing tip span station) that numerical instabilities originate when using Eq. (2) for calculations of flow over the F5 wing.

Using this grid, steady, transonic flow computations were unstable for a time-step size of

$\Delta t = 0.01$ which is ten times smaller than that used for a stable calculation in a case for a rectangular wing.⁶ However, fair steady-state results were obtained for subcritical flow at $M = 0.8$ by using a small time step of $\Delta t = 0.001$ and running the code for 2000 time steps. For the same time-step size of $\Delta t = 0.001$, at $M = 0.9$, where the flow was transonic, the calculations diverged. For most of the cases considered, the numerical instability started at the downstream boundary where the tip span station occurs. For comparison, the conventional shearing transformation Eq. (2) gives stable results for transport-type wings in which cases there is no kink in the transformation. This leads to the conclusion that this feature of transformation is causing the numerical instability. As a result, this work presents an alternate transformation procedure that does not have the property of employing metrics that have large discontinuous values. This new transformation will yield stable calculations.

Modified Shearing Transformation

The main requirement that any transformation should satisfy for the finite-difference method used in XTRAN3S is that it should map any given wing to a rectangular wing (see Fig. 1). This condition is satisfied in the modified shearing transformation by using the same conventional shearing transformation given by Eq. (2) in the region near the wing. Away from the wing, a new scheme is devised such that the grid lines have the following characteristics: 1) far field boundaries are independent of the wing planform and aligned with respect to the free-stream direction; 2) smooth first and second derivatives occur for values of the metric quantities, particularly near boundaries; and 3) grid lines are clustered near the leading and trailing edges.

A good transformation that satisfies all the above criteria is shown in Figs. 5 and 6. The computational mesh in Fig. 5 is chosen to be identical to the physical grid at the root of the wing in Fig. 6. It is noted here that any wing span station can be selected instead of the root for this matching. (However, numerical experiments for the F5 wing indicated that the best results can be obtained by selecting the root station.) By using Eq. (2), the physical grid on the wing is computed. It is assumed that the physical grid boundaries, far upstream and downstream, are perpendicular to the root. Then, for any given span station, physical grid points between the wing edges and the upstream and downstream boundaries are distributed in such a manner that they satisfy requirements (1) to (3) mentioned previously. This distribution is accomplished by employing a combination of an exponential stretching function and a coordinate smoothing function at each span station. Figure 6 shows the physical grid obtained by using the new procedure. The new properties of this grid can be seen by comparing with Fig. 3.

After applying the transformation, Eq. (1) can be rewritten as

$$\begin{aligned}
& \frac{\partial}{\partial t} \left(-\frac{A\phi_t}{\xi_x} - B\phi_\xi \right) + \frac{\partial}{\partial \xi} \left[(\xi_x E)\phi_\xi + (\xi_x^2 F)\phi_\xi^2 \right. \\
& + G(\xi_y\phi_\xi + \phi_\eta)^2 + \frac{\xi_y}{\xi_x} (\xi_y\phi_\xi + \phi_\eta) \\
& \left. + H\xi_y\phi_\xi(\xi_y\phi_\xi + \phi_\eta) \right] + \frac{\partial}{\partial \eta} \left[\frac{1}{\xi_x} (\xi_y\phi_\xi + \phi_\eta) \right. \\
& \left. + H\phi_\xi(\xi_y\phi_\xi + \phi_\eta) \right] + \frac{\partial}{\partial \zeta} \left(\frac{\phi_\zeta}{\xi_x} \right) = 0 \quad (3)
\end{aligned}$$

It is noted here that when the conventional transformation was used to obtain Eq. (3), then the ξ_x metric quantities would have been replaced by the reciprocal of the local chord. Equation (3) is solved by an ADI algorithm in XTRAN3S.²

Metric quantities required in Eq. (3) are computed by mapping the physical grid in Fig. 6 to the computational grid in Fig. 5. A plot of the metric quantity, ξ_y , versus the chord for the root section and versus the span, along a grid line starting at a distance 15.6 chords from the leading edge of the root section are shown in Figs. 4a and 4b, respectively. From these two figures, the small gradients of ξ_y , obtained by the modified transformation, can be seen particularly in Fig. 4b at the location near the tip. It is noted that the modified transformation yields metrics ξ_x that are functions of both x and y . There is no skewness in the grid at the far field boundaries and, hence, there is a smooth metric quantity for the finite differencing, particularly of cross derivatives. This improvement stabilizes the ADI scheme for low taper ratio wings.

This new coordinate transformation, along with many other improvements, is incorporated in a new version of the code, XTRAN3S-Ames.¹³

Results

Using the new transformation technique, steady and unsteady aerodynamic results are computed for the F5 wing at $M = 0.80, 0.90$, and 0.95 and are compared with experimental measurements⁹ and with results obtained from the conventional shearing transformation.

Figure 7 shows the plots of steady pressure results obtained for the mid-semispan station at $M = 0.80$ from the two transformation methods and the experiment. With the conventional shearing transformation, about 2000 time steps of size 0.001 were required to obtain a fairly converged solution, whereas, modified transformation required only about 1000 steps of size 0.01 to give a converged solution. The latter solution compares better with experiment than does the former. This illustrates that the modified shearing transformation can give more accurate results in half the computational time. Plots of steady pressure distributions obtained by the modified transformation and experiment are given for four span stations in Fig. 8. Comparisons are good at all span stations.

Figure 9 shows plots of steady pressure results obtained at $M = 0.9$ for the mid-semispan

station by the two transformation methods and experiment. In spite of using a time-step size of 0.001, results from the conventional shearing transformation eventually diverged. Also, those results were highly inaccurate after 4000 time steps as illustrated in Fig. 9. The computations diverged sometime after 4000 time steps and before 6000 time steps. With the modified shearing transformation, a converged solution was obtained by using 2000 time steps of size 0.01. In Fig. 9, it can be seen that the latter method compares well with the experiment. Plots of steady pressure distributions for four span stations obtained by the modified transformation and the experiment are given in Fig. 10. Comparisons are generally good at all span stations.

Figure 11 shows the plots of steady pressure distributions obtained by the modified transformation method and the experiment at $M = 0.95$. From the observations made at $M = 0.90$, no attempt was made to make any computations using the conventional shearing transformation. In Fig. 11, it can be observed that the shocks given by the code are stronger and shifted farther aft as compared to those observed in the experiment. This disagreement could be due to viscous effects, since the calculations assume that the flow is inviscid. At this Mach number, viscous effects can play an important role due to the strength of the shock wave, as shown in Fig. 11.

Figure 12 shows the modal motion used in the NLR experiment.⁹ The wing is pitching about an axis located at the 50% root chord and the pitching axis is normal to the wing root. Figures 13-15 show plots of the real and imaginary values of the upper surface pressures at four span stations obtained by the modified shearing transformation and the NLR experiments at $M = 0.8, 0.9$, and 0.95 , respectively. These results were obtained for the wing oscillating at a frequency of 40 cycles per second.

The same modal motion used in the NLR experiment was simulated in the code. Results from the code were obtained by forcing the wing to undergo a sinusoidal modal motion for three cycles with 1200 time steps per cycle, during which time the transients disappeared and a periodic response was obtained. No attempt was made to use the conventional shearing transformation because of the instabilities encountered during the steady calculations.

As shown in Fig. 13, at $M = 0.80$, where the flow is subsonic, both the real and imaginary parts of the unsteady pressure compare well with the experiment for all span stations as expected. At $M = 0.90$, where the flow is transonic, as shown in Fig. 14, comparisons with the experiment are good except near the root and the tip. Discrepancies near the root can be due to the wall effects which were not accounted for in this analysis. A better agreement near the tip might be obtained through the use of more computational span stations in that region. At $M = 0.95$, comparisons with the experiment are not as favorable as at the lower Mach numbers. As seen in Fig. 15, this disagreement with the NLR experiment is mainly in the region of shock wave. The results could be improved if viscous corrections were applied to the calculations. The code XTRAN3S-Ames is now capable of making such viscous corrections.¹⁴

Concluding Remarks

An efficient, modified shearing transformation method has been developed for use in the code XTRAN3S-Ames which computes unsteady transonic aerodynamics. This new method is particularly effective for low aspect ratio and small taper ratio delta-type wings. From the computations made on the F5 wing and subsequent comparisons with experiment, it can be concluded that the modified transformation makes the finite difference scheme used in XTRAN3S-Ames accurate, stable, and fast for these difficult cases. Cases can now be successfully analyzed for which the conventional shearing transformation had failed to yield results. Computations made with this new procedure demonstrate that the range of the unsteady transonic code XTRAN3S-Ames for aerodynamic and aeroelastic applications has been extended.

References

- ¹Ballhaus, W. F., Deiwert, G. S., Goorjian, P. M., Holst, T. L., and Kutler, P., "Advances and Opportunities in Transonic Flow Computations," Numerical and Physical Aspects of Aerodynamic Flows, Springer, 1981.
- ²Borland, C. J. and Rizzetta, D. P., "Transonic Unsteady Aerodynamics for Aeroelastic Applications, Vol. I - Technical Development Summary for XTRAN3S," AFWAL-TR-80-3107, June 1982.
- ³Traci, R. M., Albano, E. D., and Farr, J. L., "Small Disturbance Transonic Flows About Oscillating Airfoils and Planar Wings," AFFDL-TR-75-100, Air Force Flight Dynamics Lab., June 1975.
- ⁴Sankar, N. L., Malone, J. B., and Tassa, Y., "An Implicit Conservative Algorithm for Steady and Unsteady Three-Dimensional Transonic Potential Flows," AIAA Paper 81-1016, June 1981.
- ⁵Borland, C. J. and Rizzetta, D. P., "Non-linear Transonic Flutter Analysis," AIAA Paper 81-0608-CP, Atlanta, Ga., Apr. 1981.
- ⁶Guruswamy, P. and Goorjian, P. M., "Comparison Between Computational and Experimental Data in Unsteady Three Dimensional Transonic Aerodynamics Including Aeroelastic Applications," AIAA Paper 82-0690-CP, May 1982.
- ⁷Myers, M. R., Guruswamy, P., and Goorjian, P. M., "Flutter Analysis of a Transport Wing Using XTRAN3S," AIAA Paper 83-0922, May 1983.
- ⁸Seidel, D. A., Bennett, R. M., and Ricketts, R. H., "Some Applications of XTRAN3S," NASA TM-85641, May 1983.
- ⁹Tijdeman, J. et al., "Transonic Wind Tunnel Tests on an Oscillating Wing with External Stores; Part II - The Clean Wing," AFFDL-TR-78-194, Mar. 1979.
- ¹⁰Sotamayer, W. A., "Aerodynamic Modelling of a Fighter Wing in Transonic Flow," to be published as an AFWAL Technical Memorandum.
- ¹¹Yoshihara, H., "Formulation of the Three-Dimensional Transonic Unsteady Aerodynamic Problem," AFFDL TR-79-3030, Feb. 1979.
- ¹²Ballhaus, W. F. and Bailey, F. R., "Numerical Calculation of Transonic Flow About Swept Wings," AIAA Paper 72-677, June 1972.
- ¹³Guruswamy, P. and Goorjian, P. M., "Development and Applications of XTRAN3S-AMES," Computational Fluid Dynamics User's Workshop, The University of Space Institute, Tullahoma, Tenn., Mar. 1984.
- ¹⁴Rizzetta, D. P. and Borland, C. J., "Numerical Solution of Three-Dimensional Unsteady Transonic Flow Over Wings, Including Inviscid/Viscous Interaction," AIAA Paper 82-0352, Jan. 1982.

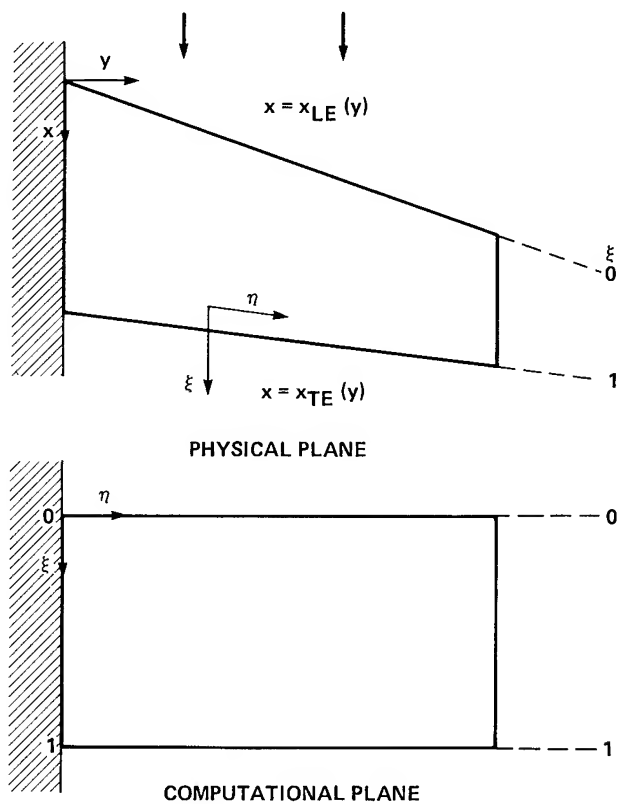


Fig. 1 Wing planform transformation.

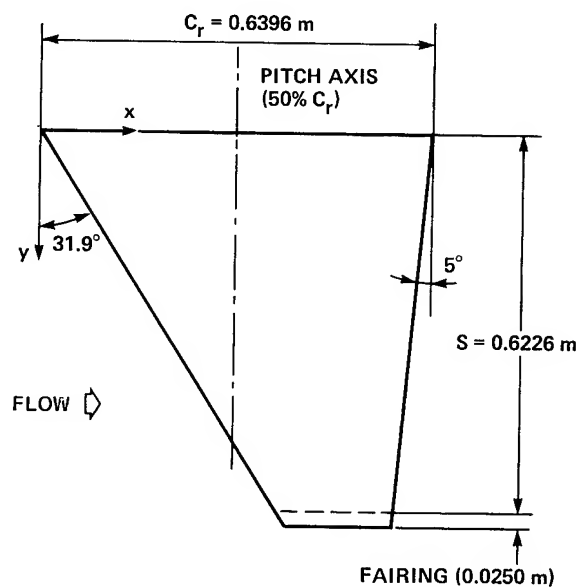


Fig. 2 Dimensions of the F5 wing.

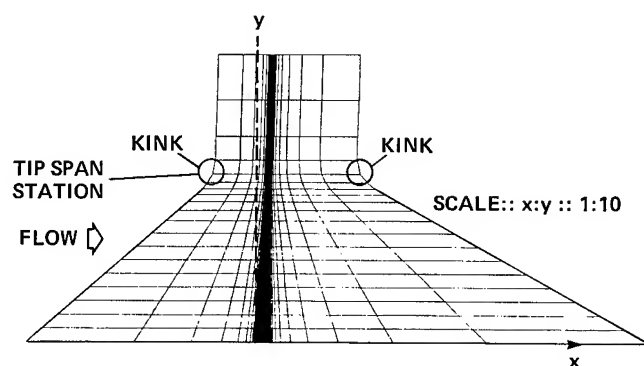
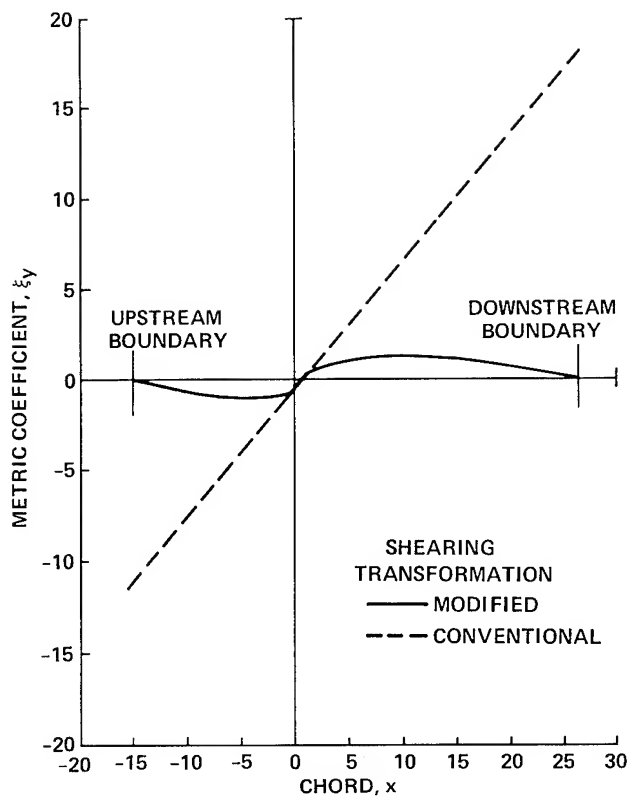
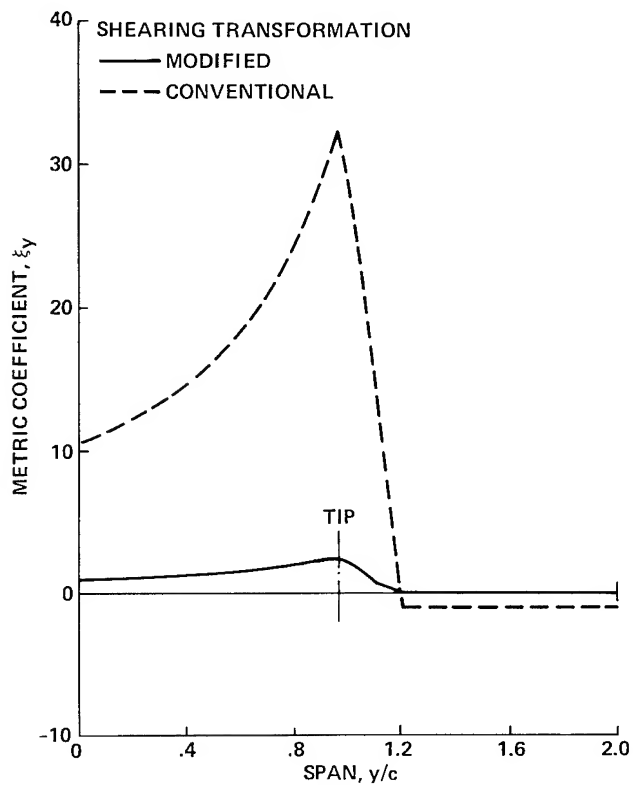


Fig. 3 Physical grid (64 × 20) in x-y plane from the conventional shearing transformation.



(a) ξ_y versus chord at the root from the two transformations.



(b) ξ_y versus span near downstream from the two transformations.

Fig. 4 Plots of the metric coefficient.

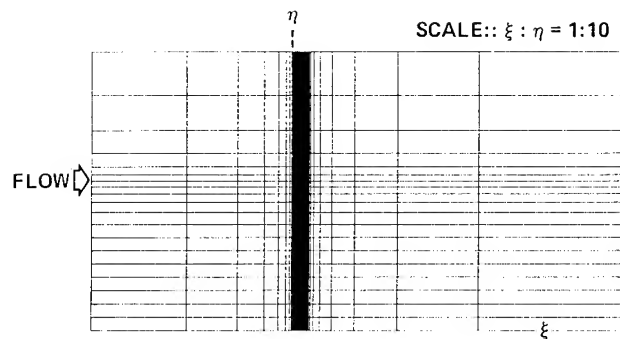


Fig. 5 Computational mesh (64×20) in ξ - η plane.

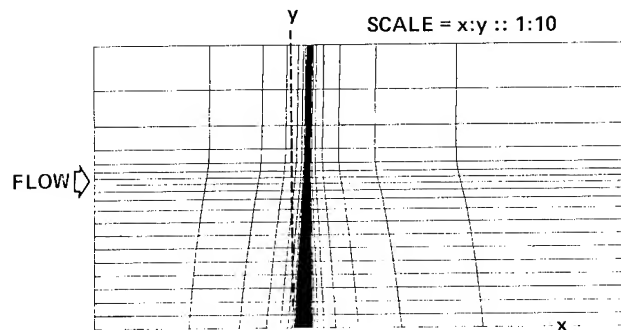


Fig. 6 Physical grid (64×20) in x - y plane by the modified shearing transformation.

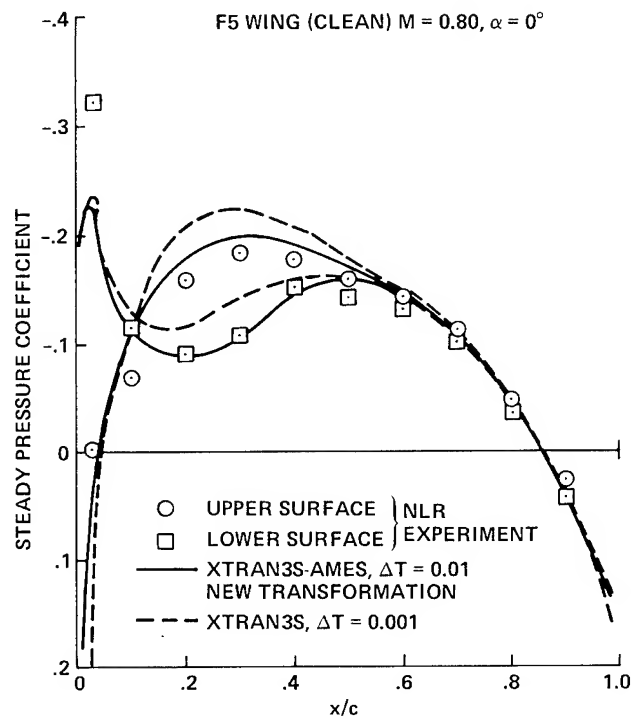


Fig. 7 Effect of transformation on steady pressures at $M = 0.80$.

F5 WING
 $M = 0.80$
 $AR = 2.98$
 $TR = 0.31$
 $\alpha = 0^\circ$

STEADY C_p
 \square UPPER } NLR EXPERIMENT
 \triangle LOWER }
 — UPPER } XTRAN 3S-AMES
 --- LOWER }

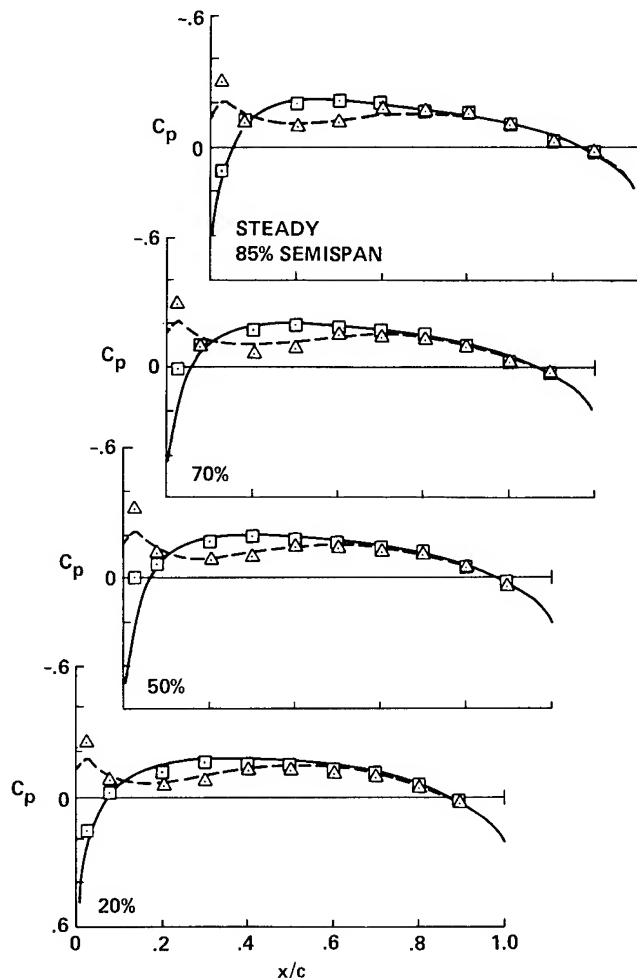


Fig. 8 Comparison of steady pressures between theory and experiment at $M = 0.80$.

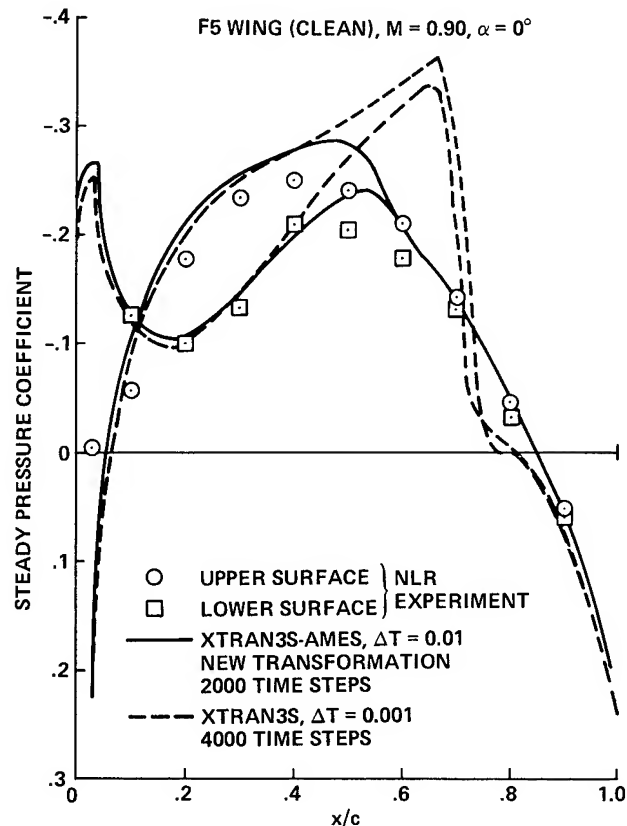


Fig. 9 Effect of transformation on steady pressures at $M = 0.90$.

F5 WING
AR = 2.98
TR = 0.31
M = 0.90
 $\alpha = 0^\circ$

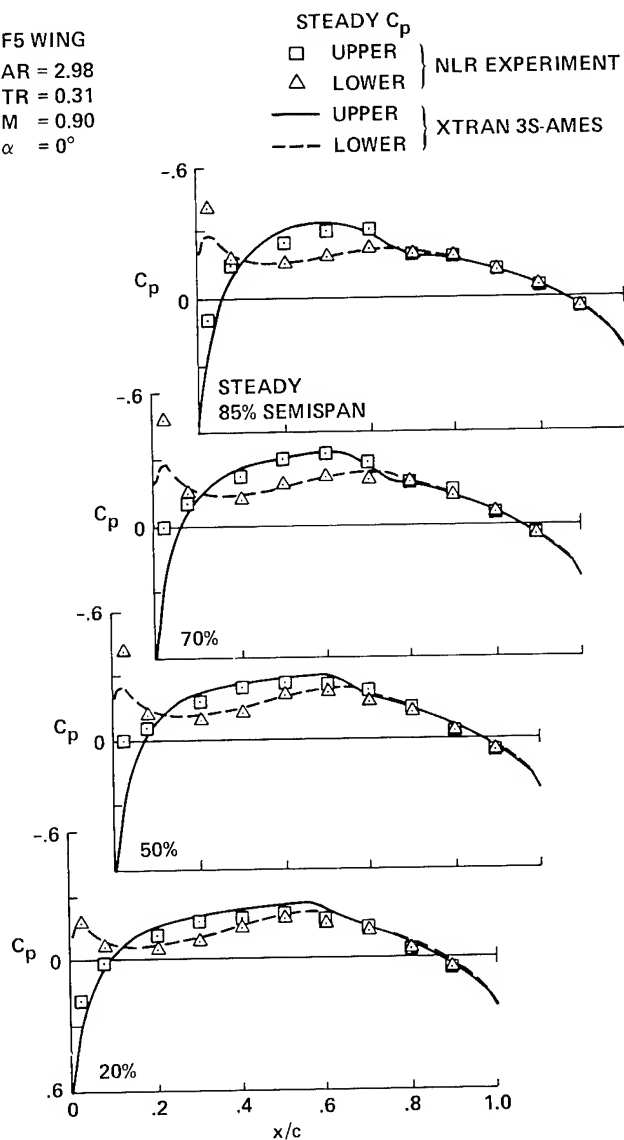


Fig. 10 Comparison of steady pressures between theory and experiment at $M = 0.90$.

F5 WING
AR = 2.98
TR = 0.31
M = 0.95
 $\alpha = 0^\circ$

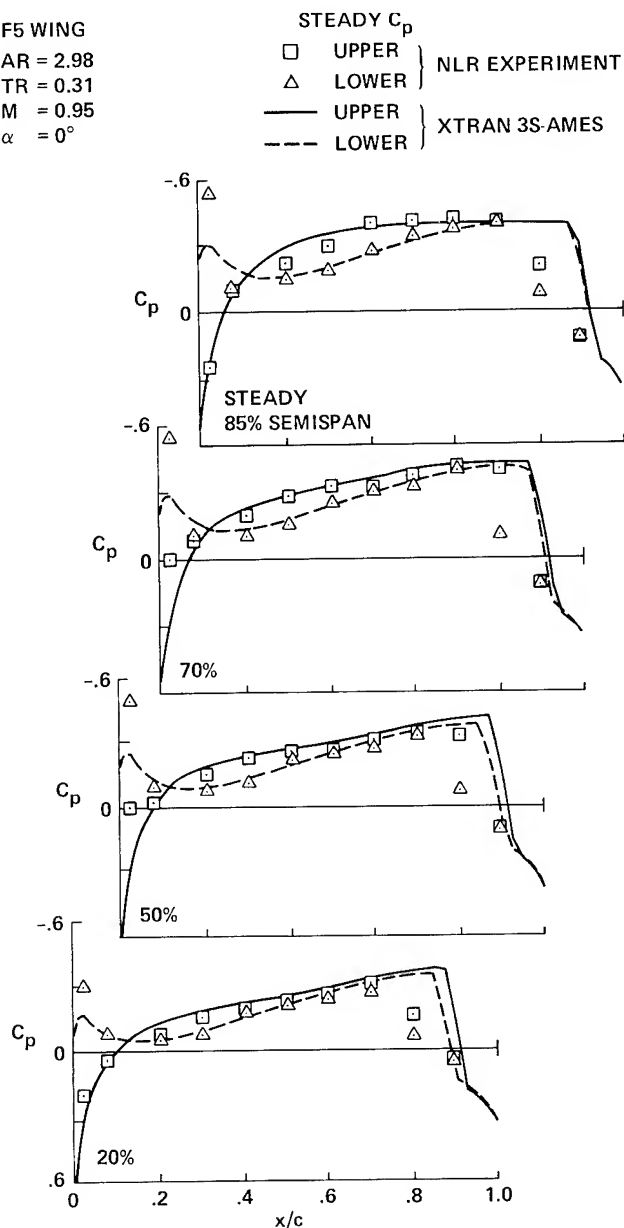


Fig. 11 Comparison of steady pressures between theory and experiment at $M = 0.95$.

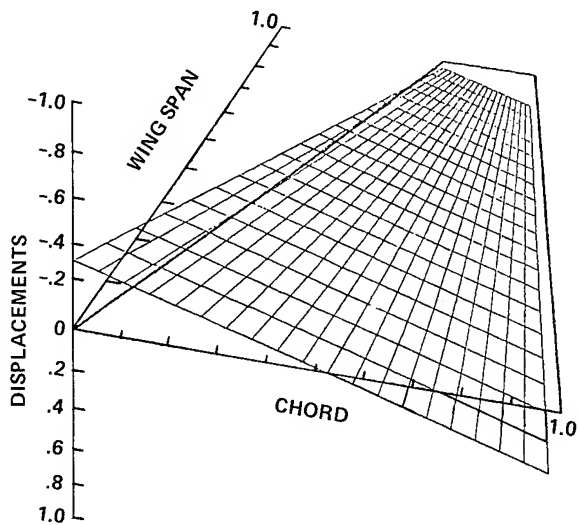


Fig. 12 Unsteady modal motion of the F5 wing.

F5 WING
 $AR = 2.98$
 $TR = 0.31$
 $M = 0.80$
 $\alpha = 0^\circ$
 $t = 40 \text{ Hz}$

UNSTEADY C_p

— REAL

- - - IMAGINARY

□ REAL

△ IMAGINARY

XTRAN 3S-AMES

NLR EXPERIMENT

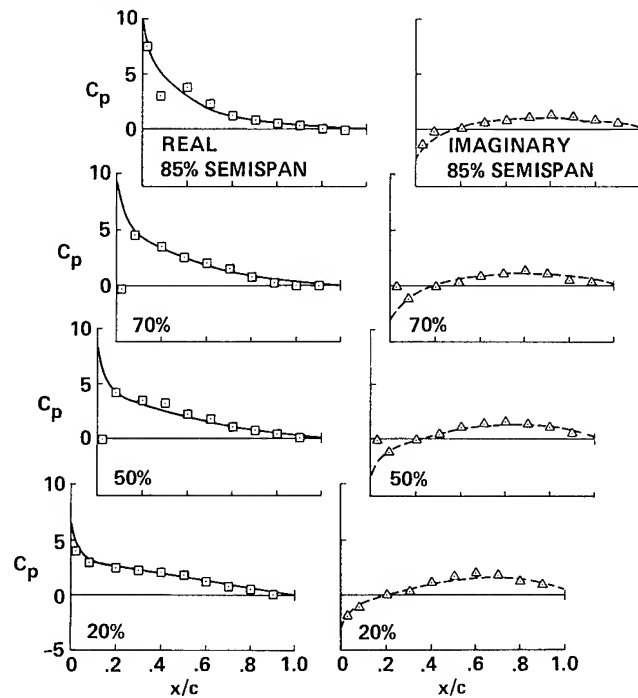


Fig. 13 Comparison of unsteady pressures between theory and experiment at $M = 0.80$.

F5 WING
AR = 2.98
TR = 0.31
M = 0.90
 $\alpha = 0^\circ$
t = 40 Hz

UNSTEADY C_p
— REAL
--- IMAGINARY } XTRAN 3S-AMES
□ REAL
△ IMAGINARY } NLR EXPERIMENT

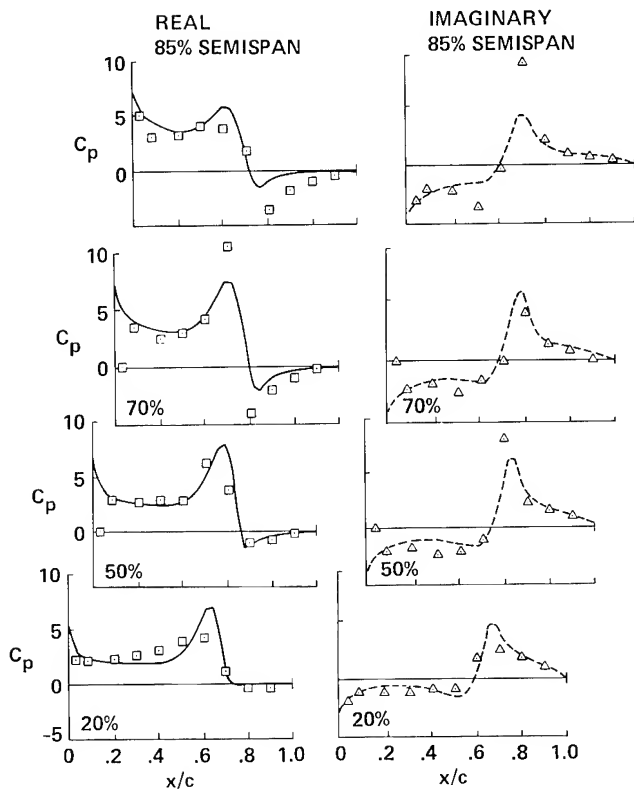


Fig. 14 Comparison of unsteady pressures between theory and experiment at $M = 0.90$.

F5 WING
AR = 2.98
TR = 0.31
M = 0.95
 $\alpha = 0^\circ$
t = 40 Hz

UNSTEADY C_p
— REAL
--- IMAGINARY } XTRAN 3S-AMES
□ REAL
△ IMAGINARY } NLR EXPERIMENT

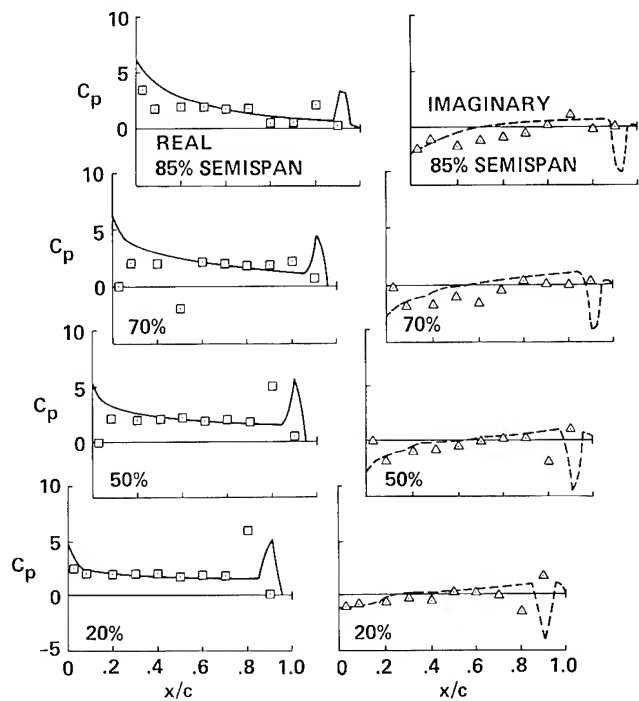


Fig. 15 Comparison of unsteady pressures between theory and experiment at $M = 0.95$.

R. M. Chi*
United Technologies Research Center
East Hartford, Connecticut 06108

Abstract

A relatively simple two dimensional subsonic unsteady aerodynamic theory has been developed to take into account the effect of flow separation on unsteady airloads for high incidence angles of thin airfoil sections approximately. The theory is an extension of the classical linear potential flow theory for thin airfoils with proper boundary conditions applied to the flow separation region along the airfoil surface. The mixed boundary value problem for the lifting unsteady aerodynamics is translated into two singular integral equations that are solved by using the collocation method. Very encouraging correlation has been obtained between the calculated and experimental pitch damping values for a thin airfoil section typical of Hamilton Standard propeller blade at large angles of attack.

Nomenclature

a_∞	Undisturbed upstream sound speed
A	Nonlifting kernel function
c	Blade full chord
$C(x, \xi)$	See Eq. (29)
C_L	Section lift coefficient
C_M	Section moment coefficient
f_n	Amplitude of harmonic f_n
f_n	Airfoil normal displacement
h	Amplitude of harmonic heaving motion
$H_n^{(2)}$	Hankel function of the second kind of nth order
$\text{Im}\{ \}$	Imaginary part of $\{ \}$
J_v	Bessel function of the first kind of order v
$K(x-\xi)$	Lifting kernel function
$\ell(x)$	See Eq. (28)
M	Mach number
\hat{p}	Amplitude of harmonic \hat{p}
p	Perturbation pressure
Δp	$\equiv p_+ - p_-$
P_0	Eigensolution for $\Delta p/\rho U^2$
P_1	Unit-upwash solution for $\Delta p/\rho U^2$ satisfying trailing-edge Kutta condition
\hat{P}_1	Unit-upwash solution for $\Delta p/\rho U^2$ satisfying leading-edge Kutta condition
$\text{Re}\{ \}$	Real part of $\{ \}$
sgn	Sign function
t	Time
U or U_∞	Undisturbed upstream flow velocity

W	Upwash velocity
\bar{W}	$\equiv \frac{1}{2} (W_+ + W_-)$
ΔW	$\equiv W_+ - W_-$
Y_v	Bessel function of the second kind of order v
x	Coordinate in direction of undisturbed upstream flow velocity
x_0	Axis about which moment is taken
x_{PCH}	Pitching axis x coordinate
x_s	Flow separation point x coordinate
z	Coordinate vertical to x
α	Fourier Transform variable
β	$\sqrt{1-M^2}$
γ	Cavitation function
$\Gamma()$	Gamma function
Γ_K	Inversion kernel corresponding to K
θ	Amplitude of harmonic pitching motion
ξ^*	$(\xi - x_s)/(1 - x_s)$
π	3.14159...
ρ	Fluid density
ϕ	Perturbation velocity potential
ω	Circular frequency
∇^2	Laplacian operator
$\frac{D}{Dt}$	$\equiv \frac{\partial}{\partial t} + U \frac{\partial}{\partial x}$

Superscript

*	Fourier Transform
---	-------------------

Subscript

NS	Nonseparated flow
COR	Correction due to flow separation
+	Upper blade surface
-	Lower blade surface
α	Pitching motion
h	Plunging motion

I. Introduction

For the major reason of high fuel efficiency, the development of advanced propfans has been of renewed interest to the general aviation industry¹. The propeller diameter of typical advanced turbo-prop propulsion systems is kept small by the use of many blades. These propeller blades are ultrathin and highly swept in order to maintain high efficiency in the tip region. As a result of the high performance aerodynamic design, stall flutter problem has been experienced in recent wind tunnel tests². Therefore, the avoidance of stall flutter of the new generation propfan blades has become a major concern in blade structural design.

*Senior Research Engineer
Member, AIAA

The major deficiency in the current flutter design system is the lack of a practical unsteady aerodynamic theory applicable to stalled compressible flow surrounding ultrathin blades. High angle of attack aerodynamics for stalled flows involving flow separation is a classical research subject. A concise discussion on the steady flow separation characteristics at low speed and transonic speeds was given by Smith³. For unsteady separated flows, Ericsson and Reding⁴⁻⁷ have developed semiempirical analysis procedures for dynamic stall airloads based on static airfoil stall performance characteristics. A more exact treatment of unsteady separated flows by carefully modeling the bound and free vortex sheets is due to Kandil and colleagues⁸⁻¹¹.

In this paper, a theoretical unsteady aerodynamic model is described to account for the effect of flow separations on stalled unsteady airloads in the subsonic flow regime. The flow model is a modification of the classical potential flow model by specifying proper boundary conditions and certain solution behaviors in the flow separation region. Flow models of similar type have been used in the past by Woods¹² in his study of airfoils with spoilers in an incompressible flow, Wu¹³ in his wake and cavity flow theory development, Perumal and Sisto¹⁴ in their study of incompressible unsteady flow with a moving flow separation point, Dowell¹⁵ in his transonic unsteady aerodynamic study for isolated airfoils, and Chi¹⁶ in his subsonic stall flutter study of cascade blades. The present work deals with subsonic flow about an isolated airfoil with fixed flow separation point. The theory provides a new derivation of the classical lifting and nonlifting kernel functions (aerodynamic influence functions or Green's functions). It utilizes both the classical lifting and nonlifting kernel functions in the analysis of separated flow lifting aerodynamics. Sample calculation results based on the present theory are compared with other theories and, more importantly, with aerodynamic damping test data for typical thin NACA airfoils used in propfan designs.

In the following discussion, the theory will be presented first followed by a discussion on the correlation between the calculated force coefficients with other theoretical and experimental data. Conclusions will then be drawn and recommendations on future work to further advance the stalled airload technology will be made.

II. Theory

Governing Equations

The perturbation velocity potential $\hat{\phi}$ is assumed to satisfy the convective wave equation

$$\nabla^2 \hat{\phi} = \frac{1}{a_\infty^2} \frac{D^2 \hat{\phi}}{Dt^2} \quad (1)$$

where a_∞ is the undisturbed upstream sound speed and

$$\frac{D}{Dt} \equiv \frac{\partial}{\partial t} + U_\infty \frac{\partial}{\partial x}$$

The perturbation pressure \hat{p} is related to the perturbation velocity potential $\hat{\phi}$ by the Bernoulli's equation

$$\hat{p} = -\rho_\infty \left(\frac{\partial \hat{\phi}}{\partial t} + U_\infty \frac{\partial \hat{\phi}}{\partial x} \right) \quad (2)$$

where

ρ_∞ = undisturbed upstream density,
 U_∞ = undisturbed upstream velocity.

The coordinate x is chosen to be in the free-stream direction, z is perpendicular to x , and t denotes time. The origin of the x, z coordinate system is fixed at the leading edge of the airfoil as shown in Fig. 1 and all linear dimensions are scaled by the blade chord c .

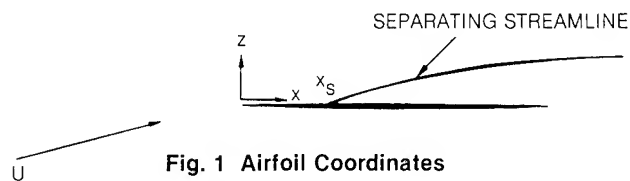


Fig. 1 Airfoil Coordinates

For simple harmonic motion, we have

$$\hat{\phi} = \phi e^{i\omega t}$$

$$\hat{p} = p e^{i\omega t}$$

$$\beta^2 \frac{\partial^2 \phi}{\partial x^2} + \frac{\partial^2 \phi}{\partial z^2} - 2i \frac{\omega}{U} M^2 \frac{\partial \phi}{\partial x} + \left(\frac{\omega}{U} M \right)^2 \phi = 0 \quad (3)$$

$$\frac{p}{\rho U} = - \left(i \frac{\omega}{U} + \frac{\partial}{\partial x} \right) \phi \quad (4)$$

where $\beta = \sqrt{1-M^2}$ and M is the upstream Mach number. For convenience, the subscript " ∞ " has been dropped for all upstream flow quantities.

Boundary Conditions

When there is no flow separation, the following boundary conditions apply:

1. On the airfoil surface, the flow tangency condition is assumed, i.e.,

$$\phi_z = \hat{W} \quad (5)$$

where \hat{W} is the prescribed upwash velocity. This boundary condition applies to both the upper and lower surfaces of the airfoil.

2. Off the airfoil, the perturbation pressure and vertical velocity (upwash) are continuous everywhere.
3. The radiation/finiteness condition is satisfied at infinity.

For simple harmonic motion, the blade displacement is simply

$$\hat{f}(x, t) = f(x)e^{i\omega t}$$

Since the upwash is related to the blade displacement by

$$\hat{W} = \frac{\partial \hat{f}}{\partial t} + U \frac{\partial \hat{f}}{\partial x}$$

or, for simple harmonic motion,

$$\hat{W} = W e^{i\omega t}$$

$$W = (i\omega + U \frac{\partial}{\partial x})f$$

The upwash $W(x)$ is given for $x \in (0, 1)$ and unknown otherwise. For combined pitching and heaving motion in nonseparated (attached) flow,

$$\begin{aligned} W(x) &= i\omega h - [i\omega(x - x_{PCH}) + U]\theta \\ &= (i\omega h - U\theta) - i\omega(x - x_{PCH})\theta \end{aligned}$$

where x_{PCH} is the pitching axis location, h and θ the heaving and pitching amplitude respectively. Therefore, the boundary condition is

$$\phi_z = W(x) = (i\omega h - U\theta) - i\omega(x - x_{PCH})\theta \quad (6)$$

For attached flows, the boundary conditions described above are adequate. For separated flow, we modify the boundary condition on the airfoil surface (Eq. (5)) by assuming that the perturbation pressure \hat{p} is known in the flow separation region and defining the cavitation function γ as

$$\gamma = \frac{p_\infty - p_+}{\frac{1}{2} \rho U^2} = \frac{-\hat{p}_+}{\frac{1}{2} \rho U^2} \quad (7)$$

The same assumption was made previously by Perumal and Sisto¹⁴, Dowell¹⁵ and Chi¹⁶ among others except that they assumed a zero cavitation. The assumption of zero cavitation is reasonable as long as $|p_+ - p_\infty| \ll |p_- - p_\infty|$. It is noted that the upwash is considered unknown on blade surfaces exposed to the separated flow. Also, it is assumed that flow separation only occurs on the suction side of the airfoil.

In summary, we will seek the solution of Eq. (3) subject to the boundary conditions, Eqs. (6) and (7), as well as the condition of pressure and velocity continuity and the radiation/finiteness condition. Note that Eq. (6) applies to the lower pressure surface ($z = 0^-$) and the portion of the upper suction surface ($z = 0^+$) where the mean flow is attached, while the upwash is considered unknown on the portion of the surface where flow separation occurs.

Solution Procedures

The Fourier Transform pair is defined as

$$\begin{aligned} \phi^* &= \int_{-\infty}^{\infty} \phi e^{-i\alpha x} dx \\ \phi &= \frac{1}{2\pi} \int_{-\infty}^{\infty} \phi^* e^{i\alpha x} d\alpha \end{aligned} \quad (8)$$

Applying Fourier Transform to Eqs. (3), (4), (6), one obtains

$$\frac{d^2 \phi^*}{dz^2} + \mu^2 \phi^* = 0 \quad (9)$$

where

$$\mu^2 = \beta^2 \left[\left(\frac{\omega}{U} \frac{M}{\beta^2} \right)^2 - \left(\alpha - \frac{\omega}{U} \frac{M^2}{\beta^2} \right)^2 \right]$$

and

$$\frac{p^*}{\rho U} = -i \left(\frac{\omega}{U} + \alpha \right) \phi^* \quad (10)$$

subject to the boundary conditions,

$$\phi_z^* = W_+^* \quad \text{at } z = 0^+ \quad (11)$$

$$\phi_z^* = W_-^* \quad \text{at } z = 0^- \quad (12)$$

where W_+^* and W_-^* are the Fourier Transforms of the upwashes on the upper and lower surfaces of the airfoil respectively. As shown in Reference 17, the transformed perturbation pressures on the airfoil surfaces are as follows:

$$\frac{p_+^*}{\rho U^2} = -\frac{\frac{\omega}{U} + \alpha}{\mu} \frac{W_+^*}{U} \quad (13)$$

$$\frac{p_-^*}{\rho U^2} = \frac{\frac{\omega}{U} + \alpha}{\mu} \frac{W_-^*}{U} \quad (14)$$

where

$$\mu = \begin{cases} i|\mu| & \text{for } \alpha < \alpha_1 \text{ or } \alpha > \alpha_2 \\ -|\mu| & \text{for } \alpha_1 < \alpha < \alpha_2 \end{cases}$$

$$|\mu| = \beta \left| \left(\frac{\omega}{U} \frac{M}{\beta^2} \right)^2 - \left(\alpha - \frac{\omega}{U} \frac{M^2}{\beta^2} \right)^2 \right|^{1/2} \geq 0$$

$$\alpha_1 = -\frac{\omega}{a+U}$$

$$\alpha_2 = \frac{\omega}{a-U}$$

Since we are interested in pressure differences, define Δp^* and \bar{p}^* as follows:

$$\Delta p^* = p_+^* - p_-^* \quad (15)$$

$$\bar{p}^* = \frac{1}{2} (p_+^* + p_-^*)$$

Similarly, define ΔW^* and \bar{W}^* as

$$\Delta W^* = W_+^* - W_-^* \quad (16)$$

$$\bar{W}^* = \frac{1}{2} (W_+^* + W_-^*)$$

Using Eqs. (15) and (16) in Eq. (13) and (14), we obtain

$$\frac{\bar{W}^*}{U} = K^* \frac{\Delta p^*}{\rho U^2} \quad (17)$$

$$\frac{\bar{p}^*}{\rho U^2} = A^* \frac{\Delta W^*}{U} \quad (18)$$

where

$$K^* = -\frac{1}{2} \frac{\mu}{\frac{\omega}{U} + \alpha} \quad (19)$$

$$A^* = -\frac{1}{2} \frac{\frac{\omega}{U} + \alpha}{\mu} \quad (20)$$

A Fourier Inversion of Eq. (17) yields

$$\frac{\bar{W}(x)}{U} = \int_0^1 K(x-\xi) \frac{\Delta p(\xi)}{\rho U^2} d\xi \quad (21)$$

where the lifting kernel K is the Fourier inversion of K^* . For attached flows, $\bar{W}(x)$ is known in terms of the airfoil vibration mode shape and Eq. (21) can be solved easily. The domain of integration of the integral in Eq. (21) covers only the airfoil surface because we consider thin wakes and assume continuous pressure across the wake itself. For separated flows, $\bar{W}(x)$ is unknown for separated region on the airfoil ($x_s < x < 1$) though prescribed for the rest of the airfoil ($0 < x < x_s$). Hence, the left hand side of Eq. (21) is partially unknown. Apparently an additional equation is needed in order to solve for the unknown upwash velocity in separated region on the airfoil. In fact, if ΔW is known \bar{W} can be calculated by

$$\bar{W} = \frac{1}{2} (W_+ + W_-) = W_- + \frac{1}{2} \Delta W \quad (22)$$

since W_- is known completely from Eq. (6).

To derive an integral equation for ΔW , we formally invert Eq. (21) to obtain

$$\frac{\Delta p(x)}{\rho U^2} = \int_0^1 \Gamma_K(x, \xi) \frac{\bar{W}(\xi)}{U} d\xi \quad (23)$$

where Γ_K is the resolvent kernel corresponding to the lifting kernel function K . General procedures are available to calculate Γ_K for a given K with fairly general singular behavior.^{18,19}

A Fourier inversion of Eq. (18) yields

$$\frac{\bar{p}(x)}{\rho U^2} = \int_{x_s}^1 A(x-\xi) \frac{\Delta W(\xi)}{U} d\xi \quad (24)$$

where we have used the condition that the upwash difference ΔW is zero both off the airfoil ($x < 0$, $x > 1$) and over attached flow portion of the airfoil ($0 < x < x_s$).

In separated region $p_+ = -1/2 \rho U^2 \gamma$ from Eq.

(7), i.e.,

$$\bar{p} + \frac{\Delta p}{2} = -\frac{1}{2} \rho U^2 \gamma \quad (25)$$

Substitution of Eq. (23) and (24) into Eq. (25) yields

$$\int_{x_s}^1 A(x-\xi) \frac{\Delta W(\xi)}{U} d\xi + \frac{1}{2} \int_0^1 \Gamma_K(x, \xi) \frac{\bar{W}(\xi)}{U} d\xi = -\frac{\gamma}{2} \quad (26)$$

Now, from Eq. (22),

$$\bar{W} = W_- + \frac{1}{2} \Delta W$$

Hence, Eq. (26) becomes

$$\int_{x_s}^1 C(x, \xi) \frac{\Delta W(\xi)}{U} d\xi = \ell(x) - \frac{\gamma}{2} \quad (27)$$

where

$$\ell(x) = -\frac{1}{2} \int_0^1 \Gamma_K(x, \xi) \frac{W_-(\xi)}{U} d\xi \quad (28)$$

$$C(x, \xi) = A(x-\xi) + \frac{1}{4} \Gamma_K(x, \xi) \quad (29)$$

Note that ΔW has been set to zero over the attached flow portion of the airfoil ($0 < x < x_s$) as assumed earlier. It is seen from Eq. (28) that the function $\ell(x)$ is actually proportional to the pressure differential for attached (i.e. nonseparated) flows, i.e.,

$$\ell(x) = -\frac{1}{2} \frac{\Delta p_{NS}(x)}{\rho U^2} \quad (30)$$

III. Formulas

This section presents the mathematical expressions and formulas required for airload calculations. Only key results are given here. For more details, the reader is referred to Reference 17.

Kernel Functions

The kernel functions K and A need to be calculated by Fourier inversions of K^* and A^* given in Eqs. (19) and (20). Physically, K is the upwash due to an impulse pressure differential; A is the perturbation pressure due to an impulse averaged upwash. Usually, K is called the lifting kernel, and A the nonlifting kernel. Analytical inversion results are given by the following formulas.

The lifting kernel $K(x)$ is simply the well known Poisson's kernel which contains a singular part K_s and a regular part, K_c :

$$K(x) = K_s(x) + K_c(x)$$

where

$$K_s(x) = \frac{\beta}{2\pi x} - \frac{i}{2\pi\beta} \frac{\omega}{U} \ln \left| \frac{\omega x}{U} \right|$$

$$K_c(x) = -\frac{\omega}{U} \frac{1}{4\beta} \left\{ \left[e^{i \frac{M^2}{\beta^2} \frac{\omega x}{U}} i M \operatorname{sgn}(x) \right] \right.$$

$$H_1^{(2)} \left(\frac{M}{\beta^2} \left| \frac{\omega x}{U} \right| \right) + \frac{2\beta^2}{\pi} \frac{U}{\beta x} \left. \right\}$$

$$- \left[e^{i \frac{M^2}{\beta^2} \frac{\omega x}{U}} H_0^{(2)} \left(\frac{M}{\beta^2} \left| \frac{\omega x}{U} \right| \right) + i \frac{2}{\pi} \ln \left| \frac{\omega x}{U} \right| \right]$$

$$+ i\beta^2 e^{-i \frac{\omega x}{U}} \left[\frac{2}{\pi\beta} \ln \frac{1+\beta}{M} + \int_0^{\frac{1}{\beta^2} \frac{\omega x}{U}} e^{-iu} H_0^{(2)}(M|u|) du \right]$$

The nonlifting kernel $A(x)$ also contains a singular part and a regular part.

$$A(x) = A_s(x) + A_c(x)$$

where

$$A_s(x) = \frac{-1}{2\pi\beta x} - \frac{i}{2\pi\beta^3} \frac{\omega}{U} \ln \left| \frac{\omega x}{U} \right|$$

$$A_c(x) = \frac{1}{4\beta^3} \frac{\omega}{U} \left\{ \left[e^{i \frac{M^2}{\beta^2} \frac{\omega x}{U}} H_0^{(2)} \left(\frac{M}{\beta^2} \left| \frac{\omega x}{U} \right| \right) + i \frac{2}{\pi} \ln \left| \frac{\omega x}{U} \right| \right] \right.$$

$$+ \left[e^{i \frac{M^2}{\beta^2} \frac{\omega x}{U}} i M \operatorname{sgn}(x) + H_1^{(2)} \left(\frac{M}{\beta^2} \left| \frac{\omega x}{U} \right| \right) + \frac{2}{\pi} \beta^2 \frac{U}{\omega x} \right] \left. \right\}$$

Inversion Kernel $\Gamma_K(x, \xi)$

If any two basic solutions of Eq. (21) are known, the inversion kernel can be written as follows.

$$\Gamma_K(x, \xi) = P_0(1-\xi)P_1(x) - \frac{\partial G(x, \xi)}{\partial \xi}$$

where

$$\frac{\partial G(x, \xi)}{\partial \xi} = [A_1 + 2A_2(\xi-x)]G_{01}(x, \xi)$$

$$+ [A_0 + A_1(\xi-x) + A_2(\xi-x)^2] \frac{\partial G_{01}(x, \xi)}{\partial \xi}$$

$$+ B_1 Q_1(x) Q_1(\xi)$$

$$+ [B_0 + B_1(\xi-x)] Q_1(x) \frac{\partial Q_1(\xi)}{\partial \xi}$$

$$- C_0 Q_2(x) \frac{\partial Q_2(\xi)}{\partial \xi}$$

$$G_{01}(x, \xi) = 2 \ln \left| \frac{\sqrt{\frac{1-\xi}{\xi}} + \sqrt{\frac{1-x}{x}}}{\sqrt{\frac{1-\xi}{\xi}} - \sqrt{\frac{1-x}{x}}} \right|$$

$$\frac{\partial G_{01}(x, \xi)}{\partial \xi} = \frac{2}{x-\xi} \cdot \frac{x(1-x)}{\xi(1-\xi)}$$

$$Q_1(x) = 2 \sqrt{x(1-x)}$$

$$Q_2(x) = 4(2x-1) \sqrt{x(1-x)}$$

$$\frac{\partial Q_1(\xi)}{\partial \xi} = \frac{1-2\xi}{\sqrt{\xi(1-\xi)}}$$

$$\frac{\partial Q_2(\xi)}{\partial \xi} = 4 Q_1(\xi) - 2(1-2\xi) \frac{\partial Q_1(\xi)}{\partial \xi}$$

$$A_0 = d_{01} + d_{03} + d_{23} - d_{12}$$

$$A_1 = 4(2d_{13} - d_{02})$$

$$A_2 = 16 d_{03}$$

$$B_0 = 4 d_{12} - 4 d_{23} - 8 d_{03}$$

$$B_1 = -16 d_{13}$$

$$C_0 = 2 d_{23}$$

$$d_{ij} = (\hat{b}_i \hat{b}_j - b_i b_j) / [\pi(b_0 - \hat{b}_0)]$$

$$b_0 = \frac{\alpha_0}{2} + \frac{\alpha_1}{8} + \frac{\alpha_2}{16} \quad \hat{b}_0 = \frac{\hat{\alpha}_0}{2} + \frac{3}{8} \hat{\alpha}_1 + \frac{5}{16} \hat{\alpha}_2$$

$$b_1 = -\frac{\alpha_0}{2} + \frac{\alpha_2}{32} \quad \hat{b}_1 = \frac{\hat{\alpha}_0}{2} + \frac{\hat{\alpha}_1}{2} + \frac{15}{32} \hat{\alpha}_2$$

$$b_2 = -\frac{\alpha_1}{8} - \frac{\alpha_2}{16} \quad \hat{b}_2 = \frac{\hat{\alpha}_1}{8} + \frac{3}{16} \hat{\alpha}_2$$

$$b_3 = -\frac{\alpha_2}{32} \quad \hat{b}_3 = \frac{\hat{\alpha}_2}{32}$$

$$\alpha_n = 2 a_n$$

$$\hat{\alpha}_n = -2 \hat{a}_n$$

Here a_n and \hat{a}_n are defined as follows:

$$P_1(x) = 2 \sqrt{\frac{1-x}{x}} \sum_{n=0}^{N-1} a_n x^n$$

$$\hat{P}_1(x) = -2 \sqrt{\frac{1-x}{x}} \sum_{n=0}^{N-1} \hat{a}_n x^n$$

where N is the number of pressure modes. The constant coefficients a_n and \hat{a}_n are chosen so that $P_1(x)$ and $\hat{P}_1(x)$ satisfy the following equations at N collocation points:

$$\int_0^1 K(x-\xi) P_1(\xi) d\xi = 1 \quad P_1(1) = 0$$

$$\int_0^1 K(x-\xi) \hat{P}_1(\xi) d\xi = 1 \quad \hat{P}_1(0) = 0$$

Finally, the eigensolution $P_0(x)$ is defined as

$$P_0(x) = \frac{P_1(x) - \hat{P}_1(x)}{\pi(b_0 - \hat{b}_0)}$$

so that

$$\int_0^1 P_0(x) dx = 1$$

Solution for Wake Upwash $\Delta W(x)$

The wake upwash solution depends on the trailing edge upwash condition imposed. Here, we discuss the solution procedures that produce the best correlation with test data. More discussion on this issue is given in Section IV. In Eq. (27) the new kernel function $C(x, \xi)$ has a predominant Cauchy type of singularity at $\xi = x$, and has a square root type of singularity at $\xi = 1$. To render the integral equation (27) to a purely Cauchy type integral equation, we write

$$\int_{x_s}^1 \frac{1}{\sqrt{1-\xi}} C(x, \xi) \left[\frac{\Delta W(\xi)}{U\sqrt{1-\xi}} \right] d\xi = \ell(x) - \frac{\gamma}{2}$$

Furthermore, from Eq. (30) $\ell(x) \sim \frac{1}{\sqrt{x}}$ as $x \rightarrow 0$. To arrive at a regular forcing function, we write

$$\int_{x_s}^1 \left[\sqrt{x(1-\xi)} C(x, \xi) \right] \left[\frac{\Delta W(\xi)}{U\sqrt{1-\xi}} \right] d\xi = \sqrt{x} \left(\ell(x) - \frac{\gamma}{2} \right) \quad (31)$$

This purely Cauchy type integral equation has the following solution:

$$\frac{\Delta W(\xi)}{U\sqrt{1-\xi}} = \sqrt{1-\xi^*} \sum_{n=1}^N a_n^W \xi^{*n-3/2} \quad (32)$$

where

$$\xi^* \equiv (\xi - x_s)/(1-x_s).$$

Here, we have imposed the condition $\Delta W(1) = 0$ consistent with the boundary condition $\Delta W(x) = 0$, for $x > 1$, for a smooth trailing edge flow. Therefore,

$$\frac{\Delta W(\xi)}{U} = \frac{1-\xi}{\sqrt{1-x_s}} \sum_{n=1}^N a_n^W \xi^{*n-3/2} \quad (33)$$

Substitution of Eq. (32) into the left-hand side of Eq. (31) gives

$$\sum_{n=1}^N a_n^W E_n(x) = \sqrt{x} \left[\ell(x) - \frac{\gamma}{2} \right] \quad (34)$$

where

$$E_n(x) = \int_{x_s}^1 \sqrt{x(1-\xi)} C(x, \xi) \sqrt{1-\xi^*} \xi^{*n-3/2} d\xi$$

Given $\ell(x)$ from Eq. (30), one can solve Eq. (34) by the collocation method to obtain a_n^W . Then Eq. (33) gives the desired $\Delta W(x)$.

Lift and Moment Formulas

The pressure differential solution of Eq. (23) can be written as

$$\Delta p(x) = \Delta p_{NS}(x) + \Delta p_{COR}(x)$$

where

$\Delta p_{NS}(x)$ = pressure differential as if no flow separation occurs

$$= \rho U^2 \int_0^1 \Gamma_K(x, \xi) \frac{\bar{w}_{NS}}{U}(\xi) d\xi$$

$\Delta p_{COR}(x)$ = additional pressure differential contribution due to flow separation or flow separation correction pressure

$$= \rho U^2 \int_{x_s}^1 \frac{1}{2} \Gamma_K(x, \xi) \frac{\Delta W(\xi)}{U} d\xi$$

Consequently, the lift and moment (about $x = x_0$) coefficients are both sums of a nonseparated flow part and a separation correction part.

$$C_L = \frac{-\int_0^1 \Delta p(x) dx}{\frac{1}{2} \rho U^2 c} = C_{LNS} + C_{LCOR}$$

$$C_M = \frac{\int_0^1 (x-x_0) \Delta p(x) dx}{\frac{1}{2} \rho U^2 c^2} = C_{MNS} + C_{MCOR}$$

where

$$C_{LNS} = -4 \sum_{j=1}^N a_j f_j$$

$$C_{MNS} = x_0 C_{LNS} - 4 \sum_{j=1}^N a_j f_{j+1}$$

$$C_{LCOR} = -2 \sum_{i=1}^N a_i^W \sum_{j=1}^N e_j (1-x_s)^j I_{ij}$$

$$C_{MCOR} = x_0 C_{LCOR} + 2 \sum_{i=1}^N a_i^W \sum_{j=1}^N (e_j - r_j) (1-x_s)^j I_{ij}$$

$$I_{ij} = \int_0^1 z^{j-3/2} (1-z)^{j-1/2} [x_s + (1-x_s)z]^{1/2} dz$$

$$f_j = \frac{\sqrt{\pi}}{2} \frac{\Gamma(j-1/2)}{\Gamma(j+1)}$$

$$f_{j+1} = \frac{j-1/2}{j+1} f_j$$

For leading-edge separation ($x_s = 0$), we have the

following simpler formulas:

$$C_{L\text{COR}} = -2 \sum_{i=1}^N a_i^w \sum_{j=1}^N e_j B_{ij}$$

$$C_{M\text{COR}} = x_0 C_{L\text{COR}} + 2 \sum_{i=1}^N a_i^w \sum_{j=1}^N (e_j - r_j) B_{ij}$$

where the beta function is defined as

$$B_{ij} = \frac{\Gamma(i)\Gamma(j+1/2)}{\Gamma(i+j+1/2)}$$

The coefficients a_j 's are the coefficients of nonseparated flow pressure expansion

$$\frac{\Delta p(x)}{\rho U^2} = 2 \sqrt{\frac{1-x}{x}} \sum_{j=1}^N a_j x^{j-1}$$

as a solution of Eq. (21). The coefficient a_j^w 's are the upwash coefficients in Eq. (33). The coefficients e_j 's and r_j 's are coefficients of expansions of two elementary solutions $P_1(x)$ and $P_2(x)$ that satisfy the leading edge kutta condition and the following singular integral equations.

$$\int_0^1 K(x-\xi) P_1(\xi) d\xi = 1 \quad P_1(1) = 0$$

$$\int_0^1 K(x-\xi) P_2(x) d\xi = x \quad P_2(1) = 0$$

$$P_1(x) = 2 \sqrt{\frac{1-x}{x}} \sum_{n=1}^N e_n x^{n-1}$$

$$P_2(x) = 2 \sqrt{\frac{1-x}{x}} \sum_{n=1}^N r_n x^{n-1}$$

IV. Remarks on Wake Upwash Solution $\Delta W(x)$

The wake upwash solution $\Delta W(x)$ of the singular integral equation, Eq. (27), is not unique unless one specifies enough constraints to the behavior of the upwash solution $\Delta W(x)$ a priori. A physically meaningful way to specify the constraints is to compare experimental lift and/or moment coefficients with theoretical prediction results assuming various types of constraints. This strategy of specifying constraints was used in Reference 16 in studying stalled airloads for cascade blades. The same constraints on the wake upwash function $\Delta W(x)$ are used in this report for isolated airfoils. These constraints require that the wake upwash $\Delta W(x)$ vanishes at the airfoil trailing edge and the wake upwash function $\Delta W(x)$ is differentiable at the airfoil trailing edge. See Eq. (32) for these constraints.

Another possible choice of constraints is to still impose the constraint of zero wake upwash at the trailing edge, $\Delta W(1) = 0$, but to assume a

square-root type wake upwash near the trailing edge, $\Delta W(x) \sim \sqrt{1-x}$. This choice of constraints does not yield good correlations between calculated and experimental data on force coefficients but it does result in force coefficients close to the theoretical results of Woods¹² and Perumal and Sisto¹⁴. It should be noted that both Woods and Perumal and Sisto assume a zero unsteady pressure not only over the airfoil surface where separation region exists but also within the wake region extending to downstream infinity. On the other hand, the separated flow theory presented in this paper assumes a constant unsteady pressure (chosen as zero in all calculations, however) over the airfoil surface where flow separation exists just as Woods¹² and Perumal and Sisto¹⁴ do but specifies a pressure continuity condition $\Delta p = 0$ across the wake boundary instead.

Based on the above discussion and the calculated results to be discussed in Section V, it appears that the assumption of zero pressure in the wake region behind the trailing edge is not physically justifiable. The present theory assuming a differentiable wake upwash function and a pressure continuity behind the trailing edge, however, yields good correlation with test data and therefore appears physically correct. The closeness between (a) the solution by assuming a zero pressure in the wake region behind the trailing edge and (b) the solution based on present theory assuming a square-root type wake upwash near the trailing edge is simply fortuitous.

V. Results

The discussion of the calculated results are divided into two parts. In the first part, comparisons are made between the results based on the present theory and other theories. In the second part, experimental data are used to validate the present theory.

1. Comparison with other theories - solution based on square-root type wake upwash near trailing edge. For a thin blade in a zero Mach number flow that separates at 60 percent chord on the upper surface, Figs. 2 through 5 show the real and imaginary parts of the calculated lift and moment coefficients for a pitching oscillation about the leading edge in the reduced frequency range from 0 to 1.0. Also shown in these figures are the corresponding force coefficients predicted by attached flow flat plate theory. Flow separation is seen to reduce the magnitudes of the airloads over the entire frequency range and tends to destabilize the pitching motion as seen in Fig. 5. The predicted imaginary parts of the lift and moment coefficients agree well with those of Perumal¹⁴ and Woods¹². This agreement however, does not imply that a physically meaningful prediction has been made as was discussed in Section IV. A successful prediction should be based on good correlations with test data from carefully performed experiments.

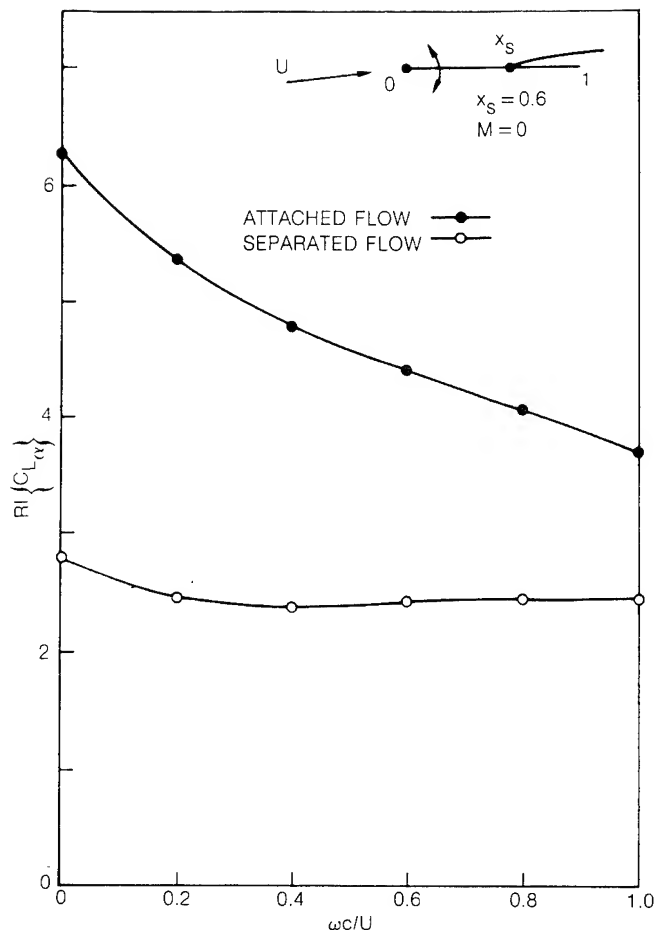


Fig. 2 Real Part of Lift Coefficient Due to Pitching Motion About Leading Edge

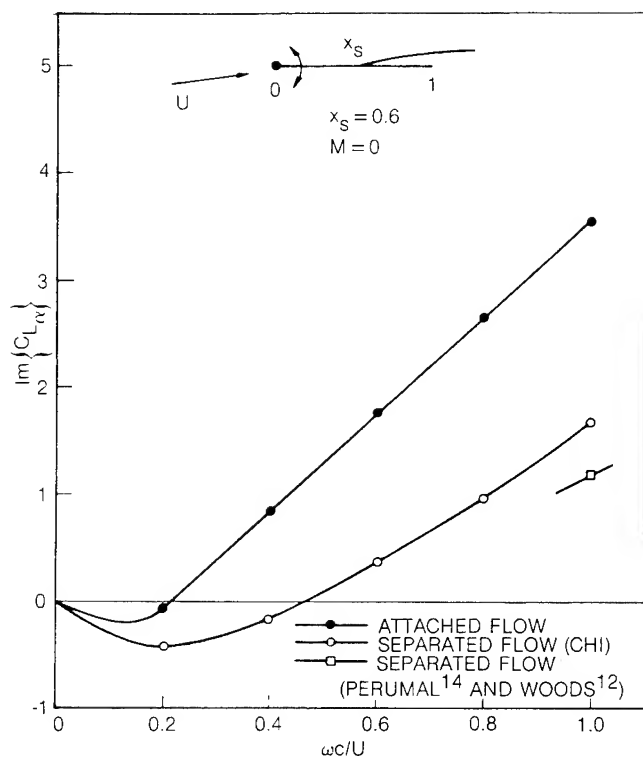


Fig. 3 Imaginary Part of Lift Coefficient Due to Pitching Motion About Leading Edge

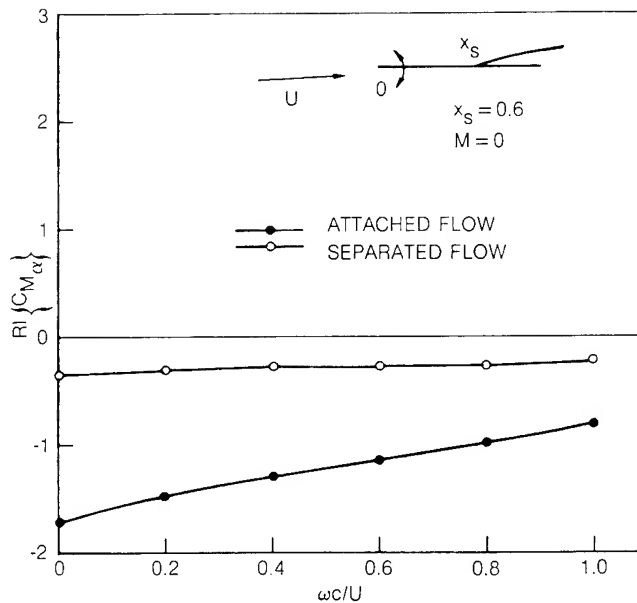


Fig. 4 Real Part of Moment Coefficient Due to Pitching Motion About Leading Edge

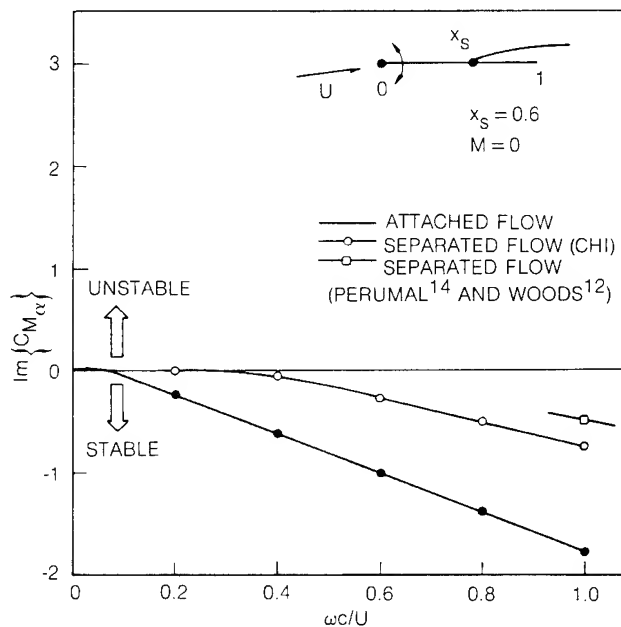


Fig. 5 Imaginary Part of Moment Coefficient Due to Pitching Motion About Leading Edge

2. Comparison with Experimental Damping - Solution based on differentiable wake upwash at the trailing edge. Lemnios²⁰ performed excellent aeroelastic tests of NACA 16-series airfoil sections for Hamilton Standard 18A20 propeller blade and Curtiss-Wright 109640 propeller blade. The blade sections are as shown in Fig. 6. The aerodynamic damping (i.e., negative of the moment coefficient for pitching motion) data for the thinnest section 16 (070)(023) of Hamilton Standard 18A20 propeller blade are used to evaluate the present theory. In Figs. 7 and 8, the measured aerodynamic dampings for a small amplitude pitching oscillation about the midchord at various mean angle of attack are compared to the classical attached flow results and

HAMILTON STANDARD 18A20
PROPELLER BLADE

CURTISS-WRIGHT 109640
PROPELLER BLADE

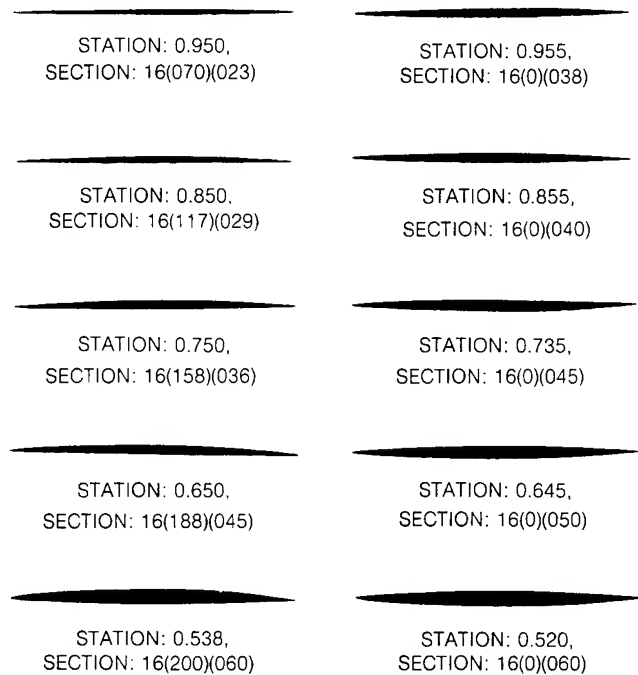


Fig. 6 Profiles of NACA 16-Series Airfoils

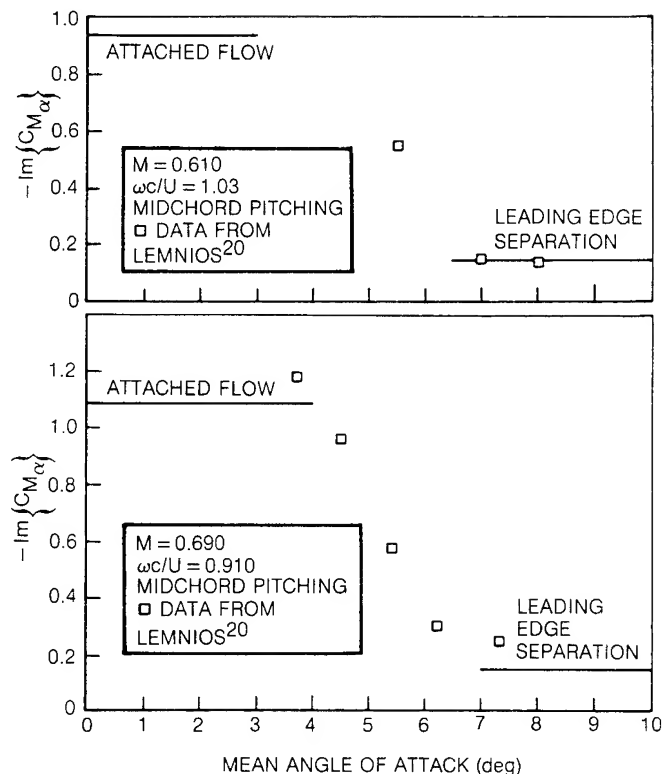


Fig. 8 Torsional Aerodynamic Damping for
16(070)(023) of HS 18A20 Propeller

the separated flow results (assuming leading edge flow separations) for four sets of Mach number-reduced frequency combinations.

The leading edge separation results appear to represent the asymptotic damping at large angles of attack in all cases. The correlation between theory and experiment here is very encouraging. The test data for intermediate angles of attack can probably be correlated with the separated flow unsteady aerodynamic theory by varying the flow separations point along the airfoil chord. This idea has not been explored further because of the lack of clear criteria to determine the flow separation point. However, by comparing theoretical calculations for various flow separation points with test data, promising flow separation criteria probably can be generated for flutter prediction purposes.

To illustrate the force coefficients for a given Mach number over a wide frequency range, the lift and moment coefficients for a midchord pitching airfoil in a subsonic flow with Mach number 0.8 are shown in Figs. 9 through 12 for both the attached flow and the leading edge separated flow. The pitch damping is seen to decrease as separation is introduced in Fig. 12. Meanwhile, a positive imaginary part of the lift coefficient due to pitching motion is predicted for separated flow as shown in Fig. 10. This implies that the bending component in a blade mode shape could be driven into instability by the destabilizing lift force due to the torsional component of the blade mode shape if leading edge flow separation occurs.

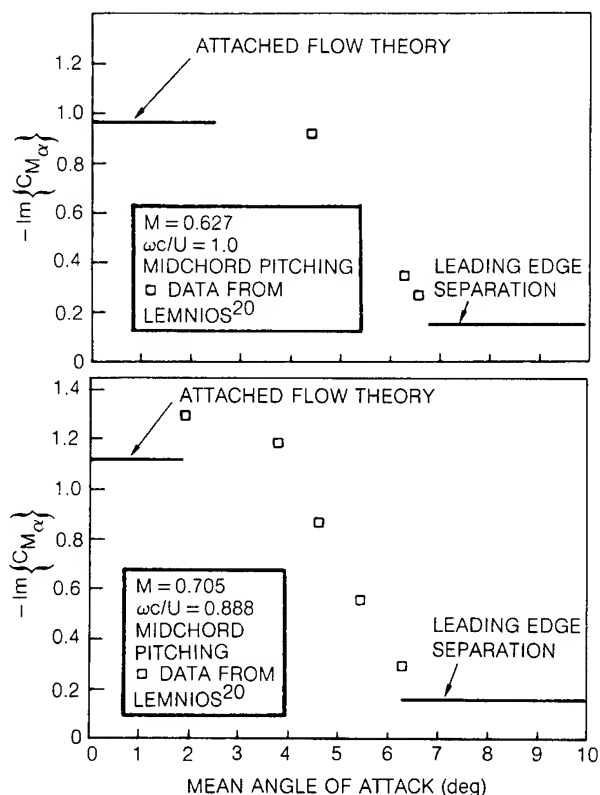


Fig. 7 Torsional Aerodynamic Damping for
16(070)(023) of HS 18A20 Propeller

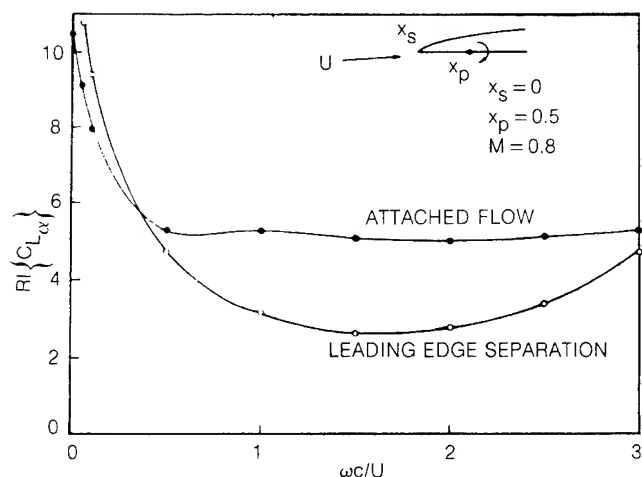


Fig. 9 Real Part of Lift Coefficient Due to Pitching Motion About Midchord

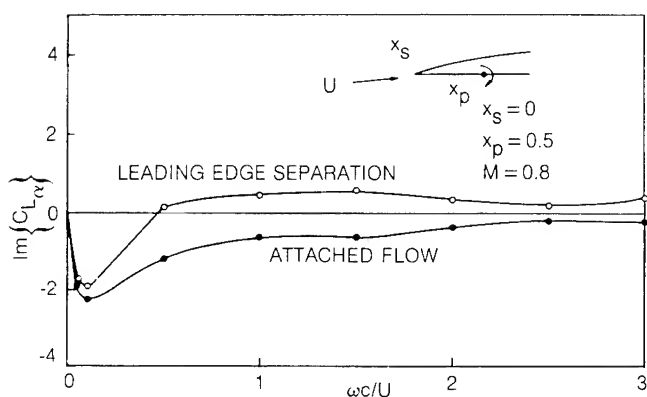


Fig. 10 Imaginary Part of Lift Coefficient Due to Pitching Motion About Midchord

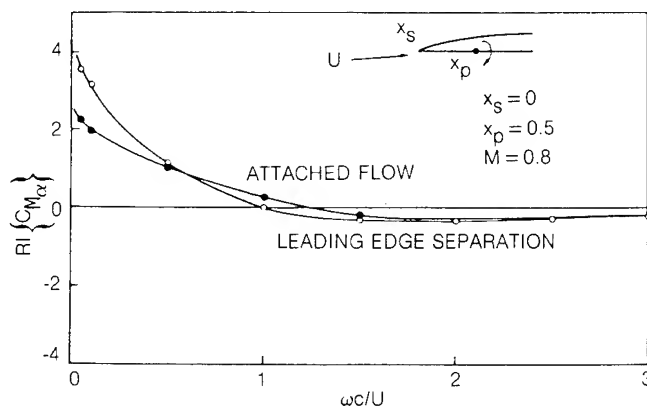


Fig. 11 Real Part of Moment Coefficient Due to Pitching Motion About Midchord

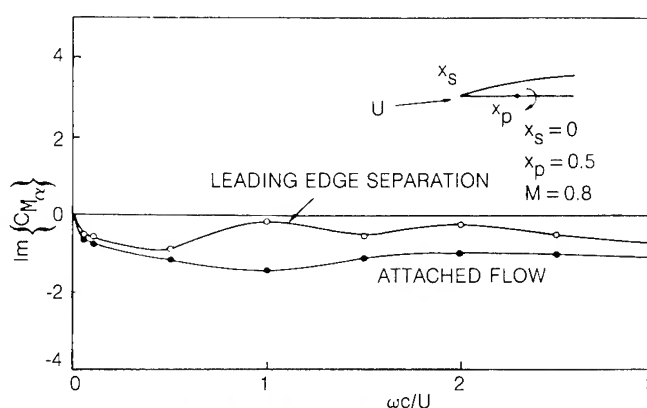


Fig. 12 Imaginary Part of Moment Coefficient Due to Pitching Motion About Midchord

VI. Conclusions and Recommendations

A relatively simple two-dimensional linear unsteady aerodynamic theory has been developed to take into account the effect of flow separation on unsteady airloads for thin airfoils oscillating in a subsonic airstream approximately. The theory is essentially a modification of the classical potential flow unsteady aerodynamic theory. The modification involves the specification of a constant (usually taken as zero) pressure in the flow separation zone along the blade surface. As a result, the upwash velocity of the separating streamline is solved as part of the problem solution. Proper constraints on the upwash velocity of the separating streamline are imposed based on the correlation between calculated and experimental aerodynamic damping data for thin airfoil sections. Two different types of upwash velocity constraints were studied. One type of constraint requires a square-root type behavior near the airfoil trailing edge and is shown to resemble closely the earlier theories of Woods, Perumal and Sisto which assume a zero pressure on the separated airfoil surface as well as the wake region behind the airfoil trailing edge. This type of constraint however, does not yield results con-

sistent with available test data. The other type of constraint requires the differentiability of the wake upwash velocity near the trailing edge and yields theoretically calculated torsional damping values in good agreement with test data of Lemnios for thin airfoils used in typical propeller designs.

The present theory assumes that the flow separation point is known either from theory or experiment. A separate theory to predict the flow separation point must be based on viscous models involving boundary layer considerations. On the other hand, experimental verification of flow separations would involve flow visualizations. Both approaches require substantial amounts of effort, but the experimental approach appears most direct in producing flow separation information as input to the present unsteady aerodynamic theory for separated flows.

For supercritical flows, the existence of shock waves is a distinct feature of the flow field and the shock movement associated with blade motion may be the major contributing mechanism to the unsteady airload. Furthermore, for high angle-of-attack flows, the effects of shock waves and flow

separations on unsteady airloads are likely to be equally important. An extension of the present separated flow theory to include shock waves appears possible and potentially significant for airfoil flutter design applications to supercritical flight conditions.

Acknowledgement

This work was sponsored by the Hamilton Standard Division and the United Technologies Research Center of the United Technologies Corporation.

References

1. Williams, L. J., Small Transport Aircraft Technology, NASA SP460, 1983.
2. Lubomski, J. F., SR5-10 Way Strain Gage Data, Personal Notes, 1982.
3. Smith, A. M. O., "Remarks on Fluid Mechanics of the Stall," Aircraft Stalling and Buffeting, AGARD-LS-74.
4. Ericsson, L. E. and Reding, J. P., "Unsteady Airfoil Stall, Review and Extension," AIAA Journal, Vol. 8, No. 8, August 1981, pp. 609-616.
5. Ericsson, L. E. and Reding, J. P., "Analytic Prediction of Dynamic Stall Characteristics," AIAA Paper No. 72-682, AIAA 5th Fluid and Plasma Dynamics Conference, Boston, Massachusetts, June 26-28, 1972.
6. Ericsson, L. E., "Dynamic Effects of Shock-Induced Flow Separation," Journal of Aircraft, Vol. 12, No. 2, February 1975.
7. Ericsson, L. E. and Reding, J. P., "Effect of Angle of Attack and Mach number on Slender Wing Aerodynamics," AIAA Paper 77-667, AIAA 10th Fluid and Plasmadynamics Conference, Albuquerque, New Mexico, June 27-29, 1977.
8. Kandil, O. A., Mook, D. T., and Nayfeh, A. H., "Effect of Compressibility on the Nonlinear Prediction of the Aerodynamic Loads on Lifting Surfaces," AIAA Paper 75-121, AIAA 13th Aerospace Sciences Meeting, Pasadena, California, January 20-22, 1975.
9. Kandil, O. A., Chu, L. C., and Yates, G. C., Jr., "Hybrid Vortex Method for Lifting Surfaces with Free Vortex Flow," AIAA Paper 80-0070, AIAA 18th Aerospace Sciences Meeting, Pasadena, California, January 14-16, 1980.
10. Kandil, O. A., Chu, L. C., and Tureaud, T., "Steady and Unsteady Nonlinear Hybrid Vortex Method for Lifting Surfaces at Large Angle of Attack," AIAA Paper 82-0351, AIAA 20th Aerospace Sciences Meeting, Orlando, Florida, January 11-14, 1982.
11. Kandil, O. A., "A Technique for Three-Dimensional Compressible Flow Past Wings at High Angles of Attack," AIAA Paper 83-2078, AIAA Atmospheric Flight Mechanics Conference, Gatlinburg, Tennessee, August 15-17, 1981.
12. Woods, L. C., "Aerodynamic Forces on An Oscillating Aerofoil Fitted With a Spoiler," Proc. Roy. Soc. London, Series A, No. 239, pp. 328-337, 1957.
13. Wu, T. Yao-Tsu, "A Wake Model for Free-Streamline Flow Theory, Part 1. Fully and Partially Developed Wake Flows and Cavity Flows Past An oblique Flat Plate," J. of Fluid Mechanics, Vol. 13, 1962, pp. 161-181.
14. Perumal, P. V. K. and Sisto, F., "Lift and Moment Prediction For An Oscillating Airfoil with a Moving Separation Point," ASME Transactions, October 1974, pp. 372-378.
15. Dowell, E. H., "A Simplified Theory of Oscillating Airfoils in Transonic Flow: Review and Extension," AIAA Paper 77-445, March 1977.
16. Chi, R. M., "Unsteady Aerodynamics in Stalled Cascade and Stall Flutter Prediction," ASME Paper 80-C2/Aero-1, 1980.
17. Chi, R. M., "Separated Flow Unsteady Aerodynamics for Propfan Applications," UTRC Report R83-356891-1, July 1983.
18. Williams, M. H., "The Inversion of Singular Integral Equations by Expansion in Jacobi Polynomials," 8th U.S. Congress of Applied Mechanics, L. A. California, June 1978.
19. Williams, M. H., "The Resolvent of Singular Integral Equations," Quarterly of Applied Mathematics, April 1977, pp. 99-110.
20. Lemnios, A. Z., "Aerodynamic Damping Tests of Propeller Blade Airfoil Sections," United Aircraft Research Laboratory Report R-0997-1, October 1957.

Modeling of Unsteady Small Disturbance Transonic Flow
Using Parametric Differentiation,
Pseudospectral Analysis and Finite-Differencing

Melvin Brown*
Wesley L. Harris†

Massachusetts Institute of Technology
Cambridge, Massachusetts 02139

Abstract

A procedure for solving the nonlinear unsteady small disturbance transonic equation is formulated. This procedure is a synthesis of a pseudospectral method, parametric differentiation, and finite differencing. It is equally applicable to lifting and nonlifting airfoils. The procedure is particularly well suited to aeroelastic stability studies that may require a set of affine solutions.

Acknowledgements

This study was supported in part by the Office of Naval Research contract N00014-82-k-0311 and the National Aeronautics and Space Administration grant NAG 1-60.

Nomenclature

$\Phi(X, Z, T)$	disturbance potential
$\phi(X, Z)$	mean disturbance potential
$\psi(X, Z, T)$	unsteady component of potential
g, \hat{g}, \tilde{g}	parametric derivatives of potentials
$C_p(X, Z, T)$	pressure coefficient
$F_1(X)$	thickness distribution
$F_2(X)$	lifting distribution
$F_3(X, T)$	distribution of unsteady disturbance
τ	thickness ratio (normalized to chord)
α	mean camber or angle of incidence
K	reduced frequency ($U\Omega/\text{Chord}$)
δ	amplitude of unsteady motion
γ	ratio of specific heats
M	freestream Mach number
U	freestream velocity
(X, Z)	cartesian coordinates
(ξ, η)	stretched coordinates
(X_c, Z_c)	collocation (Chebyshev) coordinates
$[\]$	a discontinuous change
Subscripts	
∞	freestream value
s	shock value
te	trailing edge
Le	Leading edge

*Graduate Research Assistant, Dept. of Physics.

†Professor, Dept. of Aeronautics and Astronautics. Member AIAA.

1. Introduction

Unsteady Transonics and the Small Disturbance Model

The small disturbance transonic equation is of significance to researchers concerned with the behavior of compressible fluids with embedded shock waves (see the review by Ballhaus)¹. The unsteady small disturbance transonic equation is capable of modeling mixed flows with weak shocks. The assumption of small disturbances permits one to use a linearized version of the exact boundary conditions. This model is ideally suited to the study of aerodynamic phenomena like transonic flutter. In order to map stability boundaries one would typically need a mean (or steady) solution about which the effects of perturbations could be computed. Various numerical methods have been used to study this equation, for a variety of physical situations.^{1,2}

Parametric Differentiation

The method of parametric differentiation (MPD), has been shown to be a very effective tool in the study of transonic phenomena.^{3,4,5,6} It has been combined with a number of analytical and numerical techniques. It is also used in fields as diverse as acoustics and nuclear engineering. To use MPD, one first nondimensionalizes the governing equations and associated boundary conditions. The resulting equations are differentiated with respect to the parameter of interest. Some typical aerodynamic parameters are Mach number, Reynolds number, angle of incident flow, thickness ratio, and reduced frequency. For transonic airfoils the lifting and nonlifting MPD versions of the transonic small disturbance equation are identical. Hence the method may be used to study both types of flow. In this study we have considered three parameters. They are the airfoil maximum thickness to chord ratio τ , the incident mean flow angle α and the amplitude of unsteady displacements, δ . Results have been reported for MPD combined with a relaxation procedure,⁶ with an approximate factorization procedure (ADI)³ and with an extended integral equation method.⁴ We now seek to combine the MPD with finite differencing in time and a pseudospectral spatial derivative calculator. This represents a novel use of mathematical techniques to solve the unsteady nonlinear transonic small disturbance equations.

Spectral Methods

The interest in spectral and pseudospectral methods has increased steadily over the past decade. This is due primarily to the invention of transform methods.⁷

The analysis of one dimensional model problems has been very encouraging. Spectral methods typically require substantially fewer gridpoints to obtain the same level of accuracy as a 2nd or 4th order finite difference scheme. This means a substantial saving in CPU time can be realized for systems that require a high degree of spatial resolution. The emphasis has now shifted to the solution of multidimensional problems in complex geometries with nontrivial boundary conditions. For higher dimensional problems one has the choice of a full spectral decomposition or a mixed spectral finite difference approach. The transonic codes LTRAN2 and GTRAN2^{8,9} typically require grids on the order of 100x80. Our experiments with a 33x33 Chebyshev grid indicate this is sufficient when combined with proper coordinate stretching. Chebyshev polynomials are used in this study. Other popular choices of basis functions are Fourier series, Bessel functions and sine series.

Another advantage of using a pseudospectral method is the possibility of employing only the analytic boundary conditions of the original problem. Thus the problems associated with non-physical computational modes and the formulation of additional computational boundary conditions may be avoided.

Further details on the theory and application of spectral methods may be found in^{10,11,12,13}.

2. Statement of the Problem

The Unsteady Small Disturbance Transonic Equation and Boundary Conditions

The unsteady small disturbance transonic equation is stated below, Eq. (1), a complete derivation may be found in¹⁴.

$$A \phi_{tt} + B \phi_{xt} = C \phi_{xx} + \phi_{zz} \quad (1)$$

$$A = K^2 M^2 \quad (2)$$

$$B = 2KM^2 \quad (3)$$

$$C = 1 - M^2 - M^{2b}(\gamma + 1) \phi_x \quad (4)$$

Equation (5) gives the position of airfoil surfaces:

$$0 = Z - \{ \pm \tau F_1(X) + \alpha F_2(X) + \text{Re}(\delta e^{iKt}) \} \quad (5)$$

The associated boundary conditions express the requirements of zero pressure differential at the trailing edge (assumed to be subsonic), and along the wake, Eq. (6). The normal velocity component is required to be continuous across the wake, Eq. (7). The fluid flow is tangent to the mean airfoil position, Eq. (8).

$$2 [\phi_x + \phi_t] = 0 \quad (6)$$

$$[\phi_z] = 0 \quad (7)$$

$$\phi_z^\pm = \pm \tau F_{1x}(X) + \alpha F_{2x}(X) + \text{Re} [\delta(F_{3x} + iKF_3)e^{iKt}] \quad (8)$$

When shockwaves are present, jump conditions at the shock boundary are obtained by integrating Eq. (1) across the shock boundary. All coordinates have been normalized to the chord length.

MPD Version of the Small Disturbance Transonic Equation and Boundary Conditions

Let us consider the dependence of ϕ on $\epsilon = \{\tau, \alpha \text{ or } \delta\}$. The parametric rate of change of ϕ at any point in the domain is g .

$$\phi(\epsilon + \Delta\epsilon) = \phi(\epsilon) + \int_{\epsilon}^{\epsilon + \Delta\epsilon} g(\epsilon') d\epsilon' \quad (9)$$

The MPD version of Eqs. (1), (6) to (8) are given below

$$A g_{tt} + B g_{xt} = (C g_x)_x + g_{zz} \quad (10)$$

$$2 [g_x + g_t] = 0 \quad (11)$$

$$[g_z] = 0 \quad (12)$$

$$g_z = \begin{cases} \pm F_{1x}, & \epsilon = \tau \\ F_{2x}, & \epsilon = \alpha \\ \text{Re} \{(F_{3x} + iKF_3)e^{iKt}\}, & \epsilon = \delta \end{cases} \quad (13)$$

The reader should notice that g is governed by a linear equation with a single variable coefficient. The reader should further note that the explicit dependence of g on the choice of MPD parameter enters only when applying the boundary conditions. So that the primary relations Eq. (10) to Eq. (12) are equally applicable for $\epsilon = (\tau, \alpha, \delta)$. The essence of a procedure for solving Eq. (10) to Eq. (13) is outlined. A predictor-corrector procedure is used to advance $g(\epsilon, \tau)$ in time. A pseudospectral derivative operator is used to evaluate the X and Z derivatives. Once the solution for $g(\epsilon)$ has been integrated to a steady state, the potential, $\phi(\epsilon)$ is updated to $\phi(\epsilon + \Delta\epsilon)$ via predictor-corrector step involving $g(\epsilon)$ and $g(\epsilon + \Delta\epsilon)$.

It is of particular significance that the linear partial differential equation governing $\partial\phi/\partial\epsilon$ has the same variable coefficient as the nonlinear equation governing ϕ . It is through this coefficient that type dependent differencing is introduced into conventional finite difference codes. Consider the Murman-Cole switch. In a SLOR code the term $C\phi_{xx}$ is approximated by Eq. (14). The pseudospectral difference operator would replace the centered finite difference operator.

$$(1 - \mu_{i,j}) C_{i,j} \delta_{xx} \phi_{i,j} + \mu_{i-1,j} C_{i-1,j} \delta_{xx} \phi_{i-1,j} \quad (14)$$

$$\mu_{i,j} = \begin{cases} 0 & C_{i,j} > 0 \\ 1 & C_{i,j} < 0 \end{cases} \quad (15)$$

$$\delta_x \phi_{i,j} = (\phi_{i+1,j} - \phi_{i-1,j}) / (x_{i+1} - x_{j-1}) \quad (16)$$

From the equations in the previous section we see that several methods of implementation of MPD exist.

Equation (10) could be reduced further by decomposing g into $\hat{g} + \tilde{g}$ such that $|\hat{g}| \gg |\tilde{g}|$ (see 1,9). Equations (9 - 13) may be cleanly separated. The resulting equations are no more complicated than Eq. (10). We have chosen to remain with Eq. (10). Steady solutions are obtained by integrating to a steady state.

3. Numerical Implementation

The 2nd Order Predictor-Corrector for Advancing Thickness Ratio

The potential $\Phi(\epsilon+\Delta\epsilon)$ is first predicted with Eq. (17). This is put back into the differential equation to generate a $g(\epsilon+\Delta\epsilon)$. $\Phi(\epsilon+\Delta\epsilon)$ is then corrected with Eq. (18).

$$\Phi(\epsilon+\Delta\epsilon) = \Phi(\epsilon) + \Delta\epsilon g(\epsilon) \quad (17)$$

$$\Phi(\epsilon+\Delta\epsilon) = \Phi(\epsilon) + \Delta\epsilon/2 (g(\epsilon) + g(\epsilon+\Delta\epsilon)) \quad (18)$$

The Pseudospectral Derivative Calculator

The equations below give the essence of pseudospectral derivative calculator using Chebyshev polynomials in a single variable. In practice, the procedure for evaluating functions and coefficients should take into account the size of the expansion. Generally, transform methods are recommended for very large expansions. However, for expansions involving a small number of terms, direct evaluation and matrix inversions may be advised. The derivative coefficients may be evaluated by recursion.¹¹ Multidimensional derivatives are computed in similar fashion.

$$f_N(X_j, t) = \sum_{k=0}^N A_k(t) T_k(X_j) \quad (19)$$

$$A_k(t) = \frac{2}{N} \sum_{j=0}^N f_k(X_j, t) T_k(X_j) \quad (20)$$

$$\frac{df}{dX}(X_j) = \sum_{k=0}^N B_k T_k(X_j) \quad (21)$$

$$B_k = \sum_{\substack{p=k+1 \\ p+k - \text{odd}}}^N 2p A_p(t) \quad (22)$$

$$\sum_{j=0}^N a_j = \frac{1}{2} a_0 + \sum_{j=1}^{N-1} a_j + \frac{1}{2} a_N \quad (23)$$

The Coordinate System

Before the derivative operator can be applied the coordinates must be transformed to a computational set. The Chebyshev collocation coordinates are merely the zeroes of the $N+1$ Chebyshev polynomial as defined below in equations (24) and (25)

$$X_c(j) = \cos(j\pi/N), \quad j = 0, 1, 2, \dots, N \quad (24)$$

$$T_k(X_c(j)) = \cos(jk\pi/N) \quad (25)$$

We used Chebyshev functions in this study because there is no periodic structure. Because Fourier functions are generally easier to program, in addition to being eigenvalues of the operator d/dX , they are an excellent choice for problems with some sort of periodicity. It is sometimes feasible to subtract the nonperiodic components from an equation and use Fourier functions for the remainder.

Two types of coordinate systems are being investigated. One of them is the algebraic mapping shown in Eq. (27-28). Another employs a nonuniform coordinate stretching, developed by L.A. Carlson, shown in Eq. (27-31). The stretched system is typical of the type used in numerical transonic calculations. All derivatives are modified by the scale factors as shown in Eq. (32). The constants A_1, A_2, A_3, A_4 , and X_4 control the stretch rates and position of stretching transition point.

$$X_c = (2X - (X_{\max} + X_{\min})) / (X_{\max} - X_{\min}) \quad (26)$$

$$Z_c = (2Z - (Z_{\max} + Z_{\min})) / (Z_{\max} - Z_{\min}) \quad (27)$$

$$\eta = A_1 \tan(\pi Z_c / 2) \quad (28)$$

$$X = X_4 + A_2 \tan\left(\frac{\pi}{2}(\xi + \xi_4)\right) + A_3 \tan\left(\frac{\pi}{2}(\xi + \xi_4)^3\right) \text{ when } (-1 - \xi_4) < \xi < -\xi_4 \quad (29)$$

$$X = \xi \left[\left(\frac{6X_4 - A \pi \xi_4}{4\xi_4^2} \right) + \left(\frac{A \pi \xi_4 - 2X_4}{4\xi_4^3} \right) \xi^2 \right] \text{ when } -\xi_4 \leq \xi \leq \xi_4 \quad (30)$$

$$X = X_4 + A_2 \tan \left[\frac{\pi}{2} (\xi - \xi_4) \right] + A_3 \tan \left[\frac{\pi}{2} (5 - \xi_4)^3 \right] \xi_4 < \xi < 1 + \xi_4 \quad (31)$$

$$\frac{d}{dZ} = \frac{dZ_c}{dZ} \frac{d}{dZ_c} \quad (32)$$

The pseudospectral derivative operator is used to evaluate $\left(\frac{d}{dZ_c}\right)_{op}$.

The 2nd Order Predictor-Corrector for Advancing Time

Equation (33) is the basic expression we manipulate to evolve $g(t)$ in time. This expression is derived by expanding $g(t+\Delta t)$ in a Taylor series. We then use the original differential equation to replace all temporal derivatives of $g(t)$, with space derivatives of g . The replacement of temporal derivatives is desired because it permits us to take advantage of the higher accuracy of spectrally computed derivatives. In essence we are treating all spacial derivatives of a function as known quantities (given the original function). For details see Gazdag^{15,16}.

$$G^{m+1} = 2G^m - G^{m-1} - (\Delta t B / 2A) (G_x^{m+1} - G_x^{m-1}) + (\Delta t^2 / A) \text{Flux}(m) \quad (33)$$

$$\text{Flux}(m) = \{ (CG_x^m)_x + G_{zz}^m \} \quad (34)$$

The decomposition of Eq. (33) into predictor-corrector pairs is not unique (see Gazdag¹⁶). The contribution of individual components is modified to improve overall algorithm stability. Some possible modifications are shown in Eq. (35) and Eq. (36).

$$2G_{j,k}^m < = (1/2) \{ G_{j+1,k}^m + G_{j-1,k}^m + G_{j,k+1}^m + G_{j,k-1}^m \} \quad (35)$$

$$\text{Flux}(m) < = (1/2) \{ \text{Flux}(m) + \text{Flux}(m+1) \} \quad (36)$$

$\text{Flux}(m+1)$ is computed from the predicted $G(M+1)$.

There is a severe time stepsize restriction associated with the Chebyshev representation. One way to circumvent this restriction is to use an implicit algorithm. A second method employs the use of bounded approximations to the terms $(B\Delta t/2A)$ and $(\Delta t^2/A)$. These approximations reduce to the exact expressions as Δt approaches zero (Ref.17). Both procedures permit a choice of Δt based on accuracy. An example of a bounded approximation is given in Eq. (37).

$$p\Delta t A_p < = \frac{8 \sin(\frac{B}{2A} p^2 \Delta t) - \sin(\frac{B}{A} p^2 \Delta t)}{6(\frac{B}{2A} p^2 \Delta t)} p\Delta t A_p \quad (37)$$

Equations (38) and (39) are a predictor-corrector pair we have investigated.

$$\tilde{G}_{j,k}^{m+1} = 2G_{j,k}^m - G_{j,k}^{m-1} - \frac{\Delta t B}{A} (G_{j,k}^m - G_{j,k}^{m-1})_x + \frac{\Delta t^2}{A} (\text{Flux}^m) \quad (38)$$

$$G_{j,k}^{m+1} = 2G_{j,k}^m - G_{j,k}^{m-1} - \frac{2\Delta t B}{A} (\tilde{G}_{j,k}^{m+1} - G_{j,k}^{m-1})_x + \frac{\Delta t^2}{A} (\text{Flux}^m) \quad (39)$$

A rigorous analysis of this system's stability characteristics is being undertaken. Generally, modifications like Eq. (35) and (36) improve the results.

Results

In figure 1 we give the general features of our algorithm. Formally the procedure for mean lifting and nonlifting transonic flows are identical. For example were we to examine the velocity field about a mean nonlifting profile, executing small finite amplitude harmonic oscillations in pitch we would procede as follows. First generate starting solutions $\hat{\phi}(\tau_0)$ and $g(\tau_0)$ with Eq. (40) and (41). Both are valid when $|1 - M^2| \gg \tau_0$. Starting solutions can be similarly generated for a lifting flow.

$$(1 - M^2)\hat{\phi}_{xx} + \hat{\phi}_{zz} = 0 \quad (40)$$

$$\hat{\phi}_{(x,z)} = \frac{\tau_0}{2\pi\sqrt{1-M^2}} \int_{\text{Chord}} dx_1 \frac{df_1}{dx} \ln((x-x_1)^2 + (1-M^2)z^2) \quad (41)$$

$$\hat{g} = \hat{\phi}/\tau_0 \quad (42)$$

Typically, for $M = 0.825$ we take $\tau_0 = 0.005$ and $\Delta\tau = 0.005$. Thickness Step sizes of 1/2% (0.005) are sufficient until the flow becomes supercritical.

These $\hat{\phi}(\tau_0)$ and $g(\tau_0)$ are used to predict $\hat{\phi}(\tau_0 + \Delta\tau)$. After which ϕ_x for the predicted potential is computed. A program STRAN7 is called to evolve $g(\tau_0 + \Delta\tau)$. When a final $g(\tau_0 + \Delta\tau)$ is obtained we use it to correct the original estimate of $\hat{\phi}(\tau_0 + \Delta\tau)$. This process is repeated until the final thickness ratio is achieved. A second MPD cycle is started for the oscillation amplitude, using the results of the first MPD cycle as a starting point. The majority of the computation takes place in STRAN7. A typical cycle through STRAN7 may take 10 minutes of CPU time on a VAX11/780. No attempt has been made to optimize the code. It was designed for flexibility in choice of filtering operators, time marching implementation, and MPD parameter.

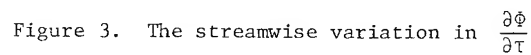
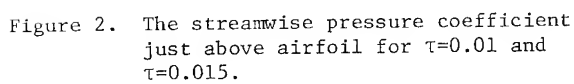
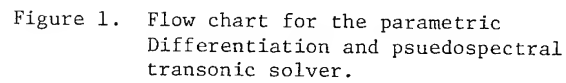
In figure 2 we present data concerning the dependence of the upper surface pressure distribution on τ . In figure 3 we present data depicting the behavior of $d\phi/d\tau$ for fixed τ as you move away from the airfoil.

The algebraic mappings of Eq. (26-27), along with Eq. (24) were used to generate the collocation grid from a physical domain bounded by $|X_p| < 2.0$ and $|Z_p| < 2.5$. This domain is too small to justify the use of asymptotic boundary conditions. We would like to use the more "standard" transonic coordinates of Eq. (28-31). Unfortunately, the amount of stretching needed to make the asymptotic boundary treatment valid causes too great a degradation in accuracy of spectrally computed derivatives. One alternative is to patch several small regions together and enforce some sort of compatibility restriction at artificial boundaries thus created¹². This procedure was used by Gottlieb, Lutzman, and Streett¹⁸ and gave good results. Boundary conditions that simulate the adsorption of outgoing disturbances have proved very useful for problems with wavelike behavior (see 19). Whitlow²⁰ derived a set of radiation boundary equations for the general frequency small disturbance equation that permits the far boundaries to be moved within 10 chords of the airfoil. We have not yet found a suitable spectral discretization of the radiation adsorbing boundary conditions suggested in references 12, 20, 21. Spectral methods are sensitive to proper boundary treatment. Work on this aspect of the numerical implementation continues.

Bounded time approximations were not used in this study. The incorporation of such approximations would permit much larger steps to be taken. The time stepsize choosen was presumably small enough to avoid stability problems. Unfortunately this requires very many time steps. For long time integration an instability does become apparent (see figure 2). The numerical noise typically starts at domain corners and propagates towards the exterior region. The periodic application of a high frequency filter improves results a great deal. The problem has not yet been completely eliminated. Some sort of filtering is mandatory for most spectral codes. The reader is referred to the work of Madja, McDonough and Osher²² for a detailed discussion of the need for spectral filtering. We expect it will be solved by extending the domain several chord lengths in each direction and further tuning of the boundary parameters.

Conclusions

This paper presents a novel formulation of the transonic problem. An approach we believe to be readily extendable to other nonlinear systems. Parametric differentiation converts the nonlinear partial differential equation to a linear partial differential equation with variable coefficients. A pseudo-spectral derivative calculator plus an appropriate filtering operator efficiently provides accurate derivatives. Work is still needed in the development of stable time integration methods. We are also working to extend these methods to treat supercritical flows.



References

1. Ballhaus, W.F., "Some Recent Progress in Transonic Flow Computations." In H.H. Wirz and J.J. Smoldern (editors), Numerical Methods in Fluid Dynamics, Von Karmen Institute, 1979.
2. Borland, C.J., "Bibliography of Recent Developments in Unsteady Transonic Flows." AFFDL-TR-189 1, February, 1979.
3. Halt, D.W. and Harris W.L., "Analysis and Design of Transonic Airfoils Using the Method of Parametric Differentiation." Master's thesis, Massachusetts Institute of Technology, August, 1981. FDRL Report No. 81-5.
4. Lamah, C. and Harris, W.L., "Calculation of Unsteady Small Disturbance Transonic Flow at Arbitrary Reduced Frequency Using an Extended Integral Equation Method." AIAA Paper (83-0884), 1983.
5. Sivaneri, N.T. and Harris, W.L., "Numerical Solution of Transonic Flows by parametric Differentiation and Integral Equation Techniques." AIAA Journal 18(12): 1534-1535, 1980.
6. Whitlow, W., Jr. and Harris, W.L., "Analysis of Nonlifting and Lifting Airfoils in Transonic Flow by Parametric Differentiation." AIAA Paper (80-1394), 1980.
7. Orazag, S.A., "Numerical Simulation of Incompressible Flows with Simple Boundaries: I. Galerkin (Spectral) Representations," Stud. Appl. Math., Vol. 50, pp. 293-327, 1971.
8. Ballhaus, W.F. and Goorigian, P.M., "Implicit Finite-Difference Computations of Transonic Flows about Airfoils." AIAA Journal 15(12), December, 1977.
9. Rizzetta, D.P. and Chin, W.C., "Effect of Frequency in Unsteady Transonic Flow." AIAA Journal 17(7), 1979.
10. Orszag, S.A. and Israeli, M., "Numerical Simulation of Viscous Incompressible Flows." Ann. Rev. Fluid Mech. (6), 1974.
11. Cottlieb, D. and Orszag, S.A., CBMS-NSF: "Numerical Analysis of Spectral Methods: Theory and Applications." SIAM, 1977.
12. Orszag, S.A., "Spectral Methods for Problems in Complex Geometries." J. Comp. Physics 37, 1979.
13. Peyret, R. and Taylor, T.D., Springer Series in Computational Physics: "Computational Methods for Fluid Flow." Springer-Verlag, 1982.
14. Landahl, M.T., "Unsteady Transonics." Pergamon Press, New York, 1961.
15. Gazdag, J., "Numerical Convective Schemes Based on Accurate Computation of Space Derivatives." J. Comp. Phys. Vol. 13, pp. 100-113, 1973.
16. Gazdag, J., "Time-Differencing Schemes and Transform Methods." J. Comp. Phys. Vol. 30, pp. 196-207, 1976.
17. Gottlieb, D. and Turkel, E., "On Time Discretizations for Spectral Methods." ICASE Report 78-1, 1978.
18. Gottlieb, D., Lutzman, L. and Streett, C.L., "Spectral Methods for Two-Dimensional Shocks." ICASE Report No. 82-38, 1982.
19. Bayliss, A. and Turkel, E., "Far Field Boundary Conditions for Compressible Flows." NASA CP 2201, 1982.
20. Whitlow, W., "XTRAN2L; A Program for Solving the General-Frequency Unsteady Transonic Small Disturbance Equation". NASA TM-85723, 1983.
21. Enquist, B. and Majda, A., "Numerical Radiation Boundary Conditions for Unsteady Transonic Flow." J. Comp. Phys. 40:91-103, 1981.
22. Majda, A., McDonough, J. and Osher, S., "The Fourier Method for Nonsmooth Initial Data." Math. of Comp., Vol. 32, Number 144, 1978.
23. Murman, E. and Cole, J.D., "Calculation of Plane Steady Transonic Flows." AIAA Journal Vol. 9, pp. 114-121, June, 1971.

DESIGN ORIENTED IDENTIFICATION OF CRITICAL TIMES IN TRANSIENT RESPONSE

Ramana V. Grandhi^{*}, Raphael T. Haftka^{**}, Layne T. Watson^{***}

Virginia Polytechnic Institute and State University
Blacksburg, Virginia

ABSTRACT

Many optimum structural design problems involve constraints which have to be satisfied for an entire range of certain parameters. For example, in a structure under dynamic loads the stress constraints have to be satisfied over a given range of time. A parametric constraint may be replaced by equivalent critical point constraints at its local minima for optimization purposes. For many real vehicle design applications, the evaluation of constraints such as stresses requires a costly finite element analysis, and finding critical points by calculating element stresses for many time points can be prohibitively expensive. This is particularly true for optimization applications because many configurations of the structure are examined.

The present paper describes two techniques for reducing the computational effort involved in identifying the critical time points. The first approach is an adaptive search technique, well suited for exactly known response. The second technique, which is useful for noisy response, is based on approximating the stress response using least squares splines. Additionally, the possibility of grouping several closely spaced local peaks to identify a single super peak from each group is investigated. The error incurred due to super peak switching is compared with the errors due to commonly employed constraint approximations. Two example problems are considered to demonstrate the computational efficiencies of the proposed techniques.

INTRODUCTION

Many optimum structural design problems involve constraints which have to be satisfied for an entire range of certain parameters. For example, when a structure is designed subject to dynamic loads, the stresses induced will vary with time and stress constraints have to be satisfied over a given range of time. One method of dealing with this type of time varying constraint is to replace it by an integrated constraint (e.g. refs. 1-6). The drawback to this integral approach is that it tends to smooth the constraint and thereby delays warning of an impending constraint violation over a small time interval.

A second method of handling a time dependent constraint is to replace it by a finite number

of constraints placed at closely spaced discrete times assuming that serious constraint violations at intermediate time points are unlikely (e.g., ref. 7). This approach has the disadvantage of increasing the number of constraints and thereby the cost of the constrained optimization problem. An attractive alternative to the above two approaches is to monitor constraints only at the critical points (constraint peaks) and to update these points as the optimization progresses (e.g. refs. 8-9). The efficiency (compared to the second method) of the critical point approach is due to the reduced number of constraints and the minimal computational effort required for calculating the derivatives of the critical point constraints with respect to the design variables during the optimization process.

The accurate calculation of critical time points without missing any of them requires that the structure be analysed at closely spaced time points. If the dependence of the constraint on time is simple enough, then the constraint evaluation is inexpensive. For many engineering design applications, however, the evaluation of behavior constraints such as stresses requires a costly finite element analysis, and the calculation of element stresses for many time points can be very expensive. The cost is particularly important in optimization applications because many configurations of the structure are examined during the optimization process. This paper describes two techniques for reducing the computational effort involved in identifying critical time points.

The first approach is an adaptive search technique, similar to a one dimensional optimization method. This technique employs the magnitude of the constraint value at a particular time point to determine the step increment for the next constraint evaluation. Since the constraint response functions can be multimodal, the search is continued throughout the given range of time to find all the critical points and corresponding constraint values. The precise location of the critical time point is obtained using a quadratic interpolation based on three data points. The second approach is based on the concept of approximating the response of the structure using splines. Splines provide a better smooth approximation to constraint functions than any other smooth approximating functions. In this study, least squares parabolic splines which accommodate noisy loading histories are used.

For optimization purposes critical time points are often assumed fixed and updated only periodically. The drift in the critical time points due to changes in design is studied. Additionally, the possibility of grouping several closely spaced local peaks to identify a single super peak from each group is described. Finally, errors involved in

* Graduate student, Engineering Science & Mechanics

** Professor, Aerospace & Ocean Engineering

*** Associate Professor, Computer Science

monitoring constraints at super peaks instead of at all local peaks are compared with errors incurred due to commonly employed constraint approximations. An analytical example and a twenty-five bar space truss structure subjected to earthquake loading are considered for demonstrating the proposed techniques.

CRITICAL POINT CONSTRAINT

Many structural optimization problems may be posed as follows: Minimize $f(X)$ subject to the constraints $g_i(X) \geq 0$, $i=1,2,\dots,n_g$ where X is a design vector. For many optimum structural design problems constraints have to be satisfied for an entire range of certain parameters. For dynamic loads, the structural design problem is characterized by constraint functions which must be enforced for an entire time interval.

$$g_i(X,t) \geq 0 \quad i = 1,2,\dots,n_g \quad (1.a) \\ 0 \leq t \leq t_f$$

For example, stress constraints may be written as

$$g_i(X,t) = 1 - \sigma_i(t)/\sigma_a \quad (1.b)$$

where $\sigma_i(t)$ is a stress component and σ_a is the corresponding allowable stress.

One common way of enforcing a time dependent constraint is to use a set of closely spaced time points t_j , where $j = 1,2,\dots,n_t$, such that serious constraint violations at intermediate time points are unlikely. With this discrete time approach, the constraints are replaced by

$$g_{ij}(X) = g_i(X,t_j) \geq 0 \quad i = 1,2,\dots,n_g \\ j = 1,2,\dots,n_t \quad (2)$$

In many practical applications, the product $n_g n_t$ is a very large number and carrying out the design process may become prohibitively expensive. The critical time point approach (refs. 8-9) replaces the monitoring of a constraint at all n_t time points by monitoring it only at its most critical points. This concept is explained by Fig. 1 which shows schematically the variation of a constraint function with time. The times of the local minima of the constraint function (A, B and C in Fig. 1) are herein called critical time points. Instead of monitoring the constraint function at all times, it is monitored only at these times. However, the critical time points drift as the design changes, and the constraint must be periodically calculated at many time points to accurately locate the critical time points.

The usefulness of the critical time points concept derives from the fact that, for portions of the design process, the drift of the critical time points may be neglected. For these portions of the design process, the constraint function has to be evaluated for only a relatively small number of time points.

To prove that the drift in the location of the critical points may be neglected to a first-order approximation, consider the constraint imposed at a critical time point t_c . Equation (1) for the constraint $g_i(X,t)$ is replaced by

$$g_{ci}(X) = g_i(X,t_c) = \min\{g_i(X,t)\} \geq 0 \quad (3)$$

The derivative of g_{ci} with respect to a design variable x_j is

$$\frac{\partial g_{ci}}{\partial x_j}(X) = \frac{\partial g_i}{\partial x_j}(X,t_c) + \frac{\partial g_i}{\partial t_c}(X,t_c) \cdot \frac{\partial t_c}{\partial x_j} \quad (4)$$

For interior critical points (A and B in Fig. 1), $\partial g_i / \partial t = 0$, and for boundary critical points (point C), $\partial t_c / \partial x_j = 0$ if $\partial g_i / \partial t = 0$, because an infinitesimal change in the design variables can not change the slope $\partial g_i / \partial t$ by a finite amount to shift the location of the peak away from the boundary. Therefore,

$$\frac{\partial g_{ci}}{\partial x_j}(X) = \frac{\partial g_i}{\partial x_j}(X,t_c) \quad (5)$$

Equation (5) shows that the drift in the critical time point may be neglected to a first-order approximation. That is, for a small change in design, the peak value constraint may be evaluated as if t_c is constant. In practice, critical time points are calculated periodically and are frozen between updatings. However, the concept remains useful, even if critical points require frequent updating, because of the large savings in the derivative calculation.

When the constraint function has more than one local peak as in Fig. 1, each critical point must be assigned a separate constraint g_{ci} ; otherwise, equation (2) may yield a discontinuous derivative of g_{ci} with respect to design variables, when the global peak is switched from one local peak to another, even if g_i is a continuously differentiable function.

EFFICIENT EVALUATION OF CRITICAL POINT CONSTRAINTS

ADAPTIVE SEARCH TECHNIQUE

The adaptive search technique has the objective of finding all the local minima of the constraint function.

We assume that the parametric constraint function data may be calculated only at uniformly spaced time points with an interval of α . We also assume that the derivatives of the constraint functions with respect to the variable t are not available. The adaptive search method first locates the approximate position of a critical point and then employs quadratic interpolation to refine the approximation.

The following adaptive search algorithm is based on the premise that only critical points where $g(t)$ is below a cut-off value g_0 are of interest. Therefore, when $g(t)$ is larger than g_0 , then large steps can be taken, while when $g(t)$ is below g_0 , then the step size is reduced. The minimum and maximum step sizes are assumed to be given as $n_{\min} \alpha$ and $n_{\max} \alpha$, respectively. In the following discussion, t is always the latest position at which $g(t)$ is evaluated.

Step 1. Start with an initial time t_0 , compute the constraint $g(t_0)$.

a. If $g(t_0) > g_0$ set $n = n_{\min}$ and proceed to step 2.

b. If $g(t_0) < g_0$, calculate the constraint at $t = t_0 + \alpha$, and if $g(t) > g(t_0)$ then $g(t_0)$ is a minimum, otherwise $g(t)$ is calculated at every data point until $g(t) > g(t - \alpha)$. When this happens, $g(t - 2\alpha)$, $g(t - \alpha)$ and $g(t)$ are used to identify the position of the minimum by using quadratic interpolation. Go to step 5.

Step 2. Set $t = t + \alpha$. If t is larger than t_f , then halt. Otherwise compute $g(t)$.

Step 3. If $g(t) > g_0$ go to step 2 with $n = \min(n+1, n_{\max})$. Otherwise go to step 4.

Step 4. Compute the constraint at p points on each side of the present time point and from the available $2p+1$ values find the lowest. It can be either one of the end points or can be an interior point. The choice of the parameter p depends on the problem and on n_{\max} . The following description is given for p equal to 2.

(i) If the first point is the lowest (i.e., Fig. 2a,b), continue the search backwards with a step size of α , until the double interval containing the minimum is trapped. Estimate the critical constraint value by quadratic interpolation.

(ii) If an interior point is the lowest (i.e., Fig. 2c-e), construct the quadratic interpolant by taking one data value on each side of the minimum.

(iii) If the last point is the lowest (Fig. 2f), compute $g(t)$ at every data point to the right until $g(t - 2\alpha) > g(t - \alpha)$ and $g(t) > g(t - \alpha)$ (when this happens, $g(t - 2\alpha)$, $g(t - \alpha)$ and $g(t)$ are used for finding the precise minimum using quadratic interpolation) or t reaches t_f ($g(t)$ is a minimum).

Step 5. Set $n = n_{\min}$.

Step 6. Set $t = t + \alpha$. If t is larger than t_f , then halt.

Step 7. Evaluate $g(t)$, if $g(t) > g_0$ go to step 3. If $g(t) \geq g(t - \alpha)$ (Fig. 2g) go to step 6. Otherwise set $t = t - \alpha$ and go to step 4(iii).

In the adaptive search technique, a quadratic least squares fit based on five points is also employed to calculate the local minima. The least squares fit is less sensitive to slight errors in the data than the direct interpolation. Furthermore, an approximation based on five points gives a better estimation of the peak values than the interpolation based on three points.

SPLINE APPROXIMATION

Interpolation of data by polynomials of high degree is often unsatisfactory because they may exhibit wild oscillations. An alternative which provides a smoother approximation is splines. A 'spline' is a function consisting of polynomial pieces on subintervals, joined together with certain smoothness conditions. Locally the spline

interpolant is always a low degree polynomial irrespective of the number of interpolating points and gives a high quality approximation. Using splines, one has the choice of either interpolating or approximating data. For a smooth and precisely known function, construction of an interpolant is effective and cheap, provided one has a reasonable way of choosing appropriate interpolation points. On the other hand, approximation is based on the belief that the given data contain a slowly varying component, the true underlying function, and a comparatively fast-varying small-amplitude component, the noise in the data.

It is reasonable to approximate noisy data from an approximation family with fewer degrees of freedom than there are data points. There should be enough degrees of freedom to approximate the underlying function well, but not enough to approximate also the high frequency noise. To this end, splines are very effective as an approximating family and least-squares approximation is very suitable for the recovery of a smooth function from noisy information.

In this work least squares spline approximation is used because of its efficiency in representing noisy data. Splines of second degree are employed here, since the calculation of critical constraint values from quadratic equations is simple. A formal definition of 'spline' is given below:

A knot sequence is a monotonically increasing sequence of numbers (e.g., 0, 1, 1, 2, 2, 3, 3, 3, ...). Breakpoints are the distinct values (strictly increasing, of course) among the knots (e.g., 0, 1, 2, 3, ...). Knot multiplicities at the breakpoints translate into smoothness conditions for the spline approximation. The spline approximation used here is computed with the aid of local basis spline functions B_i^k (the polynomial pieces have degree $\leq k-1$). For $i=1, \dots, n$, the i th B-spline B_i^k of order k for the knot sequence $t = (t_1, t_2, \dots, t_{n+k})$ is defined by the recurrence relation below (n is the dimension of the vector space generated by the B_i^k).

The B-splines of order 1 for the knot sequence t are defined by

$$B_i^1(t) = \begin{cases} 1 & \text{if } t_i \leq t < t_{i+1} \\ 0 & \text{otherwise} \end{cases} \quad (6)$$

and the higher order B-splines are defined recursively by

$$B_i^k(t) = \left(\frac{t - t_i}{t_{i+k-1} - t_i} \right) B_i^{k-1}(t) + \left(\frac{t_{i+k} - t}{t_{i+k} - t_{i+1}} \right) B_{i+1}^{k-1}(t) \quad (7)$$

where $i=1, 2, \dots, n$

Fig. 3 shows the three cubic B-splines for the knot sequence (1, 2, 3, 5, 5, 5, 7) to demonstrate that the B-splines are piecewise polynomials of order 4 with support only over $k+1 = 5$ knots.

Formally a 'spline' is defined as a linear combination of B-splines. By the Schoenberg-Whitney Theorem (ref. 10), any piecewise polynomial can be represented as a linear combination of B-splines, with an appropriate choice of order k and knot sequence t . Hence a spline can be alternatively described as a piecewise polynomial. The B-spline basis B_i is numerically very stable and inexpensive to compute.

The algorithm used for least squares spline approximation is given in Appendix A for the sake of completeness, and further details can be found in ref. 11. In this study, the constraint function is approximated as a continuous function at the breakpoints but the approximation does not have a continuous derivative.

The effectiveness of the least squares splines for noisy data is demonstrated through the following simple response function:

$$h(t) = \sin(t) \sin(2t) + 0.05 \sin(30t) \quad (8)$$

$$0 \leq t \leq 5\pi$$

In equation (8), the first term represents a slowly varying smooth function and the second term represents fast varying noise. The function $h(t)$ is shown in Fig.4 over the given time interval. A least squares spline approximation constructed using 50 piecewise polynomials is shown in Fig.5. It is clear that the least squares spline approximation removed the fast varying noise and gave a good representation for the true underlying function.

The adaptive search technique described in the previous section is a local approximation approach whereas splines provide a global approximation. Once the spline function is constructed, using the derivative information at the breakpoints, critical time points can be easily calculated in that piecewise polynomial.

SUPER PEAK CONCEPT

The critical point approach is based on monitoring the constraint only at local minima or peaks. This approach can be carried one step further by grouping several closely spaced local peaks to identify the most critical one, called herein a "super peak". The procedure for identifying super peaks starts by locating the first peak (with magnitude exceeding the cut-off value) at time t_p . The highest peak in the time interval

$(t_p, t_p + \Delta t_p)$ is taken as the first super

peak. The procedure is repeated starting at $t_p + \Delta t_p$ to locate the second super peak.

The danger of monitoring only super peaks is that as the design is changed the super peak may switch from one local peak to another. This results in a discontinuous derivative of the constraint with respect to design variables, since the location of the actual super peak is different from the location of the constraint monitored. The switching phenomenon can also become a problem when derivative based constraint approximations are employed. These constraint approximations replace the full analysis during parts of the design process. Approximations based on the super peak constraints could incur large errors because they do not account for the super peak switching. Therefore the error associated with super peak switching is compared here to errors due to other types of response function approxi-

mations used in structural optimization, e.g., linear and reciprocal approximations. The simplest form of derivative based function approximation is the linear approximation

$$\sigma_D(X) = \sigma(X_0) + \sum_{i=1}^{\ell} (x_i - x_{0i}) \frac{\partial \sigma(X_0)}{\partial x_i} \quad (9)$$

where X_0 is initial design and ℓ is the number of design variables.

An alternate expression, called the reciprocal expansion, is a first order Taylor series in the reciprocals of the design variables. The reciprocal approximation is exact for stresses of a statically determinate structure and also more accurate than the linear approximation for a statically indeterminate structure (ref. 12).

$$\sigma_R(X) = \sigma(X_0) + \sum_{i=1}^{\ell} (x_i - x_{0i}) \frac{x_{0i}}{x_i} \cdot \frac{\partial \sigma(X_0)}{\partial x_i} \quad (10)$$

RESULTS AND DISCUSSION

Two example problems were employed to demonstrate the features of the adaptive search and the least squares spline approximation techniques. The first one was a simple test problem where the exact results are known for the peak values and the second one was a twenty-five bar space truss structure. For the adaptive search technique, quadratic interpolation based on three points and least squares quadratic fit based on five points were used. In the least squares spline approximation, functions were approximated by quadratic splines continuous at breakpoints, but having discontinuous first derivatives.

The accuracy of the calculated peaks is very important for the accuracy of derivative calculation of constraints with respect to design variables. These constraint derivatives play an important role in gradient based optimization methods. In the following description, error percentages were calculated based on the absolute difference in peak values compared with the maximum amplitude of the response function. The peaks calculated with the adaptive search technique were allowed to have a maximum error of 1%. In the case of splines, root mean square (r.m.s) error was used for evaluating the quality of approximation. R.m.s. error less than the level of noise in the data was considered as an acceptable approximation. Besides the r.m.s error, the peaks were allowed an additional 1% error. The computational efficiency of the various techniques is assessed by comparing them to the "brute force" approach of calculating the stresses at equi-distanced points and finding the peaks without resorting to approximation or interpolation.

The adaptive search technique assumes the data is exact whereas the least squares spline approximation assumes the data is noisy. For demonstration purposes, both problems were solved first assuming that the data is exact, and then that it is noisy. The errors associated with the adaptive search and the least squares spline approach cannot be compared to each other because of the different assumptions on the accuracy of the data. One has the option of using either the adaptive search technique or the splines approximation depending on the problem.

ANALYTICAL EXAMPLE

The response function considered is given in equation (8). The local peaks which were greater (in absolute value) than 0.25 were considered as critical times. The peaks obtained with $\alpha = 0.0157$ sec step size, combined with quadratic interpolation were taken as exact results for comparison. The "brute force" method of finding peaks requires 350 function evaluations with a step size of 0.0449 sec for finding the peaks within 1% accuracy. 40 peaks were identified during the 5 π sec time. The number 350 was used for measuring the computational savings obtained by the adaptive search and splines techniques. Of the peaks shown in Fig. 4 some are obviously minor kinks and others are below the cut-off value of 0.25. A local peak was considered to be a mere kink if a local maximum is followed immediately by a local minimum differing by less than 3% of the response function maximum value. The function considered (Fig. 4) has several small kinks and out of the 40 peaks about 20 are considered to be important peaks; these peaks are marked in Fig. 4. Only these important peaks were considered in evaluating the adaptive search technique.

First, the adaptive search technique with quadratic interpolation based on three points was employed. n_{\min} and n_{\max} were taken as 3 and 8 respectively. 216 function evaluations with $\alpha = 0.0449$ sec were required to find 28 peaks including all the important peaks, which is a 38% savings in the number of function evaluations. The maximum error was about 0.5%. Increasing α further resulted in a decrease in the number of important peaks identified, so the results obtained with $\alpha = 0.0449$ sec are used for comparison even though the error percentages are smaller than 1%. Next, a quadratic fit based on five points was used for the adaptive search technique. 228 function evaluations with $\alpha = 0.0394$ sec were required for finding 27 peaks including all the important peaks. A savings of about 35% was realized in the number of function evaluations and the maximum error in the peaks was about 1%. Error comparisons for quadratic interpolation and quadratic fit are given in Table 1.

Next, the least squares spline approximation was employed using 50 polynomial pieces with equally spaced breakpoints. The exact magnitude of the peak values is known for the smooth function part corresponding to the first term in equation (8) and there are exactly 10 peaks. The r.m.s. error acceptable for the spline approximation was 5% (i.e., the noise in the given data). In order to find 10 peaks within 1% accuracy and also to satisfy the r.m.s. error restriction, 150 function evaluations were required with a step size α of 0.1047 sec. The peaks obtained using spline approximation are compared with the smooth function peak values in Table 2 and the differences in the peaks are very small. 57% savings was realized in the number of function evaluations and it is demonstrated that the spline approximation is successful in removing noise from the data and giving a good representation for the true underlying slowly varying function.

TWENTY-FIVE BAR SPACE TRUSS

A twenty-five bar space truss structure (Fig. 6) subject to an earthquake loading (Fig. 7) was the next example. The material properties and cross-sectional area of all members are given in Table 3. The structural analysis procedure is described in Appendix B and the stress response in each element was considered as a parametric time dependent constraint. The stress response in a typical element is shown in Fig. 8 for a time period of 10.0 sec. The goal of the procedure was to find all stress peaks which were greater (in absolute value) than 900 psi (corresponding to g_0 in the analysis).

The peaks obtained using equi-spaced data points with $\alpha = 0.01$ sec, combined with quadratic interpolation based on three points, were taken as exact for comparison since reducing α further changed peak values very little. 29 local peaks were identified in element 24 (a typical element). To achieve 1% error using equi-spaced time points, the stresses have to be evaluated at every 0.0133 sec for a total of 750 stress evaluations. The number 750 was taken as the basis for comparing the computational savings obtained by the adaptive and least squares spline techniques, since this was the minimum number of stress evaluations required by the "brute force" method of finding peaks.

Adaptive search technique

First the adaptive search technique was applied to identify the local peaks. n_{\min} and n_{\max} were taken as 3 and 5 to control minimum and maximum step sizes, respectively. Peaks were calculated from a quadratic interpolation based on three points. Twenty nine peaks were identified in element 24 using a step size of 0.02 sec with 252 stress evaluations; a savings of about 66% was realized in the number of stress evaluations. The process was repeated using the same α , n_{\min} and n_{\max} for all elements to achieve more than 75% savings for the complete twenty-five bar truss structure. The peaks obtained using the adaptive search technique have a maximum error of about 1% when compared with the results obtained using data points every 0.01 sec with quadratic interpolation (Table 4).

Next, the 3-point quadratic interpolation was replaced by a quadratic least squares fit based on five data points. 29 local peaks were identified using a step size of 0.0118 sec, with 406 stress evaluations; a savings of about 46% for element 24. For the entire structure the corresponding saving was 63% in the number of stress evaluations. The results of the 5-point quadratic fit are compared with the previous 3 point quadratic interpolation in Table 4. The total number of stress evaluations required for the complete twenty-five bar space truss structure using the quadratic interpolation and quadratic fit techniques is given in Table 5.

Least squares spline approximation

The use of least squares splines is called for when the data is assumed to be noisy. For the purpose of demonstration it was assumed that the noise amplitude is 3% of the maximum stress amplitude. The root mean square (r.m.s.) error calculated based on 1000 stress values was used for evaluating the quality of the approximation. Besides the r.m.s. error, the peaks were allowed to have 1% additional error, and thus the total error allowed in the peaks was 4%. Spline techniques require the selection of the location of the breakpoints. For this purpose stresses were calculated at a small number of points; critical regions were identified based on the magnitude of stress values. About two thirds of the breakpoints were uniformly spaced in critical regions to achieve maximum possible accuracy in peak stress values and the remaining breakpoints were uniformly spaced in other regions.

The restrictions on r.m.s. errors and peak errors were satisfied with 400 stress evaluations in each element using 90 piecewise polynomials. The approximate stress in element 24 obtained using least squares parabolic splines is shown in Fig. 9. 29 peaks were identified for element 24 with 400 stress evaluations, a saving of 46%. The stress peak values have a maximum difference of about 4% from the results obtained using 1000 data points with quadratic interpolation (Table 6). A savings of over 46% was realized in the number of stress evaluations for the complete structure. The spline approximation is more expensive than the adaptive search technique, but unlike the adaptive search technique it removes part of the noise in the data.

Super peaks

Super peaks were calculated by grouping local peaks occurring in each interval of 1.0 sec duration. Same strategy was used for the positive and negative super peaks. 10 of the 29 local peaks were identified as super peaks for element 24. The reliability of the super peak concept was studied by scaling all the cross-sectional areas by $\pm 40\%$ about the nominal design, and monitoring super peaks switching between local peaks. The error associated with super peak switching was compared to errors due to other types of constraint approximations used in structural optimization. Stress derivatives were computed using a finite difference scheme for constructing constraint approximations using equations (9) and (10). The error comparison is shown in Figs. 10-13 by constructing approximations at four different critical time points for element 24 for the nominal design where the areas of all elements was 2.0 in^2 . The four curves in Fig. 10 show the stress value monitored at the original super peak (i.e., maximum of the stress in a particular time zone), the maximum of the actual super peak value in that particular time zone, and the direct and reciprocal approximations to the original super peak as the design variables were changed. Fig. 10 shows no switching of the super peak. Super peak switching was observed only for design change larger than $\pm 25\%$ in Figs. 11 and 12. In Fig. 13 super peak switching took place even for small design changes. The location of super peak switching is marked by the letter S in

Figs. 11-13. It is seen from Figs. 10-13 that the super peak approximation does not result in excessive errors for moderate changes in the structural properties, and also, the errors involved are comparable to errors due to commonly used constraint approximations.

CONCLUSIONS

Two algorithms were developed for identifying critical times in the transient response of dynamically loaded structure. One is an adaptive search technique, where the magnitude of the constraint at a particular time point determines the time step for the next constraint evaluation. This technique is well suited for an exactly known transient response. The least squares spline approximation is suggested for a noisy response to obtain the true underlying function. Two examples were used to show that the adaptive search and the least squares spline approximation techniques can be used for efficiently finding critical times with good accuracy.

A concept of grouping peaks and analysing only "super peaks" within clusters of local peaks was investigated. It reduces the computational effort involved in the optimization due to the reduced number of design constraints. The error incurred due to super peak switching was shown to be comparable to errors due to other constraint approximations commonly used in optimization.

ACKNOWLEDGEMENT

This research work has been supported by NASA grant NAG-1-224 and NSF grant MCS-8207217.

APPENDIX A

LEAST-SQUARES SPLINE APPROXIMATION

Least-squares approximation is a best approximation with respect to a norm which derives from an inner product. Here discrete inner products of the form

$$\langle g, h \rangle = \sum_{i=1}^N g(\tau_i) h(\tau_i) w_i \quad (A1)$$

are considered, where $\tau = (\tau_1 \dots \tau_N)$ is a sequence of N data points, g and h are some functions, and $w = (w_1, \dots, w_N)$ is a sequence of positive weights. w is used to include trends in the data and/or to reflect the varying accuracy of, or confidence in, the given data. All the weights are taken as unity for the example problems.

Let S be a finite dimensional linear space of functions. We seek a best approximation from S to given function g with respect to the discrete 2-norm, i.e., we seek an $f^* \in S$ so that

$$\|g - f^*\|_2 = \min_{f \in S} \|g - f\|_2 \quad (A2)$$

where

$$\|g - f\|_2 = \langle g - f, g - f \rangle^{1/2}.$$

The function f^* is a best approximation from S to the given function g with respect to the 2-norm if and only if the function f^* is in S and the error function $g - f^*$ is orthogonal to S, i.e.,

$$\langle f, g - f^* \rangle = 0 \text{ for all } f \in S \quad (A3)$$

For the specific linear space $S = S_{k,t}$ of splines, with knot sequence $t = (t_i)_1^n$, the

B-spline basis $(B_i)_1^n$ (where n is the dimension of $S_{k,t}$) is well conditioned for moderate k (the spline order). The function f^* has a representation $\sum \alpha_i B_i$ in terms of the basis

$(B_i)_1^n$, where α_i are coefficients. The B-spline basis is easy to manipulate and inexpensive to compute. Further, the coefficient matrix for the normal equations obtained from the equation (A3)

$$\sum_{j=1}^n \langle B_i, B_j \rangle \alpha_j = \langle B_i, g \rangle \quad i = 1, 2, \dots, n \quad (A4)$$

has band width less than k . Since the matrix $(\langle B_i, B_j \rangle)$ is banded, symmetric, and positive definite, equations (A4) are inexpensively solved by Gaussian elimination without pivoting (Cholesky factorization).

APPENDIX B

STRUCTURAL ANALYSIS

The equation governing the motion of a damped linear system is

$$M \ddot{Q}(t) + C \dot{Q}(t) + K Q(t) = F(t) \quad (B1)$$

where M , C and K are mass, damping and stiffness matrices respectively. $Q(t)$ is the n -dimensional displacement vector and $F(t)$ is the associated load vector.

Equation (B1) represents a system of n coupled second order differential equations, where n is the number of degrees of freedom of the structure. A special case of interest is that of proportional damping in which damping matrix is a linear combination of the mass matrix and the stiffness matrix, or

$$C = a M + b K \quad (B2)$$

where a and b are constant scalars. In this case, the undamped vibration modes of the structure uncouples the equations of motion. These vibration modes are obtained by solving the eigenvalue problem.

$$K u = \omega^2 M u \quad (B3)$$

where ω is the natural frequency associated with the mode u .

Modal analysis techniques assume the response of n degrees of freedom system as a linear combination of m eigenvectors. The number of eigenvectors (m) is much smaller than the number of degrees of freedom, particularly for high order systems, since it is neither necessary nor feasible to retain all the modal information in deriving the response. In this case, the eigenvalue problem is not solved completely but only partially, to obtain m lower modes (ref. 13). The m eigenvectors are arranged as the columns of the modal matrix U which satisfies the orthogonality conditions

$$\begin{aligned} U^T M U &= I \\ U^T K U &= \Omega^2 \end{aligned} \quad (B4)$$

where Ω^2 is the diagonal matrix with ω_i^2 terms on the diagonal.

The response of the system at any time t can be expressed as a linear combination of the eigenvectors. The displacement vector is written as

$$Q(t) = U \eta(t) \quad (B5)$$

where $\eta(t)$ is the generalized coordinates vector of size m and U is the matrix of eigenvectors.

Substituting equation (B5) into equation (B1), premultiplying this result by U^T and using the orthogonality conditions (Eq. B4), we obtain

$$\ddot{\eta}_i(t) + 2\zeta_i \omega_i \dot{\eta}_i(t) + \omega_i^2 \eta_i(t) = N_i(t) \quad i = 1, 2, \dots, m \quad (B6)$$

where $\zeta_i = (a + b\omega_i^2)/2\omega_i$ is the damping ratio

in i th mode and $N_i = u_i^T F(t)$.

Equations (B6) are second order uncoupled ordinary differential equations for $\eta_i(t)$ and may be solved by a variety of solution procedures. The displacement vector $Q(t)$ is then computed by equation (B5). In each finite element stresses are calculated from the nodal displacements as

$$\begin{aligned} \sigma(t) &= S Q(t) \\ &\text{or} \\ &= S_g \eta(t) \end{aligned} \quad (B7)$$

where S is stress matrix and $S_g = S U$.

Stress calculation directly from generalized coordinates may be preferred because stress values are not required at all time points in all elements and also the number fundamental modes considered to represent the structural response is usually a small quantity.

REFERENCES

1. Thornton, W.A., and Schmit, L.A., Jr., "The Structural Synthesis of an Ablating Thermostructural Panel," NASA CR-1215, 1968.
2. Stroud, W.J., Dexter, C., and Stein, M., "Automated Preliminary Design of Simplified Wing Structures to Satisfy Strength and Flutter Requirements," NASA TN D-6534, 1971.
3. Fox, R.L., Optimization Methods for Engineering Design, pp.150-157, Addison-Wesley Pub. Co., Inc., 1971.
4. Schmit, L.A., Jr., and Farshi, B., "Some Approximation Concepts for Structural Synthesis," AIAA Journal, Vol 12., May, 1974, pp.692-699.
5. Cassis, J.H., and Schmit, L.A., Jr., "On Implementation of the Extended Interior Penalty Function," Intl. Journal for Numerical Methods in Engineering, Vol.10, pp. 3-23, 1976.

6. Haug, E.J., and Arora, J.S., Applied Optimal Design, pp.330-334, John Wiley, New York, 1979.

7. Adelman, H.M., "Preliminary Design Procedure for Insulated Structures Subjected to Transient Heating," NASA TP-1534, December, 1979.

8. Haftka, R.T., "Parametric Constraints with Application to Optimization for Flutter Using a Continuous Flutter Constraint," AIAA Journal, Vol.13., No.4, 1975, pp.471-475.

9. Haftka, R.T., and Shore, C.P., "Approximation Methods for Combined Thermal/Structural Design," NASA TP-1428, June, 1979.

10. Schoenberg, I.J. and Whitney, A., "On Polya Frequency Functions, III: The Positivity of Translation Determinants with Application to the Interpolation Problem by Spline Curves, Trans. Amer. Math. Soc., 1953, pp.246-259.

11. deBoor, C., A Practical Guide to Splines, Springer-Verlag, 1978.

12. Noor, A.K. and Lowder, H.E., "Structural Reanalysis Via a Mixed Method," Computers and Structures, Vol.5, pp. 9-12, April 1975.

13. Bathe, K.J., and Wilson, E.L., Numerical Methods In Finite Element Analysis, Prentice Hall Inc., 1976.

Table 1 Comparison of Critical Constraint Values Accuracy using Adaptive Search Technique for Analytical Example

Exact solution $\alpha = 0.0157$ sec		Quadratic Interpolation $\alpha = 0.0449$ sec		Percentage difference	Quadratic fit $\alpha = 0.0394$ sec		Percentage difference
Time (sec)	h(t)	Time (sec)	h(t)		Time (sec)	h(t)	
0.5060	0.4363	0.5127	0.4400	0.46*	-	-	-
0.7049	0.6769	0.7150	0.6738	0.38	0.7317	0.6787	0.22
0.8963	0.8110*	0.8980	0.8110	0.00	0.9033	0.8038	0.89
1.0850	0.7755*	1.0801	0.7742	0.16	1.0774	0.7718	0.46
2.0566	-0.7755*	2.0615	-0.7742	0.16	2.0642	-0.7718	0.46
2.2453	-0.8110*	2.2436	-0.8110	0.00	2.2383	-0.8038	0.89
3.7483	-0.5641	-	-	-	3.7685	-0.5715	0.91
3.9426	-0.7623*	3.9478	-0.7612	0.12	3.9507	-0.7589	0.42
4.1326	-0.8165*	4.1311	-0.8163	0.02	4.1269	-0.8085	0.99*
5.1055	0.6886	5.1166	0.6863	0.28	5.1320	0.6922	0.44
5.2922	0.8165*	5.2937	0.8163	0.02	5.2978	0.8085	0.99*
5.4822	0.7623*	5.4770	0.7612	0.14	5.4740	0.7589	0.42
6.7892	0.4363	6.7959	0.4400	0.46*	-	-	-
6.9880	0.6769	6.9982	0.6738	0.38	7.0149	0.6787	0.22
7.1794	0.8110*	7.1812	0.8110	0.00	7.1865	0.8038	0.89
7.3682	0.7755*	7.3633	0.7742	0.16	7.3606	0.7718	0.46
8.3398	-0.7755*	8.3447	-0.7742	0.16	8.3474	-0.7718	0.46
8.5285	-0.8110*	8.5268	-0.8110	0.00	8.5215	-0.8038	0.89
10.0314	-0.5641	-	-	-	10.0517	-0.5715	0.91
10.2257	-0.7623*	10.2310	-0.7612	0.14	10.2339	-0.7589	0.42
10.4157	-0.8165*	10.4143	-0.8162	0.02	10.4101	-0.8085	0.99*
11.3887	0.6886	11.3998	0.6863	0.28	11.4152	0.6922	0.44
11.5754	0.8165*	11.5768	0.8163	0.02	11.5810	0.8085	0.99*
11.7654	0.7623*	11.7601	0.7612	0.14	11.7572	0.7589	0.42
13.0723	0.4363	13.0791	0.4400	0.46*	-	-	-
13.2712	0.6769	13.2814	0.6738	0.38	13.2981	0.6787	0.22
13.4626	0.8110*	13.4644	0.8110	0.00	13.4697	0.8038	0.89
13.6513	0.7755*	13.6464	0.7742	0.16	13.6437	0.7718	0.46
14.6230	-0.7755*	14.6279	-0.7742	0.16	14.6306	-0.7718	0.46
14.8117	-0.8110*	14.8100	-0.8110	0.00	14.8047	-0.8038	0.89

*Maximum difference

*Important peak

Table 2 Comparison of Critical Constraint Values Accuracy
using Least Squares Splines for Analytical Example

Exact solution $\alpha = 0.0157$ sec		Spline approximation $\alpha = 0.1047$ sec		Percentage difference
Time (sec)	h(t)	Time (sec)	h(t)	
0.9553	0.7698	0.9513	0.7703	0.07
2.1863	-0.7698	2.1903	-0.7703	0.07
4.0963	-0.7698	4.0929	-0.7703	0.07
5.3279	0.7698	5.3319	0.7703	0.07
7.2385	0.7698	7.2345	0.7703	0.07
8.4695	-0.7698	8.4734	-0.7703	0.07
10.3801	-0.7698	10.3761	-0.7703	0.07
11.6111	0.7698	11.6150	0.7703	0.07
13.5217	0.7698	13.5177	0.7703	0.07
14.7527	-0.7698	14.7566	-0.7703	0.07

Table 3 Twenty-five Bar Truss Information

Material	:	Aluminium
Young's Modulus	:	10^7 psi
Material density	:	0.1 lb/in ³
Cross sectional area	:	2.0 in ²

Table 4 Comparison of Critical Times and Stresses Accuracy
using Adaptive Search Technique for Element 24

Exact solution $\alpha = 0.01$ sec		Quadratic Interpolation $\alpha = 0.02$ sec		Percentage difference	Quadratic fit $\alpha = 0.0118$ sec		Percentage difference
Time (sec)	Stress (psi)	Time (sec)	Stress (psi)		Time (sec)	Stress (psi)	
1.3977	1467.4	1.3993	1466.5	0.01	1.4000	1464.2	0.08
1.7422	-3001.9	1.7421	-3011.7	0.25	1.7419	-3007.6	0.14
2.0952	3335.4	2.0963	3332.6	0.07	2.0965	3328.9	0.16
2.2596	-3544.0	2.2603	-3543.9	0.00	2.2606	-3535.2	0.22
2.3943	3488.3	2.3945	3484.6	0.09	2.3948	3482.9	0.14
2.5078	-4184.6	2.5080	-4199.0	0.36	2.5088	-4160.3	0.61
2.6214	1479.2	2.6210	1478.2	0.03	2.6207	1458.3	0.52
2.7206	-2984.9	2.7207	-2985.0	0.00	2.7209	-2964.4	0.51
2.8301	1970.7	2.8302	1963.6	0.18	2.8302	1941.1	0.74
2.9390	-2369.4	2.9389	-2369.6	0.00	2.9388	-2359.0	0.26
3.0434	2094.3	3.0443	2100.2	0.15	3.0452	2062.5	0.79
3.1507	-1062.5	3.1507	-1062.5	0.00	3.1501	-1047.4	0.38
3.2614	1716.9	3.2618	1717.2	0.01	3.2620	1710.5	0.16
3.4010	-1552.5	3.4021	-1554.9	0.06	3.4025	-1551.2	0.03
3.9828	1956.5	3.9824	1953.9	0.07	3.9830	1933.5	0.58
4.1069	-1215.8	4.1065	-1209.0	0.17	4.1065	-1198.0	0.45
4.2374	2123.7	4.2383	2122.6	0.03	4.2386	2118.2	0.14
4.5075	-2064.6	4.5074	-2063.5	0.03	4.5083	-2049.2	0.38
4.6778	2256.6	4.6776	2257.2	0.02	4.6774	2222.2	0.86
4.8620	2399.4	4.8623	2400.1	0.02	4.8623	2354.9	1.11
4.9974	-3305.8	4.9968	-3308.7	0.07	4.9965	-3293.5	0.31
5.2221	-2160.3	5.2222	-2160.3	0.00	5.2221	-2142.4	0.45
5.6846	1717.7	5.6845	1716.8	0.02	5.6845	1704.3	0.34
8.6073	-1610.1	8.6079	-1615.2	0.13	8.6086	-1607.1	0.07
8.9687	1960.2	8.9679	1919.1	1.03*	8.9664	1914.0	1.15*
9.0958	-2026.4	9.0954	-2027.8	0.04	9.0947	-2004.0	0.56
9.2385	1897.3	9.2375	1899.6	0.06	9.2367	1873.3	0.60
9.3921	-1506.8	9.3921	-1507.9	0.03	9.3918	-1501.9	0.12
9.5395	1768.9	9.5393	1769.1	0.01	9.5391	1742.3	0.67

*Maximum difference

Table 5 Comparison of number of function evaluations required for complete truss

Members	Equispaced stress calculation	Quadratic Interpolation	Quadratic Fit
1	750	101	171
2 - 5	750	182	314
6 - 9	750	168	290
10 - 11	750	118	201
12 - 13	750	101	171
14 - 17	750	164	257
18 - 21	750	137	249
22 - 25	750	252	406
<hr/>			
Total No. of stress calculations	18750	4151	6979

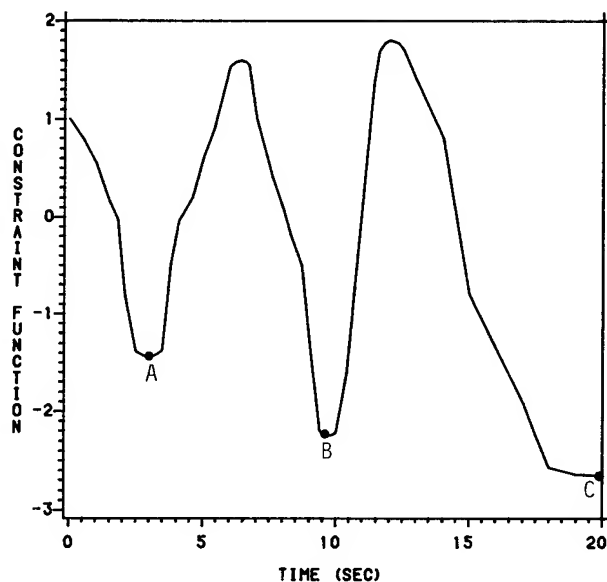


Fig.1: Typical variation of constraint with time

Table 6 Comparison of Critical Times and Stresses Accuracy using Least Squares Spline Approximation for Element 24

Exact solution $\alpha = 0.01$ sec		Spline approximation $\alpha = 0.025$ sec		Percentage difference
Time (sec)	Stress (psi)	Time (sec)	Stress (psi)	
1.3977	1467.4	1.4028	1422.1	1.12
1.7422	-3011.9	1.7459	-3027.9	0.40
2.0952	3335.4	2.0867	3329.1	0.16
2.2596	-3544.0	2.2597	-3502.7	1.04
2.3943	3488.3	2.3978	3495.9	0.20
2.5078	-4184.6	2.5003	-4221.1	0.92
2.6214	1479.2	2.6257	1509.9	0.76
2.7206	-2984.8	2.7201	-2900.6	2.12
2.8301	1970.7	2.8400	2068.9	2.46
2.9390	-2369.4	2.9376	-2331.3	0.95
3.0434	2094.3	3.0500	2096.8	0.06
3.1507	-1062.5	3.1500	-1020.2	1.06
3.2614	1716.9	3.2599	1705.9	0.28
3.4010	-1552.5	3.4035	-1579.8	0.68
3.9828	1956.5	3.9860	1813.3	3.58
4.1069	-1215.8	4.1059	-1190.6	0.63
4.2374	2123.7	4.2400	2175.1	1.29
4.5075	-2064.6	4.5107	-2019.5	1.13
4.6778	2256.6	4.6762	2180.4	1.91
4.8620	2399.4	4.8620	2281.2	2.96
4.9974	-3305.8	4.9962	-3278.4	0.68
5.2221	-2161.3	5.2109	-2270.6	2.73
5.6846	1717.1	5.6800	1846.9	3.25
8.6073	-1610.1	8.6119	-1629.8	0.49
8.9687	1960.2	8.9644	1846.6	2.84
9.0958	-2026.4	9.1000	-2109.3	2.07
9.2385	1897.3	9.2329	1876.3	0.53
9.3921	-1506.8	9.3911	-1505.6	0.03
9.5395	1768.9	9.5345	1616.1	3.82*

* Maximum difference

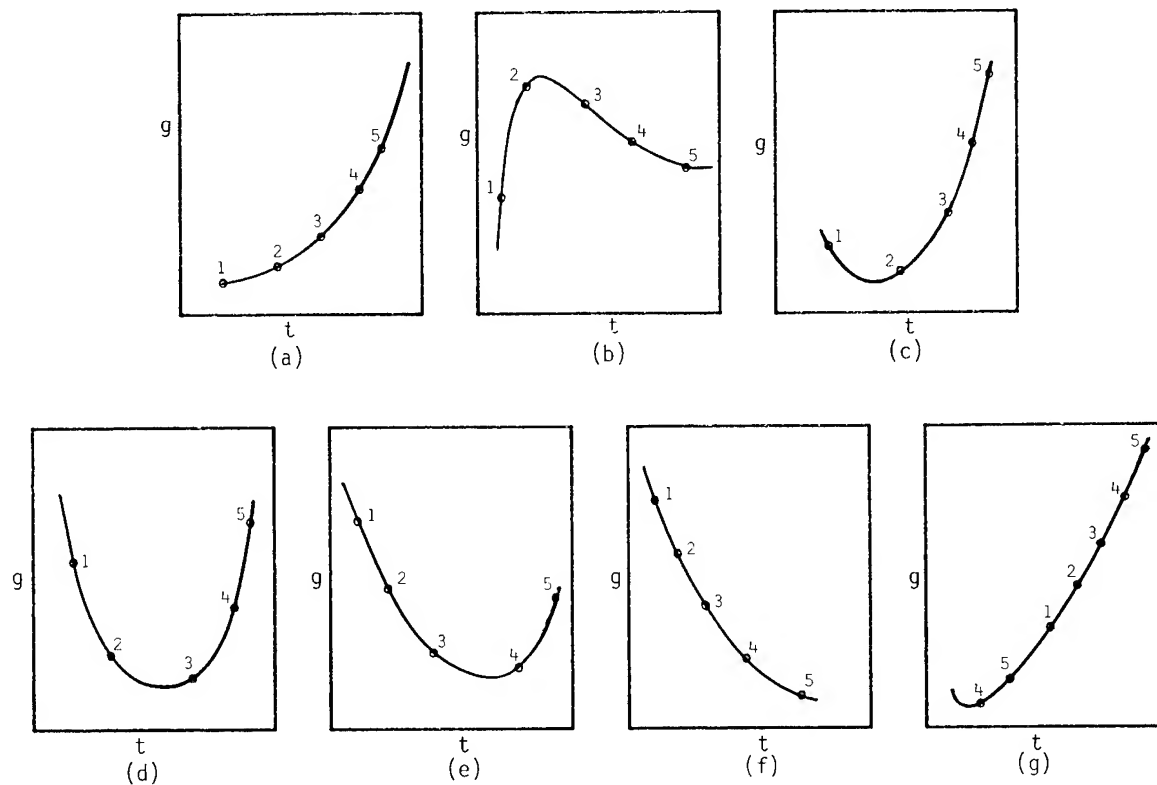


Fig.2: The various possibilities that might arise in the constraint function

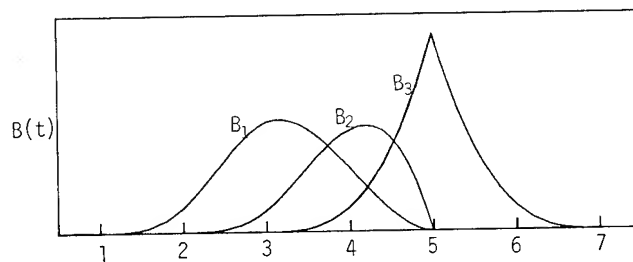


Fig.3: The three cubic B-splines for the knot sequence $(1, 2, 3, 5, 5, 5, 7)$

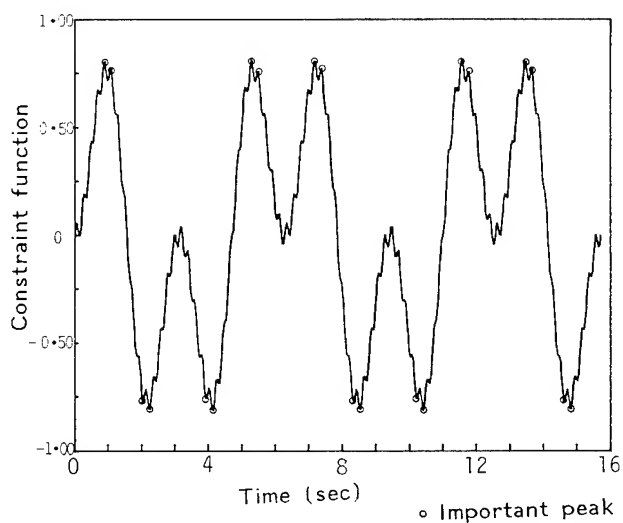


Fig.4: Constraint behavior of a noisy function

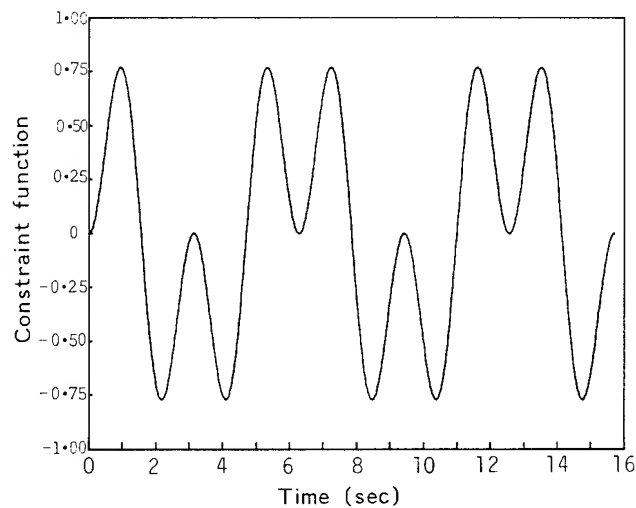


Fig.5: Least squares spline approximation for noisy constraint function

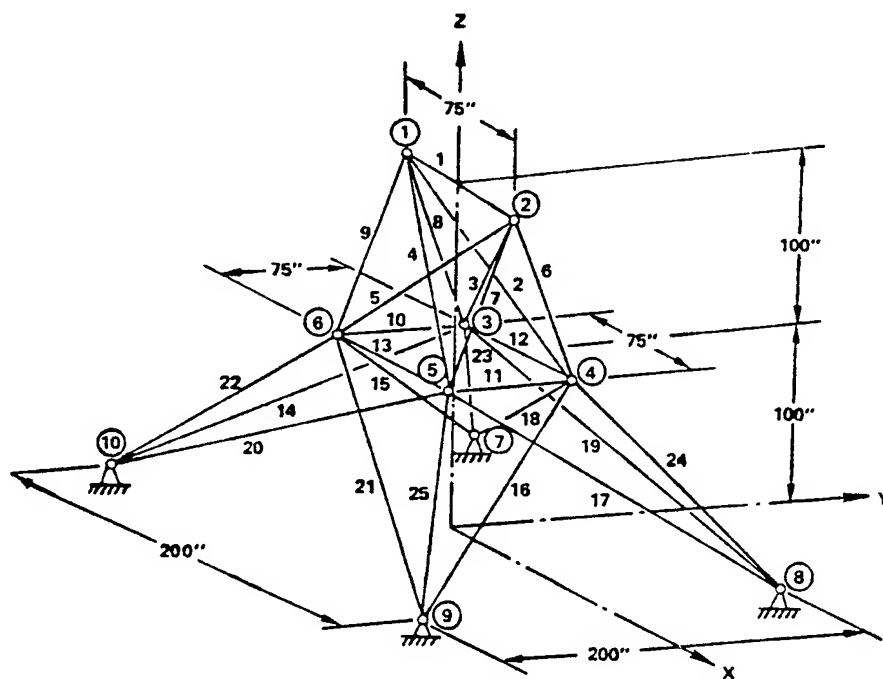


Fig.6: Twenty-five bar space truss

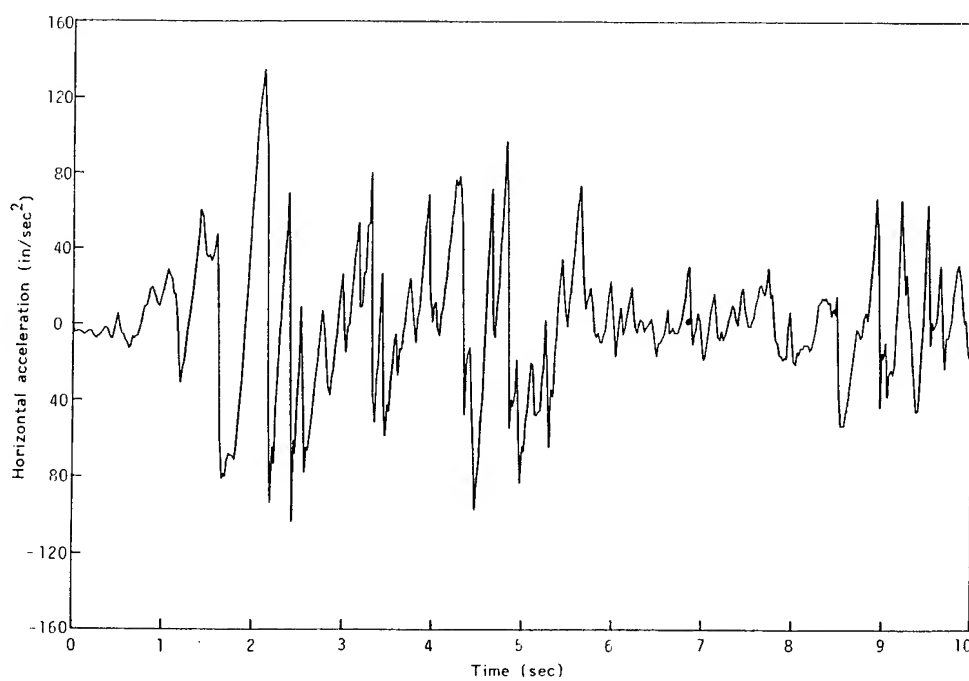


Fig.7: Earthquake data

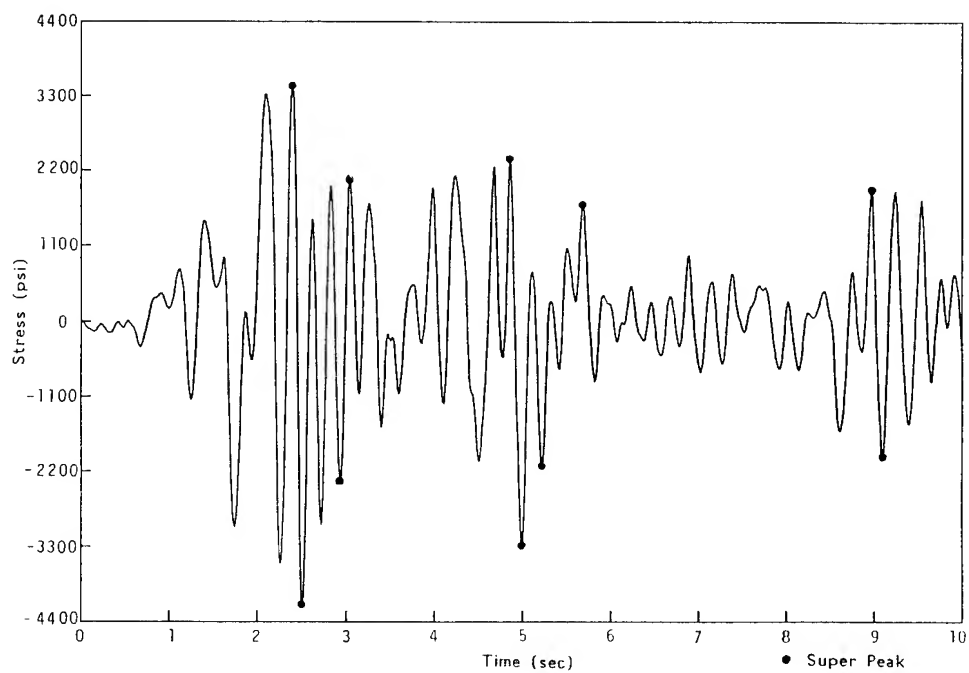


Fig 8: Stress response for element 24 of twenty five bar truss

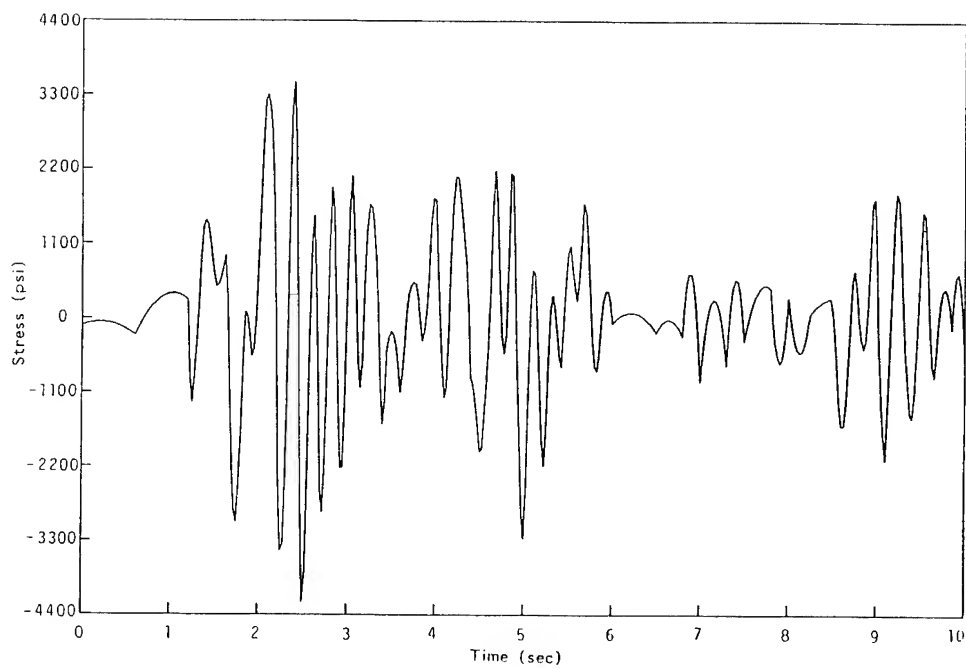


Fig.9: Least squares spline approximation for stress response in element 24

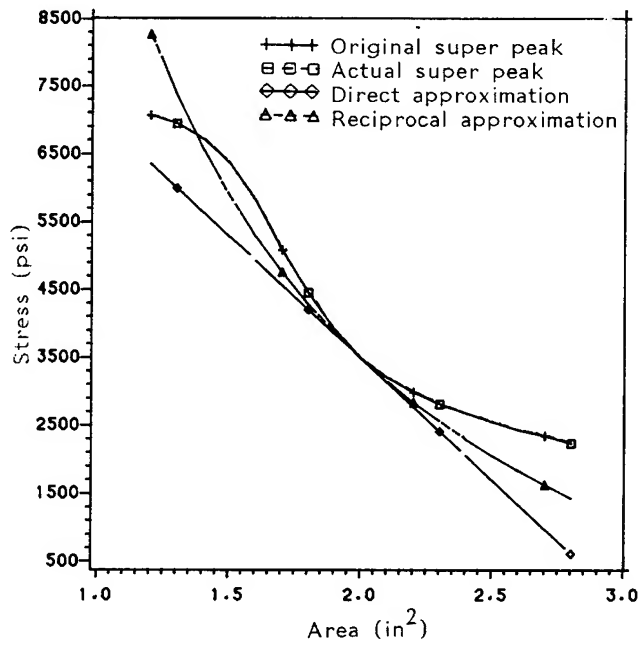


Fig.10: Study of super peak switching at 2.3945 sec for element 24 during design modification

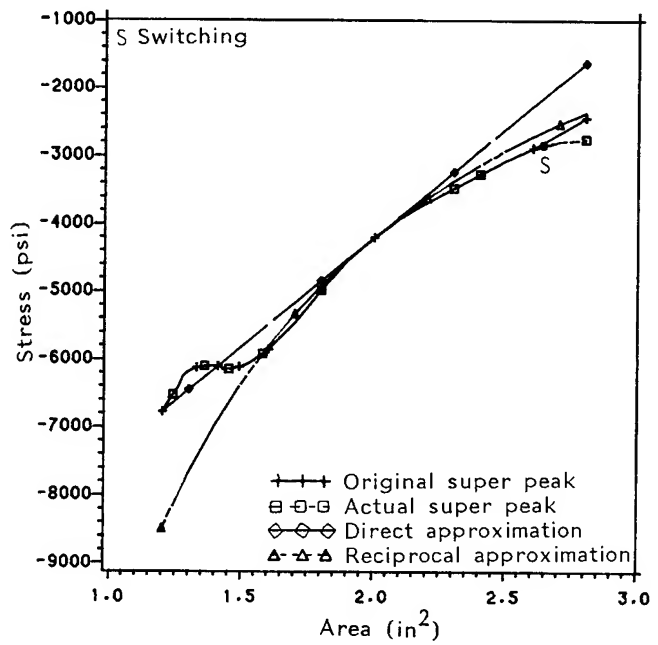


Fig.11: Study of super peak switching at 2.508 sec for element 24 during design modification

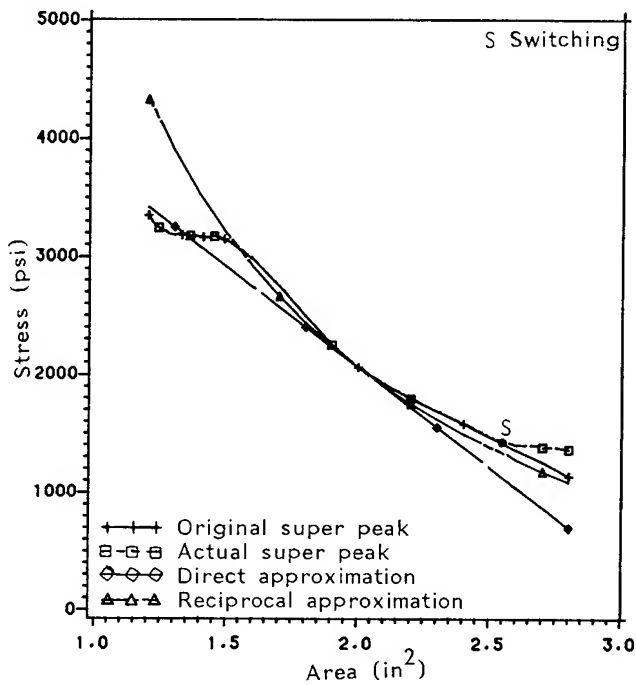


Fig.12: Study of super peak switching at 4.862 sec for element 24 during design modification

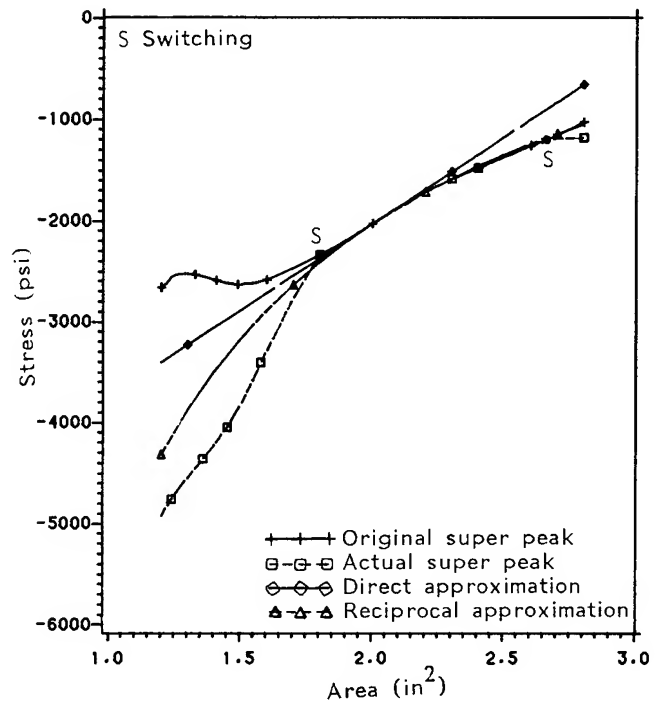


Fig.13: Study of super peak switching at 9.096 sec for element 24 during design modification

James D. Kawamoto*
The Charles Stark Draper Laboratory, Inc.
Cambridge, Massachusetts

Abstract

The development and application of an iterative frequency domain solution technique for nonlinear dynamic structural systems are presented. Numerical techniques such as zero minimization and nonlinear mode updating for improving the scheme's efficiency and artificial damping for stabilizing the solution process are illustrated by a soil amplification problem. The results indicate that the solution scheme can accurately reproduce the response, and is especially attractive when numerical integration considerations severely restrict the time step size for a time integration analysis.

Nomenclature

c	- damping
\underline{C}	- damping matrix
\underline{C}_v	- artificial viscous damping matrix
E_{sec}	- secant Young's modulus
f	- forcing function
f^h	- hysteretic damping force
\underline{F}	- external force vector
\underline{F}^{NL}	- pseudo-force vector
\underline{F}^{OD}	- off-diagonal force vector
\underline{F}^v	- artificial viscous damping force vector
$H(\omega)$	- frequency response function
k	- stiffness
\underline{K}	- stiffness matrix
$\underline{K}_{n\ell}$	- nonlinear stiffness matrix
\underline{K}_{sec}	- secant stiffness matrix
m	- mass
\underline{M}	- mass matrix
\underline{q}	- displacement response
t	- time
Δt	- time increment
T	- structural period
y	- generalized displacement response
Y	- generalized displacement response in the frequency domain
ξ	- damping ratio
ξ_h	- artificial hysteretic damping ratio
ξ_v	- artificial viscous damping ratio
$\underline{\phi}$	- eigenvector matrix
$\underline{\phi}_\ell$	- linear eigenvector matrix
$\underline{\phi}_{n\ell}$	- nonlinear eigenvector matrix
ω	- radian frequency
$\bar{\omega}$	- natural frequency
$\bar{\omega}_D$	- damped natural frequency

Introduction

Nonlinear structural dynamic problems are often solved by direct time integration techniques combined with equilibrium iteration schemes. This approach has generated an impressive algorithm for selecting time increments, equilibrium iterators, numerical integrators, convergence criteria, convergence accelerators, and divergence detectors, providing solutions whose accuracy is limited only by simplifications in the material modelling, structural discretization, and theoretical basis.

Some structural dynamic problems, however, require an excessively small time increment constrained by the accuracy of the numerical integrator, rather than the material behavior or actual structural response. Other structural systems are tremendously large, both in space and time. As a result, applications requiring extensive parameter studies to evaluate the effect of modelling uncertainties usually resort to simplified solution techniques such as the response spectra or equivalent static load approaches. Although these simplified schemes are remarkably efficient, and indeed may provide good estimates of the structural behavior, their simplifications in the material modelling and numerous assumptions of the actual behavior require that detailed direct time integration analyses be conducted initially to assess their level of accuracy.

Along the same lines, alternate solution schemes capable of producing more accurate results with less efficiency have also been investigated. Nonlinear modal analysis techniques in the time domain significantly reduce the number of degrees of freedom.^[1-4] Iterative frequency domain solution schemes have been applied to the steady state response of offshore structures.^[5,6]

A hybrid frequency-time (HFT) domain approach for evaluating the transient nonlinear dynamic response of structural systems is presented in this paper.^[7] As in the case of the direct time integration scheme the hybrid frequency-time domain method produces an accurate solution limited only by modelling considerations. Nonlinearities are evaluated in the time domain and expressed as a load vector on the RHS (right hand side) of the equations of motion (pseudo-force formulation). Combined with a mode superposition procedure to reduce the system size, the solution is efficiently extracted in the frequency domain, implying the use of a theoretically exact numerical integrator not constrained by accuracy and stability considerations. Both kinematic and material nonlinearities can be considered.

Frequency Domain Solution

A solution scheme in the frequency domain applies strictly to linear time-invariant systems whose governing equation of motion for an SDOF (single degree of freedom) system is given by

* Member AIAA

$$m\ddot{q}(t) + c\dot{q}(t) + kq(t) = f(t) \quad (1)$$

where m , c , and k are the mass, damping, and stiffness; f , the forcing function; and q , the displacement response.

The solution to Eq. (1) using a frequency domain approach is obtained by transferring the force history to the frequency domain by evaluating its Fourier transform, multiplying by the frequency response function $H(\omega)$, and then transferring the product back to the time domain using an inverse Fourier transform to yield the response history.

The frequency response function for Eq. (1) is given by

$$H(\omega) = [-\omega^2 m + i\omega c + k]^{-1} \quad (2)$$

and in general for an MDOF system it becomes

$$\underline{H}(\omega) = [-\omega^2 \underline{M} + i\omega \underline{C} + \underline{K}]^{-1} \quad (3)$$

where \underline{M} , \underline{C} , and \underline{K} are the mass, damping, and stiffness matrices.

Hybrid Frequency-Time Domain Solution Scheme

The hybrid frequency-time domain (HFT) solution scheme employs the unconventional pseudo-force approach with the equation of motion written as

$$\underline{M} \ddot{\underline{q}} + \underline{C} \dot{\underline{q}} + \underline{K} \underline{q} = \underline{F} + \underline{F}^{NL} \quad (4)$$

where \underline{M} , \underline{C} , and \underline{K} represent the linear mass, damping, and stiffness matrices; \underline{F} , the external load vector; and \underline{F}^{NL} , the pseudo-force vector containing all nonlinear terms. In conjunction with a mode superposition procedure, Eq. (4) is rewritten in normal mode form as

$$\tilde{\underline{M}} \ddot{\underline{y}} + \tilde{\underline{C}} \dot{\underline{y}} + \tilde{\underline{K}} \underline{y} = \tilde{\underline{F}} + \tilde{\underline{F}}^{NL} \quad (5)$$

where the tilda (\sim) denotes a generalized matrix and \underline{y} is the generalized displacement response vector.

Assuming the eigenproblem has been completed and the generalized matrices in Eq. (5) and frequency response function $\underline{H}(\omega)$ are available, the basic procedure for conducting the HFT analysis is as follows:

1. Obtain the frequency domain representation of the external force history $\underline{\tilde{F}}(\omega)$ by using the FFT (fast Fourier transform) to evaluate the discrete Fourier transform of $\underline{\tilde{F}}(t)$.
2. Compute the frequency domain response $\underline{y}(\omega)$ by simply multiplying $\underline{H}(\omega)$ and $\underline{\tilde{F}}(\omega)$.
3. Transfer $\underline{y}(\omega)$ to the time domain by evaluating its inverse Fourier transform.
4. Derive the geometric response $\underline{q}(t)$ from the generalized response $\underline{y}(t)$. From $\underline{q}(t)$ determine the stress-strain behavior of each degree of freedom, and calculate the system nonlinearities. Store the nonlinearities as a force vector history $\underline{F}^{NL}(t)$, and reduce $\underline{F}^{NL}(t)$ to its generalized form $\underline{\tilde{F}}^{NL}(t)$.

5. Transfer $\underline{\tilde{F}}^{NL}(t)$ to the frequency domain using the FFT.
6. The forcing function is now $\underline{\tilde{F}}(\omega) + \underline{\tilde{F}}^{NL}(\omega)$. Multiply the forcing function by $\underline{H}(\omega)$ to obtain the updated frequency domain response $\underline{y}(\omega)$.
7. Repeat steps 3-6 until a convergence criterion is satisfied.

Numerical Implementation

The basic HFT solution scheme's conceptual simplicity readily lends itself to a numerical implementation. No powerful numerical techniques are required. Actual applications to highly nonlinear systems, however, may produce stability problems characterized by response histories whose amplitudes grow with successive iterative cycles. Solutions that remain stable may converge slowly and require numerous applications of the FFT, producing an inefficient solution process. Modifications of the basic HFT solution algorithm that efficiently produce a numerically accurate solution are presented in this section. In particular, the solution formulation is examined and the zero minimization, artificial damping, and nonlinear mode updating concepts are described. A more detailed presentation is available in Ref. 7.

Solution Formulation

Steps 1-7 of the solution process can be approached from two different perspectives. The first approach, called the dual displacement formulation, evaluates the linear response \underline{y}_1 during steps 1 and 2, and obtains a correction response \underline{y}_2 by iterating from steps 3 to 7. The nonlinear response \underline{y} is then defined as

$$\underline{y} = \underline{y}_1 + \underline{y}_2 \quad (6)$$

The governing equation for the first cycle is

$$\tilde{\underline{M}} \ddot{\underline{y}}_1 + \tilde{\underline{C}} \dot{\underline{y}}_1 + \tilde{\underline{K}} \underline{y}_1 = \tilde{\underline{F}} \quad (7)$$

and for successive iterative cycles,

$$\tilde{\underline{M}} \ddot{\underline{y}}_2 + \tilde{\underline{C}} \dot{\underline{y}}_2 + \tilde{\underline{K}} \underline{y}_2 = \underline{\tilde{F}}^{NL} \quad (8)$$

Since the nonlinear correction is evaluated independently of the linear response, numerical round-off errors are minimized and, furthermore, the Fourier transform evaluation of the force history $\underline{\tilde{F}}^{NL}$ may require less points in the frequency domain than that for $\underline{\tilde{F}}$, resulting in a computational cost reduction.

Although the dual displacement formulation possesses favorable computational accuracy features, the solution may converge slowly when the nonlinear response differs significantly from the linear response. In addition, the response correction \underline{y}_2 may never approach its true value if \underline{y}_1 is inaccurate.

Considering the drawbacks of the dual displacement formulation, a total displacement formulation

was also examined. The total displacement formulation solves Eq. (5) directly, using the total force history $\bar{F} + \bar{F}^{NL}$ during all iterative cycles. Approximations in the response during initial iterative cycles are corrected in successive iterations. A "better" initial guess of the nonlinear response can be obtained by using artificial damping. Storage requirements are reduced considerably since only one response quantity y is stored, rather than both y_1 and y_2 .

Zero Minimization Technique

A frequency domain solution applies strictly to systems with periodic excitations and responses. In transient response problems, where the force history and response are aperiodic, a numerical gimmick must be employed to obtain an apparent aperiodic response. The usual procedure is to append additional zeroes to the end of the load history, thereby creating a history of sufficient length such that the residual free vibration effects at the end do not appear at the beginning. These additional zeroes may significantly increase the cost of implementing the FFT, especially when low physical damping is specified, the natural structural period is large, or a huge number of transforms must be executed. Extensions to nonlinear softening systems may further exacerbate the problem.

An alternate approach called the zero minimization technique was consequently developed. This technique eliminates the use of zeroes by subtracting the analytical expression of the residual free vibration from the incorrect response obtained with an insufficient number of zeroes. Only NB points need be used, where NB is the next power of 2 greater than the number of points in the actual load history for a radix-2 FFT, assuming that NB adequately resolves the load and response histories.

The procedure for implementing the zero minimization scheme is as follows:

1. Let N be the number of points representing the excitation history $F(t)$ and NB the total number of points used in the frequency domain ($N < NB$).
2. NB is chosen such that $N < NB < 2N$. In other words, NB is the smallest power of two greater than N (for a radix-2 FFT).
3. Using such an NB, evaluate the Fourier transform $F(\omega)$ of the load history. This transform is exact for the given time increment and NB.
4. Multiply $F(\omega)$ by the frequency response function $H(\omega)$ to obtain the frequency domain representation of the response $Y(\omega)$.
5. Evaluate the inverse Fourier transform of $Y(\omega)$ to obtain the response history $\tilde{y}(t)$.
6. $\tilde{y}(t)$ is an incorrect response because the periodic convolution executed with NB produces a significant free vibration component at $t = NB\Delta t$ that contaminates the beginning of the response.
7. Obtain the correct response $y(t)$ by realizing that the initial conditions, y_0 and \dot{y}_0 ,

should be zero (or whatever the analyst specified). Therefore, subtract from $\tilde{y}(t)$ the analytical solution of the free vibration response

$$\hat{y}(t) = e^{-\xi\bar{\omega}t} \left(\frac{\dot{\tilde{y}}_0 + \tilde{y}_0 \xi\bar{\omega}}{\bar{\omega}_D} \sin \bar{\omega}_D t + \tilde{y}_0 \cos \bar{\omega}_D t \right) \quad (9)$$

where \hat{y} is the free vibration response due to a nonzero displacement and velocity at time $t = NB\Delta t$; \tilde{y}_0 and $\dot{\tilde{y}}_0$, the initial values of the incorrect response; $\bar{\omega}$, the natural frequency; $\bar{\omega}_D$, the damped natural frequency; and ξ , the specified viscous damping ratio.

A schematic description of the zero minimization technique is provided in Figure 1.

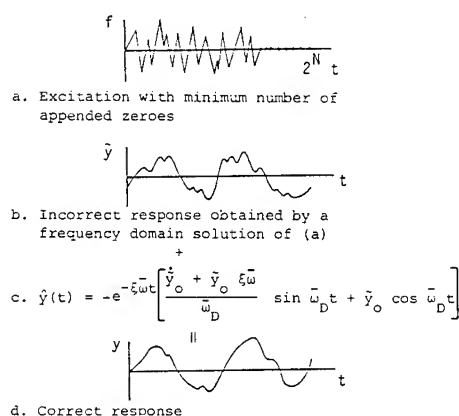


Figure 1 Zero minimization technique

Actual applications of the technique usually reduced the number of points in the frequency spectrum by a factor of four, increasing the solution efficiency considerably. The procedure is theoretically sound since the only difference between the exact response y and incorrect response \tilde{y} is the presence of the free vibration component \hat{y} . y is derived from \tilde{y} by imposing the known actual initial conditions on \tilde{y} .

Notice that the zero minimization technique applies to both linear and nonlinear analyses, with no iterative process involved for linear analyses. In the extreme case it is possible to evaluate the solution with no appended zeroes ($N = NB$).

Stabilization by Artificial Damping

Although the basic HFT solution scheme with no modifications should theoretically perform properly, actual applications involve numerical approximations such as evaluating the velocity at time zero by a finite difference expansion (used in the zero minimization technique) and extracting the Fourier transform of sequences that may possess a large maximum frequency component, producing aliasing problems (folding of high onto low frequency components). In addition, the digital computer with finite word length imposes upper and lower limits on

number sizes and produces truncation errors, possibly preventing the solution process from converging.

Due to the numerical nature of the HFT solution scheme, an artificial damping stabilization scheme was developed not to necessarily accelerate the convergence process, but to prevent divergence when used properly. Excessive vibration amplitudes due to an unconverged pseudo-force history are attenuated during the iterative process.

Artificial damping can be applied in either a viscous or hysteretic form by adding an additional damping matrix to the LHS of the equation of motion and the corresponding force vector to the RHS. For viscous type artificial damping the equation of motion becomes

$$\tilde{M} \ddot{Y} + (\tilde{C} + \tilde{C}_v) \dot{Y} + \tilde{K} Y = \tilde{F} + \tilde{F}^{NL} + \tilde{F}^v \quad (10)$$

where \tilde{C}_v is the generalized artificial viscous damping matrix and \tilde{F}^v is the artificial viscous damping force equal to $\tilde{C}_v \dot{Y}$.

Artificial hysteretic damping is defined properly only in the frequency domain where the governing equation becomes

$$\ddot{Y} + \tilde{c} \dot{Y} + \tilde{k} (1 + i2\xi_h) Y = f + f^{NL} + f^h \quad (11)$$

where Y is the generalized frequency domain displacement response; ξ_h , the artificial hysteretic damping ratio; and f^h , the hysteretic damping force equal to $i2\xi_h \tilde{k} Y(\omega)$, $i = \sqrt{-1}$.

The choice between artificial viscous and hysteretic damping depends on the actual damping dominating the response. Artificial hysteretic damping tends to be more appropriate for structural dynamic type problems since the physical damping usually arises from the frequency independent energy dissipation of the material. Viscous type damping, being well defined in the time domain, may be more appealing conceptually.

Nonlinear Mode Updating in the Frequency Domain

The numerical considerations discussed previously concern the solution of SDOF systems. The entire structure, or more specifically, the development of nonlinear mode updating schemes in the frequency domain is addressed in this section. Two problems must be considered:

1. Managing nondiagonal frequency response matrices obtained when nonlinear modes are combined with linear system matrices.
2. Evaluating modal updates to a nonlinear system.

Beginning with the first problem, suppose that n linear mode shapes ϕ_ℓ are used in the first few iterative cycles. The solution process is stopped, and m nonlinear modal updates $\phi_{n\ell}$ are evaluated. The eigenvector matrix ϕ equals $[\phi_\ell \quad \phi_{n\ell}]$. When ϕ is applied to the linear structural matrices, the resulting generalized matrices are no longer diagonal, and the frequency response matrix H cannot be evaluated by simply computing the reciprocals of

the diagonal entries in H^{-1} .

A direct evaluation of H by inverting H^{-1} is extremely costly since the matrix inversion must be executed for all frequencies in the discretized spectrum and, moreover, entails additional storage requirements since the off-diagonal terms of H must be stored in addition to the diagonal terms.

The impracticality of evaluating H directly from H^{-1} suggests an alternate approximate approach. An approximate diagonal \tilde{H} is derived by transferring all off-diagonal terms in the generalized matrices to the RHS of the equations of motion. From the remaining diagonal terms an approximate \tilde{H}^{-1} is evaluated, and the approximate \tilde{H} is easily obtained by computing the reciprocals of the diagonal terms in \tilde{H}^{-1} .

The governing equations of motion become

$$\tilde{M} \ddot{Y} + \tilde{C} \dot{Y} + \tilde{K} Y = \tilde{F} + \tilde{F}^{NL} + \tilde{F}^{OD} \quad (12)$$

where the overhead \cup refers to a generalized matrix containing only its diagonal terms and F^{OD} is the off-diagonal force vector

$$\tilde{F}^{OD} = \tilde{C} \dot{Y} + \tilde{K} Y \quad (13)$$

where the overhead \cap denotes a generalized matrix containing only off-diagonal terms. Therefore,

$$\tilde{C} = \tilde{C}^{\cup} + \tilde{C}^{\cap} \quad (14)$$

$$\tilde{K} = \tilde{K}^{\cup} + \tilde{K}^{\cap}$$

Consider next the problem of updating the mode shapes. Nonlinear mode updating schemes in the frequency domain, in contrast to those in the time domain, cannot proceed in time and be implemented whenever the nonlinearities begin to change substantially. The very nature of a frequency domain solution implies that the response at all time steps is obtained simultaneously. Mode updating is possible only after an iterative cycle. Furthermore, the stiffness matrix $K_{n\ell}$ is never evaluated, and only the pseudo-force history is extracted. These considerations significantly restrict the means for updating the mode shapes.

Two mode updating schemes were developed--the static load distribution and the least squares secant stiffness methods. Both schemes exploit the pseudo-force history's implicit portrayal of the spatial and temporal distributions of the nonlinearities. The static load distribution approach, although applied successfully to an MDOF shear beam problem,^[7] requires considerable insight on the analyst's part and will not be discussed.

The least squares secant stiffness updating method requires less insight and demands minimal participation from the analyst. Since the pseudo-force history is derived from the member forces, obtained from the current stress-strain states, the exact tangent and secant stiffness histories are available indirectly, permitting the evaluation of the exact global tangent or secant structural stiffness matrices. An HFT solution scheme, however, employs one frequency response function during each iterative cycle, thus requiring a method for select-

ing one structural stiffness that characterizes the system behavior for most of the response history. The least squares approach provides an average K_{sec} by storing the stress-strain histories of each member and then least squares fitting a Young's modulus. The method is given as follows:

1. During the evaluation of the pseudo-force histories, obtain the secant Young's modulus E_{sec} for each degree of freedom from its stress-strain diagram.
2. Store $\sum E_{sec}$ and $\sum E_{sec}^2$, where the summation is over time.
3. After evaluating the entire pseudo-force history, derive a least squares approximation of E_{sec} for each degree of freedom using the results of step 2.
4. Construct the secant stiffness matrix $K_{n\ell}$ from the E_{sec} 's of step 3.
5. Evaluate m eigenvectors $\phi_{n\ell}$ of $K_{n\ell}$.
6. Gram-Schmidt orthogonalize $\phi_{n\ell}$ with respect to the previous set of eigenvectors, and proceed with the analysis.

Notice that the mode updating can be implemented without any participation from the analyst. The nonlinear eigenvector matrix may contain eigenvectors corresponding to many different secant stiffness matrices, each representing the dominant behavior of different portions of the response history.

Sample Study

Salient features of the HFT solution scheme are illustrated by the following soil amplification problem. In particular, the total displacement formulation, zero minimization technique, hysteretic artificial damping, and least squares mode updating concepts are introduced. Additional studies are described in Ref. 7.

MDOF Soil Amplification Study

The HFT scheme was applied to a soil amplification problem investigated by Constantopoulos in 1973.^[8] In general the problem consists of determining the surface response to a seismic excitation applied at the base of a soil deposit. The problem exhibits a fairly complex response with significant nonlinearities and, moreover, has no viscous damping. These two aspects pose convergence problems for the basic HFT scheme.

The soil deposit was modelled by a closely coupled 9 degree of freedom lumped mass system and a stiffness profile varying with the square root of the depth. Each soil layer was represented by the Ramberg-Osgood material model whose governing equation is

$$\frac{q - q_i}{c q_y} = \frac{f - f_i}{c f_y} + \alpha \left[\frac{f - f_i}{c f_y} \right]^r \quad (15)$$

where the q 's are displacements and f 's are forces. For this problem, $\alpha = 0.05$ and $r = 2$. The fundamental period T_1 was 0.357 s and T_9 , 0.031 s. No viscous damping was specified, and the first ten seconds of the N69W component of the Taft record of the 1952 Kern County earthquake, scaled to 0.05 g, was used. Relevant structural properties are provided in Figure 2.

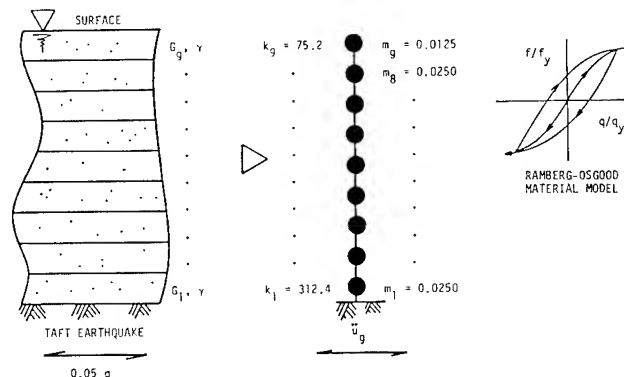


Figure 2 MDOF soil amplification system

The direct time integration analyses were conducted using the Newmark integration method ($\alpha = 0.25$, $\delta = 0.50$) and Newton equilibrium iteration scheme with a residual force tolerance of 0.00001 and iteration limit of 15. Preliminary studies indicated that a time step size of 0.005 s was adequate. The linear and nonlinear displacement responses at the soil surface are shown in Figures 3 and 4.

A time increment of 0.05 s proved adequate for the HFT analysis. An artificial hysteretic damping ratio of 0.75 was selected. Two hundred fifty-six (256) points were used in the frequency domain (200 for the 10 second earthquake and 56 appended zeroes).

The HFT results using all nine linear modes are shown in Figure 5 after 50 and 80 iterations, by which time the solution history had converged to its final shape for the specified solution parameters.

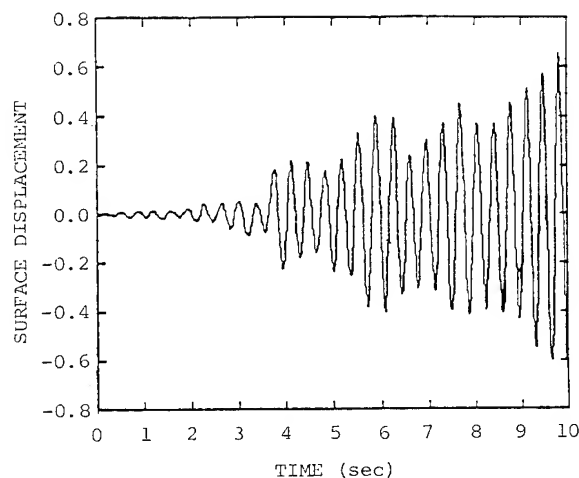


Figure 3 Linear response

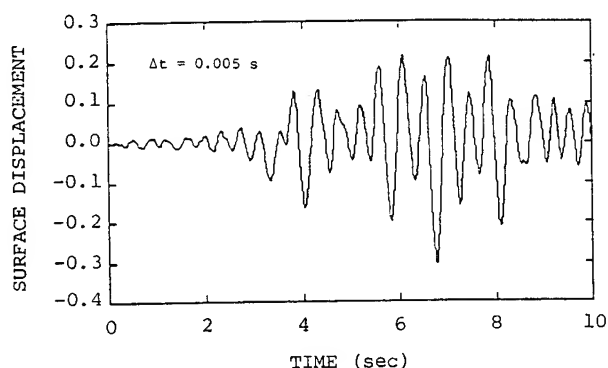


Figure 4 Nonlinear response using a direct time integration analysis

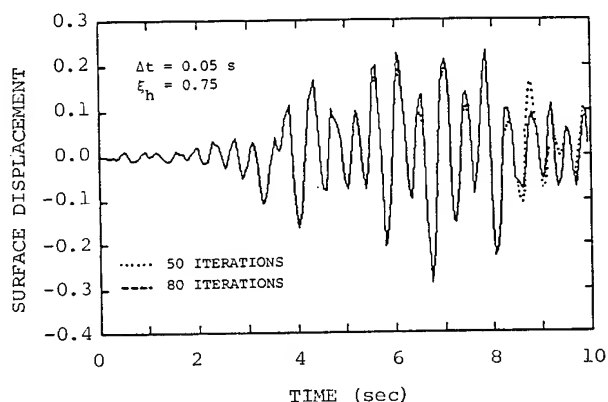


Figure 5 Nonlinear response using 9 linear modes in an HFT analysis

Notice that the results are fairly similar up to time 5 seconds. This convergence behavior indicates that the final iterations correct the latter portion of the response, implying that the initial portion converges first and proceeds in a time progressing form.

As a comparison of the efficiency of the two solution schemes, the direct time integration analysis required 650 s and the HFT analysis, 540 s.

The next portion of this study implemented the least squares secant stiffness mode updating scheme. Initial studies were conducted with a time increment of 0.05 s to determine the minimum number of linear modes necessary to adequately reproduce the response. Figure 6 shows the response after ten iterations using all 9 linear modes, 5 linear modes, and 1 linear mode. One linear mode adequately reproduces the response, although the peak amplitudes are slightly smaller. Realizing that the fundamental mode was acceptable in this particular problem, the mode updating scheme was applied in the following form:

1. Iterate the first ten cycles with one linear mode.
2. Execute the least squares mode updating algorithm.

3. Restart the analysis with the fundamental nonlinear eigenvector (one nonlinear mode).

4. Iterate for another 40 cycles.

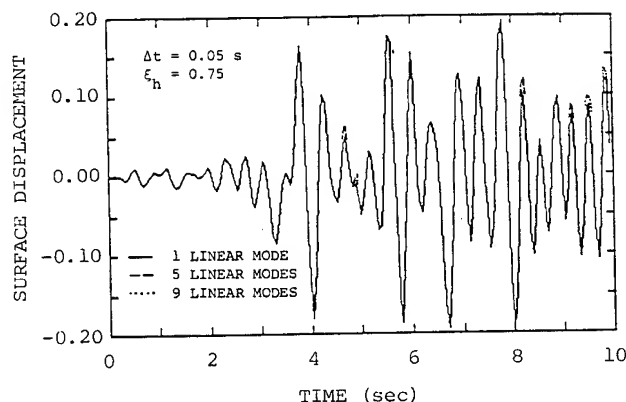


Figure 6 Nonlinear response after 10 iterations using a reduced number of linear modes

The resulting response using a time increment of 0.05 s is shown in Figure 7. For comparison purposes an additional analysis was conducted with one linear mode during all iterations and a time increment of 0.05 s, yielding the responses after 50 and 80 iterations also shown in Figure 7. It is apparent that the response converged faster with only one nonlinear mode (50 iterations for one nonlinear mode and 80 iterations for one linear mode).

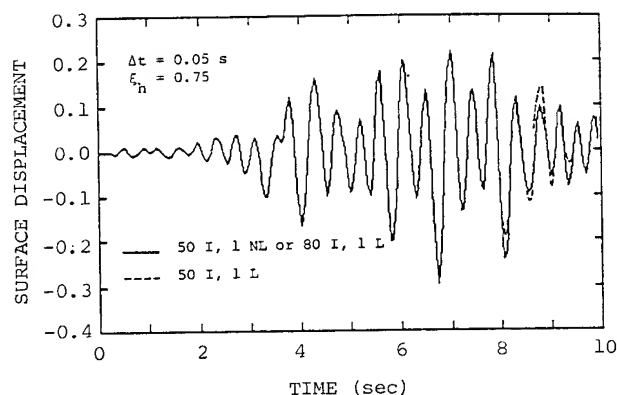


Figure 7 Nonlinear response using a mode updating scheme (I = iterations, L = linear mode, NL = nonlinear mode)

The faster rate of convergence when using one nonlinear mode, as opposed to one linear mode, stems from K_{sec} better representing the overall structural behavior than the linear stiffness, and hence providing closer initial estimates to the nonlinear response. The fundamental nonlinear mode has period 0.466 s compared to the linear mode with 0.357 s, indicating that K_{sec} portrays a softer, nonlinear structure.

The computation times for the various analyses are provided in Table 1. Notice that the HFT scheme displays significant reductions in computational cost compared to the direct time integration analyses. This efficiency originates from the use of a time increment ten times larger than that of the direct time integration analysis combined with a nonlinear mode superposition scheme.

Table 1 Computation times

Solution Scheme	Δt (sec)	Modes Used	Cycles	CPU Time (sec)
Time Integration	0.005	Direct	--	650
HFT	0.05	9 Linear	80	544
	0.05	1 Linear	80	133
	0.05	*	50	100

* 1 Linear, first 10 iterations
1 Nonlinear, next 40 iterations

Conclusions

A new hybrid frequency-time domain solution scheme for obtaining the transient nonlinear dynamic response of structural systems was presented. A sample study illustrated the application of the zero minimization technique and least squares secant stiffness mode updating procedure for increasing the computational efficiency and the artificial hysteretic damping concept for stabilizing the iterative solution process.

Advantages of the HFT approach include the following:

1. Reduction in problem size by a mode superposition procedure.
2. Use of a theoretically exact numerical integrator that produces no phase distortion and artificial damping effects, assuming that the frequency spectrum resolution is sufficiently fine and a negligible component exists at the Nyquist frequency.
3. Time increment is determined by the actual physical behavior rather than numerical considerations.
4. Frequency dependent stiffness and damping can be properly modelled.

5. Long duration excitation histories are readily handled.

The technique is limited to non-wave propagation type problems since a mode superposition approach is employed. In addition, the storage requirements may be considerable since the entire response history must be stored before transferring between the time and frequency domains.

Although the HFT scheme in its current form can accurately reproduce the nonlinear response, its efficiency must be developed further before the technique will be adapted to practical engineering problems. Additional research areas include a segmented history approach and applications to large structural systems.

References

1. Bathe, K.J., and S. Gracewski, "On Nonlinear Dynamic Analysis Using Substructuring and Mode Superposition," Computers and Structures, Vol. 13, 1981, pp. 699-707.
2. Morris, N.F., "The Use of Modal Superposition in Nonlinear Dynamics," Computers and Structures, Vol. 7, 1977, pp. 65-72.
3. Nickell, R.E., "Nonlinear Dynamics by Mode Superposition," Computer Methods in Applied Mechanics and Engineering, Vol. 7, 1976, pp. 107-129.
4. Noor, A.K., "Recent Advances in Reduction Methods for Nonlinear Problems," Computers and Structures, Vol. 13, 1981, pp. 31-44.
5. Fish, P., and R. Rainey, "The Importance of Structural Motion in the Calculation of Wave Loads on an Offshore Structure," Proceedings, BOSS Conference, London, England, 1979, pp. 43-60.
6. Taudin, P., "Dynamic Response of Flexible Offshore Structures to Regular Waves," Proceedings, Offshore Technology Conference, Houston, Texas, 1978.
7. Kawamoto, J., Solution of Nonlinear Dynamic Structural Systems by a Hybrid Frequency-Time Domain Approach, Ph.D. Thesis, MIT, Cambridge, Massachusetts, 1983.
8. Constantopoulos, I.V., Amplification Studies for a Nonlinear Hysteretic Soil Model, Sc.D. Thesis, MIT, Cambridge, Massachusetts, 1973.

H. C. BRIGGS*
Air Force Institute of Technology
Wright-Patterson AFB OH

Abstract

The results of application of the NASTRAN flutter analysis to repaired T-38 horizontal stabilizers are presented. Verification and tuning of the structural and aerodynamic models was accomplished using multiple sets of experimental data and advanced optimization techniques. Several repairs within the current field level repair limits were evaluated for their effect and none were found to significantly lower the computed flutter speed. Discussions of the novel and difficult features of the problem as well as the major assumptions are presented.

Introduction

The San Antonio Air Logistics Center (SAALC) has the primary Air Force responsibility for all engineering and maintenance for the T-38 Talon supersonic jet trainer. This responsibility includes determining whether or not a damaged T-38 stabilizer can be repaired at the field level within limits stated in T. O. 1T-38A-3. The stabilizer is an all moving control surface with a single spar of steel and aluminum. The aluminum face sheets cover an interior filled with aluminum honey comb core (see Figure 1). The results of this work have provided the SAALC with an improved repair evaluation technique for flutter of repaired stabilizers.

The repair limitations as published in the T. O. 1T-38A-3 are very restrictive in terms of allowable mass addition and repair area. For example, a trailing edge repair can cover no more than four inches. The table of limits was computed through analysis of the decrement in flutter speed caused by the mass addition. This computation was based upon the first three structural modes and quasi-steady strip theory aerodynamics.¹¹

Routinely encountered damages were consistently beyond these repair limits leading to replacement of the entire stabilizer and rapid depletion of the spares inventory. A refurbishment program was begun to salvage the major structural components of damaged articles and return newly skinned and cored parts to service. The large cost of complete replacement or refurbishment could be avoided if a new analysis could establish a safe expansion of the repair limits.

The NASTRAN flutter analysis was selected because of its unified structural and aerodynamic character. The compatibility of the structural model with a variety of analyses other than flutter allows verification of the mass and stiffness of the model. NASTRAN can handle large models by formulating the flutter problem in a modal basis and transforming the structural characteristics to modal properties and the aerodynamics to parametric modal forces. The procedure is quite well automated but, in retrospect, not well documented for practical use.

*Adjunct Professor, Aeronautical Engineering,
Member AIAA

This paper is declared a work of the U.S.
Government and therefore is in the public domain.

Verification of the Model

A flutter analysis is based upon several mathematical models that approximate a variety of physical aspects of the flight vehicle. To document and keep original data as well as the assumptions that transform the data to model parameters, a model generation computer program was constructed.⁶ The program literally creates the bulk data file for inclusion in the NASTRAN execution decks. All raw dimensional and material data with the name of the original document are contained in comments and tables of the generator program. All equations which transform these data to model parameters, such as cross-sectional area or moments of inertia, are coded in a verbose, expanded fashion for clarity. While this is computationally inefficient, it presents assumptions and manipulations clearly during later review. As the project progressed, the security of the model data base was assured by use of the generator program.

Several parameters of the stabilizer structural model were considered alterable to facilitate various analyses. The overall mesh size can be varied and extra nodes can be added to accommodate test load applications. An intermediate spar and ribs can be generated for analysis of early production model stabilizers. During subsequent model tuning investigations, material properties such as the elastic moduli were frequently altered and new models generated. This capability proved to be essential to rapidly evaluating the model errors during tuning.

The initial model verification was accomplished by comparison of calculated deflections to influence coefficient test measurements. Although the model proved too flexible, the causes could not be determined due to an inability to model the original test accurately. The resulting computed displacements agreed in form but showed excessive bending and torsional displacements.

The performance of such a faithful model was disappointing. Quite an effort had been made to eliminate numerical errors and provide a detailed model. Furthermore, interpretation and use of original test data was difficult due to the twenty year lapse. In order to investigate the detailed nature of the model's short comings, a new set of test measurements were commissioned.

To determine the modes and frequencies of vibration, a ground vibration test of a stabilizer in a free-free condition was accomplished.¹² The stabilizer was suspended from bungee cords at its four corners. While such a free-free boundary condition does not represent any service conditions, it is easily modelled and does not contain any influence of the aircraft flight control system. For verification under these boundary conditions to be useful, it must be assumed that a subsequent model change to the aircraft installed boundary conditions does not alter the accuracy of the model. While the

numerical mode shapes were predicted accurately, the frequencies were 20-40 Hz too low in the majority of cases.

A similar test was conducted at the Air Force Armament Laboratory by the Structural Dynamics Section, but on an installed stabilizer.

The flutter critical flight condition is loss of half hydraulic power since this lowers the effective pitch stiffness and the first torsion frequency. The spring constant for this condition was estimated from the full power data by matching the first torsion frequency with aircraft installed boundary conditions. The half power condition produces the lower stiffness and torsion frequencies and therefore will have the lower flutter speed. This occurs in flight with one engine out which leaves one of the two hydraulic systems operative.

To estimate the stiffness errors, the static displacement measurements similar to those conducted on the original static test article were reaccomplished.¹⁰ An antisymmetric bending boundary condition was constructed by pinning the torque tube at the aircraft center line in addition to the support near the root chord. This simulated symmetric torsion and antisymmetric down bending. While these conditions were not those of the original tests, they were easily modelled and simple to construct. As a result of these differences, the measured results are not directly comparable to the original test data but did prove to be readily modelled numerically.

Although the results are presented in detail elsewhere,^{6,10,12} a summary of the structural model verification is as follows. The cantilever root first three frequencies are low, the free-free frequencies are low, and the installed frequencies above the first two suspension modes are low. The mass and pitch inertia compare well to within the certainty of the comparison data, as does the center of gravity position. Both the original static displacement data and the new displacement measurements show the model to deflect too much in spanwise bending and in torsion. It was concluded the model mass was accurate and the stiffness too low.

Verification of the aerodynamic model was limited to comparison of the zero frequency pressures computed by a more advanced computer program.¹² Pressures computed by both programs compared well with the experimental data. No unsteady data was available.

Model Tuning

With confidence that the model was free from mistakes in the form of transcription errors, incorrect interpretation of blue line drawings, data transformation logic errors, or inaccurate approximations, the model was declared correct. The poor performance of the model could then be attributed only to neglecting to model some facet of the structure's load reaction mechanisms. Recall that the model is a two dimensional, thin sheet of plate bending elements which reacts lateral loads solely by the creation of internal moments and shears. Consider the stabilizer that is in fact a three dimensional assembly of face sheets separated by a honeycomb core. It does actually create internal bending moments in the form of equal and opposite forces in the planes of the face sheets.

The model's performance in load cases that consist of only spanwise down bending is acceptable (keep in mind that the majority of the cases included considerable torque applied about the pitch axis because of the swept spar). To react applied torques, the stabilizer creates shear stresses that are traditionally modelled as shear flows around closed cells. If modelled as a multi-celled torque box, the stabilizer has two torsion cells separated by the spar. The plate bending model is incapable of creating the reacting shear flows and is therefore too flexible.

There are at least two remedies to the inadequacy of the model. The most obvious is to construct a three dimensional model of the stabilizer. The model would consist of nodes on both surfaces of the airfoil and membranes in the planes of the face sheets. The spar and ribs would be modelled with rods in the outer surface to model the caps and membranes to model the webs. The disadvantage of having to totally reconstruct such a model would be offset by the existence of the generator program. All original data would not be retranscribed. Only the modelling assumptions about lumping and interpolating properties would be rewritten. Still considerable effort would be spent running the new model through the verification data. Furthermore, it is not at all obvious that, for the same number of degrees of freedom, such a model would perform better.

Altering the properties of the model to tune its performance to the available data was accepted in the present case since the poor performance has been attributed to the neglect of a key reaction mechanism. Since the general performance suggested an overall lack of stiffness, only those parameters that were globally effective were considered for change. That is, individual elemental properties were not changed singularly in any attempt to tune up a local section of the model. Parameters such as the elastic modulus of the entire face sheet could be tuned, in concept at least, to any of the available verification data.

The T-38 stabilizer model has been tuned to a vector of performances that included both the static displacement errors and the modal frequency errors.^{3,5,10} The result is a large set of models that do well at various combinations of load cases and modal frequencies.^{1,4} For use in flutter analysis, the best dynamic model tuned via thickness increases was selected. This model used isotropic plates and a uniformly applied 37% increase in the airfoil thickness.^{2,7} Although this model has worse total frequency error than the best orthotropic plate model, it has a better first torsion frequency.

Flutter Analysis

NASTRAN flutter analysis is based upon an iterative search of assumed Mach numbers and frequencies for neutrally stable motions of the structure existing in concert with the aerodynamic forces. The analysis is based upon a structural model, an aerodynamic model and an interface model. All models are linear and the analysis is based upon the assumption of harmonic motion. Neutrally stable perturbed motion is predicted at a computed frequency for the computed amount of assumed damping. When the amount of damping required exceeds that amount

reasonably expected to exist in the structure, flutter is indicated. Conservative practice assumes no damping in the structure so values of zero damping typically indicate flutter points. The need to presume an airspeed and reduced frequency of oscillation in the computation of the aerodynamic forces leads to the iteration. Economic considerations usually dictate the iterative refinement be reserved for the most marginal cases.

The present work investigated three of the five available NASTRAN aerodynamic theories. The doublet lattice method was selected over strip theory and the mach box method after consideration of modelling ease, accuracy and the expected flutter regime. A 8 by 8 array of boxes panelling the stabilizer planform was used for the aerodynamic model (Figure 3). Use of coarser models such as a four by five box lattice resulted in a flutter speed as much as 70 knots low. The flutter methods in NASTRAN showed significant sensitivity to common modelling assumptions about the aerodynamic grid, the interface splines and the aerodynamic force interpolations.^{2,7}

The original 830 knot flutter speed was a computed figure, assumed 3% structural damping and was 10% to 20% below expectations.⁸ The 916 knot flutter speed of the present investigation falls inside the expected range but is based upon 0% damping (Figures 4, 5, 6). The flutter frequency of 29.7 Hz is close to the computed 29 Hz of Ref. 8.

The T. O. 1T-38A-3 delineates limits for permanent field applied repairs.¹³ The usual damages are puncture holes and delaminations although water absorption may necessitate similar fixes. Typical repairs consist of removal of damaged core and skin, replacement of the aluminum core with a phenolic core and a flush patch of the skin. The repair sizes are limited based upon location and are presented in a tabular format. It is important to understand these repairs are for field application, are given only in typical terms and are not historically traced in any way. The guidelines do not address the possibility of multiple repairs to any one article.

Three repairs within the limits and one repair substantially beyond the allowables were modelled and the flutter speed recomputed (Figure 7). These represent a hole near the trailing edge, a hole near the tip, delamination of the leading edge, and an extreme case of root to tip core replacement near the trailing edge, and were modelled by the addition of a mass representative of the increased core mass in the affected elements. None of these repairs suggest a significant decrease in the flutter speed. (See Table I) This could be expected from the insignificant changes caused in the first torsion frequency.

Discussion of the Technical Assumptions

The following discussion of the more basic assumptions made in the analyses are presented here rather than earlier as a knowledge of the analytical techniques and geometric arrangement is required for their interpretation.

The structural model of the planform was verified against measured vibration data in the free-free boundary condition. This should leave only the pitch spring to be verified in the installed boundary conditions. It also simplifies the experimental setups required to take data in free-

free or other convenient conditions and does not require a fuselage under hydraulic power. Since the response of the model changes dramatically between free-free and installed conditions, this may not be valid. For example, the bending stiffness of the torque tube probably has minor impact on the free-free vibration response since it is an appendage but it dominates the installed first bending frequency. If verification has proceeded from fixed conditions to free, incorrect masses near fixed points might not be detected and not affect the fixed boundary comparisons but should alter the free boundary frequencies. In the present case, substantial confidence in the majority of the structural model was gained in the verification against the free-free vibration data.

The doublet lattice method unsteady aerodynamics were used for the entire flight envelope. Flutter procedures require the assumption of Mach number and reduced frequency followed by the computation of flutter speed and damping. If the flutter Mach number does not match the assumed Mach number, iteration may be required to match the conditions. The flutter condition is really a neutral stability point and the equations are only valid at a matched Mach number and zero damping. If the structure is judged to have some damping, say 2%, practice is to choose the flutter velocity where damping is 0.02. Further, Mach number matching is performed only if flutter conditions appear close to the flight envelope. Many simplifications are made in flutter analyses to reduce the number of computations and loops. Numerical comparisons have revealed a surprising sensitivity to common short cuts in discretizing the planform, interpolation of aerodynamic forces among the sets of reduced frequencies and Mach numbers. Standard practice seems most suited to scanning the envelope leaving the more accurate and expensive analyses for the critical points.

NASTRAN flutter evaluation of repaired structures has the advantage of including modified mode shapes in the analysis. More traditional techniques use frequencies altered by the modifications and the original mode shapes. This can be significant only for large stiffness and mass changes and appears to be an advantage for NASTRAN. Yet it is precisely these large modifications that demand reverification of the models. Nonetheless, there is apparently a significant domain of structural modifications and repairs that will appreciably alter the mode shapes but are not beyond the range of applicability of the existing model.

Repairs are limited to smooth aerodynamic shapes since the theory assumes linear aerodynamics. In particular, it is assumed that the steady load is low enough the small oscillations may be superimposed in an additive, linear fashion. This assumption may not be good near maximum lift coefficients or in the presence of shocks. Both large steps in skin thickness or holes could significantly alter the local flow and models of these effects with the present theory may produce unrealistic and unrepresentative results. With these limitations, the present method will show altered aerodynamic forces only if modal frequencies and modal shapes change due to structural repair. Earlier techniques based upon altered frequencies and the original mode shapes obviously only showed changes due to small modal frequency shifts.

The hydraulic pitch actuator is known to be non-linear in that its stiffness is a function of

frequency and temperature. The use of the operational temperature is reasonable but does not consider those cases where extreme temperatures combined with a partial hydraulic failure can reduce flutter speeds below those predicted here or in prior analyses. In any case, NASTRAN does not allow flutter computations involving a frequency dependent stiffness. Since lower pitch stiffness values lower the flutter speeds by lowering the first pitch frequency, the critical case is half hydraulic power due to one engine out. The obviously lower stiffness associated with full hydraulic failure can occur but will persist for only short periods.

Discussion of the Technical Features of the Problem

A summary of the overall features of the repaired T-38 stabilizer flutter analysis is presented as a summation of some of the lessons learned. Several were visible at the beginning and undervalued while others were discovered with much effort. While the system manager will most appreciate the models and analysis of repairs that represent the details of the results, the following are more the point for structural dynamicists.

Although the existence of a Flutter Analysis Rigid Format in NASTRAN makes this problem appear simple and straight forward, in retrospect it is very difficult. The real aircraft system is suspected to flutter in the low supersonic regime, implying a degraded or repaired aircraft would flutter in the high subsonic or transonic regimes. Few aerodynamic theories, and none available in NASTRAN, are well suited to such Mach numbers.

The original stabilizer flutter analysis showed the flutter mode to be a combination of bending and torsion with a frequency that is very sensitive to the frequency of the in-vacuum first torsion mode. This frequency is a direct function of the stiffness of the hydraulic actuator and its support structure. Tests of the actuator indicated a non-linear, frequency dependent force-displacement relation and a strong temperature dependence. These were all avoided by using a simple linear spring whose value causes the model to best match the measured, installed first torsion frequency.

Again in retrospect, bending plates were the wrong element to model the stabilizer. The single spar support arrangement leaves high levels of torsion in most of the chordwise sections. Shear flows in the double celled planform are apparently significant and suspected to be the cause of the model inaccuracies.

Although flutter analysis has been available in NASTRAN for several years, practical information on its use is passed predominantly by word of mouth. Experienced users are rare. Practitioners take many shortcuts that surprise first time users and the approximate nature of the analysis itself can cause concern. Understanding aeroelastic phenomenon requires advanced inter-disciplinary study.

Verification is a good practice but can raise tricky issues beyond the immediate scope of the analysis. Static testing requires power actuators and computerized data acquisition. Modal testing also requires significant data analysis and is undergoing changes in formulation. Both required a scale model or a test article removed from service or inventory. For test results to help reduce analysis

uncertainty, the testing techniques must not introduce much uncertainty themselves.

The actual value of aerodynamic verification at only zero frequency is open to question. Although the expected smooth behavior of pressure as a function of reduced frequency near zero frequency suggests the acceptable steady performance of the aerodynamic model might warrant confidence for some range of small reduced frequencies, there is no indication of the extent of, nor the existence of, any acceptable non-steady reduced frequency range. Nonetheless, steady verification of the stabilizer alone was all that could be accomplished.

Unsteady aerodynamic results are essentially unverifiable in their raw form. Flutter requires an unsteady aerodynamic model and the characteristics of a good aerodynamic model are quite different from those of a good structural model. Little unsteady pressure data is available that can be used to verify the analytical method much less the aerodynamic model. Significant knowledge of the flexibilities of the structure and the interacting aerodynamics of the surfaces is required to choose the extent of the model. In the present case, the original flutter design analysis indicated that the wing and stabilizer were not coupled and fuselage bending did not affect flutter.

Conclusion

This work and the models that are its basis have been presented to the SAALC T-38 system manager. They will be used to investigate a possible expansion of the repair limits and the effects of multiple repairs. The structural model and the vector optimization tuning technique will be used to model large internal flaws in stabilizers. The capability to compute steady airloads with NASTRAN developed for the verification of the aerodynamic model has been expanded to include flexibility effects. None of this research enjoyed any direct funding and could not have proceeded without the rich technical resources provided by the local engineering community.

References

1. Briggs, H. C. and DeWispelare, A. R., Finite Element Model Tuning Via Multiple Objective Optimization Techniques, Proceedings of the AIAA (Dayton-Cincinnati Section) 9th Annual Mini-Symposium on Aerospace Science and Technology, 22 March 1983.
2. Briggs, H. C. and London, G. G., Flutter Investigation of Repaired T-38 Horizontal Stabilizers Using NASTRAN, Proceedings of the AIAA (Dayton-Cincinnati Section) 9th Annual Mini-Symposium on Aerospace Science and Technology, 22 March 1983.
3. Devore, C. R., Structural Model Tuning Via Vector Optimization, AFTT/GAE/AA/82D-8, Wright-Patterson AFB OH: Air Force Institute of Technology, December 1982.
4. Devore, C. R., Briggs, H. C. and DeWispelare, A. R., Application of Multiple Objective Optimization Techniques to Finite Element Model Tuning, Paper 83-1010, Part 1 of the Proceedings of the AIAA/ASME/ASCE/AHS 24th Structures, Structural Dynamics and Materials Conference, 2-4 May 1983.

5. Dodge, L. C., Investigation of an Improved Structural Model for Damaged T-38 Horizontal Stabilizer Flutter Analysis Using NASTRAN, AFIT/GAE/AA/81D-6, Wright-Patterson AFB OH: Air Force Institute of Technology, December 1981.

6. Lassiter, J. O., Initial Development for a Flutter Analysis of Damaged T-38 Horizontal Stabilizers Using NASTRAN, AFIT/GAE/AA/80M-2, Wright-Patterson AFB OH: Air Force Institute of Technology, March 1980.

7. London, G. G., Investigation of an Improved Finite Element Model for a Repaired T-38 Horizontal Stabilizer Flutter Analysis Using NASTRAN, AFIT/GAE/AA/82D-19, Wright-Patterson AFB OH: Air Force Institute of Technology, December 1982.

8. NAI-58-11, T-38A Flutter Characteristic Summary, Vibration and Flutter Analysis, Hawthorne CA: Northrop Aircraft, Inc., June 1960.

9. Rohlman, W. H., CF-5 Horizontal Stabilizer Ground Vibration Test, Eglin AFB FL: Structural Dynamics Laboratory, Air Force Armament Test Laboratory (AFATL/DLJCS), October 1979.

10. Sawdy, J. O., Investigation of a Two-Dimensional Model for the Prediction of Static Displacement for the T-38 Horizontal Stabilizers Using NASTRAN, AFIT/GAE/AA/81D-27, Wright-Patterson AFB OH: Air Force Institute of Technology, December 1981.

11. Scanlan, R. H., and Rosenbaum, R., Introduction to the Study of Aircraft Vibration and Flutter, MacMillan Publishers, 1951.

12. Thomson, R. K., Investigation of an Improved Flutter Speed Prediction Technique for Damaged T-38 Horizontal Stabilizers Using NASTRAN, AFIT/GAE/AA/80D-21, Wright-Patterson AFB OH: Air Force Institute of Technology, December 1980.

13. T. O. 1T-38A-3, "Horizontal Stabilator Damage Repair," T-38 Maintenance and Repair Manual, Kelly AFB TX: San Antonio Air Logistics Center.

Table I

Comparison of Flutter Conditions

Repair Type	In-Vacuum 1st Torsion Frequency (cps)	Flutter Speed V_f (knots)	Flutter Frequency ω_f (cps)
Clean	44.3	916.5	29.8
Hole T.E.	44.3	916.5	29.8
Hole Tip	44.3	915.5	29.8
Delamination	44.3	919.4	29.7
Strip	44.2	911.0	29.7

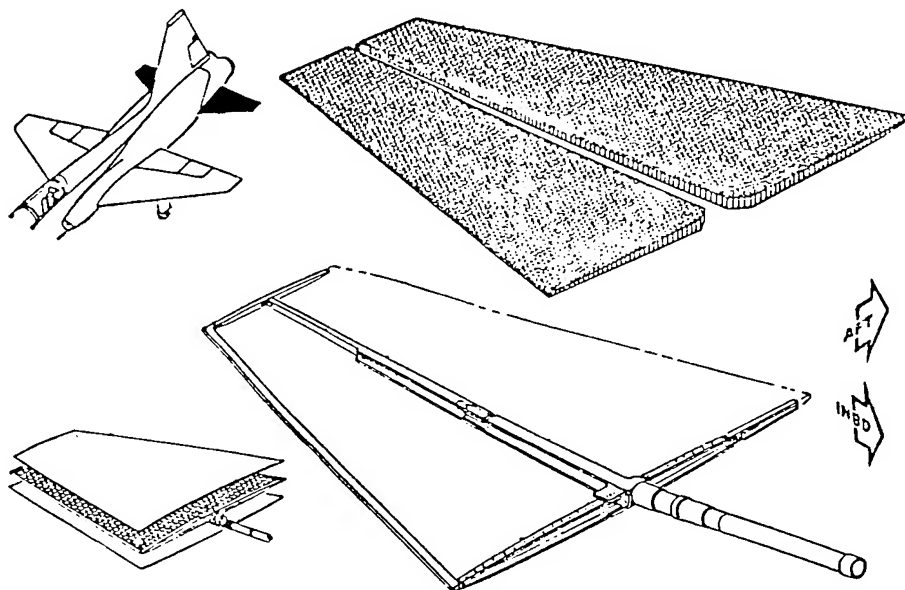


Figure 1. T-38 Stabilizer

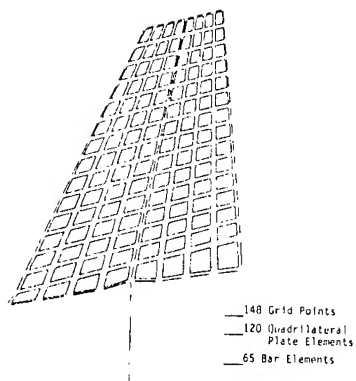


Figure 2. NASTRAN Structural Model

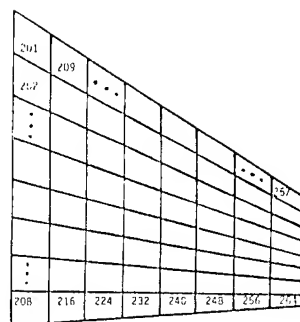


Figure 3. NASTRAN Aerodynamic Model

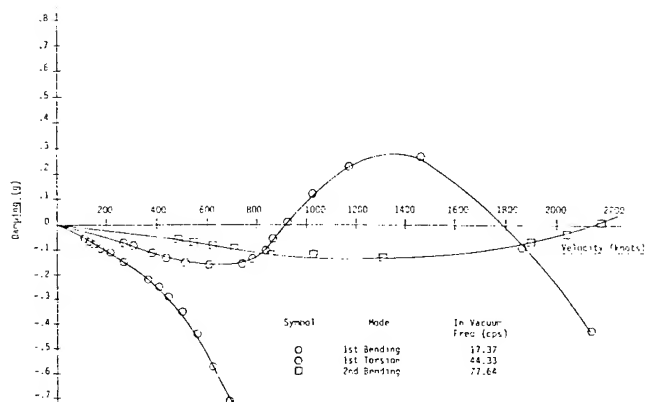


Figure 4. V-g Diagram Modes 1, 2, 3

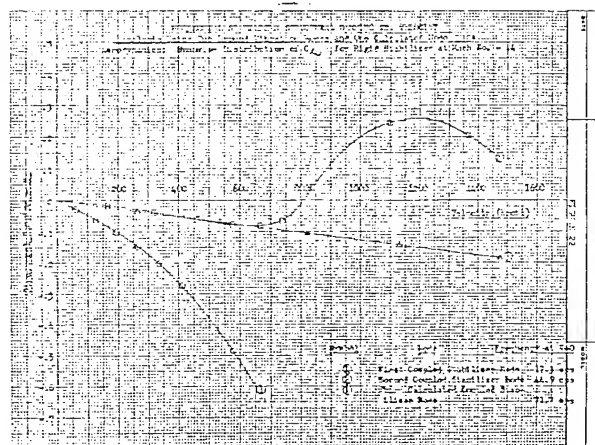


Figure 5. NAI V-g Diagram Modes 1, 2, 3

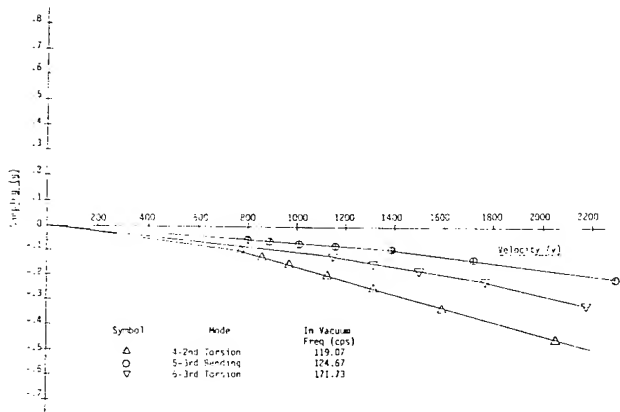
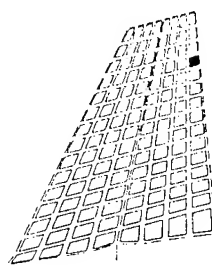
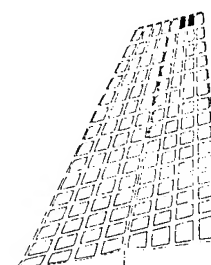


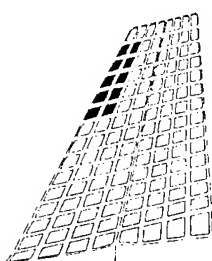
Figure 6. V-g Diagram Modes 4, 5, 6



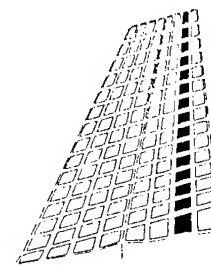
a) Trailing Edge Hole



b) Tip Hole



c) Leading Edge Delamination



d) Extreme Damage

Figure 7. Repair Simulations

Gabriel A. Oyibo*
Fairchild Republic Company
Farmingdale, New York

A generalized theory capable of predicting aeroelastic flutter speeds for all composite and isotropic aircraft wings is presented. The existence of an affine space in which the flutter analysis of composite and isotropic wings can be effected in a unified and efficient manner is established. The wing is idealized as a cantilevered flat plate-like lifting surface subjected to an incompressible flow in the physical space. The analysis assumes that the wing's construction permits the negligence of the elastic constant, D_{26} , in the Virtual Work Theorem. Using the well known bending-torsion displacement assumptions in the affine space and the variational principles, the aeroelastic equations of motion are derived. Employing the affine space unsteady aerodynamics and the uncoupled bending and torsional frequencies generated in separate analyses the flutter studies are carried out. The advantages of the present approach over the existing one include a significant reduction in the number of physical space quantities (whose relative importance and bounds are unknown), a better exposure of the interactions between the aerodynamic and elastic forces and the fact that the flutter characteristics can be efficiently compared for all materials in a preliminary design process. The results agree with previous investigations for isotropic wings.

Nomenclature

$(x, y, z), (x_0, y_0, z_0)$	= physical and affine space coordinates respectively
a_i	= chordwise integrals
$(\Delta P, \Delta P_0)$	= differential aerodynamic pressure distributions in physical and affine space respectively
r, L, D, D_0^*, ϵ	= generic nondimensionalized stiffness parameters
L_0, M_0	= affine space running aerodynamic lift and moments respectively
$L_{h_0}, L_{\alpha_0}, M_{\alpha_0}$	= complex affine space aerodynamic coefficients
\bar{U}, \bar{U}_0	= virtual work expressions in physical and affine space respectively
U, U_0	= flight velocity in physical and affine space respectively
D_{ij}	= elastic constants
$\rho_0, \bar{\rho}_\infty$	= affine space material and air density respectively

w	= displacement
\bar{h}	= wing box depth
(h_0, α_0)	= affine space bending and torsional displacement respectively
c'_0, c_0	= affine space half-chord and chord respectively
\mathcal{L}_0	= affine space half-span for the wing
e	= parameter that measures the location of the elastic axis relative to the mid-chord
r_{α_0}	= affine space nondimensionalized radius of gyration
x_{α_0}	= parameter that measures the center of gravity location relative to the elastic axis
m_0	= affine space mass per unit span
I_{α_0}	= affine space mass moment of inertia about $x_0 = e c'_0$
S_{α_0}	= affine space static mass moment about $x_0 = e c'_0$
ω	= vibration frequency
$\bar{\omega}, f$	= frequency ratio and material property/aspect ratio parameter respectively
k_0	= affine space reduced frequency/Strouhal number
$\bar{C}(k_0)$	= affine space Theodorsen's function
i	= $\sqrt{-1}$

Introduction

As the reality of operating modern high technology aircraft at supersonic and transonic speeds gathers more impetus the aeroelastician's zeal to clearly understand non-linear transonic aeroelasticity (which is believed to be capable of explaining phenomena like the 'transonic dip') has almost become an obsession. This is evidenced by the tremendous attention which has lately been given to the generation of accurate non-linear transonic unsteady aerodynamics codes. However obtaining accurate non-linear

*Senior Research and Development Engineer, Flutter and Vibration Group.

transonic unsteady aerodynamics is just one of the necessary ingredients for really understanding non-linear transonic aeroelasticity for modern advanced technology aircraft. Others include the understanding of the limit cycle theory and the anisotropic aeroelasticity. The latter is known to be plagued with the existence of too many physical constants (which tend to obstruct the physical insight expected from an analysis).

Recent studies by the author¹⁻⁵ have indicated that anisotropic aeroelasticity can be analyzed in the affine space with tremendous advantages. These advantages include a significant reduction in the number of the physical space quantities (whose relative importance and bounds are not known), a better exposure of the interaction between the aerodynamic and elastic forces, and the fact that aeroelastic characteristics can be efficiently compared for all composite materials. While references 1-4 treated the panel flutter problems, reference 5 addressed the aeroelastic divergence, a critical design problem for forwardswept wing aircraft.

The transformation of the aeroelastic equations of motion from the physical space into the affine space depends on the sophistication of the mathematical modelling of the problem involved. In general the mapping is achieved by stretching the independent¹⁻⁴ or dependent⁵ variables. The generation of the unsteady aerodynamic loads is slightly more difficult in the affine space. However, the extra effort required to solve the aerodynamic problem is certainly justified by the relative simplicity of the overall aeroelastic equations of motion⁶.

It is conceivable that if the current advances in the materials sciences continue, the use of composite materials in the design of primary structures of aerospace vehicles shall be universal in the near future. At such a time, works like those of Krone⁷, Weisshaar⁸, Hollowell and Dugundji⁹, and Librescu¹⁰, to name a few, shall be more appreciated.

In this paper, the cantilever composite wing flutter is examined in an affine space. The wing is idealized as a flat plate-like lifting surface in an incompressible flow. A sectional model is shown in Figure 1. The analysis assumes that the wing's configuration is such that the elastic constant D_{26} can be neglected in the Virtual Work Theorem. This assumption and the bending-torsion displacement assumptions make it possible to transform the aeroelastic equations of motion into the affine space by stretching the independent variables. The affine space unsteady aerodynamics generated in reference 6 and the uncoupled bending and torsional frequencies calculated in reference 11 are used in the flutter analysis, which is characterized by studying the effects of a bounded generic material parameter D_0^* (defined in the text) on the flutter boundaries.

The results show that a unified flutter analysis for all materials (isotropic results being a subset) can be achieved, since a variation of D_0^* between zero and one permits the view of the flutter continuum for all composite and isotropic materials. A comparison of the isotropic results

with results from references 12 - 14 shows an excellent agreement.

Problem Statement

Consider a cantilevered aircraft wing which is subjected to an incompressible airflow. The airfoil section, the flow speed and the forces in an affine space are shown in Figure 1. It is assumed that the wing can be constructed with metals or composites.

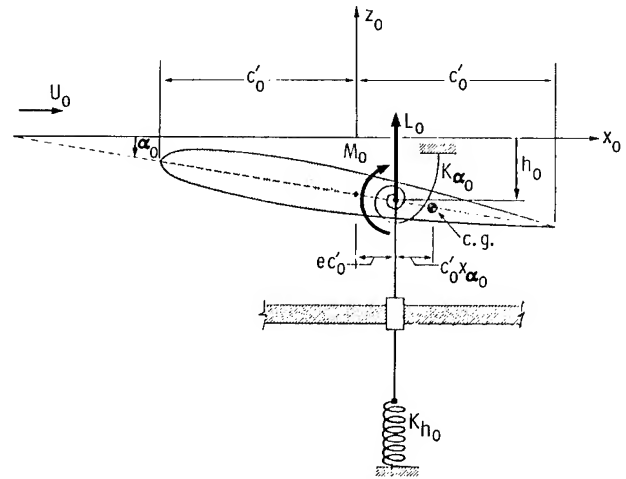


Figure 1. Oscillating Airfoil in Affine Space.

Physical Space Virtual Work Theorem

The physical space aeroelastic Virtual Work Theorem for a wing constructed with anisotropic materials is given by:

$$\begin{aligned} \delta \bar{U} = 0 = & \frac{\delta}{2} \int_0^t \iint_A \left[D_{11} (w_{,xx})^2 + 2D_{12} w_{,xx} w_{,yy} \right. \\ & + D_{22} (w_{,yy})^2 + 4D_{16} w_{,xx} w_{,xy} + 4D_{26} w_{,yy} w_{,xy} \\ & \left. + 4D_{66} (w_{,xy})^2 \right] dx dy dt - \frac{\delta}{2} \int_0^t \iint_A \rho \bar{h} \dot{w}^2 dx dy dt \\ & + \int_0^t \iint_A \Delta p \delta w dx dy dt \end{aligned} \quad (1)$$

where:

D_{ij} are the elastic constants, ρ is the material density, Δp is the differential pressure distribution, w is the displacement, t is the time, A integrals represent area integrals and h is the wing box depth. From Equation 1 the physical space aeroelastic equations can be obtained for an arbitrary displacement. However, as can be seen, the existence of so many parameters (in the equation) are bound to obstruct the physical insight expected from an analysis of the system. In what follows an attempt shall be made to show the existence of an affine space in which the aeroelastic analysis can be done in an efficient and unified manner.

Affine Space Virtual Work Theorem

Consider the affine transformations:

$$x = Ax_0, y = By_0, z = Cz_0 \quad (2)$$

where:

A, B and C are constants which if chosen properly should show that the task defined in this paper can be accomplished.

It must be pointed out before the selection of A, B and C that the usual bending-torsion displacement assumptions (which shall be used here in the affine space) would eliminate some of the parameters in equation (1). It shall also be assumed, for the purpose of this analysis, that the construction of the wing permits the negligence of the parameter D_{16} in equation (1).

Therefore if:

$$A = (D_{11}/D_{22})^{1/4}, B = C = 1 \quad (3)$$

equation (1), mapped into affine space, becomes:

$$\begin{aligned} \delta \bar{U}_0 = 0 = & \frac{\delta}{2} \int_0^t \iint_A \left\{ (w, x_0 x_0)^2 \right. \\ & + 2D^* \left[(1-\epsilon)(w, x_0 y_0)^2 + \epsilon w, x_0 x_0 w, y_0 y_0 \right] \\ & + (w, y_0 y_0)^2 + L w, y_0 y_0 w, x_0 y_0 \left. \right\} dx_0 dy_0 dt \\ & - \frac{\delta}{2} \int_0^t \iint_A \rho_0 \dot{w}^2 dx_0 dy_0 dt + \int_0^t \iint_A \Delta p_0 \delta w dx_0 dy_0 dt \end{aligned} \quad (4)$$

where:

$$\begin{aligned} \bar{U}_0 &= \frac{\bar{U}}{D_{22}} \left(\frac{D_{22}}{D_{11}} \right)^{1/4} \\ D^* &= \frac{D_{12} + 2D_{66}}{(D_{11}D_{22})^{1/2}} \\ \epsilon D^* &= \frac{D_{12}}{(D_{11}D_{22})^{1/2}} \\ L &= \frac{4D_{16}}{(D_{11})^{1/4}(D_{22})^{3/4}} \\ \Delta p_0 &= \frac{\Delta p}{D_{22}} \\ \rho_0 &= \frac{\rho \bar{h}}{D_{22}} \end{aligned} \quad (5)$$

Notice that a similar result can be obtained with $A = (D_{11})^{1/4}$, $B = (D_{22})^{1/4}$, $C = 1$.

Equation (4) is therefore the affine space aeroelastic Virtual Work Theorem, from which the equations of motion can be derived. The quantities D^* and ϵ in Equation (5), which have been studied, in references 1-5 have the following bounds for specially orthotropic composite materials

$$0 \leq D^* \leq 1, .12 \leq \epsilon \leq .65 \quad (6)$$

For isotropic materials $D^* = 1$, and ϵ becomes the Poisson's ratio. The non dimensionalized quantity L shall be made to disappear through the bending-torsion displacement assumptions to be used in the flutter analysis.

Affine Space Aeroelastic Equations of Motion

Consider the following popular bending-torsion displacement assumption,

$$w(t, x_0, y_0) = h_0(t, y_0) + x_0 \alpha_0(t, y_0) \quad (7)$$

When equation (7) is substituted into equation (4) and the variational calculus is carried out for arbitrary h and α_0 the following aeroelastic equations of motion are obtained.

$$\begin{aligned} a_1 h_0^{iv} + a_2 \alpha_0^{iv} + \rho_0 a_1 \ddot{h}_0 + \rho_0 a_2 \ddot{\alpha}_0 &= L_0 \\ a_2 h_0^{iv} + a_3 \alpha_0^{iv} - a_4 \alpha_0'' + \rho_0 a_3 \ddot{\alpha}_0 + \rho_0 a_2 \ddot{h}_0 &= M_0 \end{aligned} \quad (8)$$

where:

$$a_1 = \int_{-c_0/2}^{c_0/2} dx_0, \quad a_2 = \int_{-c_0/2}^{c_0/2} (x_0 - e c_0') dx_0 \quad (9)$$

$$a_3 = \int_{-c_0/2}^{c_0/2} (x_0 - e c_0')^2 dx_0, \quad a_4 = 2 \int_{-c_0/2}^{c_0/2} D^* (1-\epsilon) dx_0$$

$$L_0 = \int_{-c_0/2}^{c_0/2} \Delta p_0 dx_0, \quad M_0 = \int_{-c_0/2}^{c_0/2} \Delta p_0 (x_0 - e c_0') dx_0$$

$$(\quad)' = \frac{\partial}{\partial y_0}, \quad (\dot{\quad}) = \frac{\partial}{\partial t} \quad (10)$$

As can be seen from equations (8) and (9), the non dimensionalized quantity L has successfully been eliminated from the aeroelastic equations of motion by the bending-torsion displacement assumptions used in the analysis. Therefore it is now clear that in this affine space, aeroelastic analysis can be carried out for any wing configurations (isotropic or composite) by varying the

quantity D_0^* given by:

$$D_0^* = D^*(1 - \epsilon) \quad (11)$$

By examining equations (6), it becomes clear that:

$$0 \leq D_0^* \leq 1 \quad (12)$$

for all specially orthotropic composite materials. Although exact bounds of D_0^* are not established in this investigation, for laminates used in an actual wing construction, some calculations carried out seem to suggest that:

$$0 \leq D_0^* \leq 4 \quad (13)$$

would cover a substantial amount of material properties and fiber orientations. Therefore a view of the aeroelastic continuum in this range of D_0^* should be very helpful in the preliminary aircraft design process.

Unsteady Aerodynamics

In order to solve equations (8) to determine aeroelastic instability boundaries, the aerodynamic forces and moments L_0 and M_0 would have to be generated by solving the aerodynamic equations. In the affine space the aerodynamics equations are slightly more difficult to solve than in the physical space. However, the overall relative simplicity of the aeroelastic equations of motion certainly justifies the extra effort needed. Reference 6 used two dimensional linear approximations and a Theodorsen type approach to generate the incompressible harmonic unsteady aerodynamics used in this analysis. It was shown in reference (6) that:

$$\begin{aligned} L_0 &= \frac{\pi}{r} \bar{\rho} c_o'^3 \omega^2 \left\{ L_{h_0} \bar{h}_0 + \left[L_{\alpha_0} - L_{h_0} \left(e + \frac{1}{2} \right) \right] \alpha_0 \right\} \\ M_0 &= \frac{\pi}{r} \bar{\rho} c_o'^4 \omega^2 \left\{ \left[\frac{1}{2} - L_{h_0} \left(e + \frac{1}{2} \right) \right] \bar{h}_0 + \left[M_{\alpha_0} \right. \right. \\ &\quad \left. \left. + L_{h_0} \left(e + \frac{1}{2} \right)^2 - \left(L_{\alpha_0} + \frac{1}{2} \right) \left(e + \frac{1}{2} \right) \right] \alpha_0 \right\} \end{aligned} \quad (14)$$

where:

$$\begin{aligned} \bar{\rho} &= \frac{\rho_\infty}{D_{22}} \\ r &= \left(\frac{D_{22}}{D_{11}} \right)^{1/4} \\ \bar{h}_0 &= \frac{h_0}{c_o'} \\ (\bar{h}_0, \alpha_0) &= (H_0, \alpha_0) e^{i\omega t} \end{aligned} \quad (15)$$

ρ_∞ is the air density, (H_0, α_0) are the vibration amplitudes. ω is the vibration frequency and e measures the location of the elastic axis relative to the mid-chord.

L_{h_0} is the running aerodynamic lift coefficient due to the wing's bending vibrations in affine space, L_{α_0} is the running aerodynamic lift coefficient due to the wing's torsional vibrations about the affine space quarter-chord. M_{α_0} is the running aerodynamic moment coefficient due to wing's torsional vibrations about the affine space quarter-chord. These coefficients, which are functions of the affine space reduced frequency (Strouhal number), k_0 , are expressed as follows:

$$L_{h_0} = 1 - \frac{2i}{k_0} \bar{C}(k_0) \quad (15a)$$

$$L_{\alpha_0} = \frac{1}{2} - \frac{i}{k_0} \left[1 + 2\bar{C}(k_0) \right] - \frac{2\bar{C}(k_0)}{k_0^2}$$

$$M_{\alpha_0} = \frac{3}{8} - \frac{i}{k_0}$$

where:

$\bar{C}(k_0)$ is the Theodorsen's function in the affine space given by:

$$\bar{C}(k_0) = \frac{H_1^2(k_0)}{H_1^2(k_0) + iH_0^2(k_0)} \quad (15b)$$

H_0^2 and H_1^2 are Hankel functions and k_0 is given by:

$$k_0 = \frac{\omega c_o'}{U_0} \quad (16)$$

U_0 , the affine space flight velocity, is given by:

$$U_0 = rU \quad (16a)$$

The Hankel functions in equation (15b) are usually available in tabulated forms. Hence L_{h_0} , L_{α_0} and M_{α_0} can be calculated for a chosen value of k_0 from which L_0 and M_0 could be evaluated for flutter analysis.

As was pointed out in reference (6), the affine space unsteady aerodynamics is not only restricted to two dimensional space (airfoil section), but could also be evaluated in three dimensional space with various levels of sophistications (including nonlinear treatments). Ideas similar to those of references (15-16), among numerous others, can be used in the affine space. This is why the author believes that at a time when tremendous efforts are being put into the development of sophisticated computer codes for the nonlinear unsteady transonic aerodynamics, affine space aerodynamics should be considered, in the light of the current trends in the aerospace vehicle design philosophy (changing from metal to composite aerospace vehicles).

Uncoupled Vibrations Frequencies

To determine the flutter boundaries, it is necessary to estimate the so called free uncoupled vibration frequencies for the wing. To do this reference 11 examined equations (8). The results, for the wing's first bending and tor-

sional frequencies, which shall be used in the flutter analysis, were estimated as follows:

for the first bending, a fourth order approximation gives the frequency,

ω_{h1} as:

$$\omega_{h1} = \frac{(.597)^2}{\ell_0^2} \sqrt{\frac{1}{\rho_0}} \quad (17)$$

where ℓ_0 is the affine space half span of the wing.

For the first torsion, two approximations were made in reference (11); one, a second order and the other a fourth order.

The second order estimate gave the first torsional frequency, $\omega_{\alpha 01}$, as:

$$\omega_{\alpha 01} = \frac{\pi}{2 \ell_0 c_0} \sqrt{\frac{24 D_0^*}{\rho_0}} \quad (18)$$

where: c_0 ($= 2 c_0$) is the affine space wing chord. The fourth order estimate gave the first torsional frequencies as:

$$\omega_{\alpha 01} = \frac{k_{\alpha 01}}{\ell_0 c_0} \sqrt{\frac{1}{\rho_0}} \quad (19)$$

where $k_{\alpha 01} = k_{\alpha 01}(\frac{\ell_0}{c_0}, D_0^*)$ with $\frac{\ell_0}{c_0}$ as the affine space aspect ratio for the wing.

Plots of $k_{\alpha 01}$ for various $\frac{\ell_0}{c_0}$ and D_0^* are shown in reference (11).

Flutter Analysis

Without any loss of generality, equations (8) shall be specialized here to deal with the flutter arising from the coalascence between the first bending and the first torsional frequencies of the wing. Hence equations (8), no matter what order of approximation was used for estimating the uncoupled natural frequencies, reduce to:

$$m_0 \ddot{h}_0 + S_{\alpha 0} \ddot{\alpha}_0 + m_0 \omega_{h1}^2 h = L_0 \quad (20)$$

$$S_{\alpha 0} \ddot{h}_0 + I_{\alpha 0} \ddot{\alpha}_0 + I_{\alpha 0} \omega_{\alpha 01}^2 \alpha_0 = M_0$$

where:

$$m_0 = \rho_0 a_1, S_{\alpha 0} = \rho_0 a_2 = m_0 e x_{\alpha 0} \quad (21)$$

$$I_{\alpha 0} = \rho_0 a_3 = m_0 e^2 r_{\alpha 0}^2$$

$r_{\alpha 0}$ is basically a nondimensionalized radius of gyration in the affine space.

Using the simple harmonic motion assumptions in equation (15), non-dimensionalized flutter equations resulting from equations (14) and (20), are:

$$\begin{aligned} & \left\{ \frac{r m_0}{\pi \bar{\rho}_{\infty} c_0'^2} \left[1 - (f \bar{\omega})^2 \right] + L_{h_0} \right\} H_0 \\ & + \left\{ \left[L_{\alpha 0} - L_{h_0} \left(e + \frac{1}{2} \right) \right] + \frac{x_{\alpha 0} r m_0}{\pi \bar{\rho}_{\infty} c_0'^2} \right\} \bar{\alpha}_0 = 0 \\ & \left\{ \left[\frac{1}{2} - L_{h_0} \left(e + \frac{1}{2} \right) \right] + \frac{x_{\alpha 0} r m_0}{\pi \bar{\rho}_{\infty} c_0'^2} \right\} H_0 + \left\{ L_{h_0} \left(e + \frac{1}{2} \right)^2 \right. \\ & \left. + M_{\alpha 0} - \left(L_{\alpha 0} + \frac{1}{2} \right) \left(e + \frac{1}{2} \right) + \frac{r^2 m_0}{\pi \bar{\rho}_{\infty} c_0'^2} \left[1 - \bar{\omega}^2 \right] \right\} \bar{\alpha}_0 = 0 \end{aligned} \quad (22)$$

where:

$$f = \frac{\omega_{h1}}{\omega_{\alpha 01}}, \quad \bar{\omega} = \frac{\omega_{\alpha 01}}{\omega} \quad (23)$$

from equations (17), (18), (19) and (23) depending on the order of approximations,

$$f = \frac{(.597)^2 \pi}{\frac{\ell_0}{c_0} \sqrt{24 D_0^*}} \quad (24)$$

or

$$f = \frac{(.597 \pi)^2}{\frac{\ell_0}{c_0} k_{\alpha 01}} \quad (25)$$

where:

equations (24) and (25) give the second and the fourth order approximations respectively. Clearly equations (22), which can be put in the form,

$$\begin{bmatrix} M \end{bmatrix} \begin{bmatrix} H_0 \\ \bar{\alpha}_0 \end{bmatrix} = 0 \quad (26)$$

are eigenvector equations. Hence for nontrivial solutions the determinant of M must vanish identically. The fact that M is complex (resulting from the nondimensionalized unsteady aerodynamic functions) makes the computations of the eigenvalues for a set of configuration parameters a tedious exercise. However aeroelasticians have since learned to live with this fact.

Flutter Results

The computations were carried out by selecting, sets of configuration parameters and solving for k_0 and $\bar{\omega}$. These parameters are the affine space quantities,

$$\frac{rm_0}{\pi \bar{\rho}_\infty c_0'^2}, x_{\alpha_0}, r_{\alpha_0}, e, f.$$

As can be seen from equations (24) and (25) the frequency ratio parameter, f is just a function of the affine space aspect ratio, l_0/c_0 , and D_0^* . Therefore a feasibility now exists in the light of earlier discussions on the limits of D_0^* , of designing a wing (irrespective of the construction material), to meet a flutter criterion just by varying D_0^* , rather than increasing the stiffness/weight of the wing (a popular option). The plots shown in Figures 2-10 can be used to accomplish such a task. Although these figures depict the trends observed in the analysis, the intersections of the curves for some wing configuration parameters appear to indicate the danger of generalizations, a feature that has generally become inherent in flutter analysis. For example, in Figure 2, it is seen that the same nondimensionalized flutter speed can be achieved with either $x_{\alpha_0} = 0$ or .1, .2 etc., depending on the value of f .

On the other hand, the trends appear more familiar with very small f . Therefore just as has been shown by previous investigators for isotropic wings, design exercises like the incorporation of stores on an existing airplane design (which involves a variation of x_{α_0} , among other parameters) should be done with some caution. Notice also, from the figures that increases in D_0^* (say the torsional stiffness, D_{66}) does not necessarily result in higher flutter speeds.

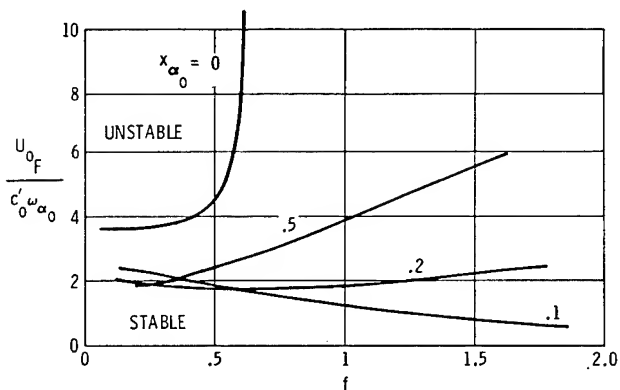


Figure 2. Affine Nondimensionalized Flutter Speed versus f

$$\frac{rm_0}{\pi \bar{\rho}_\infty c_0'^2} = 20, e = -.4 \quad r_{\alpha_0} = .333$$

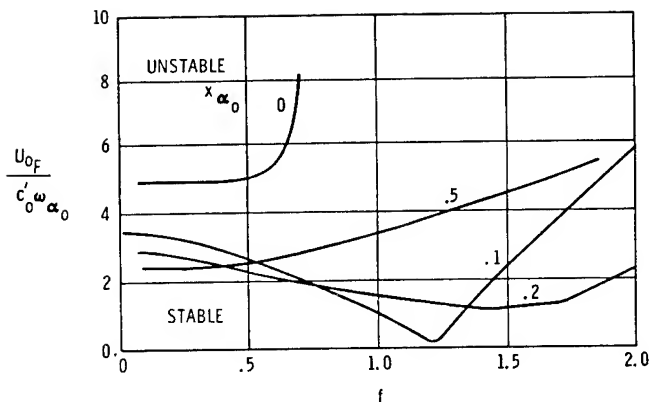


Figure 3. Affine Nondimensionalized Flutter Speed versus f

$$\frac{rm_0}{\pi \bar{\rho}_\infty c_0'^2} = 20, e = -.4 \quad r_{\alpha_0} = .5$$

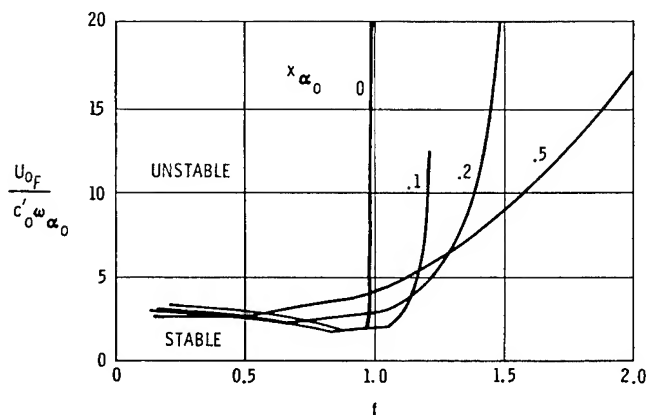


Figure 4. Affine Nondimensionalized Flutter Speed versus f

$$\frac{rm_0}{\pi \bar{\rho}_\infty c_0'^2} = 50, e = 0 \quad r_{\alpha_0} = .5$$

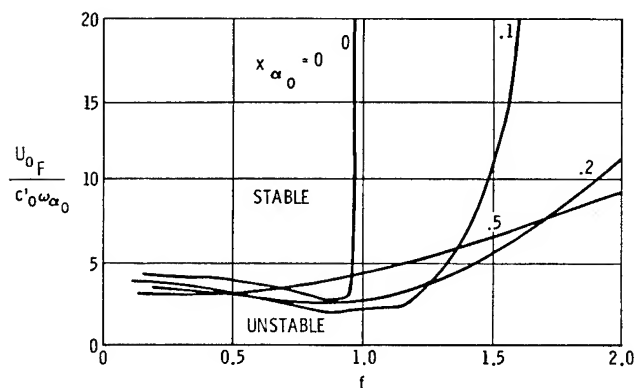


Figure 5. Affine Nondimensionalized Flutter Speed versus f

$$\frac{rm_0}{\pi \bar{\rho}_\infty c_0'^2} = 50, e = -.2 \quad r_{\alpha_0} = .5$$

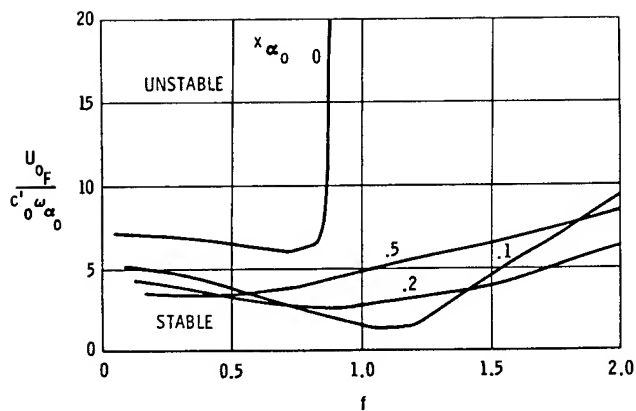


Figure 6. Affine Nondimensionalized Flutter Speed versus f

$$\frac{r_{m_0}}{\pi \bar{\rho}_{\infty} c'_{\alpha_0}{}^2} = 50, e = -.4 \quad r_{\alpha_0} = .5$$

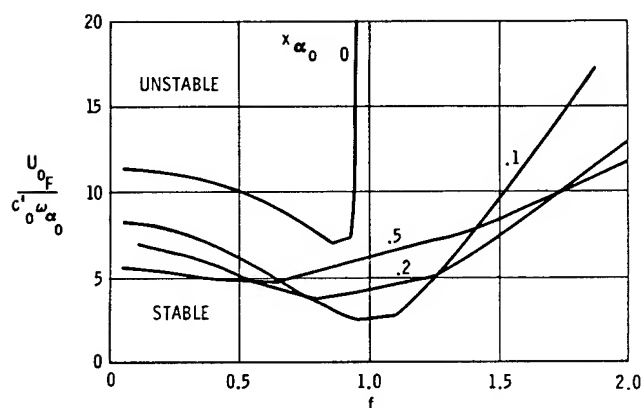


Figure 7. Affine Nondimensionalized Flutter Speed versus f

$$\frac{r_{m_0}}{\pi \bar{\rho}_{\infty} c'_{\alpha_0}{}^2} = 100, e = .4 \quad r_{\alpha_0} = .6$$

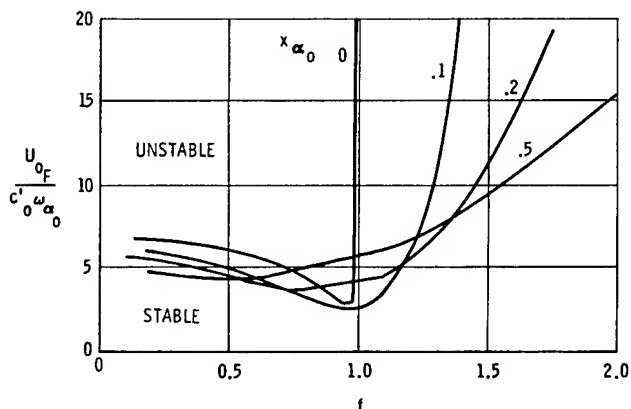


Figure 8. Affine Nondimensionalized Flutter Speed versus f

$$\frac{r_{m_0}}{\pi \bar{\rho}_{\infty} c'_{\alpha_0}{}^2} = 100, e = -.2 \quad r_{\alpha_0} = .6$$

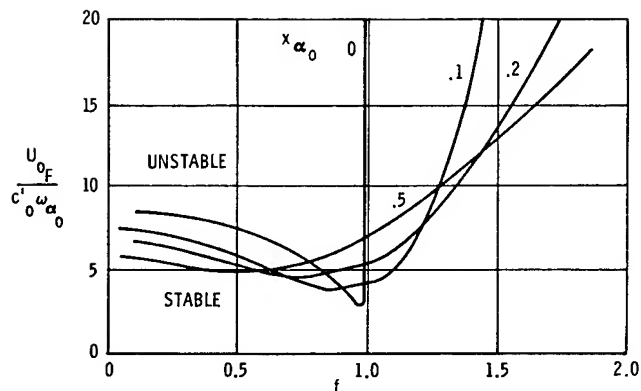


Figure 9. Affine Nondimensionalized Flutter Speed versus f

$$\frac{r_{m_0}}{\pi \bar{\rho}_{\infty} c'_{\alpha_0}{}^2} = 200, e = -.2 \quad r_{\alpha_0} = .5$$

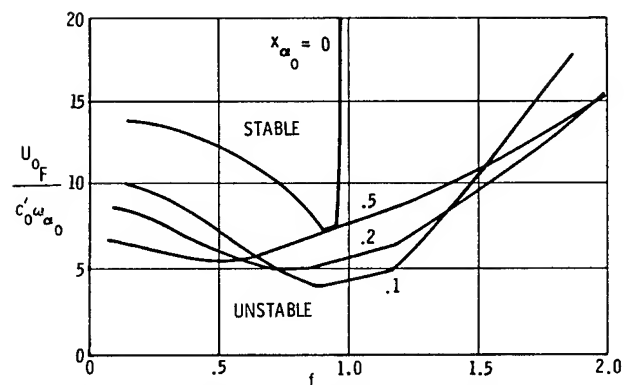


Figure 10. Affine Nondimensionalized Flutter Speed versus f

$$\frac{r_{m_0}}{\pi \bar{\rho}_{\infty} c'_{\alpha_0}{}^2} = 200, e = -.4 \quad r_{\alpha_0} = .5$$

Concluding Remarks

The development of a generalized bending-torsion flutter theory for aircraft wings constructed with either composite or isotropic materials has been attempted in this paper. With the help of some length-preserving affine transformations the aeroelastic virtual work theorem for the wing is mapped into an affine space. In this space the aeroelastic virtual work expression is not only much neater than its physical space counterpart, but also contains much fewer (and nondimensionalized) parameters which appear to be very useful in parametric-type studies. A characteristic stiffness parameter D_0^* is defined which varies between zero and one for all specially orthotropic composite materials. Although the bounds of this parameter is not established in this analysis for actual wing configurations, side calculations (not shown in the paper) seem to indicate that a variation of D_0^* between zero and four would cover a wide range of actual aircraft wing configurations.

The flutter analysis is carried out using the affine space unsteady aerodynamics and uncoupled free vibration frequencies generated in separate

analyses. The results show that the trends shown by previous investigators for isotropic wings can be established for composite materials (isotropic results being a subset) in an efficient and unified manner.

ACKNOWLEDGEMENTS

The author appreciates useful discussions with J. Berman, G. Rosenthal, Dr. S. Scala and Dr. W. Guman, all of Fairchild Republic Company. He is also grateful to R. Smith for computations, J. Constantine, T. Leonhardt, B. Berntsen and M. Gibbons for the drawings and typing.

LIST OF REFERENCES

1. Oyibo, G.A. "Flutter of Orthotropic Panels in Supersonic Flow Using Affine Transformations", AIAA Journal, Vol. 21, February 1983, pp. 283-289.
2. Oyibo, G.A., "Unified Panel Flutter Theory with Viscous Damping Effects", AIAA Journal, Vol. 21, May 1983, pp. 767-773.
3. Oyibo, G.A., "Unified Aeroelastic Flutter Theory for Very Low Aspect Ratio Panels", AIAA Journal, Vol. 21, No. 11, November 1983, pp. 1581-1587.
4. Oyibo, G.A. "The Unified Panel Flutter Theory and the Damping Effects", Presented at the Aerospace Flutter and Dynamics Council Meeting, Seattle, Washington, May 1982.
5. Oyibo, G.A., "Generic Approach to Determine Optimum Aeroelastic Characteristics for Composite Forwardswept Wing Aircraft", AIAA Journal, Vol. 22, No. 1, January 1984, pp. 117-123.
6. Oyibo, G.A., "Affine Space Unsteady Aerodynamics for Anisotropic Aeroelasticity", in preparation.
7. Krone, N.J., Jr., "Divergence Elimination with Advanced Composites", AIAA Paper No. 75-1009, presented at AIAA 1975 Aircraft Systems and Technology Meeting, Los Angeles, August 1975.
8. Weisshaar, T.A., "Divergence of Forward Swept Composite Wings", Journal of Aircraft, Vol. 17, June 1980, pp. 442-448.
9. Hollowell, S.J. and Dugundji, J., "Aeroelastic Flutter and Divergence Stiffness Coupled Graphite/Epoxy, Cantilevered Plates", AIAA Paper No. 82-0722 presented at AIAA/ASME/ASCE/AHS 23rd Structures, Structural Dynamics, and Materials Conference, New Orleans, LA, May 1982.
10. Librescu, L. "Elastostatics and Kinetics of Anisotropic and heterogeneous Shell-Type Structures", Nordhoff International Publishing, Leyden, The Netherlands, 1975.
11. Oyibo, G.A., "Generic Uncoupled Vibration Frequencies for Composite Aircraft Wings", in preparation.
12. Bisplinghoff, L.R., Ashley, H. and Halfman, R.L., Aeroelasticity, Addison-Wesley Publishing Co., Inc. 1955.
13. Theodorsen, T., "General Theory of Aerodynamic Instability and the Mechanism of Flutter, a Theoretical and Experimental Investigation of the Flutter Problem", N.A.C.A. Report 685, 1940.
14. Garrick, I.E. and Rubinow, S.I., "Flutter and Oscillating Air Force Calculations for an Airfoil in Two-Dimensional Supersonic Flow", NACA Report 846, 1946.
15. Berman, J., Shyprykevich, P., Smedfjeld, J., "A Subsonic Nonplanar Kernel Function for Oscillating Surface Inclined to the Free Stream", Journal of Aircraft; Vol. 7, No. 2, March-April, 1970.
16. Smilg, B. and Wasserman, L.S., "Application of Three-dimensional Flutter Theory to Aircraft Structures", Air Force Technical Report, 4798, 1942.

A FINITE ELEMENT METHOD FOR
NONLINEAR FORCED VIBRATIONS OF RECTANGULAR PLATES

Chuh Mei* and Kamolphan Decha-Umpai†
Department of Mechanical Engineering and Mechanics
Old Dominion University, Norfolk, Virginia

Abstract

The finite element method has been extended to determine the response of large amplitude forced vibrations of thin plates. A harmonic force matrix of a rectangular element under uniform harmonic excitation is developed for nonlinear forced vibration analysis. Inplane deformation and inertia are both considered in the formulation. Results obtained are compared with simple elliptic response, perturbation and other approximation solutions.

I. Introduction

Thin plate structures subjected to periodic lateral loading are likely to encounter severe flexural oscillations with amplitude to the order of plate thickness. The responses predicted using the small deflection linear plate theory are no longer applicable, and therefore, nonlinear theory taking account the effects of large amplitude has to be employed.

Following von Karman's large deflection plate theory, the basic governing equations for the nonlinear vibration of plates were established by Herrmann.¹ Based on these equations, various approximate procedures have been investigated by numerous researchers. For example, nonlinear forced vibration of circular and rectangular plates with various boundary conditions have been studied by applying the Galarkin or Ritz method,²⁻⁷ the Kantorovich averaging method,^{8,9} various perturbation techniques¹⁰⁻¹³ and incremental harmonic balance method.¹⁴ Studies based on the simplified Berger's hypothesis¹⁵ have also been made with the use of the Galarkin method.¹⁶ Chia¹⁷ and Yamaki et al.⁷ have presented their comprehensive and excellent reviews on both free and forced nonlinear vibrations of plates. All these studies, however, have been concerned only with circular or rectangular plates due to the difficulty of the mathematical treatment. With the increased use of thin plates in many optimum or minimum-weight designed built-up structures, it is of great importance to extend the finite element method to nonlinear forced vibration problems. In this paper, a finite element formulation is presented for the large amplitude vibrations of thin plates subjected to harmonic loading. Inplane deformation and inertia are included in the formulation. These effects were neglected in the earlier finite element nonlinear free vibrations of plates.¹⁸⁻²¹ A harmonic force matrix is developed for nonlinear oscillations of

a rectangular plate element under uniform harmonic excitation. Formulation of the harmonic forced matrix is based on the first order mathematical approximation given by Hsu²² that the simple harmonic forcing function $P_0 \cos \omega t$ is simply the first order approximation of the Fourier expansion of the Jacobian elliptic forcing function $BA \operatorname{cn}(p\tau, k)$. And the well-known perturbation solution of a Duffing system to a simple harmonic forcing function is the first order approximation of the simple elliptic response $A \operatorname{cn}(p\tau, k)$. Derivation of the harmonic force and nonlinear stiffness matrices for a rectangular plate element are given. Nonlinear response to uniform and concentrated harmonic loadings and improved nonlinear free vibration (including inplane deformation and inertia) results are presented for rectangular plates of various boundary conditions.

II. Finite Element Formulation

Strain and Kinetic Energies

From von Karman's large deflection theory of plates, the strain-displacement relations are defined as

$$\{e\} = \{e\} + z \{\kappa\} \quad (1)$$

where the membrane or midsurface strains $\{e\}$ and curvatures $\{\kappa\}$ are given by

$$\{e\} = \begin{Bmatrix} \frac{\partial u}{\partial x} + \frac{1}{2} \left(\frac{\partial w}{\partial x} \right)^2 \\ \frac{\partial v}{\partial y} + \frac{1}{2} \left(\frac{\partial w}{\partial y} \right)^2 \\ \frac{\partial u}{\partial y} + \frac{\partial v}{\partial x} + \frac{\partial w}{\partial x} \frac{\partial w}{\partial y} \end{Bmatrix} \quad (2)$$

$$\{\kappa\} = \begin{Bmatrix} -\frac{\partial^2 w}{\partial x^2} \\ -\frac{\partial^2 w}{\partial y^2} \\ -2 \frac{\partial^2 w}{\partial x \partial y} \end{Bmatrix} \quad (3)$$

The membrane or inplane forces $\{N\}$ and moments $\{M\}$ are related to the strains and curvatures by

$$\{N\} = \begin{Bmatrix} N_x \\ N_y \\ N_{xy} \end{Bmatrix} = [C] \{e\} \quad (4)$$

*Associate Professor, Member AIAA/ASME

†Graduate Student

$$\{M\} = \begin{Bmatrix} M_x \\ M_y \\ M_{xy} \end{Bmatrix} = [D] \{\kappa\} \quad (5)$$

where $[C]$ and $[D]$ are symmetric matrices of material properties. For an isotropic plate of uniform thickness h ,

$$[C] = \frac{Eh}{1-\nu^2} \begin{bmatrix} 1 & \nu & 0 \\ \nu & 1 & 0 \\ 0 & 0 & \frac{1-\nu}{2} \end{bmatrix} \quad (6)$$

$$[D] = \frac{Eh^3}{12(1-\nu^2)} \begin{bmatrix} 1 & \nu & 0 \\ \nu & 1 & 0 \\ 0 & 0 & \frac{1-\nu}{2} \end{bmatrix} \quad (7)$$

The total strain energy expression for a plate element can be obtained as

$$U = U_b + U_m \quad (8)$$

with

$$U_b = \frac{1}{2} \iint \{M\}^T \{\kappa\} dx dy = \frac{1}{2} \iint \{\kappa\}^T [D] \{\kappa\} dx dy \quad (9)$$

$$U_m = \frac{1}{2} \iint \{N\}^T \{e\} dx dy = \frac{1}{2} \iint \{e\}^T [C] \{e\} dx dy \quad (10)$$

where U_b and U_m denote the bending and membrane strain energies, respectively.

The kinetic energy of the rectangular plate element executing harmonic oscillations is

$$T = \frac{1}{2} \rho h \iint (\dot{u}^2 + \dot{v}^2 + \dot{w}^2) dx dy \quad (11)$$

where ρ is the mass density and $(\dot{})$ means differentiate with respect to time.

Rectangular Plate Finite Element

The finite element used in the present formulation is the rectangular conforming plate element with 24 degrees-of-freedom due to Bogner et al.²³ The displacement functions are assumed as

$$w = \alpha_1 + \alpha_2 x + \alpha_3 y + \alpha_4 x^2 + \alpha_5 xy + \alpha_6 y^2 + \alpha_7 x^3 + \alpha_8 x^2 y + \alpha_9 xy^2 + \alpha_{10} y^3 + \alpha_{11} x^3 y + \alpha_{12} x^2 y^2 + \alpha_{13} xy^3 + \alpha_{14} x^3 y^2 + \alpha_{15} x^2 y^3 + \alpha_{16} x^3 y^3 \quad (12)$$

$$u = \beta_1 + \beta_2 x + \beta_3 y + \beta_4 xy \quad (13)$$

$$v = \beta_5 + \beta_6 x + \beta_7 y + \beta_8 xy \quad (14)$$

The twenty four generalized coordinates

$$\{\alpha\}^T = [\alpha_1, \alpha_2, \dots, \alpha_{16}] \quad (15)$$

$$\{\beta\}^T = [\beta_1, \beta_2, \dots, \beta_8] \quad (16)$$

can be determined from the nodal displacements

$$\{\delta\}^T = [\{\delta_b\}^T, \{\delta_m\}^T] \quad (17)$$

with

$$\{\delta_b\}^T = [w_1, w_2, w_3, w_4, w_{x1}, \dots, w_{y1}, \dots, w_{xy1}, \dots, w_{xy4}] \quad (18)$$

$$\{\delta_m\}^T = [u_1, u_2, u_3, u_4, v_1, v_2, v_3, v_4] \quad (19)$$

The relationship between the generalized coordinates and the nodal displacements can be written as

$$\{\alpha\} = [T_b] \{\delta_b\} \quad (20)$$

$$\{\beta\} = [T_m] \{\delta_m\} \quad (21)$$

The bending strain energy U_b and the kinetic energy T lead to the element linear stiffness matrix $[k_b]$, and the element consistent mass matrices $[m_b]$ and $[m_m]$. They are given explicitly in reference 23.

The membrane strain energy U_m can be linearized with the utilizing of the linearizing functions defined as

$$\{f\} = \begin{Bmatrix} f_1 \\ f_2 \end{Bmatrix} = \frac{1}{2} \begin{Bmatrix} \frac{\partial w}{\partial x} \\ \frac{\partial w}{\partial y} \end{Bmatrix} = \frac{1}{2} [B] \{\alpha\} = \frac{1}{2} [B] [T_b] \{\delta_b\} \quad (22)$$

where the element displacements $\{\delta_b\}$ are obtained from the plate deflection through the iterative procedure discussed in the next section. Thus, the membrane strains become

$$\{e\} = [F] \begin{Bmatrix} \frac{\partial w}{\partial x} \\ \frac{\partial w}{\partial y} \end{Bmatrix} + \begin{Bmatrix} \frac{\partial u}{\partial x} \\ \frac{\partial v}{\partial y} \\ \frac{\partial u}{\partial y} + \frac{\partial v}{\partial x} \end{Bmatrix} = [F][B] \{\alpha\} + [G] \{\beta\} = [[F][B] \quad [G]] \begin{Bmatrix} \{\alpha\} \\ \{\beta\} \end{Bmatrix} \quad (23)$$

with

$$[F] = \begin{bmatrix} f_1 & 0 \\ 0 & f_2 \\ f_2 & f_1 \end{bmatrix} \quad (24)$$

and the linearized membrane strain energy in terms of the nodal displacements is

$$U_m = \frac{1}{2} \{ \delta_b \}^T \{ \delta_m \}^T \begin{bmatrix} [\bar{k}_b] & [\bar{k}_{bm}] \\ [\bar{k}_{mb}] & 0 \end{bmatrix} + \begin{bmatrix} 0 & 0 \\ 0 & [k_m] \end{bmatrix} \begin{Bmatrix} \delta_b \\ \delta_m \end{Bmatrix} \quad (25)$$

where the element linear membrane stiffness matrix is given by

$$[k_m] = [T_m]^T \iint [G]^T [C] [G] dx dy [T_m] \quad (26)$$

It is given explicitly in reference 23. The submatrices of the linearized nonlinear stiffness $[\bar{k}]$ are given by

$$[\bar{k}_b] = [T_b]^T \iint [B]^T [F]^T [C] [F] [B] dx dy [T_b] \quad (27)$$

$$[\bar{k}_{bm}] = [T_b]^T \iint [B]^T [F]^T [C] [G] dx dy [T_m] \quad (28)$$

$$[\bar{k}_{mb}] = [\bar{k}_{bm}]^T \quad (29)$$

Evaluation of $[\bar{k}]$ is based on numerical integration using a four-point Gaussian integration which can exactly integrate for polynomial of cubic order.

Element Harmonic Force Matrix

In the classical approach, using a standard plate deflection $w = h q(t) \phi(x, y)$, Easley⁴ and Hsu²² presented both the exact and approximate solutions of a Duffing system to forced vibrations $q, \tau\tau + q + \beta q^3 = F(\tau)$. With a simple elliptic forcing function $BA \operatorname{cn}(p\tau, k) = Bq$ as the external excitation to the system, an elliptic response $q(\tau) = A \operatorname{cn}(p\tau, k)$ is obtained as the exact solution. When the forcing function $F(\tau)$ is a simple harmonic $P_o \cos \omega\tau$, an approximate solution using the perturbation method is the well-known result,

$$\left(\frac{\omega}{\omega_L}\right)^2 = 1 + \frac{3}{4} \beta A^2 - \frac{P_o}{A} \quad (30)$$

By expanding the Jacobian elliptic forcing function to the Fourier series and comparing the orders of magnitude of the various harmonic components, Hsu²² concluded that the simple harmonic forcing function and the corresponding perturbation solution are simply the first order approximation of the elliptic forcing function and the associated elliptic response, respectively. In obtaining the exact solution, the simple elliptic forcing function is treated as a linear spring force. The potential energy of a plate element due to a uniform harmonic forcing function can thus be approximated by

$$V = \frac{B}{2} \iint w^2 dx dy \quad (31)$$

Examining Eqs. (11) and (31), the element harmonic force matrix of a plate under uniform loading $F_o \cos \omega t$ is

$$[h] = \frac{c F_o}{A h} [m_b] \quad (32)$$

The actual applied force F_o (N/m² or psi) is related to the dimensionless forcing parameter P_o and the dimensionless forcing amplitude factor B by

$$B = \frac{P_o}{A} = \frac{c F_o}{A \rho h^2 \omega_L^2} \quad (33)$$

where c is a constant. For plates under uniform harmonic excitation, $c = \iint \phi dx dy / \iint \phi^2 dx dy$ which is simply the ratio of areas under plate mode shape and square of mode shape. The harmonic force matrix depends on the maximum plate amplitude $A = w_{\max}/h$ and P_o (or F_o).

The application of the Lagrange's equation leads to the equation of motion for the present rectangular element under the influences of inertia, elastic, large deflection and uniform harmonic excitation force as

$$\begin{bmatrix} [m_b] & 0 \\ 0 & [m_m] \end{bmatrix} \{ \ddot{\delta} \} + \left(\begin{bmatrix} [k_b] & 0 \\ 0 & [k_m] \end{bmatrix} + \begin{bmatrix} [\bar{k}_b] & [\bar{k}_{bm}] \\ [\bar{k}_{mb}] & 0 \end{bmatrix} - \begin{bmatrix} [h] & 0 \\ 0 & 0 \end{bmatrix} \right) \{ \delta \} = 0 \quad (34)$$

The coupling between bending and membrane stretching is evident by the presence of $[\bar{k}_{bm}]$ and $[\bar{k}_{mb}]$ matrices in Eq. (34). Nonlinear free vibration is a special case of the more general nonlinear forced vibration problem with P_o or $[h] = 0$ in Eq. (34).

III. Solution Procedures

By assembling the finite elements and applying the kinematic boundary conditions, the equations of motion for the linear free vibration of a given plate may be written as

$$\omega_L^2 [M] \{ \phi \}_o = [K] \{ \phi \}_o \quad (35)$$

where $[M]$ and $[K]$ denote the system mass and linear stiffness matrices, respectively, ω_L is the fundamental linear frequency, and $\{ \phi \}_o$ denotes the corresponding normalized linear mode shape. The mode shape is then normalized with respect to the dimensionless maximum plate amplitude A . The plate deflection $A \{ \phi \}_o$ is then used to obtain the element nonlinear stiffness matrix $[\bar{k}]$ through Eqs. (22, 27-29). The element harmonic force matrix is obtained through Eq. (32) for given P_o and A . The nonlinear forced plate vibration is approximated by a linearized eigenvalue of the form

$$\omega^2 [M] \{ \phi \}_1 = ([K] + [\bar{K}] - [H]) \{ \phi \}_1 \quad (36)$$

where ω is the fundamental nonlinear frequency associated with amplitude A and force P_o and $\{ \phi \}_1$ is the corresponding mode shape of the first iteration. The iterative process can now be repeated until a convergence criterion is

satisfied. Three displacement convergence criteria proposed by Bergan and Clough²⁴ and a frequency convergence criterion are used in the present study. The three displacement norms are the modified absolute norm, the modified Euclidean norm and the maximum norm. The frequency norm is defined as $|\Delta\omega_i|/\omega_i$, where $\Delta\omega_i$ is the change in nonlinear frequency during the i -th iteration cycle. A typical plot of the four norms versus number of iterations for a simply supported square plate of $a/h = 240$ with immovable inplane edges subjected to a uniform harmonic force of $P_0 = 0.2$ at $A = 1.0$ is shown in Fig. 1. All four norms exhibit the important characteristics of straightness and parallelism as described in reference 24. Therefore, an upper bound or maximum error on displacement and frequency convergences can be estimated. The results presented in the following section, convergence is considered achieved whenever anyone of the norms reaches a value of 10^{-5} .

IV. Results and Discussions

Improved Nonlinear Free Vibration

The fundamental frequency ratios ω/ω_L of free vibration at various amplitude $A = w_{max}/h$ for simply supported square ($a/h = 240$) and rectangular ($a/b = 2$ and $a/h = 480$) plates with immovable inplane edges are shown in Table 1. Due to symmetry only one quarter of the plate modelled with 9 (or 3×3 gridwork) elements of equal sizes is used. Both finite element results with and without inplane deformation and inertia (IDI) are given. It shows that the improved finite element results by including IDI in the formulation are to reduce the nonlinearity. The elliptic function solution^{4,22} and perturbation solution^{4,22} are also given to demonstrate the closeness of the earlier finite element results without IDI. Raju et al.²⁵ used the Rayleigh-Ritz method in investigation of the effects of IDI on large amplitude free flexural vibrations of thin plates. It clearly demonstrates the remarkable agreement between the improved finite element and Rayleigh-Ritz solutions.

Convergence with Gridwork Refinement

Table 2 shows the frequency ratios of a simply supported square plate ($a/h = 240$) with immovable inplane edges subjected to a uniform harmonic force of $P_0 = 0.2$ with three finite element gridwork refinements. Only one quarter of the plate was used in the analysis due to symmetry. Examination of the results shows that the present finite element formulation exhibits excellent convergence characteristics. Therefore, a 3×3 (or 9 elements) in a quarter of plate was used in modeling the plates in the remainder of the nonlinear forced responses presented unless otherwise specified.

Nonlinear Forced Response of Plates with Immovable Inplane Edges

Table 3 shows the frequency ratios ω/ω_L for simply supported and clamped square plates

subjected to an uniform harmonic force of $P_0 = 0.2$. It demonstrates the closeness between the earlier finite element formulation without IDI, the simple elliptic response and the perturbation solution (with inplane deformation only). The present improved finite element results indicate clearly that the effects of IDI are to reduce the nonlinearity. The present finite element results of a square plate ($a/h = 240$) to uniform harmonic excitation of $P_0 = 0, 0.1$ and 0.2 are given in Figs. 2 and 3 for simply supported and clamped boundary conditions, respectively.

Nonlinear Forced Response of Plates with Movable Inplane Edges

The dimensionless amplitude A versus the fundamental frequency ratio ω/ω_L for a simply supported square plate ($a/h = 240$) with movable inplane edges subjected to uniform harmonic load $P_0 = 0, 0.1$ and 0.2 is shown in Fig. 4. The nonlinearity is greatly reduced with the inplane edges no longer restrained as compared to Fig. 2

Concentrated Harmonic Force

The element harmonic force matrix $[h]$ given in Eq. (32) is for an uniformly distributed harmonic load. Application of the present finite element to the case of a concentrated force is to let the area of the element becoming smaller and smaller. It is demonstrated by a concentrated force applied at the center of a simply supported square plate with immovable inplane edges. The total magnitude of the concentrated force is equal to the same plate under an uniformly distributed harmonic loading of $P_0 = 0.1$ over the total plate area. Therefore, the uniform loading for the concentrated case is $P_0 = 0.1 (a/l)^2$ where l is the length of the loaded square element. Table 4 gives the fundamental frequency ratios ω/ω_L at $(l/a) = 33.3, 10.0, 5.0$ and 2.0 %. It indicates that the convergence is rapid and $(l/a) = 5.0\%$ would yield accurate frequency response. Nonlinear response of concentrated force obtained with $(l/a) = 5.0\%$ is plotted in Fig. 5. Frequency ratios of the same plate to uniform harmonic force $P_0 = 0.1$ and 0.4 are also given. It shows that the concentrated force is approximately four times as much severe as the uniformly distributed force for the case studied.

V. Conclusions

1. The finite element method has been extended to treat nonlinear forced vibration problems. A harmonic force matrix is developed for a rectangular plate element subjected to uniform harmonic excitation.
2. Improved finite element results on nonlinear free flexural vibrations of thin plates are achieved by including inplane deformation and inertia in the formulation.
3. Nonlinear free vibration problem can be simply treated as a special case of the

more general forced vibration by setting the harmonic force matrix equal to zero.

4. The effects of inplane deformation and inertia are to reduce the nonlinearity slightly.
5. Concentrated loading yields responses several times as severe as the uniformly distributed load.

Acknowledgment

The work was sponsored by NASA-Langley Research Center under Grant NAG-1-301. The authors would like to thank their technical monitors Dr. Jerrold M. Housner and Joseph E. Walz, Structural Dynamics Branch, Structures and Dynamics Division, NASA-Langley for their encouragement and many helpful discussions.

References

1. HERRMANN, G., "Influence of Large Amplitudes on Flexural Motion of Elastic Plates," NACA TN 3578, 1956.
2. YAMAKI, N., "Influence of Large Amplitudes on Flexural Vibrations of Elastic Plates," Zeitschrift fur angewandte Mathematik and Mechanik, Vol. 41, 1961, pp. 501-510.
3. LIN, Y. K., "Response of a Nonlinear Flat Panel to Periodic and Randomly - Varying Loadings," J. Aerospace Science, Vol. 29, 1962, pp. 1029-1034, 1066.
4. EISLEY, J. G., "Nonlinear Vibration of Beams and Rectangular Plates," Zeitschrift fur angewandte Mathematik and Physik, Vol. 15, 1964, pp. 167-175.
5. SRINIVASAN, A. V., "Nonlinear Vibrations of Beams and Plates," Int. J. Non-Linear Mechanics, Vol. 1, 1966, pp. 179-191.
6. KUNG, G. C., and PAO, Y. H., "Nonlinear Flexural Vibrations of a Clamped Circular Plate," J. Applied Mechanics, Transactions of ASME, Vol. E-39, 1972, pp. 1050-1054.
7. YAMAKI, N., OTOMO, K. and CHIBA, M., "Nonlinear Vibrations of a Clamped Circular Plate with Initial Deflection and Initial Edge Displacement, Part I: Theory," J. Sound and Vibration, Vol. 79, 1981, pp. 23-42.
8. HUANG, C. L. and SANDMAN, B. E., "Large Amplitude Vibrations of a Rigidly Clamped Circular Plates," Int. J. Non-Linear Mechanics, Vol. 6, 1971, pp. 451-468.
9. HUANG, C. L. and AL-KHATTAT, "Finite Amplitude Vibrations of a Circular Plate," Int. J. Non-linear Mechanics, Vol. 12, 1977, pp. 297-306.
10. REHFELD, L. W., "Large Amplitude Forced Vibrations of Elastic Structures," AIAA J., Vol. 12, 1974, pp. 388-390.
11. SRIDHAR, S., MOOK, D. T. and NAYFEH, A. H., "Non-linear Resonances in The Forced Responses of Plates, Part I: Symmetric Responses of Circular Plates," J. Sound and Vibration, Vol. 41, 1975, pp. 359-373.
12. LOBITZ, D. W., NAYFEH, A. H. and MOOK, D. T., "Non-linear Analysis of Vibrations of Irregular Plates," J. Sound and Vibration, Vol. 50, 1977, pp. 203-217.
13. SRIDHAR, S., MOOK, D. T. and NAYFEH, A. H., "Non-linear Resonances in The Forced Responses of Plates, Part II: Asymmetric Responses of Circular Plates," J. Sound and Vibration, Vol. 59, 1978, pp. 159-170.
14. CHEUNG, Y. K. and Lau, S. L., "Incremental Time-Space Finite Strip Method for Non-linear Structure Vibrations, Earthquake Engineering and Structural Dynamics, Vol 10, 1982, pp. 239-253.
15. BERGER, H. M., "A New Approach to the Analysis of Large Deflections of Plates," J. Applied Mechanics, Transactions of ASME, Vol. 22, 1955, pp. 465-472.
16. RAMACHANDRAN, J., "Non-linear Vibrations of Circular Plates with Linearly Varying Thickness," J. Sound and Vibration, Vol. 38, 1975, pp. 225-232.
17. CHIA, C. Y., Nonlinear Analysis of Plates, McGraw-Hill, 1980.
18. MEI, C., "Finite Element Displacement Method for Large Amplitude Free Flexural Vibrations of Beams and Plates" Comp. Stru., Vol. 3, 1973, pp. 163-174.
19. RAO, G. V., RAJU, I. S. and RAJU, K. K., "Finite Element Formulation for the Large Amplitude Free Vibrations of Beams and Orthotropic Circular Plates," Comp. Stru., Vol. 6, 1976, pp. 169-172.
20. MEI, C. and ROGERS, J. R., Jr., "Application of the TRPLT1 Element to Large Amplitude Free Vibrations of Plates," NASA CP - 2018, October 1977, pp. 275-298.
21. MEI, C., NARAYANASWAMI, R. and RAO, G. V., "Large Amplitude Free Flexural Vibrations of Plates of Arbitrary Shape," Comp. Stru., Vol. 10, 1979, pp. 675-681.
22. HSU, C. S., "On the Application of Elliptic Functions in Nonlinear Forced Oscillations," Quarterly Applied Mathematics, Vol. 17, 1960, pp. 393-407.
23. BOGNER, F. K., FOX, R. L. and Schmit, L. A., "The Generation of Interelement Compatible Stiffness and Mass Matrices by the Use of Interpolation Formulas," AFFDL-TR-66-80, Wright Patterson AFB, OH, November 1966, pp. 396-443.

24. BERGAN, P. G. and CLOUGH, R. W.,
"Convergence Criteria for Iterative
Process," AIAA J., 1972, pp. 1107-1108.
25. RAJU, I. S., RAO, G. V. and RAJU, K. K.,
"Effect of Longitudinal or Inplane
Deformation and Inertia on the Large
Amplitude Flexural Vibrations of Slender
Beams and Thin Plates," J. Sound Vibration,
Vol. 49, 1976, pp. 415-422.

Table 1 Free Vibration Frequency Ratio ω/ω_L for a
Simply Supported Plate with Immovable Inplane Edges

Amplitude $A = \frac{w_{\max}}{h}$	Without IDI ^a	With Inplane Deformation		With IDI	
	Finite Element Result	Elliptic Function Solution ^{4,22}	Perturbation Solution ^{4,22}	Rayleigh Ritz Result ²⁵	Present Finite Element Result
Square Plate ($a/h = 240$)					
0.2	1.0185(3) ^b	1.0195	1.0196	1.0149	1.0134(3)
0.4	1.0716(3)	1.0757	1.0761	1.0583	1.0528(3)
0.6	1.1533(4)	1.1625	1.1642	1.1270	1.1154(4)
0.8	1.2565(6)	1.2734	1.2774	1.2166	1.1979(5)
1.0	1.3752(7)	1.4024	1.4097	1.3230	1.2967(6)
Rectangular Plate ($a/b = 2$, $a/h = 480$)					
0.2	1.0238(3)	1.0241	1.0241	1.0177	1.0168(3)
0.4	1.0918(4)	1.0927	1.0933	1.0690	1.0658(4)
0.6	1.1957(6)	1.1975	1.1998	1.1493	1.1439(5)
0.8	1.3264(8)	1.3293	1.3347	1.2533	1.2467(6)
1.0	1.4762(11)	1.4808	1.4903	1.3753	1.3701(8)

a. Inplane deformation and inertia.

b. Number inside parenthesis denotes the number of iterations to get a converged solution.

Table 2 Convergence of Frequency Ratio with Gridwork Refinement for a Simply Support Square Plate ($a/h = 240$) with Immovable Inplane Edge Subjected to $P_0 = 0.2$

$A = \frac{w_{\max}}{h}$	Gridwork		
	2 x 2	3 x 3	4 x 4
± 0.2	0.1645(3)* 1.4248(3)	0.1643(3) 1.4238(3)	0.1636(3) 1.4237(3)
± 0.4	0.7815(3) 1.2697(3)	0.7800(3) 1.2682(3)	0.7792(3) 1.2677(3)
± 0.6	0.9576(4) 1.2588(4)	0.9544(4) 1.2560(4)	0.9530(4) 1.2550(4)
± 0.8	1.0937(5) 1.3026(5)	1.0886(5) 1.2981(5)	1.0865(5) 1.2963(5)
± 1.0	1.2242(5) 1.3781(5)	1.2171(6) 1.3717(6)	1.2143(5) 1.3691(5)

*Number in parenthesis denotes the number of iterations to get a converged solution.

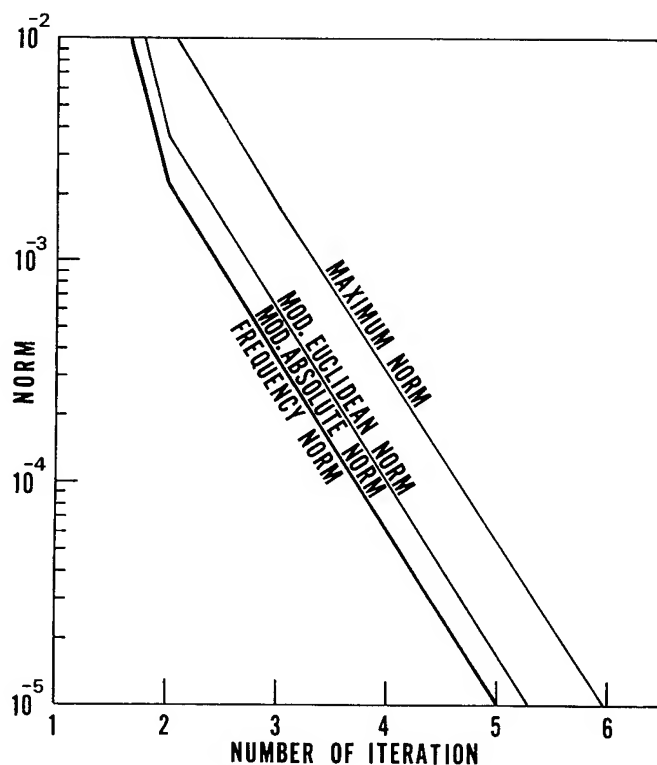


Fig. 1. Convergence characteristics.

Table 3 Forced Vibration Frequency Ratios ω/ω_L for a Square Plate ($a/h = 240$) with Immovable Inplane Edges Subjected to $P_0 = 0.2$

Amplitude $A = \frac{w_{\max}}{h}$	Simple Elliptic Response ^{4,22}	Perturbation Solution ^{4,22}	Finite Without IDI ^a	Element With IDI
Simply Supported				
± 0.2	0.1944	0.1987	0.1932(3) ^b	0.1643(3)
	1.4281	1.4281	1.4274(3)	1.4238(3)
± 0.4	0.8102	0.8111	0.8052(3)	0.7800(3)
	1.2874	1.2876	1.2839(3)	1.2682(3)
± 0.6	1.0084	1.0110	0.9984(4)	0.9544(4)
	1.2983	1.2995	1.2898(4)	1.2560(4)
± 0.8	1.1703	1.1755	1.1528(6)	1.0886(5)
	1.3686	1.3718	1.3524(6)	1.2981(5)
± 1.0	1.3283	1.3369	1.3004(7)	1.2171(6)
	1.4726	1.4789	1.4460(7)	1.3717(6)
Clamped				
± 0.2	0.1200	0.1227	0.1180(2)	0.1033(3)
	1.4195	1.4195	1.4195(2)	1.4183(3)
± 0.4	0.7483	0.7485	0.7459(3)	0.7372(4)
	1.2490	1.2491	1.2477(3)	1.2426(4)
± 0.6	0.8951	0.8956	0.8905(4)	0.8746(4)
	1.2117	1.2119	1.2083(4)	1.1966(4)
± 0.8	0.9941	0.9954	0.9863(5)	0.9617(5)
	1.2203	1.2210	1.2137(5)	1.1938(5)
± 1.0	1.0822	1.0845	1.0700(6)	1.0362(5)
	1.2540	1.2555	1.2429(6)	1.2140(5)

a. Inplane deformation and inertia.

b. Number inside parenthesis denotes the number of iterations to get a converged solution.

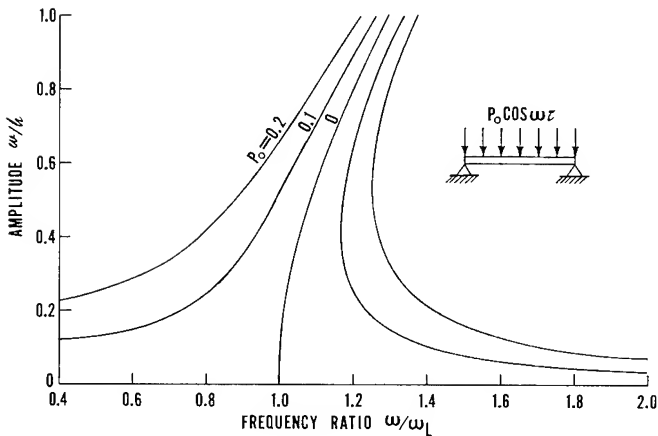


Fig. 2. Amplitude versus frequency for a simply supported square plate ($a/h = 240$) with immovable inplane edges under uniform loading.

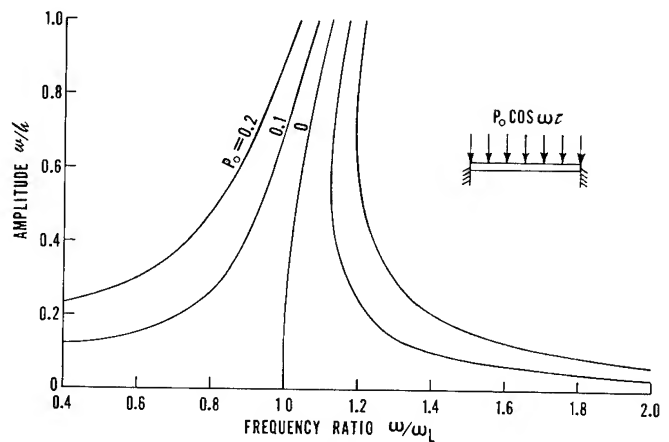


Fig. 3. Amplitude versus frequency for a clamped square plate ($a/h = 240$) with immovable inplane edges under uniform loading.

Table 4 Forced Vibration Frequency Ratios ω/ω_L for a Simply Supported Square Plate ($a/h = 240$) with Immovable Inplane Edges Subjected to a Concentrated Force $P_0 = 0.1(a/l)^2$ at the Center

Amplitude $A = \frac{W_{\max}}{h}$	$(\frac{l}{a})$ per cent			
	33.3	10	5	2
- 0.2	1.6094	1.6302	1.6269	1.6266
- 0.4	1.3880	1.4246	1.4258	1.4264
± 0.6	0.8142	0.7184	0.7074	0.7055
	1.3433	1.3789	1.3814	1.3820
± 0.8	0.9971	0.9415	0.9362	0.9358
	1.3658	1.3995	1.4025	1.4032
± 1.0	1.1502	1.1117	1.1087	1.1092
	1.4263	1.4583	1.4616	1.4624

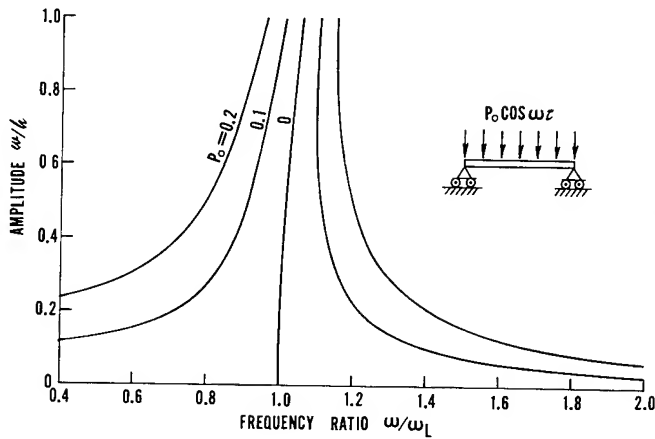


Fig. 4. Amplitude versus frequency for a simply supported square plate ($a/h = 240$) with movable inplane edges under uniform loading.

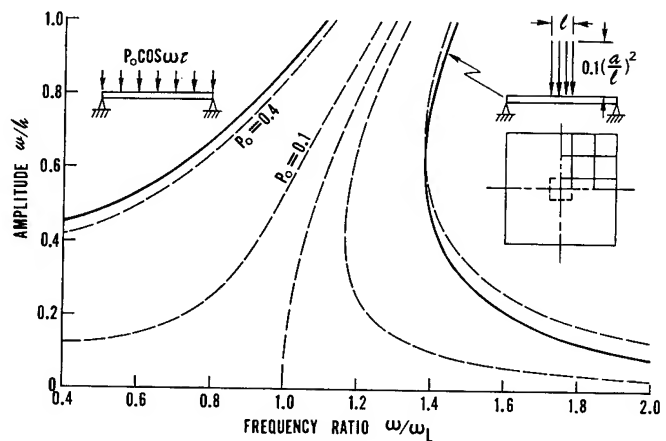


Fig. 5. Amplitude versus frequency for a simply supported square plate ($a/h = 240$) with immovable inplane edges under concentrated loading.

J. Tinsley Oden* and J. A. C. Martins+
TICOM, The University of Texas
Austin, Texas

Abstract

New variational formulations of a general class of nonlinear elastodynamics problems with contact and friction are derived which feature special models of dynamic friction effects. The friction models include effects of normal deformations of asperities.

Nomenclature

$a(\cdot, \cdot)$	a bilinear form defined on the space V of admissible motions, which represents the total virtual power developed in an elastic body Ω .
$a_0(\cdot, \cdot)$	a bilinear form representing the virtual power due to the action of the stresses σ_{ij} on the virtual strain rates ϵ_{ij} .
$a_1(\cdot, \cdot)$	a bilinear form representing the virtual power due to elastic reactions on a portion Γ_E of the boundary Γ .
b	the body force per unit volume
\tilde{C}_n, C_T	material parameters characterizing the nonlinear stiffness of the contact interface in a direction normal and tangential to the boundary, respectively.
E_{ijkl}	components of Hooke's tensor (the elasticities of the material), $1 \leq i, j, k, l \leq 3$, $E_{ijkl} = E_{jikl} = E_{ijlk} = E_{klji}$.
g	the initial gap between the elastic body Ω and a body \mathcal{N} on a foundation which contacts the body during its motion.
$H^m(\Omega), H^r(\Gamma)$	Sobolev spaces of order m and r , respectively, of functions with m -derivatives (r -derivatives) in $L^2(\Omega)$ ($L^2(\Gamma)$), respectively.
$j(\cdot, \cdot)$	a nonlinear form representing the virtual power due to frictional forces.
k_{ij}	components of an elastic stiffness tensor characterizing a deformable interface on a portion Γ_E of the boundary Γ .
K	the stiffness matrix
\tilde{m}_n, m_T	material parameters appearing in a nonlinear friction law.
M	the mass matrix
\tilde{u}	displacement field in an elastic body.
$\Gamma_D, \Gamma_F, \Gamma_E, \Gamma_C$	portions of the boundary Γ on which displacements, tractions, elastic reactions, and contact conditions are prescribed, respectively.
ρ	the mass density of the body
μ	the effective (kinetic) coefficient of friction.

We shall employ standard indicial notations, the summation convention, and standard notations

from partial differential equations and analyses throughout this paper. Other symbols are defined in the text where they first appear.

1. Introduction

For more than two centuries, it has been recognized that a decrease in the frictional forces resisting relative sliding motions of bodies in contact occurs with the initiation of a relative sliding velocity $|\dot{u}_T| > 0$. This led to the notion of "kinetic" coefficients of friction by Coulomb¹, and represented the first of many models of dynamic friction to be proposed. In 1940, Blok² showed that this apparent decrease in friction forces with sliding velocity is essential for the occurrence of stick-slip oscillations, and in the intervening forty-four years, a large volume of literature on experimental studies of such dynamic frictional behavior has accumulated.

We have recently completed a survey and critique³ of some of this literature. Among the significant qualitative features of dynamic friction of interest here, we mention the following:

- Experimental evidence suggests that the relationship between frictional forces (or, equivalently, the apparent coefficient of friction μ) and the sliding velocity \dot{u}_T is dependent upon the global dynamic properties of the system: its mass, stiffness, damping, etc., - in addition to more localized properties of the contact interface.
- The frictional force is very sensitive to the normal separation between the contacting rough bodies.
- The tangential movements observed during stick-slip motion invariably occur during jumps in the slider normal to the direction of sliding.
- External normal damping produces smooth sliding with no qualitative difference between static and kinetic friction⁴.
- If severe wear of the sliding surface is prevented, the normal deformation of metallic surfaces is (eventually) elastic, in most cases.
- The normal load increases, roughly exponentially, with penetration approach, and for small approaches, the stiffness is vanishingly small; in particular, for moderate to light normal loads (those associated with an essentially elastic normal response and no appreciable wear of the interface), the normal force is proportional to the penetrating approach raised to a power m , with $2.0 \leq m \leq 3.33$ for most metallic interfaces.

Our aim in the present paper is to present mathematical models of dynamic friction effects in elastodynamics which reflect and are consistent with the above experimental observations. We develop variational principles for these classes of elastodynamics problems and we discuss finite element methods for solving them.

*Carol and Henry Groppe Professor of Engineering Mechanics; + Graduate Student

2. A Class of Nonlinear Dynamics Problems with Friction

We begin by considering an elastic body, the interior of which is an open bounded domain Ω in \mathbb{R}^N ($N = 2$ or 3) with boundary Γ consisting of portions $\Gamma_D, \Gamma_F, \Gamma_E$, and Γ_C , as indicated in Fig. 1. The material of which the body is composed is assumed to be Hookean, so that the stress σ_{ij} at displacement field u is given by

$$\sigma_{ij}(u) = E_{ijkl} u_{k,l} \quad (1)$$

with $u_{k,l} = \partial u_k / \partial x_l$, and $1 \leq i, j, k, l \leq 3$.

As indicated in the figure, the body may come in contact with a rough sliding belt (foundation) with slides by the material surface Γ_C at a velocity \dot{u}_T^C and, initially, at a gap distance g . The body is also elastically supported along Γ_E by springs with directional stiffnesses k_{ij} and is subjected to body forces b_i and surface tractions t_i . Thus, for a time-interval $[0, T]$, we have the following equations:

Linear Momentum

$$\left. \begin{aligned} \sigma_{ij}(u)_{,j} + b_i &= \rho \ddot{u}_i \\ &\text{in } \Omega \times (0, T) \\ (\sigma_{ij}(u) &= E_{ijkl} u_{k,l}) \\ \rho &\in L^\infty(\Omega), \rho \geq \rho_0 > 0 \end{aligned} \right\} \quad (2)$$

Boundary Conditions on $\Gamma_D, \Gamma_F, \Gamma_E$

$$\left. \begin{aligned} u_i &= U_i^D \text{ on } \Gamma_D \times [0, T] \\ \sigma_{ij}(u) n_j &= t_i \text{ on } \Gamma_F \times [0, T] \\ \sigma_{ij}(u) n_j &= -k_{ij}(u_j - U_j^E) \text{ on } \\ &\Gamma_E \times [0, T] \end{aligned} \right\} \quad (3)$$

Initial Conditions

$$\left. \begin{aligned} u &= u_0 \\ \dot{u} &= u_1 \end{aligned} \right\} \text{ in } \Omega \text{ at } t = 0 \quad (4)$$

Here U_i^D, b_i, U_i^E, t_i are given (sufficiently smooth) functions.

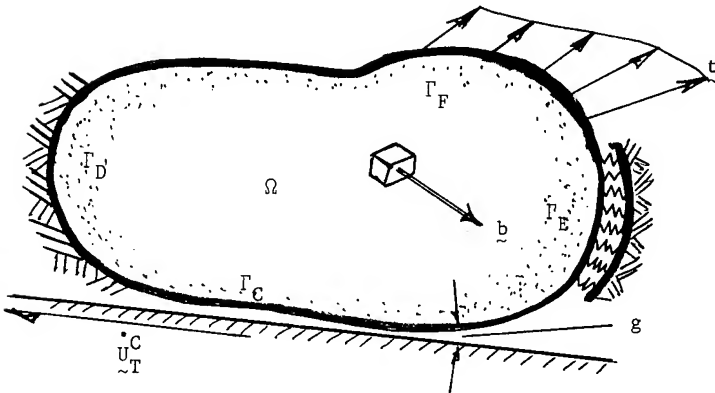


Figure 1. Elastic body in sliding contact

Interface Model of Normal Contact Forces

For \bar{n} the unit exterior normal to the candidate contact surface Γ_C and $u_n \equiv u \cdot \bar{n}$, we shall assume that the contact pressure $\sigma_n(u) = \sigma_{ij}(u) n_i n_j$ is related to the penetration approach by the power law,

$$\sigma_n(u) = -C_n (u_n - g)_+^{m_n} \text{ on } \Gamma_C \times [0, T] \quad (5)$$

where g is the initial gap between the body and the foundation and

$$(u_n - g)_+ = \sup \{0, u_n - g\}$$

Condition (5) is a constitutive equation for the interface; C_n and m_n are material constants.

Friction Conditions

As a dynamic friction law, we choose

$$\left. \begin{aligned} u_n < g &\Rightarrow \sigma_T(u) = 0 \\ u_n \geq g &\Rightarrow \left\{ \begin{aligned} |\sigma_T(u)| &\leq C_T (u_n - g)_+^{m_T} \\ |\sigma_T(u)| &\leq C_T (u_n - g)_+^{m_T} \\ &\Rightarrow \dot{u}_T = \dot{u}_T^C \\ |\sigma_T(u)| &= C_T (u_n - g)_+^{m_T} \\ &\Rightarrow \exists \lambda \geq 0, \\ &\dot{u}_T - \dot{u}_T^C = -\lambda \sigma_T \end{aligned} \right\} \end{aligned} \right\} \quad (6)$$

on $\Gamma_C \times [0, T]$

Here σ_T is the tangential (frictional) stress on Γ_C , C_T and m_T are material constants depending on interface properties (indeed, characterizing further constitutive properties of the interface), u_T is the tangential velocity of material particles on Γ_C , and \dot{u}_T^C is the prescribed tangential velocity of the foundation (adjacent body) with which Γ_C comes in contact.

The power law (5) for normal contact is motivated by empirical laws derived from many independent experiments on the contact of metallic surfaces subjected to low average pressures, characteristic of engineering sliding interfaces. That law relates the average normal pressure at each contact point with the average normal deformation of the asperities which cover the metallic surfaces. Values for the constants C_n and m_n in (5) for several combinations of metals and surface roughness can be found in ⁵. Applications of such normal contact laws to finite element static contact analysis of metallic bodies can be found in ⁶.

The friction law (6) is a generalization of the Coulomb's friction law, which is recovered if $m_n = m_T$ in (5,6). In such a case, $\mu = C_T/C_n$ is the usual coefficient of friction. The law (6) allows for a dependence of the friction coefficient on the normal contact pressure. Examples of coefficients of friction independent of the normal

load or with various types of dependence on the normal load can be found in the literature [7,8,9] for different metallic pairs. The general type of dependence compatible with (5,6) is of the form:

$$\left. \begin{aligned} \mu &= C |\sigma_n|^\alpha \\ \text{with } \alpha &= \frac{m_T}{m_n} - 1 \quad \text{and} \quad C = \frac{C_T}{C_n^{m_T/m_n}} \end{aligned} \right\} \quad (7)$$

3. Variational Formulation

We now consider the formulation of a variational principle corresponding to the elastodynamics problem outlined above. Following steps similar to those of Duvaut and Lions ¹⁰, the nonlinear elastodynamics problem can be shown to be formally equivalent to the following variational problem:

Problem 1.

$$\left. \begin{aligned} &\text{Find the function } t \rightarrow \underline{u}(t) \text{ of } [0, T] \rightarrow V \\ &\text{such that} \\ &\left\{ \begin{aligned} &\langle \ddot{\underline{u}}(t), \underline{v} - \dot{\underline{u}}(t) \rangle + a(\underline{u}(t), \underline{v} - \dot{\underline{u}}(t)) \\ &+ \langle \underline{P}(\underline{u}(t)), \underline{v} - \dot{\underline{u}}(t) \rangle \\ &+ j(\underline{u}(t), \underline{v}) - j(\underline{u}(t), \dot{\underline{u}}(t)) \\ &\geq \langle \underline{f}(t), \underline{v} - \dot{\underline{u}}(t) \rangle \quad \forall \underline{v} \in V \end{aligned} \right\} \quad (8) \end{aligned}$$

with the initial conditions:

$$\left. \begin{aligned} \underline{u}(0) &= \underline{u}_0 \\ \dot{\underline{u}}(0) &= \underline{u}_1 \end{aligned} \right\} \quad (9)$$

We have assumed here for simplicity, that $\rho \equiv 1$ and that $\underline{U}_1^0 \equiv 0$. The following notations and definitions were also used:

$$\left. \begin{aligned} V &= \text{the space of admissible displacements (velocities)} \\ &= \{ \underline{v} = (v_1, v_2, \dots, v_N) \mid v_i \in H^1(\Omega), \gamma(v_i) = 0 \text{ a.e. on } \Gamma_D \} \\ a : V \times V &\rightarrow \mathbb{R} \\ a(\underline{u}, \underline{v}) &= a_0(\underline{u}, \underline{v}) + a_1(\gamma \underline{u}, \gamma \underline{v}) \end{aligned} \right\} \quad (10)$$

where:

$a_0(\underline{u}, \underline{v})$ = virtual work (power) produced by the action of the stresses $\sigma_{ij}(\underline{u})$ on the strains (strain rates) $\epsilon_{ij}(\underline{v}) = (v_{i,j} + v_{j,i})/2$:

$$\left. \begin{aligned} a_0(\underline{u}, \underline{v}) &= \int_{\Omega} \sigma_{ij}(\underline{u}) \epsilon_{ij}(\underline{v}) \, dx \\ &= \int_{\Omega} E_{ijkl} u_{k,l} v_{i,j} \, dx \quad \underline{u}, \underline{v} \in V \end{aligned} \right\} \quad (11)$$

where \underline{u} is a displacement and \underline{v} is a virtual (velocity). $a_1(\xi, \eta)$ = virtual work (power) produced by the deformation of the linear springs on Γ_E , $a_1(\xi, \eta)$

$$= \int_{\Gamma_E} K_{ij} \xi_j \eta_i \, ds \quad \xi, \eta \in (L^2(\Gamma_E))^N \quad (12)$$

$$P : V \rightarrow V^1$$

$$\begin{aligned} \langle \underline{P}(\underline{u}), \underline{v} \rangle &= \text{virtual work (power) produced by the normal contact pressure on the displacement (velocity) } \underline{v} \\ &= \int_{\Gamma_C} C_n (u_n - g)_+^{m_n} v_n \, ds \end{aligned} \quad (13)$$

$$j : V \times V \rightarrow \mathbb{R}$$

$$\begin{aligned} j(\underline{u}, \underline{v}) &= \text{virtual power produced by the frictional force on the velocity } \underline{v} \\ &= \int_{\Gamma_C} C_T (u_n - g)_+^{m_T} |\underline{v}_T - \dot{\underline{u}}_T| \, ds \end{aligned} \quad (14)$$

$$\underline{f}(t) \in V^1$$

$$\begin{aligned} \langle \underline{f}(t), \underline{v} \rangle &= \text{virtual work (power) produced by the external forces (body forces, prescribed tractions, initial deflection of the linear springs) on the displacement (velocity) } \underline{v} : \\ &= \int_{\Omega} b_i v_i \, dx + \int_{\Gamma_F} t_i \gamma(v_i) \, ds + \\ &\quad + \int_{\Gamma_E} K_{ij} U_j^E \gamma(v_i) \, ds \end{aligned} \quad (15)$$

Here $\langle \cdot, \cdot \rangle$ denotes duality pairing on $V^1 \times V$ where V^1 is the topological dual of V ; γ is the trace operator mapping $(H^1(\Omega))^N$ onto $(H^2(\Omega))^N$ which may be decomposed into normal components $\gamma_n(v)$ and tangential components $\gamma_T(v)$. For simplicity of notation, the latter are denoted as v_n and v_T , respectively. We also observe that the boundary integrals on Γ_C are well defined for $1 \leq m_n, m_T \leq 3$ if $N = 3$ and for $1 \leq m_n, m_T$ if $N = 2$, because, for $v_i \in H^1(\Omega)$, $\gamma(v_i) \in L^q(\Gamma)$, with $1 \leq q \leq 4$, for $N = 3$, and with $1 \leq q$, for $N = 2$.

Of course, for a complete definition of Problem 1 we would need to make precise the assumed regularity of the displacements, velocity and acceleration relatively to the time variable t , i.e., we would need to specify the spaces of abstract functions to which the mappings: $\underline{u}(t)$, $\underline{u}(t) : [0, T] \rightarrow V$ and $\ddot{\underline{u}}(t) : [0, T] \rightarrow V^1$ belong. Intimately related to this question is the need for the initial conditions (9) to make sense and the need to be precise in what sense the variational inequality (8) is satisfied along the time interval $(0, T)$.

These questions will not be added herein. Instead, we will proceed formally, and we will seek a computational algorithm to obtain approximate solutions for the problem above.

4. A Regularization of the Friction Functional

Our first goal is to approximate Problem 1 by a family of regularized problems which lead to the solution of a variational equation instead of a variational inequality (as (8)).

Toward this end, we approximate the friction functional $j : V \times V \rightarrow \mathbb{R}$ which is nondifferentiable in the second argument (velocity) by a family of functionals j_ϵ convex and differentiable on the second argument:

$$\left. \begin{aligned} j_\epsilon : V \times V &\rightarrow \mathbb{R} \\ j_\epsilon(u, v) &= \int_{\Gamma_C} C_T(u_n - g)_+^{m_T} \psi_\epsilon(v_T - \dot{u}_T^C) ds \end{aligned} \right\} \quad (16)$$

where the function $\psi_\epsilon : (L^q(\Gamma_C))^N \rightarrow L^q(\Gamma_C)$ is an approximation of the function $C|\cdot| : (L^q(\Gamma_C))^N \rightarrow L^q(\Gamma_C)$ and is defined for $\epsilon > 0$, $\xi \in (L^q(\Gamma_C))^N$ and a.e. $x \in \Gamma_C$, according to :

$$\psi_\epsilon(\xi) \equiv \begin{cases} \epsilon |\frac{\xi}{\epsilon}|^2 (1 - \frac{1}{3} \frac{\xi}{\epsilon}) & \text{if } |\xi(x)| \leq \epsilon \\ \epsilon |\frac{\xi}{\epsilon}| - \frac{1}{3} & \text{if } |\xi(x)| > \epsilon \end{cases} \quad (17)$$

Remark: Since for a.e. $x \in \Gamma_C$, $|\psi_\epsilon(\xi(x))| \leq |\xi(x)|$ and since $|\xi| \in L^q(\Gamma_C)$ then $\psi_\epsilon(\xi) \in L^q(\Gamma_C)$ as stated above and no additional restrictions on m_T are required for the integral on (16) to be well defined. \square

The partial derivative of j_ϵ relative to the second argument, at (u, v) in the direction of \tilde{v} is then given by:

$$\begin{aligned} \langle j_\epsilon(u, v), \tilde{v} \rangle &\equiv \langle \partial_2 j_\epsilon(u, v), \tilde{v} \rangle \\ &= \int_{\Gamma_C} C_T(u_n - g)_+^{m_T} [\phi_\epsilon(\tilde{w}_T - \dot{u}_T^C)(\tilde{v}_T)] ds \end{aligned} \quad (18)$$

$$\forall u, v, \tilde{w} \in V$$

where, for $\epsilon > 0$, $\xi, \eta \in (L^q(\Gamma_C))^N$ and a.e. $n \in \Gamma_C$

$$\begin{aligned} \phi_\epsilon(\xi)(\eta) &\equiv \psi'_\epsilon(\xi)(\eta) \\ &= \begin{cases} \frac{1}{\epsilon} (2 - \frac{\xi}{\epsilon}) (\xi \cdot \eta) & \text{if } |\xi(x)| \leq \epsilon \\ \frac{1}{|\xi|} (\xi \cdot \eta) & \text{if } |\xi(x)| > \epsilon \end{cases} \end{aligned} \quad (19)$$

is the directional derivative of ψ_ϵ at ξ in the direction of η .

Remark: From the definition it is easy to see that for a.e. $n \in \Gamma_C$ $|\phi_\epsilon(\xi)(\eta)| \leq 2|\eta(n)|$ and consequently $[\phi_\epsilon(\xi)(\eta)] \in L^q(\Gamma_C)$. The integral on (18) is then well defined without any further restrictions on m_T . \square

We now define the regularized form of Problem 1:

Problem 1 $_\epsilon$:

Find the function $u_\epsilon(t)$ of $[0, T] \rightarrow V$ s.t.

$$\begin{aligned} \langle \dot{u}_\epsilon(t), \tilde{v} \rangle + a(u_\epsilon(t), \tilde{v}) \\ + \langle P(u_\epsilon(t)), \tilde{v} \rangle + \langle j_\epsilon(u_\epsilon(t), \dot{u}_\epsilon(t)), \tilde{v} \rangle \\ = \langle f(t), \tilde{v} \rangle \quad \forall \tilde{v} \in V \end{aligned} \quad (20)$$

with the initial conditions

$$\begin{aligned} u_\epsilon(0) &= u_0 \\ u_\epsilon(0) &= u_1 \end{aligned} \quad (21)$$

We observe that now we have a variational equation instead of a variational inequality. We also observe that this problem is formally equivalent to the problem defined by a system of equations analogous to (1) through (5) with u_ϵ replacing u and again $\rho \equiv 1$ $\dot{u}^D \equiv 0$.

However, the regularized friction conditions on Γ_C are now of the form

Regularized Friction Conditions

$$\sigma_T(u, \dot{u}) = -C_T(u_n - g)_+^{m_T} \begin{cases} (2 - |\frac{\dot{u}_T - \dot{u}_T^C}{\epsilon}|) \frac{\dot{u}_T - \dot{u}_T^C}{\epsilon} & \text{if } |\frac{\dot{u}_T - \dot{u}_T^C}{\epsilon}| \leq \epsilon \\ \frac{\dot{u}_T - \dot{u}_T^C}{|\dot{u}_T - \dot{u}_T^C|} & \text{if } |\frac{\dot{u}_T - \dot{u}_T^C}{\epsilon}| > \epsilon \end{cases} \quad (22)$$

In order to visualize the regularization procedure used above, we consider now its particularization for the case of a two dimensional ($N=2$) domain Ω with a boundary Γ_C sufficiently smooth that we can define a unit vector i_T tangent to Γ_C . In this case each vector ξ tangent to Γ_C is determined by the real number $\tilde{\xi}$ such that $\xi = \tilde{\xi} i_T$. The functions ψ_ϵ and $\phi_\epsilon \equiv \psi'_\epsilon$ are then, essentially, real valued functions of a real variable, defined by:

$$\begin{aligned} \psi_\epsilon(\xi) &= \begin{cases} \epsilon |\frac{\xi}{\epsilon}|^2 (1 - \frac{1}{3} |\frac{\xi}{\epsilon}|) & \text{if } |\xi| \leq \epsilon \\ \epsilon (|\frac{\xi}{\epsilon}| - \frac{1}{3}) & \text{if } |\xi| > \epsilon \end{cases} \\ \phi_\epsilon(\xi) &= \begin{cases} 2 - \frac{|\xi|}{\epsilon} & \text{if } |\xi| \leq \epsilon \\ \text{sgn}(\xi) & \text{if } |\xi| > \epsilon \end{cases} \end{aligned}$$

The graphs of these functions are depicted in Fig. 2 together with the graphs of the functions which they approximate: the function $|\cdot|$ and its derivative in $\mathbb{R} - \{0\}$ $\text{sgn}(\cdot)$.

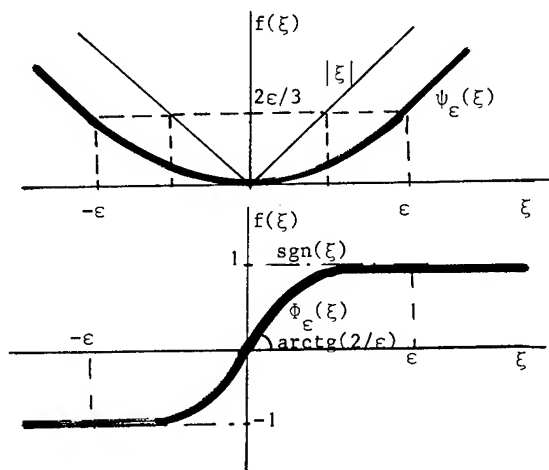


Figure 2. Graphs of the functions ψ_ϵ and ϕ_ϵ for the case of unidimensional Γ_C .

5. Finite Element Approximation of the Regularized Problem

Using standard finite element procedures, approximate versions of Problem 1_e will be solved in finite dimensional subspaces $V_h(\subset V \subset V')$. For a certain mesh (h) the approximate displacements, velocities and accelerations at each time t are elements of V_h :

$$\tilde{v}^h(t), \dot{\tilde{v}}^h(t), \ddot{\tilde{v}}^h(t) \in V_h$$

Within each element Ω_e^h ($e=1,2,\dots,E_h$) the components of the displacements, velocities and accelerations are expressed in the form:

$$\tilde{v}_j^h(x, t) = \sum_{I=1}^N \tilde{v}_j^I(t) N_I(x)$$

$$\dot{\tilde{v}}_j^h(x, t) = \sum_{I=1}^N \dot{\tilde{v}}_j^I(t) N_I(x)$$

$$\ddot{\tilde{v}}_j^h(x, t) = \sum_{I=1}^N \ddot{\tilde{v}}_j^I(t) N_I(x)$$

where $j=1,2,\dots,N_j$; N_j = number of nodes of the element; $\tilde{v}_j^I(t)$, $\dot{\tilde{v}}_j^I(t)$, $\ddot{\tilde{v}}_j^I(t)$ are the nodal values of the displacements, etc., at time t and N_I is the element shape function associated with the node I.

The finite element version of Problem 1 is then:

Problem 1_e^h:

s.t. Find the function $t \rightarrow \tilde{u}_e^h(t)$ of $[0, T] \rightarrow V_h$

$$(\ddot{\tilde{u}}_e^h(t), \tilde{v}^h) + a(\tilde{u}_e^h(t), \tilde{v}^h) + \langle \tilde{p}(\tilde{u}_e^h(t)), \tilde{v}^h \rangle + \langle \tilde{j}_e(\tilde{u}_e^h(t), \dot{\tilde{u}}_e^h(t)), \tilde{v}^h \rangle = \langle \tilde{f}(t), \tilde{v}^h \rangle$$

$$\forall \tilde{v}^h \in V^h \quad (23)$$

with the initial conditions

$$(\tilde{u}_e^h(0), \tilde{v}^h) = (\tilde{u}_0, \tilde{v}^h)$$

$$(\dot{\tilde{u}}_e^h(0), \tilde{v}^h) = (\tilde{u}_1, \tilde{v}^h)$$

$$\forall \tilde{v}^h \in V^h \quad (24)$$

If N_h is the number of nodes of the finite elements mesh, then this problem is equivalent to the following:

s.t. Find the function $t \rightarrow \tilde{r}(t)$ of $[0, T] \rightarrow \mathbb{R}^{N_h \times N_h}$

$$M \ddot{\tilde{r}}(t) + K \tilde{r}(t) + P(\tilde{r}(t)) + J(\tilde{r}(t), \dot{\tilde{r}}(t)) = F(t) \quad (25)$$

with the initial conditions

$$\tilde{r}(0) = \tilde{p}_0$$

$$\dot{\tilde{r}}(0) = \tilde{p}_1 \quad (26)$$

Here we have introduced the following matrix notations:

$\tilde{r}(+)$, $\dot{\tilde{r}}(+)$, $\ddot{\tilde{r}}(+)$ = the column vectors of nodal displacements, velocities and accelerations

$M(K)$ = standard mass (linear stiffness) matrix
 $F(t)$ = consistent nodal applied forces
 $\tilde{P}(\tilde{r}(t))$ = vector of consistent nodal normal forces on Γ_C
 $J(\tilde{r}(+), \dot{\tilde{r}}(+))$ = vector of consistent nodal friction forces on Γ_C
 $\tilde{p}_0(\tilde{p}_1)$ = initial nodal displacement (velocity)

The components of the element vector $(e)_P$ are of the form:

$$(e)_{P_{I_j}} = - \int_{\Gamma_C^e} \sigma_n n_j N_I ds \quad (27)$$

and the components of the element vector $(e)_J$ are of the form:

$$(e)_{J_{I_j}} = - \int_{\Gamma_C^e} \sigma_{Tj} N_I ds \quad (28)$$

5. Time Discretization

Consider a partition P of the time domain $[0, T]$ into M intervals of length Δt such that $0 = t_0 < t_1 < \dots < t_K < \dots < t_M = T$ with $t_{K+1} - t_K = \Delta t$.

Using the Newmark's scheme the velocities and accelerations at time t_K can be obtained as functions of the displacement velocities and accelerations at time t_{K-1} and of the displacements at time t_K , by the following relations:

$$\dot{\tilde{u}}_K = \frac{\gamma}{\beta \Delta t} (\tilde{u}_K - \tilde{u}_{K-1}) + (1 - \frac{\gamma}{\beta}) \dot{\tilde{u}}_{K-1} + \Delta t (1 - \frac{\gamma}{2\beta}) \ddot{\tilde{u}}_{K-1}$$

$$\ddot{\tilde{u}}_K = \frac{1}{\beta \Delta t^2} (\tilde{u}_K - \tilde{u}_{K-1}) - \frac{1}{\beta \Delta t} \dot{\tilde{u}}_{K-1} - (\frac{1}{2\beta} - 1) \ddot{\tilde{u}}_{K-1} \quad (29)$$

where $\tilde{u}_K \equiv \tilde{u}_e^h(t_K)$, etc. Similar simplifications of notation will be used in the foregoing, if no confusion is likely to arise.

Introducing the above relations in the variational equation (23), the following variation equation is obtained at time t_K :

$$\frac{1}{\beta \Delta t^2} (\tilde{u}_K, \tilde{v}) + a(\tilde{u}_K, \tilde{v}) + \langle \tilde{p}(\tilde{u}_K), \tilde{v} \rangle + \langle \tilde{J}(\tilde{u}_K), \tilde{v} \rangle = \langle \tilde{f}_K, \tilde{v} \rangle \quad \forall \tilde{v} \in V^h \quad (30)$$

where

$$\langle \tilde{J}(\tilde{u}_K), \tilde{v} \rangle \equiv \langle \tilde{J}(\tilde{u}_K, \dot{\tilde{u}}_K), \tilde{v} \rangle = \langle \tilde{J}(\tilde{u}_K, \frac{\gamma}{\beta \Delta t} (\tilde{u}_K - \tilde{u}_{K-1}) + (1 - \frac{\gamma}{\beta}) \dot{\tilde{u}}_{K-1} + \Delta t (1 - \frac{\gamma}{2\beta}) \ddot{\tilde{u}}_{K-1}), \tilde{v} \rangle$$

$$\langle \hat{\tilde{f}}_K, \tilde{v} \rangle = \langle \tilde{f}_K, \tilde{v} \rangle + (\frac{1}{\beta \Delta t^2} \tilde{u}_{K-1} + \frac{1}{\beta \Delta t} \dot{\tilde{u}}_{K-1} + (\frac{1}{2\beta} - 1) \ddot{\tilde{u}}_{K-1}, \tilde{v})$$

The above variational equation can be put in the operator form:

$$R_K(\tilde{u}_K) = 0 \quad \text{in } V_h' \quad (31)$$

with $R_K : V_h \rightarrow V'_h$ being the nonlinear operator defined by

$$\begin{aligned} \langle R_K(u_K), v \rangle_{V_h \times V'_h} &= \frac{1}{\beta \Delta t^2} (u_K, v) + a(u_K, v) \\ &+ \langle P(u_K), v \rangle + \langle J(u_K), v \rangle \\ &- \langle \hat{f}_K, v \rangle \quad \forall u_K, v \in V_h \end{aligned}$$

6. The Newton-Raphson Iteration

Let $\tilde{K}_K(u_K) = DR_K(u_K) \in \mathcal{L}(V_h, V'_h)$ be the derivative of the map R_K at $u_K \in V_h$. Then the Newton-Raphson iteration technique to obtain a solution of (31) consists of, given an initial guess $u_K^{(0)} \in V_h$, to obtain successive approximations of the solution u_K by using the following recurrence formula:

$$u_K^{(i+1)} = u_K^{(i)} - [\tilde{K}_K(u_K^{(i)})]^{-1} R_K(u_K^{(i)}) \quad (32)$$

where $i=0,1,\dots$ is the iteration counter. Thus, at each iteration i , the following variational equation has to be solved:

$$\begin{aligned} \langle \tilde{K}_K(u_K^{(i)})(\Delta u_K^{(i)}), v \rangle_{V_h \times V'_h} &= -\langle R_K(u_K^{(i)}), v \rangle_{V_h \times V'_h} \\ \forall v \in V_h \end{aligned} \quad (33)$$

with $\Delta u_K^{(i)} = u_K^{(i+1)} - u_K^{(i)}$

In the present problem we have, for $u_K, w, v \in V_h$

$$\begin{aligned} \langle \tilde{K}_K(u_K)(w), v \rangle_{V_h \times V'_h} &= \\ &= a(w, v) + \frac{1}{\beta \Delta t^2} (w, v) + \\ &+ \langle P(u_K)(w), v \rangle \\ &+ \langle J(u_K)(w), v \rangle \end{aligned}$$

where

$$\begin{aligned} \langle P(u_K)(w), v \rangle &= \\ &= \int_{\Gamma_C} c_n m_n(u_n - g)_+^{m_n-1} w_n v_n ds \\ \langle J(u_K)(w), v \rangle &= \\ &= \langle \partial_1 J_\epsilon(u_K, \dot{u}_K)(w), v \rangle + \frac{\gamma}{\beta \Delta t} \langle \partial_2 J_\epsilon(u_K, \dot{u}_K)(w), v \rangle \\ &= \int_{\Gamma_C} c_T m_T(u_{nK} - g)_+^{m_T-1} [\phi_\epsilon(\dot{u}_{TK} - \dot{u}_T^C)(v_T)] w_n ds \\ &+ \int_{\Gamma_C} c_T (u_{nK} - g)_+^{m_T} [\pi_\epsilon(\dot{u}_{TK} - \dot{u}_T^C)(w_T, v_T)] ds \end{aligned}$$

where, for $\epsilon > 0, \xi, \eta, \zeta \in (L^q(\Gamma_C))^N$ and a.e. $x \in \Gamma_C$ $\pi_\epsilon(\xi)(\eta, \zeta) \equiv \psi_\epsilon(\xi)(\eta, \zeta)^C =$

$$= \begin{cases} -\frac{1}{\epsilon^2 |\xi|} (\xi \cdot \eta) (\xi \cdot \zeta) + \frac{1}{\epsilon} (2 - \frac{\xi}{\epsilon}) (\eta \cdot \zeta) & \text{if } |\xi(x)| \leq \epsilon \\ -\frac{1}{|\xi|^3} (\xi \cdot \eta) (\xi \cdot \zeta) + \frac{1}{|\xi|} (\eta \cdot \zeta) & \text{if } |\xi(x)| > \epsilon \end{cases} \quad (34)$$

is the second directional derivative of ψ_ϵ at ξ on the directions of η and ζ .

Remark: From the above definition it can be seen that for a.e. $x \in \Gamma_C$

$$|[\pi_\epsilon(\xi)(\eta, \zeta)](x)| \leq \frac{3}{\epsilon} |\eta(x)| |\zeta(x)|$$

and consequently $[\pi_\epsilon(\xi)(\eta, \zeta)] \in L^{q/2}(\Gamma_C) \square$

It is also important to note that if $N=2$ the above definition reduces to

$$\pi_\epsilon(\xi)(\eta, \zeta) = \begin{cases} \frac{2}{\epsilon} (1 - \frac{\xi}{\epsilon}) (\eta, \zeta) & \text{if } |\xi(x)| \leq \epsilon \\ 0 & \text{if } |\xi(x)| > \epsilon \end{cases}$$

for $\epsilon > 0$ and $\xi, \eta, \zeta \in (L^q(\Gamma_C))^2$

We will now recast equation (33) in matrix form:

$$\tilde{K}_K^{(i)} \Delta r_K^{(i)} = -R_K^{(i)}$$

where :

$$\begin{aligned} \tilde{K}_K^{(i)} &= K + \frac{1}{\beta \Delta t^2} M + K_K^{n(i)} + K_K^{Tn(i)} + \\ &+ \frac{\gamma}{\beta \Delta t} C_K^{T(i)} \end{aligned}$$

$$\Delta r_K^{(i)} = r_K^{(i+1)} - r_K^{(i)}$$

$$R_K^{(i)} = [\frac{1}{\beta \Delta t^2} M + K] r_K^{(i)} + P_K^{(i)} + J_K^{(i)} - \hat{F}_K$$

and

$$\begin{aligned} \hat{F}_K &= F_K + M[\frac{1}{\beta \Delta t^2} r_{K-1} + \frac{1}{\beta \Delta t} \dot{r}_{K-1} + (\frac{1}{2\beta} - 1) \\ &\quad \ddot{r}_{K-1}] \end{aligned}$$

The element components of the matrices K_K^{Tn} , and $C_K^{T(i)}$ are of the form:

$${}^{(e)}K_{M_1 N_1}^{Tn} = \int_{{}^{(e)}\Gamma_C} c_n m_n(u_n - g)_+^{m_n-1} n_{i,j} n_{M_1 N_1} ds$$

where ${}^{(e)}\Gamma_C$ is the part of Γ_C belonging to element e

$${}^{(e)}K_{M_1 N_j}^{Tn} = \int_{\Gamma_C} C_T m_T (u_n - g)_+^{m_T-1} \left\{ \begin{array}{l} \frac{1}{\epsilon} (2 - \frac{|\dot{u}_T - \dot{u}_T^C|}{\epsilon}) \\ \text{if } |\dot{u}_T - \dot{u}_T^C| \leq \epsilon \\ \frac{1}{|\dot{u}_T - \dot{u}_T^C|} \\ \text{if } |\dot{u}_T - \dot{u}_T^C| > \epsilon \end{array} \right\}$$

$$\cdot (u_{Ti} - u_{Ti}^C) n_j N_M N_N \, ds$$

$${}^{(e)}C_{M_1 N_j}^T = \int_{\Gamma_C(\leq)} C_T (u_n - g)_+^{m_T} \frac{2}{\epsilon} (1 - \frac{|\dot{u}_T - \dot{u}_T^C|}{\epsilon})$$

$$(\delta_{ij} - n_i n_j) N_M N_N \, ds$$

where ${}^{(e)}\Gamma_C(\leq)$ is the part of $\Gamma_C^{(e)}$ where

$$|\dot{u}_T - \dot{u}_T^C| \leq \epsilon$$

Physically, the matrix K^n produces a variation of the normal nodal forces due to a variation of the nodal normal displacements; the matrix K^{Tn} produces a variation of the nodal friction forces due to a variation of the nodal normal displacements; finally, the matrix C^T produces a variation of the nodal friction forces due to a variation of the nodal sliding velocities.

Both K^n and C^T are symmetric matrices because both are associated with terms of $\langle \tilde{K}_k(u_k)(w), v \rangle$ which can be considered as second derivatives of functionals. In fact :

$$\langle DP(u)(w), v \rangle = \langle D^2 p(u)(w), v \rangle$$

for $u, v, w \in V$, with $p : V \rightarrow \mathbb{R}$ being the deformation energy associated with the nonlinear springs on Γ_C

$$p(u) = \int_{\Gamma_C} \frac{c_n}{m_n+1} (u_n - g)_+^{m_n+1} \, ds$$

We also have that :

$$\langle \partial_2 J_1(u, \dot{u})(w), v \rangle = \langle \partial_2^2 j_\epsilon(u, \dot{u})(w), v \rangle$$

is the second partial derivative of the friction functional j_ϵ relative to the second variable (velocity). We also observe that, in the two-dimensional case ($N=2$) C^T is the incremental damping matrix associated with the region of Γ_C which is "stuck" at some instant (the modulus of the sliding velocity is smaller than ϵ). Finally, we observe that the matrix K^{Tn} is not symmetric. This results from the fact that, according to the contact laws (5, 22), the normal stresses on Γ_C depend only on the penetration $(u_n - g)_+$. A change on the sliding velocity does not produce any change on the normal contact forces.

A complete program has been developed to implement the above algorithms. Numerical experiments are to be run soon and full tests of these

methodologies should be forthcoming.

Acknowledgement

Research was sponsored by the Air Force Office of Scientific Research (AFSC), under Contract F49620-84-C-0024. We are especially grateful to Dr. Anthony Amos for his enthusiastic support of this work. The U. S. Government is authorized to reproduce and distribute reprints for governmental purposes notwithstanding any copyright notation hereon.

References

1. Coulomb, A. C., "Theorie des Machines," Memoire de Mathematique et de Physique de l'Academie Royale, pp. 161-342, 1785.
2. Blok, H., "Fundamental Mechanical Aspects of Boundary Lubrication," S.A.E. Journal, 46(2), pp. 54-68, 1940.
3. Martins, J.A.C. and Oden, J. T., "Dynamic Friction Laws for Metallic Surfaces - A Survey and Critique of Literature," Research Report, TR-84-1, Austin, 1984 (to appear, Computer Methods in Applied Mechanics and Engineering).
4. Tolstoy, D. M., "Significance of the Normal Degree of Freedom and Natural Normal Vibrations in Contact Friction," Wear, 10, pp. 199-213, 1967.
5. Back, N., Burdekin, M. and Cowley, A., "Review of the Research on Fixed and Sliding Joints," Proc. 13th International Machine Tool Design and Research Conference, ed. by S. A. Tobias and F. Koenigsberger, MacMillan, London, 1973.
6. Back, N., Burdekin, M. and Cowley, A., "Analysis of Machine Tool Joints by the Finite Element Method," Proc. 14th International Machine Tool Design and Research Conference, ed. by S. A. Tobias and F. Koenigsberger, MacMillan, London.
7. Bowden, F. P. and Tabor, D., The Friction and Lubrication of Solids, Part II, Clarendon Press, Oxford, 1964.
8. Bay, N. and Wanheim, T., "Real Area of Contact and Friction Stresses at High Pressure Sliding Contact," Wear, 38, pp. 201-209, 1976.
9. Madakson, P. B., "The Frictional Behavior of Materials," Wear, 87, pp. 191-206, 1983.
10. Duvaut, G. and Lions, J. L., Inequalities in Mechanics and Physics, Springer-Verlag, Berlin, Heidelberg, New York, 1976.

Shlomo Ginsburg*
The University of Kansas, Department of Civil Engineering
Lawrence, Kansas

Abstract

A study of shock wave propagation in one-dimensional configurations consisting of layered media is presented. The layers of concrete, sand, and steel are subjected to high-pressure short-duration pulses simulating the effects of conventional H.E. explosions. Time histories and stress profiles are used to explain the influence of geometrical and material parameters. Guidelines are provided for design and further research.

Nomenclature

a	acceleration
L	thickness of layer
t	time
u	particle velocity
U	specific energy
x	Lagrangian coordinate
ρ	density
σ	stress
$\sigma_{,x}$	denote spatial derivative
$\dot{\cdot}$	denotes time derivative
*	denotes nondimensional quantity

I. Introduction

Systematic optimization of protective structures requires a large amount of computer resources as nonlinear transient response is involved. Several techniques which are employed for practical problems are based on simple structure modeling^(1,2) approximate loading⁽¹⁾, simple attenuation expressions^(1,3) and constitutive equations^(1,4). In many cases these models lead to oversized structures, but they might also result in unsafe solutions. A more realistic approach which employs accurate although complex material models, and which accounts for wave propagation is necessary to avoid the shortcomings of the simplified models. The major disadvantage of the more accurate models is excessive computer time required for the analysis. This problem becomes crucial when optimization is performed, since the analysis is repeated whenever parameter changes are introduced.

Optimization of protective structures involves a relatively large number of parameters which change during the design process. These include the design variables, parameters related to the structural model, and parameters associated with the numerical method used for the analysis. The first effort in a design process should be aimed towards reducing the number of variables, as this will result in a reduction in the number of analyses. For the sake of simplicity, it will be assumed here that a set of parameters associated with the numerical method can be determined by the designer for any set of design variables. But, it should be recognized that this is not always the case, and that repeated analyses may be required for choosing appropriate meshes, artificial viscosity, and other quantities when one changes physical parameters.

Reduction in the number of variable quantities is an important step taken prior to the optimization. Simple test cases such as 1-D problems can be employed for various parameters^(4,5). The comprehensive study of several materials⁽⁵⁾ indicates the influence of changes in material properties on attenuation curves and provides qualitative explanations of the observed influence. Correct interpretation of such observations is not always straightforward, especially when the geometrical configurations involved in the problem are complex. This paper describes some simple test cases which are used to explain and demonstrate the challenges a designer may encounter. Section II describes the nature of the problem and the governing equations. In Section III specific cases are used to demonstrate the influence of geometrical variables. Guidelines for design are provided in Section IV. The concluding remarks in Section V include recommendations for further research.

II. Protective Layers

The protected structure is often covered by layers of concrete, steel, geological materials, or others^(1,6). In many instances the optimization process is based on a multi-level approach⁽⁶⁾, and the structure's cover will consist of a distinct subsystem. Here, simple configurations will be employed to represent the protective layers (or cover), with two or more different materials (see Fig. 1). The load is simulated by a pressure pulse, which sometimes may be used as an approximation for the attenuated shock propagating in the ground; but often does not provide a good representation of the real response⁽⁴⁾. Although the model is simplified, it will provide an insight to the dominant phenomena. The structure is represented by an interface, and again this simplification is used for demonstration purposes only. Constraints are imposed on stresses at that interface. For the purpose of this discussion the total length of the cover is kept constant.

For one-dimensional problems in rectangular Cartesians the governing equations are:

$$\text{equation of motion } \rho a = \sigma_{,x} \quad (1)$$

where ρ is the density, x is the Lagrangian coordinate, and σ is the stress. The particle velocity is $u = \dot{x} \equiv dx/dt$, and the acceleration is $a = \dot{u} = \ddot{x}$.

$$\text{conservation of mass } \rho dx = \text{constant} \quad (2)$$

which applies to any element dx (the constant may of course differ from one element to another, e.g., for different materials).

$$\text{conservation of energy } \rho \dot{U} = \sigma \dot{\epsilon} / \rho \quad (3)$$

where U is the specific energy. For simplicity it is assumed that heat flux due to conduction or heat sources is absent. Also, body forces have been neglected in the formulation.

To the field equations it is necessary to add the constitutive equations. Materials used in this study are described by various laws ranging from

*Assistant Professor

compressible fluids, through elastic-plastic solids to porous solids^(7, 8). The field equations applied to the states behind and ahead of a shock front result in the Rayleigh line which joins the possible states in the pressure-specific volume plane. Shock experiments are required to relate shock velocity to the particle velocity, resulting together with the field equations in the Hugoniot curve in the pressure-specific volume plane.

The initial-boundary value problem can be solved numerically by using a discrete rather than continuous model, i.e., by finite differences or finite elements. Special techniques are required to assure stability of the solution⁽⁹⁾. The formulation of the approximate discrete problem may even influence the governing equations, e.g., by introducing artificial viscosity to spread shock fronts (avoid discontinuities) into the stress term.

The solution of the equations has been obtained by employing finite differences⁽⁸⁾. Parameters associated with the method, such as mesh size, have been chosen such that solutions are optimal in terms of accuracy rather than computer time. Materials used in this study include concrete, steel, sand, and air. The applied loads consist of triangular pulses. Results are illustrated by using nondimensional values. The specific values of sound speeds and pulse durations are of less importance, since general aspects rather than special cases are of major concern in this paper.

III. Configurations

We shall assume that the design problem consists of choosing a cover of given length which minimizes the peak stress at the structure's interface. Of course, this is a simplified case which does not represent the general design problem. With two materials, e.g., concrete and sand, the possibilities range from a single-material cover to two-materials covers with either concrete or sand adjacent to the structure, and multiple-layer covers.

The load histories at the structure's interface for single-material covers are illustrated for concrete and sand (see Figs. 2 and 3 respectively). As expected, the porous sand absorbs more energy during shock transition, it attenuates the shocks at higher rate than concrete, and reduces the peak stresses to a lower value. Concrete has a higher value of wave velocity, which results in the sharp short-duration peaks. The designer may be tempted at this point to use sand alone for the cover, or if a concrete layer is required (to avoid penetration, say) put the latter adjacent to the structure's interface, and employ a minimum thickness for that layer.

A comparison between two configurations having the same amounts of concrete and sand, but different relative locations show clearly (see Figs. 4, 5) that when the sand layer is adjacent to the structure the peak pressure is lower than that corresponding to a concrete layer located near the structure. Similar results are obtained with steel layers substituting the concrete. In order to gain insight into the problem it is necessary to follow the propagation of waves within the layers. When a shock propagates in concrete and reaches the sand (see Fig. 6) a compression wave is induced in the sand, and rarefaction propagates in concrete.

Sand, having a lower shock impedance than concrete, transmits a front with a lower peak stress. While this wave still propagates in the sand, the rarefaction in concrete reaches the boundary at which the load is applied. Waves reflected from that boundary travel towards the concrete-sand boundary, and several changes (the number of which depends on the geometrical dimension) in the nature of this front take place while the compression wave still propagates in sand.

When concrete is located adjacent to the structure, the first compression front propagating in sand will induce compression of approximately equal magnitude in concrete. The latter travels fast towards the structure with little attenuation taking place. A pressure wave is reflected back into the concrete, which once it reaches the concrete-sand interface, becomes a rarefaction propagating towards the structure. Again, waves traveling in the concrete bounce back and forth rapidly.

More complicated configurations (see Fig. 7) can also be evaluated in a similar manner. The qualitative analysis provides guidelines for topology but cannot account for specific dimensions or even the number of layers to be used. Actually, the same limitations apply to the usefulness of parametric studies aimed towards estimating attenuation properties, etc. For example, in the study of material properties^(5,7), unless several solutions are obtained, only a rough estimate of the influence of any particular parameter can be determined. It is also important to note that the influence of several parameters on the attenuation can accumulate. For example, changing parameters such as the Grüneisen ratio and Hugoniot curvature does not have a dramatic influence as changing the porosity. Yet, accumulation of their influence may be significant. Moreover, when complex geometrical configurations rather than simple attenuation in a single material are involved, it is hard to choose "conservative" values for various parameters. The latter may include variables associated with uncertainties, or design variables. This is quite obvious when one considers the two-layer configurations, where an optimum (maximum reduction in peak stress) is obtained for some intermediate values of the concrete and sand thickness. As the previous discussion indicates, the stress histories are influenced by the waves propagating in both materials. For given boundary conditions, the latter are functions of material properties and the configuration.

IV. Guidelines

Systematic optimization of protective structures undoubtedly requires a preliminary design which produces a starting point for a detailed final design process. The preliminary design requires a parametric study and a simplified model. These two tools are interrelated, as the determination of dominant parameters serves for development of the simple model, and since the extent of the parametric study depends on the required accuracy of the simple model.

Practical design problems are three-dimensional, but sometimes can be approximated by a two-dimensional model. Yet, one-dimensional parametric studies provide useful guidelines for elimination of variables. Thus, such cases, applied to material and geometrical variables can serve as a natural first step of the design process. These studies

can provide guidelines for topology, such as location of materials, as well as bounds on the influence of material properties, e.g., maximum expected attenuation. The designer should be careful when assessing such bounds, as true solutions depend on interaction between waves, where influence of some parameters may be favorable for some aspects and unfavorable for others. As an example, the low impedance of the material adjacent to the structure (e.g., sand) may be advantageous for decreasing the pulse amplitude at the structure's interface. But, this configuration results in longer pressure pulses acting on the structure. In realistic cases, both pressure and time-duration are important quantities for damage threshold determination.

Several parametric studies of 1-D configurations⁽⁴⁾ including spherical symmetry (to simulate geometrical divergence) indicate that quantitative estimates can also be obtained by employing a few analyses. For example, the total length of the cover has been changed keeping the relative (material) thicknesses constant. The influence of the applied load has been studied, together with several material properties such as fracture criteria. Results of these studies are given elsewhere⁽⁷⁾. As a rough estimate, errors in peak pressures at the structure's interface can be limited to less than 25%, by using merely a few accurate analyses. For a preliminary design aimed at determining topology and size of covers, this is a reasonable approximation.

The next step required for systematic design is an economical model. Several attempts have been made towards obtaining lumped mass models to represent continuous media^(4,10). These models have several shortcomings, mainly they "lose" some wave components, which result in errors in both amplitude and frequency. Yet, they are attractive for preliminary design, as ordinary rather than partial equations need to be solved.

A configuration of concrete, air, and sand has been studied, with an approximate model consisting of three nonlinear springs with two masses. A typical stress history at the structure's interface (see Fig. 8) shows that the simple model closely approximates the accurate model. Of course, successful application of a simple model in this case is due to the low shock impedance of air. But, the same approach has been applied to several solid covers and results were within a 20% error in peak pressures. Again, these results can be considered acceptable for preliminary design.

The final stages of the design process require accurate analyses. Obviously, the wave propagation rather than spring motion has to be studied, in order to take advantage of optimal materials and configuration. The starting point for this stage, provided by the approximate model, may require a number of additional parametric studies in order to establish the influence of material properties on the specific configurations tested.

V. Conclusions and Recommendations

Optimization of protective structures requires to take into account wave phenomena in order to provide safe and economical designs. The analysis of such problems imposes a severe restriction on optimum search algorithms, as a large amount of computer resources, mainly time, is necessary.

Correct interpretation of the physical phenomena can be achieved by qualitative analysis. Parametric studies of simple cases can provide guidelines for configurations and materials which are most liable to produce improved designs. Simple approximate models can be employed for the preliminary design.

No general approach is yet available for developing approximate models. Lumped mass models seem to be promising, but they are problem dependent. Employing such models is suitable for preliminary design, but more accurate analyses are required for verification and modification of the design. Especially, such parameters to which the simple models are insensitive should be checked.

Emphasis should be put on development of approximate models which enable repeated analyses at reasonable computer effort. The other necessary means for efficient synthesis involve the optimization algorithm. This area requires basic research for both lumped mass and continuous models subjected to shocks.

References

1. TM 5-1300, "Structures to Resist the Effects of Accidental Explosions," Depts. of the Army, Navy Air Force, 1969 (with amendments).
2. Buyukozturk, O., and Connor, J. J. "Nonlinear Dynamic Response of Reinforced Concrete Under Impulsive Loadings: Research Status and Needs," Nuclear Engineering and Design, Vol. 50, No. 1, 1978.
3. Crawford, R. E., "Protection from Nonnuclear Weapons," Air Force Weapons Laboratory, AFWL-TR-70-127, 1971.
4. Ginsburg, S., Tene, Y., and Kirsch, U., "Optimization of Protective Layers," Report No. 010-766, Technion Research and Development Foundation, 1980 (in Hebrew).
5. Herrmann, W., and Lawrence, R. J., "The Effect of Material Constitutive Models on Stress Wave Propagation Calculations," Proc. ASME Winter Annual Meeting, 1977.
6. Ginsburg, S., and Kirsch, U., "Design of Protective Structures Against Blast," ASCE, J. Struct. Div., Vol. 109, No. 6, 1983.
7. Ginsburg, S., "Parametric Studies of Shock Wave Propagation in Layered Media," to appear in Proc. 5th ASCE-EMD Specialty Conf., August 1984.
8. Lawrence, R. J., and Mason, D. S., "WONDY IV, A Computer Program for One-Dimensional Wave Propagation with Rezoning," Sandia Nat'l. Lab., SC-RR-71-0284, 1975.
9. Richtmyer, R. D., and Morton, K. W., Difference Methods for Initial-Value Problems, John Wiley, 1967.
10. Belytschko, T., and Midle, W. L., "Flexural Wave Propagation Behavior of Lumped Mass Approximations," J. Computers & Structures, Vol. 12, 1980.

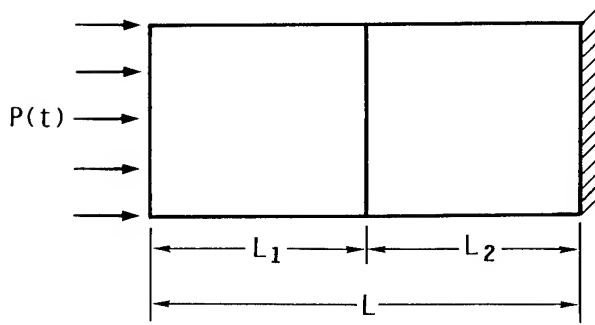


Fig. 1 The configuration.

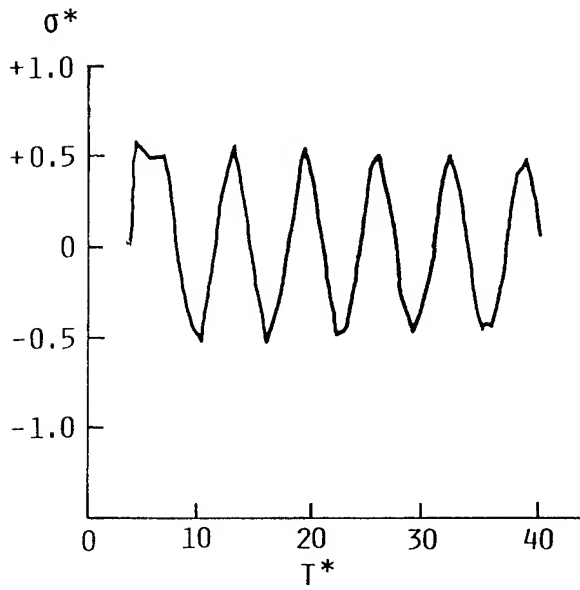


Fig. 2 Sand layer.

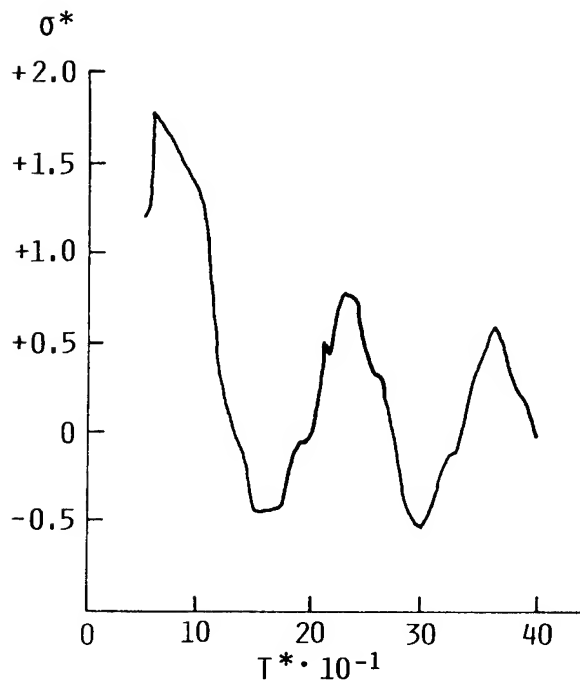


Fig. 3 Concrete layer.

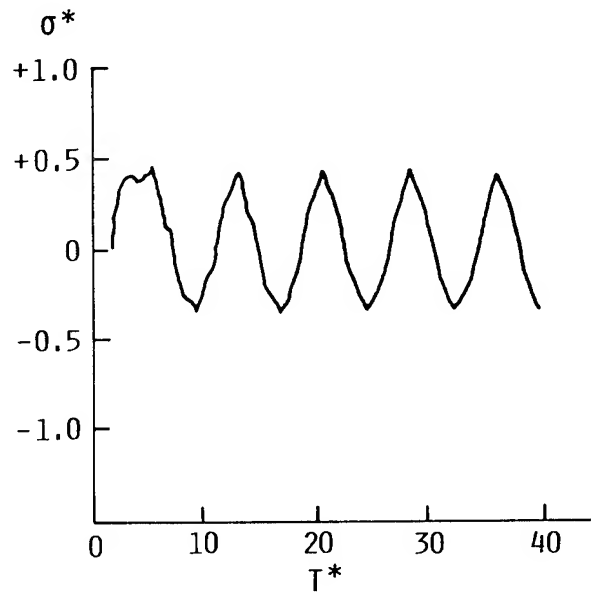


Fig. 4 Concrete-sand cover.

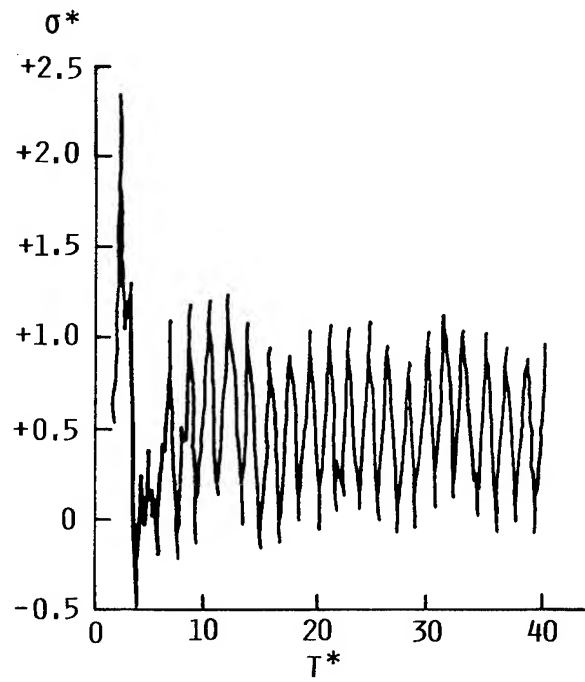


Fig. 5 Sand-concrete cover.

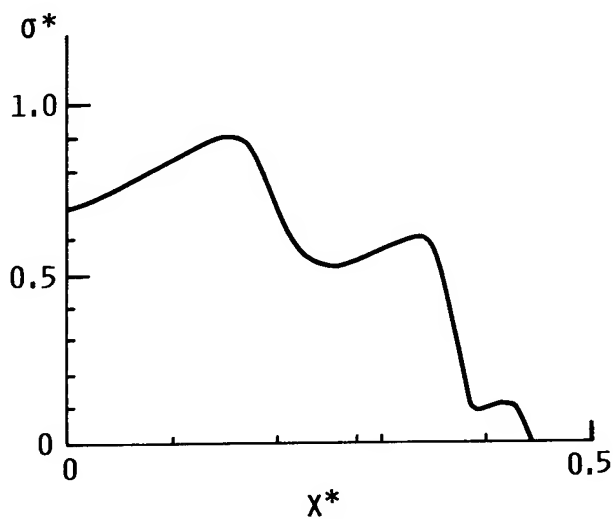


Fig. 6 Stress profile in concrete-sand cover.

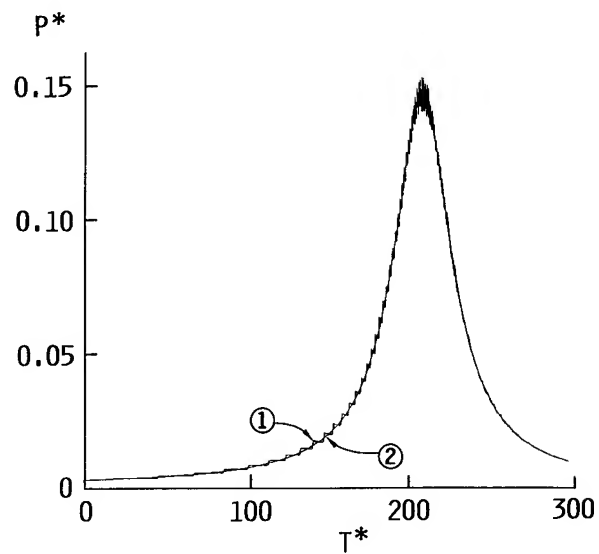


Fig. 8 Accurate (1) and approximate (2) solutions for cover with air layer.

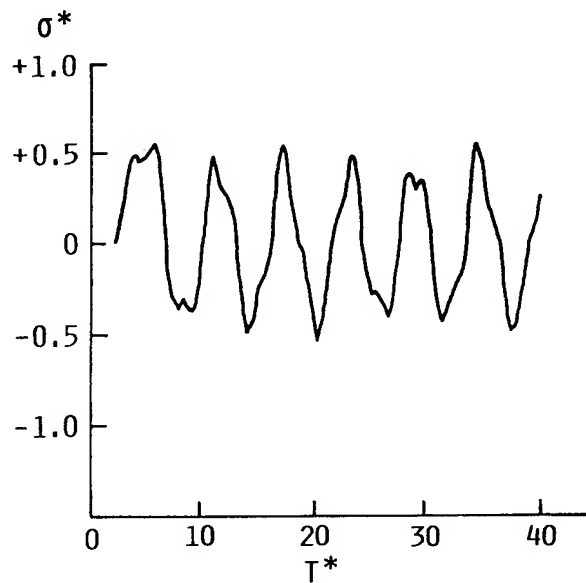


Fig. 7 Four-layer cover with sand adjacent to structure.

LIMIT CYCLE OSCILLATIONS OF A NONLINEAR ROTORCRAFT MODEL*

Benson Tongue
Assistant Professor
School of Mechanical Engineering
Georgia Institute of Technology
Atlanta, Georgia

Abstract

The limit cycle behavior of a rotorcraft model having a nonlinear damping characteristic is examined. The effect of parameter variations on the system's response is discussed and differences between a linear and nonlinear model are presented. It is shown that, for the model examined, the nonlinear analysis yields qualitatively different results from the linear case.

Nomenclature

a	frequency of system's oscillations
\tilde{a}	nondimensional frequency of system's oscillations; $\tilde{a} = a/p_0$
C_b	blade damping coefficient
C_o	fuselage damping coefficient
I	moment of inertia of blade relative to vertical hinge
K_b	rotating blade spring coefficient
K_o	fuselage spring constant
ℓ_{vh}	vertical hinge offset from rotor axis of rotation
m_o	mass of fuselage
m_b	mass of blade
M	total mass of craft, $M = nm_b + m_o$
n	number of blades
n_b	blade damping coefficient, $n_b = C_b/I$
\tilde{n}_b	nondimensional blade damping coefficient, $\tilde{n}_b = n_b/p_o$
n_o	fuselage damping coefficient, $n_o = C_o/M$
\tilde{n}_o	nondimensional fuselage damping coefficient, $\tilde{n}_o = n_o/p_o$
p_o	natural frequency of fuselage on its spring support, $p_o^2 = K_o/M$
p_{b_o}	natural frequency of nonrotating blade relative to vertical hinge, $p_{b_o}^2 = K_b/I$
S	static imbalance relative to vertical hinge
t	time
x	fuselage motion coordinate
\tilde{x}	nondimensional fuselage motion coordinate, $\tilde{x} = xy$
X_o	amplitude of fuselage coordinate
\tilde{X}	amplitude of nondimensional fuselage coordinate
α_k	angular spacing between arms of rotor
β_k	k^{th} rigid blade
γ	nonlinear fuselage damping coefficient
ϵ	hinged mass ratio, $\epsilon = \frac{n}{2} \frac{S^2}{MI}$

η	nonphysical blade coordinate
$\tilde{\eta}$	nondimensional nonphysical blade coordinate
H_o	amplitude of nonphysical blade coordinate, $\tilde{\eta} = \eta \gamma \frac{S}{M}$
v_o	nondimensional blade parameter, $v_o^2 = \frac{\ell_{vh} S}{I}$
ξ_k	individual blade angular displacement
ρ	mass per unit length of blade
τ	nondimensional time; $\tau = p_o t$
ϕ	nonphysical blade coordinate
$\tilde{\phi}$	nondimensional nonphysical blade coordinate $\tilde{\phi} = \phi \gamma \frac{S}{M}$
ϕ_o	amplitude of nonphysical blade coordinate
ψ_k	individual blade angular orientation referenced to fuselage, $\psi_k = \omega t + \alpha_k$
ω	rotor speed
$\tilde{\omega}$	nondimensional rotor speed $\tilde{\omega} = \omega/p_o$
ω_b	effective natural frequency of rotating blade, $\omega_b^2 = p_{b_o}^2 + v_o^2 \omega^2$
ω_s	$\omega_s^2 = p_{b_o}^2 + \omega^2(v_o^2 - 1)$
(\cdot)	differentiation with respect to time, t
$(\cdot)'$	differentiation with respect to non-dimensionalized time, τ

Introduction

It has been observed for approximately fifty years that vehicles having a rotor on a flexible support can experience a destructive instability known as ground resonance. The first vehicles to exhibit this phenomenon were the autogiros, followed in short order by the first helicopters.¹ The motion was initially thought to be a resonance between the ground and the rotorcraft, but in 1957 Coleman presented his now classic analysis of the process and showed it to be a self excited instability.² Basically, some external disturbance will perturb the rotor blades. This moves their center of gravity off from the center of the rotor and so forms an inertial force which acts against the helicopter fuselage (Fig. 1). Since the fuselage is flexibly connected to the ground through the landing gear, the fuselage will start to rock. When the rotor speed is within a critical band of rotational speeds, this rocking will act to increase the amplitude of vibration that the blades are undergoing. This increase blade motion leads to a larger inertial force and one has an unstable situation between fuselage and blade motion. If left unchecked, the vibrations will increase until some nonlinear restoring force brings the system into a limit cycle or

until some part of the rotorcraft fails.

Previous studies of ground resonance have concerned themselves with the purely linear problem, 2-7 i.e., their mathematical models employed linear springs and dampers. This paper will analyze a system in which damping nonlinearities are present and will examine the role of these nonlinearities in altering the system's response. Other possible nonlinearities are neglected in this basic study.

Figure 2 illustrates a simplified model of a helicopter. The fuselage, F, is constrained to translate along the x-axis, giving it one degree of freedom. This motion represents the lateral motion of a helicopter on its landing gear. The motion is constrained by a spring (S) and a damper (D). The spring-damper combination represents the landing gear's resistance to lateral motions. A rigid, massless, rotor (R) rotates at an angular speed ω and is supported by the fuselage. The blades (β_k) are attached to the rotor through vertical hinges, V.H., and these hinges are offset from the central axis of the rotor by a distance $l_{V.H.}$. The blades are rigid and they are constrained by the vertical hinge to move in a plane perpendicular to the angular velocity vector of the rotor. This type of blade motion is termed lag motion and the angular displacements of the blades are given by ξ_k . Only lag motions of the blades contribute substantially to the ground resonance phenomenon and so other degrees of freedom such as flap or twist are neglected. ² ψ_k equals $\omega t + \alpha_k$ and gives the angular displacements of the different rotor arms. Aerodynamics are not important in ground resonance and are therefore neglected. ²

The full equations of motion of the model are nonlinear. A linear analysis will neglect all but the first order terms. The damping nonlinearities considered in this paper are of the second order; it is indeed because of these that limit cycle behavior is observed. However, the second order inertial nonlinearities inherent in the original equations of blade motion are not retained in the following analysis. In Appendix A it is shown that retaining these terms will not affect the single frequency limit cycle behavior that is the object of study in this paper.

Analysis-Linear Theory

The following linear analysis follows that of Mil. ³ Applying D'Alembert's principle yields:

$$\begin{aligned} I\ddot{\xi}_k + 2C_b\dot{\xi}_k + (K_b + \omega^2 l_{VH} S) \xi_k &= S \ddot{x} \sin\psi_k \\ M\ddot{x} + 2C_0\dot{x} + K_0 x &= \frac{S}{M} \sum_{k=1}^n [(\ddot{\xi}_k - \omega^2 \xi_k) \sin\psi_k + 2\omega\dot{\xi}_k \cos\psi_k] \end{aligned}$$

Dividing the first and second equation by I and M respectively and putting the equations in canonical form yields:

$$\ddot{\xi}_k + 2n_b\dot{\xi}_k + \omega_b^2 \xi_k = \frac{S}{I} \ddot{x} \sin\psi_k \quad (1)$$

$$\ddot{x} + 2n_0\dot{x} + p_0^2 x = \frac{S}{M} \sum_{k=1}^n [(\ddot{\xi}_k - \omega^2 \xi_k) \sin\psi_k + 2\omega\dot{\xi}_k \cos\psi_k] \quad (2)$$

The coupling between the fuselage and blades is now clear. Equation (2) is in the form of a normalized spring-mass-damper being driven by some force. n_0 is the damping coefficient and p_0 is the natural frequency of the fuselage-landing gear combination. Since $\psi_k = \omega t + \alpha_k$ the forcing function has an explicitly time dependent part ($\sin\psi_k$ and $\cos\psi_k$) and also depends on the blade's displacement, velocity and acceleration, as well as on the rotor speed ω . Similarly, the blade motion is described in Eq. (1) where n_b is the blade damping coefficient and ω_b^2 represents the blade's restoring spring. Note that $\omega_b^2 = p_b^2 + v_0^2 \omega^2$, where

p_b^2 represents an actual restoring spring, and $v_0^2 \omega^2$ is the additional spring force due to centrifugal stiffening. The blades are driven by both the fuselage's acceleration and by the position of the blades (\ddot{x} , $\sin\psi_k$).

The problem with these equations is that they are variable coefficient, linear differential equations. It would be desirable to transform them into a constant coefficient form since one could then use standard solution techniques such as the Laplace transform method. A possible transformation is to define two new variables such that:

$$\eta = \sum_{k=1}^n \xi_k \sin\psi_k \quad (3)$$

$$\phi = \sum_{k=1}^n \xi_k \cos\psi_k \quad (4)$$

η and ϕ represent motions of the center of mass of the blades. Since the center of mass is the driving force of the fuselage motion, it at least seems reasonable that such a transformation could be useful. Similar transformations exist that represent blade motions in which the center of mass remains fixed with respect to the fuselage. ⁸ To clarify the role of η and ϕ , one can examine the case of a four blade rotor. For $n = 4$, $\alpha_1 = 0$, $\alpha_2 = \pi/2$, $\alpha_3 = \pi$, $\alpha_4 = 3\pi/2$ and:

$$\eta = \sin\omega t(\xi_1 - \xi_3) + \cos\omega t(\xi_2 - \xi_4) \quad (5)$$

$$\phi = \cos\omega t(\xi_1 - \xi_3) - \sin\omega t(\xi_2 - \xi_4) \quad (6)$$

Let N and P represent a coordinate system originally aligned with the rotor and attached to the fuselage, (Figure 3). To begin, let $t = 0$. One then has from eqs. (5) and (6):

$$\eta = \xi_2 - \xi_4$$

$$\phi = \xi_1 - \xi_3$$

From Figure 3a it is clear that only blades 1 and 3 contribute to any movement of the center of mass along the P axis. Similarly, only movements of blades 2 and 4 will move the center of mass along the N axis. The position of the center of mass is

(within a linear angular approximation) located at $\eta = (\xi_2 - \xi_4) B$, $\phi = (\xi_1 - \xi_3) B$ where B is the distance from an individual blade's center of mass to the blade's vertical hinge. Thus the above expressions for η and ϕ are seen to be proportional to the position of the center of mass of the blades. If $t = \pi/2\omega$ then:

$$\eta = \xi_1 - \xi_3$$

$$\phi = -(\xi_2 - \xi_4)$$

and the rotor system rotates 90° to yield Figure 3B. Note again the expressions for η and ψ are proportional to the position of the blades' center of mass.

Now that a physical feel for η and ϕ has been obtained, one can proceed to use them. If Eq. (1) is multiplied by $\cos\psi_k$ and summed from 1 to k , and similarly is multiplied by $\sin\psi_k$ and summed from 1 to k :

$$\sum_{k=1}^n (\text{Eq. (1)}) \cos\psi_k = 0$$

$$\sum_{k=1}^n (\text{Eq. (1)}) \sin\psi_k = 0$$

the following equations result:

$$\ddot{x} + 2n_0 \dot{x} + p_0^2 x - \frac{S}{M} \ddot{\eta} = 0$$

$$\ddot{\eta} + 2n_b \dot{\eta} + \omega_s^2 \eta - 2\omega(\dot{\phi} + n_b \phi) - \frac{n}{2} \frac{S}{I} \ddot{x} = 0$$

$$\ddot{\phi} + 2n_b \dot{\phi} + \omega_s^2 \phi + 2\omega(\dot{\eta} + n_b \eta) = 0$$

where

$$\omega_s^2 = p_b^2 + \omega^2(v_0^2 - 1)$$

Letting $\tau = p_0 t$ and defining $\tilde{n}_0 = n_0/p_0$, $\tilde{n}_b = n_b/p_0$, $\tilde{\omega} = \omega/p_0$ and $\tilde{\omega}_s = \omega_s/p_0$ yields:

$$x'' + 2\tilde{n}_0 x' + x - \frac{S}{M} \eta'' = 0 \quad (7)$$

$$\eta'' + 2\tilde{n}_b \eta' + \tilde{\omega}_s^2 \eta - 2\tilde{\omega}(\phi' + \tilde{n}_b \phi) - \frac{n}{2} \frac{S}{I} x'' = 0 \quad (8)$$

$$\phi'' + 2\tilde{n}_b \phi' + \tilde{\omega}_s^2 \phi + 2\tilde{\omega}(\eta' + \tilde{n}_b \eta) = 0 \quad (9)$$

One now has a set of linear, constant coefficient, homogeneous equations which can easily be solved. To find the stability boundaries, let $x = X_0 e^{i\tilde{a}\tau}$, $\eta = H_0 e^{i\tilde{a}\tau}$ and $\phi = \Phi_0 e^{i\tilde{a}\tau}$ where X_0 , H_0 , and Φ_0 are complex quantities and \tilde{a} is real. Substituting these relations into Eqs. (7), (8), and (9) will yield a set of three linear, algebraic equations:

$$X_0 (1 - \tilde{a}^2 + 2i\tilde{a}\tilde{n}_0) + \frac{S}{M} \tilde{a}^2 H_0 = 0 \quad (10)$$

$$H_0 (\tilde{\omega}_s^2 - \tilde{a}^2 + 2i\tilde{a}\tilde{n}_b) - 2\tilde{\omega}\Phi_0 (2\tilde{n}_b + i\tilde{a}) + \frac{n}{2} \frac{S}{I} \tilde{a}^2 X_0 = 0 \quad (11)$$

$$\Phi_0 (\tilde{\omega}_s^2 - \tilde{a}^2 + 2i\tilde{a}\tilde{n}_b) + 2\tilde{\omega}H_0 (2\tilde{n}_b + i\tilde{a}) = 0 \quad (12)$$

Setting the determinant of these equations to zero produces a sixth order, complex equation for the unknowns \tilde{a} and $\tilde{\omega}$. The real and imaginary parts of this equation are individually equal to zero and so this complex equation can be written as two real equations:

$$A_1 \tilde{a}^6 + A_2 \tilde{a}^4 + A_3 \tilde{a}^2 + A_4 = 0 \quad (13)$$

$$B_1 \tilde{a}^4 + B_2 \tilde{a}^2 + B_3 = 0 \quad (14)$$

where the A 's and B 's depend on the system parameters S , M , I , n , $\tilde{\omega}$, \tilde{n}_b , \tilde{n}_0 , and $\tilde{\omega}_s$.

A quick way to analyze these equations is to note that Eq. (14) is second order in \tilde{a}^2 . Therefore one can use Eq. (14) to solve for \tilde{a}^2 . The resulting \tilde{a}^2 can then be inserted into Eq. (13) and the result examined. If it yields a result unequal to zero, $\tilde{\omega}$ is altered and the procedure is continued until both Eqs. (13) and (14) are satisfied. This allows one to obtain a plot similar to Figure 4 in which the linear blade damping \tilde{n}_b is plotted versus the rotor speed $\tilde{\omega}$ for all other parameters fixed. With this, one can predict the region of unstable $\tilde{\omega}$. For $\tilde{\omega}$ between $\tilde{\omega}_1$ and $\tilde{\omega}_2$ the motion variables have a form $x \sim e^{i\tilde{a}\tau} e^{b\tau}$. At $\tilde{\omega}_1$ and $\tilde{\omega}_2$ the response has the form $x \sim e^{i\tilde{a}\tau}$. Lastly, for all other $\tilde{\omega}$ the form of the motion is $x \sim e^{i\tilde{a}\tau} e^{-b\tau}$ where a and b are real and greater than zero.

Analysis-Nonlinear Theory

The first extension to this linear theory is to model the landing gear damper as being composed of a linear and nonlinear element in parallel. In this analysis, the nonlinear element is represented by $F_d = \gamma \dot{x}|\dot{x}|$, where γ controls the degree of nonlinearity in the system.

Thus one now has:

$$\ddot{x} + 2n_0 \dot{x} + \gamma \dot{x}|\dot{x}| + p_0^2 x = \frac{S}{M} \ddot{\eta} \quad (15)$$

$$\ddot{\phi} + 2n_b \dot{\phi} + \omega_s^2 \phi + 2\omega(\dot{\eta} + n_b \eta) = 0 \quad (16)$$

$$\ddot{\eta} + 2n_b \dot{\eta} + \omega_s^2 \eta - 2\omega(\dot{\phi} + n_b \phi) = \frac{nS}{2I} \ddot{x} \quad (17)$$

These equations can now be rewritten by letting $\tau = p_0 t$:

$$x'' + 2\tilde{n}_0 x' + \gamma x'|\dot{x}| + x = \frac{S}{M} \eta'' \quad (18)$$

$$\phi'' + 2\tilde{n}_b \phi' + \tilde{\omega}_s^2 \phi + 2\tilde{\omega}(\eta' + \tilde{n}_b \eta) = 0 \quad (19)$$

$$\eta'' + 2\tilde{n}_b \eta' + \tilde{\omega}_s^2 \eta - 2\tilde{\omega}(\phi' + \tilde{n}_b \phi) = \frac{nS}{2I} x'' \quad (20)$$

Multiplying all three equations by γ and Eqs. (19) and (20) by $\frac{S}{M}$ and defining $\tilde{x} = \gamma x$,

$\tilde{\eta} = \frac{S}{M} \eta$ and $\tilde{\phi} = \frac{S}{M} \phi$ yields:

$$\tilde{x}'' + 2\tilde{n}_0 \tilde{x}' + |\dot{\tilde{x}}|\dot{\tilde{x}} + \tilde{x} = \tilde{\eta}'' \quad (21)$$

$$\ddot{\phi}'' + 2\tilde{n}_b \dot{\phi}' + \tilde{\omega}_s^2 \phi + 2\tilde{\omega}(\tilde{n}' + \tilde{n}_b \tilde{n}) = 0 \quad (22)$$

$$\ddot{\eta}'' + 2\tilde{n}_b \dot{\eta}' + \tilde{\omega}_s^2 \eta - 2\tilde{\omega}(\dot{\phi}' + \tilde{n}_b \dot{\phi}) = \epsilon \tilde{x}'' \quad (23)$$

$$\text{where } \epsilon = \frac{nS^2}{2IM}$$

The parameter γ has been eliminated and thus the solution of the equations will be valid for all values of γ . ϵ is an inertial parameter of the rotorcraft that depends on the number of blades, mass of the fuselage and blades, and mass distribution of the blades.

The equations of motion are now in their final form. Recall that \tilde{n}_0 and \tilde{n}_b are nondimensional landing gear and blade damping coefficients, respectively. $\tilde{\omega}$ is the nondimensional rotor speed. $\tilde{\omega}_s^2$ appears as a nondimensional natural frequency. Note however, that from the previous definitions, $\tilde{\omega}_s^2 = \tilde{n}_b^2 + \tilde{\omega}^2(\tilde{v}_0^2 - 1)$. \tilde{v}_0^2 is of order .1 for modern helicopters and the blade restoring springs are weak or, more commonly, absent. (In this analysis the spring is absent). Therefore $\tilde{\omega}_s^2$ will have a negative value. Thus one might immediately suspect the existence of unstable behavior. ϵ is a fixed inertial property of the rotorcraft structure. Lastly, \tilde{x} represents a nondimensional motion of the fuselage and ϕ and η are nondimensional, transformed blade coordinates.

Consider now the term $\tilde{x}'|\tilde{x}'|$. The physical nature of $\tilde{x}'|\tilde{x}'|$ versus \tilde{x}' for $\tilde{x}' \sim \sin(\tilde{a}\tau)$ is shown in Figure 5. This nonlinearity will be approximated by constructing a describing function for it.⁹ For $\tilde{x}'|\tilde{x}'|$, assuming an \tilde{x} motion of $\tilde{x} = |\tilde{x}| \cos(\tilde{a}\tau)$, one has:

$$F_d = \begin{cases} \tilde{a}^2 |\tilde{x}|^2 \sin^2(\tilde{a}\tau) ; & \tau \leq \frac{\pi}{\tilde{a}} \\ -\tilde{a}^2 |\tilde{x}|^2 \sin^2(\tilde{a}\tau) ; & \frac{\pi}{\tilde{a}} \leq \tau \leq \frac{2\pi}{\tilde{a}} \end{cases}$$

Express F_d as

$$F_d = \sum_{n=1}^{\infty} b_n \sin(\tilde{a}n\tau)$$

then

$$b_n = \frac{\tilde{a}}{\pi} \int_0^{2\pi/\tilde{a}} F_d \sin(\tilde{a}n\tau) d\tau$$

Retaining the first harmonic produces:

$$F_d = \frac{8}{3\pi} \tilde{a}^2 |\tilde{x}|^2 \sin(\tilde{a}\tau) \quad (24)$$

Note that the amplitude is nonlinearly related to the input (proportional to \tilde{x} and \tilde{a}) but the output frequency is the same as the input frequency. It is for this reason that the method is often called quasi-linearization; the approximation is not fully nonlinear, but is more than just linear.

The most important question at this point is whether this is a good approximation. A straightforward test is to run numerical simulations of the following two equations and compare the results.

$$\ddot{x} + b\dot{x}|\dot{x}| + \omega_n^2 x = F \sin(\omega t) \quad (25)$$

$$\ddot{x} + \frac{8\omega Ab}{3\pi} \dot{x} + \omega_n^2 x = F \sin \omega t,$$

$$x = A \sin(\omega t + \beta) \quad (26)$$

By varying b , F , ω_n , and ω one can find how closely Eq. (25)'s response matches Eq. (26)'s over a range of input parameters.

An example of such a comparison in which the deviations are of a worst case type is shown in Figure 6. The quasilinear response is in the form of a circle, so any noncircularity of the nonlinear response is due to the higher order terms generated by the nonlinear element. The main point is that even in this case, which is among the most nonlinear of the responses, the quasilinear approximation is still quite good. Noting this, one can proceed with the helicopter analysis.

Equation (21) is now modified by replacing

$$\tilde{x}'|\tilde{x}'| \text{ with } \frac{8}{3\pi} \tilde{a} |\tilde{x}| \tilde{x}':$$

$$\ddot{\tilde{x}}'' + [2\tilde{n}_0 + \frac{8\tilde{a}|\tilde{x}|}{3\pi}] \tilde{x}' + \tilde{x} = \tilde{n}'' \quad (27)$$

Once again assume motion of the form $\tilde{x} = \tilde{x} e^{i\tilde{a}\tau}$, etc., substitute these expressions into Eqs. (22), (23), and (27) and solve the resulting set of algebraic equations. The final characteristic equation is:

$$\begin{aligned} & \tilde{a}^6(1 - \epsilon) - \tilde{a}^5 \left(\frac{32 \tilde{n}_b \tilde{x}}{3\pi} \right) - \tilde{a}^4 (4\tilde{\omega}^2 + 4\tilde{n}_b (2\tilde{n}_0 + \tilde{n}_b)) \\ & + 1 + \tilde{\omega}_s^2 (2 - \epsilon)) \\ & + \tilde{a}^3 (\tilde{\omega}_s^2 + 2\tilde{\omega}^2) \frac{32 \tilde{x} \tilde{n}_b}{3\pi} + \tilde{a}^2 [\tilde{\omega}_s^2 (2 + \tilde{\omega}_s^2 + 8 \tilde{n}_0 \tilde{n}_b) \\ & + 4\tilde{n}_b^2 + 4\tilde{\omega}^2 (1 + \tilde{n}_b^2 + 4\tilde{n}_b \tilde{n}_0)] - \tilde{\omega}_s^4 - 4\tilde{\omega}^2 \tilde{n}_b^2 \\ & - i [\tilde{a}^5 \left(\frac{4\tilde{x}}{3\pi} \right) + \tilde{a}^4 (\tilde{n}_b (2 - \epsilon) + \tilde{n}_0) - \tilde{a}^3 [2\tilde{n}_b^2 + \tilde{\omega}_s^2 + \\ & 2\tilde{\omega}^2] \frac{8\tilde{x}}{3\pi} - 2\tilde{a}^2 (\tilde{\omega}_s^2 (\tilde{n}_0 + \tilde{n}_b) + \tilde{n}_b (1 + 2\tilde{n}_0 \tilde{n}_b) + \\ & 2\tilde{\omega}^2 (\tilde{n}_b + \tilde{n}_0)) + \tilde{a} (\tilde{\omega}_s^4 + 4\tilde{n}_b^2 \tilde{\omega}^2) \frac{4\tilde{x}}{3\pi} + \tilde{\omega}_s^2 (\tilde{\omega}_s^2 \tilde{n}_0 + \\ & 2\tilde{n}_b) + 4\tilde{n}_b \tilde{\omega}^2 (1 + \tilde{n}_b \tilde{n}_0)] = 0 \end{aligned}$$

Note that this is sixth order in \tilde{a} , not third order in \tilde{a}^2 as before. Also, the \tilde{X} amplitude now appears explicitly. This means that the limit cycle amplitude of the nonlinear system is directly related to \tilde{a} , the frequency of oscillation, and both must be solved for simultaneously.

In this study the Newton Raphson method was used to solve the above equation. The real and imaginary parts of the characteristic equation define two new equations, f_1 and f_2 , which are both set to zero. The Newton Raphson procedure requires one to form $J(f_1, f_2)$ where J is defined as:

$$J = \begin{bmatrix} \frac{\partial f_1}{\partial \tilde{X}} & \frac{\partial f_1}{\partial \tilde{a}} \\ \frac{\partial f_2}{\partial \tilde{X}} & \frac{\partial f_2}{\partial \tilde{a}} \end{bmatrix}$$

The equations

$$[J] \begin{Bmatrix} \Delta \tilde{X} \\ \Delta \tilde{a} \end{Bmatrix} = - \begin{Bmatrix} f_1 \\ f_2 \end{Bmatrix}, \quad \begin{aligned} \tilde{X}_{\text{new}} &= \tilde{X} + \Delta \tilde{X}, \\ \tilde{a}_{\text{new}} &= \tilde{a}_0 + \Delta \tilde{a} \end{aligned}$$

are then used to iterate an initial guess of \tilde{a}_0 and \tilde{X}_0 to the correct values of \tilde{a} and \tilde{X} .

Results

Figure 7 illustrates the expected behavior for the linear case. $\tilde{\omega}_1 < \tilde{\omega} < \tilde{\omega}_2$ implies motion of the form $x \sim e^{i\tilde{a}\tau}$. When a nonlinear restoring element is added, one would expect to find finite limit cycle behavior between $\tilde{\omega}_1$ and $\tilde{\omega}_2$

($x \sim e^{i\tilde{a}\tau}$). Between $\tilde{\omega}_1$ and $\tilde{\omega}_2$ as $\tilde{\omega}$ approaches

$\tilde{\omega}_1$ or $\tilde{\omega}_2$ the amplitude should decrease to zero since the linear destabilizing terms, b , is approaching zero and so the motion is only weakly unstable. This means that only a small amplitude of oscillation is needed for the nonlinear term to balance out the unstable linear behavior. Correspondingly, one expects the maximum limit cycle amplitude to occur in the middle of the region between $\tilde{\omega}_1$ and $\tilde{\omega}_2$ since this is where the linear model shows the strongest unstable behavior, (Fig. 8). Thus one could start the nonlinear search near $\tilde{\omega}_1$ in Figure 8, where one expects $\tilde{X} \approx 0.0$ and the oscillation frequency, \tilde{a} , has the value found from a linear analysis. Once the combined solution of \tilde{a} and \tilde{X} for a given $\tilde{\omega}$ is known, $\tilde{\omega}$ can be incremented and the corresponding \tilde{a} and \tilde{X} determined.

In actuality, the simple behavior described above is only found for large values of blade damping (Fig. 9, $\tilde{n}_b = .20$). As the blade damping decreases, the absolute magnitude of the response increases, as expected (Fig. 9, $\tilde{n}_b = .10$). However, a surprising result is that the response

eventually becomes triple valued and the range of limit cycle oscillations increases beyond $\tilde{\omega}_2$, the limit predicted by linear theory ($\tilde{n}_b = .04$ in Fig. 9).

Physically this means that hysteresis now exists in the amplitude response. Figure 11 illustrates this motion. If $\tilde{\omega}$ increases from zero, the amplitude builds to point A. Any further increment in $\tilde{\omega}$ will cause the response to drop down to B, which in addition to being a different amplitude also entails a new (lower) frequency of oscillation. Correspondingly, if the lower branch is being traversed, then when $\tilde{\omega}$ decreases below the speed corresponding to point C, the amplitude will increase dramatically (to D) and the frequency of oscillation will increase as well. Thus when increasing or decreasing $\tilde{\omega}$ through these critical points the response will change abruptly. This behavior would be quite disturbing to an operator since the craft would suddenly experience greatly increased (or decreased) shaking for a very small change in $\tilde{\omega}$. Note that points on the middle curve (between A and C) are not physically realizable; they represent unstable limit cycles and so motion that starts on this branch will jump to either the top or bottom branch. This alteration of stable and unstable limit cycles is quite common in nonlinear systems.⁹ The lower branch of the triple valued curve is not visible in Figure 9 due to its small magnitude relative to the other solutions.

An interesting numerical problem is how to solve for the unstable branch of the response. If $\tilde{\omega}$ is simply increased, the solution will drop to the lower branch upon moving beyond point A. One could attempt to jump directly onto the root by trial and error, but this is a very slow process. The method used to overcome this problem was to realize that plotting f_1 and f_2 as functions of \tilde{a} and \tilde{X} would yield a solution surface in the three dimensional space defined by $f_1(\tilde{a}, \tilde{X})$ and $f_2(\tilde{a}, \tilde{X})$. By specifying $f_1 = f_2 = 0$, one cuts this surface and a curve similar to that illustrated in Figure 12 is obtained. This curve shows the top and bottom branch solutions, as well as the middle one. These middle solution values can now be used as initial conditions for charting the unstable limit cycles. This method lends itself very well to a general search for solutions. If one has a solution for some value of \tilde{a} , then one can find all the other possible solutions by branching $f_1 = 0$ and $f_2 = 0$ from these initial values.

Now return to Figure 9. If \tilde{n}_b is further decreased the response curves bifurcate ($\tilde{n}_b = .036$, Fig. 9). This is a fundamentally different behavior from that for larger \tilde{n}_b . For all larger values of \tilde{n}_b , the oscillations stop when one increases $\tilde{\omega}$ through the unstable regime. The transition to zero may be gradual ($\tilde{n}_b = .10$) or abrupt ($\tilde{n}_b = .037$), but it always occurs. Now one has the situation in which the stable limit cycle will persist for all $\tilde{\omega} > \tilde{\omega}_1$. The bottom branch represents unstable limit cycle behavior which continues as $\tilde{\omega}$ approaches infinity. In this situation there exists no way to leave the top branch once it has been entered except by reducing

$\tilde{\omega}$ or by disturbing the system sufficiently strongly that the response moves through the middle branch to the underlying stable region.

The bifurcation phenomenon can be understood by extending the domain of input rotor speeds. Figure 10 illustrates the response in this expanded range. Several points can now be made.

First, one notes that multiple limit cycle solutions exist over a greater range than previously indicated. Examine the case of $\tilde{\eta}_b = .04$, for example. It had appeared that for all rotor speeds above approximately 1.8, only a zero amplitude solution existed. Now it is seen that this is only true up to $\tilde{\omega} = 3.1$. Above this speed, multiple solutions exist, both stable and unstable. Figure 10 therefore shows that the existence of a finite limit cycle solution is the rule rather than the exception, since only for two finite frequency intervals ($0 < \tilde{\omega} < \text{lower limit of left solution branch}$ and $\text{upper limit of left solution branch} < \tilde{\omega} < \text{lower limit of right solution branch}$) can a zero amplitude solution exist with no associated finite limit cycle solutions.

Second, although the zero amplitude solution is stable for all rotor speeds above approximately 1.6, the stability becomes relatively weaker since the unstable locus, (indicated by the dashed line), has an asymptotic behavior of the form, $\tilde{X} \sim 1/\tilde{\omega}$ as $\tilde{\omega} \rightarrow \infty$. Therefore a progressively smaller perturbation to the system is required to drive the oscillation amplitude from zero, through the unstable locus, and to the stable, high amplitude solution locus.

Third, as the damping decreases, the rotor speed at which the second solution branch occurs will decrease. For $\tilde{\eta}_b = .04$, the point A indicates the lower rotor speed limit of the right branch. As $\tilde{\eta}_b$ is decreased, to .037, the minimum speed of the right branch decreases, (shown in Figure 10 by the point B). Finally, for a level of damping between .036 and .037, the two branches touch. After this level of damping is passed, the loci join to form the previously noted bifurcation. Thus the loci at which the two branches join is analogous to the well known separatrix, found in the phase plane representation of the solution of the equations of motion of a pendulum, in that it separates two distinct solution regions from each other.

A further interesting result is that the $\tilde{\eta}_b$ necessary for bifurcation is the same regardless of variations in $\tilde{\eta}_0$ (Figure 13). If one wishes to eliminate the bifurcation phenomenon, one must increase $\tilde{\eta}_b$; altering $\tilde{\eta}_0$ will be ineffective. This is not at all intuitive. One would usually think that adding damping to either the blades or the landing gear would effect the response in some broadly similar way. However, analysis shows that even though the overall amplitude of the motion will change for varied $\tilde{\eta}_0$, the bifurcation itself will always occur for the same value of $\tilde{\eta}_b$. There is a final observation that is useful for determining the value of $\tilde{\eta}_b$ necessary for bifurcation. Figure 13 shows that

the relation between ϵ and the value of $\tilde{\eta}_b$ necessary for bifurcation is quite linear. Therefore one can predict the bifurcation $\tilde{\eta}_b$ from a knowledge of ϵ . Numerical integrations of the equations of motion were performed to verify the above results. As expected from the analysis of Eqs. (25) and (26), the amplitudes and frequencies found from numerical integrations agreed with the results of the harmonic balance procedure.

For typical dimensional values, and $\tilde{\eta}_b = .02$, the x oscillations range from 0 to 1 foot and the blade lag oscillations range from 0 to 360° . For $\tilde{\eta}_b = .20$, x and ξ range from 0 to 1/2 inch and 0 to 2° respectively. The distance from the center of rotation of the actual helicopter to its rotor hub is approximately five feet. Thus it is clear that for certain parameter ranges the results may not always be physically meaningful. The size of the actual oscillations is dependent on the non-dimensional parameter, γ . For a given helicopter, if the degree of nonlinearity in the landing gear is increased, γ will increase and the actual x and ξ corresponding to \tilde{x} , $\tilde{\eta}$, and ϕ will decrease. Therefore, the question of whether the above phenomena, such as bifurcation, will occur depends on the specific helicopter being examined.

Conclusions

By including nonlinearities in the helicopter model, one can predict both the frequency and amplitude of the solution. Moreover, the addition of a nonlinear element to the landing gear of a simplified helicopter model will cause large qualitative changes in the response curves from those predicted by linear theory. For large values of linear blade damping, the response follows one's intuitive notion of how the limit cycles should behave. That is, within a critical band of rotor speeds a finite amplitude limit cycle will exist, the amplitude of which will decrease as the rotor speed approaches these boundaries from within. For rotor speeds outside of the instability range predicted by linear theory, the system will not support a limit cycle and disturbances to the system will decay. As blade damping is decreased however, new phenomena occur. The solutions become triple valued and finally bifurcate. Thus when increasing the nondimensional rotor speed, $\tilde{\omega}$, from zero, the response can include limit cycles that increase to a maximum and then smoothly decay to zero, solutions that abruptly jump to zero and solutions that keep limit cycling for all $\tilde{\omega}$ above some critical value. This behavior has important consequences with regard to piloting a rotorcraft.

The most dramatic nonlinear feature of the solutions, the bifurcation, depends only on the blade damping and is independent of variations in fuselage damping. This phenomenon (and the bowing out of the solutions in the triple valued response region) implies that the range of unstable rotor speeds can actually be greater than that predicted by linear theory. Thus linear theory will sometimes give overly optimistic results with regard to stability boundaries. The various values of $\tilde{\eta}_b$ which produce bifurcation can be easily predicted if one knows the parameter ϵ , which involves the parameters S , I , M and n . Finally, the results

must be translated back into dimensional quantities in order to determine their physical significance.

Future work will involve introducing a nonlinear blade, as well as a nonlinear fuselage, damper.

Acknowledgement

The author would like to thank Professors Earl H. Dowell and Howard C. Curtiss, Jr. for their invaluable advice during this investigation. Thanks must also go to Mr. Robert Blackwell of Sikorsky Aircraft Company for sharing some of his expertise.

References

1. Gregory, H. F., The Helicopter, A. S. Barnes and Co. Inc., 1976.
2. Coleman, R. P. and Feingold, A. M., "Theory of Self Excited Mechanical Oscillations of Helicopter Rotors with Hinged Blades", NACA Report 1351, Langley Aeronautical Laboratory, Langley Field, VA, February 1957.
3. Mil, M. L. et al., Helicopters - Calculation and Design, Vol. II, Vibrations and Dynamic Stability, NASA TT F-519, May 1968.
4. Hammond, C. E., "An Application of Floquet Theory to Prediction of Mechanical Instability", JAHS, Vol. 19, No. 4, October 1974.
5. Peters, D. A. and Hohenemser, K. H., Applications of the Floquet Transition Matrix to Problems of Lifting Rotor Stability", JAHS Vol. 16, No. 2, April 1971.
6. Gabel, R. and Capurso, V. "Exact Mechanical Instability Boundaries as Determined from the Coleman Equation", JAHS Vol. 7, No. 1, January 1962.
7. Warming, Troeis, "Some New Conclusions About Helicopter Mechanical Instability", JAHS Vol. 1, July 1956.
8. Hohenemser, K. H. and Yin, S. K., "Some Applications of the Methods of Muliblade Corrdinates", JAHS Vol. 17, No. 3, July 1972.
9. Minorsky, N., Theory of Nonlinear Control Systems, McGraw-Hill Book Company, New York, 1969.

Appendix A

The full nonlinear equations of motion corresponding to the model of Figure 2 including blade nonlinearities and nonlinear fuselage damping are:

$$\ddot{\xi}_k + 2n_b \dot{\xi}_k + p_{b_0}^2 \xi_k + \omega_v^2 \sin \xi_k = \frac{S}{I} \ddot{x} \sin(\psi_k + \xi_k)$$

$$\ddot{x} + 2n_0 \dot{x} + \gamma \dot{x} |\dot{x}| + p_0^2 x = \frac{S}{M} \sum_{k=1}^n$$

$$[\ddot{\xi}_k \sin(\psi_k + \xi_k) + (\omega + \dot{\xi}_k)^2 \cos(\psi_k + \xi_k)] \quad (A1)$$

If all terms greater than second order are neglected and the previously used nondimensionalizations are used, the resulting equations are:

$$\begin{aligned} \ddot{\xi}_k + 2\tilde{n}_b \dot{\xi}_k + (\tilde{p}_{b_0}^2 + \tilde{\omega}_v^2) \xi_k &= \frac{S^2}{IM^2} \ddot{x} \\ &+ [\sin \psi_k + \sigma \cos \psi_k \xi_k] \\ \ddot{x} + \tilde{x}' |\tilde{x}'| + 2\tilde{n}_0 \tilde{x}' + \tilde{x} &= \sum_{k=1}^n [\sin \psi_k (\ddot{\xi}_k - \tilde{\omega}^2 \xi_k) \\ &+ \cos \psi_k (2\tilde{\omega} \xi_k')] + \sigma \sum_{k=1}^n [\sin \psi_k (-2\tilde{\omega} \xi_k' \xi_k + \\ &\cos \psi_k (\xi_k'' \xi_k - \tilde{\omega}^2 \frac{\xi_k^2}{2} + \xi_k'^2))] \end{aligned} \quad (A2)$$

$$\text{where } \sigma = \frac{1}{S \gamma_M}$$

To determine the importance of the second order blade inertial nonlinearities that occur in Eq's A2, numerical simulations were run for the same input parameters as those used in Figure 9. The outputs of the numerical runs were recorded for several cycles and then the Fourier series coefficients of the resulting data were calculated. The resulting amplitudes and frequencies present in the outputs are compared with the previous limit cycle results, which neglected blade inertial nonlinearities, in Fig's A1-A6. As can be seen, the amplitude and frequency of the limit cycle motion found by the previous analysis remains relatively unchanged when blade inertial nonlinearities are included.

The major effects of the blade inertial nonlinearities is to increase the amplitude response of the off-peak frequencies which occur below the fundamental harmonic. Thus the importance of these frequencies must be ascertained for the particular parameters being used.

Clearly, the results of the main paper are correct, as far as the single frequency limit cycle response is concerned. In practice, one should run one or two time simulations to ensure that the limit cycle amplitude at the fundamental frequency is sufficiently large in comparison to the amplitude at other frequencies so that blade inertial nonlinearities may be neglected.

* This work was supported by the National Science Foundation under Grant MEA-8119883 with the Division of Mechanical Engineering and Applied Mechanics.

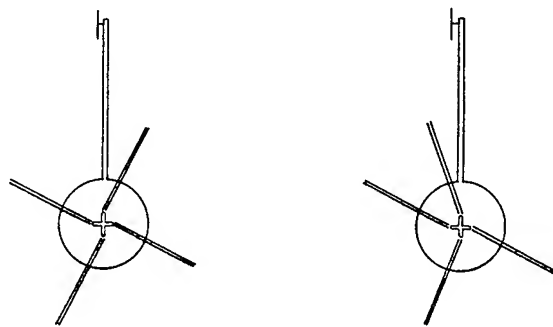


FIGURE 1

a) HELICOPTER IN A STATE OF EQUILIBRIUM.

b) HELICOPTER WITH ONE OF ITS BLADES PERTURBED FROM EQUILIBRIUM.

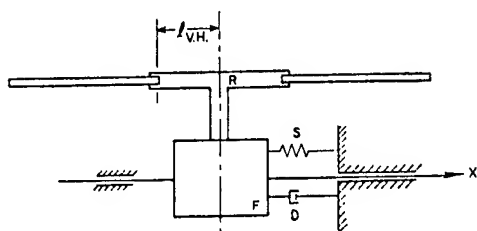


FIGURE 2. SIMPLIFIED MODEL OF A ROTOR ON A MOVABLE FUSELAGE.

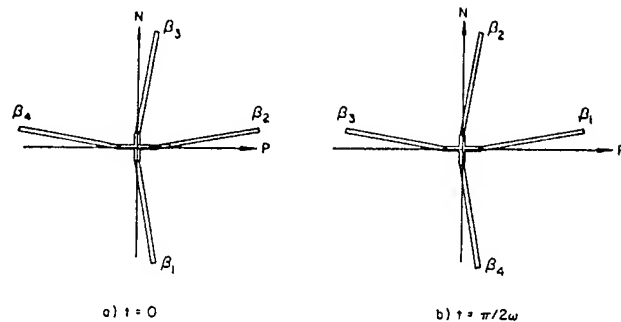
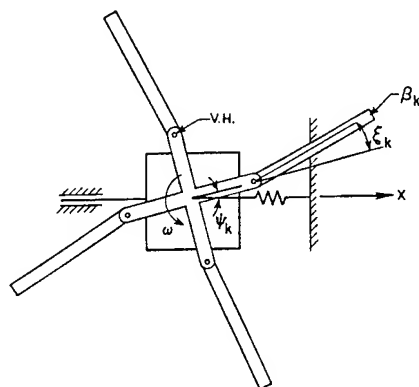


FIGURE 3. SCHEMATIC SHOWING HOW η AND ϕ REPRESENT MOTIONS OF THE CENTER OF MASS OF OPPOSED BLADES.

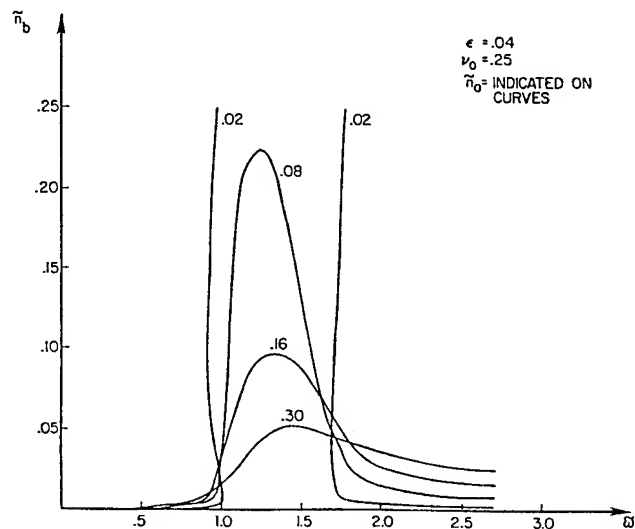


FIGURE 4. PLOT SHOWING RELATION BETWEEN \tilde{n}_b (BLADE DAMPING), \tilde{n}_o (FUSELAGE DAMPING) AND $\tilde{\omega}$ (ROTOR SPEED) FOR NEUTRALLY STABLE MOTION IN A LINEAR SYSTEM.

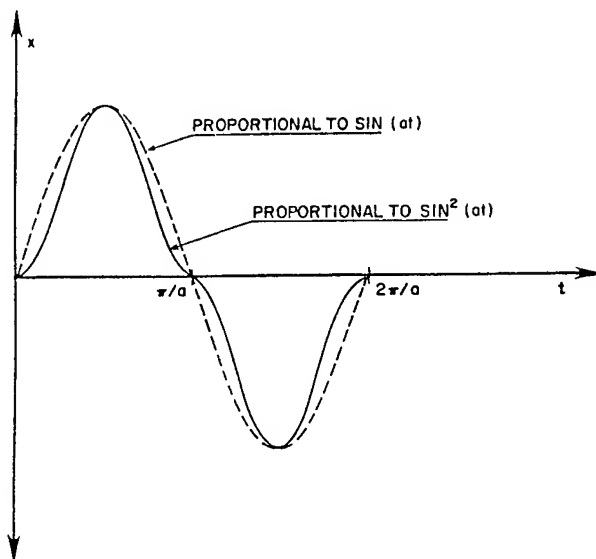


FIGURE 5. PLOT SHOWING DIFFERENCE BETWEEN A HYDRAULIC DAMPER ($\sin^2 at$) AND A LINEAR ONE ($\sin at$)

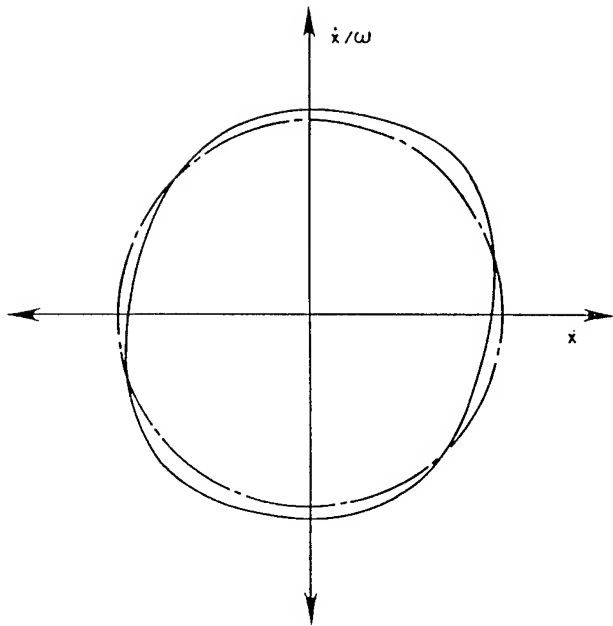


FIGURE 6. COMPARISON BETWEEN MOTION OF NONLINEAR SYSTEM (UNBROKEN LINE) vs. THE QUASILINEARIZED SYSTEM (BROKEN LINE) WITH HIGH LEVEL OF NONLINEARITY PRESENT.

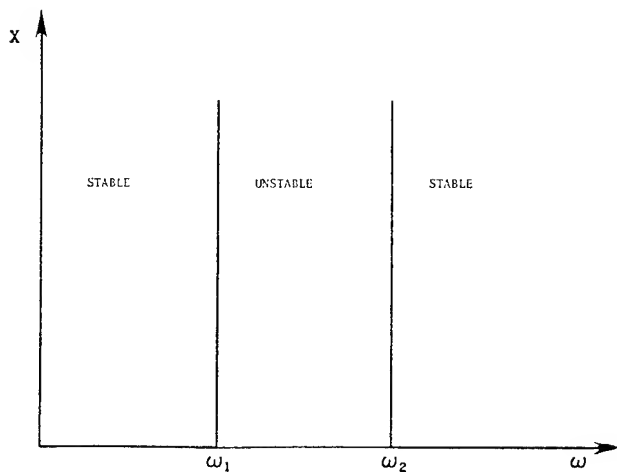


FIGURE 7. REGIONS OF INSTABILITY AND STABILITY FOR LINEAR CASE.

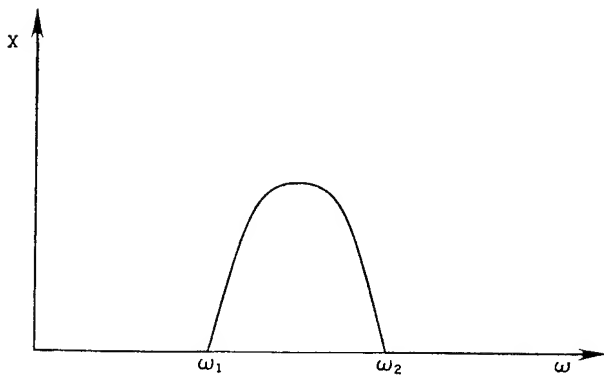


FIGURE 8. INTUITIVELY EXPECTED MOTION FOR LIMIT CYCLE BEHAVIOR WHEN RESTORING NONLINEARITY IS PRESENT IN LINEAR UNSTABLE REGIME.

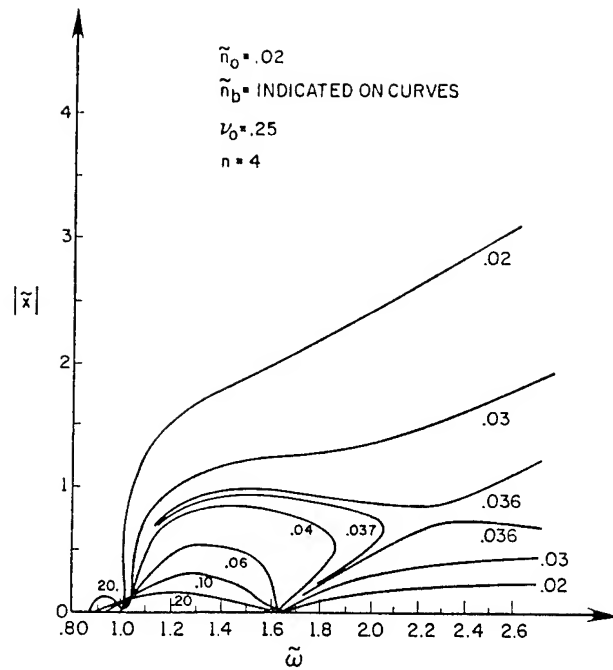


FIGURE 9. ACTUAL LIMIT CYCLE BEHAVIOR WHEN HYDRAULIC NONLINEARITY IS PRESENT IN THE LANDING GEAR DAMPER.

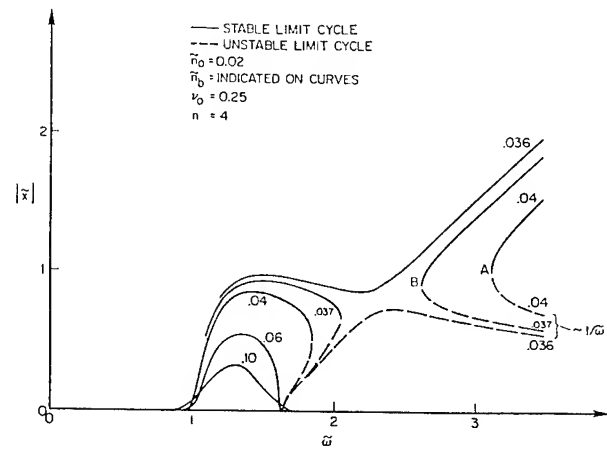


FIGURE 10. LIMIT CYCLE BEHAVIOR WHEN HYDRAULIC NONLINEARITY IS PRESENT IN THE LANDING GEAR DAMPER.

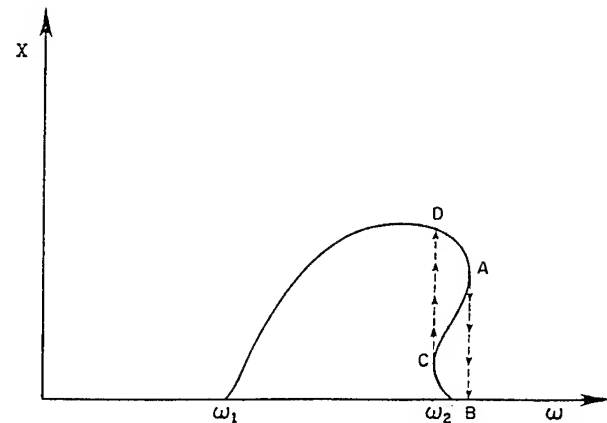


FIGURE 11. PLOT ILLUSTRATING HYSTERETIC RESPONSE FOR TRIPLE VALUED SOLUTION.

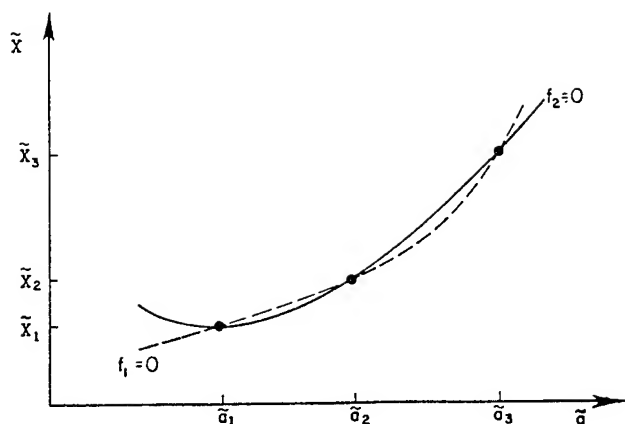


FIGURE 12. PLOT OF THE TWO SOLUTION FUNCTIONS, f_1 AND f_2 , AS FUNCTIONS OF a (FREQUENCY OF OSCILLATION) AND X (AMPLITUDE OF FUSELAGE MOTION).

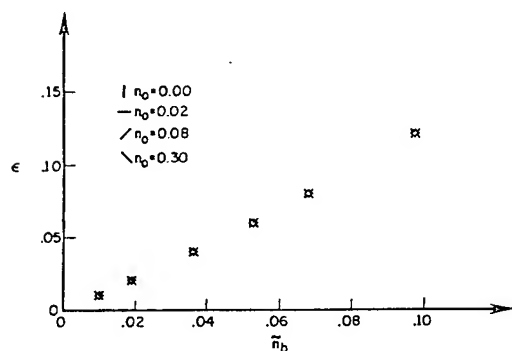


FIGURE 13 Plot of ϵ (hinged mass ratio) versus n_b (linear blade damping) Required for Bifurcation in Solution Curves

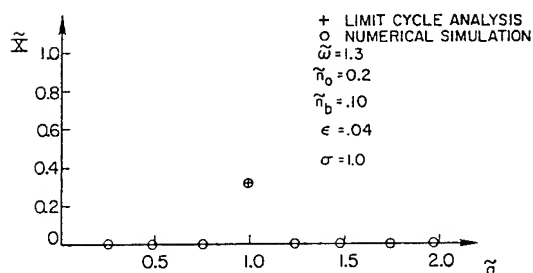


FIGURE A-1.

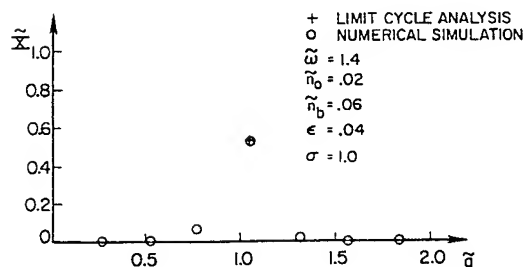


FIGURE A-2.

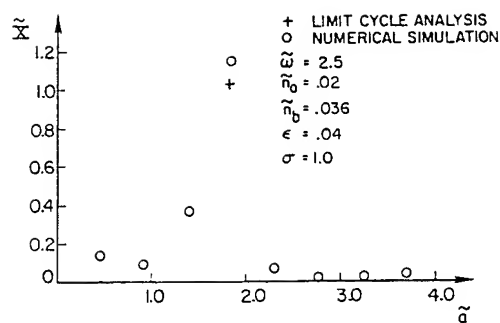


FIGURE A-3.

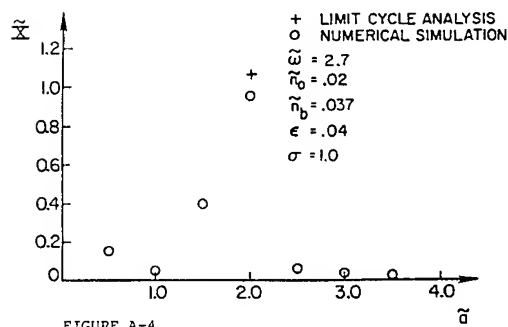


FIGURE A-4.

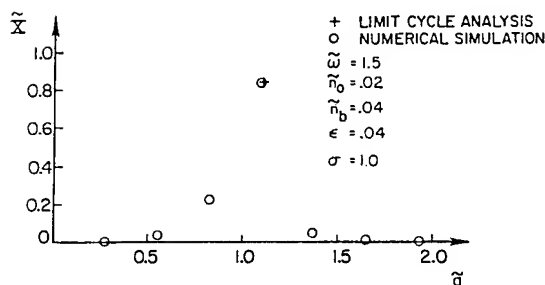


FIGURE A-5.

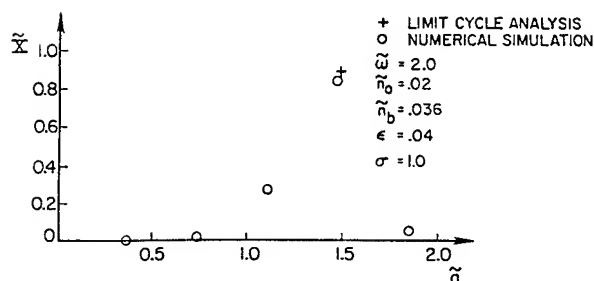


FIGURE A-6.

Jon-Shen Fuh**, Shyi-Yaung Chen[†], and Alex Berman^{††}
Kaman Aerospace Corporation
Bloomfield, Connecticut

Abstract

A procedure is presented for identifying linear non-proportionally damped system. The system damping is assumed to be representable by a real symmetric matrix. Analytical mass, stiffness and damping matrices which constitute an approximate representation of the system are assumed to be available. Given also are an incomplete set of measured natural frequencies, damping ratios and complex mode shapes of the structure, normally obtained from test data. A method is developed to find the smallest changes in the analytical model so that the improved model can exactly predict the measured modal parameters. The present method uses the orthogonality relationship to improve mass and damping matrices and the dynamic equation to find the improved stiffness matrix.

Nomenclature

A	matrix defined in Eq. (4)
B	matrix defined in Eq. (5)
C	system damping matrix
D	GQG*, Eq. (29f)
E	coefficient matrix, Eq. (14)
F	GH, defined in Eq. (29c)
f	matrix defined in Eq. (1b)
G	matrix defined in Eq. (29b)
g	matrix defined in Eq. (24a)
H	matrix defined in Eq. (29a)
h	matrix defined in Eq. (24b)
I	identity matrix
K	system stiffness matrix
k	$W_K K W_K^T$
M	system mass matrix
m	number of measured modes
n	number of degrees of freedom
P	matrix defined in Eq. (29d)
Q	matrix defined in Eq. (29e)
R	real part of ϕ
S	imaginary part of ϕ
U	real part of $\phi\Omega$
V	imaginary part of $\phi\Omega$
W	weighting matrix
X	displacement vector, Eq. (1)
Y	vector of system state variables, Eq. (3)
α	matrix consisting of Lagrange multipliers, Eq. (18)
β	matrix consisting of Lagrange multipliers, Eq. (18)
γ	matrix consisting of Lagrange multipliers, Eq. (18)
Δ	matrix defined in Eqs. (14a, b)
ϵ	weighted matrix norm
θ	$\gamma - \gamma^T$
Λ	matrix consisting of Lagrange multipliers, Eq. (12)
ϕ	rectangular complex mode shape matrix
ϕ	$W_K^{-1} \phi$

*This work was carried out under Contract NAS1-15805 to the Langley Research Center

**Senior Research Engineer, Member AIAA

[†]Senior Research Engineer

^{††}Assistant Director for Research, Member AIAA

ψ	Lagrangian function
Ω	diagonal complex matrix consisting of damping ratios and natural frequencies
(\cdot)	one differentiation with respect to time
($\bar{\cdot}$)	complex-conjugate of a matrix

Superscripts

T	matrix transpose
*	conjugate transpose of a matrix
+	Moore-Penrose inverse of a matrix

Subscripts

A	analytical matrix
C	system damping
I	imaginary part
K	system stiffness
M	system mass
R	real part

Introduction

With the increasing complexity and accuracy demands of modern aerospace structures, system identification has become a necessity. In recent years, within the framework of linear undamped systems, many procedures have been proposed to improve an analytical model by using measured modal parameters¹⁻⁷. Analytical mass and stiffness matrices are often available from some source, for example, a finite element analysis. Certainly, the resulting model is only an approximate representation to the structure and contains errors of undetermined magnitude. On the other hand, vibration test results in incomplete sets of natural frequencies and mode shapes of the structure. These data also contain errors whose magnitudes are unknown. Assuming it is desired to have an analytical model which will be consistent with the analysis and the test, Berman⁴ applied the Lagrange multiplier method to minimize a weighted matrix norm³ and obtained an improved model which predicted exactly the measured modal data and minimized the changes in the analytical model. The requirement for a small modification implies that the analytical model is a good representation of the structure. Applications of this procedure to improve the analytical models of large structural systems have been reported^{6,7}.

The procedure mentioned above among others is based on the assumption that the system possesses only negligible damping level or that the damping is proportional and that the measured modal parameters are real. However, there are cases in which damping effects must be taken into account. For instance, ground vibration tests of a helicopter fuselage have shown that the modal damping ratio of several lowest modes are over 12 percent and the mode shapes are essentially complex-valued⁸. Therefore, it was necessary to refine the previous method so that the more realistic, nonproportionally damped system and the modal parameters

may be equally treated. In the analyses reported hereafter, the system damping can be of any type so long as it can be represented by a real symmetric matrix coefficient of the velocity vector in the dynamic equation.

Primary concerns in the present study are as follows:

1. The method must be applicable to large structural systems. Let the number of degrees of freedom be n and the number of measured modes be m . Typically, n is of the order of hundreds and m is much less than n . Methods involving extensive iteration or repeated eigensolution would be prohibitively expensive and convergence problem would always involve some uncertainty.
2. Besides the analytical mass (M_A) and stiffness (K_A) matrices, the present procedure needs an analytical damping matrix (C_A). It is acknowledged that no general rules currently exist for formulating a damping matrix as are those for mass and stiffness matrices. One way to obtain C_A in the first approximation is to represent it as a proportional matrix which is a linear combination of M_A and K_A . This step, of course, involves considerable engineering judgement and the accuracy may not be high.
3. Unlike its undamped counterpart, a damped system has complex-valued modal matrices Ω and Φ . To guarantee the improved matrices being real symmetric, appropriate constraints had to be imposed on the system equations which rendered the problem considerably more complicated than would otherwise be the case.

A method was developed which is applicable to realistically large models, is computationally efficient, and satisfies all the theoretical requirements.

Theoretical Background

A linear structural system of n degrees of freedom is described by the matrix equation

$$M\ddot{X} + C\dot{X} + KX = 0 \quad (1)$$

where M , C and K are real symmetric constant coefficient matrices. With the state-space representation, (1) can be rewritten as

$$A\dot{Y} + BY = 0 \quad (2)$$

where

$$Y = \begin{Bmatrix} \dot{X} \\ X \end{Bmatrix} \quad (3)$$

$$A = \begin{bmatrix} 0 & M \\ M & C \end{bmatrix} \quad (4)$$

$$B = \begin{bmatrix} -M & 0 \\ 0 & K \end{bmatrix} \quad (5)$$

By the use of (2)-(5), the following orthogonality relationships are obtained:

$$\begin{bmatrix} \Phi\Omega \\ \Phi \end{bmatrix}^T A \begin{bmatrix} \Phi\Omega \\ \Phi \end{bmatrix} = I \quad (6)$$

$$\begin{bmatrix} \Phi\Omega \\ \Phi \end{bmatrix}^T B \begin{bmatrix} \Phi\Omega \\ \Phi \end{bmatrix} = -\Omega \quad (7)$$

or equivalently,

$$\Phi^T M \Phi \Omega + \Omega \Phi^T M \Phi + \Phi^T C \Phi = I \quad (6a)$$

and

$$\Omega \Phi^T M \Phi \Omega - \Phi^T K \Phi = \Omega \quad (7a)$$

where Ω is a complex-valued diagonal matrix containing modal damping ratios (real part) and natural frequencies (imaginary part) and Φ the corresponding mode shape matrix. Attention must be called that in identification problem Φ is a rectangular matrix and Ω is $m \times m$. With these modal parameters, the dynamic equation (1) can be cast in the form of

$$M \Phi \Omega^2 + C \Phi \Omega + K \Phi = 0 \quad (1a)$$

Given Ω and Φ , it can be shown that if M , C and K satisfy (1a) and (6) then they also satisfy (7). In other words, (1a) and (6) imply (7), but (1a) and (7) do not imply (6) unless Ω is non-singular. Therefore, Eqs. (1a) and (6) have been selected to improve the analytical model since it is desired to include rigid body modes if the system has free boundary conditions.

Intuitively, it might seem appropriate to improve M , C and K by directly identifying A and B of Eqs. (4) and (5). Unfortunately, this cannot be done. The reason is that the optimization techniques would distribute variations to all variables involved and, for example, the upper-left portion of the modified matrix will no longer to be precisely zero, which is certainly unacceptable. Thus it is necessary to take the more difficult analytical approach of specifically identifying the physical matrices.

Full Mode Computation

Since in practice, the degrees of freedom measured in a vibration test are only a small portion of those specified in the analytical model, a procedure is required to compute the modal displacements at the unmeasured degrees of freedom. This preprocessing procedure referred to as "full-mode computation" has been discussed in Ref. 6. A slight modification is made here to include the system damping.

Let Φ_i be the i th column of the mode shape matrix Φ . The portion of Φ_i whose elements are measured is denoted by Φ_{1i} and the rest by Φ_{2i} . With this coordinate transformation, Eq. (1a) can be partitioned into

$$\left(\Omega_i^2 \begin{bmatrix} M_1 & M_2 \\ M_2^T & M_4 \end{bmatrix} + \Omega_i \begin{bmatrix} C_1 & C_2 \\ C_2^T & C_4 \end{bmatrix} + \begin{bmatrix} K_1 & K_2 \\ K_2^T & K_4 \end{bmatrix} \right) \begin{Bmatrix} \Phi_{1i} \\ \Phi_{2i} \end{Bmatrix} = 0 \quad (8)$$

where, for the i th mode, Ω_i is the measured eigenvalue and M , C and K partitioned are the system matrices update. At the start of the identification procedure, M , C and K are the analytical matrices M_A , C_A and K_A . It is apparent from (8) that

$$\phi_{2i} = - (\Omega_i^2 M_A + \Omega_i C_A + K_A)^{-1} (\Omega_i^2 M_A^T + \Omega_i C_A^T + K_A^T) \phi_{1i} \quad (9)$$

Because analytical matrices are involved in the equation, the accuracy of ϕ_{2i} solved from (9) is expected to be of the order of M_A , C_A or K_A even if ϕ_{1i} is exact. The analysis following will deal with full modal matrices $\Phi(n \times m)$ and $\Omega(m \times m)$.

Improvement of Mass and Damping Matrices

The basic equation to be used for improving analytical mass and damping matrices is the orthogonality relationship (6a). Since $m < n$, given Φ and Ω , there are infinite sets of $M(n \times n)$ and $C(n \times n)$ satisfying (6a). A unique set of mass and damping matrices will result if, in addition to satisfying the orthogonality relationship, a norm

$$\epsilon = || W_M (M - M_A) W_M || + || W_C (C - C_A) W_C || \quad (10)$$

is also minimized, where $W_M(n \times n)$ and $W_C(n \times n)$ are arbitrary real symmetric, nonsingular weighting matrices. Let $\Phi = R + iS$ and $\Phi\Omega = U + iV$ then the real and imaginary parts of (6a) are separated into

$$R^T M U + U^T M R - S^T M V - V^T M S + R^T C R - S^T C S = I \quad (11a)$$

$$R^T M V + V^T M R + S^T M U + U^T M S + R^T C S + S^T C R = 0 \quad (11b)$$

Define the Lagrangian function

$$\begin{aligned} \psi = \epsilon + \sum_{i=1}^m \sum_{j=1}^m (\Lambda_R)_{ij} (R^T M U + U^T M R - S^T M V - V^T M S \\ + R^T C R - S^T C S - I)_{ij} \\ + \sum_{i=1}^m \sum_{j=1}^m (\Lambda_I)_{ij} (R^T M V + V^T M R + S^T M U + U^T M S \\ + R^T C S + S^T C R)_{ij} \end{aligned} \quad (12)$$

Differentiating ψ with respect to M and C respectively and equating the results to 0 yield

$$\begin{aligned} M = M_A - 1/2 W_M^{-2} (R \Lambda_R U^T + U \Lambda_R R^T - S \Lambda_R V^T - V \Lambda_R S^T \\ + R \Lambda_I V^T + V \Lambda_I R^T + S \Lambda_I U^T + U \Lambda_I S^T) W_M^{-2} \end{aligned} \quad (13a)$$

$$C = C_A - 1/2 W_C^{-2} (R \Lambda_R R^T - S \Lambda_R S^T + R \Lambda_I S^T + S \Lambda_I R^T) W_C^{-2} \quad (13b)$$

Obviously, imposing Λ_R and Λ_I being symmetric in Eqs. (13a, b) is equivalent to imposing the constraints of M and C being symmetric to Eqs. (11a, b). The Lagrange multipliers $(\Lambda_R)_{ij}$ and $(\Lambda_I)_{ij}$ may

be solved numerically from the following set of equations obtained by substituting (13a, b) into (11a, b),

$$\begin{bmatrix} (E_{11})_{iklj} & (E_{12})_{iklj} \\ (E_{21})_{iklj} & (E_{22})_{iklj} \end{bmatrix} \begin{Bmatrix} (\Lambda_R)_{kl} \\ (\Lambda_I)_{kl} \end{Bmatrix} = \begin{Bmatrix} (\Lambda_R)_{ij} \\ (\Lambda_I)_{ij} \end{Bmatrix} \quad (14)$$

where

$$\begin{aligned} \Delta_R = 2 (I - R^T M_A U - U^T M_A R + S^T M_A V + V^T M_A S \\ - R^T C_A R + S^T C_A S) \end{aligned} \quad (14a)$$

$$\begin{aligned} \Delta_I = 2 (R^T M_A V + V^T M_A R + S^T M_A U + U^T M_A S \\ + R^T C_A S + S^T C_A R) \end{aligned} \quad (14b)$$

and the submatrices E_{11} , E_{12} , E_{21} and E_{22} are

functions of R , S , U , V , W_M^{-2} and W_C^{-2} . Repeated index in a product denotes summation over the range of the index. Since Δ_R and Δ_I are symmetric, there are $m(m+1)$ unknowns along with $m(m+1)$ equations in (14). In the implementation of the techniques the coefficient matrix E which has $m(m+1) \times m(m+1)$ elements is formulated by a FORTRAN program. The improved mass and damping matrices, M and C , result when Λ_R and Λ_I are solved from (14) and are substituted into (13a, b).

In this section, a numerical method has been used to solve $m(m+1)$ equations. In practice the number of measured modes is small enough to make this solution economically practical.

Improvement of Stiffness Matrix

Given the full modal matrices Φ and Ω , the improved M and C , and the analytical stiffness matrix K_A , an improved stiffness matrix K must satisfy the dynamic equation

$$\Phi^T K = - (\Omega^2 \Phi^T M + \Omega \Phi^T C) W_K = f \quad (1b)$$

and the constraints

$$k = k^* \quad (15)$$

$$k = k^T \quad (16)$$

in which an asterisk denotes the conjugate transpose of a matrix, $\Phi = W_K^{-1} \phi$, $k = W_K^T K W_K$ and $W_K(n \times n)$ is an arbitrary, real symmetric, nonsingular weighting matrix. The constraints (15) and (16) guarantee the improved stiffness matrix to be real symmetric. A unique set of K will result if k satisfies (1b), (15), (16) and also minimizes the norm

$$\epsilon = || W_K (K - K_A) W_K || = || k - k_A || \quad (17)$$

Define

$$\begin{aligned} \psi = \varepsilon + \sum_{i=1}^m \sum_{j=1}^n \left[\alpha_{ij} (\phi^T k - f)_{ij} \right. \\ \left. + \alpha_{ij}^* (\phi^T k - f)^*_{ij} \right] + \sum_{i=1}^n \sum_{j=1}^n \left[\beta_{ij} (k - k_A)_{ij} \right. \\ \left. + \beta_{ij}^* (k - k_A)^*_{ij} + \gamma_{ij} (k - k^T)_{ij} \right. \\ \left. + \gamma_{ij}^* (k - k^T)^*_{ij} \right] \end{aligned} \quad (18)$$

Note that it is no longer practical to solve the equations numerically for the Lagrange multipliers β and γ because their order is n^2 . A closed-form representation for the improved stiffness matrix is necessary. Differentiating ψ with respect to k and equating the result to zero yields

$$(k - k_A)^* + \phi \alpha + \beta - \beta^* + \gamma - \gamma^T = 0 \quad (19)$$

Taking the conjugate transpose of (19) and adding it to (19) results in

$$2(k - k_A) + \phi \alpha + (\phi \alpha)^* + \theta + \theta^* = 0 \quad (20)$$

where $\theta = \gamma - \gamma^T$ and the relationship $k - k_A = (k - k_A)^*$ has been used in the equation. Premultiplying (20) by ϕ^T , applying (1b) and noting that $\phi^T \phi$ is non-singular, then

$$\alpha = -(\phi^T \phi)^{-1} [2(f - f_A) + \phi^T (\theta + \theta^*)] - (\phi^T \phi)^{-1} \phi^T \alpha^* \phi^* \quad (21)$$

in which $f_A = \phi^T k_A$. Substituting (21) into (20) gives

$$\begin{aligned} 2(k - k_A) + \theta + \theta^* - \phi (\phi^T \phi)^{-1} [2(f - f_A) \\ + \phi^T (\theta + \theta^*)] - \phi (\phi^T \phi)^{-1} \phi^T \alpha^* \phi^* \\ - [2(f^* - f_A^*) + (\theta + \theta^*) \bar{\phi}] (\phi^* \bar{\phi})^{-1} \phi^* \\ - \phi \alpha \bar{\phi} (\phi^* \bar{\phi})^{-1} \phi^* = 0 \end{aligned} \quad (22)$$

where an overbar denotes the complex conjugate of a matrix. Substituting (21) into (22) results in

$$\begin{aligned} 2(k - k_A) + \theta + \theta^* - \phi (\phi^T \phi)^{-1} [2(f - f_A) \\ + \phi^T (\theta + \theta^*)] - [2(f^* - f_A^*) \\ + (\theta + \theta^*) \bar{\phi}] (\phi^* \bar{\phi})^{-1} \phi^* \\ + \phi (\phi^T \phi)^{-1} \phi^T [2(f^* - f_A^*) \\ + (\theta + \theta^*) \bar{\phi}] (\phi^* \bar{\phi})^{-1} \phi^* \\ + \phi (\phi^T \phi)^{-1} [2(f - f_A) \\ + \phi^T (\theta + \theta^*)] \bar{\phi} (\phi^* \bar{\phi})^{-1} \phi^* \\ + \phi \alpha \bar{\phi} (\phi^* \bar{\phi})^{-1} \phi^* + \phi (\phi^T \phi)^{-1} \phi^T \alpha^* \phi^* = 0 \end{aligned} \quad (23)$$

The Lagrange multipliers α and α^* can be eliminated by adding (23) to (22), which after some algebraic manipulations results in

$$k = k_A + g + h \quad (24)$$

where

$$\begin{aligned} g = \phi (\phi^T \phi)^{-1} (f - f_A) + [\phi (\phi^T \phi)^{-1} (f - f_A)]^* \\ - 1/2 \phi (\phi^T \phi)^{-1} \{ \phi^T (f - f_A)^* \\ + [\phi^T (f - f_A)]^* \} [\phi (\phi^T \phi)^{-1}]^* \end{aligned} \quad (24a)$$

$$\begin{aligned} h = -1/2 [I - \phi (\phi^T \phi)^{-1} \phi^T] (\theta + \theta^*) \\ [I - \phi (\phi^T \phi)^{-1} \phi^T]^* \end{aligned} \quad (24b)$$

Apply the symmetric condition (16) to (24)

$$g + h = g^T + h^T \quad (25)$$

Premultiply (25) by ϕ^T and note that $\phi^T h = 0$, then

$$h \phi = (g^T - g) \phi \quad (26)$$

Solving (26) for h

$$h = (g^T - g) \phi \phi^+ \quad (27)$$

in which $\phi^+ = (\phi^* \phi)^{-1} \phi^*$ is the Moore-Penrose inverse of ϕ . Therefore, the improved stiffness matrix becomes

$$k = k_A + g + (g^T - g) \phi \phi^+ \quad (28)$$

or, equivalently

$$\begin{aligned} K = K_A - W_K^{-2} F - (W_K^{-2} F)^* + W_K^{-2} (F - \bar{F}) P W_K^{-2} \\ + (F - \bar{F})^* W_K^{-2} P W_K^{-2} + 1/2 W_K^{-2} D W_K^{-2} \\ + 1/2 W_K^{-2} (D^T - D) W_K^{-2} P W_K^{-2} \end{aligned} \quad (29)$$

where

$$H = \Omega^2 \phi^T M + \Omega \phi^T C + \phi^T K_A \quad (29a)$$

$$G = \phi (\phi^T W_K^{-2} \phi)^{-1} \quad (29b)$$

$$F = GH \quad (29c)$$

$$P = \phi (\phi^* W_K^{-2} \phi)^{-1} \phi^* \quad (29d)$$

$$Q = \phi^T H^* + (\phi^T H^*)^* \quad (29e)$$

$$D = GQG^* \quad (29f)$$

The matrix inversions required for the evaluation of the improved damping matrix are W_K^{-2} , $(\phi^T W_K^{-2} \phi)^{-1}$ and $(\phi^* W_K^{-2} \phi)^{-1}$. None will cause difficulty since the first one is a chosen weighting matrix and the other two are of order m .

Conclusions

A method is developed to find smallest changes in the analytical model of a nonproportional damped structure so that the improved model exactly predicts the measured damping ratios, natural frequencies and complex mode shapes. The only assumption to the system damping is that it can be represented by a real symmetric matrix. The reported procedures use an orthogonality relationship to improve mass and damping matrices and the dynamic equation to improve stiffness matrix and are applicable to a structural system with rigid body modes. Since this method has not invoked any iterative scheme, it is especially suited to the identification of large systems.

References

1. Rodden, W.P., "A Method for Deriving Structural Influence Coefficients from Ground Vibration Tests," AIAA Journal, Vol. 5, 1967, pp. 991-1000.
2. Berman, A. and Flannelly, W.G., "Theory of Incomplete Models of Dynamic Structures," AIAA Journal, Vol. 9, 1971, pp. 1481-14787.
3. Baruch, M. and Bar Itzhack, I.Y., "Optimal Weighted Orthogonalization of Measured Modes," AIAA Journal, Vol. 16, 1978, pp. 346-351.
4. Berman, A., "Mass Matrix Correction Using an Incomplete Set of Measured Modes," AIAA Journal, Vol. 17, 1979, pp. 1147-1148.
5. Chen, J.C. and Garba, J.A., "Analytical Model Improvement Using Modal Test Results," Vol. 18, 1980, pp. 684-690.
6. Berman, A., Wei, F.S. and Rao, K.V., "Improvement of Analytical Dynamic Models Using Modal Test Data," AIAA Paper 80-0800, 1980.
7. Berman, A. and Nagy, E.J., "Improvement of a Large Analytical Model Using Test Data," AIAA Journal, Vol. 21, 1983, pp. 1168-1173.
8. Flannelly, W.G., Fabunmi, J.A. and Nagy, E.J., "Analytic Testing," NASA CR 3429, 1981.
9. Ben-Israel, A. and Greville, T.N.E., "Generalized Inverses: Theory and Applications," John Wiley and Sons, 1974.

Samir R. Ibrahim*
Department of Mechanical Engineering
and Mechanics
Old Dominion University
Norfolk, Virginia 23508

Abstract

This paper discusses the damping identification accuracy of the time domain modal identification algorithm referred to as the "ITD" technique. It is shown here that the biased, but bound, errors in the identified damping factors are due to the inherent statistically biased numerical errors in the least squares approach used to compute the matrix of eigenvalues and eigenvectors. A modified least squares solution is presented and shown to eliminate the damping bias and improve its identification accuracy without affecting either the simplicity or the other acknowledged merits of the technique.

Introduction

Modal identification techniques, in general, use experimentally obtained responses from a structure under test to determine its natural frequencies, damping factors and mode shapes. The modal parameters thus obtained may be used for a wide variety of applications such as trouble shooting, responses and loads prediction, control system design, dynamic modeling and incipient failure detection.

The accuracy requirements in modal identification techniques are very much dependent on the specific application for which they are used. In some applications, the mere determination of dominant resonant frequencies or just a qualitative analysis of the responses may be sufficient. The others may require accurate estimation of all modal parameters of the system over a wide range of frequency. For example in modal identification for mathematical modeling and control system design, requirements such as high accuracy and the need for the identification technique to possess high frequency resolution to separate closely spaced modes become crucial factors for judging the suitability of the technique for such applications. When modal analysis is used for incipient failure detection and structural integrity monitoring, the ability of the identification technique to repeatedly identify modal parameters with high accuracy to determine any changes in them becomes a must. In such application, and also in flutter margins predictions, strong emphasis is needed in the accuracy of damping factors determination. Another example where high accuracy is desirable is in the application of linear modal identification algorithms to nonlinear systems in a quasi-modal fashion¹ to determine the types of nonlinearities.

The modal identification technique referred to as the Ibrahim Time Domain, ITD, technique²⁻⁵ proved to be promising when accuracy is highly required. The technique is capable of accurately resolving closely spaced modes. Extremely good accuracy characterized the technique in identifying modal parameters even when high levels of noise corrupted the responses. Only the accuracy of the identified damping factors did not match those of natural frequencies and mode shapes. Damping factors frequently showed biased but bound errors. Reasons for such errors are explained and an algorithm is proposed to eliminate or reduce such errors.

Basic Theory of the ITD Technique

The technique uses free decay responses, containing n structural modes, to construct the $2m \times 2r$ system's response matrices $[\phi]$ and $[\hat{\phi}]$ such that

$$\phi_{ij} = x_i(t_j) \quad (1)$$

$$\hat{\phi}_{ij} = x_i(t_j + \Delta t_1) \quad (2)$$

with x_i being a physical measurement at location i on the structure under test or a physical measurement delayed in time Δt_2 which in such case represents a pseudo measurement. In constructing these response matrices the value of m (number of degrees of freedom in the identification model) is greater than the number of modes n . This is to allow the use of an oversized identification models. The number of columns in these response matrices, $2r$, is greater than $2m$ to allow for the implementation of least squares solution.

Since the free decay responses are linear combinations of the system's modes, then $[\phi]$ and $[\hat{\phi}]$ can be written as

$$[\phi] = [\Phi] [A] \quad (3)$$

$$\text{and } [\hat{\phi}] = [\Phi] [\alpha] [A] \quad (4)$$

where $[\Phi]$ is the matrix of complex mode shapes, $[\alpha]$ is a diagonal matrix,

$$A_{ij} = e^{\lambda_i t_j} \quad (5)$$

$$\text{and } \alpha_i = e^{\lambda_i \Delta t_1} \quad (6)$$

where λ 's are the characteristic roots of the system. By eliminating $[A]$ from equations (3)

*Associate Professor; Member AIAA

and (4) the problem reduces to the left eigenvalue equation

$$[A] [\psi]^{-1} [\phi] = [\psi]^{-1} [\hat{\phi}] \quad (7)$$

To convert equation (7) to the more classical right eigenvalue problem

$$[A] \{\psi\} = \alpha \{\psi\} \quad (8)$$

the [A] matrix must satisfy the equation

$$[A] [\phi] = [\hat{\phi}] \quad (9)$$

(2mx2m) (2mx2r) (2mx2r)

Since equation (9) is an over specified set of linear equations, the solution for [A] maybe obtained by using the least squares approach.

It is important to note here that the eigenvalues and eigenvectors of the matrix [A] contain information not only related to the modal parameters of the structure under test but also on the computational noise modes⁵ representing the noise in the measurements.

When noise exists and an oversized identification model is used, the [A] matrix is never unique but the eigenvalues and eigenvectors corresponding to the structural modal parameters are uniquely identified.

The purpose of the algorithm is not to identify [A] but to identify its eigenvalues and eigenvectors. For that purpose the inverse of [A] contain the same information. If a solution for [A] is to be computed from equation (9) by the least squares approach, then

$$[A] = [\hat{\phi} \hat{\phi}^T] [\phi \phi^T]^{-1} \quad (10)$$

on the other hand equation (9) may be post-multiplied by $[\phi]^T$ to obtain the least squares solution for the inverse of [A]

$$[A]^{-1} = [\hat{\phi} \hat{\phi}^T]^{-1} [\phi \phi^T] \quad (11-a)$$

$$\text{or } [A] = [\hat{\phi} \hat{\phi}^T]^{-1} [\phi \phi^T] \quad (11-b)$$

The Solution in equation (10) is the solution frequently used in the ITD technique. It was always pointed out that the solution in equation (11) is another possible solution.

Analysis of Existing Damping Accuracy

The [A] matrix obtained from either solution, equations (10) or (11), yields frequencies and mode shapes with high accuracy but has always showed biased errors in the identified damping factors. The high accuracy of the identified frequencies and mode shapes as compared to the biased errors in the identified damping factors, should not confuse the fact that all these parameters are obtained from the same matrix. The difference in the accuracy is readily explained by the procedure for computing λ 's from α 's.

If

$$\alpha_i = \beta_i + j\gamma_i \quad (12)$$

and

$$\lambda_i = a_i + jb_i \quad (13)$$

then

$$b_i = \frac{1}{\Delta t} \tan^{-1} \frac{\gamma_i}{\beta_i} \quad (14)$$

$$a_i = -\frac{1}{2\Delta t} \ln (\beta_i^2 + \gamma_i^2) \quad (15)$$

The fact is that even though the eigenvalues of the [A] matrix may be of very high accuracy, the damping factors, which are related to the real part of λ , may show much higher errors because of the exponential nature of equation (15). Actually, if ϵ is the percent error in the magnitude of the identified eigenvalue, the percent error in the corresponding damping factor is

$$\delta = -\frac{100f_a}{\pi f \zeta_{ex}} \ln (1 + \epsilon/100) \%$$

where f_a is the aliasing frequency, corresponding to the time delay Δt_1 , f is the frequency of the identified mode and ζ_{ex} is the exact damping factor.

To further elaborate on this correlation in errors, an example may be appropriate here. For a 20 Hz mode and 2% damping factor, the percent error in the identified damping factor versus the error in the magnitude of eigenvalue α is shown in Figure 1 for aliasing frequencies of 60 and 30 Hz. From this figure and from past experiences with the ITD technique, it may be said that the errors in the computed damping factors were always bound and even though they may seem large, they are still a testimony to the identification accuracy of the technique as far as the frequencies and mode shapes are concerned. For example, if the error in the magnitude of the identified eigenvalue is -2%, the corresponding error in the identified damping factor will be about 96.5% and 48.2% for aliasing frequencies of 60 Hz and 30 Hz.

This difference in accuracy may also be substantiated by the theoretical and identified parameters listed in Table 1. The two modes responses that were used to obtain these identified parameters contained 200% noise to signal RMS ratio. By using the errors correlation formula and the errors in the identified damping factors, the accuracy of the identified eigenvalues turn to be 99.2% and 99.1% for the two modes respectively.

Proposed Approach

The analysis in the previous section reveals that the technique under consideration has high accuracy in identifying frequencies and mode shapes. Identified damping factors show biased errors due to the following reasons:

- i) The solution for the matrix of eigenvalues and eigenvectors is obtained by least squares method which is known to have statistically biased numerical errors.
- ii) Even though the eigenvalues are accurately identified, the damping factors show much higher errors since they are computed from an exponential formula.

Recognizing these two reasons and also considering that there exist two possible least squares solutions for the [A] matrix, equations (10) and (11), the following solutions will be proven to have less bias than either of those solutions:

Let $[\phi]$ and $[\hat{\phi}]$ be as earlier defined. Another matrix $[\hat{\phi}]$ is defined such that

$$\hat{\phi}_{ij} = x_i (t_j + 2\Delta t_1)$$

then a better estimate for the [A] matrix may be obtained in one of the following manners:

Solution One

The A matrix theoretically satisfies the following equations:

$$[A][\phi] = [\hat{\phi}] \quad (16-a)$$

and

$$[A][\hat{\phi}] = [\phi] \quad (16-b)$$

by postmultiplying equations (16-a) and (16-b) by $[\phi]^T$, which is equivalent to the solution in equation (10) and equation (11) respectively, two estimates of [A] are obtained and multiplied to give

$$[A] = [A_2][A_1] = [\hat{\phi}\hat{\phi}]^T [\phi\phi]^T^{-1} \quad (19)$$

The eigenvalues of [A] in such case are

$$\alpha_i = e^{(\lambda_{11} + \lambda_{21})\Delta t_1} \quad (20)$$

in which an average value for λ may be obtained.

Solution Two

Since the bias in equations (10) and (11) are expected to be opposite to each other, averaging the two solutions will give a better estimate for the eigenvalues. In such case

$$[A] = \frac{1}{2} ([\hat{\phi}\hat{\phi}]^T [\phi\phi]^T^{-1} + [\phi\phi]^T [\hat{\phi}\hat{\phi}]^T^{-1}) \quad (21)$$

Solution Three

A better estimate for the [A] matrix may be obtained by postmultiplying equations (16-a) and (16-b) by $[\phi]^T$ and then adding. In this case the

solution for [A] is

$$[A] = [\hat{\phi} + \phi] [\hat{\phi}]^T ([\phi + \hat{\phi}][\hat{\phi}]^T)^{-1} \quad (22)$$

The three solutions presented here are expected to have less biased errors than those of equations (10) or (11). These proposed solutions have the advantage of reducing the errors in the identified damping factors while maintaining the accuracy of the identified frequencies and mode shapes. The computational requirements are about the same as the previous solutions. Only one matrix inversion, except for solution two, and one eigenvalue problem are performed in one identification run.

Using this new approach for the same case discussed in Table 1, the identified frequencies and damping factors are listed in Table 2. While the same levels of accuracy are noticed in identified frequencies, the accuracy of damping factors is improved. Furthermore the usual biased errors in damping factors are not noticed. Instead, the errors seem to be random. Results in Table 2 were obtained by a smaller identification model than that used for Table 1 (65 D.O.F versus 300 D.O.F)

Simulated Experiments

Two different sets of responses are generated and used as data for the identification program to test the proposed procedure and compare it to the previous one. The mode shapes used to generate the free decay responses are for a simply supported beam with ten measurements located at spacings of one eleventh of the beam's length. The first set of data contain responses from the first three modes while the second set has five modes in the responses. Frequencies were arbitrarily assigned as 10, 12, 15, 20 and 21 Hz while damping factors were 2% for all modes. A sampling frequency of 100.00 Hz is used and the record length is 300 samples. Randomly generated numbers were used to simulate noise in the data and the noise to signal RMS ratio was adjusted to 30 percent.

The simulated experimental responses were used to identify the systems modal parameters. Identification models of 15 and 20 modes were used for both the previous approach, equation (10), and the new proposed approach. The two approaches are here referred to as single least squares (SLS) and double least squares (DLS) solutions.

Tables 3 and 4 list the identified frequencies and damping factors for the three modes responses and tables 5 and 6 for the five modes responses. Damping results obtained by using the proposed approach show noticeable improvement. Errors in damping factors seem to be more random and always less than the noise to signal ratio of the input data. Frequencies maintained their high identification accuracy.

Concluding Remarks

In time domain modal identification algorithms, in which least squares solutions are

implemented, identified damping factors show biased errors. This is due to the inherent statistically biased numerical errors of the least squares method. A modified approach for least squares solution is presented. The averaging of two oppositely biased solutions is shown here to reduce the bias and improve the damping identification accuracy.

Acknowledgement

This work is partially supported by a research contract from the Air Force Wright Aeronautical laboratories; Mr. K. R. Wentz, technical monitor.

References

1. Ibrahim, S. R., "Time Domain Quasi Linear Identification of Nonlinear Dynamic Systems." Proceedings of the 24th Structures, Structural Dynamics and Materials Conference AIAA Paper No. 83-0811, May 1983. To appear in the AIAA Journal.
2. Ibrahim, S. R. and Miluleik, E. C., "A Method for the Direct Identification of Vibration Parameters from Free Response." Shock and Vibration Bulletin, Bulletin 47, Part 4, September 1977, pp. 183-198.
3. Ibrahim, S. R., "Random Decrement Technique for Modal Identification of Structures." J. Spacecraft and Rockets, Vol. 14, No. 11, November 1977, pp. 696-700.
4. Ibrahim, S. R., "Modal Confidence Factor in Vibration Testing." J. Spacecraft and Rockets, Vol. 15, no. 5, September 1978, pp. 313-316.
5. Ibrahim, S. R. and Pappa R. S., "Large Modal Survey Testing Using the Ibrahim Time Domain (ITD) Modal Identification Algorithm." J. Spacecraft and Rockets, Vol. 19, No. 5, Sept. - Oct. 1982, pp. 459-465.
6. Goodwin, G. C. and Payne R. L., Dynamic Identification, Experimental Design and Data Analysis, Academic Press, 1977.

Table 1. Identification Errors for 200% N/S Ratio (Single Least Squares Approach)

Parameter	Theoretical	Identified	% Error
f_1 (Hz)	20.0000	20.0062	0.03
f_2	30.0000	29.9894	0.04
ζ_1 (%)	1.00	2.23	123.00
ζ_2	1.00	1.98	98.00

Table 2. Identification Errors for 200% N/S Ratio (Double Least Squares Approach)

Parameter	Theoretical	Identified	% Error
f_1 (Hz)	20.000	19.992	0.040
f_2	30.000	30.014	0.047
ζ_1 (%)	1.000	0.834	-16.600
ζ_2	1.000	1.135	+13.500

Table 3. Three Modes, 30% Noise 15 DOF Identification Results

Parameter	Theoretical	Identified			
		SLS Approach		DLS Approach	
		Value	% Error	Value	% Error
f_1 (Hz)	10.0000	10.0100	0.10	10.0091	0.04
f_2	12.0000	12.0222	0.19	12.0282	0.24
f_3	15.0000	15.0092	0.06	14.9945	-0.09
ζ_1 (%)	2.00	3.57	19.80	1.94	-2.92
ζ_2	2.00	2.86	42.81	2.14	6.98
ζ_3	2.00	3.57	78.69	1.87	-6.58

Table 4. Three Modes, 30% Noise 20 DOF Identification Results

Parameter	Theoretical	Identified			
		SLS Approach		DLS Approach	
		Value	% Error	Value	% Error
f_1 (Hz)	10.0000	10.0047	0.05	10.0069	0.07
f_2	12.0000	12.0355	0.30	12.0399	0.33
f_3	15.0000	15.0194	0.13	15.0116	0.08
ζ_1 (%)	2.00	2.32	16.00	1.93	-3.40
ζ_2	2.00	2.81	40.50	2.06	2.87
ζ_3	2.00	3.60	80.00	2.01	0.57

Table 5. Five Modes, 30% Noise 15 DOF Identification Results

Parameter	Theoretical	Identified			
		SLS Approach		DLS Approach	
		Value	% Error	Value	% Error
f_1 (Hz)	10.0000	9.9747	-0.25	9.9976	-0.02
f_2	12.0000	12.0110	0.09	11.9893	-0.09
f_3	15.0000	15.0063	0.04	14.9965	-0.02
f_4	20.0000	20.0598	0.30	20.0494	0.25
f_5	21.0000	21.0140	0.07	21.0460	0.22
ζ_1 (%)	2.00	3.71	85.28	1.78	-10.99
ζ_2	2.00	3.85	92.58	2.06	3.11
ζ_3	2.00	3.14	57.13	1.69	-15.73
ζ_4	2.00	3.57	78.67	1.69	-15.31
ζ_5	2.00	3.53	76.68	1.82	-9.08

Table 6. Five Modes, 30% Noise 20 DOF Identification Results

Parameter	Theoretical	Identified			
		SLS Approach		DLS Approach	
		Value	% Error	Value	% Error
f_1 (Hz)	10.0000	10.0170	0.17	10.0163	0.16
f_2	12.0000	11.9987	-0.01	11.9978	-0.02
f_3	15.0000	15.0082	0.05	14.9869	-0.09
f_4	20.0000	20.1145	0.57	20.0460	-0.23
f_5	21.0000	20.9165	-0.33	20.9764	-0.11
ζ_1 (%)	2.00	2.79	39.47	1.78	-10.81
ζ_2	2.00	3.24	62.10	1.90	-4.94
ζ_3	2.00	2.89	44.64	2.25	12.47
ζ_4	2.00	3.59	79.26	1.72	-13.99
ζ_5	2.00	3.05	52.56	1.63	-18.26

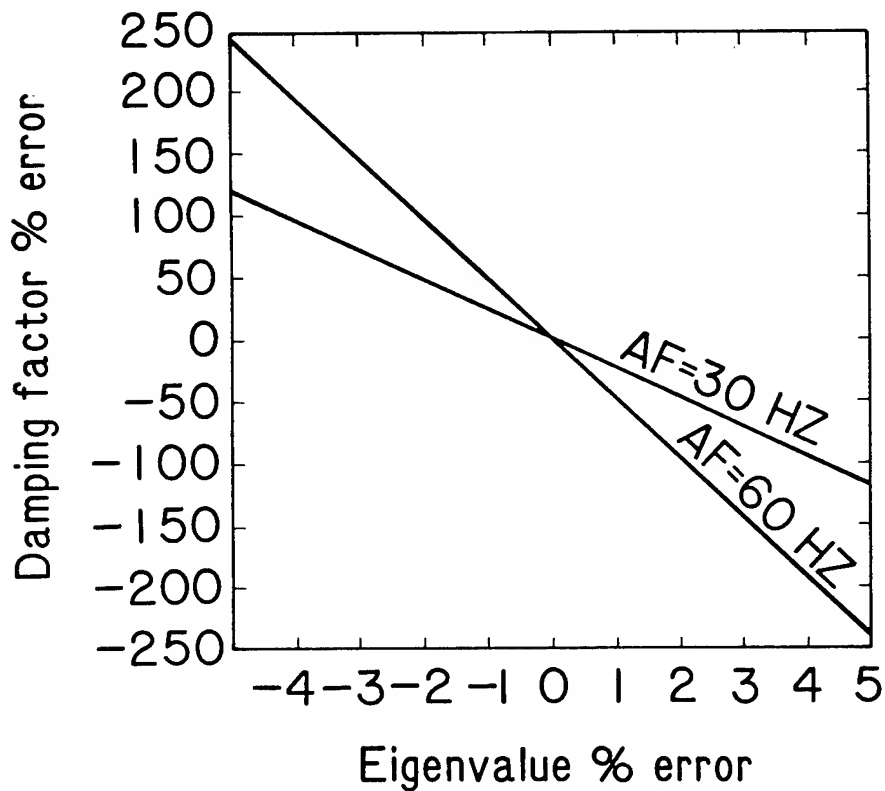


Figure 1. Damping Factor Error Versus Eigenvalue Error for a 20 Hz Mode Identified with 30 and 60 Hz Aliasing Frequency

A. Berman *

Kaman Aerospace Corporation
Bloomfield, Connecticut

Abstract

This paper discusses the general field of technology in which a linear mass, damping, and stiffness matrix model of a structure is identified using data obtained from dynamic tests of the structure. The data may be used alone or in conjunction with an approximate analytical model. It is shown that there are severe limitations on this process and that algebraically correct procedures may have no chance of achieving their goals. The topics discussed are: Relationships between a linear continuous structure (the test article) and a valid discrete analytical model (the objective of the procedure); relationships between the classes of parameters of the analytical model and those measured in a test and the effects of measurement uncertainties. The general conclusions are: there is no unique valid linear discrete model to be identified; a valid physically realistic model cannot be identified using test data alone; the identification of a limited set of specific physical parameters of a complex structure is not possible; the most promising approaches to obtaining valid useful models will use test data to minimally modify a realistic analytical model, subject to a set of physical constraints.

Nomenclature

C	damping matrix
f	force vector
i	$\sqrt{-1}$
Im	imaginary part of
K	stiffness matrix
M	mass matrix
m	order of equations of analytical model
Re	real part of
S	static influence coefficient matrix
s	order of equations of structure
X	displacement vector
Y, Y(ω)	displacement mobility matrix at frequency ω
Z, Z(ω)	impedance matrix at frequency ω
ϕ	normal mode vector
Ω	natural frequency
ω	frequency of steady state force

Superscripts

T	transpose of matrix
-1	inverse of matrix
.	time derivative

Subscripts

m	model degrees of freedom
s	structure degrees of freedom
1	partition of matrix containing model degrees of freedom
2	partition of matrix coupling 1, 4
4	partition of matrix containing non-modeled degrees of freedom
ω	frequency domain

*Assistant Director for Research, Member AIAA, AHS

Introduction

One of the most important sources of information for the design and analysis of aerospace structures are discrete linear dynamic analytical models of the structures. Good models can be used to predict responses to applied forces and the stability characteristics of the structure and are also necessary for the design of control system algorithms. In addition, the effects of various operational configurations may be predicted, as well as the effects of potential design changes and damage conditions.

Regardless of the care and the detail considered in the derivation of a dynamic model, it is generally accepted that one cannot have complete confidence in its predictions without a dynamic test of the structure to validate the analysis. Validation itself is a "yes", "no", or "maybe" process and is normally followed by intuitive improvement of the model based on an analysis of the discrepancies between the analytical predictions and the results of the test. This may be a costly and uncertain process and rarely results in completely satisfactory agreement between the two sets of data.

A more appealing approach is to use the test data to directly identify the necessary changes in the model. An alternate possibility is to use test data alone to determine a valid analytical model of the structure. Such a process would eliminate the need to develop an analysis and would also apply when an analysis is not available. Procedures of these types have become known as "structural system identification."

Numerous publications in recent years have addressed this area of technology. Surveys of the literature may be found in Refs. 1-4. A brief summary of selected relevant publications follows. In 1967, Rodden⁵ used measured modes to identify static influence coefficients. Berman and Flannelly⁶, 1971, used measured modes to improve an analytical mass matrix and to identify an "incomplete" stiffness matrix. In 1974, Collins, Hart, Hassleman, and Kennedy⁷, applied an iterative statistical procedure to improve estimated physical parameters. Baruch and Bar Itzhack⁸, 1978, modified measured modes based on an analytical mass matrix and developed a closed form solution for a corrected stiffness matrix. Chen and Garba⁹, 1980, and Grossman¹⁰, 1982, presented more efficient techniques for iteratively improving physical parameters. Berman, Wei, and Rao¹¹, 1980, and Berman and Nagy¹², 1983, improved mass and stiffness matrices for full models using measured modal data. During 1982, Leuridan, Brown, and Allemang¹³ used response data to estimate mass, damping, and stiffness matrices; Hart and Martinez¹⁴ applied

frequency response data and a form of iterated Kalman filtering to improve estimated parameters; and Baruch¹⁵ generalized the methods of Refs. 8, 11 to include several alternate procedures. Ibrahim¹⁶, 1983, obtained real normal modes based on measured complex modes and used these to identify mass, damping and stiffness matrices. In 1984, Fuh, Chen and Berman¹⁷ and Hanagud, Cheng, and Craig¹⁸ developed techniques to identify non-proportionally damped systems.

In 1982, Caughey¹⁹, states the following conclusion: "Modal testing (and indeed any other technique) cannot be used as a method for uniquely determining the mass, damping, and stiffness matrices of real aerospace structures, which are usually continuous in nature, and the modal testing thereby cannot provide a means for improving the analytical techniques for determining dynamics response." In a recent paper (Berman²⁰, 1984) an analyses of similar considerations was presented with similar conclusions.

System identification, however, does have important valid applications. It is the purpose of this present paper to examine the basis of structural system identification and to identify those classes of techniques which have a potential for success.

The Structure and the Model

The relationships between the actual equations of the real structure, which are and will remain unknown, and the equations of a realistic analytical model of the structure are important considerations in this study.

Structure Equations

The structure for which an analytical model is desired is the structure which is being tested. It is effectively a continuous structure which may be thought of as being analytically representable by a discrete model of order s where s approaches infinity. For the purposes of this analysis, the structure shall be assumed to be linear with non-proportional viscous damping and that it may be accurately represented by a very large order linear discrete model, as follows.

$$M_s \ddot{X}_s + C_s \dot{X}_s + K_s X_s = f_s \quad (1)$$

where M , C , K , X , f represent the symmetric mass, damping, stiffness matrices, the displacement and force vectors, and the subscript s refers to the large order model of the structure.

The frequency domain form of Eq.(1) is:

$$(K_s - \omega^2 M_s + i\omega C_s) X_{s\omega} = f_{s\omega} \quad (2)$$

where ω is the frequency of the forcing and the response, and $f_{s\omega}$ and $X_{s\omega}$ are the steady state complex force and displacement vectors.

Model Equations

The matrices representing the actual structure (M , C , K) are unknown. What is desired is a model of practical order, m , which is a good representation of the structure. This will be the order of the matrices resulting from a detailed finite element analysis. The m coordinates of the model are a subset of the coordinates of the structure.

Eq.(2) may be written as

$$Z_s(\omega) X_{s\omega} = f_{s\omega} \quad (3)$$

where $Z(\omega)$ is the displacement impedance of the structure at the frequency ω . For convenience, consider that the structure matrices are arranged so that the elements corresponding to the model elements are in the upper left. $Z_s(\omega)$ may be written in partitioned form

$$Z_s(\omega) = \begin{bmatrix} Z_1 & Z_2 \\ Z_2^T & Z_4 \end{bmatrix} \quad (4)$$

The mobility, $Y_s(\omega)$, represents the response of the structure per unit force. This may be written as

$$Y_s(\omega) = Z_s(\omega)^{-1} = \begin{bmatrix} Y_1 & Y_2 \\ Y_2^T & Y_4 \end{bmatrix} \quad (5)$$

Y_1 is the response per unit force of the coordinates of the model, and based on the inverse of the partitioned $Z_s(\omega)$ (Eq.(4))

$$Y_m(\omega) = Y_1 = (Z_1 - Z_2 Z_4^{-1} Z_2^T)^{-1} \quad (6)$$

By definition, a valid impedance of the model is the inverse of $Y_m(\omega)$ (see Ref. 21)

$$Z_m(\omega) = Y_m(\omega)^{-1} = Z_1 - Z_2 Z_4^{-1} Z_2^T \quad (7)$$

If it is assumed that the model may be represented in the same analytical form as the structure, then

$$Z_m(\omega) = K_m - \omega^2 M_m + i\omega C_m \quad (8)$$

Using the same partitioning notation as above, from Eqs.(7), (8)

$$\begin{aligned} K_m - \omega^2 M_m + i\omega C_m &= Z_1 - Z_2 Z_4^{-1} Z_2^T \\ &= (K_1 - \omega^2 M_1 + i\omega C_1) \\ &\quad - (K_2 - \omega^2 M_2 + i\omega C_2) (K_4 - \omega^2 M_4 + i\omega C_4)^{-1} (K_2^T - \omega^2 M_2^T + i\omega C_2^T) \end{aligned} \quad (9)$$

The model stiffness matrix may be obtained from Eq.(9) when $\omega = 0$,

$$K_m = K_1 - K_2 K_4^{-1} K_2^T \quad (10)$$

Then

$$M_m = M_1 - \frac{1}{\omega^2} K_2 K_4^{-1} K_2 + \frac{1}{\omega^2} \text{Re}(Z_2 Z_4^{-1} Z_2^T) \quad (11)$$

and

$$C_m = C_1 - \frac{1}{\omega} \text{Im}(Z_2 Z_4^{-1} Z_2^T) \quad (12)$$

For the special case of $C = 0$ and $M_2 = 0$, Eq.(11) becomes

$$M_m = M_1 + K_2 K_4^{-1} M_4 (I - \omega^2 K_4^{-1} M_4)^{-1} K_4^{-1} K_2^T \quad (13)$$

Note that Eq.(10) is that of Turner²² and Eq.(13) reduces to that of Guyan²³ when $\omega = 0$.

Interpretation of Relationships

It is apparent from Eq. 11, 12, 13 that a discrete model representation of a linear continuous structure (or a reduced model of a linear discrete structure) is nonlinear. A linearized version of the model can only be approximately valid over a limited range of frequencies.

While it has not been shown quantitatively, it is commonly accepted in practice that, at most, only the first half of the natural frequencies of the model correspond to those of the structure.

When one is attempting to identify an m^{th} order model based on test data taken at m points on the structure, less than $m/2$ of the modes of the structure are appropriate for this purpose.

Since less than the full set of measured modal data may be used there are an infinite number of models which will predict these results of the test.

Note that the above discussion specifically refers to measured modal data. Actually any measured dynamic response is a combination of modal responses and similar conclusions may be drawn for any type of dynamic measurements.

Numerical illustration of some of the phenomena described may be found in Ref. 20.

Quantitative Evaluation of Relationships

An approach to a quantitative assessment of the linearity of the reduction relationships may be based on a consideration of the nonlinear term in Eq.(13), $\omega^2 K_4^{-1} M_4$. If one imagines that the structure (test article) were constrained to ground at all the retained degrees of freedom (sensor locations), then K_4 and M_4 are the stiffness and mass matrix representing this condition. K_4^{-1} may be written in terms of the natural frequencies, Ω_i , and modes, ϕ_i , of this constrained structure:

$$K_4^{-1} = \sum_{i=1}^{s-m} \frac{1}{\Omega_i^2} \phi_i \phi_i^T \quad (14)$$

The relationship in Eq.(13) which produces the non linearity is then

$$(I - \omega^2 K_4^{-1} M_4)^{-1} = (I - \sum_{i=1}^{s-m} \frac{\omega}{\Omega_i} \phi_i \phi_i^T M_4)^{-1} \quad (15)$$

The linear model obtained by ignoring $\omega^2 K_4^{-1} M_4$ may be considered valid when the frequency, ω , is much less than (by some factor) the lowest natural frequency of the artificially constrained system previously described.

Physically modeling this condition is, of course, impossible in a test. However, given a reasonably valid analytical model of greater order than that to be identified, it may be possible to numerically estimate this limit. This may also be true for the more general case of Eqs.(11), (12).

Classes of Parameters

There are separate sets of parameters associated with analysis and with testing*. The differences in the characteristics of these sets of parameters have important influences on the practicality of system identification methods.

Intuitive Parameters

In the process of forming a discrete model of a structure, the analyst makes use of geometrical and physical characteristics of the material, such as mass and moduli of elasticity. Parameters of the model which are directly derived from this information are the mass, damping, stiffness matrices, and the impedance matrix. These are classified as "intuitive" parameters. The numerical values are specifically dependent on the particular set of coordinates selected as degrees of freedom of the model. Changing coordinates will cause changes in the numerical values of the parameters.

The intuitive parameters may be consistently computed to any degree of precision. They may be inaccurate because of imprecise data or inexact theoretical assumptions. It is the intuitive parameters which are desired to be identified in a structural system identification procedure.

Measurable Parameters

The parameters which may be directly obtained from test data include transient and steady state responses, mobility matrices, normal modes, and natural frequencies. These data, as distinguished from the intuitive parameters, are not dependent on any analytically defined set of degrees of freedom. Each numerical value depends only on the point of measurement and, if appropriate, the location of the exciting force.

Measurable data are considered to be accurate since they represent the actual behavior of the structure, however, they are

*Briefly discussed by Flannelly and Berman in Ref. 1 (p, 122) and also in Ref. 2.

imprecise because of the limitations on precision of measurement and in the extraction of data (such as mode shapes) from the raw test data. It is the measurable parameters which are used in system identification to identify intuitive parameters of the model.

Relationships Between Parameters

Intuitive parameters are inaccurate but precise and depend on the coordinates of the model. Measurable parameters are accurate but imprecise and are independent of the coordinates of the model. The transformation from one class to the other always involves a matrix inversion or the equivalent (solution of a differential equation or an eigenanalysis.)

Because of the precision of the intuitive parameters, matrices may be inverted or eigenanalyses may be performed to yield meaningful measurable type data. This computed data will contain inaccuracies due to the inaccuracies of the original model. If the intuitive model is reasonably accurate the computed measurable data will agree reasonably well with the actual measured data. (This is shown below.)

The converse to this conclusion, however, is not true. It is not possible to invert a measured matrix and have meaningful results (except possibly for trivially small models) because of the imprecision of the data, even though it may be accurate. There is a fine discussion of this point in Ref. 24. This conclusion may be specifically illustrated. Consider the static influence coefficient matrix (mobility at $\omega = 0$) and the possibility of inverting it to obtain the stiffness matrix. These matrices may be expressed in terms of the modes of the model, as follows. (See Ref. 6, for example.)

$$K = M \sum_{i=1}^m \Omega_i^2 \phi_i \phi_i^T \quad (16)$$

$$S = K^{-1} = \sum_{i=1}^m 1/\Omega_i^2 \phi_i \phi_i^T \quad (17)$$

where Ω_i , ϕ_i are the natural frequencies and mode shapes of the model and the modes are normalized so that $\phi_i^T M \phi_i = 1$.

It is observed that the dominant terms in K are the highest frequency modes of the model and the dominant terms in S are the lowest frequency modes. It is apparent that accurate measurement of the static influence coefficient matrix is possible since it mainly depends on the low frequency modes. It is also apparent that S cannot be measured with sufficient precision to include the necessary information (high frequency modes) to define the stiffness matrix. The effect of the high frequency modes in the S matrix decreases by Ω^2 .

It is important to note that, in practice a valid measured static influence coefficient matrix will likely invert numerically with no indications of ill-conditioning and may even result in a K

matrix which appears to be of reasonable magnitude. The reason is the pollution of the data with small random errors. It will be found that the inverse is extremely sensitive to small changes in the measured data.

Consider now the inversion of an analytical K matrix. Since K can be computed to any (within limits) level of precision, it can include the effects of all the modes of the model. Thus, it is possible to invert this matrix to obtain a meaningful static influence coefficient.

The above discussion, of course, applies equally well to the relationships between the more general case of measured mobility and analytically derived impedance matrices.

Additional Considerations

If S could be measured with sufficient precision to include the effects of the first m modes, there are other problems to consider. The modes in K (Eq.(16)) are the modes of the model, but the modes in the measured S matrix (Eq.(17)) are the modes of the structure. The measured S matrix would in fact include the effects of more than m modes. The question of the physical meaning of a precisely measured matrix is not resolved. This is a moot point at present, however, since there is no possibility of performing such measurements in the foreseeable future.

The possibility of synthesizing the K matrix from Eq.(16) by identifying the first m modes of the structure also fails because of the differences between the higher measured modes of the structure and the model modes of Eq.(16). The inability to define the shapes of the higher modes by the use of only m sensors adds to the uncertainty of such a procedure.

Another observation which affects this consideration is as follows. It is well known that an eigenanalysis of a detailed finite element model will yield many more modes in a given frequency range than will be identified in a test. If the first m measured modes were summed as in Eq.(16), the highest frequencies would be very much higher than Ω_m .

Discussion of Findings

The objective of structural system identification is to obtain an analytical model of a structure that is representative of the physical characteristics as well as the dynamic behavior and thus may be used to analyze conditions which were not tested. The sources of information are dynamic test data and possibly an approximate analytical model.

In the previous discussions, two sizes of models were considered, that of the structure (which must remain unknown) and the analytical model which has the same degrees of freedom as the coordinates measured in a test. No significant changes in the general conclusions result if the test points were in fact fewer than the degrees of freedom of the analytical model to be identified.

The findings of the previous sections may be summarized as follows:

- (1) The true discrete model representing the structure is nonlinear. A linearized version has a frequency range of applicability which is much less than the range of eigenfrequencies of the model.
- (2) Only the lower frequency modes of the structure contain information relevant to the linear model.

Since only a limited ("incomplete") set of test data is relevant, the following conclusions are made. ((2) logically follows from (1).)

- (1) There are an infinite number of analytical models which will duplicate the test results (within the limits of uncertainty.)
- (2) It is not possible to identify a physically realistic model directly from test data.

Comments on Specific Techniques

A number of techniques and variations have been suggested in the literature. The following comments on classes of these techniques are based on the conclusions of this analysis.

Use of Test Data Alone

Since an infinite number of models exist which are consistent with the data, as stated above, this approach cannot successfully identify a valid model without other information relevant to the structural parameters. The amount of information cannot be increased by taking more measurements since within a finite frequency range a limited number of parameters (e.g., modes and frequencies) determine all the dynamic characteristics. (More measurements may, however, be used to increase the precision.) Thus, measurement of forced responses (including velocities, accelerations, and displacements) at a large number of closely spaced frequencies will not circumvent this basic limitation.

Use of Test Data and Analysis

There are a number of variations on this general procedure which have been published. In general, this approach has possibilities since the information regarding the model (intuitive) parameters is also used. The approaches may be divided into two general classes, those which have a unique solution and those which have an infinite number of solutions. Consider these two groups separately.

Unique Solutions - A possible method could form a full set of modes by performing an eigenanalysis on the approximate analytical model and replacing an appropriate lower frequency set by measured modes. This procedure would then allow a unique solution that includes both physical and test data. An obvious advantage is that the stiffness matrix could remain nearly

equal to the analytical formulation since the dominant high frequency modes would not be changed. The mass matrix could be modified, as in some procedures, to make the complete set of modes orthogonal. Such a procedure, however, may not result in the set of modes satisfying the dynamic eigenequation, which must be a necessary condition. A procedure which includes this constraint is certainly worthy of further study.

One other consideration regarding methods of this type is that, of the infinite set of possible solutions, the analyst is arbitrarily choosing one by his selection of the full set of measured and analytical modes. Within the frequency range tested, there are analytical modes which are not identified in the test. Assuming that these remain invariant while the physical parameters are modified is unrealistic. However, since the undetected modes may be considered "minor", this effect may not be very important. Additional research is required to resolve this issue.

Another class of procedures involves a comparison of model and measured frequencies and/or modes and an iteration process to modify the model to yield the measured quantities within the limits of estimated errors. In these procedures a set of physical parameters are selected as unknowns and these are perturbed during the iteration process. An advantage of these procedures is that the resulting model matrices will exactly represent a physical structure. A disadvantage is that the resulting parameters may have no relation to the actual parameters of the structure. This is due to the usual selection of a relatively small set of specific parameters. Another set of parameters may result in a physical representation of a quite different structure. For a set of parameters greater than the number required for a unique solution, their variations will depend on the sensitivity of the eigensolutions to their values and the solution may also have no relation to their true physical values. The necessity of a one-to-one pairing of the numerous analytical modes and the measured modes also introduces uncertainty.

The last mentioned methods for large models often will be quite expensive to execute and there are often convergence difficulties. Since there are an infinite number of physically realistic solutions possible, the arbitrary forcing of a specific solution does not appear to be a valid approach. An extension of this method to include all or many physical parameters and minimizing the changes may be theoretically sound but most likely prohibitively expensive.

Non-Unique Solutions - There are a class of procedures which find minimum changes in the matrix elements to make them consistent with the test data. A disadvantage is that the resulting matrices may not be representative of a physical structure and may imply coupling which does not physically exist. Extension of such methods to contain a comprehensive set of constraint conditions to satisfy physical reality would be

desirable if practically possible. If, upon the application of such a method, the changes in the matrix elements were within the expected ranges of uncertainty, the model may be expected to be a valid dynamic and physical representation of the structure. This condition implies a reasonably good analytical model and accurate test data. These methods appear to offer the best chance for success.

Correction of Modeling Errors

From the above discussion, it is apparent that a single realistic solution is not possible. This implies that system identification cannot be used to identify particular errors since the errors will be compensated for by an equivalent distribution of minimum changes depending on the specific algorithm used.

It follows that system identification cannot be used as a tool to improve analytical modeling techniques or to detect topographical errors.

Summary

The field of structural system identification is very important and has great potential but it has certain rather stringent limitations.

It has been shown that structural system identification must be a non-unique process.

Methods which attempt to identify a physically realistic model from test data alone are not possible.

Methods which force a unique solution are arbitrary and there is no rationale for expecting the particular solution to be physically meaningful or even useful.

The most promising methods select a solution which minimizes changes in a reasonably good analytical model. These methods should include constraints to force physical reality of the solution.

Structural identification cannot be used to identify modeling errors or as an educational tool to improve modeling techniques.

References

1. Pilkey, W. D., and Cohen, R., (Eds.), System Identification of Vibrating Structures, ASME, New York, N.Y., 1972
2. Berman, A., "Determining Structural Parameters from Dynamic Testing", Shock and Vibration Digest, Volume 7, No. 1, January, 1975
3. Berman, A., "Parameter Identification Techniques for Vibrating Structures", Shock & Vibration Digest, Volume 11, No. 1, January, 1979
4. Ibanez, P., "Review of Analytical and Experimental Techniques for Improving Structural Dynamic Models", Welding Research Council, Bulletin 249, New York, N.Y., June, 1979

References (continued)

5. Rodden, W. P., "A Method for Deriving Structural Influence Coefficients from Ground Vibration Tests", AIAA Journal, Vol. 5, No. 8, May, 1967, pp. 991-1000
6. Berman, A., Flannelly, W. G., "Theory of Incomplete Models of Dynamic Structures", AIAA Journal, Vol. 9, No. 8, August, 1971, pp. 1481-1487
7. Collins, J. D., Hart, G. C., Hassleman, T. K., and Kennedy, B., "Statistical Identification of Structures", AIAA Journal, Vol. 12, 1974, pp. 185-190
8. Baruch, M., Bar Itzhack, I. Y., "Optimal Weighted Orthogonalization of Measured Modes", AIAA Journal, Vol. 16, 1978, pp. 346-351
9. Chen, J. C., and Garba, J. A., "Analytical Model Improvement Using Modal Test Results" AIAA Journal, Vol. 18, 1980, pp. 684-690
10. Grossman, D. T., "An Automated Technique for Improving Modal Test/Analysis Correlation", AIAA SDM Conference, Paper 82-0640, 1982
11. Berman, A., Wei, F. S., Rao, K. V., "Improvement of Analytical Dynamic Models Using Modal Test Data", AIAA SDM Conference, Paper 80-0800, 1980
12. Berman, A., Nagy, E. J., "Improvement of a Large Analytical Model Using Test Data", AIAA Journal, Vol. 21, 1983, pp. 1168-1173
13. Leuridan, J. M., Brown, D. L., Allemang, R. J., "Direct System Parameter Identification of Mechanical Structures with Application to Modal Analysis", AIAA SDM Conference, Paper 82-0767, 1982
14. Hart, G. C., and Martinez, D. R., "Improving Analytical Dynamic Models Using Frequency Response Data - Application", AIAA SDM Conference, Paper 82-0637, 1982
15. Baruch, M., "Methods of Reference Basis for Identification of Linear Dynamic Structures", AIAA SDM Conference, Paper 82-0769, 1982
16. Ibrahim, S. R., "Dynamic Modeling of Structures from Measured Complex Modes", AIAA Journal, Vol. 21, 1983, pp. 898-901
17. Fuh, J., Chen, S., and Berman, A., "System Identification of Analytical Models of Damped Structures", AIAA Structures, Structural Dynamics and Materials Conference, Paper 84-0926, Palm Springs, California, 1984

References (continued)

18. Hanagud, S., Cheng, Y. P., and Craig, J. I., "Identification of Structural Dynamic Systems with Nonproportional Damping", AIAA Structures, Structural Dynamics and Materials Conference, Paper 84-993, Palm Springs, California, 1984
19. Caughey, T. K., "Structural Dynamics Analysis Testing and Correlations", JPL Publication 81-72, Jet Propulsion Laboratory, Pasadena, California, May 1, 1982
20. Berman, A., "Limitations on the Identification of Discrete Structural Dynamic Models", Second International Conference on Recent Advances in Structural Dynamics, Southampton, England, April, 1984
21. Berman, A., "Vibration Analysis of Structural Systems Using Virtual Substructures", The Shock and Vibration Bulletin, No. 43, June, 1973
22. Turner, J. J., Clough, R. W., Martin, H. C., and Topp, L. J., "Stiffness and Deflection Analysis of Complex Structures", Journal of the Aeronautical Sciences, Vol. 23, 1956, pp. 805-823
23. Guyan, R.J., "Reduction of Stiffness and Mass Matrices", AIAA Journal, Vol. 2, 1965, p. 380
24. Rosanoff, R. A., "A Survey of Modern Nonsense as Applied to Matrix Computations", AIAA Structural Dynamics and Aeroelasticity Specialist Conference, New Orleans, Louisiana, April 16-17, 1969.

IDENTIFICATION OF STRUCTURAL PROPERTIES OF A CONTINUOUS LONGERON SPACE MAST

Y. Soucy* and F.R. Vigneron**
Communications Research Centre
Department of Communications, Ottawa, Canada

Abstract

This paper describes test and modal parameter identification results for a deployable coilable continuous longeron space mast of a type planned for several space missions. Four different types of tests were needed to obtain good results over the range of natural frequencies 0-60 Hz. Modal damping factors were in the range 0.02-0.09 and were essentially the same in air and vacuum.

Experimental frequencies are compared to results generated by an equivalent continuum beam model and a finite element model. The models correlate with test data for lower frequency modes, but fall short for higher modes.

Introduction

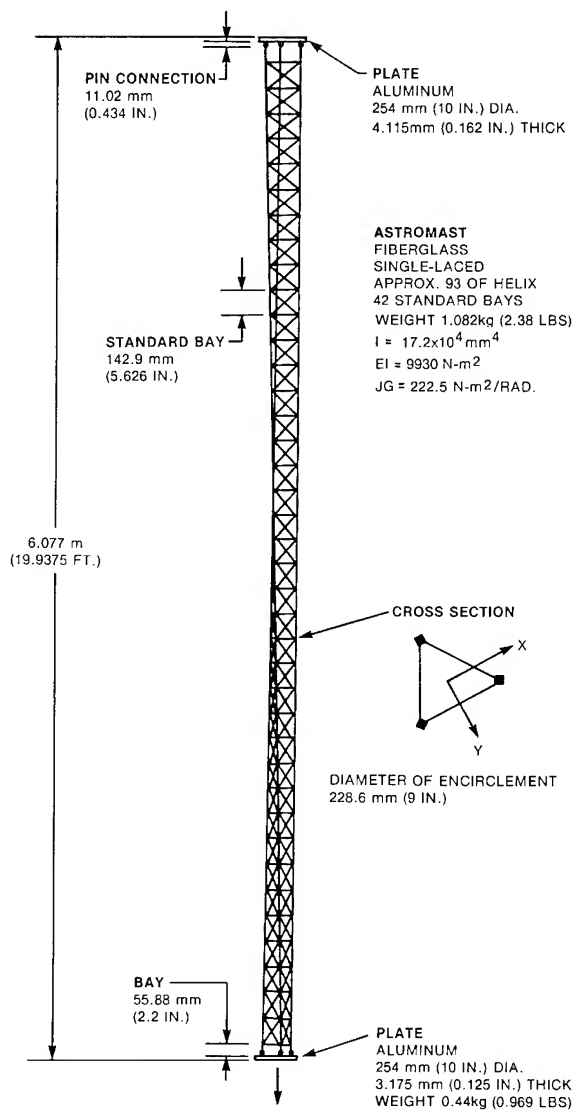
A number of space projects during the coming decade will use large light-weight deployable lattice-type structures as masts, beams, or trusses, for antennas, solar arrays, and other structures. This type of structure is not yet in wide use, and consequently there is little published information or experience with actual hardware. The intent of this paper is to describe test and modeling experience for a representative structure of this type with particular attention to the test techniques that were found to be useful, the degree to which test-derived results correlated with analytical modeling, and the measured modal damping factors.

The structure of this paper is a deployable, coilable, continuous longeron mast, manufactured by Astro Research Corporation under the trade name Astromast and depicted in Fig. 1. Astromasts of this type are part of the European LSAT satellite to be launched in 1987, and are part of the baseline design of the Canadian MSAT and RADARSAT satellites.

Description of the Structure

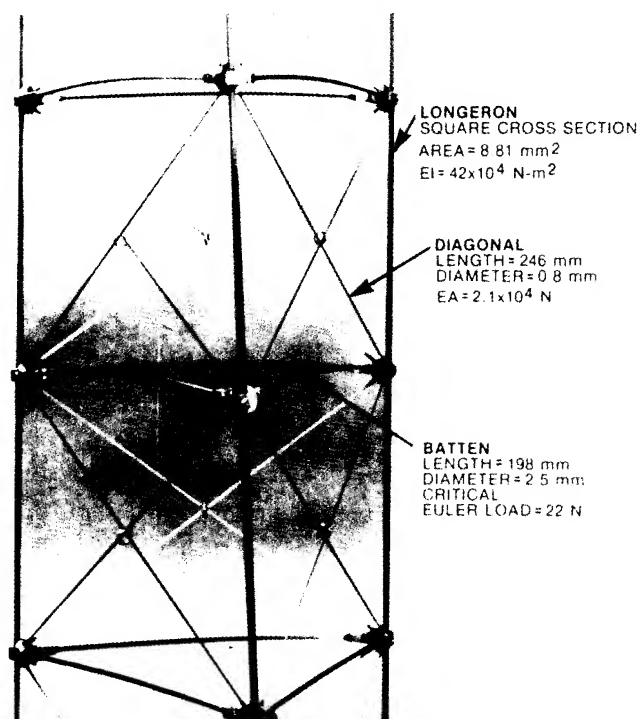
The Astromast is a continuous longeron structure made of fiberglass (Fig. 1). It is about 608 cm long and 229 mm diameter. It is composed of 42

storeys or bays and has a helical rotation of 93° from one end to the other for reduction of in-space solar-induced thermal deformation. The post-buckled state of the battens creates the rigidity of the structure by producing compression in the longerons and tension in the diagonals (Fig. 2). The structure has a high stiffness to weight ratio. Reference 1 contains additional parametric information for this design of mast.



1. Astromast in fully deployed configuration

* Engineer, Structural Dynamics
** Research Scientist, Member AIAA



2. Photograph of the Astromast. The structure is maintained in tension by the diagonals, and the battens are in the post-buckled state.

Analytical Modal Characteristics

Modeling with both finite element and simple continuum methods was done. The results were used initially as a guide for planning the experimental tests. After the tests, experimental and theoretical results were compared.

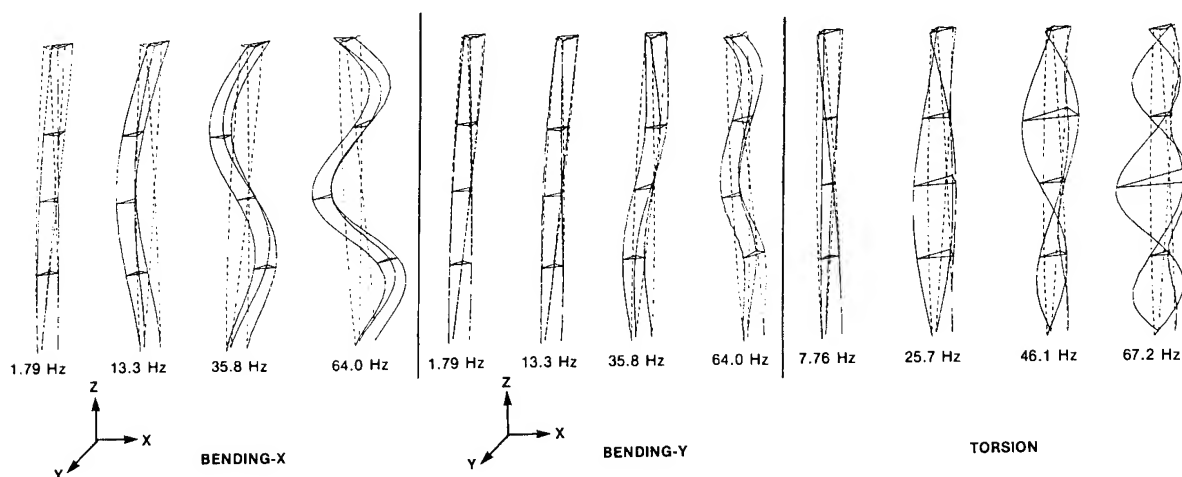
Finite Element Modeling

A computer program based on finite element analysis was developed to

calculate fixed-base (cantilever) natural frequencies and mode shapes². The model assumes that the longerons and diagonals are axial tension/compression members which remain in their linear elastic range. The bending and twist energy of the longerons is neglected. It is further assumed that the battens always maintain their post-buckled state and thus exert the constant tension force at the connectors (joints). The effects of damping and gravity are neglected. The mass and inertia of one end plate are included in the modelling, as is consistent with the fixed-end cantilever configuration. The mass is modelled by concentrated masses located at the joints. The finite element program accounts for 3 degrees of freedom (DOF) per joint in the X, Y and Z directions respectively, or 9 DOF for each bay. With 42 bays, the mast is represented by 378 degrees of freedom. The stiffness matrix is an 378 X 378 square banded matrix with half-band width of 18. To reduce memory requirements, the program replaces the stiffness matrix by a rectangular one with dimensions 378 X 18.

Figure 3 depicts the natural frequencies and mode shapes of the first twelve modes. In the figure, the triangles represent levels at which accelerometers were placed in tests described later. The input values for the axial stiffnesses of the longeron and diagonal elements were experimentally derived. The modes may be classified into three categories: transverse bending - X direction, transverse bending - Y direction, and torsion.

The bending modes are the same in the X and Y directions, and this is explained from simple strength-of-materials beam theory by the fact that, for any cross-section of the mast, the moment of inertia is the same in all



3. Mode Shapes and Frequencies from Finite Element Program

directions. The first five modes appear to be either pure bending or pure torsion. The third and higher bending modes have, with different intensity, some coupling with torsion; as is evidenced by a change in shape of the top triangle. The second and higher torsion modes exhibit a "breathing" characteristic: i.e., the post-buckled battens admit small axial displacements, which result in an extension of the length of the sides of the triangles.

The continuous longerons are modeled by pinned-end axial elements at each bay, with no elemental bending resistance accounted for. This approaches continuum modeling for beams, and achieves a large reduction in DOF by contrast with modeling using bending elements. As a result of the pinned-end assumption, the program calculates certain extraneous modes with discontinuities in slope of the longerons³.

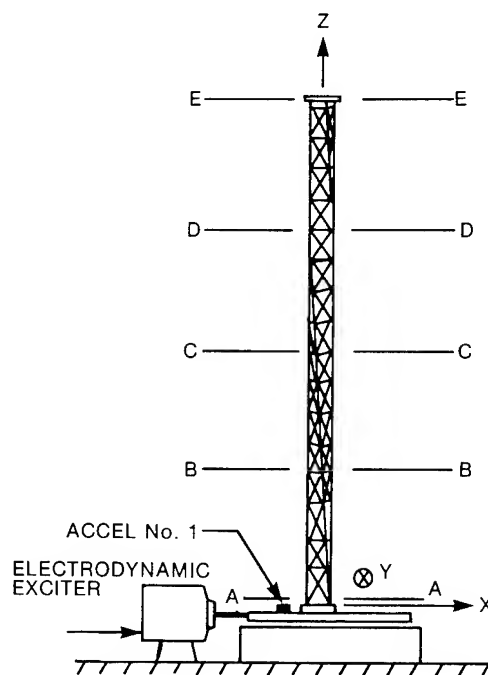
Continuum Modeling

A simple model of the mast as a slender uniform cantilevered beam with a tip mass and bending and twist properties was developed. The effect of earth's gravity in test configuration was included. Damping was not considered. The effective bending modulus (EI) and stiffness modulus (JG) for the model were obtained by static load vs deflection tests on the structure in a configuration where the mast was suspended vertically and fixed at the top end.

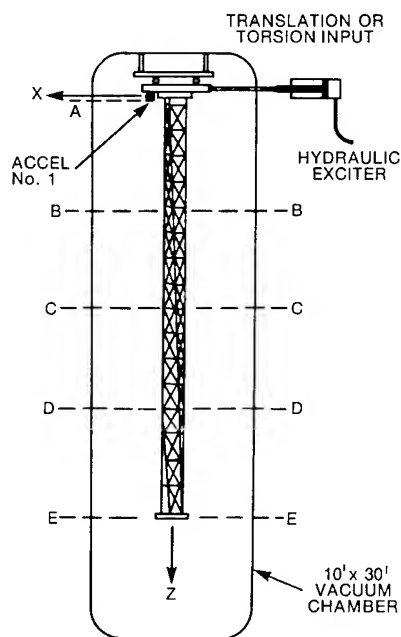
Sensitivity analysis was performed with this model. For example a change of 10% in bending stiffness results in a change of about 5% in the first three bending frequencies. A 10% variation in mast density changes the third mode by 5%. An increase of 10% in tip mass decreases the first mode frequency by 3%.

Structural Dynamics Tests

Four different test configurations were found to be needed to obtain sound experimental parameters over the frequency range of interest. (1) Tests in air with unidirectional translational input at the base of the structure with an electrodynamic exciter (Fig. 4) provided results for the frequency range 5-60 Hz. (2) Tests were done in vacuum and in air with a hydraulic exciter over the frequency range 1-30 Hz (Fig. 5), to observe the effect of aerodynamic forces on the measured damping factors. (3) Step relaxation tests were done to obtain parameters in the low frequency range, 0 to 10 Hz. (4) An impact test was done to confirm a torsion mode at about 30 Hz.



4. Configuration for uni-directional base excitation in air. Six accelerometer locations at each of the levels B to E.

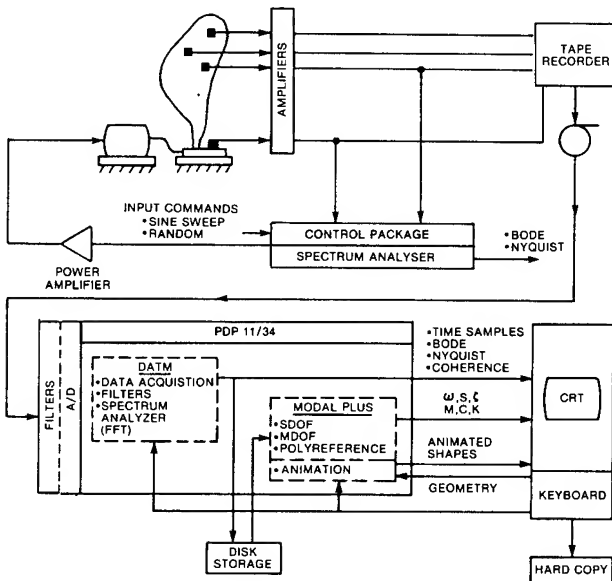


5. Configuration for base excitation in vacuum. Six accelerometer locations at each of levels B to E.

The effect of gravitational forces on the mast under test may be ignored. Calculations with the continuum model show that gravitational loads decrease the effective stiffness of the mast in

the configuration of Fig. 4 and cause a decrease in the fundamental natural frequency of less than 1%. The gravitational loads increase the fundamental frequency in the configuration of Fig. 5 by 1%.

For each of the four test configurations, the data acquisition and modal parameter identification software obtained from the Structural Dynamics Research Corporation was used. A Gen Rad 2503 system was employed. The flow of data handling and processing is depicted schematically in Fig. 6 for a typical test configuration. The basic input and response data are created in a particular test and stored on analog tape. The data are then acquired in digital form using the DATM software. Frequency response and coherence functions are also calculated using digital Fast Fourier Transform techniques and displayed in an interactive mode for data prescreening and verification. Modal parameters are then extracted from the frequency response information using the MODAL-PLUS software.



6. Data flow and processing stages.

MODAL-PLUS contains routines for identification of the modal parameters (natural frequencies, damping coefficients, mode shapes, modal mass, and related parameters) by analysis of the frequency response functions. The routines are based on the underlying assumption that the system to be identified can be represented by a linear modal model of the form

$$\frac{\bar{x}_j(\omega)}{\bar{f}_k(\omega)} = \bar{H}_{jk}(\omega; \omega_r, \zeta_r, \alpha_r, \psi_{jr}), \quad (1)$$

where

$$\bar{H}_{jk} = \sum_{r=1}^n \frac{\psi_{jr} \psi_{kr}}{\alpha_r (i\omega + \zeta_r \omega_r - i\omega_r \sqrt{1 - \zeta_r^2})} + \frac{\psi_{jr}^* \psi_{kr}^*}{\alpha_r^* (i\omega + \zeta_r \omega_r + i\omega_r \sqrt{1 - \zeta_r^2})} \quad (2)$$

In the above, the f_k are input forces and x_j are response states at discrete points on the structure. The f_k and x_j are both required to correspond directly to measureable quantities (the software can accept measurements of x , \dot{x} , or \ddot{x}). $\bar{H}_{jk}(\omega)$ is the Fourier transform of the unit impulse response function (i.e., the response at location j , to a single unit impulse at location k). The $\{\omega_r, \zeta_r, \alpha_r, \psi_{jr}\}$ and the order, n , are the modal parameters to be identified.

Measurements of f_k and x_j are acquired in the tests. Then, an experimental $\bar{H}_{jk}(\omega)$ (in element, column, or full matrix form as appropriate to a particular exercise) is constructed from the measurements using Eq (1). Then, using one or more of the routines of MODAL-PLUS, the parameters ($\omega_r, \zeta_r, \psi_{jr}$) that result in a curve fit of the analytical H_{jk} of Equation (2) to the measurement-based H_{jk} are found; the parameters are the identified modal parameters.

MODAL-PLUS has routines for classical single-degree-of-freedom (SDOF) curve fits equivalent to the Kennedy-Pancu technique. The technique is limited to single-force-input tests. The SDOF routine derives modal frequency and damping ratio from a curve fit of a single scalar element of H represented in the frequency domain, and requires that the modal frequencies be separately spaced. Mode shapes are constructed from the maximum amplitudes of a column of $\bar{H}(\omega)$ at a value of ω equal to the modal frequencies.

The Polyreference routine of MODAL-PLUS is based on the complex exponentials technique. The measurement-based matrix, $\bar{H}(\omega)$, is first converted to the time domain by the inverse Fast Fourier Transform. Then a time domain equivalent of Eq. (2) is fit to the time domain samples of the measurement-based matrix, H using a Prony-type algorithm and least squares⁴.

A Multiple-Degree-Of-Freedom (MDOF) curve fit technique of Version 6 is

essentially the Polyreference Method, applied to single force input data (i.e., a curve fit of a single column of the H matrix by the complex exponentials method).

All vibrational measurements were made with ENDEVCO piezoresistive accelerometers (Series 7265), having ranges of either 10 or 20 g in tension and compression, and a response range of 0 to 300 Hz. The weight per accelerometer was 6 g plus 9.2 g/m for cables.

Tests in Air with Input at the Base - Electrodynamic Exciter

A number of exploratory and major dynamic tests were done with the Astromast base mounted (fixed-free) to a 178 kN electrodynamic exciter as depicted in Fig. 4. The lower frequency limit of the exciter was about 5 Hz. The upper limit was set at 100 Hz, this being a reasonable limit of interest for the structure. The second and higher bending modes were expected to be identifiable with this exciter.

The exciter was operated under digital control to input the desired excitation waveform at the base of the structure. The accelerations corresponding to base input and the mast structural deformations were measured with accelerometers.

Figures 4 and 7 show the accelerometer locations and directions. A total of 12 response locations were chosen. Two accelerometers at each location were

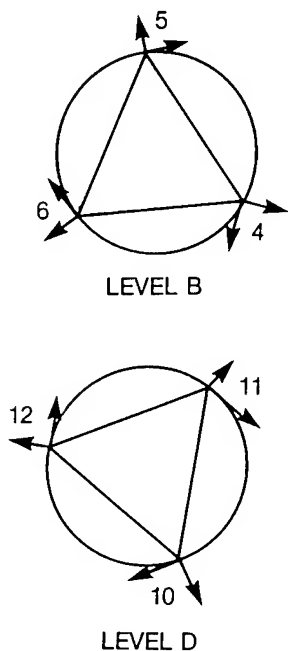
used to measure radial and tangential motions. No accelerometers were pointed in the z direction since a preliminary test showed the vertical accelerations to be negligible. The input was measured with an accelerometer fixed on the base plate and pointing in the direction of excitation.

Two types of base input signals were used, swept sine and random. Exciter control was implemented with either an HP 5427A system or the Gen Rad 2503 system, depending on availability.

For operation of MODAL-PLUS (parameter estimation), the frequency response functions are obtained (with DATM) with the base acceleration as the input, and the astromast mounted accelerometers as the output channels. However, it should be noted that the mathematical model of the configuration (i.e. excitation at the base of the structure, base acceleration as measured input, and mast accelerations as measured outputs) is slightly different than the model upon which the MODAL-PLUS software is based (Eqs. 1 and 2). The differences are discussed in Ref. 5. The modal frequencies and damping factors deduced from the frequency response functions are shown to correspond to "fixed-base" mode shapes. However, the mode shapes and modal coefficients given by MODAL-PLUS are not rigorously correct. MODAL-PLUS has been used directly herein, with an awareness of these factors.

Added Mass, Stiffness, and Damping Contributed by Accelerometers. Due to the structure being very light, it was necessary to explore experimentally, the level of stiffness mass, and damping contributed by the accelerometers and their cables.

To observe the effect of the cables, a sine sweep was performed from 5 to 100 Hz at 0.2 g peak acceleration level, for three different conditions: (1) 6 accelerometers at level E (Figure 7); (2) 2 accelerometers at level E for radial and tangential directions; and (3) 1 accelerometer at level E, either radial or tangential. For conditions (2) and (3), the accelerometers taken off were replaced by dummy masses having the same weight as the accelerometers and part of their cables, so that any modification of the responses would be caused only by the presence of the cables. The conclusion was that the response for the three cases was essentially the same for frequency up to 30 Hz for swept sine; but beyond, there were unacceptable differences. Similar tests were done for random excitation. No difference appeared in the frequency response functions for frequencies up to 60 Hz. Above that frequency, the energy dissipation in the structure was too



7. Examples of accelerometer locations of the test configurations (Figs 4 and 5). Directions are radial and tangential.

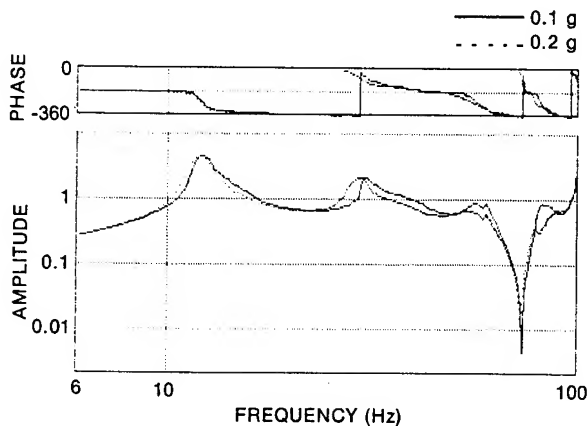
high and thus the signals were too noisy.

To observe the effect of added masses, runs with one, three, and six accelerometers at a level were done, and responses compared. Frequency and amplitude shifts of up to 1.5% and 10% respectively were observed for various modes.

On the basis of the above types of experimental tests, it was concluded that the use of three accelerometers simultaneously on the structure could be permitted for random input.

Non-Linearity of the Astromast. The main sources of non-linearity are: free play in some connections between longeron and battens; buckling of battens which causes local changes in the sectional inertia (and thus in the effective EI); local buckling associated with compression in the longeron in the region close to the fixed end (for high stress levels). Several experimental exercises were conducted to determine the magnitude and influence of these non-linearities on the dynamics of the structure.

Sine sweep runs were performed at 0.1, 0.2, 0.3 and 0.4 g levels to determine the amount of non-linearity. Figure 8 shows an example comparison of magnitude and phase of a frequency response function for 0.1 and 0.2 g inputs. There is a definite small change. The non-linearity effect stabilizes between 0.2 and 0.4 g for frequencies lower than 30 Hz.

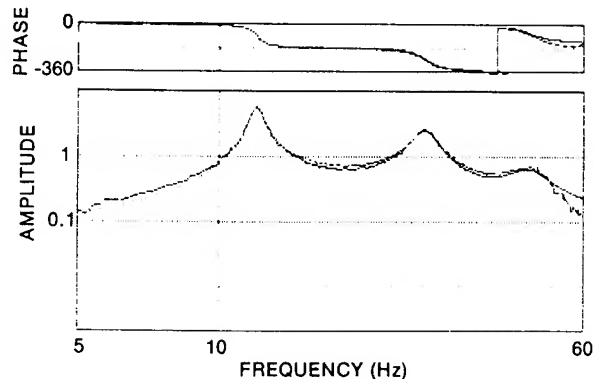


8. Example of non-linearity. Two sine sweep with input amplitudes of 0.1 g and 0.2 g.

Random vibration was input at the two different levels, 2 and 3 g rms (0-100 Hz). Frequency response functions were identical for frequencies below 60 Hz, meaning that the results contained no non-linearity distortion.

The invariance to different random input levels was not unexpected, since it is known that random input tends to eliminate, through averaging, any non-linearity.

Parameter Determinations. A complete set of response functions were acquired with random base excitation, 2.0 g Rms (0-100 Hz) over an effective range of 5 to 60 Hz. The responses were acquired in eight successive runs, with three accelerometers per level for each run. A sample frequency response function that illustrates the quality of the data is given in Fig. 9. A curve fit mode using the MDOF routine is also shown in Fig. 9. Reasonable curve fits covering three resonances over the range 5 to 60 Hz were possible from the random data.



9. Example of frequency response function obtained with random base excitation (solid), and curve fit with the MDOF (single input complex exponential) routine of MODAL-PLUS (dotted).

A complete set of response functions were also acquired with swept sine base excitation, 0.2 g over 5 to 100 Hz. The responses were acquired in four successive runs with six accelerometers at each level per run. This data did not submit to curve-fitting as well as the random data due to previously discussed accelerometer effects. These effects plus the non-linearity of the structure rendered the data above 30 Hz questionable.

The modal frequencies and damping factors estimated using the MDOF routine and the above data are summarized in Table 1. Mode shapes were also determined in tabular and graphic animation form.

Tests in Air and Vacuum with Input at the Base - Hydraulic Exciter

The configuration of Fig. 5 was used to test the mast in air and vacuum. The hydraulic exciter was capable of being configured to provide unidirectional translation, or torsion, over the range 1 to 30 Hz.

In this test configuration, the base acceleration is used as the input measurement, and thus the remarks of the previous section concerning the limitations of MODAL-PLUS processing apply also.

The main data was acquired with swept sine input. The data clearly showed the first and second bending frequencies at 1.9 and 11.9 Hz and the first torsion at 10.3 Hz. The shape of the peak of the first mode was not confidently established because of low signal to noise ratio in the input and high non-linear effect due to excessive compression in part of the longeron; thus, the estimates of the damping factor are of low confidence. Except for a few of the frequency response functions, curve fits with MDOF were of poor quality. The SDOF routine provided acceptable curve fits in most cases for the second frequency.

There was no significant difference in frequency response functions between tests in air and tests in vacuum, thus establishing that aerodynamic effects are negligible for this type of astromast.

The modal frequencies and damping factors determined from the tests with the hydraulic base exciter are given in Table 1.

The Step Relaxation Method

The previously-described tests did not obtain parameters satisfactorily for frequencies below about 2 Hz due to the contribution of input noise to the very small accelerometer signals and the lack of control of the exciter at low amplitude inputs. To obtain the low frequency parameters, the Step Relaxation described herein was implemented.

For Step Relaxation, the input excitation is achieved by initially applying a single force to deform the structure statically and then releasing the force suddenly. The force and the response accelerations at a number of points are measured before, during, and after release as the structure vibrates freely and damps to a motionless state.

The equations that model the configuration are not directly in the form of Eqs (1) and (2). However with appropriate mathematical manipulation it can be proved rigorously that

$$\frac{\ddot{a}_i(\omega)}{f_j(\omega)} = \bar{H}_{ij}(\omega; \omega_r, \zeta_r, \alpha_r, \psi_{ir}) \quad (3)$$

Table 1(a) Measured frequencies (Hz) for Astromast

Mode	Base Excitation Electrodynamic	Base Excitation Hydraulic	Step Relaxation	Impact
1st Bending-X		1.94	1.81	
1st Bending-Y			1.88	
2nd Bending-X or Y	11.9	11.9		
3rd Bending-X or Y	27.6			
4th Bending-X or Y	45.9			
1st Torsion		10.3		10.9
2nd Torsion				33.7

Table 1(b) Measured damping factors for Astromast

Mode	Base Excitation Electrodynamic	Base Excitation Hydraulic	Step Relaxation	Impact
1st Bending-X		0.035	0.020	
1st Bending-Y			0.032	
2nd Bending-X or Y	0.031	0.032		
3rd Bending-X or Y	0.058			
4th Bending-X or Y	0.085			
1st Torsion		0.012		0.013
2nd Torsion				0.024

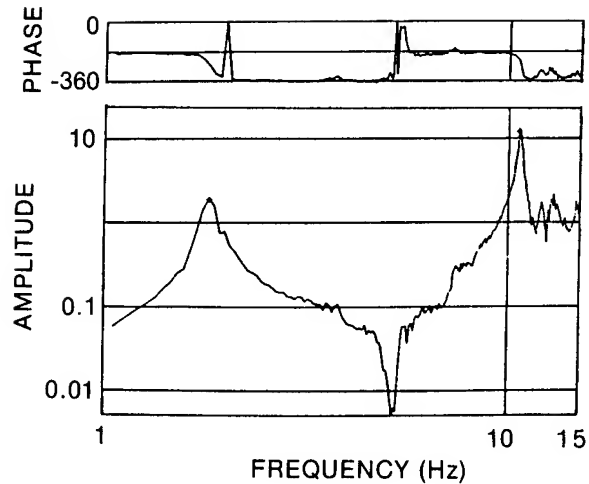
Hence a measurement-based frequency response function can be constructed from the Fourier transforms of the derivatives of the accelerometers and force measurements. The various curve fit routines of MODAL-PLUS can then be used to fit the analytical \bar{H} of Equation (2) to the measurement-derived \bar{H} , and so identify the parameters.

Appropriate software was developed by Dr. Gordon Mutch of SDRC in collaboration with the authors for this exercise⁶. A force, f_1 , is applied and released. The $f_1(t)$ and response at j locations, $a_j(t)$, are acquired and digitized. They are then differentiated using a simple difference algorithm, to obtain $\dot{f}_1(t)$ and $\dot{a}_j(t)$. The Fast Fourier Transform routines then obtain $\dot{f}_1(\omega)$ and $\dot{a}_j(\omega)$, and from Eq. (3), $\bar{H}_{1j}(\omega)$. f_1 may be reapplied several times, the acquisition/preprocessing repeated, and the resulting multiple samples of $\bar{H}_{1j}(\omega)$ averaged. With reconfiguration of the experimental set-up, other single forces, f_k , can be applied sequentially, and the preprocessing repeated to obtain additional columns, $\bar{H}_{kj}(\omega)$. At this stage the graphs of elements of the matrix can be screened visually, and reciprocity can be checked. The Polyreference software of MODAL-PLUS is then invoked; i.e. the $\bar{H}(\omega)$ matrix is then converted to the time domain, $H(t)$, and the complex exponentials technique is used to identify the modal parameters.

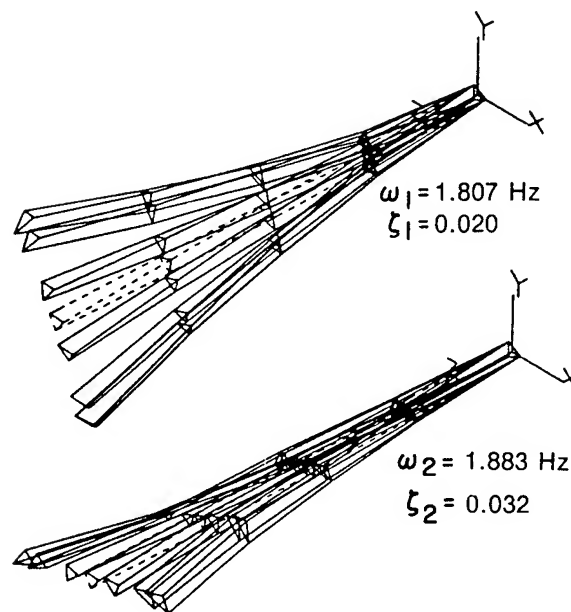
An apparatus for release of the load using a solenoid-activated release mechanism was designed for test of the mast. Two configurations of force were set up to deform the structure in a manner that excited the transverse X and Y deformations and torsion.

Response accelerometers were mounted at the locations depicted in Figs. 4 and 7. The accelerometers were limited to two per test run in order to avoid cable and mass loading effects.

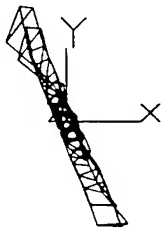
Figure 10 shows the frequency response function for the driving point 11y. This example illustrate the quality of data obtained by Step Relaxation. The first bending mode in the X and Y directions were jointly identified successfully, and are depicted in Figure 11. The results demonstrate the ability of the complex exponentials technique to separate two very closely-spaced modes. The damping factors are noted to be different, and the two modes are seen to be orthogonal to each other (Fig. 12).



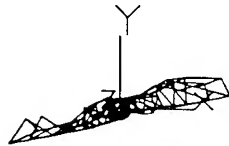
10. Example of frequency response function obtained with step relaxation. The response was at the driving point 11y.



11. Successive frames of an animation of the first two modes that were derived from step relaxation data by the Polyreference routine.



$\omega_1 = 1.807 \text{ Hz}$



$\omega_2 = 1.883 \text{ Hz}$

12. End view of the modes of Fig. 11. The graphs demonstrate orthogonality of the transverse bending modes.

Impact Tests in Torsion

Tests using an impact force hammer were performed mainly to confirm the first and second torsion modes. The Astromast was hung with the top end plate fixed. The lower end of the mast was attached to a fixture which allowed torsion, but had no degree of freedom in translation.

A PCB impact hammer with a quartz force transducer was used to impart the force. A rubber tip, chosen to keep the input energy in the low frequency range, caused the input spectrum to roll off at about 100 Hz. This configuration of test is modelable directly with Eq (1), and is within the scope of operation of MODAL-PLUS.

The test was performed by mounting a limited number of accelerometers in the tangential directions and hitting the structure in the tangential directions at many locations. Five samples were taken and averaged at each input location.

In general, the quality of the data was poor relative to that of other tests. The main cause was the high degree of flexibility which provoked impedance mismatch problems. The experimental curves could not be fit well with the MODAL-PLUS algorithms, with the exception of a few frequency response functions. The data yielded conclusive torsional frequencies, and somewhat less confident damping factors.

Table 1 presents the parameters derived from the tests.

Comparison of Theoretical and Measured Modal Data

Finite Element Model

Table 2 gives the comparison of measured to calculated frequencies with the finite element model described earlier (the experimental values in Tables 1 and 2 are regarded as correct and not in question). The input masses

were determined by carefully conducted weighings of the individual components and the total structure. The modulus of elasticity of the longeron and diagonal elements were determined by lab tests of samples. No attempt has been made to adjust parameter values to optimize the correlation in Table 2.

The general character and shape of the theoretical and experimental modes were in agreement as determined by visual comparisons of plots.

However Table 2 shows that the FEM model has some shortcomings as regards quantitative agreement. The shortcomings are under further study. They are possibly due to the ignoring of unit longitudinal flexural and or torsional energy.

Continuum Model Comparison

Table 2 gives the comparison of measured to calculated frequencies for the continuum model described earlier. The general character and shape of the theoretical and experimental modes were in agreement. The input values of EI and JG were determined in static tests. No attempt has been made in Table 2 to optimize results by parameter value adjustments. The model calculates the first two torsional and first bending frequencies well. Higher modes are substantially in error, which indicates that simple continuum modeling is an oversimplification as regards the higher modes of the Astromast.

Table 2 Comparison of Experimental and Theoretical Frequencies.

Mode	Exp (Hz)	Finite Freq (Hz)	Element % Error	Continuum Freq (Hz)	% Error
1st Bending	1.85	1.79	- 3	2.16	+16
2nd Bending	11.9	13.3	+12	17.4	+46
3rd Bending	27.6	35.8	+30	52.9	+92
4th Bending	45.9	64.0	+39	---	---
1st Torsion	10.3	7.76	-25	12.2	+18
2nd Torsion	33.7	25.7	-24	41.6	+23

Conclusions

The measured structural characteristics, in particular the damping factors and observations on non-linearities, are representative of this type of space mast, and should be useful in the design of dynamics and control of spacecraft that employ this type of component.

Four different types of tests were needed to obtain good quality modal parameter values. For the lower modes, the Step Relaxation technique worked

well, mainly because it provided appropriate noise-free excitation in the low frequency range where the accelerometer outputs are very small. For 5-60 Hz, base excitation with electrodynamic or hydraulic actuators worked well; random input led to consistent results, and slow-sine sweep showed up non-linearity to some extent. Above 60 Hz, consistent results were not obtained because of structural non-linearities and added damping and mass of accelerometer cables. The data acquisition and parameter estimation software of MODAL-PLUS supported all tests in a very effective interactive manner.

A simple continuum (beam) model of the Astromast gave the qualitative character of the mode shapes, and quantitative estimates of modal frequencies shown in Table 2. For higher modes a more refined model appears to be needed.

The finite element model described herein forecasted the qualitative nature of the mode shapes correctly and gave correct quantitative estimates for the lower frequencies. Further refinement of the model would be needed to accurately predict the higher modal frequencies.

There was no difference between test results in air and in vacuum, thus establishing that aerodynamic effects are negligible in test of this type of space mast.

Acknowledgements

The authors wish to acknowledge the support to the test work provided by Mr. Tom Steele, Mr. John Giurgevich, Mr. E.G. Williams, and the David Florida Laboratory facilities under Dr. R. Mamen and Mr. B. Kinney. Contribution to the modeling and test were also made by Dr. Béliveau, Mr. Lauzier, and Dr. Massoud of University of Sherbrooke, and Dr. K. Lips.

List of References

1. "Astromasts for Space Applications", ARC-B-004, Astro Research Corporation, Carpinteria, California, August 1978.
2. Massoud, M., Béliveau, J.-G., and Bourassa, P., "Méthode d'identification pour la détermination des caractéristiques structurelles d'une sous-structure d'un satellite", Contractor Report DOC-CR-SP-82--019, Space Technology and Applications Branch, Department of Communications, Ottawa, Canada, March 1982.
3. Soucy, Y., and Vigneron, F., "Modeling and Identification of the Structural Properties of an Astromast", to be issued as a CRC Report (in press), Department of Communications, Ottawa, Canada.
4. Vold, H., Kundrat, J., Rocklin, G.T. and Russel, R., "A Multi-Input Modal Estimation Algorithm for Mini-Computers", SAE Technical Paper Series (820194), 1982.
5. Vigneron, F.R., "Comparison of Test Configurations for Modal Parameter Identification", Tech. Memo No. DSM-29, Directorate of Space Mechanics, Communications Research Centre, Ottawa, May 1983.
6. Mutch, G., Vigneron, F.R. and Vold, H., "The Dynamic Analysis of a Space Lattice Structure Via the Use of Step Relaxation Testing", Proc. 2nd International Modal Analysis Conference, Orlando, Florida, February 6-9, 1984.

David R. Martinez*
Engineering Analysis Department

Thomas G. Carne**
Dan L. Gregory***
Environmental Testing Department

A. Keith Miller****
Advanced Systems Development Department

Sandia National Laboratories
Albuquerque, New Mexico

ABSTRACT

This study evaluates the accuracy of computed modal frequencies and mode shapes obtained from a combined experimental/analytical model for a simple beam structure. The structure was divided into two subsystems and one subsystem was tested to obtain its free-free modes. Using a Component Mode Synthesis (CMS) technique, the experimental modal data base for one subsystem was directly coupled with a finite element model of the other subsystem to create an experimental/analytical model of the total structure. Both the translational and rotational elements of the residual flexibilities and mode shapes at the interface of the experimental subsystem were measured and used in the coupling. The modal frequencies and mode shapes obtained for the combined experimental/analytical model are compared to those for a reference finite element model of the entire structure. The sensitivity of the CMS model predictions to errors in the modal parameters and residual flexibilities, which are required to define a subsystem, is also examined.

INTRODUCTION

Component mode synthesis (CMS) is a technique for assembling a system model using individual models of the components or subsystem parts. CMS techniques are a class of reduction or substructure coupling methods for dynamic analysis. They have proven very useful in solving large structural dynamics problems, especially where the structure consists of several distinct components. In CMS, a series of elastic modes and static displacement shapes are utilized in a transformation to obtain a reduced set of generalized coordinates. Either free or fixed interface elastic modes may be used as trial vectors for a subsystem. These are augmented with appropriate static displacement shapes. Invoking displacement and force compatibility at the interface permits coupling of subsystems to obtain a lower order or reduced system model.

CMS techniques are also useful for coupling experimental and analytical models. A modal description of a subsystem, consisting of the modal frequencies, mode shapes, modal mass, and modal damping, can be generated analytically or provided from tests in a modern vibration test laboratory. In addition, a quantity referred to as residual flexibility may be obtained with many of the curve fitting algorithms which are currently available in commercial modal analysis software¹. Advances in experimental modal analysis and testing have resulted in increased utility of this data base². Instead of using the measured modes only to verify an existing finite element (FE) model, attempts are being made to directly utilize the measured data in a combined experimental/analytical model. Many applications utilize frequency response or impedance substructure coupling techniques³⁻⁵; however, CMS may also be used for the coupling. When using free subsystem modes plus residuals to describe a subsystem, the experimental data base contains all the information required for the CMS formulation of the total system.

These synthesis techniques have been used in the aerospace and automotive industries for several years⁶⁻⁸. In the aerospace industry, fixed interface modes have most often been measured. Then a detailed FE model of the subsystem is used to orthogonalize the measured modes⁹ and also to obtain the generalized mass and stiffness terms due to the static displacement shapes. For the fixed CMS formulation, the static displacement shapes are columns of the Guyan reduction transformation matrix which reduces the interior degrees of freedom (DOF) to the interface DOF. These static displacement shapes, referred to as constraint modes, are difficult to determine experimentally, requiring either static testing or measurements of the interface forces during the modal test¹⁰. In automotive applications free modes are usually measured. The subsystems are then coupled using elastic stiffness elements representing local flexibilities and body or engine mounts¹¹. Due to the relatively soft coupling elements, the need to include residual terms and rotational behavior at the subsystem interfaces is not as great as in those aerospace applications which involve stiffer structures.

* Member of Technical Staff, Member AIAA

** Member of Technical Staff, Member AIAA and ASME

*** Member of Technical Staff

**** Member of Technical Staff, Member ASME

This paper is declared a work of the U.S. Government and therefore is in the public domain.

For many aerospace structures, free interface modes are much easier to obtain experimentally than fixed modes. A very useful CMS technique¹², using free modes, is one which includes static displacement shapes which are determined from the residual flexibility that is associated with a truncated set of modes. These are referred to as residual attachment modes and are columns of the residual flexibility matrix. As in the case with fixed modes, the static portion of the subsystem description must be determined either from a finite element model or from test. To experimentally account for the static effects, either mass loading of the interface must be included when measuring the modes, or the residual flexibility properties of the test item must be measured^{13,14}.

For structures which do not contain a large number of interface degrees of freedom; i.e., beam-type structures, the rotational information at the interface is required for proper subsystem coupling. Measurements of rotational frequency response functions and rotational residual flexibilities are necessary to properly describe the rotational displacements in a combined experimental/analytical model. Several successful attempts have been made to determine rotational frequency response functions. Either finite difference techniques have been applied to translational displacement and force measurements¹⁵, or fixtures have been designed to impart a moment to the structure using forces with a small offset between the points of application¹⁶.

The general method of CMS which utilizes free modes and residuals was used in this study. Our specific method is similar to the technique employed by Craig and Chang^{17,18}; however, we modify the final form of the equations to explicitly retain the interface DOF in the reduced system model. This greatly simplifies the coupling of subsystems and is directly amenable for systematic incorporation into existing finite element codes. The technique uses free elastic subsystem modes, rigid body modes, and residual flexibility displacement shapes. A previous analytic study for a beam structure was performed to evaluate variations of this CMS method¹⁹. That study demonstrated that neglecting the residual terms in the mass matrix for the subsystem introduced only a small error in the system modes; therefore, this approach was selected for the current study, eliminating the need for determining the residual mass associated with the high frequency modes. Further, neglecting the off-diagonal residual terms of the residual flexibility matrix also caused only a small increase in the modal frequency errors and a modest decrease in the mode shape correlation.

This paper evaluates the accuracy of computed modal frequencies and mode shapes using this CMS method for a simple beam structure. The beam was chosen because it is simple to model, has widely separated modes, but the importance of the rotational coupling at the interface is significant. Both the translational and rotational elements of the residual flexibilities and mode shapes at the interface of the two subsystems were measured and used in the coupling. The rotational

frequency response functions were generated from translational frequency response functions at closely spaced measurement points and a finite differencing technique. The translational and rotational residual flexibilities were obtained from the measured frequency response functions. The modal frequencies and mode shapes obtained for the combined experimental/analytical model are compared to those for a reference finite element model of the entire structure. A study is included which examines the sensitivity of the CMS model predictions to errors in the measured quantities needed to define a subsystem.

The following sections of the paper describe the beam structure and model, followed by a development of the CMS equations. Results of the sensitivity studies are then given, followed by the experimental procedures used to measure the data, and the results of an application of this technique using experimental data for the beam.

BEAM STRUCTURE AND MODEL DESCRIPTION

Figure 1 shows the structure which was studied. Figure 2 gives a description of the beam and finite element model. Two identical beams were manufactured and one was physically cut into two subsystems. MSC/NASTRAN²⁰ was used to assemble the combined model. The residual flexibility CMS technique is not available as one of the standard options in MSC/NASTRAN and was DMAP programmed into the normal modes rigid format solution. Modal frequencies and mode shapes were experimentally and analytically obtained for the entire beam as well as one of the subsystems. The modal frequencies and mode shapes for the original FE model of the entire beam were used as the reference model results for all comparisons. The experimental modal frequencies of the entire beam were in very close agreement with those of the reference FE model.

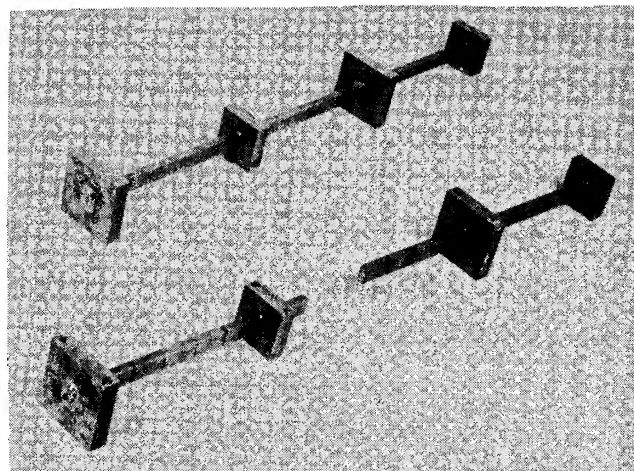


Figure 1. Beam Structure

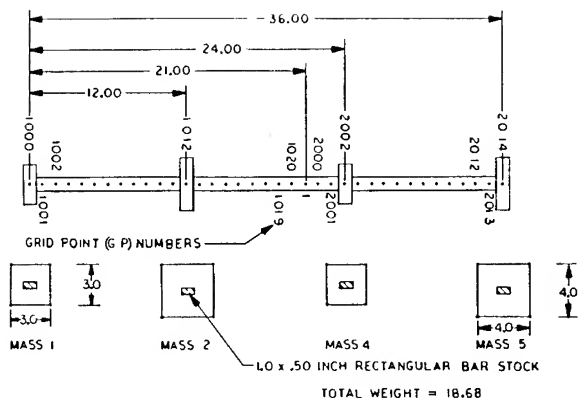


Figure 2a. Test Beam Description

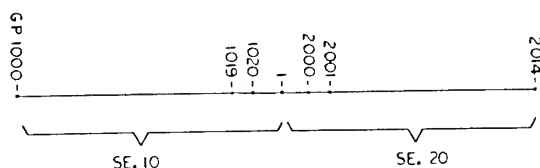


Figure 2b. Substructure Definition

The beam was modeled using standard beam (CBAR) ²⁰ elements and a diagonal mass matrix, including rotational inertias for every grid point (GP). The concentrated rectangular masses were assumed to be rigid with their total mass and inertia lumped at their center. The model was divided into two subsystems or superelements, denoted SE10 and SE20 as shown in Figure 2. The subsystem interface was at GP-1 and the reduced system model consisted of one physical grid point, GP-1 plus generalized coordinates for the rigid body, elastic, and residual attachment modes associated with each subsystem. Only the software bending modes were considered for this study. The total number of DOF for the FE model of the entire beam was 74, 44 DOF in SE10 and 32 DOF in SE20.

COMPONENT MODE SYNTHESIS TECHNIQUE USING FREE MODES AND RESIDUAL FLEXIBILITY

General Comments

A brief development of the residual flexibility CMS technique which was used is given below. A more detailed derivation has been presented ²¹ which applies to the general, forced-response problem. Provision is made to include residual flexibilities for interior DOF where external forces are applied. In this study, we are interested only in the real eigenvalue problem. Therefore, damping is neglected and the only forces which exist are boundary or interface forces from adjacent subsystems. The total transformation of the subsystem matrices is divided into two steps. The first is a Ritz transformation which utilizes free interface elastic modes and residual attachment modes ¹² For unrestrained

ed subsystems, rigid body modes must also be used, and the residual attachment modes must be calculated using inertia relief loading ^{12,19}. The results of this first transformation are subsystem matrices which are expressed entirely in terms of generalized coordinates. When expressed in this form, the effects of truncated modes are clearly seen and the elements in the reduced subsystem matrices retain physical and intuitive interpretation. The second transformation replaces those generalized coordinates which are associated with the residual modes, with the physical coordinates associated with the interface DOF. This greatly simplifies coupling of the subsystem equations and is directly amenable for systematic incorporation into existing finite element codes. However, the elements in the subsystem matrices lose physical interpretation.

Subsystem Equations

The original equation of motion describing one of the subsystems is

$$M \ddot{\underline{x}} + K \underline{x} = \underline{F} \quad (1)$$

where M and K are the $(N \times N)$ mass and stiffness subsystem matrices; $\ddot{\underline{x}}$ and \underline{x} are the acceleration and displacement vectors; and \underline{F} is the total subsystem forcing function. \underline{x} and \underline{F} are partitioned as follows;

$$\underline{x} = \begin{Bmatrix} \underline{x}_I \\ \underline{x}_B \end{Bmatrix} \quad \underline{F} = \begin{Bmatrix} \underline{0} \\ \underline{f}_B \end{Bmatrix} \quad (2)$$

where \underline{x}_B are the interface or boundary DOF, \underline{x}_I are the interior DOF, and \underline{f}_B are the interface forces due to adjacent subsystems. (Note that K may be singular due to rigid body modes of the subsystem.) An eigenvalue analysis is performed on Equation (1). The eigenvectors are then used in the following approximate transformation for \underline{x} ,

$$\underline{x} = \phi_k \underline{q}_k + G_B \underline{q}_B = [\phi_k \ G_B] \begin{Bmatrix} \underline{q}_k \\ \underline{q}_B \end{Bmatrix} = T_1 \underline{q} \quad (3)$$

where ϕ_k is an $(N \times n_k)$ matrix of kept dynamic modes (rigid body and elastic), n_k is the number of kept modes, \underline{q}_k , \underline{q}_B , and \underline{q} are the generalized coordinate vectors, G_B is a partition of the $(N \times N)$ residual flexibility matrix G , and T_1 is the total transformation matrix. The columns of G_B are static displacement shapes associated with the residual flexibility attachment modes at the interface DOF. G is defined as follows:

$$G = \sum_{i=n_k+1}^N \begin{bmatrix} \phi_i \phi_i^T \\ \frac{\phi_i \phi_i^T}{\omega_i^2} \end{bmatrix} \quad (4)$$

where ϕ_i is the i -th deleted eigenvector, ω_i is the i -th modal frequency, and the eigenvectors have been normalized to unity modal mass. G may be partitioned by columns, consistent with \bar{x} and \bar{E} , as $G = [G_I \ G_B]$. The full partitioning for G is

$$G = \begin{bmatrix} \overbrace{G_{II}}^{n_I} & \overbrace{G_{IB}}^{n_B} \\ \underbrace{G_{BI}}_{n_I} & \underbrace{G_{BB}}_{n_B} \end{bmatrix} \quad (5)$$

where n_B is the number of interface DOF and n_I the number of interior DOF. Note that for analytical implementations of this method for free subsystems, the rigid body modes are easily calculated and cause no difficulty in obtaining the residual flexibility matrix. When using experimental data from free interface modal tests, the effects of low frequency or rigid body modes may be determined by a quantity denoted as residual inertance, which accounts for mass-like effects of low frequency modes. Then, the residual flexibility may be calculated and is still defined by Equation (4). The transformation showing the full partitioning for T_1 is

$$\bar{x} = \begin{Bmatrix} \bar{x}_I \\ \bar{x}_B \end{Bmatrix} = \begin{bmatrix} \phi_{kI} & G_{IB} \\ \phi_{kB} & G_{BB} \end{bmatrix} \begin{Bmatrix} q_k \\ q_B \end{Bmatrix} = T_1 q \quad (6)$$

where the first column partition of T_1 is simply the partitioning of ϕ_k consistent with the partitioning of \bar{x} . Because G may be calculated using only the deleted elastic modes, it can be shown^{17,21} that ϕ_k and G are orthogonal with

respect to the M and K matrices, i.e., $\phi_k^T K G = \phi_k^T M G = 0$. Using the partitioning of G , we obtain $\phi_k^T K G_I = \phi_k^T K G_B = 0$, and $\phi_k^T M G_I = \phi_k^T M G_B = 0$. Also, although it is not obvious, it

may be shown²¹ that $G^T K G = G$. Note, this does not imply that $K G = I$ because G is not the total flexibility matrix but only the residual flexibility. In fact G is an $(N \times N)$ singular matrix of rank $(N - n_k)$. Expanding this last expression, we obtain

$$G^T K G = \begin{bmatrix} G_I^T K G_I & G_I^T K G_B \\ \text{Sym} & G_B^T K G_B \end{bmatrix} = \begin{bmatrix} G_{II} & G_{IB} \\ \text{Sym} & G_{BB} \end{bmatrix} = G \quad (7)$$

Substituting the transformation Equation (3) into Equation (1), the subsystem equation becomes

$$M^R \ddot{q} + K^R q = F^R \quad (8)$$

where $M^R = T_1^T M T_1$, $K^R = T_1^T K T_1$, and $F^R = T_1^T F$. Expanding Equation (8) and using the orthogonality results, we obtain

$$K^R = \begin{bmatrix} \Omega_{kk}^2 & 0 \\ 0 & G_{BB} \end{bmatrix} \quad M^R = \begin{bmatrix} I_{kk} & 0 \\ 0 & H_{BB} \end{bmatrix}$$

$$F^R = \begin{bmatrix} \phi_{kB}^T \\ G_{BB} \end{bmatrix} f_B \quad (9)$$

where $\Omega_{kk}^2 = \phi_k^T K \phi_k$, $I_{kk} = \phi_k^T M \phi_k$, and $H_{BB} = G_B^T M G_B$. Note $G_B^T K G_B = G_{BB}$ as shown in Equation (7). Ω_{kk}^2 is a diagonal matrix of kept dynamic modal frequencies, and I_{kk} is the identity modal mass matrix associated with the dynamic displacement shapes. G_{BB} and H_{BB} are the generalized stiffness and mass associated with the residual flexibility modes; i.e., the static displacement shapes. Note that the reduced subsystem matrices are uncoupled. Also, only the G_{BB} partition of the transformation matrix T_1 is needed to define K^R . Equations (8,9) describe the CMS equations for the subsystem.

The above formulation is a consistent Ritz transformation technique. Residual effects due to the static displacement shapes are included in both the reduced mass (denoted residual mass) and stiffness matrices. An inconsistent but often used transformation¹⁷ neglects the residual mass effects, H_{BB} . If these terms are neglected it may be shown²¹ that $q_B = f_B$, by partitioning Equation (8). This is equivalent to using a less accurate transformation \bar{T}_1 to reduce M where

$$\bar{x} = \phi_k q_k = [\phi_k \ 0] \begin{Bmatrix} q_k \\ q_B \end{Bmatrix} = \bar{T}_1 q \quad (10)$$

Although this inconsistent formulation is less accurate, it is much easier to implement. Only the residual stiffness terms are needed, which are defined by certain partitions of the residual flexibility matrix G .

When the subsystem equations are expressed entirely in terms of generalized coordinates as in Equation (9), the residual mass terms are clearly seen. An alternate method to derive the reduced subsystem matrices is to use a direct modal expansion of the subsystem equations, including interface forces rather than generalized coordinates for the interface DOF. In that case, the residual mass is implicitly neglected, although this fact is not apparent in the derivation²¹

To permit simple and general coupling between subsystems, it is convenient to obtain an alternate formulation for the subsystem equations. From the lower partition of Equation (6), it can be shown that

$$\begin{aligned} \mathbf{q}_B &= \mathbf{G}_{BB}^{-1} (\mathbf{x}_B - \bar{\phi}_{kB} \mathbf{q}_k) \\ &= -\mathbf{G}_{BB}^{-1} \bar{\phi}_{kB} \mathbf{q}_k + \mathbf{G}_{BB}^{-1} \mathbf{x}_B \end{aligned} \quad (11)$$

Let $\mathbf{q}_2 = \{\mathbf{q}_k, \mathbf{x}_B\}^T$. Then, a transformation \mathbf{T}_2 can be introduced incorporating Equation (11) as follows,

$$\mathbf{q} = \begin{Bmatrix} \mathbf{q}_k \\ \mathbf{q}_B \end{Bmatrix} = \mathbf{T}_2 \mathbf{q}_2 = \begin{bmatrix} \mathbf{I} & \mathbf{0} \\ -\mathbf{G}_{BB}^{-1} \bar{\phi}_{kB} & \mathbf{G}_{BB}^{-1} \end{bmatrix} \begin{Bmatrix} \mathbf{q}_k \\ \mathbf{x}_B \end{Bmatrix} \quad (12)$$

Using $\mathbf{K}_2^R = \mathbf{T}_2^T \mathbf{K}^R \mathbf{T}_2$, $\mathbf{M}_2^R = \mathbf{T}_2^T \mathbf{M}^R \mathbf{T}_2$, and $\mathbf{F}_2^R = \mathbf{T}_2^T \mathbf{F}^R$, the alternate subsystem equation becomes

$$\mathbf{M}_2^R \ddot{\mathbf{q}}_2 + \mathbf{K}_2^R \mathbf{q}_2 = \mathbf{F}_2^R \quad (13)$$

where

$$\mathbf{K}_2^R = \begin{bmatrix} \Omega_{kk}^2 + \bar{\phi}_{kB}^T \mathbf{G}_{BB}^{-1} \bar{\phi}_{kB} & -\bar{\phi}_{kB}^T \mathbf{G}_{BB}^{-1} \\ \text{Symmetric} & \mathbf{G}_{BB}^{-1} \end{bmatrix} \quad (14a)$$

$$\mathbf{M}_2^R = \begin{bmatrix} \mathbf{I}_{kk} + \bar{\phi}_{kB}^T \mathbf{J}_{BB} \bar{\phi}_{kB} & -\bar{\phi}_{kB}^T \mathbf{J}_{BB} \\ \text{Symmetric} & \mathbf{J}_{BB} \end{bmatrix} \quad (14b)$$

$$\mathbf{F}_2^R = \begin{Bmatrix} \mathbf{0} \\ \mathbf{f}_B \end{Bmatrix} \quad (14c)$$

and $\mathbf{J}_{BB} = \mathbf{G}_{BB}^{-1} \mathbf{H}_{BB} \mathbf{G}_{BB}^{-1}$. Because the \mathbf{x}_B now appear explicitly as physical coordinates, the CMS equations for the coupled system may now be easily obtained from direct matrix assembly using Equation (14); however, interpretation of the elements in \mathbf{K}_2^R and \mathbf{M}_2^R lose the physical significance which is apparent in Equation (9). As must be the case, because the generalized coordinates are now $\{\mathbf{q}_k, \mathbf{x}_B\}^T$, the generalized forces associated with the \mathbf{q}_k DOF are zero, and those associated with the \mathbf{x}_B DOF are the original interface forces, \mathbf{f}_B . The only matrix inverse required in this technique is \mathbf{G}_{BB}^{-1} , the partitioned residual flexibility matrix associated with the interface DOF. It is informative to write out the

total transformation $\mathbf{T}_{\text{tot}} = \mathbf{T}_1 \mathbf{T}_2$, which when partitioned, simplifies to

$$\begin{aligned} \mathbf{x}_I &= \mathbf{G}_{IB} \mathbf{G}_{BB}^{-1} \mathbf{x}_B + (\bar{\phi}_{kI} - \mathbf{G}_{IB} \mathbf{G}_{BB}^{-1} \bar{\phi}_{kB}) \mathbf{q}_k \\ &= \bar{\mathbf{G}}_{IB} \mathbf{x}_B + \bar{\phi}_{kI} \mathbf{q}_k \end{aligned} \quad (15a)$$

$$\mathbf{x}_B = \mathbf{x}_B \quad (15b)$$

This final form of the reduced subsystem matrices

utilizes modified free elastic modes, $\bar{\phi}_{kI}$ and

modified residual attachment modes $\bar{\mathbf{G}}_{IB}$ as trial vectors for the Rayleigh-Ritz transformation. Note that if residual mass is neglected,

$$\mathbf{M}^R = \mathbf{M}_2^R = \begin{bmatrix} \mathbf{I}_{kk} & \mathbf{0} \\ \mathbf{0} & \mathbf{0} \end{bmatrix} \quad (16)$$

One of the various forms of the residual flexibility CMS technique which has been studied neglects the off-diagonal residual terms. The proper implementation of this variation requires that the off-diagonal terms be neglected in \mathbf{G}_{BB} and \mathbf{H}_{BB} . Note that this is not the same as neglecting the off-diagonal terms in \mathbf{K}_2^R and \mathbf{M}_2^R .

ANALYTICAL MODEL SENSITIVITY STUDIES

General Comments

An analytical CMS model was used to examine the sensitivity of system modes to errors in the three basic quantities needed to define the subsystem matrices: 1) modal frequencies, 2) mode shapes at the subsystem interface, and 3) residual flexibilities at the interface. Also, the effect of neglecting the residual mass and off-diagonal residual flexibility terms was determined. Both modal frequency and mode shape convergence were studied. When evaluating convergence for either analytical or combined models, care must be taken to ensure that corresponding modes are compared. Mismatching of some modes can easily occur due to truncation effects or experimental error, as well as in areas of high modal density. The proper matching of modes is accomplished through the use of a mode shape correlation coefficient (MSCC) ²² The MSCC determines the correlation or "resemblance" between any two mode shapes but may also be used to determine mode shape accuracy. A more discriminating measure of mode shape convergence is given by the mode shape error (MSERR). The value of $(1.0 - \text{MSERR})$ gives the accuracy for the mode shapes from an approximate model as compared to those of a reference model. For real modes, the MSCC and MSERR are defined as follows:

$$MSCC = \frac{|\phi_{app}^T \phi_{ref}|^2}{|\phi_{app}^T \phi_{app}| |\phi_{ref}^T \phi_{ref}|} \times 100\% \quad (17a)$$

$$MSERR = \frac{(\phi_{ref} - \phi_{app})^T (\phi_{ref} - \phi_{app})}{\phi_{ref}^T \phi_{ref}} \times 100\% \quad (17b)$$

where ϕ_{app} is the approximate mode shape and ϕ_{ref} is the reference mode shape. Although the MSCC is a more forgiving measure of convergence than the direct percentage error given by MSERR¹⁹, it is more easily implemented and is the measure used for mode shape convergence in this study.

Sensitivity Results

Pertinent results from a previous study are first given which show the effect of neglecting residual mass and off-diagonal residual flexibility terms¹⁹. Component modes to 2000 Hz were retained for both subsystems (2 rigid body and 5 elastic modes for SE10, and 2 rigid body and 3 elastic modes from SE20). Figure 3 shows the modal frequency errors and MSCC convergence. The RKM curve shows results for the CMS formulation which includes residual terms for both mass and stiffness, the RK curve includes residual terms only for stiffness, and the RK-DIAG curve includes only diagonal residual stiffness terms. Comparing the RKM and RK curves shows that although there is a definite loss of accuracy introduced by neglecting the residual mass, the absolute error in the RK formulation is very small. Further, neglecting the off-diagonal residual flexibility terms results in increased errors whose magnitudes are acceptable for practical applications.

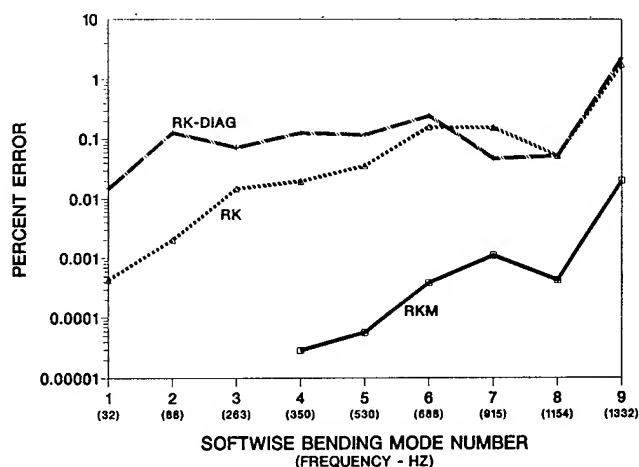


Figure 3a. Modal Frequency Convergence, Variations of CMS Technique

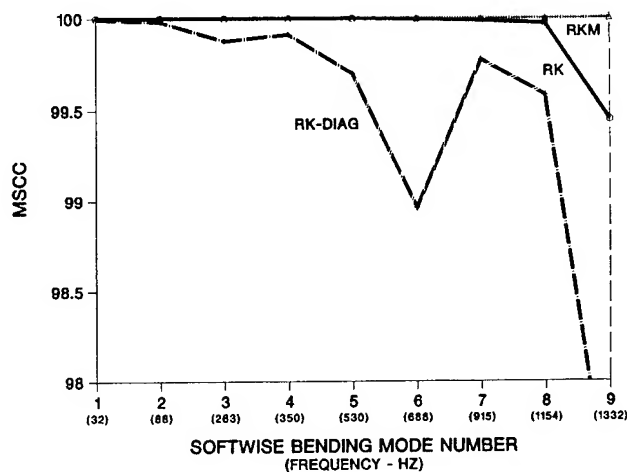


Figure 3b. Mode Shape Convergence, Variations of CMS Technique

The analytical RK model was then used to determine the relative sensitivity of the system modes to errors in the three basic quantities needed to specify a subsystem description; i.e., modal frequency (denoted Ω_{kk}), translational and rotational mode shapes at the boundary (denoted ϕ^u, ϕ^θ), and translational and rotational residual flexibilities at the boundary, (denoted G_{BB}^u, G_{BB}^θ).

Figure 4 shows the system modal frequency errors and MSCC convergence due to errors of +25% in subsystem modal frequency, +100% in subsystem interface mode shapes, and +200% in subsystem residual flexibilities. Similar results were seen for errors of -25%, -50%, and -67% in these same quantities. The results indicate that for the beam (i.e. rigidly connected substructures), system modal frequencies are sensitive to errors in the subsystem description in the following order of importance: modal frequency, rotational and translational mode shapes, rotational residual flexibility, and lastly, translational residual flexibility. In fact, for this structure, there was no noticeable effect on either modal frequency error or mode shape correlation due to very large positive or negative errors in the translational residual flexibility.

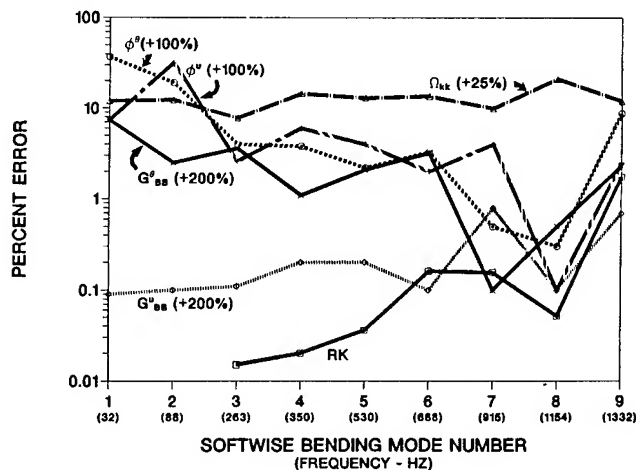


Figure 4a. Modal Frequency Convergence, Positive Subsystem Errors

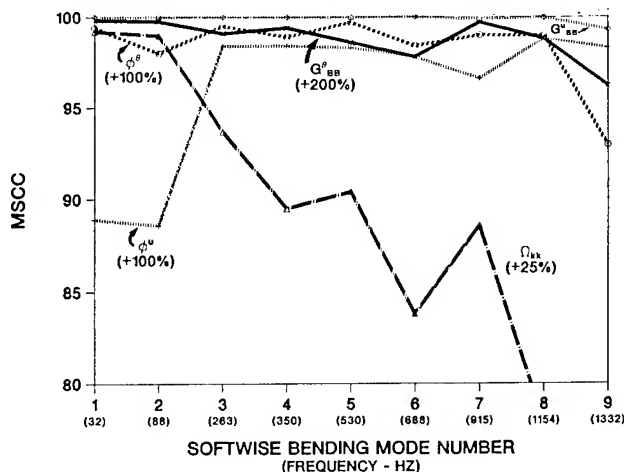


Figure 4b. Mode Shape Convergence, Positive Subsystem Errors

The rotational residual flexibility terms for the beam are much more important. A comparison was made of the modal frequency errors as a function of the number of elastic modes retained both with and without residual flexibilities for SE10. To simulate neglecting residuals, the diagonal rotational and translational residuals for SE10 were simply set equal to 1% of the correct values, and the off-diagonal residuals were set equal to zero. Modes for both subsystems were retained up to 2000Hz, 1000Hz, and 300Hz, respectively. This corresponds to retaining five, three, and one elastic modes, respectively, for SE10; and three, two and one elastic modes, respectively, for SE20. Figure 5 shows the modal frequency results, indicating the importance of the residuals. The errors seen in the curves without residuals are almost entirely due to neglecting the rotational residual term and not the translational residual, as verified by other sensitivity studies whose results are not included here. As can be seen, the accuracy for the first system mode is much greater when retaining only one elastic mode plus residuals, than for five elastic modes without residuals. MSCC convergence showed similar results.

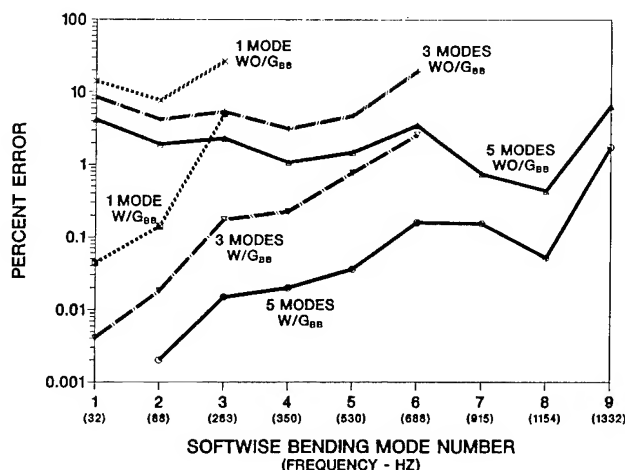


Figure 5. Modal Frequency Convergence, Effect of Neglecting Residuals

EXPERIMENTAL PROCEDURES

In this section we discuss the procedures used to experimentally obtain the data required by the CMS technique to describe one subsystem entirely from test. The required data includes the modal frequencies, mode shapes including rotational DOF at the interface, and the translational and rotational residual flexibilities at the interface.

Measuring the free modes of the beam structure presented no unusual difficulties. The beam was supported very softly with elastic cords. A single light-weight accelerometer was attached at the interface grid point. The structure was excited using a 0.25 lb. instrumented impact hammer, and six averages were used to compute the resulting frequency response functions (FRF). Since the structure was very lightly damped, a negative exponential damping window was applied to the responses to prevent leakage. Since rotational data were to be computed from the translational measurements, accuracy in the point of impact during the tests was tightly controlled. The measured translational FRF's were then used in the Poly Reference ¹ modal parameter extraction algorithm to extract the modal frequencies and mode shapes. Translational FRF's and mode shapes were determined at two inch stations along the beam, except near the interface where the spacing was one inch. Using the driving point FRF, the modal mass scale factor was derived for each of the measured modes and subsequently used to scale the mode shapes to unity modal mass.

Two approaches ^{15,16} were examined to compute the required rotational mode shapes and residuals at the interface, and the finite differencing technique ¹⁵ was used due to its ease of implementation. To generate the rotational FRF's at the interface, the translational FRF's near the interface are used in finite difference equations, as follows:

$$H_{\theta 1} F_1 = \frac{3H_{11} - 4H_{21} + H_{31}}{2\Delta} \quad (18a)$$

$$H_{\theta 1} M_1 = \frac{9H_{11} - 24H_{21} + 6H_{31} + 16H_{22} - 8H_{32} + H_{33}}{4\Delta^2} \quad (18b)$$

where H_{ij} is the x/F frequency response function between points i and j, and Δ is the spatial distance between the points. Point 1 is at the subsystem interface, while points 2 and 3 are at one and two Δ away from the interface, respectively.

Using these equations directly with the measured translational FRF's resulted in rotational FRF's which were unacceptably noisy. This is simply due to the fact that we are differencing data which itself contains a certain amount of noise. In particular, the implementation of Equations (18) resulted in the subtraction of quantities which are very nearly equal, thus increasing the effect of the noise. These very

noisy rotational FRF's were not acceptable for further curve fitting and extraction of the residual terms; therefore a slightly different approach was taken. First, rather than applying Equation (18a) to the FRF's, it was applied directly to the translational mode shapes at points 1, 2, and 3 to obtain the rotational element of the mode shape. Thus the θ/F frequency response function was not needed to determine the rotational mode shape at the interface. Because the translational mode shape coefficients have been determined from a fitting process, they reflect average or smoothed values which are less affected by the noise in individual spectral lines. This approach resulted in values for the rotational mode shapes which were very accurate and well within the requirements necessary for use in the combined experimental/analytical model.

The other rotational quantity that was required for the combined model is the residual flexibility from the θ/M frequency response function at the interface. An estimate of the measured FRF is required. Here again, using Equation (18b) directly with the data resulted in a FRF that was much too noisy. Also using a block floating point representation of the FRF's in a sixteen bit computer resulted in large round-off errors. Consequently, the following procedure was adopted. First, all the translational FRF's used in Equation (18b) were synthesized using the computed modal parameters. Residual inertance and residual flexibility terms were then calculated and added to the synthesized FRF's to obtain corrected FRF's, resulting in a very "close" fit to the experimental data. These fully corrected analytical translational FRF's are very smooth curves and contain no random noise as do the measured FRF's. However, they do contain the residual effects of deleted high frequency modes. These data were then used in Equation (18b) to produce a smooth estimate of the experimental θ/M FRF, which contains the residual effects. Figure 6a shows a Bode plot of the experimentally measured driving point FRF at the interface. This is typical of all the translational FRF's measured. Figure 6b shows the noisy FRF for θ/M using Equation (18b) directly with the measured data, and Figure 6c shows the smoothed estimate of θ/M using the procedure described above. The difference between Figure 6b,c is quite evident

Having obtained the θ/M and x/F FRF's at the interface, the last experimental quantities needed are the residual flexibilities. To obtain the residuals, modes in the identified frequency range of interest were first used to synthesize analytical FRF's. These synthesized FRF's were compared to the experimental FRF's for x/F and the smoothed estimate of the experimental FRF for θ/M . Data in the frequency range 10-100Hz were used to compute the residual inertance. This correction accounts for the rigid body modes not included in the synthesis. The residual inertance terms were then added to the synthesized FRF's to obtain partially corrected FRF's. Finally, the data between 1000-1500Hz were used to compute the residual flexibility. This procedure worked very well, producing a very good fit over the whole frequency range 10-1500Hz. Figure 7a compares the experimental FRF with the synthesized FRF using only the five modes in the frequency range of interest. The discrepancy at the low frequency end is quite evident and is due to neglecting the

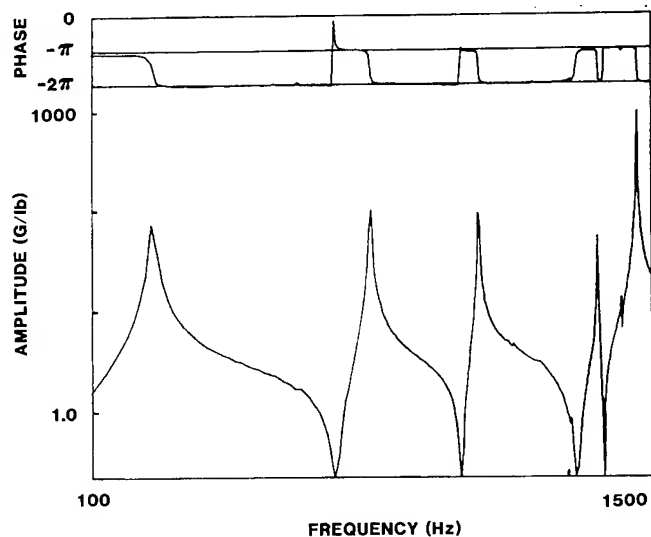


Figure 6a. Driving Point Frequency Response Function at the Interface

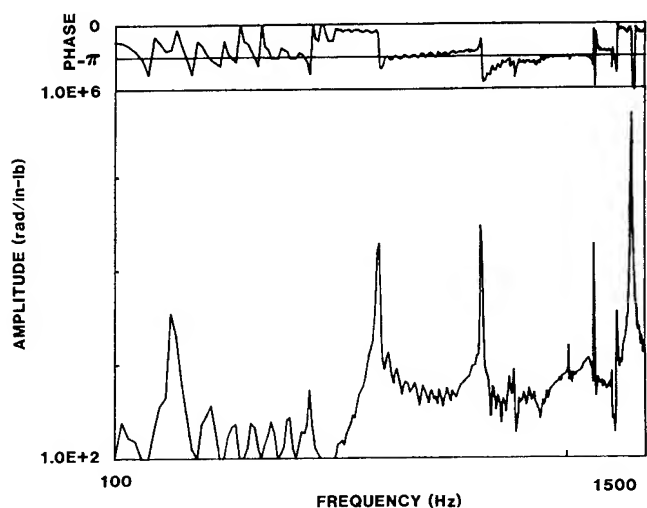


Figure 6b. θ/M Frequency Response Function, Raw Data

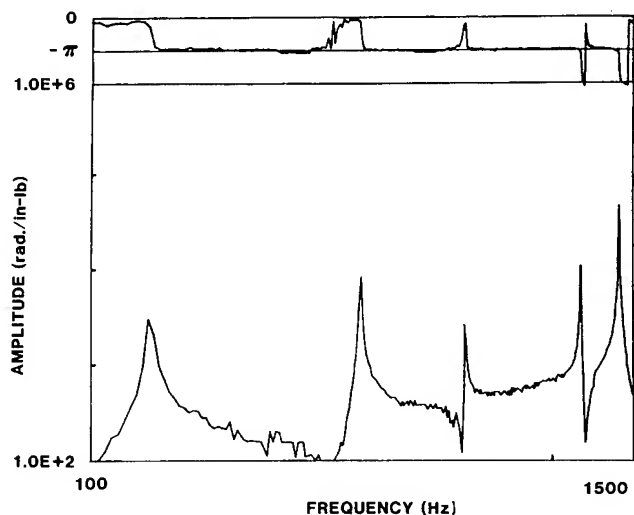


Figure 6c. θ/M Frequency Response Function, Smoothed Data

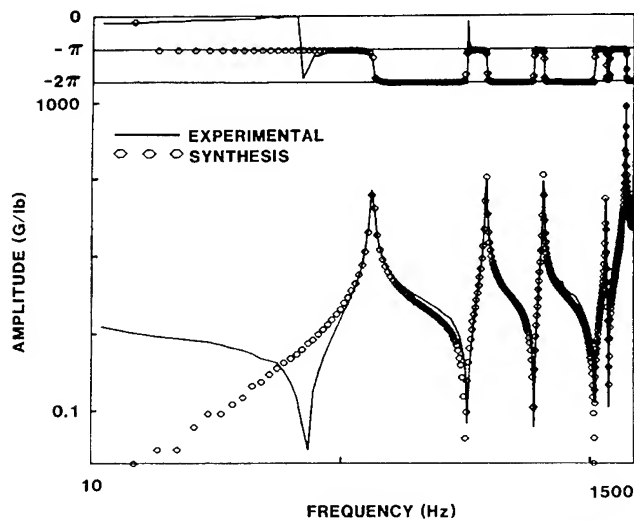


Figure 7a. Comparison of Frequency Response Functions, Experimental vs Synthesis Using Modes Only.

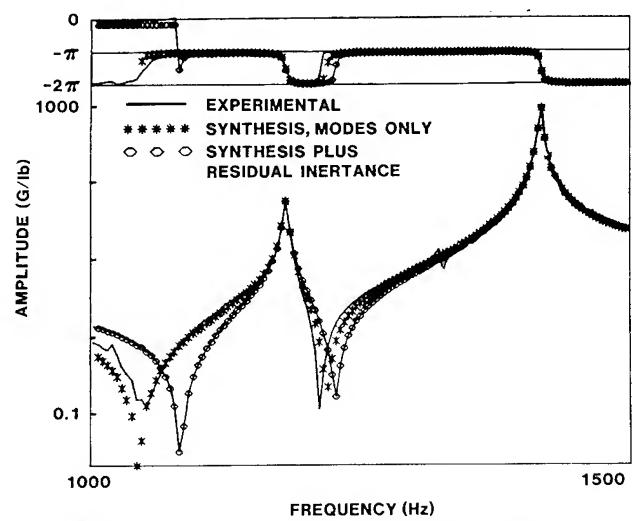


Figure 7c. Comparison of Frequency Response Functions, Experimental vs Synthesis (1000-1500 Hz)

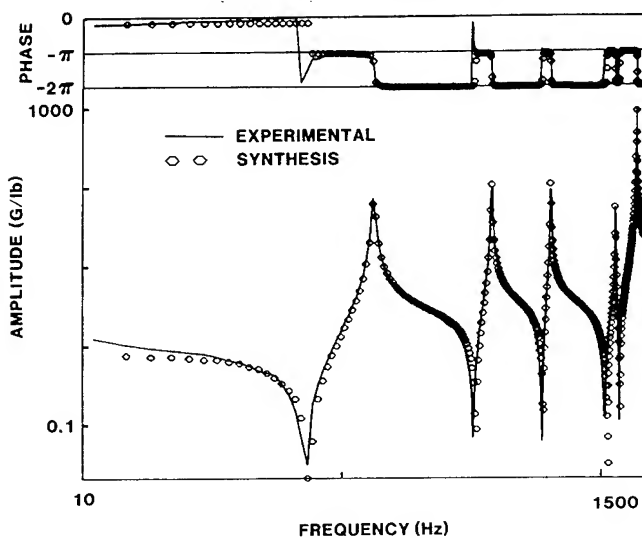


Figure 7b. Comparison of Frequency Response Functions, Experimental vs Synthesis With Residual Inertance

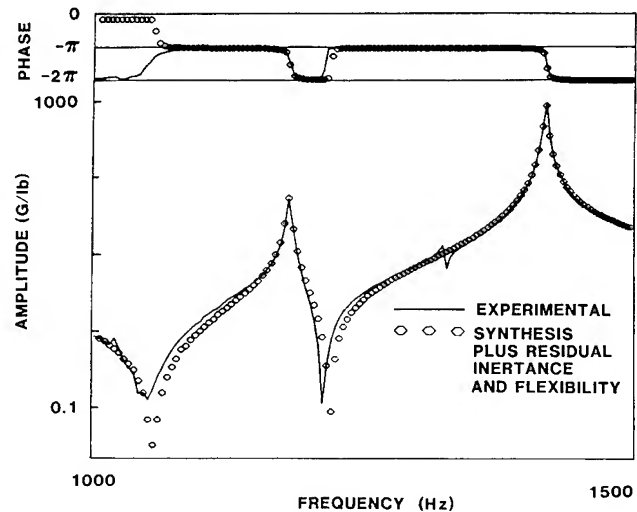


Figure 7d. Comparison of Frequency Response Functions, Experimental vs Synthesis With Both Residuals (1000-1500 Hz)

rigid body modes. Figure 7b compares the experimental data with the partially corrected FRF, i.e., including the residual inertance. Figure 7c expands this data in the frequency range from 1000-1500Hz. The solid line represents the experimental data, the line plotted with symbol '*' is the synthesis including only the modes, and the line plotted with the symbol 'o' is the synthesis including the modes and the residual inertance. As can be seen, adding the residual inertance did not improve the fit in this high frequency range. Figure 7d shows the final comparison of the experimental data with the synthesized FRF in the frequency range 1000-1500Hz, including both the residual inertance and residual flexibility. This clearly shows the improvement by adding the residual flexibility. With the residual flexibility correction, the synthesized data fits the experimental data extremely well over the entire frequency range, as shown in Figure 7e. The residual flexibilities which provided the final corrections to the synthesized FRF's were then used as the residual terms in the combined model.

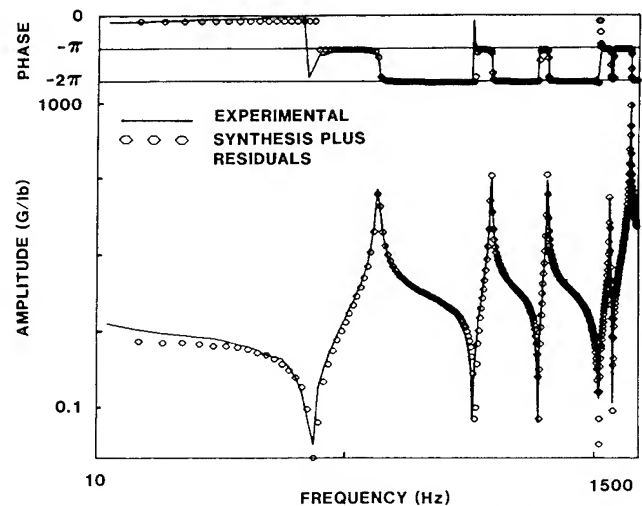


Figure 7e. Comparison of Frequency Response Functions, Experimental vs Synthesis With Both Residuals

General Comments

In this section results are presented from an application of the residual CMS technique using measured data for one subsystem. A combined experimental/analytical model for the beam structure was assembled using a description of SE10 that was obtained entirely from test. That is, except for the subsystem rigid body modes, every parameter for this subsystem was derived from measured data, without the use of an analytical model. The measured modal frequencies, translational and rotational mode shapes at the interface, and the translational and rotational residual flexibilities at the interface were used in the coupling. The results indicate the modeling accuracy which can be obtained for combined models of beam-type structures using experimentally determined elastic modes and residuals.

Combined Experimental/Analytical Model Results

Figure 8 shows the first two experimentally determined elastic modes for SE10, and Figure 9 shows the first two experimentally determined elastic modes for the total beam structure. For the combined model cases that were studied, component modes to 2000Hz were retained for both the experimental and finite element subsystems. Table 1 compares the experimental values of modal frequency and mass normalized mode shapes at the interface for SE10 with those predicted from the finite element model of that subsystem. Percentage errors are given relative to the reference FE model. For subsystem modes less than 1000Hz, modal frequency errors are less than 1.6% and mode shape errors are less than 5%. For subsystem modes between 1000 and 2000Hz, modal frequency errors are less than 3.4% and mode shape errors, including rotations, are less than 16.5%, except for mode four which had a node point near the interface. Considering that the mode shape accuracy is dependent on two experimentally obtained quantities; i.e., the modal vectors estimated from the modal extraction algorithm and the modal mass scaling constant, this is extremely good agreement, particularly for the rotations. Table 2 compares the experimental and finite element predictions of residual flexibilities from the translation/force and rotation/moment FRF's. The zero mode values indicate the total flexi-

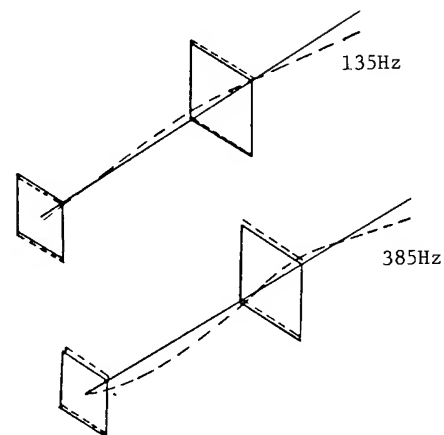


Figure 8. First and Second Modes of Experimental Subsystem

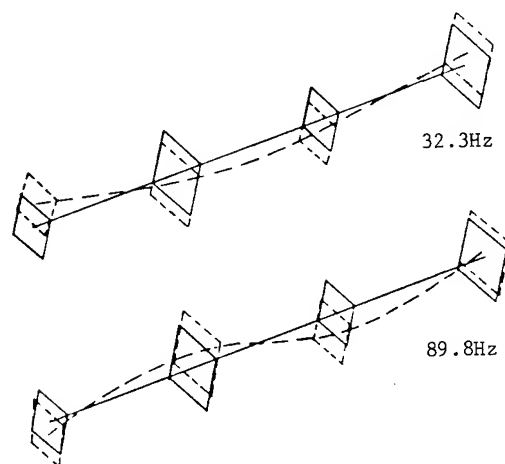


Figure 9. First and Second Modes of Total Beam Structure

bility for the beam at the interface. The percentage error is also given relative to the reference FE model. As can be seen, the error for the translational residuals varies from between 3% to 109%, while the rotational residuals have smaller errors. These errors are probably typical for estimating residuals. The reason for the large errors is due to the basic problem of

TABLE 1

Mode No.	Modal Frequency (Hz)			Interface Mode Shapes					
	Anal.	Exp.	% Error	Translation			Rotation		
				Anal.	Exp.	% Error	Anal.	Exp.	% Error
1	132.7	135	1.7	-25.3	-24.4	3.7	3.7	3.83	3.5
2	381	385	1.0	-17.5	-17.4	0.5	4.4	4.6	4.5
3	651	651	0.0	-14.6	-13.9	5.0	5.4	5.2	3.7
4	1135	1159	2.1	10.1	7.7	24	-5.3	-4.46	15.8
5	1356	1403	3.4	29.0	30.2	4	-17.1	-19.93	16.5

Experimental vs Analytical Modal Frequencies
and Mode Shape Comparison for SE10

TABLE 2

Interface Residual Flexibilities ($\times 10^{-6}$)

No. of Retained Modes	Translational (G_{BB}^u , in/lb)			Rotational (G_{BB}^θ , rad/in lb)		
	Analytical (FE)	Experimental	% Error	Analytical (FE)	Experimental	% Error
5	2.5	5.2	108	5.14	4.6	10.5
4	14.1	19.8	40	9.17	7.5	18.2
3	16.1	20.9	29	9.73	8.5	12.6
2	28.8	60.2	109	11.4	---	---
1	82.1	166	102	14.8	---	---
0	1010	1040	3	34.3	---	---

Experimental vs Analytical Residual Flexibilities for SE10

estimating a small quantity which is the difference of two large quantities. Because of the relative insensitivity of results to the translational residuals for this beam, no attempt was made to obtain more accurate measurements for these terms.

Retaining modes to 2000Hz, the RK-DIAG model was used to couple the experimental description of SE10 with the finite element model for SE20. System modes were obtained for the combined model. Figure 10 shows the modal frequency errors and MSCC convergence for the combined model. To permit a relative comparison of these errors with those of the sensitivity studies, the reference finite element model was used as the basis for comparison. This is somewhat inconsistent due to the fact that the reference model did not exactly correlate with the experimental data for the total beam, however, similar trends resulted when using the experimental modes of the entire beam as the basis for comparison.

In practical applications, accurate values for the residual terms are difficult to determine from the experiment. Therefore, the effect of neglecting the residuals for the combined model are also shown in the Figure 10. These results indicate that for a beam structure, relatively small error is introduced when using the experimental data, and although a much larger modal frequency error is introduced when neglecting the

residuals, seven of the nine system modal frequency errors were less than 3%, and only one was greater than 6%. The MSCC convergence is even less sensitive to neglecting the residual flexibilities.

If recovery of mode shapes at interior DOF of the experimental subsystem are not of interest, only a moderate amount of data is required from the modal test. Only the subsystem modal frequencies for the retained modes, the components of the retained mode shape vectors at the interface degrees of freedom, and the residual flexibility terms at the interface are required. However, if mode shapes are desired at interior points, then Equation (15a) may be used. But this requires values for ϕ_{kI} , the experimental mode shapes at interior points, as well as G_{IB} , the residuals at interior points. Because values for G_{IB} as well as rotational values for ϕ_{kI} are not ordinarily obtained from test, the following alternative procedure was used. Only the translational mode shape information at interior points was used in an approximate back transformation. Specifically, $\underline{x}_I = \phi_{kI} \underline{q}_k$ was used for the translational DOF instead of the more correct expression given in Equation (15a). For this calculation, the experimental data for ϕ_{kI} was used for SE10. The results indicate very good MSCC convergence as shown in Figure 10b.

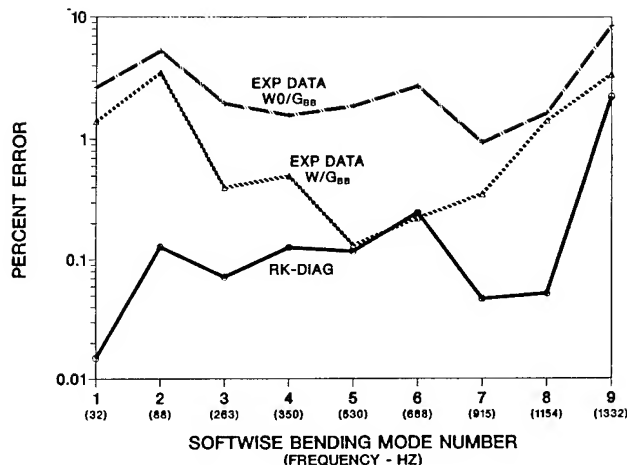


Figure 10a. Modal Frequency Convergence, Combined Experimental/Analytical Model

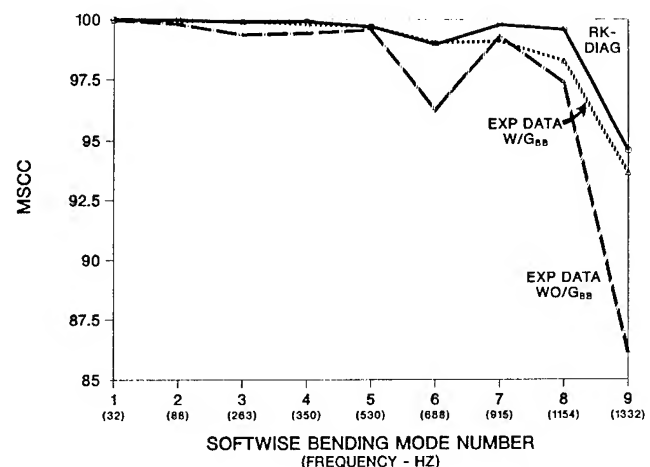


Figure 10b. Mode Shape Convergence, Combined Experimental/Analytical Model

Additional combined model studies were performed utilizing fewer elastic modes and the corresponding residual flexibilities. Modes to 1000 Hz (three elastic modes for SE10) and modes to 300Hz (one elastic mode for SE10) were retained, with conclusions similar to those discussed above. The convergence for both modal frequencies and mode shapes, which was achieved when using the experimental data, was very good.

CONCLUSIONS

A combined experimental/analytical model of a simple beam structure was successfully assembled using a component mode synthesis technique which employs free modes and residuals. The accuracy of system modal frequencies and mode shapes for the combined model are quite adequate for practical applications. Only a moderate amount of data is required from the modal test to describe the subsystem. All of the required experimental data, including rotational components and residuals, were obtained with careful testing and the application of two special procedures for obtaining the rotational quantities. The rotational mode shapes at the interface were measured and compared to finite element data with excellent agreement.

The sensitivity study for this beam indicated that system modal frequency errors are sensitive to errors in the subsystem description in the following order of importance: errors in modal frequency, rotational and translational mode shapes, rotational residual flexibility, and lastly, translational residual flexibility. The translational residual flexibility had almost no effect on the system modes, but the rotational residual flexibility was more significant. Further, measurement capabilities in the modern vibration test lab comfortably exceeds the requirements necessary to obtain a sufficiently accurate subsystem description for incorporation into a system model using component mode synthesis techniques employing free modes and residuals.

Future efforts should be expended to verify the potential for using this residual component mode synthesis technique to couple experimental/analytic models of complex structures with redundant interface conditions. Included should be simple consistency checks of the experimental residual flexibilities, and orthogonality checks of the measured modes.

REFERENCES

1. Modal-Plus Reference Manual, Version 7, The SDRC Corporation, Milford, Ohio, August, 1982.
2. First International Modal Analysis Conference, Proceedings, Orlando, Florida, sponsored by Union College, November, 1982.
3. Ewins, D. J. and Sainsbury, M. G., "Vibration Analysis of Damped Machinery Foundation Structure using the Dynamic Stiffness Coupling Technique," ASME Journal of Industrial Engineering, 96B, 3, 1974.
4. Ewins, D. J., Silva, J. M. M. and Maleci, G., "Vibration Analysis of a Helicopter Plus an Externally-Attached Structure," Shock and Vibration Bulletin, 50, 1980.
5. Goyder, H. G. D., "Methods and Application of Structural Modelling From Measured Structural Frequency Response Data," Journal of Sound and Vibration, 68(2), p. 209-230, 1980.
6. Bamford, R., Wada, B. K., Garba, J. A., and Chisholm, J., "Dynamic Analysis of Large Structural Systems," Synthesis of Vibrating Structures, presented at ASME Winter Annual Meeting, 1971, p. 57-71.
7. SAMSO Pamphlet 800-5, "Independent Structural Loads Analysis of Integrated Payload/Launch Vehicle Systems," February 15, 1975.
8. Klosterman, A. L. and McClelland, W. A., "Combining Experimental and Analytical Techniques for Dynamic System Analysis," Theory and Practice in Finite Element Structural-Analysis, University of Tokyo Press, 1973, pp. 339-356.
9. Targoff, W. P., "Orthogonality Check and Correction of Measured Modes," AIAA Journal, Vol. 14, No. 2, February, 1976, pp. 164-167.
10. Klosterman, A. L., On the Experimental Determination and Use of Modal Representations of Dynamic Characteristics, Ph.D. Dissertation, University of Cincinnati, 1971.
11. Kamal, M. K., and Wolf, J. A., eds, Modern Automotive Structural Analysis, Van Nostrand Reinhold Co., 1982.
12. Craig, R. R., Jr., Structural Dynamics. An Introduction to Computer Methods, John Wiley and Sons, 1981, chapter 19.
13. Coppolino, R. N., "Employment of Residual Mode Effects in Vehicle/Payload Dynamic Loads Analysis," Payload Flight Loads Prediction Methodology Workshop, Proceedings, NASA CP-2075, November, 1978, pp. 323-346.
14. Benfield, W. A. and Hrudu, R. F., "Vibration Analysis of Structures by Component Mode Substitution," AIAA Journal, Vol. 9, No. 7, July 1971, pp. 1255-1261.
15. Sattinger, S. S., "A Method for Experimentally Determining Rotational Mobilities of Structures," Shock and Vibration Bulletin, 50, Pt2, p. 17, September 1980.
16. Ewins, D. J. and Gleeson, P. T., "Experimental Determination of Multidirectional Mobility Data for Beams," Shock and Vibration Bulletin, 45, 5, 1975.
17. Craig, R. R., Jr. and Chang, C-J, "On the Use of Attachment Modes in Substructure Coupling for Dynamic Analysis," 18th Structural Dynamics and Materials Conference, San Diego, California, March 1977.

18. Chang, Ching-Jone, A General Procedure for Substructure Coupling in Dynamic Analysis, Ph.D Dissertation, Applied Mechanics Department, University of Texas at Austin, 1977.
19. Martinez, D. R. and Gregory, D. L., "A Comparison of Free Component Mode Synthesis Techniques Using MSC/NASTRAN," SAND83-0025, Sandia National Laboratories, and MSC/NASTRAN Users' Conference Proceedings, March, 1983, The MacNeal-Schwendler Corporation, Los Angeles, California.
20. MSC/NASTRAN User's Manual, Version 62, 1982, C. W. McCormick, ed.
21. Martinez, D. R. and Miller, A. K., "Component Mode Synthesis for Forced Response Using Free Modes," Sandia National Laboratories, 1984, to be published.
22. Ibrahim, S. R. and Pappa, R. S., "Large Modal Survey Testing Using the Ibrahim Time Domain (ITD) Identification Technique," 22nd Structural Dynamics and Materials Conference, Atlanta, Georgia, April 1981.

COMPONENT MODE SYNTHESIS METHODS FOR TEST-BASED,
RIGIDLY CONNECTED, FLEXIBLE COMPONENTS

Mary Baker*

Structural Dynamics Research Corporation
San Diego, California 92121

Abstract

With the objective of enhancing test-based modal synthesis and planning the development of test methods, simple examples were run using finite-element-based components to compare accuracy and define test requirements for the following approaches to component mode synthesis: restrained modal component, residual flexibility, mass-loaded connect degrees of freedom, and rotational connect degrees of freedom.

1. Introduction

Recent advances in modal testing methods and software (Vold and Leuridan, 1982; Vold and Rocklin, 1982; Vold, et al., 1982; Stroud, et al., 1984; Allemang, et al., 1982; Leuridan and Kundrat, 1982) have reduced the time and increased the accuracy and confidence associated with experimental determination of modal properties. This is particularly true for structures which formerly were considered very difficult to test such as lightweight flight components with closely spaced modes or rocket motors which have high damping. These new modal testing techniques motivate consideration of new uses for test methods in structural design, analysis, and validation. Typically for aerospace structures, modal testing is used only to verify analytical models. The work reported here was initiated to increase the feasibility of using modal testing methods in the following two areas:

- (1) Experimental component structural characterization as an alternative to analysis in conceptual or early design activities; and
- (2) Component testing and component mode synthesis as an alternative to large scale total space vehicle testing.

For design purposes, components of dynamic systems are often analytically modeled in order to obtain sufficient understanding to select a design concept. For some components, the analysis requires substantial time and cost commitment or unacceptable uncertainty because of the complexity of the structure.

With recent new capabilities, component modal testing, instead of analysis, may be the most effective way to obtain a simple simulation of the system dynamics. Although the actual article being designed does not yet exist, representative components or subunits of the structure are often available or easily fabricated. As long as confidence exists in the component mode synthesis techniques, these test-based component characteristics can be assembled into a simulation of new design concepts. The achievement of design models from test is one of the objectives of reviewing component mode synthesis techniques and expanding test methods to include all data needed for system synthesis from test-defined components.

The other objective is to meet the demands of verifying the structural integrity of very large dynamic systems. As space vehicles get larger, the feasibility of testing the complete assembled system is lost due to the size of currently available test facilities. If confidence exists in test-based modal synthesis techniques, only the components of the vehicle need to be tested. Final system performance can be verified through analysis using component mode synthesis.

The structural definition of components totally from test has been accomplished before and used successfully for design purposes (Klosterman 1972). This past success has been with relatively stiff structures connected with flexible elements such as an automobile frame and body connected with isolation mounts. For this situation, components can be tested with free boundaries to obtain a free-free modal data base. This modal data is sufficient to use in component mode synthesis to simulate system dynamic performance. However, in the case of aerospace vehicles, the components are typically more flexible and connected more rigidly. For large space structures, greater extremes in flexibility of rigidly connected components are expected. In general, using a truncated set of free-free modes to simulate aerospace systems leads to intolerable errors in the system response predictions. Typical aerospace vehicle components such as stages of missiles, panels of

*Director of Projects
Member AIAA

a satellite, aircraft components, and payloads mounted in the space shuttle cannot be accurately simulated by free-free modal analysis without defining a very large number of modes or some additional data to accurately define the local flexibility near the connect locations.

Many methods for obtaining a more accurate component definition have been developed for component analytical modeling. The exercise described here was undertaken to help in planning the development of improved experimental methods. The main interest is in selecting what additional measurement methods should be developed to obtain accurate definition for flexible components to be rigidly connected. Specific additional measurements under consideration are modal restraint forces, residual flexibility, static stiffness between connect locations, rotational accelerations, and modes of the component with mass-loaded connect locations.

2. Approach

The approach to evaluating the importance of various additional or different modal test measurements was to solve a simple system, representative of the actual system of interest, with different component mode synthesis methods. For this study, modal analysis was carried out by finite element analysis.

The system synthesis was in each case carried out with the SDRC SYSTAN dynamic analysis program. The component finite element analysis was performed using either SDRC SUPERB or MODEL SOLUTION or MSC NASTRAN programs, all of which are interfaced with SYSTAN as part of the SDRC I-DEAS™ software package. The accuracy of the various methods was assessed by comparing the frequencies, mode shapes, and strain energy distribution to a finite element solution of the whole system with both components included.

The structural configuration selected for this study is a simple representation of a flexible satellite supported in a relatively rigid cradle structure. The cradle structure was represented by beams and the satellite by parabolic shells. This structure and simplified model are shown in Figure 1.

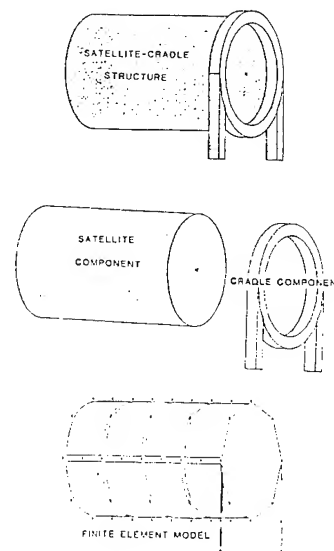


Figure 1. Satellite-cradle system used as example to compare methods.

The various component synthesis methods studied were applied to the satellite component definition while the cradle structure was always represented by the same modal data base, which consisted of twenty modes with degrees of freedom to be connected left free during the modal analysis.

The results from the total finite element model of the system in terms of frequencies and strain energy distribution are given in Table 1.

Table 1. Frequency and strain energy results for first five system modes of the total finite element model.

	Mode 1	Mode 2	Mode 3	Mode 4	Mode 5
Frequency (Hz)	1.16	1.63	1.71	2.15	3.00
Satellite Strain Energy (%)	19	67	74	25	29
Cradle Strain Energy (%)	81	33	26	75	71
Connection Strain Energy (%)	none	none	none	none	none

These results were treated as the reference for evaluating the accuracy of the other methods. The strain energy distributions for each mode were especially valuable for making comparisons particularly related to the accuracy of the load determination for a component. The example problem was selected to have a significant amount of strain energy in

the satellite component so that changes in the methods for definition of this component would show an effect in the system response predictions.

The first form of component mode synthesis tried was to perform free-free modal analysis on the satellite defined by just ten modes. Within the SYSTAN program, a system was formed with these ten satellite modes connected with very stiff translational springs to the twenty modes of the cradle. The results are summarized in terms of frequencies and strain energy distribution in Table 2.

Table 2. Frequency and strain energy results for first five system modes using a free-free satellite modal component with ten modes and only translational degree-of-freedom connections.

	Mode 1	Mode 2	Mode 3	Mode 4	Mode 5
Frequency (Hz)	1.27	2.50	3.29	3.94	6.11
Satellite Strain Energy (%)	1	0	0	3	0
Cradle Strain Energy (%)	99	99	100	97	100
Connection Strain Energy (%)	0	1	0	0	0

The results in Table 2 when compared with Table 1 illustrate the difficulties which occur when free-free testing and a severely truncated set of modes are used to define a component. Although some modes are reasonably close in frequency, the distribution in strain energy is not at all accurate and would lead to a very poor estimate of satellite loads. The total finite element model results of Table 1 show that, in modes 2 and 3 in particular, most of the strain energy should be in the satellite; yet the free-free component definition leads to zero strain energy in the satellite in these important modes.

Extending the satellite model to include twenty free-free modes led to the results in Table 3.

Table 3. Frequency and strain energy results for first five system modes using a free-free satellite modal component with twenty modes and only translational degree-of-freedom connections.

	Mode 1	Mode 2	Mode 3	Mode 4	Mode 5
Frequency (Hz)	1.27	2.22	2.31	2.49	3.56
Satellite Strain Energy (%)	1	36	10	8	4
Cradle Strain Energy (%)	99	64	90	92	96
Connection Strain Energy (%)	0	0	0	0	0

Doubling the number of satellite component modes leads to an improvement in system response predictions. However, the simulation still does not provide a close approximation of the total finite element result or a good representation of loads in the satellite.

Several methods for improving component mode synthesis over these results for a free-free modal satellite component were tried on this model. These candidate methods are summarized next.

3. Summary of Candidate Methods For Accuracy Improvement

In order to avoid using an unreasonable number of free-free modes, other synthesis methods are often used. The literature includes many different methods of component mode synthesis (Benfield and Hrudá 1971; Craig and Bampton 1968; Craig and Chang 1977; Dowell 1972; Hasselman and Kaplan 1974; Hurty 1964, 1971; MacNeal 1971; Rubin 1975) as well as reviews comparing methods (Benfield, et al. 1972; Craig and Chang 1976; Hou 1969; Engels and Harchow 1981; Rubin 1975). Although a single review may recommend a particular method which appears the most accurate, there is not a clear consensus of one method over all others. The accuracy of a particular method depends in part on the problem used to test it. Moreover, the practical difficulty (cost, time, equipment, software, experience) of acquiring the information needed to carry out each method varies. Therefore, selecting a method for test-based modal models still requires sample problems to assess the relative practicability, accuracy, and overall acceptability of the candidate methods.

For convenience in this study, the various methods were grouped into four general

types defined below. The first two groups of methods were considered because they have been described in the literature as the most accurate, particularly for rigid connection of flexible components.

3.1. Restrained Modal Component

The methods grouped here use modal data from a test or analysis with the connect degrees of freedom fixed; that is, those degrees of freedom which will be used to connect a component to other components when the system is assembled have a boundary condition of zero displacements. The methods of Hurty and Craig-Bampton are the best known examples of this approach. In general, these methods are expected to be most accurate when the final system allows the component of interest to have little motion near the connect degrees of freedom. Another way to describe this situation is that flexible component is rigidly attached to a relatively stiff component. The mass associated with the connect degrees of freedom is often neglected, while the local stiffness is accurately included with methods that take this general approach.

3.2. Free-Free Modal Component with Residuals

These methods, due to MacNeal and Rubin, improve the truncated free-free modal representation of a component by including estimates of the residual effects due to modes which are higher in frequency than the cut-off frequency for including modes in the component representation. In general, the residual effects are obtained by calculating the component flexibility due to those modes to be retained and subtracting this from the total flexibility of the component, which is obtained either from a finite element stiffness matrix or an experimentally determined frequency response function for the component. Once this "residual" flexibility has been obtained, it can be used to enhance the component modal stiffness representation before the component is connected into the system. In the Rubin approach, the first-order response based on the residual stiffness is used further to estimate the residual inertial and damping effects of higher-order modes.

For the sample problems reported in the literature (Rubin 1975), the inclusion of residuals appears as accurate as or even more accurate than restrained modal approaches. For components from test, the residual flexibility approach is particularly appealing because the free-free modal testing can be used. Free-free modal testing with the inclusion of residual flexibility has been proven to be feasible (Klosterman 1972). The

limitation of the residual flexibility in defining a flexible component to be rigidly connected is not known. If the stiffness of a very localized structural region near a connection is important in response of the component and in component loads, the constrained-mode approaches are likely to be more accurate.

The two remaining approaches were tried more from potential test feasibility rather than published or proven accuracy improvements.

3.3. Mass-Loaded Connect Degrees of Freedom

The limitations of any free-free modal approach in defining the local flexibility at connect locations is the lack of deformation in these areas in the lower frequency modes. It has been suggested that mass loading these boundary degrees of freedom during the modal analysis would force measurable deformation in this critical area in the first few component modes. By removing the mass (adding negative mass) in the system synthesis, the true system could be simulated--perhaps with more accuracy for a given number of modes than could be obtained with the unaugmented component free-free modes.

3.4. Rotational Connect Degrees of Freedom

Another approach at better definition of local flexibility at connect locations is to measure rotational degrees of freedom as well as translations during the modal test. These additional degrees of freedom could potentially include enough added information to allow a more accurate component definition. (Smiley and Brinkman 1984.) Since the system synthesis will remove these added degrees of freedom, the computation time for the final system solution will not increase as it would for additional modes.

Rotational degrees of freedom are not normally included in the modal test because they are not particularly helpful in plotting and visualizing mode shapes and because translational accelerometers are the usual transducer used to record motion in a modal test. However, various indirect methods for measuring rotations have been developed (Padgaonkar et al. 1975, Brinkman and Smiley 1984, Yasuda et al. 1984). In addition, a practical rotational accelerometer may be available soon, if not already.

4. Results for Candidate Approaches Applied to Satellite-Cradle Example

Results for each of the candidate approaches are summarized here for the

satellite-cradle system shown in Figure 1. Also included here is an explanation of each method and a discussion of data that must be measured for experimental definition of a component via each method.

4.1. Restrained Modal Component

In order to determine the accuracy and feasibility of simulating the satellite component with a restrained modal approach, a modal analysis of the satellite was performed using SDRC SUPERB with zero deflections boundary conditions at connect degrees of freedom. These modes were then assembled using the Hurty method to define the satellite component, which was then connected to in the same cradle component used before. (In this system, no connectors are required because the connect degrees of freedom are not constrained by the mode shapes.) The results are summarized in Table 4.

Table 4. Frequency and strain energy results for first five system modes using a restrained modal component with ten satellite modes and only translational degree-of-freedom connection.

	Mode 1	Mode 2	Mode 3	Mode 4	Mode 5
Frequency (Hz)	1.17	1.64	1.71	2.18	3.09
Satellite Strain Energy (%)	20	68	74	26	29
Cradle Strain Energy (%)	80	32	26	74	71
Connection Strain Energy (%)	none	none	none	none	none

The comparison of Table 4 and Table 1 shows that the constrained mode approach provides very accurate results. The satellite strain energy distribution matches that of the total finite element case.

Although other constrained mode methods are sometimes considered even more accurate, the above agreement is sufficient so that other restrained methods were not treated.

In order to understand requirements for a restrained modal test for component mode synthesis, the elements required to formulate the component stiffness and mass matrices for system assembly are reviewed here.

A general schematic of the type of system being considered is shown in Figure 2.

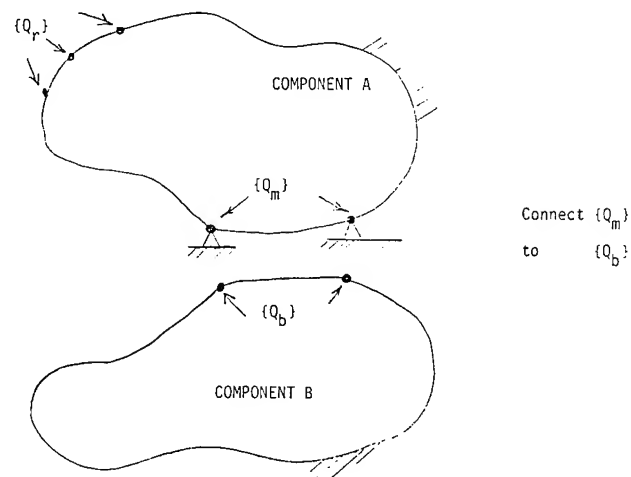


Figure 2. General schematic of a system with a constrained modal component.

For a component A, the mass and stiffness matrices, $[K]$ and $[M]$, can be partitioned into the following sets of degrees of freedom:

$\{Q_m\}$ = Connection degrees of freedom which were fixed during the subsystem analysis.

$\{Q_r\}$ = Remaining degrees of freedom in component A.

The equations of motion for the component A can then be written as:

$$\left(-\omega^2 \begin{bmatrix} M_{rr} & M_{rm} \\ M_{rm}^T & M_{mm} \end{bmatrix} + \begin{bmatrix} K_{rr} & K_{rm} \\ K_{rm}^T & K_{mm} \end{bmatrix} \right) \begin{Bmatrix} Q_r \\ Q_m \end{Bmatrix} = \begin{Bmatrix} F_r \\ F_m \end{Bmatrix} \quad (1)$$

Assume that $[M_{rm}] \approx [M_{mm}] \approx 0$. Inherent in the assumption that system modes are more like restrained modes than free-free modes is the assumption that the degrees of freedom $\{Q_m\}$ will not move very much in the system; therefore, their mass is neglected. In order to obtain system equations, these degrees of freedom have zero mass. Rewriting component A equation (1) with zero mass at connect degrees of freedom results in the following equation:

$$\begin{bmatrix} [K_{rr} - \omega^2 M_{rr}] & [K_{rm}] \\ [K_{rm}^T] & [K_{mm}] \end{bmatrix} \begin{Bmatrix} Q_r \\ Q_m \end{Bmatrix} = \begin{Bmatrix} F_r \\ F_m \end{Bmatrix} \quad (2)$$

Component A is tested with $\{Q_m\} = 0$. The result is a matrix of mode shape vectors, $[\Psi]$ for which

$$[\Psi]^T [K_{rr}] [\Psi] = [-k_-]$$

$$[\Psi]^T [M_{rr}] [\Psi] = [-m_-]$$

Let $\{n\}$ represent the modal coordinates and $\{F_n\}$ the modal forces such that

$$\{Q_r\} = [\Psi] \{n\}$$

$$\{F_n\} = [\Psi]^T \{F_r\}$$

Multiply upper partition of equation (2) by $[\Psi]^T$ and use the above definitions to obtain the following component definition equation:

$$\begin{bmatrix} [-k_-] - \omega^2 [-m_-] & [\Psi]^T [K_{rm}] \\ [K_{rm}]^T & [K_{mm}] \end{bmatrix} \begin{Bmatrix} \{n\} \\ \{Q_m\} \end{Bmatrix} = \begin{Bmatrix} \{F_n\} \\ \{F_m\} \end{Bmatrix} \quad (3)$$

The modal stiffnesses $[-k_-]$, modal masses $[-m_-]$, and mode shape vectors $[\Psi]$ are readily obtained from the restrained modal test or analysis, but the stiffnesses, $[K_{mm}]$ and $[K_{rm}]$, associated with the restrained connect degrees of freedom are not directly defined by a modal test or analysis. These additional stiffnesses must be obtained from measurements of modal reaction forces in the restrained modal test and from static measurements of stiffnesses between connect points. This process of obtaining these additional stiffnesses is explained further in the following paragraphs.

During the modal test, $\{Q_m\} = 0$; from equation (3)

$$[K_{rm}]^T [\Psi] \{n\} = \{F_m\} \quad (4)$$

The matrix $[K_{rm}]^T [\Psi]$ is a matrix of reaction forces associated with each mode.

Therefore,

$$[K_{rm}]^T [\Psi] = [\{R\}^1 \{R\}^2 \dots \{R\}^n] = [R]$$

where $\{R\}^i$ is the vector of forces at restrained degrees of freedom for a unit displacement of the i^{th} mode.

The matrix of modal reaction forces can be measured directly from modal test by using a force transducer at the connect locations and extracting modal forces as part of the eigenvectors during modal analysis. Thus equation (3) becomes

$$\begin{bmatrix} [-k_-] - \omega^2 [-m_-] & [R]^T \\ [R] & [K_{mm}] \end{bmatrix} \begin{Bmatrix} \{n\} \\ \{Q_m\} \end{Bmatrix} = \begin{Bmatrix} \{F_n\} \\ \{F_m\} \end{Bmatrix} \quad (5)$$

in which the only unknown for definition of component A is the matrix $[K_{mm}]$.

In order to evaluate $[K_{mm}]$ in terms of known or measurable quantities, rearrange equation (5) into the following form:

$$\begin{bmatrix} [-k_-]^{-1} & -[-k_-]^{-1} [R]^T \\ [R] [-k_-]^{-1} & [K_{mm}] - [R] [-k_-]^{-1} [R]^T \end{bmatrix} \begin{Bmatrix} \{F_n\} + \omega^2 [-m_-] \{n\} \\ \{Q_m\} \end{Bmatrix} = \begin{Bmatrix} \{n\} \\ \{F_m\} \end{Bmatrix} \quad (6)$$

The term,

$$\{ \{F_n\} + \omega^2 [-m_-] \{n\} \} = \{F'\}$$

represents the forces on the free degrees of freedom. For the static case, $\{F\}$ is equal to zero. Therefore, from equation 6, the following term is the static stiffness among connect degrees of freedom:

$$[K'_{mm}] = [K_{mm}] - [R] [-k_-]^{-1} [R]^T \quad (7)$$

If the component restraints are statically nonredundant--that is, the restraints are the minimum required to prevent rigid body motion--then there is zero stiffness among the restraints and

$$[K'_{mm}] = 0$$

and

$$[K_{mm}] = [R] [-k_-]^{-1} [R]^T \quad (8)$$

In this special case the $[K_{mm}]$ matrix can be formed from the modal reaction forces and modal stiffness values alone.

For most structures, the restraints $\{Q_m\}$ are redundant, and $[K'_{mm}]$ does not equal zero and must be evaluated. In order to make this evaluation, consider partitions of $\{Q_m\}$ into nonredundant subset $\{Q_c\}$ and other degrees of freedom $\{Q_f\}$.

$$\{Q_m\} = \begin{Bmatrix} \{Q_f\} \\ \{Q_c\} \end{Bmatrix}$$

The evaluation of $[K'_{mm}]$ requires an additional static analysis or test for which only a nonredundant set of degrees of freedom $\{Q_c\}$ is restrained. With these restraints, the static deflection due to some applied force $\{F_f\}$ of the other $\{Q_f\}$ degrees of freedom can be expressed as the sum of rigid body motion and elastic deformation of the component:

$$\{Q_f\} = \underbrace{[G]^{-1} \{F_f\}}_{\text{elastic deformation}} + \underbrace{[T] \{Q_c\}}_{\text{rigid body motion}} \quad (9)$$

Also from static equilibrium, the forces applied at $\{Q_f\}$ must be balanced by forces at $\{Q_c\}$ at $\{F_c\}$; therefore,

$$-[T]^T \{F_f\} = \{F_c\} \quad (10)$$

Rearranging equations (9) and (10) and writing as a matrix results in the following equations:

$$\underbrace{\begin{bmatrix} [G]^{-1} & -[G]^{-1} [T] \\ -[T]^T [G]^{-1} & -[T]^T [G]^{-1} [T] \end{bmatrix}}_{[K'_{mm}]} \begin{Bmatrix} \{Q_f\} \\ \{Q_c\} \end{Bmatrix} = \begin{Bmatrix} \{F_f\} \\ \{F_c\} \end{Bmatrix} \quad (11)$$

Therefore, the total $[K_{mm}]$ matrix has been evaluated--and, thereby, the total component A definition matrix.

What must be measured in a separate static test is the stiffness matrix $[G]^{-1}$. Therefore, the following items must be measured in the modal test: $[m]$, $[k]$, $[\psi]$, $[R]$, $[G]^{-1}$, $[T]$. The first three items are just the modal mass, stiffness, and mode shape vectors, which are obtained from a modal test with the component clamped. The next item $[R]$ is the matrix of modal reaction forces which can easily be extracted as part of the eigenvectors but requires transducers to record the forces required to restrain the structure during the modal test. The matrix $[G]^{-1}$ requires a static test for which a non-redundant subset of the connect degrees of freedom is constrained and the stiffness matrix of the redundant set is measured. The matrix $[T]$ is just a rigid body transformation between connect degrees of freedom which can

easily be obtained from the geometry alone. Therefore, the new challenges for test are the measurement of restraint forces and stiffness matrix $[G]^{-1}$.

4.2. Residual Flexibility

If all modes are retained in a component definition, the modal representation would be exact. Therefore, the accuracy of the truncated mode representation can be improved by estimating the residual effects of the higher order modes. Because residual flexibility can easily be obtained experimentally to supplement the free-free component definition and because the first-order residual flexibility correction is readily available in SYSTAN, NASTRAN, and MODAL-PLUS, this approach was tried next on the same sample problem used above with the results shown in Table 5.

Table 5. Frequency and strain energy results for ten free-free satellite modes using residual flexibility.

	Mode 1	Mode 2	Mode 3	Mode 4	Mode 5
Frequency (Hz)	1.16	2.15	2.70	3.00	4.82
Satellite Strain Energy (%)	19	25	19	31	30
Cradle Strain Energy (%)	81	75	81	69	70
Connector Strain Energy (%)	none	none	none	none	none

Although this set of natural frequencies shows closer agreement with the full finite element result than use of the free-free modes alone, the accuracy in satellite strain energy distribution is still poor, particularly in comparison to the restrained mode approach.

In order to better understand the information used for this example, the calculation of residual flexibility is reviewed here. The dynamic flexibility or frequency response function G_{ab} can be expressed in terms of the modal stiffness, k_r ; mass, m_r ; and mode shape vectors ψ_r by the following summation over the modes where the subscript r refers to the r^{th} mode and the subscripts a and b refer to physical degrees of freedom, which in this case will be connect degrees of freedom.

$$G_{ab} = \sum_{r=1}^N \frac{\psi_{ra} \psi_{rb}}{k_r - \omega^2 m_r} + \sum_{r=N+1}^{\infty} \frac{\psi_{ra} \psi_{rb}}{k_r - \omega^2 m_r} \quad (12)$$

In this expression, N is the number of retained modes; and the second term above is called the residual flexibility, Z_{ab} , due to

modes truncated in a simulation. Experimentally the term Z_{ab} can be obtained by exciting the structure at point a, measuring the response at point b, and subtracting the first sum in equation 12, which can be evaluated after the modal analysis has determined the properties of the first N modes. Using finite element analysis, Z_{ab} is approximated assuming that truncated modes have only a stiffness contribution. The static stiffness contribution of the retained modes is then subtracted from the physical static stiffness matrix to obtain a first-order or static approximation to Z_{ab} . Once an estimate of the residual effects at connect degrees is obtained, it is necessary to include these in the component stiffness and mass matrices.

From the free-free modal test, the stiffness and mass matrices have only modal degrees of freedom. In order to add the residual effects at the connect degrees of freedom and to expand the stiffness matrix to include the connect degrees of freedom, the definition of residual effects is rewritten into the following stiffness matrix form.

$$\begin{bmatrix} K_{\text{resid}} \end{bmatrix} \begin{Bmatrix} \{n\} \\ \{Q_c\} \end{Bmatrix} = \begin{Bmatrix} \{F_n\} \\ \{F_c\} \end{Bmatrix} \quad (13)$$

residual
effects
stiffness

where $\{n\}$ are the modal degrees of freedom, $\{Q_c\}$ are the physical connect degrees of freedom, and $\{F_c\}$ are the forces applied to the connect degrees of freedom.

The physical displacements $\{Q_c\}$ are given by the following equation

$$\{Q_c\} = [\Psi] \{n\} + [Z] \{F_c\} \quad (14)$$

which can be rearranged to obtain

$$\{F_c\} = [Z]^{-1} \{Q_c\} - [Z]^{-1} [\Psi] \{n\} \quad (15)$$

Equation (15) is one of the equations needed to fill out the K_{resid} matrix, and the other can be obtained by multiplying equation 15 by $-[\Psi]^T$ to obtain an expression for $\{F_n\}$. The resulting residual effects stiffness matrix formulation is the following:

$$\begin{bmatrix} [\Psi]^T [Z]^{-1} [\Psi] & -[\Psi]^T [Z]^{-1} \\ -[Z]^{-1} [\Psi] & [Z]^{-1} \end{bmatrix} \begin{Bmatrix} \{n\} \\ \{Q_c\} \end{Bmatrix} = \begin{Bmatrix} \{F_n\} \\ \{F_c\} \end{Bmatrix} \quad (16)$$

The whole stiffness and mass matrix for the component can be obtained by adding the free-free modal mass and stiffness from the modal

test into the upper partition of equation (16). When this formulation is included in the system synthesis, the connect degrees of freedom are now independent in the system formulation, and no auxiliary connectors are required.

We have not yet implemented the second-order correction suggested by Rubin (1975). Including the estimate of inertial and dissipative effects of the truncated modes should improve the accuracy of the residual flexibility approach further.

4.3. Mass-Loaded Connect Degrees of Freedom

Adding mass to exercise the local structure near connect locations was studied next as a potential experimental approach. This method consisted of attaching lumped masses at connect degrees of freedom during the modal analysis. Then, in the system synthesis, this modal component was attached with a connector which had equivalent negative mass at the connect locations. Cases were tried with ten satellite modes run with the lumped mass at each of the eight connect locations equal to 0.01, 0.1 and 1.0 times the mass of the entire satellite. No improvements in accuracy over the free-free case of Table 2 were obtained. The most accurate results are shown in Table 6. These results are for each lumped mass equal to one tenth the entire satellite mass.

Table 6. Frequency and strain energy results for first five system modes using a free-free modal component with ten modes. Mass equal to .1 times the mass of the was added used at connect DOF in component analysis and removed in system analysis.

	Mode 1	Mode 2	Mode 3	Mode 4	Mode 5
Frequency (Hz)	1.27	2.51	3.29	4.12	6.31
Satellite Strain	0	0	0	0	0
Energy (%)					
Cradle Strain	99	100	100	99	100
Energy (%)					
Connection Strain	1	0	0	1	0
Energy (%)					

The strain energy which is observed in the connectors indicates a modal insufficiency problem: the condition that satellite connect degrees of freedom and corresponding cradle connect degrees of freedom have zero relative motion is not being satisfied. Several cases were run with increased number of modes. At

twenty modes, there is no strain energy in the connectors, but still no improvement over the twenty mode free-free case of Table 3. Even at forty modes, the results are still not as accurate as ten modes with residual flexibility.

4.4. Rotational Degrees of Freedom

The fourth approach tried was the inclusion of rotational degrees of freedom. Again using the above models and ten free-free modes of the satellite the system synthesis included stiff translational and rotational springs connecting the satellite and cradle degrees of freedom. For this case, the results are summarized in Table 7.

Table 7. Frequency and strain energy results for first five system modes using a free-free modal satellite component with ten modes and translational and rotational degrees of freedom connected in system analysis.

	Mode 1	Mode 2	Mode 3	Mode 4	Mode 5
Frequency (Hz)	4.17	7.78	15.12	19.1	32.2
Satellite					
Strain	0	0	0	0	0
Energy (%)					
Cradle					
Strain	99	68	35	81	1
Energy (%)					
Connection					
Strain	1	32	65	19	99
Energy (%)					

The results again show large deviations from the total finite element result. Note the strain energy in the connection indicating insufficient modes to satisfy the connection equations. The same example was run with twenty satellite modes and then with forty satellite modes. Even for forty modes, the connection equations are not satisfied and the results are not at all accurate as shown in Table 8.

Table 8. Frequency and strain energy results for first five system modes using a free-free modal satellite component with forty modes and translational and rotational degrees of freedom connected in a system analysis.

	Mode 1	Mode 2	Mode 3	Mode 4	Mode 5
Frequency (Hz)	4.04	6.48	7.93	10.8	12.6
Satellite					
Strain	1	13	86	16	32
Energy (%)					
Cradle					
Strain	96	55	13	61	36
Energy (%)					
Connection					
Strain	3	32	1	23	32
Energy (%)					

Even with four times the modes, a satisfactory synthesis cannot be obtained with rotational degrees of freedom included.

This result was at first surprising because the addition of more degrees of freedom suggests a more accurate definition of a component. Because the example here showed a reduced accuracy with the addition of rotations, two other independent analyses of this same general configuration were run. One involved a cradle component of 1/20 the stiffness (1/20 the bending moment in the beams), and the other had this same flexible cradle but double the nodes and elements in both the cradle and satellite components. In both additional cases a decrease in accuracy or an increased difficulty in satisfying the connecting condition was obtained with the addition of rotational degrees of freedom.

Although it seems counter intuitive that increasing the number of degrees of freedom can reduce the accuracy, the effect observed could be described instead as increasing the difficulty in the synthesis rather than reducing accuracy. The strain energy in the connectors indicates that the synthesis equations, which call for degrees of freedom on the satellite to be fixed to corresponding ones on the cradle, are not satisfied and therefore the synthesis has not been accomplished. With the addition of rotational degrees of freedom, more modes are required to approximate the synthesis constraint equations before a valid comparison in accuracy can be obtained.

5. Conclusions

The main objective of this current effort was to determine what measurements were required to accurately define, by experimental modal analysis, a flexible component for mode

synthesis of a system with rigid connections and a configuration similar to the satellite-cradle example. In this example, the satellite is flexible enough to allow significant strain energy in this component.

The conclusion based on the work to date is that no significant improvement over unaugmented free-free modes can be expected from the inclusion of either rotational degrees of freedom or mass loaded boundary degrees of freedom. Too many modes are required for either of these approaches to even allow a valid system synthesis. The use of residual flexibility with free-free modes is much more promising and is the only method which is immediately feasible experimentally. However, achieving acceptable accuracy for rigidly connected flexible components requires more modes than the restrained modal component approach does.

For the configuration tried here, the restrained modal component approach was significantly more accurate than even the residual flexibility approach. Therefore, the implementation of a second-order correction in residual effects (Rubin's approach) and consideration of the feasibility of measurement of restrained modes should be investigated further.

Another conclusion apparent from the examples reported in the literature and from the execution of the examples in this paper is that the relative accuracy of a method depends greatly on the nature of the example. Certainly the relative flexibility of the components in the system determines the importance of the local flexibility and local mass at the connect degrees of freedom. This conclusion suggests that it is worthwhile to make a very simple conceptual model which is representative of the system in question yet small enough for a total finite element model check. Once various methods have been tried on the small model, the most accurate feasible method can be readily identified.

Acknowledgements

Contributions to this effort were made by many others at SDRC. Wayne McClelland provided the discussion of the various approaches to component mode synthesis, Havard Vold suggested the use of rotational connect degrees of freedom, Bob Ryan (currently at Stanford) and David Hunt prepared software to formulate restrained modal components, Dan Kammer and Mark Rashid prepared independent examples including rotational degrees of freedom. Jeff Young, Joe Klahs, and Matt Peffley provided discussion helpful in implementation of the

various methods. This work was performed as part of ongoing SDRC consulting methods development activities.

References

- Allemang, R.J. and D.L. Brown. "A Correlation Coefficient for Modal Vector Analysis." International Modal Analysis Conference, November 1982.
- Allemang, R.J., R.W. Rost, D.L. Brown. "Dual Input Estimation of Frequency Response Functions for Experimental Modal Analysis of Aircraft Structures." International Modal Analysis Conference, 1982.
- Bajan, R.L., C.C. Feng, I.J. Jaszlics. "Vibration Analysis of Complex Structural Systems by Modal Substitution." Shock and Vibration Bulletin, Vol. 39, 1969, pp. 99-105.
- Benfield, W.A. and R.F. Hruda. "Vibration Analysis of Structures by Component Mode Substitution." AIAA Journal, Vol. 9, 1971, pp. 1255-1261.
- Benfield, W.A., C.S. Bodley, G. Morosow. "Modal Synthesis Methods." Space Shuttle Dynamics and Aerolasticity Work Group Symposium on Substructuring, Marshall Space Flight Center, August 30, 1972.
- Brown, David L., Randall J. Allemang, Paul J. Riehle, Chiaki Yasuda. "Estimation Method for Rotational Degrees of Freedom Using a Mass Additive Technique." 2nd International Modal Analysis Conference, February 1984.
- Caughey, T.K. and M.E.J. O'Kelley. "Classical Normal Modes in Damped Linear Dynamic Systems." Journal of Applied Mechanics, Vol. 32, 1965, pp. 583-588.
- Chen, J.C. "Comparison of Various Modal Analysis Test Results." 2nd International Modal Analysis Conference, Orlando, Florida, 1984, pp. 820-824.
- Chen, J.C. and M. Trubert. "Galileo Modal Test and Pre-Test Analysis." 2nd International Modal Analysis Conference, Orlando, Florida, 1984, pp. 796-802.
- Collins, J.C., G.C. Hart, W.C. Hurty. "Formulation of System Modal Damping for Complex Structures." Symp. Substructure Testing and Synthesis, NASA Marshall Space Flight Center, Ala., 1972.
- Craig, R.R. Jr. and C-J Chang. "On the Use of Attachment Modes in Substructure Coupling for Dynamic Analysis." Paper No. 77-405, AIAA/ASME 18th SDM Conference, Vol. 8, March 1977, pp. 89-99.
- Craig, R.R. Jr. and C-J. Chang. "A Review of Substructure Coupling Methods for Dynamic Analysis." Advances in Engineering Science, Vol. 2, NASA CP-2001, Nov. 1976.

Craig, R.R. Jr. and M.C.C. Bampton. "Coupling of Substructures for Dynamic Analysis." AIAA Journal, Vol. 6, No. 7, 1968, pp. 1313-1319.

Dowell, E.H. "Free Vibration of an Arbitrary Structure in Terms of Component Modes." Journal of Applied Mechanics, Vol. 34, 1972, pp. 727-732.

Engels, R.C. and Harcrow, H.W. "A Survey of Payload Integration Methods." AIAA/ASME/ASCE/ANS 22nd Structures, Structural Dynamics and Materials Conference April 6-8, 1981, Atlanta, Georgia, Paper No. 81-0568-CP.

Gladwell, G.M.L. "Branch Mode Analysis of Vibrating Systems." Journal of Sound and Vibration, Vol. 1, 1964, pp. 41-59.

Goldman, R.L. "Vibration Analysis by Dynamic Partitioning." AIAA Journal, Vol. 7, 1969, pp. 1152-1154.

Hart, G.C., W.C. Hurty, J.D. Collins. "A Survey of Modal Synthesis Methods." Proc. National Aeronautics and Space Engineering and Manufacturing Meeting, Los Angeles, California, September 28-30, 1971.

Hasselman, T.K. and A. Kaplan. "Dynamic Analysis of Large Systems by Complex Mode Synthesis." Journal of Dynamic Systems, Measurement, and Control, Trans. ASME, Vol. 96, Ser. G., Sept. 1974, pp. 327-333.

Hintz, R.M. "Analytical Methods in Component Modal Synthesis." AIAA Journal, Vol. 12, 1975, pp. 1007-1016.

Hou, S.N. "Review of Modal Synthesis Techniques and a New Approach." Shock and Vibration Bulletin, Vol. 40, No. 4, 1969, pp. 25-30.

Hurty, W.C. "Dynamic Analysis of Structural Systems Using Component Modes." AIAA Journal, Vol. 3, No. 4, April 1965, pp. 678-85 (based upon JPL Tech. Memo 32-530, January 1964).

Hurty, W.C. "Vibration of Structural Systems by Component Mode Synthesis." Journal of the Engineering Mechanics Division, ASCE, Vol. 1, 1960, pp. 56-69.

Hurty, W.C., J.D. Collins, G.C. Hart. "Dynamic Analysis of Large Structures by Modal Synthesis Techniques." Computers and Structures, Vol. 1, 1971, pp. 535-563.

Klosterman, A.L. "A Combined Experimental and Analytical Procedure for Improving Automotive System Dynamics." Paper no. 720093, SAE Transactions, 1972, pp. 343-353.

Klosterman, A.L. and W.A. McClelland. "Combined Experimental and Analytical Techniques for Dynamic System Analysis." 1973 Tokyo Seminar on Finite Element Analysis, 1973.

Leuridan, J. and J. Kundrat. "Advanced Matrix Methods for Experimental Modal Analysis--a Multi-Matrix Method for Direct Parameter Extraction." International Modal Analysis Conference, November 1982.

MacNeal, R.H. "A Hybrid Method of Component Mode Synthesis." Computers and Structures, Vol. 1, 1971, pp. 581-601.

Padgaonkar, A.J., K.W. Krieger, A.I. King. "Measurement of Angular Acceleration of a Rigid Body Using Linear Accelerometers." Transactions of the ASME, September 1975, p. 552ff.

Rubin, S. "Improved Component-Mode Representation for Structural Dynamic Analysis." AIAA Journal, Vol. 13, 1975, pp. 995-1006.

Stroud, R.C., R.N. Coppolino, D.L. Hunt, S.R. Ibrahim. "Advanced Methods Used on the Galileo Spacecraft Modal Survey." 2nd International Modal Analysis Conference, Orlando, Florida, 1984, pp. 813-819.

Vold, H. and J. Leuridan. "A Generalized Frequency Domain Matrix Estimation Method for Structural Parameter Identification." University of Leuven, September 1982.

Vold, H., G.T. Rocklin. "The Numerical Implementation of a Multi-Point Modal Estimation Method for Mini-Computers." International Modal Analysis Conference, November 1982.

Vold, H., J. Kundrat, G.T. Rocklin, R. Russell. "A Multi-Input Model Estimation Algorithm for Mini-Computers." SAE Paper No. 820194, February 22-26, 1982.

A SUBSTRUCTURE COUPLING PROCEDURE APPLICABLE TO GENERAL
LINEAR TIME-INVARIANT DYNAMIC SYSTEMS

Thomas G. Howsman*
Control Dynamics Co.
Huntsville, AL

Roy R. Craig, Jr.**
The University of Texas at Austin
Austin, TX

Abstract

A substructure synthesis procedure applicable to structural systems containing general nonconservative terms is presented. In their final form, the non-self-adjoint substructure equations of motion are cast in state vector form through the use of a variational principle. A reduced-order model for each substructure will be implemented by representing the substructure as a combination of a small number of Ritz vectors. For the method presented, the substructure Ritz vectors are identified as a truncated set of substructure eigenmodes, which are typically complex, along with a set of generalized real attachment modes. The formation of the generalized attachment modes does not require any knowledge of the substructure flexible modes; hence, only the eigenmodes used explicitly as Ritz vectors need to be extracted from the substructure eigenproblem. An example problem is presented to illustrate the method.

Nomenclature

A, B	- substructure state matrices
A_{bk}, B_{bk}	- system block-diagonal matrices
A_{sys}, B_{sys}	- system state matrices
C, K, M	- substructure damping, stiffness and mass matrices
C_x, C_y	- standard, and adjoint, transformation matrices
D	- denotes dependent coordinate
e	- denotes single finite element
E_1	- interface locator matrix
E	- generalized interface locator matrix
f	- force vector
F	- state space force vector
F_A	- unit interface force vector
F_{sys}	- system force vector

I	- denotes independent coordinate
n	- number of physical substructure degrees of freedom
n_k	- number of kept eigenmodes
N_x	- total number of Ritz vectors approximating X
N_y	- total number of Ritz vectors approximating Y
v	- substructure velocity vector
w	- Lagrange multiplier vector
x	- substructure displacement vector
X	- substructure state vector
y	- substructure adjoint displacement vector
Y	- substructure adjoint state vector
η	- time-varying generalized coordinate
λ, ψ	- substructure eigenpair
σ_1, σ_2	- Lagrange multiplier vectors
ϕ	- set of generalized Ritz vectors
ϕ_{sys}, ϕ_{xsys}	- block diagonal matrices of generalized Ritz vectors
$(\cdot)^i$	- denotes interface portion
$(\cdot)^T$	- denotes matrix transpose
$(\cdot)_x$	- denotes standard quantity
$(\cdot)_y, (\cdot)^*$	- denotes adjoint quantity
$(\cdot)_{\alpha, \beta}$	- denotes substructure α, β

Introduction

Over the past several decades a multitude of substructure coupling techniques for undamped structural systems have been developed, but comparatively few authors have concerned themselves with the coupling of damped systems. It has only been in the last several years that procedures for treating systems containing veloci-

* Senior Associate Engineer
Formerly Graduate Student, Aerospace Engineering
The University of Texas at Austin

** Professor, Aerospace Engineering and Engineering Mechanics
Associate Fellow, AIAA

ty-dependent terms have been actively pursued. Several situations in which velocity-dependent terms play an important role in the dynamics of the system include those where Coriolis, aerodynamic, and perhaps most importantly, control system forces are present.

Several recent papers have established procedures applicable to damped systems, and it is from these developments that many of the ideas in the present paper are drawn.^{1,2} The Chung-Craig paper¹ develops a generalized modal synthesis procedure applicable to substructures containing symmetric mass, damping, and stiffness matrices. The equations of motion are cast into state vector form, and the substructure Ritz vectors are identified as free-interface normal modes and residual attachment modes. The residual attachment modes are formed from a linear combination of the substructure normal modes not employed explicitly as Ritz vectors.

The technique advanced by Hale² has as its basis a variational principle applicable to non-self-adjoint systems, i.e. those containing damping terms or nonsymmetries in the defining matrices (M,C,K). The variational formulation used by Hale results in an unconditionally nonsymmetric state vector equation of motion, along with its adjoint, for each substructure. The substructure Ritz vectors employed by Hale are formed by a variant of subspace iteration.

The present paper formulates a substructure coupling procedure which is applicable to systems containing velocity-dependent terms. No assumptions regarding the symmetry of the defining matrices are made. The equations of motion will be derived from a variational principle which, unlike the principle suggested by Hale, does not exclude a symmetric formulation of the substructure state matrices. Free-interface substructure state modes along with a set of generalized attachment modes serve as the substructure Ritz vectors. Contrary to the attachment modes used by Chung, the attachment modes used in the present paper do not require knowledge of the entire set of substructure eigenmodes.^{1,3} Hence, only the low-frequency eigenmodes used explicitly as Ritz vectors need to be extracted from the substructure eigenproblem.

Substructure Equations of Motion

For the purposes of this paper, it will be assumed that a discrete model of the substructure is available. When one considers the popularity of finite element modeling, the restrictions imposed by this assumption are recognized as being quite minimal.

The substructure equation of motion, written in the standard second-order form, is

$$\ddot{Mx} + \dot{C}\dot{x} + Kx = F \quad (1)$$

When written in the above form, the equation of motion possesses two properties worthy of note at this point. Perhaps the most important property of Eq. (1) is that it does not conveniently fit into an eigenproblem format. Additionally, Eq. (1) is recognized as being a non-self-adjoint differential equation - a fact that complicates the variational principle associated with the substructure equation of motion. The reason for representing the substructure by a variational principle is the ease in which approximations and

constraints can be applied to the substructure displacement field.

It can be demonstrated that the differential adjoint equation corresponding to Eq. (1) is

$$M^T \ddot{y} - C^T \dot{y} + K^T y = f^* \quad (2)$$

and that the bilinear functional whose Euler equations duplicate Eqs. (1) and (2) is

$$\pi_1 = \int_0^t [y^T (\ddot{Mx} + \dot{C}\dot{x} + Kx) - \dot{y}^T f - x^T f^*] dt \quad (3)$$

In order to cast the substructure equation of motion, along with its adjoint, into a form compatible with an eigenproblem format, a state vector substitution will be made. An obvious choice for such a substitution is

$$v = \dot{x} \quad (4)$$

The above equation is equivalent to

$$M(\dot{x} - v) = 0 \quad (5)$$

if the mass matrix is nonsingular, a condition assumed in this paper.

To derive the state vector formulation of the substructure equation of motion, the π_1 functional is modified by making the state variable substitution and by appending the constraint equation, i.e. Eq. (5), to the functional with a Lagrange multiplier vector. The modified substructure functional, to be called π_2 , is

$$\pi_2 = \int_0^t [y^T (\ddot{Mx} + \dot{C}\dot{x} + Kx) - \dot{y}^T f - x^T f^* + w^T M(\dot{x} - v)] dt \quad (6)$$

Since there are four vectors of variables (w,y,v,x) to be considered independent in the π_2 functional, there will, of course, be four Euler equations. The Euler equations are

$$M\dot{x} - Mv = 0 \quad (7a)$$

$$M\dot{v} + C\dot{x} + Kx = f \quad (7b)$$

$$-M^T \dot{y} - M^T w = 0 \quad (7c)$$

$$-M^T w - C^T \dot{y} + K^T y = f^* \quad (7d)$$

These four equations can be conveniently represented by the following two matrix equations

$$A\dot{X} + BX = F \quad (8a)$$

and

$$-A^T \dot{Y} + B^T Y = F^* \quad (8b)$$

where

$$A = \begin{bmatrix} 0 & M \\ M & C \end{bmatrix} \quad B = \begin{bmatrix} -M & 0 \\ 0 & K \end{bmatrix}$$

$$X = \begin{bmatrix} v \\ x \end{bmatrix} \quad Y = \begin{bmatrix} w \\ y \end{bmatrix} \quad F = \begin{bmatrix} 0 \\ f \end{bmatrix} \quad F^* = \begin{bmatrix} 0 \\ f^* \end{bmatrix}$$

Equation (8a) is the substructure state vector equation of motion, and Eq. (8b) is the corresponding adjoint equation. As noted in Ref. (2), the vector of Lagrange multipliers, w , plays the role of the adjoint velocity in Eq. (8b). This fact will be utilized when compatibility between substructures is considered.

It should be noted that the state vector equation of motion represented by Eq. (8a) is identical to the equation of motion employed by Chung-Craig in Ref. (1), although derived by different means. References (1) and (3), however, do not concern themselves with the substructure adjoint equation of motion, since symmetry of the defining matrices is assumed by the author. The variational principle employed herein to obtain the state vector equation of motion and its adjoint is similar to the procedure used by Hale in Ref. (2), but with an important difference. The functional used in Ref. (2) produces a state matrix which is unconditionally unsymmetric, whereas the π_2 functional, given in Eq. (6), produces state matrices which will be symmetric if the defining matrices are symmetric - a computationally favorable situation when the substructure Ritz vectors are to be calculated.

Compatibility at Substructure Interfaces

Physically, it is clear that the displacements experienced by each adjacent substructure must be identical at the common interface. For two substructures, α and β , this idea can be expressed by

$$x_{\alpha}^i = x_{\beta}^i \quad (9)$$

where i denotes the interface coordinates.

The concept of a locator matrix can be used to select out the interface degrees of freedom from the entire substructure displacement vector, thus producing

$$(E_1 x)_{\alpha} = (E_1 x)_{\beta} \quad (10)$$

Similarly, the substructure velocities must be compatible across the interface. The time derivative of Eq. (10) results in the velocity compatibility equation, i.e.

$$(E_1 \dot{v})_{\alpha} = (E_1 \dot{v})_{\beta} \quad (11)$$

While it is clear that the substructure interface velocities are indeed compatible, it is not nearly so obvious whether or not Eq. (11) must be enforced in the system functional. It would appear that the combination of Eqs. (4) and (10) implicitly produces Eq. (11). Pragmatically, Ref. (5) has shown with test problems that similar results occur with and without the inclusion of Eq. (11) in the system functional. Reference (2) draws a similar conclusion based upon the work done by Hughes et al. in Ref. (6).

Although it is not mandatory to append Eq. (11) to the system functional, it can prove to be computationally advantageous. Inclusion of the velocity constraint equation in the formulation can provide useful conditioning to the system state matrices, one of which may be singular without the explicit enforcement of Eq. (11).^{2,5}

Equations (10) and (11) can be combined into the following single matrix equation,

$$\begin{bmatrix} E_1 & 0 \\ 0 & E_1 \end{bmatrix} \begin{Bmatrix} v \\ x \end{Bmatrix}_{\alpha} = \begin{bmatrix} E_1 & 0 \\ 0 & E_1 \end{bmatrix} \begin{Bmatrix} v \\ x \end{Bmatrix}_{\beta} \quad (12)$$

or, more compactly

$$E_{\alpha} X_{\alpha} = E_{\beta} X_{\beta} \quad (13)$$

Force compatibility between adjacent substructures can be easily deduced from Newton's Third Law. The interface reaction forces are equal in magnitude and opposite in direction, a fact represented by the following equation

$$f_{\alpha}^i + f_{\beta}^i = 0 \quad (14)$$

Since the variation procedure employed involves adjoint quantities, compatibility equations between these "adjoint substructures" need to be developed. Although a physical interpretation of the adjoint equations of motion is evasive, it seems logical to assume that the adjoint compatibility equations will correspond exactly to those of the physical substructures. Hence, the adjoint compatibility equations are taken to be

$$E_{\alpha} Y_{\alpha} = E_{\beta} Y_{\beta} \quad (15)$$

and

$$f_{\alpha}^{*i} + f_{\beta}^{*i} = 0 \quad (16)$$

Development of the Coupling Procedure

As in the development of the substructure equations of motion, a variational principle will be utilized to obtain the system equation of motion.² The interface compatibility conditions developed previously will be appended to the system functional, thereby insuring the satisfaction of interface constraints. A Ritz approximation to the substructure state vector, X , and its adjoint vector, Y , will be incorporated into the final form of the system functional.

Before constructing the system functional, it will prove useful to write the substructure state vector equation of motion, and its adjoint, in the following form

$$A\dot{X} + BX = F^i + F \quad (17a)$$

and

$$-A^T \dot{Y} + B^T Y = F^{*i} + F^* \quad (17b)$$

where the interface reaction forces have been separated from the externally applied forces. The substructure functional corresponding to Eqs. (17a) and (17b) is

$$\pi_3 = \int_0^t [Y^T (A\dot{X} + BX) - Y^T (F^i + F) - X^T (F^{*i} + F^*)] dt \quad (18)$$

The system functional will be composed of each substructure functional plus the appended constraint equations. Hence, for a system con-

taining two substructures, the system functional will be

$$\pi = \pi_3^\alpha + \pi_3^\beta + \quad (19)$$

$$\int_0^t \{ \sigma_1^T [(EX)_\alpha - (EX)_\beta] + \sigma_2^T [(EY)_\alpha - (EY)_\beta] \} dt$$

where the appended constraint equations are those represented by Eqs. (13) and (15). Equation (18) can be substituted into Eq. (19) to yield

$$\begin{aligned} \pi = & \int_0^t \{ [Y^T(A\dot{X} + BX) - Y^T(F^i + F) - X^T(F^{*i} + F^*)]_\alpha \\ & + [Y^T(A\dot{X} + BX) - Y^T(F^i + F) - X^T(F^{*i} + F^*)]_\beta \\ & + \sigma_1^T [(EX)_\alpha - (EX)_\beta] + \sigma_2^T [(EY)_\alpha - (EY)_\beta] \} dt \end{aligned} \quad (20)$$

When the terms containing the interface reaction forces in Eq. (20) are examined in conjunction with the interface compatibility equations, it becomes clear that the reaction force terms vanish from the system functional.

Introduction of Ritz Vectors

In order to implement a reduced-order model, a Ritz vector approximation to the substructure generalized displacement vectors (i.e. state vectors X and Y) will be incorporated into the system functional. This Ritz approximation can be expressed as

$$X = \sum_{j=1}^{N_x} \phi_{xj} \eta_{xj} = \phi_x \eta_x \quad (21)$$

and

$$Y = \sum_{j=1}^{N_y} \phi_{yj} \eta_{yj} = \phi_y \eta_y \quad (22)$$

Clearly the number of Ritz vectors used in the approximation must not be larger than the total number of substructure degrees of freedom, i.e.

$$N_x, N_y \leq 2n \quad (23)$$

The approximate system functional is formed by substituting the Ritz approximations into the previous expression for the system functional. This new functional takes the form

$$\begin{aligned} \pi_a = & \int_0^t \{ (\eta_y^T \phi_y^T [A \phi_x \dot{\eta}_x + B \phi_x \eta_x] - \eta_y^T \phi_y^T F - \eta_x^T \phi_x^T F^*)_\alpha \\ & + (\eta_y^T \phi_y^T [A \phi_x \dot{\eta}_x + B \phi_x \eta_x] - \eta_y^T \phi_y^T F - \eta_x^T \phi_x^T F^*)_\beta \\ & + \sigma_1^T [(E \phi_x \eta_x)_\alpha - (E \phi_x \eta_x)_\beta] \\ & + \sigma_2^T [(E \phi_y \eta_y)_\alpha - (E \phi_y \eta_y)_\beta] \} dt \end{aligned} \quad (24)$$

The actual form of the Ritz vectors will be discussed after the system equation of motion is developed.

The System Equation

The Euler equations of the approximate system functional, π_a , will be the system equations of motion as well as the appropriate constraint equations. In order to insure stationarity of π_a , six quantities must be varied - $\eta_{y\alpha}$, $\eta_{x\alpha}$, $\eta_{y\beta}$, $\eta_{x\beta}$, σ_1 , and σ_2 . Accordingly, the approximate system functional will produce six Euler equations. These Euler equations are easily shown to be

$$(\phi_y^T A \phi_x \dot{\eta}_x)_\alpha + (\phi_y^T B \phi_x \eta_x)_\alpha \quad (25a)$$

$$= (\phi_y^T F)_\alpha - (\phi_y^T E^T)_\alpha \sigma_2$$

$$(\phi_y^T A \phi_x \dot{\eta}_x)_\beta + (\phi_y^T B \phi_x \eta_x)_\beta \quad (25b)$$

$$= (\phi_y^T F)_\beta + (\phi_y^T E^T)_\beta \sigma_2$$

$$-(\phi_x^T A \phi_y \dot{\eta}_y)_\alpha + (\phi_x^T B \phi_y \eta_y)_\alpha \quad (25c)$$

$$= (\phi_x^T F^*)_\alpha - (\phi_x^T E^T)_\alpha \sigma_1$$

$$-(\phi_x^T A \phi_y \dot{\eta}_y)_\beta + (\phi_x^T B \phi_y \eta_y)_\beta \quad (25d)$$

$$= (\phi_x^T F^*)_\beta + (\phi_x^T E^T)_\beta \sigma_1$$

$$(E \phi_x \eta_x)_\alpha - (E \phi_x \eta_x)_\beta = 0 \quad (25e)$$

$$(E \phi_y \eta_y)_\alpha - (E \phi_y \eta_y)_\beta = 0 \quad (25f)$$

Equations (25a) and (25b) are equivalent to the following block-diagonal matrix equation

$$\begin{bmatrix} \phi_{y\alpha} & 0 \\ 0 & \phi_{y\beta} \end{bmatrix}^T \begin{bmatrix} A_\alpha & 0 \\ 0 & A_\beta \end{bmatrix} \begin{bmatrix} \phi_{x\alpha} & 0 \\ 0 & \phi_{x\beta} \end{bmatrix} \begin{Bmatrix} \dot{\eta}_{x\alpha} \\ \dot{\eta}_{x\beta} \end{Bmatrix} +$$

$$\begin{bmatrix} \phi_{y\alpha} & 0 \\ 0 & \phi_{y\beta} \end{bmatrix}^T \begin{bmatrix} B_\alpha & 0 \\ 0 & B_\beta \end{bmatrix} \begin{bmatrix} \phi_{x\alpha} & 0 \\ 0 & \phi_{x\beta} \end{bmatrix} \begin{Bmatrix} \eta_{x\alpha} \\ \eta_{x\beta} \end{Bmatrix} = \quad (26)$$

$$\begin{bmatrix} \phi_{y\alpha} & 0 \\ 0 & \phi_{y\beta} \end{bmatrix}^T \begin{Bmatrix} F_\alpha \\ F_\beta \end{Bmatrix} + [-(E \phi_y)_\alpha \quad (E \phi_y)_\beta]^T \sigma_2$$

or, more compactly

$$\dot{\phi}_{ysys}^T A_{bk} \phi_{xsys} + \phi_{ysys}^T B_{bk} \phi_{xsys} \eta = \quad (27)$$

$$\phi_{ysys}^T F + [-(E\phi_y)_\alpha \quad (E\phi_y)_\beta]^T \sigma_2$$

where ϕ_{ysys} , ϕ_{xsys} , A_{bk} , B_{bk} are simply the block-diagonal matrices represented in Eq. (26). Logically, Eqs. (25c) and (25d) can be combined into a single equation corresponding to the adjoint of Eq. (27).

At this point, the equations of motion for each substructure have yet to be coupled in their final form. Indeed, the system equation represented by Eq. (27) is coupled only by the unknown vector of Lagrange multipliers, which can be directly related to the substructure interface reaction forces. The system equation of motion cannot be solved until σ_2 is in some way eliminated. The elimination of σ_2 will be achieved by applying the constraint equations to Eq. (26).⁷

Equation (25f), which represents a constraint on the adjoint Ritz coordinates, can be cast in a more convenient form such as

$$[(E\phi_y)_\alpha - (E\phi_y)_\beta] \begin{Bmatrix} \eta_{y\alpha} \\ \eta_{y\beta} \end{Bmatrix} = 0 \quad (28)$$

By its very existence, the above constraint equation implies that not all of the substructure generalized adjoint coordinates (η_v 's) are independent. If Eq. (28) is partitioned into user-defined dependent and independent coordinates, the following equation results

$$[(E\phi_y)_I - (E\phi_y)_D] \begin{Bmatrix} \eta_{yI} \\ \eta_{yD} \end{Bmatrix} = 0 \quad (29)$$

where the number of dependent coordinates is equal to the number of constraints to be enforced.

Manipulation of Eq. (29) leads directly to the following transformation

$$\begin{Bmatrix} \eta_{yI} \\ \eta_{yD} \end{Bmatrix} = \begin{bmatrix} I_I & - & - & - \\ - & - & - & - \\ -(E\phi_y)_D & I & - & - \\ - & - & - & - \end{bmatrix} \eta_{yI} \quad (30)$$

The transformation matrix in the above equation will be designated as C_y for brevity. An important property of the above transformation matrix, to be applied shortly, is the following identity,

$$[(E\phi_y)_I \quad (E\phi_y)_D] C_y = 0 \quad (31)$$

Naturally, a set of equations corresponding to Eqs. (28-31) exists for the standard substructure generalized coordinates (η_x 's). For example, the complement to Eq. (30) can be written as

$$\begin{Bmatrix} \eta_{xI} \\ \eta_{xD} \end{Bmatrix} = C_x \eta_{xI} \quad (32)$$

If Eq. (32) is substituted into Eq. (27), and the result premultiplied by C_y^T , the following form of the system equation of motion results

$$C_y^T \dot{\phi}_{ysys}^T A_{bk} \phi_{xsys} C_x \dot{\eta}_{xI} + \quad (33)$$

$$C_y^T \phi_{ysys}^T B_{bk} \phi_{xsys} C_x \eta_{xI} =$$

$$C_y^T \phi_{ysys}^T F + C_y^T [-(E\phi_y)_I \quad (E\phi_y)_D]^T \sigma_2$$

In the formulation of the above equation, it has been implicitly assumed that the substructure Ritz vectors have been arranged in such a manner as to be compatible with the arrangements in Eq. (29) and its complement.

The coefficient of the σ_2 term in Eq. (33) is seen to be the transpose of Eq. (31); thus the unknown Lagrange multiplier vector is eliminated from the system equation of motion. The system equation of motion can now be written in its final form, i.e.

$$A_{sys} \dot{\eta}_{sys} + B_{sys} \eta_{sys} = F_{sys} \quad (34)$$

where

$$A_{sys} = C_y^T \dot{\phi}_{ysys}^T A_{bk} \phi_{xsys} C_x \quad (35a)$$

$$B_{sys} = C_y^T \phi_{ysys}^T B_{bk} \phi_{xsys} C_x \quad (35b)$$

$$F_{sys} = C_y^T \phi_{ysys}^T F \quad (35c)$$

and

$$\eta_{sys} \equiv \eta_{xI} \quad (35d)$$

A system adjoint equation of motion can be formed in a manner analogous to the procedure used to form Eq. (34). However, unless one wishes to diagonalize Eq. (34) by making use of the bi-orthogonality property of the adjoint eigenvectors, it appears that the system adjoint equation of motion is of little interest.

Component Ritz Vectors

Throughout the evolution of substructure coupling techniques, the formation and selection of component Ritz vectors has been a topic of much investigation, and justifiably so. The less computational effort spent defining the component Ritz vectors, the "cheaper" the overall coupling process. The vast majority of substructure coupling techniques employ a truncated set of component modes along with a set of static displacement vectors as the component Ritz vectors, hence the term "component mode synthesis." This is not to say that alternate methods of defining substructure Ritz vectors don't exist, for they do. Hale and Meirovitch have advocated the use of so-called "admissible vectors," which have ranged in sophistication from finite element shape functions to variants of subspace iteration

generated vectors.^{2,8,9,10} Unfortunately, a comparison between the different types of Ritz vectors which takes into account system accuracy versus computational cost has yet to be undertaken.

For the coupling procedure being developed, a truncated set of substructure modes augmented by a set of generalized attachment modes will be employed as the set of substructure Ritz vectors. There are two primary reasons for choosing this particular combination of Ritz vectors - first, the relative ease of obtaining these types of Ritz vectors, and second, the proven accuracy of methods employing normal and attachment modes for undamped systems.⁷

The only requirements that the Ritz vectors must satisfy are that they be independent and that they satisfy the geometric boundary conditions of the substructure. This being the case, there is nothing to preclude choosing the two classes of Ritz vectors, standard and adjoint, to be identical², i.e.

$$\phi_y = \phi_x \quad (36)$$

The computational effort saved by implementing the above equation can be quite substantial when large systems are considered.

Substructure Modes

The term "substructure mode" will apply to the eigenvectors of the substructure state vector equation. These free-interface modes are obtained by substituting $X = \psi_x e^{\lambda t}$ into the homogeneous form of Eq. (8a), i.e.

$$\lambda A \psi_x + B \psi_x = 0 \quad (37)$$

Equation (37) is recognized as a generalized eigenproblem, and can be readily solved by a number of algorithms. Generally the eigenvectors obtained from Eq. (37) are complex, and commonly come in complex conjugate pairs.

As stated previously, the reduced-order system model will utilize a number of the substructure modes as Ritz vectors. Typically, the low frequency modes are considered the most significant to the system dynamics, and are therefore used as Ritz vectors. The high frequency modes are usually not employed as Ritz vectors, therefore eliminating the need for their calculation.

Attachment Modes

Intuitively, it is clear that if only a portion of the substructure modes are utilized as Ritz vectors, then the substructure has lost the flexibility of the discarded modes. The so-called attachment modes represent an attempt to regain a significant portion of the flexibility lost due to the modal truncation.

A number of papers have dealt with attachment modes for undamped systems, and Ref. (7) offers a review of these. Chung has developed a procedure for forming a type of attachment mode for damped systems which results in excellent system accuracies.^{1,3} However, the attachment modes developed by Chung require the solution of the entire

substructure eigenproblem, since the attachment modes are formed as a combination of the substructure modes not kept explicitly as Ritz vectors. The solution of the entire substructure eigenproblem may prove to be an enormous occupational burden if the substructure contains a large number of degrees of freedom; therefore, an alternate method of defining the attachment modes is desirable.

In a manner paralleling the traditional definition of an attachment mode, this paper will consider a generalized standard attachment mode to be the pseudo-static response of the substructure to a unit load applied at the interface. This idea can be represented by the following equation

$$B \psi_A = F_A \quad (38)$$

The fact that F_A can have only one non-zero element makes it clear ψ_A is simply a column of the generalized flexibility matrix, B^{-1} . The block-diagonal nature of B indicates that the upper n elements in the state vector represent velocity coordinates.

It can be shown that if ψ_x and ψ_y are normalized such that

$$\psi_y^T A \psi_x = 1 \quad (39)$$

then

$$B^{-1} = \sum_{i=1}^{n_k} \frac{\psi_{ix} \psi_{iy}^T}{-\lambda_i} + \sum_{i=n_k+1}^{2n} \frac{\psi_{ix} \psi_{iy}^T}{-\lambda_i} \quad (40)$$

where n_k is the number of substructure modes kept explicitly as Ritz vectors.⁵ The residual flexibility matrix can be defined from Eq. (40) as

$$B_{RES}^{-1} = \sum_{i=n_k+1}^{2n} \frac{\psi_{ix} \psi_{iy}^T}{-\lambda_i} \quad (41)$$

or

$$B_{res}^{-1} = B^{-1} - \sum_{i=1}^{n_k} \frac{\psi_{ix} \psi_{iy}^T}{-\lambda_i} \quad (42)$$

Generalized residual attachment modes can be defined as the columns of the above residual flexibility matrix, as was done for the generalized standard attachment modes. It is clear from Eq. (42) that the computation of residual attachment modes requires at least the calculation of the first n_k adjoint eigenvectors - a situation that was avoided previously.

For substructures possessing rigid-body modes, it is clear that B^{-1} does not exist, thus invalidating Eqs. (38) and (42). A simple, yet effective, method of defining attachment modes for unrestrained substructures is to constrain the substructure at user-defined degrees of freedom.⁷ The degrees of freedom are chosen such that rigid-body motion is prevented, thus allowing equations similar to Eq. (38) or (42) to be written.

Due to the potentially large computational costs associated with the formation of the generalized residual attachment modes, it is felt that the computationally "cheap" generalized standard attachment modes provide the most advantageous method of reintroducing the flexibility lost in the modal truncation.

Since some of the substructure Ritz vectors are complex, it is clear that the system state matrices will be complex, as can be seen from Eqs. (35a) and (35b). Naturally, the system eigenproblem will also be complex, and will be of order $n_k + n_k$ if an attachment mode is calculated for each interface degree of freedom and if all displacement and velocity constraints are explicitly enforced.

Example Problem

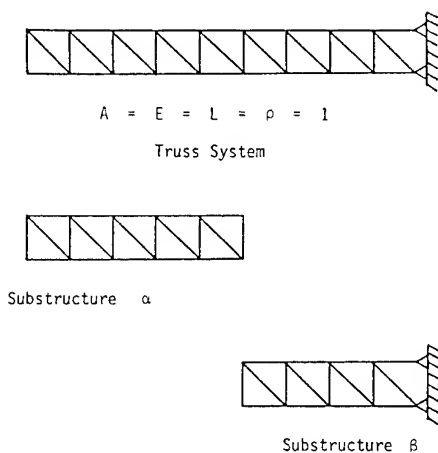


Figure 1 - 36 DOF Pin-Jointed Truss

As an example of the substructure coupling method presented in this paper, the truss structure shown in Fig. 1 will be analyzed. The entire system contains 36 physical degrees of freedom, which corresponds to 72 state variables. The horizontal members of the truss have nonsymmetric damping matrices associated with them, and are of the form

$$[C]_{\alpha}^e = .05 [C]^e \quad \text{and} \quad [C]_{\beta}^e = .075 [C]^e$$

where

$$[C]^e = \begin{bmatrix} 1 & 1 \\ -1 & 1 \end{bmatrix}$$

The nature of this problem permits an assessment to be made of the ability of the coupling procedure to deal with such potential problems as nonsymmetric, nonproportional damping and rigid-body modes simultaneously. The substructure Ritz vectors are accounted for below.

Substructure α :	18	complex flexible modes
	6	real rigid-body modes
	4	real attachment modes
Substructure β :	14	complex flexible modes
	4	real attachment modes

Since there are 4 interface degrees of freedom, the approximate system eigenproblem is of order 38. A comparison between the exact and the approximate system eigenvalues ($\lambda_{\text{sys}} = \sigma + i\omega_d$) is given in Table 1. As Table 1 indicates, the coupling procedure provides 8 pairs of complex conjugate system eigenvalues that have a maximum error of less than 4% in the damping coefficient. The oscillatory portion of the eigenvector is seen to be quite accurate for all eigenvalue pairs shown.

Summary

A substructure coupling procedure that is applicable to systems containing nonproportional, even nonsymmetric, damping terms has been presented in this paper. A state vector formulation of the equation of motion is arrived at through a variational principle which recognizes the non-self-adjointness of the equations of motion. The combination of substructure generalized eigenmodes and attachment modes serving as the substructure Ritz vectors appears to represent the dynamics of the low-frequency system modes quite well.

Acknowledgment

This work was supported by NASA Contract NAS8-35338 with Marshall Space Flight Center. The interest and encouragement of the contract monitor, Mr. Larry Kiefling, are gratefully acknowledged.

References

1. Chung, Y.T. and Craig, R.R., "State Vector Formulation of Substructure Coupling For Damped Systems," Paper No. 83-0965, AIAA/ASME/ASCE/AHS 24th Structures, Structural Dynamics, and Materials Conference, Lake Tahoe, May, 1983. pp. 520-528.
2. Hale, A.L., "Substructure Synthesis and Its Iterative Improvement for Large Nonconservative Vibratory Systems," *AIAA Journal*, Vol. 22, No. 2, Feb. 1984, pp. 265-272.
3. Chung, Y.T., "Application and Experimental Determination of Substructure Coupling for Damped Structural Systems," Ph.D. Dissertation, The University of Texas at Austin, Austin, TX, 1982.
4. Finlayson, B.A., *The Method of Weighted Residuals and Variational Principles*, Academic Press, Inc., New York, 1972.

5. Howsman, T.G., "A Substructure Coupling Procedure Applicable to General Linear Time-Invariant Damping Systems," M.S. Thesis, The University of Texas at Austin, Austin, TX, 1983.
6. Hughes, T.J.R., Hilber, H.M., and Taylor, R.L., "A Reduction Scheme for Problems of Structural Dynamics," International Journal of Solids and Structures, Vol. 12, 1976, pp. 749-767.
7. Craig, R.R., Jr. and Chang, C.J., "On the Use of Attachment Modes in Substructure Coupling for Dynamic Analysis," Paper No. 77-405, AIAA/ASME/ASCE/AHS 18th Structures, Structural Dynamics and Materials Conference, San Diego, March, 1977, pp. 89-99.
8. Hale, A.L. and Meirovitch, L., "A General Substructure Synthesis Method for the Dynamic Simulation of Complex Structures," Journal of Sound and Vibration, Vol. 69, 1980, pp. 309-326.
9. Meirovitch, L. and Hale, A.L., "A General Dynamic Synthesis for Structures with Discrete Substructures," Paper No. 80-0798, AIAA/ASME/ASCE/AHS 21st Structures, Structural Dynamics, and Materials Conference, Seattle, May, 1980, pp. 790-800.
10. Meirovitch, L. and Hale, A.L., "On the Substructure Synthesis Method," AIAA Journal, Vol. 19, No. 7, July, 1981, pp. 940-947.

Eigenvalue Number	σ	Exact ω_d	σ	Approximate ω_d	σ % Error	ω_d % Error
1	-.852E-3	.209E0	-.825E-3	.210E0	-3.266	.524
2	-.874E-2	.195E0	-.883E-2	.196E0	.993	.580
3	-.695E-3	.151E0	-.678E-3	.152E0	-2.480	.634
4	-.622E-3	.951E-1	-.621E-3	.952E-1	-.239	.034
5	-.726E-2	.646E-1	-.729E-2	.651E-1	.430	.743
6	-.499E-3	.421E-1	-.498E-3	.422E-1	-.197	.105
7	-.112E-3	.853E-2	-.112E-3	.853E-2	.026	.004
8	-.127E-2	.262E0	-.128E-2	.265E0	.939	1.275
9	-.556E-2	.304E0	-.650E-2	.308E0	16.861	1.338
10	-.234E-2	.320E0	-.156E-2	.327E0	-33.258	2.293
11	-.934E-2	.323E0	-.935E-2	.329E0	.128	2.080
12	-.108E-2	.365E0	-.111E-2	.369E0	2.728	.993
13	-.735E-2	.381E0	-.845E-2	.395E0	14.921	3.638

Table 1 - Comparison of Exact and Approximate System Eigenvalues for Example Problem.
All eigenvalues shown are one of a pair of complex conjugates.

THE SPACE SHUTTLE PAYLOAD TRANSIENT LOADS ANALYSIS BY THE FLEX-BASE DRIVE METHOD

By

Kenji Kubomura
Member of the Technical Staff
Rockwell International
Downey, California

Abstract

A flex-base drive method has been developed for analysis of linear transient loads. Results of an analysis are presented, and investigations needed for implementation of this method for Space Shuttle payload transient load are discussed. Two payload configurations of the orbiter landing model were analyzed by both the proposed and conventional methods. The first configuration contained only one payload, the second three payloads. Results show that the method can be substituted for the current coupled loads analysis method for certain types of payload. The flex-base drive method involves time integration of the payload equations of motion and the simultaneous calculation of the interface reaction forces without structurally coupling the orbiter. It enables a payload design organization to perform a design/loads analysis cycle independently with minimal information from the Space Shuttle orbiter, while still adequately predicting the effects of orbiter/payload dynamic interaction. This method has a great advantage over the conventional linear transient loads analysis when the analysis involves determination of payload configuration and frequent changes of payload structure.

1. Introduction

While each Space Transportation System (STS) flight is being prepared, payloads are being designed and analyzed. Severe structural dynamic environments are expected during lift-off and landing of the Space Shuttle orbiter. The analysis of linear transient loads is performed for verification analysis of the structural loads. The Space Shuttle system is subjected to transient loads that represent propulsive forces, aerodynamic forces, acoustic forces, etc. The system substructures such as a Space Shuttle orbiter, one external tank, two solid rocket boosters, and payloads are represented in terms of stiffness, damping, and mass matrices called mathematical models. The matrix size of each substructure mathematical model is reduced and coupled by substructure modal synthesis.¹ The system equations of motion are decoupled by eigenanalysis and modally truncated. The decoupled equations of motion are time-integrated, and dynamic responses are calculated to assess orbiter and payload structural integrity. Considerable time and cost are required to integrate the composite models and response analysis. This is because (1) the model is very large and (2) typically each payload is developed and designed by a different organization and then integrated with the Space Shuttle orbiter by still another organization. Since the mathematical models of payloads are based on payload structural design, the design/analysis is an iterative process. Whenever a design change occurs, all costly and time-consuming analysis processes are repeated in the present loads analysis procedure. Thus, methods of analyzing transient loads have been sought that separate the payload analysis from the orbiter to the maximum and eliminate the need for repetition of similar processes in the analysis.

When a design change in the minor structure (payload) is small, the perturbation technique can be applied for the transient loads analysis of the system structure.² In this technique, a transient loads analysis solution of the original structure is used in conjunction with slightly modified system mass and stiffness matrices.

When the payload supports are statically determined in a launch vehicle, the reaction forces on the payloads from the launch vehicle can be expressed with payload mass and accelerations at the payload/launch vehicle interfaces. Taking account of this, Payne computed the Fourier coefficients of interface accelerations without coupling the payloads and launch vehicle.³ The launch vehicle and payload eigenvalues and eigenvectors are used for computation of the transfer function from the Fourier coefficients of external forces. Trubert and Salama developed a method called the Generalized Modal Shock Spectra Method for payloads that are supported in a statically determinant manner in a launch vehicle.⁴ When the stiffness and mass matrices are reduced in size with the Craig-Bampton method, the reduced stiffness and mass matrices become nearly orthogonal, except for the degrees of freedom pertinent to the interface.⁵ Engels et al. applied this to the transient loads analysis of the Space Shuttle structure without performing an eigenanalysis of the payloads and Shuttle-coupled structure.⁶ Chen et al. decomposed the response of the system structure into (a) the response of the launch vehicle and determinantly supported payload and (b) the response arising from the elastic coupling of them.⁷ The equation of motion for the coupled structure is rewritten for the latter response, with the former response being considered as an applied load to this equation.

As discussed by Chen et al., applications and advantages of these methods are limited to special conditions because of the assumptions used in their development.⁸ The analysis methods have been sought to accommodate all the following needs of the Space Shuttle payload dynamic loads analysis:

1. To simplify the analytical process, thus providing results in a timely manner due to minimal interaction between the various payload design organizations.
2. To enable a payload design organization to perform a design/load analysis cycle independently while adequately predicting the effects of orbiter and payload dynamic interaction.
3. To minimize repetition of analytic processes so that payload structural design changes can be evaluated in a timely manner with the minimum possible expense.

It appears that no one method among those discussed can accommodate even one of the needs of the Space Shuttle payload dynamic loads analysis method.

The method proposed in this paper is aimed at the third item. The analysis by the proposed method requires the following information:

1. The eigenvalues of the orbiter and payloads
2. The interface partitioned free-free modes of the orbiter and payloads
3. The displacement and velocity time histories of the empty orbiter at the interface

4. The initial values of accelerations at the empty orbiter interface degree of freedom.

When Space Shuttle and payload-coupled systems are analyzed, analysis results can be converted to satisfy the aforementioned requirements.

The method involves solving the payload equations of motion and simultaneously calculating the orbiter and payload reaction forces. The influence of the applied forces and orbiter structure on the payload dynamic response is accounted for through the displacements and velocities of the empty orbiter at the interface. The reaction forces on payloads from the orbiter are treated as external forces during the time integration of the payload equations of motion in a time incremental form. The equilibrium and compatibility conditions at the orbiter and payload interfaces determine reaction forces while accounting for orbiter and payload structural properties.

Generally, response of a linear structure is expressed as the sum of the free and forced vibration responses. Response of the substructure is also expressed as the sum of the free and forced vibration responses by the reaction and applied forces. The reaction forces acting during a sufficiently small time interval are interpolated by using known values at the beginning of the interval and the unknown values at the end of the interval. The response by reaction forces during this interval consists of responses pertinent to known and unknown reaction forces. From the equilibrium and compatibility conditions at the interface of the orbiter and payload, the unknown reaction forces can be solved and expressed as a function of orbiter and payload structural properties, the response to known reaction forces, and the free and forced vibration responses by applied forces. With the calculated reaction forces and the applied forces acting on the orbiter, the response at the end of the interval is calculated, and time integration advances to the next time step.

2. Formulation of Flex-Base Drive Method

Presently, several payload structures are coupled to a Space Shuttle structural model to construct a system equation of motion for analysis of transient loads. The system equation is decoupled by eigenanalysis, and then decoupled equations of motion are time-integrated. The method presented here does not involve structural coupling of payloads and an orbiter. Instead, the equations of motion for payloads are solved by calculating reaction forces from the orbiter structure. The reaction forces are calculated so that compatibility and equilibrium are satisfied at the payload and orbiter interfaces. The displacement and velocity compatibility in the least-square sense is used in formulation of equations to calculate the reaction forces.

In this section, development of the flex base drive method for the Space Shuttle orbiter and payload transient loads analysis will be summarized. The response of a substructure at time $t + dt$ is expressed as the sum of responses due to the forced vibration during the time interval t and $t + dt$, and the free vibration from time t . The forces acting on the substructure are decomposed into externally applied forces, $F(t)$, and reaction forces, $R(t)$, from adjacent substructures. The response at time $t + dt$ due to the free vibration can be decomposed into those associated with external forces and reaction forces. Thus, the response such as displacement, velocity, and acceleration at the interface are written in the form

$$\begin{aligned} \underline{g}_b^{t+dt} = & \int_t^{t+dt} \underline{G}_{bb}(t+dt-z) \underline{R}(z) dz + \underline{R}_g b^{t+dt} \\ & + \int_t^{t+dt} \underline{G}_b(t+dt-z) \underline{F}(z) dz + \underline{A}_g b^{t+dt} \end{aligned} \quad (1)$$

The first term represents the interface response by the reaction forces, where matrix $\underline{G}_{bb}(z)$ is a matrix of the interface partitioned impulse response of the substructure. The second term represents the response of substructure vibration from time t with the initial values (displacements and velocities) of time t which were activated solely by the reaction forces up to time t from the beginning of the analysis. The third represents the response of forced vibration by the applied forces during the time interval. The fourth term represents the response of free vibration with the initial displacements and velocities activated by the applied forces. The sum of third and fourth terms represents the interface response of the substructure caused solely by the applied forces. The sum of first two terms represents the interface response caused solely by the reaction forces. The reaction forces, $\underline{R}(z)$, on the substructure are calculated from compatibility and equilibrium at all substructure interfaces, while the applied forces are known during the time interval. The reaction forces during the interval must be calculated before the payload equations of motion are integrated if a system equation of motion is not formulated. For this purpose the reaction forces during the time interval t and $t + dt$ are linearly interpolated with known values, \underline{R}^t , at the beginning of the interval and unknown values, \underline{R}^{t+dt} , at the end of the interval, i.e.

$$\underline{R}(z) = (1 - z/dt) \underline{R}^t + z/dt \underline{R}^{t+dt} \quad (2)$$

Introducing the interpolation of reaction forces into equation (1), performing the time integration and rearranging the terms result in the form for the interface displacement \underline{U}_b^{t+dt} at time $t + dt$:

$$\underline{U}_b^{t+dt} = \underline{A}_{bb} \underline{R}^t + \underline{B}_{bb} \underline{R}^{t+dt} + \underline{R}_U b^{t+dt} + \underline{A}_U b^{t+dt} \quad (3)$$

where

$\underline{A}_U b^{t+dt}$ is a vector of interface displacements at time $t + dt$ by the applied forces and $\underline{R}_U b^{t+dt}$ is a vector of free vibration displacements by the reaction forces. Matrices \underline{A}_{bb} and \underline{B}_{bb} are obtained from the corresponding integrations in equation (1). The similar expression for the interface velocity \underline{U}_b^{t+dt} is derived; i.e.

$$\dot{\underline{U}}_b^{t+dt} = \dot{\underline{A}}_{bb} \underline{R}^t + \dot{\underline{B}}_{bb} \underline{R}^{t+dt} + \underline{R}_{\dot{U}} b^{t+dt} + \underline{A}_{\dot{U}} b^{t+dt} \quad (4)$$

where

$\underline{A}_{\dot{U}} b^{t+dt}$ is the velocity associated with the applied forces and $\underline{R}_{\dot{U}} b^{t+dt}$ is the free vibration velocity associated with the interface reaction forces. Vectors $\underline{A}_U b^{t+dt}$ and $\underline{A}_{\dot{U}} b^{t+dt}$, which are associated with the applied forces, can be calculated independently for the orbiter. Reaction forces \underline{R}^t are assumed known from the previous time interval. Free vibration displacement $\underline{R}_U b^{t+dt}$ and velocity $\underline{R}_{\dot{U}} b^{t+dt}$ are time-integrated by using the displacement and velocity at time t . Thus, the displacement and velocity at time $t + dt$ can be integrated if reaction forces \underline{R}^{t+dt} at time $t + dt$ are known. The transient loads analysis can advance to the next time step if the reaction forces, displacement, and velocity at the end of the time interval are used as those at the beginning of the next time interval. Both displacement and velocity compatibilities are used for calculation of reaction forces at time $t + dt$. The reaction forces at the very beginning of the analysis are calculated through the displacement compatibility and equilibrium conditions.

3. The Calculation of Interface Reaction Forces

For convenience of the formulation, consider one payload, S , to be mounted in the bay of the Space Shuttle orbiter, O . The

displacements and velocities of structures O and S are continuous across the interface. The reaction forces are the same in magnitude and opposite in direction. Superscripts o and s are assigned to equations (3) and (4) to indicate quantities to be pertinent to structures O and S, respectively. There is one unknown reaction force at each interface degree of freedom and there are two compatibility conditions to be constrained. Therefore, the compatibilities are forced by a means of the least square. Now, the problem is to seek the reaction forces \underline{R}_b^{t+dt} which minimize function W defined by

$$W = (\underline{o}\underline{U}_b^{t+dt} - \underline{s}\underline{U}_b^{t+dt})^2 + (\underline{o}\underline{U}_b^{t+dt} - \underline{s}\underline{U}_b^{t+dt})^2 \quad (5)$$

Introducing equations (3) and (4) into equation (5), taking derivatives of W with respect to \underline{R}_b^{t+dt} , equating the resulting equations zero and rearranging the terms result in the form

$$\underline{H}_{bb}\underline{R}_b^{t+dt} = \underline{L}_{bb}\underline{R}_b^t + \underline{L}_{bb}\underline{DU} + \underline{K}_{bb}\underline{DU} \quad (6)$$

where

$$\underline{H}_{bb} = (\underline{o}\underline{B}_{bb} + \underline{s}\underline{B}_{bb})^T (\underline{o}\underline{B}_{bb} + \underline{s}\underline{B}_{bb}) + (\underline{o}\underline{B}_{bb} + \underline{s}\underline{B}_{bb})^T (\underline{o}\underline{B}_{bb} + \underline{s}\underline{B}_{bb})$$

$$\underline{L}_{bb} = (\underline{o}\underline{B}_{bb} + \underline{s}\underline{B}_{bb})^T (\underline{o}\underline{A}_{bb} + \underline{s}\underline{A}_{bb}) + (\underline{o}\underline{B}_{bb} + \underline{s}\underline{B}_{bb})^T (\underline{o}\underline{A}_{bb} + \underline{s}\underline{A}_{bb})$$

$$\underline{L}_{bb} = (\underline{o}\underline{B}_{bb} + \underline{s}\underline{B}_{bb})^T$$

$$\underline{K}_{bb} = (\underline{o}\underline{B}_{bb} + \underline{s}\underline{B}_{bb})^T$$

$$\underline{DU} = \underline{o}(\underline{R}_b^{t+dt}) + \underline{o}(\underline{A}_b^{t+dt}) - \underline{s}(\underline{R}_b^{t+dt}) - \underline{s}(\underline{A}_b^{t+dt})$$

$$\underline{DU} = \underline{o}(\underline{R}_b^{t+dt}) + \underline{o}(\underline{A}_b^{t+dt}) - \underline{s}(\underline{R}_b^{t+dt}) - \underline{s}(\underline{A}_b^{t+dt})$$

Free vibration displacements $\underline{o}(\underline{R}_b^{t+dt})$ and $\underline{s}(\underline{R}_b^{t+dt})$ and velocities $\underline{o}(\underline{U}_b^{t+dt})$ and $\underline{s}(\underline{U}_b^{t+dt})$, which are associated with reaction forces, are calculated from displacements and velocities at the beginning of the time interval. Displacements $\underline{o}(\underline{A}_b^{t+dt})$ and $\underline{s}(\underline{A}_b^{t+dt})$ and velocities $\underline{o}(\underline{U}_b^{t+dt})$ and $\underline{s}(\underline{U}_b^{t+dt})$, which are associated with the applied forces, are obtained from the time integration of the Space Shuttle empty orbiter equation of motion subjected to the applied forces only. Thus, the right-hand side of equation (5) can be solved for the reaction forces at the end of the interval.

4. Analysis

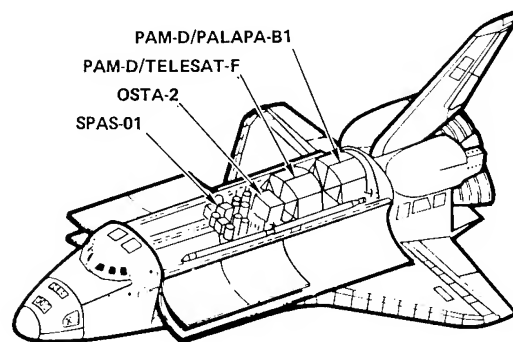
The STS-7 landing Space Shuttle orbiter and payload models are used in conjunction with a landing forcing function in the flex-base drive method of analysis. The Space Shuttle orbiter consists of many substructures: two wings, a vertical tail, a cabin, a fuselage, and bridges that support payload structures in the orbiter bay (Fig. 1). Each substructure is modeled by a very large number of finite elements. The Guyan method is used for the substantial reduction of substructure degrees of freedom of the finite element models.⁹ The orbiter landing dynamic model is developed by syn-

thesizing the reduced finite element models. The model is described by 1044 physical degrees of freedom. The mass description is contained in Fig. 1.

Three STS-7 payload models are used in the analysis: OSTA-2, PAM-D/Telesat-F, and PAM-D/PALAPA-B1. In the STS-7 load verification analysis, SPAS-01 and four GAS beams are included, in addition to the aforementioned payloads. The models were generated for the STS-7 loads verification analysis and documented by Chao et al.¹⁰

The OSTA-2 original stiffness and mass matrices were generated by NASTRAN and truncated first by the Guyan and then Craig-Bampton methods down to 21 degrees of freedom.^{9,5} The model is characterized by seven attach degrees of freedom and 16 modal coordinates associated with cantilever modes of frequencies up to 72.93 Hz. The PAM-D/Telesat-F and PAM-D/PALAPA-B1 models were provided by the Hughes Aircraft Company Space and Communications Group, El Segundo, California. Both models consist of 70 degrees of freedom, and their stiffness and mass matrices are labeled by seven attach degrees of freedom and 63 modal coordinates associated with cantilever modes of frequencies up to about 60 Hz. All three payloads are supported at seven degrees of freedom with the orbiter. The descriptions of these support degrees of freedom are right-hand forward bridge fitting X-DOF (RH FWD X), right-hand forward bridge fitting Z-DOF (RH FWD Z), right-hand after bridge fitting Z-DOF (RH AFT Z), left-hand forward bridge fitting X-DOF (LH FWD X), left-hand forward bridge fitting Z-DOF (LH FWD Z), left-hand after bridge fitting Z-DOF (LH AFT Z) and keel bridge fitting Y-DOF (KEEL Y). They are illustrated in Fig. 2.

The model used in calculation of the landing forcing function consists of complex nonlinear representations of the main landing gear attached to the orbiter plus STS-7 cargo elements. Aerodynamic forces and an active control system are included. No cross wind is included. The vehicle is considered to be in aerodynamic trim at the moment of main gear impact. The low horizontal speed of 153 knots and high sink speed of 9.6 feet per second were considered. The angle of attack is 17.12 degrees.



STS-7 CARGO CONFIGURATION MASS AND C.G.

PAYLOAD	PAYLOAD CENTER OF GRAVITY (IN.)			PAYLOAD WEIGHT (LB)
	X CG	Y CG	Z CG	
SPAS-01	899.94	0.53	399.97	4000
OSTA-2	994.725	-3.552	413.705	4717.82
TELESAT-F	1096.174	2.372	378.797	9803.42
PALAPA-B1	1241.674	2.372	378.797	9803.42
COMBINED PAYLOADS	1101.92	1.13	387.60	28324.66

COORDINATES GIVEN IN THE ORBITER COORDINATE SYSTEM

Fig. 1 STS-7 payload configuration.

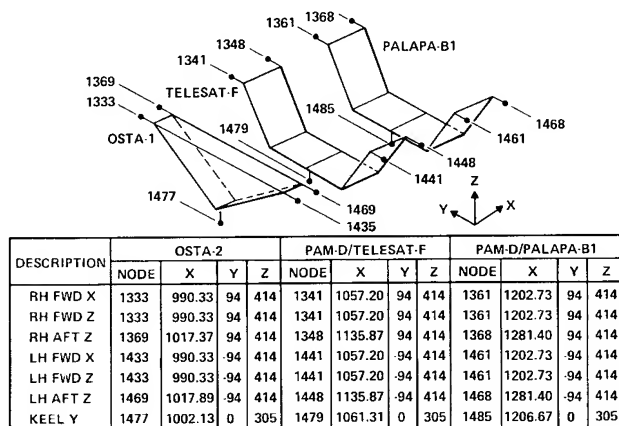


Fig. 2 STS-7 payload attach point definition.

First, the landing forcing function is used to analyze the empty landing orbiter model without coupling any payload in its bay. The orbiter stiffness and mass matrices are reduced by the Rubin-MacNeal method down to 277 degrees of freedom.^{11,12} The reduced matrices of the orbiter are characterized by 27 attach degrees of freedom and 250 modal coordinates associated with free-free modes of frequencies up to 54 Hz. The free-free mode eigenvectors and eigenvalues are calculated from the empty orbiter reduced stiffness and mass matrices. The empty orbiter equation of motion is decoupled by transforming it into the modal coordinate system. Decoupled equations of motion are time-integrated for 197 modal coordinates of frequency up to 40 Hz. The time increment used for integration is 0.001 seconds, which is the same time increment used in the landing payload loads verification analysis.

When proportional damping is used for orbiter and payload structures, the damping matrix in the orbiter and payload-coupled system equation becomes nonproportional. Thus, the assumption of proportional damping in the present loads verification analysis is an approximation of the coupled damping matrix. The flex-base drive method calculates solutions for the orbiter and payload proportional damping. No damping is included in the present analysis so that assumptions concerning structural damping do not obscure the comparison of results by the present and conventional methods. Displacements, velocities, and accelerations are calculated at 21 attach degrees of freedom from solved modal coordinates. The empty orbiter displacement, velocity, and acceleration time histories are used in the flex-base drive analysis to account for the influence of applied forces through the orbiter to payloads.

The stiffness and mass matrices of OSTA-2, PAM-D/Telesat-F and PAM-D/PALAPA-B1 models are reduced to the Craig-Bampton forms 6 of 21, 70, and 70 degrees of freedom, respectively. The free-free mode eigenvectors and eigenvalues of these three payload models are calculated. No damping is considered for payloads for the same reason as that for the empty orbiter. With the payload free-free modes eigenvectors and eigenvalues, the responses of the empty orbiter at the interface degree of freedom, and interface partitioned empty orbiter eigenvectors and eigenvalues, the flex-base drive method is ready for payload transient loads analyses.

First, the Telesat model is considered. Ten different combinations are chosen for selection of orbiter and Telesat free-free modes. The numbers of orbiter modes are 192 (up to 40 Hz) and 231 (up to 50 Hz) and those of Telesat modes are 32 (up to 40 Hz), 46 (up to 45 Hz), 55 (up to 50 Hz), 63 (up to 63 Hz), and 70 (all). The equations of motion for Telesat models represented with five

different numbers of free-free modes are time-integrated. The displacement, velocity, and acceleration time histories at the empty orbiter and Telesat interface are supplied to the equations. Orbiter flexibility is accounted for by the interface partitioned orbiter free-free modes and associated eigenvalues. Calculations of the Telesat displacements, velocities, and accelerations at the interface use 32 Telesat free-free modes. The interface acceleration maximum and minimum values are tabulated in Table 1 for all combinations. The columns and rows of the table represent the frequencies of Telesat and orbiter modes, respectively, used in the analysis. Table 2 gives the interface displacement, velocity, and acceleration minimum and maximum values from the analysis results with use of Telesat and orbiter modes of frequencies up to 40 Hz. Figures 3 through 5 present plots of displacement, velocity, and acceleration time histories of about 0.6 seconds for the analysis with up to 40-Hz frequency free-free modes of both orbiter and Telesat. A time segment of 0.6 seconds is chosen out of 2 seconds so that the maximum and minimum interface responses are included in the figures.

Next, the equation of motions for three payloads are solved: OSTA-2, Telesat, and PALAPA. The empty orbiter structure is modeled with empty orbiter free-free modes of frequencies up to 40 Hz. The 19, 32, and 32 modes of frequencies up to about 40 Hz are used for OSTA-2, Telesat, and PALAPA payload's models, respectively. The empty orbiter interface displacements, velocities, and accelerations are calculated, with empty orbiter free-free modes of frequencies up to 40 Hz used. No damping is considered. The payload interface displacement, velocities, and accelerations are calculated by using each payload modes of frequencies up to 40 Hz. The Z-direction acceleration time histories of the forward bridge fitting are plotted in Fig. 6 by solid lines. The maximum and minimum values of displacements, velocities, and accelerations at the Telesat interface are tabulated in Table 2.

For comparison, the PAM-D/Telesat-F alone and then the OSTA-2, PAM-D/Telesat-F and PAM-D/PALAPA-B1 models are analyzed by the conventional transient loads analysis method. Two system equations of motion are constructed by coupling the 277 degrees of freedom of the empty orbiter model with the Telesat Craig Bampton model and with the OSTA-2, Telesat, and PALAPA Craig Bampton models. No damping is considered. Each equation of motion is decoupled by transforming it into modal coordinates and time-integrated. A value of 0.001 second is used for the time increment. The displacements, velocities, and accelerations at the interfaces are calculated, with 220 (up to 40 Hz) system free-free modes used for the Telesat-only structure and 268 (up to 40 Hz) modes for the three-payload system structure. The displacement, velocity, and acceleration time histories are plotted by dotted lines in Figs. 3 through 5 for single payload and Fig. 6 for triple payloads for corresponding time histories by the flex-base drive method. Also the maximum and minimum values of displacements, velocities, and accelerations are tabulated in Tables 1 and 2, respectively, for one and three-payload structures. Table 3 gives absolute maximum accelerations from Tables 1 and 2 and percent differences between those by the flex-base drive and conventional methods.

5. Discussion and Conclusion

The present analysis has three objectives. The first is to find possible applicable areas of the flex-base drive method to Space Shuttle payloads transient loads analysis. The second is to have an understanding of the attainable accuracy of the present method. The third is to define future works needed for the completion of the present method.

When all substructure free-free modes are included in the analysis by the present and conventional methods, the solutions by

Table 1. Telesat/orbiter interface responses by flex-base drive method and conventional coupled loads analysis method (in./sec)

Telesat/Orbiter Interface Response	Three-Payload Analysis		One-Payload Analysis	
	Flex-Base Drive	Coupled Analysis	Flex-Base Drive	Coupled Analysis
	Min/Max (ips)	Min/Max (ips)	Min/Max (ips)	Min/Max (ips)
Displacement				
Right-hand Forward X	-17.3/0.0048	-17.3/0.0046	-18.8/0.0038	-18.8/0.0041
Right-hand Forward Z	0.458/155	0.453/155	0.52/166	0.52/166
Right-hand Aft Z	0.371/156	0.368/156	0.43/168	0.43/168
Left-hand Forward X	-17.3/0.0059	-17.3/0.0062	-18.8/0.0052	-18.8/0.0060
Left-hand Forward Z	0.458/155	0.452/155	0.52/167	0.52/167
Left-hand Aft Z	0.369/156	0.368/156	0.43/168	0.43/168
Keel Y	-0.22/0.00069	-0.20/0.00088	-0.19/0.001	-0.19/0.001
Velocity				
Right-hand Forward X	-43.3/0	-46.2/0	-47.9/0	-48.5/0
Right-hand Forward Z	0/393	0/393	0/418	0/419
Right-hand Aft Z	0/391	0/388	0/418	0/419
Left-hand Forward X	-43.4/0	-46.1/0	-48.4/0	-48.9/0
Left-hand Forward Z	0/395	0/395	0/419	0/421
Left-hand Aft Z	0/393	0/390	0/420	0/421
Keel Y	-1.25/1.97	-1.58/0.95	-1.23/0.11	1.07/0.52
Acceleration				
Right-hand Forward X	-477/220	-538/387	-569/269	-588/289
Right-hand Forward Z	-1148/2130	-1279/2299	-1153/2243	-1243/2275
Right-hand Aft Z	-780/1714	-1152/1954	-1060/1834	-1124/1940
Left-hand Forward X	-475/212	-528/288	-572/278	-602/304
Left-hand Forward Z	-1216/2135	-1336/2316	-1184/2241	-1305/2304
Left-hand Aft Z	-869/1723	-779/2029	-1119/1834	-1232/1972
Keel Y	-50/65	-108/136	-53/68	-69/83

Table 2. Effects of mode truncation (no damping, DT=0.001: one-payload configuration) (inch/sec²)

Empty Orbiter Retained Modes (Hz)	Telesat Interface	PAM-D/Telesat Payload Retained Modes (Hz)				
		40	45	50	60	All
		Min/Max	Min/Max	Min/Max	Min/Max	Min/Max
40	RH Forward X	-569/270	-564/2713	-561/260	-645/396	-679/372
	RH Forward Z	-1154/2243	-1166/2201	-1146/2161	-1298/2084	-922/1903
	RH Aft Z	-1060/1834	-1065/1839	-986/1783	-827/1758	-956/1873
	LH Forward X	-572/279	-559/325	-648/360	-724/692	-780/463
	LH Forward Z	-1184/2241	-1171/2253	-1220/2193	-1652/1943	-1072/1794
	LH Aft Z	-1119/1832	-1152/1827	-1035/1714	-829/1764	-964/2034
	Keel Y	-53/68	-70/75	-70/83	-146/182	-131/142
50	RH Forward X	-568/287	-561/270	-565/264	-598/379	-678/372
	RH Forward Z	-1141/2240	-1175/220	-1155/2162	-962/1877	-923/1903
	RH Aft Z	-1045/1832	-1054/1841	-990/1780	-928/1844	-956/1873
	LH Forward X	-570/278	-551/318	-655/375	-784/509	-780/463
	LH Forward Z	-1179/2234	-1176/225	-1234/2191	-1833/1808	-1072/1794
	LH Aft Z	-1119/1824	-1154/1820	-1047/1705	-1899/1998	-964/2034
	Keel Y	-54/61	-72/70	-77/73	-118/133	-131/142
Interface acceleration calculations used Telesat free-free modes of frequencies up to 40 Hz.						

INPUT RESPONSE—40 Hz, ORB—40 Hz, P/L—40 Hz, OUTPUT—40 Hz
BRIDGE FITTING, RIGHT-HAND SIDE, Z TELESAT

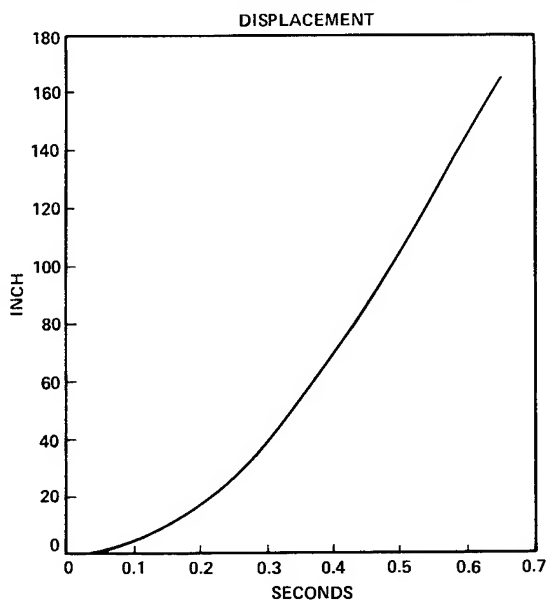


Fig. 3 Telesat interface displacement (single-payload configuration).

INPUT RESPONSE—40 Hz, ORB—40 Hz, P/L—40 Hz, OUTPUT—40 Hz
BRIDGE FITTING, RIGHT-HAND SIDE, Z TELESAT

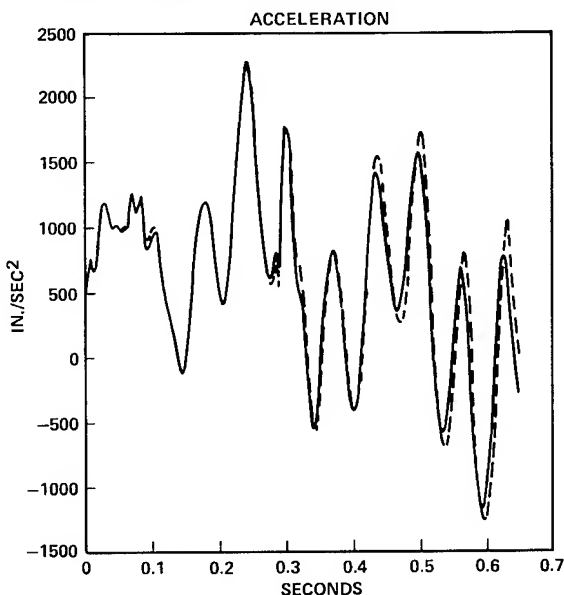


Fig. 5 Telesat interface acceleration (single-payload configuration).

INPUT RESPONSE—40 Hz, ORB—40 Hz, P/L—40 Hz, OUTPUT—40 Hz
BRIDGE FITTING, RIGHT-HAND SIDE, Z TELESAT

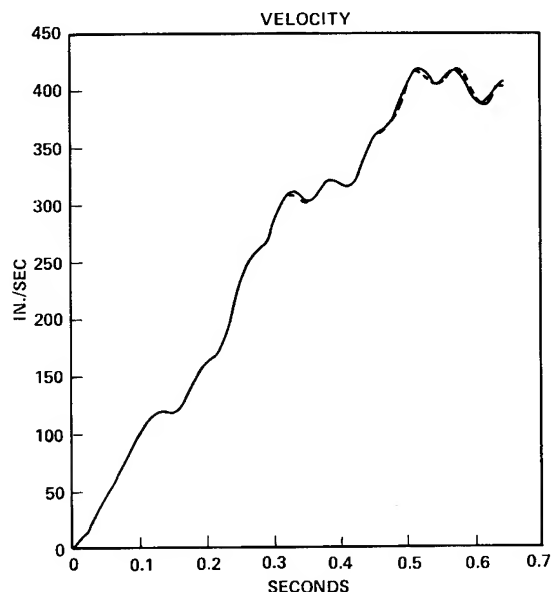


Fig. 4 Telesat interface velocity (single-payload configuration).

INPUT RESPONSE—40 Hz, ORB—40 Hz, P/L—40 Hz, OUTPUT—40 Hz
BRIDGE FITTING, RIGHT-HAND SIDE, Z TELESAT

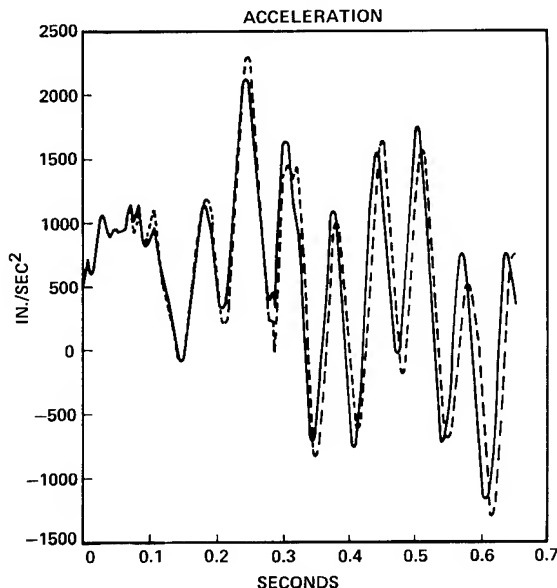


Fig. 6 Telesat interface acceleration (triple-payload configuration).

both methods coincide. For a modal transient loads analysis of a complex Space Shuttle structure with payloads in the orbiter bay, the matrices of payload and orbiter mathematical models are reduced with component modal analysis and coupled to construct a system equation of motion. The system equation of motion is decoupled by eigenanalysis, and higher modes are truncated out for the transient loads analysis. A solution by the present method never coincides with the one by the conventional method if truncated system modes are used. Generally, it is impossible to find substructure modes representing the system truncated modes if substructure modes to be included are weighted equally. When higher system modes are truncated out, it is assumed that forces transmitted through the substructure interface are the linear com-

bination of forces associated with retained lower frequency modes. The present method can only approximate reaction forces as the linear combination of forces associated with substructure modes. Thus, a reaction force calculated by the present method is an approximation of those calculated by the conventional method using modal truncation. This problem seems to be associated with any type of transient loads analysis method that foregoes the coupling of substructure equations of motion.

In the present analysis, both empty orbiter and payload free-free modes are truncated. The solutions are compared to those obtained by the conventional method and it appears that the solutions obtained by using up to 40 Hz frequency free-free modes for

**Table 3. Telesat interface acceleration percent difference
[LB4461 (Main Gear Contact) Landing Analysis;
Damping = 0, 2 Seconds With DT = 0.001] (% , in./sec²)**

Telesat Interface	Three-Payload Analysis			One-Payload Analysis		
	Three-Payload Analysis			One-Payload Analysis		
	Flex-Base Drive Absolute Maximum	Coupled Absolute Maximum	Percent Difference	Flex-Based Drive Absolute Maximum	Coupled Absolute Maximum	Percent Difference
Right-hand Forward X	477	538	11.0	569	588	3.0
Right-hand Forward Z	2130	2299	7.4	2243	2275	1.4
Right-hand Aft Z	1714	1954	12.2	1834	1940	5.5
Left-hand Forward X	475	528	10.0	572	602	5.0
Left-hand Forward Z	2135	2316	7.8	2241	2304	2.7
Left-hand Aft Z	1723	2029	15.0	1834	1972	7.0
Keel Y	65	136	52.0	68	83	18.0
Coupled = conventional coupled loads analysis method						
Percent Difference = $\frac{(\text{Coupled}) - (\text{Flex-Base Drive})}{(\text{Coupled})} \times 100$						

both the payload and orbiter agree best with those by the conventional method (Tables 1 and 2). The more modes included in the analysis by the present method, the more flexibility is involved in the analysis. It is understood that an analysis using more orbiter and payload modes could better account for the orbiter and payload dynamic interaction. However, the solutions with fewer modes compare better with the coupled solutions. This suggests that more investigation should be done to find a better combination of orbiter and payload free-free modes in the flex-base drive method analysis. A method to calculate payload responses should also be sought, along with calculating the empty orbiter responses. In the present analysis, payload responses are calculated by using frequency modes up to 40 Hz and compared with a coupled analysis result also calculated by using system modes up to 40 Hz, even though higher orbiter and payload modes are involved. A better understanding should be developed for the payload and orbiter higher modes participation in dynamic interaction. This understanding may lead to a better choice of the empty orbiter responses and combination of orbiter and payload free-free modes.

The compatibilities of displacements and velocities are implemented in the least square sense during each time increment for calculation of the reaction forces. As long as the compatibilities are satisfied at the end of the time increment, the distribution of reaction forces during the time increment is not questioned, although linear distribution is assumed. Thus, the instantaneous values of reaction forces may lack accuracy. The calculation of accelerations involves this possibly inaccurate instantaneous reaction force. Therefore, other methods should be investigated for calculating accelerations, such as a method to take time derivatives of velocity, thus avoiding the direct participation of instantaneous reaction forces.

The differences between Z-direction accelerations at the Telesat/orbiter interface by the present and conventional methods are about 15 percent, those for the X direction are 11 percent, and for the Y direction are 50 percent. It should be noted that the magnitudes of Y-direction responses are very small and well within the magnitude differences between Z-direction responses. The landing forcing function generates an almost symmetric response about the X axis, and, therefore, the Y-direction response is very

small compared with the X- and Z-direction responses. From the nature of the Space Shuttle orbiter structure, the X-direction response is minimally influenced by the introduction of payloads in its orbiter bay when modes are truncated after 40 Hz. The Z-direction accelerations at orbiter bridges are significantly influenced by payload structures and are large. The large response values are associated with about 12-Hz resonance vibration. The empty orbiter accelerations are approximated well with sinusoidal curves having many peaks and valleys. Because of the nature of the forcing function LB4461, landing response is primarily activated by the resonance of orbiter modes by the forcing function. Different from impact response, the resonance response is highly sensitive to a slight difference in mathematical models. The conventional coupled loads analysis generates significantly different responses (20 to 30 percent) when slight differences are introduced in orbiter mathematical models, even though the identical payload models are used. The orbiter and payload mathematical models used in the present analysis are significantly different due to modal truncations compared with the slight orbiter model differences in the conventional method. The differences between responses obtained by the present and conventional methods appear small compared with the differences in the responses of slightly different mathematical models by the conventional coupled loads analysis method.

The orbiter and payload dynamic interaction is included in the analysis by the flex-base drive method. When a payload mass and stiffness distribution, and its location in the orbiter bay is selected, the payload responses should reflect different mass and stiffness distributions and payload and orbiter interactions at different locations. The more different payload mass and stiffness distributions and locations that are analyzed, the more favorable design and location of the payload. The conventional coupled loads analysis method is too expensive to analyze many different payload designs and orbiter bay locations. This is because expensive calculations of system eigenvectors and eigenvalues and generalized forces are repeated whenever the payload structure and orbiter bay location change. The present method avoids these repeated expensive calculations, also saving computation time. This is an area potentially benefitted from the introduction of the flex-base drive method to the Space Shuttle payload transient loads analysis.

The flex-base drive method for Space Shuttle payload transient loads analysis has been developed and demonstrated with STS-7 payloads and comparing the results with the conventional coupled loads analysis method. Though more work is needed for the completion of the method, results of the analysis show a great potential for Space Shuttle payload transient loads analysis. The advantages of this method are where following needs arise:

1. Frequent changes of payload design
2. Determination of the mass and stiffness distribution of payload structures
3. Selection of payload locations in the orbiter bay
4. Last-minute changes of payload configurations

References

1. Kubomura, K. "A Theory of Substructure Modal Synthesis," *ASME Journal of Applied Mechanics*, Vol. 49, pp. 903-909 (1982).
2. Chen, J. C., and B. K. Wada. "Matrix Perturbation for Structural Dynamic Analysis," *AIAA Journal*, pp. 1095-1100 (August 1977).
3. Payne, K. R. "An Impedance Technique for Determining Low Frequency Payload Environments," *The Shock and Vibration Bulletin*, No. 49, Part II, pp. 1-4 (September 1979).
4. Trubert, M. and M. Salama. "Generalized Shock Spectra Method for Spacecraft Loads Analysis," *AIAA Journal*, Vol. 18, No. 8, pp. 988-994 (August 1980).
5. Craig, R. R., and M. C. Bampton. "Coupling of Substructures for Dynamic Analysis," *AIAA Journal*, Vol. 7, pp. 1313-1319 (July 1968).
6. Engles, R. C., H. W. Harcrow, and T. G. Shanahan. "An Integration Scheme to Determine the Dynamic Response of a Launch Vehicle With Several Payloads," *AIAA/ASME/ASCE/AMS 23rd Structural Dynamics & Material Conference*, (April 1, 1982) Paper No. 82-C632.
7. Chen, J. G., J. A. Garba, and B. K. Wada. "Estimation of Payload Loads Using Rigid-Body Interface Accelerations," *Journal of Spacecraft and Rockets*, Vol. 16, No. 2, pp. 74-80 (1979).
8. Chen, J. C., J. A., Garba, M. Salama, M. Trubert. "A Survey of Load Methodologies for Shuttle Orbiter Payloads," *JPL Publication 80-37*, Jet Propulsion Laboratory, Pasadena, California (June 15, 1980).
9. Guyan, R. J. "Reduction of Stiffness and Mass Matrices," *AIAA Journal*, Vol. 3, No. 2, (February 1965).
10. Chao, R. S., J. L. Leang, H. S. Fan, and S. J. Yahata. *Load Data Book for STS-7 Verification Loads Analysis*, Rockwell International Report STS 82-0782, Rockwell International Space Operation/Integration & Satellite Systems Division, Downey, California (November 1982).
11. MacNeal, R. H. "A Hybrid Method of Component Mode Synthesis," *Computer & Structures*, Vol. 1, pp. 581-601 (December 1971).
12. Rubin, S. "Improved Component-Mode Representation for Structural Dynamic Analysis," *AIAA Journal*, Vol. 13, No. 8, pp. 995-1006 (August 1975).

SIMULATING THE DYNAMIC SEPARATION OF LAUNCH VEHICLES
FROM THEIR SUPPORT STRUCTURES

D.J. Olberding*
RTS Technical Services
Scottsdale, Arizona

Abstract

A technique is presented for generating the transient response of a launch vehicle during separation from its support structure. The method utilizes a complete dynamic model of the launch vehicle and support structure, with no limitations on the number of interface degrees of freedom. Changes occurring in the structural math model during the point-by-point separation are accounted for by introducing terms to the right-hand-side of the equations of motion. This allows the analyst to employ a single set of system modes to simulate the vehicles transition from the constrained to the free-free configuration.

Nomenclature

X_v	vehicle discrete displacement vector.
X_s	support discrete displacement vector.
\ddot{X}_v	vehicle discrete acceleration vector.
\ddot{X}_s	support discrete acceleration vector.
F_v	vehicle discrete force vector.
F_s	support discrete force vector.
$R_{I/F}$	interface reactions.
M_v	vehicle discrete mass matrix.
M_s	support discrete mass matrix.
K_v	vehicle discrete stiffness matrix.
K_s	support discrete stiffness matrix.
Q	generalized displacement vector.
\ddot{Q}	generalized acceleration vector.
ω	system natural frequencies.
ϕ	system modes.
I	identity matrix.
LTM	load transformation matrix.

Introduction

For the structural analyst, whose job it is to simulate the dynamic response of launch vehicles, a clear understanding of the separation process is essential. During a typical liftoff sequence the vehicle is subjected to a variety of external excitations, including: Engine thrust, guidance control forces, ignition over pressure, and gusting winds. However, a good deal of the dynamic activity occurring at liftoff is a result of the vehicle's abrupt separation from its support structure. This is due, in part, to a redistribution of the internal structural energy as support of the vehicle shifts from the launch

mount attach points to the thrust structure of the booster. In addition, its sudden release from a constrained configuration - resulting from such things as structural misalignment, cryogenic shrinkage, element pre-loads, or base bending moment - produces additional excitation of the vehicle. These factors combine to form a difficult problem for the dynamic analyst. One whose complexities require thorough examination to insure a realistic simulation.

The principal obstacle to overcome in an analysis of this nature is accommodating the multiple changes occurring at the boundary or interface of the vehicle and its support structure during separation. A traditional approach - using a set of normal modes to decouple the equations of motion - is hampered as each intermediate configuration would require a unique set of normal modes. Also, the use of load transformation matrices, which often contain elements of the structure's flexibility matrix, would be restricted because each new configuration has a unique flexibility, requiring re-inversion of the discrete stiffness matrix.

Faced with these choices the analyst might opt for a direct numerical integration of the discrete equations of motion. This would allow for a straightforward modification of the structural math model as changes at the boundary occurred. However, as is normally the case, direct numerical integration of large multiple degree of freedom systems is costly and usually beyond the means of those with limited computational resources.

Past attempts at simulating a launch vehicle's liftoff have involved simplifications of the structural math model. One approach employed a simple static reduction transformation to cut down the number of boundary degrees of freedom¹. This reduced the number of intermediate configurations and simplified the separation simulation. However, this process altered the true characteristics of the structure and made for a crude and abnormally abrupt release. Another approach treated the vehicle's launch mount as a rigid structure^{2,3}. Here a complete description of the boundary was preserved but at the expense of the support structure's dynamic properties.

Presented in this paper is a technique that enables the analyst to simulate the dynamic separation of a launch vehicle from its support structure. The method is rigorous in that it employs a complete dynamic model of the vehicle and its launch mount, with no unusual simplifications of the interface. No limitations are placed on the number of boundary degrees of freedom, or on the complexity of the restraining mechanism. The approach utilizes a single set of normal modes and interface load transformations matrices to simulate the vehicle's transition from the constrained to free-free condition, accounting for each intermediate configuration along the way. In general, the technique is easy to implement and should prove useful to those working with launch vehicles.

* Consultant under contract to the Space Transportation and Systems Group of Rockwell International Corp., Downey, California.

Analytical Development

The objective of the dynamic liftoff simulation is to generate reactions between the vehicle and its support structure, for all coupled and partially coupled configurations. Later, these reactions are combined with those forces originally applied to the vehicle to form a complete dynamic environment for the vehicle as a free-free structure (see figure 1). The resulting free-free equations of motion are easily written as

$$[M] \ddot{X}_v + [K] X_v = \{F_v\} + \{R_{I/F}\}, \quad (1)$$

where F_v is a vector of externally applied forces and $R_{I/F}$ a vector of the pre-determined interface reactions.

This feature of the liftoff simulation, often referred to as a parallel analysis, is not new. For years it has been, and continues to be, a practical technique for defining the time dependent forces acting on a launch vehicle during liftoff. The difficulty with this method has been the generation of interface reactions as the structure transitions through the many intermediate configurations of separation. What follows is a scheme that minimizes this difficulty.

Separation Equations of Motion

The generation of interface reactions begins with a single set of normal modes, and associated interface load transformation matrices, for the fully coupled launch vehicle/support structure configuration. This allows for a simple closed-form solution of the equations of motion during the period in which no separation has occurred. Equations (2) and (6) illustrate graphically the coupled equations of motion, in discrete and generalized coordinates respectively, of a vehicle and its support. Notice, in equation (2), that coupling between the two structures occurs in the stiffness matrix only. This form of coupling is

not uncommon and easily achieved through selected modeling techniques.

$$\begin{bmatrix} M_v & 0 \\ 0 & M_s \end{bmatrix} \begin{bmatrix} \ddot{X}_v \\ \ddot{X}_s \end{bmatrix} + \begin{bmatrix} K_v & K_{vs} \\ K_{sv} & K_s \end{bmatrix} \begin{bmatrix} X_v \\ X_s \end{bmatrix} = \begin{bmatrix} F_v \\ F_s \end{bmatrix}, \quad \begin{matrix} \text{VEHICLE} \\ \text{SUPPORT} \end{matrix} \quad (2)$$

Proceeding in the normal fashion the associated eigenvalue problem is solved to obtain the identities

$$\begin{bmatrix} X_v \\ X_s \end{bmatrix} = \begin{bmatrix} \phi \end{bmatrix} \begin{bmatrix} q \end{bmatrix}, \quad (3)$$

$$\begin{bmatrix} \phi^T \end{bmatrix} \begin{bmatrix} M_v & 0 \\ 0 & M_s \end{bmatrix} \begin{bmatrix} \phi \end{bmatrix} = \begin{bmatrix} I \end{bmatrix}, \quad (4)$$

$$\begin{bmatrix} \phi^T \end{bmatrix} \begin{bmatrix} K_v & K_{vs} \\ K_{sv} & K_s \end{bmatrix} \begin{bmatrix} \phi \end{bmatrix} = \begin{bmatrix} \omega^2 \end{bmatrix}. \quad (5)$$

Incorporating equations (3) through (5) into equation (2) yields a diagonal equation of motion in generalized coordinates

$$\begin{bmatrix} I \end{bmatrix} \ddot{q} + \begin{bmatrix} \omega^2 \end{bmatrix} q = \begin{bmatrix} \phi^T \end{bmatrix} \begin{bmatrix} F_v \\ F_s \end{bmatrix}. \quad (6)$$

Equations of this type are easily solved in closed-form for q and \dot{q} . Likewise the interface reactions can be computed using any of a number of well established techniques. These can be summarized with the general expression

$$\{R_{I/F}\} = [LTM] \{G_i(F, q, \ddot{q})\}, \quad (7)$$

where G_i is a vector function of the discrete force and the generalized displacements and accelerations.

As separation begins, changes occurring in the equations of motion are accounted for, not by

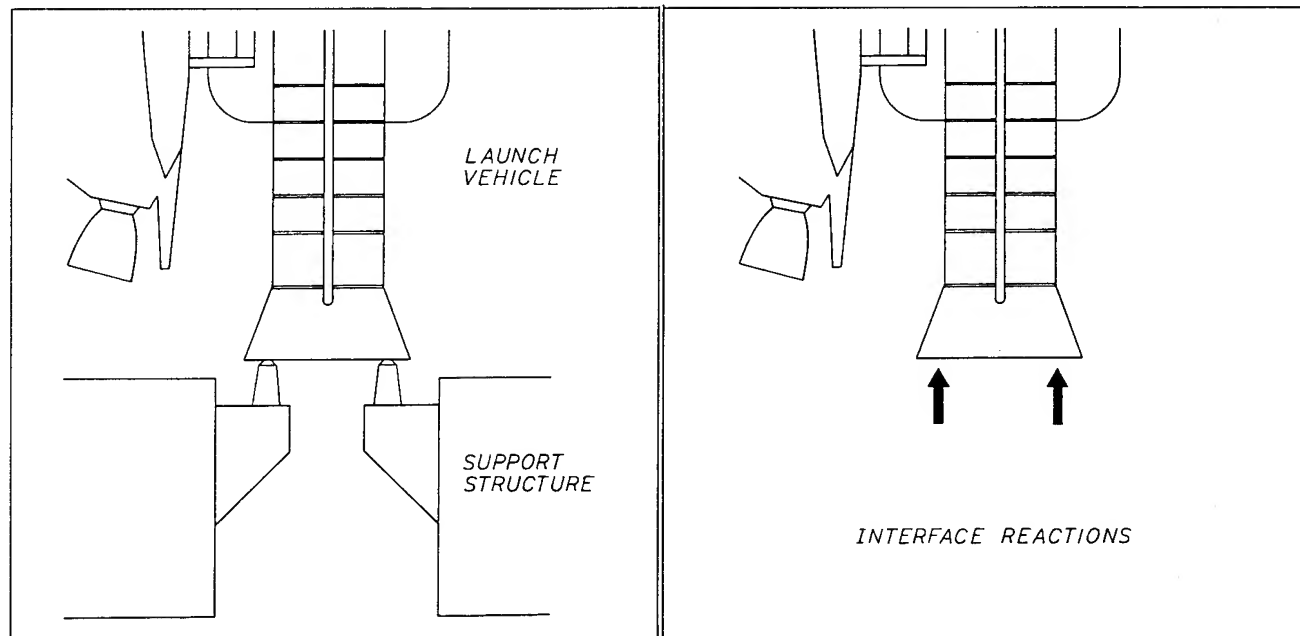


Figure 1. Parallel Analysis.

altering the original mass and stiffness matrices, but by introducing terms that reflect these changes to the right-hand-side of the equations. Equations (8) through (10) illustrate how different configurations of separation - in this case the completely separated configuration - are simulated.

$$\begin{bmatrix} M_v & \\ & M_s \end{bmatrix} \begin{Bmatrix} \ddot{X}_v \\ \ddot{X}_s \end{Bmatrix} + \begin{bmatrix} K_v & \\ & K_s \end{bmatrix} \begin{Bmatrix} X_v \\ X_s \end{Bmatrix} = \begin{Bmatrix} F_v \\ F_s \end{Bmatrix} \quad (8)$$

$$= \begin{bmatrix} M_v & \\ & M_s \end{bmatrix} \begin{Bmatrix} \ddot{X}_v \\ \ddot{X}_s \end{Bmatrix} + \begin{bmatrix} K_v & \\ & K_s \end{bmatrix} \begin{Bmatrix} X_v \\ X_s \end{Bmatrix} - \begin{bmatrix} \\ \end{bmatrix} \begin{Bmatrix} X_v \\ X_s \end{Bmatrix} = \begin{Bmatrix} F_v \\ F_s \end{Bmatrix} \quad (9)$$

$$= \begin{bmatrix} M_v & \\ & M_s \end{bmatrix} \begin{Bmatrix} \ddot{X}_v \\ \ddot{X}_s \end{Bmatrix} + \begin{bmatrix} K_v & \\ & K_s \end{bmatrix} \begin{Bmatrix} X_v \\ X_s \end{Bmatrix} = \begin{Bmatrix} F_v \\ F_s \end{Bmatrix} + \begin{bmatrix} \\ \end{bmatrix} \begin{Bmatrix} X_v \\ X_s \end{Bmatrix} \quad (10)$$

Substituting equations (3) through (5) into equation (10) yields an equation whose left-hand-side is diagonalized and whose right-hand-side contains the dependent variable.

$$\begin{bmatrix} I \\ \omega^2 \end{bmatrix} \begin{Bmatrix} \ddot{q} \\ q \end{Bmatrix} = \begin{bmatrix} \phi^T \\ \phi \end{bmatrix} \left\{ \begin{bmatrix} F_v \\ F_s \end{bmatrix} + \begin{bmatrix} \\ \end{bmatrix} \begin{bmatrix} X_v \\ X_s \end{bmatrix} \right\} \quad (11)$$

In this form, the analyst forgoes a closed-form solution and must revert to some type of numerical integration. As before the interface reactions are given by the general expression

$$\begin{Bmatrix} R_{ij} \end{Bmatrix} = \begin{bmatrix} LTM \end{bmatrix} \begin{Bmatrix} G_2(F, q, \ddot{q}) \end{Bmatrix}. \quad (12)$$

Discussion and Conclusion

A technique was presented which allows the analyst to generate the transient response of a launch vehicle during its point-by-point separation from its support structure. The method required no unusual simplifications of the interface, placed no restrictions on the number of interface degrees of freedom, and made no compromise of the structure's dynamical properties. Changes occurring in the structural math model were accounted for by introducing terms to the right-hand-side of the equations of motion, requiring a numerical integration. However, this is a minor shortcoming when compared with the task of generating eigensolutions for a multitude of configurations, simply for the sake of the closed-form solution. In addition, dynamic analyses of this type usually employ a truncated set of normal modes. Numerical integration of this small set of generalized equations, with diagonal coefficient matrices, is by far easier than a direct integration of a large set of discrete equations with their fully populated coefficient matrices.

References

1. Kaminsky, J. A.: Structural Design Loads Data Book, SD73-SH-0069. Shuttle Orbiter Division, Rockwell International Corporation, Downey, California, 1981.
2. Wilkening, H., Kessler, R., and Ikard, R.: Program Titan IIIB Design Loads Report. SSD-CR-66-105. Martin Marietta Corporation, Denver, Colorado, October 1969.
3. White, C.: Category B Study Titan EEEB-36, Dynamics and Loads Study, MCR-70-442. Martin Marietta Corporation, Denver, Colorado, November 1970.
4. Meirovitch, L., Analytical Methods in Vibrations, Macmillan, New York, 1967.
5. Meirovitch, L., Elements of Vibration Analysis, McGraw-Hill, New York, 1975.

THERMAL AND ELECTROMAGNETIC DAMPING ANALYSIS AND ITS APPLICATION

Usik Lee*
Stanford University
Stanford, California

Abstract

This paper discusses the thermoelastic damping and the electromagneto-elastic damping of vibrating solids. It is found that the former is dependent on structure, boundary conditions and structural geometry and that the latter has certain analogies to thermoelastic damping within an elastic body. Some design conditions are discussed for controlling damping in typical configurations. Finally, the influence of thermal damping on aeroelastic stability is investigated.

Nomenclature

a	Plate length in x-direction
a_p	Fourier coefficients
A	Vector potential
\tilde{C}_H, \tilde{C}_U	Electromagneto-elastic coupling vectors
C_k	Magnification factors
c_v	Constant-strain specific heat (unit mass)
D	Plate flexural rigidity, $Eh^3/12(1-\nu^2)$
e	Dilatation, $\epsilon_{11} + \epsilon_{22} + \epsilon_{33}$
E	Young's modulus
$f(a_3)$	Function defined in Eq. (2-5)
F, \tilde{f}	Represent external forces
h	Shell thickness
\tilde{h}	Perturbation in magnetic field, $\tilde{H} - H_0$
H_0	Constant reference magnetic field
i	Imaginary unit, $\sqrt{-1}$
k	Thermal conductivity
K	$Eh/(1-\nu^2)$
K_{11}, K_{22}	Bending strains (Ref (13))
L	Characteristic length
L_1, L_2	Dimensions along α_1, α_2 coordinates
m_{ij}	Maxwell stress tensor, Eq. (3-15(c))
M	Mach number
M_k, M_m	Quantities defined in Eqs. (2-11), (4-4(b))
R_1, R_2	Radii of shell curvatures in α_1, α_2 coordinates
R	Quantity defined in Eq. (3-17)
t	Time coordinate
t_{ij}	Total stress tensor, $\sigma_{ij} + m_{ij}$
ΔT	Temperature disturbance, $(T - T_0)$
T_0	Constant reference absolute temperature
\tilde{u}	Displacement field vector
U	Strain energy
ΔU	Energy dissipated
U_∞	Fluid velocity
w	Deflection of shell in α_3 -coordinate
W	Normal modes (with subscripts)
α	Velocity of longitudinal wave
$\alpha_1, \alpha_2, \alpha_3$	Orthogonal curvilinear coordinates
α_t	Linear thermal coefficient of expansion
β	Velocity of transverse wave

γ	Dimensionless mass ratio, $\rho_\infty a / \rho h$
λ	Eigenvalues, Eq. (3-7(a))
Γ^n	Quantity defined in Eq. (2-2)
δ	Logarithmic decrement (with subscripts)
$\delta(\dots)$	Delta function
δ_{kl}	Kronecker delta
$\Delta k\ell$	Thermal relaxation strength, $T \alpha_t^2 E / \rho c_v$
$\epsilon, \epsilon_1, \epsilon_2$	Electromagneto-elastic coupling constants
ϵ_{ij}	Mechanical strain tensor
η	Damping loss factors (with subscripts)
η_D	Debye formula, $\Delta[\omega\tau/(1 - \omega^2\tau^2)]$
η_t	Quantity defined in Eq. (2-14)
θ	Dimensionless constants (≈ 1)
μ_H	Magnetic permeability
ν	Poisson's ratio
ν_H	Magnetic viscosity, $1/\sigma\mu_H$
ξ_H	Dimensionless quantity (with subscripts)
Π	Factor defined by Eq. (2-22)
ρ	Material density
ρ_∞	Fluid density
σ	Electric conductivity
σ_{ij}	Mechanical stress tensor
τ_{ij}	Dimensionless time, $\rho c_v h^2 / \pi^2 k$
ϕ	Scalar potential
ψ	Normal modes (with subscripts)
χ	Dimensionless quantity (with subscripts)
ω	Frequency
ω^*	Characteristic frequency
$\Delta\omega$	Half-power bandwidth, $\omega_1 - \omega_2$
$\nabla, \tilde{\nabla}$	Vector Nabla operator
$(\dots)_k$	Property of k-th vibration mode
$(\dots)_{\max}$	Maximum value of (\dots)
\cdot	Time derivative, $\partial/\partial t$

1. Introduction

Material damping arises from several physical sources, and it is therefore difficult to predict accurately. Nevertheless, reasonably accurate damping information is often required to design a system properly for dynamic loadings. There exists considerable literature on both analytical and experimental aspects of the subject. Lazan⁽¹⁾ and Nowick and Berry⁽²⁾ provide useful summaries of what was known up to their dates of publication. The author has found, however, relatively few fundamental theoretical studies of internal energy dissipation (or material damping).

The inherent dissipation in monolithic solids tends to be small compared to the damping furnished artificially by dashpots, constrained viscoelastic layers or interconnections, joints and bearings. This is believed to explain why the role of material damping is frequently omitted or underplayed in the extensive literature on damping analysis and active control of Large Space Structures (LSS). Several authors (e.g., Gerarter,⁽³⁾ Ashley⁽⁴⁾) have given some consideration to the possibly important role of material damping on the stabilization of structures. Reference 4 observed that a tiny amount of structural damping is useful

*Graduate Student and Research Assistant,
Department of Mechanical Engineering.

for meeting the control system requirements of LSS like telescopes and antennas in space.

In order to analyze the internal energy dissipation of a given structure, one should take into account all possible damping mechanisms, depending upon the specific material. In practical cases, however, one or two mechanisms generally predominate, the others being comparatively negligible.

In 1938 Zener⁽⁵⁾ predicted that thermoelastic damping (simply thermal damping) of monolithic crystalline solids is often much greater than that due to all other mechanisms. Experiments of Bennewitz and Rotger⁽⁶⁾ confirmed that his predictions are accurate. Thermal damping is almost universal. But, under certain conditions with high electromagnetic (EM) field, the electro-magneto-elastic damping (simply electromagnetic damping) is even of a larger order of magnitude.

2. Thermal Damping Analysis

2.1 Background

Zener^(5,7) was apparently the first to point out that the energy dissipation in vibrating metals must be sought in stress inhomogeneities, giving rise to temperature gradients and hence to local thermal currents which increase the entropy. Biot⁽⁸⁾ discussed irreversible thermodynamics in vibrating systems and applied a generalized coordinate method to the calculation of internal energy dissipation. Tasi and Herrmann^(9,10), investigated a crystal plate by means of a variational principle. Chadwick⁽¹¹⁾, in 1962, showed that his results from normal mode analysis agree with Zener's theory⁽⁵⁾. Later, Alblas⁽¹²⁾ developed a general theory of energy dissipation in a three-dimensional finite body.

2.2 Basic Formulation

The two governing equations of the linearized coupled thermoelasto-dynamics are given by^(13,14)

$$D\nabla_1^4 w + \left(\frac{E}{1-\nu}\right) \nabla_1^2 \int_{-\frac{h}{2}}^{\frac{h}{2}} \alpha_t \Delta T \alpha_3 d\alpha_3 + \Gamma w + \rho h \ddot{w} = F, \quad (2-1)$$

where

$$\Gamma = K \left[\frac{1}{R_1^2} + \frac{1}{R_2^2} + \frac{2\nu}{R_1 R_2} \right] \quad (2-2)$$

and

$$\nabla^2 (\alpha_t \Delta T) - \left(\frac{\rho C_v}{k}\right) \frac{\partial (\alpha_t \Delta T)}{\partial t} = \frac{T_o \alpha_t^2 E}{k(1-2\nu)} \frac{\partial e}{\partial t} \quad (2-3)$$

Here ∇_1^2 is the Laplacian operator for in-plane orthogonal curvilinear coordinates (α_1, α_2) and ∇^2 is for $(\alpha_1, \alpha_2, \alpha_3)$, where α_3 is normal to the in-plane coordinates (α_1, α_2) . F is the external force and the other symbols are defined in nomenclature.

Equation (2-1) is the equation of transverse motion, which is believed sufficiently accurate to estimate quickly the effects of curvature in relatively shallow shells. Equations for plates and beams are readily recovered by forcing the radii of shell curvatures, $R_1 = R_2 = \infty$ and Poisson's ratio, $\nu = 0$. Because of this

adaptability plates and beams are easily recovered from the results obtained by solving Eqs. (2-1) and (2-3) for shallow shells. Equation (2-3) is the heat conduction equation, in which the influence of the curvatures of shell on thermal flux is neglected. One notes that the two governing equations include small coupling terms between elastomechanical and thermodynamic behaviors which give rise to the damping of the vibration.

The general theory of shallow shells usually assumes as above the normal stress σ_{33} is negligible along with shear strains ϵ_{13} and ϵ_{23} . Under this assumption, the reduced Hooke's law and the strain-displacement relations⁽¹³⁾ approximately give the dilatational part of the displacement field (simply dilatation) in the form

$$e = \epsilon_{11} + \epsilon_{22} + \epsilon_{33} \\ \approx - \left[\frac{1-2\nu}{1-\nu} \right] \alpha_3 \nabla_1^2 w + \left[\frac{1+\nu}{1-\nu} \right] \alpha_t \Delta T \quad (2-4)$$

From the physics of the situation and the forms of Eqs. (2-3) and (2-4), a logical approximation to the elastomechanical coupling would seem to be

$$\alpha_t \Delta T (\alpha_1, \alpha_2, \alpha_3, t) \approx f(\alpha_3) \nabla_1^2 w (\alpha_1, \alpha_2, t), \quad (2-5)$$

which reduces Eqs. (2-1) and (2-3) into the forms:

$$D(1+i\eta_t) \nabla_1^4 w + \Gamma w + \rho h \ddot{w} = F \quad (2-6)$$

$$\frac{d^2 f}{d\alpha_3^2} + \left[\frac{\nabla_1^4 w}{\nabla_1^2 w} - \left(\frac{\rho C_v \theta}{k} \right) \frac{\nabla_1^2 \dot{w}}{\nabla_1^2 w} \right] f + \frac{\rho C_v \Delta}{k(1-\nu)} \frac{\nabla_1^2 \dot{w}}{\nabla_1^2 w} \alpha_3 = 0, \quad (2-7)$$

where

$$\eta_t \equiv \text{Real part of } \left\{ \frac{E}{D(1-\nu)} \int_{-\frac{h}{2}}^{\frac{h}{2}} f(\alpha_3) \alpha_3 d\alpha_3 \right\} \quad (2-8)$$

$$\Delta = \frac{T_o \alpha_t^2 E}{\rho C_v}$$

$$\theta = 1 + \Delta \left\{ \frac{1+\nu}{(1-\nu)(1-2\nu)} \right\} \approx 1$$

One notes that only the imaginary part of the integration in Eq. (2-8) is taken because of its contribution to the damping of vibration. The modified equation of motion (2-6) now contains the complex plate flexural rigidity $D(1+i\eta_t)$. θ is approximately equal to unity because always the thermal relaxation strength $\Delta \ll 1$ ⁽⁷⁾.

In order to investigate free vibration, one assumes harmonic motion in the form

$$w = \sum_{mn} C_{mn} W_{mn} e^{i\omega t} = \sum_k C_k W_k e^{i\omega t} \quad (2-9)$$

(Indices mn are replaced by k for convenience) Here C_k is the amplification factor of the k -th normal mode, W_k , which satisfies the following equations:

$$D\nabla_1^4 W_k + (\Gamma - \rho h \omega_k^2) W_k = 0 \quad (2-10)$$

$$\iint_A W_k W_l dA = M_k \delta_{kl}, \quad (2-11)$$

where $dA = da_1 da_2$ is the plate area element and δ_{kl} is the Kronecker delta. It is convenient to expand $f(\alpha_3)$ in Fourier series, following the lead of Zener⁽⁵⁾,

$$f(\alpha_3) = \sum_{p=0}^{\infty} a_p \sin(2p+1) \frac{\pi \alpha_3}{h}, \quad (2-12)$$

which satisfies insulated boundary conditions at the upper and lower shell surfaces. These are appropriate to the vacuum of space, and one assumes no energy loss due to heat convection and radiation. Substituting Eqs. (2-9), (2-12) into Eq. (2-7) and using the orthogonality property of Fourier series, one may solve for the coefficients a_p of Eq. (2-12) to find that $a_p \ll a_0$ for $p > 1$. Therefore a one-term approximation is acceptable with an error typically < 1.0%:

$$f(\alpha_3) \approx [f_R + if_I] \sin \frac{\pi \alpha_3}{h}, \quad (2-13)$$

where

$$f_R = \frac{1}{\pi} \frac{4h}{1-\nu} \Delta \frac{\omega^2 \tau^2}{1+\omega^2 \tau^2}$$

$$f_I = \frac{1}{\pi} \frac{4h}{1-\nu} \Delta \frac{\omega \tau}{1+\omega^2 \tau^2}$$

Here we used the approximations $\theta \approx 1$ and $O[(h/L)^2] = 0$ for the shallow shells. τ is the characteristic time, which controlled by the choice of material, specimen shape and size, defined by

$$\tau = \frac{\rho c_v h^2}{\pi^2 k}$$

Substituting Eq. (2-13) into Eqs. (2-8) gives

$$\eta_t \approx \frac{96}{\pi} \left(\frac{1+\nu}{1-\nu} \right) \left[\Delta \frac{\omega \tau}{1+\omega^2 \tau^2} \right] \quad (2-14)$$

Here the square-bracketed portion of Eq. (2-14) is called the Debye formula, η_D .

2-3 Free Vibration

Consider free vibration with forcing $F = 0$ and assume harmonic motion, Eq. (2-9). Then, using the orthogonality property of Eq. (2-11), the equation of motion can be reduced in the form

$$\rho h(\omega_k^2 - \omega^2) + i\eta_t(\Gamma - \rho h \omega_k^2) = 0,$$

which gives the complex circular frequency. For small η_t , the k -th mode of vibration is found approximately to be

$$w_k \sim W_k e^{-\frac{1}{2} \eta_t \left[\frac{\omega_k}{\omega_k} \right]^2 t} e^{i\omega t},$$

where

$$\frac{-2}{\omega_k} = \omega_k^2 - \frac{\Gamma}{\rho h}$$

One measure of free-oscillation decay is the logarithmic decrement, which yields the modal

damping loss factor, as follows:

$$\frac{\delta_k}{\pi} \approx \frac{96}{\pi} \left[\frac{1+\nu}{1-\nu} \right] \Delta \frac{\omega_k \tau}{1+\omega_k^2 \tau^2} \left[\frac{\omega_k}{\omega_k} \right]^2 \quad (2-15)$$

2-4 Forced Vibration

Consider the vibration forced by a concentrated load acting at point (α_1, α_2) . In terms of modal modes governed by Eq. (2-10), Eq. (2-6) can be written

$$\begin{aligned} \rho h \sum_k (\omega_k^2 - \omega^2) C_k W_k - i\eta_t \sum_k (\Gamma - \rho h \omega_k^2) C_k W_k \\ = P_0 \delta(\alpha_1 - \bar{\alpha}_1) \delta(\alpha_2 - \bar{\alpha}_2) \end{aligned}$$

Using again the orthogonality property of Eq. (2-11), one finds the amplification factors C_k , as follows:

$$C_k = \frac{P_0 W_k(\bar{\alpha}_1, \bar{\alpha}_2)}{\rho h M_k [(\omega_k^2 - \omega^2) + i\eta_t(\omega_k^2 - \frac{\Gamma}{\rho h})]} \quad (2-16)$$

As an estimate of damping, the half-power bandwidth $\Delta\omega = \omega_1 - \omega_2$ is readily obtained from the magnification factor C_k . Then one measure of damping for the k -th mode of vibration is simply

$$\frac{\Delta\omega}{\omega_k} \approx \frac{96}{\pi} \left[\frac{1+\nu}{1-\nu} \right] \Delta \frac{\omega_k \tau}{1+\omega_k^2 \tau^2} \left[\frac{\omega_k}{\omega_k} \right]^2, \quad (2-17)$$

which proved identical to the logarithmic decrement, Eq. (2-15).

Another classical measure of damping is the loss factor η , defined as the ratio of energy dissipated in unit volume per radian of oscillation to the maximum strain energy per unit volume, that is

$$\eta = \frac{\Delta U}{2\pi U_{\max}} \quad (2-18)$$

Here

$$U \approx \frac{1}{2} \int_A \int_{\frac{h}{2}}^{\frac{h}{2}} [\sigma_{11} \epsilon_{11} + \sigma_{22} \epsilon_{22}] d\alpha_3 dA \quad (2-19)$$

$$\Delta U \approx \frac{1}{2} \int_A \int_{\frac{h}{2}}^{\frac{h}{2}} \int_0^{2\pi} [\alpha_{11} \dot{\epsilon}_{11} + \sigma_{22} \dot{\epsilon}_{22}] d\omega t d\alpha_3 dA \quad (2-20)$$

In Eqs. (2-19) and (2-20) approximations have been made consistent with the foregoing derivations. Since limitations prevent reproducing detail of a consistent analysis, which leads to the expression

$$\eta \approx \frac{96}{\pi} \left[\frac{1+\nu}{1-\nu} \right] \Delta \frac{\omega \tau}{1+\omega^2 \tau^2} \Pi \quad (2-21)$$

with

$$\Pi = \frac{\int_A [K_{11} + K_{22}]^2 dA}{\int_A [K_{11}^2 + 2\nu K_{11} K_{22} + K_{22}^2] dA}, \quad (2-22)$$

where K_{11} and K_{22} are bending strains.⁽¹³⁾ In any practical examples, $\Pi > 1$ since $\nu < 0.5$. However,

one notes that $\Pi = 1$ for the structures vibrating one-dimensionally like beam-plates. For the simply supported structures, considered in this paper, Π has the general form:

$$\Pi = \frac{\sum_k \bar{C}_k^2 \left[\left(\frac{\pi n}{L_1} \right)^2 + \left(\frac{\pi n}{L_2} \right)^2 \right]^2 M_k}{\sum_k \bar{C}_k^2 \left[\left(\frac{\pi n}{L_1} \right)^4 + 2\nu \left(\frac{\pi n}{L_1} \right)^2 \left(\frac{\pi n}{L_2} \right)^2 + \left(\frac{\pi n}{L_2} \right)^4 \right] M_k} \quad (2-23)$$

where \bar{C}_k is the magnitude of C_k , Eq. (2-16). L_1 and L_2 are the full dimensions of a structure along the coordinates α_1 and α_2 , respectively.

Investigation of magnification factor C_k shows that the k -th normal mode predominates when the circular frequency ω is near the k -th natural frequency ω_k . Then one can use the approximation

$$\eta \approx \left[\frac{1+\nu}{1-\nu} \right] \Delta \frac{\omega \tau}{1 + \omega^2 \tau^2} \Pi_k \quad (\omega = \omega_k), \quad (2-24)$$

where the Π_k (or Π_{mn}) for simply supported structures are given by

$$\Pi_{mn} = \frac{\left[\left(\frac{\pi m}{L_1} \right)^2 + \left(\frac{\pi n}{L_2} \right)^2 \right]^2}{\left[\left(\frac{\pi m}{L_1} \right)^4 + 2\nu \left(\frac{\pi m}{L_1} \right)^2 \left(\frac{\pi n}{L_2} \right)^2 + \left(\frac{\pi n}{L_2} \right)^4 \right]} \quad (2-25)$$

The k -th modal loss factors for simply supported structures, without further approximation, are readily obtained from Eq. (2-21) in the form:

$$\eta_k \approx \frac{96}{\pi^4} \left[\frac{1+\nu}{1-\nu} \right] \Delta \frac{\omega_k \tau}{1 + \omega_k^2 \tau^2} \Pi_k \quad (\omega = \omega_k) \quad (2-26)$$

2-5 Discussion

Equations (2-15), (2-17) and (2-26) provide measures of modal damping at frequencies near natural frequencies. For structures vibrating one-dimensionally, such as beams and beam-plates, these equations give exactly identical results as the case of mass-spring-dashpot system. In general, however, there exists no unique expression suitable as a measure of damping, even at a natural frequency. One may therefore ask which measure of damping is the most meaningful and accurate. The author has concluded that this question has no definitive answer. As Jones⁽¹⁵⁾ observed, this ambiguity is really not a serious problem. When comparing different materials and configurations, one must simply employ consistent, clearly-defined measures. As far as small damping is concerned, every measure must provide the same useful information. For this reason, the author has adopted the loss factor η as a vehicle for further investigations.

How to maximize the loss factor seems to be the most interesting issue for damping analysis. Maximization of damping is not a simple matter, because of the complicated characteristics of vibration problem. Figures 1 through 4 have been calculated to illustrate factors, Π , and loss factors, η , for simply supported structures with same surface areas (i.e., $L_1 = L_2 = 2m$). As a

preliminary, Fig. 1 and study of C_k and Eq. (2-16) demonstrate that factor Π is nearly independent of circular frequency and structural thickness. These factors are clearly important for the part of η_D of Eq. (2-14). Figure 2 shows that loss factor increases at very low frequencies and decreases at high frequencies as the thickness increases. It also demonstrates that loss factor is almost proportional to the reference absolute temperature.

From earlier development, for a given material and structure, η_D and Π can be represented by

$$\eta_D \approx \eta_D(\omega, h); \quad \Pi \approx \Pi(L_1, L_2, m, n)$$

Then it is obvious that η_D has its maximum value at frequency $\omega = \tau^{-1}$, which is called the Debye peak. The thickness for maximum η_D is readily obtained from

$$h \approx \pi \sqrt{\frac{k}{\rho c_v \omega}} \quad (2-27)$$

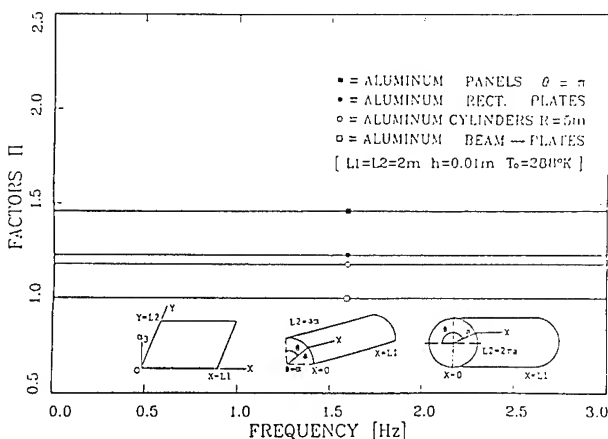


Fig. 1 Frequency dependence of the factor, Π , for simply supported structures vs. frequency (H_z).

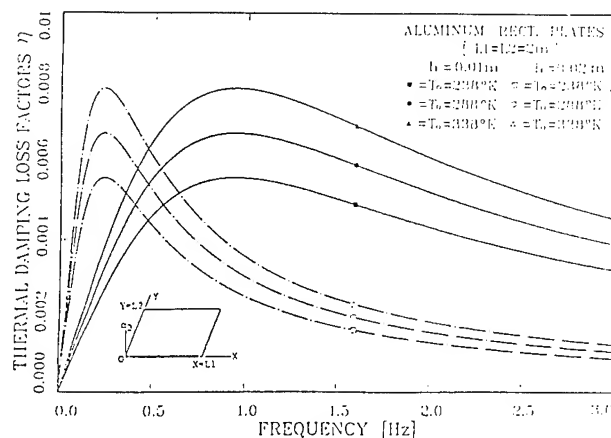


Fig. 2 Temperature and thickness dependence of the loss factor η , for a simply supported plate vs. frequency (H_z).

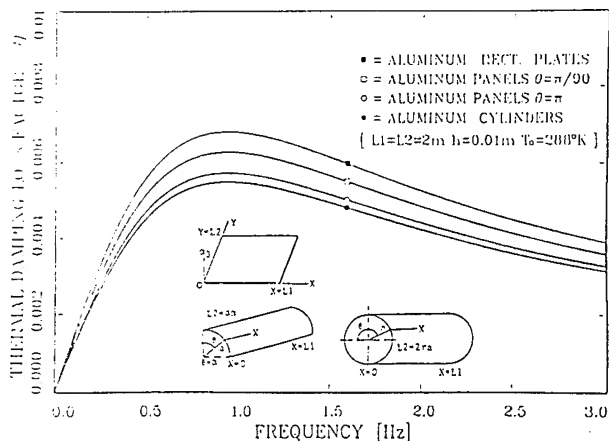


Fig. 3 Panel-curvature dependence of the loss factor η , for simply supported structures vs. frequency (H_z).

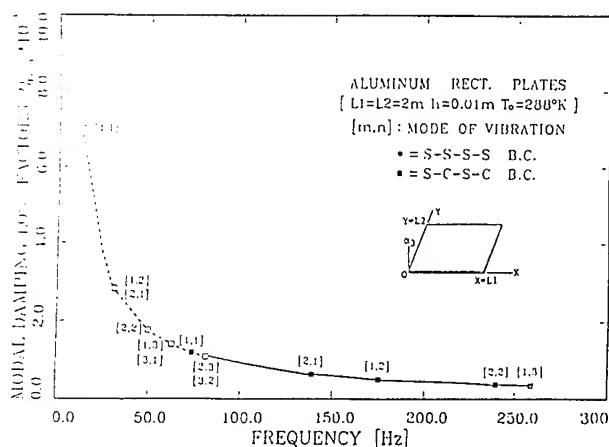


Fig. 4 Boundary condition dependence of the modal loss factor, η , for a plate at the first five fundamental natural frequencies (H_z).

Since damping plays its most important role at frequencies near natural frequencies, it is valuable to maximize the modal factor Π_{mn} of Eq. (2-25). An optimal combination of geometry and mode of vibration for the maximum value of Π_{mn} is found to be

$$\frac{L_2}{L_1} \approx \frac{n}{m} \quad (2-28)$$

Equations (2-27) and (2-28) will be useful for designers who wish to maximize the damping of vibration of the sort considered here.

Consider the modal loss factors of the plates and shells which are made of same material. At a natural frequency, when the same dimensions (L_1 , L_2) and mode (m, n) are selected for the plate and shell, it follows that

$$\frac{\eta_s}{\eta_p} = \frac{\omega_s}{\omega_p} \frac{1 + \frac{2}{\omega_s^2 \tau}}{1 + \frac{2}{\omega_p^2 \tau}}$$

Since $\omega_s \omega_p > \tau^{-1}$ in general, the modal loss factor of a plate tends to be larger than that of a shell. Figures 1 and 3 show that plates do indeed have the largest damping, followed by panels, cylinders, beam-plates and simple beams. The damping of a panel gets closer to that of a plate as it gets flatter. Also the damping of a curved panel gets closer to that of cylinder as it approaches the shape of the cylinder (Fig. 3). It is also found that the damping of a barrel-shaped shell is larger than that of a cylinder, but again it gets closer to the other as the radius of barrel curvature increases. Figure 4 shows the influence of boundary conditions. Simply supported plates show higher damping than partially-clamped plates.

Without observation of what is really happening inside the material, it seems to be very difficult to clarify the foregoing results with a reasonable physical interpretation. From the heat conduction Eq. (2-3), however, one can conclude that the structure will experience higher damping when the rate of dilatation gets larger. When the geometry and boundary conditions for a particular structure are likely to increase the rate of dilatation, the structure will achieve great damping. Constraints on a structure seem to prevent increasing the rate of dilatation with increasing natural frequency. Curved and clamped structures have more constraints than flat and simply supported structures.

3. Electromagnetic Damping Analysis

3-1 Background

Electromagneto-solid mechanics deals with the effects of an EM field on the elastic deformations of a solid body. In order to avoid an excessively long bibliography, the reader is referred to the articles by Brown,⁽¹⁶⁾ Pao⁽¹⁷⁾ and Grot.⁽¹⁸⁾

There are two main reasons, in the author's judgment, why until recently there existed relatively few applications of magneto-elasticity. First, EM effects were not a significant industrial problem at least until the appearance of very powerful magnets. Secondly, continuum mechanics cannot avoid to resort to complicated formulations for predicting the internal forces in a magnetized body.

On the other hand, industrial activity could not avoid dealing with instruments working in a strong EM field. Alers and Fleury⁽¹⁹⁾ recognized experimentally in 1963 that the influence of magneto-elastic interactions is considerable in many such situations. Moon⁽²⁰⁾ and Paria⁽²¹⁾ discussed many practical applications of magneto-solid mechanics.

Even though there exists an extensive literature on the subject, very few studies of internal energy dissipation due to EM field are known. Zener⁽⁵⁾ is believed to be the first who predicted energy dissipation by eddy currents in vibrating ferromagnetic metals. Chadwick⁽²²⁾ investigated the effect of a static magnetic field on wave motion in a conducting solid. Subsequently, Smith and Herrmann⁽²³⁾ discussed the effect of a type of magnetic damping upon the stability of some circulatory elastic systems. Nayfeh and Nasser⁽²⁴⁾ examined the influence of

small thermoelastic and magneto-elastic couplings on the propagation of plane electromagneto-elastic waves through an infinite isotropic medium.

In this paper, the author investigates the electromagnetic damping due to electric conduction currents within a homogeneous, isotropic and electromagnetically linear conducting elastic body. The underlying theory is linear magneto-elasticity^(23,25).

3-2 Basic Formulation

A complete set of equations of the linear magneto-elasticity is given by⁽²⁵⁾

$$\alpha^2 \nabla \nabla \cdot \underline{u} - \beta^2 \nabla \times (\nabla \times \underline{u}) + \frac{\mu_H}{\rho} (\nabla \times \underline{h}) \times \underline{H}_0 + \underline{f} = \ddot{\underline{u}} \quad (a) \quad (3-1)$$

$$\nabla^2 \underline{h} - \frac{1}{v_H} \underline{h} = - \frac{1}{v_H} \nabla \times (\underline{u} \times \underline{H}_0) \quad (b)$$

Where \underline{u} is the displacement field and \underline{h} is a small perturbation in a constant reference magnetic field \underline{H}_0 . $v_H = 1/\sigma\mu_H$ is the magnetic viscosity, where σ is electric conductivity and μ_H is the magnetic permeability. Application of vector identities and properties of Maxwell's equations into Eqs. (3-1) yields the equations as follows:

$$\alpha^2 \nabla \nabla \cdot \underline{u} - \beta^2 \nabla \times (\nabla \times \underline{u}) + \nabla \times (\underline{h} \times \underline{C}_H) - \nabla (\underline{h} \cdot \underline{C}_H) + \underline{f} = \ddot{\underline{u}} \quad (a) \quad (3-2)$$

$$\nabla^2 \underline{h} - \frac{1}{v_H} \underline{h} - \underline{C}_u (\nabla \cdot \underline{u}) - \underline{C}_u \times (\nabla \times \underline{u}) + \nabla (\underline{u} \cdot \underline{C}_u) = 0 \quad (b)$$

where \underline{C}_H and \underline{C}_u are the electromagnetic-elastic coupling vectors defined by

$$\underline{C}_H = \frac{\mu_H \underline{H}_0}{\rho} \quad \underline{C}_u = \frac{\underline{H}_0}{v_H}$$

Parabolic Eq. (3-2(b)) contains three types of coupling terms: dilatational, rotational and gradient parts. In the case of the heat conduction equation, one sees by comparison that only a dilatational part exists.

To simplify the analysis without losing generality, one assumes that the gradient part can be rendered negligible by applying a properly oriented magnetic field. That is,

$$\nabla (\underline{u} \cdot \underline{C}_u) = 0 \quad (3-3)$$

With the assumption, Eq. (3-3), one introduces the Helmholtz theorem⁽²⁶⁾

$$\underline{u} = \nabla \phi + \nabla \times \underline{A} \quad \nabla \cdot \underline{A} = 0 \quad (3-4)$$

Assuming $\underline{f} = \nabla F$ and inserting Eq. (3-4) into (3-2), one finds the equations as follows:

$$\alpha^2 \nabla^2 \phi - \underline{h} \cdot \underline{C}_H + F = \ddot{\phi} \quad (a)$$

$$\beta^2 \nabla^2 \underline{A} + \underline{h} \times \underline{C}_H = \ddot{\underline{A}} \quad (b) \quad (3-5)$$

$$\nabla^2 \underline{h} - \frac{1}{v_H} \underline{h} + \underline{C}_u \times \nabla^2 \underline{A} - \underline{C}_u \nabla^2 \phi = 0 \quad (c)$$

These three equations govern longitudinal (P-), transverse (S-) and EM waves. P and S waves are coupled to the EM wave.

Modal analysis is useful for the solution of Eqs. (3-5) in the form:

$$\phi(\underline{r}, t) = \sum_n \phi_n^0 \psi_n(\underline{r}) e^{i\omega t} \quad (a)$$

$$\underline{h}(\underline{r}, t) = \sum_n [\underline{\psi}_n] \underline{h}_n^0 e^{i\omega t} \quad (b) \quad (3-6)$$

$$\underline{A}(\underline{r}, t) = \sum_n [\underline{\psi}_n] \underline{A}_n^0 e^{i\omega t} \quad (c)$$

with the harmonic excitation given by

$$F(\underline{r}, t) = \sum_n F_n \psi_n(\underline{r}) e^{i\omega t} \quad (d)$$

Here \underline{r} is a collective symbol for the coordinates x, y, z , and $\phi_n^0, \underline{h}_n^0, \underline{A}_n^0$ are constant magnification factors. The eigenfunctions of ψ_n corresponding eigenvalues λ_n are determined byⁿ

$$\nabla^2 \psi_n + \lambda_n^2 \psi_n = 0 \quad \text{on } V \quad (a)$$

$$\underline{\psi}_n \cdot \underline{n} = 0 \quad \text{on } S \quad (b) \quad (3-7)$$

$$\int \psi_m \psi_n dV = \delta_{mn}, \quad (c)$$

where \underline{n} is the unit outward vector normal to surface S . Even though the boundary conditions (3-7(b)) do not embrace all possible realistic conditions at bounding surfaces,⁽²⁵⁾ the corresponding solutions should provide an acceptable basis for the analytical study of electromagnetic damping. Introducing assumed solutions into Eqs. (3-5), one may obtain

$$(\alpha^2 \lambda_n^2 - \omega^2) \phi_n^0 + \underline{h}_n^0 \cdot \underline{C}_H = F_n \quad (a)$$

$$(\beta^2 \lambda_n^2 - \omega^2) \underline{A}_n^0 - \underline{h}_n^0 \times \underline{C}_H = 0 \quad (b) \quad (3-8)$$

$$(\lambda_n^2 + \frac{i\omega}{v_H}) \underline{h}_n^0 + i\omega \lambda_n^2 \underline{C}_u \times \underline{A}_n^0 - i\omega \lambda_n^2 \underline{C}_u \phi_n^0 = 0 \quad (c)$$

Here F_n is usually prespecified. When a constant magnetic field is applied in such a way that $\underline{C}_H = (C_{H1}, C_{H2}, 0)$, then Eqs. (3-8) are reduced to a two-by-two matrix equation with unknown variables $\underline{h}_n^0 = (h_{n1}, h_{n2}, 0)$.

3-3 Free Vibration

Put $F_n = 0$ in order to study free vibration at a natural frequency ω_n . Then Eqs. (3-8) yield two algebraic equations, as follows:

$$\chi_{n1}^3 - i\epsilon_1 \chi_{n1}^2 - \epsilon_1^2 (1 + \epsilon_1) \chi_{n1} + i\epsilon_1^4 = 0 \quad (a) \quad (3-9)$$

$$\chi_{n2}^3 - i\epsilon_2 \chi_{n2}^2 - \epsilon_2^2 (1 + \epsilon_2) \chi_{n2} + i\epsilon_2^4 = 0 \quad (b)$$

Here ϵ_1 and ϵ_2 are electromagneto-elastic coupling constants with standing P and S waves, respectively. The new notations are defined as follows:

$$\left(\frac{\beta^2}{v_H}, \frac{\alpha^2}{v_H}\right) = (\omega_1^*, \omega_2^*) \quad \left(\frac{\omega_n}{\omega_1}, \frac{\omega_n}{\omega_2}\right) = (\chi_{n1}, \chi_{n2})$$

$$\left(\frac{\lambda_n^2}{\omega_1}, \frac{\mu_n \lambda_n^2}{\omega_2}\right) = (\zeta_{n1}^2, \zeta_{n2}^2) \quad \left(\frac{\rho \sigma \zeta_H^2}{\omega_1}, \frac{\rho \sigma \zeta_H^2}{\omega_2}\right) = (\epsilon_1, \epsilon_2)$$

where ω_1^*, ω_2^* are characteristic frequencies and the others are non-dimensional quantities. When $\epsilon_1 = \epsilon_2 = 0$, the algebraic equations for uncoupled elastic P and S waves are recovered.

It is interesting to find that each of the algebraic equations (3-9) has a form identical to that for the thermal damping of an elastic body, solved by Chadwick.⁽¹¹⁾ This implies that electromagnetic damping is analogous to thermal damping. With the help of Chadwick's solutions obtained for the same type of algebraic equation, the modal damping loss factor can be obtained from

$$\frac{\delta_{ni}}{\pi} \approx \epsilon_i \frac{\zeta_{ni}}{1 + \zeta_{ni}^2} \quad (i=1,2), \quad (3-10)$$

where higher terms $O(\epsilon_i^2)$ are neglected. Since $\epsilon_1 > \epsilon_2$, standing S waves are seen to have larger damping than standing P waves.

As an example, consider an infinite plate with uniform thickness h . To obtain maximum dampings for P and S waves, the thicknesses can be shown to be

$$h_1 = (2n+1) \frac{v_H \pi}{\beta} \quad \text{for the P wave}$$

$$h_2 = (2n+1) \frac{v_H \pi}{\alpha} \quad \text{for the S wave}$$

Therefore the standing P wave requires larger thickness than the standing S wave to achieve peak damping.

3-4 Forced Vibration

It is convenient to introduce a new notation, defined by

$$\frac{\omega}{\omega_2} = \chi$$

For the forced vibration Eqs. (3-8) can readily be solved for ϕ_n^0 , A_n^0 and h_n^0 . Without reproducing complicated calculations, one finds the real parts of solutions as follows:

$$\bar{u} = \sum_n [\phi_n^0 \cos \omega t] \bar{\psi}_n \quad (3-11)$$

$$\bar{h} = \sum_n [\bar{h}_{nR}^0 \cos \omega t - \bar{h}_{nI}^0 \sin \omega t] \bar{\psi}_n, \quad (3-12)$$

where

$$\bar{h}_{nR}^0 \approx \frac{F C_H}{\zeta_H^2} \frac{\epsilon \chi^2 \zeta_n^2}{(\zeta_n^4 + \chi^2)(\chi^2 - \zeta_n^2) - \epsilon \zeta_n^2 \chi^2}$$

$$\bar{h}_{nI}^0 \approx \frac{F C_H}{\zeta_H^2} \frac{\epsilon \chi \zeta_n^4}{(\zeta_n^4 + \chi^2)(\chi^2 - \zeta_n^2) - \epsilon \zeta_n^2 \chi^2}$$

The result shows that only the dilatation contributes to the damping of forced vibration.

Equation (2-18) will be adopted as a measure of electromagnetic damping in forced vibration. In the present case, the energies U and ΔU are given in the form

$$U = \frac{1}{2} \int_V t_{ij} \epsilon_{ij} dV \quad (3-13)$$

$$\Delta U = \int_V \int_0^{2\pi} m_{ij} \dot{\epsilon}_{ij} d\omega t dV \quad (3-14)$$

Note that t_{ij} is the total stress, which is the sum of mechanical stress and linearized Maxwell stress:

$$t_{ij} = \sigma_{ij} + m_{ij} \quad (a)$$

$$\sigma_{ij} = \frac{E}{(1+\nu)(1-2\nu)} [\nu e \delta_{ij} + (1-2\nu) \epsilon_{ij}] \quad (b) \quad (3-15)$$

$$m_{ij} = \mu_H [H_{oi} h_j + H_{oj} h_i] - \bar{H}_0 \cdot \bar{h} \delta_{ij} \quad (c)$$

It is obvious that the mechanical stress does not contribute to the energy dissipation. Thus only the Maxwell stress is considered in Eq. (3-14). It can be shown, by using the assumption (3-3), that the round bracketed part of m_{ij} also does not contribute to the energy dissipation. A substantial series of calculations, with application of the orthogonality property (3-7(c)), leads to

$$\eta \approx \epsilon R \sum_m P_m \frac{\chi \zeta_m^2}{\zeta_m^4 + \chi^2} \quad (3-16)$$

Here

$$R \approx \frac{\int_V e_{\max}^2 dV}{\int_V [e^2 + \left(\frac{1-2\nu}{1-\nu}\right)(\epsilon_{ij}^2 - e^2)]_{\max} dV} \quad (3-17)$$

In Eqs. (3-16), P_m satisfies the Parseval properties⁽¹¹⁾. The perturbation of EM field generated in a solid body is likely to be so small that its contribution to R is neglected. Equation (3-16) is exactly analogous to the key results of Zener⁽¹⁵⁾ and Chadwick⁽¹¹⁾, which are for thermo-elastic damping. Zener worked out a number of simple cases in which he estimated the values of P_m . It is found that $P = 1$ and $P_m \ll 1$ for $m > 1$. Equation (3-16) can then be approximated by

$$\eta \approx \epsilon R \frac{\psi \zeta_o^2}{\chi^2 + \zeta_o^4} \quad (3-18)$$

which has the maximum value $\epsilon R/2$ when $\chi = \zeta_o^2$. The modal loss factor at a natural frequency $\chi \approx \zeta_n$ is found to be

$$\eta_n \approx \epsilon R \frac{\xi_n}{1 + \xi_n^2} \quad (3-19)$$

This result agrees with δ_{n2}/π apart from factor $R(\approx 1)$. η_n has the maximum value $\epsilon R/2$ when $\xi_n = 1$.

Modal damping loss factor, defined by the half-power bandwidth, is found from the magnification factor ϕ_n^0 of Eq. (3-11(a)) in the form:

$$\frac{\dot{\omega}}{\omega_n} = \frac{\Delta \chi}{\chi_n} \approx \epsilon \frac{\xi_n}{1 + \xi_n^2}$$

which is exactly the same as Eq. (3-10) with index $i = 2$ and Eq. (3-19) with $R \approx 1$.

The general expression for electromagnetic damping shows that it takes the form of the Debye formula and that it is proportional to the square of the magnitude of the reference EM field. Therefore the contribution of electromagnetic damping to total material damping will be considerable in high fields.

4. Thermal Damping Effects on the Aeroelastic Stability of Beam-Plates

4-1 Analysis

Consider a simply supported or damped beam-plate vibrating one dimensionally. Dowell's equation of aeroelastic equilibrium⁽²⁸⁾ is modified into the form

$$D(1+i\eta_t) \frac{\partial^4 w}{\partial x^4} + \rho h \ddot{w} + \Delta p^M + \Delta p^E = 0 \quad (4-1)$$

This now includes a thermal damping source η_t . Familiar aerodynamic theory will be directly applied as given by:

$$\Delta p^M = \frac{\rho_\infty U_\infty^2}{\sqrt{M^2 - 1}} \left[\frac{\partial w}{\partial x} + \frac{M^2 - 2}{M^2 - 1} \frac{1}{U_\infty} \frac{\partial w}{\partial t} \right] \quad (4-2)$$

which is the unsteady aerodynamic pressure due to plate motion in supersonic flow ($M > 1$) and low frequency. Δp^E in Eq. (4-1) is the external aerodynamic pressure independent of plate motion.

Application of modal analysis and the assumption of harmonic motion lead to a characteristic equation in matrix form:

$$|M_{mn} [\omega^2 - (1+i\eta_t)\omega_n^2] \delta_{mn} - \rho_\infty U_\infty^2 \frac{\partial^2 M}{\partial mn}| = 0 \quad (4-3)$$

Here the following relations have been used:

$$D \frac{\partial^4 w_n}{\partial x^4} - \rho h \omega_n^2 w_n = 0 \quad (a)$$

$$\int_0^a w_m w_n dx = M_{mn} \delta_{mn} \quad (b) \quad (4-4)$$

$$\overline{Q}_{mn}^M = \begin{cases} \sqrt{M^2 - 1} \frac{M^2 - 2}{M^2 - 1} \frac{i\omega}{U_\infty} M_{nn} & \text{for } m = n \\ \sqrt{M^2 - 1} \int_0^a \frac{dw_m}{dx} w_n dx & \text{for } m \neq n \end{cases} \quad (c)$$

with a the plate length in the streamwise x -direction. One may replace η_t with its maximum value, independent of frequency to simplify the analysis without compromising the main objective of the study.

4-2 Case I: Single Mode ($N=1$)

For the n -th mode of vibration, Eq. (4-3) can be reduced to the form

$$K^2 - i\gamma \frac{1}{\sqrt{M^2 - 1}} \frac{M^2 - 2}{M^2 - 1} K - (1+i\eta_t)K_n^2 = 0 \quad (4-5)$$

where K and K_n are reduced frequency defined by

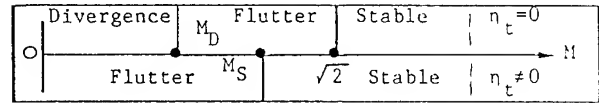
$$K = \frac{\omega a}{a_\infty} \quad K_n = \frac{\omega_n a}{a_\infty}$$

and γ is the non-dimensional mass ratio. The roots of characteristic Eq. (4-5) determine the stability of the beam-plate. The stability boundaries are at $M = \sqrt{2}$ when $\eta_t = 0$ and $M_S \approx \sqrt{2} - (K/4\gamma)\eta_t$ when $\eta_t \neq 0$. This result implies that energy dissipation due to thermal damping is helpful for stability, by the order $O(\eta_t)$. It is also found that divergence instability and thermal damping cannot coexist. A divergence boundary M_D is determined by the equation

$$\gamma M_D^2 (M_D^2 - 2) + 2K_n (M_D^2 - 1) \sqrt{M_D^2 - 1} = 0 \quad (4-6)$$

Typical results are shown in Fig. 5.

Fig. 5 Instability of Single Mode ($N=1$)



4-3 Case II: Multiple Mode ($N=2$)

Flutter may also occur as a result of coupling between modes. This normally is observed at high supersonic Mach numbers ($M > \sqrt{2}$), where Eq. (4-3) can be approximately written

$$K^4 - (1+i\eta_t)(K_1^2 + K_2^2)K^2 + (1+i\eta_t)K_1^2 K_2^2 = 0, \quad (4-7)$$

where

$$\phi^2 = \left[\frac{M^4}{M^2 - 1} \right] \frac{\left[\int_0^1 \frac{dw_1}{d\xi} w_2 d\xi \right]^2}{\int_0^1 w_1^2 d\xi \int_0^1 w_2^2 d\xi} = \left[\frac{M^4}{M^2 - 1} \right] \phi^2 \quad (4-8)$$

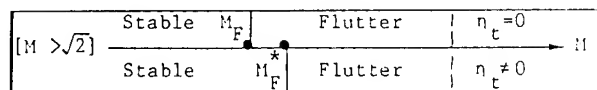
Flutter boundaries are given analytically as follows:

$$4\gamma\phi^2 M_F^2 + (K_1^2 - K_2^2)(M_F^2 - 1) = 0 \quad (4-9)$$

$$M_F^* = M_F + \left[\frac{(K_1^2 + K_2^2)^2}{16M_F^2 \gamma \phi^2} \right] \eta_t^2 \quad (4-10)$$

Figure 6 shows the effects of thermal damping on the flutter of coupled multiple modes. These results again demonstrate that thermal damping is favorable for stability, by the order of $O(\eta_t^2)$.

Fig. 6 Instability of Coupled Multiple Modes ($N = 2$)



Acknowledgements

This research was supported by Air Force Office of Scientific Research under contract AFOSR 0062. The contents of this paper will be contained in the author's upcoming Ph.D dissertation. The author is appreciative of valuable discussions with professor Holt Ashley.

References

1. Lazan, B.J., Damping of Materials and Members in Structural Mechanics, Pergamon Press, Oxford, 1960.
2. Nowick, A.S., and Berry, B.S., Anelastic Relaxation in Crystalline Solids, Academic Press, New York, 1972.
3. Gevarter, W.B., "Basic Relations for Control of Flexible Vehicles," AIAA Journal, Vol. 8, No. 4, April 1970, pp. 666-672.
4. Ashley, H., "On Passive Damping Mechanisms in Large Space Structures," AIAA 82-0639-CP, Proceedings, AIAA/ASME/ASCE/AHS 23rd Structures, Structural Dynamics and Materials Conference, New Orleans, LA., May, 1982, pp. 56-67.
5. Zener, C., "Internal Friction in Solids," Parts I, II, III, IV, V, Phys. Review, Vol. 53, 1938.
6. Bennewitz, K., and Rötger, H., "On the Internal Friction of Solid Bodies: Absorption Frequencies of Metals in the Acoustic Range," (in German), Phys. Zeitschrift, Vol. 37, 1936, PP. 578-588.
7. Zener, C., Elasticity and Anelasticity of Metals, The University of Chicago Press, Chicago, Illinois, 1948.
8. Biot, M.A., "Thermoelasticity and Irreversible Thermodynamics," Journal of Applied Physics, Vol. 27, No. 3, March 1956, PP.240-253.
9. Tast, J., "Thermoelastic Dissipation in Vibrating Plates," Transactions of the ASME, Journal of Applied Mechanics, Vol. 30, No.4, Dec. 1963, PP. 562-567.
10. Tasi, J., and Herrmann, G., "Thermoelastic Dissipation in High-Frequency Vibrations of Crystal Plates," Journal of the Acoustical Society of America, Vol. 36, No.1, Jan. 1964, PP. 100-110.
11. Chadwick, P., "Thermal Damping of A Vibrating Elastic Body," Mathematika, Vol. 9, 1962, PP. 38-48.
12. Alblas, J.B., "A Note on the Theory of Thermoelastic Damping," Journal of Thermal Stresses, Vol. 4, 1981, PP. 333-355.
13. Soedal, W., Vibrations of Shells and Plates, Marcel Dekker Inc., New York, 1981.
14. Nowacki, W., Dynamic Problems of Thermoelasticity, Noordhoff Int. Publishing, Leyden, The Netherlands, 1975.
15. Jones, D.I.G., "Behaviour of Damping Materials," Lecture Note at ASME Short Course Program on Damping Control of Design Flexibility, Norfolk, Virginia, March 21-24, 1983.
16. Brown, W.F., Magnetoelastic Interactions, Springer-Verlag, New York, 1966, P. 50.
17. Pao, Y.H., "Electromagnetic Forces in Deformable Continua," Section IV, Mechanics Today, Vol. 4, Pergamon Press Inc., 1978.
18. Grot, R.A., "Relativistic Continuum Physics: Electromagnetic Interactions," Part II, Continuum Physics, Vol. III, Academic Press, New York, 1976, PP. 129-172.
19. Alers, G.A. and Fleury, P.A., "Modification of the Velocity of Sound in Metals by Magnetic Fields," Phys. Rev. 129, No. 6, March 1963, PP. 2425-2429.
20. Moon, F.C., "Problems in Magneto-Solid Mechanics," Section V, Mechanics Today, Vol. 4, Pergamon Press Inc., 1978.
21. Paria, G., "Magneto-Elasticity and Magneto-Thermo-Elasticity," Advances in Applied Mechanics, Vol. 10, Fascicle 1, Academic Press, New York, 1967, PP. 73-112.
22. Chadwick, P., "Elastic Wave Propagation in a Magnetic Field," 9th Int. Congress for Applied Mechanics, Brussels, 1956.
23. Smith, T.E., and Herrmann, G., "Stability of Circulatory Elastic Systems in the presence of Magnetic Damping," Acta Mechanica 12, 1971, PP. 175-188.
24. Nayfeh, A.H., and Nemat-Nasser, S., "Electromagneto-Thermoelastic Plane Waves in Solids with Thermal Relaxations," Transaction of the ASME, Journal of Applied Mechanics, March 1972, PP. 108-113.
25. Nowacki, W., "Electromagnetic Interactions in Elastic Solids," Chapter II, International Centre For Mechanical Sciences, Courses and Lectures - No. 357, Edited by H. Parkus, Springer-Verlag, Wien-New York.
26. Fung, Y.C., Foundation of Solid Mechanics, Prentice-Hall Inc., N.J., 1965.
27. Knopoff, L., "The Interaction between Elastic Wave Motions and A Magnetic Field in Electrical Conductors," Journal of Geophysical Research, Vol. 60, No. 4, Dec. 1955, PP. 441-456.
28. Dowell, E.H., Aeroelasticity of Plates and Shells, Noordhoff Int. Publishing, Leyden, The Netherlands, 1975.

ACTIVE CONTROL OF DECOUPLED UNDERDAMPED SYSTEMS

Chi K. Ng*

Member of Technical Staff
AT and T Bell Telephone Laboratories
Whippany, New Jersey 07981
(201) 386-4147

Daniel J. Inman**

Assistant Professor
Department of Mechanical and Aerospace Engineering
State University of New York at Buffalo
Buffalo, New York 14260
(716) 636-2733

Abstract

The implementation of a state feedback controller for a class of underdamped distributed parameter systems (DPS) possessing classical normal modes is studied. In this control scheme, a continuous system in time and space is reduced and decoupled into a sufficiently large but finite system described by its time dependent harmonic or modal amplitudes. This model is then divided into two parts, the controlled and the residual (uncontrolled) subsystems. For the controlled subsystem, controllability and observability conditions are derived. It is demonstrated that, in theory, only one actuator and one sensor are required for controllability and observability. In this case, these controllability and observability conditions are expressed simply as functions of eigenfunctions and eigenvalues of the DPS. The authors note that these results on controllability and observability are consistent with the results on more restricted models obtained by previous investigators. Upper bounds for the residual modal amplitudes of the DPS have been derived. These bounds show that the control spillover does not destabilize the residual subsystem.

1. Introduction

One method of vibration control of DPS is to reduce the system into a set of decoupled modal equations. From this set of equations, a number of vibration modes that have been determined to be undesirable is selected for control. These modes are called the controlled modes, while the rest of the uncontrolled modes are termed the residual modes. According to modern control theory, if the controlled system satisfies controllability and observability conditions, then a controller can be designed for manipulation of the eigenvalues of the system. In other words, the controller can add damping and prescribe "natural frequencies" to the controlled system. However, the control force and the unfiltered sensor output couple the residual modes with the controlled modes of the system, creating phenomena known as control spillover and observation

spillover. The control spillover effect has been shown to cause instabilities in undamped systems⁽¹⁻²⁾. Recognizing the fact that all systems have some structural damping, this paper intends to show that the control spillover cannot create instability in the residual modes of the underdamped DPS. Since most of the engineering problems need concern for the first several modes of vibration, a low bandpass filter is recommended to filter out the higher modes thereby eliminating observation spillover.

The other approach to active vibration control of DPS relies on the so called modal filters, which can be designed to extract the modal information from the sensors data with minimal residual modal contaminations. The concept is based on distributed actuators and sensors. In practice, though, a sufficiently large number of point actuators and sensors are to be employed. The rationale behind this approach is the concern for the destabilizing effect of the control and observation spillover on undamped systems⁽³⁻⁴⁾.

In this study, the controllability and observability conditions of the controlled system are demonstrated to be guaranteed by one actuator and one sensor. They are also shown to be dependent on the locations of the point actuators and sensors as well as the eigenvalues of the system. Although these conditions are derived in a manner different from [1] and [5], they can still be applied to the undamped systems of [1] and [5]. The use of controllability and observability norms here follows analogously to those found in [5].

Bounds on the residual modal solutions have been derived in a straight forward manner from a well known closed form solution. These bounds may be used for estimating the residual system response due to excitations from initial conditions and from control spillover.

The distributed parameter systems discussed here is described by the following⁽⁶⁾:

$$u_{tt}(\underline{x}, t) + L_1[u_t(\underline{x}, t)] + L_2[u(\underline{x}, t)] = F(\underline{x}, t) \text{ in } \Omega$$

$$B[u(\underline{x})] = 0 \quad \text{on } \partial\Omega \quad (1.1)$$

where the assumptions and notations are:

- a. $(\cdot)_t$ indicates partial differentiation of (\cdot) with respect to the time, t ;

* Formerly, a graduate student in the Department of Mechanical and Aerospace Engineering, State University of New York at Buffalo. This work was performed while at the University of Buffalo.

** Member of AIAA, work supported under AFOSR Grant 820242.

- b. Ω is a bounded, open region in R^n , $n=1,2$, or 3 with boundary $\partial\Omega$;
- c. L_1 and L_2 are linear spatial differential operators of order n_1, n_2 , respectively, and are self-adjoint* on the domain $D(L) = \{u(\cdot, t) \in L_2(\Omega) \text{ such that all partial derivatives with respect to } \underline{x} \text{ of order up to and including } k \text{ are in } L^2(\Omega) \text{ where } k = \max(2n_1, n_2) \text{ and } B[u(\underline{x})] = 0 \text{ for } \underline{x} \in \partial\Omega, \text{ for all } t \geq 0\}$;
- d. L_1 and L_2 commute on $D(L)$; L_1, L_2 are positive definite operators on $D(L)$ and each has a compact resolvent;
- e. $4L_2 - L_1^2$ is positive definite on $D(L)$ ensuring that all the modes are underdamped⁶.
- f. B is a linear spatial operator (and may be a differential operator of order up to $\max(n_1, n_2) - 1$ which reflects time independent boundary conditions).
- g. $F(\underline{x}, t)$ is an applied force distribution.

Note that the system described above is more general than the one considered in [1] which requires L_1 to be expressible as $2\zeta L_2^{1/2}$ (ζ denotes damping ratio).

The applied force distribution is obtained from n point force actuators. The force distribution may be written as

$$F(\underline{x}, t) = \sum_{i=1}^n \delta(\underline{x} - \underline{x}_i) f_i(t) \quad (1.2)$$

where $\delta(\underline{x} - \underline{x}_i)$ denotes the Dirac delta function, \underline{x}_i is the position vector of the i th point force actuator, $f_i(t)$ is the i th actuator force amplitude.

Following from assumption (d), system (1.1) has solution of the form

$$u(\underline{x}, t) = \sum_{k=1}^e u_k(t) \phi_k(\underline{x}) \quad (1.3)$$

where $\phi_k(\underline{x})$ is a complete set of real orthonormal functions which satisfies the boundary conditions specified on $\partial\Omega$.

In theory, e is taken to be at infinity but in practice, e is taken to be a sufficiently large number. Clearly, e should be chosen such that $u(\underline{x}, t)$ can be faithfully represented by the truncated series with acceptable errors.

Substituting (1.3) into (1.1) and making use of the orthonormality property of the eigenfunctions and noting that (1.3) is uniformly convergent due to L_1, L_2 having compact resolvent, we get

$$\ddot{\underline{u}}(t) + [\Lambda^{(1)}] \dot{\underline{u}}(t) + [\Lambda^{(2)}] \underline{u}(t) = [B] \underline{f}(t) \quad (1.4)$$

where

$$[\Lambda^{(1)}] = \text{diag}[\lambda_1^{(1)}, \dots, \lambda_1^{(1)}]$$

* n_1, n_2 are necessarily even numbers.

$$[\Lambda^{(2)}] = \text{diag}[\lambda_1^{(2)}, \dots, \lambda_1^{(2)}]$$

$$\underline{u}(t) = [u_1(t), \dots, u_e(t)]^T$$

$$\underline{f}(t) = [f_1(t), \dots, f_e(t)]^T$$

and

$$B = \begin{bmatrix} \phi_1(\underline{x}_1) & \dots & \phi_1(\underline{x}_n) \\ \vdots & & \vdots \\ \phi_e(\underline{x}_1) & \dots & \phi_e(\underline{x}_n) \end{bmatrix}$$

We note that the left side of (1.4) becomes decoupled under our assumption (d) (i.e., $L_1 L_2 = L_2 L_1$) stated earlier.

In general, there are p point sensors that feed back both position and velocity information. The point sensors described above may be composed of collocation of both position and velocity sensors or may be a combined unit that can produce information for position and velocity. The sensor equation can be written as

$$\underline{y}(t) = [\bar{C}] u(\underline{x}, t) + [\bar{D}] \dot{u}(\underline{x}, t) \quad (1.5)$$

where

$$[\bar{C}] = \text{diag}[c_1 \delta(\underline{x} - \underline{x}_1), \dots, c_p \delta(\underline{x} - \underline{x}_p)]$$

$$[\bar{D}] = \text{diag}[d_1 \delta(\underline{x} - \underline{x}_1), \dots, d_p \delta(\underline{x} - \underline{x}_p)]$$

$$\underline{y}(t) = [y_1(t), \dots, y_p(t)]$$

Note that $\delta(\underline{x} - \underline{x}_i)$ is a Dirac delta function denoting the location of the i th sensor at \underline{x}_i .

Substitution of (1.3) into (1.5) yields

$$\underline{y}(t) = [C] [E] \underline{u}(t) + [D] [E] \dot{\underline{u}}(t) \quad (1.6)$$

where

$$[C] = \text{diag}[c_1, \dots, c_p]$$

$$[D] = \text{diag}[d_1, \dots, d_p]$$

and

$$[E] = \begin{bmatrix} \phi_1(\underline{z}_1) & \dots & \phi_e(\underline{z}_1) \\ \vdots & & \vdots \\ \phi_1(\underline{z}_p) & \dots & \phi_e(\underline{z}_p) \end{bmatrix}$$

We partition the large but truncated system into controlled and residual modal states, $\underline{v}(t)$ and $\underline{w}(t)$ respectively. We have

$$\underline{v}(t) = [\underline{v}_N^T(t) \quad \dot{\underline{v}}_N^T(t)]^T \quad (1.7a)$$

$$\underline{w}(t) = [\underline{w}_R^T(t) \quad \dot{\underline{w}}_R^T(t)]^T \quad (1.7b)$$

The subscripts N and R will now be used to denote controlled and residual parts of the large, truncated system respectively.

We now rewrite (1.4) and (1.6) in the following

first order form.

$$\dot{\underline{y}}(t) = [\bar{A}_N] \underline{y}(t) + [\bar{B}_N] \underline{f}(t) \quad (1.8)$$

$$\dot{\underline{w}}(t) = [\bar{A}_R] \underline{w}(t) + [\bar{B}_R] \underline{f}(t) \quad (1.9)$$

$$\underline{y}(t) = [\bar{C}_N] \underline{y}(t) + [\bar{C}_R] \underline{w}(t) \quad (1.10)$$

where the system coefficient matrices are:

$$[\bar{A}_N] = \begin{bmatrix} [0] & [I_N] \\ -[\Lambda_N^{(2)}] & -[\Lambda_N^{(1)}] \end{bmatrix} \quad [\bar{A}_R] = \begin{bmatrix} [0] & [I_R] \\ -[\Lambda_R^{(2)}] & -[\Lambda_R^{(1)}] \end{bmatrix}$$

$$[\bar{B}_N] = \begin{bmatrix} [0] \\ [B_N] \end{bmatrix} \quad [\bar{B}_R] = \begin{bmatrix} [0] \\ [B_R] \end{bmatrix}$$

$$[\bar{C}_N] = [C][E_N] \quad [\bar{C}_R] = [C][E_R] \quad [D][E_R]$$

with the appropriate partitions,

$$[\Lambda^{(1)}] = \begin{bmatrix} [\Lambda_N^{(1)}] & [0] \\ [0] & [\Lambda_R^{(1)}] \end{bmatrix} \quad [\Lambda^{(2)}] = \begin{bmatrix} [\Lambda_N^{(2)}] & [0] \\ [0] & [\Lambda_R^{(2)}] \end{bmatrix}$$

$$[E] = [[E_N] \quad [E_R]]$$

We define the term $[\bar{C}_R] \underline{w}(t)$ to be observation spillover and the term $[\bar{B}_R] \underline{f}(t)$ to be control spillover (see Fig. 1).

The following control law is used for the subsystem $[\bar{A}_N]$

$$\underline{f}(t) = [G] \underline{y}(t) \quad (1.11)$$

where $[G]$ is the control gain matrix.

If the modal states, $\underline{y}(t)$, are estimated by an asymptotic observer, then (1.11) takes the following form

$$\underline{f}(t) = [G] \hat{\underline{y}}(t) \quad (1.12)$$

where $\hat{\underline{y}}(t)$ are the states estimated by the observer.

The combined controller-observer system can be described by

$$\underline{y}(t) = [\bar{A}_N] \underline{y}(t) + [\bar{B}_N] [G] \underline{y}(t) \quad (1.13)$$

$$\dot{\hat{\underline{y}}}(t) = ([\bar{A}_N] - [K][\bar{C}_N]) \hat{\underline{y}}(t) + [\bar{B}_N] [G] \hat{\underline{y}}(t) + [K][\bar{C}_N] \underline{y}(t),$$

$$\hat{\underline{y}}(0) = \underline{0}$$

Note that $[K]$ is the gain matrix for the observer.

The error between the actual and estimated states is defined by

$$\underline{e}(t) = \underline{y}(t) - \hat{\underline{y}}(t)$$

Substituting (1.14) into (1.13), we have

$$\dot{\underline{y}}(t) = ([\bar{A}_N] + [\bar{B}_N][G]) \underline{y}(t) - [\bar{B}_N][G] \underline{e}(t) \quad (1.15a)$$

$$\dot{\underline{e}}(t) = ([\bar{A}_N] - [K][\bar{C}_N]) \underline{e}(t), \quad \underline{e}(0) = \underline{y}(0) \quad (1.15b)$$

Or, equivalently, (1.15) can be written as

$$\underline{z}(t) = \begin{bmatrix} [\bar{A}_N] + [\bar{B}_N][G] & -[\bar{B}_N][G] \\ [0] & [\bar{A}_N] - [K][\bar{C}_N] \end{bmatrix} \underline{z}(t) \quad (1.16)$$

where $\underline{z}(t) = [\underline{y}^T(t) \quad \underline{e}^T(t)]$

Since (1.16) is in block triangular form, the associated eigenvalues are simply those of the controller, $[\bar{A}_N] + [\bar{B}_N][G]$, and those of the observer, $[\bar{A}_N] - [K][\bar{C}_N]$. Furthermore, the modes of controller and observer do not interact. Therefore, the controller and the observer can be designed independently. This property is called the separation property.

To write (1.16) in a more compact form, we let

$$[\tilde{A}_N] = \begin{bmatrix} [\bar{A}_N] + [\bar{B}_N][G] & -[\bar{B}_N][G] \\ [0] & [\bar{A}_N] - [K][\bar{C}_N] \end{bmatrix}$$

then (1.16) becomes

$$\dot{\underline{z}}(t) = [\tilde{A}_N] \underline{z}(t) \quad (1.17)$$

2. Controllability and Observability Conditions

2.1 Modal Matrix of $[\bar{A}_N]$

We first examine (1.4) with the removal of the forcing term $[B] \underline{f}(t)$. Eqn. (1.4) is now rewritten as follows (with concern only for the controlled modal amplitudes).

$$\ddot{\underline{u}}_N(t) + [\Lambda_N^{(1)}] \dot{\underline{u}}_N(t) + [\Lambda_N^{(2)}] \underline{u}_N(t) = \underline{0} \quad (2.1)$$

Again, the subscript N denotes the controlled part of (1.4) and (2.1) is equivalent to (1.8) without $[\bar{B}_N] \underline{f}(t)$, i.e.

$$\dot{\underline{y}}(t) = [\bar{A}_N] \underline{y}(t) \quad (2.2)$$

The scalar form of (2.1) is

$$\ddot{u}_i(t) + \lambda_i^{(1)} \dot{u}_i(t) + \lambda_i^{(2)} u_i(t) = 0 \quad (i=1, \dots, n) \quad (2.3)$$

To solve the above equation, one assumes the solution of the form

$$u_i(t) = q e^{st} \quad (2.4)$$

Substituting (2.4) into (2.3), get

$$(s^2 + \lambda_i^{(1)} s + \lambda_i^{(2)}) q = 0 \quad (2.5)$$

The nontrivial solution of 2.5 is obtained by using the quadratic formula,

$$s_j, s_{j+1} = (-\lambda_i^{(1)} \pm \sqrt{(\lambda_i^{(1)})^2 - 4\lambda_i^{(2)}}) / 2 \quad (2.6)$$

Since system (1.1) is underdamped, the s_j and s_{j+1} are always complex conjugates of each other, therefore $s_j \neq s_{j+1}$, i.e. each pair of adjacent roots are distinct.

We now claim that the following transformation, $[T]$, is a modal matrix of $[\bar{A}_N]$. The reason for this particular choice of $[T]$ will enable us to simplify controllability and observability conditions of $([\bar{A}_N], [\bar{B}_N], [\bar{C}_N])$.

$$[T] = \begin{bmatrix} 1 & 1 & 0 & 0 & \dots & 0 & 0 \\ 0 & 0 & 1 & 1 & & . & . \\ . & . & 0 & 0 & & . & . \\ . & . & . & . & & . & . \\ . & . & . & . & & 0 & 0 \\ 0 & 0 & . & . & & 1 & 1 \\ s_1 & s_2 & 0 & 0 & & 0 & 0 \\ 0 & 0 & s_3 & s_4 & & . & . \\ . & . & 0 & 0 & & . & . \\ . & . & . & . & & . & . \\ . & . & . & . & & . & . \\ 0 & 0 & 0 & 0 & \dots & s_{2n-1} & s_{2n} \end{bmatrix} \quad (2.7)$$

Since s_1 and s_2 , s_3 and s_4 , ..., and s_{2n-1} and s_{2n} are pairs with distinct elements, one can easily see that $[T]$ has a complete set of linearly independent eigenvectors. In other words, $[T]^{-1}$ exists. The inverse of $[T]$ takes the following form:

$$[T]^{-1} = \begin{bmatrix} \frac{s_2}{s_2-s_1} & 0 & \dots & 0 & \frac{-1}{s_2-s_1} & 0 & 0 \\ \frac{-s_1}{s_2-s_1} & 0 & . & \frac{1}{s_2-s_1} & 0 & . & . \\ 0 & \frac{s_4}{s_4-s_3} & & 0 & \frac{-1}{s_4-s_3} & & . \\ . & \frac{-s_3}{s_4-s_3} & & . & \frac{1}{s_4-s_3} & & . \\ 0 & 0 & \frac{s_{2n}}{s_{2n}-s_{2n-1}} & 0 & \frac{-1}{s_{2n}-s_{2n-1}} & & . \\ . & . & . & . & . & . & . \\ 0 & 0 & \frac{-s_{2n-1}}{s_{2n}-s_{2n-1}} & 0 & 0 & \frac{1}{s_{2n}-s_{2n-1}} & . \end{bmatrix} \quad (2.8)$$

One can easily verify that $[T][T]^{-1}$ yields $[I]$, the identity matrix. Therefore (2.7) and (2.8) are truly inverse of each other.

Now, to establish that $[T]$ is a modal matrix of $[\bar{A}_N]$, we will show that

$$[T]^{-1}[\bar{A}_N][T] = [D] \quad (2.9)$$

where $[D]$ is a diagonal matrix with the eigenvalues s_1, s_2, \dots, s_{2n} of $[\bar{A}_N]$ on the diagonal of $[D]$.

By actually carrying out the calculation of the left side of (2.9), we find that

$$[T]^{-1}[\bar{A}_N][T] = \begin{bmatrix} \frac{s_1 s_2 - s_1^2}{s_2 - s_1} & & & & 0 \\ & \frac{-s_1 s_2 + s_2^2}{s_2 - s_1} & & & \\ & & \frac{s_3 s_4 + s_3^2}{s_4 - s_3} & & \\ & & & \frac{s_{2n-1} s_{2n} - s_{2n-1}^2}{s_{2n} - s_{2n-1}} & \\ 0 & & & & \end{bmatrix} \quad (2.10)$$

Eqn (2.10) can further be simplified to

$$[T]^{-1}[\bar{A}_N][T] = \begin{bmatrix} s_1 & & & 0 \\ & s_2 & & \\ & & . & \\ 0 & & & s_{2n} \end{bmatrix} \quad (2.11)$$

The above is identically equal to $[D]$. Our claim that $[T]$ is the modal matrix of $[\bar{A}_N]$ is now justified.

2.2 Controllability

We define our controlled system with the forcing term $[\bar{B}_N]f(t)$ by the following

$$\dot{\bar{y}}(t) = [\bar{A}_N]\bar{y}(t) + [\bar{B}_N]f(t) \quad (2.12)$$

$$\bar{y}(t) = [\bar{C}_N]\bar{y}(t) \quad (2.13)$$

The observation spillover, $[\bar{C}_R]w(t)$, is presumed to be eliminated by means of a prefilter such as a low bandpass filter.

With the aid of $[T]$ and $[T]^{-1}$, we perform similarity transformation of (2.12) and (2.13). Letting $\underline{y}(t) = [T]\bar{y}(t)$, and premultiplying (2.12) with $[T]$, we have

$$\dot{\underline{y}}(t) = [T]^{-1}[\bar{A}_N][T]\underline{y}(t) + [T]^{-1}[\bar{B}_N]f(t) \quad (2.14)$$

$$\underline{y}(t) = [\bar{C}_N][T]\underline{y}(t) \quad (2.15)$$

Using (2.9), we may write (2.14) and (2.15) as

$$\dot{\underline{y}}(t) = [D]\underline{y}(t) + [\tilde{B}]f(t) \quad (2.16)$$

$$\underline{y}(t) = [\tilde{C}]\underline{y}(t) \quad (2.17)$$

where $[\tilde{B}] = [T]^{-1}[\bar{B}_N]$ and $[\tilde{C}] = [\bar{C}_N][T]$

Since the elements of $[D]$ are distinct, one may use the corollary on p.420 of [5] for investigating the controllability condition. For the reader's convenience, we restate the corollary here:

If $[D]$ is a diagonal matrix, partition $[B]$ into rows thus

$$[\tilde{B}] = \begin{bmatrix} \tilde{b}_1^T \\ \vdots \\ \tilde{b}_{2n}^T \end{bmatrix} \quad (2.18)$$

then the necessary and sufficient conditions for controllability are

$$\|\tilde{b}_i\| > 0 \quad i=1, \dots, 2n \quad (2.19)$$

where $\|\cdot\|$ denotes a norm.

Observe that if $[B]$ is a vector and each of its rows is non-zero, then each row of $[T]^{-1}B$ is non-zero, therefore satisfying (2.19). We conclude, based on the above observation, that the minimum number of actuators required for controllability is one actuator. This conclusion is similar to those comments made in [1] and [5] for undamped systems with distinct eigenvalues. We now go one step further to express the controllability conditions in terms of eigenfunctions and eigenvalues of the distributed parameter system (1.1).

Recall that (with one actuator)

$$\bar{B}_N = \begin{bmatrix} 0 \\ B_N \end{bmatrix} = \begin{bmatrix} 0 \\ \vdots \\ b_1 \\ \vdots \\ b_n \end{bmatrix} = \begin{bmatrix} 0 \\ \vdots \\ \phi_1(x_1) \\ \vdots \\ \phi_n(x_1) \end{bmatrix} \quad (2.20)$$

Multiplying out (2.20) and (2.8), yields

$$\tilde{B} = \begin{bmatrix} b_1 \\ b_2 \\ \vdots \\ b_{2n-1} \\ b_{2n} \end{bmatrix} = \begin{bmatrix} -\phi_1(x_1)/(s_2-s_1) \\ \phi_1(x_1)/(s_2-s_1) \\ \vdots \\ -\phi_n(x_1)/(s_{2n}-s_{2n-1}) \\ \phi_n(x_1)/(s_{2n}-s_{2n-1}) \end{bmatrix} \quad (2.21)$$

Noting again that the complex conjugate poles s_i and s_{i+1} are distinct due to the underdamping condition of (1.1), \tilde{B} will always be a bounded vector.

The controllability condition, as expressed by (2.19) is now reduced to

$$\|\tilde{b}_i\| = \|\phi_i(x_1)/(s_{2j}-s_{2j-1})\| > 0 \quad (2.22)$$

$$i=1,1,2,2, \dots, n,n$$

$$j=1,2,3, \dots, 2n$$

We summarize the above results in the following theorem.

Thm. 3.1 - For one actuator, the system $([D],B)$ is controllable if and only if

$$c_j \triangleq \|\phi_1(x_1)/(s_{2j}-s_{2j-1})\| > 0, \quad (2.23)$$

$$i=1,1,2,2, \dots, n,n$$

$$j=1,2,3, \dots, 2n$$

One clearly sees that if the actuator is located at a node of a controlled mode, then the system $([D],\tilde{B})$ will be rendered uncontrollable.

Observe that the modes associated with complex conjugate poles have the same controllability norm (which is of no surprise). The controllability norm provides us a way to measure the degree of controllability for that particular mode. It follows that one can maximize the controllability of the controlled system by optimizing the placement of the actuator. Similar comments can also be found in [5]. We note that these norms are not invariant as the system undergoes similarity transformation. Therefore, these norms are meaningful only when one compares them to those of their own transformed system or to others which has undergone the same similarity transformations.

2.3 Observability

Here, results similar to those derived in the controllability section are also obtained for the observability of $([\bar{A}_N],[\bar{C}_N])$. The output matrix $[\bar{C}]$ and the modal matrix $[T]$ are partitioned as follows:

$$[\bar{C}] = [[C][E_N] \quad [D][E_N]] [T] \quad (2.24)$$

and

$$[T] = \begin{bmatrix} [T_{11}] & [T_{12}] \\ [T_{21}] & [T_{22}] \end{bmatrix} \quad (2.25)$$

where $\dim([T_{ij}]) = nxn$.

Furthermore, we note that $[T_{ij}]$ has a "1" in each of its columns and $[T_{2j}]$ has an eigenvalue, s_i , in every column. The rest of the elements in $[T]$ consists of zeroes.

Letting $[P]=[C][E_N]$ and $[R]=[D][E_N]$, and using (2.25), we may simplify (2.24) into the following form,

$$[\bar{C}]=[P][T_{11}]+[R][T_{21}][P][T_{12}]+[R][T_{22}] \quad (2.26)$$

Denoting the j th column of $[\bar{C}]$ as \tilde{c}_j , we state the following theorem.

Thm 2.2 - The system $([D],[\bar{C}])$ is observable if and only if

$$o_j \triangleq \|\tilde{c}_j\|, \quad j=1, \dots, 2n \quad (2.27)$$

Proof: Direct application of the Jordan-form controllability theorem on p.191 of ref. 7.

Corollary 2.2.1 - For one position sensor with unit gain and no velocity sensor, i.e., $C=1$ and $D=0$, $([D], [\tilde{C}])$ is observable if and only if

$$\theta_j = ||\phi_i(z_1)|| > 0, \quad i=1,1, \dots, n,n, \quad j=1, \dots, 2n \quad (2.28)$$

Proof: For this case, $[C]$ is a row vector expressed as $[C] = [\phi_1(z_1), \phi_1(z_1), \phi_2(z_1), \phi_2(z_1), \dots, \phi_n(z_1), \phi_n(z_1)]$. Application of Thm 2.2

Corollary 2.2.2 - For one velocity sensor with unit gain and no position sensor, i.e. $C=0$ and $D=1$, $([D], [C])$ is observable if and only if

$$\theta_j = ||s_j \phi_i(z_1)|| > 0, \quad i=1,1, \dots, n,n, \quad j=1, \dots, 2n \quad (2.29)$$

Proof: Here, $[C] = [s_1 \phi_1(z_1), s_2 \phi_1(z_1), s_3 \phi_1(z_1), s_4 \phi_2(z_1), \dots, s_{2n-1} \phi_n(z_1), s_{2n} \phi_n(z_1)]$. Application of Thm 2.2

From corollaries 2.2.1 and 2.2.2, we conclude that only one sensor (position or velocity) is needed for observability of $([D], [\tilde{C}])$, provided the sensor is appropriately placed.

These corollaries indicate to us that z_i 's should be chosen to be away from the nodes of the controlled modes. Again the observability norm, θ_j , gives us a quantitative way of computing the relative degree of observability provided that one is comparing norms with the same similarity transformations. One may deduce that, as for controllability, the appropriate placement of the sensor can enhance the observability of the controlled modes by maximizing the observability norms.

Since similarity transformations preserve controllability and observability properties, we say that the above controllability and observability theorems and corollaries also apply to the controlled system $([\tilde{A}_N], [\tilde{B}_N], [\tilde{C}_N])$.

3. Bounds on Solutions of Residual Modes

With the aid of modal decomposition, solutions are obtained for the controller-observer system (1.17). Using these results, we derive a closed form solution for the subsystem with the residual modes. From the solution, a convenient bound is then selected.

The solution the controller-observer system (1.17) can be written as

$$\underline{z}(t) = \sum_{i=1}^{4n} a_i e^{\tilde{\lambda}_i t} \underline{\psi}_i, \quad \underline{z} = \begin{bmatrix} \underline{v}(o) \\ \underline{v}(o) \end{bmatrix} \quad (3.1)$$

where a_i 's are the modal participation coefficients, $\tilde{\lambda}_i$ and $\underline{\psi}_i$ are the eigenvalues and eigenvectors of the controller-observer system, respectively. The residual modal system is

$$\ddot{\underline{w}}(t) = [\tilde{A}_R] \underline{w}(t) + [\tilde{B}_R] [G] [\underline{v}(t) + \underline{e}(t)] \quad (3.2)$$

or (3.2) can be written equivalently as

$$\ddot{\underline{w}}(t) + [\Lambda_R^{(1)}] \dot{\underline{w}}(t) + [\Lambda_R^{(2)}] \underline{w}(t) = [\tilde{B}_R] [G] [\underline{v}(t) + \underline{e}(t)] \quad (3.3)$$

Noting that the left side of (3.3) is decoupled, we write any one of its equations as

$$\ddot{u}_r(t) + \lambda_r^{(1)} \dot{u}_r(t) + \lambda_r^{(2)} u_r(t) = \bar{F}_r(t), \quad r=n+1, n+2, \dots, \infty \quad (3.4)$$

where $\bar{F}_r(t)$ is a linear combination of elements of $\underline{v}(t)$ and $\underline{e}(t)$.

Using one actuator, $\bar{F}_r(t)$ can be expressed as follows.

$$\bar{F}_r(t) = \sum_{j=1}^{4n} c_j \bar{f}_j(t) = \phi_r(x_1) (g_1 v_1(t) + g_2 v_2(t) + \dots + g_{2n} v_{2n}(t) + g_1 e_1(t) + g_2 e_2(t) + \dots + g_{2n} e_{2n}(t)) \quad (3.5)$$

where the g_i 's are the gain constants of the controller.

Clearly, when $\phi_r(x_1)$ vanishes (i.e. the location of the actuator is a node of the i th mode), (3.4) is then reduced to a homogeneous equation. In other words, the control spillover does not affect this particular residual mode.

One can write down the general solution for (3.4). (For lightly damped structures, the damped frequency can be taken to be equal to the corresponding undamped frequency with sufficient accuracy.)

$$u_r(t) = e^{-\beta_r t} \left[\frac{\dot{u}_r(o) + \beta_r u_r(o)}{\omega_r} \sin \omega_r t + u_r(o) \cos \omega_r t \right] + \sum_{j=1}^{4n} \int_0^t q_j \bar{f}_j(\tau) e^{-\beta_r(t-\tau)} \sin \omega_r(t-\tau) d\tau \quad (3.6)$$

where $\beta_r = \lambda_r^{(1)}/2$

and $\omega_r = \sqrt{\lambda_r^{(2)}}$

The time dependent term, $\bar{f}_j(t)$, takes the following form,

$$e^{-\sigma_j t} \quad \text{or} \quad e^{-\sigma_j t} \sin(\omega_j t - \phi_j) \quad (3.7)$$

where ϕ_j is a phase angle and σ_j and ω_j are positive real numbers prescribed by the controller-observer system.

Since

$$e^{-\sigma_j t} e^{-\beta_r(t-\tau)} \begin{cases} \sin(\omega_j \tau - \phi_j) \sin \omega_r(t-\tau) \\ \text{or} \\ \sin \omega_r(t-\tau) \end{cases} \quad (3.8)$$

then the integral of the above functions will

also have the same relationship. Integrating the larger function above, yields

$$\int e^{-\sigma_j \tau} e^{-\beta_r(t-\tau)} d\tau = \bar{g}_j(t) = \begin{cases} \frac{(\beta_r - \sigma_j)t}{e^{\beta_r t}(\beta_r - \sigma_j)} - 1 & \text{if } \beta_r \neq \sigma_j \\ t e^{-\beta_r t} & \text{if } \beta_r = \sigma_j \end{cases} \quad (3.9)$$

A bound for $u_r(t)$ is

$$u_{r_{\max}}(t) = H_r e^{-\beta_r t} + \sum_{j=1}^{4n} q_j \bar{g}_j(t) \quad (3.10)$$

where $H_r = \{[\dot{u}_r(0) + \beta_r u_r(0)]^2 / \omega^2 + (u_r(0))^2\}^{1/2}$

From inspection, (3.10) is stable for all t . This implies that the control spillover cannot create instability in the residual system. Furthermore, (3.10) represents one method by which we can estimate the peak response of some residual modes.

3.1 Illustrative Example

This example is intended to demonstrate the design procedure for the vibration control of a distributed parameter system. Meanwhile, an effort is made to apply the important results obtained in this paper. Let us consider the longitudinal vibration of a clamped uniform rod with external damping. The dynamics of the linear model can be written as

$$u_{tt}(x,t) + u_t(x,t) - \frac{\partial^2 u(x,t)}{\partial x^2} = F(x,t) \quad (4.1)$$

for $x \in (0,1) = \Omega$ and $t > 0$

where $u(x,t)$ is the axial displacement of the rod.

Since the rod is clamped on both ends, the boundary conditions are

$$u(0,t) = u(1,t) = 0$$

The eigenfunctions for this model are

$$\phi_k(x) = \sqrt{2} \sin k\pi x, \quad k=1,2,3, \dots \quad (4.2)$$

and note that $\phi_k(x)$ are normalized such that

$$\int_0^1 \phi_k(x) \phi_k(x) dx = 1, \quad k=1,2,3, \dots \quad (4.3)$$

The rod is controlled by one actuator whose location is chosen to be at $x=(5/8)$ so that Thm 2.1 is satisfied.

$$F(x,t) = \delta(x-5/8)f(t) \quad (4.4)$$

The rod is measured by a position sensor selected to be located at $z=(1/8)$. This particular choice of location satisfies Corollary 2.2.1.

Now, the placement of the sensor and actuator

will assure us the controllability and observability of $([D],[B],[C])$ or equivalently $([\bar{A}_N],[\bar{B}_N],[\bar{C}_N])$. This will be checked by the traditional method of inspecting the rank of controllability matrix and observability matrix of $([\bar{A}_N],[\bar{B}_N],[\bar{C}_N])$.

A low bandpass filter is chosen to filter out the higher frequencies from the sensor output so that observation spillover is eliminated.

Note that all of the assumptions stated for (1.1) are satisfied.

The DPS has the following solution,

$$u(x,t) = \sum_{k=1}^{\infty} u_k(t) \phi_k(x) \quad (4.5)$$

where $\phi_k(x)$ are defined in (4.2) and $u_k(t)$ are the modal amplitudes.

Substituting (4.5) into (4.1) and using the orthonormality property of $\phi_k(x)$, yields

$$\ddot{u}_k(t) + \dot{u}_k(t) + (k\pi)^2 u_k(t) = (\sqrt{2} \sin 5k\pi/8) f(t), \quad (4.6)$$

$$k=1,2,3, \dots$$

It can be easily checked that the unforced equation has underdamped frequencies. For convenience, we control the first mode (i.e. $k=1$) by using one actuator and one sensor, (4.6) is written into an equivalent state space representation. Again, letting $v(t) = [u_1(t) \dot{u}_1(t)]^T$,

$$\dot{v}(t) = [\bar{A}_N]v(t) + [\bar{B}_N]f(t) \quad (4.7)$$

where

$$[\bar{A}_N] = \begin{bmatrix} 0 & 0 \\ -\pi^2 & 1 \end{bmatrix}, \quad [\bar{B}_N] = \begin{bmatrix} 0 \\ 1.31 \end{bmatrix}$$

The accompanying sensor equation is,

$$y(t) = [\bar{C}_N]v(t) \quad (4.8)$$

where $[\bar{C}_N] = [0.541 \ 0.541]$ with $C=1$ and $D=0$ in (1.6)

Note: $\sqrt{2} \sin \frac{5\pi}{8} = 1.31$ and $\sqrt{2} \sin \frac{\pi}{8} = 0.541$

From (4.7) we can calculate the controllability matrix, $[C]$

$$[C] = [\bar{B}_N : [\bar{A}_N][\bar{B}_N]] = 1.31 \begin{bmatrix} 0 & 1 \\ 1 & -1 \end{bmatrix} \quad (4.9)$$

By inspection, $[C]^{-1}$ exists which implies our controlled system $([\bar{A}_N],[\bar{B}_N],[\bar{C}_N])$ is controllable.

We can also calculate the observability matrix, $[O]$

$$[O] = [\bar{C}_N : [\bar{A}_N]^T [\bar{C}_N]^T]^T = 0.541 \begin{bmatrix} 1 & 1 \\ -\pi^2 & 0 \end{bmatrix} \quad (4.10)$$

Also, by inspection, $[O]^{-1}$ exists. Therefore,

the system $([\bar{A}_N], [\bar{B}_N], [\bar{C}_N])$ is observable.

The above results are expected since we have put our sensor and actuator away from the node of the first mode.

Since we have guaranteed the controllability and observability of the system described by (4.7) and (4.8), we can now proceed to design the active controller. A direct pole placement technique is used for designing the asymptotic observer and controller. The algorithm used for calculating the controller gains can be found on p.275 of [7]. The method for calculating the observer can be derived analogously. The poles selected for the controller and observer are -2, -3, and -4, -5, respectively.

The gains calculated for the controller are

$$G = [2.96 \quad -3.06] \quad (4.11)$$

The gains calculated for the observer are

$$K = [-0.400 \quad 15.2] \quad (4.12)$$

The combined controller-observer system is then assembled. It is simple exercise to find that the eigenvalues of this combined system are indeed -2, -3, -4, and -5. This confirms that our gains of the controller and observer are calculated correctly.

If there is an initial axial displacement to the rod such that only the first vibration mode gain an unit amplitude.

$$\underline{v}_1(0) = [\underline{u}_1(0) \quad \dot{u}_1(0)]^T = [1 \quad 1]^T \quad (4.13)$$

Or,

$$\underline{z}(0) = [1 \quad 1 \quad 1 \quad 1]^T \quad (4.14)$$

Using (4.14) and the inverted modal matrix from the controller-observer system, we may compute \underline{g} , yielding

$$\underline{g} = [-15 \quad 54 \quad -57 \quad 19] \quad (4.15)$$

The solution for the combined controller system is,

$$z_1(t) = u_1(t) = -15e^{-2t} + 54e^{-3t} - 57e^{-4t} + 19e^{-5t} \quad (4.16)$$

$$z_2(t) = \dot{u}_1(t) = 30e^{-2t} - 162e^{-3t} + 228e^{-4t} - 95e^{-5t} \quad (4.17)$$

$$z_3(t) = e_1(t) = 6.43e^{-4t} - 5.42e^{-5t} \quad (4.18)$$

$$z_4(t) = \dot{e}_1(t) = -22.3e^{-4t} + 23.2e^{-5t} \quad (4.19)$$

Simple calculation shows us that for $t=0^+$, the above set of equations will give us back our stated initial conditions within acceptable round off error.

We will only calculate the residual solution for the second mode. The forcing function for the equation of the second mode is obtained as follows.

$$B_R = \phi_2(5/8) = \sqrt{2} \sin \frac{10\pi}{8} = -1$$

And from (3.5), we may write $\bar{F}_2(t)$ as

$$\bar{F}_2(t) = (-1)[g_1 v_1(t) + g_2 v_2(t) + g_1 e_1(t) + g_2 e_2(t)] \quad (4.20)$$

where g_i 's are elements of the gain vector \underline{g} .

Putting the appropriate values into (4.20) and simplifying, get

$$\bar{F}_2(t) = 136e^{-2t} - 656e^{-3t} + 779e^{-4t} - 260e^{-5t}$$

After calculating the needed constants for (3.10) and substituting, we have

$$u_{r_{\max}}(t) = e^{-1/2t} \{-2.3(e^{-1.5t} - 1) + 6.6(e^{-2.5t} - 1) - 5.6(e^{-3.5t} - 1) + 1.46(e^{-4.5t} - 1)\}$$

For $t=0^+$, this bounds estimates that the peak response of the second mode will gain no more than 16% of the initial amplitude of the first mode. This bound value is also true for the rest of the residual modes, since the other modes have the same degree of damping.

3.2 Conclusions

The results from this study suggest that the considered control scheme is a viable alternative in the field of vibration control. One clear advantage of this method is that you can theoretically control many vibration modes with one actuator and one displacement/velocity sensor. Insight is gained from the controllability and observability conditions, which are expressed explicitly as a function of the eigenvalues and eigenfunctions of the distributed parameter system. For example, these conditions reinforce one's intuition for the appropriate placement of the actuators and sensors. Although the derived bounds for the residual modal solutions are conservative, nevertheless, they offer us a way to estimate the degradation of the controlled system response from the residual modes.

References

- [1] Balas, M., "Feedback Control of Flexible Systems", IEEE Trans. Automat. Contr., AC-23, 1978, pp.673-679.
- [2] Balas, M., "Modal Control of Certain Flexible Dynamic Systems", SIAM J. Contr. Optimiz., vol. 16, 1978, pp.450-462.
- [3] Meirovitch, L., and Baruh, H., "Control of Self-Adjoint Distributed-Parameter Systems", J. of Guidance, Control and Dynamics, vol. 5, 1982, pp.60-66.
- [4] Oz, H., and Meirovitch, L., "Stochastic Independent Modal-Space Control of Distributed-Parameter Systems", J. of Optimiz. Theory and Appl., vol. 40, 1983, pp.121-154.
- [5] Hughes, P.C., and Skelton, R.E., "Controllability and Observability of Linear Matrix-Second-Order Systems", J. of Appl. Mech., vol. 47, 1980, pp.415-420.

- [6] Inman, D.J., Andry, A.N. Jr., "The Nature of the Temporal Solutions of Damped Distributed Systems with Classical Normal Modes", J. of Appl. Mech., vol. 49, 1982, pp.867-870.
- [7] Chen, C.T., Introduction to Linear System Theory. Holt, Rinehart and Winston, 1970.

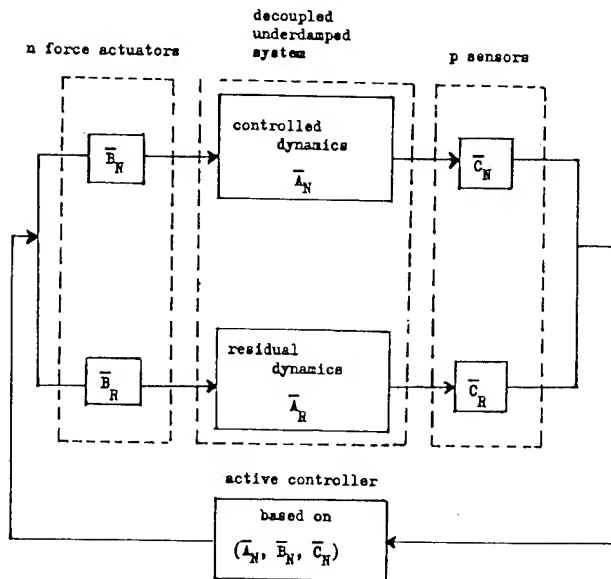


Fig. 1

J. N. Reddy[†] and N. D. Phan^{*}
Virginia Polytechnic Institute and State University
Blacksburg, Virginia 24061

Abstract

This paper deals with the dynamic analog of the higher-order shear deformation plate theory developed by the senior author. The theory is based on a displacement field in which the inplane displacements are expanded as cubic functions of the thickness coordinate and the transverse deflection is assumed to be constant through the thickness. The additional dependent unknowns introduced with the quadratic and cubic terms of the thickness coordinate are eliminated by requiring the transverse shear stresses to vanish on the bounding planes of the plate. The theory accounts for the parabolic distribution of the transverse shear stresses, and hence no shear correction coefficients are required.

Nomenclature

a, b	planeform dimensions of the plate
$A_{ij}, B_{ij}, \text{etc.}$	laminate stiffnesses
E_1, E_2	Young's moduli in material directions 1 and 2, respectively
G_{12}, G_{13}, G_{23}	shear moduli in 1-2, 1-3, and 2-3 planes, respectively
I_i ($i = 1, 2, \dots, 7$)	inertias defined in Eq. (6)
M_i, N_i, P_i, Q_i, R_i	stress resultants defined in Eq. (7)
q	distributed transverse load
u, v, w	displacement of a point in the midplane of the laminate
ϕ_i^α ($\alpha = 1, 2$)	finite-element interpolation functions
ψ_x, ψ_y	rotations of normals to the midplane about the y and x axes, respectively.

I. Introduction

Due to the high ratio of inplane modulus to transverse shear modulus, the shear deformation effects are more pronounced in the composite laminates subjected to transverse loads than in the isotropic plates under similar loading. The classical plate theory (CPT), in which the Kirchhoff-Love assumption that normals to the mid-surface before deformation remain straight and normal to the mid-surface after deformation is used, is not adequate for the dynamic analysis of

moderately thick laminates (unless the dynamic excitations are within the low frequency range).

Many refined theories have been introduced to account for the transverse shear strains. The extension of the Mindlin plate theory for isotropic plates to laminated anisotropic plates (see Whitney and Pagano¹ provides a first-order correction to the classical plate theory. In this theory the transverse shear strains are constant through the thickness, and hence shear correction coefficients are used to estimate the transverse shear stiffnesses. It is known that the true distribution of transverse shear stresses is approximately parabolic through the thickness of the plate. To account for higher-order variations of the transverse shear stresses, other higher-order theories have been also proposed². These theories are based on expansions of the displacements (about the midplane displacements) in terms of the thickness coordinate. A shortcoming of these theories is that with each power of the thickness coordinate an additional dependent unknown is introduced. For certain order expansions, it is possible to express the new dependent unknowns in terms of those in the first-order theory by imposing constraints on the stress field. For example, for the cubic expansion of the inplane displacements and zeroth expansion of the transverse displacement, we have a total of nine dependent unknowns (compared to the five in the first-order theory). The additional four dependent variables can be eliminated by requiring the transverse shear stresses to vanish at the top and bottom inplanes of the laminate. Such a theory was presented by Levinson³ for isotropic plates and by Reddy⁴ for laminated plates. The present study deals with the dynamic analysis of laminated plates using the higher-order theory.

II. A Review of the Equations

Consider a rectangular laminate with planeform dimensions a and b and thickness h . The coordinate system is taken such that the x - y plane coincides with the mid-plane of the plate, and the z -axis is perpendicular to that plane. The plate is composed of perfectly bonded orthotropic layers with the principal material axes of each layer oriented arbitrarily with respect to the plate axes.

Following the developments presented by Reddy⁴, the equations of motion for the higher-order theory can be shown to be of the form,

$$N_{1,x} + N_{6,y} = I_1 \ddot{u} + I_2 \ddot{\psi}_x - \frac{4}{3h^2} I_4 \ddot{w}_{,x} \quad (1)$$

[†]Professor, Engineering Science and Mechanics Department

^{*}Graduate Research Assistant

$$N_{6,x} + N_{2,y} = I_1 \ddot{v} + I_2 \ddot{\psi}_y - \frac{4}{3h^2} I_4 \ddot{w}_{,y} \quad (2)$$

$$\begin{aligned} Q_{1,x} + Q_{2,y} - \frac{4}{h^2} (R_{1,x} + R_{2,y}) \\ + \frac{4}{3h^2} (P_{1,xx} + 2P_{6,xy} + P_{2,yy}) \\ = I_1 \ddot{w} - \frac{16}{9h^4} I_7 (\ddot{w}_{,xx} + \ddot{w}_{,yy}) + \frac{4}{3h^2} I_4 (\ddot{u}_{,x} + \ddot{v}_{,y}) \\ + \frac{4}{3h^2} \bar{I}_5 (\ddot{\psi}_{x,x} + \ddot{\psi}_{y,y}) + q \end{aligned} \quad (3)$$

$$\begin{aligned} M_{1,x} + M_{6,y} - Q_1 + \frac{4}{h^2} R_1 - \frac{4}{3h^2} (P_{1,x} + P_{6,y}) \\ = \bar{I}_2 \ddot{u} + \bar{I}_3 \ddot{\psi}_x - \frac{4}{3h^2} \bar{I}_5 \ddot{w}_{,x} \end{aligned} \quad (4)$$

$$\begin{aligned} M_{6,x} + M_{2,y} - Q_2 + \frac{4}{h^2} R_2 - \frac{4}{3h^2} (P_{6,x} + P_{2,y}) \\ = \bar{I}_2 \ddot{v} + \bar{I}_3 \ddot{\psi}_y - \frac{4}{3h^2} \bar{I}_5 \ddot{w}_{,y} \end{aligned} \quad (5)$$

where

$$\begin{aligned} \bar{I}_2 = I_2 - \frac{4}{3h^2} I_4, \quad \bar{I}_5 = I_5 - \frac{4}{3h^2} I_7 \\ \bar{I}_3 = I_3 - \frac{8}{3h^2} I_5 + \frac{16}{9h^4} I_7 \end{aligned} \quad (6)$$

and N_i, M_i, P_i , and Q_i are the stress resultants,

$$\begin{aligned} (N_i, M_i, P_i) &= \int_{-h/2}^{h/2} \sigma_i(1, z, z^3) dz \quad (i = 1, 2, 6) \\ (Q_1, Q_2) &= \int_{-h/2}^{h/2} (\sigma_5, \sigma_4) dz \\ (R_1, R_2) &= \int_{-h/2}^{h/2} (\sigma_5, \sigma_4) z^2 dz \end{aligned} \quad (7)$$

III. Exact Spatial Variation of the Solution

As discussed in Reference 4, the Navier type solution for simply supported cross-ply and antisymmetric angle-ply plates subjected to static transverse loads can be obtained. Similar results are also valid for the determination of the natural frequencies. In the case of plates subjected to transient loads, the Navier method

can be used to determine the exact spatial variation of the solution, provided that the spatial and time variations of the generalized displacements can be separated. In the present study we assume that the loads applied are such that the spatial and time variations can be separated.

The following two types (which differ from each other in the form of the inplane displacements) of boundary conditions permit the construction of the Navier type solution:

$$\left. \begin{aligned} u(x, 0) = u(x, b) = v(0, y) = v(a, y) = 0 \\ N_2(x, 0) = N_2(x, b) = N_1(0, y) = N_1(a, y) = 0 \end{aligned} \right\} \quad S-1$$

$$\left. \begin{aligned} u(0, y) = u(a, y) = v(x, 0) = v(x, b) = 0 \\ N_6(0, y) = N_6(a, y) = N_6(x, 0) = N_6(x, b) = 0 \end{aligned} \right\} \quad S-2$$

$$\left. \begin{aligned} w(x, 0) = w(x, b) = w(0, y) = w(a, y) = 0 \\ P_2(x, 0) = P_2(x, b) = P_1(0, y) = P_1(a, y) = 0 \\ M_2(x, 0) = M_2(x, b) = M_1(0, y) = M_1(a, y) = 0 \\ \psi_x(x, 0) = \psi_x(x, b) = \psi_y(0, y) = \psi_y(a, y) = 0 \end{aligned} \right\} \quad \begin{array}{l} \text{for both} \\ S-1 \text{ and} \\ S-2 \end{array} \quad (8)$$

For the above boundary conditions, the exact spatial variations of the displacements can be determined for laminates with two sets of plate stiffnesses.

$$\left. \begin{aligned} A_{16} = A_{26} = B_{16} = B_{26} = D_{16} = D_{26} = 0 \\ E_{16} = E_{26} = F_{16} = F_{26} = H_{16} = H_{26} = 0 \\ A_{45} = D_{45} = F_{45} = 0 \end{aligned} \right\} \quad \text{and SS-1}$$

$$\left. \begin{aligned} A_{16} = A_{26} = B_{11} = B_{12} = D_{16} = D_{26} = 0 \\ E_{11} = E_{12} = F_{16} = F_{26} = H_{16} = H_{26} = 0 \\ A_{45} = D_{45} = F_{45} = 0 \end{aligned} \right\} \quad \text{and SS-2} \quad (9)$$

These two sets of conditions are satisfied by general cross-ply and antisymmetric angle-ply laminates, respectively.

Following the Navier solution procedure, we assume the following form of solution, which satisfy the boundary conditions in eq. (8).

$$\left. \begin{aligned} u &= \sum_{m=1}^{\infty} \sum_{n=1}^{\infty} U_{mn} \cos \alpha x \sin \beta y \cos \omega t \\ v &= \sum_{m=1}^{\infty} \sum_{n=1}^{\infty} V_{mn} \sin \alpha x \cos \beta y \cos \omega t \end{aligned} \right\} \quad S-1 \quad (10a)$$

$$\left. \begin{aligned} u &= \sum_{m=1}^{\infty} \sum_{n=1}^{\infty} U_{mn} \sin \alpha x \cos \beta y \cos \omega t \\ v &= \sum_{m=1}^{\infty} \sum_{n=1}^{\infty} V_{mn} \cos \alpha x \sin \beta y \cos \omega t \end{aligned} \right\} \quad S-2 \quad (11a)$$

$$w = \sum_{m=1}^{\infty} \sum_{n=1}^{\infty} W_{mn} \sin \alpha x \sin \beta y \cos \omega t$$

$$\phi_x = \sum_{m=1}^{\infty} \sum_{n=1}^{\infty} X_{mn} \cos \alpha x \sin \beta y \cos \omega t \quad (10b, 11b)$$

$$\phi_y = \sum_{m=1}^{\infty} \sum_{n=1}^{\infty} Y_{mn} \sin \alpha x \cos \beta y \cos \omega t$$

where $\alpha = \frac{m\pi}{a}$ and $\beta = \frac{n\pi}{b}$, and m, n are integers.

In addition, we assume that the transverse load can be expanded in the double Fourier series,

$$q(x, y, t) = \sum_{m=1}^{\infty} \sum_{n=1}^{\infty} Q_{mn} \sin \alpha x \sin \beta y \cos \omega t \quad (12)$$

Substitution of Eqs. (10) and (12) or (11) and (12) into Eq. (1)-(7), gives

$$[M]\{\ddot{\Delta}\} + [S]\{\Delta\} = \begin{Bmatrix} 0 \\ 0 \\ 0 \\ Q_{mn} \\ 0 \end{Bmatrix} \quad (13)$$

where $[M]$ and $[S]$ are the mass and stiffness matrices. Equation (13) can be solved for $\{\Delta\}$ at time $t = n\Delta t$, where Δt is the time step, using a time-approximation scheme. Here we used the Newmark direct integration scheme.

IV. Finite Element Model

In the interest of solving more general problems than those permitted by the Navier procedure, we construct a finite element model of Eqs. (1)-(7). Over a typical finite element we assume (see Reddy⁵ for details) that the displacements are interpolated by expressions

$$u(x, y, t) = \sum_{i=1}^n U_i(t) \phi_i^1(x, y)$$

$$v(x, y, t) = \sum_{i=1}^n V_i(t) \phi_i^1(x, y)$$

$$w(x, y, t) = \sum_{i=1}^m W_i(t) \phi_i^2(x, y)$$

$$\phi_x(x, y, t) = \sum_{i=1}^n X_i(t) \phi_i^1(x, y)$$

$$\phi_y(x, y, t) = \sum_{i=1}^n Y_i(t) \phi_i^1(x, y) \quad (14)$$

and ϕ_i^1 and ϕ_i^2 are the interpolation functions. For simplicity, the same shape functions are used for the inplane displacements and the two rotations. The variational formulation of Eqs. (1)-(7) requires that the transverse deflection

and its derivatives be continuous across the interelement boundary; hence, the Hermit cubic interpolation functions for w are used in the present model.

Substituting Eq. (14) into Eqs. (1)-(7), we obtain the element equations

$$[M^e]\{\ddot{\Delta}^e\} + [K^e]\{\Delta^e\} = \{F^e\} \quad (15)$$

where $[M^e]$ and $[K^e]$ denote the element mass and stiffness matrices, respectively, and $\{F^e\}$ denotes the element force vector that contains both applied and reactive loads of the element (see Reddy⁵). Equation (15) should be approximated, like Eq. (13), to determine the vector of nodal values, $\{\Delta\}_n$, at time $t = n\Delta t$. The Newmark direct integration scheme is used to approximate Eq. (15).

V. Numerical Results for Some Sample Problems

Here the exact and finite element solutions of laminated plates predicted by the higher-order shear deformation theory (HSDT) are presented and compared with the results obtained using the first order shear deformation theory (FSDT) and the classical plate theory (CPT). The effects of transverse shear deformation, material anisotropy and coupling between stretching and bending on the deflections are investigated. The finite element model developed herein is validated by comparing the results with the exact solutions. Once the accuracy of the finite element model has been verified, analysis of general laminates with arbitrary edge conditions are conducted. All of the computations were carried on an IBM 3081 processor with double precision arithmetic.

In all laminate problems considered, the following material parameters are used:

$$E_1/E_2 = 25, G_{12}/E_2 = 0.5, G_{23}/E_2 = 0.2, \nu_{12} = 0.25$$

It is assumed further that $G_{12} = G_{13}$ and $\nu_{12} = \nu_{13}$ and $\rho = 1$. For the analysis based on the FSDT, shear correction coefficient of

$$k_1^2 = k_2^2 = \frac{5}{6} \text{ are used. Also, the initial}$$

conditions were assumed to be zero.

1. Simply supported rectangular isotropic plate under uniformly distributed load at the central square area (see Fig. 1).

This problem was solved by Reisman and Lee⁶ analytically using the three-dimensional elasticity theory. The plate dimensions and material properties are shown in Fig. 1. The plots of the nondimensional center deflection ($\bar{w} = wEah/qb^3$) versus time for the higher-order theory, the first-order theory and the classical theory are presented in Fig. 1. Both the first-order and the higher-order theories are found to be in excellent agreement with the analytical solution⁶. For this isotropic plate problem, there is no significant difference between the solutions predicted by the first-order theory and the higher-order theory, and therefore cannot be distinguished in the graph. Also, the finite element solution is in excellent agreement with the exact solution. The effect of shear

deformation on the deflection is significant even for the isotropic case.

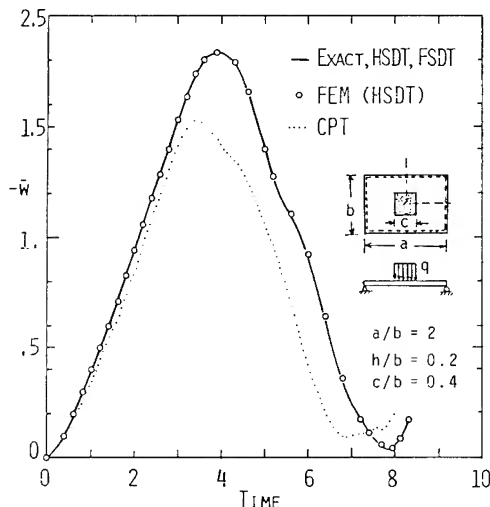


Fig. 1 Nondimensionalized center deflection versus time for an isotropic rectangular plate under uniform load at the center square area ($\nu = .3$, $\Delta t = 0.1$)

2. Two-layer cross-ply $[0^\circ/90^\circ]$ plate under sinusoidal load.

Figure 2 contains plots of the center deflection versus time for simply supported square plates under sinusoidally distributed transverse loads. The first order theory slightly overestimates the deflection and underestimates stresses (see Fig. 3) compared to the higher-order theory. The finite element solution is in good agreement with the exact solution. Once again, we note that the neglect of shear deformation in CPT causes it to underpredict both displacements and stresses.

3. Two-layer angle-ply $[45^\circ/-45^\circ]$ square laminate under sinusoidal load.

Figures 4 and 5 contain plots of center deflection vs. time and stress vs. time, respectively, for two-layer antisymmetric angle-ply plates. The effect of shear coupling (B_{16} , $B_{26} \neq 0$ for this case) on the deflection and stress is clear from a comparison of the plots in Figs. 2 and 3 with those in Figs. 4 and 5. The shear coupling causes increase in the center deflection and stress. Once again we note that the first-order theory overpredicts deflection and underpredicts stress.

V. Summary and Conclusions

The higher-order (cubic in the thickness coordinate) shear deformation theory developed by Reddy⁴ is used to determine the transient response of laminated plates. The theory accounts for the parabolic distribution of the transverse shear stresses and principal and coupled rotatory inertias. The major features of the present theory are: no shear correction coefficients are used; the same dependent unknowns as in the first-order shear deformation theory are present in the

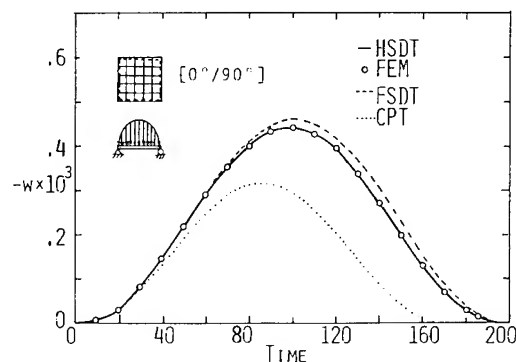


Fig. 2 Comparison of the central deflections obtained using various plate theories for two-layer cross-ply laminates: $[0^\circ/90^\circ]$, $a/h=5$, $\Delta t=5\mu\text{sec.}$, sinusoidal distribution of the transverse load

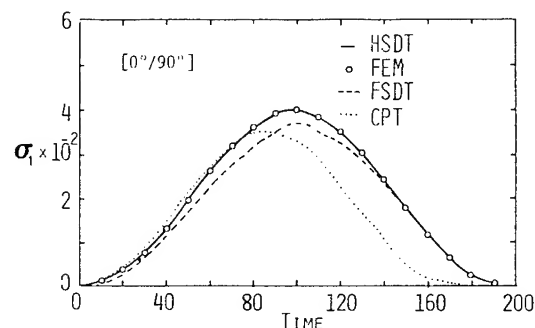


Fig. 3 Comparison of the central normal stress obtained by various theories for two-layer cross-ply laminates (see Fig. 2)

higher-order theory. The exact spatial variation of the solution for simply supported rectangular plates with cross-ply and antisymmetric angle-ply laminations are presented. A displacement finite element model of the theory is also developed.

A comparison of the center deflections and stresses obtained by the first-order theory and the higher-order theory for antisymmetric cross-ply and angle-ply laminates show that the first-order theory overpredicts deflections and underpredicts stresses. The accuracy of the present theory when compared to the three-dimensional elasticity theory is established for static bending case earlier by the senior author⁷. On the basis of this, the transient response results obtained using the present theory are believed to be more close to the true response than those of the first-order theory.

Acknowledgements

The results reported herein were obtained during investigations supported, in parts, by the Air Force Office of Scientific Research and NASA Langley Research Center. Thanks are also due to Mrs. Vanessa McCoy for typing the manuscript on special mats.

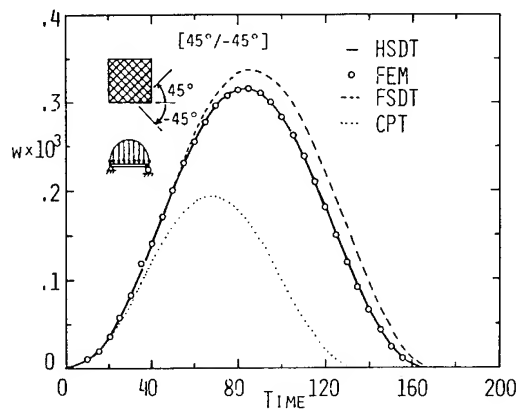


Fig. 4 Comparison of the central deflection vs. time plots obtained using various plate theories for two-layer antisymmetric angle-ply plates: $[45^\circ/-45^\circ]$, $a/h = 5$, $t = 5$ sec., sinusoidal distribution of the transverse load.

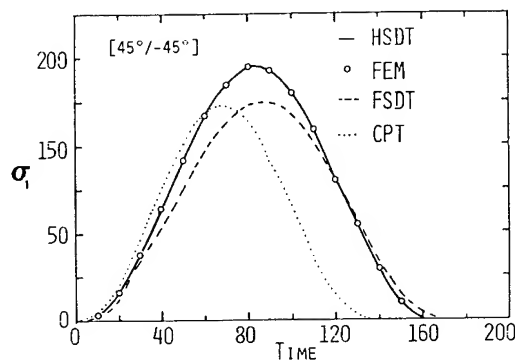


Fig. 5 Comparison of the central normal stress versus time obtained by various plate theories (see Fig. 4)

References

1. Whitney, J. M. and Pagano, N. J., "Shear Deformation in Heterogeneous Anisotropic Plates," *J. Applied Mechanics*, Vol. 37, pp. 1031-1036, Dec. 1970.
2. Lo, K. H., Christensen, R. M., and Wu, E. M., "A Higher-Order Theory of Plate Deformation, Part 2: Laminated Plates," *J. Applied Mechanics*, Vol. 44, No. 5, pp. 669-676, Dec. 1977.
3. Levinson, M., "An Accurate, Simple Theory of the Statics and Dynamics of Elastic Plates," *Mechanics Research Communications*, Vol. 7, No. 6, pp. 343-350, 1980.
4. Reddy, J. N., "A Refined Nonlinear Theory of Plates with Transverse Shear Deformation," *Int. J. Solids and Structures*, to appear.
5. Reddy, J. N., *An Introduction to the Finite Element Method*, McGraw-Hill, New York, 1984.
6. Reismann, H. and Lee, Y., "Forced Motions of Rectangular Plates," in *Developments in Theoretical and Applied Mechanics*, Vol. 4, edited by D. Frederick, Pergamon Press, New York, pp. 3-18, 1969.
7. Reddy, J. N., "A Simple Higher-Order Theory for Laminated Composite Plates," Report VPI-E-83.28, ESM Department, Virginia Polytechnic Institute, Blacksburg, VA, June 1983.

VIBRATION AND BUCKLING OF GENERAL PERIODIC LATTICE STRUCTURES

M. S. Anderson*
 NASA Langley Research Center
 Hampton, Virginia 23665

F. W. Williams§
 University of Wales Institute of Science and Technology
 Cardiff CF1 3EU, Wales

Abstract

A method is presented for vibration and buckling analysis of arbitrary lattice structures having repetitive geometry in any combination of coordinate directions. The approach is based on exact member theory for representing the stiffness of an individual member subject to axial load, and in the case of vibration, undergoing harmonic oscillation. The method is an extension of previous work that was limited to specific geometries. The resulting eigenvalue problem is of the size associated with the repeating element of the structure. A computer program has been developed incorporating the theory and results are given for vibration of rectangular platforms and a large antenna structure having rotational symmetry. Buckling and vibration results for cable-stiffened rings are also given.

Nomenclature

A_p terms in member stiffness matrix
 a_p $(-1)^{p-1}$
 b_p $(-1)^p$
 c_j $\cos \theta_j$
 c_b r_1/L
 C defined by equation (A14)
 D_0 displacement vector of fundamental repeating element
 D_a displacement vector of node on axis of rotational symmetry
 D_j displacement vector of j th repeating element
 EA axial rigidity of a member
 EA_T EA_C times total number of cables in cable-stiffened ring
 EI bending rigidity of member
 f frequency in Hz
 H depth of truss
 j_k bay index for j th repeating element in the k th coordinate direction
 J_0 number of eigenvalues exceeded if all nodes are clamped

k_{pq} submatrices of stiffness matrix of an individual member
 K_0 assembled global stiffness matrix that multiplies D_0
 K_1 global stiffness that couples D_a and D_1 defined by equation (A12)
 K_a global stiffness matrix that multiplies D_a defined by equation (A9)
 K_j global stiffness matrix that couples D_0 and D_j
 K_{pq}^j global stiffness submatrix for a member connecting D_a and D_j
 L member length
 m mass per unit length of member
 N_k number of bays in the k th coordinate direction for which mode is repetitive
 n_k index for harmonic response in k th coordinate direction, without subscript refers to θ direction
 P_0 compressive force in ring
 r radial coordinate or radius of ring
 r_0 radius of hub
 r_1 radial coordinate of node 1
 s_j $\sin \theta_j$
 s_b $(z_1 - z_a)/L$
 T, T' transformation matrices
 W submatrix contained in T
 z_a, z_1 axial coordinate of nodes a and 1
 θ circumferential coordinate
 θ_j circumferential coordinate of node j
 ρ radius of gyration
 ϕ_j defined by equation (2)
 ω circular frequency

*Principal Scientist, Structural Dynamics Branch, Structures and Dynamics Division. Associate Fellow AIAA

§Professor of Civil Engineering, Department of Civil Engineering and Building Technology

Subscripts

c cable

p,q denotes partitioning of member stiffness matrix or a general integer

r ring

Superscripts

H Hermitian transpose of a matrix

T transpose of a matrix

Introduction

Large lattice structures, such as booms, antennas, and platforms proposed for future space applications, have many members and joints that result in very large and expensive analysis problems if the complete structure is modeled in detail. However, these configurations may have only a few different member types and a structural arrangement that has repetitive geometry. The analysis of such structures is greatly facilitated and a considerable savings in computer time is made by using techniques which take advantage of the periodic nature of the structure. Such an analysis for vibration and buckling of a certain class of periodic configurations by Anderson^{1,2} demonstrated that accurate results could be obtained for very large systems with a simple and rapid analysis. The use of exact member theory, and an algorithm for determining eigenvalues that assured that no modes were omitted, were significant factors in achieving accurate results. In the present paper, this analysis has been extended to include any lattice structure having repetitive geometry and loading. The repeating element may have an arbitrary number and arrangement of nodes. For structures having rotational symmetry, there may be nodes along the axis of symmetry which are accounted for in the theory. A description of the theory and results for several example problems are given.

Theory

Equilibrium at the nodes of a repeating element is written in terms of displacements as follows

$$K_0 D_0 + \sum_j K_j D_j = 0 \quad (1)$$

where K_0 , K_j are transcendental stiffness matrices derived from exact member theory using the exact solution of the linear beam-column equation. These stiffnesses, sometimes referred to as stability functions for buckling problems and dynamic stiffness matrices for vibration problems are summarized for space frame members by Anderson^{1,2}. The displacement vector, D_0 is for all the nodes of the basic repeating element, and the D_j are the displacement vectors of other repeating elements connected to the basic repeating element. There is no restriction on the number or arrangement of the nodes in the basic repeating element. Because the stiffnesses are based on exact member theory, the effect of member axial load, mass, and frequency are implicitly accounted for in the elements of K_0 and K_j . The key step for the repetitive analysis is to relate D_j to D_0 as follows

$$\begin{aligned} D_j &= D_0 \exp[2i\pi(n_{1j1}/N_1 + n_{2j2}/N_2 + n_{3j3}/N_3)] \\ &= D_0 \exp(i\phi_j) \end{aligned} \quad (2)$$

where j_k is the number of bays in the k th coordinate direction by which the repeating element must be incremented to reach the j th repeating element, and N_k is the number of bays in the k th coordinate direction for which the mode is repetitive. Note the structure may be repetitive in any combination of the three coordinate directions and that indexing the repeating element by N_k bays in each coordinate direction generates the complete structure that is analyzed. For ϕ_j not an integer multiple of π , the stiffness matrix is complex and its eigenvalues correspond to pairs of structural modes. For rotational structures, cylindrical coordinates are used and the structure repeats in the θ direction and could also repeat in the axial direction. To ensure that all possible modes are considered, it is necessary to consider separately the following integer values of n_k

$$n_k = 0, \pm 1, \pm 2, \dots, \pm \text{integer}(N_k/2) \quad (3)$$

It is only necessary to consider combinations of n_k that produce different absolute values of ϕ_j since changing the sign of ϕ_j only changes the stiffness matrix to its complex conjugate which has the same eigenvalues. Thus if a structure is repetitive in only one coordinate direction, only positive values of n_k are required. For structures repetitive in two directions, values of n_k need to be taken in the combination $p \pm q$. However for many structures having the proper symmetry, the eigenvalue for $p - q$ will be the same as for $p + q$. The above theory, which is a generalization of the analysis by Anderson^{1,2}, has been implemented by modifying an existing general space frame buckling and vibration analysis program (BUNVIS) by Banerjee and Williams³. The program determines vibration frequencies or buckling loads and can include the effects of transverse shear and rotary inertia in individual members. To adapt the program to include repetitive structures, the member stiffnesses (K_j) that couple one repeating element to another are multiplied by $\exp(i\phi_j)$ prior to assembly resulting in a complex Hermitian global stiffness matrix governing D_0 to give

$$K D_0 = 0 \quad (4)$$

In the modified computer program, the matrix K is declared complex and the original coding in BUNVIS for determining eigenvalues is essentially unchanged. A brief description of the eigenvalue analysis used is given in the Appendix. In the case of cylindrical coordinates, the equations correspond to those of MacNeal et al.⁴ or Thomas⁵ for structures having cyclic symmetry, except that in references 4 and 5, conventional finite element stiffness and mass matrices were used rather than stiffness matrices based on exact member theory. MacNeal et al.⁴ developed the real form of the equations and limited their results to connections only between adjacent repeating elements. Thomas⁵ however, pointed out that no additional complexity results from connections to any other repeating element. Many structures having cyclic symmetry also have nodes along the axis that are not repeated. The theory accounting for such cases is given in the Appendix.

Results

The results given by Anderson^{1,2} were primarily for vibration and buckling of simple beam and ring structures where the repeating element has only one node. The present theory and computer program duplicate all of those results exactly. For structures that are repetitive in rectangular coordinate directions, results for modes that repeat at various wavelengths may not satisfy desired boundary conditions. For such cases, modes with wavelengths small compared to the size of the structure may still provide useful information. For example, a buckling load may be associated with a short wavelength mode. If simply supported boundary conditions are desired, the repetitive mode solution satisfies these boundary conditions exactly for many structures and loadings. A very useful application of the theory is to structures having rotational symmetry where the mode must be repetitive in the θ direction and results are obtained without approximation. Examples of the application of the theory are given in the following sections.

Hexagonal Frame

Belvin⁶ analyzed and performed vibration tests on a number of cable-stiffened frames which have repetitive geometry in the θ direction. Comparison of these results with those from the present method illustrates how all the eigenvalues of a complete structure can be obtained. The radial rib platform from Belvin⁶ is shown in figure 1 and consists of 6 radial beams emanating from the center and connected at the outer ends by tensioned cables. When the repeating element shown in the upper left corner of figure 1 is rotated 6 times about the central node in increments of 60° , the complete hexagonal frame is generated. Vibration modes must be repetitive over 6 bays so $N_2 = 6$ and according to equation (3), it is necessary to consider harmonics n from 0 to 3 inclusive. The configuration was analyzed as a free-free structure. Several of the lower elastic modes and associated frequencies for inplane vibration are shown in figure 1. The solutions for $n = 1$ and 2 correspond to two independent vibration modes which are taken as the real and imaginary mode shapes determined from the complex eigenvalue problem. The mode shapes shown are from the present analysis and the beam dominated modes agree well with those presented

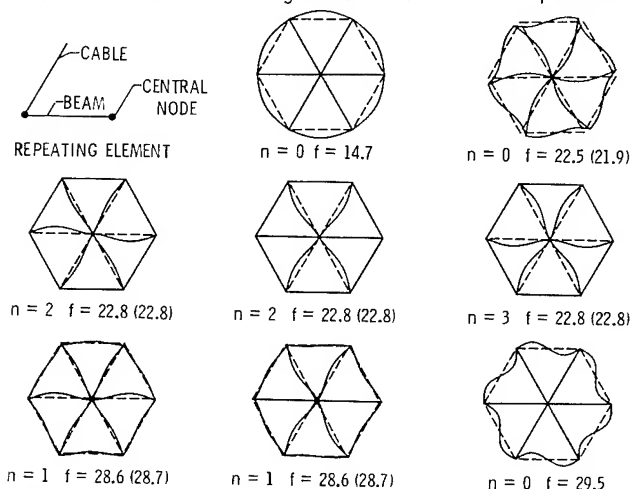


Figure 1. - Vibration modes and frequencies of cable-stiffened hexagonal frame. Values in parenthesis from Belvin⁶.

by Belvin⁶. The exact modes were obtained from the deflections of the two nodes used in the repeating element along with equation (2) and the solutions of the member differential equations. The complete frame was also analyzed with BUNVIS and the results obtained were identical to those shown in figure 1. The finite element results of Belvin⁶ for the complete configuration used many nodes in each bending member but no interior nodes for the cable so that cable frequencies were not obtained. The only difference in the results of the two analyses for the beam dominated modes are those for which some observable cable motion is present. For each of the two cable modes shown in figure 1, five additional modes were found at the same or nearly the same frequency for the harmonics $n = 1$ to 3.

Hexahedral Truss Platform

Vibration of a simply supported rectangular hexahedral truss platform of the type shown in figure 2 was considered by Noor et al.⁷ using a continuum and a complete finite element analysis. The truss configuration has members oriented at $\pm 45^\circ$ and at 0° - 90° in both surfaces with the pattern repeating in an offset manner. Members with different cross-sectional areas were used in the two surfaces as well as in the core that connects the two surfaces. Because of the symmetry of the configuration, the eigenvalues for the harmonic response n_1, n_2 are the same as those for $n_1, -n_2$. It can be shown that the modes for these two solutions can be combined to satisfy simply supported boundary conditions at intervals of one half the distance over which the mode is repetitive. Thus, modes that repeat over 16 bays in both directions then give results for a structure simply supported over a span of 8 bays in each direction. Only the 8 bays analyzed in the complete model are shown in figure 2 along with the nodes which are simply supported. Because the figure was generated from the repeating element, members that may be missing from an edge node do appear at the opposite edge. The complete model has 162 nodes while only a four noded repeating element is required in the present analysis as shown in figure 2. A comparison of the results from the present theory with the finite element results using the complete model is given in table 1. The subscripts on f denote the number of half waves in each direction for the vibration mode. The analysis gave $f_{pq} = f_{qp}$ as expected for a square symmetric configuration

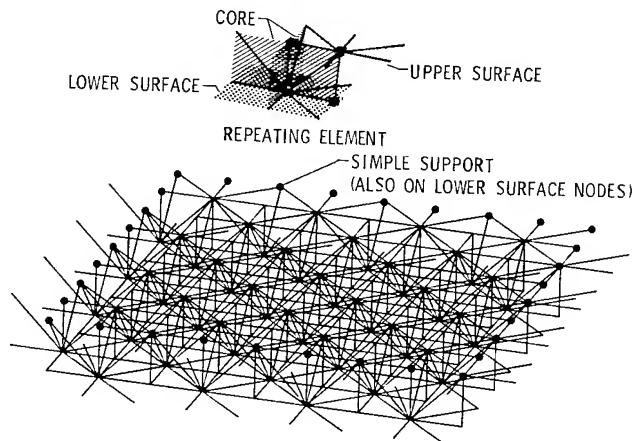


Figure 2. - Simply supported hexahedral truss platform.

Table 1. Frequencies of hexahedral truss calculated from complete model and repetitive model

mode	Noor ⁷ rod elements	Frequency, Hz	
		present theory rigid joints	pinned joints
f ₁₁	4.50	4.57	4.44
f ₁₂	7.73	7.78	7.43
f ₂₂	10.08	10.04	9.44
f ₁₃	11.22	11.15	10.37
f ₀₁	12.84	12.99	12.02
f ₂₃	13.06	12.86	11.74
f ₁₄	14.66	14.42	12.91
f ₃₃	15.58	15.18	13.37
f ₂₄	16.18	15.80	13.79
f ₁₅	17.82	17.60	14.91
f ₃₄	18.32	17.77	14.77

so only one frequency value is shown. The finite element model used a linear stiffness and mass matrix derived by representing each member by a single rod element without bending stiffness. In the repetitive analysis, the bending members used have moment of inertias which give $H/\rho = 30$ for each of the three different area truss members, where H is the depth of the truss and ρ is the member radius of gyration. The results for pinned joints were obtained by modifying the stiffness matrix of the individual members by conventional techniques to set all end moments to zero. The comparison is quite good, especially for the lower modes, but there is a tendency for the results from the complete model, using the linear eigenvalue analysis, to be high at the higher modes. The pin-ended frequency for the longest member is about 17.8 Hz and the clamped frequency is about 40.3 Hz. The results for pinned joints are in close agreement with the others for the lower modes, but the higher modes are appreciably affected by the nearness of the pin-ended member frequencies. A mode with a zero subscript will not in general satisfy simply-supported boundary conditions. However, the second eigenvalue of the f_{01} mode is given in table 1 because the displacements were parallel to the truss surfaces, hence satisfying the simply-supported boundary condition.

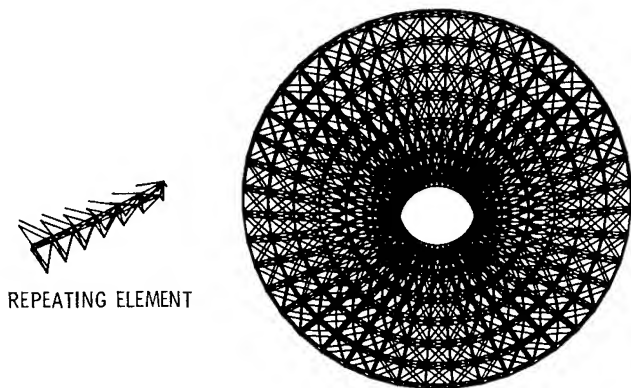


Figure 3. - 100m diameter parabolic dish antenna structure.

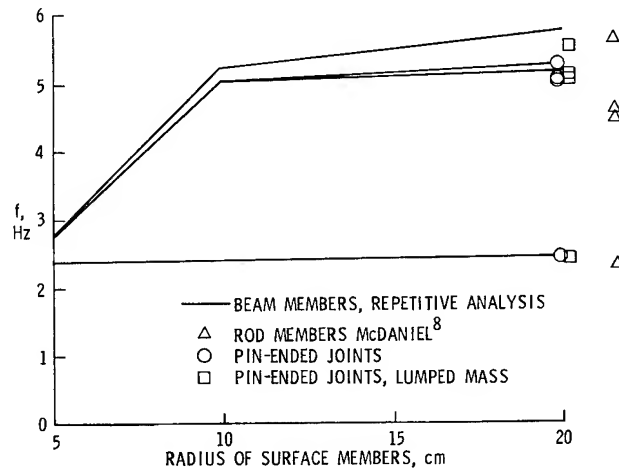


Figure 4. - Four lowest frequencies of 100m antenna structure.

Antenna Structure

The capability to analyze a complex structure is illustrated by the vibration analysis of the parabolic dish antenna structure shown in figure 3 and first analyzed by McDaniel and Chang⁸. The repeating element has 14 nodes. The original analysis modeled the members as rod elements. The present analysis used tubular members that matched the area of the rod elements by adjusting the radius and thickness of the individual members. The radius to thickness ratio of different size members was held constant for each analysis. Several calculations were made for various size members. The first four frequencies are plotted in figure 4 as a function of the surface member radius and are compared with previous results. Three sets of results are shown from the present analysis. Besides the results from direct application of the theory, results are given for pin joints with distributed and lumped mass at a radius of 20 cm. The lumped mass results were obtained by reducing the member mass to essentially zero, and placing the appropriate concentrated mass at each joint. For small radii, the individual members vibrate at frequencies below the frequencies of the antenna modeled with rod elements. As the member radius increases, these modes become sufficiently high that the overall dish modes appear at frequencies about 10 percent higher than that found previously. There appears to be some discrepancy in the present model as developed from the information provided in reference 8 and the actual model analyzed by McDaniel and Chang⁸. To check the present modeling, an independent analysis of the complete structure was made using

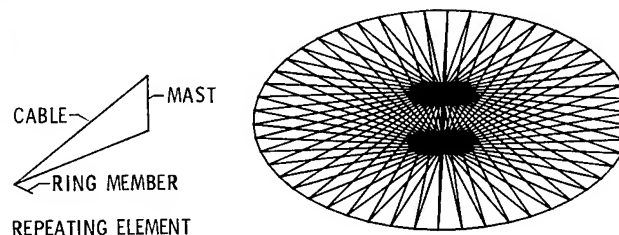


Figure 5. - Cable-stiffened ring.

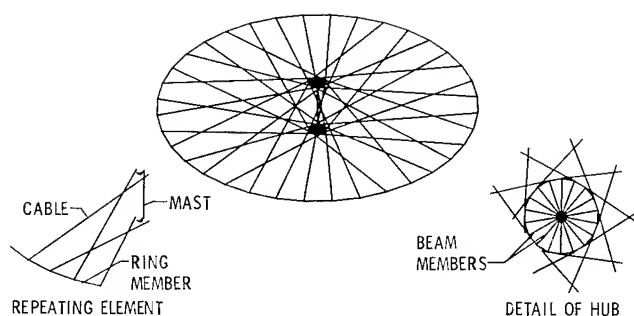


Figure 6. - Cable-stiffened ring with bicycle spoke lacing.

the EAL⁹ computer program and data derived from reference 8. These results were essentially identical to those from the repetitive analysis for the larger radius members with pinned joints.

Cable Stiffened Ring

Buckling and vibration of the cable stiffened ring shown in figure 5 was analyzed by Anderson^{1,2}. However, in that analysis, the attachment at the mast had to be considered clamped which is correct only for the higher harmonics ($n > 1$, see Appendix). The present analysis can include the mast but results in an essentially zero torsion frequency in addition to the rigid body torsion mode for the configuration of figure 5. This problem can be eliminated by using cables arranged like bicycle wheel spokes, as shown in figure 6. This model demonstrates two of the unique capabilities of the analysis: (1) the ability to connect a member between elements that are not adjacent, and (2) the treatment of a central member. For this case, the θ coordinate at the hub is plus or minus 80° from the ring attachment which provides torsional stiffness to the structure. The hub itself (shown in detail in figure 6) is modeled with bending members of the same cross-sectional properties as the ring members. The variation of the square of the lowest frequency with compressive ring force, P_0 , produced by cable tension is shown in figure 7. Nondimensional parameters are used that make results essentially independent of number of cables.

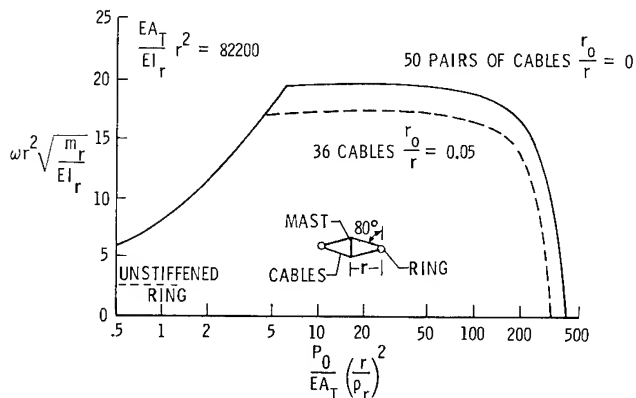


Figure 7.- Frequency of cable-stiffened ring as a function of preload.

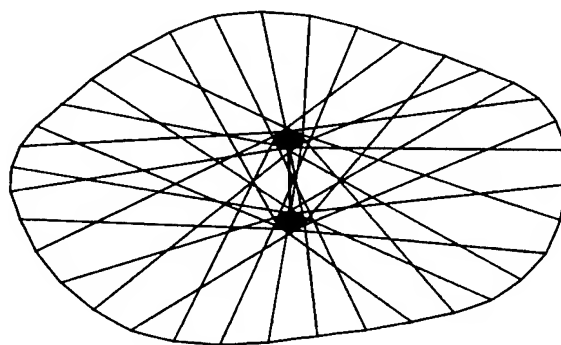


Figure 8. - Buckling mode of cable-stiffened ring with bicycle lacing.

The definition of all the parameters used can be found in the nomenclature. The solid curve is for 50 pairs of centrally directed cables ignoring any zero frequencies. The results for the 36-cable bicycle wheel lacing are shown as the dashed curve. In the left portion of figure 7, cable modes control and the results for both models coincide. At higher loadings, the frequencies of the ring modes for the bicycle arrangement are somewhat lower than for the centrally directed cables. This is attributed to flexibility of the members in the vicinity of the hub. When the lowest frequency goes to zero, the ring buckles. For the bicycle arrangement, the mode has 4 waves around the circumference as shown in figure 8.

The radius of the hub was sufficient to drive the torsion frequency above the fundamental frequency shown in figure 7. Additional calculations have shown that even a much smaller hub is adequate. In an actual design, requirements for torsional stiffness or strength probably would control.

Concluding Remarks

A method is developed to determine, without approximation, vibration or buckling eigenvalues for lattice structures having repetitive geometry and having modes that also are repetitive. The method involves nodes of only one repeating element and uses stiffness matrices that are based on exact solutions to the beam-column equations. Thus accurate values can be obtained for all eigenvalues without introduction of nodes between points of connection. For structures that are repetitive in rectangular coordinate directions and having the proper symmetry, the solution corresponds to boundary conditions of simple support over a length one half of the length over which the mode is assumed to be repetitive. Such a solution is useful for other boundary conditions if the response wavelengths of interest are small with respect to the size of the structure. For structures having rotational symmetry, such as large antenna configurations proposed for space, the mode must be repetitive around the circumference; thus, the method gives results that are identical to an analysis of the complete structure. Such configurations often have a central mast that is connected to all the repetitive segments. The necessary equations to treat this case are also

developed.

A computer program has been developed incorporating the repetitive analysis features and results have been obtained for several platform, ring and antenna configurations. Comparison of these results with previous analyses of the complete structures generally showed good agreement for the lower modes. For higher modes, conventional finite element analysis results tend to be unconservative and thus are higher than those obtained using stiffness matrices based on the exact solution of the beam-column equations. For problems having many identical elements, the savings in computer time and storage can be very large compared to methods which analyze the complete structure.

Appendix

Stiffness matrices when node is on axis of rotational symmetry

Consider N identical members which connect a node on the axis of rotational symmetry to nodes which have identical axial coordinates and are uniformly spaced in the θ direction as shown in figure 9. In the analysis of the complete structure, that set of members would contribute to the global stiffness matrix as follows

$$\begin{bmatrix} \sum K_{11}^j & K_{12}^1 & K_{12}^2 & \dots & K_{12}^N \\ K_{21}^1 & K_{22}^1 & 0 & \dots & \\ K_{21}^2 & 0 & K_{22}^2 & \dots & \\ \dots & \dots & \dots & \dots & \\ K_{21}^N & \dots & \dots & \dots & K_{22}^N \end{bmatrix} \begin{bmatrix} D_a \\ D_1 \\ D_2 \\ \dots \\ D_N \end{bmatrix} \quad (A1)$$

where

$$\sum = \sum_{j=1}^N$$

The displacement vector corresponding to each row in equation (A1) is also shown. The K_{pq}^j are 6×6 submatrices resulting from transformation of

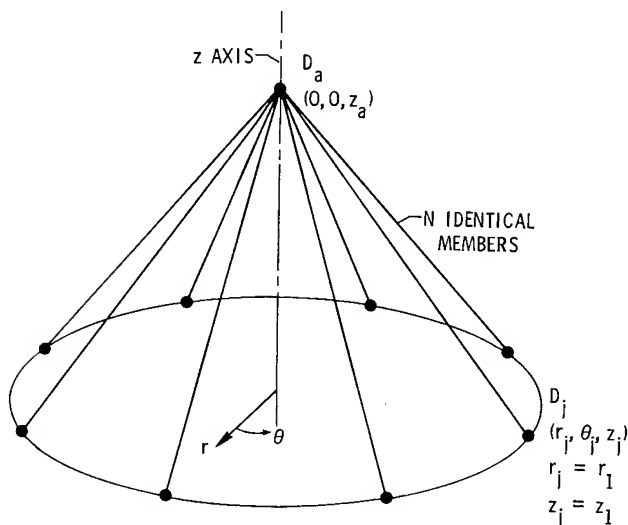


Figure 9. - Central node on z axis connected to several repetitive nodes.

the local member stiffness matrices. For mode shapes that are repetitive in the θ direction, D_j may be related to D_1 as in equation (2) by

$$D_j = D_1 \exp(2i\pi n(j-1)/N) \quad (A2)$$

The first row of the matrix of (A1) times the corresponding displacement vector can then be written as

$$\sum [K_{11}^j D_a + K_{12}^j D_1 \exp(2i\pi n(j-1)/N)] \quad (A3)$$

or

$$K_a D_a + K_1 D_1 \quad (A4)$$

The matrices K_a and K_1 can be determined as follows. The member stiffness matrix in local coordinates can be expressed as the four 6×6 submatrices

$$k_{pq} = \begin{bmatrix} A_1 & 0 & 0 & 0 & a_p A_7 & 0 \\ 0 & A_2 & 0 & b_p A_8 & 0 & 0 \\ 0 & 0 & A_3 & 0 & 0 & 0 \\ 0 & b_q A_8 & 0 & A_4 & 0 & 0 \\ a_q A_7 & 0 & 0 & 0 & A_5 & 0 \\ 0 & 0 & 0 & 0 & 0 & A_6 \end{bmatrix} \quad (A5)$$

where

$$a_p = (-1)^{p-1}$$

$$b_p = (-1)^p$$

The matrix (A5) is written assuming that the nodal displacement vector is given in the order of three displacements followed by three rotations in a right handed coordinate system and that the member is aligned along the third local coordinate direction. The terms A_p are in general different for the four submatrices. For a nonvibrating member without axial load, they are equal to the conventional finite element stiffness terms. The member global stiffness matrix can be obtained using the transformation matrices T and T' .

$$T = \begin{bmatrix} W & 0 \\ 0 & W \end{bmatrix} \quad (A6)$$

where

$$W = \begin{bmatrix} s_j & -c_j & 0 \\ c_j s_b & s_j s_b & -c_b \\ c_j c_b & s_j c_b & s_b \end{bmatrix} \quad (A7)$$

and

$$\begin{aligned} c_j &= \cos \theta_j & c_b &= r_1/L \\ s_j &= \sin \theta_j & s_b &= (z_1 - z_a)/L \\ \theta_j &= \theta_1 + 2(j-1)\pi/N & & \\ T' &= T|_{\theta_j=0} & & \end{aligned} \quad (A8)$$

where r_1 , θ_1 , z_1 are the coordinates of the first repetitive node and z_a is the axial coordinate of the central node. The transformation of equation (A7) assumes that one of the principal axis of inertia lies in a meridional plane. The real symmetric matrix K_a can be obtained as

$$K_a = \sum K_{11}^j = \sum T^T k_{11} T \quad (A9)$$

The nonzero terms in the upper triangle are

$$\begin{aligned} K_a(1,1) &= K_a(2,2) = (A_1 + A_2 s_b^2 + A_3 c_b^2)N/2 \\ K_a(1,5) &= -K_a(2,4) = (A_7 + A_8)s_b N/2 \\ K_a(3,3) &= (A_2 c_b^2 + A_3 s_b^2)N \\ K_a(4,4) &= K_a(5,5) = (A_4 + A_5 s_b^2 + A_6 c_b^2)N/2 \\ K_a(6,6) &= (A_5 c_b^2 + A_6 s_b^2)N \end{aligned} \quad (A10)$$

The terms A_p in equation (A10) come from the k_{11} matrix and use has been made of the relations

$$\begin{aligned} \sum \cos^2 \theta_j &= \sum \sin^2 \theta_j = N/2 \\ \sum \cos \theta_j \sin \theta_j &= 0 \\ \sum \cos \theta_j &= \sum \sin \theta_j = 0 \end{aligned} \quad (A11)$$

The matrix K_1 is obtained as

$$\begin{aligned} K_1 &= \sum K_{12}^j \exp(2i\pi n(j-1)/N) \\ &= \sum T^T k_{12} T' \exp(2i\pi n(j-1)/N) \end{aligned} \quad (A12)$$

The nonzero elements are

$$\begin{aligned} K_1(1,1) &= C(A_2 s_b^2 + A_3 c_b^2) \\ K_1(1,2) &= -CiA_1 \\ K_1(1,3) &= C(-A_2 + A_3)c_b s_b \\ K_1(1,4) &= CiA_7 s_b \\ K_1(1,5) &= CA_8 s_b \\ K_1(1,6) &= -CiA_7 c_b \\ K_1(3,1) &= (-A_2 + A_3)c_b s_b N\delta_{0n} \\ K_1(3,3) &= (A_2 c_b^2 + A_3 s_b^2)N\delta_{0n} \\ K_1(3,5) &= -A_8 c_b N\delta_{0n} \\ K_1(4,1) &= CiA_8 s_b \\ K_1(4,2) &= CA_7 s_b \\ K_1(4,3) &= -CiA_8 c_b \\ K_1(4,4) &= C(A_5 s_b^2 + A_6 c_b^2) \\ K_1(4,5) &= -CiA_4 \\ K_1(4,6) &= C(-A_5 + A_6)c_b s_b \\ K_1(6,2) &= -A_7 c_b N\delta_{0n} \\ K_1(6,4) &= (-A_5 + A_6)c_b s_b N\delta_{0n} \\ K_1(6,6) &= (A_5 c_b^2 + A_6 s_b^2)N\delta_{0n} \end{aligned} \quad (A13)$$

$$\begin{aligned} K_1(2,k) &= iK_1(1,k) \\ K_1(5,k) &= iK_1(4,k) \end{aligned} \quad k = 1, 2, \dots, 6$$

where

$$\begin{aligned} C &= (\cos \theta_1 - i \sin \theta_1)\delta_{1n}N/2 \\ \delta_{pq} &= 1 \quad p = q \\ \delta_{pq} &= 0 \quad p \neq q \end{aligned} \quad (A14)$$

The terms A_p in equation (A13) come from the k_{12} matrix and the following relationships have been used

$$\begin{aligned} \sum \cos \theta_j \exp(2i\pi(j-1)n/N) &= C \\ \sum \sin \theta_j \exp(2i\pi(j-1)n/N) &= iC \\ \sum \exp(2i\pi(j-1)n/N) &= \delta_{0n}N \end{aligned} \quad (A15)$$

The matrix K_{22}^j is defined as

$$K_{22}^j = (T')^T k_{22} T' \quad (A16)$$

Since T' is not a function of θ_j ,

$$K_{22}^j = K_{22}^1 \quad (A17)$$

If succeeding rows of equation (A1), starting at the second row, are multiplied by $\exp(-2i\pi n(j-1)/N)$ and summed, the result is

$$K_1^H D_a + N K_{22}^1 D_1 \quad (A18)$$

where the superscript H denotes Hermitian transpose. Thus the matrix coefficient of D_1 is the same as that obtained by considering only one member and multiplying the result by N. In the analysis of the complete structure, all stiffness matrices involving members not connected to a central node are multiplied by N to be compatible with equations (A9) and (A12). For members that lie along the axis, the stiffness matrices are generated in the usual way without multiplication by N.

Eigenvalue analysis

Vibration or buckling eigenvalues are determined in BUNVIS by the theory described by Williams and Wittrick¹⁰. The theory involves reducing the stiffness matrix for some trial value of the eigenvalue by Gaussian elimination and determining the sign count which is the number of negative signs on the leading diagonal. The number of eigenvalues exceeded is the sign count plus J_0 , the number of eigenvalues exceeded by individual members if their ends were clamped. An iterative procedure is used to converge to the desired eigenvalue. The procedure is equally valid for the complex matrix of the repetitive analysis, recognizing that eigenvalues occur in pairs except for the special cases when the matrix is real. These procedures must be modified somewhat to account for a central node. Examination of the matrix K_1 shows that for $n = 0$ only the 3rd and 6th rows are nonzero, corresponding to axial displacement and torsion about the axis. For this case the other degrees of freedom are suppressed and only the contribution to J_0 from the axial and torsion modes of members along the axis are counted. For $n = 1$, rows 3 and 6 of K_1 are zero. Therefore the corresponding displacements

are suppressed. In addition, the contribution to the sign count and J_0 must reflect the fact that the displacement vector is a combination of vectors D_a which are not periodic, and vectors D_j that are periodic around the circumference. This can be accomplished by restricting motion of all nodes along the axis to one plane only (suppressing displacements corresponding to rows 2 and 4 of K_a for example) and multiplying K_a by one half. In addition the stiffness matrix for any member along the axis must be multiplied by one half. Contributions to J_0 from members along the axis are from bending only and are counted singly (for the theory to apply, the central members must have equal principle moments of inertia and ordinarily the contributions to J_0 for such a member is in multiples of two). This procedure effectively weights the contribution of the central nodes by one half compared to other nodes so that final eigenvalues may be considered as occurring in pairs as for structures without central nodes and having rotational symmetry. For $n > 1$, $K_1 = 0$ and the central node displacements do not couple with exterior node displacements. In this case all degrees of freedom of the central node are suppressed and no contribution to J_0 from a member along the axis is made.

References

¹Anderson, M. S., "Buckling of Periodic Lattice Structures," AIAA Journal, Vol. 19, June 1981, pp. 782-788.

²Anderson, M. S., "Vibration of Prestressed Periodic Lattice Structures," AIAA Journal, Vol. 20, April 1982, pp. 551-555.

³Banerjee, J.R. and Williams, F. W., "User's Guide to the Computer Program BUNVIS (BUckling or Natural Vibration of Space Frames)," The University of Wales Institute of Science and Technology Department of Civil Engineering and Building Technology, Cardiff, UK, Dept. Rept. No. 5, February 1982.

⁴MacNeal, R. H., Harder, R. L. and Mason, J. B., "NASTRAN Cyclic Symmetry Capability," NASTRAN Users Experience-3rd Coll. NASA TM X-2893 pp.395-421.

⁵Thomas, D. L., "Dynamics of Rotationally Periodic Structures," International Journal for Numerical Methods in Engineering, Vol. 14, 1979, pp.81-102.

⁶Belvin, W. K., "Vibration Characteristics of Hexagonal Radial Rib and Hoop Platforms," Presented at the AIAA/ASME/ASCE/AHS 24th Structures, Structural Dynamics and Materials Conference, Paper No. 83-0822CP, Lake Tahoe, Nevada May 2-4, 1983.

⁷Noor, A. K., Anderson, M.S. and Greene, W. H. "Continuum Models for Beam- and Platelike Lattice Structures," AIAA Journal, Vol. 16, Dec. 1978, pp. 1219-1228.

⁸McDaniel, T. J. and Chang, K. J., "Dynamics of Rotationally Periodic Large Space Structures," Journal of Sound and Vibration, Vol. 68, No. 3, 1980, pp. 351-368.

⁹Whetstone, W. D., "Engineering Analysis Language," Proceedings of the Second Conference on Computing in Civil Engineering, American Soc. Civil Eng., 1980, pp.276-285.

¹⁰Williams, F. W. and Wittrick, W. H., "Exact Buckling and Frequency Calculations Surveyed," Journal of Structural Engineering, Vol. 109, No. 1, Jan., 1983, pp. 169-187.

C.W. Bert*
University of Oklahoma
Norman, Oklahoma

T.G. Gardner**
Gulfstream Aerospace Corporation
Bethany, Oklahoma

Abstract

A new theory for the in-plane dynamic behavior of shear-deformable ring-type structures, i.e., curved beams and complete rings, is presented. In classical thin-ring theory, transverse shear deformation is neglected altogether, while in Bresse-Timoshenko-type ring theory, the shear strain is assumed to be distributed uniformly through the thickness with a shear correction factor determined in an *ad hoc* fashion. The thick ring problem has also been treated using two- and three-dimensional elasticity theory, but these solutions involve extensive computation. The present theory is an advancement over Bresse-Timoshenko theory in that it satisfies the physical requirements of zero shear strain at the inner and outer ring surfaces. Its accuracy lies between that of the shear-correction and elasticity methods and yet it involves no more effort than the former method. Finally, it is emphasized that transverse shear effects are much more significant for composite materials than for homogeneous materials of the same geometric configuration and in the same vibration mode.

Nomenclature

A	stretching stiffness constant
B, B'	bending-stretching stiffness constants
C	extensional shear stiffness constant
D	bending stiffness constant
E	Young's modulus
F	bending shear stiffness constant
G	shear modulus
H	coefficient matrix
h	ring depth
I_0, I_1, I_4	mass moments of inertia
J_2, J_3, J_5, J_6	rotatory inertias
L	coefficient matrix
M	circumferential bending moment
m	mode number
N	circumferential normal force
P_i	externally distributed loading
Q	circumferential shear force
R	midsurface radius
r	radial dimensional variable
S	shear stiffness constant
S'	rotational shear stiffness constant
t	time
V, v, \underline{v}	circumferential displacement
W, w, \underline{w}	radial displacement
y	circumferential dimensional variable (= $R\theta$)
z	radial position measured from mid-surface
$\alpha, \underline{\alpha}$	angular displacement (1st order)
β	angular displacement (2nd order)
ϵ	normal strain
γ	shear strain

κ	midsurface curvature
η	modal constant
θ	angular dimensional variable
ϕ	angular displacement (3rd order)
ρ	material density
σ	normal stress
τ	shear stress
Ω	modal frequency

Introduction

Because of the varied use of ring elements in the machines and structures of our present-day world, the necessary models and applied mathematics must be developed as design tools. Ring structures such as flywheel rims, shell and cylinder rims, casings for load rings and vibration and pressure transducers, and others are common examples of this important class of structures. Furthermore, the increasing use of more fiber reinforced composite materials in ring structures is prompting the need for an accurate description of transverse shear strain in ring analysis.

The classical thin-ring theory of Hoppe¹ is very inaccurate when applied to thick homogeneous rings and composite-material rings in which transverse shear effects are of significant magnitude. The work of Bresse² (and similarly Timoshenko for straight beams³) is an improvement which includes a uniform distribution of transverse shear strain through the thickness. However, the physical requirement of rings requires that the shear strains vanish at the free surfaces, namely the intrados and extrados. In fact, the actual shear-strain distribution through the thickness of a ring structure is a somewhat distorted parabola. To correct the poor shear description, the Bresse-Timoshenko theory uses a shear correction factor which must be determined independently of the ring analysis. Mindlin and Deresiewicz⁴ and Cowper⁵ have suggested various methods for determining this shear correction factor.

To avoid the inaccuracies of the shear-correction analysis, some investigators have modeled ring structures using two- and three-dimensional elasticity theory^{6,7}. This approach is, of course, quite accurate, but at the same time quite laborious. Levinson⁸ has recently proposed a new, straight beam theory which allows for a more realistic shear strain distribution. However, this and analogous earlier plate theories by Ambartsumyan⁹, Reissner¹⁰, and Schmidt¹¹ were derived for macroscopically homogeneous materials only. Levinson's plate theory¹² has been extended to include laminated plates by Murthy¹³ and Bert¹⁴. However, Levinson's theory cannot be directly extended to ring structures, since for such a geometry, it does not satisfy the physical conditions of zero shear strain at the inner and outer surfaces.

The new theory reported in this paper is motivated by the need for a realistic shear strain

*Perkinson Professor of Engineering, Associate Fellow AIAA

**Structural/Fluid Dynamics Engineer, Member AIAA

distribution and the requirement to satisfy the zero shear strain conditions. Following Levinson, the circumferential displacement will contain the same terms plus those necessary to apply the surface boundary conditions. The new theory is also of the nature of a first-order approximation in the sense that the terms involving $(h/R)^2$ in the expanded circumferential displacement field are neglected. The accuracy of this new theory is greater than the classical and shear-correction theories, yet is much more practical than an elasticity analysis in the amount of effort required to arrive at a satisfactory engineering solution. An additional motivation for this new theory is the increasing use and importance of fiber-reinforced composite construction rings. The transverse shear effects of composite rings are much more pronounced because of the relatively low shear modulus of such materials. For this reason, designers need an analysis method which offers an accurate description of the shear effects and at the same time requires only modest computational effort.

Bert¹⁵ recently applied this notion to the development of a new static-ring theory. The present paper presents the dynamic analysis counterpart for shear-deformable ring structures.

Theoretical Development

The displacement field considered is shown in Fig. 1, where the circumferential displacement is

$$V(\theta, z, t) = v(\theta, t) + z\alpha(\theta, t) + z^2\beta(\theta, t) + z^3\phi(\theta, t), \quad (1)$$

and the radial displacement is

$$W(\theta, z, t) = w(\theta, t). \quad (2)$$

Then the linear strain-displacement relations can be written

$$\begin{aligned} \epsilon_\theta &= \epsilon_y = W/R + v_{,y} \\ \epsilon_z &= W_{,z} = 0 \\ \gamma_{\theta z} &= \gamma_{yz} = w_{,y} - v/R + v_{,z} \end{aligned} \quad (3)$$

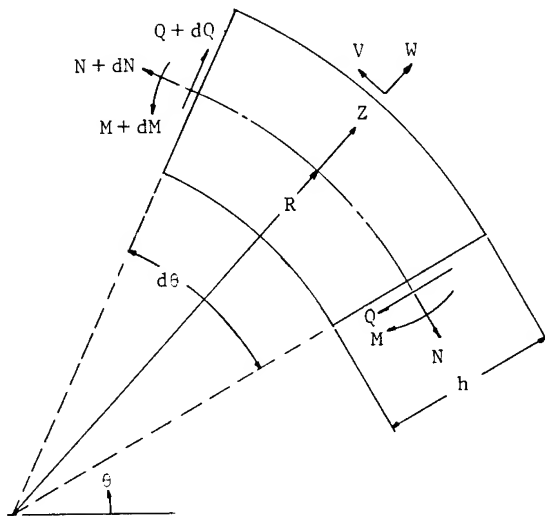


Fig. 1 Coordinates and generalized forces.

Using equations (1) through (3), the stress-strain relation for the element $d\tau$ can be written.

$$\sigma_\theta = \sigma_y = E\epsilon_y = E\{w/R + v_{,y} + z\alpha_{,y} + z^2\beta_{,y} + z^3\phi_{,y}\} \quad (4a)$$

$$\begin{aligned} \tau_{\theta z} = \tau_{yz} &= G\gamma_{yz} = G\{w_{,y} - v/R + \alpha(1 - z/R) \\ &+ \beta(2z - z^2/R) + \phi(3z^2 - z^3/R)\} \end{aligned} \quad (4b)$$

Since the shear stress must vanish at the inner and outer surfaces of the ring $\{\tau_{yz}(y, \pm h/2) = 0\}$, equation (4b) leads to

$$\begin{aligned} w_{,y} - v/R + \alpha(1 - h/2R) + \beta(h - h^2/4R) \\ + \phi(3h^2/4 - h^3/8R) &= 0 \\ w_{,y} - v/R + \alpha(1 + h/2R) + \beta(-h - h^2/4R) \\ + \phi(3h^2/4 + h^3/8R) &= 0 \end{aligned} \quad (5)$$

Equations (5) can be solved to isolate β and ϕ leaving,

$$\begin{aligned} \beta &= - (1/6R)(w_{,y} - v/R - 2\alpha) \\ \phi &= - (4/3h^2)(w_{,y} - v/R + \alpha) \end{aligned} \quad (6)$$

where $h^2/8R^2$ is neglected compared to unity. Now the normal and shear strains ϵ_y and γ_{yz} can be written in terms of the circumferential, radial, and angular deflections of the middle surface v , w , and α , respectively.

From the theory of elasticity, the dynamic equations of motion neglecting body forces can be written in polar coordinates $(R + z, \theta)$ as follows. The circumferential equation of motion is

$$\tau_{\theta z,z} + (\sigma_{\theta,\theta} + 2\tau_{\theta z})/(R + z) = \rho v_{,tt} \quad (7)$$

and the radial equation is

$$\tau_{\theta z,\theta} + (R + z)\sigma_{r,z} + \sigma_r - \sigma_\theta = (R + z)\rho w_{,tt}. \quad (8)$$

Equation (7) can be integrated over z to obtain an equation for the normal force, N , per unit width for any arbitrary point within the ring.

$$\begin{aligned} \int_{-h/2}^{h/2} \{(R + z)\tau_{\theta z,z} + \sigma_{\theta,\theta} + 2\tau_{\theta z}\} dz &= \int_{-h/2}^{h/2} \rho(R + z) \\ &\cdot \{v_{,tt} + z\alpha_{,tt} + z^2\beta_{,tt} + z^3\phi_{,tt}\} dz \end{aligned} \quad (9)$$

Similarly, multiplying equation (7) by z and integrating from $z = -h/2$ to $z = h/2$, yields an equation from which is obtained a description of the unit moment for any arbitrary point.

$$\int_{-h/2}^{h/2} z \{ (R+z) \tau_{\theta z, z} + \sigma_{\theta, \theta} + 2 \tau_{\theta z} \} dz = \int_{-h/2}^{h/2} \rho z (R+z) \cdot \{ v_{,tt} + z \alpha_{,tt} + z^2 \beta_{,tt} + z^3 \phi_{,tt} \} dz \quad (10)$$

The shear force, Q , per unit width results from integrating equation (8) over z .

$$\int_{-h/2}^{h/2} \{ (1/R) \tau_{\theta z, \theta} + (1+z/R) \sigma_{r, z} + (1/R) \sigma_r - (1/R) \sigma_{\theta} \} dz = \int_{-h/2}^{h/2} \rho (1+z/R) w_{,tt} dz \quad (11)$$

From Fig. 1 the stress resultants (N, Q) and stress couple (M) are defined as

$$(N, M) \equiv \int (1, z) \sigma_{\theta} dz \quad ; \quad Q \equiv \int \tau_{\theta z} dz \quad (12)$$

Completing the integrations in equations (9) through (11) and using equations (6) and the definitions in equations (12) results in three equations of motion involving v , w , and α .

$$\begin{aligned} N_{,y} + Q/R &= I_1 v_{,tt} + J_2 \alpha_{,tt} - J_3 w_{,ytt} \\ M_{,y} - Q &= I_4 v_{,tt} + J_5 \alpha_{,tt} - J_6 w_{,ytt} \\ Q_{,y} - N/R &= I_0 w_{,tt} - P_1 \end{aligned} \quad (13)$$

where P_1 is the external distributed loading. Equations (13) are written in this form recognizing that

$$N_{,y} = \frac{1}{R} \frac{\partial N}{\partial \theta} \quad ; \quad M_{,y} = \frac{1}{R} \frac{\partial M}{\partial \theta} \quad ; \quad Q_{,y} = \frac{1}{R} \frac{\partial Q}{\partial \theta}$$

The inertial terms in equations (13) are derived from the right side of equations (9) through (11).

$$\begin{aligned} I_0 &= \int_{-h/2}^{h/2} \rho (1+z/R) dz \\ I_1 &= \int_{-h/2}^{h/2} \rho (1+z/R) \{ 1 + z^2/6R^2 + 4z^3/3h^2R \} dz \\ J_2 &= \int_{-h/2}^{h/2} \rho (1+z/R) \{ z + z^2/3R - 4z^3/3h^2 \} dz \\ J_3 &= \int_{-h/2}^{h/2} \rho (1+z/R) \{ z^2/6R + 4z^3/3h^2 \} dz \\ I_4 &= \int_{-h/2}^{h/2} \rho z (1+z/R) \{ 1 + z^2/6R^2 + 4z^3/3h^2R \} dz \\ J_5 &= \int_{-h/2}^{h/2} \rho z (1+z/R) \{ z + z^2/3R - 4z^3/3h^2 \} dz \\ J_6 &= \int_{-h/2}^{h/2} \rho z (1+z/R) \{ z^2/6R + 4z^3/3h^2 \} dz \end{aligned} \quad (14)$$

$$I_4 = \int_{-h/2}^{h/2} \rho z (1+z/R) \{ 1 + z^2/6R^2 + 4z^3/3h^2R \} dz$$

$$J_5 = \int_{-h/2}^{h/2} \rho z (1+z/R) \{ z + z^2/3R - 4z^3/3h^2 \} dz$$

$$J_6 = \int_{-h/2}^{h/2} \rho z (1+z/R) \{ z^2/6R + 4z^3/3h^2 \} dz$$

The force and moment definitions in equations (12) can be expanded using the stress-strain relationships of equations (4), resulting in descriptions of the normal and shear force and couple with respect to the midplane normal and shear strain and curvature;

$$\begin{Bmatrix} N \\ M \end{Bmatrix} = \begin{bmatrix} A & B' \\ B & D \end{bmatrix} \begin{Bmatrix} \epsilon^0 \\ \kappa \end{Bmatrix} - \begin{Bmatrix} C \\ F \end{Bmatrix} \gamma_{,y}^0 \quad (15)$$

$$Q = S \gamma^0 - S' \alpha$$

where

$$\begin{aligned} \epsilon^0 &= v_{,y} + w/R && \text{(midsurface normal strain)} \\ \kappa &= \alpha_{,y} && \text{(midsurface curvature)} \\ \gamma^0 &= w_{,y} - v/R + \alpha && \text{(midsurface shear strain)} \end{aligned}$$

The stiffness terms in equations (15) are defined as follows:

$$\begin{aligned} (A, B) &= \int_{-h/2}^{h/2} (1, z) E dz \\ (B', D) &= \int_{-h/2}^{h/2} (1, z) \{ E(z + z^2/2R) \} dz \\ (C, F) &= \int_{-h/2}^{h/2} (1, z) \{ E(z^2/6R + 4z^3/3h^2) \} dz \\ S &= \int_{-h/2}^{h/2} G \{ 1 - z/3R + z^2(1/6R^2 - 4/h^2) + 4z^3/3h^2R \} dz \\ S' &= \int_{-h/2}^{h/2} G(z^2/2R^2) dz \end{aligned} \quad (16)$$

Returning to equations (13), these relationships can now be expanded and terms collected in v , w , and α .

$$A\epsilon^0_{,y} + B'\kappa_{,y} - C\gamma^0_{,yy} + (1/R)(S\gamma^0 - S'\alpha) - I_1 v_{,tt} - J_2 \alpha_{,tt} + J_3 w_{,ytt} = 0$$

$$B\epsilon^0_{,y} + D\kappa_{,y} - F\gamma^0_{,yy} - (S\gamma^0 - S'\alpha) - I_4 v_{,tt} - J_5 \alpha_{,tt} + J_6 w_{,ytt} = 0$$

$$S\gamma^0_{,y} - S'\alpha_{,y} - (1/R)(A\epsilon^0 + B'\kappa - C\gamma^0_{,y}) - I_0 w_{,tt} = -P_i$$

Substituting the definitions of ϵ^0 , γ^0 , and κ and rearranging terms leads to the following set of simultaneous equations.

$$\begin{bmatrix} L_{11} & L_{12} & L_{13} \\ L_{21} & L_{22} & L_{23} \\ L_{31} & L_{32} & L_{33} \end{bmatrix} \begin{bmatrix} v/R \\ \alpha \\ w/R \end{bmatrix} = \begin{bmatrix} 0 \\ 0 \\ -P_i \end{bmatrix} \quad (17)$$

The coefficients of matrix $\{L\}$ are defined as follows where dy and dt are differential operators acting on the variable terms v , α , and w such that

$$dy = d/dy \quad ; \quad dt = d/dt$$

$$L_{11} = (AR + C)dy^2 - S/R - I_1 R dt^2$$

$$L_{12} = (B' - C)dy^2 + (1/R)(S - S') - J_2 dt^2$$

$$L_{13} = (A + S)dy - CRdy^3 + J_3 R dy dt^2$$

$$L_{21} = (BR + F)dy^2 + S - I_4 R dt^2$$

$$L_{22} = (D - F)dy^2 - (S - S') - J_5 dt^2$$

$$L_{23} = (B - SR)dy - FRdy^3 + J_6 R dy dt^2$$

$$L_{31} = - (S + A + C/R)dy$$

$$L_{32} = (S - S' - B'/R + C/R)dy$$

$$L_{33} = (SR + C)dy^2 - A/R - I_0 R dt^2$$

When $dv/dt = d\alpha/dt = dw/dt = 0$, equations (17) reduce to the static case as described in the work by Bert¹⁵.

In order to calculate the natural or free modes of vibration for any ring, solutions for v , α , and w will be assumed which are continuous over the circumference of the ring, i.e.,

$$v/R = \underline{v} \sin n\gamma \cos \Omega t$$

$$\alpha = \underline{\alpha} \sin n\gamma \cos \Omega t \quad (18)$$

$$w/R = \underline{w} \cos n\gamma \cos \Omega t$$

where $n = m/R$, m = mode number, and Ω = frequency in radians/second.

Substituting equations (18) into equations (17) and setting $P_i = 0$ (free vibration) yields a simultaneous set of equations for \underline{v} , $\underline{\alpha}$, and \underline{w}

with coefficients containing terms in Ω^2 .

$$\begin{bmatrix} H_{11} & H_{12} & H_{13} \\ H_{21} & H_{22} & H_{23} \\ H_{31} & H_{32} & H_{33} \end{bmatrix} \begin{bmatrix} \underline{v} \\ \underline{\alpha} \\ \underline{w} \end{bmatrix} = \begin{bmatrix} 0 \\ 0 \\ 0 \end{bmatrix} \quad (19)$$

The terms of $\{H\}$ are,

$$H_{11} = -\eta^2(AR + C) - (S/R) + \Omega^2 I_1 R$$

$$H_{12} = -\eta^2(B' - C) + (1/R)(S - S') + \Omega^2 J_2$$

$$H_{13} = -\eta(A + S) - \eta^3 CR + \eta \Omega^2 J_3 R$$

$$H_{21} = -\eta^2(BR + F) + S + \Omega^2 I_4 R$$

$$H_{22} = -\eta^2(D - F) - (S - S') + \Omega^2 J_5$$

$$H_{23} = -\eta(B - SR) - \eta^3 FR + \eta \Omega^2 J_6 R$$

$$H_{31} = -\eta(S + A + C/R)$$

$$H_{32} = \eta(S - S' - B'/R + C/R)$$

$$H_{33} = -\eta^2(SR + C) - (A/R) + \Omega^2 I_0 R$$

If arbitrary values of \underline{v} , $\underline{\alpha}$, and \underline{w} are considered, a nontrivial solution for equations (19) exists only if the determinant of matrix $\{H\}$ equals zero.

As a special reduced case, mode $m = 0$ (breathing mode) is considered. In this case, matrix $\{H\}$ reduces to

$$\begin{bmatrix} -S/R + \Omega^2 I_1 R & 1/R(S - S') + \Omega^2 J_2 & 0 \\ S + \Omega^2 I_4 R & -(S - S') + \Omega^2 J_5 & 0 \\ 0 & 0 & -A/R + \Omega^2 I_0 R \end{bmatrix}$$

The determinant, $\{H\}$, is simplified and the lowest real root is,

$$(\Omega^2)_1 = A/R^2 I_0 \quad ; \quad \Omega_1 = (1/R) \sqrt{E/\rho}$$

Since the zeroth mode has no shear action present, this should agree exactly with the classic solution for thin rings. From reference (16), page 454, the classic equation for pure extensional vibration of a thin ring is

$$\begin{aligned} \Omega &= (1/R) \{1 + m^2\} \sqrt{E/\rho} \} , \\ &= (1/R) \sqrt{E/\rho} \quad (\text{for } m = 0) . \end{aligned}$$

Discussion

The present analysis has been used to reduce the two-dimensional equilibrium equations (7,8) to a set of simultaneous equations (19) involving the normalized displacements \underline{v} , $\underline{\alpha}$, and \underline{w} . This technique is an improvement over the shear-correction theory by including a nonlinear shear strain distribution which allows the shear strain

to vanish at the inner and outer ring surfaces. In order to predict the modal frequencies for a given ring, the determinant of $\{H\}$ is simply set to zero, resulting in a cubic equation in Ω^2 . The lowest real root of this characteristic equation is the natural frequency for the given mode. The coefficients of matrix $\{H\}$ combine geometric properties relating bending, stretching, shear, and coupled actions as well as mass and rotatory inertial effects.

The present theory can be applied to shear-deformable rings of any cross-sectional shape or any material construction. However, the advantages of a more accurate nonlinear shear strain description should be more obvious when considering laminated rings made of composite materials. The low shear modulus of polymer-matrix composite materials greatly enhances the shear action in composite parts. As a result, composite-material rings of relatively thin laminates ($h/R \sim 0.1$) can exhibit appreciable shear effects. The terms in the coefficient matrix $\{H\}$ are readily determined by piecewise integration through each layer of the laminate.

Application

The present theory can now be applied to the case of a thick steel ring for which experimental data by Kuhl¹⁷ have been published by Kirkhope¹⁸.

The ring under consideration has a rectangular cross section as shown in Fig. 2. The appendix shows the calculated values of the coefficients involved in matrix $\{H\}$ for the given geometry and material properties. Table 1 shows the results of the present theory and the experimental and theoretical results published by Kirkhope¹⁸.

Table 2 shows the calculated and experimental results for a similar ring of rectangular cross section where $R = 1.282$ in. and $h = 0.967$ in. Again, the comparative data are from Kirkhope¹⁸.

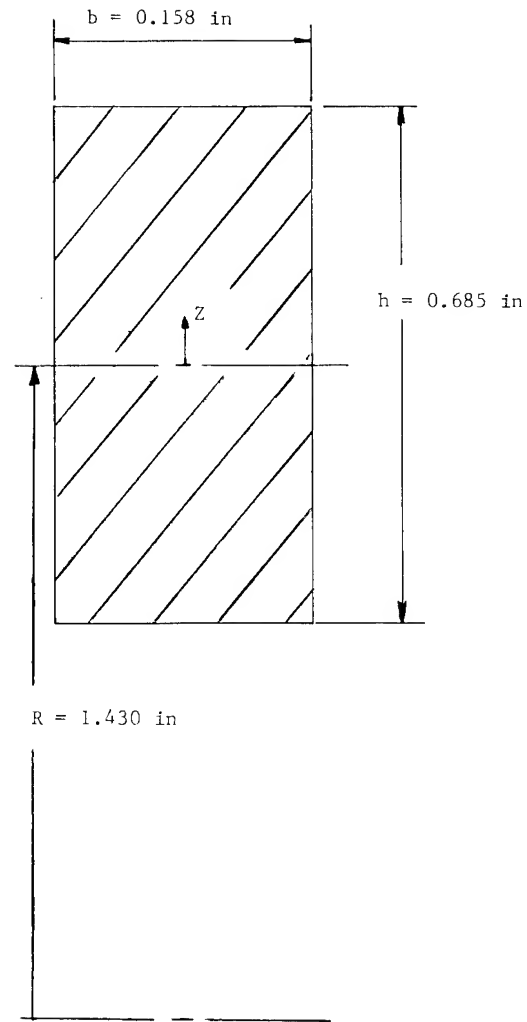


Fig. 2. Rectangular ring cross section $h/R = 0.479$.

Table 1 In-plane modes of a rectangular cross-section ring, $h/R = 0.479$

Mode No. m	Experimental	Classical Thin		Present Theory		Kirkhope Approximation Equation (2) of Ref. (18)	
	Freq (Hz)	Freq (Hz)	% Error	Freq (Hz)	% Error	Freq (Hz)	% Error
2	7,635	8,371	10	7,378	-3.4	7,257	-5.0
3	19,060	23,675	24	18,517	-2.8	19,122	0.3
4	32,150	45,396	41	31,338	-2.5	32,529	1.2
5	46,050	73,415	59	44,910	-2.5	46,614	1.2
6	60,400	107,699	78	58,815	-2.6	60,857	0.8
7	74,200	148,234	100	72,820	-1.9	75,045	1.1
8	88,000	195,014	122	86,833	-1.3	89,104	1.3

Table 2 In-plane modes of a rectangular cross-section ring, $h/R = 0.750$

Mode No. m	Experimental	Classical Thin		Present Theory		Kirkhope Approximation Equation (2) of Ref. (18)	
	Freq (Hz)	Freq (Hz)	% Error	Freq (Hz)	% Error	Freq (Hz)	% Error
2	12,070	14,538	20	11,211	-7.1	11,563	-4.2
3	28,650	41,119	44	26,088	-8.9	27,077	-5.5
4	44,750	78,841	76	41,815	-6.6	43,257	-3.3
5	60,200	127,503	112	57,661	-4.2	59,268	-1.6
6	73,900	187,044	153	73,387	-0.7	74,971	1.5
7	86,300	257,443	198	88,952	3.1	90,394	4.7
8	97,950	338,688	246	104,356	6.5	105,593	7.8

Summary

The classical thin-ring theory is very inaccurate when applied to thick homogeneous rings. The shear-correction theory is an improvement; however, it still cannot satisfy the physical requirement of rings, namely that the shear strains vanish at the free surfaces. The actual shear strain distribution is far from the uniform distribution allowed by the shear-correction theory. The present theory provides a more realistic shear strain description while satisfying the surface boundary requirements. For the case shown in Table 1, the present theory predicts very well (less than 5% error) the lower natural frequencies for a homogeneous thick ring. The amount of effort is limited to calculating the coefficients of matrix $\{H\}$ and finding the lowest real root of the cubic equation in Ω^2 resulting from setting the determinant $|H|$ equal to zero. This is clearly much less effort than that required of a two-dimensional elasticity solution. In contrast to a shear-correction type analysis, the separate calculation of a shear-correction factor is not required and thus the associated inaccuracies are not present.

The increasing use and importance of fiber-reinforced composite rings provides another incentive for the present theory. The advantages of a more accurate nonlinear description of the shear strain in rings should be more obvious when considering laminated composite-material rings since the transverse shear effects of composite rings are much more pronounced. Therefore, the present theory should provide a new and valuable tool for the design and analysis of composite rings, offering a more accurate description of the shear effects and at the same time requiring a manageable effort.

References

- ¹Hoppe, R., "Vibration en eines ringes in seiner ebene," *J. für reine und angewandte Math. (Crelle's J.)*, Vol. 73, 1871, pp. 158-170.
- ²Bresse, J.A.C., *Cours de mécanique appliquée*, Mallet-Bachelier, Paris, 1859; 2nd ed., Gauthier-Villars, Paris, 1866.
- ³Timoshenko, S.P., "On the Correction for Shear of the Differential Equation for Transverse Vibrations of Prismatic Bars," *Philosophical Magazine*, Ser. 6, Vol. 41, 1921, pp. 744-746.

⁴Mindlin, R.D. and Deresiewicz, H., "Timoshenko's Shear Coefficient for Flexural Vibrations of Beams," *Proc. 2nd U.S. Nat. Congr. Appl. Mech.*, ASME, 1954, pp. 175-178.

⁵Cowper, G.R., "The Shear Coefficient in Timoshenko's Beam Theory," *Journal of Applied Mechanics*, Vol. 33, 1966, pp. 335-340.

⁶Federhofer, K., "Zweidimensionale theorie der Biegungsschwingungen des kreisringes mit rechteckigem querschnitt," *Sitzungsber. Akad. Wiss., Wien*, Vol. 144, 1935, pp. 561-575.

⁷Endo, M., "Flexural Vibrations of a Ring with Arbitrary Cross Section," *Bulletin of Japan Soc. of Mech. Engrs.*, Vol. 15, 1972, pp. 446-454.

⁸Levinson, M., "A New Rectangular Beam Theory," *Journal of Sound and Vibration*, Vol. 74, 1981, pp. 81-87.

⁹Ambartsumyan, S.A., *Theory of Anisotropic Plates* (English translation), Technomic Publishing Co., Stamford, CT, 1970.

¹⁰Reissner, E., "On Transverse Bending of Plates, Including the Effect of Transverse Shear Deformation," *International Journal of Solids and Structures*, Vol. 11, 1975, pp. 569-573.

¹¹Schmidt, R., "A Refined Nonlinear Theory of Plates with Transverse Shear Deformations," *Journal of the Industrial Mathematics Society*, Vol. 27, 1977, pp. 23-38.

¹²Levinson, M., "An Accurate, Simple Theory of the Statics and Dynamics of Elastic Plates," *Mechanics Research Communications*, Vol. 7, 1980, pp. 343-350.

¹³Murthy, M.V.V., "An Improved Transverse Shear Deformation Theory for Laminated Anisotropic Plates," NASA TP-1903, 1981.

¹⁴Bert, C.W., "Comparison of New Plate Theories Applied to Laminated Composites," *Mechanics of Composite Materials*, ASME Applied Mechanics Division, Vol. 58, ASME Winter Annual Meeting, Boston, MA, Nov. 1983, pp. 9-17.

¹⁵Bert, C.W., "A New Theory for Shear-Deformable Rings," presented at the 17th Israel Conference on Mechanical Engineering, Tel Aviv University, July 1983; *Israel Journal of Technology*, to appear.

¹⁶Love, A.E.H., *A Treatise on the Mathematical Theory of Elasticity*, Dover Publications, New York, 4th Ed., 1927.

¹⁷Kuhl, W., "Messungen zu den Theorien der Eigenschwingungen von Kreisröhrer Beliebiger Wandstärke," *Akustische Zeitschrift*, Vol. 2, 1942, pp. 10-152.

¹⁸Kirkhope, J., "In-Plane Vibration of a Thick Circular Ring," *Journal of Sound and Vibration*, Vol. 50, 1977, pp. 219-227.

Appendix

The ring under consideration in Table 1 and shown in Fig. 2 has a rectangular cross section with the following geometric dimensions and material properties.

$$h = 0.685 \text{ in}$$

$$R = 1.430 \text{ in}$$

$$E = 30 \times 10^6 \text{ psi}$$

$$G = 11.9 \times 10^6 \text{ psi}$$

$$\rho = 7.33 \times 10^{-4} \text{ lb-sec}^2/\text{in}^4$$

The stiffness and inertial terms included in the coefficients of matrix {H} can be calculated from equations (14) and (16). They are:

$$A = 2.055 \times 10^7 \text{ lb/in}$$

$$B = 0$$

$$B' = 2.8096 \times 10^5 \text{ lb}$$

$$C = 9.3654 \times 10^4 \text{ lb}$$

$$D = 8.0355 \times 10^5 \text{ in-lb}$$

$$F = 1.6071 \times 10^5 \text{ in-lb}$$

$$S = 5.4603 \times 10^6 \text{ lb/in}$$

$$S' = 7.7929 \times 10^4 \text{ lb/in}$$

$$I_0 = 5.0211 \times 10^{-4} \text{ lb-sec}^2/\text{in}^3$$

$$I_1 = 5.0563 \times 10^{-4} \text{ lb-sec}^2/\text{in}^3$$

$$J_2 = 1.556 \times 10^{-5} \text{ lb-sec}^2/\text{in}^2$$

$$J_3 = 5.034 \times 10^{-6} \text{ lb-sec}^2/\text{in}^2$$

$$I_4 = 1.6554 \times 10^{-5} \text{ lb-sec}^2/\text{in}^2$$

$$J_5 = 1.5932 \times 10^{-5} \text{ lb-sec}^2/\text{in}$$

$$J_6 = 4.0393 \times 10^{-6} \text{ lb-sec}^2/\text{in}$$

S. Ramamurthy, D. Bhargava,
B. Niyogi, and N. A. Muni
Stone & Webster Engineering Corporation
Cherry Hill, NJ 08034

Abstract

Piping or other subsystems, attached to a larger structure that is subjected to any dynamic loading, will have different acceleration time histories (TH) at the attachment points. Where there are many dynamic load cases, analysis of the subsystems becomes very expensive. This paper presents an economical method of obtaining the response of a subsystem, when subjected to differing TH at the support attachment points. This method combines transfer functions (TF) of the subsystem and the Fourier transform (FT) of the input TH to obtain the output response in the frequency domain. By combining individual responses due to distinct loadings at each support point obtained from the inverse FT, the final response for any specific load case can be obtained. An example is presented to illustrate the accuracy of this method.

Introduction

The subsystems, and their parent containment structures in Boiling Water Reactor (BWR) nuclear power plants, are subjected to transient hydrodynamic loads resulting from safety relief valve (SRV) blowdown and loss-of-coolant-accident (LOCA) events. Each event consists of several load cases. For each load case, the subsystems are excited by multiple, distinctly different, support time histories (TH). For the dynamic analysis an adapted model (Figure 1) is created by adding very stiff springs to the mathematical model (Figure 2) of the structure. The input forcing functions for the adapted model are derived from the original TH multiplied by the spring stiffnesses.

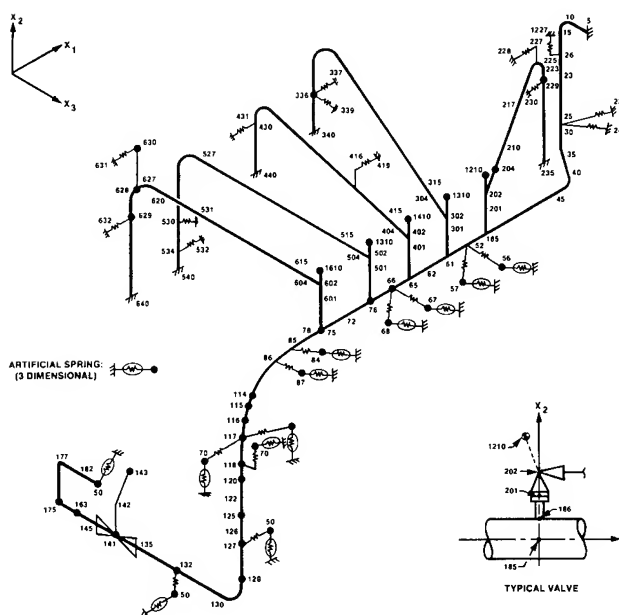


Fig. 1 Adapted Model of the Piping System

Repetition of this time-consuming dynamic analysis for each load case is expensive. An alternative method reduces computer time and cost by combining the time-domain and frequency-domain analyses.⁶ This mixed-domain analysis exploits the common spatial distribution of the input time histories of several load cases. However, the multiple support excitation problems do not have common spatial distributions. The method outlined in this paper extends the mixed-domain analysis to systems excited by multiple and distinct support time histories while using a novel approach to solve multiple support excitation problems.

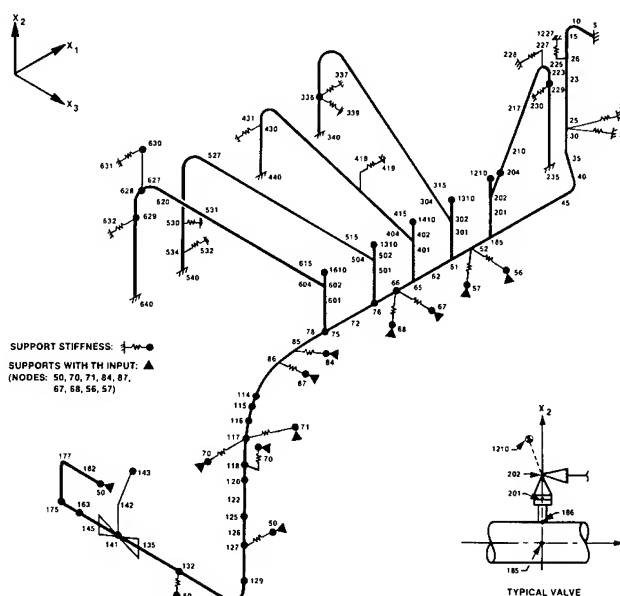


Fig. 2 Mathematical Model of the Main Support Piping System

The proposed method, employing an impulse function TH (Figure 3), generates as many transfer functions as there are distinct support THs. The FT of the impulse function TH is presented in Figure 4. One distinct TH means that the direction and magnitude of these histories should be the same even though it may excite the structure at many support points simultaneously. Development and use of the individual transfer functions to obtain the combined response are described in the method of analysis.

A numerical example is given and a comparison of the results of the computations using impulse function and conventional single-step analyses to illustrate the accuracy of the proposed method is discussed. The cost saving of the proposed method is stated and future work is discussed in the conclusion.

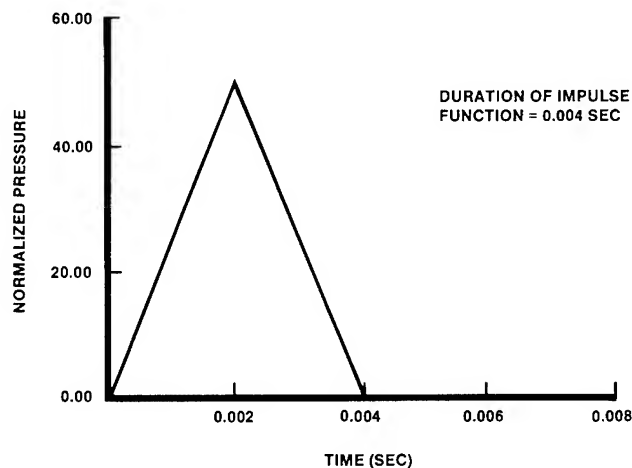


Fig. 3 Impulse Function Time History

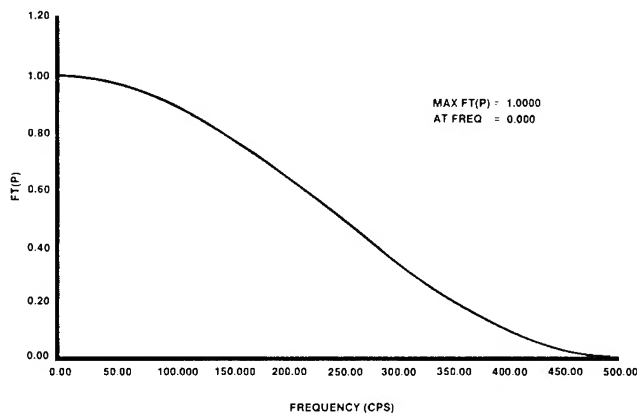


Fig. 4 Fourier Transformation for Triangular Impulse Function

Method of Analysis

Dynamic Analysis of the Adapted Model

The adapted model results from adding springs with an arbitrary stiffness of 10^{13} lb/ft (K_{sp}) to the supports that will be excited.¹ The number of added springs (Figure 5) will be equal to the number of directions in which acceleration time histories are input. Therefore, this model consists of the elements in the earlier mathematical model plus the added springs. This adapted model is analyzed with forces applied to each node having the arbitrary spring and a small mass (Figure 1). The magnitude of the forces equal 10^{13} times support acceleration time history.

The proposed method will have a pseudo force time history equal to K_{sp} times \ddot{x}_s where \ddot{x}_s equals support acceleration time history. This approach is very helpful as acceleration time histories are readily available.

However, the required actual acceleration response time history corresponds to the available displacement response time history of the adapted model obtained from the dynamic analysis discussed later.

The decomposition of the dynamic analysis of a multiple distinct excitation problem into multiple simple dynamic analysis problems. The simple analyses, discussed in the following section, will have only one distinct input time history (the same time history can be applied at several points). The solution of each of these single time history dynamic analyses via impulse functions also follows.

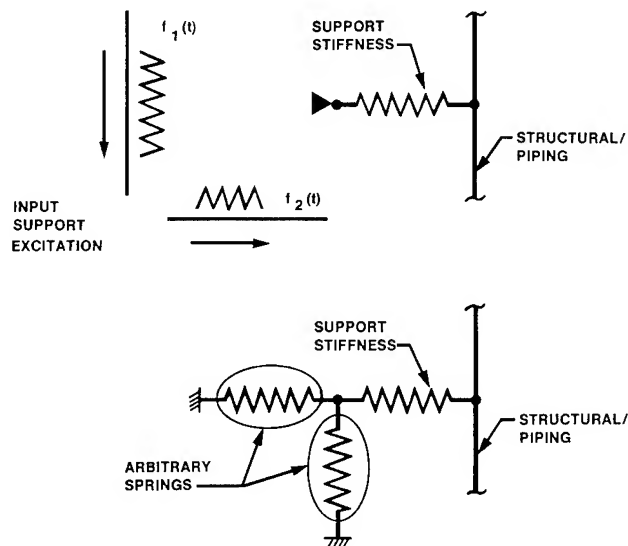


Fig. 5 Adaptation of Supports

Decomposition of Multiple Input Analysis

The equation of motion relating to the multiple DOF system with viscous damping is stated as follows:²

$$[M] \{\ddot{x}(t)\} + [C] \{\dot{x}(t)\} + [K]\{x(t)\} = \{f(t)\} \quad (1)$$

Where $[M]$ and $[C]$ and $[K]$ are the mass damping and stiffness matrices, respectively, of the adapted mathematical model; $x(t)$ is a generalized response function TH vector, and $\dot{x}(t)$ and $\ddot{x}(t)$ denote first and second derivatives of $x(t)$, respectively and $\{f(t)\}$ is a loading TH vector that can be expressed as a sum of distinct time history (in a case with four distinct time histories) vectors as follows:

$$\begin{aligned} \{f(t)\} &= \{a_1\} f_1(t) + \{a_2\} f_2(t) \\ &= \{a_3\} f_3(t) + \{a_4\} f_4(t) \end{aligned} \quad (2)$$

$$\text{where } \{a_1\} = \begin{Bmatrix} 1 \\ 0 \\ 0 \\ 0 \\ 0 \end{Bmatrix}$$

A vector consisting of "1's" and "0's", and $f_1(t)$ is applied at DOF corresponding to "1's" appearing in vector $\{a_1\}$.

The same holds true between $\{a_2\}$ and $f_2(t)$, $\{a_3\}$ and $f_3(t)$, and between $\{a_4\}$ and $f_4(t)$.

Thus Equation 1 is written:

$$[M]\{\ddot{x}_i(t)\} - [C]\{\dot{x}_i(t)\} + [K]\{x_i(t)\} = \{a_i\} f_i(t) \quad (3)$$

Here $i = 1, 2, 3$, and 4 and

$$\{x_1(t)\} + \{x_2(t)\} + \{x_3(t)\} + \{x_4(t)\} = \{x(t)\} \quad (4)$$

Thus, the solution of the equation for the subscripts $i = 1, 2, 3, 4$ can be obtained and summed as shown in Equation 4 to obtain the final response $x(t)$.

Each of these individual analyses can be carried out using mixed domain analysis, which is summarized here.

Mixed Domain Analysis Using Impulse Function Approach

Transfer Function Related to i th Subproblem

The subproblem of Equation 3 is stated as follows:

$$[M]\{\ddot{x}_i(t)\} + [C]\{\dot{x}_i(t)\} + [K]\{x_i(t)\} = \{a_i\} f_i(t) \quad (5)$$

Fourier transform (FT) of $f_i(t)$, $F_i(w)$

$$= \int f_i(t) e^{-iwt} dt \quad (6)$$

$$\text{Defining } [H(w)] = [-w^2[M] + iw[C] + [K]]^{-1} \quad (7)$$

$\{STF_i(w)\} = [H(w)]\{a_i\}$ where w is the frequency parameter.

$$\{x_i(w)\} \text{ can be obtained thus:} \quad (8)$$

$$\{x_i(w)\} = \{STF_i(w)\} F_i(w) \quad (9)$$

$$\text{An inverse FT of } \{x_i(w)\} \text{ yields } \{x_i(t)\} \quad (10)$$

Solving Equation 3 for $i = 1, 2, 3, 4$ in the case of four distinct time histories $\{x(t)\}$ can be obtained as shown in Equation 4.

Transfer Function Using Impulse Function

Defining w_j as the discrete value of the frequency that falls within the range of frequencies characterizing the structural system, the following procedure obtains $STF_i(w_j)$ from the time domain direct integration analysis with impulse function.

1. Perform a direct integration dynamic analysis with STARDYNE using the impulse function TH (Figure 3) to obtain response THs.⁷ The FT of the impulse function TH, denoted as $SF(w_j)$, shows a wide range of input frequencies of the structural system.
2. Using TRANFUN, the determined response TH due to impulse input TH is run through an FT procedure to obtain a function denoted as $SR_i(w_j)$, and the transfer function $STF_i(w_j)$ is then obtained as $STF_i(w_j) = SR_i(w_j) / SF(w_j)$.⁸

Mixed Domain Analysis to Obtain Response Function Using INVTRAN⁵

From the $STF_i(w_j)$, and the FT of any input forcing function TH, $f_i(t)$, the response function $PR_i(w_j)$, in terms of frequency parameter w_j , is obtained from:

$$PR_i(w_j) = STF_i(w_j) PF_i(w_j) \quad (11)$$

Where $PF_i(w_j)$ is the FT of the corresponding actual input forcing function TH, one $PR_i(w_j)$ is computed for all discrete values of w_j . The inverse FT provides the response TH, $\{x_i(t)\}$.

Numerical Example

Mathematical Model Description

The mathematical model (Figure 2) is a typical main steam piping layout of a power plant. The pipe is supported at various points along its route. To illustrate the proposed method, two sets of acceleration time histories acting in x_1 and x_2 directions will be input at Support Nodes 84, 87, 67, 56, and 57, (Group A nodes). Another two sets of acceleration time histories acting along x_1 and x_2 directions will be input at Support Nodes 50, 70, and 71 (Group B nodes). Thus, there are four distinct input time histories.

Adapted Model

There are two distinct time histories that will be applied at Group A nodes. Consequently, two springs with stiffness = K_{sp} will be added at each of these nodes. In the same manner, two springs will be introduced in each nodal support of Group B.

Input Time Histories

The input acceleration time histories are typical response time histories of SRV discharge loading of a BWR nuclear power plant reactor containment. The applied time histories (Figures 6a, 6b, 6c, and 6d) are 1.98 second duration, and for the dynamic analysis, an integration time step of 0.001 second will be used.

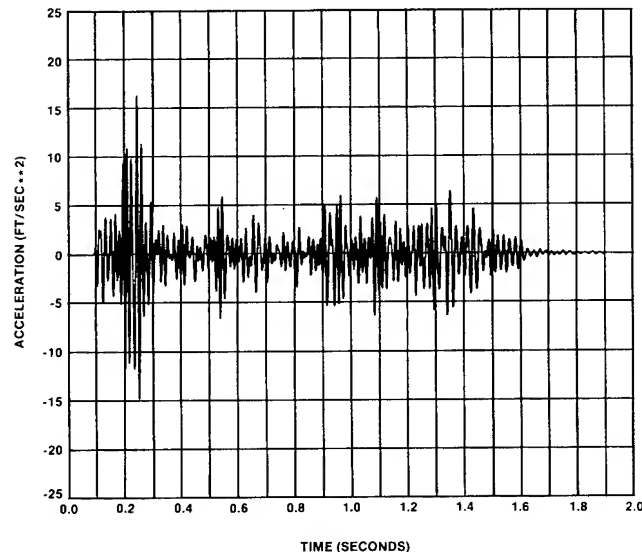


Fig. 6a Input Acceleration Time History:
Node Group A X1 Direction

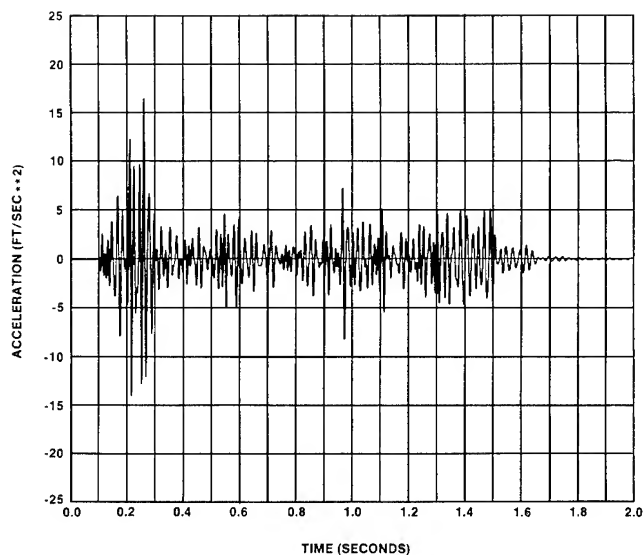


Fig. 6b Input Acceleration Time History:
Node Group A X2 Direction

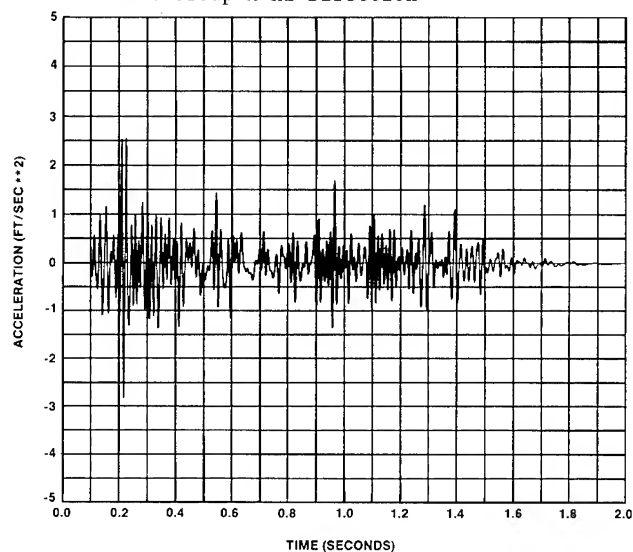


Fig. 6c Input Acceleration Time History:
Node Group B X1 Direction

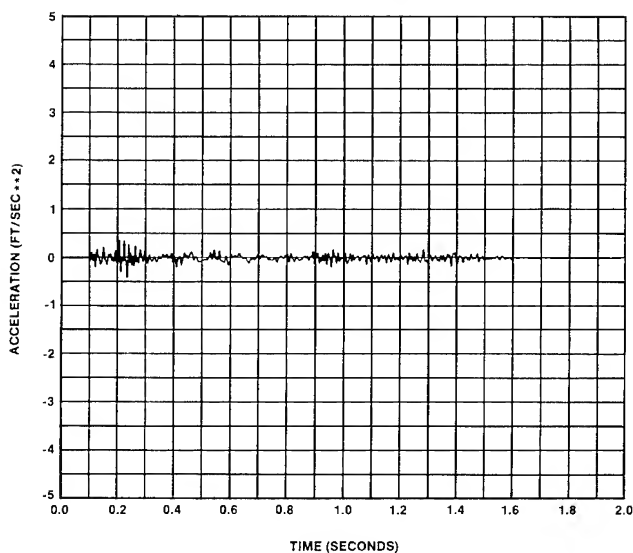


Fig. 6d Input Acceleration Time History:
Node Group B X2 Direction

Conventional Analysis

Using the input time histories (described previously) that are applied at Group A and Group B nodes of the adapted model, the conventional time history analysis was performed. A flow chart of this analysis is provided as Figure 7. From the response acceleration time history at Node 401 the amplified response spectra (ARS) were obtained.⁴ The ARS (Figure 8) were obtained for 2 percent oscillator damping.

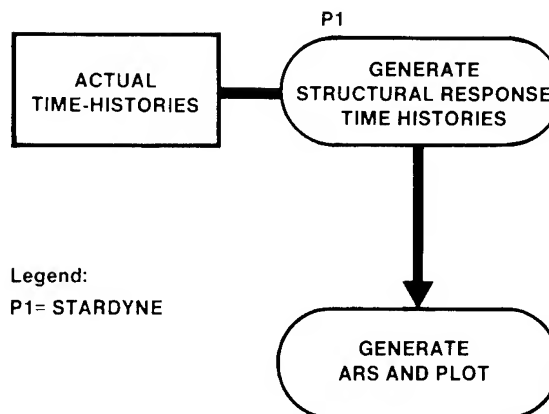


Fig. 7 Flow Chart for Conventional Analysis

Mixed Domain Analysis for Multiple Input Time History

Using the same adapted model the conventional time history analysis is performed four times with impulse TH as input (Figure 9). From these responses the transfer functions (TFs) for responses at selected locations can be obtained using TRANFUN. (This information can be used for any combination of input excitations that would result in significant savings in the subsequent analysis.)

With these TFs, the actual responses can be obtained using INVTRAN. After adding their responses, the ARS were obtained for 2 percent oscillator damping. The ARS results are presented in Figure 10.

Validation

Comparison of the two plots (Figures 8 and 10) shows that the results from these alternative approaches are indistinguishable.

Economy of Proposed Method

For a single load case, the computational effort required for both methods is comparable. For additional load cases, the incremental effort required to obtain individual responses using INVTRAN, which uses fast Fourier transform techniques, is far less than the total re-analysis.³ Further analysis for any additions or changes in support excitation will be more economical than the total re-analysis required by the conventional analysis.

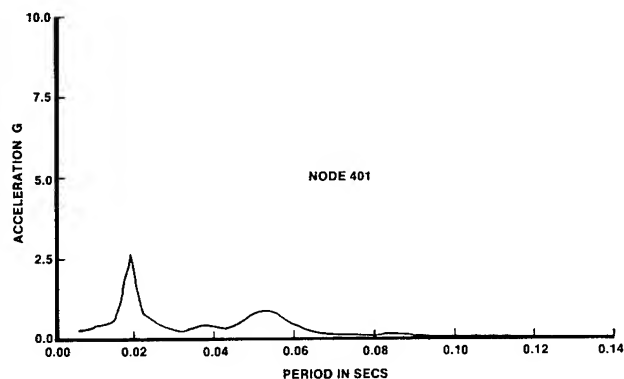


Fig. 8 X1 Direction ARS, Conventional Analysis

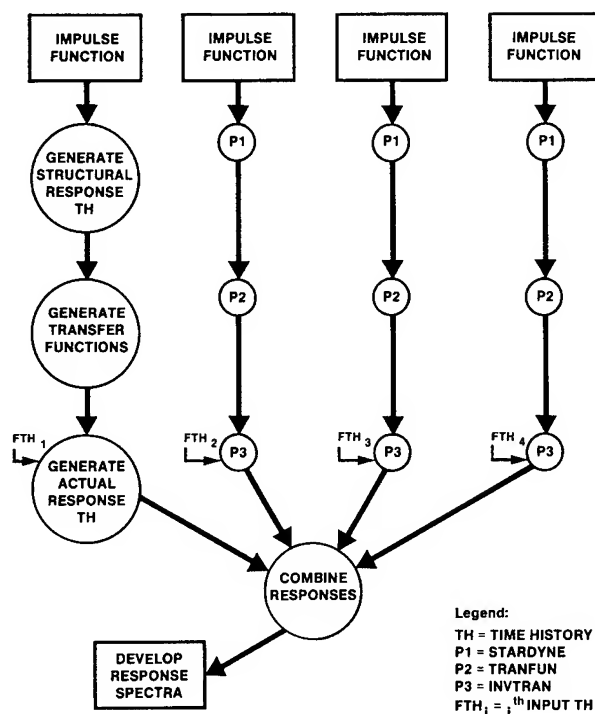


Fig. 9 Flow Chart for Mixed Domain Analysis

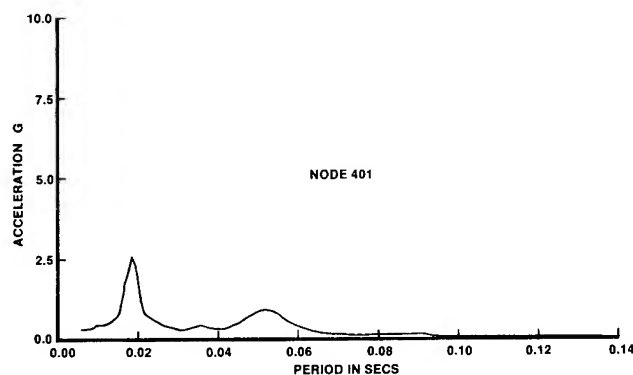


Fig. 10 X1 Direction ARS, Mixed Domain Analysis

Conclusion

The adapted model with acceleration forcing function as input is a viable approach to solving the multiple support excitation problem. The adapted model can be solved economically by mixed domain analysis with impulse function.

Future work will examine the reduction in computational effort with shorter duration impulse function dynamic analyses for longer duration input loads.⁶ The computational aspects on the addition of responses in the frequency domain before the inverse FT (Equation 9) stage also will be studied.

References

1. Chan, A.N., C.H. Chen, and B. J. Mitchell. Model Dynamic Analysis of Linear Elastic Systems with Specified Displacement Time Histories. Presented at Century 2 Pressure Vessel & Piping Conference, ASME, San Francisco, CA August 12 - 15, 1980. Reprint No. 80-C2/PVP-91.
2. Clough, R. W. and Penzien, J. Dynamics of Structures. McGraw-Hill, NY, 1975.
3. Cooley, J.W., Lewis, Peter A.W., and Welch, P.D. The Fast Fourier Transform and its Applications. IEEE Transaction on Education, Vol. 12, 1, P27-34, 1969.
4. GETARS - A Program to Compute Amplified Response Spectra, Program No. ST-339. Stone & Webster Engineering Corporation, Cherry Hill, NJ, 1978.
5. INVTRAN - A Program to Compute Response in Time Domain, Program No. ST-341. Stone & Webster Engineering Corporation, Cherry Hill, NJ, 1978.
6. Ramamurthy, S. and Shah, M. J. Mixed Domain Analysis of Nuclear Containment Structures Using Impulse Functions, Computers and Structures, No. 1-4, p. 573-579, 1983.
7. STARDYNE-3 User's Manual. Systems Development Corporation, 1977.
8. TRANFUN - A Program to Compute System Characteristic Function, Program No. ST-340. Stone & Webster Engineering Corporation, Cherry Hill, NJ 1978.

Terrence A. Weisshaar* and Rosemary J. Ryan**
 School of Aeronautics and Astronautics
 Purdue University
 West Lafayette, Indiana 47907

Abstract

This study examines the effects of directional stiffness upon the flutter and divergence behavior of swept and unswept wings. An idealized aeroelastic model is developed for this purpose. A stiffness cross-coupling parameter is defined and then used to develop guidelines for flutter and divergence enhancement. Results indicate that it may be possible to preclude flutter by a judicious choice of stiffness cross-coupling. It appears that this type of passive flutter prevention is more difficult when applied to swept back wings. However, it is shown that combinations of directional stiffness orientation and inertia balancing may lead to flutter and divergence free surfaces.

Introduction

The use of directional stiffness or "elastic" cross-coupling to favorably affect aircraft performance is commonly known as aeroelastic tailoring. A significant number of papers devoted to tailoring studies of a wide variety of aircraft configurations have appeared during the past decade. A review of the literature suggests that it may be possible to develop some general guidelines and conclusions related to the use of tailoring to improve flutter and divergence characteristics of lifting surfaces.

This paper will identify several features of structural tailoring for aeroelastic stability improvement. An analytical model that has many of the characteristics requisite for an aeroelastic stability study, with tailoring included, is described. With this model, the potential for design improvement, and more importantly, the limitations of structural tailoring for stability enhancement will be explored and discussed. In addition, the relationships that exist among non-dimensional system parameters that influence classical flutter and divergence will be identified and discussed. The end result will be a better understanding of the design option that aeroelastic tailoring represents.

Background

A laminated composite material can be designed or tailored to match design requirements. As a result there are an unlimited number of possible configurations that one may encounter. In the case of beam-like wings, several authors have suggested categorizing laminated wings through the use of characteristic parameters that

arise in the analysis of laminated wings [1, 2, 3]. Use of these parameters allows the study of aeroelastic characteristics of laminated wings independent of actual laminate geometry. For instance, if wing deformation is to be characterized as beam-like, the relationship between: bending curvature along a reference axis; nose-up twist about that same axis; and, the resultant cross-sectional bending and twisting moments, M and T respectively, can be written as:

$$\begin{bmatrix} EI & -K \\ -K & GJ \end{bmatrix} \begin{Bmatrix} h'' \\ \alpha' \end{Bmatrix} = \begin{Bmatrix} M \\ T \end{Bmatrix} \quad (1)$$

where h'' represents curvature while α' is twist rate. The parameter K may be positive or negative; it establishes the magnitude of bend/twist coupling [4]. Strain energy considerations require that the cross-sectional stiffness matrix in Eqn. 1 be positive definite. This establishes bounds on K .

$$K^2 < EI GJ \quad \left(\text{or } \frac{K^2}{EI GJ} < 1 \right) \quad (2)$$

Therefore, three variables can be used to characterize laminated beam stiffness; these are:

$$GJ \text{ (or } EI), R = GJ/EI, \psi = K/\sqrt{EI GJ} \quad (3)$$

where

$$-1 < \psi < 1 \quad (4)$$

The three variables in Eqn. 3 are functions of laminate geometry with respect to a spanwise reference axis. If a laminate is reoriented or otherwise changed, changes in all three parameters result. This makes it difficult to discern the relative importance of each parameter in the tailoring process if, for instance, a ply angle is chosen as a design variable.

Austin, et al. [3] also present a method of computing the coefficients necessary to define the cross-sectional stiffnesses in Eqn. 1. Reference 3 includes a study of wing flutter and divergence in which the stiffness ratio R is fixed, while a ratio equivalent to K/EI is varied. Their results indicate that high flutter speeds and low divergence speeds exist when K/EI is positive.

In Reference 5, Weisshaar and Foist examined the effects of ply orientation upon flutter and divergence of swept and unswept wings. Their results are based upon an *ad hoc* example. Since both R and ψ change as ply angle changes, one is unsure about which parameter is responsible for changes in flutter and divergence speeds. Because of this, an example, presented in Reference 6, was chosen to illustrate the effects of independent variations of R and ψ . This result is of sufficient interest to be reproduced in Figure 1 of this

* Professor, Member AIAA

** Graduate Research Assistant, presently with Rockwell International, North American Aircraft Division

study.

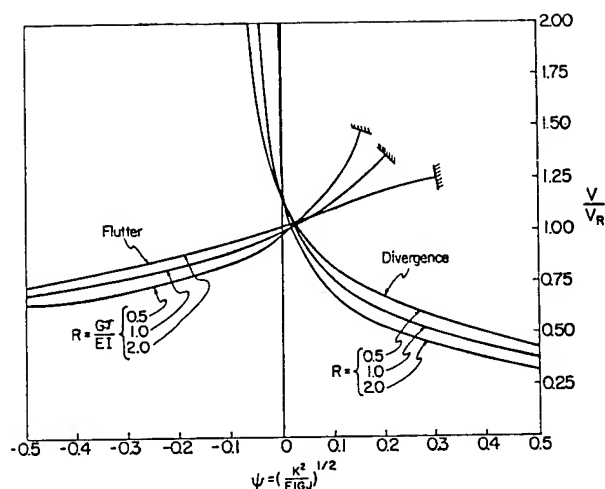


Fig. 1 - Flutter and divergence speeds, as a function of the nondimensional parameter ψ , for three values of $R = GJ/EI$.

Figure 1 shows the effects, on flutter and divergence, of changing the bend/twist cross-coupling parameter, ψ , while holding $R = GJ/EI$ fixed. For this example GJ is fixed while EI is allowed to assume three different values. The uniform planform wing is unswept and has an aspect ratio of 12.8. Both EI and GJ are constant along the span. Figure 1 shows that bend/twist cross-coupling affects flutter and divergence in an opposite manner. This figure also shows that, beyond certain values of ψ , flutter does not appear because of modal decoupling. These results were sufficiently interesting to warrant a closer look at the mechanism for modal decoupling and the potential for flutter elimination. To do so, a simple model was developed for the present study to investigate and to illustrate the effects of bend/twist coupling on divergence and flutter and to see if correlations between the results of the present study and previous archival studies could be found. It is to this model and to this investigation that attention now turns.

Aeroelastic Model Development

The most important feature of aeroelastic tailoring is the treatment of directional stiffness as an independent design variable to control aeroelastic behavior. There are a number of analytical models and procedures available to assist one in tailoring studies. These procedures range from highly sophisticated theoretical models suitable for detailed design evaluation to those with considerably less complexity. A sometimes delicate balance exists between the quantitative validity of the numbers one can generate and the qualitative understanding that comes from an examination of the results. It would be desirable to have a model possessing both accuracy and ease of interpretation. Such is not the case in

aeroelastic work. As a result, to understand the innermost workings of that portion of aeroelastic tailoring that relies upon directional stiffness, or stiffness cross-coupling, we will develop an analytical model in which parameter groupings clearly appear. This model will have the characteristic that numeric manipulation is simplistic and can be delayed until the last possible moment. As a result, some accuracy is sacrificed, but interpretive benefits are present and outweigh this cost.

When one reviews the history of aeroelastic studies, the progression in the sophistication of theoretical models is readily apparent. Also apparent is the reliance upon experience gained from simple models to explain and to understand, in a qualitative fashion, the results and trends present in wind tunnel tests and in sophisticated mathematical analysis. The workhorse of all simplistic math models is, of course, the 2-dimensional, "typical section" (see, for instance, Ref. 6). This model traces its origins to the 1930's; it is still used extensively, both in educational pursuits and in serious, sophisticated research efforts such as the study of transonic aeroelasticity. The advantages of such a model are twofold. Algebraic expressions for the equations of motion of such a system reveal a great deal about inertial and aerodynamic interaction. For certain assumptions or restrictions, closed-form solutions for flutter and divergence speeds may be found. Equally important is the extensive experience that enables one to tell when the 2-D results are likely to be valid and when they are not.

The present study seeks to examine the interaction among such variables as wing sweep, directional stiffness and inertia. Consider the idealized lifting surface shown in Figure 2. This surface is rigid and has its mass uniformly distributed along the span. The reference axis for determining the equations of motion is swept at an angle, Λ , to the free stream. The offset of the line of aerodynamic centers (located at the 1/4 chord) and the reference axis is denoted as e , while the offset of the line of centers of mass and the reference axis is denoted as x_α ; this latter coordinate is positive when the sectional centers of mass are located aft of the reference axis. The chordwise dimension c and spanwise dimension b determine the planform area $S = bc$ and the structural aspect ratio $b/c = \bar{A}R$.

To model the influence of aerodynamic forces upon the stability of this system, a simplified aerodynamic model was chosen. As a result, this model contains many of the parameters present in any study of inertial-structural-aerodynamic interactions. To formulate the aerodynamic model, loads on 2-D strips perpendicular to the y -axis in Figure 2 were used to compute moments about the x and y -axes at the pivot, in terms of θ and ϕ . The effects of the wake and damping were neglected in the development. Neglect of damping is not serious, provided that the mass ratio of the wing/fluid combination is large, implying that the fluid density is low in comparison to that of the wing. The neglect of the unsteady nature of the flow is potentially more serious. However, since the present study will focus on the ability of the directional stiffness to decouple motion, the results should still be valid in a qualitative sense.

$$\frac{K_{12}^2}{K_{11}K_{22}} < 1 \quad (8)$$

A nondimensional stiffness cross-coupling parameter is now defined as follows:

$$\psi = \frac{-K_{12}}{\sqrt{K_{11}K_{22}}} \quad (-1 < \psi < 1) \quad (9)$$

The minus sign is included in Eqn. 9 so that positive ψ values indicate that upward "bending" ($+\phi$) is accompanied by nose-up "twist" ($+\theta$). Thus, positive values of ψ will lead to a so-called "wash-in" wing (bend up/twist up) while negative values lead to a "wash-out" (bend up/twist down) wing.

In addition to the definition of ψ , an additional stiffness parameter is defined as:

$$R = \frac{K_{11}}{K_{22}} \quad (10)$$

This parameter is similar to the ratio of torsional stiffness to bending stiffness in an actual wing cross-section.

The three variables, K_{11} (which represents torsional stiffness), R and ψ now describe the stiffness characteristics of the model in the same manner as those for beam-like wings constructed of composite materials. While these latter parameters are controlled by ply orientation and laminate construction instead of structural sweep and springs, nevertheless, an obvious analogy exists between this model and an actual structure with tailoring present.

If the spring values K_T and K_B in Figure 2 are fixed while γ is changed, the values of K_{11} , K_{22} and K_{12} change simultaneously. However, what we wish to accomplish in the present study is to examine the effects of changes in R and ψ independently. Thus, both γ and the combination K_T and K_B are changed to preserve values of certain stiffness parameters. Thus, we will not be concerned as to the actual values of K_T , K_B and γ ; we merely point out that this configuration is possible and has a physical interpretation.

The inertia matrix, also presented in the Appendix, is coupled because of the use of a reference axis that does not coincide with the line of centers of mass. The matrix contains elements M_{ij} .

Despite efforts to keep the aeroelastic model simple, the resulting equations of motion are quite complicated. The dimensional equations of motion involve the inertia, structural stiffness and aerodynamic stiffness matrices discussed above. As a final step in equation development, these equations were nondimensionalized, with the result that a number of characteristic aeroelastic, inertial and structural parameters appear. Definitions of these terms appear in the Appendix. With motion assumed to be of the form:

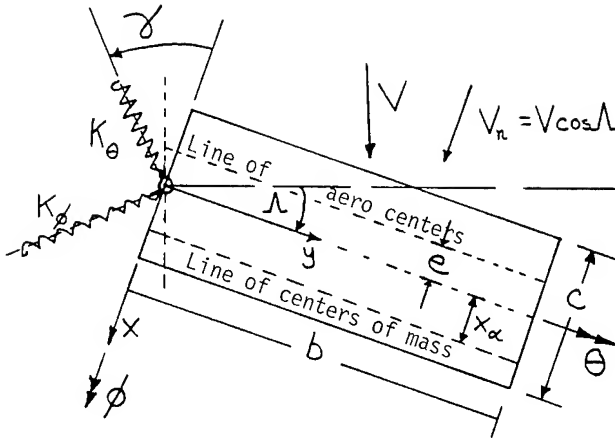


Fig. 2: Idealized semi-rigid swept wing.

This quasi-steady approximation provides loads (moments M_θ and M_ϕ) on the wing due to θ and ϕ motion as follows:

$$\begin{Bmatrix} M_\theta \\ M_\phi \end{Bmatrix} = qSC_L \cos^2 \Lambda \begin{bmatrix} e & -e \tan \Lambda \\ y_{cp} & -y_{cp} \tan \Lambda \end{bmatrix} \begin{Bmatrix} \theta \\ \phi \end{Bmatrix} \quad (5)$$

The co-ordinate y_{cp} locates the spanwise center of pressure.

Next, the equations of motion for free vibration of this semi-rigid swept wing were developed by deriving mass and stiffness matrices for the wing. In terms of θ and ϕ , the stiffness matrix is written as

$$[K] = \begin{bmatrix} K_{11} & K_{12} \\ K_{12} & K_{22} \end{bmatrix} \quad (6)$$

The expressions for the K_{ij} elements are given in the Appendix to this paper. The term K_{12} cannot exceed the geometric mean value of the primary stiffness terms K_{11} and K_{22} . This must be true if the stiffness matrix is to be positive definite.

The determinant of the stiffness matrix may be written as follows:

$$\Delta = K_{11}K_{22} \left[1 - \frac{K_{12}^2}{K_{11}K_{22}} \right] \quad (7)$$

The condition that this stiffness matrix be positive definite results in the following requirement:

$$\begin{Bmatrix} \bar{\theta} \\ \bar{\phi} \end{Bmatrix} = \begin{Bmatrix} \bar{\theta} \\ \bar{\phi} \end{Bmatrix} e^{st} \quad (11)$$

The equations of motion for vibration in the air-stream are:

$$\begin{bmatrix} (\bar{s}^2 + 1) & (\bar{s}^2 \left[\frac{-\bar{x}_\alpha \bar{A}R}{2\bar{r}_\alpha^2} \right] - \frac{\psi}{\sqrt{R}}) \\ (\bar{s}^2 \left[\frac{-\bar{x}_\alpha \bar{A}R}{2\bar{r}_\alpha^2} \right] - \frac{\psi}{\sqrt{R}}) & (\bar{s}^2 \frac{\bar{A}R^2}{3\bar{r}_\alpha^2} + \frac{1}{R}) \end{bmatrix} \begin{Bmatrix} \bar{\theta} \\ \bar{\phi} \end{Bmatrix} + \frac{1}{2} \frac{(\bar{V} \cos \Lambda)^2 C_{L\alpha}}{\pi \mu \bar{r}_\alpha^2} \begin{Bmatrix} \bar{\theta} \\ \bar{\phi} \end{Bmatrix} = \begin{Bmatrix} 0 \\ 0 \end{Bmatrix} \quad (12)$$

$$X \begin{bmatrix} -\bar{e} & \bar{e} \tan \\ -\bar{y} \bar{A} R & \bar{y} \bar{A} R \tan \end{bmatrix} \begin{Bmatrix} \bar{\theta} \\ \bar{\phi} \end{Bmatrix} = \begin{Bmatrix} 0 \\ 0 \end{Bmatrix}$$

In Eqn. 12,

$$\bar{s}^2 = s^2 / \omega_p^2 \quad (13)$$

where a reference frequency, ω_p is defined as:

$$\omega_p^2 = K_{11} / M_{11} \quad (14)$$

(see the Appendix for the definition of M_{11}).

The reduced velocity, \bar{V} , is defined as:

$$\bar{V} = \frac{V}{\omega_p (c/2)} \quad (15)$$

The frequency determinant of this system has the form

$$a\bar{s}^4 - b\bar{s}^2 - d\bar{V}_n^2 \bar{s}^2 + f + \bar{V}_n^2 g = 0 \quad (16)$$

where the normal component of velocity is

$$\bar{V}_n = \bar{V} \cos \Lambda \quad (17)$$

Equation 17 is quadratic in \bar{s}^2 . The lengthy expressions for the coefficients of this quadratic (a, b, d, f, g), are functions of the parameters that appear in Eqn. 12 and are given in the Appendix.

Equation 16 can be rearranged and written as follows:

$$-\frac{1}{\bar{V}_n^2} = \frac{d\bar{s}^2 - g}{a\bar{s}^4 - b\bar{s}^2 + f} \quad (18)$$

In this form, the aeroelastic system can be made to resemble a system with feedback control (see, for instance Refs. 7, 8). Expressed in the form shown in Eqn. 18, the square of reduced normal velocity, \bar{V}_n^2 , resembles a feedback gain whose value determines the values of \bar{s}^2 . Equations for feedback control parameters such as open loop poles and zeroes can be identified by inspection of Eqn. 18.

Although one need not resort to the complexities of control theory to solve this simple stability problem, nevertheless, some interesting

features of aeroelastic tailoring are discernable if one adopts this perspective. Two zeroes occur in Eqn. 18; these are found from the equation

$$\bar{s}^2 = g/d \quad (19)$$

As may be verified from the expressions in the Appendix, the coefficient g has a term that is proportional to ψ . The poles of this system are found by setting the denominator of Eqn. 18 equal to zero. The result is

$$\bar{s}^2 = \frac{b \pm \sqrt{b^2 - 4af}}{2a} \quad (20)$$

An examination of the coefficients a, b and f shows that they are independent of airspeed but depend upon ψ . In addition, \bar{s}^2 must be less than zero. These poles correspond to the system natural frequencies at zero airspeed.

One may therefore view the problem of aeroelastic tailoring as a passive feedback control problem. The structural parameter ψ may be used to modify both the location of poles and zeroes of the system. Thus, the stability of the wing may be controlled to some extent by ψ . In addition, there are similarities between the objectives of both active control, the "plant" is modified through the use of control laws, sensors, and already existing control surfaces. Aeroelastic tailoring, while passive in the sense that no internal energy source is used, also uses a form of control law to modify the behavior of the flexible system. It does so by using the flexible lifting surface as both sensor and actuator; the "control law" is embedded within the structure in the form of constitutive relations that govern the deformation of the surface under applied loads. In this case, ψ acts as a gain that may be set either by judicious design or by accident.

The simplicity of the present equations does not warrant the complexity of control theory to solve the dynamic stability problem. Instead, let us assume that motion is harmonic, so that

$$\bar{s} = i\Omega \quad (21)$$

In this case, the characteristic equation becomes

$$a\Omega^2 + (b + \bar{V}_n d)\Omega^2 + (f + \bar{V}_n^2 g) = 0 \quad (22)$$

Equation (22) provides a relationship between Ω^2 and \bar{V}_n^2 that may be used to plot \bar{V}_n^2 versus Ω^2 , and vice versa. The frequency ratio, Ω , is determined from the following relationship.

$$\Omega^2 = \frac{-(b + \bar{V}_n d) \pm \sqrt{(b + \bar{V}_n d)^2 - 4a(f + \bar{V}_n^2 g)}}{2a} \quad (23)$$

Thus, frequency is a function of airspeed. With damping excluded, stability is, at best, neutral. However, flutter occurs when the two natural frequencies of this system coalesce or merge [9]. This occurs if the term in the radical in Eqn. 23 equals zero. The condition for the onset of flutter thus becomes

$$(b + \bar{V}_n^2 d)^2 = 4a(f + \bar{V}_n^2 g) \quad (24)$$

$$\text{or } \bar{V}_F^2 = \frac{-(bd-2ag) \pm 2\sqrt{a(-bdg+ag^2+d^2f)}}{d^2(\cos^2\Lambda)} \quad (25)$$

Eqn. 25 expresses the relationship between the air speed at frequency coalescence and the aerodynamic, structural and inertial parameters of the system. Two speeds result from the computation suggested in Eqn. 25. Motion is unstable between these speeds. The lower speed is the flutter speed. The higher speed given in Eqn. 25 provides the speed at which the system regains stability; at this speed, the natural frequencies are again real. This upper speed seldom is a physical reality.

An interesting feature of Eqn. 25 is that the predicted flutter speed can become complex under two conditions. The first condition occurs if the radical becomes negative as previously discussed. The second condition occurs if the coefficient of \bar{V}_n^2 in the equation that results when Eqn. 24 is expanded is positive (see, for instance, Ref. 6, pp. 269-274). The onset of this event is when

$$db = 2ag \quad (26)$$

A complex value of \bar{V} implies that flutter is impossible. An examination of the terms contained within the radical shows that this term is a quadratic in the cross-coupling parameter, ψ . Thus, in theory, two values of ψ exist that lead to the merging of the upper and lower flutter boundaries.

Returning to Eqn. 22, we see that divergence will occur when

$$\bar{V}_n^2 = -f/g \quad (27)$$

since, at this velocity, a frequency becomes zero. At speeds in excess of $\bar{V}_n^2 = -f/g$, a root of Eqn. 22 is imaginary, implying that the system is exponentially divergent in time. Note that both f and g are functions of ψ .

The expressions that have been presented are still quite complicated. However, at this point, a model has been developed to allow the examination of the effects of stiffness cross-coupling upon dynamic and static instability of a swept wing aeroelastic model. At this point it would be wise to exercise the model via a set of parameter variations to demonstrate some important features of tailoring and then attempt to interpret results. We now turn our attention to a set of examples.

Applications

To provide further insight into the tailoring process, an example will be discussed. The parameters for this example are as follows:

$\bar{e} = 0.10$	$\bar{y} = 0.50$	$\bar{x}_\alpha = 0.10$
$r_\alpha^2 = 0.25$	$C_{L_\alpha} = 4.0/\text{radian}$	$\mu = 10.0$
$b/c = \bar{AR} = 4.0$		

Table 1 - Wing parameters

The sweep angle, Λ , the stiffness ratio, R , and the cross-coupling parameter, ψ , are independent variables for this illustration.

First, let us examine a case in which the wing is unswept. For this case, three values of R were chosen; then, values of ψ ranging from -1 to +1 were input into the equations for flutter and divergence. The results are shown in Figure 3. Dashed lines represent the locus of divergence speeds versus ψ . Note that these speeds, shown in nondimensional form in Figure 3, decline rapidly when ψ increases from zero. Furthermore, this decline is more pronounced when the stiffness ratio, R , is large.

Equation 27 provides the equation for divergence speed. It can be shown that this speed will become infinite when ψ is less than the value ψ_D , given by the equation:

$$\psi_D = \frac{\bar{e} - R\bar{y}\bar{AR}\tan\Lambda}{\sqrt{R}(\bar{e}\tan\Lambda - \bar{y}\bar{AR})} \quad (28)$$

Note the dependence of ψ_D on R and Λ .

In all cases shown in Figure 3, the flutter speed is relatively low when ψ is negative; there is a value of ψ , above which flutter does not occur. This unique value of cross-coupling is denoted as ψ_{CR} . Where flutter is concerned, a decrease in the stiffness ratio R results in lower flutter speeds if all other parameters remain fixed.

Sweeping the wing aft 15° causes somewhat different flutter and divergence behavior. As shown in Figure 4, aft sweep of the wing 15° causes a rightward shift of the divergence speeds as compared to those shown in Figure 3. In addition, Figure 4 indicates that a larger value of ψ_{CR} is necessary to eliminate flutter from this configuration. An additional feature of the flutter and divergence behavior, also present in Figure 3, but more visible in Figure 4, is the fact that the flutter speed curves and the divergence curves have a common point for each value of R . However, the curves of flutter speed and divergence speed do not cross.

Figure 5 shows flutter and divergence results for a wing sweepback angle of 30° . This figure is included to illustrate the fact that elastic cross-coupling may be unable to eliminate flutter if R is large and the wing is swept back. Even when R is small, large values of ψ are necessary to preclude flutter. In addition, a comparison of the divergence behavior versus ψ in Figures 3 and 5 shows that the relative positions of the dashed curves, as a function of R , has been reversed because of sweepback. With moderate sweepback, a low value of R is disadvantageous for divergence prevention.

Figures 6 and 7 illustrate the effects of forward sweep upon tailoring for stability enhancement. In Figure 6, it is seen that, unlike the unswept wing, relatively large negative values of ψ are necessary to preclude divergence of a forward swept wing. This is particularly so if R is large. This latter difficulty is indicative of the fact that tailoring relies upon bend/twist

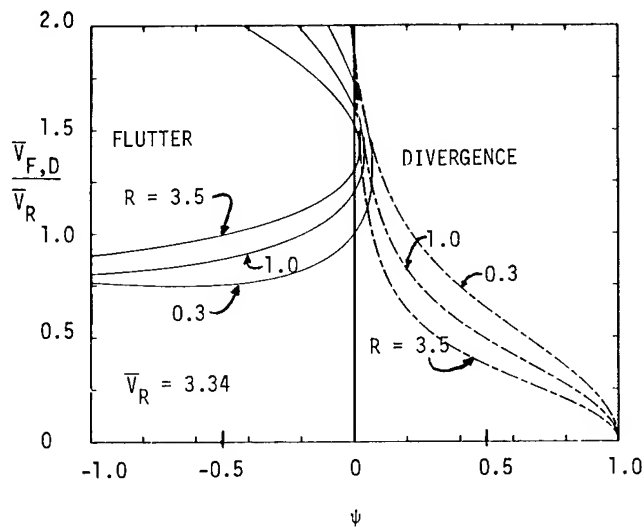


Figure 3 - Nondimensional flutter and divergence speeds for three values of $R = K_{11}/K_{22}$; unswept wing.

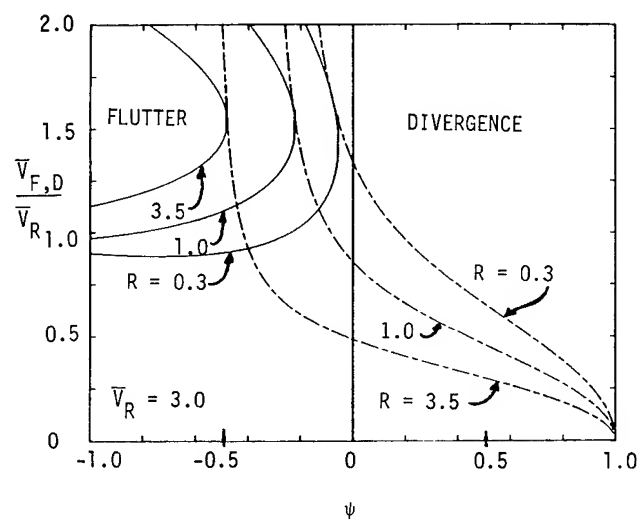


Figure 6 - Nondimensional flutter and divergence speeds for a 15° sweptforward wing.

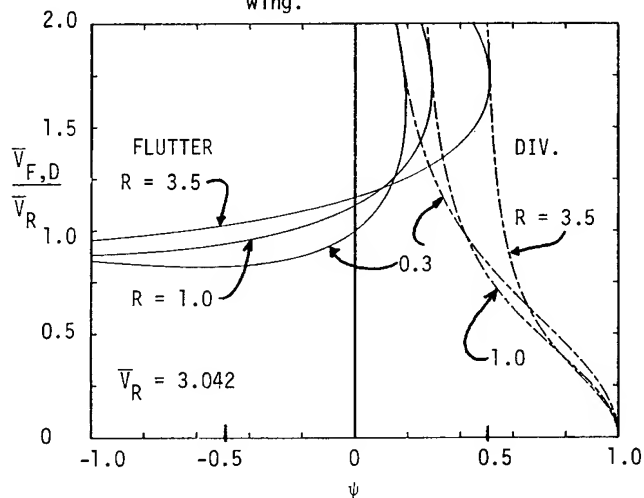


Figure 4 - Nondimensional flutter and divergence speeds for a 15° sweptback wing; three values of R .

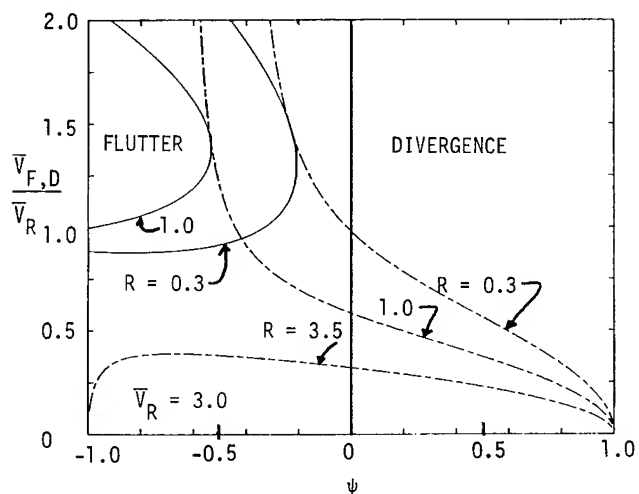


Figure 7 - Nondimensional flutter and divergence speeds for a 30° sweptforward wing.

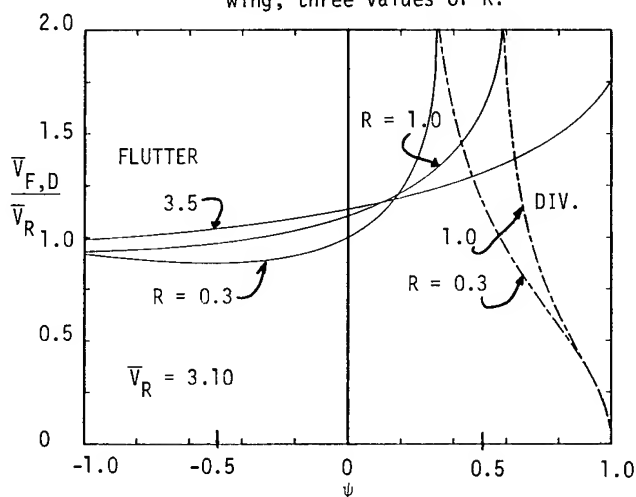


Figure 5 - Nondimensional flutter and divergence speeds for a 30° sweptback wing.

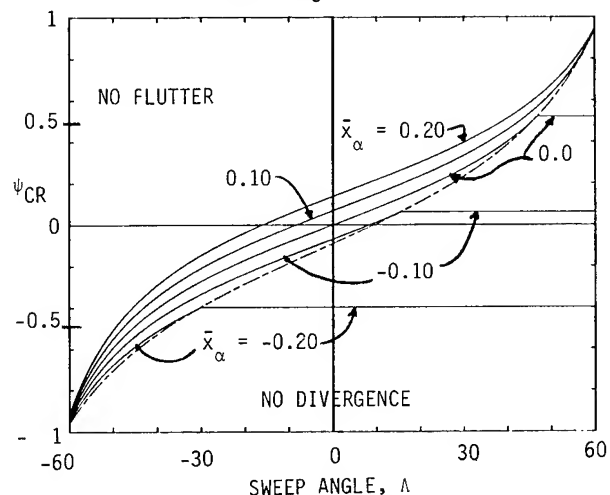


Figure 8 - Values of cross-coupling, ψ_{CR} , and sweep angle, Λ , necessary to prevent flutter (solid lines) or divergence (dashed line) for several values of static (inertia) unbalance, \bar{x}_α .

interaction. Bending deformation is responsible for the low divergence speeds of forward swept wings. These speeds can be raised if the wing can be tailored to twist down (and thus relieve the load) when the wing bends upward. This interaction will be increasingly difficult to achieve if the torsional stiffness becomes large in comparison to the bending stiffness. (R is large). A similar observation was made by Niblett [2] in RAE studies of forward swept wing flutter and divergence.

Figure 7 reinforces the conclusions about the potential difficulties involved in divergence enhancement. In this case, the sweep angle is $\Lambda = -30^\circ$; note that it is now impossible to eliminate divergence at any value of ψ when $R = 3.5$. On the other hand, flutter is nonexistent when $R = 3.5$.

Although the results presented are based upon an analytical model with rather extreme assumptions, one cannot help but notice qualitative agreement between previous, more sophisticated, studies and the present results. A comparison of Figures 1 and 3 shows that they are qualitatively similar. An important difference is that no upper bound on the flutter region is present in Figure 1; in addition, the flutter speed boundary penetrates the divergence boundary in Figure 1. A close inspection of the present equations will convince the reader (after an exhaustive algebraic exercise) that the flutter and divergence curves can never cross.

In addition, although the results in Figure 1 are based upon an analysis that retains the first nine normal modes in an unsteady aerodynamic model, nevertheless, the flutter event is decidedly a binary event. The present model is restricted to binary flutter. Flutter can (and does) appear through coupling between and among other modes in real-life situations. Nevertheless, the present model seems attractive and surprisingly demonstrative, all things considered.

The fact that our model predicts the possibility of both divergence and flutter elimination at certain values of ψ is of potential importance. A closed-form algebraic solution for the values of ψ necessary to merge the upper and lower flutter boundaries can be determined from Eqn. 25. These values of ψ are denoted as ψ_{CR} ; they are functions of wing sweep angle, Λ , static unbalance, \bar{x}_α , and other problem parameters.

The most interesting combination of parameters for tailoring is the group containing ψ , Λ and \bar{x}_α . As a result, a study was conducted with $R = 0.3$ and the parameters in Table 1 held fixed, with the exception of \bar{x}_α which was allowed to take on different values. With the values $\bar{x}_\alpha = -0.20, -0.10, 0.0, 0.10, 0.20$, combinations of ψ and Λ for which flutter vanishes were determined. In addition, combinations of ψ and Λ for which divergence vanishes were also determined. Note that divergence is not a function of \bar{x}_α . The results of this study are shown in Figure 8.

In Figure 8, the dashed line indicates the boundary between regions in which divergence is possible and impossible. Combinations of ψ and Λ lying below this line are those for which

divergence is impossible. Note the interesting tradeoff between wing sweep and structural cross-coupling, ψ . To eliminate divergence with ψ equal to zero, we must sweep the wing back 9.45° . If the wing is unswept, divergence can be eliminated if $\psi < -0.0913$. This illustrates, at least conceptually, the aeroelastic tradeoff between sweep and structural cross-coupling for stability enhancement.

For flutter, the situation is somewhat different. Combinations of ψ and Λ lying above the solid lines in Figure 8 represent those which provide a flutter free design. For instance, with $\bar{x}_\alpha = 0.20$ and $\psi = 0$, a forward sweep angle of 19.35° is necessary to eliminate flutter. If wing sweep is not permitted, then a value of ψ equal to 0.137 will accomplish the same purpose.

Since aft c.g. placement has an adverse effect on flutter, reducing the value of \bar{x}_α also leads to reduced requirements for structural cross-coupling, as indicated in Figure 8. Notice that, with $\bar{x}_\alpha = 0$, any amount of forward sweep eliminates flutter. This is due to the reasonably well-known, but often overlooked, fact that wing wash-out due to aft sweep causes a disadvantageous situation for flutter while the wash-in tendency of a forward swept wing causes a reverse effect. However, because of the change in the effective C_{L_α} due to sweep, these effects are moderated.

Negative mass offset results in unusual, yet interesting, behavior of the flutter boundary. If $\bar{x}_\alpha = -0.10$, then the locus of sectional centers of mass lies on the locus of aerodynamic centers (AC). It is well-known that a quasi-static analysis will predict an infinite flutter speed in such a case. This behavior is observed when one examines Figure 8 for $\psi = 0, \Lambda = 0$. However, if ψ is decreased, while Λ is fixed at zero, flutter will reappear. This once more confirms the observation that wash-out behavior, whatever its source, is disadvantageous for flutter.

The flutter boundaries for $\bar{x}_\alpha = 0, -0.10$ and -0.20 each consist of both a curved line and a straight line segment. The intersection point of these segments occurs at the divergence boundary; at this point both flutter and divergence are impossible for certain $\psi, \Lambda, \bar{x}_\alpha$ combinations. This point is given by the relationship

$$\tan \Lambda_{DF} = \left[\frac{\frac{2}{3} \bar{e} + \bar{y} \bar{x}_\alpha}{2 \bar{y} \bar{r}_\alpha^2 + \bar{x}_\alpha \bar{e}} \right] \bar{AR} \quad (29)$$

where Λ_{DF} is that value of Λ for which flutter and divergence disappear simultaneously. The value of ψ for this simultaneous disappearance is found by substituting Eqn. 29 into Eqn. 28. Note that Λ_{DF} is not a function of R .

For certain values of static unbalance, Figure 8 shows that there exists a region in which the wing can be tailored to be both divergence and flutter free beyond a certain sweep angle. Unless

the static unbalance is negative, this region is likely to only involve aft sweep.

Two solutions for ψ_{CR} exist. In all cases examined to date, the second value of ψ_{CR} has been found to occur at a value either outside the region $-1 \leq \psi \leq 1$ or else will occur when the coefficient of the \bar{V}_n^2 term is negative. Thus, no upper bound to the flutter free region was encountered. However, given the complexity of the equations, such cases cannot be ruled out entirely.

As a final example, consider the case for for which the parameters in Table 1 are fixed, but with $R = 0.1, 0.3, 1, 2, 3$. In this case, interest will be focused upon combinations of ψ and Λ necessary to preclude flutter or divergence.

Figure 9 shows the effects of R upon the value ψ_D , the value of cross-coupling below which divergence is not possible. Notice that, if R is small and $\psi = 0$, then rather large values of aft sweep are necessary to preclude divergence. If torsional stiffness K_{11} is fixed, then small R values occur when bending stiffness K_{22} is large. In such cases, the well-known load attenuating effect of swept wing bending will be minimal. On the other hand, without wing sweep, divergence can never be eliminated without some elastic coupling, no matter how large the ratio R becomes. To see this, notice that the curve for $R = 3$ lies close to, but not on, the origin of Figure 9. From Figure 9, it appears that divergence of forward swept wings may be difficult (or even impossible) to prevent if R is large. For aft swept wings, the reverse is true.

Figure 10 shows the effects of R upon ability to control flutter of swept wings through stiffness cross-coupling. These curves indicate that the flutter speed of a sweptforward wing is easily controlled by structural cross-coupling if ψ is allowed to be positive. In the sweptback region, large positive values of ψ are necessary to preclude flutter, especially when R is large.

The Mechanism For Aeroelastic Control

There are a number of approaches to explaining the results presented in this paper. The behavior of the two system natural frequencies as airspeed increases might be examined to attempt to show why frequency merging is precluded. Or, the interplay between inertial cross-coupling, as exemplified by \bar{x}_α , and elastic cross-coupling, in the form of ψ/\sqrt{R} might be scrutinized. In both cases, the emphasis would be upon "structural coupling" and its interaction with "inertial coupling." Such an approach is coordinate dependent. On the other hand, Crisp [10] presents the viewpoint that the prevention or elimination of flutter (divergence should be thought of as a special case) can be regarded as a problem in aerodynamic balancing rather than mass balancing or stiffness balancing. Whether this aerodynamic balancing is done by means of inertial or structural stiffness redistribution, the result is the same. With this approach, eigenfunctions (mode

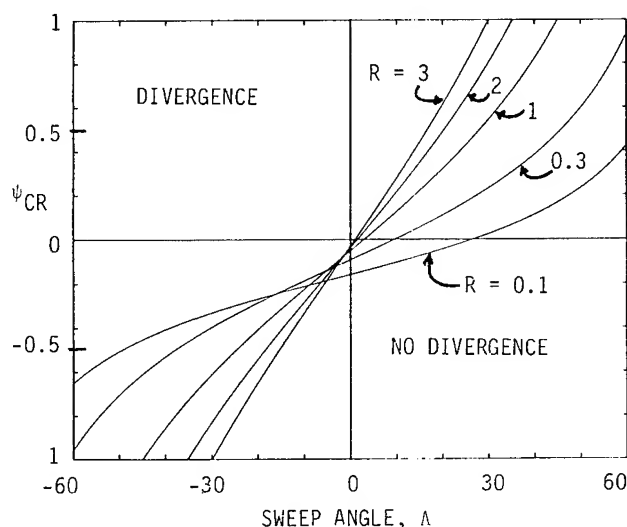


Figure 9 - Combinations of ψ and Λ for which divergence does not occur. Divergence cannot occur in the region below each curve.

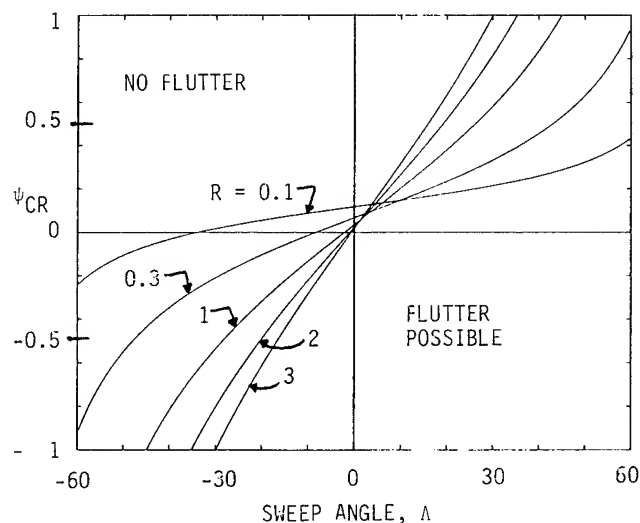


Figure 10 - Values of ψ and Λ for which flutter speed is precluded. Flutter will not occur in the region above each curve.

shapes) assume particular importance, since these mode shapes (together with reduced frequency) determine the motion dependent air forces that act upon the structure.

Biot and Arnold [11] present a similar viewpoint in a paper that pre-dates that of Crisp. Reference 11 points out the importance of the position of the node line of a normal mode (they discuss a two-degree-of-freedom, typical section) with respect to the 3/4 chord point on the cross-section. It is noted that the closer a node line position lies to the 3/4 chord point, the lower the flutter speed.

Reference 3 discusses that influence of laminate ply orientation upon node line position. In terms of the cross-coupling parameter, ψ , it is shown that such a parameter exerts substantial control over the position of node lines. For the present model, if ψ is positive, the node line for the first mode (usually a "bending" mode) originates at the x-y origin of Figure 2 and sweeps aft, nearly parallel to the root chord. On the other hand, a positive value of ψ will cause the node line associated with the "torsion" mode to sweep slightly forward (of the order of 2-4°) of the y-axis in Figure 2. This behavior is similar to that encountered when the sectional centers of gravity are placed forward of the reference axis. Therefore, if aft placement of the sectional c.g. leads to node lines that, in turn, lead to lower flutter speeds due to a node line shift aft of the reference axis, positive elastic cross-coupling can reposition the node line forward, away from the 3/4 chord line "danger zone." Thus, positive elastic cross-coupling (bend up/twist up) is equivalent to forward mass balancing as regards its effect on node line position and flutter speed. A forward rotation of the structural axis in Figure 2 leads to negative values of ψ . Such values have been shown to enhance divergence performance. Such rotations can place the principal stiffness direction ahead of the aerodynamic center. Thus, the offset between the line of aerodynamic centers and the structural axis is effectively decreased. Conversely, the distances between the sectional centers of mass and the stiffness axis is effectively increased by negative ψ , thus leading to lowered flutter speeds.

Conclusion

The reader is again reminded about the limitations imposed upon this study by the model restrictions and assumptions, as previously detailed. Despite these limitations, the authors have developed and illustrated the use of an aeroelastic tailoring model that contains mechanical features essential to the study and understanding of tailoring for stability enhancement. In doing so, a combination of features, previously observed in other more sophisticated studies, together with new results have been demonstrated with this idealization.

An interesting aspect of aeroelastic tailoring shown in these studies is the required trade-off, or compromise, between flutter speed and divergence speed. The objective of increased flutter speed leads to a wash-in (bend-up/twist-up) condition that is undesirable for divergence. Conversely, an increase in the diver-

gence speed due to a structural wash-out (bend-up/twist-down) condition are likely to lower the flutter speed. The inclusion of wing sweep and stiffness cross-coupling as design variables leads to further trade-offs between aerodynamic sweep and structural sweep. The present model indicates that forward sweep of the wing will raise the flutter speed and lower the divergence speed. The use of tailoring to increase the wing wash-out can achieve a harmonious balance between the flutter and divergence speeds. The same is true of the sweptback wing.

For aeroelastic stability purposes, stiffness cross-coupling, as given by ψ , has been shown to be aeroelastically analogous to fore or aft sweep, because of the similarities between the induced wash-in/wash-out behavior. In addition, because this effect depends upon the interaction between bending and torsional deformation, the ratio of torsional to bending stiffness is an important parameter in the analysis. From an aeroelastic optimization standpoint, one must be careful then that the objective of increasing the flutter speed does not decrease the fixed-root divergence speed to the extent that an attitude instability is triggered similar to that suffered by forward swept wings (see Ref. 5).

The most interesting feature of this study is the theoretical finding that both flutter and divergence can be precluded for certain circumstances. The ability of directional stiffness to modify the vibration characteristics to the extent that the system is uncoupled or "balanced" aerodynamically is a feature worthy of further attention by designers and researchers alike.

References

1. Austin, F., Hadcock, R., Hutchings, D., Sharp, D., Tang, S. and Waters, C., "Aeroelastic Tailoring of Advanced Composite Lifting Surfaces in Preliminary Design," Proceedings of the AIAA/ASME/SAE 17th Structures, Structural Dynamics and Materials Conference, King of Prussia, Penn., May 1976, pp. 69-79.
2. Niblett, L.L.T., "Divergence and Flutter of Swept-Forward Wings with Cross-Flexibilities," Royal Aircraft Establishment TR 80047, April 1980.
3. Weisshaar, T.A. and Foist, B.L., "Vibration and Flutter of Advanced Composite Lifting Surfaces," AIAA Paper No. CP-83-0961, Proceedings of the 24th Structures, Structural Dynamics and Materials Conference, Lake Tahoe, Nevada, May 1983, pp. 498-508.
4. Weisshaar, T.A., "Divergence of Forward Swept Composite Wings," Journal of Aircraft, Vol. 17, No. 6, June 1980, pp. 442-448.
5. Weisshaar, T.A. and Foist, B.L., "Aeroelastic Tailoring of Aircraft Subject to Body Freedom Flutter," AFWAL-TR-3123, Air Force Wright Aeronautical Laboratories, Wright-Patterson Air Force Base, Ohio, November 1983.
6. Bisplinghoff, R.L. and Ashley, H., Principles of Aeroelasticity, Dover Publications, 1975.
7. Reinfurth, M.H. and Swift, F.W., "A New Approach to the Explanation of the Flutter Mechanism," AIAA Symposium on Structural Dynamics

and Aeroelasticity, Boston, 1965, pp. 1-9.

8. Horikawa, H. and Dowell, E.H., "An Elementary Explanation of the Flutter Mechanism with Active Feedback Controls," Journal of Aircraft, April 1979, pp. 225-232.
9. Hermann, G., "Dynamics and Stability of Mechanical Systems with Follower Forces," NASA CR-1782, Nov. 1971.
10. Crisp, J.D.C., "The Equation of Energy Balance for Fluttering Systems with Some Applications in the Supersonic Regime," Journal of the Aerospace Sciences, November 1959, pp. 703-716, 738.
11. Biot, M.A. and Arnold, L., "Low-Speed Flutter and Its Physical Interpretation," Journal of the Aeronautical Sciences, April 1948, pp. 232-236.

Appendix

The equations of motion for free vibration of the semi-rigid swept wing model are written as:

$$[M_{ij}] \begin{Bmatrix} \ddot{\theta} \\ \ddot{\phi} \end{Bmatrix} + [K_{ij}] \begin{Bmatrix} \theta \\ \phi \end{Bmatrix} + [A_{ij}] \begin{Bmatrix} \theta \\ \phi \end{Bmatrix} = \begin{Bmatrix} 0 \\ 0 \end{Bmatrix} \quad (A-1)$$

(i, j = 1, 2)

In terms of the rotational spring constants K_θ and K_ϕ measured along the axes shown in Figure 2, the K_{ij} terms in Eqn. A-1 are

$$K_{11} = K_\theta \cos^2 \gamma + K_\phi \sin^2 \gamma \quad (A-2)$$

$$K_{12} = (K_\phi - K_\theta) \sin \gamma \cos \gamma \quad (A-3)$$

$$K_{22} = K_\theta \sin^2 \gamma + K_\phi \cos^2 \gamma \quad (A-4)$$

The inertia terms are:

$$M_{11} = m(r_0^2 + x_\alpha^2) = mr_\alpha^2 \quad (A-5)$$

$$M_{12} = -mx_\alpha b/2 \quad (A-6)$$

$$M_{22} = m b^2/3 \quad (A-7)$$

where m is the total mass of the wing and r_0 is the radius of gyration of the wing about the line of centers of mass of the wing. The factor of 3 in Eqn. A-7 reflects the fact that the mass distribution is uniform along the span. The terms in the matrix A_{ij} have been given in Eqn. 5. Note that the expression for moments in Eqn. 5 must be transferred to the left-hand side of Eqn. A-1 to obtain A_{ij} .

The nondimensionalization of Eqn. A-1 results in the definition of several nondimensional parameters, some of which have been defined previously. Parameters with a bar (—) indicate nondimensionalization with respect to either the chord dimension, c , or the span, b . These parameters are

$$\bar{x}_\alpha = x_\alpha / c \quad (A-8)$$

$$\bar{r}_\alpha = r_\alpha / c \quad (A-9)$$

$$\bar{AR} = b/c \quad (A-10)$$

$$\bar{y} = y_{cp}/b \quad (A-11)$$

$$\bar{e} = e/c \quad (A-12)$$

In addition, the mass ratio, μ , is

$$\mu = m/\pi \rho b (c/2)^2 \quad (A-13)$$

The frequency determinant that results from the equations of motion is expressed in Eqns. 16 and 22 in terms of constants a , b , d , f , g . Note that b in Eqn. 16 and the ensuing equations does not refer to the swept span dimension in Figure 2.

In terms of the nondimensional parameters in the problem, the expressions for a , b , d , f , g are:

$$a = \frac{R \bar{AR}^2}{12 \bar{r}_\alpha^2} \left[\frac{4 \bar{r}_\alpha^2 - 3 \bar{x}_\alpha^2}{\bar{r}_\alpha^2} \right] \quad (A-14)$$

$$b = - \left[1 + \frac{R \bar{AR}^2}{3 \bar{r}_\alpha^2} - \frac{\bar{x}_\alpha \bar{AR} \psi \sqrt{R}}{\bar{r}_\alpha^2} \right] \quad (A-15)$$

$$d = -R \bar{\xi} \bar{AR} [\bar{y} \tan \Lambda - \frac{\bar{AR} \bar{e}}{3 \bar{r}_\alpha^2} + \frac{\bar{x}_\alpha}{2 \bar{r}_\alpha^2} (\bar{e} \tan \Lambda - \bar{y} \bar{AR})] \quad (A-16)$$

where $\bar{\xi} = C_L / \pi^2 \mu \bar{r}_\alpha^2$

$$f = 1 - \psi^2$$

$$g = \bar{\xi} [-\bar{e} + R \bar{y} \bar{AR} \tan \Lambda + \psi \sqrt{R} (\bar{e} \tan \Lambda - \bar{y} \bar{AR})] \quad (A-17)$$

Note that "a" is always positive. The combination $f + g \bar{V}_n^{-2}$ is positive unless divergence has occurred. If $d + g$ is positive and divergence has not occurred, then flutter cannot occur.

Acknowledgement

The authors gratefully acknowledge financial support from the Naval Air Systems Command, without which this study could not have been completed.

EQUATIONS OF MOTION OF AN ELASTIC FLIGHT VEHICLE
UTILIZING STATIC AEROELASTIC CHARACTERISTICS
OF THE RESTRAINED VEHICLE

William P. Rodden* and J. Richard Love**
Northrop Corporation, Pico Rivera, Calif.

Abstract

Principal axes provide the usual reference in maneuvering and dynamic response analyses of flexible vehicles. Attached or structural axes have also been used because the flexibility characteristics of the structure are only determined for a restrained structure. If the structural axes are employed, a relationship is required for the orientations of the structural axes relative to the principal axes, since the equations of motion determine the orientations of the principal axes. If this relationship is not considered, as it has not been in a number of publications, the solution to the equations of motion of the structural axes is not invariant with the choice of support configuration used in the calculation of the structural flexibility influence coefficients, and is therefore incorrect. This relationship and the correct equations of motion for the structural axes are presented, and the correctness of the formulation is demonstrated numerically in studies of longitudinal maneuvering of an example forward-swept wing airplane at constant forward velocity. The basic derivations assume quasi-steady equilibrium of the structure during the motion, but this assumption is later relaxed by the addition of vibration modes and aerodynamic lag functions in an application of the mode acceleration method of dynamic response analysis. Although the paper assumes constant airspeed in the basic developments, it concludes with discussions of aeroelastic speed derivatives and aeroelastic effects on drag.

Nomenclature

A = deflection amplification factor
a = flexibility; a_f is free-body flexibility
 a_s = amplitude of motion of support reference point
 a_F = amplitude of vibration mode
 a_0 = airfoil two-dimensional lift curve slope
B = aerodynamic amplification factor
 B_g = equivalent viscous damping
b = reference span
 b_{ijk} = coefficient in exponential approximation to aerodynamic lag function
C = generalized aerodynamic force coefficient; C_F is static value for vibration modes; C_F is first order damping value

for vibration modes; C_i is inertial value; C_q is angular rate value; C_α is incidence and control surface value; $C_{\dot{\alpha}}$ is incidence rate value; C_0 is initial value
 C_e = experimental control point force coefficient
 C_h = aerodynamic influence coefficient for transient lift deficiency
 C_h = complex oscillatory aerodynamic influence coefficient
 C_{hDh} = aerodynamic damping influence coefficient
 C_{hD^2h} = aerodynamic inertial influence coefficient
 C_{hs} = static aerodynamic influence coefficient
 C_m = aerodynamic pitching moment coefficient
 C_z = aerodynamic normal force coefficient
 \bar{c} = mean aerodynamic chord
D = modal generalized aerodynamic force coefficient; D_F is static value for vibration modes; D_F is first order damping value for vibration modes; D_i is inertial value; D_q is angular rate value; D_α is incidence and control surface value; $D_{\dot{\alpha}}$ is incidence rate value; D_0 is initial value
 c_{λ_α} = local lift curve slope
 EI_x = bending stiffness
F = control point force; F_a is aerodynamic force; F_i is inertial force
GJ = torsional stiffness
g = acceleration of gravity; structural damping coefficient
H = generalized reference deflection; H_q includes steady angular rates; H_α includes changes in incidence and control surface rotations; $H_{\dot{\alpha}}$ includes incidence rates
h = control point deflection; h_F is modal deflection; h_f is flexible deformation; h_p is relative to the principal axis; h_r is due to rigid body modes; h_0 is initial value
I = unit matrix
 I_y = pitching moment of inertia about support reference point
 i_t = horizontal tail setting
K = structural stiffness
k = reduced frequency
M = mass matrix; Mach number
 \mathcal{M} = generalized rigid body mass

* Consultant. Fellow AIAA

** Senior Technical Specialist, Dynamics and Loads, Advanced Systems Division

n_z = normal load factor
 q = pitch rate
 \bar{q} = dynamic pressure
 R = inertial relief factor
 $R\&$ = real part of complex variable
 S = reference surface area
 S_y = static unbalance about support reference point
 t = time
 V = velocity
 v = perturbation velocity
 \bar{x} = distance from support origin to center of gravity
 z_s = deflection of origin of structural support
 α = incidence (angle of attack); α_p is incidence of principal axis, α_s is incidence of structural axis
 $\dot{\alpha}$ = incidence rate defined in Eq. (38)
 β = sideslip angle
 β_{ijk} = exponential coefficient in exponential approximation to aerodynamic lag function
 ΔC_α = supplementary incidence coefficient
 ΔC_q = supplementary rate coefficient
 Δh_f = dynamic structural deflection
 δ = control surface rotation
 θ = pitch angle of principal axis

Subscripts and Superscripts

α = $\partial/\partial\alpha$
 $\dot{\alpha}$ = $\partial/\partial(\dot{\alpha}\bar{c}/2V)$
 q = $\partial/\partial(\dot{\theta}\bar{c}/2V)$
 \ddot{z} = $\partial/\partial(\ddot{z}_s/g)$
 $\ddot{\theta}$ = $\partial/\partial(\ddot{\theta}\bar{c}/2g)$
 v = $\partial/\partial(v/V)$
 0 = intercept value at zero incidence
 $(\dot{})$ = $d()/dt$
 $(\ddot{})$ = $d^2()/dt^2$
 $()''$ = denotes FLEXSTAB value

Matrices

$[\]$ = square
 $[\]^T$ = transpose
 $[\]^{-1}$ = inverse
 $\{ \}$ = column

Introduction

The use of a principal axis system as a reference for the equations of motion has been a standard in vibration and flutter analysis of unrestrained vehicles for many years. In 1962 a comprehensive statement of the various structural dynamics problems of the unrestrained vehicle was given by Bisplinghoff and Ashley¹ using a centroidal principal axis system. The use of attached, mean, and principal axes was discussed by Milne in 1964² and the distinction between mean and principal axes was further clarified in 1968³. The mean and principal axes are the same

when transverse displacement is the primary degree of freedom, i.e., when rotatory inertia effects can be neglected (as we assume in the present development). The use of a principal axis system in flight mechanics was further refined in the FLEXSTAB computer program developed by Dusto and his associates at the Boeing Co. from 1968⁴ to 1974⁵. The conclusion from these investigations is that principal axes, rather than attached axes, must be used in the equations of motion.

In 1965 Wykes and Lawrence⁶ utilized both principal and attached axes in a study of aero-thermoelastic effects on the stability and control of a typical canard-delta configuration. Their "modal technique" used the principal axes and their "direct influence coefficient technique" used the attached axes. Wykes and Lawrence recognized both the need for the principal axes and the difficulties associated with the attached axes: "The main problem stems from the fact that it is very difficult to obtain readily a transformation relating the angle-of-attack reference used in the influence coefficient problem analyses to the angle-of-attack reference of the dynamic stability problem formulation. In the influence coefficient analyses, the angle-of-attack reference was a line tangent to the wing surface slope at the wing apex. This was a convenient choice, for it permitted the most expedient joining of vehicle component effects to form the whole. In the dynamic stability analyses, the reference line for angle of attack was a body axis related to mass characteristics and rigid vehicle main lifting surface orientation. This axes system was the one for which the equations of motion were written. It is pertinent also to emphasize that this axes system is the same one used for the modal analyses described earlier. For this reason, the difficulty being discussed is avoided in the modal technique and constitutes another advantage in its application in connection with most dynamic aerothermoelastic problems. Although one does know the orientation of the velocity vector (and, consequently, the angle of attack) with respect to the reference system attached at the wing apex, the relationship difficult to define is the angle between the flexible vehicle wing apex axes and the equations of motion axes."

In spite of all foregoing developments, two textbooks and one NASA report have appeared subsequently that prefer the convenience of the attached axes without regard to the requirements for the principal axes. In his two books on airplane flight dynamics, where Roskam^{7,8} addresses stability and control of the elastic airplane, he chooses the origin of the attached axis system at "a reference point in the jig shape" which "is also the material point that represents the center of gravity (c.g.) of the jig shape." The facts that there may be no structural connection to the c.g., and that the c.g. does not remain fixed during a mission, are not addressed. Then, Kemp⁹ chooses the origin of his attached axis system at 33% of the mean aerodynamic chord because the structural influence coefficients (SIC's) used in a Boeing study of a high-performance supersonic transport airplane configuration were fixed there. However, he notes that "when a complete and consistent set of

stability derivatives is used in the equations of motion derived from the conditions for dynamic equilibrium, the reactions at the fixity point vanish and the deformed shape at any instant is, in a coordinate-free sense, independent of fixity point location."

References 7-9 have one assumption in common: that the solution to the equations of motion will be invariant with the choice of support system used to determine the SIC's if this support system is unloaded in the unrestrained flight condition. This is a necessary and sufficient condition for a trimmed loads solution only, and the loads solution of Rowan and Burns¹⁰ is therefore correct. However, it is not sufficient for the maneuvering solution. The conditions for a correct maneuvering solution require not only an unloaded support system but also, and obviously, that the moments equal the rate of change of angular momenta. These conditions will be realized if the principal axis formulation of the equations of motion is employed. However, an alternate formulation that retains the convenience of an arbitrary attached axis system can still be used if the location of the principal axes is duly noted in the formulation. This alternate formulation is the subject of the present paper.

The attached axes will be called structural axes in this paper because they will be referred to the statically determinate support system for which the SIC's are determined and, in general, the assumption of constant forward velocity will be made here, although the problem of calculating speed derivatives by numerical differentiation of the present results will be discussed briefly.

Aeroelastic Characteristics of a Restrained Vehicle

For the analysis of the aeroelastic characteristics of a restrained vehicle, the vehicle flexibility can be represented by a matrix of SIC's which permit the calculation of the structural deflections relative to a statically determinate support system (the SIC constraint point(s)) located conveniently within the vehicle (e.g., near the intersection of primary wing and fuselage structural components). The aeroelastic analysis must consider not only the aerodynamic forces that arise from vehicle incidence and control surface rotations, but also the aerodynamic forces that arise from the deflections (considered as initial deflections such as camber and twist) caused by the inertial forces that would exist in free flight. This approach leads to a series of inertial aeroelastic coefficients corresponding to unit accelerations in addition to the more conventional aeroelastic coefficients. An example of this approach is given in Sect. 8-3 of Ref. 11, in which the effect of normal load factor on a wing is considered.

The net force distribution $\{F\}$ acting on a flexible lifting surface or body is the difference between the aerodynamic forces $\{F_a\}$ and the inertial forces $\{F_i\}$,

$$\{F\} = \{F_a\} - \{F_i\} \quad (1)$$

The aerodynamic forces are found from experimentally corrected* steady aerodynamic influence coefficients (AIC's) $[C_{hs}]$ defined in Ref. 12, and a set of experimentally determined control force coefficients $\{C_e\}$.

$$\{F_a\} = (\bar{q}S/\bar{c})[C_{hs}]\{h\} + \bar{q}S\{C_e\} \quad (2)$$

The use of the experimental force coefficients may be necessary to account for aerodynamic effects that are not predictable, such as some interference loads, or not accurately predictable, such as camber loads. The inertial forces are found from the mass matrix $[M]$ and the accelerations

$$\{F_i\} = [M]\{\ddot{h}\} \quad (3)$$

The accelerations are written in terms of the rigid body modal matrix $[h_R]$ of Ref. 14 and the accelerations of a reference point in the SIC support system, and by neglecting any dynamic structural response

$$\{\ddot{h}\} = [h_R]\{\ddot{a}_s\} \quad (4)$$

The accelerations $\{\ddot{a}_s\}$ are assumed to be known.

The deflections $\{h\}$ are given by the sum of the deflections of the rigid vehicle $\{h_r\}^{**}$ and the flexible deflections $\{h_f\}$ relative to the support system.

$$\{h\} = \{h_r\} + \{h_f\} \quad (5)$$

The last equation required for the aeroelastic analysis is the flexibility relationship. The flexible deflections are found from the SIC's $[a]$ and the net forces.

$$\{h_f\} = [a]\{F\} \quad (6)$$

Substituting Eqs. (1)-(5) into Eq. (6) permits solution for the flexible deflections

$$\{h_f\} = [A][a]\{F_r\} \quad (7)$$

where $\{F_r\}$ is the net force distribution on the rigid system

* A premultiplying correction matrix derived from experimental data on loads arising from vehicle rotations of incidence and control surfaces is discussed in Refs. 12 and 13; Ref. 13 also considers a postmultiplying correction matrix.

** These deflections may arise from a number of sources: built-in twist, camber, or thermal distortions; changes in angle of attack or control surface rotations; steady angular motions. A number of terms to account for these effects separately are introduced in Eq. (13).

$$\{F_r\} = (\bar{q}S/\bar{c})[C_{hs}]\{h_r\} + \bar{q}S\{C_e\} \quad (8)$$

$$- [M][h_R]\{\ddot{a}_s\}$$

and $[A]$ is the aeroelastic deflection amplification (or attenuation) matrix

$$[A] = ([I] - (\bar{q}S/\bar{c})[a][C_{hs}])^{-1} \quad (9)$$

The net force distribution on the flexible system is obtained by substituting Eqs. (2)-(8) into Eq. (1)

$$\{F\} = [B]\{F_r\} \quad (10)$$

where $[B]$ is the aeroelastic load amplification (or attenuation) matrix

$$[B] = [I] + (\bar{q}S/\bar{c})[C_{hs}][A][a] \quad (11a)$$

$$= ([I] - (\bar{q}S/\bar{c})[C_{hs}][a])^{-1} \quad (11b)$$

The alternate form for $[B]$ shown in Eq. (11b) would have been obtained if the order of solution for $\{h_f\}$ and $\{F\}$ above had been reversed. The use of Eq. (11a) is more computationally efficient since a second matrix inversion is not required. A singularity in $[A]$ (and $[B]$) occurs* at the eigenvalues of

$$(\bar{c}/S\bar{q})\{h_f\} = [a][C_{hs}]\{h_f\} \quad (12)$$

Aeroelastic divergence of the restrained system corresponds to positive values of $\bar{c}/S\bar{q}$.

The analysis of equilibrium and the determination of stability derivatives requires the generalization of the initial deflections $\{h_r\}$ introduced above. We write

$$\{h_r\} = \{h_0\} + [h/H_\alpha]\{H_\alpha\} + [h/H_q]\{H_q\} \quad (13)$$

The first term $\{h_0\}$ accounts for initial deflections such as camber and twist, and thermoelastic deflections which may be important in flight at high supersonic speeds at low altitudes. The second term accounts for changes in attitude and control surface deflections; if in the longitudinal case the elements of $\{H_\alpha\}$ are angle of attack and elevator rotation, then the elements of the first column of $[h/H_\alpha]$ are streamwise distances of the aerodynamic control points from the pitch axis and the second column consists of non-zero elements on the control surface equal to the streamwise distances from the hinge line. The third term in Eq. (13) accounts for steady angular velocities such as pitch rate or roll rate; if one element of $\{H_q\}$ is pitch rate the elements in the corresponding column of $[h/H_q]$ are proportional to the square of the streamwise

distances of the aerodynamic control points from the pitch axis¹⁵.

The rigid body modal matrix $[h_R]$ also provides the basis for the equilibrium condition, viz., that there are no net resultant forces in any direction or resultant moments about any axis, i.e.,

$$[h_R]^T\{F\} = 0 \quad (14)$$

Substituting Eqs. (8), (10), and (13) into Eq. (14) leads to the basic equilibrium equation which can be written

$$\begin{aligned} \bar{q}S\{C_0\} + [C_\alpha]\{H_\alpha\} + [C_q]\{H_q\} \\ + [C_i]\{\ddot{a}_s\} - [M]\{\ddot{a}_s\} = 0 \end{aligned} \quad (15)$$

where the initial coefficient matrix is

$$\{C_0\} = [h_R]^T[B]((1/\bar{c})[C_{hs}]\{h_0\} + \{C_e\}) \quad (16)$$

the incidence coefficient matrix is

$$[C_\alpha] = (1/\bar{c})[h_R]^T[B][C_{hs}][h/H_\alpha] + [\Delta C_\alpha] \quad (17)$$

and the rate coefficient matrix is

$$[C_q] = (1/\bar{c})[h_R]^T[B][C_{hs}][h/H_q] + [\Delta C_q] \quad (18)$$

We have introduced a supplementary incidence coefficient matrix $[\Delta C_\alpha]$ and a supplementary rate coefficient matrix $[\Delta C_q]$ above because there are certain theoretical difficulties in estimating lateral-directional stability derivatives from AIC's (e.g., the wing rotary cross-derivatives and the adverse yawing moment from ailerons); these correction matrices must be obtained from other considerations than those presented here. The aerodynamic loads induced by inertial forces have been separated from the rigid body inertial forces so the inertial coefficient matrix is given by

$$\bar{q}S[C_i] = [h_R]^T([I] - [B])[M][h_R] \quad (19a)$$

$$= -(\bar{q}S/\bar{c})[h_R]^T[C_{hs}][A][a][M][h_R] \quad (19b)$$

and the rigid body inertial matrix is

$$[M] = [h_R]^T[M][h_R] \quad (20)$$

Unsteady aerodynamic effects, contained in $\dot{\alpha}$ - and $\dot{\beta}$ -derivatives, have not yet been considered in the present development. They may be obtained by using complex AIC's $[C_h]$, defined in a similar manner to $[C_{hs}]$, and utilizing the method of Ref. 15. Accordingly, Eq. (15) will be extended to include these effects by adding the term $[C_\alpha]\{H_\alpha\}$. The method of Ref. 15 leads to the rigid $\dot{\alpha}$ - and $\dot{\beta}$ - loadings which, when introduced into the foregoing development, results in the expression

$$[C_\alpha] = -R\lambda(1/2k^2\bar{c})[h_R]^T[B][\bar{C}_h][h/H_\alpha] \quad (21)$$

* Note that Eqs. (9) and (11b) have identical singularities.

where k is the reduced frequency based on some characteristic frequency of the vehicle, e.g., the short period mode or Dutch roll mode, for which the oscillatory AIC's are obtained, and the columns of $[h/H_\alpha]$ are the displacements for unit plunging and sidesway. The extended form of Eq. (15) then appears as

$$\begin{aligned} \bar{q}S\{[C_0] + [C_\alpha]\{H_\alpha\} + [C_\alpha]\{H_\alpha\} \\ + [C_q]\{H_q\} + [C_i]\{\ddot{a}_s\}\} - [m]\{\ddot{a}_s\} = 0 \end{aligned} \quad (22)$$

The stability derivative data are all contained in the coefficient matrices in Eq. (22). Some of the terms in these coefficient matrices are dimensional and obtaining dimensionless aerodynamic coefficients from them depends on the rigid body motions considered. Different reference lengths are used to nondimensionalize the longitudinal coefficients from what are used for the lateral-directional coefficients, viz., the reference chord \bar{c} in the longitudinal case, and the reference span b in the lateral-directional case. In the longitudinal case, the trim parameters are angle of attack α_s and elevator deflection δ

$$\{H_\alpha\} = \{\alpha_s\} \quad (23)$$

and the rigid body degrees of freedom are plunge and pitch so that

$$[C_\alpha] = \begin{bmatrix} C_{z_\alpha} & C_{z_\delta} \\ C_{m_\alpha} \bar{c} & C_{m_\delta} \bar{c} \end{bmatrix} \quad (24)$$

Just as the attitude and control effectiveness derivatives are found from $[C_\alpha]$, in a similar manner the initial aerodynamic derivatives can be found from $[C_0]$ and the aerodynamic damping derivatives can be found from $[C_\alpha]$ and $[C_q]$. Finally, the aerodynamic inertial derivatives are found from $[C_i]$.

In the longitudinal case

$$\{\ddot{a}_s\} = \begin{Bmatrix} \ddot{z}_s \\ \ddot{\theta} \end{Bmatrix} \quad (25)$$

and if we define dimensionless inertial derivatives by

$$C_z = C_{z_z}(\ddot{z}_s/g) + C_{z_\theta}(\ddot{\theta}\bar{c}/2g) \quad (26)$$

and

$$C_m = C_{m_z}(\ddot{z}_s/g) + C_{m_\theta}(\ddot{\theta}\bar{c}/2g) \quad (27)$$

we find

$$[C_i] = \begin{bmatrix} C_{z_z} & C_{z_\theta} \bar{c} \\ C_{m_z} \bar{c} & C_{m_\theta} \bar{c}^2 \end{bmatrix} \quad (28)$$

The FLEXSTAB Formulation for an Unrestrained Vehicle

It can be inferred from the FLEXSTAB documents, Refs. 4 and 5, that the foregoing development for the restrained vehicle also applies to the unrestrained vehicle if the free-body flexibility matrix $[a_f]$ replaces the restrained SIC's $[a]$, where

$$[a_f] = [R][a][R]^T \quad (29)$$

and $[R]$ is the inertial relief matrix

$$[R] = [I] - [h_R][m]^{-1}[h_R]^T[M] \quad (30)$$

Substituting Eq. (29) into Eqs. (9), (11), and (16)-(18) leads to aerodynamic coefficients for the unrestrained vehicle; the inertial coefficients, Eq. (19), do not exist in the FLEXSTAB formulation because all inertial relief effects have been accounted for in the free-body SIC's. Equation (22) (with the term $[C_i]\{\ddot{a}_s\}$ deleted)

becomes the equation of motion and $\{\ddot{a}_s\}$ is the set of accelerations of a point on the principal axis at the longitudinal location of the origin of the support system, and it then appears as

$$\begin{aligned} \bar{q}S\{[C_0] + [C_\alpha]\{H_\alpha\} + [C_\alpha]\{H_\alpha\} \\ + [C_q]\{H_q\}\} - [m]\{\ddot{a}_s\} = 0 \end{aligned} \quad (31)$$

where the doubly primed coefficients are the FLEXSTAB values (see Ref. 16 for an alternate derivation of the FLEXSTAB coefficients beginning with the restrained values of the preceding section).

Maneuvering of an Unrestrained Vehicle

Equation (31) is the correct equation of motion for the quasi-steady maneuvering vehicle. However, Eq. (22) was implicitly assumed to be valid in Refs. 7-9, but, as noted in the Introduction, it contains no reference to the principal axis. The problem has been succinctly summarized by Letsinger 17: "If angular accelerations are not measured with respect to the mean plane,...equations 1 and 2 (Eq. (22) here) will not be valid. The motion of the axes system will not represent the motion of the airplane. Figure 2 (Fig. 1 here) illustrates the problem. Three possible clamp locations are shown. A 'clamped axis' is shown at each clamp point. If the load on the airplane is changing, the airplane shape is also changing. If the airplane shape is changing, the three clamped axes are rotating relative to each other. Therefore, no more than one of the axes shown can possibly have a pitch acceleration time history proportional to the pitching moment time history. Or, at any given instant, no more than one clamped axis can have a pitch rate proportional to the angular momentum of the system. In general, the clamped axes system does not relate to the equations of motion."

Accordingly, the accelerations $\{\ddot{a}_s\}$ in Eq. (22) are interpreted to be the accelerations of Eq. (31), i.e., of a point on the principal axis at the support station. Then, since the equations of motion now contain the angle of attack at the support and the rotation angle of the principal axis, a relationship is needed between the angles; this is the relationship that Wykes and Lawrence⁶ did not obtain (see Introduction). Figure 2 illustrates the geometry.

The deflections of the structure relative to the principal axes $\{h_p\}$ may be written

$$\{h_p\} = \{h_f\} + \{h_R\}\{a_s\} \quad (32)$$

in which $\{a_s\}$ now represents the set of displacements (translations and rotations) of the support point relative to the principal axes. The requirement for the principal axes is that deformation occurs about them such that the center of gravity does not move and the axes do not rotate^{2,3}. In terms of the rigid-body modal matrix and the mass matrix, this condition is expressed by

$$\{h_R\}^T [M] \{h_p\} = 0 \quad (33)$$

Equations (32) and (33) lead to

$$\{a_s\} = -[\mathbf{m}]^{-1} \{h_R\}^T [M] \{h_f\} \quad (34)$$

The rotations (pitch and yaw) of the longitudinal structural axis relative to the longitudinal principal axis are given by elements of $\{a_s\}$. If the deflections $\{h_f\}$ are calculated independently for each source of loading, viz., initial deflections, incidence and control surface deflections, angular rates, and accelerations of the support point, via Eq. (7) for the restrained system, then the negative values of the appropriate elements in $\{a_s\}$ can be used as coefficients in the following equation for the angles of attack (longitudinal and sideslip) of the principal axis.

$$\begin{aligned} \{\alpha_p\} = \{\alpha_{p_0}\} &+ \left[\frac{\partial \alpha_p}{\partial \alpha} \right] \{H_\alpha\} + \left[\frac{\partial \alpha_p}{\partial \dot{\alpha}} \right] \{\dot{H}_\alpha\} \\ &+ \left[\frac{\partial \alpha_p}{\partial \ddot{\alpha}} \right] \{\ddot{H}_\alpha\} + \left[\frac{\partial \alpha_p}{\partial \dot{q}} \right] \{\dot{H}_q\} + \left[\frac{\partial \alpha_p}{\partial \ddot{q}} \right] \{\ddot{H}_q\} \end{aligned} \quad (35)$$

It will be demonstrated by numerical calculations that Eq. (22) coupled with Eq. (35) is equivalent to Eq. (31). An example airplane in a typical pitch maneuver will be investigated using three significantly different support configurations, and the solutions will be compared to the FLEXSTAB solution.

The Quasi-Steady Longitudinal Equations of Motion

We now rewrite Eqs. (22) and (35) for the specific case of longitudinal motion so that specific details in their solution will become apparent. Equation (22) is expanded to read

$$\begin{aligned} \bar{q} S \left(\begin{Bmatrix} \bar{C}_{z_0} \\ \bar{C}_{m_0} \bar{c} \end{Bmatrix} + \begin{bmatrix} \bar{C}_{z_\alpha} & \bar{C}_{z_\delta} \\ \bar{C}_{m_\alpha} \bar{c} & \bar{C}_{m_\delta} \bar{c} \end{bmatrix} \begin{Bmatrix} \alpha_s \\ \delta \end{Bmatrix} + \begin{bmatrix} \bar{C}_{z_{\dot{\alpha}}} & \bar{C}_{z_{\dot{q}}} \\ \bar{C}_{m_{\dot{\alpha}}} \bar{c} & \bar{C}_{m_{\dot{q}}} \bar{c} \end{bmatrix} \begin{Bmatrix} \frac{\dot{\alpha}_s \bar{c}}{2V} \\ \frac{\dot{\delta} \bar{c}}{2V} \end{Bmatrix} \right) \\ + \begin{bmatrix} \bar{C}_{z_{\ddot{z}}} & \bar{C}_{z_{\ddot{\theta}}} \\ \bar{C}_{m_{\ddot{z}}} \bar{c} & \bar{C}_{m_{\ddot{\theta}}} \bar{c} \end{bmatrix} \begin{Bmatrix} \ddot{z}_s/g \\ \ddot{\theta} \bar{c}/2g \end{Bmatrix} - \begin{bmatrix} M & S_y \\ S_y & I_y \end{bmatrix} \begin{Bmatrix} \ddot{z}_s \\ \ddot{\theta} \end{Bmatrix} = 0 \end{aligned} \quad (36)$$

Equation (35) becomes

$$\begin{aligned} \alpha_p = \alpha_{p_0} &+ \alpha_{p_\alpha} \alpha_s + \alpha_{p_\delta} \delta \\ &+ \alpha_{p_{\dot{\alpha}}} \frac{\dot{\alpha}_s \bar{c}}{2V} + \alpha_{p_{\dot{q}}} \frac{\dot{\delta} \bar{c}}{2V} \\ &+ \alpha_{p_{\ddot{z}}} \frac{\ddot{z}_s}{g} + \alpha_{p_{\ddot{\theta}}} \frac{\ddot{\theta} \bar{c}}{2V} \end{aligned} \quad (37)$$

The rate of change of angle of attack is proportional to the centripetal acceleration of the vehicle, and is given by

$$\dot{\alpha} = (\ddot{z}_s - \bar{x} \ddot{\theta} + V \dot{\theta} + g \cos \theta)/V \quad (38)$$

where \bar{x} is the distance from the origin of the support to the center of gravity.

The solution of Eqs. (36) and (37) requires their combination into a single matrix differential equation that results from the elimination of α_s . Substituting Eq. (38) into Eq. (37) and solving for α_s yields

$$\begin{aligned} \alpha_s = (1/\alpha_{p_\alpha}) [\alpha_p - \alpha_{p_0} - (\alpha_{p_{\dot{\alpha}}} + \alpha_{p_{\dot{q}}}) \frac{\dot{\alpha}_s \bar{c}}{2V} \\ - (2\alpha_{p_{\ddot{z}}} + \alpha_{p_{\ddot{\theta}}} \bar{c} g) \frac{\ddot{z}_s}{2gV^2} \\ - (\alpha_{p_{\ddot{\theta}}} V^2 - \alpha_{p_{\ddot{z}}} \bar{x} g) \frac{\ddot{\theta} \bar{c}}{2gV^2} - \alpha_{p_{\ddot{\theta}}} \bar{c} g \cos \theta / 2V^2] \end{aligned} \quad (39)$$

Substituting Eqs. (38) and (39) into Eq. (37) eliminates α_s and the equations of motion become

$$\begin{bmatrix} \bar{M} & \bar{S}_1 \\ \bar{S}_2 & \bar{I} \end{bmatrix} \begin{Bmatrix} \ddot{z}_s \\ \ddot{\theta} \end{Bmatrix} = \bar{q} S \left(\begin{Bmatrix} \bar{C}_{z_0} \\ \bar{C}_{m_0} \bar{c} \end{Bmatrix} + \begin{bmatrix} \bar{C}_{z_\alpha} & \bar{C}_{z_\delta} \\ \bar{C}_{m_\alpha} \bar{c} & \bar{C}_{m_\delta} \bar{c} \end{bmatrix} \begin{Bmatrix} \alpha_s \\ \delta \end{Bmatrix} + \begin{Bmatrix} \bar{C}_{z_{\dot{\alpha}}} \\ \bar{C}_{m_{\dot{\alpha}}} \bar{c} \end{Bmatrix} \frac{\dot{\alpha}_s \bar{c}}{2V} \right) \quad (40)$$

where

$$\begin{aligned} \bar{M} &= M - [C_{Z\ddot{z}}/g + C_{Z\ddot{\alpha}} \bar{c}/2V^2 \\ &- C_{Z\alpha} (2\alpha_{p\ddot{z}} V^2 + \alpha_{p\ddot{\alpha}} \bar{c}g)/2gV^2 \alpha_{p\alpha}] \bar{q} S \end{aligned} \quad (41)$$

$$\begin{aligned} \bar{S}_1 &= S_y - [C_{Z\ddot{\theta}} \bar{c}/2g - C_{Z\ddot{\alpha}} \bar{c} \bar{x}/2V^2 \\ &- C_{Z\alpha} (\alpha_{p\ddot{\theta}} V^2 - \alpha_{p\ddot{\alpha}} \bar{x}g)/2gV^2 \alpha_{p\alpha}] \bar{q} S \end{aligned} \quad (42)$$

$$\begin{aligned} \bar{S}_2 &= S_y - [C_{m\ddot{z}}/g + C_{m\ddot{\alpha}} \bar{c}/2V^2 \\ &- C_{m\alpha} (2\alpha_{p\ddot{z}} V^2 + \alpha_{p\ddot{\alpha}} \bar{c}g)/2gV^2 \alpha_{p\alpha}] \bar{q} S \end{aligned} \quad (43)$$

$$\begin{aligned} \bar{I} &= I_y - [C_{m\ddot{\theta}} \bar{c}/2g - C_{m\ddot{\alpha}} \bar{c} \bar{x}/2V^2 \\ &- C_{m\alpha} (\alpha_{p\ddot{\theta}} V^2 - \alpha_{p\ddot{\alpha}} \bar{x}g)/2gV^2 \alpha_{p\alpha}] \bar{q} S \end{aligned} \quad (44)$$

$$\begin{aligned} \bar{C}_{Z_0} &= C_{Z_0} - C_{Z\alpha} \alpha_{p_0} / \alpha_p \\ &+ (C_{Z\ddot{\alpha}} - C_{Z\alpha} \alpha_{p\ddot{\alpha}} / \alpha_{p\alpha}) \bar{c} g \cos \theta / 2V^2 \end{aligned} \quad (45)$$

$$\begin{aligned} \bar{C}_{m_0} &= C_{m_0} - C_{m\alpha} \alpha_{p_0} / \alpha_{p\alpha} \\ &+ (C_{m\ddot{\alpha}} - C_{m\alpha} \alpha_{p\ddot{\alpha}} / \alpha_{p\alpha}) \bar{c} g \cos \theta / 2V^2 \end{aligned} \quad (46)$$

$$\bar{C}_{Z_\alpha} = C_{Z_\alpha} / \alpha_{p\alpha} \quad (47)$$

$$\bar{C}_{m_\alpha} = C_{m_\alpha} / \alpha_{p\alpha} \quad (48)$$

$$\bar{C}_{Z_\delta} = C_{Z_\delta} - C_{Z\alpha} \alpha_{p_\delta} / \alpha_{p\alpha} \quad (49)$$

$$\bar{C}_{m_\delta} = C_{m_\delta} - C_{m\alpha} \alpha_{p_\delta} / \alpha_{p\alpha} \quad (50)$$

$$\bar{C}_{Z_q} = C_{Z_q} + C_{Z\ddot{\alpha}} - C_{Z\alpha} (\alpha_{p_q} + \alpha_{p\ddot{\alpha}}) / \alpha_{p\alpha} \quad (51)$$

$$\bar{C}_{m_q} = C_{m_q} + C_{m\ddot{\alpha}} - C_{m\alpha} (\alpha_{p_q} + \alpha_{p\ddot{\alpha}}) / \alpha_{p\alpha} \quad (52)$$

The solution of Eq. (40) is a routine problem in numerical integration. The Runge-Kutta method was used in the example problem after the equation was rewritten in state-variable form (the computer program utilized also has the capability of including autopilots). The initial conditions on α_p and δ are provided by the level flight trim solution, and the angle of attack is updated during the integration via

$$\alpha_p = (1/V) \int_0^t (\ddot{z}_s + V\dot{\theta} + g \cos \theta) d\tau \quad (53)$$

An Example of a Forward-Swept Wing Configuration

The example problem selected is a forward-swept wing (FSW) configuration with a gross weight of 16,000 lbs, because of its importance in the current literature on static aeroelasticity. An extremely idealized configuration is shown in Fig. 3. The wing has an aspect ratio of 4.0, no taper, no twist or camber, and a forward sweep angle of 30°; the canard has an aspect ratio of 1.0 and no taper, twist, camber, or sweep. The chords of the wing and canard are both 10.0 ft; the reference chord is chosen as $\bar{c} = 10.0$ ft and the reference area is $S = 400$ sq ft. The semi-span of the wing is divided into two equal width strips, as shown on the left wing in Fig. 3, for analysis by strip theory and the canard is analyzed as a single strip. Aerodynamic forces on the fuselage are neglected. In the subsonic strip theory for the wing and canard, a rigid chord is assumed* and the approximation for the strip lift curve slope $c_{L\alpha} = a_0 \cos \lambda$ is utilized

where a_0 is the airfoil lift curve slope and λ is the sweep angle; a_0 is taken as 5.0 per radian. The right wing in Fig. 3 shows the structural idealization. Four weights on each wing semispan are located along the centerlines of their respective strips and at the one-quarter and three-quarter chord locations, and are assumed to be connected to the 50% chord elastic axis by rigid streamwise bars; the weights are assumed to be 600 lbs forward and 400 lbs aft, giving a wing centroid at 45% of the wing chord. Each wing is assumed to be uniform with equal bending (EI_x) and torsion (GJ) stiffnesses of 25×10^7 lb-ft² and connected at its root to the fuselage. The fuselage is assumed to have the same bending stiffness as the wing and is shown with four equal and equidistant weights (1500 lbs each per side); the fuselage length is 30.0 ft. The total weight per side is 8000 lbs, the center of gravity is 12.82 ft forward of the intersection of the fuselage and wing elastic axis, and the centroidal moment of inertia in pitch per side is $I_y = 892,900$ lb-ft².

* The assumption of only two chordwise control points on the lifting strips precludes accurate evaluation of the q -derivatives since pitch rate is equivalent to a static parabolic camber deflection¹⁵.

Three structural support configurations are investigated to illustrate the magnitudes of variations in the stability derivatives and response characteristics: one is a clamp at the forward end of the fuselage, the second is a clamp at the center of gravity (in order to assess Roskam's recommendation), and the third is a clamp at the intersection of the wing elastic axis and the fuselage centerline.

Vibration and flutter analyses have been performed on the example airplane to determine a speed regime for the maneuvering study in which the airplane is stable. The first three unrestrained frequencies are 9.886, 18.40, and 43.22 Hz. The modes are highly coupled and not readily described, although the first two appear to be primarily first wing bending and first fuselage bending, respectively. The flutter analysis utilized the British flutter method in NASTRAN¹⁸, assumed strip theory aerodynamics with the W. P. Jones approximation to the Theodorsen function (in order to avoid the singular effects of the Theodorsen function at low reduced frequency), and structural damping coefficients of 0.02 in each mode. The flutter speed at sea level was found to be 1310 fps which corresponds to a dynamic pressure of $q = 2040$ psf. The flutter mode is a coupling between rigid body pitch and the first vibration mode; the flutter frequency is 4.48 Hz. This flutter mode is similar to that observed in the design studies of Miller, Wykes, and Brosnan¹⁹.

Space does not permit tabulating the basic matrices required to determine the equations of motion. However, all of the derivatives are summarized in Table 1, which presents the three sets of derivatives for the airplane restrained at the forward point, at the centroid, and at the aft point, and also the derivatives for the unrestrained airplane calculated by the FLEXSTAB method; the results are shown for the single value of dynamic pressure, $\bar{q} = 1200$ psf, which corresponds to $V = 1005$ fps and a Mach number of 0.90 at sea level (in addition to the rigid values ($\bar{q} = 0.0$) referred to the centroid and given in the second column).

The example control inputs are shown in Fig. 4. The airplane is in trimmed flight for 0.10 sec with an angle of attack $\alpha_p = 0.128^\circ$ and canard incidence $\delta = 0.611^\circ$. Then a pullup is initiated and the control input rotates the canard at 50 deg/sec to 3.611° at 0.16 sec. At 0.66 sec a pushover is begun and the canard incidence reaches -2.389° at 0.78 sec. At 1.28 sec the control is reversed and returns to the trim setting at 1.34 sec. The time histories of centroidal load factors and pitching accelerations using the four sets of stability stability derivatives and α_p -derivatives in Table 1 are found to be identical in five degree-of-freedom maneuvering analyses. The basic data were calculated with six significant figures and between five and six significant figures were found to agree among the four sets of response accelerations. The common results from the four separate calculations are tabulated in the first column of Table 2 and are also presented graphically in Fig. 4.

We may now evaluate the consequences of disregarding the requirements for the principal axes, i.e., if we assume that $\alpha_p = \alpha_s$, as is implied in Refs. 7-9, in Eq. (36). In this case,

all the α_p -derivatives vanish except for $\frac{\partial \alpha_p}{\partial \alpha} = 1.0$ in Eq. (37). The resulting incorrect solutions for the three different structural supports are compared numerically with the correct solution in the last three columns of Table 2. In this example, the differences are not dramatic, and the assumption that $\alpha_p = \alpha_s$ is not an unreasonable approximation. However, in general, the magnitudes of the differences would be expected to be configuration-dependent. The accuracy of the assumption $\alpha_p = \alpha_s$ could be a subject for further investigation on more practical configurations, but the present development should make the assumption no longer necessary.

Addition of Dynamic Structural Effects

Equation (22) is the equation of motion assuming the structure is in quasi-steady equilibrium with the transient loading. If the loads are applied abruptly, as in the example, or the flight velocity is close to the flutter speed, also as in the example, dynamic structural effects should be included. The addition of these to the present formulation constitutes an application of the mode acceleration method, discussed extensively in Ref. 11 (pp. 642-650) with regard to its rapid convergence characteristics.

We begin by adding the dynamic loads to the quasi-steady loads of Eq. (10).

$$\begin{aligned} \{F\} = & [B]\{F_r\} - [M]\{\Delta h_f\} - [B_g]\{\dot{\Delta h}_f\} \\ & - [K]\{\Delta h_f\} + (qS/\bar{c}) ([C_{hs}]\{\Delta h_f\} \\ & + [C_{hdh}]\{\Delta h_f \bar{c}/2V\}) \end{aligned} \quad (54)$$

in which $\{\Delta h_f\}$ is the dynamic structural deflections, $[K]$ is the unrestrained vehicle stiffness matrix, $[B_g]$ is the equivalent viscous structural damping matrix, (assumed to be such that its modal form is diagonal) and $[C_{hdh}]$ is the first order aerodynamic matrix of Ref. 12. We express the dynamic structural deflections as a series of free vehicle vibration modes $[h_F]$ with modal amplitudes $\{a_F\}$.

$$\{\Delta h_f\} = [h_F]\{a_F\} \quad (55)$$

$$\{\dot{\Delta h}_f\} = [h_F]\{\dot{a}_F\} \quad (55)$$

The rigid body modal equations of motion follow from the Galerkin method by premultiplying Eq. (40) by $[h_R]^T$ and we obtain

$$\begin{aligned} & \bar{q}S(\{C_0\} + [C_\alpha]\{H_\alpha\} + [C_{\dot{\alpha}}]\{\dot{H}_\alpha\} + [C_q]\{H_q\} \\ & + [C_i]\{\ddot{a}_s\}) - [\mathbf{m}]\{\ddot{a}_s\} \\ & + (\bar{q}S/\bar{c})([C_F]\{a_F\} + [C_{\dot{F}}]\{\dot{a}_F\bar{c}/2V\}) = 0 \end{aligned} \quad (56)$$

where

$$[C_F] = [h_R]^T [C_{hs}] [h_F] \quad (57)$$

and

$$[C_F^*] = [h_R]^T [C_{hdh}] [h_F] \quad (58)$$

The last two terms are the additions to Eq. (22). No new mechanical terms appear because of the orthogonality of the rigid body modes with the free vehicle vibration modes.

The vibration equations follow by premultiplying Eq. (40) by $[h_F]^T$ and we obtain

$$\begin{aligned} & \bar{q}S(\{D_0\} + [D_\alpha]\{H_\alpha\} + [D_{\dot{\alpha}}]\{\dot{H}_\alpha\} + [D_q]\{H_q\} \\ & - [D_i]\{\ddot{a}_s\}) - ([\mathbf{m}_F]\{\ddot{a}_F\} \\ & + [\mathbf{m}_F\omega g]\{\dot{a}_F\} + [\mathbf{m}_F\omega^2]\{a_F\} \\ & + (\bar{q}S/\bar{c})([D_F]\{a_F\} + [D_{\dot{F}}]\{\dot{a}_F\bar{c}/2V\}) = 0 \end{aligned} \quad (59)$$

where

$$[\mathbf{m}_F] = [h_F]^T [\mathbf{M}] [h_F] \quad (60)$$

$$[\mathbf{m}_F\omega g] = [h_F]^T [B_g] [h_F] \quad (61)$$

and

$$[\mathbf{m}_F\omega^2] = [h_F]^T [K] [h_F] \quad (62)$$

are diagonal matrices by virtue of the assumed orthogonality, and

$$\{D_0\} = [h_F]^T [B]((1/\bar{c})[C_{hs}]\{h_0\} + \{C_e\}) \quad (63)$$

$$[D_\alpha] = (1/\bar{c})[h_F]^T [B][C_{hs}][h/H_\alpha] \quad (64)$$

$$[D_{\dot{\alpha}}] = -R\lambda(1/2k^2\bar{c})[h_F]^T [B][\bar{C}_h][h/H_{\dot{\alpha}}] \quad (65)$$

$$[D_q] = (1/\bar{c})[h_F]^T [B][C_{hs}][h/H_q] \quad (66)$$

$$[D_i] = (1/\bar{c})[h_F]^T [C_{hs}][A][a][M][h_R] \quad (67)$$

$$[D_F] = [h_F]^T [C_{hs}][h_F] \quad (68)$$

$$[D_F^*] = [h_F]^T [C_{hdh}][h_F] \quad (69)$$

Equation (67) utilizes Eq. (11a) and the orthogonality condition between the flexible and rigid modes.

The inclusion of aerodynamic lags in the above formulation customarily begins by adding the inertial AIC's and the convolution integral of Ref. 12 to the force equation,

$$\begin{aligned} & (\bar{q}S/\bar{c})\left([C_{hd^2h}]\left\{\frac{\ddot{h}\bar{c}^2}{4V^2}\right\}\right. \\ & \left. + \int_0^t [C_h]\left(\frac{V(t-\tau)}{\bar{c}/2}\right)\left\{\frac{dh(\tau)}{d\tau}\right\}d\tau\right) \end{aligned} \quad (70)$$

where here the transient AIC's $[C_h(\frac{Vt}{\bar{c}/2})]$ must be regarded as accounting for the deficiency in the unsteady aerodynamic forces from the deficiencies already accounted for by the first order rate and inertial AIC's. The transient deficiency AIC's may be approximated by exponentials at subsonic speeds

$$C_h\left(\frac{Vt}{\bar{c}/2}\right)_{ij} = - \sum_k b_{ijk} \exp\left(-\frac{b_{ijk}Vt}{\bar{c}/2}\right) \quad (71)$$

With the exponential approximation, the convolution integral may be replaced by a summation of aerodynamic lag functions obtained from a series of first order differential equations, as in Ref. 20. Any further discussion of aerodynamic lags and the form they assume in the modal reduction is beyond the scope of the present paper.

The use of Padé approximants and other curve fitting techniques to determine the constants in the exponential approximations is discussed, e.g., in Refs. 21-25. Inclusion of the unsteady aerodynamic terms in the equations of motion is also discussed in the literature on design of control systems for ride comfort, load alleviation, and flutter suppression, e.g., Refs. 26-33.

The convergence characteristics of the vibration modes of the example airplane in the example maneuver are presently under investigation.

The Speed Derivatives

Although the assumption of constant forward velocity has been made throughout the preceding development, the speed derivatives for lift and moment are readily found from the foregoing. The lift and moment coefficients at trim are functions of the incidence variables, accelerations ($\ddot{z} = g \cos\theta$, $\ddot{\theta} = 0$). Mach number, and dynamic pressure. If the trim airspeed V is perturbed by an amount v , the speed derivative is defined by

$$C_v = \frac{\partial C(\alpha, \delta, \ddot{z}, M, \bar{q})}{\partial (v/V)} \bigg|_{v=0} \quad (72a)$$

$$= V \frac{\partial C}{\partial M} \frac{\partial M}{\partial v} + V \frac{\partial C}{\partial \bar{q}} \frac{\partial \bar{q}}{\partial v} \quad (72b)$$

which becomes simply

$$C_V = M \frac{\partial C}{\partial M} + 2\bar{q} \frac{\partial C}{\partial \bar{q}} \quad (73)$$

At trim, the lift coefficient is

$$C_Z = C_{Z_0} + C_{Z_\alpha} \alpha + C_{Z_\delta} \delta + C_{Z_{\ddot{z}}} \cos \theta \quad (74)$$

so the speed derivative for lift is

$$\begin{aligned} C_{Z_V} = M \frac{\partial C_{Z_0}}{\partial M} + 2\bar{q} \frac{\partial C_{Z_0}}{\partial \bar{q}} \\ + \alpha_S \left(M \frac{\partial C_{Z_\alpha}}{\partial M} + 2\bar{q} \frac{\partial C_{Z_\alpha}}{\partial \bar{q}} \right) \\ + \delta \left(M \frac{\partial C_{Z_\delta}}{\partial M} + 2\bar{q} \frac{\partial C_{Z_\delta}}{\partial \bar{q}} \right) \\ + \cos \theta \left(M \frac{\partial C_{Z_{\ddot{z}}}}{\partial M} + 2\bar{q} \frac{\partial C_{Z_{\ddot{z}}}}{\partial \bar{q}} \right) \end{aligned} \quad (75)$$

The speed derivative for moment is given by a similar expression.

The derivatives with respect to M and \bar{q} may be obtained numerically, as suggested by Kemp⁹ by using the central difference formulae

$$\frac{\partial C}{\partial M} = \frac{C(M+\Delta M, \bar{q}) - C(M-\Delta M, \bar{q})}{2\Delta M} \quad (76)$$

$$\frac{\partial C}{\partial \bar{q}} = \frac{C(M, \bar{q}+\Delta \bar{q}) - C(M, \bar{q}-\Delta \bar{q})}{2\Delta \bar{q}} \quad (77)$$

The small perturbations ΔM and $\Delta \bar{q}$ must be large enough that the close differences do not lose significance.

Concluding Remarks

The correct formulation of the equations of motion of an elastic flight vehicle has been presented for the case in which the structural flexibility is given in terms of the flexibility matrix of the vehicle restrained in a statically determinate manner. The relationship that has been missing in previous analyses of the problem has been established in the rotations of the principal axes relative to the structural axes as caused by each aerodynamic and inertial loading. The modified form of the equations of motion that results from inclusion of the principal axis rotations has been presented and the correctness of the formulation has been demonstrated by identical numerical results from four case studies of longitudinal maneuvering of an example forward-swept airplane using the principal axis formulation (FLEXSTAB) and three significantly different structural axis formulations. The errors consequent to disregarding the require-

ments for the principal axes have been evaluated on the example airplane for the three different structural axes, but it is noted that the errors would be configuration-dependent.

The primary analysis has assumed quasi-steady structural equilibrium during maneuvering, considered unsteady aerodynamic effects only to the extent of $\dot{\alpha}$ - and $\dot{\beta}$ -terms, and assumed constant airspeed. However, brief discussions have also been given of the addition of dynamic structural effects, unsteady aerodynamic lag effects, and aeroelastic speed derivatives for inclusion in a longitudinal equation of motion.

The longitudinal equation of motion has not been discussed since it was secondary to our basic concerns, although aeroelastic speed derivatives have been discussed briefly. Aeroelastic effects on drag are another matter. It is commonly assumed^{7,8,34,35} that these are negligible. This is not entirely the case. Aeroelastic effects have a negligible effect only on the drag polar of the individual components of an airplane but not for the entire vehicle trimmed drag polar, as has been shown by an elementary analysis in Ref. 36. A drag polar measured³⁷ on a low-speed aeroelastic (flutter) model of the Douglas XA3D-1 airplane is presented in Fig. 5 for an intermediate horizontal tail incidence ($i_t = 1^\circ$; settings of $i_t = -2^\circ, +4^\circ$ and tail-off were also measured). Since only the wing was flexible on the model, the data of Fig. 5 verify the conclusion of Ref. 36 that the component drag polar is not affected by flexibility. However, the trim drag requires further investigation. A theoretical investigation would require an accurate aerodynamic method for estimating induced drag on flexible surfaces, such as the subsonic quasi-vortex lattice method of Lan³⁸. The inclusion of dynamic structural effects in the longitudinal equation of motion would also result in small aerodynamic propulsion terms that could be obtained, e.g., from the unsteady version of Lan's method³⁹.

Acknowledgements

The authors wish to thank Dr. Malcolm J. Abzug of ACA, Inc., for stimulating discussions and helpful suggestions during the preparation of this paper. They would also like to express their appreciation to him for his computation of the time histories presented using his FLY4 six degree-of-freedom maneuvering analysis, modified to account for the principal axis rotations of the flexible vehicle.

The authors also wish to thank E. Dean Bellingier of The MacNeal-Schwendler Corp., for obtaining the flexibility matrices for the three support conditions and performing the flutter analysis of the example configuration using MSC/NASTRAN.

References

- 1 Bisplinghoff, R.L. and Ashley, H., Principles of Aeroelasticity, John Wiley and Sons, New York, 1962; reprinted by Dover Publications, New York, 1975.

2 Milne, R.D., "Dynamics of the Deformable Aeroplane," British A.R.C. R&M 3345, 1964.

3 Milne, R.D., "Some Remarks on the Dynamics of Deformable Bodies," AIAA Journal, Vol. 6, March 1968, pp. 556-558.

4 Anon., "An Analysis of Methods for Predicting the Stability Characteristics of an Elastic Airplane - Summary Report", NASA CR-73277, Nov. 1968.

5 Dusto, A.R., Brune, G.W., Dornfeld, G.M., Mercer, J.E., Pilet, S.C., Rubbert, P.E., Schwanz, R.C., Smutny, P., Tinoco, E.N., and Weber, J.A., "A Method for Predicting the Stability Derivatives of an Elastic Airplane; Vol. I - FLEXSTAB Theoretical Description, NASA CR-114712, Oct. 1974; or AFFDL TR-74-91, Vol. 1, Nov. 1974, pp. 4-4 to 4-26, 5-11 to 5-14.

6 Wykes, J.H., and Lawrence, R.E., "Aerothermoelasticity: Its Impact on Stability and Control of Winged Aerospace Vehicles", Journal of Aircraft, Vol. 2, Nov.-Dec. 1965, pp. 517-526.

7 Roskam, J., Flight Dynamics of Rigid and Elastic Airplanes, Roskam Aviation and Engineering Corp., Lawrence, Kansas, 1972.

8 Roskam, J., Airplane Flight Dynamics and Automatic Flight Controls, Roskam Aviation and Engineering Corp., Lawrence, Kansas, 1979.

9 Kemp, W.B., Jr., "Definition and Application of Longitudinal Stability Derivatives for Elastic Airplanes," NASA TN D-6629, 1972.

10 Rowan, J.C., and Burns, T.A., "Aeroelastic Loads Predictions Using Finite Element Aerodynamics", Journal of Aircraft, Vol. 12, Nov. 1975, pp. 890-898.

11 Bisplinghoff, R.L., Ashley, H., and Halfman, R.L., Aeroelasticity, Addison-Wesley Publishing Co., Reading, Mass., 1955, p. 449.

12 Rodden, W.P. and Revell, J.D., "The Status of Unsteady Aerodynamic Influence Coefficients," Institute of the Aeronautical Sciences, Fairchild Publication Fund Paper No. FF-33, Jan. 23, 1962.

13 Giesing, J.P., Kalman, T.P., and Rodden, W.P., "Correction Factor Techniques for Improving Aerodynamic Prediction Methods," NASA CR-144967, May 1976.

14 Rodden, W.P., "On Vibration and Flutter Analysis with Free-Free Boundary Conditions," Journal of the Aeronautical Sciences, Vol. 28, Jan. 1961, pp. 65-66.

15 Rodden, W.P., and Giesing, J.P., "Application of Oscillatory Aerodynamic Theory to Estimation of Dynamic Stability Derivatives," Journal of Aircraft, Vol. 7, May-June 1970, pp. 272-275; also Errata and Addenda, Journal of Aircraft, Vol. 21, Jan. 1984, pp. 92-94.

16 Rodden, W.P., "Errata, 'Aeroelastic Divergence of Unrestrained Vehicles'," Journal of Aircraft, Vol. 21, Jan. 1984, pp. 94-96.

17 Letsinger, G.R., "Effect of Aeroelasticity on Airplane Stability and Control with Special Reference to an Application of FLEXSTAB to the F-111 TACT I Airplane," Symposium on Transonic Aircraft Technology, Technical Report AFFDL-TR-78-100, Aug. 1978.

18 Rodden, W.P., Harder, R.L., and Bellinger, E.D., "Aeroelastic Addition to NASTRAN," NASA CR 3074, March 1979.

19 Miller, G.D., Wykes, J.H., and Brosnan, M.J., "Rigid-Body Structural Mode Coupling on a Forward Swept Wing Aircraft," Journal of Aircraft, Vol. 20, Aug. 1983, pp. 696-702.

20 Rodden, W.P., and Stahl, B., "A Strip Method for Prediction of Damping in Subsonic Wind Tunnel and Flight Flutter Tests," Journal of Aircraft, Vol. 6, Jan.-Feb. 1969, pp. 9-17.

21 Roger, K.L., "Airplane Math Modeling Methods for Active Control Design; Structural Aspects of Active Controls," AGARD-CP-228, Aug. 1977, pp. 4-1 to 4-11.

22 Vepa, R., "Finite State Modeling of Aeroelastic Systems," NASA CR-2779, 1977.

23 Edwards, J.W., "Unsteady Aerodynamic Modeling and Active Aeroelastic Control," SUDAAR 504, Stanford University, Feb. 1977; also available as NASA CR-148019.

24 Burkhart, T.H., "Subsonic Transient Lifting Surface Analysis," Journal of Aircraft, Vol. 14, Jan. 1977, pp. 44-50.

25 Dunn, H.J., "An Analytical Technique for Approximating Unsteady Aerodynamics in the Time Domain," NASA Tech. Paper 1738, 1980.

26 Wykes, J.H., "Structural Dynamic Stability Augmentation and Gust Alleviation of Flexible Aircraft," AIAA Paper 68-1067, Oct. 1968.

27 Burris, P.M. and Bender, M.D., "Aircraft Load Alleviation and Mode Stabilization (LAMS)," AFFDL TR-68-158, Apr. 1969.

28 Roger, K.L., Hodges, G.E., and Felt, L., "Active Flutter Suppression - A Flight Test Demonstration," Journal of Aircraft, Vol. 12, June 1975, pp. 551-556.

29 Many authors, "Flutter Suppression and Structural Load Alleviation," AGARD-CP-175, July 1975.

30 Wykes, J.H., and Borland, C.J., "B-1 Ride Control," AGARDograph No. 234, Active Controls in Aircraft Design, Nov. 1978.

31 Armstrong, E.S., "ORACLS - A system for Linear-Quadratic Gaussian Control Law Design," NASA TP-1106, Apr. 1978.

³² O'Connell, R.F., and Messina, A.F., "Development of an Active Flutter Margin Augmentation System for a Commercial Transport," Journal of Guidance and Control, Vol. 3, July-Aug. 1980, pp 352-360.

³³ Mahesh, J.K., Stone, C.R., Garrard, W.L., and Dunn, H.J., "Control Law Synthesis for Flutter Suppression Using Linear-Quadratic Gaussian Theory," Journal of Guidance and Control, Vol 4, July-Aug. 1981, pp. 415-422.

³⁴ Etkin, B., "The Dynamics of Atmospheric Flight," John Wiley & Sons, New York, 1972.

³⁵ Seckel, E., "Stability and Control of Airplanes and Helicopters," Academic Press, New York, 1964.

³⁶ Rodden, W.P., Surber, T.E., and Vetter, H.C., "The Effect of Flexibility on the Drag Polar of an Aircraft," Journal of the Aeronautical Sciences, Vol. 24, June 1957, pp. 456-458.

³⁷ Ogawa, H., "Report of Wind-Tunnel Tests on a 1/12 Scale Aeroelastic Model of the Douglas (El Segundo) XA3D-1 Airplane," GALCIT Report 601, California Institute of Technology, Pasadena, California, April 30, 1953.

³⁸ Lan, C.E., "A Quasi-Vortex-Lattice Method in Thin Wing Theory," Journal of Aircraft, Vol. 11, Spet. 1974, pp. 518-527.

³⁹ Lan, C.E., "The unsteady quasi-vortex-lattice method with applications to animal propulsion," Journal of Fluid Mechanics, Vol. 93, Part 4, 1979, pp. 747-765.

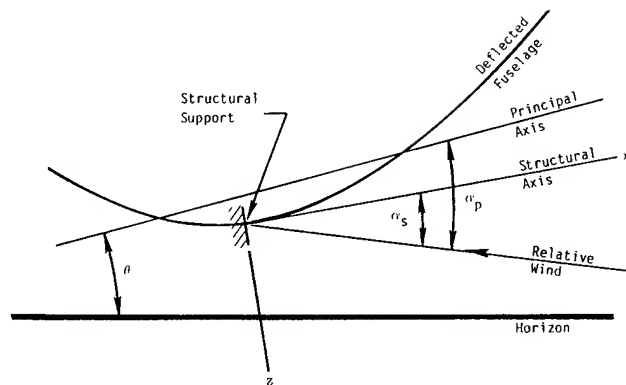


Fig. 2 Geometry of deformed flight vehicle

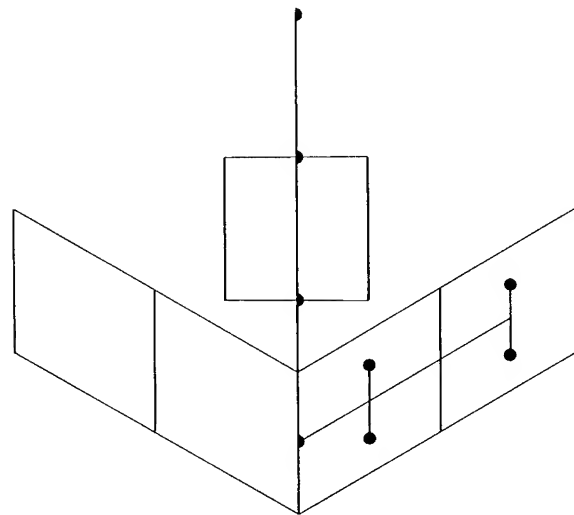


Fig. 3 Idealization of FSW configuration

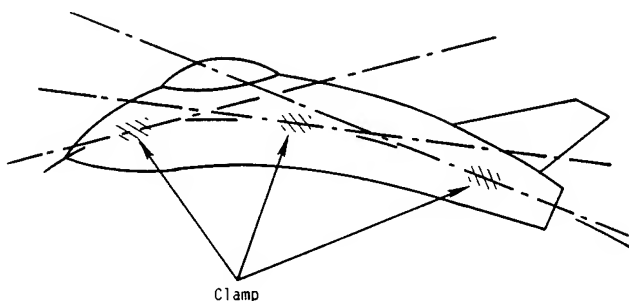


Fig. 1 Axes acceleration

Table 1 Derivatives for example FSW airplane

Derivative	Rigid value	Forward restraint	Centroidal restraint	Aft restraint	Unrestrained (FLEXSTAB)
C_{z_0}	0.0	0.0	0.0	0.0	0.0
C_{m_0}	0.0	0.0	0.0	0.0	0.0
C_{z_α}	-5.580	-3.168	-7.884	-7.206	-8.784
C_{m_α}	-1.383	-6.326	-2.295	7.481	-2.716
C_{z_δ}	-1.250	-0.9220	-1.256	-1.524	-1.284
C_{m_δ}	0.5852	-0.9028	0.5951	2.668	0.5690
$C_{z_{\dot{\alpha}}}$	8.521	5.450	12.82	11.30	14.22
$C_{m_{\dot{\alpha}}}$	1.414	10.288	3.122	-12.42	3.782
C_{z_q}	-5.556	-12.86	-7.610	11.603	-8.694
C_{m_q}	-3.750	-28.00	-4.592	-14.73	-5.077
$C_{z_{\ddot{z}}}$	0.0	0.01825	0.001044	-0.006958	-
$C_{m_{\ddot{z}}}$	0.0	0.03716	0.0008483	0.010679	-
$C_{z_{\ddot{\theta}}}$	0.0	0.09358	0.010477	0.02937	-
$C_{m_{\ddot{\theta}}}$	0.0	0.1915	0.003465	-0.04850	-
α_{p_0}	0.0	0.0	0.0	0.0	-
α_{p_α}	1.0	0.4943	0.9578	1.1607	1.0
$\alpha_{p_{\dot{\alpha}}}$	0.0	0.7891	0.05824	-0.2634	-
α_{p_δ}	0.0	-0.03560	0.010978	0.1960	-
α_{p_q}	0.0	-2.337	-0.07668	-0.5342	-
$\alpha_{p_{\ddot{z}}}$	0.0	-0.001796	0.0001772	0.003726	-
$\alpha_{p_{\ddot{\theta}}}$	0.0	-0.008427	-0.001630	-0.01886	-

Table 2 Accelerations during maneuver for various SIC supports

Centroidal load factor - n_z (g's)				
t(sec)	Correct solutions	Incorrect solutions assuming $\alpha_p = \alpha_s$		
	(FLEXSTAB) et. al.	Forward fixity	Centroidal fixity	Aft fixity
0.10	1.0	1.0	1.0	1.0
0.16	2.996	3.346	2.912	2.876
0.36	6.768	6.611	6.811	6.784
0.66	5.631	5.708	5.601	5.235
0.78	0.836	0.388	0.955	1.095
0.96	-5.619	-5.300	-5.706	-5.639
1.28	-3.726	-3.818	-3.682	-2.937
1.34	-1.987	-1.597	-2.071	-1.525
1.40	-0.916	-0.762	-0.972	1.116
1.60	1.763	1.568	1.828	2.086
1.80	0.697	0.821	0.657	0.602
2.00	1.120	1.054	1.140	1.071

Pitching acceleration - $\ddot{\theta}$ (deg/sec ²)				
t(sec)	Correct solutions	Incorrect solutions assuming $\alpha_p = \alpha_s$		
	(FLEXSTAB) et. al.	Forward fixity	Centroidal fixity	Aft fixity
0.10	0.0	0.0	0.0	0.0
0.16	144.0	127.1	148.0	149.8
0.36	-54.7	-46.2	-57.0	-58.8
0.66	4.3	0.6	5.8	25.7
0.78	-233.2	-212.5	-238.7	-246.5
0.96	99.0	82.0	103.8	106.4
1.28	1.3	5.4	-0.8	-39.9
1.34	157.6	138.1	161.9	135.6
1.40	93.2	86.6	95.7	105.1
1.60	-37.3	-27.5	-40.7	-56.9
1.80	14.9	8.5	17.0	22.3
2.00	-5.9	-2.5	-7.0	-4.9

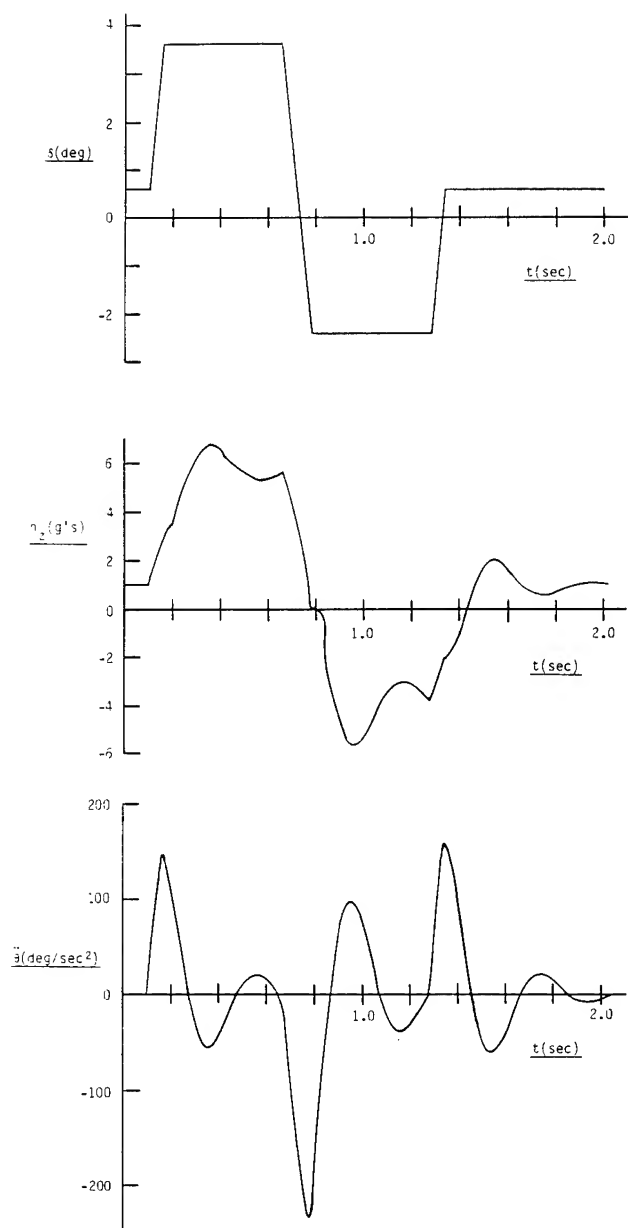


Fig. 4 Control input and maneuvering accelerations

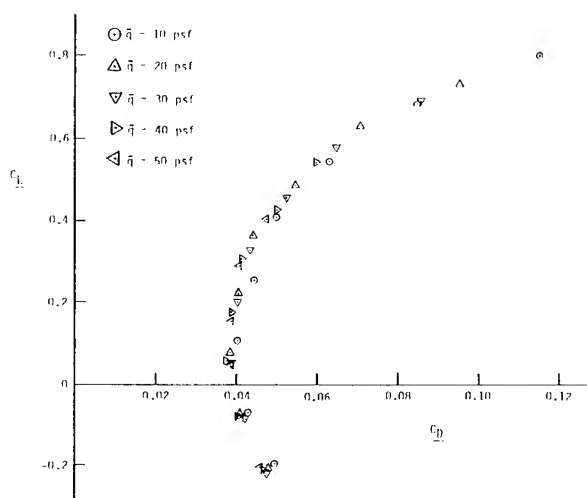


Fig. 5 Drag polar of flexible wing

VEHICLE MODEL REPRESENTING A HYBRID HEAVY LIFT AIRSHIP (HHLA)*

C. Venkatesan[†] and P.P. Friedmann^{††}
 Mechanics and Structures Department
 School of Engineering and Applied Science
 University of California
 Los Angeles, California 90024, U.S.A.

Abstract

Hybrid Heavy Lift Airship (HHLA) is a proposed candidate vehicle aimed at providing heavy lift capability at low cost. This vehicle consists of a buoyant envelope attached to a supporting structure to which four rotor systems, taken from existing helicopters are attached. Nonlinear equations of motion capable of modelling the dynamics of this coupled multi-rotor/support frame/vehicle system have been developed. Using these equations of motion the aeroelastic and aeromechanical stability analysis is performed aimed at identifying potential instabilities which could occur for this type of vehicle. The coupling between various blade, supporting structure and rigid body modes is identified. Furthermore, the effects of changes in buoyancy ratio (Buoyant lift/total weight) on the dynamic characteristics of the vehicle are studied. The dynamic effects found are of considerable importance for the design of such vehicles. The analytical model developed is also useful for studying the aeromechanical stability of single rotor and tandem rotor coupled rotor/fuselage systems.

Nomenclature

I_{xx}, I_{yy}	= Rotary inertia of the vehicle in roll and pitch respectively
$[K]$	= Stiffness matrix
K_{SBXY}, K_{SBXZ}	= Supporting structure bending stiffness in x-y (Horizontal) plane and in x-z (Vertical) plane respectively (in fundamental mode)
K_{ST}	= Supporting structure torsional stiffness (in fundamental mode)
$K_{\beta}, K_{\zeta}, K_{\phi B}$	= Root spring constant of the blade in flap, lag and torsion respectively
$K_{\phi C}$	= Control system stiffness
K_{ϕ}	= Equivalent spring stiffness in torsion of the blade
ℓ_{F1}, ℓ_{F2}	= Distance between origin O_s and the center of gravity of the fuselages, F_1 and F_2 respectively, Fig. 2
$[M]$	= Mass matrix
M_x, M_y, M_z	= Moments about x,y,z axes acting on the vehicle
$M_{\beta}, M_{\zeta}, M_{\phi}$	= Blade root moments in flap, lag and torsion respectively
N	= Number of blades in a rotor ($N \geq 2$)
P_z^S	= Static buoyancy on the envelope
$\{q\}$	= Generalized coordinate vector
R_x, R_y, R_z	= Rigid body perturbational motion in x,y,z directions respectively
s_k	= k^{th} eigenvalue ($\sigma_k \pm j\omega_k$)
T_1, T_2	= Thrust developed by rotor systems R_1 and R_2 respectively
W	= Total weight of the vehicle
W_{EN}	= Weight of the envelope
W_{F1}, W_{F2}	= Weight of the fuselages F_1 and F_2
W_S	= Weight of the supporting structure
W_{S1}	= Weight of passenger compartment
a	= Lift curve slope
BR	= Buoyancy ratio (Buoyant lift/total weight of the vehicle)
$[C]$	= Damping matrix
C_T	= Thrust coefficient of the rotor
f	= Rotating natural frequency
F_x, F_y, F_z	= Forces along x,y,z directions of the body axes
h_1	= Distance between origin O_s and under-slung load, Fig. 2
h_2	= Distance between centerline and rotor hub, Fig. 2
h_3	= Distance between centerline and center of volume of the envelope, Fig. 2
h_4	= Distance between centerline and C.G. of the envelope, Fig. 2
h_5	= Distance between the origin O_s and C.G. of the structure, Fig. 2

* This work was supported by NASA Ames Research Center under Grant NAG 2-116

[†] Assistant Research Engineer

^{††} Professor of Engineering and Applied Science

© 1984 by C. Venkatesan and P.P. Friedmann, released to AIAA to publish in all forms.

W_{UN}	= Underslung weight
$\{y_1\}, \{y_2\}$	= State vector
β_k, ζ_k, ϕ_k	= Flap, lead-lag and torsion angles of the k^{th} blade
$\beta_{k0}^i, \zeta_{k0}^i, \phi_{k0}^i$	= Equilibrium angles in flap, lag and torsion of the k^{th} blade in the i^{th} rotor system $i = 1, 2$
β_0, ζ_0, ϕ_0	= Equilibrium angles in flap, lag and torsion respectively
$\Delta\beta_k, \Delta\zeta_k, \Delta\phi_k$	= Perturbational quantities in flap, lag and torsion respectively
β_M, ζ_M, ϕ_M	= Generalized coordinates for collective flap, lag and torsion modes
$\beta_{-M}, \zeta_{-M}, \phi_{-M}$	= Generalized coordinates for alternating flap, lag and torsion modes
$\beta_{1C}, \zeta_{1C}, \phi_{1C}$	= Generalized coordinates for 1-cosine flap, lag and torsion modes
$\beta_{1S}, \zeta_{1S}, \phi_{1S}$	= Generalized coordinates for 1-sine flap, lag and torsion modes
β_P, ζ_P, ϕ_P	= Progressing (or high frequency) flap, lag and torsion modes
β_R, ζ_R, ϕ_R	= Regressing (or low frequency) flap, lag and torsion modes
ϵ	= Basic order of magnitude for blade slopes employed in ordering scheme
λ	= Inflow ratio
ω_k	= Modal frequency in k^{th} mode (imaginary part of s_k)
$\bar{\omega}_{SBXY}$	= Nondimensional uncoupled fundamental bending frequency of the supporting structure in x-y plane
$\bar{\omega}_{SBXZ}$	= Nondimensional uncoupled fundamental bending frequency of the supporting structure in x-z plane
$\bar{\omega}_{ST}$	= Nondimensional uncoupled fundamental torsion frequency of the supporting structure
Ω	= Rotor r.p.m.
σ_k	= k^{th} modal damping (real part of s_k)
σ	= Solidity ratio
θ_0, θ	= Collective pitch of the blade
θ_0^i	= Collective pitch setting for the i^{th} rotor
$\theta_x, \theta_y, \theta_z$	= Perturbational rotation in roll, pitch and yaw respectively
ξ_1, ξ_2	= Generalized coordinate for the fundamental mode bending of the supporting structure in x-y plane and x-z plane respectively

ξ_3	= generalized coordinate for the fundamental torsion mode of the supporting structure
$(\bar{})$	= Nondimensional quantity

1. Introduction

Hybrid Heavy Lift Airship (HHLA) or Hybrid Heavy Lift Helicopter (HHLH) is a candidate vehicle for providing heavy lift capability. Potential applications of this vehicle are for logging, construction, coast guard surveillance and military heavy lift. These vehicles combine buoyant envelope lift with lift and control forces generated by a multi-rotor system. A rough sketch of a typical HHLA vehicle is shown in Fig. 1. Clearly such a vehicle is quite different from the conventional rotorcraft. It is well known that aeroelastic and structural dynamic considerations are of primary importance in the successful design of rotary-wing vehicles. The aeroelastic and structural dynamic behavior of HHLA type vehicles has not been considered in the technical literature to date, therefore it is reasonable to consider these topics so that potential aeroelastic instability modes and structural dynamic aspects of such vehicles can be simulated and identified in the design process. Recent studies on HHLA type vehicles dealt with the overall dynamic stability and control of the vehicle under the assumption that it behaves like a rigid body having six degrees of freedom^{1,2}. However, the aeroelastic stability of the rotor and the aeromechanical stability of the coupled rotor/support system as well as the interaction of the buoyant lift with these vehicle dynamic characteristics have not been considered in the literature before.

The main objectives of this paper are to develop a fundamental understanding of the aeroelastic and aeromechanical problems which can be encountered in a HHLA type vehicle due to their unique features such as: buoyancy, multiple rotor systems, flexible supporting structure and underslung load.

This study is based on a simplified model of a HHLA type vehicle, in which the salient features are still retained. These simplifying assumptions consist of using two rotor systems instead of four, and a beam type structure representing the flexible supporting structure (Fig. 1), which in reality consists of a three dimensional frame (or truss). The essential features of this configuration, illustrated in Fig. 2, are described below:

- two rotor systems, providing lift, each having arbitrary number of blades $N(N \geq 2)$ are attached rigidly to the two ends of a flexible supporting structure;
- the flexible supporting structure is capable of bending in two orthogonal planes (horizontal and vertical) and it can also twist about its longitudinal axis;
- an envelope providing buoyant lift, acting at its center of buoyancy, is attached at the center of the supporting structure;
- two masses are attached at the two ends of the flexible structure, these two masses represent helicopter fuselages;

- e) a weight W_{UN} simulating an underslung load is attached to the structure.

The dynamic equations of motion for this model were derived in Ref. 3. The equations of motion are nonlinear coupled differential equations and they represent the dynamics of the coupled rotor/support frame/vehicle system in forward flight. The equations of motion can be divided into three groups, each group representing an appropriate subsystem of equations. These are:

- 1) rotor blade equations of motion in flap, lead-lag and torsion, respectively;
- 2) rigid body equations of motion of the complete vehicle;
- 3) equations of motion of the flexible supporting structure.

These coupled equations of motion have considerable versatility and can be used to study different classes of rotary-wing dynamic problems which are listed below in an ascending order of complexity:

- a) isolated rotor blade aeroelastic stability;
- b) coupled single rotor/supporting structure dynamics, which is representative of coupled rotor/body aeromechanical stability;
- c) stability of tandem rotor and side by side rotor helicopters;
- d) dynamics of HHLA type vehicles, in hover and forward flight.

The results presented in this paper deal primarily with the aeroelastic and aeromechanical stability analysis of an HHLA type of vehicle, shown in Fig. 2. The total number of degrees of freedom used in modeling this system which consists of two four bladed rotor systems and a flexible supporting structure is 31. Thus the stability analysis yields a total of 62 eigenvalues corresponding to these 31 degrees of freedom. Based on a careful parametric study, the various blade and vehicle modes have been identified. The physical interpretation of the various eigenvalues is determined from a systematic study of the eigenvalue changes caused by variations of the vehicle system parameters. Furthermore the coupling between various blade and vehicle modes is identified. Finally vehicle stability is analyzed at different buoyancy ratios ($BR = \text{Buoyancy of the envelope}/\text{total weight of the vehicle}$) so as to determine the influence of buoyancy on the aeromechanical stability of the vehicle.

2. Equations of Motion

Recent research on rotary-wing aeroelasticity⁴ has indicated that geometrically nonlinear effects, due to moderate blade deflections, are important for this class of problems. Thus a proper treatment of rotary-wing aeroelastic problems requires the development of a consistent mathematical model, which includes the geometrically nonlinear effects associated with finite blade slopes in the aerodynamic, inertia and structural operators. Retention of the nonlinear terms is based on an ordering

scheme^{3,4}. All the important parameters of the problem are assigned orders of magnitude in terms of a nondimensional quantity ϵ , which represents the typical blade slope ($0.1 < \epsilon < 0.15$). The ordering scheme consists of neglecting terms of the order $O(\epsilon^2)$ when compared to unity, i.e., $1 + \epsilon^2 \approx 1$.

The most important assumptions used in formulating the equations of motion are: (1) each rotor consists of three blades or more, (2) the rotors are lightly loaded, (3) the rotor is in uniform inflow, (4) the rotor blade is modelled as a rigid blade with orthogonal root springs (Fig. 3). This blade model is useful for simulating configurations which are either hingeless or articulated, (5) there is no aerodynamic interference between the rotor and the buoyant envelope, (6) the aerodynamic model used for the rotor is a quasi-steady blade element theory based on Greenberg's⁵ derivation of unsteady aerodynamic loads on an oscillating airfoil in a pulsating flow, and (7) the elastic supporting structure is modelled as a free-free beam for which the bending and torsional structural dynamics are modelled by the corresponding free vibration modes.

The various degrees of freedom considered for the model vehicle are: flap (β_k), lead-lag (ζ_k), torsion (ϕ_k) for each blade, rigid body translation (R_x, R_y, R_z) and rigid body rotation ($\theta_x, \theta_y, \theta_z$) of the vehicle as a whole and the generalized coordinates representing the uncoupled normal modes of vibration of the supporting structure (ξ_1, ξ_2, ξ_3). The equations of motion for the blade are obtained by enforcing moment equilibrium, of the various forces on the blade, at the root. The blade equations are written in a hub fixed rotating reference frame and these equations have periodic coefficients. The rigid body equations of motion are obtained by imposing the force and moment equilibrium of the vehicle. The equations of motion for the elastic modes of the supporting structure are obtained using a normal mode approximation. The complete details and the derivation can be found in Ref. 3. An overview of the coupling process between the blade motion and the body motion is presented in Fig. 4, which can be considered to be a schematic diagram describing the basic operations involved in the derivation of equations of motion for the coupled multi-rotor/vehicle system. It can be seen from Fig. 4 that the rigid body motions of the vehicle and the elastic deformations of the supporting structure are affected by the rotor loads. In turn, these rotor loads are related to the rigid body motions and the elastic deformation through the hub motions.

The final set of equations of motion are nonlinear ordinary differential equations with periodic coefficients. These equations have to be solved so as to determine the aeroelastic and aeromechanical stability characteristics of the vehicle.

3. Method of Solution

The method of solution for the coupled rotors/vehicle problem follows essentially the procedure outlined in Refs. 4 and 6. A brief description of the procedure aimed at determining the aeroelastic and aeromechanical stability characteristics of the vehicle is provided below.

1. Calculation of the equilibrium state of an

individual blade and the trim setting of the blade collective pitch angle.

2. Linearization of the nonlinear ordinary differential equations about the equilibrium position (linearized equations will have periodic coefficients).
3. Transformation of the linearized equations with periodic coefficients to linearized equations with constant coefficients, using multiblade coordinate transformation^{7,8}.
4. Evaluation of the eigenvalues of the linearized system with constant coefficients to obtain information on the stability of the vehicle.

The four steps described above represent essentially two separate stages of the analysis. The first stage consists of a trim analysis by which the equilibrium position of the blade is determined. Subsequently in the second stage a stability analysis of the linearized perturbational equation about the equilibrium state is carried out.

3.1 Trim or Equilibrium State Solution

In the trim analysis, the force and moment equilibrium of the complete vehicle together with the moment equilibrium of the individual blade about its root in flap, lead-lag and torsion are enforced. It is important to recognize that only the generalized coordinates representing the blade degrees of freedom will have a steady state value representing the equilibrium position. The generalized coordinates associated with the rigid body motions of the vehicles are essentially perturbational quantities and hence their equilibrium, or trim values are identically zero. In deriving the equations of motion for the flexible supporting structure, it was assumed that the vibrations of the structure occur about a deflected equilibrium position. The determination of the equilibrium of the supporting structure is unimportant, for the case considered in this study. The lack of dependence between these two items is due to the following: (a) The equilibrium deflection (or position) of the supporting structure does not affect the equilibrium values of the blade degrees of freedom, since the blade equations contain only the terms with the time derivatives of the degrees of freedom representing the elastic modes of the supporting structure. The physical reason for this mathematical dependence is due to the fact that the blade inertia and aerodynamic loads depend on the hub motion and not on the hub equilibrium position (the hub motion is related to the fuselage motion and the vibration of the supporting structure), and (b) The final linearized differential equations used for the stability analysis do not contain any term dependent on the static equilibrium deflection of the supporting structure. Hence, the generalized coordinates for the vibration modes of the supporting structure can also be treated as perturbational quantities. However, it should be noted that the evaluation of the static equilibrium deflection of the supporting structure could be important in the proper design of the supporting structure.

The k^{th} blade degrees of freedom can be written as

$$\begin{aligned}\beta_k &= \beta_{k0} + \Delta\beta_k(\psi) & \text{Flap} \\ \zeta_k &= \zeta_{k0} + \Delta\zeta_k(\psi) & \text{Lead-Lag} \\ \phi_k &= \phi_{k0} + \Delta\phi_k(\psi) & \text{Torsion}\end{aligned}\quad (1)$$

where β_{k0} , ζ_{k0} , ϕ_{k0} are the steady state values and $\Delta\beta_k$, $\Delta\zeta_k$, $\Delta\phi_k$ are the perturbational quantities.

Linearization of the equations is accomplished by substituting these expressions into the nonlinear coupled differential equations and neglecting terms containing the products or squares of the perturbational quantities. The remaining terms are then separated into two groups: one group of terms contains only the steady state quantities and constants (i.e., time independent quantities). These represent the trim or equilibrium equations. For the case of hover, these are nonlinear algebraic equations which represent the force and moment equilibrium equations determining the steady state. The second group contains the time dependent perturbational quantities and represents the equations of motion about the equilibrium position. These linearized dynamic equations of equilibrium are used for the stability analysis.

The steady state equilibrium equations can be written symbolically as:

for the complete vehicle

$$F_x = F_y = F_z = 0 \quad (2)$$

$$M_x = M_y = M_z = 0 \quad (3)$$

and for the individual blade

$$M_\beta = M_\zeta = M_\phi = 0 \quad (4)$$

In the above equations F_x , F_y and M_x are identically zero. The remaining equations for the vehicle can be written as

$$F_z = T_1 + T_2 + P_z^s - W = 0 \quad (5)$$

$$M_y = 0 \quad (6)$$

$$M_z = 0 \quad (7)$$

where T_1 and T_2 are the thrust developed by the two rotor systems R_1 and R_2 respectively, P_z^s is the static buoyancy due to the envelope and W is the weight of the complete vehicle. The quantities T_1 and T_2 are functions of the steady state flap, lead-lag and torsion angles, collective pitch angles and the operating conditions of the rotor. Equation (7) for M_z represents the torques developed by the two rotor systems. These torques can either be balanced by having a tail rotor for each main rotor or by having two counter-rotating main rotors. In the present study, it is assumed that the torques are balanced by tail rotors. Equation (6) for M_y consists of the pitching moments developed by the thrust due to the rotors and the gravity loads acting on the various components.

The steady state moment equilibrium equations for the individual blade will have the following symbolic form

$$M_\beta = f_1^i (\beta_{k0}^i, \zeta_{k0}^i, \phi_{k0}^i, \theta_0^i) = 0 \quad (8)$$

$$M_{\zeta} = f_2^i (\beta_{k0}^i, \zeta_{k0}^i, \phi_{k0}^i, \theta_0^i) = 0 \quad (9)$$

$$M_{\phi} = f_3^i (\beta_{k0}^i, \zeta_{k0}^i, \phi_{k0}^i, \theta_0^i) = 0 \quad (10)$$

where $i = 1, 2$ refer to the two rotor systems R_1 and R_2 respectively and k refers to the k^{th} blade in the i^{th} rotor system. For the case of hover, all the blades in one particular rotor system will have the same steady state values (i.e. equilibrium quantities). Thus the subscript 'k' can be deleted.

Equations (5), (6), (8)-(10) are nonlinear algebraic equations. These are a total of eight equations and 8 variables ($\beta_0^i, \zeta_0^i, \phi_0^i, \theta_0^i$; $i = 1, 2$). These eight equations are solved iteratively using the Newton-Raphson method, to obtain the steady state values. Failure to converge during iteration is attributed to divergence or static instability of the blade.

In deriving the equations of motion, the inflow ratio λ is assumed to be constant over the rotor disc. The typical value chosen for the inflow ratio is its value at 75% of the blade span. It is given as

$$\lambda = \frac{\sigma a}{16} \left(-1 + \sqrt{1 + \frac{24\theta_0}{\sigma a}} \right) \quad (11)$$

3.2 Description of Stability Analysis

The perturbational equations of motion, linearized about the equilibrium position, can be written in the following form

$$[M]\{\ddot{q}\} + [C]\{\dot{q}\} + [K]\{q\} = 0 \quad (12)$$

where $\{q\}$ contains all the degrees of freedom representing the blade motion, the rigid body motions of the vehicle and the flexible modes of the supporting structure.

The matrices $[M]$, $[C]$ and $[K]$ can be identified as representing mass, damping and stiffness matrices respectively and the elements of these matrices are functions of the equilibrium values.

The stability of the vehicle about the trim condition is obtained by solving the eigenvalue problem represented by Eq. (12). For convenience Eq. (12) is rewritten in state variable form

$$\{\dot{y}\} = [F]\{y\} \quad (13)$$

where $\{y\}^T = \{y_1\}^T, \{y_2\}^T$

and $\{y_1\} = \{\dot{q}\}; \{y_2\} = \{q\}$

and

$$[F] = \begin{bmatrix} -[M]^{-1}[C] & -[M]^{-1}[K] \\ [I] & 0 \end{bmatrix}$$

Assuming a solution for Eq. (13) in the form of $\{y\} = \{\bar{y}\}e^{s\psi}$, yields the standard eigenvalue problem

$$[F]\{y\} = s\{y\} \quad (14)$$

The eigenvalues of Eq. (14) can be either real or complex conjugate pairs

$$s_k = \sigma_k \pm i\omega_k$$

The complex part of the k^{th} eigenvalue (ω_k) refers to the modal frequency and the real part (σ_k) refers to the modal damping. The mode is stable when $\sigma_k < 0$ and the stability boundary is represented by $\sigma_k = 0$.

This relatively simple procedure can become complicated depending on the form of the matrices $[M]$, $[C]$ and $[K]$. In the aeroelastic stability analysis of a isolated rotor in hover, these matrices contain constant elements. Thus the solution of this eigenvalue problem is straight-forward. However when dealing with the stability analysis of a coupled rotor/vehicle system in hover, as required in the present case, these matrices will have elements which are time dependent. The reason for the appearance of time dependent or periodic coefficients is due to the vehicle perturbational motion and vibration of the supporting structure. These perturbational motions introduce, through the hub motion, periodic terms in inertia and aerodynamic loads of the blade.

For the cases, when the matrices in the linearized perturbational equations are time dependent, the stability analysis can be performed by applying either Floquet theory or by using a multiblade coordinate transformation^{7,8}. It is well known that for the coupled rotor/vehicle type of analysis for the case of hover, the multiblade coordinate transformation is successful in eliminating the time dependency of the coefficients, in the equations of motion. During this transformation, the individual blade degrees of freedom will transform into a new set of rotor degrees of freedom. (It is worthwhile mentioning that this transformation is also frequently denoted by the terms Fourier transformation, Coleman transformation and more recently rotor plane coordinate transformation⁸.) These rotor degrees of freedom are basically representative of the behavior of the rotor as a whole when viewed from a non-rotating reference frame. The various rotor degrees of freedom are known as collective, cyclic and alternating degrees of freedom. For example, in a four bladed rotor, the flap degree of freedom corresponding to each blade (β_k ; $k = 1, 4$) will transform into collective flap (β_M), cyclic flap (β_{1c}, β_{1s}) and alternating flap (β_{-M}) degrees of freedom. Alternating degree of freedom will appear only when the rotor consists of an even number of blades. In a similar fashion, the lead-lag and torsional degrees of freedom will also transform into corresponding rotor degrees of freedom.

As a result of the application of the multiblade coordinate transformation, the linearized perturbational equations with periodic coefficients will transform into linearized perturbational equations with constant coefficients. Using these equations, with constant coefficients, a stability analysis is performed as described above. The eigenvalues corresponding to the cyclic degrees of freedom of the rotor ($\beta_{1c}, \beta_{1s}, \zeta_{1c}, \zeta_{1s}, \phi_{1c}, \phi_{1s}$) are referred in this paper as high frequency (or progressing) and low frequency (or regressing or regressing) mode. The designation of high frequency or low frequency mode is based on the rotating natural frequency of the rotor. Suppose, the rotating natural frequency, say in lead-lag, is f/rev , then the two frequencies corresponding to the cyclic modes (ζ_{1c}, ζ_{1s}) will be usually $(f+1)/\text{rev}$ and $(f-1)/\text{rev}$. The mode with the frequency $(f+1)/\text{rev}$

is called a high frequency lag mode and that corresponding to $(f-1)/\text{rev}$ is called a low frequency lag mode. The mode with the frequency f/rev is known as the collective lag mode. Since the HHLA model vehicle (Fig. 2) consists of two rotor systems coupled by a supporting structure, the stability analysis will provide a pair of eigenvalues for each rotor degree of freedom. Hence for the purpose of identification, in the presentation of the results the rotor modes will be referred to as mode 1 and mode 2, such as collective flap mode 1, collective flap mode 2 and high frequency flap mode 1 and high frequency flap mode 2, etc.

4. Results and Discussion

The validity of the equations of motion for the coupled rotor/vehicle system was first verified by using them to solve the aeromechanical stability problem of a single rotor helicopter in ground resonance and comparing the analytical results, obtained using our equations, with experimental data presented in Ref. 9. We found that our analytical results are in good agreement with the experimental results indicating that the equations of motion for the coupled rotor/vehicle system are valid. Sample results taken from Ref. 10, are included in this paper to illustrate the degree of correlation. Figure 5 presents the variation of rotor and body frequencies with rotor speed Ω . Fig. 6 presents the variation of damping in the lead-lag regressing mode with Ω . These figures show that our analytical predictions are in good agreement with the experimental results.

The stability of the model vehicle (Fig. 2) representing an HHLA is analyzed for the case of hovering flight. The various degrees of freedom considered for this problem are flap, lead-lag, torsion (for each blade), rigid body translation (R_x, R_y), rigid body rotation (θ_x, θ_y) and three normal modes of vibration of the supporting structure. The three normal modes represent the fundamental symmetric bending mode (ξ_1) in the horizontal (x-y) plane, the fundamental symmetric bending mode (ξ_2) in the vertical (x-z) plane and the fundamental antisymmetric torsion (ξ_3) about the longitudinal axis. For a four bladed rotor, there are in total 31 degrees of freedom, namely 12 rotor degrees of freedom for each rotor plus four rigid body degrees of freedom plus three elastic vibration modes of the supporting structure. Hence a stability analysis for this system will yield 62 eigenvalues corresponding to these 31 degrees of freedom. The primary aim is to identify the 62 eigenvalues and relate them to the various modes of the rotor/vehicle assembly. This relatively complicated identification process is based on physical insight gained by performing some preliminary calculations augmented by additional considerations described below:

1. Comparison of the imaginary part of the eigenvalue (ω) with the uncoupled frequencies of the various modes, and
2. employing an extensive parametric study in which the primary parameters allowed to vary are the bending and torsional stiffness of the supporting structure ($K_{SBXY}, K_{SBXZ}, K_{ST}$) combined with the rotary inertia of the vehicle in pitch (I_{yy}) and roll (I_{xx}).

Based on the results obtained in the parametric

study, the various eigenvalues and the coupling among different modes are identified. It should be noted that for the cases studied, the trim (or equilibrium) quantities are the same because the trim values are independent of the quantities varied in the parametric study. A complete description of this study can be found in Ref. 6.

For the example problem analyzed, the rotors are articulated and they are identical. The data used for this study is presented in Appendix A. The result presented below are obtained for the model vehicle without the sling load.

The results of the trim (or equilibrium) analysis are presented in Appendix B. Since the two rotors have identical geometrical properties and identical operating conditions and furthermore the model vehicle possesses a symmetry about y-z plane, the equilibrium angles of the blade are the same for both rotor systems. For the buoyancy ratio of $BR = 0.792$, the thrust coefficient in the rotors is $C_T = 0.00158$. The equilibrium blade angles are in flap $\beta_0 = 2.302$ deg., in lead-lag $\zeta_0 = -3.963$ deg. and in torsion $\phi_0 = -0.115$ deg. The collective pitch angle is $\theta_0 = 4.206$ deg.

The results of the stability analyses are presented in Figs. 7-11. Figure 7 illustrates the variation of the eigenvalues of blade lead-lag modes and the supporting structure bending modes as a result of an increase in the bending stiffness (K_{SBXY}) of the supporting structure in x-y (horizontal) plane. The bending stiffness K_{SBXY} was increased in increments from 5.09×10^7 N/m to 1.74×10^8 N/m, such that the corresponding uncoupled nondimensional bending frequency in x-y plane ($\bar{\omega}_{SBXY}$) assumed the values $\bar{\omega}_{SBXY} = 1.2, 1.499, 1.754, 2.192$, where the frequencies are nondimensional with respect to the rotor speed of rotation Ω , where $\Omega = 217.79$ R.P.M.. The arrows in the figure indicate the direction along which the eigenvalues of the modes change due to an increase in K_{SBXY} . The eigenvalues of the other modes, which are not shown in the figure, remain unaffected by the variation in K_{SBXY} . It can be seen from Fig. 7 that the bending mode, in x-y plane, of the supporting structure is strongly coupled with the high frequency lag mode 2. The high frequency lag mode 2 which was initially unstable becomes more stable as K_{SBXY} is increased. The damping in the bending mode in x-y plane decreases asymptotically with an increase in frequency and this mode is always stable. The low frequency lead-lag mode 2 shows a slight decrease in damping as K_{SBXY} is increased. The eigenvalues corresponding to the bending mode in x-z plane and the high frequency lag mode 1 are not affected by the changes in K_{SBXY} . However, since these two modes have nearly equal frequencies it can be seen that the high frequency lag mode 1 is unstable.

Figure 8 presents the variation of eigenvalues of the blade lead-lag modes and the supporting structure bending modes as a result of an increase in the bending stiffness (K_{SBXZ}) of the supporting structure in x-z (vertical) plane. The bending stiffness K_{SBXZ} was increased in increments from 7.96×10^6 N/m to 1.74×10^8 N/m and the corresponding nondimensional uncoupled bending frequency in x-z plane ($\bar{\omega}_{SBXZ}$) assumed the values $\bar{\omega}_{SBXZ} = 1.499, 1.754, 2.192$. It can be seen from Fig. 8 that the bending mode in x-z plane is strongly coupled with high frequency lag mode 1. The high

frequency lag mode 1 which was initially unstable becomes a stable mode as K_{SBXZ} is increased from 7.96×10^7 N/m ($\bar{\omega}_{SBXZ} = 1.499$) to 1.09×10^8 N/m ($\bar{\omega}_{SBXZ} = 1.754$). But a further increase in K_{SBXZ} to 1.74×10^8 N/m does not affect the eigenvalue corresponding to the high frequency lag mode 1, indicating that these two modes are decoupled. Damping in the bending mode in x-z plane decreases drastically at the beginning and once the bending mode and the high frequency lag mode 1 are decoupled, the decrease in damping of the bending mode in x-z plane is very small. Damping in the torsion mode of the supporting structure and low frequency lag mode 1 are slightly affected as K_{SBXZ} is increased. Since the torsion mode and the low frequency lag mode 1 have frequencies which are close to each other, the figure clearly indicates that the lag mode 1 is unstable. The eigenvalues corresponding to the rest of the modes are unaffected.

Figure 9 shows the eigenvalue variation in the rotor lead-lag modes and the torsion mode of the supporting structure as a result of an increase in the torsional stiffness (K_{ST}) of the supporting structure. The torsional stiffness, K_{ST} , was increased in increments from $K_{ST} = 1.59 \times 10^6$ N.m to 3.99×10^7 N.m and the corresponding uncoupled nondimensional torsional frequency ($\bar{\omega}_{ST}$) of the supporting structure are $\bar{\omega}_{ST} = 0.4, 0.55, 0.846, 1.096, 1.2, 1.3, 1.4, 1.5, 1.754, 2.0$. It is evident from the figure that the low frequency lag mode 2 and high frequency lag mode 2 remain unaffected during the variations in K_{ST} and these modes are stable. In Fig. 9, the different curves are divided into three segments represented by points A, B, C and D. The curves between points A to B refer to the range of $K_{ST} = 3.01 \times 10^6$ N.m to 7.20×10^6 N.m ($\bar{\omega}_{ST} = 0.55$ to 0.846); the curves between points B to C refer to the range $K_{ST} = 7.20 \times 10^6$ N.m to 1.685×10^7 N.m ($\bar{\omega}_{ST} = 0.846$ to 1.3); and the curves between points C to D refer to the range $K_{ST} = 1.685 \times 10^7$ N.m to 3.1×10^7 N.m ($\bar{\omega}_{ST} = 1.3$ to 1.754).

It is evident from Fig. 9 that in the range A to B, as the torsional stiffness K_{ST} is increased, the torsion mode of the supporting structure becomes increasingly stable and its frequency is increasing; the low frequency lag mode 1 becomes increasingly unstable with its frequency slightly increased. This clearly indicates that the torsion mode is strongly coupled with the low frequency lag mode 1. The high frequency lag mode 1 experiences a slight increase in frequency but its damping remains almost the same. In this range, A to B, the eigenvalues of these three modes have been distinctly identified based on their uncoupled nondimensional frequencies. In the range B to C, as the torsional stiffness K_{ST} is increased, the damping in the low frequency lag mode 1 decreases and its frequency tends to increase towards 1.0. At the same time, the damping in torsional mode of the supporting structure decreases drastically and a slight change in the frequency is observed (i.e., the frequency initially increases and then decreases). The high frequency lag mode 1 shows an increase in frequency with no appreciable change in damping. In this range B to C, the eigenvalues of these three modes do not exhibit a direct one to one correspondence to the uncoupled nondimensional frequencies, implying that all these modes are coupled. Hence in this range, B to C, the reference to the various modes, as torsion mode, low

frequency lag mode 1 and high frequency lag mode 1, is only for the convenience of explaining the variation of the eigenvalues. When the torsional stiffness K_{ST} was increased still further, i.e. the range C to D, the eigenvalues start exhibiting a correspondence to nondimensional uncoupled frequencies indicating that these three modes are slowly decoupled. In this range, C to D, the torsional mode of the supporting structure has low damping and it tends to decrease asymptotically while the frequency increases from 1.5 to 1.75. The high frequency lag mode 1 shows an increase in the frequency and the mode becomes stable at the point D. The damping in the low frequency lag mode 1 decreases while the frequency undergoes a slight reduction. Beyond the point D i.e. for $K_{ST} \geq 3.1 \times 10^7$ N.m the eigenvalues of low frequency lag mode 1 and high frequency lag mode 1 show negligible change and the damping in torsion mode remains the same but its frequency increases. Beyond point D all the three modes are stable.

Another interesting observation which can be made from Fig. 9 is associated with the effect due to the increase in torsional stiffness K_{ST} . When K_{ST} is increased from 1.685×10^7 N.m to 3.99×10^7 N.m (curve in the range C to D and beyond), the eigenvalues corresponding to the high frequency lag mode 1 tend to approach the eigenvalue corresponding to the high frequency lag mode 2 (which remains unaffected during the variation in K_{ST}) and similarly the low frequency lag mode 1 approaches the low frequency lag mode 2. This behavior seems to indicate that as the torsional stiffness of the supporting structure is increased the coupling between the two rotors due to the torsional deformation of the supporting structure is eliminated. As a result of this lack of coupling the eigenvalues corresponding to the high frequency lag modes 1 and 2 and low frequency lag modes 1 and 2 approach each other. It should be noted that elimination of the coupling of the two rotors, due to the torsional deformation of the supporting structure, does not imply that the two rotors are totally decoupled. The rotors are still coupled through the bending deformation of the supporting structure and rigid body pitch motion of the vehicle. The presence of this coupling causes the eigenvalues of the low frequency and high frequency lag modes to approach each other rather than coalescing.

The last observation which can be made using Fig. 9 is that the high frequency lag mode 1, low frequency lag mode 1 and torsion mode of the supporting structure undergo a reversal in their characteristics as K_{ST} is increased from 1.59×10^6 N.m to 3.99×10^7 N.m. Thus, the mode which was initially a distinct torsion mode becomes a low frequency lag mode 1; the low frequency lag mode 1 becomes a high frequency lag mode 1 and the high frequency lag mode 1 becomes a torsion mode. For low and high values of the torsional stiffness (i.e., $K_{ST} \leq 1.59 \times 10^6$ N.m ($\bar{\omega}_{ST} \leq 0.4$) and $K_{ST} \geq 3.10 \times 10^7$ N.m ($\bar{\omega}_{ST} \geq 1.754$)) the torsional mode of the supporting structure, the low frequency lag mode 1 and high frequency lag mode 1 are all stable. For intermediate values of the torsional stiffness of the supporting structure, one of the lag modes is unstable.

The variation of the eigenvalues of the collective flap modes and body pitch mode due to increase in body inertia in pitch is presented in Fig. 10. It is evident from the figure that the

pitch mode is a pure damped mode. An increase in pitch inertia causes the eigenvalues, corresponding to the pitch mode, to approach each other. The eigenvalues of the collective flap mode 2 tend to approach the eigenvalue of the collective flap mode 1. The pure damped nature of the pitch mode is associated with the presence of two rotors. During pitch motion, the net inflow in the two rotor system changes. If in one rotor system the net inflow increases, then in the other one the inflow decreases and vice versa. These changes in inflow results in changes in the thrust in the two rotor systems. The rotor system which moves up, during pitch motion, experiences a reduction in thrust due to the increased inflow and the rotor system which moves down produces more thrust due to the decreased flow. These changes in the thrust tend to restore the vehicle to its equilibrium position. Since this restoring force is proportional to the pitch rate, this mechanism produces a damping in pitch. In the present case, the pitch motion is overdamped. Hence an increase in inertia causes the eigenvalues, corresponding to the pitch mode, to approach each other, as shown in Fig. 10.

Figure 11 illustrates the variation of eigenvalues corresponding to the low frequency lag mode 2 and body roll mode as a result of an increase in inertia in roll. An increase in roll inertia tends to decrease the damping in roll, furthermore its frequency is also reduced. The low frequency lag mode 2 tends to become more stable. The roll mode, for the model vehicle, is a damped oscillatory mode. This is different from the pure damped mode⁷ normally observed in a conventional tandem rotor helicopter. The reason for this oscillatory nature of the roll mode is due to the presence of the buoyancy of the envelope.

For all the cases analyzed, it was found that the flap and torsional modes of the rotor are always stable. The eigenvalues corresponding to the cyclic flap modes and all the torsion modes are not affected by the variation in the quantities used in this parametric study. The alternating modes of the rotor were also found stable.

The degree of coupling, as well as the relative strength of the coupling between the various blade modes and the body modes is presented in a qualitative manner in Table I. It is evident from this table that the supporting structure elastic modes are strongly coupled with the low frequency and high frequency lead-lag modes.

The effects of varying the buoyancy ratio on the stability of the vehicle represented in Table II and Figs. 12 and 13. Table II shows the results from the trim analysis, at various buoyancy ratios. As the buoyancy ratio is decreased, the equilibrium angles of the blade and the thrust coefficient of the rotors are increased.

Figure 12 depicts the variation of eigenvalues in supporting structure elastic modes with decrease in buoyancy ratio. The direction of arrows in the figure indicate the variation of the eigenvalues as a result of the decrease in buoyancy ratios. The frequencies corresponding to these modes are not affected by the variation in buoyancy ratio. However, the damping in bending in x-y plane increases, the damping in bending in x-z plane decreases while the damping in torsion mode increases.

Figure 13 presents the variation of the eigenvalues of pitch and roll modes with buoyancy ratio. As the buoyancy ratio is decreased, one of the eigenvalues corresponding to the pitch mode decreases while the other eigenvalue increases. The pitch mode always remains as a pure damped mode. The roll mode which was initially a stable mode becomes unstable for buoyancy ratios $BR \leq 0.6$.

The results obtained also indicate that as the buoyancy ratio is decreased, the damping in lead-lag modes of the rotors increases while the damping in flap and torsion modes of the rotor decreases. However changes in the buoyancy ratio have only a minor effect on the frequencies of the blade modes. A quantitative indication for the magnitude of the changes in damping in the blade modes produced by changes in the buoyancy ratio is illustrated by the following results: for a 40% reduction in buoyancy ratio, the damping in torsion modes decreases by 12%; the damping in flap modes decreases by 12% and the damping in lag modes increases by 200%.

5. Concluding Remarks

This paper presents the results of an aeromechanical stability analysis of a model vehicle representative of a HHLA configuration in hovering flight. The most important conclusions obtained in this study are presented below.

- 1) The rotor cyclic lead-lag modes couple strongly with the bending modes and the torsion mode of the supporting structure, as a consequence, the stability of the lead-lag modes is sensitive to changes in stiffness (or the natural frequencies) of the supporting structure in bending and torsion. Therefore the natural frequencies of the supporting structure must be designed so as to be well separated from the frequencies of the rotor lead-lag modes. This also emphasizes the importance of modelling the supporting structure with an adequate number of elastic modes.
- 2) The low frequency and high frequency lead-lag modes of the rotor and the torsion mode of the supporting structure undergo a change in their basic characteristics, as the torsional stiffness of the supporting structure is increased from a low value to a high value (i.e., $K_{ST} = 1.59 \times 10^6$ N.m to 3.99×10^7 N.m).
3. The lead-lag modes of the rotor are stable only when the torsional stiffness of the supporting structure has low or high values ($K_{ST} \leq 1.59 \times 10^6$ N.m and $K_{ST} \geq 3.10 \times 10^7$ N.m). For intermediate values of K_{ST} , one of the lead-lag modes is unstable.
- 4) The body pitch mode is a pure damped mode.
- 5) The body roll mode is a damped oscillatory mode. However, as the buoyancy ratio is decreased, this mode becomes unstable.
- 6) The stability analysis of the coupled rotor/vehicle dynamics clearly illustrates the fundamental features of the aeroelastic stability of the rotor, coupled rotor/support system aeromechanical stability and the vehicle dynamic stability in longitudinal and lateral planes.

Furthermore, it should be mentioned that the analytical model developed in this study, for the aeromechanical stability study of an HHLA type vehicle, can be also applied to various other types of vehicles, such as a tandem rotor helicopter configuration and the coupled rotor/body aeromechanical problem of a single rotor helicopter. Finally, it should be noted that the analytical model is capable of representing not only aeroelastic and aeromechanical problems but it is also suitable for investigating rigid body stability and control problems associated with these types of vehicles.

Acknowledgement

The authors would like to express their gratitude to the grant monitor Dr. H. Miura for providing a large part of the data used in these calculations, and also for his constructive comments and suggestions.

References

1. "A Preliminary Design Study of a Hybrid Airship for Flight Research", by Goodyear Aerospace Corporation, NASA CR 166246, July 1981.
2. Tischler, M.B., Ringland, R.F., and Jex, H.R., "Heavy-Lift Airship Dynamics", *Journal of Aircraft*, Vol. 20, No. 5, May 1983, pp. 425-433.
3. Venkatesan, C. and Friedmann, P.P., "Aeroelastic Effects in Multirotor Vehicles with Application to Hybrid Heavy Lift System, Part I: Formulation of Equations of Motion", Submitted to NASA for publication as a Contractor Report.
4. Friedmann, P.P., "Formulation and Solution of Rotary-Wing Aeroelastic Stability and Response Problems", *Vertica*, Vol. 7, No. 2, pp. 101-141, 1983.
5. Greenberg, J.M., "Airfoil in Sinusoidal Motion in a Pulsating Flow", NACA TN 1326, 1947.
6. Venkatesan, C. and Friedmann, P.P., "Aeroelastic Effects in Multirotor Vehicles, Part II: Method of Solution and Results Illustrating Coupled Rotor/Body Aeromechanical Stability", NASA CR Report being reviewed for publication.
7. Johnson, W., *Helicopter Theory*, Princeton University Press, Princeton, New Jersey, 1980.
8. Levin, J., "Formulation of Helicopter Air-Resonance Problem in Hover with Active Controls", M.Sc Thesis, Mechanics and Structures Department, University of California, Los Angeles, Sept. 1981.
9. Bousman, W.G., "An Experimental Investigation of the Effects of Aeroelastic Couplings on Aeromechanical Stability of a Hingeless Rotor Helicopter", *Journal of the American Helicopter Society*, Vol. 26, No. 1, Jan. 1981, pp. 46-54.
10. Friedmann, P.P. and Venkatesan, C., "Comparison of Experimental Coupled Helicopter Rotor/Body Stability Results with a Simple Analytical Model", Paper Presented at the Integrated Technology Rotor (ITR) Methodology Workshop, NASA Ames Research Center, Moffett Field, California, June 20-21, 1983.
11. Bisplinghoff, R.L., Ashley, H., and Halfman, R.L., *Aeroelasticity*, Addison-Wesley, 1955.

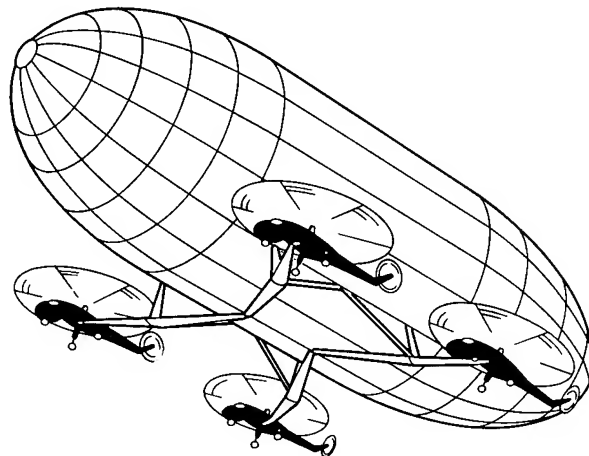
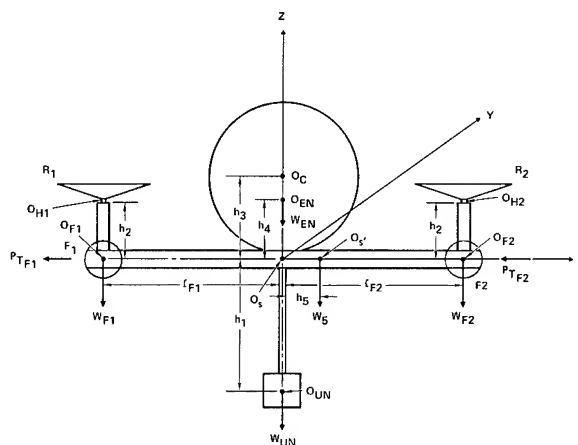


Fig. 1 Hybrid Heavy Lift Airship - Approximate Configuration



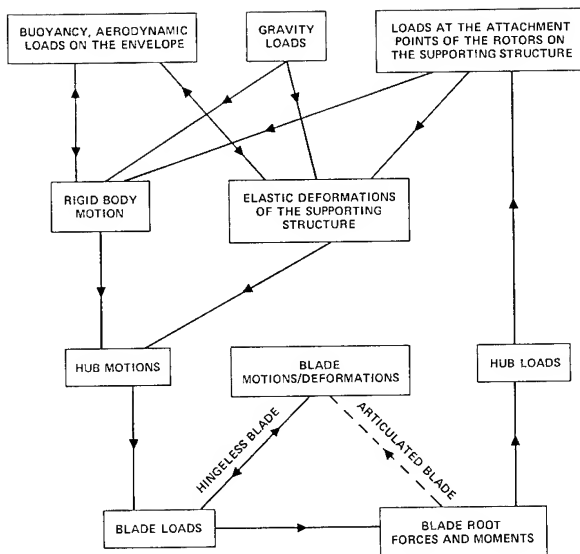


Fig. 4 Schematic Diagram of Coupled Rotor/Vehicle Dynamic Interactions

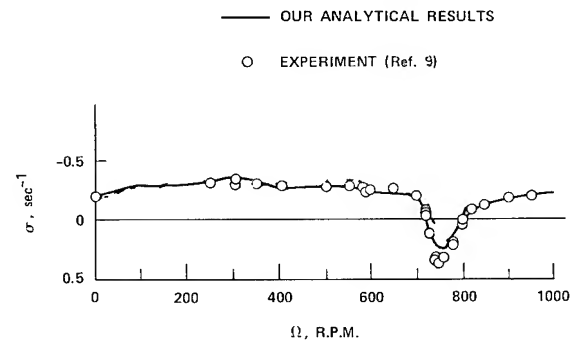


Fig. 6 Regressing Lag Mode Damping as a Function of $\Omega, \theta = 0$

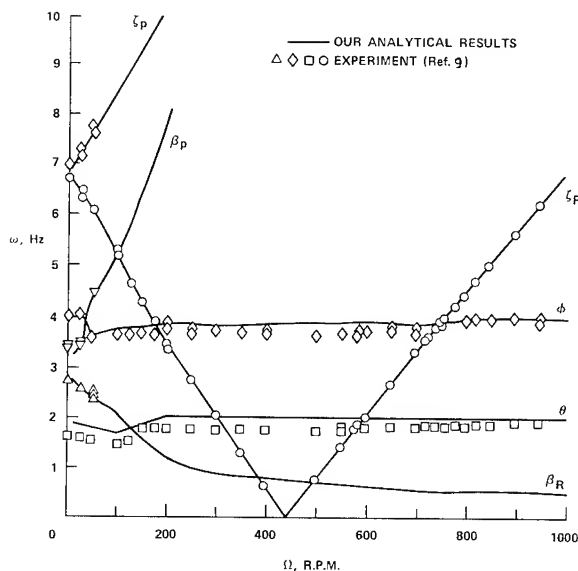


Fig. 5 Modal Frequencies as a Function of $\Omega, \theta = 0$

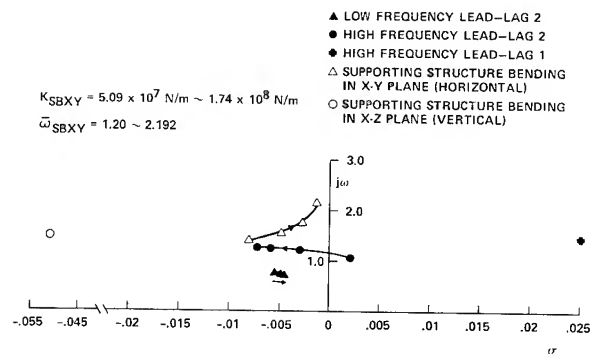
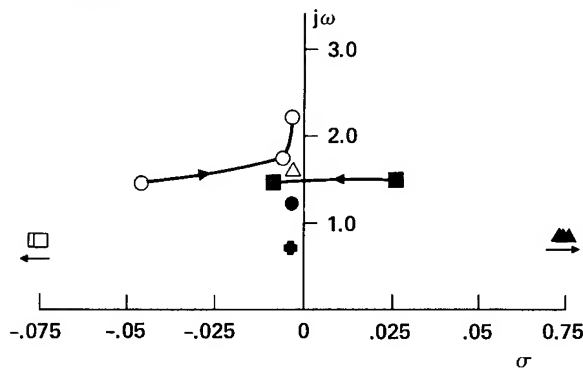


Fig. 7 Variation of Nondimensional Eigenvalues of Blade Lead-Lag Modes and Supporting Structure Bending Modes with Increase in K_{SBX2} ($\omega_{SBXZ} = 1.499, \bar{\omega}_{ST} = 1.096, I_{xx} = 6.44 \times 10^5 \text{ kg.m}^2, I_{yy} = 2.59 \times 10^6 \text{ kg.m}^2, BR = 0.792, C_T = 0.00158$)

$$K_{SBXZ} = 7.96 \times 10^7 \text{ N/m} \sim 1.74 \times 10^8 \text{ N/m}$$

$$\bar{\omega}_{SBXZ} = 1.499 \sim 2.192$$



- SUPPORTING STRUCTURE TORSION
- SUPPORTING STRUCTURE BENDING IN X-Z PLANE (VERTICAL)
- △ SUPPORTING STRUCTURE BENDING IN X-Y PLANE (HORIZONTAL)
- HIGH FREQUENCY LEAD-LAG 1
- HIGH FREQUENCY LEAD-LAG 2
- ▲ LOW FREQUENCY LEAD-LAG 1
- ◆ LOW FREQUENCY LEAD-LAG 2

Fig. 8 Variation of Nondimensional Eigenvalues of Blade Lead-Lag Modes and Supporting Structure Bending Modes with Increase in K_{SBXZ} ($\bar{\omega}_{SBXY} = 1.499$, $\bar{\omega}_{ST} = 1.096$, $I_{xx} = 6.44 \times 10^5 \text{ kg.m}^2$, $I_{yy} = 2.59 \times 10^6 \text{ kg.m}^2$, $BR = 0.792$, $C_T = 0.00158$)

- ▲ COLLECTIVE FLAP 1
- △ COLLECTIVE FLAP 2
- BODY PITCH

$$I_{yy} = 2.59 \times 10^6 \text{ kg.m}^2 \sim 4.75 \times 10^6 \text{ kg.m}^2$$

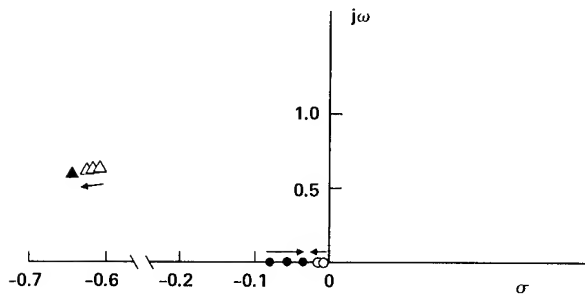
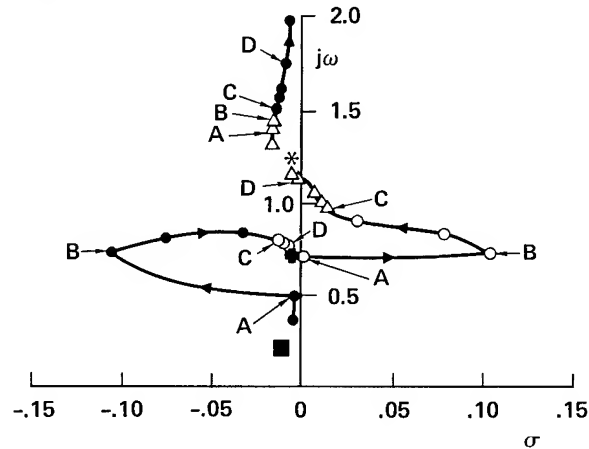


Fig. 10 Variation of Nondimensional Eigenvalues of Blade Collective Flap Modes and Body Pitch Mode with Increase in I_{yy} ($\bar{\omega}_{SBXY} = \bar{\omega}_{SBXZ} = 2.192$, $\bar{\omega}_{ST} = 1.754$, $I_{xx} = 2.0 \times 10^6 \text{ kg.m}^2$, $BR = 0.792$, $C_T = 0.00158$)

- COLLECTIVE LEAD-LAG 1, 2
- SUPPORTING STRUCTURE TORSION
- LOW FREQUENCY LEAD-LAG 1
- ◆ LOW FREQUENCY LEAD-LAG 2
- △ HIGH FREQUENCY LEAD-LAG 1
- * HIGH FREQUENCY LEAD-LAG 2

$$K_{ST} = 1.59 \times 10^6 \text{ N.m} \sim 3.99 \times 10^7 \text{ N.m}$$

$$\bar{\omega}_{ST} = 0.4 \sim 2.0$$



$$A - B \quad K_{ST} = 3.01 \times 10^6 \sim 7.20 \times 10^6 \text{ N.m}$$

$$B - C \quad K_{ST} = 7.20 \times 10^6 \sim 1.685 \times 10^7 \text{ N.m}$$

$$C - D \quad K_{ST} = 1.685 \times 10^7 \sim 3.10 \times 10^7 \text{ N.m}$$

Fig. 9 Variation of Nondimensional Eigenvalues of Blade Lead-Lag Modes and Supporting Structure Torsion Mode with Increase in K_{ST} ($\bar{\omega}_{SBXY} = \bar{\omega}_{SBXZ} = 2.192$, $I_{xx} = 6.44 \times 10^5 \text{ kg.m}^2$, $I_{yy} = 2.59 \times 10^6 \text{ kg.m}^2$, $BR = 0.792$, $C_T = 0.00158$)

- BODY ROLL
- LOW FREQUENCY LEAD-LAG 2

$$I_{xx} = 6.44 \times 10^5 \text{ kg.m}^2 \sim 2.0 \times 10^6 \text{ kg.m}^2$$

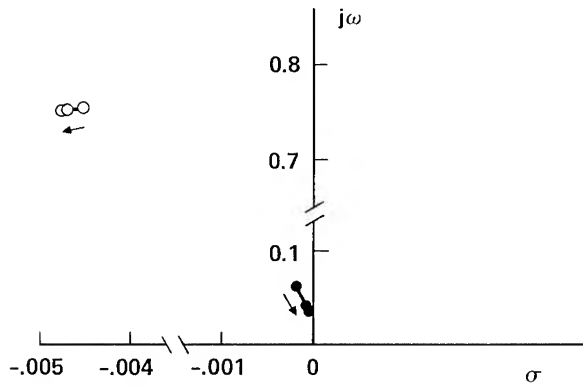


Fig. 11 Variation of Nondimensional Eigenvalues of Blade Lead-Lag Mode and Body Roll Mode with Increase in I_{xx} ($\bar{\omega}_{SBXY} = \bar{\omega}_{SBXZ} = 2.192$, $\bar{\omega}_{ST} = 1.754$, $I_{yy} = 2.59 \times 10^6 \text{ kg.m}^2$, $BR = 0.792$, $C_T = 0.00158$)

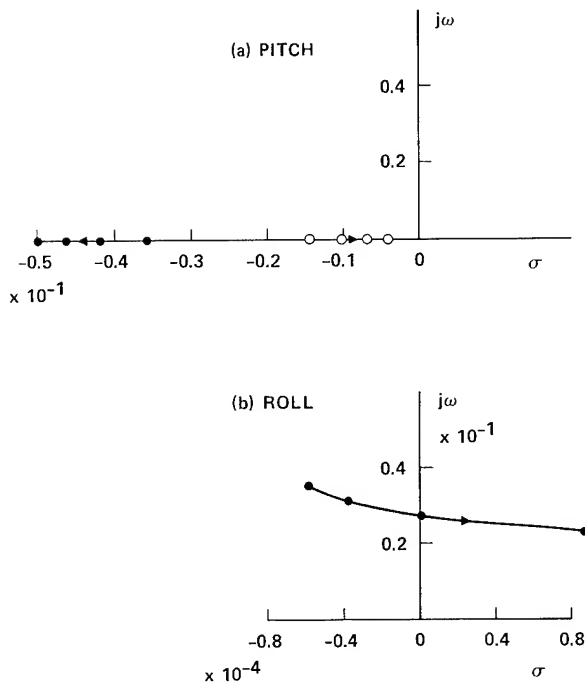


Fig. 13 Variation of Nondimensional Eigenvalues in (a) Body Pitch and (b) Body Roll Modes with Decrease in Buoyancy Ratio, $BR = 0.792, 0.7, 0.6, 0.5$ ($\bar{\omega}_{SBXY} = \bar{\omega}_{SBXZ} = 2.192$, $\bar{\omega}_{ST} = 1.754$, $I_{yy} = 4.75 \times 10^6 \text{ kg.m}^2$, $I_{xx} = 2.0 \times 10^6 \text{ kg.m}^2$)

- BENDING IN X-Y PLANE (HORIZONTAL)
- BENDING IN X-Z PLANE (VERTICAL)
- ◇ TORSION

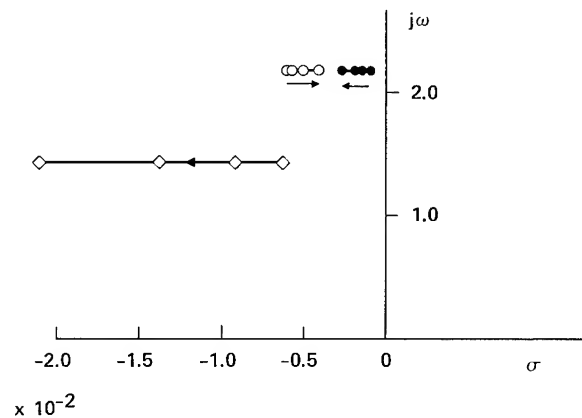


Fig. 12 Variation of Nondimensional Eigenvalues of the Supporting Structure Elastic Modes with Decrease in Buoyancy Ratio, $BR = 0.792, 0.7, 0.6, 0.5$ ($\bar{\omega}_{SBXY} = \bar{\omega}_{SBXZ} = 2.192$, $\bar{\omega}_{ST} = 1.754$, $I_{yy} = 4.75 \times 10^6 \text{ kg.m}^2$, $I_{xx} = 2.0 \times 10^6 \text{ kg.m}^2$)

Modes	Lead-lag Modes						Flap Modes					
	High frequency		Collective frequency		Low frequency		High frequency		Collective frequency		Low frequency	
	1	2	1	2	1	2	1	2	1	2	1	2
Supporting structure symmetric bending in x-y (horizontal) plane		XXX				XX						
Supporting structure symmetric bending in x-z (vertical) plane	XXX		X		XX				X			
Supporting structure torsion (antisymmetric)	XXX				XXX							
Body pitch		X		X		X				X		
Body roll		X				XX						

Legend:

XXX = Strongly coupled

XX = Moderately coupled

X = Weakly coupled

TABLE I COUPLING BETWEEN VARIOUS BODY MODES AND BLADE MODES

Buoyancy Ratio BR	θ_0	β_0	ζ_0	ϕ_0	λ	C_T
0.792	4.206°	2.302°	-3.963°	-0.115°	0.03272	.00158
0.7	5.243°	3.209°	-5.074°	-0.161°	0.03820	.00228
0.6	6.259°	4.179°	-6.453°	-0.236°	0.04313	.00304
0.5	7.207°	5.142°	-7.994°	-0.352°	0.04743	.00380

$$\bar{\omega}_{ST} = 1.754, \bar{\omega}_{SBXY} = \bar{\omega}_{SBXZ} = 2.192, I_{yy} = 4.74 \times 10^6 \text{ kg.m}^2, I_{xx} = 2.0 \times 10^6 \text{ kg.m}^2$$

TABLE II EQUILIBRIUM VALUES AT DIFFERENT BUOYANCY RATIOS

Appendix A

Blade data

The HHLA model (Fig. 2) has identical rotors.

Type of rotor: Articulated rotor

Number of blades N 4

Blade chord c = 2b 41.654 cm

Hinge offset e 30.48 cm

Rotor radius R 8.6868 m

Blade precone β_p 0

Distance between elastic center and aerodynamic center

X_A 0

Distance between elastic center and mass center X_I 0

Mass/unit length of the blade m 7.9529 kg/m

Principal mass moment of inertia of the blade/unit length I_{MB3} 1.1503x10⁻¹kg.m

I_{MB2} 6.6723x10⁻³kg.m

Aerodynamic data

Blade airfoil NACA 0012

Lift curve slope a 2 π

Lock number γ 10.9

Solidity ratio σ 0.0622

Density of air ρ_A 1.2256 kg/m³

Blade profile drag coefficient c_{d0} 0.01

Rotor R.P.M. Ω 217.79 R.P.M.

Nonrotating blade frequencies
(Articulated blade)

Flap frequency	$\omega_F = \left(\frac{K_S}{mR^3} \right)^{1/2}$	0
Lead-lag frequency	$\omega_L = \left(\frac{K_\zeta}{mR^3} \right)^{1/2}$	0
Torsional frequency	$\omega_T = \left(\frac{K_\phi}{mR^3} \right)^{1/2}$	(Assumed) 1.895 rad/sec
Damping in flap	ξ_{SF}	0
Damping in lead-lag	ξ_{SL}	0
Damping in torsion	ξ_{ST}	0

Vehicle data

Weight of fuselage F_1	W_{F1}	$3.5919 \times 10^4 \text{ N}$
Weight of fuselage F_2	W_{F2}	$3.5919 \times 10^4 \text{ N}$
Weight of underslung load	W_{UN}	0.0
Weight of envelope	W_{EN}	$8.5539 \times 10^4 \text{ N}$
Weight of supporting structure	W_S	$9.4302 \times 10^3 \text{ N}$
Weight of passenger compartment	W_S'	$6.6723 \times 10^3 \text{ N}$
(Treated as a lumped structural load attached at the point O_s on the structure (Fig. 2))		

Buoyancy on the envelope	P_z^S	$1.3748 \times 10^5 \text{ N}$
--------------------------	---------	--------------------------------

Geometric data

Distance between origin O_s and F_1	l_{F1}	-21.946m
Distance between origin O_s and F_2	l_{F2}	21.946m
Distance between origin O_s and underslung load (Assumed)	h_1	-15.24m
Distance between center-line and rotor hub	h_2	2.591m
Distance between center-line and center of volume of envelope	h_3	14.64m
Distance between center-line and C.G. of the envelope	h_4	8.544m
Distance between origin O_s and C.G. of the structure	h_5	0.0

Structural Dynamic Properties of the Supporting Structure

The supporting structure is modelled as an elastic structure with three normal modes of vibration: two normal modes for bending in vertical and in horizontal plane and one mode for torsion. The two bending modes are symmetric modes and the torsion is an anti-symmetric mode. It was assumed that the envelope and the underslung load are attached to the supporting structure at the origin O_s . The data given above shows that the vehicle is symmetric about Y-Z plane. Furthermore due to the presence of a heavy mass attached at the center (O_s) of the supporting structure, the mode shapes in bending and torsion for each half of the model are assumed to be the modes of a cantilever with a tip mass.

Modal Displacement at F_1 , F_2 and O_s

The symmetric mode shape in bending for each half of the supporting structure can be written as [Ref. 11, Page 140]

$$\eta_1 \left(\frac{X}{L} \right) = 6 \left(\frac{X}{L} \right)^2 - 4 \left(\frac{X}{L} \right)^3 + \left(\frac{X}{L} \right)^4$$

(Bending in X-Y plane)

and

$$\eta_2 \left(\frac{X}{L} \right) = 6 \left(\frac{X}{L} \right)^2 - 4 \left(\frac{X}{L} \right)^3 + \left(\frac{X}{L} \right)^4$$

(Bending in X-Z plane)

where X is the coordinate of any section of the supporting structure from origin O_s and L is the length of the supporting structure, $L = 21.946\text{m}$. The mode shape for torsion, for each half of the supporting structure is [Ref. 11, Page 99]

$$\eta_3 \left(\frac{X}{L} \right) = \sin \frac{\pi}{2} \left(\frac{X}{L} \right)$$

Generalized mass and stiffness data

Generalized mass and generalized stiffness for the i^{th} mode of vibration of the supporting structure is defined as

$$M = \int_{F1}^{F2} m \eta_i^2 dx$$

and

$$K = \omega_i^2 M$$

where ω_i is the i^{th} modal frequency

η_i is the i^{th} mode shape

and m is the mass per unit length (for bending modes), or m is the mass moment of inertia per unit length (for torsion modes).

Bending in x-y plane (horizontal)
generalized mass M_{SBXY} $6.801 \times 10^4 \text{ kg}$

Bending in x-z plane (vertical)
generalized mass M_{SBXZ} $6.801 \times 10^4 \text{ kg}$

Torsion
generalized mass M_{ST} $1.936 \times 10^4 \text{ kg.m}^2$

Appendix B

An equilibrium analysis is carried for the vehicle in hover, using the data given in Appendix A.

Total weight of the vehicle

$$\begin{aligned} W &= W_{EN} + W_S + W_{F1} + W_{F2} + W_{S1} + W_{UN} \\ &= 8.5539 \times 10^4 + .9430 \times 10^4 + 2 \times 3.5919 \times 10^4 \\ &\quad + .6672 \times 10^4 + 0 \\ &= 1.7348 \times 10^5 \text{ N} \end{aligned}$$

$$\text{Buoyancy of the envelope } P_z^S = 1.3748 \times 10^5 \text{ N}$$

$$\text{Weight to be supported by the rotors} = 0.36 \times 10^5 \text{ N}$$

$$\begin{aligned} \text{Thus each rotor has to develop a thrust} &= \\ 0.18 \times 10^5 \text{ N} \end{aligned}$$

Since the two rotors are identical and the model vehicle has a symmetry about y-z plane, the equilibrium values for both rotor systems are identical. They are:

Equilibrium

$$\text{Flap angle of the blade } \beta_0 = 2.302 \text{ degrees}$$

$$\text{Lead-lag angle } \zeta_0 = -3.963 \text{ degrees}$$

$$\text{Torsion angle } \phi_0 = -0.115 \text{ degrees}$$

$$\text{Inflow ratio } \lambda = 0.03272$$

Collective pitch angle of the blade

$$\theta_0 = 4.206 \text{ degrees}$$

Thrust coefficient for each rotor

$$C_T = 0.00158$$

$$\text{Buoyancy ratio } BR = 0.792$$

M.A.H. Dinyavari[†] and P.P. Friedmann^{††}
 Mechanics and Structures Department
 School of Engineering and Applied Science
 University of California
 Los Angeles, California 90024, U.S.A.

Abstract

Several incompressible finite-time arbitrary-motion airfoil theories suitable for coupled flap-lag-torsional aeroelastic analysis of helicopter rotors in hover and forward flight are derived. These theories include generalized Greenberg's theory, generalized Loewy's theory, and a staggered cascade theory. The generalized Greenberg's and staggered cascade theories were derived directly in Laplace domain considering the finite length of the wake and using operational methods. The load expressions are presented in Laplace, frequency, and time domains. Approximate time domain loads for the various generalized theories, discussed in the paper, are obtained by developing finite state models using the Pade approximant of the appropriate lift deficiency functions. Three different methods for constructing Pade approximants of the lift deficiency functions were considered and the more flexible one was used. Pade approximants of Loewy's lift deficiency function, for various wake spacing and radial location parameters of a helicopter typical rotor blade section, are presented.

Nomenclature

A_1, A_2	= constants defined by Eq. 14
a_i	= incompressible two dimensional lift curve slope
a_m	= coefficients in the numerator of the Dowell's form of approximation for the lift deficiency function
$\bar{a}bR$	= cross sectional elastic center (E.C.) offset from midchord
b_m	= time constants in the Dowell's form of rational approximation (coefficients in the denominator)
$bR, \bar{b}R$	= blade semi-chord $\bar{b}R = bR/\ell$
$C(k), C(\bar{s})$	= Theodorsen's lift deficiency function and its generalized form
$C'(k, \bar{m}_e, \bar{h}_e)$ $C'(\bar{s}, \bar{s}r_e, \bar{s}h_e)$	= Loewy's lift deficiency function and its generalized form

$C''(\bar{s}, \bar{T}_{Re}, \bar{T}_{He})$	= cascade wake model lift deficiency function in the Laplace and frequency domains
$C''(ik, \bar{T}_{Re}, \bar{T}_{He})$	
C_T	= rotor thrust coefficient
e	= offset of the elastic blade root from the rotor axis of rotation
$(\hat{e}_x, \hat{e}_y, \hat{e}_z)$	= triad of undeformed precone rotating blade unit vectors (Figs. 4 and 5)
$(\hat{e}'_x, \hat{e}'_y, \hat{e}'_z)$	= triad of deformed blade section unit vectors, coincident with $(\hat{e}_x, \hat{e}_y, \hat{e}_z)$ prior to deformation (Fig. 5)
$(\hat{e}''_x, \hat{e}''_y, \hat{e}''_z)$	= triad of untwisted deformed blade section unit vectors obtained by rotating $(\hat{e}'_x, \hat{e}'_y, \hat{e}'_z)$ by the amount $-\phi$ (Fig. 5)
$(F, G), (F', G')$ (F'', G'')	= real and imaginary parts of $C, C',$ and C'' , respectively
$F(\bar{s}; n, m, \bar{T}_{Re}, \bar{T}_{He})$	= a family of double integrals defined by Eq. 22b
$H_n^{(2)}(k)$	= Hankel function of the second kind of order $n: H_n^{(2)} = J_n - iY_n$
$\Delta h(t)$	= vertical displacement of elastic center for the airfoil, positive downward
Δh_0	= amplitude of $\Delta h(t)$ in the simple-harmonic motion case
$h, \bar{h}_e, \bar{h}, \bar{h}_e$	= vertical wake spacing beneath the the rotor in Loewy's model for single and multi-bladed rotors; $\bar{h}_e = h/Q, (\bar{\cdot}) = (\cdot)/bR, h = 2\pi U_{p0}/\Omega$
H^*, H_e^*	= vertical wake spacing beneath the rotor, cascade wake model theory for single and multi-bladed rotors; $H^* = h, H_e^* = \bar{h}_e$
i	= $\sqrt{-1}$
$\hat{i}, \hat{j}, \hat{k}$	= unit vectors in the directions of the rotating blade-fixed coordinate system

* This work was supported by NASA Ames Research Center under grant NASA NAG 2-209.

[†] Research Assistant, Student Member AIAA and AHS.

^{††} Professor of Engineering and Applied Science, Associate Fellow AIAA.

$I_n(\)$	= modified Bessel function of the first kind of order n	$r, r_e, \bar{r}, \bar{r}_e$	= radial station for the blade section; $r_e = r/Q$, $(\bar{\ }) = (\)/bR$
$IN(ik:n,m,\bar{T}_{Re},\bar{T}_{He})$	= a family of double integrals associated with the numerator and denominator of cascade wake model lift deficiency function defined by Eqs. (23b) and (23c)	s, \bar{s}	= Laplace transform variable: $s = (sbR/U_{T0})$
$ID(ik:n,m,\bar{T}_{Re},\bar{T}_{He})$		$T_H, T_{He}, \bar{T}_H, \bar{T}_{He}$	= time required for a fluid particle to travel one wake spacing with the mean oncoming flow velocity U_{T0} ; $T_H = H^*/U_{T0}$, $T_{He} = H^*/U_{T0}$, $(\bar{\ }) = (\)/T$ (Note: $\bar{T}_H = \bar{h}$, and $\bar{T}_{He} = \bar{h}_e^{sc}$)
$J_n(\)$	= Bessel function of the first kind of order n		
$K_n(\)$	= modified Bessel function of the second kind of order n		
k	= reduced frequency; $k = \omega bR/U_{T0}$	$T_R, T_{Re}, \bar{T}_R, \bar{T}_{Re}$	= time required for a fluid particle to travel the distance between identical airfoils on consecutive blades with the mean oncoming flow velocity U_{T0} ; $T_R = 2\pi r/U_{T0}$, $T_{Re} = 2\pi r_e/U_{T0}$, and $(\bar{\ }) = (\)/T_{sc}$
ℓ	= length of the elastic part of the blade		
$L(t), L_C(t), L_{NC}(t)$	= total, circulatory, and non-circulatory components of lift	T_{sc}	= time required for a fluid particle to travel the semichord length bR with the mean oncoming velocity U_{T0} ; $T_{sc} = bR/U_{T0}$
$\bar{L}_{Ce}, \bar{L}_{Nc}$	= nondimensional circulatory and noncirculatory components of the lift per unit rotor blade length in \hat{e}_z direction for the equilibrium and perturbation states; $(\bar{\ }) = (\)/[a_1 \rho_A (bR) (\Omega \ell)^2]$	$U_T(t), U_p(t)$	= freestream velocity in x^* , and negative z^* directions respectively; $U_T(t) = U_{T0} + \Delta U_T(t)$, $U_p(t) = U_{p0} + \Delta U_p(t)$
$\Delta \bar{L}_C(\psi), \Delta \bar{L}_{NC}(\psi)$		ΔU_{p0}	= amplitude of $\Delta U_p(t)$ for the case of simple harmonic motion
$M(t), M_C(t), M_{NC}(t)$	= total, circulatory and non-circulatory components of moment	U_x'', U_y'', U_z'' $\bar{U}_x'', \bar{U}_y'', \bar{U}_z''$	= components of blade cross section elastic center velocity vector relative to air in \hat{e}_x'' , \hat{e}_y'' , and \hat{e}_z'' directions; $(\bar{\ }) = (\)/\Omega \ell$
$\bar{M}_{Ce}, \bar{M}_{Nc}$	= nondimensional circulatory and noncirculatory components of the moment per unit rotor blade length in direction \hat{e}_x'' for the perturbation and equilibrium states; $(\bar{\ }) = (\)/[a_1 \rho_A (bR) (\Omega \ell)^2]$	$U_{ye}'', U_{ze}'', \Delta \bar{U}_y''(\psi), \Delta \bar{U}_z''(\psi)$	= equilibrium and perturbation components of \bar{U}_y'' and \bar{U}_z''
\bar{m}, \bar{m}_e	= frequency ratio: $\bar{m} = \omega/\Omega$, $\bar{m}_e = \omega/\Omega Q$ (collective mode)	u, v, w $\bar{u}, \bar{v}, \bar{w}$	= blade displacement components in x_0, y_0 , and z_0 direction (see Fig. 5); $(\bar{\ }) = (\)/\ell$
NL	= number of wake layers beneath the rotor included in the cascade wake model lift deficiency function	$\bar{u}_e, \bar{v}_e, \bar{w}_e$ $\Delta \bar{u}(\psi), \Delta \bar{v}(\psi), \Delta \bar{w}(\psi)$	= nondimensional blade displacement components for the equilibrium and perturbation states
NP	= number of poles in the Pade approximant of the lift deficiency function	$\Delta \bar{v}_0, \Delta \bar{w}_0$	= the complex amplitude of the perturbation lead-lag and flap displacements for the case of decaying, stable or increasing oscillations
$\bar{P}_F, \bar{P}_L, \bar{P}_P, \bar{P}_{if}$	= nondimensional complex frequencies in flap, lag, torsion, and unsteady inflow for the decaying stable or increasing blade motion; $(\bar{\ }) = (\)/\Omega$	$W(k\bar{h}_e, \bar{m}_e), W(s\bar{h}_e, s\bar{r}_e)$	= Loewy's wake weighting function and its generalized form
$Q(t), Q(s)$	= downwash velocity at the 3/4 chord point; $Q(s) = \mathcal{L}[Q(t)]$	X, Z	= coordinate axes in Joukowski's plane (Fig. 2)
Q	= number of blades	x^*, z^*	= coordinate axes in plane of airfoil (Fig. 1)
$\bar{Q}(\psi), \bar{Q}_e, \Delta \bar{Q}(\psi)$	= nondimensional 3/4-chord point downwash velocity of blade sections in the negative \hat{e}_z'' direction; $(\bar{\ }) = (\)/\Omega \ell$	$X_0^*(\tau)$	= location of trailing edge of the wake behind the reference airfoil at time $t = \tau$ (Figs. 2 & 15)
R, \bar{R}	= blade radius; $R = (R/\ell)$		

$x_n^*(\tau)$	= location of trailing edge of wake behind the n-th imaginary airfoil below the reference airfoil at time $t = \tau$ in the cascade wake model theory (Fig. 15)	$\Delta\phi_0$	= amplitude of $\Delta\phi(\psi)$ for the case of simple harmonic motion
$x_1(t), x_2(t), \bar{x}_1(\psi), \bar{x}_2(\psi), \bar{x}_{1e}, \bar{x}_{2e}, \Delta\bar{x}_1(\psi), \Delta\bar{x}_2(\psi)$	= the augmented aerodynamic state variables; $\bar{x}_1 = (\Omega/\ell)(x_1)$, $\bar{x}_2 = (1/\ell)(x_2)$	ψ	= azimuth angle of blade from straight aft position: $\psi = \Omega t$
x_A, \bar{x}_A	= blade actual cross sectional aerodynamic center (A.C.) offset from elastic center (E.C.), positive for A.C. in front of E.C.; $(\bar{x}_A) = (x_A)/bR$	Ω	= rotor speed of rotation
$Y_n(\)$	= Bessel function of second kind of n th order	$\omega_\alpha, \omega_h, \omega_v, \omega_{if}$	= frequency of steady state simple harmonic oscillations in pitch and plunge motions and oncoming and inflow velocities, respectively
$\alpha(t), \alpha_0, \Delta\alpha(t)$	= time variant angle of incidence of the airfoil around the elastic center, measured clockwise from the horizontal x^* axis (Fig. 1); $\alpha(t) = \alpha_0 + \Delta\alpha(t)$	$(\dot{\ })$ or $(\)'$	= $\partial/\partial t$
$\Delta\alpha_0$	= amplitude of $\Delta\alpha(t)$ for the case of simple harmonic motion	$(^*)$	= $\partial/\partial\psi = \partial/\Omega\partial t$
β_p	= precone angle of the blade	$(\)'$	= $\partial/\partial(\bar{x}_0)$
$\gamma_a(\xi^*, t)$	= bound vortex strength distribution, positive clockwise	$\mathcal{L}[\]$	= Laplace transform operator
γ_e	= Euler's constant		
$\gamma_\omega(\xi^*, \tau)$	= wake vortex strength distribution behind the airfoil at time $t = \tau$, positive clockwise		
$\gamma_t(t')$	= trailing edge vortex strength shed at time $t = \tau'$		
θ_G	= total geometric pitch angle about feathering axis for the blade cross section (Fig. 5)		
$\lambda, \lambda_e, \Delta\lambda(\psi)$	= inflow ratio and its equilibrium and perturbation components		
$\Delta\lambda_0$	= complex amplitude of perturbation inflow for decaying, stable or increasing motion		
λ_1, λ_2	= the eigenvalues of the system of differential equations for augmented states (Eq. 13)		
$\xi^*(t', \tau)$	= location of the vortex which was shed at time $t = t'$ observed at time $t = \tau$		
ρ_A	= air density		
σ	= a number determining the magnitude of stream fluctuations for the case of simple harmonic motion		
$\phi, \phi_e, \Delta\phi(\psi)$	= torsional elastic deflection of the blade about the elastic axis		

1. Introduction and Problem Statement

Modeling of unsteady aerodynamic loads required for rotary aeroelastic analysis presents major challenges to the analyst. When dealing with this complex problem a wide array of assumptions can be made which lead to a variety of models, starting with simple and computationally efficient models and culminating in computationally expensive models which are capable of simulating the more intricate details of the unsteady flow. Most rotary-wing aeroelastic analyses use unsteady or quasisteady two dimensional aerodynamic theories and neglect three dimensional effects except near the blade tips where these effects are important. All unsteady aerodynamic expressions used in theories which have closed form analytical solutions are based on the assumption of simple harmonic motion. In this study, such theories will be referred to as frequency domain theories.

A brief summary of frequency domain type theories developed for either fixed wing or rotary wing applications is provided here for convenience; Theodorsen's incompressible fixed-wing theory¹; Greenberg's theory which extends Theodorsen's theory to account for pulsating velocity and constant angle of attack² and its modification by Kottapalli and Pierce³; Loewy's rotary wing theory for hover which accounts approximately for the effects of the returning wake^{4,5}; Jones and Rao's theory⁶ and Hammond and Pierce's theory⁷ which are extensions of Loewy's theory accounting for effects of compressibility; Friedmann and Yuan's modification of these strip theories accounting for fully coupled flap-lag-torsional dynamics⁸; and Shipman and Wood's theory⁹ which attempts to account for forward flight and certain returning wake effects in an approximate manner.

An important shortcoming of these theories is that they are suitable only for determining stability boundaries in aeroelastic problems, since the assumption of simple harmonic motion holds only at the stability boundary. Thus standard stability analysis techniques such as the root locus method cannot be used in conjunction with these theories and special techniques representing variations on the well known V-g method have to be used.

The prevalence of frequency domain theories can be attributed to two reasons: (1) Exact closed-

form solutions for aerodynamic pressure distributions and loads do not exist in terms of familiar mathematical functions, unless the motion of airfoil is restricted to steady state simple harmonic form. (2) Historically the earlier attempts to deal with arbitrary motion encountered some computational difficulties due to a mathematical error in analytical continuation of certain Bessel functions. It should be emphasized that in this paper the term arbitrary motion is used to denote growing or decaying oscillations with a certain frequency. Edwards¹⁰ circumvented these difficulties for the case of a two-dimensional airfoil oscillating in incompressible flow. The most serious objection to the previous attempts to directly generalize the Theodorsen's lift deficiency function has been that Theodorsen's wake model extends to infinity behind the airfoil and is not directly applicable to finite-time arbitrary motion. Sears¹¹ had previously applied operational techniques to a finite wake model, due to evolution of the motion, to solve the Wagner indicial lift problem. However the generality of this formulation was left unrecognized for over three decades. Edwards recognized the generality of this derivation and showed that the generalized Theodorsen's lift deficiency function acts as a Laplace domain operator between the Laplace transforms of the circulatory loads and the $3/4$ -chord downwash velocity, for any arbitrary finite time motion. Rock¹² presented the experimental verification of arbitrary-motion incompressible aerodynamic theories of the type developed by Edwards by comparing analytically obtained aeroelastic root loci with experimentally identified ones. Due to the use of a small wind tunnel for testing, Rock was forced to generalize Timman's Theory¹³ to arbitrary motions by replacing the reduced frequency (ik) by the Laplace transform variable (s).

There are a number of aeroelastic stability and response calculations where it is convenient and important to be able to model arbitrary motions in both Laplace and time domains. Some typical examples for such cases are: 1) Aeroelastic systems with geometric nonlinearities, which are typical of many rotary-wing applications. 2) Rotary-wing aeroelastic problems in forward flight, where time domain unsteady aerodynamics are much more convenient to use due to the presence of periodic coefficients in the equations of motion. 3) Simulation of subcritical flutter testing of rotors where the determination of damping levels is important before actual flutter boundaries are encountered. 4) Calculation of aerodynamic loads in the sub-stall regions of rotor blades which undergo dynamic stall in a certain portion of their periodic motion. 5) Treatment of rotary-wing aeroelastic systems with feedback control systems, such as higher harmonic controls in helicopters. Despite these needs, to this date there is a lack of unsteady strip theories which have the capability for arbitrary motion modeling intended for rotary-wing applications.

The primary objective of this paper is to present several incompressible finite-time arbitrary-motion airfoil theories suitable for coupled flap-lag-torsional aeroelastic analysis of rotary wings in hover and forward flight. An important attribute of these theories is their validity for subcritical as well as supercritical conditions. These theories can be applied to the development of augmented state (finite state) aeroelastic models for rotary-wing problems.

Two types of theories are considered in this study; theories which ignore the effect of returning wake beneath the rotor and theories which include this effect. It is well known that depending on rotor loading and flight conditions the returning wake effects can be either very important or they can be less important.

In the first part of the paper, Greenberg's theory is extended to arbitrary motion in both the Laplace and time domains, for both hover and forward flight. An example illustrating the application of this theory to the calculation of the unsteady lift and moment on a typical blade cross section undergoing coupled flap-lag-torsional motion is presented.

Next, two separate theories representing extensions of Loewy's theory (which includes the effects of the returning wake), for the case of arbitrary motions are also presented. Different Pade approximants for the unsteady loads are obtained, and numerical results showing the accuracy of various approximations are given.

The detailed derivations of these theories are not presented here, due to their length. However, the final detailed expressions obtained from these theories are presented, for the unsteady loads with and without the effects of the returning wake for both decaying and growing oscillations.

It is envisioned that the arbitrary-motion unsteady aerodynamic theories presented in this paper will make a useful contribution towards improving the state-of-the-art in unsteady aerodynamic modeling for rotary-wing applications.

2. Arbitrary Motion Unsteady Airfoil Theory, Without Returning Wake Effects, for Rotary-Wing Applications

2.1 Extension of Greenberg's Theory to Arbitrary Motion

Greenberg's theory² has received considerable attention in rotary-wing aeroelasticity in recent years^{3,8,14-21}. This theory models approximately the effect of time-varying free stream velocity, resulting either from lead-lag motion or the forward flight speed, and nonzero steady state angle of incidence. Subsequently Greenberg's theory was modified by Friedmann and Yuan^{6,14} to incorporate returning wake effects and constant inflow at the blade section. This was simply achieved by replacing Theodorsen's lift deficiency function in Greenberg's expressions for lift and moment by Loewy's modified lift deficiency function, and by incorporating in the downwash velocity expression with the appropriate inflow velocity.

In this study an approach similar to that used by Edwards¹⁰, to generalize Theodorsen's theory¹, is applied to Greenberg's theory. Expressions for the calculation of unsteady lift and moment of an airfoil undergoing arbitrary plunge and pitch motion about a steady pitch angle in presence of time-varying oncoming velocity and variable inflow are obtained. The aerodynamic loads are derived in Laplace, frequency, and time domains. The time-varying oncoming velocity allows for modeling streamwise blade motion as well as time variation of velocity due to forward flight. Similar to Greenberg's theory, the flow is assumed to be two-

dimensional, incompressible, and irrotational. In addition, the disturbances due to airfoil motion and the free-stream fluctuations are assumed to be small.

The geometry of motion of a typical airfoil is illustrated in Fig. 1. The unsteady aerodynamic problem is linear, thus the solution may be obtained as the superposition of mean-camber line and thickness problems. Due to symmetry the thickness problem can not provide any lift or moment, hence it is not discussed. Furthermore, the camber-line problem can be also separated into two problems; namely, (1) a flat plate in motion about a non-zero incidence angle, representing a symmetric airfoil, and (2) a stationary cambered airfoil with zero thickness at zero incidence.

Due to its length, the complete mathematical derivation of the expressions for the unsteady lift and moment is not presented in this paper. Only the essential elements of the derivation are outlined here, and some of the more important equations are presented. The complete mathematical details and the lengthy equations are presented in Ref. 29.

The governing equations for this problem consist of the boundary conditions of zero disturbance upstream at infinity, tangent velocity over the airfoil, Kutta condition at the trailing edge, zero pressure discontinuity on the wake, and the condition of conservation of circulation. The solution is obtained from the combination of two contributions representing circulatory and noncirculatory flows, respectively. The noncirculatory portion of the flow is obtained by placing an appropriate distribution of sources and sinks on the upper and lower surfaces of the airfoil so that the tangent-flow boundary condition is satisfied at every instant of time. The expressions for the noncirculatory loads in the time domain for any arbitrary motion are given by

$$L_{NC}(t) = \rho_A \pi (bR)^2 \{ [\Delta \dot{h}(t) - U_p(t)] + U_T(t) \Delta \dot{\alpha}(t) + \dot{U}_T(t) [\alpha_0 + \Delta \alpha(t)] - \bar{a} b R \Delta \ddot{\alpha}(t) \} \quad (1a)$$

$$M_{NC}(t) = \rho_A \pi (bR)^3 \{ (\bar{a} - \frac{1}{2}) U_T(t) \Delta \dot{\alpha}(t) + \bar{a} [\Delta \dot{h}(t) - U_p(t)] + \bar{a} \dot{U}_T(t) [\alpha_0 + \Delta \alpha(t)] - b R (\frac{1}{8} + \bar{a}^2) \Delta \ddot{\alpha}(t) \} \quad (1b)$$

It should be noted that the portion of the moment which cancels out between noncirculatory and circulatory parts is left out. The above expressions can readily be converted to the frequency and Laplace domains.

To satisfy the Kutta condition a circulatory flow must be added. A pattern of vortices is placed on the segment of the wake which has been influenced by the shed vortices since the beginning of the motion. In addition bound vortices which are images of the wake vortices are placed on the airfoil. The bound vortices are located so that the normal velocity on the airfoil due to circulatory flow is zero at every instant of time, hence the tangent-flow boundary condition, already satisfied by noncirculatory flow, remains valid. This

concept is illustrated in Figs. 2-3. The imposition of Kutta condition yields a singular integral equation over the finite wake length of the shed vortices in terms of wake vortex strength

$$- \frac{1}{2\pi bR} \int_{bR}^{X_0^*(\tau)} \sqrt{\frac{\xi^* + bR}{\xi^* - bR}} \gamma_w(\xi^*, \tau) d\xi^* = Q(\tau) \quad (2a)$$

where

$$Q(t) = U_T(t) [\alpha_0 + \Delta \alpha(t)] + [\Delta \dot{h}(t) - U_p(t)] + bR(\bar{a} - \frac{1}{2}) \Delta \dot{\alpha}(t) \quad (2b)$$

The circulatory lift and moment in terms of the wake vortex distribution are given by

$$L_C(t) = - \rho_A U_T(t) \int_{bR}^{X_0^*(\tau)} \frac{\xi^*}{\sqrt{\xi^{*2} - (bR)^2}} \gamma_w(\xi^*, \tau) d\xi^* \quad (3a)$$

$$M_C(t) = \rho_A (bR) U_T(t) \int_{bR}^{X_0^*(\tau)} [\frac{1}{2} \sqrt{\frac{\xi^* + bR}{\xi^* - bR}} - (\bar{a} + \frac{1}{2}) \frac{\xi^*}{\sqrt{\xi^{*2} - (bR)^2}}] \gamma_w(\xi^*, \tau) d\xi^* \quad (3b)$$

The condition of zero pressure discontinuity across the wake requires the vortices shed at the trailing edge to travel downstream with the freestream velocity

$$\frac{\partial \xi^*}{\partial t} = - U_T(t') \quad (4a)$$

where ξ^* is the position of a vortex shed at time t' as a function of time τ and can be expressed in terms of the oncoming velocity as

$$\xi^*(t', \tau) = bR + \int_{t'}^{\tau} U_T(t) dt \quad (4b)$$

Using the exact downstream velocity of shed vortices, but assuming a mean value for their position, yields

$$\xi^*(t', \tau) \approx bR + U_{T0}(\tau - t') \quad (4c)$$

A change of variable from position along the wake to the time variable can be introduced. Using this change of variable, the integral equation of downwash (Eq. 2a) and the circulatory lift and moment expressions (Eqs. 3) can be transformed into convolution form. Application of Laplace transformation to the integral equation of downwash and the circulatory loads in the convolution form allows for the elimination of the unknown trailing edge vortex strength, and the solution for the circulatory lift and moment in the Laplace domain as

$$\mathcal{L} \left[\frac{L_C(t)}{U_T(t)} \right] = 2\pi \rho_A (bR) C(\bar{s}) \mathcal{L} [Q(t)] \quad (5a)$$

$$\mathcal{L} \left[\frac{M_C(t)}{U_T(t)} \right] = 2\pi \rho_A (bR)^2 (\bar{a} + \frac{1}{2}) C(\bar{s}) \mathcal{L} [Q(t)] \quad (5b)$$

where

$$C(\bar{s}) = \frac{K_1(\bar{s})}{K_1(\bar{s}) + K_0(\bar{s})}, \quad \bar{s} = \frac{sbR}{U_0} \quad (5c)$$

From Eq. (5c) is evident that the lift deficiency function $C(\bar{s})$, identical to generalized Theodorsen's lift deficiency function, acts as a Laplace domain operator between the 3/4-chord downwash velocity and the circulatory loads divided by the time-varying oncoming velocity.

Whereas Edwards' generalized Theodorsen's theory is directly applicable to Laplace-domain aeroelastic analysis using iterative search procedures for finding aeroelastic roots¹⁰, the theory discussed above is not. The reason is that the present theory does not yield the Laplace transform of the circulatory loads themselves, instead it gives the Laplace transform of the circulatory loads divided by the time-varying oncoming velocity. This feature does not pose any difficulty in the case of finite state time domain representation. This is due to the fact that in the time domain the time-varying oncoming velocity can be simply transferred to the right hand side of the equations, which results in a direct expressions for the loads.

2.1.1 Frequency Domain Representation

Assuming steady state simple harmonic form for the airfoil motion as well as for the far field velocities yields

$$\begin{aligned} \Delta h(t) &= \Delta h_0 e^{i\omega_h t}, & k_h &= \frac{\omega_h bR}{U_0} \\ \Delta \alpha(t) &= \Delta \alpha_0 e^{i\omega_\alpha t}, & k_\alpha &= \frac{\omega_\alpha bR}{U_0} \\ U_T(t) &= U_0(1 + \sigma e^{i\omega_v t}), & k_v &= \frac{\omega_v bR}{U_0} \\ U_p(t) &= U_{p0} + \Delta U_{p0} e^{i\omega_{if} t}, & k_{if} &= \frac{\omega_{if} bR}{U_0} \end{aligned} \quad (6)$$

The exact frequency domain circulatory load expressions for the steady state simple harmonic motion are derived by performing inverse Laplace transform of Eqs. (5) using the Bromwich inversion integral, Cauchy's theorem and the calculus of residues

$$\begin{aligned} L_C(t) &= 2\pi\rho_A bRU_T(t) \{ (U_0\alpha_0 - U_{p0}) + \sigma U_0\alpha_0 C(k_v) e^{i\omega_v t} \\ &\quad + C(k_\alpha) [bR(\frac{1}{2} - a)\dot{\Delta\alpha}(t) + U_0\Delta\alpha(t)] \\ &\quad + C(k_h)\dot{\Delta h}(t) - C(k_{if})\Delta U_p(t) + \sigma U_0\Delta\alpha(t) C(k_v + k_\alpha) e^{i\omega_v t} \} \end{aligned} \quad (7a)$$

$$M_C(t) = bR(\bar{a} + \frac{1}{2}) L_C(t) \quad (7b)$$

When inflow is set to zero, these equations reduce to the classical Greenberg's relations. This serves as the formal proof that the wake assumption made in deriving the arbitrary motion theory is consistent with that made by Greenberg.

2.1.2 Finite State Time Domain Representation

In his study of unsteady lift on fixed wings, of finite aspect ratio, Jones²² used an operational method. Jones expressed the lift on each unit strip as a convolution integral of Wagner's indicial lift function for infinite wings with an effective downwash velocity. The effective downwash velocity includes both the induced downwash velocity due to the motion of the entire wing and the physical downwash velocity due to the motion of the wing section itself. Using Ref. 22 a generalized Theodorsen lift deficiency function, in the Laplace domain, can be obtained as²⁹

$$C(\bar{s}) = \frac{0.5(\bar{s})^2 + 0.2808(\bar{s}) + 0.01365}{(\bar{s})^2 + 0.3455(\bar{s}) + 0.01365} \quad (8)$$

Several researchers have constructed higher order Pade approximants for the generalized Theodorsen's lift deficiency function using various least squares techniques or by truncating a continued fraction series²³⁻²⁵. However the second order Pade approximant obtained from Jones approximation of the indicial lift has proved itself to be both accurate and efficient^{23,24}. These higher order approximations yield only limited additional accuracy and substantially increase the size of the problem. Using the Pade approximant given in Eq. (8), a second order finite-state time domain representation of the circulatory loads is obtained in terms of the airfoil degrees of freedom and their time derivatives, and two additional augmented state variables

$$\begin{aligned} L_C(t) &= 2\pi\rho_A(bR)U_T(t) [0.00685(U_{T0}/bR)^2 X_1(t) \\ &\quad + 0.10805(U_{T0}/bR) X_2(t)] + \pi\rho_A(bR)U_T(t)Q(t) \end{aligned} \quad (9a)$$

$$M_C(t) = (bR)(\bar{a} + \frac{1}{2}) L_C(t) \quad (9b)$$

The augmented state variables X_1 and X_2 are governed by a system of ordinary differential equations which is associated with the 3/4-chord downwash velocity $Q(t)$

$$\begin{aligned} \begin{Bmatrix} \dot{X}_1(t) \\ \dot{X}_2(t) \end{Bmatrix} &= \begin{bmatrix} 0 & 1 \\ -0.01365(U_{T0}/bR)^2 & -0.3455(U_{T0}/bR) \end{bmatrix} \begin{Bmatrix} X_1(t) \\ X_2(t) \end{Bmatrix} \\ &\quad + \begin{Bmatrix} 0 \\ Q(t) \end{Bmatrix} \end{aligned} \quad (10)$$

Where the augmented states, Eq. (10), have to be appended to the equations of motion of the blade.

3. Application to Helicopter Rotor Blade Sections in Hover and Forward Flight

The two dimensional arbitrary motion airfoil theory in time domain described above is applied to a unit strip of a flexible hingeless helicopter rotor blade undergoing flap, lead-lag, and torsional motion in hover or forward flight. The undeformed and deformed blade geometry is illustrated by Figs. 4-6. The blade is assumed to have a blade root offset, precone, and pretwist. The undeformed elastic axis of the blade is assumed to

be a straight line. The rotary-wing aeroelastic problem, for hingeless or bearingless type of rotor blades is known to be sensitive to geometrically nonlinear effects due to moderate deflections^{15,16}. Therefore these geometrically nonlinear terms have to be incorporated in the aerodynamic, structural, and inertia operators associated with this aeroelastic problem.

The preconed undeformed blade coordinate system together with the deformed blade coordinate system ($\hat{e}_x'', \hat{e}_y'', \hat{e}_z''$) are shown in Fig. 5. The position of a typical blade cross section before and after the deformation is shown in Fig. 6. The ($\hat{e}_x'', \hat{e}_y'', \hat{e}_z''$) coordinate system, shown in Fig. 6, is one which excludes the contribution of the time-varying twist. The proper evaluation of aerodynamic loads requires identification of the components of the velocity vector of the elastic center, due to motion, relative to the oncoming airflow in the directions \hat{e}_y'' and \hat{e}_z'' , denoted by U_y'' and U_z'' . This is accomplished by writing the position vector of a point on the blade elastic axis in its deformed state, in the blade fixed rotating system, and differentiating it with respect to time to obtain the velocity due to the blade motion. Combining the velocities due to the airflow with those due to the blade motion and applying an ordering scheme¹⁶ yields the expressions for the relative velocity of the elastic axis with respect to the air in the deformed blade coordinate system (U_y'', U_z''). The velocities and incidence angles required for the two-dimensional theories can be identified in terms of relative elastic center velocities U_y'' and U_z'' and blade elastic and geometric twist angle.

Using these velocities and incidence angles and combining them with the time domain aerodynamic theory described in Section 2.1.2 yields the expressions for both equilibrium and perturbational aerodynamic lift and moment for a typical blade section undergoing coupled flap-lag-torsional motion in hover. For the equilibrium condition in hover, these reduce to the usual expressions for the static lift and moment. The perturbational loads for a general motion of the blade in hover are given by the noncirculatory contribution

$$\Delta \bar{L}_{NC}(\psi) = (b\bar{R}/2) \{ \bar{U}_{ye}'' \Delta \phi^* + \Delta \bar{U}_y'' \Delta \phi^* - \Delta \bar{U}_z'' b\bar{R}(\bar{x}_A - \frac{1}{2}) \Delta \phi^* + (\theta_G + \phi_e) \Delta \bar{U}_y'' + \Delta \phi \Delta \bar{U}_y'' \} \quad (11a)$$

$$\Delta \bar{M}_{NC}(\psi) = (b\bar{R}/2) \{ (\bar{x}_A - 1) \bar{U}_{ye}'' \Delta \phi^* - (\bar{x}_A - \frac{1}{2}) \Delta \bar{U}_z'' + (\bar{x}_A - \frac{1}{2}) (\theta_G + \phi_e + \Delta \phi) \Delta \bar{U}_y'' - b\bar{R}(3/8 + \bar{x}_A^2 - \bar{x}_A) \Delta \phi^* \} \quad (11b)$$

and the circulatory contribution

$$\begin{Bmatrix} \Delta \bar{X}_1(\psi) \\ \Delta \bar{X}_2(\psi) \end{Bmatrix} = \begin{bmatrix} 0 & -1 \\ -0.01365 \left(\frac{\bar{U}_0}{b\bar{R}} \right)^2 & -0.3455 \left(\frac{\bar{U}_0}{b\bar{R}} \right) \end{bmatrix} \begin{Bmatrix} \Delta \bar{X}_1(\psi) \\ \Delta \bar{X}_2(\psi) \end{Bmatrix} + \begin{Bmatrix} 0 \\ \Delta \bar{Q}(\psi) \end{Bmatrix} \quad (12a)$$

where

$$\Delta \bar{X}_1(0) = \Delta \bar{X}_2(0) = 0 \quad (12b)$$

$$\begin{aligned} \Delta \bar{L}_C(\psi) = & [\bar{U}_{ye} + \Delta \bar{U}_y''(\psi)] \left\{ 0.006825 \left(\frac{\bar{U}_0}{b\bar{R}} \right)^2 \Delta \bar{X}_1(\psi) + \right. \\ & 0.10805 \left(\frac{\bar{U}_0}{b\bar{R}} \right) \Delta \bar{X}_2(\psi) \} + [\bar{U}_{ye}''(\theta_G + \phi_e) - \bar{U}_{ze}''] \Delta \bar{U}_y''(\psi) + \\ & \frac{1}{2} [\bar{U}_{ye}'' + \Delta \bar{U}_y''(\psi)] \{ \bar{U}_{ye}'' \Delta \phi + [\theta_G + \phi_e + \Delta \phi(\psi)] \Delta \bar{U}_y''(\psi) \\ & - \Delta \bar{U}_z''(\psi) + b\bar{R}(1 - \bar{x}_A) \Delta \phi^*(\psi) \} \end{aligned} \quad (12c)$$

$$\Delta \bar{M}_C(\psi) = \bar{X}_A \Delta \bar{L}_C(\psi) \quad (12d)$$

Using the theory of ordinary differential equations with constant coefficients, the solution of Eqs. (12a) with the initial conditions of Eq. (12b) can be expressed in a Duhamel's integral form as

$$\begin{Bmatrix} \Delta \bar{X}_1(\psi) \\ \Delta \bar{X}_2(\psi) \end{Bmatrix} = \frac{1}{(\lambda_2 - \lambda_1)} \int_0^\psi \left\{ \frac{\lambda_2(\psi - \psi')}{\lambda_2 e^{\lambda_2(\psi - \psi')}} - \frac{\lambda_1(\psi - \psi')}{\lambda_1 e^{\lambda_1(\psi - \psi')}} \right\} \Delta \bar{Q}(\psi') d\psi' \quad (13)$$

where $\lambda_1 = -0.0455 (\bar{U}_0/b\bar{R})$, and $\lambda_2 = -0.3000 (\bar{U}_0/b\bar{R})$. Hence the expression associated with the augmented state appearing in the loads can be expressed as

$$\begin{aligned} [0.006825 \left(\frac{\bar{U}_0}{b\bar{R}} \right)^2 \Delta \bar{X}_1 + 0.10805 \left(\frac{\bar{U}_0}{b\bar{R}} \right) \Delta \bar{X}_2] = \\ \int_0^\psi \left[A_1 e^{\lambda_2(\psi - \psi')} + A_2 e^{\lambda_1(\psi - \psi')} \right] \Delta \bar{Q}(\psi') d\psi' \end{aligned} \quad (14)$$

where $A_1 = 0.10055 (\bar{U}_0/b\bar{R})$, and $A_2 = 0.007499 (\bar{U}_0/b\bar{R})$.

This form of the solution is particularly useful when the mathematical form of the motion is known and the above integral can be solved in closed form. The expressions for the lift and moment can be also specialized to the case of typical decaying, stable, or increasing flap-lag-torsional motion about an arbitrary equilibrium state with different damping, frequency and phase angle values for each of the degrees of freedom. A typical decaying, stable, or growing motion of a blade about its equilibrium state can be expressed as

$$\begin{aligned} \bar{w}(\bar{x}_0, \psi) &= \bar{w}_e(\bar{x}_0) + \Delta \bar{w}_0(\bar{x}_0) e^{\bar{P}_F \psi} \\ \bar{v}(\bar{x}_0, \psi) &= \bar{v}_e(\bar{x}_0) + \Delta \bar{v}_0(\bar{x}_0) e^{\bar{P}_L \psi} \\ \phi(\bar{x}_0, \psi) &= \phi_e(\bar{x}_0) + \Delta \phi_0(\bar{x}_0) e^{\bar{P}_P \psi} \\ \lambda(\bar{x}_0, \psi) &= \lambda_e(\bar{x}_0) + \Delta \lambda_0(\bar{x}_0) e^{\bar{P}_{if} \psi} \end{aligned} \quad (15)$$

For such a motion, the Duhamel integral expression associated with the augmented states, Eq. (14) is solved in Ref. 29 where the relatively lengthy expression for this solution are presented.

The derivations for the unsteady equilibrium and perturbational loads for forward flight are similar to the hover case, except that the additional component of the forward flight velocity along the blade section must be included. In addition the geometric pitch angle will have a time varying cyclic component as well as the collective component. The expressions for the equilibrium and perturbational loads both for a general arbitrary flap-lag-torsional blade motion and a decaying, stable, or growing oscillations are presented in Ref. 29. Due to their length and lack of space these expressions are not given here. A few remarks about the form of these equations and their compatibility with various techniques used to solve the complete aeroelastic response and stability problem¹⁶ should be made. Since the equilibrium state in forward flight is time-varying and periodic, the augmented states can not be solved a priori. These equations have to be appended to the complete aeroelastic equations for equilibrium of the blade. It is important to mention that the equations for the equilibrium loads in forward flight are in a form entirely consistent with the response analysis techniques such as quasilinearization and Floquet theory which have been frequently used with the quasisteady aerodynamic theories¹⁶. The main difference is that the size of the matrices to be manipulated is larger due to the addition of augmented state variables.

4. Arbitrary Motion Unsteady Airfoil Theory Including The Effects of the Returning Wake

Experimental evidence obtained by Ham, Moser, and Zvara²⁶ clearly shows that the returning wakes can significantly change the rotor blade response levels at low inflows in hover condition. Furthermore there is evidence, both theoretical and experimental¹⁵ showing that under certain conditions the returning wakes can have a significant influence also on the aeroelastic stability of the blade. In this section two separate arbitrary motion airfoil theories are developed which account for both the wake structure beneath and behind the airfoil.

4.1 Generalized Loewy's Theory

Loewy's rotary-wing unsteady airfoil theory is an incompressible two-dimensional theory, somewhat similar to Theodorsen's theory, which accounts for the effect of the spiral returning wake beneath the rotor in an approximate manner for situations which are characterized by low inflow and hovering flight. The geometry of the two-dimensional wake model postulated in this theory is illustrated in Fig. 7. The horizontal returning wake layers beneath the reference airfoil are the two dimensional approximation of the wakes shed by the reference airfoil in the previous revolutions and identical airfoils on the other blades in the previous revolutions. In Loewy's model the returning wake layers are extended to infinity both aft and fore of the reference airfoil for mathematical convenience. Loewy's theory is primarily intended to be used in studying unsteady effects on hovering rotors operating at low inflows, as well as unsteady effects at larger inflows, for cases when the

oscillatory frequency is significantly larger than the rotational speed. Like other frequency domain theories, this theory also assumes a simple harmonic motion.

The Loewy's lift deficiency function in frequency domain for the case of collective mode of motion, where all blades move in phase, is given by

$$C'(k, \bar{m}_e, \bar{h}_e) = \frac{H_1^{(2)}(k) + 2J_1(k)W(k\bar{h}_e, \bar{m}_e)}{H_1^{(2)}(k) + iH_0^{(2)}(k) + 2\{J_1(k) + J_0(k)\}W(k\bar{h}_e, \bar{m}_e)} \quad (16a)$$

where

$$W(k\bar{h}_e, \bar{m}_e) = \begin{cases} \frac{1}{e^{k\bar{h}_e} e^{i2\pi\bar{m}_e} - 1} & k > 0 \\ 0 & k = 0 \end{cases} \quad (16b)$$

In which \bar{m}_e , and \bar{r}_e for a blade section at a radial distance r , for a rotor with Q blades, are given by

$$\bar{m}_e = \frac{\omega}{\Omega Q} = k \frac{\bar{r}}{Q} = k \bar{r}_e \quad (16c)$$

$$\bar{h}_e = \frac{2\pi U_p}{bRQ} \quad (16d)$$

$$\bar{r} = r/bR, \quad \bar{r}_e = \bar{r}/Q \quad (16e)$$

Before attempting to generalize Loewy's theory to arbitrary motion it is useful to examine certain features of this theory which have not been noted previously. For a given blade section at a radial distance r away from the axis of rotation, the equivalent frequency ratio, m , is dependent on k by virtue of Eq. 16c. The ascending series given in the literature for Loewy's lift deficiency function, such as the series presented in Wayne Johnson's book, Ref. 27, page 509 does not capture this dependence.

$$C' \approx \frac{1 - i \frac{\pi}{2} k^2 W}{1 + \frac{\pi}{2} k - ik(\ln \frac{k}{2} + \gamma_e) + (1 - \frac{i}{2} k) \pi kW} \quad (17)$$

where $W = \frac{1}{i2\pi\bar{m}_e - 1}$ is assumed constant for non-integer \bar{m}_e values. An ascending series which takes into account this dependence has been derived in this study²⁹ and is given below

$$C'(s, sr_e, sh_e) \approx \frac{1 + \frac{\pi i}{2(2\pi\bar{r}_e - i\bar{h}_e)} \bar{s}}{1 - (\ln(\frac{\bar{s}}{2}) + \gamma_e) \bar{s} - \frac{\pi i}{2\pi\bar{r}_e - i\bar{h}_e} (1 - \frac{\bar{s}}{2})}, \quad \bar{s} = ik, \quad (18)$$

The zero frequency limit of C' is obtained by letting \bar{s} in the ascending series approach zero

$$\lim_{|\bar{s}| \rightarrow 0} C'(\bar{s}, \bar{s}\bar{r}_e, \bar{s}\bar{h}_e) = \frac{1}{1 + \frac{\pi}{\bar{h}_e + i(2\pi\bar{r}_e)}} \quad (19a)$$

Hence the real and imaginary parts become

$$\lim_{|\bar{s}| \rightarrow 0} F' = \frac{\left[1 + \frac{\pi \bar{h}_e}{\bar{h}_e^2 + (2\pi \bar{r}_e)^2}\right]}{\left[1 + \frac{\pi \bar{h}_e}{\bar{h}_e^2 + (2\pi \bar{r}_e)^2}\right]^2 + \left[\frac{2\pi^2 \bar{r}_e}{\bar{h}_e^2 + (2\pi \bar{r}_e)^2}\right]^2} \quad (19b)$$

$$\lim_{|\bar{s}| \rightarrow 0} G' = \frac{\left[\frac{(2\pi^2 \bar{r}_e)}{\bar{h}_e^2 + (2\pi \bar{r}_e)^2}\right]}{\left[1 + \frac{\pi \bar{h}_e}{\bar{h}_e^2 + (2\pi \bar{r}_e)^2}\right]^2 + \left[\frac{2\pi^2 \bar{r}_e}{\bar{h}_e^2 + (2\pi \bar{r}_e)^2}\right]^2}$$

This limit is different from unity and is a function of \bar{h}_e and \bar{r}_e . The reason for this behavior is that k and \bar{m}_e , which have been treated as independent quantities in Ref. 5, thus k was allowed to approach zero while \bar{m}_e was kept constant. This condition would not be encountered in a real rotor blade section at a fixed radial distance away from the hub.

Another item which can be noted in Loewy's lift deficiency is a jump type discontinuity at $k = 0$ in the wake weighting function $W(k\bar{h}_e, \bar{m}_e)$. This discontinuity is associated with the validity of the solution for a certain improper integral used by Loewy to obtain the relation for W at $k = 0$, as shown in Ref. 29. The implication of this discontinuity is that the low-frequency limit of C' , as k approaches zero is different than the value of C' obtained for $k = 0$. While the latter is equal to unity, as can be expected for fully steady conditions, the former is a function of \bar{h}_e and \bar{r}_e and can amount to significantly large reductions in the lift and moment. This means that even for very slow oscillations the cumulative wake effects may be significant.

Next Loewy's theory is extended to arbitrary motion by using an approach similar to that used in Section 2. Loewy's lift deficiency function in the frequency domain is analytically continued to the entire Laplace plane by replacing the frequency domain variable (ik) with the complex variable (\bar{s}). To accomplish this objective the argument of the various Bessel and Hankel functions in the Loewy's lift deficiency function has to be changed from k to ik . This was accomplished using a number of identities which are valid for various Bessel, modified Bessel, and Hankel functions. The parameter \bar{m}_e in the wake weighting function W had to be also expressed in terms of k before it could be generalized. Replacing the lift deficiency function in the theory presented in Section 2, with the new generalized lift deficiency function, the returning wake effects are approximately accounted for. The generalized lift deficiency function is given by

$$C'(\bar{s}, \bar{s}\bar{r}_e, \bar{s}\bar{h}_e) = F' + iG' =$$

$$\frac{K_1(\bar{s}) + \pi i I_1(\bar{s}) W(\bar{s}\bar{h}_e, \bar{s}\bar{r}_e)}{K_1(\bar{s}) + K_0(\bar{s}) + \pi i [I_1(\bar{s}) - I_0(\bar{s})] W(\bar{s}\bar{h}_e, \bar{s}\bar{r}_e)} \quad (20a)$$

where

$$W(\bar{s}\bar{h}_e, \bar{s}\bar{r}_e) = \begin{cases} \frac{1}{-i\bar{s}\bar{h}_e} \frac{1}{2\pi\bar{s}\bar{r}_e} & |\bar{s}| > 0 \\ 0 & |\bar{s}| = 0 \end{cases} \quad (20b)$$

Pade approximants are constructed for the generalized Loewy lift deficiency function using three different techniques; namely (1) Dowell's quadratic least-squares technique²⁴, (2) Vepa's quadratic least-squares technique²³, and (3) a general nonlinear least-squares technique using Fletcher Reeves optimization algorithm. It should be mentioned that Dowell's method yields results which are as good as those obtained from the other two methods, while being numerically more efficient. Furthermore Dowell's method also provides flexibility in selecting the poles in the stable region of the Laplace plane, i.e. on the negative real axis.

A number of Pade approximants for Loewy's lift deficiency function are obtained for various discrete values of nondimensionalized wake spacing, \bar{h}_e , and blade section radial distance, \bar{r}_e , typical of existing helicopters. A selected sample of these results are presented in Figs. 8 through 14 for two cases of ($\bar{h}_e = 4.0$, $\bar{r}_e = 3.0$) and ($\bar{h}_e = 1.5707$, $\bar{r}_e = 1.5$). The first case corresponds to a blade section located at a radial distance of 0.8R of a four bladed rotor with a semichord $bR = 0.0667R$ operating at an inflow ratio of 0.15 ($C_T = 0.046$). The second case corresponds to a blade section of radial distance 0.3R of a four bladed rotor with a semichord $bR = 0.005R$. The thrust coefficients C_T are calculated from inflow velocities based on simple momentum theory in hover

$$\lambda = \sqrt{C_T/2} \quad (21)$$

While the C_T in the first case is unreasonable for the helicopter rotors, it was selected as such to avoid the oscillatory nature of Loewy's lift deficiency function. Loewy's lift deficiency function for small wake spacing parameters, or small inflow ratios, becomes highly oscillatory and is not amenable to rational approximations. The zero-frequency limit of the generalized lift deficiency function C' for the first case is ($0.9448 + i 0.1457$), corresponding to 4.40% reduction and 8.77° phase lead in circulatory loads, while for the second case one obtains $C' = (0.8667 + i 0.2667)$, corresponding to 9.32% reduction and 17.10° phase lead in circulatory loads. The zero-frequency values of C' for both cases is unity, which means no amplitude reduction or phase lead in loads. The Pade approximants constructed for the first case are based on the assumption that the zero-frequency value is matched. For the Pade approximants constructed for the second case, however, the zero frequency value was repeatedly adjusted to achieve a better overall agreement.

The imaginary part of the exact C' , denoted by G' , has an oscillatory form for a large range of the wake spacing parameters. Based on a somewhat simplistic argument, Dowell²⁴ suggests that the poles should be selected as the negative values of the reduced frequencies where G' has its extrema. While this argument is valid for the case of one extremum, it loses its validity for the cases where the shape of the curve is oscillatory, such as in

the present case. In an attempt to capture the oscillatory nature of G' , many possible relative arrangements of poles as well as their locations in the complex plane were examined. The results of various representative pole arrangements are summarized for the first case in Table A.1, and for the second case in Table A.2. Figures 8-14 show the comparison between the real and imaginary parts of the Pade approximant for these cases. Based on these results, and additional results not presented here²⁹, the following conclusions can be drawn:

1. The marginal improvement in the approximation realized by having a large number of poles as opposed to three or four poles does not justify using the higher order approximations.
2. When the proximity of the poles to each other and the origin is excessive, the quality of approximation deteriorates.
3. The imaginary part does not exhibit extrema at $k = b_m$. Hence selecting these poles does not necessarily lead to a better overall quality of approximation.
4. In general the results are insensitive to the differences in error weighting coefficients for the low and high frequency ranges because major contribution to the error is associated to a narrow frequency band of $0.0 < k < 1.0$.
5. It appears that the Pade approximation, which consists of a ratio between two polynomials, does not have the capability of capturing the oscillatory type functions. Rather, it yields a result which represents the average of the oscillatory curve.

The last columns of Tables A.1 and A.2 are estimates on the quality of the approximation based on the sum of the squares of the errors in the real and imaginary parts for the reduced frequency range $0.0 < k < 3.0$. While the Pade approximants obtained are not a good approximation of the lift deficiency function in the frequency domain, the time domain representation is better due to the error cancellations which occur, as indicated in item (5) above. The oscillatory nature of Loewy's lift deficiency function could be partially attributed to the fact that returning wake layers have been artificially extended to infinity on both sides. The staggered cascade wake model described in the following section was developed in an attempt to remedy this situation.

Using the Pade approximants obtained, the approximate finite-state time domain representation of the generalized Loewy's theory combined with the generalized Greenberg's theory are derived²⁹.

4.2 Cascade Wake Model Theory

It was mentioned previously that Loewy's wake model is not entirely compatible with the finite-time arbitrary motion representation of the blade dynamics, because each wake layer beneath the rotor is assumed to extend to infinity on both sides (see Fig. 7). Therefore one would be unable to derive a generalized Loewy's theory directly from the fundamental governing equation and Loewy's wake model. In this section an alternative theory capable of capturing the effects associated with the returning wake is derived. A new finite time

wake structure, shown in Fig. 15*, is proposed in which an infinite number of identical staggered airfoils are flying beneath the reference airfoil, separated by the wake spacing H^* . Each airfoil is leading the previous airfoil by the distance $2\pi r$. The wake behind each of the imaginary airfoils is of a finite length corresponding to the time elapsed from the beginning of motion.

Using this wake model, the integral equation of downwash is formulated for an airfoil undergoing coupled flap-lag-torsional motion in a stream having time-varying oncoming velocity. It should be noted that the shed vortices behind the airfoil in each parallel wake layer, are assumed to travel at the mean velocity, as was done in the extension of Greenberg's theory in Section 2.1.

The approach used by Johnson for deriving Theodorsen's theory (Sec. 10, Ref. 27) was found to be suitable for this problem, and thus the mathematical derivation presented in this study follows along similar lines, except that changes accounting for time-varying oncoming velocity, finite-time arbitrary motion, and the cascade form of the wake are introduced.

The complete flow is obtained as the sum of three components; far field oncoming and inflow velocities, system of bound vortices representing the airfoil, and system of shed vortices representing the wake. The condition of tangent flow over the airfoil, gives an integral equation. Using the Söhngen inversion integral²⁸ on this integral equation combined with the Kutta condition, enables one to write a relation for the bound vortex system in terms of integral of the wake induced downwash velocities. By representing different velocities over the airfoil by their respective Fourier series expansions, the circulatory component of the bound vortex system, which amounts to the entire circulation around the airfoil but corresponds to zero downwash velocity over the chord, can be calculated. Similarly the noncirculatory component of the bound vortex system, which amounts to the entire downwash velocity over the airfoil but corresponds to zero circulation around it, is found in terms of the Fourier coefficients of downwash and wake induced downwash velocities. Using small disturbance unsteady Bernoulli's equation, antisymmetry of the problem, and integration over the airfoil chord, the unsteady lift and moment can be written in terms of different integrals of circulatory and noncirculatory bound vortex systems, which can in turn be expressed by the Fourier coefficients of the downwash and wake induced downwash velocities. The assumption of downstream convection of shed vortices allows one to relate directly the wake vortices, which depend on both time and position, to the vortices which have been shed at the trailing edge of reference airfoil and which are only a function of time. Using this approach the lift deficiency function for a multibladed rotor can be written as

$$C''(\bar{s}, \bar{t}_{Re}, \bar{t}_{He}) = \quad (22a)$$

$$K_1(\bar{s}) - \frac{\bar{s}}{2} \sum_{n=1}^{NL} e^{-n\bar{s}\bar{t}_{Re}} [F(\bar{s}; n, 0, \bar{t}_{Re}, \bar{t}_{He}) - F(\bar{s}; n, 2, \bar{t}_{Re}, \bar{t}_{He})]$$

$$K_1(\bar{s}) + K_0(\bar{s}) + \sum_{n=1}^{NL} e^{-n\bar{s}\bar{t}_{Re}} [F(\bar{s}; n, 0, \bar{t}_{Re}, \bar{t}_{He}) + F(\bar{s}; n, 1, \bar{t}_{Re}, \bar{t}_{He})]$$

*Figure 15 appears after Fig. 3.

where

$$F(\bar{s}; n, m, \bar{T}_{Re}, \bar{T}_{He}) =$$

$$\int_{1-n\bar{T}_{Re}}^{\infty} \left[\frac{1}{\pi} \int_0^{\pi} \frac{(t' - \cos\theta) \cos(m\theta) d\theta}{(t' - \cos\theta)^2 + (n\bar{T}_{He})^2} \right] e^{-st'} dt' \quad (22b)$$

and the various other quantities are given by

$$T_{sc} = \left(\frac{bR}{U_{T0}} \right) \quad (22c)$$

$$\bar{T}_{He} = \left(\frac{2\pi U_{p0}}{\Omega Q U_{T0}} \right) / T_{sc} = (\bar{h}_e) \quad (22d)$$

$$\bar{T}_{Re} = \left(\frac{T_R}{T_{sc}} \right) / Q = (2\pi \bar{r}_e) \quad (22e)$$

This Laplace-domain lift deficiency function involves two integrals and two infinite summations which do not lend themselves to closed form solutions in terms of familiar mathematical functions. In Reference 29 two important properties of the new lift deficiency function are proved, namely: 1) It always approaches unity as reduced frequency goes to zero, whereas Loewy's lift deficiency function does not. 2) It approaches Theodorsen's lift deficiency function both for infinite wake spacing and the case where a single wake layer behind the reference blade is considered, as can be expected.

4.2.1 Frequency Domain Lift Deficiency Function

The frequency domain lift deficiency function is needed for constructing Pade approximants and also for the time domain representation of the unsteady aerodynamic loads. The frequency domain lift deficiency function is obtained by specializing the generalized lift deficiency function, C'' to the case of $\bar{s} = (ik)$.

$$C''(ik, \bar{T}_{Re}, \bar{T}_{He}) =$$

$$\frac{K_1(ik) - \left(\frac{ik}{2}\right) \sum_{n=1}^{NL} e^{-ink\bar{T}_{Re}} IN(ik:n, \bar{T}_{Re}, \bar{T}_{He})}{K_1(ik) + K_0(ik) + \sum_{n=1}^{NL} e^{-ink\bar{T}_{Re}} ID(ik:n, \bar{T}_{Re}, \bar{T}_{He})} \quad (23a)$$

where

$$IN(ik:n, \bar{T}_{Re}, \bar{T}_{He}) =$$

$$\int_{LL}^{UL} \left[\frac{1}{\pi} \int_0^{\pi} \frac{(t' - \cos\theta)(1 - \cos 2\theta) d\theta}{(t' - \cos\theta)^2 + (n\bar{T}_{He})^2} \right] e^{-ikt'} dt' \quad (23b)$$

$$ID(ik:n, \bar{T}_{Re}, \bar{T}_{He}) =$$

$$\int_{LL}^{UL} \left[\frac{1}{\pi} \int_0^{\pi} \frac{(t' - \cos\theta)(1 + \cos\theta) d\theta}{(t' - \cos\theta)^2 + (n\bar{T}_{He})^2} \right] e^{-ikt'} dt' \quad (23c)$$

For the case where the wake is allowed to extend to infinity behind the imaginary airfoils, the upper and lower limits of the integrals are given by²⁹

$$\begin{aligned} LL &= 1 - n\bar{T}_{Re} \\ UL &= \infty \end{aligned} \quad (24)$$

However only the wake contained within a double azimuth angle straddling the blade has physical meaning. For this case

$$\begin{aligned} LL &= \begin{cases} -\bar{T}_{Re} & n \neq 1 \\ -\bar{T}_{Re} + 1 & n = 1 \end{cases} \\ UL &= \bar{T}_{Re} \end{aligned} \quad (25)$$

An efficient method of evaluating the lift deficiency function for practical range of reduced frequencies, wake spacing, and radial position of the blade section was developed²⁹. The frequency domain lift deficiency function is evaluated by a combined analytical and numerical approach. The approach is based on the recognizing that the integrand of the unknown integrals Eq. (23b) and (23c), for the wake layers sufficiently far from the rotor plane can be approximated accurately by their binomial expansions. These expressions can be integrated in closed form and the results can be found in Ref. 29. Plots of this lift deficiency function for various values of wake spacing, and radial position along the blade are calculated as a function of the reduced frequency and compared with the corresponding values obtained from Loewy's lift deficiency function. The representative results for the case of $\bar{T}_{He} = 1.5707$ and $\bar{T}_{Re} = 9.4248$, which corresponds to $\bar{h}_e = 1.5707$ and $\bar{r}_e = 1.5$ for Loewy's theory, with different number of wake layers beneath the rotor are shown in Figs. 16a and b. The real and imaginary parts of cascade wake model lift deficiency for this case with 100 wake layers beneath the rotor are compared with the Loewy's lift deficiency function in Figures 17a and b. The cascade wake model lift deficiency function agrees very well with that of Loewy, except in two regions: 1) in the proximity of the regions where $m_e = (k) \cdot (\bar{r}_e)$ is an integer, 2) near the origin where the cascade wake model tends to the correct quasisteady values. From these plots it is evident that Loewy's lift deficiency function tends to smooth out the effect of the returning wakes near the integer frequency ratios when compared to the cascade wake model. Therefore the extension of the wake to infinity on both sides of the rotor, in Loewy's model, tends to reduce the unsteady effects rather than to enhance them. However both theories indicate very large load reductions in these regions. It is also evident from Figures 17a and b that the extension of the wake to infinity on both sides of the rotor in Loewy's theory has relatively small effects on the lift deficiency function except in regions of low reduced frequency and integer frequency ratios.

Due to highly oscillatory nature of the cascade wake model lift deficiency function, no attempt was made to construct any Pade approximant. Further investigations of time domain modeling for this theory will be undertaken.

5. Concluding Remarks

In this study a number of different arbitrary-motion type of unsteady two dimensional airfoil theories, aimed at rotary-wing aeroelastic applications, were derived. The first is an extension of Greenberg's theory to arbitrary coupled flap-lag-torsional motion. This theory is derived for both hover and forward flight, however it does not include the effect of the returning wake.

Two additional theories for hover, which incorporate the effect of returning wakes, were also developed. The first is an extension of Loewy's theory to arbitrary motion. The development of Pade approximants for this theory are presented and the time domain unsteady aerodynamic loads for a typical section are derived. A cascade wake model is developed in the Laplace domain and specialized to frequency domain. A combined numerical and analytical scheme is developed to deal with various integrals and infinite summations involved. The cascade wake model lift deficiency function is compared with Loewy's. It is found that the cascade wake model predicts somewhat larger unsteady aerodynamic effects at integer frequency ratios than Loewy's theory. Furthermore the low frequency limit of this theory tends to the quasi-steady limit, whereas Loewy's theory predicts very large reductions in loads near zero frequency.

It is envisioned that these theories could have useful applications in rotary wing aeroelastic stability and response analyzes.

References

1. Theodorsen, T., "General Theory of Aerodynamic Instability and the Mechanism of Flutter", NACA Report 496, 1935.
2. Greenberg, J.M., "Airfoil in Sinusoidal Motion in Pulsating Stream", NACA TN No. 1326, 1947.
3. Kottapalli, S.B.R., and Pierce, G.A., "Drag on an Oscillating Airfoil in a Fluctuating Free Stream", ASME Journal of Fluids Engineering, Vol. 101, September 1979, pp. 391-399.
4. Loewy, R.G., "A Two-dimensional Approximation to the Unsteady Aerodynamics of Rotary Wings", Journal of Aeronautical Sciences, Vol. 24, No. 2, Feb. 1957.
5. Loewy, R.G., "A Two-dimensional Approximation to the Unsteady Aerodynamics of Rotary Wings", Cornell Aeronautical Laboratory, Inc., CAL Report No. 76, October 1955.
6. Jones, W.P., and Rao, B.M., "Compressibility Effects on Oscillating Rotor Blades in Hovering Flight", AIAA Journal, Vol. 8, No. 2, Feb. 1970, pp. 321-329.
7. Hammond, C.E., and Pierce, G.C., "A Compressible Unsteady Aerodynamic Theory for Helicopter Rotors", AGARD Specialists Meeting on the Aerodynamics of Rotary Wings, Marseille, France, September 1972.
8. Friedmann, P.P., and Yuan, C.H., "Effect of Modified Aerodynamic Strip Theories on Rotor Blade Aeroelastic Stability", AIAA Journal, Vol. 15, No. 7, July 1977, pp. 932-940.
9. Shipman, K.W., and Wood, E.R., "A Two-Dimensional Theory for Rotor Blade Flutter in Forward Flight", Journal of Aircraft, Vol. 8, No. 12, December 1971.
10. Edwards, J.W., "Unsteady Aerodynamic Modeling and Active Aeroelastic Control", Guidance and Control Laboratory, Department of Aeronautics and Astronautics, Stanford, SUDAAR 504, Feb. 1977.
11. Sears, W.R., "Operational Methods in the Theory of Airfoils in Nonuniform Motion", Journal of Franklin Institute, Vol. 230, No. 1, July 1940, pp. 95-111.
12. Rock, S.M., "Transient Motion of an Airfoil: an Experimental Investigation in a Small, Subsonic Wind Tunnel", Guidance and Control Laboratory, Department of Aeronautics and Astronautics, Stanford University, May 1978.
13. Timman, R., "The Aerodynamic Forces on an Oscillating Aerofoil Between Two Parallel Walls", Appl. Sci. Res. (The Hague), Vol. A3, No. 1, 1951, pp. 31-57.
14. Cheng-hsein Yuan, "A Study of the Effect of Unsteady Aerodynamics on the Aeroelastic Stability of Rotor Blades in Hover", Ph.D. Dissertation, University of California at Los Angeles, 1976.
15. Friedmann, P.P., "Recent Developments in Rotary-Wing Aeroelasticity", Journal of Aircraft, Vol. 14, No. 11, November 1977, pp. 1027-1041.
16. Friedmann, P.P., "Formulation and Solution of Rotary-wing Aeroelastic Stability and Response Problems", Vertica, Vol. 7, No. 2, 1983, pp. 101-141.
17. Hodges, D.H., and Ormiston, R.A., "Stability of Elastic Bending and Torsion of Uniform Cantilever Rotor Blades in Hover with Variable Structural Coupling", NASA TN D8192, 1976.
18. Kaza, K.R., and Kvaternik, R.G., "Nonlinear Aeroelastic Equations for Combined Flapwise Bending, Chord-wise Bending, Torsion, and Extension of Twisted Nonuniform Rotor Blades in Forward Flight", NASA Technical Memorandum 74059, August 1977.
19. Johnson, W., "Application of Unsteady Airfoil Theory to Rotary Wings", Journal of Aircraft, Vol. 17, No. 4, April 1980, pp. 285-286.
20. Kaza, K.R.V., and Kvaternik, R.G., "Application of Unsteady Airfoil Theory to Rotary Wings", Journal of Aircraft, Vol. 18, No. 7, July 1981, pp. 604-605.
21. Kottapalli, S.B.R., "Drag on an Oscillating Airfoil in a Fluctuating Free Stream", Ph.D. Dissertation, School of Engineering, Georgia Institute of Technology, August 1977.
22. Jones, R.T., "The Unsteady Lift of a Wing of Finite Aspect Ratio", NACA Report 681, 1940.

23. Vepa, R., "On the Use of Pade Approximants to Represent Unsteady Aerodynamic Loads for Arbitrary Small Motions of Wings", AIAA Paper No. 76-17, January 1976.
24. Dowell, E.H., "A Simple Method for Converting Frequency-domain Aerodynamics to the Time Domain", NASA Langley Research Center, Hampton, Virginia, NASA TM-81844, 1980.
25. Desmarais, R., "A Continued Fraction Representation for Theodorsen's Circulation Function", NASA TM-81838, 1980.
26. Ham, N.D., Moser, H.H., and Zvara, J., "Investigation of Rotary Response to Vibratory Aerodynamic Inputs, Part I. Experimental Results and Correlation with Theory", WADC TR 58-87, October 1958.
27. Johnson, W., *Helicopter Theory*, Princeton University Press, 1980, Chapters 10 & 11.
28. Söhngen, H., "Die Lösungen der Integralgleichung und deren Anwendung in der Tragflugel Theorie", *Mathematische Zeitschrift*, Band 45, 1939, pp. 245-264.
29. Asghar-Hessari-Dinyavari, M., "Unsteady Aerodynamics in Time and Frequency Domains for Finite-time Arbitrary Motion of Rotary Wings in Hover and Forward Flight", Doctoral Dissertation, Department of Mechanics and Structures, University of California at Los Angeles, Los Angeles, California, to be published in June 1984.
30. Gradshteyn, I.S., and Ryzhik, I.M., *Table of Integrals, Series, and Products*, 2nd Edition, Academic Press, 1980.

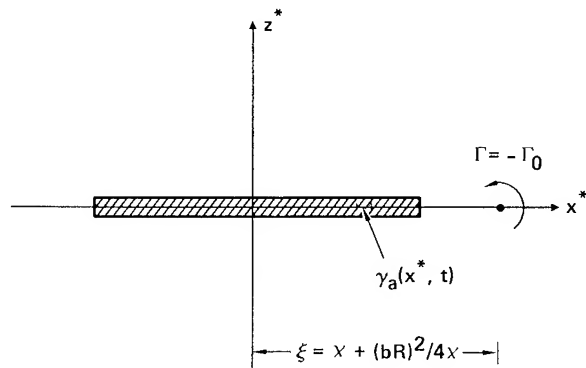


Fig. 2 Bound and Wake Vortices in x^*z^* -plane and the XZ -plane

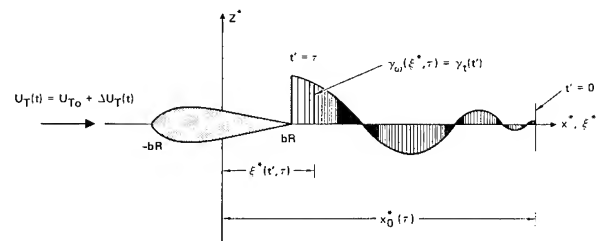


Fig. 3 Schematic of Wake Vortex Distribution at Time $t=\tau$ Due to an Arbitrary Finite Time Airfoil Motion Between $t=0$ and $t=\tau$

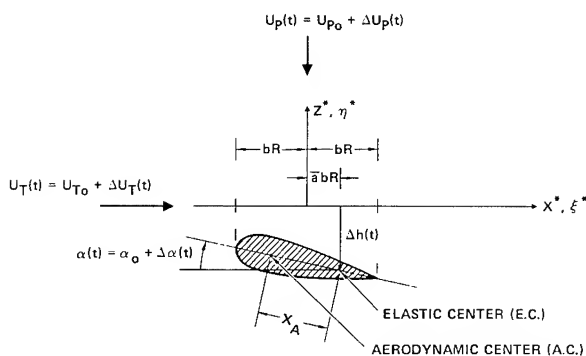


Fig. 1 Geometry of Motion of a Typical Airfoil

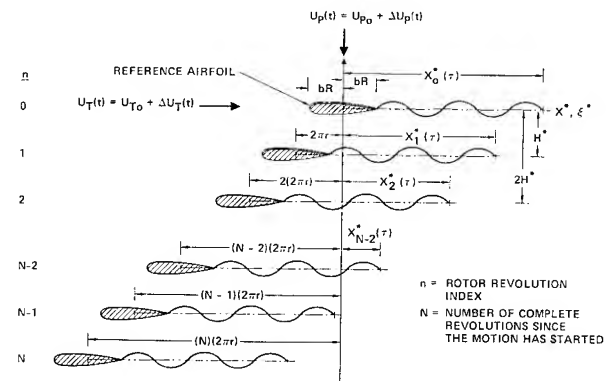


Fig. 15 Schematic of the Cascade Wake Model for the Arbitrary-Motion Rotary-Wing Aerodynamic Theory for a Single-Bladed Rotor

Table A.1. Summary of Numerical Results for Pade Approximant of Loewy's Lift Deficiency Function for $\bar{r}_e=3.0$, and $\bar{h}_e=4.0$

Fig. No.	Error Weighting Coefficients	Arrangement	Pole Locations	Pade Approximant for $C'(\bar{s}, \bar{r}_e=3.0, \bar{h}_e=4.0)$	Relative Quality
8	<u>For $k < 1.0$</u> $W_F' = 5$ $W_G' = 15$ <u>For $k > 1.0$</u> $W_F' = 1.0$ $W_G' = 1.0$	4 Regularly Spaced Poles on Negative Real Axis	$b_1 = 0.0$ $b_2 = -0.045$ $b_3 = -0.18$ $b_4 = -0.3$	$1.0 - \frac{(0.020516)\bar{s}}{(\bar{s}+0.045)} - \frac{(0.3021)\bar{s}}{(\bar{s}+0.18)} - \frac{(0.17738)\bar{s}}{(\bar{s}+0.3)}$	Good
9	<u>For all k's</u> $W_F' = 1.0$ $W_G' = 1.0$	6 Regularly Spaced Poles on Negative Real Axis	$b_1 = 0.0$ $b_2 = -0.045$ $b_3 = -0.24$ $b_4 = -0.38$ $b_5 = -0.56$ $b_6 = -0.76$	$1.0 + \frac{(0.03744)\bar{s}}{(\bar{s}+0.045)} - \frac{(0.9419)\bar{s}}{(\bar{s}+0.24)} + \frac{(0.47791)\bar{s}}{(\bar{s}+0.38)}$ $+ \frac{(0.27946)\bar{s}}{(\bar{s}+0.56)} - \frac{(0.35992)\bar{s}}{(\bar{s}+0.76)}$	Good
10	<u>For $k < 1.0$</u> $W_F' = 1.0$ $W_G' = 1.0$ <u>For $k > 1.0$</u> $W_F' = 1.0$ $W_G' = 1.0$	4 Closely Spaced Poles Near the Origin on Negative Real Axis	$b_1 = 0.0$ $b_2 = -0.015$ $b_3 = -0.03$ $b_4 = -0.045$	$1.0 - \frac{(3.8441)\bar{s}}{(\bar{s}+0.015)} + \frac{(9.5829)\bar{s}}{(\bar{s}+0.03)} - \frac{(6.2388)\bar{s}}{(\bar{s}+0.045)}$	Bad

Table A.2. Summary of Numerical Results for Pade Approximant of Loewy's Lift Deficiency Function for $\bar{r}_e = 1.5$, $\bar{h}_e = 1.570$ ($W_F' = W_G' = 1.0$ for all k 's)

Fig. No.	Arrangement of Poles	Pole Locations	Zero Frequency Value	Pade Approximant for $C'(\bar{s}, \bar{r}_e=1.5, \bar{h}_e=1.5707)$	Relative Quality
11	3 poles similar to the poles of Jones' approximation of Theodorsen's C	$b_1 = 0.0$ $b_2 = -0.0455$ $b_3 = -0.3$	$a_1 = 1.0$	$1.0 - \frac{(0.006294)\bar{s}}{\bar{s}+0.0455} - \frac{(0.49371)\bar{s}}{(\bar{s}+0.3)}$	Good
12	3 poles similar to the poles of Jones' approximation of Theodorsen's C	$b_1 = 0.0$ $b_2 = -0.0455$ $b_3 = -0.3$	$a_1 = 0.8667$	$0.8667 + \frac{(0.15084)\bar{s}}{\bar{s}+0.0455} - \frac{(0.51754)\bar{s}}{\bar{s}+0.3}$	Good
13	3 regularly spaced poles on negative real axis	$b_1 = 0.0$ $b_2 = -0.3$ $b_3 = -0.45$	$a_1 = 0.9254$	$0.9254 - \frac{(0.36196)\bar{s}}{\bar{s}+0.3} - \frac{(0.063444)\bar{s}}{\bar{s}+0.45}$	Good
14	8 regularly spaced poles on the negative real axis, with some within proximity of the origin	$b_1 = 0.0$ $b_2 = -0.05$ $b_3 = -0.1$ $b_4 = -0.15$ $b_5 = -0.2$ $b_6 = -0.25$ $b_7 = -0.3$ $b_8 = -0.35$	$a_1 = 0.9254$	$0.9254 - \frac{(4.5127)\bar{s}}{\bar{s}+0.05} + \frac{(48.395)\bar{s}}{\bar{s}+0.1}$ $- \frac{(226.900)\bar{s}}{\bar{s}+0.15} + \frac{(540.000)\bar{s}}{\bar{s}+0.2} - \frac{(673.760)\bar{s}}{\bar{s}+0.25}$ $+ \frac{(419.330)\bar{s}}{\bar{s}+0.3} - \frac{(102.980)\bar{s}}{\bar{s}+0.35}$	Bad

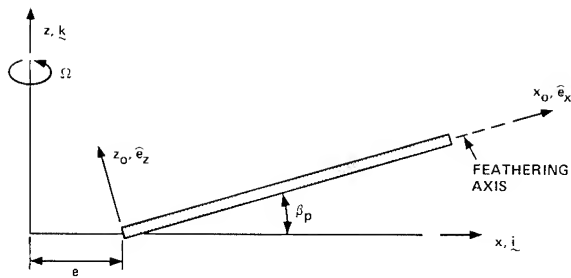


Fig. 4 Typical Description of the Undeformed Blade in the Rotating System x,y,z (i,j,k)

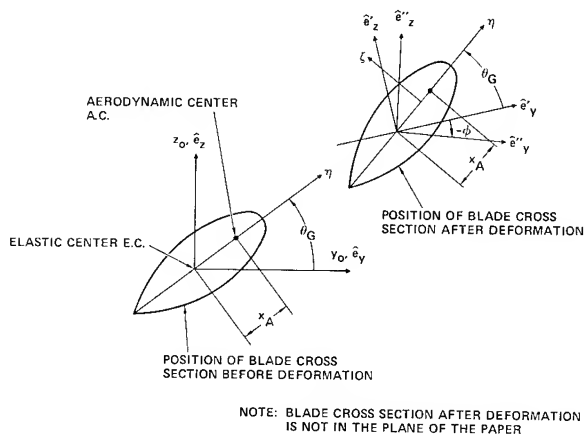


Fig. 6 Blade Cross Section Positions Before and After the Deformation

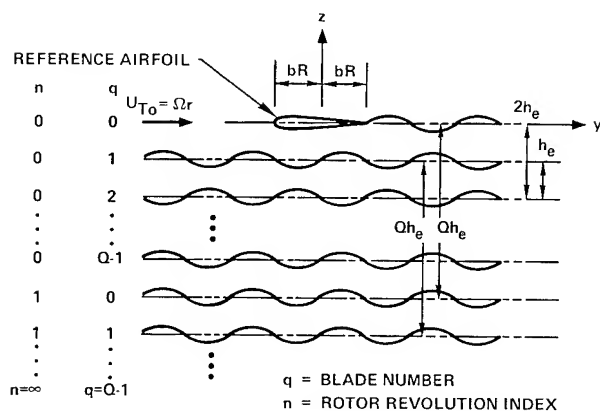


Fig. 7 Loewy's Incompressible Aerodynamic Model

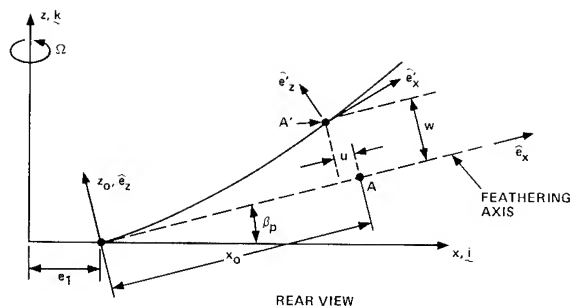


Fig. 5 Geometry of the Elastic Axis of the Deformed Blade

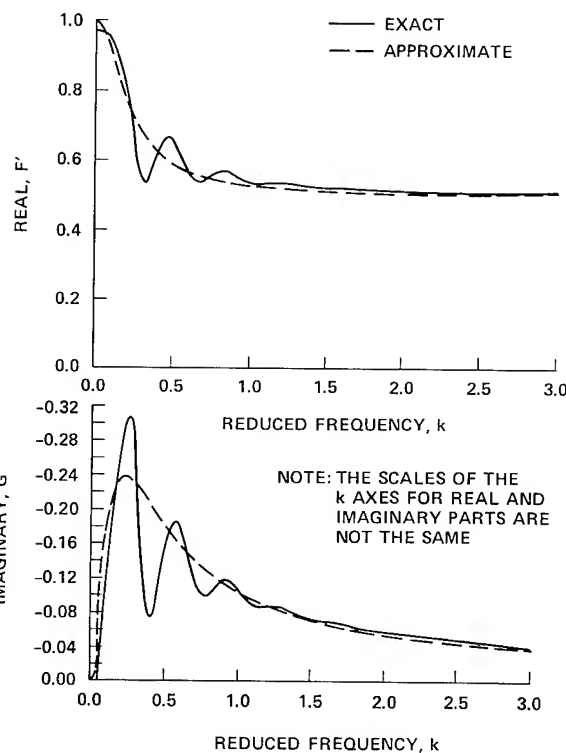
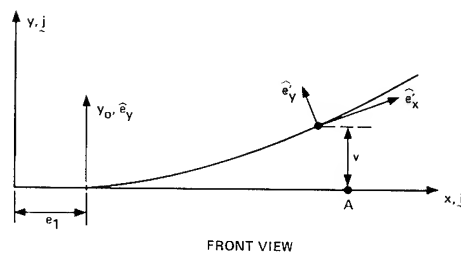


Fig. 8 Loewy's Lift Deficiency Function and Its Pade Approximant Using Dowell's Method (for $\bar{r}_e=3.0$, and $\bar{h}_e=4.0$: $NP=4$; $b_1=0.0$, $b_2=-0.045$, $b_3=-0.18$, $b_4=-0.3$; $a_1=1.0$, $a_2=-0.020516$, $a_3=-0.30210$, $a_4=-0.17738$)

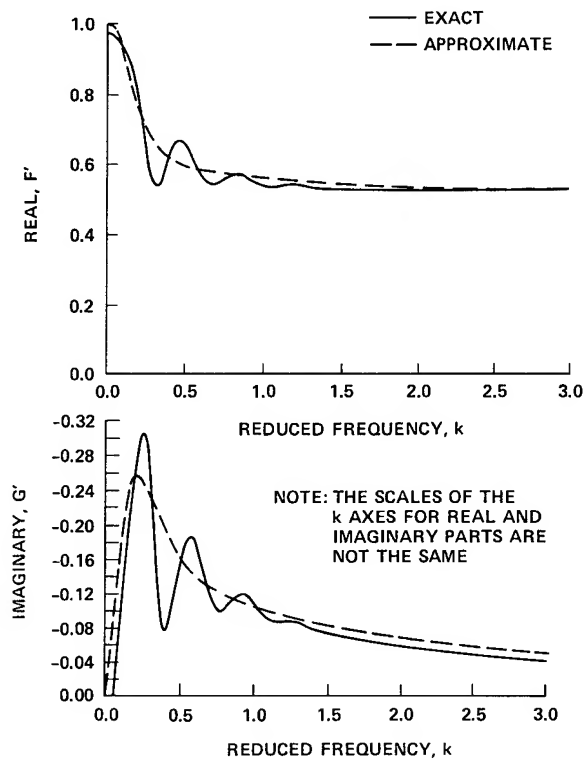


Fig. 9 Loewy's Lift Deficiency Function and Its Padé Approximant Using Dowell's Method (for $\bar{r}_e=3.0$, and $\bar{h}_e=4.0$: NP=6; $b_1=0.0$, $b_2=-0.045$, $b_3=-0.24$, $b_4=-0.38$, $b_5=-0.56$, $b_6=-0.76$; $a_1=1.0$, $a_2=0.037443$, $a_3=-0.94190$, $a_4=-0.47791$, $a_5=0.27946$, $a_6=-0.35292$)

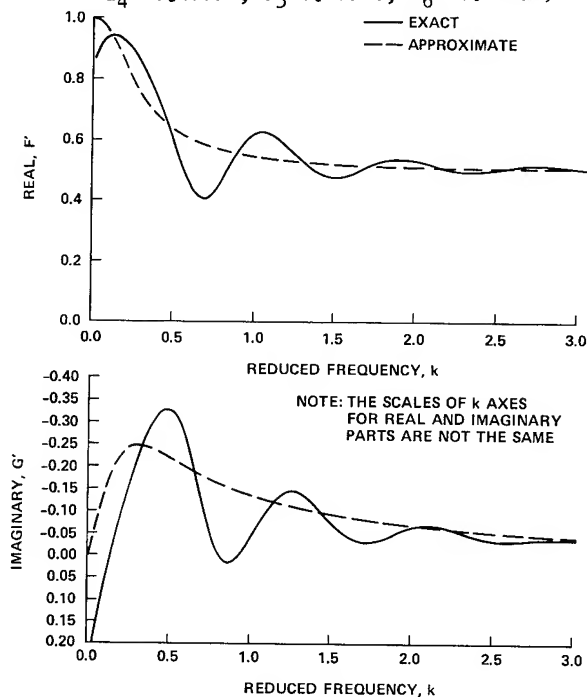


Fig. 11 Loewy's Lift Deficiency Function and Its Padé Approximant Using Dowell's Method (for $\bar{r}_e=1.5$, and $\bar{h}_e=1.5707$: NP=3; $b_1=0.0$, $b_2=-0.0455$, $b_3=-0.3$; $a_1=1.0$, $a_2=0.006294$, $a_3=-0.49371$)

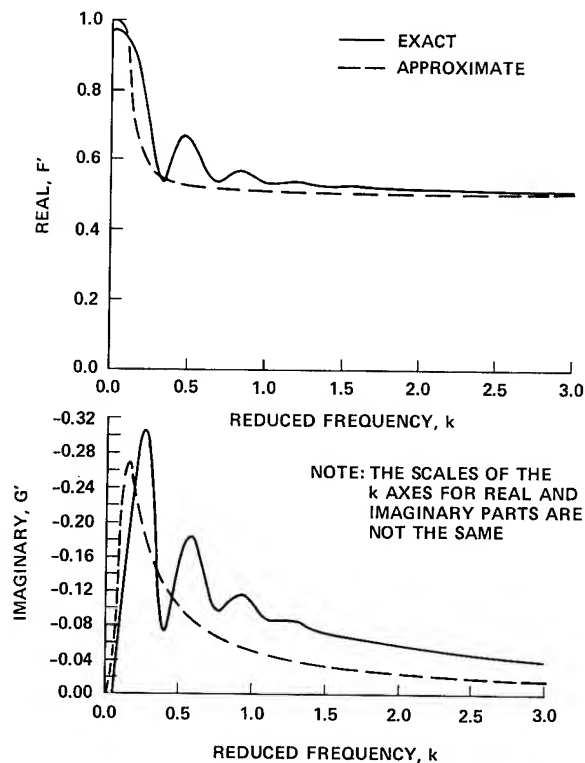


Fig. 10 Loewy's Lift Deficiency Function and Its Padé Approximant Using Dowell's Method (for $\bar{r}_e=3.0$, and $\bar{h}_e=4.0$: NP=4.0; $b_1=0.0$, $b_2=-0.015$, $b_3=-0.03$, $b_4=-0.045$; $a_1=1.0$, $a_2=-3.8441$, $a_3=9.5829$, $a_4=-6.2388$)

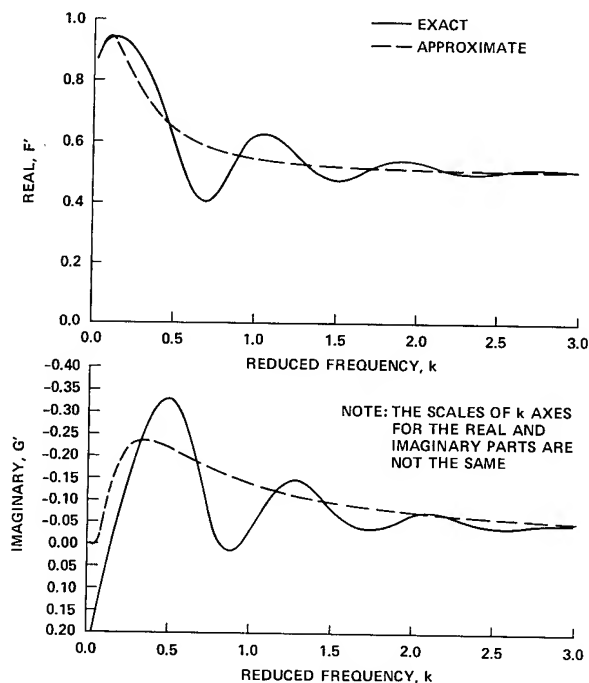


Fig. 12 Loewy's Lift Deficiency Function and Its Padé Approximant Using Dowell's Method (for $\bar{r}_e=1.5$, and $\bar{h}_e=1.5707$: NP=3; $b_1=0.0$, $b_2=-0.0455$, $b_3=-0.3$; $a_1=0.8667$, $a_2=0.15084$, $a_3=-0.51754$)

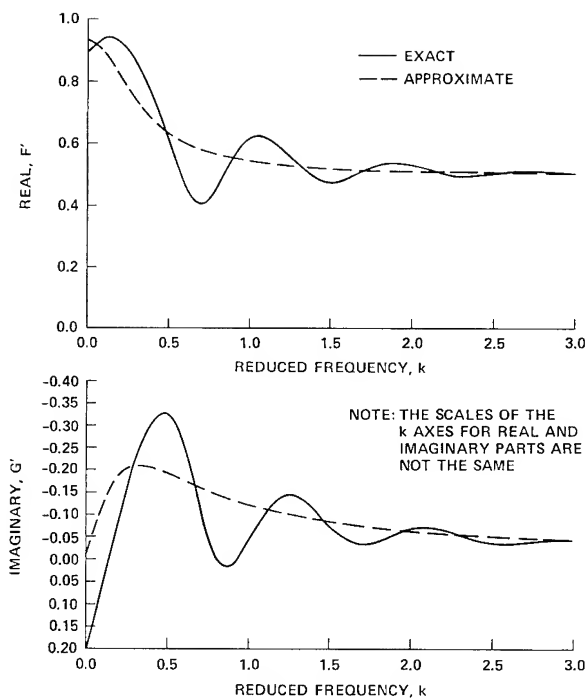


Fig. 13 Loewy's Lift Deficiency Function and Its Pade Approximant Using Dowell's Method (for $\bar{r}_e=1.5$, and $\bar{h}_e=1.5707$: NP=3; $b_1=0.0$, $b_2=-0.3$, $b_3=-0.45$; $a_1=0.925$, $a_2=-0.36196$, $a_3=-0.06344$)

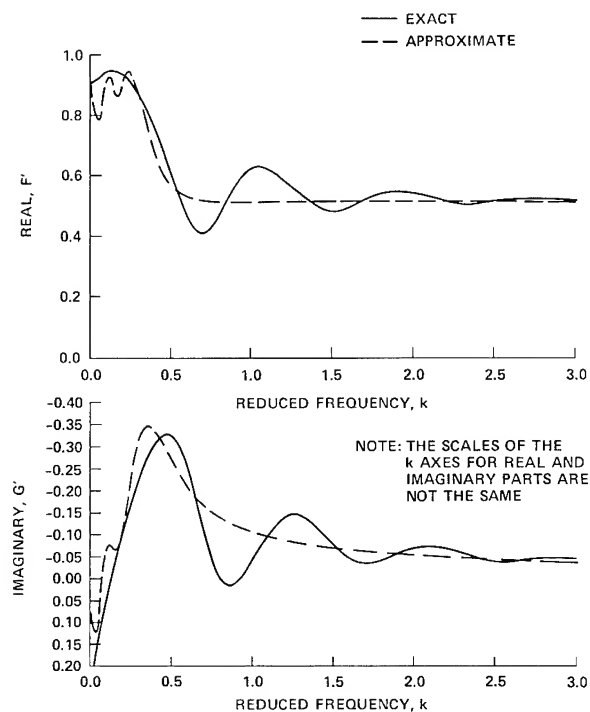


Fig. 14 Loewy's Lift Deficiency Function and Its Pade Approximant Using Dowell's Method (for $\bar{r}_e=1.5$, and $\bar{h}_e=1.5707$: NP=8; $b_1=0.0$, $b_2=-0.05$, $b_3=-0.1$, $b_4=-0.15$, $b_5=-0.2$; $b_6=-0.25$, $b_7=-0.3$, $b_8=-0.35$; $a_1=0.9254$, $a_2=-4.5127$, $a_3=48.395$, $a_4=-226.9$, $a_5=540.0$, $a_6=-673.76$, $a_7=419.330$, $a_8=-102.98$)

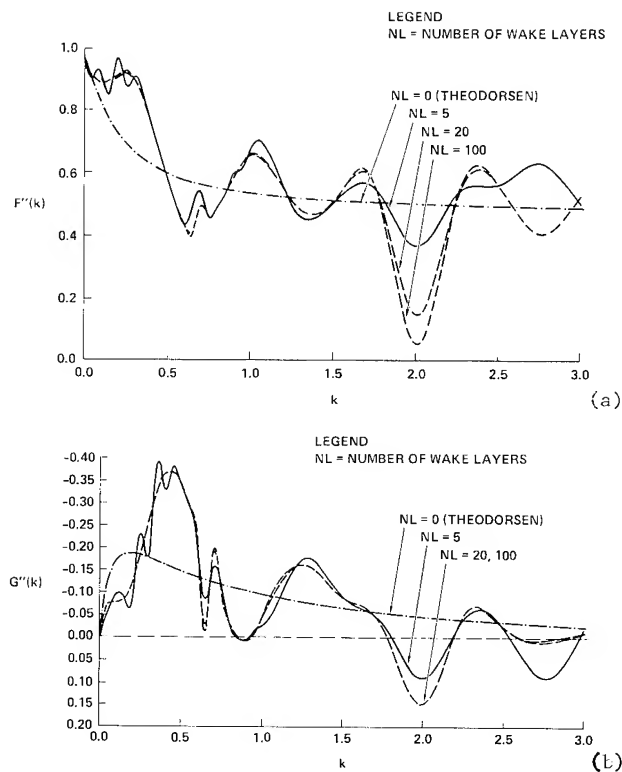


Fig. 16 Cascade Wake Model Lift Deficiency Function for Increasing Numbers of Wake Layers (for $\bar{T}_{Re}=9.4248$, $\bar{T}_{He}=1.5707$; $\bar{r}_e=1.5$, $\bar{h}_e=1.5707$)

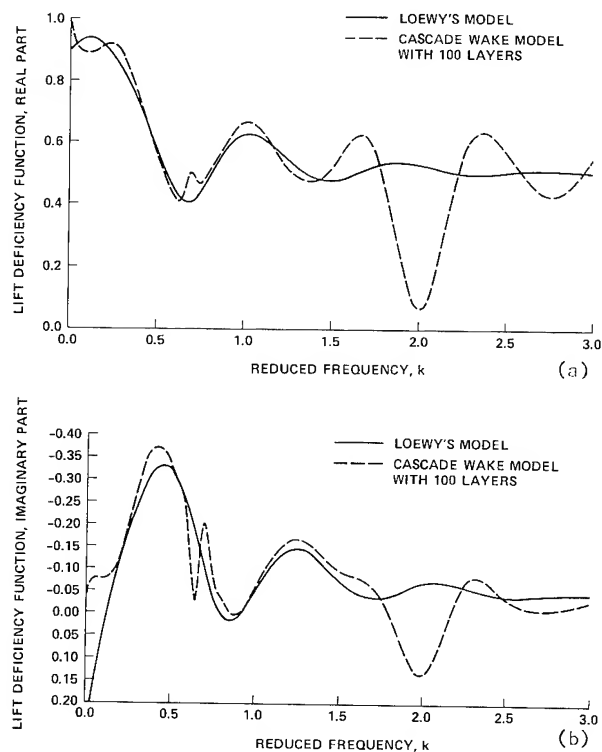


Fig. 17 Comparison of Cascade Wake Model and Loewy's Lift Deficiency Functions (for $\bar{T}_{Re}=9.4248$, $\bar{T}_{He}=1.5707$; $\bar{r}_e=1.5$, $\bar{h}_e=1.5707$)

by

S. Hanagud, M. Meyyappa, Y. P. Cheng, and J. I. Craig
Georgia Institute of Technology
School of Aerospace Engineering
Atlanta, Georgia 30332

Abstract

A method to identify the mass, damping and stiffness matrices from measured modal parameters is discussed. The procedure consists of minimizing a matrix norm of the error in the eigenvalue equation. It is assumed that some of the coefficients in the mass matrix are known a priori. The unknown coefficients of the mass matrix and the coefficients of stiffness and damping matrices are then obtained. Both numerical examples and examples using real experimental data are considered. Cases of proportional and nonproportional damping are discussed.

Introduction

A linear structural dynamic system is usually represented mathematically by a set of second order linear differential equations. The inertia, damping and stiffness effects are quantified in terms of mass, damping and stiffness matrices whose order is equal to the number of degrees of freedom chosen in modelling the physical system. An identification problem involving such systems reduces to the determination of these matrices from a given set of information about the dynamic behavior of the system. For example, the information can be in the form of the system output in the time domain for a specified input. Although a substantial number of techniques have been developed by various researchers to identify undamped or proportionally damped systems, methods capable of handling generalized damping matrices are relatively scarce. Currently existing procedures in this area include the estimation of system matrices using time domain output (1-3), frequency domain output (4) and modal parameters (5,6).

Caravani, Watson, and Thomson (1) have described a time domain recursive least square technique to identify the general damping matrix. In this method, only the parameters of the mass matrix are assumed to be known initially. However, a knowledge of the displacement, velocity and acceleration at all nodes and the forcing vector are assumed to be determined by measurements on the system. Another procedure that involves the use of time domain data is described by Kozin and Kozin (2). Yun and Shinozuka (3) discuss a nonlinear Kalman filtering technique for the problem.

Caravani and Thomson (4) present a frequency domain technique for systems with nonproportional damping. In their method, the parameters of mass and stiffness matrices are assumed to be known. It is also assumed that the Fourier transforms of the forcing vector and the response vector are determined from measurements on the system. The parameters of the damping matrix are then estimated by minimizing a function involving the difference between actual and measured responses over a specific frequency range of interest. Beliveau (5) presents a Bayesian approach to the problem. The method is based on a modified Newton-Raphson scheme and perturbations of eigenvalues and eigenvectors.

Copyright © American Institute of Aeronautics and Astronautics, Inc., 1984. All rights reserved.

In a recent paper, Ibrahim (6) presents a different approach to the problem. He formulates the problem of nonproportional damping in the form of a system of first order equations. He assumes that the parameters of the mass matrix are known. It is also assumed that the complex eigenvalues and complex eigenvectors are determined by measurements on the system. First, the case where all the eigenvalues and eigenvectors corresponding to the assumed degrees of freedom are measured is discussed. Next, the case where only some of the eigenvalues and eigenvectors are measured is discussed. The method depends on solving a system of simultaneous equations for the parameters of the $K^{-1}M$ and $K^{-1}C$ matrices. The method does not assure the determination of symmetric stiffness and damping matrices even though the real passive system contains symmetric matrices.

In this paper a different approach to the problem is presented. The technique is based on the assumption that either some or all of the elements of the mass matrix for example, are known. It is also assumed that the complex eigenvalues and the complex eigenvectors of the system have been measured (7-9). The parameters of the remaining elements of the mass matrix, the stiffness matrix, and the damping matrix are determined by minimizing the Euclidean norm of a matrix that assures the satisfaction of the equations of the eigenvalue problem and the appropriate orthogonality conditions. The minimization of the norm has been performed subject to the constraints of symmetry of the appropriate matrices. In order to simplify the computational procedure, new real matrices are defined which are functions of real and imaginary parts of the complex eigenvalues and eigenvectors.

The Eigenvalue Problem

The equations of motion that describe a freely vibrating n degree of freedom structural dynamic system are

$$M\ddot{y} + C\dot{y} + Ky = 0 \quad (1)$$

where M , C , and K are the $n \times n$ mass, viscous damping and stiffness matrices; y , \dot{y} and \ddot{y} are the $n \times 1$ vectors of displacement, velocity and acceleration measured at the n degrees of freedom. Equation (1) yields the following eigenvalue problem

$$\lambda_i^2 M \phi_i + \lambda_i C \phi_i + K \phi_i = 0 \quad (i = 1, 2, \dots, 2n) \quad (2)$$

where λ_i and ϕ_i are the i^{th} eigenvalue and the i^{th} eigenvector, which in general occur in complex conjugate pairs. When the damping matrix is proportional, the eigenvectors are real. In terms of the natural frequencies and the damping ratios of the system, the eigenvalues can be expressed as

$$\lambda_i = -\rho_i \omega_i + j \sqrt{1 - \rho_i^2} \omega_i \quad (3a)$$

$$\lambda_{n+i} = -\rho_i \omega_i - j \sqrt{1 - \rho_i^2} \omega_i \quad (3b)$$

for i varying from 1 to n .

Defining the following complex $n \times n$ matrices

$$\begin{aligned} U &= [\lambda_1^2 \phi_1 \quad \lambda_2^2 \phi_2 \quad \dots \quad \lambda_n^2 \phi_n] \\ V &= [\lambda_1 \phi_1 \quad \lambda_2 \phi_2 \quad \dots \quad \lambda_n \phi_n] \\ W &= [\phi_1 \quad \phi_2 \quad \dots \quad \phi_n] \end{aligned} \quad (4)$$

the eigenvalue problem in Equation (2) can be restated as

$$MU + CV + KW = 0. \quad (5)$$

It is to be noted that in this equation only the first n modes are included. This is because of the fact that when Equation (5) is satisfied for a given set of M , C , and K with the first n modes, it is also satisfied for their complex conjugates, which, by definition, are the higher order modes. Also note that when Equation (5) is satisfied, the orthogonality conditions are also satisfied.

The identification problem consists of finding the matrices M , C , and K when all the eigenvalues and eigenvectors are known through experiments or otherwise. If all the eigenvalues and eigenvectors are not known and/or all the eigenvector components are not known, the missing part of the data must be synthesized by some other means. Refs. 6 and 10 suggest several methods that are applicable when approximate mass and stiffness matrices of the system are known.

Identification of System Matrices

If inexact values for the mass, damping and stiffness matrices are substituted into Equation (5), it will not be satisfied exactly and will give rise to some error so that

$$MU + CV + KW = E \quad (6)$$

where E is the matrix of error coefficients whose components are given by

$$E_{ij} = \sum_{m=1}^n (M_{im} U_{mj} + C_{im} V_{mj} + K_{im} W_{mj}) \quad (7)$$

Equations (6) and (7) have been derived from Equation (2). When the eigenvalue problem is written in the form Equation (2), the higher modes will contribute more to the error as defined in Equation (6).

Consequently, the dynamic system identified by minimizing the error will reproduce the higher modes with greater accuracy. For most systems, however, it is the lower modes that are of interest. Experimental data is usually available for the lower modes only. In any case, analytical models are less exact in predicting the response in the higher modes due to the assumptions involved in deriving the models. As a result, it is more desirable to force the identified system to yield the lower modes as accurately as possible. In order to achieve this, Equation (2) is rewritten as

$$K \frac{1}{\lambda_i^2} \phi_i + C \frac{1}{\lambda_i} \phi_i + M \phi_i = 0$$

With the eigenvalue problem expressed in this form, the lower modes will dominate the error, and will therefore be reproduced more accurately. Using this form, however, is equivalent to using Equation (2), provided that the roles of the mass and stiffness

matrices are interchanged and reciprocals of eigenvalues are used instead of the eigenvalues themselves. Hence, all the equations derived hereafter will be based on Equations (2), (5), and (6).

Since structural dynamic systems usually possess symmetric mass, damping and stiffness matrices, it is necessary to ensure that the identification technique gives rise to symmetric matrices. This can be done by incorporating the following constraint equations in the procedure.

$$M - M^T = 0 \quad (8)$$

$$C - C^T = 0 \quad (9)$$

$$K - K^T = 0 \quad (10)$$

where T is used to denote the matrix transpose.

In the method proposed here, the system matrices are identified by minimizing the norm of E subject to the constraints in Equations (8) - (10). A constrained objective function is formulated as

$$\beta = \alpha^E + \alpha^M + \alpha^C + \alpha^K \quad (11)$$

in which β is the function to be minimized and

$$\alpha^E = \sum_{j=1}^n \sum_{i=1}^n |E_{ij}|^2 = \sum_{i=1}^n \sum_{j=1}^n E_{ij} \bar{E}_{ij} \quad (12)$$

$$\alpha^M = \sum_{i=1}^n \sum_{j=1}^n \gamma_{ij}^M (M_{ij} - M_{ji})$$

$$\alpha^C = \sum_{i=1}^n \sum_{j=1}^n \gamma_{ij}^C (C_{ij} - C_{ji}) \quad (13)$$

$$\alpha^K = \sum_{i=1}^n \sum_{j=1}^n \gamma_{ij}^K (K_{ij} - K_{ji})$$

where a bar denotes complex conjugate and γ^M , γ^C and γ^K are Lagrange multiplier matrices such that

$$\gamma^M = -(\gamma^M)^T, \quad \gamma^C = -(\gamma^C)^T, \quad \gamma^K = -(\gamma^K)^T \quad (14)$$

By differentiating Equation (11) with respect to the unknown mass coefficient M_{kl} and equating to zero, one obtains

$$\begin{aligned} \frac{\partial \beta}{\partial M_{kl}} &= \sum_{j=1}^n \sum_{i=1}^n (E_{ij} \frac{\partial \bar{E}_{ij}}{\partial M_{kl}} \\ &+ \frac{\partial E_{ij}}{\partial M_{kl}} \bar{E}_{ij}) + 2 \gamma_{kl}^M = 0 \end{aligned} \quad (15)$$

Written in matrix form, this equation reduces to

$$E \bar{U}^T + \bar{E} U^T + 2 \gamma^M = 0 \quad (16)$$

in which Equation (7) has been used. Upon taking the transpose, adding and using Equation (14), Equation (16) yields

$$E \bar{U}^T + \bar{E} U^T + \bar{U} E^T + U \bar{E}^T = 0 \quad (17)$$

Substituting for E from Equation (6),

$$\begin{aligned}
& M(UU^* + \bar{U}U^T) + (UU^* + \bar{U}U^T)M + \\
& C(VU^* + \bar{V}U^T) + (UV^* + \bar{U}V^T)C + \\
& K(WU^* + \bar{W}U^T) + (UW^* + \bar{U}W^T)K = 0 \quad (18)
\end{aligned}$$

where an asterisk denotes complex conjugate transpose. This equation can be written in a more compact form by defining the following matrices.

$$\begin{aligned}
L_1 &= \text{Re}(UU^*), \quad L_2 = \text{Re}(VU^*), \\
L_3 &= \text{Re}(WU^*) \quad (19)
\end{aligned}$$

where $\text{Re}(z)$ denotes the real part of complex number z . Equation (18) now becomes

$$\begin{aligned}
ML_1 + L_1M + CL_2 + L_2^T C + KL_3 \\
+ L_3^T K = 0 \quad (20)
\end{aligned}$$

Following a similar procedure, two additional equations are derived by differentiating the objective function with respect to the damping and the stiffness parameters. These equations can be expressed as follows.

$$ML_2^T + L_2M + CL_4 + L_4C + KL_5 + L_5^T K = 0 \quad (21)$$

$$ML_3^T + L_3M + CL_5^T + L_5C + KL_6 + L_6K = 0 \quad (22)$$

where

$$L_4 = \text{Re}(VV^*), L_5 = \text{Re}(WV^*), L_6 = \text{Re}(WW^*) \quad (23)$$

Equations (20) - (22) can be assembled together to form a set of homogeneous linear equations with the mass, stiffness and damping elements as unknowns. This results in

$$Ax = 0 \quad (24)$$

where A = coefficient matrix consisting of the elements of $L_1 - L_6$

$$\begin{aligned}
\text{and } x^T &= [M_{11} \ M_{12} \dots M_{1n} \ M_{22} \dots M_{2n} \dots M_{nn} \\
&\quad C_{11} \dots C_{nn} \ K_{11} \dots K_{nn}]
\end{aligned}$$

The length of the vector x when all the matrix elements are treated as unknown is $3n(n+1)/2$. To obtain a nontrivial solution however, at least one nonzero element of any one of the matrices M , C , and K must be specified. If this condition is satisfied, the set of equations in Equation (24) can be solved for by neglecting the rows obtained by differentiating with respect to the known elements and substituting the values of these elements into the remaining equations, thus converting the system into an inhomogeneous one.

If the total mass of the system is known and if the mass matrix is assumed to be diagonal, the above procedure can be used to get a unique solution. This is accomplished by first assigning an arbitrary value to one of the elements of the diagonal mass matrix and solving for the remaining unknowns in M , C , and K . The identified matrices are then multiplied by a scalar so that the sum of the diagonal elements of the revised

mass matrix is equal to the total mass and the ratios between the diagonal elements are preserved. Note that if a set of matrices M , C , and K satisfies Equation (5), this set multiplied by a scalar (or in the more general case, premultiplied by a constant $n \times n$ matrix) also satisfies the same equation.

The matrices $L_1 - L_6$ in Equation (19) and (23) are expressed in terms of U , V , and W which are complex. To avoid the use of complex arithmetic and facilitate computation, the relevant equations can be transformed so that they involve only real matrices. The eigenvalue problem in Equation (5), for example, is equivalent to

$$MZF^2 + CZF + KZ = 0 \quad (25)$$

where

$$\begin{aligned}
Z &= [\text{Re}(\phi_1) \ \text{Re}(\phi_2) \dots \text{Re}(\phi_n) \\
&\quad \text{Im}(\phi_1) \ \text{Im}(\phi_2) \dots \text{Im}(\phi_n)] \\
F &= \begin{bmatrix} \Lambda_R & \Lambda_I \\ -\Lambda_I & \Lambda_R \end{bmatrix}
\end{aligned}$$

$$\Lambda_R = \text{diag} [\text{Re}(\lambda_1) \ \text{Re}(\lambda_2) \dots \text{Re}(\lambda_n)]$$

$$\Lambda_I = \text{diag} [\text{Im}(\lambda_1) \ \text{Im}(\lambda_2) \dots \text{Im}(\lambda_n)]$$

By going through the error minimization process, it can be shown that in place of Equations (19) and (23), one obtains

$$\begin{aligned}
L_1 &= ZF^2(F^T)^2Z^T, \quad L_2 = ZF(F^T)^2Z^T \\
L_3 &= Z(F^T)^2Z^T, \quad L_4 = ZFF^TZ^T \\
L_5 &= ZF^TZ^T, \quad L_6 = ZZ^T \quad (26)
\end{aligned}$$

where all the required matrices are expressed in terms of the real and imaginary components of the measured eigenvalues and eigenvectors.

Numerical Results

To evaluate the performance of the identification method described, two numerical examples are considered in this section. In the first example, an assumed set of M , C , and K is used to determine the eigenvalues and eigenvectors which in turn are treated as experimental data and utilized in the identification. The resulting mass, stiffness and damping coefficients are compared with the exact values. The second example consists of experimental data for the first three bending modes obtained from a cantilever beam (Fig. 1) by curve fitting measured transfer functions. A three degree of freedom system is identified for the beam for each of the several cases considered and the eigenvalues and eigenvectors predicted by the identified system are compared with the test data. Since the imaginary parts of the experimental mode shapes of the beam were negligibly small, the eigenvectors in all cases were treated as real.

The mass, damping and stiffness matrices assumed in the first example were

$$M = \begin{bmatrix} 100 & 0 \\ 0 & 200 \end{bmatrix}, \quad C = \begin{bmatrix} 40 & -20 \\ -20 & 20 \end{bmatrix}, \quad K = \begin{bmatrix} 500 & -400 \\ -400 & 400 \end{bmatrix}$$

The identified coefficients of M, C, and K using the complex frequencies and mode shapes with different amounts of error are given in Table 1. The first element of the diagonal mass matrix was assumed to be known in obtaining these results. It is seen that when the error is of the order of 1% in eigenvalues and 5% in eigenvectors, the deviations of the coefficients from their exact values are of the order of 2%.

For the cantilever beam, an a priori finite element model was first constructed using three beam elements. A three degree-of-freedom model was obtained by removing the rotational degrees-of-freedom using Guyan reduction.⁽¹¹⁾ The mass and stiffness coefficients of this model are listed in Table 2. The a priori eigenvalues and eigenvectors are compared with their experimental counterparts in Table 3.

Identification of the matrix elements by using all the modes, and by treating the entire mass matrix to be known and equal to the a priori mass matrix, produced the values given in Table 4. The modal parameters of the identified model are listed in Table 5 along with those specified (experimental) in the identification. Noticeable differences are observed for the 2nd and 3rd modes, particularly in the mode shapes. To improve these values, only the diagonal elements of the a priori mass matrix were used next. The results are shown in Tables 6 and 7, and they indicate that the experimental modal parameters are simulated to a very high degree of accuracy by the identified system.

Cases in which experimental data are not available for all the modes were investigated by considering the test results for higher modes as unknown. A priori analytical modal parameters were substituted for the higher modes for which experimental data were assumed to be lacking. Following Ibrahim,⁽⁶⁾ these modes were assumed to possess damping values equal to the average of all the experimentally measured damping values. Results for the case in which the 3rd analytical mode was used with the first two experimental modes are given in Tables 8 and 9. When one experimental and two analytical modes were taken into account, the values shown in Tables 10 and 11 were obtained. As before, the model identified in each case using a priori diagonal mass elements is found to reproduce the specified modal parameters very accurately.

The experimental results that were used in the example consisted primarily of real eigenvectors. As a further test of the technique with complex eigenvectors, mass and stiffness matrices of Table 4 were used with a nonproportional damping matrix (Table 12) to obtain eigenvalues and eigenvectors. These are listed in Table 13. The identification procedure was then used with these eigenvalues, eigenvectors, and only the diagonal elements of the mass matrix shown in Table 12. The procedure totally reproduced the remaining elements, of the mass matrix, stiffness matrix, and the damping matrix of Table 12.

In some cases where some of the coefficients of the stiffness matrix were assumed to be known a priori and the coefficients of the mass and damping matrices were identified, the results were not always satisfactory. Even though the matrices obtained satisfied the equations of the eigenvalue problem, they were found not to be positive-definite, which would be considered unacceptable for most physical systems.

CONCLUSIONS

An identification procedure has been developed to estimate the mass, damping and stiffness matrices from experimental eigenvalues and eigenvectors. The method is based on the minimization of the eigenvalue equation error subject to the conditions of symmetry of the matrices involved. If one or more nonzero coefficients in any of the matrices are given, the remaining coefficients in all the matrices can be found. The identified matrices are symmetric and satisfy the eigenvalue problem as accurately as possible. The method is applicable in all cases of damping, either proportional or nonproportional. Example problems are solved to indicate the validity of the approach. Results obtained in these examples also demonstrate that the procedure is capable of identifying systems that simulate experimental modal data to high levels of accuracy. Application of the technique to systems with large degrees of freedom is still to be evaluated.

References

1. Caravani, P., Watson, M. L., and Thomson, W. T., "Recursive Least-Squares Time Domain Identification of Structural Parameters," *Journal of Applied Mechanics*, Vol. 44, No. 1, March 1977, pp. 135-140.
2. Kozin, F., and Kozin, C. H., "Identification of Linear Systems, Final Report on Simulation Studies," NASA CR-98738, April 1968.
3. Yun, C. B., and Shinozuka, M., "Identification of Nonlinear Structural Dynamic Systems," *Journal of Structural Mechanics*, Vol. 8, No. 2, 1980, pp. 187-203.
4. Caravani, P., and Thomson, W. T., "Identification of Damping Coefficients in Multidimensional Linear Systems," *Journal of Applied Mechanics*, Vol. 41, No. 2, June 1974, pp. 379-382.
5. Beliveau, J. G., "Identification of Viscous Damping in Structures from Modal Information," *Journal of Applied Mechanics*, Vol. 43, No. 2, June 1976, pp. 335-339.
6. Ibrahim, S. R., "Dynamic Modeling of Structures from Measured Complex Modes," AIAA Paper No. 82-0770.
7. Richardson, M., and Potter, R. W., "Identification of the Modal Properties of an Elastic Structure from Measured Transfer Function Data," *Proceedings of the 20th ISA Symposium held at Albuquerque, New Mexico*, May 1974, pp. 239-246.
8. Brown, D. L., Allemang, R. J., Zimmerman, R., and Mergeay, M., "Parameter Estimation Techniques for Modal Analysis," SAE Paper No. 790221.
9. Ibrahim, S. R., and Mikulcik, E. C., "A Method for the Direct Identification of Vibration Parameters from the Free Response," *Shock and Vibration Bulletin*, Vol. 47, Pr. 4, 1977, pp. 183-198.
10. Baruch, M., "Methods of Reference Basis for Identification of Linear Dynamic Structures," AIAA Paper No. 82-0769.
11. Guyan, R. J., "Reduction of Stiffness and Mass Matrices," *AIAA Journal*, Vol. 3, No. 2, Jan. 1965, p. 380.

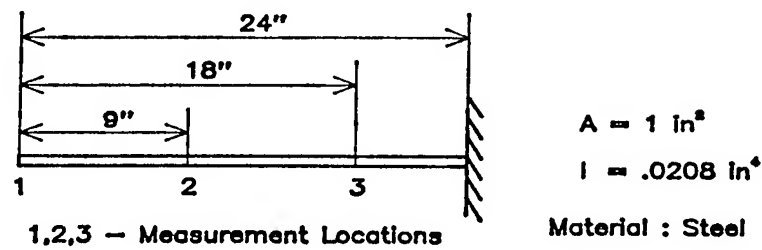


Fig. 1. Cantilever Beam Used in Experiments

Table 1. Identified Matrix Elements for the 2 Degree-of-Freedom System

Case	M_{11}	M_{12}	M_{22}	C_{11}	C_{12}	C_{22}	K_{11}	K_{12}	K_{22}
No error in eigenparameters	100	0	200	40	-20	20	500	-400	400
-1% Error in λ_i s +5% Error in ϕ_i s	100	0	200	39.6	-19.8	19.8	490	-392	392
+1% Error in λ_i s +5% Error in ϕ_i s	100	0	200	40.4	-20.2	20.2	510	-408	408
Exact Values	100	0	200	40	-20	20	500	-400	400

Table 2. Matrix Elements of the A Priori Beam Model

Element Index	(11)	(21)	(22)	(31)	(32)	(33)
Mass ($\times 10^{-2}$)lb sec ² /in	0.185	0.109	0.606	-.054	0.085	0.538
Damping	-	-	-	-	-	-
Stiffness ($\times 10^4$)lb/in	0.136	-.316	0.904	0.283	-1.198	3.179

Table 3. Comparison of Experimental and A Priori Analytical Modal Parameters

Mode No.	Experimental Values			A Priori Values		
	λ	Φ^T		λ	Φ^T	
1	-0.73+j 158.3	[1	.52 .12]	-0.00+j 174.8	[1	.49 .10]
2	-0.76+j 947.5	[1	-.55 -.73]	-0.00+j1110.1	[1	-.52 -.41]
3	-1.62+j2693.6	[1	-.69 .83]	-0.00+j3173.0	[1	-.66 .97]

Table 4. Identified Matrix Elements When the Entire Mass Matrix is Specified

Element Index	(11)	(21)	(22)	(31)	(32)	(33)
Mass ($\times 10^{-2}$)lb sec ² /in	0.185	0.109	0.606	-.054	0.085	0.538
Damping ($\times 10^{-2}$)lb sec/in	0.300	0.076	1.098	0.013	-.131	1.143
Stiffness ($\times 10^4$)lb/in	0.172	-.382	0.960	0.283	-.916	1.680

Table 5. Comparison of Identified and Specified Modal Parameters When the Entire Mass Matrix is Known

Mode No.	Specified Values			Identified Values		
	λ	Φ^T		λ	Φ^T	
1	-0.73+j 158.3	[1	.52 .12]	-0.73+j 158.2	[1	.52 .12]
2	-0.76+j 947.5	[1	-.55 -.73]	-0.76+j 962.4	[1	-.46 -.67]
3	-1.62+j2693.6	[1	-.69 .83]	-1.66+j2762.4	[1	-.63 .69]

Table 6. Identified Matrix Elements When Only the Diagonal Mass Elements are Specified

Element Index	(11)	(21)	(22)	(31)	(32)	(33)
Mass ($\times 10^{-2}$)lb sec ² /in	0.185	0.069	0.606	0.047	-.143	0.538
Damping ($\times 10^{-2}$)lb sec/in	0.326	-.049	1.281	0.250	-.700	1.424
Stiffness ($\times 10^4$)lb/in	0.257	-.638	1.678	0.692	-1.939	2.732

Table 7. Comparison of Modal Parameters When the Diagonal Mass Elements are Known

Mode No.	Specified Values			Identified Values		
	λ	Φ^T		λ	Φ^T	
1	-0.73+j 158.3	[1	.52 .12]	-0.73+j 158.3	[1	.52 .12]
2	-0.76+j 947.5	[1	-.55 -.73]	-0.76+j 947.5	[1	-.55 -.73]
3	-1.62+j2693.6	[1	-.69 .83]	-1.62+j2694.0	[1	-.69 .83]

Table 8. Identified Matrix Elements Using the 3rd Analytical Mode and Diagonal Mass Elements

Element Index	(11)	(21)	(22)	(31)	(32)	(33)
Mass ($\times 10^{-2}$)lb sec ² /in	0.185	0.019	0.606	-.008	-.063	0.538
Damping ($\times 10^{-2}$)lb sec/in	0.699	-1.121	3.950	1.424	-3.944	5.671
Stiffness ($\times 10^4$)lb/in	0.326	-.803	2.080	0.827	-2.332	3.333

Table 9. Comparison of Modal Parameters When the 3rd Analytical Mode is Used

Mode No.	Specified Values			Identified Values		
	λ	Φ^T		λ	Φ^T	
1	-0.73+j 158.3	[1	.52 .12]	-0.73+j 158.3	[1	.52 .12]
2	-0.76+j 947.5	[1	-.55 -.73]	-0.76+j 947.5	[1	-.55 -.73]
3	-8.57+j3173.0	[1	-.66 .97]	-8.56+j3172.6	[1	-.66 .97]

Table 10. Identified Matrix Elements Using 2 Analytical Modes and Diagonal Mass Elements

Element Index	(11)	(21)	(22)	(31)	(32)	(33)
Mass ($\times 10^{-2}$)lb sec ² /in	0.185	0.142	0.606	-.019	0.003	0.538
Damping ($\times 10^{-2}$)lb sec/in	0.875	-1.090	4.188	0.560	-3.636	12.031
Stiffness ($\times 10^4$)lb/in	0.134	-.334	1.017	0.394	-1.586	3.717

Table 11. Comparison of Modal Parameters When 2 Analytical Modes are Used

Mode No.	Specified Values			Identified Values		
	λ	Φ^T		λ	Φ^T	
1	-0.73+j 158.3	[1	.52 .12]	-0.73+j 158.3	[1	.52 .12]
2	-5.11+j1110.1	[1	-.52 -.41]	-5.11+j1110.1	[1	-.52 -.41]
3	-14.60+j3173.0	[1	-.66 .97]	-14.59+j3172.5	[1	-.66 .97]

Table 12. Assumed Matrix Elements of a Nonproportionally Damped System

Element Index	(11)	(21)	(22)	(31)	(32)	(33)
Mass ($\times 10^{-2}$) lb sec ² /in	0.184	0.109	0.606	-.054	0.085	0.538
Damping ($\times 10^{-2}$) lb sec/in	5.000	0.200	4.000	0.100	0.200	6.000
Stiffness ($\times 10^4$) lb/in	0.172	-.382	0.960	0.283	-.916	1.680

Table 13. Modal Parameters of the Nonproportionally Damped System

Mode No.	λ	Φ^T		
1	-6.88+j 158.1	[1.+j0.	0.52+j0.13 $\times 10^{-2}$	0.12+j0.69 $\times 10^{-3}$]
2	-7.20+j 962.3	[1.+j0.	-.46+j0.79 $\times 10^{-2}$	-.67+j0.46 $\times 10^{-2}$]
3	-11.59+j2762.4	[1.+j0.	-.63+j0.42 $\times 10^{-2}$	0.69-j0.50 $\times 10^{-2}$]

N. Niedbal*

Deutsche Forschungs- und Versuchsanstalt für
Luft- und Raumfahrt (DFVLR-AVA)
Göttingen, W. GermanyAbstract

Normal mode parameters are required in order to solve dynamic problems. These parameters can be determined either analytically by means of a Finite Element Method (FEM) or experimentally by means of a Ground Vibration Test or Modal Survey Test. The classical Phase Resonance Method determines directly the undamped normal mode parameters. To overcome the problem of structures with limited accessibility, phase separation methods have to be taken into account. In order to ensure comparability between the results of the FEM analysis and the proposed experimental method, a matrix transformation is presented to transform the damped (complex) normal mode parameters into undamped (real) normal mode parameters.

Nomenclature

D	generalized damping matrix
K	generalized stiffness matrix
K*	complex generalized stiffness matrix containing the stiffness and damping matrix, see Eq. (6)
M	generalized mass matrix
T ₁	complex transformation matrix
T ₂	real transformation matrix
X	modal matrix

Special symbols:

() ^d	appertaining matrix formulated by means of damped normal modes
() ^r	real part
() ⁱ	imaginary part
() ⁻	matrices obtained by means of the transformation matrix T ₁
() ^T	matrix transposed

Introduction

The determination of normal mode parameters has become an important tool in structural dynamics. Mathematical description of the structural dynamics can be formulated in an efficient manner by means of normal mode parameters. The parameters are:

- the normal frequency,
- the damping coefficient,
- the generalized mass and
- the normal mode shape.

Classical applications of these normal mode formulations include flutter clearance of aircraft and the dynamic qualification of spacecraft structures. Even changes of the dynamic behavior due to structural modification can be calculated on the basis of normal mode parameters. Moreover, it is possible to

determine the dynamic behavior of complicated, branched structures by means of the dynamic behavior of the various substructures using normal mode parameters.

Depending on the course of development of an aerospace structure, the normal mode parameters can be determined in two different ways:

- During the design phase of a structure the normal mode parameters are determined analytically by means of finite element methods (FEM).
- After production of the real structure the normal mode parameters can be measured in a ground vibration test, also called modal survey test (MST).

Comparison and correlation of both the analytically and experimentally determined normal mode parameters offer maximum reliability and accuracy which are important criteria for aerospace constructions. When analyzing modern ground vibration test techniques, this aspect has to be kept in mind.

Until recently, the ability to model a realistic damping distribution within an FEM analysis was very limited. On the one hand, a host of results and data have been published to describe the damping behavior of structures while, on the other hand, no general theory could be established to calculate accurately a physical damping distribution. For this reason, FEM calculations are performed without taking damping effects into account. Therefore, the results of an FEM analysis are the normal mode parameters of the undamped structure. The mode shapes of the undamped system are real and therefore are called real normal modes. Contrary to the equation of motion described above, the equation of motion could be formulated to include damping, as is the case for all newer experimental methods, called Phase Separation Methods (PSM). The results of such an approach are the damped normal mode parameters. In the case of a real structure with disproportionate damping distribution¹, the mode shapes are complex and are therefore called complex normal modes.

Due to the different ways of formulating the equations of motion, a comparison of FEM results and PSM data may be erroneous. The only experimental method which determines undamped normal mode parameters is the classical phase resonance method². By virtue of essential improvements made in electronic measurement as well as process computer techniques, this method has been developed into an efficient and reliable procedure³. The improved version of the classical phase resonance method is based on the indicator function and on-line presentation of the normal modes in order to aid the test engineer in identifying and isolating normal modes. Reduction of test duration³ using the classical phase resonance method is shown in Table 1.

* Dr.-Ing., Institute of Aeroelasticity

Year	Configuration	Number of Measured Eigenmodes	Test Duration
1966	clean wing	21	6 weeks
1974	5 configurations with 2-6 external stores	110	6 weeks
1978	clean wing and 5 configurations with 2-6 external stores	125	10 days

Table 1: Reduction of test duration using the classical phase resonance method

Despite these improvements, analytical determination of undamped normal mode parameters from measured complex responses is desired for structures with limited accessibility. Limited accessibility means that a desired excitation of the structure is not possible due to physical barriers. In such cases, only the complex responses of a structure can be measured. The present task entails analytical determination of the undamped normal mode parameters from such measured complex responses.

Determination of the Damped Normal Mode Parameters

In the past, many alternative spectral decomposition techniques⁴⁻¹⁰ have been proposed for determination of normal mode parameters. Assessment of the individual methods is difficult because published results are based on quite different test items. Furthermore, different weighting of the selection criteria will lead to diverse assessments of the individual methods. Taking all these aspects into account and analyzing the mathematical formulation of the various procedures, the author³ selected an improved version¹¹ of Natke's method¹² as the most appropriate to determine the damped normal mode parameters from measured complex responses.

Determination of the Undamped Normal Mode Parameters

If the damped normal mode parameters, designated with the superscript "d", are known, then the damped normal mode parameters have to be transformed

$$\bar{X} = X^d T_1 \quad (1)$$

or, in terms of real and imaginary parts,

$$\bar{X}' + j \bar{X}'' = X^{d'} T_1' - X^{d''} T_1'' + j (X^{d''} T_1' + X^{d'} T_1'') \quad (2)$$

The undamped normal mode parameters are characterized by the following conditions:

- real normal modes, i.e. a real modal matrix X ,
- a diagonal generalized mass matrix M and a diagonal generalized stiffness matrix K and

- a non-diagonal damping matrix D .

Comparing these characteristics with those of the damped normal mode parameters, only the first condition enables formulation of a mathematical procedure. The condition of real modes requires that the imaginary part of the matrix \bar{X} vanishes, which leads to:

$$X^{d'} \cdot T_1'' = -X^{d''} \cdot T_1' \quad (3)$$

Eq.(3) contains two unknowns, T_1' and T_1'' . In order to solve Eq.(3), matrix T_1' is assumed a unity matrix. Premultiplying Eq.(3) by the transposition of $X^{d'}$, matrix T_1'' can be calculated from Eq.(3) as follows:

$$T_1'' = -[(X^{d'})^T X^{d'}]^{-1} (X^{d'})^T X^{d''} \quad (4)$$

The transformed normal modes are calculated from Eq.(1), while the transformed generalized mass, stiffness and damping matrices are obtained from

$$\bar{M} = T_1^T M^d T_1 \quad \text{and} \quad (5a)$$

$$\bar{K}^* = T_1^T K^{*d} T_1 \quad (5b)$$

whereby the complex matrix K^{*d} contains the stiffness and damping matrices

$$K^{*d} = K^d + j D^d \quad (6)$$

Performing the transformation according to Eq.(5) discloses that matrix \bar{M} as well as the real part \bar{K} of matrix \bar{K}^* are both non-diagonal matrices. The assumption that matrix T_1' in Eq.(3) is a unity matrix produces this result.

The second condition of a diagonal generalized mass matrix M and generalized stiffness matrix K can now be used. In order to obtain the diagonal matrices, an eigenvalue approach can be applied:

$$(-\omega^2 \bar{M} + \bar{K}) T_2 = 0 \quad (7)$$

The diagonalization of \bar{M} and \bar{K} by means of transformation matrix T_2 yields:

$$M = T_2^T \bar{M} T_2 \quad (8a)$$

$$K = T_2^T \bar{K} T_2 \quad (8b)$$

$$X = \bar{X} T_2 \quad (8c)$$

The transformation of damping matrix \bar{D} by means of T_2 ,

$$D = T_2^T \bar{D} T_2 \quad (8d)$$

produces a non-diagonal matrix. This is the complete generalized damping matrix. The non-diagonal terms express the damping coupling effects.

Results

In order to verify the proposed transformation, the three-degrees-of-freedom system shown in Figure 1 was simulated. The influence of damping coupling was studied by selecting the following local damping factors:

$$\gamma_1 = 0.3, \quad \gamma_2 = \gamma_3 = 0.04$$

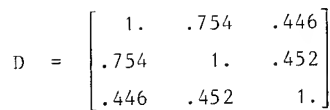
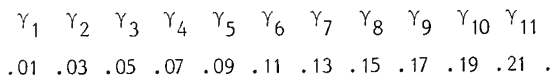


Table 2: Damping matrix of the disproportionate damped system with three degrees of freedom

The generalized damping matrix is the most sensitive and may well be the most interesting one. For an expanded eleven-degrees-of-freedom system, this matrix was calculated from the damped normal mode parameters. The simulated physical damping factors are as follows:



The appertaining generalized damping matrix in orthonormalized form is shown in Table 3. These results are based on the complete eleven-degrees-of-freedom system. In practice, only a limited number of modes are of interest. Therefore, only the third through sixth normal modes were extracted. The resulting damping matrix is also included in Table 3. Comparison with the complete number of modes shows nearly the same results.

$$\begin{array}{rrrr} 100 & & & \\ -52 & 100 & & \\ -19 & -29 & 100 & \\ -10 & 11 & -51 & 100 \end{array}$$

3rd - 6th
normal modes

[illegible]

Table 3: Generalized damping matrix of a disproportionate damped system with eleven degrees of freedom

The same comparisons were performed simulating in addition "measurement" errors of the deformations up to 7.5%. The results of the complete number of modes as well as of the limited number of modes are not influenced significantly, see Table 4.

$$\begin{array}{ccccccc}
 & & & & & & 100 \\
 & & & & & -51 & -100 \\
 & & & & -18 & -27 & 100 \\
 & & & -10 & -60 & 100 \\
 \hline
 100 & & & & & & \\
 -35 & & & & & & \\
 -21 & & -31 & & & & \\
 -17 & & 12 & & & & \\
 3 & & 4 & & & & \\
 2 & & -2 & & & & \\
 -3 & & -3 & & & & \\
 -1 & & 2 & & & & \\
 2 & & 2 & & & & \\
 1 & & -1 & & & & \\
 -1 & & -4 & & & &
 \end{array}
 \begin{array}{ccccccc}
 & & & & & & 100 \\
 & & & & & -51 & -100 \\
 & & & & -18 & -27 & 100 \\
 & & & -10 & -60 & 100 \\
 \hline
 & & & & & & \\
 & & & & & & \\
 & & & & & & \\
 & & & & & & \\
 & & & & & & \\
 & & & & & & \\
 & & & & & & \\
 & & & & & & \\
 & & & & & & \\
 & & & & & &
 \end{array}
 \begin{array}{l}
 \text{3rd - 6th} \\
 \text{normal modes}
 \end{array}$$

Table 4: Generalized damping matrix of a disproportionate damped system with eleven degrees of freedom (simulated measurement error 7.5%)

N. S. Khot*

V. B. Venkayya*

Air Force Wright Aeronautical Laboratories
Wright-Patterson Air Force Base, Ohio

and

F. E. Eastep**

Department of Aerospace Engineering
University of Dayton, OhioAbstract

This paper deals with the study of the dynamic behavior of large space structures due to changes in the stiffness of the members. The stiffness of the members was modified to satisfy an optimum design criterion, to satisfy static displacements associated with the line-of-sight (LOS) and to satisfy frequency constraints. The response of the LOS to different initial displacement conditions was investigated for various modified designs.

Introduction

There are different stringent requirements on Large Space Structures (LSS) because of their use, environment and the methods used to deploy them. LSS have to be a minimum weight design and also satisfy all the imposed performance requirements. One of the important requirement is the Line-of-Sight (LOS) pointing. The error associated with this has to be within a specified value for proper operation of the vehicle. The LOS error may be defined as the movement of a node point or a linear combination of movements at different locations in the structure due to a dynamic disturbance. The LOS error depends on the stiffness of the structure, the distribution of nonstructural mass and the control system used to minimize the error. The correct procedure to obtain an optimum design would be to include all the design variables in the formulation of the problem and to derive a proper algorithm to minimize the specified objective functions and satisfy all the constraints. In order to solve this problem it would be necessary to deal with two disciplines of LSS design such as structural design and control theory. This is a difficult problem to solve because it would be necessary to take into consideration the interaction of the two disciplines.

In this paper a simple procedure to investigate the effect of structural modifications on the passive control of the LOS error is used. The structure is modified to satisfy constraints on static displacements associated with the LOS and the frequency distribution. Different designs are then compared for their dynamic behavior. The structure used in this investigation is a tetrahedral truss discussed in Ref. 1. This structure was devised by Draper Labs as one of the simplest nonplanar geometries capable of representing a Large Space Structure. A short description of the methods used to modify and analyze the structure is given in the next section.

Static Analysis

The relation between the static load vector $\{P\}$ and the displacement vector $\{u\}$ for a structure with n degrees of freedom is given by

$$[K]\{u\}=\{P\} \quad (1)$$

where $[K]$ is the $n \times n$ symmetric stiffness matrix of the structure. The displacement u_j at a node point j in the structure is given by

$$u_j = \sum_{i=1}^m \frac{Q_{ij}}{A_i} \quad (2)$$

where m is the number of elements and Q_{ij} is the flexibility coefficient given by

$$Q_{ij} = A_i \{u\}_i^t [k]_i \{s^j\}_i \quad (3)$$

Here $\{u\}_i$ and $\{s^j\}_i$ are the displacements associated with the i th element due to the applied load vector $\{P\}$ and the virtual load vector $\{S^j\}$. In Eq 3 $[k]_i$ is the stiffness matrix of the i th element and A_i is the i th design variable, which in the case of bar elements will be the cross-sectional area. The solution to Eq 1 gives the displacements in the structure, and Eq 2 and 3 can be used to determine the displacement at a specified node point.

Dynamic Analysis

The equations of motion for a structure are given by

$$[M]\{\ddot{u}(t)\} + [E]\{\dot{u}(t)\} + [K]\{u(t)\} = [D]\{F(t)\} \quad (4)$$

where $[M]$ is a $n \times n$ mass matrix which includes the contribution from the structural and the nonstructural mass of the structure, $[E]$ is a $n \times n$ damping matrix and $[D]$ is the $n \times p$ applied load distribution matrix relating the applied load vector $\{F(t)\}$ and the coordinate system. For the free undamped motion Eq 4 becomes

$$[M]\{\ddot{u}(t)\} + [K]\{u(t)\} = 0 \quad (5)$$

Since the free oscillations are simple harmonic, the displacement $u(t)$ can be written as

$$\{u(t)\} = \{u\} e^{i\omega t} \quad (6)$$

*Aerospace Engineer, Member AIAA

**Professor, Associate Fellow AIAA

where ω is the circular frequency and $\{U\}$ is the vector defining the amplitudes of motion. Substituting Eq 6 in Eq 5 and cancelling $e^{i\omega t}$ gives the homogeneous set of equations,

$$[K] - \omega^2 [M] \{U\} = 0 \quad (7)$$

Multiplying this equation by $\{U\}^t$ and rearranging gives

$$\omega_j^2 = \frac{\{U_j\}^t [K] \{U_j\}}{\{U_j\}^t [M] \{U_j\}} \quad (8)$$

where ω_j is the j th circular frequency associated with the j th eigenvector $\{U_j\}$. Using the coordinate transformation,

$$\{U\} = [\phi] \{\eta\} \quad (9)$$

where $[\phi]$ is the modal matrix whose columns are eigenvectors $\{\tilde{U}\}_j$ (normalized with respect to the mass matrix $[M]$), Eq 4 can be transformed into n uncoupled system of differential equations as

$$[\bar{M}]\{\ddot{\eta}\} + [\bar{E}]\{\dot{\eta}\} + [\bar{K}]\{\eta\} = [\phi]^t [D] \{F\} \quad (10)$$

where

$$[\bar{M}] = [I]_{n \times n} \text{ identify matrix} \quad (11)$$

$$[\bar{E}] = [2\xi\omega]_{n \times n} \text{ diagonal damping matrix} \quad (12)$$

$$[\bar{K}] = [\omega^2]_{n \times n} \text{ matrix of eigenvalues} \quad (13)$$

In Eq 12 $\{\xi\}$ is the vector of modal damping factors. The second order Eq 10 can be reduced to a first order equation by using the state variable vector $\{x\}$ given by

$$\{x\}_{2n} = \begin{bmatrix} \eta \\ \dot{\eta} \end{bmatrix} \quad (14)$$

The state space representation of Eq 10 using Eq 14 can be written as

$$\{\dot{x}\} = [A]\{x\} + [B]\{f\} \quad (15)$$

where $[A]$ is $2n \times 2n$ plant matrix, $[B]$ is $2n \times p$ input matrix and $\{f\}$ is an $p \times 1$ control input vector. The plant matrix and the input matrix are of the form

$$[A] = \begin{bmatrix} 0 & I \\ -\omega^2 & -2\xi\omega \end{bmatrix} \quad (16)$$

$$[B] = \begin{bmatrix} 0 \\ \frac{1}{t_D} \end{bmatrix} \quad (17)$$

Eq 15 is known as the state input equation and the state output equation is given by

$$\{y\} = [C]\{x\} \quad (18)$$

where $\{y\}$ is a $q \times 1$ output vector and $[C]$ is a $q \times 2n$ output matrix.

The complete solution to Eq 15 is given by²

$$\underline{x}(t) = \psi(t) \underline{x}(0) + \int_0^t \psi(t-\alpha) B \underline{f}(\alpha) d\alpha \quad (19)$$

where $\psi(t)$ is the state transition matrix and is given by

$$\psi(t) = e^{At} = 1 + \frac{At}{1!} + \frac{(At)^2}{2!} + \dots \quad (20)$$

In Eq 19 \underline{x} and \underline{f} are the vectors and ψ , B , A are the matrices. For discrete time steps Eq 19 can be suitably modified and evaluated at each time interval. In the case where there are no externally applied loads or the input vector $\{f\}$ is zero, Eq 19 becomes

$$\underline{x}(t) = e^{At} \underline{x}(0) \quad (21)$$

The numerical solution to Eqs 19 or 21 can be obtained by using available subroutines.³

Algorithm to Minimize Displacements

The optimization problem for minimizing the displacements in a structure for a given weight of the structure \bar{W} can be stated as:

minimize the displacement function 'G' subject to

$$\bar{W} = \sum_{i=1}^m \rho_i A_i l_i = \bar{W} \quad (22)$$

where ρ_i is the density of the material, A_i is the design variable and l_i is the volume parameter associated with the i th element. Using Eq 2 the function G may be written as

$$G = \sum_{i=1}^m \frac{Q_{i1}}{A_i} \text{ a single displacement} \quad (23)$$

can be written as^{4,5}

$$G = \sum_{j=1}^{p_1} R_j \sum_{i=1}^m \frac{Q_{ij}}{A_i} \text{ a linear combination of the displacements} \quad (24)$$

$$G = \sum_{j=1}^{p_1} R_j \left(\sum_{i=1}^m \frac{Q_{ij}}{A_i} \right)^2 \text{ a linear combination of the squares of the displacements} \quad (25)$$

where R_j is a set of specified parameters and p_1 is the number of parameters. Using Eqs 22 and 23 through 25, the Lagrangian can be written as

$$L(A, \lambda) = G + \frac{1}{\lambda} (W - \bar{W}) \quad (26)$$

where λ is the Lagrange multiplier. Differentiating Eq 26 with respect to the design variables A_i and setting the resulting equations to zero, the optimality conditions can be written as

$$\frac{\partial G}{\partial A_i} + \frac{1}{\lambda} \rho_i \ell_i = 0 \quad i=1, \dots, m \quad (27)$$

Using Eqs 23 through 25 the optimality conditions for the three objective functions can be written as

single displacement

$$1 = \lambda \frac{Q_{i1}}{A_i^2 \rho_i \ell_i} \quad (28)$$

linear combination of the displacements

$$1 = \lambda \sum_{j=1}^{p_1} R_j \frac{Q_{ij}}{A_i^2 \rho_i \ell_i} \quad (29)$$

linear combination of the square of the displacements

$$1 = \lambda \sum_{j=1}^{p_1} 2R_j G_j \frac{Q_{ij}}{A_i^2 \rho_i \ell_i} \quad (30)$$

In Eq 30 $G_j = \sum_{i=1}^m \frac{Q_{ij}}{A_i}$. Eqs 28 through 30 can be written as

$$1 = \beta_i \quad (31)$$

where the value of β_i depends on the nature of the objective function. Using the optimality criterion a recurrence relation to modify the design variables

$$A_i^{v+1} = A_i \left(1 - \frac{1}{r} (\beta_i - 1) \right)^{-1}_v \quad (32)$$

where $v+1$ and v are the iteration numbers and r is the parameter that controls the step size. The value of the Lagrange parameter λ which is required to use in Eq 32 can be calculated by solving Eqs 28 through 30 for A_i substituting in Eq 22 and solving for λ . This gives

$$\lambda^{1/2} = \frac{\bar{W}}{\sum_{i=1}^m \sqrt{Q_{i1} \rho_i \ell_i}} \quad (33)$$

for a single displacement,

$$\lambda^{1/2} = \frac{\bar{W}}{\sum_{i=1}^m \sqrt{\sum_{j=1}^p R_j Q_{ij} \rho_i \ell_i}} \quad (34)$$

for a linear combination of displacements,

$$\lambda^{1/2} = \frac{\bar{W}}{\sum_{i=1}^m \sqrt{\sum_{j=1}^p 2R_j G_j Q_{ij} \rho_i \ell_i}} \quad (35)$$

for a linear combination of the square of the displacements.

The algorithm to minimize the displacements then consists of modifying the design variables by using Eq 32 until the optimality criterion is satisfied.

Algorithm to Satisfy Frequency Constraints

The optimization problem for the minimum weight of the structure with constraints on the fundamental frequency and the frequency distribution of the higher vibration modes can be defined as:

minimize the weight of the structure

$$W = \sum_{i=1}^m \rho_i A_i \ell_i \quad (36)$$

subjected to

$$g_j^* = g_j - \bar{g}_j \quad (37)$$

$$= (\omega_j^2 - \alpha_j \bar{\omega}_1^2) \leq 1 \quad j=1, \dots, p_1 \quad (38)$$

where g_j and \bar{g}_j are the actual and the desired values of the constraints. $\bar{\omega}_1$ is the specified value of the fundamental frequency and $\alpha_j \bar{\omega}_1^2$ is the desired value of the square of the j th frequency. Using Eqs 36 and 38 the Lagrangian can be written as:

$$L(A, \lambda) = \sum_{i=1}^m \rho_i A_i \ell_i - \sum_{j=1}^{p_1} \lambda_j (\omega_j^2 - \alpha_j \bar{\omega}_1^2) \quad (39)$$

Differentiating this equation with respect to the design variable A_i and setting the resulting equations to zero gives⁶

$$\rho_i \ell_i - \sum_{j=1}^{p_1} \lambda_j \frac{\partial \omega_j^2}{\partial A_i} = 0 \quad (40)$$

or

$$1 = \sum_{j=1}^{p_1} \lambda_j \frac{\tilde{Q}_{ij}}{A_i^2 \rho_i \ell_i} \quad (41)$$

or

$$1 = \beta_i \quad (42)$$

where

$$\tilde{Q}_{ij} = A_i \{ \{\tilde{U}_j\}_i^T [k]_i \{\tilde{U}_j\}_i - \omega_j^2 \{\tilde{U}_j\}_i^T [m]_i \{\tilde{U}_j\}_i \} \quad (43)$$

In Eq 43 $\{\tilde{U}_j\}$ is the j th vibration mode normalized with respect to the mass matrix, and $[m]_i$ is the structural mass matrix associated with the i th element. The format of this optimality criterion for frequency constraints (Eq 42) has the same form as Eq 31, and the recurrence relation to modify the design variables can be written as⁶

$$A_i^{v+1} = A_i^v \left(1 - \frac{1}{r} (\beta_i - 1) \right)^{-1} \quad (44)$$

where $v+1$ and v are the iteration numbers and r is the step size parameter. In order to use Eq 45 it is necessary to evaluate the Lagrange multiplier λ_j associated with the active constraints. A set of equations to determine the Lagrange multipliers can be written by using the condition that a change in the design variables should satisfy the constraint relations. This would give⁶

$$\sum_{k=1}^{p_1} \lambda_k^{v+1} \sum_{i=1}^m \left(\frac{\tilde{Q}_{ij} \tilde{Q}_{ik}}{\rho_i \ell_i A_i^3} \right) = r (\alpha_j \bar{\omega}_1^2 - \omega_j^2) + \left(\sum_{i=1}^m \frac{Q_{ij}}{A_i} \right) \quad (45)$$

Eq 45 was derived by assuming that all the elements would satisfy the optimality criterion. However, the cross sectional areas of some of the elements would be governed by the minimum size requirement. In that case these elements are not included in the summation in Eq 45. One of the design requirements can be that the fundamental frequency or some other frequency of the structure should be equal to a specified value. This would require the scaling of all the design variables. The scaling factor δ_j is given by⁶

$$\delta_j = \frac{\bar{F}_j \frac{\alpha_j \bar{\omega}_1^2}{\omega_j^2} - \bar{H}_j \alpha_j \bar{\omega}_1^2}{\bar{F}_j - \bar{H}_j \alpha_j \bar{\omega}_1^2} \quad (46)$$

where

$$\bar{F}_j = \{\tilde{U}_j\}^T [K] \{\tilde{U}_j\} \quad (47)$$

$$\bar{H}_j = \{\tilde{U}_j\}^T [M_1] \{\tilde{U}_j\} \quad (48)$$

In Eq 48 the mass matrix $[M_1]$ includes the contribution from the structural mass only. When nonstructural mass is present, it is required to iterate a couple of times before the j th frequency is exactly equal to the j th desired frequency.

Illustrative Examples

The structural model selected for this study is shown in Fig. 1. In spite of its simplicity it models the feed-tower in a generic class of large antenna applications. This structure is defined in unspecified consistent units. The edges of the tetrahedron are each 10 units long, and the bipod legs are each $2\sqrt{2}$ units long. The horizontal base of the tetrahedron formed by nodes 2, 3 and 4 is 2 units above the base plane of reference. The coordinates of the node points are given in Table 1. The structure has twelve degrees of freedom, and four masses of 2 units are attached at nodes 1 through 4. Young's modulus of the members is 1.0, and the density of the structural material is assumed to be 0.001.

The tetrahedral apex (node 1) represents the antenna feed and its motion defines the LOS (line of sight). The motion of this point in the X direction and the Y direction are denoted by LOS-X and LOS-Y respectively. The sum of the squares of these displacements i.e., $(\text{LOS-X})^2 + (\text{LOS-Y})^2$ is denoted by LOS-(2). A comparison of the different design modifications discussed below will be made with respect to the response of LOS-X, LOS-Y and LOS-2 to changes in the stiffness of members of the structure. The four designs used for comparison are described first.

Design A

This was a nominal design with the cross-sectional areas of the members as given in Table 2. This design was used by the Charles Stark Draper Lab¹ for their preliminary investigation on the

design of the active control system.

Design B

This design was obtained by using the algorithm discussed previously to minimize the displacement function by keeping the weight of the structure the same. The weight of the structure was equal to that of Design A, and the displacement function was the sum of the squares of the displacements in the X and Y direction of node 1, which is the line of sight. The nonstructural masses attached at nodes 1 through 4 were assumed to be the static loads acting in the three coordinate directions. For the first iteration the cross-sectional areas were assumed to be the same as those of Design A. The design variables were modified by using the recurrence relation in Eq 32. The step size parameter r was set equal to 100 for the first twenty-five iterations, and was reduced to 10 thereafter. The small step size was used to obtain a design that satisfies the optimality criterion exactly, i.e. $\beta_i=1$ for all the elements. The initial value of the objective function was .313 and this was reduced to .041 after about fifty iterations. The cross-sectional areas of the optimum design are given in Table 2.

Design C

An algorithm that minimizes the weight of the structure with constraints on the frequency distribution was used to obtain this design. It was specified that the square of the fundamental frequency (ω_1^2) and the second frequency (ω_2^2) should be equal to 1.76 and 2.69 respectively. These values were the same as that for Design A. The remaining ten frequencies were unconstrained. The cross-sectional areas of the members for the first iteration were assumed to be equal to those of Design A. The design variables were modified by using Eq 44, and the Lagrange multipliers were evaluated by using Eq 45. The step size parameter r was set equal to 2. The initial weight of the structure was .0437 and the optimum design weighed 0.015. The optimum design was obtained with twenty iterations. The optimality criterion, i.e., $\beta_i=1$ was satisfied for all elements. The cross-sectional areas of the members for Design C are given in Table 2.

Design D

This design was obtained by scaling Design C so that the weight of the structure was the same as that of Design A or Design B. This was achieved by multiplying all the areas of Design C by the ratio 0.0437/0.0150. The cross-sectional areas of the members for this design are given in Table 2.

Frequency Separation of Different Designs

The distribution of the frequencies for the four designs are given in Table 3. In this table the square of the frequencies listed under columns I and II were determined by including and not including respectively, the contribution of the structural mass to the mass matrix $[M]$ in Eq 7. The square of the frequencies under column II are given here for information; since a computer program such as NASTRAN with CROD elements would give these values. Comparing the values under columns I and II for the four designs, it is seen that the difference between them is small. The difference between the components of the vibration modes for the two cases was also small. The results presented in this

paper were obtained by using the square of the frequencies under column I and the associated vibration modes. Comparing the distribution of the square of the frequencies for the four designs, the following observations can be made:

Design A: The lowest and the highest square of the frequencies for this design are 1.76 and 161.30 respectively. The ω_7^2 associated with the 7th and 8th mode are 21.73 and 21.76 which are close to each other.

Design B: The square of the first and the twelfth frequencies for this design are 1.57 and 187.0 respectively. The frequencies for this design are more widely separated than for all other designs. This wide distribution is considered desirable for designing an active control system.

Design C: The ω_1^2 and ω_2^2 for this design are equal to those for Design A. The square of the highest frequency is 50.77 which is substantially lower than for Designs A or B. The frequencies associated with the 9th and 10th modes are closer to each other.

Design D: The square of the fundamental frequency for this design is 5.01 which is nearly three times that of Design A. The square of the highest frequency is 145.10. The frequencies associated with the 9th and 10th modes for this design are closer to each other.

LOS Response to Initial Displacement

In order to investigate the response of the different designs, each structure was subjected to the same initial conditions. The transient response of the structure was then simulated by using Eq 21 for the period $t=0$ to $t=20$ sec. at the time interval of $t=0.1$ sec. The magnitudes of LOS-X, LOS-Y and LOS-(2) were than calculated at each time interval. Two conditions were imposed to initiate the response. For Case I, the structure was subjected to a unit displacement in the X-direction at node 2 at $t=0$. The time histories for the four designs for the three quantities LOS-X, LOS-Y, LOS-(2) are given in Figs. 2 through 4. In the second case at $t=0$, a displacement of 1 unit was assumed in the Z direction at node 1. The time histories for this case are given in Figs. 5 through 7. For both cases a modal damping of 10% was assigned to all the modes.

Comparing the time histories for the two cases the following observations may be made.

Case I

1. The amplitudes of the LOS-X curve for Design B (Fig. 2(b)) are generally smaller than those for the nominal Design A (Fig. 2(a)), and also for Designs C and D (Figs. 2(c), 2(d)). Design C or D has not reduced LOS-X over the nominal Design A. The amplitudes of LOS-X for Design C (Fig. 2(c)) damped out faster than those for Design D (Fig. 2(d)).

2. The magnitudes of LOS-Y are initially larger for Design B (Fig. 3(b)) than for Design A (Fig. 3(a)), however after about three seconds they become smaller. The amplitudes of LOS-Y for Design C (Fig. 3(c)) or Design D (Fig. 3(d)) are larger than those for Design A or B. The amplitudes of LOS-Y for Design D are larger than those for Design C.

3. The amplitudes of LOS-(2) for Design A (Fig. 4(a)) are initially smaller than those for Design B (Fig. 4(b)), however they become larger after about 3 sec. The amplitudes of LOS-(2) for Design C (Fig. 4(c)) or Design D (Fig. 4(d)) are larger than those for Designs A or B. The magnitude of LOS-(2) for Design C and D are nearly equal, however LOS-(2) for Design C damped out faster.

Case II

1. The amplitudes of LOS-X for Design C (Fig. 5(c)) and Design D (Fig. 5(d)) are smaller than those for Design A (Fig. 5(a)) and Design B (Fig. 5(b)). The amplitudes of LOS-X for Design D damp out faster than those for Design C. Design B in this case has not reduced LOS-X over that of Design A.

2. The magnitudes of LOS-Y for Design C (Fig. 6(c)) and Design D (Fig. 6(d)) are smaller than those for Design A (Fig. 6(a)) or Design B (Fig. 6(b)). The amplitudes of LOS-Y for Design B (Fig. 6(b)) are generally larger than those for Design A (Fig. 6(a)).

3. The magnitudes of LOS-(2) for both Design C (Fig. 6(c)) and Design D (Fig. 6(d)) are substantially smaller than those for Design A (Fig. 6(a)) or Design B (Fig. 6(b)). For Design D (Fig. 6(d)), the amplitudes of LOS-(2) damped out faster than those for Design A (Fig. 6(a)).

Conclusions

It has been shown that by changing the stiffness of the members based on an optimum design criterion, an improvement in the response of the structure to a dynamic disturbance can be made to reduce the line of sight error. From the preliminary results presented in this paper, it is seen that the improvement depends upon the criterion used to design the structure and the initial conditions used to start the dynamic response. Additional study is required to investigate the effect of different disturbances. Further study should include the effect of design modifications on active control of the LOS on large space structures.

Acknowledgements

The authors would like to thank Ms. Elizabeth Copenhagen for her assistance in the preparation of the response curves.

References

1. Strunce, R. R. et. al., "Acos Four (Active Control of Space Structures) Theory Appendix" RADC-TR-80-78, Vol II, 1980.
2. D'Azzo, J. J., and Houpis, "Linear Control System Analysis and Design," 2nd Ed. McGraw-Hill, New York, 1981, pp. 93-99.
3. Sandel, N. R., and Athans, M., "Modern Control Theory - A Self-Study Subject, Computer Manual," Center for Advanced Engineering Study, MIT.
4. Khot, N. S., Berke, L., and Venkayya, V. B., "Comparison of Optimality Criteria Algorithms for Minimum Weight Design of Structures," AIAA Journal, Vol 17, Feb 1979, pp. 182-190.

5. Khot, N. S., "Algorithms Based on Optimality Criteria to Design Minimum Weight Structures," Engineering Optimization, Vol 5, 1981, pp. 73-90.
6. Khot, N. S., "Optimization of Structures with Multiple Frequency Constraints," To be published in Int. J. of Computers and Structures.

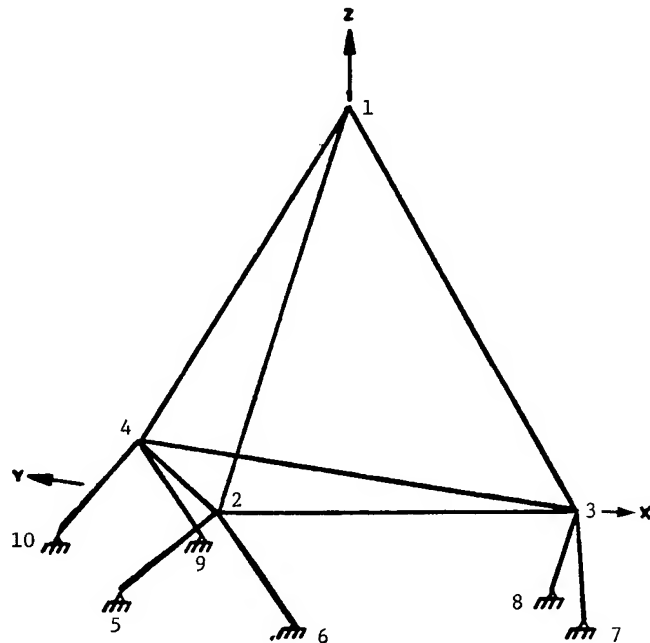
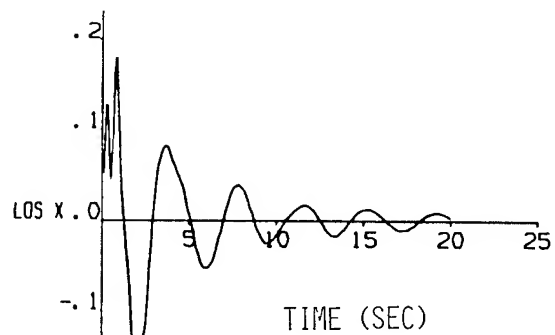
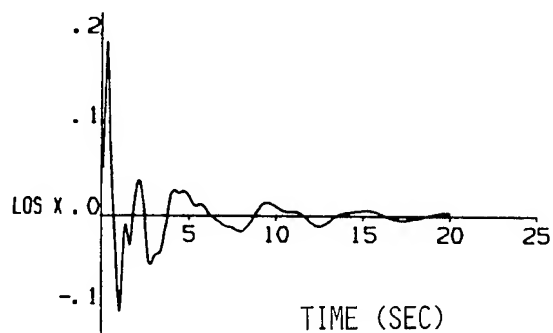


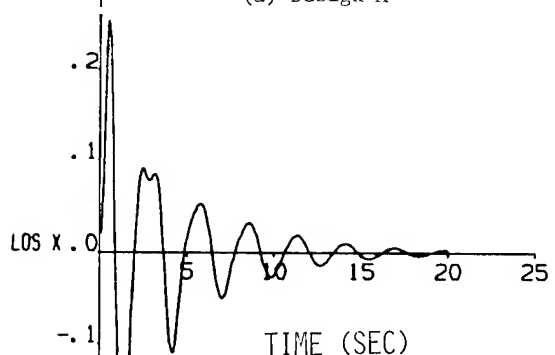
Fig. 1 CSDL Tetrahedral Finite Element Model



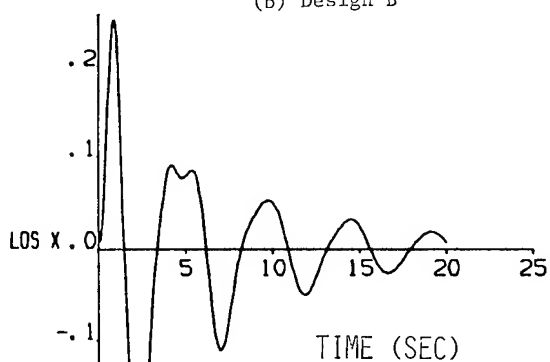
(a) Design A



(b) Design B

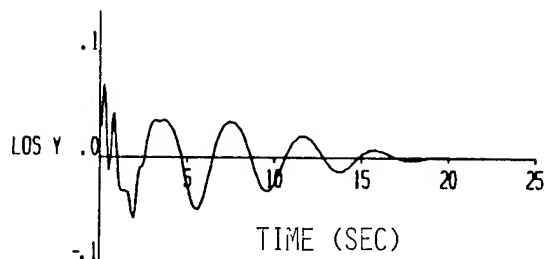


(c) Design C

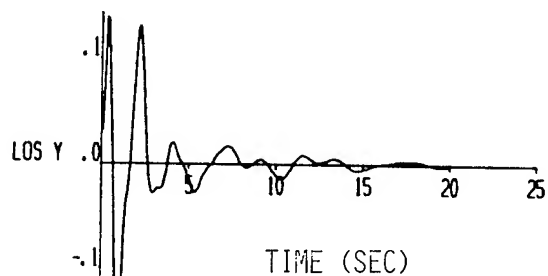


(d) Design D

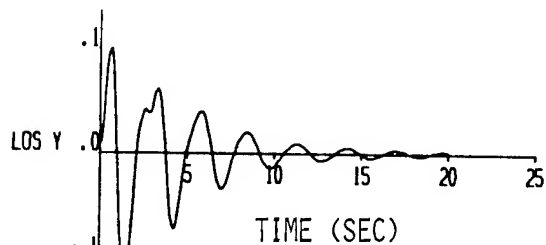
Fig. 2 LOS-X Transient Response for Case I



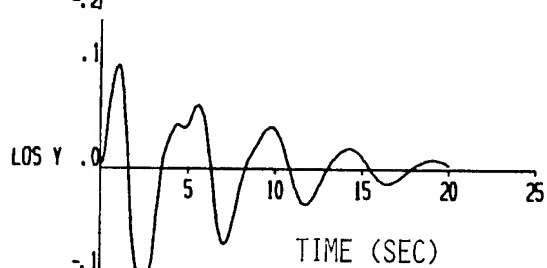
(a) Design A



(b) Design B

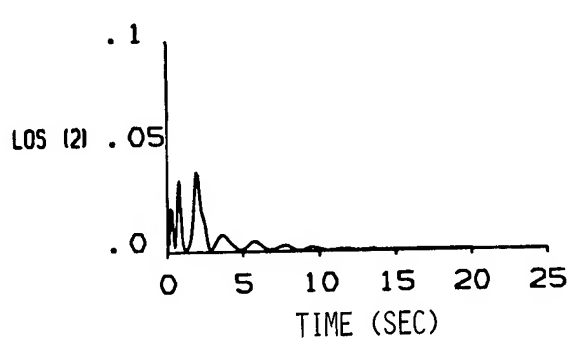


(c) Design C

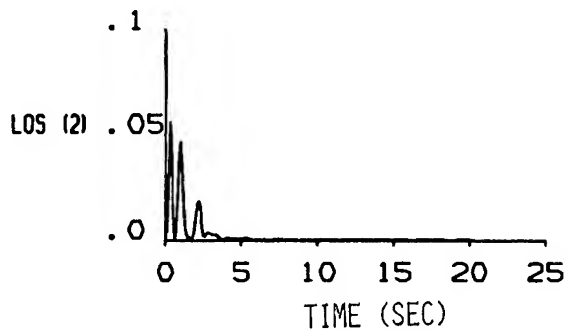


(d) Design D

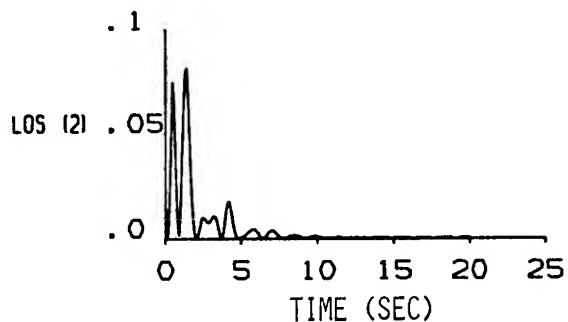
Fig. 3 LOS-Y Transient Response for Case I



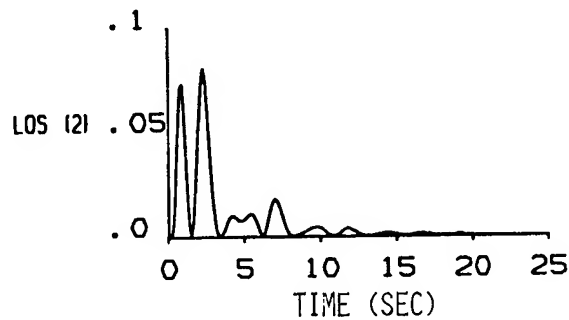
(a) Design A



(b) Design B

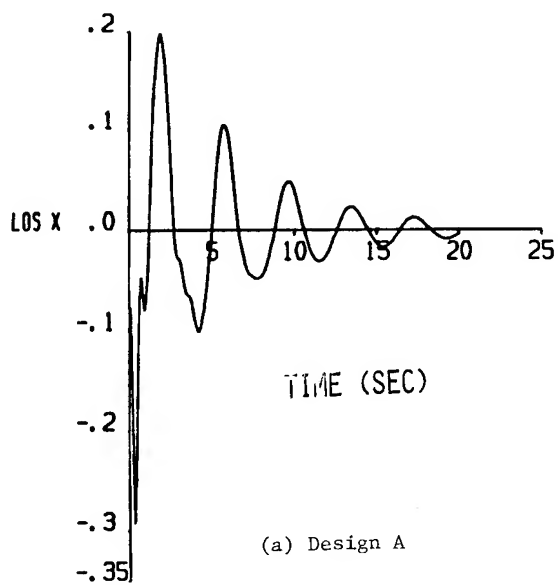


(c) Design C

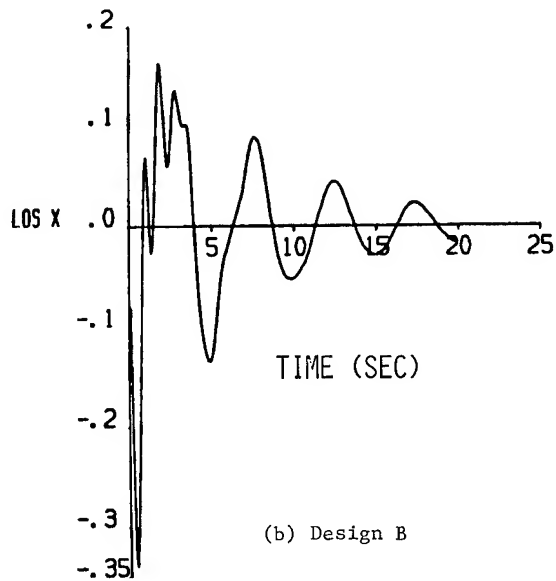


(d) Design D

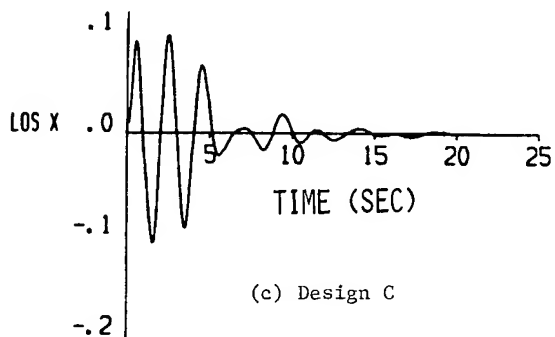
Fig. 4 $(LOS-X)^2 + (LOS-Y)^2$ Transient Response for Case I



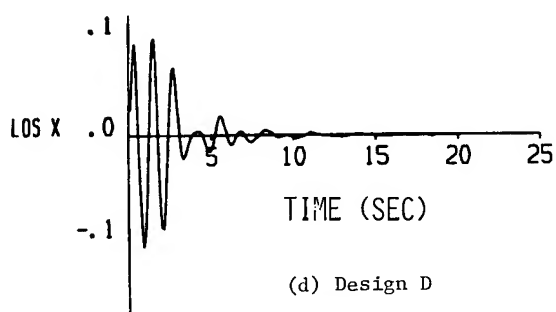
(a) Design A



(b) Design B



(c) Design C



(d) Design D

Fig. 5 LOS-X Transient Response for Case II

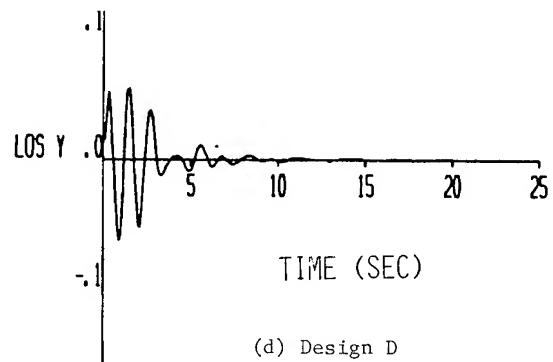
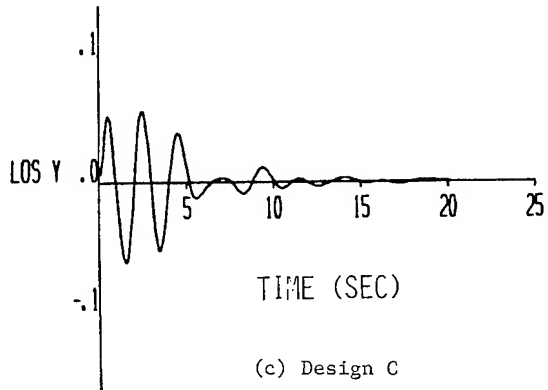
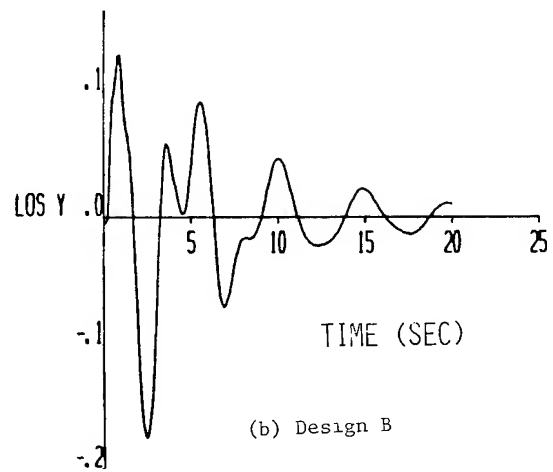
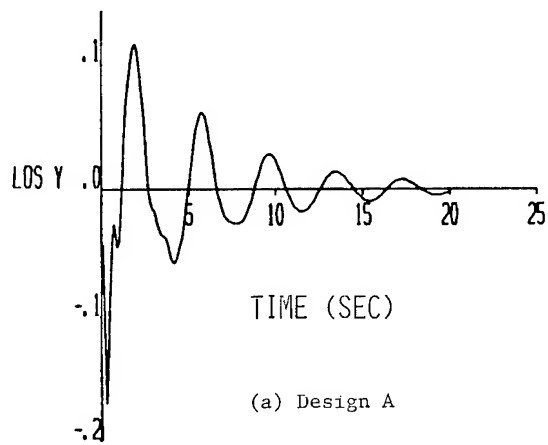


Fig. 6 LOS-Y Transient Response for Case II

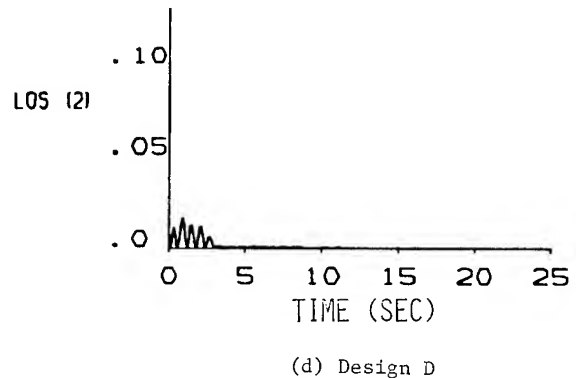
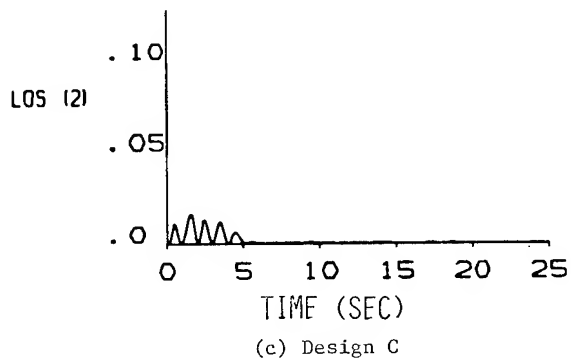
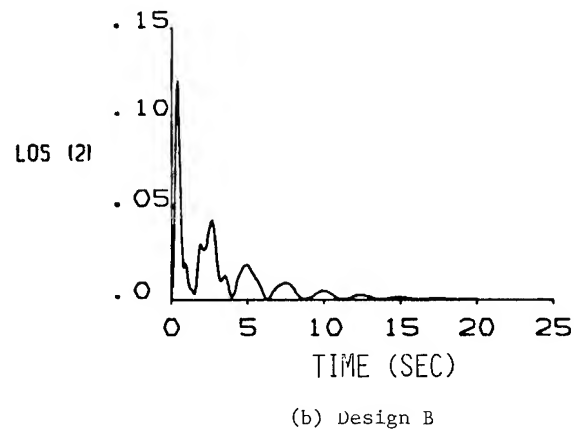
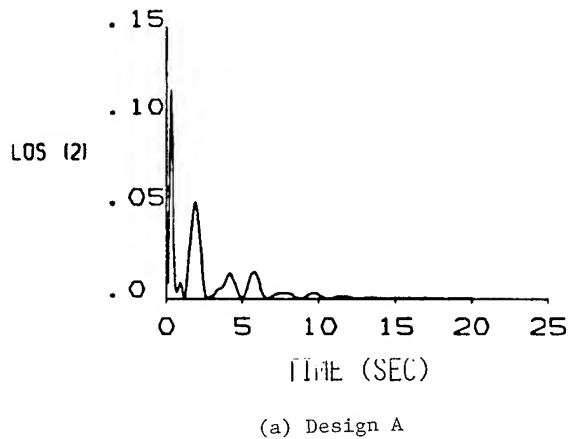


Fig. 7 $(\text{LOS-X})^2 + (\text{LOS-Y})^2$ Transient Response for Case II

Table 1. Node Point Coordinates

Node	X	X	Z
1	0.0	0.0	10.165
2	-5.0	-2.887	2.00
3	5.0	-2.887	2.00
4	0.0	5.7735	2.00
5	-6.0	-1.1547	0.0
6	-4.0	-4.6188	0.0
7	4.0	-4.6188	0.0
8	6.0	-1.1547	0.0
9	2.0	5.7735	0.0
10	-2.0	5.7735	0.0

Table 2. Cross-Sectional Areas of the Members

Element No.	Design A	Design B	Design C	Design D
1(1-2)	1000.	993.5	122.74	353.17
2(2-3)	1000.	614.9	242.96	712.86
3(1-3)	100.	56.58	224.22	643.42
4(1-4)	100.	453.30	224.25	643.50
5(2-4)	1000.	352.60	242.93	712.77
6(3-4)	1000.	909.00	133.90	392.35
7(2-5)	100.	565.00	195.58	576.58
8(2-6)	100.	873.00	195.60	576.64
9(3-7)	100.	420.30	227.76	669.75
10(3-8)	100.	763.00	124.78	366.53
11(4-9)	100.	151.10	227.74	669.68
12(4-10)	100.	727.00	124.80	366.60
Weight	.0437	.0437	.0150	.0437

Table 3. Natural Frequencies (ω_j^2)

Mode	Design A		Design B		Design C		Design D	
	Case I	Case II	Case I	Case II	Case I	Case II	Case I	Case II
1	1.76	1.80	1.57	1.61	1.76	1.79	5.01	5.18
2	2.69	2.77	7.50	7.74	2.69	2.81	7.67	7.94
3	7.98	8.35	10.41	10.83	7.37	7.46	20.99	21.69
4	8.30	8.74	21.09	21.79	9.68	9.99	27.69	28.58
5	10.99	11.54	44.64	46.01	13.31	13.95	37.82	39.15
6	17.12	17.67	48.74	50.33	25.33	25.59	72.39	74.85
7	21.15	21.73	79.06	81.72	28.09	28.73	80.70	83.16
8	21.76	22.61	101.90	105.51	37.40	37.96	107.70	111.00
9	70.61	72.92	130.05	134.30	42.95	43.82	123.60	127.30
10	82.76	85.57	140.06	144.70	43.12	43.86	123.80	127.50
11	102.90	105.77	153.80	159.00	47.08	47.92	135.30	139.80
12	161.30	166.54	187.00	193.40	50.77	52.70	145.10	149.80

Wm. L. Hallauer Jr.^{*}, Gary R. Skidmore^{**}, and Russell N. Gehling^{**}
 Department of Aerospace and Ocean Engineering
 Virginia Polytechnic Institute and State University
 Blacksburg, Virginia

Abstract

This paper first reviews a theory of multiple-actuator modal-space active damping (control) which uses spectral filtering for modal estimation; then it describes an experiment in which the control technique was applied in analog form to a laboratory plane grid structure having a dozen modes under 10 Hz. Experimental observations and corresponding theoretical calculations are presented. Active damping of five modes, including a closely spaced pair, was attempted with the use of five control actuators. But coupling between the two close modes and their filters produced a mild system instability. Subsequently, a stable four-mode controller was produced by disabling the control of the mode that had driven the instability. The spectral filtering played an unexpectedly dominant and counterproductive role in the active damping process.

1. Introduction

This paper pertains to the active damping (control) of structural vibration, excluding self-excited vibration such as aeroelastic flutter. As preparations are made for greatly expanded operations in Earth orbit, the dynamics and control of highly flexible satellites become increasingly important. The anticipated application of the type of active damping considered in this paper is vibration control of large space structures.

In the past several years, there have been a large number of studies of active vibration damping. Most of these studies have been purely theoretical, but recently an increasing number of experimental studies have been reported; see, for examples, Refs. 1-8. Most previous reports of experimental studies either have not presented comparisons of experimental data with corresponding theoretical calculations, or have presented only very limited comparisons. But experimental-theoretical comparisons are required in order either to validate theoretical concepts for practical application, or to reveal the factors which prevent evidently promising theoretical concepts from being successful in practice. Therefore, the present authors' general objectives are to design and execute experimental implementations of active vibration damping and to compare quantitatively the experimental measurements of control system performance with theoretical predictions.

The version of modal-space active damping used in this study has been described previously⁹ and is reviewed below. The object of control is a flexible structure which either is being disturbed by environmental and/or maneuvering actions or is vibrating freely following such disturbances. It is presumed that the inherent passive damping is too light to adequately suppress the vibration, so that additional damping is required. Modal-space active damping is a method for producing this additional damping actively with the use of sensors, a feedback controller, and actuators; in the ideal case, it essentially provides a modal linear viscous dashpot individually to each vibration mode that requires active damping.

The authors have studied modal-space active damping because it is conceptually simple and it is well suited for comparison of experiment and theory. We do not necessarily advocate this control technique; indeed, we believe that insufficient information is available as yet to justify advocacy of any particular vibration control technique for large space structures.

2. Description of Modal-Space Active Damping

Consider a structure idealized to be linear with viscous inherent damping that does not couple the undamped normal modes of vibration. Suppose that one knows the natural frequencies and mode shapes of a particular set of n_c modes which are to be actively damped, the controlled modes, and that one has available n_a independently controllable actuators at specified positions on the structure. It will be specified in this theoretical development that the number of actuators equals the number of modes to be controlled, $n_a = n_c$. Suppose further that one wishes to impose the actuator forces and/or moments so as to effect each of the controlled modes independently of all other controlled modes.

If the structure is represented theoretically as an N-degree-of-freedom (DOF) finite element model, the matrix equation of motion in physical coordinates is

$$[m]\ddot{q} + [c]\dot{q} + [k]q = \underline{e}(t) + \underline{c}. \quad (1)$$

The $N \times N$ matrices $[m]$, $[c]$, and $[k]$ are mass, noncoupling inherent viscous damping, and stiffness matrices, respectively; $q(t)$ is the vector of all time-dependent DOF, consisting of grid point translations and rotations; $\underline{e}(t)$ is the vector of all possible grid-point excitations, consisting of discrete forces and moments; and \underline{c} is the vector of all possible grid-point control actions.

^{*} Associate Professor, Member AIAA

^{**} Graduate Research Assistant,
Student Member AIAA

Standard structural dynamics eigenanalysis decouples the left-hand side of Eq. (1), giving the modal equations of motion,

$$[M]\ddot{\xi} + [C]\dot{\xi} + [K]\xi = [\Phi]^T(\underline{e}(t) + \underline{c}). \quad (2)$$

$[\Phi]$ is the $N \times N$ modal matrix, whose columns are mode shape vectors; the modal coordinates $\xi(t)$ are related to the physical coordinates $\underline{q}(t)$ through the modal transformation, $\underline{q} = [\Phi]\xi$; and the generalized mass, inherent viscous damping, and stiffness matrices are

$$[M] = [\Phi]^T[m][\Phi] = \text{diag}(M_r, r = 1, 2, \dots, N),$$

$$[C] = \text{diag}(2M_r\zeta_r\omega_r, r = 1, 2, \dots, N),$$

$$[K] = \text{diag}(M_r\omega_r^2, r = 1, 2, \dots, N),$$

where ω_r and ζ_r denote, respectively, the natural frequency and inherent viscous damping factor of the r th mode.

The n_a actuators are applied at points and in directions corresponding to a specific subset \underline{q}^a of DOF. Accordingly, the $n_a \times 1$ actuator

submatrix of \underline{c} is denoted as \underline{c}^a , all other elements of \underline{c} being zero. Hence, Eq. (2) can be written as

$$[M]\ddot{\xi} + [C]\dot{\xi} + [K]\xi = [\Phi]^T\underline{e}(t) + [\Phi^a]^T\underline{c}^a, \quad (3)$$

where the $n_a \times N$ matrix $[\Phi^a]$ consists of the appropriate rows of $[\Phi]$.

Feedback control vector \underline{c}^a depends on the measured motion, so in general it can be a function of all ξ_i 's and/or their derivatives. This paper

considers only velocity feedback, so that $\underline{c}^a = \underline{c}^a(\dot{\xi})$.

The essence of modal-space active damping is selection of \underline{c}^a so as to decouple that portion of the right-hand side of Eq. (3) associated with the specified controlled modes. The matrix equation describing only the controlled modes is

$$[M^c]\ddot{\xi}^c + [C^c]\dot{\xi}^c + [K^c]\xi^c = [\Phi^c]^T\underline{e}(t) + [\Phi^{ac}]^T\underline{c}^a(\dot{\xi}^c), \quad (4)$$

where superscript c denotes appropriate partitions of the matrices in Eq. (3); in particular, matrix $[\Phi^{ac}]$ is square (since it has been specified that $n_c = n_a$) and consists of the columns of $[\Phi^a]$ associated with the controlled modes.

Use of the form $\underline{c}^a(\dot{\xi}^c)$ in Eq. (4) presumes that it is possible at least to estimate with reasonable accuracy the instantaneous modal velocity of each of the controlled modes. The present authors have chosen to do this by measuring physical response with a single sensor at a point which is non-nodal for all controlled modes and by directing this signal through parallel narrow-band spectral filters, one centered at the natural frequency of each controlled mode, to

separate the response into individual modal contributions. (Meirovitch et al.¹ have used another type of response observer, a spatial modal filter, which requires several sensors but no spectral filtering.) Suppose that an ideal velocity sensor is placed at, say, the i th DOF. The output of this sensor is

$$\dot{q}_i(t) = \sum_{j=1}^N \dot{q}_{ij} = \sum_{j=1}^N \Phi_{ij} \dot{\xi}_j.$$

Suppose that this output is directed through n_c ideal spectral filters, as described above. The ideal filter for a mode would introduce no phase lag and would have a sufficiently narrow passband and sufficiently steep rolloffs to completely exclude response from all other modes. Hence, the output of the filter for mode s is $\Phi_{is} \dot{\xi}_s$, and the collective output of all the controlled mode filters is $\dot{\underline{q}}_i^c = [\Phi_i^c] \dot{\xi}^c$, where $[\Phi_i^c] = \text{diag}(\Phi_{is}, s \text{ over the controlled modes})$.

Considering again Eq. (4), one defines as \underline{A}_s^a the unknown (at this point) apportioning of control actions which will isolate controlled mode s from all other controlled modes. If only the s th mode were to require control in the form of modal viscous damping, then one would produce that control by feeding back to the structure control actions of the form $\underline{c}^a = \underline{A}_s^a \dot{\underline{q}}_i^c$. But to suppress independently all of the controlled modes, one must use the summation

$$\underline{c}^a = \sum_s \underline{A}_s^a \dot{\underline{q}}_i^c = [C^{ac}] \dot{\underline{q}}_i^c \quad (5)$$

where $[C^{ac}]$, whose s th column is \underline{A}_s^a , is the square control apportioning matrix. Hence, the matrix equation describing the controlled modes can be written as

$$[M^c]\ddot{\xi}^c + [C^c]\dot{\xi}^c + [K^c]\xi^c = [\Phi^c]^T\underline{e}(t) + [\Phi^{ac}]^T[C^{ac}][\Phi_i^c]\dot{\xi}^c. \quad (6)$$

In order for Eq. (6) to be fully uncoupled and to have a specified degree of active viscous damping in each controlled mode (in addition to the inherent damping), it is necessary that

$$[\Phi^{ac}]^T[C^{ac}][\Phi_i^c] = -[D^c], \quad (7)$$

where $[D^c] = \text{diag}(D_s = 2M_s\zeta_s^c\omega_s, s \text{ over the controlled modes})$, and ζ_s^c is the viscous active damping factor specified for mode s . Hence, the control apportioning matrix is the solution of Eq. (7),

$$[C^{ac}] = -[\Phi^{ac}]^{-T}[D^c][\Phi_i^c]^{-1}, \quad (8)$$

provided that the inverse matrices exist. Substituting Eq. (8) into Eq. (6) gives the uncoupled scalar equation governing each controlled

mode,

$$M_s \ddot{\xi}_s + (C_s + D_s) \dot{\xi}_s + K_s \xi_s = \phi_s^T e(t),$$

s over the controlled modes, where ϕ_s is column s of $[\Phi]$.

Clearly, the ideal control apportioning (8) allows each controlled mode to be suppressed independently of all other controlled modes. Note, however, that this control apportioning generally produces excitation of all modes other than the controlled modes, which are called residual modes. One can demonstrate this by substituting equations (8) and (5) into Eq. (3) and observing that the right-hand-side terms due to control in the scalar equations of motion for all residual modes are, in general, nonzero. This control spillover into the residual modes is a consequence of the presence of fewer control actuators than structural modes, and it can seriously impair control effectiveness.⁹ There are also other practical factors that can influence effectiveness, including imperfect knowledge of modal parameters and nonideal sensing, filtering, and actuation. The effects of nonideal filtering and inaccuracies in theoretical models are of particular interest in this paper.

3. Plane Grid Laboratory Structure

Almost all previously reported experimental studies of active control have considered relatively simple one-dimensional laboratory structures, primarily beams. References 1-8 are examples. But such structures generally cannot exhibit some of the dynamic characteristics that may complicate active damping of large space structures, such as high modal density and complex patterns of nodal lines. The plane grid illustrated in Figs. 1 and 2 was designed to provide these characteristics in a small laboratory structure. Details of its design and theoretical modeling are given in Refs. 10 and 11. Only relevant aspects of those reports are summarized here.

The basic structure was a combination of highly flexible aluminum grid beams, a horizontal steel top beam assembly supported in nearly frictionless bearings, and rigid eccentric weights. Grid skew angle θ and eccentricity \bar{Y} of the rigid weights were variable. For this paper, $\theta = 46^\circ$ and $\bar{Y} = 8.5$ inches. Grid members were bolted together tightly at joints, twelve of which are labeled on Fig. 2.

The principal dynamic response of the plane grid consisted of out-of-plane motion. The structure had a dozen out-of-plane vibration modes with natural frequencies under 10 Hz, including a very low frequency pendulum mode (the frequency of which is strongly dependent on \bar{Y}), and a pair of modes with closely spaced frequencies around 3.5 Hz. Natural frequencies and nodal lines were measured accurately in sine dwell modal tests with the use of noncontacting exciters (see Sections 5 and 6) in single-point and two-point excitation configurations. Nodal points were detected by a noncontacting, inductive-type proximity probe (with 0.3 inch probe tip diameter), which was moved along the aluminum beams by a finely adjustable traverse mechanism.¹¹ Measured natural frequencies are listed in Table 1, and measured nodal lines for modes 2-5 are shown on Figs. 3.

Table 1 Plane Grid Natural Frequencies

Structure Mode r	Natural Frequency (Hz)	
	Experimental	Theoretical
1	0.60	0.60
2	0.95	0.96
3	1.44	1.43
4	3.42	3.40
5	3.65	3.72
6	5.15	5.16
7	5.48	5.49
8	5.67	5.67
9	6.27	6.59
10	8.25	8.54
11	8.36	8.75
12	9.47	9.77

Two refined finite element models of the plane grid were evaluated.¹¹ Three DOF were assigned to each analysis grid point (node): translation out of the plane, rotation about a vertical in-plane axis, and rotation about a horizontal in-plane axis. The first model was of lower order and consisted of analysis grid points at each of the twelve bolted joints of the aluminum grid, at the two bearing supports of the steel top beam, and at six points in the interior of the steel top beam; with three DOF per grid point and with out-of-plane translation prevented at each bearing support, this model had 58 DOF. In the second model, each beam between adjacent bolted joints of the aluminum grid was represented as two finite elements of equal length, rather than one; otherwise, it was identical to the first model. Consequently, the second model had 121 DOF.

Corresponding natural frequencies calculated for the two finite element models differ by less than 1% for all modes under 10 Hz, and corresponding calculated nodal points representative of the mode shapes are also nearly identical. One concludes, therefore, that for practical purposes the 58-DOF model converged mathematically for modes under 10 Hz. Natural frequencies are listed for the 121-DOF model in Table 1 (and for the 58-DOF model in Table 2), and nodal lines for modes 2-5 of the 121-DOF model are shown on Figs. 3.

Comparison of experimental and theoretical natural frequencies in Table 1 shows good agreement, especially for modes 1-8. Experimental and theoretical nodal lines also match reasonably well for all of modes 1-8 except, as shown on Fig. 3a, mode 2. At this writing, the authors are unable to explain this mismatch. All testing was done in air at one atmosphere pressure, so the mismatch may be due to air resistance on the very light aluminum grid moving at the low frequency of the second mode. This and other possible sources of modeling error are analyzed in Ref. 11.

4. Active Damping Configuration

The active damping task attempted was to provide $\zeta_s^c = 0.1$, $s = 2-6$; that is, it was desired to produce 10% active damping in modes 2-6 of the plane grid. Hardware availability limited the number of controlled modes to five. Modes 4 and 5 were included among the controlled modes because their frequencies were close to each other. The other modes were chosen, somewhat arbitrarily, to complete a sequence of adjacent low frequency modes that did not include the fundamental (pendulum) mode.

The single control sensor was positioned at bolted joint 1 to measure out-of-plane translational velocity. This location was selected because theoretical mode shapes indicated that it was a point of substantial response for all of the controlled modes. However, as was shown by subsequent measurements (Fig. 3a), bolted joint 1 was actually very close to a nodal line of mode 2.

Force actuators exerting control forces perpendicular to the plane were positioned at bolted joints 1, 2, 4, 5, and 8. These positions were selected in a semi-quantitative manner, rather than by mathematical optimization. The candidate positions were restricted to bolted joints 1-12, but joints 9-12 were eliminated because response of the controlled modes was generally much greater in the lower half of the plane grid. Equation (8) for control gain matrix $[C^{ac}]$ was evaluated with theoretical mode shapes for several different five-joint combinations from among joints 1-8. The combination 1,2,4,5, and 8 was chosen because it produced the most uniform spatial distribution of control forces.

5. Control System Hardware

Active damping was effected by the velocity sensor, an analog controller, and the force actuators, all of which were custom designed and assembled in-house. The control system implemented the version of Eq. (5) accounting for actual filter characteristics. The circuit design of the filters is that of Forward⁴; this design is analyzed in detail in Ref. 7. The response of the filter for controlled mode s is described by

$$\ddot{y}_s + B_s \dot{y}_s + \omega_{cs}^2 y_s = B_s \ddot{q}_i, \quad (9)$$

in which \ddot{q}_i is input, y_s is output, B_s is half-power bandwidth, and ω_{cs} is passband center frequency. Hence, the version of Eq. (5) actually implemented is

$$\tilde{c}^a = \sum_s^{n_c} \tilde{A}_s^a y_s = [C^{ac}] \tilde{y}. \quad (10)$$

Control gain matrix $[C^{ac}]$ was calculated from Eq. (8) with theoretical (rather than experimental) mode shapes.

Half-power bandwidth B_s was set at 1.00 Hz for modes 2, 3, and 6, and at 0.333 Hz for close modes 4 and 5. For each controlled mode, the filter center frequency was set at the mode's

experimental (rather than theoretical) natural frequency. Figure 4 shows the frequency response functions calculated from Eq. (9) for modes 4 and 5.

The complete physical implementation of the active damping technique used in this study is summarized as follows. The velocity transducer provided sensor signal \dot{q}_i , and this signal was the input for the filter of each controlled mode. Implementation of Eq. (10) consisted of three principal operations: (i) filter output y_s was

multiplied into control gain vector \tilde{A}_s^a by a gain circuit; (ii) the outputs from all gain circuits were added together by a summation circuit; and (iii) each output of the summation circuit was directed into a power amplifier, which generated the input signal proportional to $c_j^a(t)$ for the j th control force actuator. It is noted for later reference that the control for any individual mode could be disabled by simply grounding the input to that mode's filter.

The analog controller, consisting of buffers, filters, and gain and summation circuits, was built around integrated circuit operational amplifiers.⁷

The velocity sensor and force actuators consisted of structure-borne conducting coils interacting with magnetic fields produced by stationary, noncontacting magnetic field structures⁶ (Fig. 5). These devices were linear provided that coil displacement was less than about 2 mm from the static position. In order to minimize current flow in the velocity sensor coil (and hence additional but unwanted passive damping), it was necessary to pass the velocity signal into the filters through a unity gain buffer having extremely high input impedance.⁷

The power amplifiers driving the actuators were designed to have controlled current output; this was necessary to establish a linear transduction of summation circuit output voltage into actuator output force, eliminating the effect of voltage induced by motion of the actuator coil.

6. Experimental Procedure

Measured displacement-to-force frequency response functions (FRF's) were the principal type of experimental data used to evaluate the validity of the structure-control system theoretical model. The experimental procedure is summarized in this section, and the corresponding theoretical analysis is developed in the next.

Experiments were conducted with the use of an STI-11/23 data acquisition-analysis system developed by Synergistic Technology Incorporated. This system both generated the excitation signal and acquired and processed the data signals.

Frequency response was measured directly in incremental sine sweeps. In such a sweep, an excitation signal is imposed at a driving frequency, and the force excitation and displacement response at that frequency are measured after a settling period in which transients are allowed to decay. Then the driving frequency is changed by an

increment and the process is repeated. The sweeps covered the range 0.4-6.4 Hz (including the nine lowest natural frequencies) in increments of 0.0122 Hz, and they generally took 2-3 hours.

It was necessary that dynamic displacements remain small in order not to exceed the ± 2 mm linear range of the control sensor and actuators. Therefore, low frequency excitation forces on the light and flexible plane grid had to be small. Even the smallest commercially available shakers and piezoelectric force gauges proved too heavy-handed and insensitive for the task. However, the noncontacting force actuators provided a simple solution to the problem: in each frequency response sweep, the excitation signal from the ST1-11/23 was added to the control feedback signal in the input to the power amplifier of a selected actuator. Thus, that actuator served simultaneously as the exciter and a control actuator. The excitation force was related through a calibration constant to the excitation signal. A typical force level required was on the order of 0.01 lb, and this was generated by an excitation signal on the order of 50 millivolts.¹¹ Because dynamic displacements were kept small, amplitude servo-control was not required.

Frequency response displacements were measured at bolted joints of the plane grid by sensitive proximity probes (see Section 3). Light, half-inch square steel targets were used.

In order to minimize unwanted disturbances, it was necessary to conduct testing during periods of low personnel activity in the laboratory. Air currents produced by normal air conditioning, or by doors being opened and closed, or even by a person walking within a few feet of the plane grid could disturb the structure and reduce the quality of measured data.

7. Theoretical Frequency Response and System Roots

The basic theoretical model of the complete structure-control system consists of the structural Eq. (1), n_c equations (9) describing the filters, and Eq. (10) for the vector of control actions.

The filter equations can be cast into the matrix form

$$[I]\ddot{\underline{y}} + [B]\dot{\underline{y}} + [\omega_c^2]\underline{y} = [B][T_s]\ddot{\underline{q}}, \quad (11)$$

where \underline{y} is the vector of n_c filter outputs, $[I]$ is the identity matrix of order n_c , $[B]$ is the diagonal matrix of filter half-power bandwidths, and $[\omega_c^2]$ is the diagonal matrix of filter center frequencies squared. Also, $[T_s]$ is an $n_c \times N$ transformation matrix relating the sensor velocity \dot{q}_i to the full velocity vector $\dot{\underline{q}}$; accordingly, $[T_s]$ is null, except that column i (corresponding to DOF i) is a column of ones.

From Eq. (10), the vector of all N control actions, including $N - n_a$ zero elements is

$$\underline{z} = [T_a][C^{ac}]\underline{y}, \quad (12)$$

where $[T_a]$, the $N \times n_a$ actuator transformation matrix, consists of appropriate zero and unit elements.

Now the complete, coupled physical system of order $N + n_c$ is described by the combination of Eqs. (1), (11), and (12). It is desirable to reduce the order of this system by assuming that structural response can be adequately described by a truncated set of n_t normal modes: $\underline{q} =$

$[\xi^t]\underline{\xi}^t$, where $[\xi^t]$ and $\underline{\xi}^t$ are appropriate submatrices of $[\xi]$ and $\underline{\xi}$. Hence, the structural response is represented by the subset of modal Eq. (2),

$$[M^t]\ddot{\underline{\xi}}^t + [C^t]\dot{\underline{\xi}}^t + [K^t]\underline{\xi}^t = [\xi^t]^T(\underline{e} + [T_a][C^{ac}]\underline{y}), \quad (13)$$

where $[M^t]$, $[C^t]$, and $[K^t]$ are appropriate partitions of $[M]$, $[C]$, and $[K]$.

The vector of all retained modal coordinates and all filter outputs is defined as

$$\underline{z} = \begin{bmatrix} \underline{\xi}^t \\ \underline{y} \end{bmatrix}. \quad (14)$$

Combining Eqs. (11)-(14) into a single matrix equation of order $n_t + n_c$ gives

$$[AM]\ddot{\underline{z}} + [AC]\dot{\underline{z}} + [AK]\underline{z} = \underline{f}, \quad (15)$$

where augmented mass, damping, and stiffness matrices are defined as

$$[AM] = \begin{bmatrix} [M^t] & [0] \\ -[B][T_s][\xi^t] & [I] \end{bmatrix},$$

$$[AC] = \begin{bmatrix} [C^t] & [0] \\ [0] & [B] \end{bmatrix},$$

$$[AK] = \begin{bmatrix} [K^t] & -[\xi^t]^T[T_a][C^{ac}] \\ [0] & [\omega_c^2] \end{bmatrix},$$

and the augmented excitation vector is

$$\underline{f} = \begin{bmatrix} [\xi^t]^T \underline{e} \\ 0 \end{bmatrix}.$$

To calculate the FRF of displacement in any DOF for excitation in DOF k , one solves directly for $\underline{z} = [\underline{\xi}^T \underline{y}^T]^T$ using the form of Eq. (15),

$$([AK] - \omega^2[AM] + i\omega[AC])\underline{z} = \underline{F}, \quad (16)$$

where $i = \sqrt{-1}$ and $\underline{F} = [\underline{E}^T \ 0^T]^T$, in which \underline{E}^T is the k th row of $[\xi^t]$.

Calculation of the system complex roots (eigenvalues) is expedited by definition of the state vector $\underline{x} = [\underline{\dot{z}}^T \ \underline{z}^T]^T$. Thus, one casts the homogeneous form of Eq. (15) into the state-space form,

$$[B]\ddot{X} - [A]\dot{X} = 0,$$

where

$$[B] = \begin{bmatrix} [0] & [I] \\ [AM] & [AC] \end{bmatrix},$$

$$[A] = \begin{bmatrix} [I] & [0] \\ [0] & -[AK] \end{bmatrix},$$

in which $[I]$ is the identity matrix of order $n_t + n_c$. Hence, the system roots are the complex eigenvalues p of

$$[A]\dot{X} = p[B]\dot{X}. \quad (17)$$

For each complex conjugate pair $p = \sigma \pm i\omega$, one defines damping factor $\zeta = -\sigma / \sqrt{\sigma^2 + \omega^2}$ and frequency $f_o = \sqrt{\sigma^2 + \omega^2} / 2\pi$.

8. Experimental Results and Comparison with Theory

Figures 6 and 7 show two different FRF's, in both measured and calculated versions, and for both active damping turned off (open loop) and active damping turned on (closed loop). These two FRF's are the most illustrative of several that were evaluated.

To establish parameters of the theoretical model for use in numerical solutions of Eqs. (16) and (17), the open loop experimental FRF's (dashed curves of Figs. 6a and 7a) were considered first. The open loop theoretical model was produced by nulling the off-diagonal submatrices in augmented matrices $[AM]$ and $[AK]$, thus decoupling structure and filters. The ten lowest normal modes were used to represent the structure's dynamics, $n_t =$

10. The adequacy of this modal truncation was confirmed by comparison of experimental and theoretical results. Inherent damping matrix $[C^*]$ was estimated in a semi-quantitative fashion: modal inherent viscous damping factors ζ_r were

adjusted iteratively until reasonable agreement in resonance peak magnitudes was achieved between measurements and calculations. Modal damping ratios estimated in this manner are listed in Table 2. Note that damping values for modes 1-6 are surprisingly high in view of the nature of the plane grid structure. These high values are almost certainly due to aerodynamic damping.

It is clear in retrospect that a mathematical curve-fitting procedure would probably have produced more accurate modal damping values. The method used did not account for mode shape errors in the theoretical results. One can see the effects of these errors, especially for modes 2 and 5, by examining the open loop resonance peaks on Figs. 6 and 7 in light of the nodal lines on Figs. 3.

Table 2 Open loop and closed loop system roots

System Mode r	Open Loop System Type *	Structure-Control Systems					
		Five-Mode Control		Four-Mode Control		Control	
		ζ_r	$f_{or}(Hz)$	ζ_r	$f_{or}(Hz)$	ζ_r	$f_{or}(Hz)$
1	SM 1	0.043	0.597	0.153	0.421	0.152	0.421
2	SM 2	0.050	0.965	0.074	0.913	0.074	0.914
3	FM 2	0.518	0.965	0.425	1.296	0.425	1.294
4	SM 3	0.035	1.432	0.046	1.290	0.048	1.290
5	FM 3	0.349	1.432	0.221	1.809	0.219	1.798
6	SM 4	0.010	3.413	0.026	3.104	0.027	3.156
7	FM 4	0.049	3.413	-0.010	3.559	0.029	3.675
8	SM 5	0.009	3.728	0.068	3.561	0.009	3.728
9	FM 5	0.045	3.730	0.022	3.987	0.045	3.730
10	SM 6	0.013	5.151	0.058	4.680	0.056	4.654
11	FM 6	0.097	5.152	0.041	5.640	0.047	5.659
12	SM 7	0.0035	5.494	0.011	5.480	0.0068	5.478
13	SM 8	0.0030	5.667	0.0044	5.666	0.0041	5.666
14	SM 9	0.0060	6.630	0.0092	6.747	0.0080	6.658
15	SM 10	0.0060	8.618	0.0061	8.642	0.0060	8.615

* SM r - denotes structure mode r
FM r - denotes filter for structure mode r

When five-mode active damping was activated, the structure-control system exhibited a mild dynamic instability at 3.55 Hz. It was determined by selective disabling of the controls for closely spaced modes 4 and 5 (see Section 5) that, essentially, the control for mode 5 was driving mode 4 unstable. This circumstance is quite plausible in view of the considerable overlapping of the filter bandwidths for modes 4 and 5 (Fig. 4): each of those modes could contribute significant, possibly destabilizing error signals to the input of the other mode's gain circuit. Roots calculated theoretically for the five-mode control are listed in Table 2. The single root with negative damping factor matches exactly the experimentally observed instability.

A stable structure-control system was produced by disabling the control for mode 5. Thus, the four modes 2, 3, 4, and 6 were actively damped by the five control actuators at bolted joints 1, 2, 4, 5, and 8. This is the system for which the closed loop FRF's in Figs. 6 and 7 were measured and calculated and for which the four-mode control roots in Table 2 were calculated. There is reasonable agreement between measurements and calculations. The discrepancies are due primarily to errors in the theoretical mode shapes.

9. Discussion of Results

Figures 6 and 7 indicate that four-mode active damping reduced substantially the resonance peak magnitudes of controlled modes 3, 4, and 6. It also provided unexpected additional damping to mode 1, which was not among the controlled modes; this damping was probably a modal rate feedback effect permitted by the 1-Hz half-power bandwidth of the filter for mode 2 (Section 5). Experimentally, mode 2 received almost no active damping, probably because the control gains were calculated on the basis of the theoretical shape of mode 2, which is significantly different from the actual shape (Fig. 3a).

There is a serious general discrepancy between the actual damping achieved, as represented adequately by the theoretical four-mode control roots in Table 2, and the active damping that was expected on the basis of the theory in Section 2. The active damping factor specified for each controlled mode in the calculation of control gains was $\zeta_s^c = 0.10$; but the damping factors achieved were much lower for all controlled modes. Observation of this discrepancy led to a search for an explanation, and the search culminated in the analysis in the Appendix of an oscillator (1-DOF structure) subjected to modal-space active damping with the use of a single spectral filter. The surprising and counterintuitive conclusion of the analysis is that, for practical purposes, the active damping actually achieved is a strong function of the filter half-power bandwidth, but is functionally independent of the specified active damping factor ζ_s^c .

Direct extrapolation of the result for the oscillator-filter system to the actual structure-control system is not appropriate because the filter bandwidths overlapped, and this certainly affected the damping achieved. However, it was relatively

easy to simulate theoretically cases in which the filter bandwidths were made so narrow that they did not overlap. These calculations were performed for the five-mode control case. When all filter bandwidths were reduced in simulation to 10% of their actual values, the system became stable and each mode had essentially only its own inherent damping. This result substantiates the conclusion that filter bandwidth is the primary factor determining the degree of active damping achieved.

10. Concluding Remarks

The research reported in this paper evaluated a form of modal-space active damping which uses spectral filtering for modal estimation. It was demonstrated that the particular type of spectral filter used has a serious deficiency: in order to avoid instability due to mode-filter coupling, the bandwidth of the filter for a given controlled mode must be so narrow as to reject response from all other modes; but, by virtue of being narrow, the filter bandwidth can reduce the active damping to such a low level as to be useless.

Generally satisfactory agreement was achieved between experimental measurements and theoretical calculations. However, the nature of the inevitable differences observed suggests a practical guideline: any active vibration control technique implemented on a dynamically complicated large space structure should be insensitive to errors in the structure model used to design the control, because that model is unlikely to predict accurately the parameters of all modes affected by the control.

Appendix: Oscillator-Filter System

Consider the case in which the structure is a simple 1-DOF damped oscillator with mass m , inherent viscous damping c , and stiffness k , and the filter has center frequency ω_f and half-power bandwidth B . For the version of modal-space active damping considered in this paper, the coupled structure-filter equations are

$$m\ddot{q} + c\dot{q} + kq = -dy,$$

$$\ddot{y} + B\dot{y} + \omega_f^2 y = B\ddot{q},$$

where d is the active damping feedback constant. One defines structure natural frequency $\omega_s = \sqrt{k/m}$ and structure, filter, and active damping ratios, respectively, $\zeta_s = c/2m\omega_s$, $\zeta_f = B/2\omega_f$, and $\zeta_a = d/2m\omega_s$. The coupled equations become

$$\ddot{q} + 2\zeta_s\omega_s\dot{q} + \omega_s^2 q = -2\zeta_a\omega_s y,$$

$$\ddot{y} + 2\zeta_f\omega_f\dot{y} + \omega_f^2 y = 2\zeta_f\omega_f\ddot{q}.$$

Seeking solutions of these equations with time variation $\exp(\omega_s pt)$, one finds the following quartic characteristic equation for the dimensionless roots p ,

$$(p^2 + 2\zeta_s p + 1)(p^2 + 2\zeta_f\Omega_f p + \Omega_f^2) + 2\zeta_a(2\zeta_f\Omega_f)p^2 = 0,$$

where $\Omega_f = \omega_f/\omega_s$. If the roots are denoted $p = \sigma \pm i\Omega$, then the system damping ratio and dimensionless frequency are $\zeta = -\sigma/\sqrt{\sigma^2 + \Omega^2}$ and $\omega = \sqrt{\sigma^2 + \Omega^2}$.

The variation of system roots with dimensionless filter bandwidth $B/\omega_s = 2\zeta_f\Omega_f$ is of interest. Numerical parameters representative of the cases considered in the main body of this paper are $\Omega_f=1$, $\zeta_s=0.016$, and $\zeta_a=0.1$. For these parameters, the loci of roots having positive imaginary parts are shown in Fig. A1. Two ζ_f values are identified on the curved portions of the loci to illustrate a general observation, namely that on these portions, the active damping ratio ζ_a affects the system frequencies but has negligible influence on the system damping ratios. These damping ratios are equal and are approximated closely by $\zeta = (\zeta_f + \zeta_s)/2$. The third point identified on the solid branch illustrates the other general observation: only when the filter bandwidth becomes very large does the active damping ratio take effect over system damping and provide the structure with the expected total damping ratio, $\zeta_a + \zeta_s$.

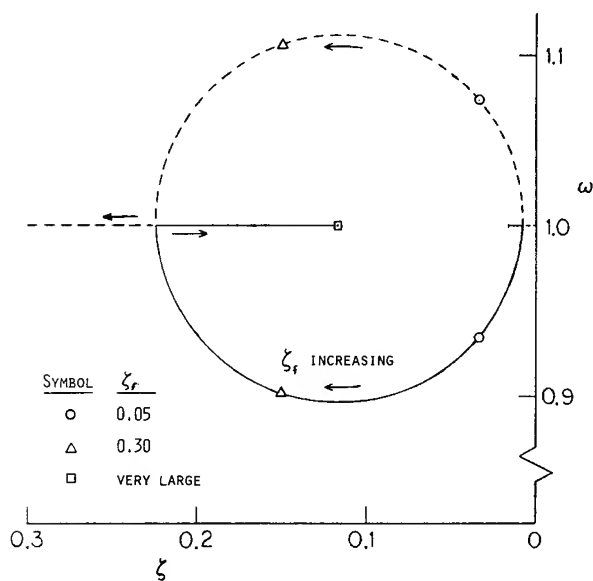


Fig. A1

Acknowledgments

This work was supported by the U.S. Air Force Office of Scientific Research, Grant AFOSR-82-0217 and Contract F49620-83-C-0158. The data acquisition and analysis system was purchased with Grant No. CME-8014059 from the U.S. National Science Foundation. Carolyn Russillo and David Russillo assisted greatly in the preparation of the manuscript.

References

1. Meirovitch, L., Baruh, H., Montgomery, R. C., and Williams, J. P., "Nonlinear Control of an Experimental Beam by IMSC," AIAA Paper 83-0855, Collection of Technical Papers, 24th Structures, Structural Dynamics, and Materials Conference, pp. 185-192, 1983.
2. Schaechter, D. B., "Hardware Demonstration of Flexible Beam Control," Journal of Guidance, Control and Dynamics, Vol. 5, pp. 48-53, 1982.
3. Montgomery, R. C., Horner, G. C., and Cole, S. R., "Experimental Research on Structural Dynamics and Control," Dynamics and Control of Large Flexible Spacecraft, Proceedings of the Third VPI & SU/AIAA Symposium, pp. 365-377, 1981.
4. Forward, R. L., "Electronic Damping of Orthogonal Bending Modes in a Cylindrical Mast--Experiment," Journal of Spacecraft, Vol. 18, pp. 11-17, 1981.
5. Stroud, R. C., Hama, G. A., Smith, S., and Lyons, M. G., "Developments Toward Active Control of Space Structures," SAE Paper 801234, Society of Automotive Engineering Aerospace Meeting, Los Angeles, 1980.
6. Hallauer, W. L. Jr., Skidmore, G. R., and Mesquita, L. C., "Experimental-Theoretical Study of Active Vibration Control," Proc. 1st International Modal Analysis Conf., pp. 39-45, 1982.
7. Skidmore, G. R., "A Study of Modal-Space Control of a Beam-Cable Structure," M. S. Thesis, Virginia Polytechnic Institute and State University, 1983.
8. Skidmore, G. R., Hallauer, W. L. Jr., and Gehling, R. N., "Experimental-Theoretical Study of Modal-Space Control," Proc. 2nd International Modal Analysis Conf., pp. 66-74, 1984.
9. Hallauer, W. L. Jr. and Barthelemy, J.-F. M., "Sensitivity of Modal-Space Control to Nonideal Conditions," Journal of Guidance and Control, Vol. 4, pp. 564-566, 1981.
10. Masse, M. A., "A Plane Grillage Model for Structural Dynamics Experiments: Design, Theoretical Analysis, and Experimental Testing," M. S. Thesis, Virginia Polytechnic Institute and State University, 1983.
11. Gehling, R. N., "Experimental and Theoretical Analyses of a Plane Grillage Structure with High Modal Density," M. S. Thesis, Virginia Polytechnic Institute and State University, 1984.

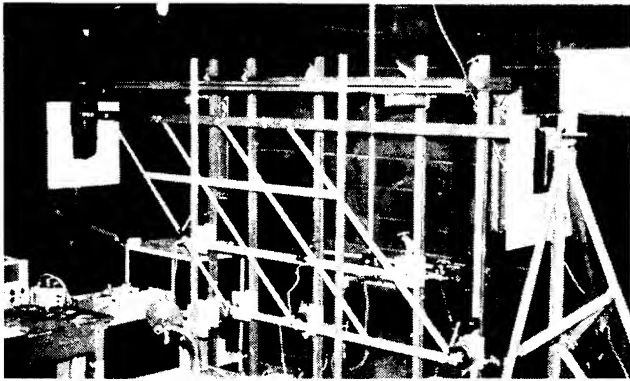


Fig. 1 Photograph of plane grid and support framework

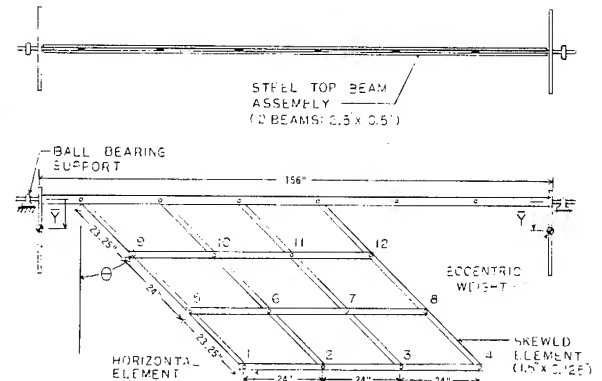
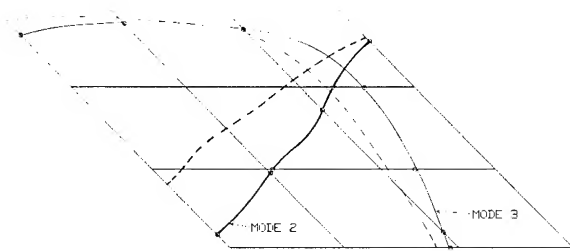
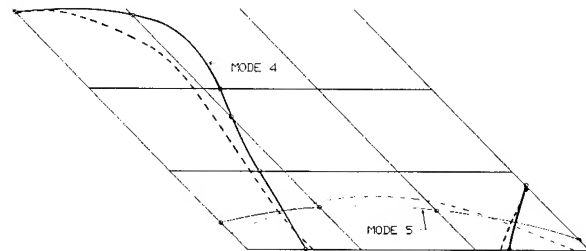


Fig. 2 Line drawing of plane grid



a) Modes 2 and 3



b) Modes 4 and 5

Figs. 3 Experimental (solid) and theoretical (dashed) nodal lines

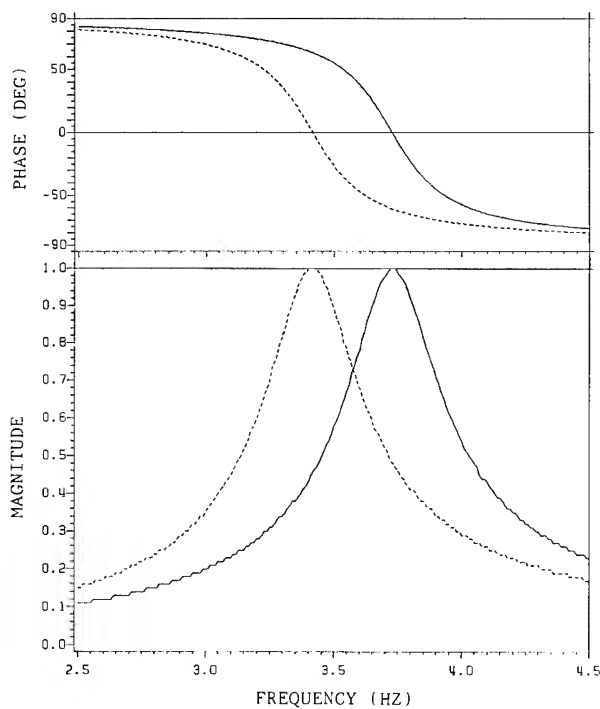


Fig. 4 Theoretical frequency response of the filters for modes 4 and 5

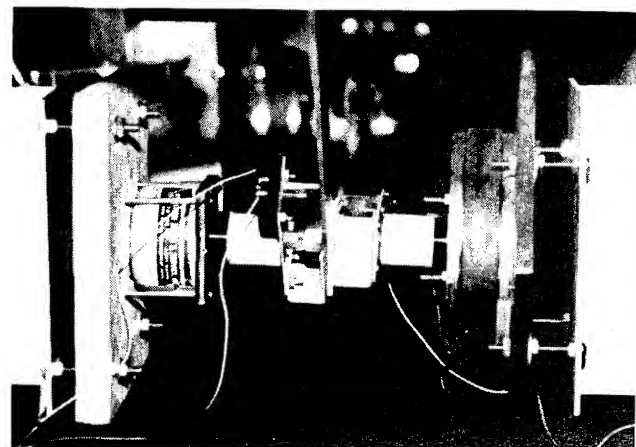
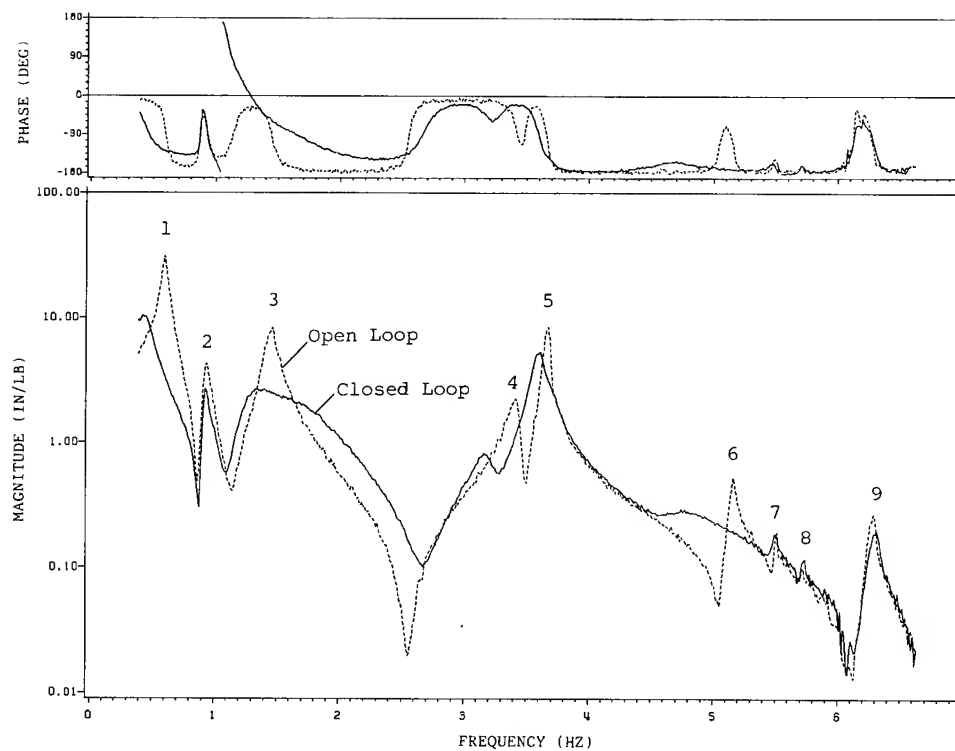
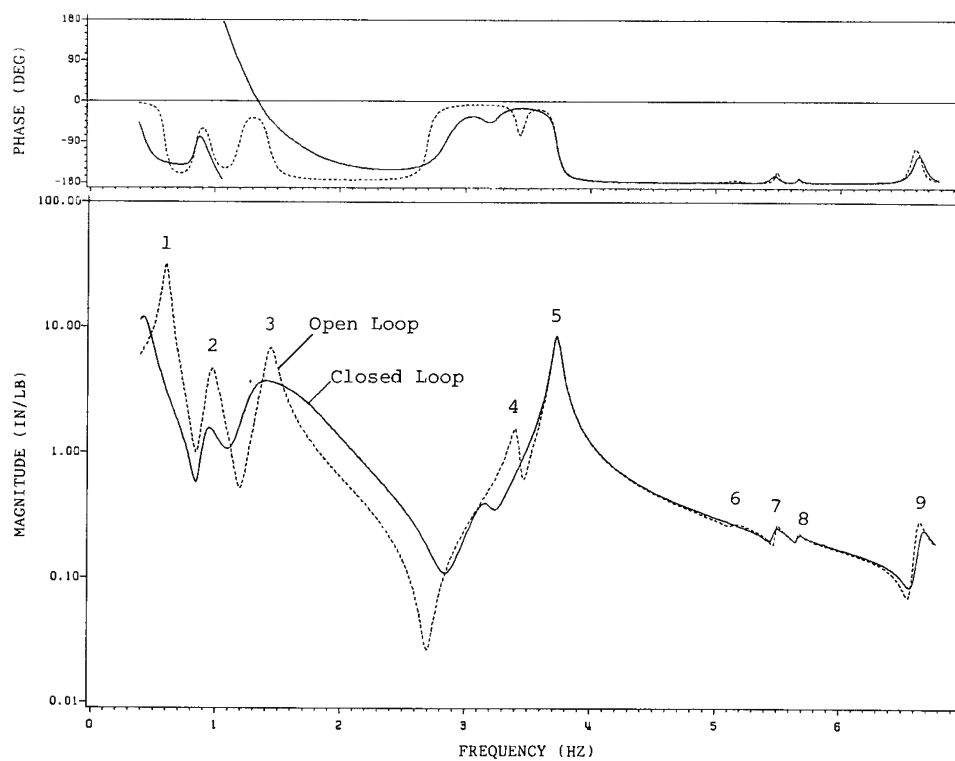


Fig. 5 Force actuator (at left) and velocity sensor (at right) at bolted joint 1 of the plane grid as viewed from the left of joint 1 in Fig. 2

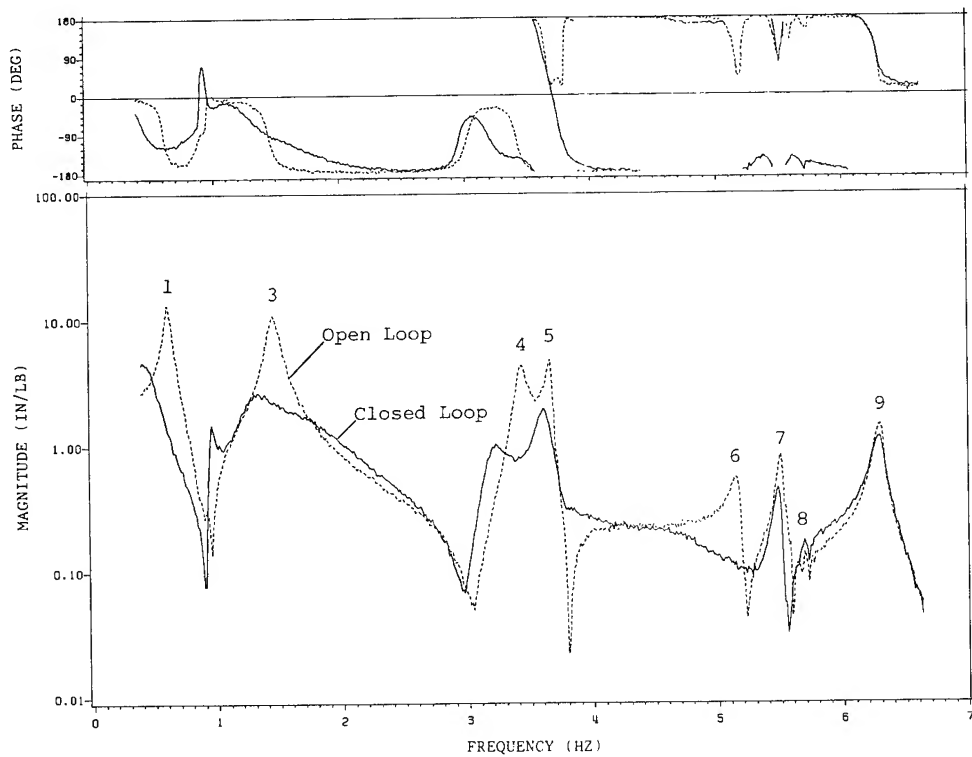


a) Experimental

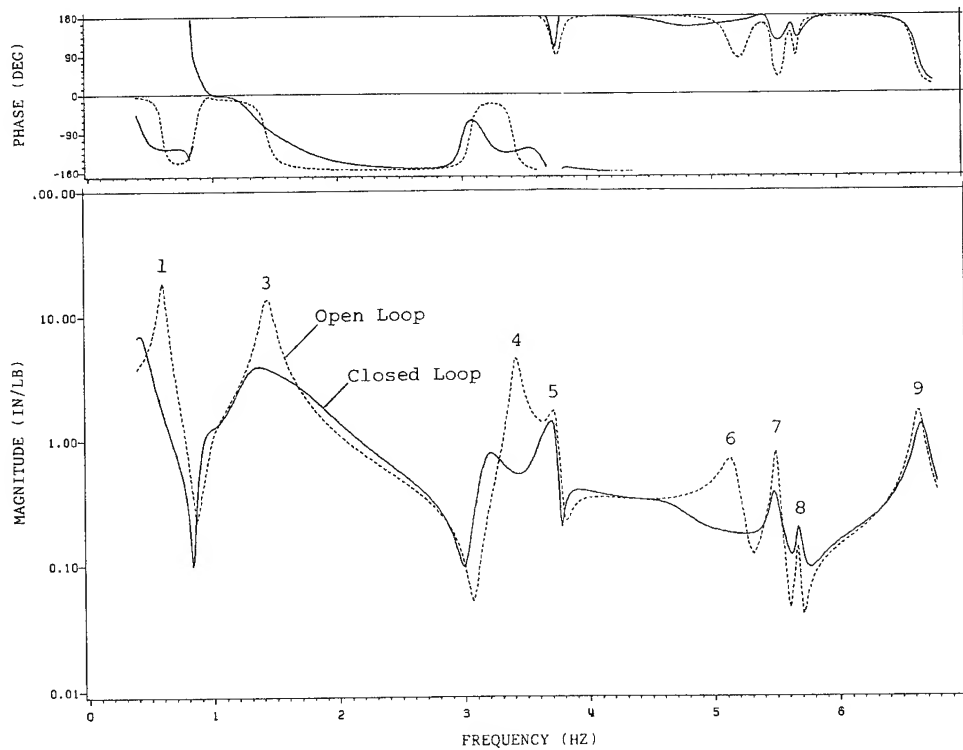


b) Theoretical

Figs. 6 Frequency response functions of displacement at joint 2 due to excitation at joint 2. Resonance peaks of open loop structure modes are labeled by mode number.



a) Experimental



b) Theoretical

Figs. 7 Frequency response functions of displacement at joint 5 due to excitation at joint 1. Resonance peaks of open loop structure modes are labeled by mode number.

EXPERIMENTAL RESEARCH ON FLEXIBLE BEAM MODAL CONTROL

B. Schäfer

H. Holzach

Deutsche Forschungs- und Versuchsanstalt für Luft-
und Raumfahrt e.V. (DFVLR)

8031 Oberpfaffenhofen

Federal Republic of Germany

Abstract

A hardware experiment has been constructed for active vibration control (low-authority control) of a clamped-free flexible beam, where the design methodology is based on direct velocity feedback control. The objective of the experiment is to demonstrate and verify the dynamics and the advanced control laws for the structural element. A further important feature of the experiment is the feasibility of a hardware realization, especially the dedicated non-contacting sensors and actuators. Sensing is provided by a purely optical displacement sensor while an in-house developed electrodynamic force system provides for actuating. Experimental results in comparison with computer simulations are presented for open and closed loop performance for both collocated and dislocated actuator/sensor positions. In most cases of different positioning good agreement could be achieved between experiment and theoretical predictions.

w	deflection function of beam
W	mode shape
x	spatial variable
\dot{y}	velocity vector
δ	Dirac delta function
δ_{kl}	Kronecker symbol
ζ	modal damping factor
η	efficiency factor
Δ	eigenvalue
λ	eigenvalue
ν	Poisson's ratio
ξ	non-dimensional spatial variable
ρ	density
τ	non-dimensional parameter including gravity
ϕ	comparison function
Ω	diagonal frequency matrix
ω	circular natural frequency
(\cdot)	time derivative
$(\cdot)^T$	spatial derivative
$()^T$	vector or matrix transpose

Nomenclature

A	cross section of beam
B	input matrix
b	width of beam
b_{ki}	entry of matrix B
C	measurement matrix
\underline{c}	eigenvector
c_{jk}	entry of matrix C
D_0	damping matrix
d	coefficient of linear damping
E	Young's modulus
E_D	dissipation energy
E_0	total energy
F	external forces
f	natural frequency
\underline{f}	vector of input forces
\underline{G}	transfer function
g	acceleration of gravity
h	thickness of beam
I	moment of inertia; identity matrix
K	feedback gain matrix
k_{11}	first diagonal element of K
l	length
M	dynamical matrix
m	mass; number of force actuators
m_{kl}	entry of matrix M
n	truncation number
\underline{q}	generalized coordinate vector
r	number of sensors
S	transform parameter
S	tensile force
T_1, T_2	time constants
t	time variable
v_0	initial velocity

I. Introduction

Advanced spacecraft systems become increasingly complex with large light weight structural elements being integral parts of the configuration. Furthermore, future systems are considered which no longer will have a central rigid body. One essential characteristic of these space structures is given by their very low critical frequencies which are falling within the attitude control system bandwidth. Hence, the question of vibration suppression by active modal control reveals fundamental importance. Although there exists already a great variety of theoretical control law approaches [1], the development of control experiments has grown much more slowly. Representative first major attempts are described in [2]. Interesting experimental studies on active vibration damping (low-authority control) have been performed on a flexible beam structure having various supporting devices and using different actuator and sensor types [3,4,5]. Controllers have been designed using full-state feedback and observer theory [3] or discrete Kalman filter [4].

Controllers based on direct velocity feedback (described in [6]) appear extremely simple compared to other approaches. The objective of the present experiment therefore is to demonstrate and verify this advanced approach on the basis of a new method for optimal positioning of actuators and sensors on the structure together with optimal feedback gains [7]. Further important features of the experiment are to demonstrate the feasibility of the dedicated non-contacting actuating and sensing devices.

2. Flexible Beam Configuration and Analysis

2.1 Test Setup

Since the main objective of the experiment has been directed towards the demonstration and verification of the dynamics and controller design, a simple structure with respect to dynamical modelling and to technical realization is required. In this sense the clamped-free homogeneous flexible beam hanging in the vertical direction (flexible pendulum) has been chosen as a suitable test structure. This configuration can be regarded as being typical for a large variety of flexible elements (e.g. booms, antenna) in many spacecraft systems. The beam consists of austenitic stainless steel with a length of 2.90 m with rectangular cross-section of width 10 cm and thickness 1 mm. A rigid, reinforced double-T-girder of about 500 kg weight, being mounted in parallel to the flexible beam in a distance of 5 cm, serves as the supporting mechanism and is fixed at the wall (Fig. 1). At its upper end a clamp is mounted to support the flexible beam. An optical guide rail, as long as the beam, is attached along the supporting girder serving as a well-defined reference frame for carrying the actuating system. Furthermore, the guide rail enables easy positioning only by displacing of the actuator, if further locations are required to be investigated in the closed loop tests.

Dynamic tests of the supporting mechanism have been performed in order to be aware of possible disturbances which are likely to occur by the interaction of the supporting beam with the flexible structure. The results show minimum resonant frequencies at 56 and 82 Hz which appeared to be of no importance during the subsequent controller tests. In all experimental dynamical tests a structural dynamics analyzer (of type HP 5423A) has been employed which served as a useful tool for performing the studies and interpreting the results by means of time histories, frequency responses and transfer functions.

2.2 Dynamical Model

For the controller design a dynamical model of the flexible beam is required. The model is based on the EULER-BERNOULLI theory including longitudinal loads due to gravity effects (Fig. 2). The partial differential equation of motion including structural linear damping is

$$EIw^{IV} - (Sw')' + d\dot{w} + \rho A\ddot{w} = F \quad (1)$$

together with the boundary conditions

$$\begin{aligned} w(0,t) &= 0, \quad w'(l,t) = 0, \\ w'(0,t) &= 0, \quad w'''(l,t) = 0, \end{aligned} \quad (2)$$

where

$$S(x) = \rho Ag(l-x) \quad (3)$$

is the tensile force due to gravity [8]. At the clamped end this force is equal to the beam's weight while S is zero at the free end. The force distribution $F(x,t)$ comprises the applied forces due to control action. For the free vibration analysis considered here, damping and control forces vanish.

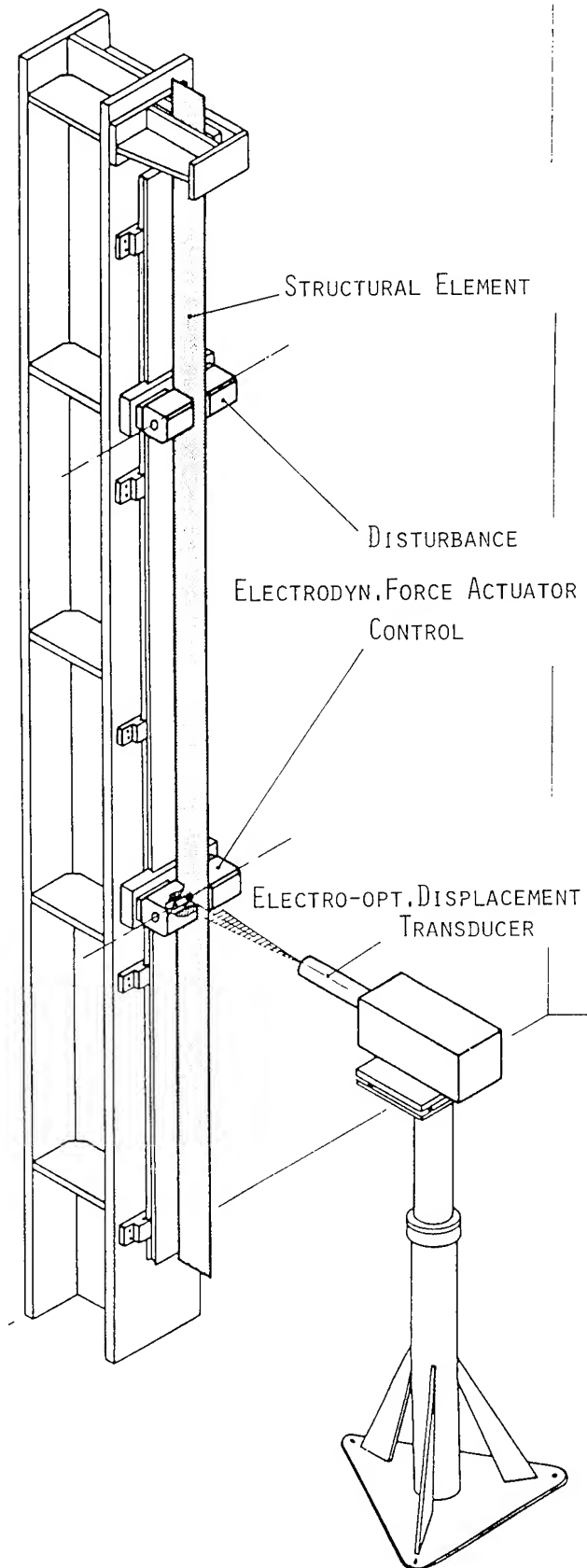


Fig. 1 Flexible Beam Test Setup.

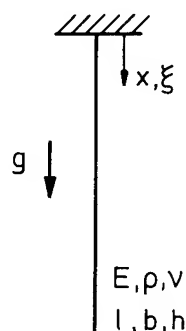


Fig. 2 Flexible Beam Model.

A transverse harmonic motion of the form

$$w(x, t) = W(x) \cdot \sin \omega t \quad (4)$$

is assumed, where ω is the natural frequency and W is the corresponding mode shape. With $\xi = x/l$, $\tau = \rho A g l^3 / EI$, $\Delta = \rho A \omega^4 l^4 / EI$ Eq. (1) is replaced by

$$W^{IV}(\xi) - \tau[(1-\xi)W'(\xi)]' - \Delta W(\xi) = 0. \quad (5)$$

Up to now no exact solutions are known for this boundary value problem. Therefore an approximate approach for achieving a closed form analytical solution is performed using GALERKIN'S method [9] using beam eigenfunctions φ_i (without gravity) as comparison functions in the RITZ expansion:

$$W(\xi) = \sum_{i=1}^n c_i \varphi_i(\xi) \quad (6)$$

where the

$$\begin{aligned} \varphi_i(\xi) = & \cosh \lambda_i \xi - \cos \lambda_i \xi \\ & - \frac{\cosh \lambda_i + \cos \lambda_i}{\sinh \lambda_i + \sin \lambda_i} (\sinh \lambda_i \xi - \sin \lambda_i \xi) \end{aligned} \quad (7)$$

are orthogonal and normalized with respect to

$\int_0^1 \varphi_k \varphi_l d\xi = \delta_{kl}$. Inserting Eq. (6) in Eq. (5) finally leads to the special eigenvalue problem

$$(M - \Delta I)\underline{c} = 0 \quad (8)$$

where the symmetric and positive definite matrix M consists of the matrix elements

$$m_{kl} = \int_0^1 \varphi_k [\varphi_l^{IV} - \tau((1-\xi)\varphi_l')] d\xi. \quad (9)$$

Numerical results for the eigenvalue Δ and the corresponding eigenvector \underline{c} have been achieved by standard methods, with truncation number $n = 20$. A final design for a homogeneous flat beam yielded the parameter set listed in Table 1. Because flat beams are plate-like structures, a correction on the assumption of pure bending is necessary [10]: transverse contraction will be restrained by additional transverse normal stresses which finally result simply in an increase of YOUNG'S modulus according to $E' = E/(1-\nu^2)$.

Table 1 Beam Characteristics

material	austenitic stainless steel	
length	l	2.90 m
width	b	0.10 m
thickness	h	1.00 mm
density	ρ	8 g/cm ³
mass $m = \rho A l$		2.32 kg
POISSON'S ratio ν		0.3
$\sqrt{E'/\rho}$		4685 m/s
$I = \frac{1}{12} b h^3$		8.33 mm ⁴
$\tau = \rho A g l^3 / E' I$		130.8

Table 2 Natural Frequencies and Modal Damping Parameters for Beam

j	natural frequencies f_j [Hz]			exp. modal damping
	theor. (without g)	theor. (with g)	exp. (with g)	
1	0.09	0.37	0.37	0.30
2	0.56	1.02	1.02	0.24
3	1.58	2.14	2.14	0.16
4	3.09	3.73	3.72	0.14
5	5.12	5.79	5.80	0.13
6	7.64	8.35	8.39	0.12
7	10.67	11.41	11.41	0.1
8	14.21	14.96	15.1	<0.1
9	18.25	19.01	19.2	<0.1
10	22.80	23.57	23.9	<0.1

Moreover in most practical cases E is known only with poor accuracy, while the density can be measured easily. Therefore the modified wave velocity $\sqrt{E'/\rho}$ has been determined such that the five lowest natural frequencies agree very well with the corresponding experimental data, giving finally a value of E that is about 20% lower than the expected one of $2 \cdot 10^{11}$ N/m².

Table 2 comprises a comparison of theoretically and experimentally determined natural frequencies together with experimental modal damping parameters, where the experimental values of the first five modes have been determined by a modal survey test, the others by frequency response measurements using strain gauges. Moreover, the first column contains the theoretical natural frequencies of a clamped-free beam without gravity in order to exhibit the great impact by gravity effects, especially on the lower frequencies. The corresponding mode shapes are influenced only little by gravity when comparing with the gravity-free modes not shown here. Figure 3 shows a graph of the first six mode shapes.

For experimental verification of the model a modal survey test has been performed by means of the impact method. To identify the various mode shapes, the beam has been stimulated at different locations and the deflection has been measured by a displacement transducer. The transfer functions, generated by the spectral analyzer, yield the frequency and damping behaviour (Table 2) together with the mode shapes, where good agreement with the

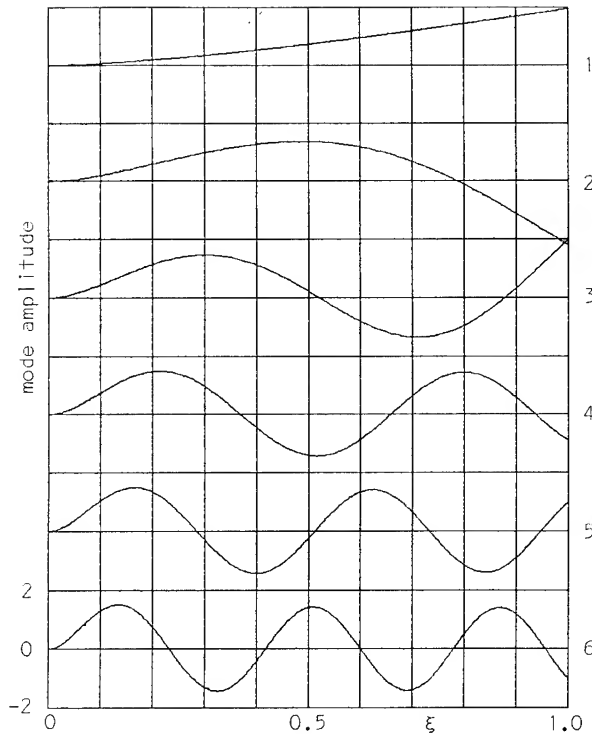


Fig. 3 Six Lowest Mode Shapes.

theoretical predictions has been achieved. Additional informations about the higher frequency range has been obtained by a strain gauge mounted at the clamped end (Fig. 4).

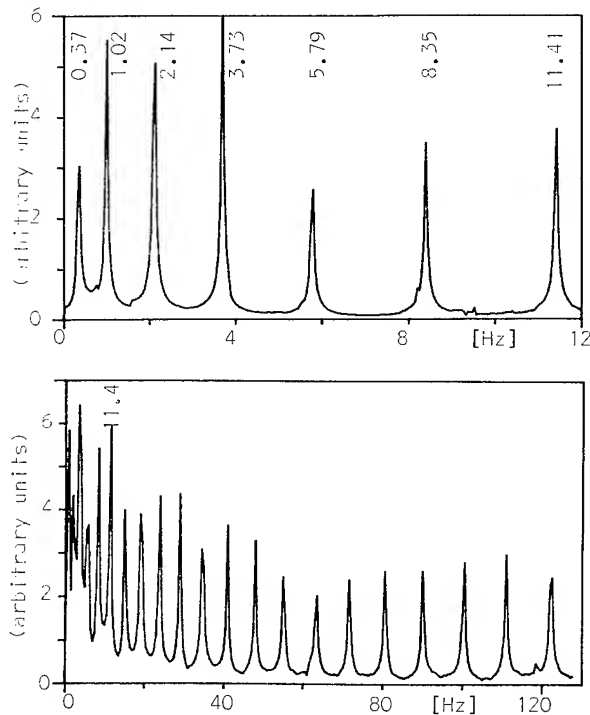


Fig. 4 Transfer Function (Strain gauge at $\xi = 0$, Impact at $\xi = 1$) Showing the Lowest 7 (Upper Graph, 0.05 Hz Resolution) and the Lowest 22 (Lower Graph, 0.8 Hz Resolution) Natural Frequencies.

3. Controller Design

The objective of the controller to be designed is to increase damping of the structure by direct velocity feedback. The flexible beam dynamics with structural damping and m point-force actuators

$$F(x, t) = \sum_{i=1}^m f_i(t) \cdot \delta(x - x_i) \quad (10)$$

are described by Eq. (1). The velocities are measured by r point-sensors:

$$\dot{y}_j(t) = \dot{w}(x_j, t), \quad j = 1, \dots, r. \quad (11)$$

The solution of Eq. (1) can be expanded in the mode shapes given by Eq. (6)

$$w(x, t) = \sum_{k=1}^m W_k(x) \cdot q_k(t), \quad (12)$$

where $\underline{q} = [q_1, \dots, q_m]^T$ is the vector of generalized coordinates satisfying the modal state space equation

$$\ddot{\underline{q}} + D_0 \dot{\underline{q}} + \Omega \underline{q} = \frac{1}{m} B \underline{f}, \quad (13)$$

with $\Omega = \text{diag}(\omega_k^2)$, $D_0 = \text{diag}(2\zeta_k \omega_k)$, B is a $n \times m$ matrix with entries $b_{ki} = W_k(x_i)$ and the vector of input forces is $\underline{f} = [f_1, \dots, f_m]^T$. The sensor Eq. (11) becomes

$$\underline{y}(t) = C \dot{\underline{q}}(t) \quad (14)$$

with $\underline{y} = [y_1, \dots, y_r]^T$ and C is a $r \times n$ matrix with entries $c_{jk} = W_k(x_j)$. For direct velocity feedback the control law is obtained by

$$\underline{f}(t) = -K \underline{y}(t), \quad (15)$$

where K is the $m \times r$ gain matrix. Then the dynamical behaviour of the closed loop system is described by

$$\ddot{\underline{q}} + (D_0 + \frac{1}{m} BKC) \dot{\underline{q}} + \Omega \underline{q} = 0. \quad (16)$$

In case of collocated actuators and sensors (i.e. $m = r$ and $B^T = C$), K non-negative definite and no zero frequencies it can be shown [6] that Eq. (16) has asymptotically stable solutions if $\zeta > 0$ (even if the truncated residual modes are implemented), which is fulfilled since internal damping is present in all flexible structures. In the case of dislocation instability may occur as soon as truncated residual modes are implemented in the model which have nodal points between actuator and sensor positions (spillover effect).

The important problem of positioning suitably actuators and sensors has been solved by SCHULZ and HEIMBOLD [7] who presented a new method for an integral determination of actuator/sensor positions (included in B and C) and feedback gains (matrix K) for the system of Eq. (16). The method is based on the maximization of dissipation energy

$$E_D = - \int_0^\infty \dot{\underline{q}}^T \cdot BKC \cdot \dot{\underline{q}} dt \quad (17)$$

due to control action, which represents an optimization criterion guided only by physical considerations. Additionally, constraints (upper bounds of

+ 50 Ns/m) have been posed to the feedback matrix K because of restricted maximum control forces exerted by real actuators.

In spite of these constraints it is expected that yet high feedback gains will result, which are likely to produce spillover on the residual modes. Hence an alternative optimization criterion has been envisaged minimizing the dissipation energy in Eq. (17) in conjunction with minimum damping constraints. A minimum value of 5% modal damping has been considered for all modes implemented in the design model.

Initial disturbance force is realized by an impulsive point-force acting on the beam and producing an initial velocity v_0 . The energy distribution on the mode shapes of the total energy E_0 stored in the flexible structure is influenced very strongly by the position of the originating disturbance, and hence it influences the optimal actuator/sensor positions and the feedback gains. In order to excite many of the lower structural modes the initial force has been applied near the clamped end at $\xi = 0.2$ rather than at the free end (in order to avoid an ideal disturbance compensation at the free end). To comply with realistic conditions the force impact has been chosen as to achieve $v_0 = 30$ mm/s which gives a maximum amplitude of about 5 mm at the free end.

The design model accounts for the lowest $n = 5$ vibration modes. An evaluation model including higher modes has been considered with $n = 10$ in order to investigate stability of the residual five modes on the basis of the design model. The natural frequencies and mode shapes determined analytically together with the experimentally obtained structural damping factors (Table 2) entered into the controller design. Furthermore, an efficiency factor $\eta = E_p/E_0$ has been considered in order to judge the optimal solutions. Computer programs for numerical determination of optimal controller parameter with respect to both energy criteria have been available.

4. Actuators and Sensors

Great emphasis has been directed towards the proper selection of the actuating and sensing system, since an almost ideal performance is preferred. Many different possibilities have been eliminated by the requirement of minimum sensor/actuator interaction with the flexible beam dynamics. Requirements referring to range and sensitivity restricted the selection to few types. The sensor is considered to provide for expected maximum vibration amplitudes of 10 mm and a frequency range of about 100 Hz since the designed controller will be based on the first 5 or 6 lowest modes, and signals of higher frequency should be observable in order to account for possible spillover effects. Expected force amplitudes range up to about 1 N. High accurate accelerometers, have been discarded by physical considerations: When mounted on the beam, they cannot separate between the interesting horizontal acceleration and the undesired vertical component due to gravity, which might be in the same order of magnitude as the horizontal one.

On this basis non-contacting systems with laboratory fixed references have been selected: A purely electro-optical displacement transducer together with an in-house developed electrodynamic force actuator [11]

provide for sensing and actuating. The actuator is of high resolution ($< 1\%$) with a range of 1.1 N and nonlinearity of 1% for a displacement range of + 12 mm. It consists of a permanent magnetic bar attached to the structural element being free to move in a cylindrical laboratory fixed electromagnetical coil (Fig. 5). The dimensions of coil and magnet have been determined such that the applied force is almost independent from their relative motion, resulting in

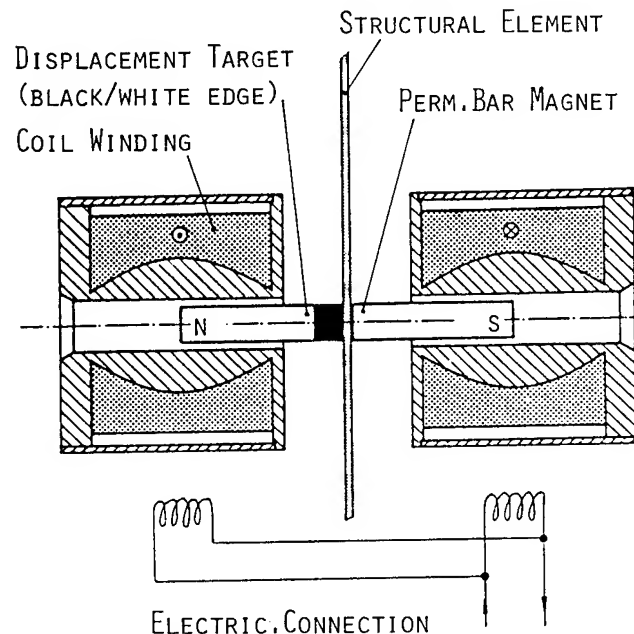


Fig. 5 Electrodynamical Force Actuating System.

an almost parabolic coil shape. To minimize errors in motion, a pair of actuators is arranged at opposite sides of the structure. Driving these actuators in parallel, the axial motion induced error will be essentially cancelled. The small tilt angle of the vibrating flexible beam proved to be of no remarkable influence upon system nonlinearities. Additional mass concentrations due to the mounted pair of cylindrical, rare earth magnetic bars are negligible, considering a weight of 25 g for one bar with a length of 4 cm and a diameter of 1 cm. This could be shown experimentally by frequency analysis when varying the location of the bar along the beam in discrete spatial steps. Frequency shifts have been below 3%.

The electro-optical transducer with very low noise levels has an excellent resolution of about 0.01% full scale considering a range of about 10 mm. The range easily can be varied by changing the imaging optics. Nonlinearity is below 0.1% and frequency range extends to 1 kHz. The transducer is placed perpendicular to the plane of the beam vibrations at a distance of 30 cm to the beam's symmetry axis.

The actuating/sensing system provides for an almost ideal realization of collocated actuator/sensor positioning since the plate mounted magnetic bar vibrating with the structure serves as the reference point for sensing (Fig. 1). Non-collocated actuator/sensor positioning has been realized by a similar configuration fixing a small black/white edge sheet at the specified position.

The controller to be designed requires velocity in-

formation for feedback which is extracted out of the optical displacement signal by a differentiation procedure. Since no other controller algorithms have been proposed, it was preferred to realize differentiation by analog technique rather than by a data processing system. It is characterized by a transfer function of type $G(s) = T_1s/(1+T_2s)$, with time constants of $T_1 = 0.01$ s and $T_2 = 0.0015$ s, yielding a roll-off frequency of 667 Hz.

Bandwidth limitation of the sensor signal is necessary to avoid saturation effects of the differentiation loop. During the tests no instability has been observed due to phase shifts in sensor signal and differentiation circuit.

5. Experimental and Numerical Results

An inherent basic problem of the optimization procedures used is that no global optimum can be found. The optimal parameters achieved depend upon their initial values. Hence, several optima may result which are regarded being only locally optimal. An important feature of the experimental investigations therefore is to judge the closed loop behaviour for different optima. The studies are performed for 1 actuator/sensor configuration for both collocated and dislocated positions. Furthermore, to get a first insight experimentally in the treatment of multiple actuator/sensor locations, a configuration of two actuators/two sensors is realized. Here, the study is confined to collocated positions in order to avoid excessive parameter combinations for the positions. In all studies the control law is based on maximization of dissipation energy, unless mentioned explicitly different from that (minimization of dissipation energy).

For verification of the designed control law the variation of the closed loop system eigenvalues with respect to the open loop values has been determined by means of a transfer function, measured between the force impact input at $\xi = 0.2$ and the displacement output at the optimized sensor position. In case of highly damped systems excitation by white noise has been preferred rather than by impact, in order to introduce more energy into the system.

The disturbance impulse has been realized experimentally by a separate electrodynamic actuator system. A further electro-optical displacement sensor has been positioned at $\xi = 0.2$ to determine the initial velocity v_0 by subsequent analog differentiation of the sensor signal. Pulse height and width could be adjusted to defined initial conditions to comply with the desired value of v_0 , yielding 0.15 N and 50 ms. The adjustment of v_0 is necessary for comparison of experimentally and numerically obtained time histories, since the closed loop system of Eq. (16) is linear in q .

5.1 1 Actuator/1 Sensor (Collocation)

Nine locally optimal positions have been obtained, each of them lying between adjacent zero crossings of the mode shapes as presented in Fig. 6a. The feedback gain matrix K now consists of only one element k_{11} . Table 3 comprises the optimized position, feedback gain k_{11} and the corresponding efficiency factor η for the various optima. The striking position number 1 could be expected due to an ideal disturbance compensation which causes the optimizer

Table 3 1 Act./1 Sens. (Coll.): Opt. Parameters.

number	ξ	k_{11} [Ns/m]	η [%]
1	0.2	50.0	99.4
2	0.329	15.43	88.4
3	0.445	14.29	93.1
4	0.602	13.30	92.2
5	0.699	12.33	84.1
6	0.774	10.05	85.7
7	0.830	10.33	91.3
8	0.900	10.60	76.5
9	1.0	3.96	79.1

to move the actuator at the position of the originating disturbance, thus giving an extremely high gain which is identical to the upper bound constraint in the present case. The position numbers 2 to 8 show gains of comparatively size but with quite different efficiency. This means that high gains do not automatically yield low decay time constants in order to damp out the vibrations very quickly, since the damping behaviour obviously is influenced strongly by the modal amplitude at the actuator/sensor position. This behaviour is evident for position number 5, where the size of the mode shapes with number 2,4 and 5 is much lower than the size of number 1 and 3. In contrary to that, at the free end a very low gain factor is achieved, mainly due to the large deflection of the mode shapes there.

Fig. 7 presents graphs of experimental and numerical open loop time behaviour of displacement at three different positions. To be lucid closed loop behaviour will be demonstrated just for two optimized positions: one at $\xi = 0.602$ (Fig. 8 shows time histories of displacement and control force) and the other at the free end (Fig. 9). Experimentally determined transfer functions for open and closed loop system are shown in Fig. 10 (with white noise excitation) and 11 for both positions. The resulting eigenvalues, i.e. shifted eigenfrequencies and modal damping factors, are listed in Tables 4 and 5 together with the numerical values for the lowest six modes. Although almost good agreement is indicated, proper determination at lower frequent modes often appears difficult due to the high damping rates, especially for position at $\xi = 0.602$. In accordance with theoretical predictions no instable modes could be observed during these tests.

In a further test, for optimized position at $\xi = 1.0$ the optimal gain factor has been drastically increased by a factor of 10 in order to enhance strongly damping and stiffness of the structure. The purpose of this study has been to investigate if due to the enhanced control action the free end could be fixed in order to prevent the actuator from energy extraction. But no such effect could be observed, on the contrary the vibrations have been damped out in much less time than before.

Minimization of dissipation energy with 5% minimum modal damping constraints yielded similar results as in case of maximization. Optimal positions are not much different but the feedback gains take considerably smaller values, depending upon the constraints. Just one example should be mentioned: the optimized position at $\xi = 0.593$ gives $k_{11} = 5.47$ Ns/m which is about three times smaller when compared to the similar case at $\xi = 0.602$.

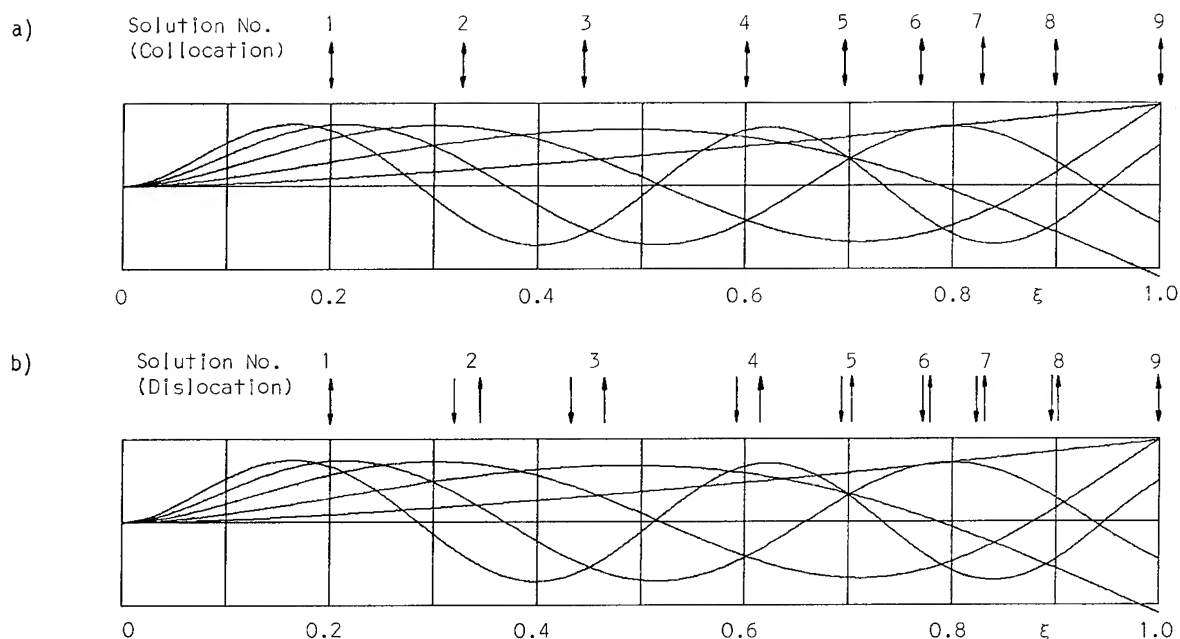


Fig. 6 Five Mode Shapes and Optimal Actuator/Sensor Positions for Collocated and Dislocated Configurations (\downarrow Actuator \uparrow Sensor).

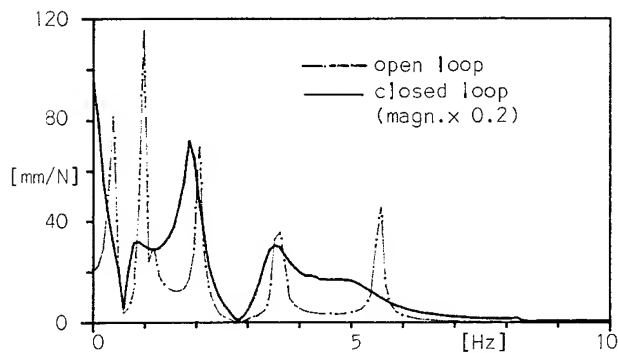


Fig. 10 Open and Closed Loop Transferfunction for Optimized Collocated Position at $\xi=0.602$ (Impact at $\xi = 0.2$, Displacement Sensor at $\xi = 0.602$).

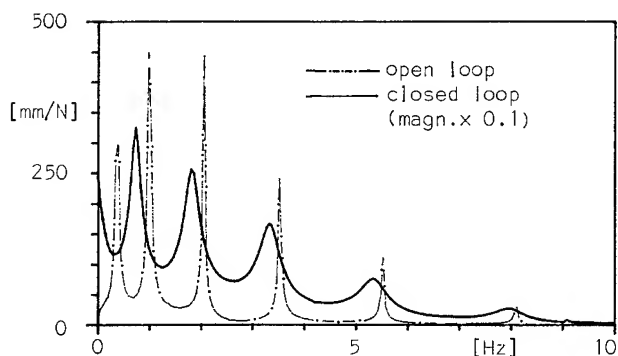


Fig. 11 Open and Closed Loop Transferfunction for Optimized Collocated Positions at $\xi = 1.0$ (Impact at $\xi = 0.2$, Displacement Sensor at $\xi = 1.0$).

Table 4 1 Actuator/1 Sensor (Collocated): Closed Loop Eigenvalues for Optimized Position at $\xi = 0.602$.

mode number	frequency [Hz]		modal damping [%]	
	exp.	num.	exp.	num.
1	-	-	-	100.0
2	0.7	0.70	10.2	15.0
3	1.9	1.96	8.3	7.6
4	3.5	3.57	7.6	7.7
5	4.9	5.33	12.7	11.5
6	8.3	8.35	1.1	0.5

Table 5 1 Actuator/1 Sensor (Collocated): Closed Loop Eigenvalues for Optimized Position at $\xi = 1.0$.

mode number	frequency [Hz]		modal damping [%]	
	exp.	num.	exp.	num.
1	-	-	-	100.0
2	0.7	0.73	11.9	12.1
3	1.8	1.88	7.3	7.6
4	3.3	3.67	5.4	1.9
5	5.3	5.73	4.6	2.1
6	8.0	8.30	3.3	1.8

5.2 1 Actuator/1 Sensor (Dislocation)

Again, nine locally optimal positions are obtained, where the initial values for both actuator and sensor have been chosen such as to lie between adjacent zero crossings of the five lowest mode shapes. The results are presented in Fig. 6b and in Table 6, indicating a very close spacing between actuator and sensor position. Obviously this spacing becomes closer if more modes are implemented

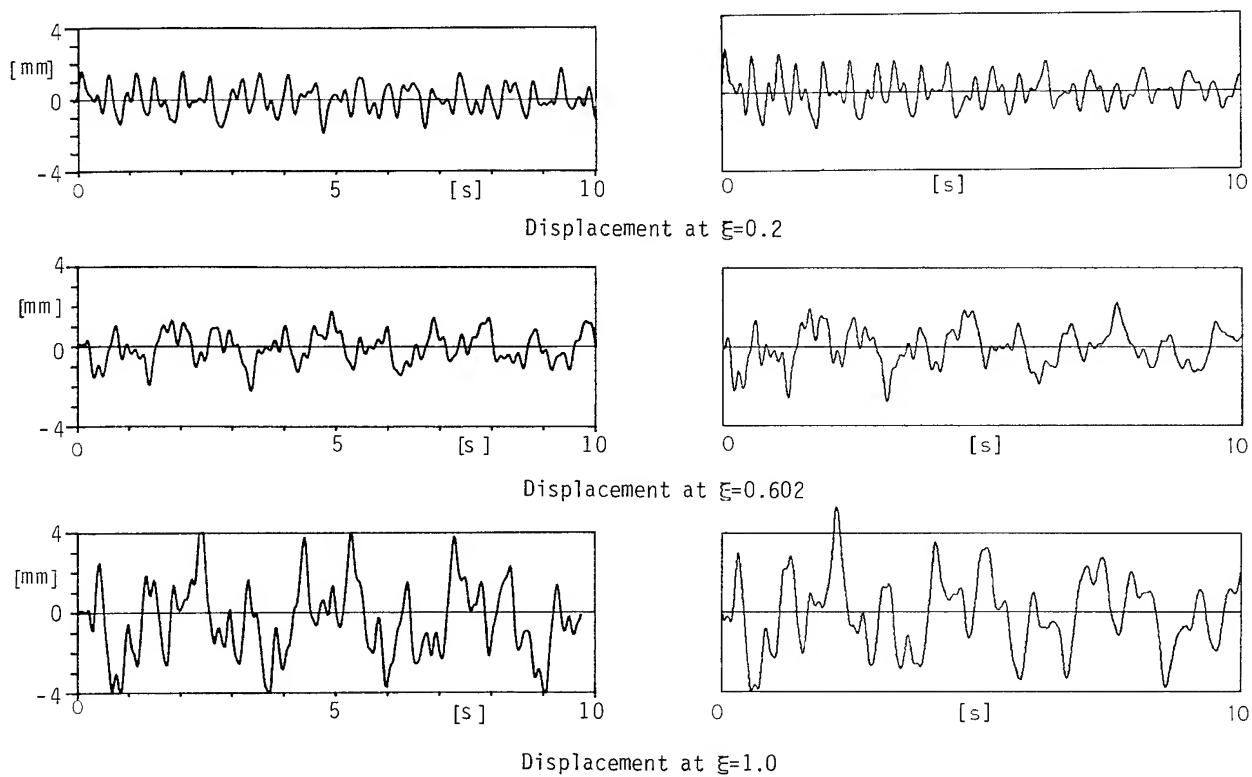


Fig. 7 Open Loop Time Histories of Displacement after Impact at $\xi=0.2$ (Left Side: Experimental, Right Side: Numerical).

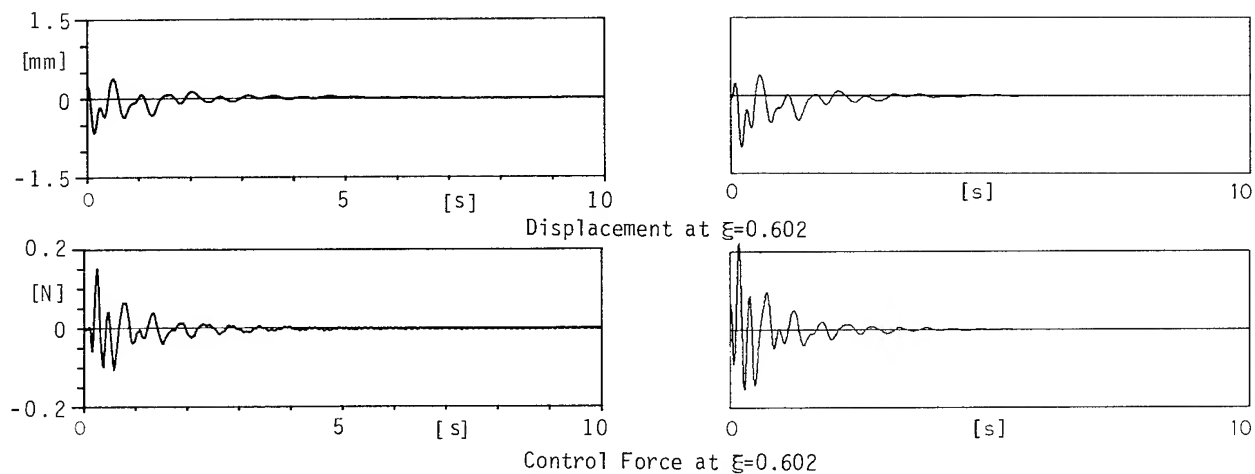


Fig. 8 Closed Loop Time Histories (Collocation) for Optimized Position at $\xi=0.602$ (Left Side: Experimental, Right Side: Numerical).

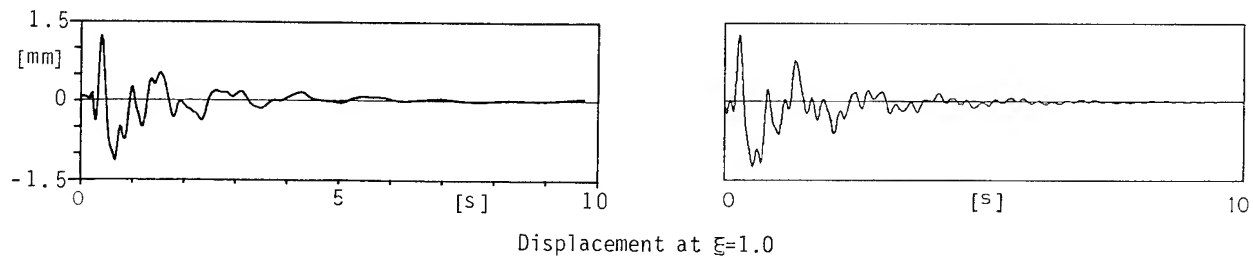


Fig. 9 Closed Loop Time History (Collocation) for Optimized Position at $\xi=1.0$ (Left Side: Experimental, Right Side: Numerical).

Table 6 1 Actuator/1 Sensor (Dislocated): Optimal Parameters

number	$\xi(\text{actuator})$	$\xi(\text{sensor})$	$k_{11}[\text{Ns/m}]$	$\eta[\%]$
1	0.2	0.2	50.0	99.7
2	0.317	0.343	18.72	89.3
3	0.429	0.463	16.59	93.5
4	0.591	0.614	14.31	92.4
5	0.695	0.702	12.57	84.3
6	0.772	0.776	10.14	85.7
7	0.825	0.835	10.47	91.3
8	0.898	0.901	10.63	76.5
9	1.0	1.0	3.96	79.1

in the design model in order to avoid zero crossings between actuator and sensor position; hence approaching the collocated case. The energy extracted by the actuator and the feedback gains are only insignificantly higher than in the collocated case. Moreover, it turns out that in the collocated case the actuator/sensor position always lies about in the middle of the corresponding dislocated positions.

Spillover is predicted in cases number 3 and 4 when implementing the residual five modes in the evaluation model, caused by nodal points of higher mode shapes between actuator and sensor positions. For experimental demonstration of spillover only position number 4 will be investigated. Here, sensor and actuator positions are separated by a distance of only 6.7 cm. The closed loop time history of the displacement at sensor location is presented in Fig. 12 and shows that the lower vibration modes are damped out but mode number 6 with frequency of 8.4 Hz and a nodal point at $\xi=0.6$ (Fig. 3) is excited very strongly.

To avoid spillover an extension of the controller design has been attempted on the basis of a six

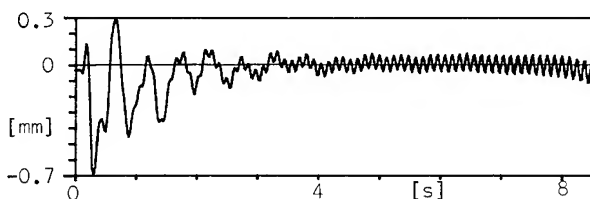


Fig. 12 Closed Loop Time History of Displacement at $\xi(\text{sensor})=0.614$ for Optimized Dislocated Solution No.4 (Table 6) Showing Spillover with Unstable Sixth Mode.

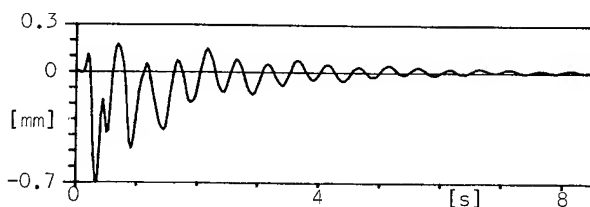


Fig. 13 Closed Loop Time History of Displacement at $\xi(\text{sensor})=0.579$ (Dislocation) for Extended 6 Modes Design Model to Prevent from Spillover (cf. Fig. 13).

modes design model, thus including the unstable vibration mode. In that case actuator and sensor move closer in order to exclude the critical zero crossing, yielding $\xi(\text{actuator})=0.5692$, $\xi(\text{sensor})=0.5787$, $k_{11}=12.85$ Ns/m and $\eta=96.6\%$. Fig. 13 indicates stability of the closed loop system. The very close distance of 2.7 cm appears almost collocated and it is conjectured that in the collocated case the optimal position will be somewhere between these two dislocated positions. A subsequent controller design proves this suggestion, yielding optimal parameters of $\xi=0.5741$, $k_{11}=12.53$ Ns/m and $\eta=96.5\%$, which are not much different from the dislocated case.

5.3 2 Actuators/ 2 Sensors (Collocation)

The gain matrix now comprises four elements to be optimized. Different choice of a specific form of K has been followed in the design, depending upon the choice of number of sensor signals to be fed back. This has been realized numerically by equating zero the corresponding matrix elements of K . The purpose of different feedback strategies is to investigate the possibility of successful operation with only a few number of sensors. To be more clear, actuator and sensor positions have been determined from the optimized 1 actuator/1 sensor case at $\xi=0.602$ and $\xi=1.0$ rather than optimizing these positions here. Three different feedback schemes have been considered:

Scheme 1:

$$K = \begin{bmatrix} 7.53 & -0.95 \\ 8.38 & 3.31 \end{bmatrix} [\text{Ns/m}], \quad \eta = 94.7\%,$$

i.e. all sensor signals are fed back to all actuators (global feedback);

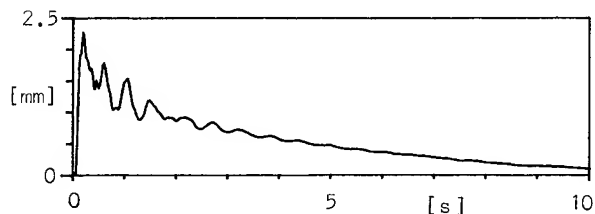


Fig. 14 Closed Loop Time History of Displacement at $\xi=1.0$ for Collocated 2 Actuators/ 2 Sensors Global Feedback.

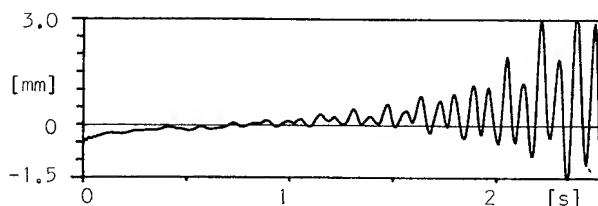


Fig. 15 Closed Loop Time History of Displacement at $\xi=1.0$ for Collocated 2 Actuators/ 2 Sensors Scheme 3 Feedback (Here: Increasing Oscillation from Equilibrium Position).

Scheme 2:

$$K = \begin{bmatrix} 12.21 & 0 \\ 0 & 2.35 \end{bmatrix} \text{ [Ns/m], } \eta = 98.0 \% ,$$

i.e. each sensor signal is fed back locally to the collocated actuator (axial feedback);

Scheme 3:

$$K = \begin{bmatrix} 0 & 11.36 \\ -11.38 & 0 \end{bmatrix} \text{ [Ns/m], } \eta = 2.6 \% ,$$

i.e. sensor signal at position 1 is fed back to actuator at position 2 and vice versa.

Since in all three feedback schemes K is non-negative definite, the five modes closed loop system is asymptotically stable. Evidently, axial feedback gives the largest efficiency with low feedback gains which remember the equivalent gains in the 1 actuator/1 sensor case (Table 3) for both positions. On the contrary, feedback scheme 3 produces an extremely low efficiency factor but with comparatively high gain factors. Moreover regarding the evaluation model with 10 modes spillover is predicted and observed experimentally for mode number 7 with frequency of 11.4 Hz. Figures 14 and 15 present the corresponding time histories.

An important result is that a configuration of two actuators and two sensors can be more efficient than a configuration of only one actuator/one sensor, depending upon the selected feedback strategy. But an overall sensor information (global feedback) may not be as useful as in axial feedback, when comparing the amount of dissipated energy.

6. Conclusions

A flexible beam experiment has been constructed in order to demonstrate and verify advanced control laws based on direct velocity feedback. The new actuating/sensing system of electrodynamic force actuator and electro-optical displacement transducer revealed almost ideal performance which allowed to investigate the interaction of controller/structure without the impact of hardware constraints. The structural dynamics of the gravity-loaded beam could be modelled with good accuracy, being an essential input for the controller design. Detailed studies on collocated and dislocated 1 actuator/1 sensor positions favoured the collocated configuration since dislocation proved to produce spillover due to higher modes not implemented in the design model or, moreover, in the evaluation model. By realization of two actuators/two sensors positioning a better closed loop behaviour could be achieved: The amount of dissipated energy was increased when applying special feedback strategies (global or axial feedback), but an overall sensor information for feedback appeared to be not necessary. For investigation of the closed loop system dynamics the experimental determination of complex eigenvalues by means of transfer functions proved to be most practicable. Only in cases of highly damped systems eigenvalues could be determined very inaccurately. In all studies performed no remarkable difference between experimental

results and theoretical predictions could be exhibited.

Future work will be directed towards the digital realization of controller feedback. Further studies shall involve structures with a frequency spectrum including closely spaced frequencies being more typical for large space structures.

Acknowledgement

Experimental investigations require much team effort. All members of the group 'Satellite Dynamics' therefore deserve recognition. Many thanks are returned to G. Schulz who made his optimization software routines available to the authors.

References

- 1 Balas, M.J.; "Trends in Large Space Structure Control Theory: Fondest Hopes, Wildest Dreams", IEEE Trans. Automatic Control, Vol. 27, 1982, pp. 522-535.
- 2 Aubrun, J.-N.; Ratner, M.J.; Lyons, M.G.; "Structural Control for a Circular Plate", Lockheed Palo Alto Research Laboratory, 1983.
- 3 Herrick, D.; Canavin, J.; Strunce, R.; "An Experimental Research of Modern Modal Control", AIAA 17th Aerospace Sciences Meeting, Paper No. 79-0199, New Orleans, La., Jan. 15-17, 1979.
- 4 Schaechter, D.B.; "Hardware Demonstration of Flexible Beam Control", AIAA Guidance and Control Conference, Paper No. 80-1794, Denver, Mass., Aug. 11-13, 1980.
- 5 Montgomery, R.C.; Horner, G.C.; Cole, S.R.; "Experimental Research on Structural Dynamics and Control", NASA Conference on Structural Dynamics and Control of Large Space Structures, Publ. No. 2187, Hampton, Va., Oct. 30-31, 1980.
- 6 Balas, M.J.; "Direct Velocity Feedback Control of Large Space Structures", J. Guidance and Control, Vol. 2, 1979, pp.252-253.
- 7 Schulz, G.; Heimbold, G.; "Integrated Actuator/Sensor Positioning and Feedback Design for Large Flexible Structures", AIAA Guidance and Control Conference, Paper No. 82-1590 CP, San Diego, Cal., Aug. 9-11, 1982.
- 8 Schäfer, B.; "Auslegung eines flexiblen Balkens als dynamisches Modell für die aktive Schwingungsdämpfung großer Leichtbaustrukturen", DFVLR Contractor Report, Oberpfaffenhofen, Germany, 1982.
- 9 Collatz, L.; "Eigenwertaufgaben mit technischen Anwendungen", Akademische Verlagsgesellschaft, Leipzig, 1949.
- 10 Szabo, I.; "Einführung in die Technische Mechanik", Springer Verlag, Berlin, 1961.
- 11 Holzach, H.; Lange, Th.; "Development of an Electromagnetical Force Actuator System for Active Vibration Control", DFVLR, Oberpfaffenhofen, Germany, TN-1/84, 1984.

DYNAMICS OF FLEXIBLE BODIES IN TREE
TOPOLOGY - A COMPUTER ORIENTED APPROACH

Ramen P. Singh* and Richard J. VanderVoort**
Honeywell Incorporated
Clearwater, FL.

Peter W. Likins***
Lehigh University
Bethlehem, PA.

Abstract

An approach suited for automatic generation of the equations of motion for large mechanical systems (i.e., large space structures, mechanisms, robots, etc.) is presented. The system topology is restricted to a tree configuration. The tree is defined as an arbitrary set of rigid and flexible bodies connected by hinges characterizing relative translations and rotations of two adjoining bodies. The equations of motion are derived via Kane's method. The resulting equation set is of minimum dimension. Dynamical equations are imbedded in a computer program called TREETOPS. Extensive control simulation capability is built in the TREETOPS program. The simulation is driven by an interactive set-up program resulting in an easy to use analysis tool.

Introduction

In the last two decades considerable efforts have been made in the efficient formulation and solution of the dynamic equations of multi-body mechanical systems. Examples of such systems include spacecraft, large space structures, manipulators, mechanisms and bio-systems. This paper deals with an improved approach to the solution of the dynamics and control problem that is applicable in each of these areas. This approach will accommodate structures with an open tree topology including flexibility in any or all of the individual bodies along with large angle rotations and translations at the hinges. This formulation reduces the problem to a minimum dimension set which is very desirable from a computational standpoint.

The emphasis of researchers working with multibody systems has been the expanded generality of mathematical models and the formulation of equations of motion that are amenable to computer solution. Dynamical equations of motion for multibody systems can be derived by Newton-Euler methods or by analytical mechanics methods (e.g. Lagrange's

equations, Hamilton's canonical equations, the Boltzman-Hamel equations, etc.). The relative advantages and disadvantages of these various approaches depend upon: (1) the choice of dependent (kinematic) variables, (2) the geometrical organization and accounting procedure for a unique kinematic description and (3) the systematic implementation. Comparative studies in recent years¹⁻⁴ suggest that Kane's method of generalized speed⁵ or some related generalization of Lagrange's form of D'Alembert's principle is most useful. These methods are ideally suited for computer generation of the equations of motion⁶ Kane's method combines the computational advantages of both Newton's Laws and Lagrangian formulation - the nonworking constraint forces and torques do not appear and tedious differentiation of scalar energy functions is avoided. The resulting equation set is of minimum dimension. Methods of analytical dynamics best suited for automatic generation of the equations of motion are reviewed in Reference 7.

The interest in multibody dynamics modeling has arisen, almost simultaneously, in three distinct fields: spacecraft dynamics, mechanisms and robotics. In what follows the extensive literature in multibody dynamics in these three fields will be very briefly reviewed.

In the early years space vehicles were idealized as rigid bodies or elastic beams for control system design purposes. In response to needs of the aerospace industry in mid-sixties, the equations of motion were published^{8,9} for a point connected set of interconnected rigid bodies in a topological tree. A model combining rigid bodies and elastic appendages was developed and applied extensively¹⁰⁻¹² in the 1970's. Incorporation of body flexibility in the topological tree model was the next logical step, taken in some cases concurrently with the inclusion of relative translation between the bodies.¹³ In the most general case considered to date,

*Staff Engineer, Associate Fellow AIAA

**Senior Staff Engineer

***President, Fellow AIAA

the prohibition of closed loops in the topology is also relaxed.¹⁴⁻¹⁷

In parallel with the preceding development the same problems were being considered for complex machinery with floating links (e.g. reciprocating engines, printing, textile and agricultural machinery). The "kinetostatic" approach (calculation of the applied forces and reactions associated with an assumed state of the motion with the aid of graphical kinematics) did not seem adequate. Graphically oriented thinking was abandoned to reframe the pertinent problems of kinematics and dynamics in a form better suited to numerical methods of analysis. Since early 1970's much work has been done in the formulation of dynamical equations of motion for mechanisms with rigid links.¹⁸⁻²⁷ Based on these formulations, a number of general purpose computer programs have been developed. But most of these computer programs are limited to analyzing planar machines. The distributed elasticity of the links can be modeled by the introduction of massless elastic springs at selected hinges in References 18-27. Reference can be made²⁸⁻³³ on direct methods for including distributed flexibility.

Researchers in robotics make extensive use of 4x4 transformation matrices of Denavit and Hartenberg.³⁴ These 4x4 transformations may be interpreted as a product of rotation and translation transformation and may be readily used to describe the positions and orientations of coordinate frames in space. Uicker³⁵ presented a derivation of the exact equations of motion for rigid-link spatial mechanical systems, using 4x4 transformation matrices. These results were specifically adapted for open kinematic chains³⁶⁻³⁸, the most common manipulator configuration. Although these early derivations served as a theoretical frame work, the results were too complicated and computations cost prohibitive to be practical. Several simplifications of the basic equations of motion have been made³⁹⁻⁴⁰ to reduce the computation time. The most promising methods, from a computational point of view, are the recursive formulations⁴¹⁻⁴³ presented in the last few years. Some robot formulations include the influence of member flexibility,⁴⁴⁻⁴⁵ and Dubowsky and Gardner³² have also incorporated a model for joint clearance.

Although all three areas of interest deal with the same class of

multi-body systems, the equation formulation and corresponding computer programs from one area are in general of little use in the other areas. Particular care was taken in formulating the equations presented in this paper so that the resulting computer program, TREETOPS, would be useful to all areas of interest that deal with multi-body structures in an open tree topology. Some features of the TREETOPS program are: (1) Any or all bodies can be rigid or deformable, (2) Loop closures are permitted if the constraints are kinetic rather than kinematic, (3) The hinges can have 0 to six degrees of freedom and hinge rotations can be large, (4) The dimension of the problem equals the number of the degrees of freedom (constraint forces do not appear in the formulation), (5) Individual body deformations can be described by any set of modal vectors, (6) An interactive program helps the user set up his problem, (7) Extensive control simulation capability (a full set of sensors and actuators, a linear time invariant control law in block diagram format, a non-linear controller in user supplied subroutine format) is built in the program, (8) Equations can be linearized (via Taylor series expansion) about a nominal state.

The design of TREETOPS is such that the generic formulation does not compromise the computational efficiency of the program. For example, in the case of a planar mechanism the problem is defined by the user with no out of plane degrees of freedom. The computer program, which formulates equations only for the user defined degrees of freedom knows only of the planar motion and will perform no computations for out of plane motion. Computationally, this is an attractive feature of TREETOPS.

This paper consists of four sections. The first section describes the geometry of open tree multibody system. The second section presents the derivation of motion equations via Kane's method. The third section gives a guideline for choosing modal displacement vectors. The fourth section is an overview of the TREETOPS program. An illustrative example is presented.

System Description

A multibody system in a topological tree configuration is shown in Figure 1. Body 1 is arbitrarily selected as the reference body. A non-sequential numbering of the bodies has been deliberately indicated in Figure 1. For convenience, the reference body is assumed to be connected to an imaginary

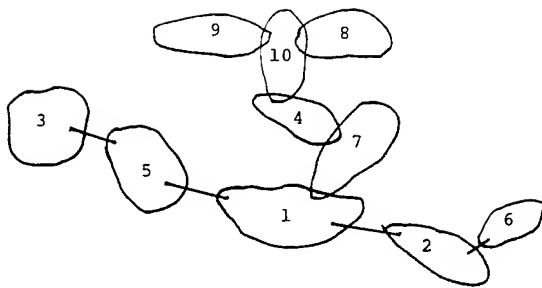


Figure 1. A General Tree Configuration

inertially fixed body numbered 0. Development of an accounting procedure for a unique kinematic description requires the knowledge of a direct path from the inertial frame (body 0) to any body of the system. A direct path array can be constructed as follows. To any body j assign a number $c(j)$ which is the body number of the adjacent body leading inboard to body 0 (or the reference body). In Figure 1, for example, for $j=10$, $c(10)=4$ and for $j=1$, $c(1)=0$. Given j and $c(j)$, one could readily draw Figure 1. Every j has a unique path set whose elements are j , 0, and all the bodies in the path from j to 0. A set $P(j)$ can be constructed from the knowledge of j and $c(j)$ as a set of all the bodies outboard of j including j . Similarly, $E(j)$ can be defined as another set having all the elements of $P(j)$ excluding j .

A hinge, as shown in Figure 2, is defined as a pair of two material points, with a point situated on each of two adjoining bodies. The discrete degrees of freedom of the j th body in the tree are characterized by the relative translations and rotations of two sets of reference axes having origins located respectively at P_j (a point of body $c(j)$ leading to body j) and h_j (a point located in body j). Points P_j and h_j and the reference frames at these

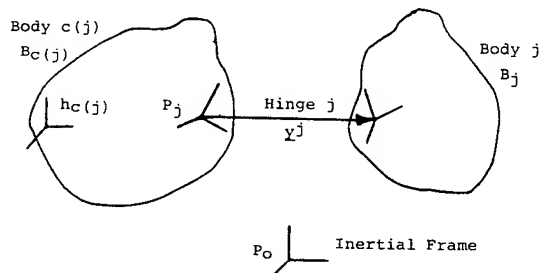


Figure 2. A Typical Hinge

two points constitute the j th hinge. A fictitious hinge is assigned to the reference body by assuming P_0 an inertial point. Thus the number of hinges equals the number of bodies in the system.

Following symbols are used to describe the configuration:

NB = number of bodies

NT_j = translational degrees of freedom of the j th hinge

NR_j = rotational degrees of freedom of the j th hinge

NM_j = deformational degrees of freedom of the j th body

NS = total number of degrees of freedom of the tree

NB

$$\sum_{j=1} (NT_j + NR_j + NM_j)$$

Formulation Methodology

The equations of motion are derived via Kane's method.⁵ This approach is expressed in terms of generalized and "quasi" coordinates (e.g. the scalar components of angular velocity vectors). In a previous paper⁶ this method was employed to derive the equation of motion for structures in a topological chain. In what follows, the approach will be extended to accommodate bodies in a tree configuration.

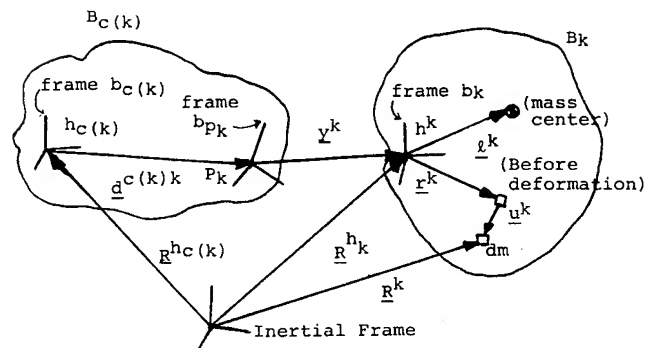


Figure 3 - Geometry of Deformable Body j

Figure 3 shows B_k , the k th body in the tree, in a deformed state. An elemental mass dm of B_k is located inertially by

$$\underline{R}^k = \underline{R}^{hk} + \underline{r}^k + \underline{u}^k \quad (1)$$

where underscore represents a vector quantity, \underline{r}^k is fixed in a reference frame at h_k and \underline{u}^k represents the elastic deformation. A set of NM_k modal vectors ϕ_ℓ^k , $\ell=1, \dots, NM_k$ is chosen to approximately represent the elastic deformation by a finite number of kinematic variables η_ℓ^k (modal coordinates) by

$$\underline{u}^k = \sum_{\ell=1}^{NM_k} \phi_\ell^k (\underline{r}^k) \eta_\ell^k \quad (2)$$

Time differentiation in inertial space provides

$$\dot{\underline{R}}^k = \dot{\underline{R}}^{hk} + \underline{\omega}^k \times (\underline{r}^k + \underline{u}^k) + \underline{\dot{u}}^k \quad (3)$$

where $(\dot{})$ implies time differentiation in the local reference frame (here b_k), and $\underline{\omega}^k$ is the angular velocity vector of the frame b_k . Since the modal vectors in eq. (2) are fixed in frame b_k , the relative deformation velocity is given by

$$\underline{\dot{u}}^k = \sum_{\ell=1}^{NM_k} \phi_{\ell}^k(\underline{r}^k) \dot{\eta}_{\ell}^k \quad (4)$$

Let a set of generalized speeds w_1, \dots, w_{NS} represent the degrees of freedom of the system. Then $\dot{\underline{R}}^k$ can always be written as

$$\dot{\underline{R}}^k = \sum_{p=1}^{NS} \underline{v}_p^k w_p + \underline{v}_t^k \quad (5)$$

where \underline{v}_p^k and \underline{v}_t^k are functions of NS generalized coordinates and time.

From Newton's Law

$$d\underline{f} - \ddot{\underline{R}}^k dm = 0 \quad (6)$$

where $d\underline{f}$ is the force on the differential element and $\ddot{\underline{R}}^k$ is the inertial acceleration of dm .

The equations of motion for the tree structure can be written as

$$\sum_{k=1}^{NB} \int_{B_k} \underline{v}_p^k \cdot (d\underline{f} - \ddot{\underline{R}}^k dm) = 0, p=1, \dots, NS \quad (7)$$

or

$$\sum_{k=1}^{NB} \int_{B_k} \underline{v}_p^k \cdot d\underline{f} - \sum_{k=1}^{NB} \int_{B_k} \underline{v}_p^k \cdot \ddot{\underline{R}}^k dm = 0, p=1, \dots, NS$$

Symbolically, Eq. (7) can be expressed as a system of NS equations given by

$$\underline{f}_p + \underline{f}_p^* = 0, p=1, \dots, NS \quad (8)$$

where \underline{f} and \underline{f}^* are the generalized active and the generalized inertia forces respectively.

Identification of \underline{v}_p^k is made easier by the following definitions.

$$\underline{R}^{hk} = \sum_{p=1}^{NS} \underline{v}_p^{hk} w_p + \underline{v}_t^{hk} \quad (9)$$

$$\underline{\omega}^k = \sum_{p=1}^{NS} \underline{\omega}_p^k w_p + \underline{\omega}_t^k \quad (10)$$

$$\underline{\dot{u}}^k = \sum_{p=1}^{NS} \underline{v}_p^{\eta k} \dot{\eta}_p \quad (11)$$

Substituting the above in eq. (3), one obtains

$$\begin{aligned} \dot{\underline{R}}^k = & \sum_{p=1}^{NS} \underline{v}_p^{hk} w_p + \underline{v}_t^{hk} + \left(\sum_{p=1}^{NS} \underline{\omega}_p^k w_p + \underline{\omega}_t^k \right) \\ & \times \left(\underline{r}^k + \sum_{\ell=1}^{NM_k} \phi_{\ell}^k(\underline{r}^k) \eta_{\ell}^k \right) + \sum_{p=1}^{NS} \underline{v}_p^{\eta k} \dot{\eta}_p \end{aligned} \quad (12)$$

Note that $\underline{v}_p^{\eta k}$ is zero unless the generalized speed w_p corresponds to one of the modal velocities $\dot{\eta}_{\ell}^k$ in body B_k .

Comparison of eqs. (5) and (12) provides

$$\underline{v}_p^k = \underline{v}_p^{hk} + \underline{\omega}_p^k \times \left(\underline{r}^k + \sum_{\ell=1}^{NM_k} \phi_{\ell}^k(\underline{r}^k) \eta_{\ell}^k \right) + \underline{v}_p^{\eta k}$$

and

$$\underline{v}_t^k = \underline{v}_t^{hk} + \underline{\omega}_t^k \times \left(\underline{r}^k + \sum_{\ell=1}^{NM_k} \phi_{\ell}^k(\underline{r}^k) \eta_{\ell}^k \right) \quad (13)$$

Substitution of eq. (13) in the expression for the pth generalized active force yields (after some labor)

$$\underline{f}_p = \sum_{k=1}^{NB} \int_{B_k} \underline{v}_p^k \cdot d\underline{f} \quad (14)$$

$$= \sum_{k=1}^{NB} \left(\underline{M}^{hk} \cdot \underline{\omega}_p^k + \underline{F}^k \cdot \underline{v}_p^{hk} + \int_{B_k} \underline{v}_p^{\eta k} \cdot d\underline{f} \right)$$

Here \underline{M}^{hk} is the moment on B_k with respect to the hinge point h_k of working forces (eliminating non-working constraint forces) and \underline{F}^k is the force on B_k obtained by summing the working forces (eliminating non-working constraint forces).

Similarly, the expression for the pth generalized inertia force is as follows.

$$\begin{aligned} -\underline{f}_p^* = & \sum_{k=1}^{NB} \int_{B_k} \underline{v}_p^k \cdot \ddot{\underline{R}}^k dm \\ = & \sum_{k=1}^{NB} \left\{ m_k (\ddot{\underline{R}}^{hk} + \ddot{\underline{u}}^k) \cdot \underline{v}_p^{hk} + (\dot{\underline{H}}^{hk} + m_k \underline{\dot{u}}^k \times \underline{R}^{hk}) \cdot \underline{\omega}_p^k \right. \\ & + \ddot{\underline{R}}^{hk} \cdot \int_{B_k} \underline{v}_p^{\eta k} dm + \underline{\omega}^k \cdot \int_{B_k} (\underline{r}^k + \underline{u}^k) \times \underline{v}_p^{\eta k} dm \\ & + 2 \underline{\omega}^k \cdot \int_{B_k} \underline{\dot{u}}^k \times \underline{v}_p^{\eta k} dm + \int_{B_k} \underline{\ddot{u}}^k \cdot \underline{v}_p^{\eta k} dm \\ & \left. - \underline{\omega}^k \cdot \underline{D}_p^k \cdot \underline{\omega}^k \right\} \end{aligned} \quad (15)$$

where m_k is the mass of B_k , $\underline{\ell}^k$ locates the mass center of the deformed body B_k with respect to h_k , $(\dot{})$ and $(\ddot{})$ symbolize first and second derivative in the

inertial frame respectively, $(^{00})$ indicates second derivative in the frame b_k (Figure 3), \underline{u}^k is defined by eq. (2), $\underline{\dot{h}}^{hk}$ and \underline{D}_p^k (double underscore implies a dyadic quantity) are defined below.

\underline{H}^{hk} is the angular momentum of B_k with respect to h_k .

$$\underline{H}^{hk} = \int_{B_k} (\underline{r}^k + \underline{u}^k) \times \frac{d}{dt} (\underline{r}^k + \underline{u}^k) dm \quad (16)$$

By forming the time derivative of \underline{H}^{hk} in the inertial frame, we find

$$\begin{aligned} \dot{\underline{H}}^{hk} &= \underline{I}^{hk} \cdot \underline{\dot{\omega}}^k + \underline{\omega}^k \times \underline{I}^{hk} \cdot \underline{\omega}^k + m_k \sum_{\ell=1}^{NM_k} \\ &\left\{ \underline{h}_\ell^k \ddot{\eta}_\ell^k + \left[(\underline{N}_\ell^k + \underline{M}_\ell^k) \cdot \underline{\dot{\omega}}^k \right] \eta_\ell^k + 2 \underline{N}_\ell^k \cdot \underline{\omega}^k \eta_\ell^k + \underline{\omega}^k \times \left[\underline{N}_\ell^k + \underline{M}_\ell^k \right] \cdot \underline{\omega}^k \eta_\ell^k \right\} \\ &+ \int_{B_k} \left[\underline{u}^k \times \underline{\dot{u}}^k + \underline{u}^k \times (\underline{\dot{\omega}}^k \times \underline{u}^k) \right. \\ &\left. + 2 \underline{u}^k \times (\underline{\omega}^k \times \underline{\dot{u}}^k) + \underline{u}^k \times \{ \underline{\omega}^k \times (\underline{\omega}^k \times \underline{u}^k) \} \right] dm \end{aligned} \quad (17)$$

where \underline{I}^{hk} is the inertia dyadic of B_k (undeformed) referred to h_k , \underline{h}_ℓ^k and the dyadic quantities \underline{N}_ℓ^k and \underline{M}_ℓ^k are defined below.

$$\underline{h}_\ell^k = \frac{1}{m_k} \int_{B_k} \underline{r}^k \times \underline{\phi}_\ell^k(\underline{r}^k) dm \quad (18)$$

$$\underline{N}_\ell^k = \frac{1}{m_k} \int_{B_k} \left[(\underline{r}^k \cdot \underline{\phi}_\ell^k(\underline{r}^k)) \underline{U} - \underline{r}^k \underline{\phi}_\ell^k(\underline{r}^k) \right] dm \quad (19)$$

$$\underline{M}_\ell^k = \frac{1}{m_k} \int_{B_k} \left[(\underline{\phi}_\ell^k(\underline{r}^k) \cdot \underline{r}^k) \underline{U} - \underline{\phi}_\ell^k(\underline{r}^k) \underline{r}^k \right] dm \quad (20)$$

where \underline{U} is the unit dyadic. \underline{D}_p^k , appearing in eq. (15), is given as follows.

$$\begin{aligned} \underline{D}_p^k &= \int_{B_k} \left[(\underline{r}^k + \sum_{\ell=1}^{NM_k} \underline{\phi}_\ell^k(\underline{r}^k) \eta_\ell^k) \cdot \underline{v}_p^k \underline{U} \right. \\ &\left. - (\underline{r}^k + \sum_{\ell=1}^{NM_k} \underline{\phi}_\ell^k(\underline{r}^k) \eta_\ell^k) \underline{v}_p^k \right] dm \end{aligned} \quad (21)$$

The mass center of B_k in a deformed state can be expressed by

$$\underline{g}^k = \frac{1}{m_k} \int_{B_k} \left[(\underline{r}^k + \sum_{\ell=1}^{NB_k} \underline{\phi}_\ell^k(\underline{r}^k) \eta_\ell^k) \right] dm \quad (22)$$

Substitution of eqs. (14) and (15) into eq. (8) provides the basic equations of motion for a system of NB flexible bodies.

From Figure (3)

$$\underline{R}^{hk} = \underline{R}^{hc(k)} + \underline{d}^{c(k)k} + \underline{y}^k \quad (23)$$

where

$$\underline{d}^{c(k)k} = \underline{D}^{c(k)k} + \sum_{\ell=1}^{NM_k} \underline{\phi}_\ell^k(p_k) \eta_\ell^k$$

$\underline{D}^{c(k)k}$ is the vector from $h_{c(k)}$ to p_k prior to the deformation of $B_{c(k)}$ and $\underline{\phi}_\ell^k(p_k)$ are the modal displacements (fixed in $b_{c(k)}$ frame) at p_k .

The time derivative of \underline{R}^{hk} in the inertial frame is given by

$$\begin{aligned} \dot{\underline{R}}^{hk} &= \dot{\underline{R}}^{hc(k)} + \sum_{\ell=1}^{NM_k} \underline{\phi}_\ell^k(p_k) \dot{\eta}_\ell^k \\ &+ \underline{\omega}^{c(k)} \times \underline{d}^{c(k)k} + \underline{y}^{ok} \\ &+ \left[\underline{\omega}^{c(k)} + \sum_{\ell=1}^{NM_k} \underline{\phi}_\ell^k(p_k) \dot{\eta}_\ell^k \right] \times \underline{y}^k \end{aligned} \quad (24)$$

where \underline{y}^{ok} is the time differentiation of \underline{y}^k in the frame b_{p_k} located at p_k (Figure 3), $\underline{\omega}^{c(k)}$ is the angular velocity of the frame $b_{c(k)}$ and $\underline{\phi}_\ell^k(p_k)$ are the modal rotations at p_k .

The angular velocity of the frame b_k can be expressed as

$$\underline{\omega}^k = \underline{\omega}^{c(k)} + \sum_{\ell=1}^{NM_k} \underline{\phi}_\ell^k(p_k) \dot{\eta}_\ell^k + \underline{\omega}^{kc(k)} \quad (25)$$

where $\underline{\omega}^{kc(k)}$ is the rotational velocity vector of the frame b_k relative to b_{p_k} . Notice that $\dot{\underline{R}}^{hk}$ and $\underline{\omega}^k$ (and similarly $\dot{\underline{R}}^{hk}$ and $\underline{\dot{\omega}}^k$) have been written in a recursive form. Thus one can express $\dot{\underline{R}}^{hk}$, $\underline{\omega}^k$, $\dot{\underline{R}}^{hk}$ and $\underline{\dot{\omega}}^k$ for $k=1, \dots, NB$ by simply knowing k and $c(k)$.

The following choice of the generalized speeds is made

- $\dot{\theta}_m^k$ for the k th hinge relative rotational velocity $\underline{\omega}^{kc(k)} = \frac{NR_k}{\sum_{m=1}^{NR_k} \dot{\theta}_m^k \underline{e}_m^k}$, where \underline{e}_m^k is a unit vector along the m th gimbal (rotational) axis of the k th hinge.
- \dot{y}_n^{ok} for the k th hinge relative translational velocity $\underline{y}^{ok} = \frac{NT_k}{\sum_{n=1}^{NT_k} \dot{y}_n^{ok} \underline{g}_n^k}$, where \underline{g}_n^k is a unit vector, fixed in b_{p_k} , along the translational degree of freedom of the k th hinge.
- $\dot{\eta}_1^k, \dots, \dot{\eta}_{NM_k}^k$ for the deformation rates of the k th body.

Let p in eqs (14) - (15) correspond to the m th rotational degree of freedom axis of the q th hinge.

$$\begin{aligned} \underline{v}_{-p}^{hj} &= \begin{cases} \underline{l}_m^q \times \underline{x}^{qj} & ; \text{ for } j \in P(q) \\ \underline{0} & ; \text{ otherwise} \end{cases} \\ \underline{l}_{-p}^j &= \begin{cases} \underline{l}_m^q & ; \text{ for } j \in E(q) \\ \underline{0} & ; \text{ otherwise} \end{cases} \end{aligned} \quad (26)$$

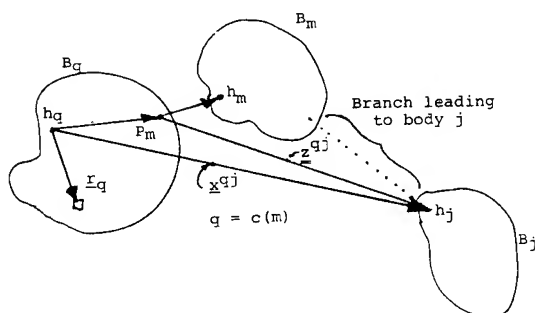
$$\frac{v_p^{nj}}{x_p^{qj}} = \frac{0}{1}$$


Figure 4
Vectors Defining Coefficients of
Generalized Speeds

Let p in eqs. (14)-(15) represent the translational degree of freedom along the n th axis of the q th hinge (along \underline{g}_n^q).

$$\begin{aligned} \underline{v}_p^{hj} &= \begin{cases} \underline{a}_n^q; & \text{for } j \in E(q) \\ \underline{0} & \text{otherwise} \end{cases} \\ \underline{\omega}_p^j &= \underline{0} \\ \underline{v}_p^{nj} &= \underline{0} \end{aligned} \quad (27)$$

Let p in eqs (14)-(15) correspond to the k th modal degree of freedom of the k th body

$$\begin{aligned} \underline{v}_p^{hj} &= \begin{cases} \phi_{\ell}^q(p_m) + \phi_{\ell}^{-q}(p_m) \times \underline{z}^{qj}; & \text{for } j \in P(q) \\ \underline{0}; & \text{otherwise} \end{cases} \\ \underline{\omega}_p^j &= \begin{cases} \phi_{\ell}^{-q}(p_m); & \text{for } j \in P(q) \\ \underline{0}; & \text{otherwise} \end{cases} \\ \underline{v}_p^{nj} &= \begin{cases} \phi_{\ell}^q(\underline{r}^q); & \text{for } j=q \\ 0; & j \neq q \end{cases} \end{aligned} \quad (28)$$

where $\underline{\phi}^q(p_m)$ and $\underline{\phi}^{'q}(p_m)$ are the modal displacements and the modal rotations at p_m (see Figure 4) respectively. $\underline{\phi}_{\ell}^q(r^q)$ represents the modal displacement at a generic point of the q th body. \underline{z}^{qj} is shown in Figure 4.

Eqs. (26)-(28) are the coefficients of generalized speeds identified by p , the kinematical coordinate associated with the tree configuration. When substituted into eqs. (14) and (15) they yield a complete set of equations of motion for the topological tree system.

Choice of Mode Shapes

Any set of modal displacement vectors $\phi_l^k(\underline{r}^k)$ (l th mode of k th body) can be chosen that satisfy the following

$\underline{\phi}_\ell^k(h_k) = \underline{\phi}_\ell^k(h_k) = \underline{0}$ where point h_k is the reference point of the k th body as shown in Figure 3.

For spacecraft application (unrestrained motion of the multibody system) the mode shapes for the reference body (say B_1) might be chosen as the "free-free" modes with h_1 being the mass center of B_1 , and for bodies beyond B_1 one might choose the "fixed-free" modes with translation and rotation at h_k constrained. Alternatively, one might use the "augmented body" concept as defined in Refs. 8, 9 and use the "free-free" modes of the augmented form of B_1 and the

"fixed-free" modes of the remaining augmented bodies. An augmented body, in an open topology, is the body itself augmented at the points of connection to other bodies by particles each having the mass of the set of bodies attached through that connection point. Modal coordinates of augmented bodies may be preferable to those for unaugmented bodies because the former reflect at least in part the influence of the inertial loading of attached bodies. Care must be taken to ensure that the augmented mass elements are not doubly accounted for.

Computer Program (TREETOPS)

The simulation consists of three major parts: (1) a tree topology of flexible structures, (2) a controller, (3) a set of sensors and actuators.

(1) Based on eqs. (14)-(15) the simulation numerically forms the first order differential equations

$$\dot{\underline{x}}_p = M^{-1} \underline{y}_p \quad (29)$$

$$\dot{\underline{z}}_p = \underline{x}_p \quad (30)$$

where \underline{x}_p is the system state vector (dimensioned NS) formed of all the generalized speeds, $\dot{\underline{x}}_p$ and \underline{z}_p are the

first derivative (second derivative of kinematic variables) and integral of the state vector respectively and M is the system "inertia" matrix.

(2) The emphasis of the simulation is on high-fidelity modeling of multi-body structures but the intent of the effort is to build a control system design tool. To this end a set of sensors and actuators are built into the simulation along with a controller specified in a linear, block-diagram format or a user supplied subroutine.

a. Linear, block-diagram controller format. This format is intended to provide a quick, first cut analytical capability. The controller is a multi-input, multioutput system composed of transfer functions and summing junctions with gains included in the interconnections between elements. The block diagram is reduced within the simulation to a set of matrix quadruples A, B, C, D corresponding to the vector form of the control equations

$$\dot{\underline{x}} = \underline{A}\underline{x} + \underline{B}\underline{u} \quad (31)$$

$$\underline{r} = \underline{C}\underline{x} + \underline{D}\underline{u} \quad (32)$$

where \underline{x} , \underline{u} and \underline{r} are the controller state vector, input and output vectors respectively and A, B, C, D are constant coefficient matrices.

When the linear controller is continuous eq. (31) is integrated simultaneously with the structure equations, eqs. (29)-(30). A discrete linear controller may also be defined in which case the discrete equations corresponding to eqs. (31)-(32) are updated only at the sample times.

b. User Supplied Control Subroutine. For more advanced control studies where the user wishes to try optimal, non-linear or time varying controllers then the user may supply his own control subroutine. This is also a multi-input, multi-output system and it offers unrestricted control capability but the burden of software development is on the user. It should be noted that the continuous linear controller, the discrete controller and the user supplied subroutine may all be used simultaneously and interconnected as desired.

(3) A set of seven sensors has been built into the simulation (rate gyro, accelerometer, resolver, angular accelerometer, position and velocity sensors, a tachometer). The user needs only define the type of sensor, its mounting point node and input axis orientation. Likewise a set of four actuators has been defined - reaction jet, hydraulic cylinder, momentum wheel and torque motor. The user can generate disturbance or control forces (torques) on the structure by simply specifying the actuator type, mounting point node, output axis orientation and actuator command input. The user need not be concerned with how the actuator output

forces enter into the \underline{M}^h_j , \underline{F}^j and $d\dot{\underline{f}}$ terms in eq. (14).

The simulation has an option for computing a linear structure model for preliminary controller design using off-line linear analysis tools. In this sense the structure includes the sensors and actuators as shown in Figure (5) because control analysis requires end-to-end transfer functions from actuator inputs to sensor outputs.

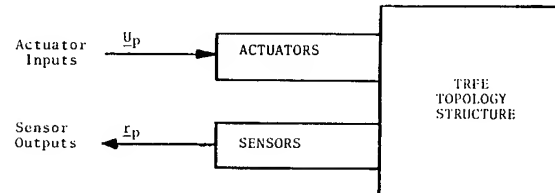


Figure 5
Plant Model For Linear Analysis
(Structures + Sensors + Actuators)

In control terminology the "plant" consists of the structure, sensors and actuators and is described by non-linear differential equations.

$$\dot{\underline{x}}_p = \underline{f}_x(\underline{x}_p, \underline{z}_p, \underline{u}_p) = \underline{M}^{-1} \underline{y}_p \quad (33)$$

$$\dot{\underline{z}}_p = \underline{x}_p \quad (34)$$

$$\underline{r}_p = \underline{f}_r(\underline{x}_p, \underline{z}_p, \underline{u}_p) \quad (35)$$

where \underline{u}_p and \underline{r}_p are the plant input and output vectors and \underline{f}_x and \underline{f}_r are non-linear vector functions.

Linearization is accomplished by expanding eqs. (33), (35) (eq. (34) is already linear) about the nominal operating point $(\underline{x}_{p_0}, \underline{z}_{p_0}, \underline{u}_{p_0})$ and retaining only the first order terms.

$$\delta \dot{\underline{x}}_p = \underline{A}_p \delta \underline{x}_p + \underline{B}_p \delta \underline{z}_p + \underline{C}_p \delta \underline{u}_p \quad (36)$$

$$\delta \underline{r}_p = \underline{D}_p \delta \underline{x}_p + \underline{E}_p \delta \underline{z}_p + \underline{F}_p \delta \underline{u}_p \quad (37)$$

$$\begin{aligned} \underline{A}_p &= \frac{\partial \underline{f}_x}{\partial \underline{x}_p}; \underline{B}_p = \frac{\partial \underline{f}_x}{\partial \underline{z}_p}; \underline{C}_p = \frac{\partial \underline{f}_x}{\partial \underline{u}_p} \\ \underline{D}_p &= \frac{\partial \underline{f}_r}{\partial \underline{x}_p}; \underline{E}_p = \frac{\partial \underline{f}_r}{\partial \underline{z}_p}; \underline{F}_p = \frac{\partial \underline{f}_r}{\partial \underline{u}_p} \end{aligned} \quad (38)$$

where $\underline{A}_p, \underline{B}_p, \underline{C}_p, \underline{D}_p, \underline{E}_p, \underline{F}_p$ are constant coefficient matrices obtained by numerically computing each of the partial derivatives at the nominal operating point. A typical matrix element $(\underline{A}_{p_{ij}} = \partial f_{x_i} / \partial x_{pj})$ is found by computing f_{x_i} at 3 values of x_{pj} ($x_{pj_0}, x_{pj_0} \pm h$) with all other \underline{x}_p elements at their nominal values. A second order Lagrange interpolating polynomial is fitted to these

three points and the partial derivative is the derivative of the interpolating function evaluated at x_{pj_0} .

Software Overview

The TREETOPS software consists of three separate computer programs and a number of files as shown in Figure 6.

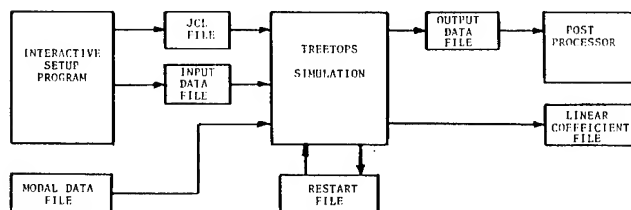


Figure 6. Treetops Software Overview

The motivation for having 3 separate programs is that the set-up program and post-processor run in an interactive mode while the simulation program which requires more execution time is normally run in a batch mode.

The interactive set-up program provides a user-friendly interface with the simulation via the following features:

- The user is prompted for input so that essential elements are not omitted.
- Free format inputs are accepted so a knowledge of data format and column number is not required.
- Editing capability is provided for high level changes (delete or add bodies) and low level changes (change a data value).
- The file structure and JCL (Job Control Language) files are set up automatically so the user doesn't need a high level knowledge of the computer operating system.
- Error checking is performed in the interactive session reducing the possibility that the simulation batch job will bomb-out.

The simulation program is the heart of TREETOPS. It formulates the structure equations and performs numerical integration to obtain the time history response of the system. It also computes and outputs the linear structure model coefficients. A restart file is created at the end of each simulation run so that subsequent runs can be started at that point at a later date.

The post-processor is interactive so that data can be examined and output modified based on simulation results. This makes it possible to obtain all the simulation output but doesn't make it necessary. Since the output data files have a standard format, it is possible to cross plot data from different runs for comparison purposes. By making the post-processor a stand along program it enables the addition of special print or plot capabilities for special simulation cases.

An example test case demonstrated the usefulness of basic capability of the TREETOPS program. For this test case a TREETOPS simulation of the Ku Band antenna mounted in the Space Shuttle orbiter cargo bay is compared to an ad-hoc simulation developed by Rockwell International.⁴⁶ The configuration is illustrated in Figure 7 and was modeled as a four body, 20 mode problem. The antenna dish and electronics assembly were modeled as flexible bodies while the outer gimbal and orbiter were rigid. In this example a control system is used to stabilize the two gimbals so the test validates not only the structure equation generator but also the controller, sensors and actuators. Comparisons included the linearization option and off-line programs to generate Nichols plots which agreed closely with corresponding plots obtained from the ad-hoc simulations. Figure 8 shows an open loop frequency response for the β -gimbal with the α -gimbal loop closed and illustrates the good agreement between the two simulations. Variations at higher frequencies are attributed to differences in mode selection. A key observation of this test is that the three man weeks required to set up and run the TREETOPS simulation was significantly less than that required to build the ad-hoc simulation, excluding data collection which is required for either approach.

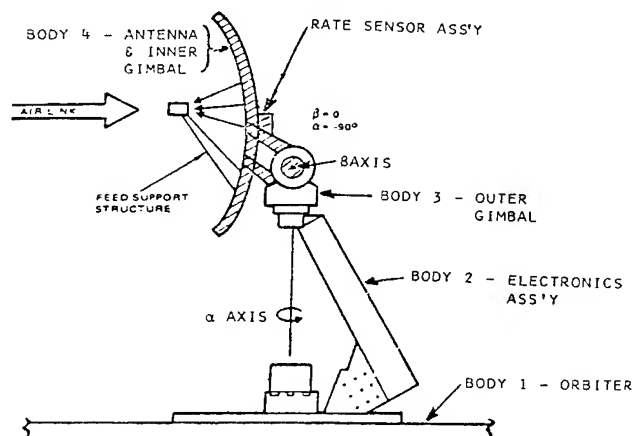


Figure 7
Ku-Band Antenna Test Case

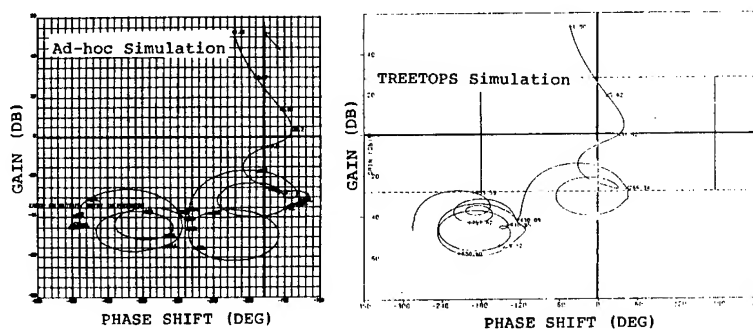


Figure 8
A Comparison of the Frequency Response (Gain vs. Phase Shift) From a Torque Command to a Sensor Output For the Ku-Band Test Case.

TREETOPS is operational at Honeywell and also at Marshall Space Flight Center where it is now being used to study the control problems relating to Instrument Pointing System (IPS), Pinhole-Occulter Experiment and other spacecraft projects.

Summary

An efficient computer-oriented method for formulating equations of motion for large mechanical systems in a topological tree has been presented. It is shown that these equations can be obtained by recursive relations (eqs. (24)-(28)). Non-working constraint forces do not appear in the formulation. The resulting equation set is of minimum dimension. The emphasis of the simulation presented has been on the high-fidelity modeling of the structure with the intent that the simulation be used for control system studies. The dynamic equations have been formulated and programmed in a general sense. Furthermore, the simulation has an easy-to-use, interactive set-up program that creates all the necessary data files. Also included in the simulation are easy-to-use sensor and actuator models.

ACKNOWLEDGEMENT

The computer software mechanization was partially sponsored by NASA, Marshall Space Flight Center. The authors wish to acknowledge the contributions of Dr. Henry Waites, the NASA program sponsor, who has been instrumental in developing the detailed simulation requirements.

References

1. Kane, T. R. and D. A. Levinson, "Formulation of Equations of Motion for complex Spacecraft", J. Guidance and Control, Vol. 3, No. 2, March-April 1980.
2. Likins, P. W., "Analytical dynamics and Non-rigid Spacecraft Simulation", JPL TR 32-1593, July 1974.
3. Likins, P. W., "Point-connected Rigid Bodies in a Topological Tree", Celestial Mechanics II, 1975.
4. Levinson, D. A., "Equations of Motion for Multiple-Rigid Body Systems via Symbolic Manipulation", J. Spacecraft and Rockets, Vol. 14, No. 8, August 1977.
5. Kane, T. R. and C. F. Wang, "On the Derivation of Equations of Motion", J. SIAM, Vol. 13, No. 2, June 1965.
6. Singh, R. P. and P. W. Likins, "Manipulator Interactive Design with Interconnected Flexible Elements", 1983 Automatic Control Conference, San Francisco, CA., June 1983.
7. Paul, B. "Analytical Dynamics of Mechanisms - A Computer Oriented Overview", Mechanism and Machine Theory, Vol. 10, 1975.
8. Hooker, W. W. and G. Margulies, "Dynamical Attitude Equations for an n-Body Satellite", J. Astronaut. Sci. 12, 1965.
9. Roberson, R. E. and J. Wittenburg, "A Dynamical Formalism for an Arbitrary Number of Interconnected Rigid Bodies, with Reference to the Problem of Satellite Attitude Control", Proc. Third Congress IFAC, London 1966.
10. Likins, P. W., "Dynamics and Control of Flexible Space Vehicles", JPL TR 32-1329, 1970.
11. Likins, P. W., "Dynamic Analysis of a System of Hinge-connected Rigid Bodies with Non-rigid Appendages", Int. J. Solids Structures, 9 1973.
12. Ho, J.Y.L., "Direct Path Method for Flexible Multibody Spacecraft Dynamics", J. Spacecraft and Rockets, Vol. 14, Feb. 1977.

13. Roberson, R. E. , " A Form of the Translational Dynamical Equations for Relative Motion in Systems of Many Non-Rigid Bodies", *Acta Mechanica*, Vol. 14, 1972.
14. Bodley, C., A. Devers, A. Park, and H. Frisch, "A Digital Computer Program for Dynamic Interaction and Simulation of Controls and Structures (DISCOS)", NASA Technical Paper 1219, May 1978.
15. Boland, P., J. Samin, and P. Willems, "Stability Analysis of Interconnected Deformable Bodies in a Topological Tree", *AIAA Journal*, Vol. 12, 1974.
16. Boland, P., J. Smain, and P. Willems, "Stability Analysis of Interconnected Deformable Bodies in a Closed-Loop Configuration", *AIAA Journal*, Vol. 13, 1975.
17. Keat, J. E. and J. D. Turner, "Dynamical Equations of Multibody System with application to Space Structure Deployment", CSDL-T-822, The Charles Stark Draper Lab., Inc., Cambridge, MA, May 1983.
18. Chace, M. A. and Y. O. Bayazitoglu, "Development and Application of a Generalized D'Alembert Force for Multifreedom Mechanical Systems", *J. Eng. for Ind.*, Vol. 93, Feb. 1971.
19. Vance, J. M. and A. Sitchin, "Derivation of First-order Difference Equation for Dynamical systems by Direct Application of Hamilton's Principle", *J. App. Mech.* Vol. 37, 1970.
20. Smith, D. A., "Reaction Force Analysis in Generalized Machine System", *J. Eng. for Ind.*, Vol. 95, 1973.
21. Sadler, J. P., "Dynamic Analysis of Mechanisms including Coulomb Friction via Equilibrium Equations", *Proc. Third App. Mech. Conf.*, Oklahoma State Univ., 1973.
22. Dillon, S. R. and H. Hemami, "Automated Equation Generation and Its Application to Problems in Control", *Proc. FQ 15th Joint Automatic Control Conf.*, Austin, Texas, June 1974.
23. Gupta, V. K., "Dynamical Analysis of Multi-Rigid-Body Systems", *J. Eng. for Ind.*, Vol. 96, 1974.
24. Stepanenko, Y. and M. Vukobratovic, "Dynamics of Articulated Open Chain Active Mechanism", *Math. Biosci.* 28 (112), 1976.
25. Vukobratovic, M., "Computer Method for Dynamic Model Construction of Active Articulated Mechanism Using Kinetostatic Approach", *Mechanism and Machine Theory*, Vol. 13, 1978.
26. Haug, E. J., R. A. Wehage and N. C. Barman, "Dynamic Analysis and Design of constrained Mechanical systems", *J. Mechanical Design*, Vol. 103, 1981.
27. Nikravesh, P. E. and I. S. Chung, "Application of Euler Parameters to the Dynamic Analysis of Three-Dimensional Constrained Mechanical Systems", *J. Mechanical Design*, Vol. 104, 1982.
28. Winfrey, R. C. "Elastic Link Mechanism Dynamics", *J. Eng. for Ind.*, Vol. 93, 1971.
29. Erdman, A. G., G. N. Sandor and R. G. Oakberg, "A General Method for Kinetostatic analysis and Synthesis of Mechanisms", *J. Eng. for Ind.*, Vol. 94, 1972.
30. Imam, I., G. N. Sandor and S. N. Kramer, "Deflection and Stress Analysis in High Speed Planar Mechanisms with Elastic Links", *J. Eng. for Ind.*, Vol. 95, 1973.
31. Sadler, J. P. and G. N. Sandor, "A Lumped Parameter Approach to Vibration and Stress Analysis of Elastic Linkages" *J. Eng. for Ind.*, Vol. 95, 1973.
32. Dubowsky, S. and T. N. Gardner, "Design and Analysis of Multi-Link Flexible Mechanisms with Multiple Clearance Connections", *J. Eng. for Ind.*, Vol. 99, 1977.
33. Sunada, W. and S. Dubowsky, "The Application of Finite Element Methods to the Dynamic Analysis of Spatial and Coplanar Linkage Systems", *J. Mechanical Design*, Vol. 103, 1981.
34. Denavit, J. and R. S. Hartenberg, "A Kinematic Notation for Lower-Pair Mechanisms Based on Matrices", *J. App. Mech.*, Vol. 22, June 1955.
35. Uicker, J. J., Jr., "On the Dynamic Analysis of Spatial Linkages Using 4x4 Matrices", Ph.D. Dissertation, Northwestern University, 1965.
36. Kahn, M.E. and B. Roth, "The Near-Minimum Time Control of Open-Loop Articulated Kinematic Chains", *Stanford Artificial Intelligence Memo #106*, Dec. 1969.

37. Woo, L. S. and F. Freudenstein,
"Dynamic Analysis of Mechanisms
Using Screw Coordinates", J. Eng.
for Ind. Vol. 93, Feb. 1971.
38. Yang, A. T., "Inertia Force Analysis
of Spatial Mechanisms", J. Eng. for
Ind., Vol. 93, Feb. 1971.
39. Bejczy, A. K., "Robot Arm Dynamics
and Control", NASA TM 33-669, JPL,
CA, Feb. 1974.
40. Raibert, M. H., "Mechanical Arm Con-
trol Using a State-Space Memory",
Society of Manufacturing Engineers,
Technical Paper MS-77-742, 1977.
41. Paul, R. P., "Advanced Industrial
Robot Control Systems", Purdue Uni-
versity, TR-EE-78-25, West
Lafayette, IN., 1978.
42. Hollerbach, J. M., "A Recursive For-
mulation of Lagrangian Manipulator
Dynamics", Proc. 1980 Joint Automa-
tic Controls Conference, San
Francisco, CA., 1980.
43. Hollerbach, J. M., "A Recursive
Lagrangian Formulation of
Manipulator Dynamics and a Compara-
tive Study of Dynamics Formulation
Complexity", IEEE Trans. Systems,
Man and Cybernetics, Vol. SMC-10,
No. 11, 1980.
44. Book, W. J., "Modeling, Design and
Control of Flexible Manipulator
Arms", Ph.D. Th., MIT, April 1974.
45. Book, W. J., "Recursive Lagrangian
Dynamics of Flexible Manipulator
Arms via Transformation Matrices",
IFAC Symposium on Computer Aided
Design of Multivariable Technologi-
cal Systems, Purdue University, IN,
Sept. 1982.
46. Andrew, L. V. and G. Cortez,
"Results of Stability Analysis of
the KU Band Antenna", Rockwell I.L.
280-304-83-009, 20 May 1983.

REQUIREMENTS AND ISSUES FOR THE CONTROL OF FLEXIBLE SPACE STRUCTURES

J.F. Garibotti*

HR Textron Inc.

2485 McCabe Way, Irvine, CA 92714

Abstract

This paper is a summary of the Final Report of the NASA Space Systems and Technology Advisory Committee's Ad Hoc Subcommittee on Controls/Structures Interaction. The subcommittee was charged on August 2, 1982 with addressing NASA's need for a flight-ready capability for accurate shape control, vibration suppression, and pointing control for future space structures such as antennas and platforms. The subcommittee objectives were to determine where and to what extent this is a problem for NASA, and what controls/structures research and development is required for future NASA missions.

The paper discusses candidate NASA missions that might involve or benefit from Controls/Structure Interaction technology, key technical issues, and on-orbit testing philosophy. The paper concludes with a recommendation for a NASA R&D program.

Background

The technology for controlling the attitude and dynamic deformations of large space structures is one of the key considerations for future space initiatives. The need to assess the state of readiness of this technology and evaluate potential NASA alternative activities to remedy any deficiencies led to the formation of the NASA Space Systems and Technology Advisory Committee (SSTAC) Ad Hoc Subcommittee on Controls/Structures Interaction on August 2, 1982. The subcommittee was charged with addressing NASA's need for a flight-ready capability for accurate shape control, vibration suppression, and pointing control for future flexible space structures including antennas and platforms. The subcommittee objectives were to determine where and to what extent this is a problem for NASA, and what controls/structures research and development is required for future NASA space missions. With this information the subcommittee would assess the existing NASA program and make recommendations.

The subcommittee's formation is one initial step in providing for flight-readiness of this technology for future national space programs. The achievement of this technology is a formidable objective since a number of potentially significant problem areas require resolution before this technology can be considered a proven option for space program applications. The subcommittee report¹ presents findings and recom-

mends a course of action for NASA which is, in the subcommittee's opinion, necessary for establishing a flight-ready technology in a timely manner. This paper is a summary of the subcommittee report and emphasizes those aspects of the report dealing with mission requirements and key technical issues.

In the context of the subcommittee report Controls/Structures Interaction (CSI) technology implies the active suppression of flexible body responses, as distinct from the present practice of control of rigid body motions and avoidance of flexible structure and control interaction.

The members of the Ad Hoc Subcommittee were:

Chairman

J.F. Garibotti, HR Textron Inc.

Materials and Structures - SSTAC

Robert Herzberg, Lockheed Missiles and Space Company

Keto Soosaar, Charles Stark Draper Laboratories, Inc.

Space Electronics - SSTAC

Narendra K. Gupta, Integrated Systems, Inc.

John Keigler, RCA

Space Systems - SSTAC

Bernard Morais, Lockheed Missiles and Space Company

C. Allan Nathan, Grumman Aerospace Corp.

Ex-Officio Members

John Hedgepeth, Astro Research, Chairman Materials and Structures - SSTAC

Raj Reddy, Carnegie Mellon University, Chairman Space Electronics - SSTAC

Charles Bersch, NASA Headquarters Executive Secretary

The subcommittee evaluation of the status of CSI technology was based on a number of comprehensive presentations by NASA, DOD and Industry representatives and extensive committee discussions. A sizable body of data was acquired, and sufficient information was obtained for substantive recommendations. These are discussed in some detail in this paper. The major findings and recommendations of the subcommittee are summarized here for overview purposes.

Summary of Major Findings

1. CSI technology is a significant change

*Director, Space Technology Associate Fellow AIAA

from present spacecraft controls design practice and its application will have substantial impact on future space programs which require this option.

2. A number of important NASA and DOD space initiatives planned for the 1990+ time frame would face serious performance constraints without the CSI technology option.

3. The present rate of development of this technology represents minimal progress towards establishing its flight-readiness, with no predictable flight-ready date.

4. Flight-readiness for this technology will require a coordinated overall development program including analysis and design, ground testing, and on-orbit testing.

Summary of Major Recommendations

1. NASA should aggressively take the lead in developing CSI technology to a state of flight-readiness by initiating a high priority R&D program directed to this purpose. This program should recognize DOD needs and be closely coordinated with DOD technology development activities.

2. CSI technology should be treated as an entity consisting of analysis and design, ground testing, implementation (sensors, actuators, processors, etc.) and on-orbit testing.

3. A very significant improvement in the rate of CSI technology development by NASA can be realized with the present CSI R&D budget, (approximately \$4M for FY 83) by establishing a CSI Program Manager at NASA Headquarters who is responsible for overall direction of CSI technology development and validation.

4. The subcommittee recommended an augmentation, beginning in fiscal year '85 or '86, of \$3M to \$5M per year for four years to the presently planned CSI R&D budget. This augmentation is primarily intended to address the need for an increase in ground and on-orbit testing specifically needed for resolving generic technology issues. This latter activity would specifically include the validation of analytical and ground test simulations.

5. Specific space program initiatives may require on-orbit demonstration(s) or validation of CSI technology applied to particular spacecraft configurations. Such demonstration(s) can aid in developing CSI technology, but should not be considered as an alternative to the testing identified in recommendation (4).

Introduction

One of the more significant design problems for all spacecraft programs is the need to stabilize the vehicle with respect to a desired coordinate system and to point the vehicle and/or its sensors with some

prescribed accuracy relative to this coordinate system. This is accomplished by providing a system of sensors and positioning actuators together with associated electronics which constitute the spacecraft control system. The "associated electronics", loosely stated, interprets the sensor data vis-a-vis the desired attitude and "commands" the actuators to provide the necessary corrections. This requires that an analytical model which defines the relationship between actuation force and vehicle response be incorporated in the control electronics with some degree of precision.

If the vehicle can be considered to be a rigid body for these purposes, the design problem is greatly simplified, since at most only six degrees-of-freedom are needed to describe the system, and only six actuation forces and sensors need be considered. Also, the controller logic is relatively straight-forward, since only a rigid body model is required for the vehicle. An important analytical consequence of this simplification is the ability to treat the actuation forces independently (i.e. they are uncoupled), and to thereby develop single-input, single-output relationships between forces and resultant motions. Such relationships are widely exploited in the design of present spacecraft control systems, and, for example, are the basis for the "gain margin" specifications which are generally used to define acceptable control system performance.

In general, present practice is to specify a minimum structural elastic mode frequency which is well beyond the highest control frequency (i.e. outside the control bandwidth). If this minimum frequency is sufficiently high, the elastic effects at frequencies within the control bandwidth will be small, and any uncertainties regarding such effects can be encompassed by the gain and phase control margins. All present spacecraft control systems are basically designed using this approach, and it has proven adequate as witnessed by successful stabilization and pointing performance of our present space vehicles.

It is clear, however, that this rigid-body approach becomes inadequate when, for whatever reason, it is impractical to design a spacecraft with the necessary separation between the control bandwidth and the lowest elastic mode of the structure. This can be the case when the structural configuration is necessarily very large, or when mission requirements dictate a very fast controls response with an associated relatively high frequency bandwidth. In either case, the control system must take on a quite different form. The control strategy in these cases must consider control of elastic modes as well as the standard rigid body control.

A further complication is encountered in the more flexible satellites where dynamic response caused by rigid-body maneuvers

or on-orbit mechanical sources can result in significant internal misalignments such as defocusing within optical or antenna structures. The control system is then required to reduce the dynamic response to acceptable performance levels.

The analytic approaches for accomplishing the above mentioned control strategies have been developed by a number of investigators over the past years, and may generally be referred to as "flexible-body" control approaches as distinct from traditional "rigid-body" methodology in present use. This new approach is referred to as the CSI approach in the following discussion.

It is important to note the very significant implications of the newer approach as regards our present state-of-the-art spacecraft controls design industrial capabilities. Since more than rigid-body control is required, the number of actuators and sensors must increase accordingly, and the force-motion relationships must reflect elastic as well as rigid effects. As a result, much of the rigid-body controls technology is no longer applicable. For example, single-input, single-output relationships no longer can be used, making the present gain and phase margin concepts inapplicable. Also, since the analytic model of the vehicle must now include both elastic and inertial effects, the accuracy of the structural-elastic models becomes a significant consideration - especially since the controls design requires considerably more accurate modeling of modal characteristics than for the stress and deflection analyses which have been the primary motivation for our present structural modeling capabilities.

CSI technology has considerable recent development history, but, almost exclusively, this has been in a basic research context. No present spacecraft system uses this controls approach, and relatively little work has been done to transition this technology to engineering application. A significant start has been made via the DARPA sponsored ACOSS program, and a number of aerospace firms have Independent and Contract Research and Development studies under way in this area.

Mission Requirements

Large Structure Candidate Missions

As the Ad Hoc Subcommittee reviewed the proposed NASA and DOD spaceflight missions that might involve CSI technology, it was apparent that there are two distinct types of missions under consideration: applications missions (see Figure 1) and generic technology missions. Accomplishment of many of the applications and generic missions depends on the use of as-yet undeveloped or unproven technology for the control of flexible space vehicle structures.

In addition to the applications mis-

sions with their respective scientific or applications goals, there have been several generic CSI technology missions proposed. These generic missions such as MAST and SAFE support the investigation, development, and validation of CSI technology.

A key issue for NASA consideration is whether a) the generic missions should be considered a prerequisite for validation of CSI technology prior to any applications missions, b) the CSI technology can be developed and validated as an element of the applications missions or c) basically generic missions can include an applications objective in order to realize some economy of combining the two mission objectives on one flight. Approach (a) is technically the soundest and most conservative, while (b) has the programmatic appeal of potentially lower agency cost (if the applications missions are necessary and successful). (c) is a compromise, i.e. the middle ground between technical risk and program cost.

The subcommittee recommended that generic on-orbit testing should be used to validate CSI technology and therefore be considered a prerequisite for applications missions. The subcommittee recommended against alternatives that include development and validation of CSI technology as an element of applications missions, or the inclusion of applications objectives in a basically generic mission.

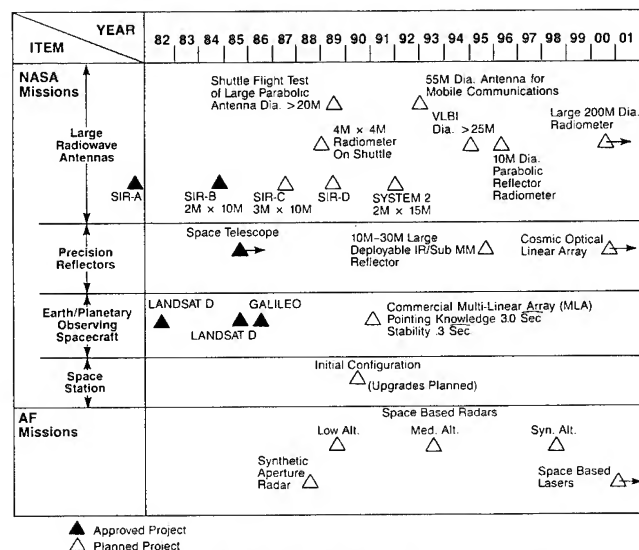


Figure 1 NASA/AF Relevant (Technology) Missions

Status of Control System Requirements

Based on the candidate mission descriptions and the likely evolution of U.S. space initiatives, the subcommittee undertook an evaluation of the significance of CSI technology for space programs in the 1990+ time frame. This evaluation was necessarily limited in scope because of the preliminary nature of most of the defined missions. Determining the level of need

for CSI technology for specific future space programs requires a reasonably complete preliminary design process. A configuration for the satellite must be established, pointing and configuration tolerances or accuracies must be estimated, a preliminary dynamic model developed, disturbances assumed, and the resulting vehicle responses calculated and compared to the tolerances. This establishes the control system requirements.

Using the available information, attempts were made to categorize the candidate missions in terms of whether CSI can be considered enhancing, enabling, or not needed. This was not productive, however, due to the lack of systems studies of sufficient depth to identify the significance of CSI approaches on system performance in comparison with other approaches. A more general evaluation was then undertaken with the objective of evaluating the probable need for CSI technology as a design option for future space programs.

The most obvious consideration in this evaluation is the lowest structural-mode frequency of a candidate mission configuration. For a number of missions of Figure 1 this will clearly be lower than present satellite experience. The need to package large aperture antennas to fit within the STS cargo bay and deploy them on-orbit, for example, leads to flexible configurations and low structural frequencies, much lower than 1 Hz in some cases.

The configuration deformation tolerances, both static and dynamic, are strong control system design drivers for many of the identified missions. For example, for a given disturbance, a large flexible antenna operating at a wavelength of 30 microns will require much more control than one operating at 30 cm. Table 1 lists some of the tolerances that could be inferred from the mission concepts of Figure 1. A review of these tolerances shows that even relatively smaller systems (i.e. 20 meters) could be susceptible to CSI technology needs. If the disturbances are found to be particularly severe, then even smaller systems (i.e. 5 meters) could be of concern.

An examination of Figure 1 and Table 1 suggests therefore that the following systems may require considerable attention to the subject of CSI:

Shuttle Flight Large Antenna
VLBI
Large Diameter Radiometer
Large IR Reflector (LDR)
Cosmic Linear Array
Space Station (Upgrades)

It should be noted that the lack of data to complete Table 1 is indicative of the preliminary nature of the defined missions and, hence, the system requirements.

Mission	Size M	Wavelength λ	Tolerances				Point. Acc. $2\sqrt{D}$ *	Point. Stab.
			Surface $\lambda/50$	Defocus 2λ	Lateral 1λ			
Shuttle Flight Large Antenna	50M Reflector	3 cm	($\lambda/50$) .06 cm	6 cm	3 cm		.12 mR	
Mobile Communication Antenna	55M Reflector	30 cm	($\lambda/25$) 1.2 cm	60 cm	3 cm		1.1 mR	~3 mR
Very Large Baseline Interferometer	50M Reflector	3 cm	($\lambda/30$) .1 cm	6 cm	3 cm		.12 mR	
Radiometer On Shuttle	4M x 4M Planar	21 cm	.42 cm	42 cm	2.1 cm		10.5 mR	
Parabolic Refl. Radiometer	10M Reflector	1.4-18 GHz 21.4-1.7 cm	4-.03 cm	43 cm-3.4 cm	2.1-.17 cm		4-.34 mR	
Large Radiometer	200M Reflector	1.4 GHz 21.4 cm	.43 cm	43 cm	2.1 cm		.2 mR	
SIR B	2.1 x 10.6M Array	1.4 GHz 21.4 cm	.43 cm	43 cm	2.1 cm		4 mR	
SIR C	2.6 x 12M Array	10 GHz 3 cm	.06 cm	6 cm	3 cm		5 mR	
SIR D	4 x 12M Array	40 GHz .8 cm	.016 cm	1.6 cm	.08 cm		.13 mR	
System Z	2 x 15M							
Large IR (LDR)	20M	30 μ	($\lambda/30$) 1 μ	60 μ	3 μ		.3 μ R	
'Cosmic' Array	1.8M Spaced AT 14M	0.4 μ	($\lambda/20$) .02 μ	8 μ	.04 μ		.006 μ R	
Multi-Linear Array								
Space Station								
STEP								
MAST								
SADE								

*D = Antenna Diameter

Table 1 Large Structure Mission Control Requirements

While the above discourse presents a preliminary sifting of the proposed missions, it is incumbent upon NASA to generate further data in this area. It is desirable to develop appropriate normalized parameters which will indicate in a preliminary way the degree of control complexity to be expected. Some of these normalized parameters might include those shown in Table 2,

Pointing Accuracy, Stability	D/λ
Surface Accuracy	$D/(\text{rms Surface})$
Dynamic Susceptibility	$D/(\lambda f_0)$
Disturbance Acceleration	$\frac{T}{I}$

Table 2 Normalized CSI Parameters Indicating Degree of Expected Control Complexity

where D = Antenna Diameter, λ = wavelength, f_0 = fundamental structural frequency, T = torque, and I = moment of inertia.

In summary, the subcommittee finding regarding the future mission requirement or need for CSI technology was that a number of major future NASA and DOD space initiatives would face serious design constraints if CSI is not available as a controls option. Of the 17 missions listed in Figure 1, half were identified as having a strong potential for CSI application, and others may benefit substantially from this approach. A similar study of the USAF Military Space Systems Technology Model (MSSTM) indicated CSI as important for 15 of the 27 Air Force mission concepts.

In order to determine more specifically the nature of the CSI problem for the various missions, it was recommended that NASA perform preliminary systems studies on these missions to obtain better quantified mission-related requirements down to the control system level. Ideally this should progress to tolerances and open-loop

behavior estimates. The development of normalized parametric measures and their application would be a major contribution, and this was recommended. This latter is illustrated in Table 3.

Mission	D/A	f_0 (Hz)	$\frac{D}{f_0 K_A}$ ($f_0 K_A$)	Estimated Control Magnitude**	Disturbances
Shuttle Flight Large Antenna	1667	.029	5.75×10^4	~ 10	Shuttle
Mobile Communication Antenna	183	.087	2.10×10^5	~ 1	
Very Large Baseline Interferometer	1667	.056	2.98×10^4	~ 5	Shuttle
Radiometer On Shuttle	(D=4) 19				Shuttle
Parabolic Refl. Radiometer	47-588	1.5	31-392		60 RPM Spin
Large Radiometer	935	.04	2.34×10^5	~ 200	
SIR B	(D=10.6) 49.5				
SIR C	(D=12M) 400				
SIR D	(D=12M) 1500				
System Z					
Large IR (LDR)	6.7×10^5	3.7	1.81×10^5	~ 150	2 Hz Chop Slew
'Cosmic' Array	3.5×10^7	4.5	7.78×10^6	$\sim 10^3$	
Multi-Linear Array					
Space Station					
STEP					
MAST					
SADE					

Table 3 Large Structure Mission Control Requirements

Key Technical Issues

It is clear that the CSI control problem discussed here is many times more complex than the control problem experienced in previous generations of satellites. In general the control system must be able to provide two or three orders of magnitude of vibration alteration beyond what is obtained through natural damping. To do so, it may be necessary to have as many as 100 flexible modes in the control bandwidth, although only some of these will be excited by the disturbances, and fewer yet will contribute to the control cost function.

Three major control functions may need to be addressed when using the CSI approach. The classical attitude and pointing control will be needed to stabilize the satellite in rigid body coordinates while minimizing the effect of many flexible modes that are excited. Vibration attenuation control will be necessary in the absence of flexible body response in instances such as the dynamic defocus of flexible optics or antennas. Finally the flexible surfaces of optics and antennas will be excited by dynamic disturbances and will require appropriate corrections to maintain the wave-front quality. Mathematically these problems are similar, if not identical, but their major impact will occur in sensor, actuator, and avionics considerations.

A major consideration is associated with the performance wavelength of optical and RF systems. One group of missions will be associated with large antennas (>50m) and long wavelength (>5cm) while the other group involves smaller reflectors (<20m) and very short wavelengths (<30 μ). The resolution of sensors and actuators will define completely separate components technologies. Ground testing of the large antennas may be difficult due to atmospheric, gravity, and size effects, while the control of structures at micron levels re-

quires the extrapolation of elastic and damping properties to extremely small motions.

The theoretical foundations of CSI, and some of the analytical methodology is well developed, and has been reasonably well absorbed by the aerospace industry. As previously noted, however, current missions have not required its application, and the analysis/design tools and the experience base (i.e., ground and flight testing) are lagging. It would be very difficult, if not impossible, to develop a meaningful specification for a control system involving CSI at the present time. The technology requiring resolution in order to remedy this situation is complex but it useful to identify some of the major subelements of this technology as a framework for establishing specific technology development objectives.

The following list, while not all inclusive, summarizes key technical issues requiring attention in CSI technology development:

- 1) Analytic modeling and model reduction
- 2) Structural concepts
- 3) System identification
- 4) Control law design methodology
- 5) Robustness criteria
- 6) Sensor and actuator development
- 7) Digital implementation technology
- 8) Synthesis and design software tools
- 9) Ground testing
- 10) On-orbit testing
- 11) Reliability issues (fault-tolerance)

The subcommittee strongly recommends an organized program that identifies key technical issues, e.g. Analytical Modeling and Model Reduction, as the framework for establishing and implementing a technical development plan for CSI.

Technical readiness levels should be established for the key issues. The key technical issues discussed in this paper are very similar to those for DOD and as a result would enable NASA to support DOD as well, with or without additional funding.

The following paragraphs present brief discussions of each of these subelements of CSI technology together with an evaluation of their status with respect to flight readiness.

Key Issues

1) Analytical Modeling and Model Reduction

The CSI problem could be mathematically defined as the effect of a distributed multi-input, multi-output control system on a continuous structure. At present, the continuous structure is replaced by its finite element model, and then the modal representation is obtainable which allows the analyst to neglect those modes that no longer appear of interest. The model reduction, or truncation process needs to be

performed to limit the size of the controls design problem, as well as to fit the controller inside the flight computer. The means whereby this reduction is made is a very crucial step since the criteria are not always obvious, depending very much on the controls methodology chosen. If energy should spill over from the controlled modes to the uncontrolled ones, and the latter have been truncated, it is entirely possible that instability will not be observed analytically but will be experienced in flight. Development of appropriate reduction criteria and techniques is therefore a crucial area in CSI technology and is far from mature.

Independent of the model reduction process, the quality of the structural model, too, requires close attention. Since the fiftieth mode may require control, it and many higher ones need to be determined with fidelity appropriate to the robustness of the controller. It is clear that the accuracy of the model extraction process, or its experimental relative--the systems identification process--needs to be extended to deal with these requirements.

Of the physical parameters of the structure, the damping may be most difficult to model. Since many of the controls approaches need to know the damping properties with some precision, CSI will lead to requirements for improved measurement and characterization of damping phenomena.

Quick turnaround design evaluation tools, including structural modeling programs, are needed in order to rapidly determine, for example, the effect of structural or material changes on the control design and on the ensuing system performance.

The final key element of the analytical model is the interaction between the rigid and flexible dynamic behavior. Large angle maneuvers, hinged-linked structural assemblies, and on-board rotors that cause gyroscopic coupling of the modes, alter the original models considerably and need to be taken into account. The present DISCOS program developed by NASA is very useful here but needs to be brought up to date and made more user friendly.

2) Structural Concepts

Controlling a flexible structure generally involves minimizing the deviation of the structure from some desired shape or position. This minimization should be achieved by not only varying the control parameters but the structural parameters, i.e., the structural design. As a result development of new structural concepts should be pursued that recognize the goal of an optimal control system design, in addition to conventional goals such as light weight, efficient packaging, and reliable and predictable deployment. A development of importance here would be a procedure for "designing in" passive damp-

ing in an efficient manner.

3) Systems Identification

While the technology of satellite structural and dynamic modeling has progressed immensely since the early days of space activities, the demands of the CSI problem have probably outstripped this capability. In order to achieve the high controls performance levels expected in the CSI problem, the controlled "plant" needs to be characterized with great accuracy. This puts great demand on the eigenvalue analyzers currently available since it may be necessary to determine the fiftieth mode of a structure with some fidelity. It is expected, further, that the physical parameters of the satellite structure will change with orbital position (e.g., solar panels) and with time (e.g., depletion of attitude gas). Non-linear phenomena and idealized damping characterization become yet further error sources.

A suggested approach is systems identification, where the structural and dynamic characteristics are inferred from observed response to known disturbances. The control system can also be part of the system to be characterized, and it is likely that the control sensors, actuators and processor will be used for the identification process.

Like many of the topics under consideration here, identification has been studied by the community in the area of satellites. Whether the state of the art is sufficient remains problematical. Reliable identification accuracy requirements based on robustness considerations remain yet to be developed for the general case, and it is not clear just how many modes can be identified with sufficient accuracy. Substantial work needs to be done in this area.

4) Control Law Design Methodology

A large body of theoretical knowledge has been generated in the past few years dealing with the control of structures. Much of this has remained academic with few attempts to reduce to practice, so that the methodology is mainly untempered by physical experience.

A major area of utmost interest where only few contributions exist is the trade-off between control authority, parameter uncertainty, and robustness. With increasing parameter uncertainty, the robustness can be shown to decrease rapidly, thus the control authority that can be applied decreases rapidly as well. In the limit, where little is known of the structure to be controlled, the controller must simulate natural damping to remain stable. It is recommended that work in Control Law Design methodology be encouraged in order to provide a unified conceptual and theoretical architecture for the CSI design methodology.

5) Robustness Criteria

The engineering approach to producing a

spacecraft system with a high level of flight confidence is based on the concept of demonstrable performance margins. In the case of control systems, typical margin measures are "gain" and "phase" margins. As previously discussed, these concepts are largely unusable for CSI designs, and some new methods are required. This subject is generally referred to as the need for a "robustness" criteria, and several possibilities have been developed. They have not been tested against realistic cases, however, and no attempts have been seriously made to establish numeric measures that could be used as a specification basis. This area could be a serious problem, since the degree of configuration dependency of the various approaches is unknown, and could be substantial.

Progress in this area is highly dependent on establishing a methodical experimental program which would include a number of different test article configurations that are representative of the range of potential future spacecraft configurations. Also, the probable variability of structural and control elements within a specific configuration would have to be addressed in the testing program. This experimental confirmation of the criteria defining the range of acceptable performance of CSI control system designs would be a major step towards establishing the flight readiness of CSI controls systems technology.

6) Sensor and Actuator Development

It is generally accepted that CSI control systems will require new types of control sensors and actuators. The actuators will have to provide precise response at very low force levels and will, in some applications, need to be compact and light weight. The increased bandwidth and stringent performance requirements associated with most CSI applications will require new types of structural response sensors. This is especially the case for those applications utilizing figure control (i.e., contour control of large antennas). Only very preliminary work has been done to date in this area - mostly because of the lack of a specific application need. However, conceptual developments and, in some cases, bread-board models have been achieved. The most significant present problem appears to be providing adequate sensor and actuator systems for the various experimental programs.

7) Digital Implementation Technology

Since any significant application of CSI technology to future space systems will surely require digital implementation and, most likely, some form of distributed processing approach, the status of on-board computation technology is a consideration when assessing CSI readiness for future space missions. The increased number of sensors and actuators together with the need for in-flight characterization and

relatively complex near real-time matrix calculations create a substantial computational requirement. Present flight computers are not, in general, usable for these applications, and new systems will be needed. However, given the tremendous development pace of microprocessor technology, which is being driven by various technical and mission needs, it is likely that adequate digital devices will be available when the CSI needs materialize. Here again, the immediate need is in the experimental area, since commercially available test electronics that are affordable for test programs are often inadequate for CSI experiments. The availability of laboratory microprocessor equipment specially designed for this purpose (and at reasonable cost) would substantially improve the timeliness and usefulness of important ground test programs.

8) Synthesis and Design Software Tools

The engineering process for designing a spacecraft controls system requires the use of a variety of computer programs which must be efficient, reliable, and generally usable by the aerospace industry's engineering groups. Since CSI technology differs from present approaches, new software tools are needed. Several important and useful computer programs are available for these purposes and most companies have some or all of these included as part of their computational capabilities. In general, the computational tools needed for control systems design purposes fall into the following categories:

- 1) Model construction programs
- 2) Control system synthesis tools
- 3) Stability analysis tools
- 4) Performance evaluation programs

Since the development and improvement of such tools is an ongoing process in the aerospace industry, it is reasonable to expect that adequate progress will be made in this area and it will not require substantial NASA attention. Category (2) may need some attention when design studies become widespread, and category (4) may pose difficulties due to the increased size and complexity of the system models used for CSI approaches, but this is not considered a major problem for CSI readiness.

9) Ground Testing

The need for test programs to evaluate and demonstrate CSI technology has resulted in a number of projects, many of which are presently under way in NASA and aerospace company laboratories. The summary report of Strunce and Carman² presents a comprehensive annotated list of these projects. It includes fourteen projects undertaken at seven NASA and aerospace industry laboratories. An evaluation of these programs indicates the absence of overall coordination. As a result, although the total activity level is significant, the disper-

sion of the effect to a number of relatively small projects makes progress difficult and the overall value of the current CSI ground test program questionable. Specific objectives of the activities, are in most cases not clear, and it is difficult to identify their individual contributions to the enhancement of CSI technology. Also, with few exceptions, the tests have been restricted to fairly simple configurations such as plates and beams. While these have the advantage of being analytically tractable, such testing cannot provide the needed confirmation of CSI technology and its applicability to realistic spacecraft structural configurations. At best these tests represent proof of principle tests with little or no traceability to real flight systems.

Since experimental confirmation of the assumptions inherent in the CSI technology is critically important to establishing its readiness for space program applications, this area requires first priority attention. A second issue which must also be addressed is the eventual need for developing valid and effective ground test procedures which can be used as part of the qualification/acceptance test sequences which are ultimately required for any space program that will use CSI control strategies. Most likely, some form of on-orbit test/demonstration segment will be needed for such programs, at least for initial applications. The need for on-orbit testing for qualification of a space structure should, however, be eliminated by proper validation of analytical and ground test techniques. This validation should be a major objective of NASA's CSI technology program and will involve on-orbit testing. It should be noted that qualification/acceptance via on-orbit test has not been used for current space programs.

Valid real time closed loop hardware/software test beds as well as extensive simulation tools should be developed as part of any ground test procedure. The ground test segment objectives would be to demonstrate adequate margins before proceeding to any required flight test segment. The development of effective methods for performing this coordinated ground/flight qualification sequence, if it is required, should be one of the objectives of the CSI ground test program.

10) On-orbit Testing

There is little doubt that the differences between CSI controls designs and conventional approaches and the inevitable uncertainties in extrapolating ground test results to on-orbit environments will make on-orbit testing a prerequisite to space program applications. Such tests are a logical part of a CSI technology readiness program and are the most critical consideration when planning activities in this area. Due to the importance of this subject, it is discussed as a separate case in

the following section of this paper. In the context of the overall CSI discussion, however, it is important to recognize the role of on-orbit testing as part of the complete CSI technology development and validation sequences. Close coordination of all elements of a CSI technology development program will be needed if the flight program is to be a success.

11) Reliability

The implementation of CSI control systems to flight articles will require significant attention to reliability and fault-tolerance. Large numbers of highly distributed sensors, actuators and perhaps even processors need to be networked together to obtain the desired performance from a satellite. The fact that the space systems requiring this control will be costly will place stringent demands on system confidence. Such systems will also have long-life specifications and, in the case of national defense systems, have some form of survivability requirements. Fortunately, a large amount of theoretical and applied work has been performed in the fault-tolerant technology area, and the application to the CSI problem is not expected to be unusually difficult. Since reliability issues may become significant to the users of these systems, this area will require some attention in an overall CSI readiness initiative.

On-orbit Testing

Due to the importance of on-orbit testing in the demonstration of the CSI technology readiness, this issue received major attention during the subcommittee deliberations. As pointed out earlier, successful on-orbit tests are pivotal to demonstrating the acceptability of this technology for future space program applications. They are the logical centerpiece for a CSI technology development initiative, and they will surely be the most expensive element of such a program. The following paragraphs discuss the orbital test issue in the context of the general question of CSI technology development and validation, and present constructive observations and recommendations relative to this important area. It is clear that all on-orbit tests should be a means to an end, rather than the end itself, i.e. a means to achieve a flight-ready CSI technology.

On-orbit Testing Objectives

The basic objectives of a flight test program for CSI technology should be carefully considered. Figure 2 displays the relationship between developing analytical tools and ground test procedures, and on-orbit tests using the shuttle. A flight demonstration is indicated to complete validation of CSI technology. This figure shows the interactive loops that are necessary to develop and validate the technology. The results of the ground and on-orbit tests will be necessary to support

the development and validation of the analysis tools just as the on-orbit test results will modify and validate the procedures used in the ground tests. On-orbit testing will also reveal unknown or unexpected interactions. The conclusions of the activity shown are a) the provision of the necessary analytical tools and ground test procedures to support the trade analyses necessary to assess the cost and risk of applying the CSI technology to a program specific application, and b) the ability to implement the technology as required.

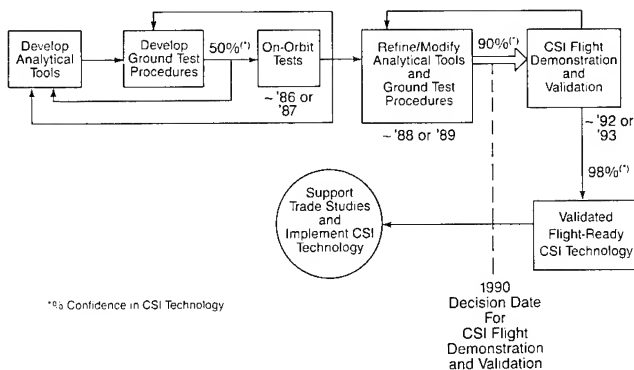


Figure 2 On-Orbit Testing

The shuttle provides a convenient means of performing these on-orbit tests and provides the capability of near real time adjustment of testing objectives based on the results of the flight. The shuttle also provides a test bed for performing scaling experiments related to CSI technology. With proper instrumentation and thorough analysis, scaled testing may be an effective way of performing a flight demonstration, for specific applications.

The purpose of the flight demonstration of Figure 2 is to validate that the technology is ready to support design application and not to develop the technology. This demonstration should not be undertaken until there is very high confidence that it will be unconditionally successful. The flight demonstration is to provide proof to program managers that the technology is understood, that the tools are available and that there is a series of ground tests that allow for the qualification of a system that has used the CSI technology.

The subcommittee advised against combining the CSI technology demonstration with experiments of another technology. There is too much risk in developing the generic CSI technology to have the demonstration clouded by unforeseen results of experimentation.

Recommended NASA R&D Program

The summaries of NASA technology development programs relating to CSI which were presented to the subcommittee showed

substantial attention being given to this area and a high level of awareness of the need for advances in most of the critical areas of technical deficiency. While accurate figures on the level of present and planned NASA expenditures on tasks that are directly supportive of CSI technology were difficult to obtain, it appears that the 1983 OAST Program included approximately \$4M in this area, with some increase planned for the next year. This represents a considerable amount of emphasis.

A major CSI technology initiative is required which includes scheduled, coordinated activity involving on-orbit testing and which leads to a convincing flight demonstration. In view of NASA's space technology development role, it would be both appropriate and effective for NASA to undertake such an initiative. The following presents subcommittee recommendations for and R&D program which would support such an initiative. As a focus for the recommendations, a date of 1990 was assumed, at which time a decision would be made for a flight demonstration and validation test (see Figure 2).

As an approach, the overall CSI program can be considered in terms of the following major segments:

- 1) Analysis and design studies
- 2) Ground testing
- 3) Implementation developments
- 4) On-orbit testing
- 5) Flight demonstration and validation

Table 4 suggests a segment of a CSI R&D program consisting of coordinated activities with defined objectives which is based on current expenditure levels including NASA personnel. Although on-orbit tests and flight demonstration and validation are recognized as necessary elements of an overall CSI development program, such activities are not included in Table 4 due to the fact that they cannot adequately be funded with current expenditure levels. In order to more completely address the program needs identified in previous sections of this report, an augmentation of the R&D program beginning in FY 85 or FY 86 of \$3M to \$5M per year for four years, is needed.

	'84		'85		'86		'87		'88		'89		'90		Total (Man-Yrs)
I. Analysis and Design Studies	32	32	32	30	28	28	22	24	19	15	9	7	7	7	146
Methodology R&D		3					2								
Modeling Studies		7					6					2			
System Characterization		8				9	3						1		
Robustness Criteria		9				7			2						
Design Studies		5			4			6					2		
II. Testing Program	24	24	30	30	33	33	24	22	16	16	12	12	12	12	150
Theory Verification		10				8		4				2			
System Level Eval		6			10						5				
Qual./Accept. Proc. Dev.		3				8			6			4			
Readiness Demonstration		5			7			2			1				
III. Implementation	5	5	13	15	20	20	23	23	21	21	9	9	8	8	100
Sensor/Actuator Dev		2			4			7				3			
On-Board Dig. Processing		1				6							3		
Test Facility Dev				5				4							
Reliability		1		5				6					2		
IV. On-Orbit Tests, Flight Demonstration & Validation															
Planning															
System Design															
Fabrication															
Ground Testing															
Flight & Evaluation															
Totals (Man-Years)	61		75		81		69		54		29		27		396
Man-Years of Effort															

*Man Years of Effort

Table 4 Representative CSI Development Schedule

It is important to note that the subcommittee strongly felt that structures technology and controls technology must both contribute equally to the development and validation of CSI technology.

References

1. NASA Space Systems and Technology Advisory Committee Ad Hoc Subcommittee on Controls/Structures Interaction, "Final Report," June 8, 1983.
2. R.R. Strunce and R.W. Carman, "Active Control of Space Structures (ACOSS), A Status Report," The Charles Stark Draper Laboratory, Inc. Report CSDL-P-1707, February, 1983.

Robert R. Strunce, Jr.
General Research Corporation
McLean, Virginia 22102

Richard W. Carman
Rome Air Development Center
Griffiss Air Force Base, New York 13441

Abstract

The Active Control Of Space Structures (ACOSS) is one of the key enabling technologies for future Large Space Structures (LSS). This paper presents a summary status of the ACOSS technology as well as the relevant technologies necessary for implementation: algorithm sizing, avionics data processing, sensors, actuators, fault tolerant considerations, relevant LSS experiments and LSS vacuum chambers. The reference list included at the end of the paper provides a comprehensive overview of the ACOSS program.

Introduction

During the Apollo era, the control designers became increasingly aware of the flight-control system dynamic interaction with complex vehicle motion.¹⁻⁴ With the advent of large space structures⁵⁻⁸ and increasing demands on precision pointing and control, active control of flexible space structures¹⁰⁻¹⁴ will be necessary in order to satisfy stringent performance goals.

Historically structures for optical systems have been massive, stiff, heavily damped and isolated from sources of vibration (noise). These structures are monolithic and dedicated to maintaining the optical elements in proper alignment. The NASA Space Telescope represents the current state-of-the-art (SOA) in space structures for large optical systems and has many of the above characteristics. Future systems will require Large Space Structures (LSS) that can be deployed from NASA's Space Shuttle. LSSs inherently have characteristics which make them unsatisfactory for use as optical systems structures. They are lightly damped, have lumped masses interconnected by slender structural members, use many joints and hinges and have many low frequency modes of vibration. The problem can be better understood by looking at some proposed future space systems.

Typical large precision systems of the future are: (1) High Altitude Large Optics (HALO) is a passive surveillance system; (2) High Energy Large Optics (HELO) is a laser weapon system; (3) MM Wave Radiometer is a passive surveillance system. Each of these systems has three characteristics in common: large size, low stiffness, and very stringent structural and performance tolerances. The result is a generic problem (as shown in Fig. 1) where mechanical disturbances can create structural vibration and deformation that results in line-of-sight (LOS) error, wavefront error (WE) and figure distortion that translates into overall reduced system performance. The degree of per-

formance degradation depends upon the particular system and the particular disturbances.

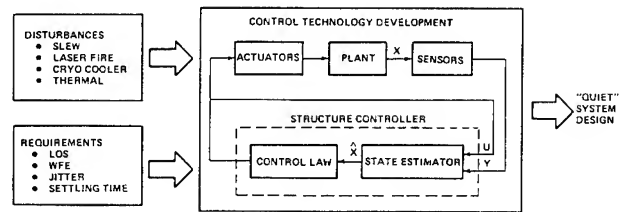


Figure 1. Generic Problem

Reference 15 addressed the issue of passive and active suppression of vibration response in precision structures from a structural point of view. The results of this 1977 state-of-the-art assessment showed that the 1-3% achievable damping was insufficient for 1990 requirements. It is this study which motivated the DARPA ACOSS program. The objectives of the ACOSS program are threefold:

1. Develop a unified technology base in structural dynamics and control for large precision space structures
2. Demonstrate the applications of this technology through analysis and simulations
3. Verify this technology through ground-based proof-of-concept experiments

For successful control of large space structures, it is recognized by the control community that the fundamental problem is the design of a finite-dimensional compensator to control an infinite dimensional system. The LSS control technology issues are:

1. Modeling Accuracy--LSS modeling inaccuracies will limit achievable control system performance. The more stringent the mission performance requirements, the greater the LSS model fidelity required. These modeling errors are grouped into three categories:
 - a. LSS Structural/Dynamic Models. These errors may be introduced through initially assumed structural properties or the truncation process implicit in the finite-element method. In space, LSS parameters may vary as a function of thermal gradients, configuration changes, or depletion of consumables.

- b. Environmental Models. These models must be investigated and verified by appropriate experiments. Accurate knowledge of the external forces (e.g., earth magnetic and gravitational fields, solar wind and radiation pressure, and drag) acting upon an LSS may be necessary to satisfy precision control requirements.
 - c. Disturbance Models. Internal/external disturbance phenomenon must be understood and sufficient models developed. The achievable control system performance will be a function of disturbance model fidelity.
2. System Identification. LSS structural model verifications will be accomplished through system identification. Identification techniques must be developed to determine structural parameters, modal frequencies, damping ratios, and mode shapes. Such methods could be used to determine environmental and disturbance models. Consideration must be given to the type of sensors, onboard processing requirements, data reduction, and post-processing requirements.
 3. Control Law Design Methodology. The control law design approach will be a function of the structural/dynamic models, disturbance models, and mission performance requirements. The design methodology must address the following:
 - a. The model reduction process which reduces the high dimensional finite-element model to a tractable (lower order) design model.
 - b. Reduced-order compensator design methods need to be developed which ensure overall closed-loop system stability. These methods must address the direct digital design problem.
 - c. Implementation of these control laws will require analog/digital mechanizations which must consider centralized vs. decentralized processing, sensor/actuator configuration, fault-tolerant systems, redundancy management and reconfiguration.
 4. Sensors and Actuators. Techniques will be required to determine sensor/actuator placement as a function of the control objectives. The type of sensor/actuator must be determined which meets the necessary performance specification. The dynamic characteristics of these devices will be essential for evaluation of controller closed-loop stability and robustness.
 5. Avionics. The high computational needs and sensor/actuator data rates will require development of advanced system architecture and integration in order to meet the 1990 type requirements. Fault detection, isolation, and reconfiguration

must be an integral part of this development.

ACOSS Program Summary

Precision pointing and control trends⁹ through the year 2000 will require pointing accuracies ranging from 10 arcsec down to 0.1 arcsec with corresponding stability requirements ranging from 1 arcsec down to 0.001 arcsec. These stringent requirements and the large space structure (LSS) characteristics (closely packed, lightly damped, low frequency modes) have motivated a plethora of research in active control of space structures (ACOSS).¹¹⁻¹⁴ A hierarchy of vibration suppression methods (Fig. 2) is a function of the LSS characteristics, performance requirements, and disturbance characteristics. Naturally, structural response minimization methods such as tuning, stiffening, and material damping should receive first consideration.

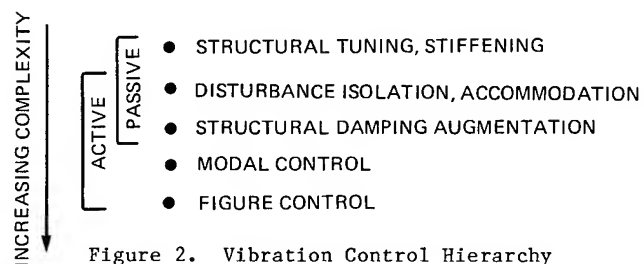


Figure 2. Vibration Control Hierarchy

The ACOSS program products are¹⁶⁻³⁵

1. Control theory
2. Structural models^{19,36,37}
 - Tetrahedron (ACOSS Model #1)
 - ACOSS Model #2, #3
3. Analytical verifications
4. Laboratory demonstrations
 - Plate experiment
 - POC experiment
5. Hardware
 - Pivoted proof mass actuator
 - Microphase multichannel sensor
6. Flight-test plan

Figure 3 presents a summary of the ACOSS program with respect to control theory, control design and analysis, and experiments.

Slewing Maneuvers

The subject of spacecraft slewing maneuvers has received the attention of many authors. A summary of the recent work in slewing maneuvers for flexible spacecraft is presented in Fig. 4. The work to date encompasses many important subjects including: (1) linear/nonlinear open-loop methods, (2) distributed control, (3) on-off thruster control, (4) feedback control, and (5)

Company	Control Theory	Control Design & Analysis	Experiments
Convair	Model Error Sensitivity Suppression (MESS)	MESS Disturbance Accommodation	Flyswatter Plate (IR&D)
Draper	Reduced-Order Modeling Reduced-Order Controller Output Feedback Sensor/Actuator Placement Optimal Slewing Maneuvers High Resolution System Identification	Structural Damping Augmentation (SDA) Modern Modal Control (MMC) SDA/MMC Actuator Synthesis Disturbance Rejection Sensor/Actuator Placement Optimal Slewing Maneuvers High Resolution System Identification	Beam (IR&D)
Honeywell	System Identification	Singular Values	
Hughes	Electronic Damping	Electronic Damping	Hollow Cylinder
Lockheed	Low Authority Control (LAC) High Authority Control (HAC) Modal Cost Analysis (MCA)	LAC, HAC LAC/HAC Frequency Shaping System Identification	Mini-Beam Maxi-Beam Vertical Pipe Circular Plate Wheel (frame) Toysat POC
TRW	Stability Ensuring Methodology System Identification Adaptive Control	Stability Ensuring Methodology System Identification	Plate (IR&D)

Figure 3. ACOSS Program Summary

Subject	Turner & Chen	Turner & Junkins	Breakwell	Forrenkopt	Swigert	Vander Velde & He	Longman & Alfriend	Markley	Lassen & Elliot
Rigid +1-Flexi-Mode Plant	✓	✓	✓	✓	✓	✓	✓	✓	✓
Rigid + Flexi-Modes Plant	✓	✓	✓			✓			
Distributed Control	✓					✓			
Parameter Variation Sensitivity			✓	✓				✓	
Open-Loop Control of Nonlinear Plants	✓	✓							
On-Off Thruster Control						✓		✓	
Control Smoothing Techniques	✓				✓				✓
Feedback Control	✓		✓			✓			
General End Condition Problems	✓								
Experimental Results			✓		✓				
Suboptimal Control				✓				✓	
Large-Angle Maneuvers	✓	✓				✓			
Small-Angle Maneuvers	✓	✓	✓	✓	✓	✓	✓	✓	✓

Figure 4. Overview of Recent Work in Slewing Maneuvers for Flexible Spacecraft

experimental results. Nevertheless, much additional theoretical and analytical work is required before reliable techniques will be commonly available for LSS applications.

Virtually everyone has investigated rigid body plus one-mode flexible dynamic models and small-angle maneuvers. Distributed feedback control of a multimode flexible model for large-angle maneuvers is very immature. Utilization of on-off thrusters has also been neglected.

Computational Considerations

It is not possible to simply use high gain to suppress all of the structural modes by brute force because of modeling accuracy, computational considerations, sensor and actuator limitations and considerations of stability. The approach taken by Lockheed Missiles and Space Company (LMSC) and by others, is a two level design which LMSC calls "High Authority Control/Low Authority Control (HAC/LAC)." The basic concept²⁰ uses LAC to provide a low gain over a broad bandwidth to suppress all the modes. Modes which interact within the performance metric are identified and HAC is applied to them. HAC uses high gain against these selected modes. The overall effect is a stable, efficient controller as shown in Fig. 5.

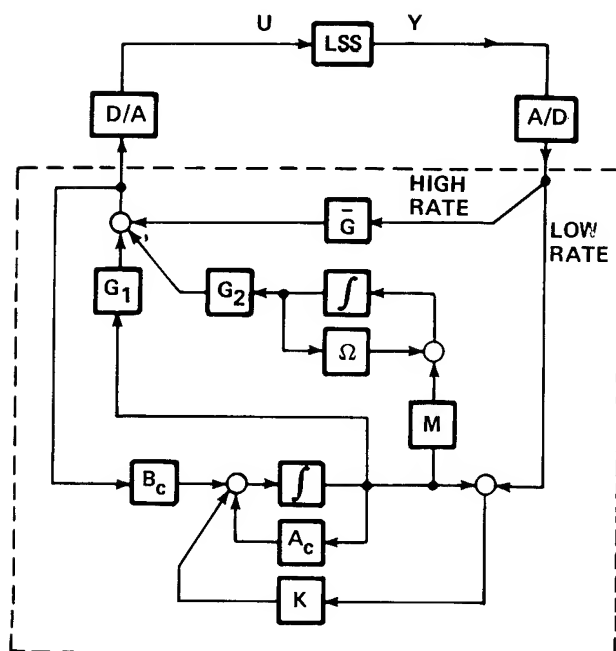


Figure 5. HAC/LAC Approach

The computational requirements for the HAC/LAC control algorithm were determined.³⁸ Sizing this control-law algorithm assumed a 50-Hz control bandwidth, 250-Hz sampling frequency, 2 bytes/word accuracy, and a data flow rate of 500 bytes/s per sensor or actuator. The floating point operations (FLOP) per control cycle were computed as a number

of the control states ($2n_H$ states/mode) and the number of sensor/actuator pairs (m) (see Fig. 6).

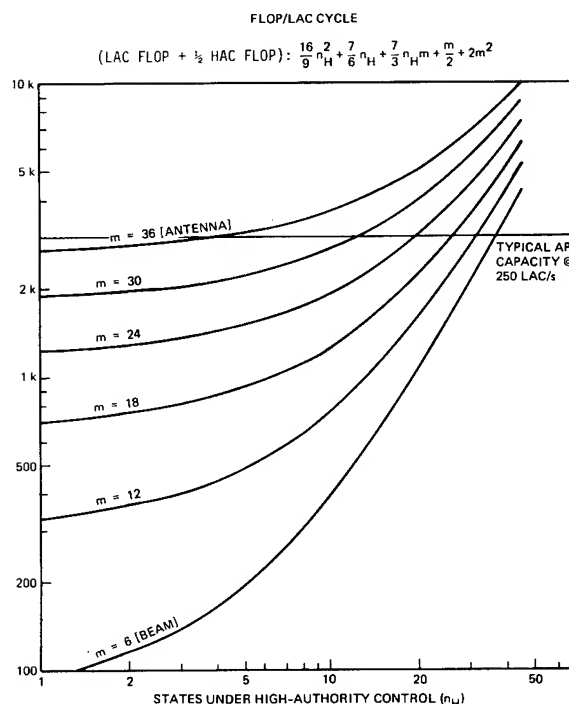


Figure 6. Control Law Algorithm Sizing

Note that the control of 10 modes ($n_H = 20$) with 18 sensor/actuator pairs ($m = 18$) pushes the state-of-the-art in current commercially available array processors.

Array Processors

Figure 7 shows the array processors surveyed.³⁹ The primary function of these devices is signal processing which requires high throughput while performing filtering on data collected in real time. Because of their speed, the array processors would appear to be candidates for closed-loop control. Several array processors are ruled out for closed-loop control application because of their fixed-point arithmetic. The loss in speed incurred by the host/array processor transfer of sensor/actuator data prohibits those which have no direct I/O capability. Hence, FPS-100, FPS-164, AP-120B, AP-180R, AP-190L, Datawest 460, MAP 300, MAP 200, MAP 6400, Magnavox (Mil Spec of CSPI MAPs), and CDA MSP-300 are the major contenders. There are mixed reports concerning the success of array processors in real-time closed-loop control. Conflicting reports have indicated that a major rewrite of the operating system was necessary. Despite the negative tone, closed-loop control with an array processor capable of direct, programmed I/O poses no fundamental problem. It simply appears that no one has thought or has had the need to use them in such an application. In collecting data for this survey, array processor engineers were unfamiliar

with closed-loop control applications but saw no difficulty in their implementation. The MCP-100^{40,41} is an untried prototype processor which was designed specifically to implement LQ controllers.

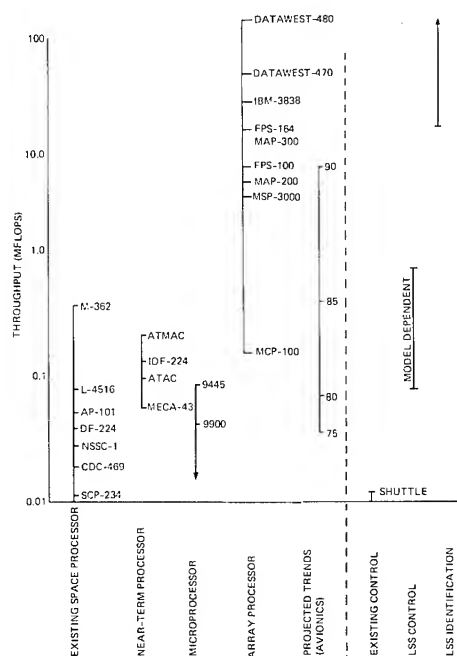


Figure 7. Avionics Data Processing

Sensor Technology

Sensor technology³⁹ (see Fig. 8) for sensing submicron vibration in large precision space systems is not available off-the-shelf. Optical

Type	Device	Bandwidth (Hz)	Range	Resolution	Power (W)	Weight (lb)	Size (in.)	Comments
Position	LVDT	0-500	±10 mm	6 μm	0.3	2.3	0.75 D × 2.1	
	Capacitive probes	0-500	0.1-152 mm	0.001 μm	—	17.6	0.63 D × 3.7	
	Interferometer	0-50	±0.01 m	0.08 μm	0.0004	—	—	LMSC @ 100 M
	metaphase sensor	0-250	±0.01 m	0.08 μm	—	—	—	LMSC
	SAMS	0-8	±30 cm	±0.2 mm	0.3	—	0.47 × 0.53 × 1.6	TRW @ 45 M
	BIRD II	0-8	±30 cm	±0.3 mm	—	192	—	Bell @ 32 M
Angle	RVDI	0-500	±1 rad	0.01 rad	1.0	1.9	1.1 D × 1.9	
	Optical encoder	0-750	—	0.0008 rad	—	—	3.0 D × 6.5	
Acceleration	Inertial accelerometer	0-100	100 g	0.1 μg	1.5	1.7	0.8 D × 1.4	Modified Bell XI
	Piezoelectric accelerometer	2-100	±84 g	800 μg	—	1.4	0.75 D × 1.5	
Force	Piezoelectric transducer	0-75	±2.5 kN	18 mN	—	0.4	0.4 D × 1.0	Force link
	Strain gauge	0-500	±80 μm/m	5 μm/m	0.025	0.04	0.25 × 0.02 × 0.002	
Rate	Inertial gyro	0-200	—	0.003 sec	—	28.2	2.5 D × 3.6	CSPL ITGG

Figure 8. Table of Typical Sensors

measurement techniques provide the best potential because of their high and low bandwidth, accuracy and resolution. Piezoelectric sensors are another candidate. Lockheed, Hughes, TRW, and Itek are pursuing these technologies. The only inertial grade space accelerometer is the BELL XI which is expensive by comparison to optical devices. The Charles Stark Draper Laboratory is investigating

the potential of a Three-Axis Angular Rate Accelerometer (TAARA) and a Six-Axis Space Sensor (SASS). The high cost of inertial grade space gyros is the major disadvantage. Even though these gyros exhibit low noise and drift, their bandwidth is less than 50 Hz. Fundamentally, the sensor technology for submicron vibration sensing is available but exists only as a laboratory demonstration.

Actuator Technology

Actuator technology³⁹ (see Fig. 9) for submicron vibration control relevant to the large precision space systems problem is virtually nonexistent. Piezoelectric devices provide the best potential. A pivoted proof mass (PPM) actuator was developed by Lockheed. This actuator produces a force on a structure by inertial reaction on a small proof mass. The prototype PPM used on the ACOSS experiments delivers a 1N (0.22 lb) force at 10 Hz with a 0.80-kg (1.76 lb) proof mass.

Type	Device	Bandwidth (Hz)	Characteristics	Weight (lb)	Power (W)	Size (in.)
Torque	Reaction wheel	0-100	5 lb-in./7 ft-lb-s	12	15	12 D × 7.8
	Control momentum gyro	0-50	500 ft-lb/2300 ft-lb-s	418	50	49 sphere
Force	Pulsed plasma thrusters	—	0.0003 N/1000 s SPI	14.5	25	15 × 7 × 9
	Piezoelectric actuators	0-5k	1 Nm/15 μm range	1	—	0.7 D × 2
	LMSC Proof Mass actuator PPM	2-200	10N	—	—	—

Figure 9. Table of Typical Actuators

Control Moment Gyro/Reaction Wheel (CMG/RW) technology is 10 years old. CMG/RWs are not capable of satisfying the slew maneuver requirements of high torque/high bandwidth characteristics. Low noise/high torque/high bandwidth characteristics are necessary for precision tracking. For attitude control, the CMG/RW is required to have low noise/low torque/low bandwidth characteristics. Today's CMGs and RWs fall in between these diverse requirements as presented in Fig. 10.

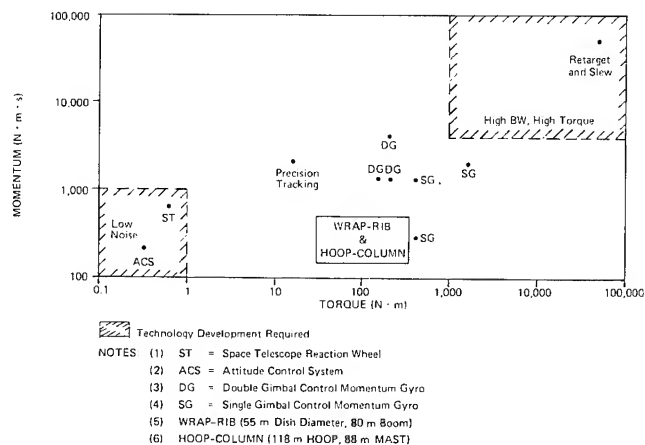


Figure 10. Torque/Momentum Capabilities and Requirements

Thruster technology has the potential for high torque; however, these devices lack a continuously variable thrust level.

Fault Tolerant Considerations

Very little work has been done in the area of Fault Detection, Isolation, and Reconfiguration for large space systems per se.^{42,43} Therefore, a broad, well-planned technical effort is needed to successfully apply fault-tolerant technology to large space systems and gain the benefits of improved system performance and reliability which can result from it. Fortunately, a large amount of theoretical and applied work has been done in the fault-tolerant technology area, which forms a solid and broad basis for the development of a fault-tolerant large space system. This is especially true in the areas of computation, failure detection, and isolation algorithm development, reliability analysis, digital system architecture, and the application of fault-tolerant technology to space, naval, and aircraft systems.

A simple example which demonstrates the need for fault tolerant systems is shown in Fig. 11 where a system with 50 components ($N = 50$) whose mean time between failure is 100,000 hours (12 years) can expect 4 component failures each year.

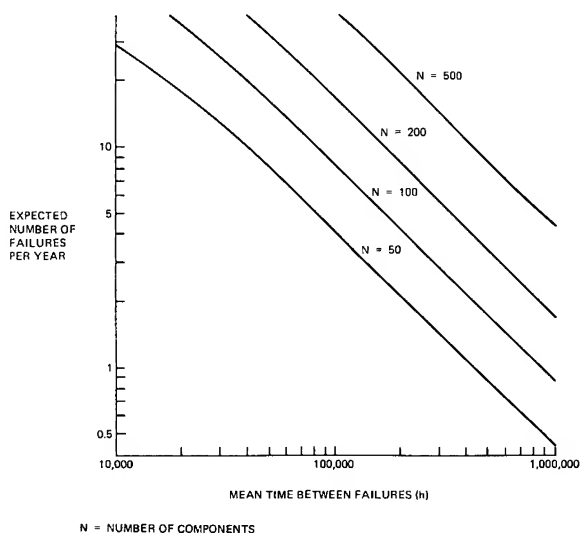


Figure 11. Fault-Tolerant Consideration

LSS Experiments

The relevant large space structure experiments³⁹ to date (Fig. 12) considered either beams or plates with one exception, Lockheed's Proof-of-Concept (POC). The advantage of these choices is the ability to analytically predict the dynamic behavior of the structure and thus compare the analysis to the experimental results. The obvious drawback of these experiments is the fact that

almost no realistic large space structures has the characteristics of a beam or a plate, although it might contain a flexible beam (e.g., the boom connecting the feed and the reflector of an antenna). None of the experiments employed a truss structure--a likely large space structure configuration. The current level of performance in these experiments was for large deflections and not in the submicron range which is anticipated for large precision space systems. The Draper RPL-EXP is the only experiment which incorporates thrusters.

The most complex experiment is the Lockheed POC. The intent of the POC is to design and test a brassboard that is as large and complex as a real spacecraft. An equipment section representing the satellite body is a 4-ft (1.21 m) cube and the largest single mass. An antenna support boom extends from the equipment section to one edge of a large offset parabolic reflector. The overall structure floats near its center of gravity on an air bearing. The structure is 8 m (25.25 ft) long and has a 2.95 m (9.69 ft) diameter antenna. The overall weight is 600 lb (272.16 kg) with much of the mass concentrated in the equipment section. The structure has many closely spaced, low frequency modes of vibration. There are pendulum (rigid body) modes lower than 0.1 Hz. The first two bending modes are between 1 and 2 Hz. The first six bending modes are under 9 Hz. The antenna dish modes are over 20 Hz.

The size of the structure is such that realistic hardware can be used for sensors and actuators. Actuation is accomplished with 3 control moment gyros (CMGs) units spaced 120 degrees apart in the equipment section and Pivoted Proof Mass (PPM) actuators. Sensing is accomplished with rate gyros and accelerometers. A LOS is simulated with a laser mounted in the equipment section that reflects off a mirror on the parabolic reflector structure to an external detector. Control is implemented on a PDP 11/45 with a CSPI Array Processor and VAMP software.

LSS Vacuum Chambers

Ground-based environmental testing of large space structures sections or components may be required prior to actual space construction. The issues of zero-g and seismic disturbances cannot be ignored; however experience has shown that prudent ground-based testing of spacecraft can reduce operational risk. Large environmental space chambers which could be utilized in an appropriate large space structure ground-based test program were surveyed.

Figure 13 shows the major potential large space structures tests facilities: Air Force Rocket Propulsion Laboratory, Arnold Engineering Development Center, Boeing, Ford Aerospace, General Dynamics, Johnson Space Center, McDonnell-Douglas, and the TRW Systems Group.

Company	Type	Description	Sensor	Actuator	Demonstration
Convair	Plate	Fixed-free 68" x 103" aluminum 4" x 5/16" welded beams	Rate gyros	Torque wheels	Model error sensitivity suppression
Draper	Beam	Fixed-free 1/4" x 1" x 60" aluminum	Piezoelectric accelerometers	Electrodynamic shaker	Observation/control spillover modern modal control
	RPL-EXP	4 beams (1/8" x 6" x 48" aluminum) cantilevered to hub on air bearing table	Angle encoder accelerometers	Cold gas thrusters	RCS controller Design methods for flexible space- craft
Hughes	Cylindrical mast	Hollow fiberglass cylinder (0.23 cm x 4.3 cm dia. x 66 cm long)	Piezoelectric ceramic strain transducers	Piezoelectric ceramic strain transducers	Electronic damping
JPL	Beam	Pinned-free 150" x 6" x 1/32" stainless steel	Eddy current position sensor	Brushless dc torque motor	Modern modal control
LaRC	Beam	Suspended 12' x 6" x 3/16" aluminum	Noncontacting deflection sensor, load sensor	Electrodynamic shaker	
Lockheed	Beam	Fixed-free 40" magnesium	Optical rate sensor	Proof-mass	Low authority control
	I-Beam	Fixed-free 25' x 16" (400 lb) aluminum	Optical rate sensor	Single gimbal CMG	Low authority control
	Vertical Beam	Fixed-free 6' aluminum lead tip masses	Accelerometers, quad-detector photo diodes	Pivoted proof-mass	Low authority control System identification
	Circular plate	Suspended, 2 meter diameter, aluminum	Multi-channel micro-phase optics	Pivoted proof-mass	Low authority control Low/high authority control System identification
	Frame	Suspended 2 meter diameter aluminum tubes	Accelerometers, optics	Pivoted proof-mass	
	Toysat	Suspended rigid body 1.6 m cantilever beams aluminum	Accelerometers, LVDT velocity pickoffs	Electrostatic actuators	Open loop torque profile high authority control
	POC	4.5 meter boom with 3 meter reflector, aluminum on air bearing sphere	Accelerometers, rate gyro, laser	CMG Proof mass	Classical and modern control of vibration and slew
TRW	Plate	Clamped 1.73 m x 1.22 m x 1.66 mm aluminum	Rate sensors, accelerometers	Bending moment actuator	Vibration suppression and damping augmentation

Figure 12. Relevant LSS Experiments

Observations

The success of future high performance control systems will depend on our knowledge of the structural dynamics. New modeling techniques may be required. Ground and space-based testing must be conducted to better understand the phenomena associated with structural damping, deployment dynamics, joint characteristics, etc.

System identification is a key first step in support of model validation and control-law performance verification. Algorithms as well as sensors/actuators must be developed to accommodate the broad dynamic range of LSS characteristics.

Multi-input/multi-output control system design and analysis methodologies require further research in order to bring practical designs to fruition. Laboratory experiments are necessary to drive the control theory research and development in the proper direction of digital implementation. New efficient and numerically stable control design and analysis software tools are needed.

Sensor/actuator technology is lagging. High torque capability is necessary as well as micron sensing and actuation. There does not appear to be research and development in either of these two areas that goes beyond laboratory prototypes.

The computational requirements for future LSS controllers are beyond today's avionic architectures. Innovative hardware and software concepts are necessary. Flight qualifiable hardware will drive fabrication materials and techniques.

Well-conceived LSS ground-based demonstrations, correlated with an equivalent flight experiment, can go a long way in resolving the LSS control technology issues.

ACKNOWLEDGEMENTS

The authors would like to acknowledge Lt. Col. Alan Herzberg (DARPA) for his efforts in furthering the state-of-the-art in ACROSS technology. This paper draws upon briefing material prepared by Robert R. Strunce, Jr. during his

Organization	Equipment	Size (ft)	Pressure (torr)	Heat	Cooling	Solar	Comments
Air Force Rocket Propulsion Laboratory	SPEF	30 ft sphere	1×10^{-6}	Heated panel +400°F	Cryo panel -300°F	Solar heat simulator	
Arnold Engineering Development Center	Mark I	42 D x 82 L vertical	5×10^{-9}		Cryo	Yes	
	7V	7 D x 12 L horizontal	---		Cryo	No	Used for simulation of space mission for cold-optics and specialized infrared equipment
	10V	10 D x 20 L horizontal	---		Cryo	No	Used for low density aerodynamic studies and testing of small rocket engines
	12V	12 D x 35 L vertical	---		Cryo	Xenon arc	Heat flux system to simulate planet albedo and radiance
Boeing	Space Chamber	28 D x 40 L vertical					Structure mounted on 1×10^6 lb mass. Used to make optical level measurements
Ford Aerospace	Solar Simulation Chamber	10 D x 22 L	1×10^{-7}	NA	Yes	Off axis xenon arc	LN ₂ cold wall
General Dynamics		12 D x 30 L horizontal					
Johnson Space Center	SESL Chamber A	55 D x 90 L vertical	1×10^{-6}	Heat flux of 150 W/ft ²	90° K	Top and side	
	SESL Chamber B	25 D x 26 L vertical	1×10^{-6}	Heat flux of 150 W/ft ²	90° K	Yes	
McDonnell Douglas	39' spherical	30 x 30	---	NA	Cryo shrouds		Isolated seismic base vibration shaker
TRW System Group	Sphere	30 ft sphere		Shroud temp +275°F	Shroud temp -30°F	84 in diameter	-300°F cold wall
	Cylinder	22 D x 46 L vertical		Shroud temp +200°F	Shroud temp -80°F	10 feet square	-300°F cold wall

Figure 13. Large Space Structure Vacuum Chamber Summary

employment with The Charles Stark Draper Laboratory, Inc., Cambridge Massachusetts. In addition, the authors would like to mention the ACOSS contractors: The Charles Stark Draper Laboratory, General Dynamics (Convair Division), Hughes Aircraft Company, Lockheed Missiles and Space Company, TRW (Defense and Space Systems Group), Control Dynamics Company, and Honeywell (Systems and Research Center).

References

1. Effects of Structural Flexibility on Spacecraft Control Systems, NASA SP-8016, April 1969.
2. Noll, Richard B., John J. Deyst, Curtis H. Spenny, "A Survey of Structural Flexibility Effects on Spacecraft Control Systems," AIAA Paper No. 69-116, AIAA 7th Aerospace Sciences Meeting, New York, New York, January 20-22, 1969.
3. Farrenkopf, R. L., A Survey of Case Histories Involving Spacecraft Dynamic Interaction, TRW Report, March 30, 1968.
4. Likins, Peter W., H. Karl Bouvier, "Attitude Control of Nonrigid Spacecraft," Astronautics and Aeronautics, May 1971.
5. Disher, John H., "Next Steps in Space Transportation and Operations," Journal of Astronautics and Aeronautics, January 1978.
6. Hagler, Thomas, Herbert G. Patterson, and Allan C. Nathan, "Learning to Build Large Structures in Space," Journal of Astronautics and Aeronautics, December 1977.
7. Daros, Charles J., Robert F. Freitag, and Richard L. Kline, "Toward Large Space Systems," Journal of Astronautics and Aeronautics, May 1977.
8. Powell, Robert V., and Albert R. Hibbs, "An Entree for Large Space Antennas," Journal of Astronautics and Aeronautics, December 1977.
9. Dahlgren, J. B., and S. M. Gunter, "Pointing and Control Technology Needs for Future Automated Space Systems," AIAA Convention of Large Space Platforms, Los Angeles, California, September 1978.

10. Mode, V. J., "Attitude Dynamics of Satellites with Flexible Appendages - A Brief Review," Journal of Spacecraft and Rockets, Vol. 11, No. 11, September 1974.
11. "Special Issue on Dynamics and Control of Large Space Structures," The Journal of the Astronautical Sciences, Volume XXVII, No. 2, April-June 1979.
12. Seltzer, Sherm M., "Active Control of Flexible Space Structures," AAS 80026, Annual Rocky Mountain Guidance and Control Conference, February 17-21, 1980, Keystone, Colorado.
13. Likins, Peter, "The New Generation of Dynamic Interaction Problems," AAS-78-101, Annual Rocky Mountain Guidance and Control Conference, March 10-13, 1978, Keystone, Colorado.
14. Balas, Mark J., "Trends in Large Space Structure Control Theory: Fondest Hopes, Wildest Dreams," IEEE Trans. Automat. Contr., Vol. AC-27, No. 3, June 1982.
15. Passive and Active Suppression of Vibration Response in Precision Structures: State of the Art Assessment, Vol. 1 and 2, R-1138, The Charles Stark Draper Laboratory, Inc., Cambridge, Massachusetts, 1978.
16. Actively Controlled Structures Theory, Theory of Design Methods, Vol. 1 (of 2), Draper, RADC TR-79-268.
17. ACOSS ONE (Active Control of Space Structures), Phase I, General Dynamics, RADC TR-80-79.
18. ACOSS THREE (Active Control of Space Structures), Phase I, Lockheed, RADC TR-80-131.
19. ACOSS FOUR (Active Control of Space Structures, Theory, Vol. I and Vol. II, Draper, RADC TR-80-78.
20. ACOSS FIVE (Active Control of Space Structures, Phase IA, Lockheed, RADC TR-82-21.
21. ACOSS SIX (Active Control of Space Structures), Draper, RADC TR 80-377.
22. ACOSS SEVEN (Active Control of Space Structures), General Dynamics RADC TR-81-241.
23. ACOSS EIGHT (Active Control of Space Structures), Phase II, TRW, RADC TR-81-242.
24. ACOSS Nine (Active Control of Space Structures), Control Dynamics Company, RADC TR-82-240.
25. ACOSS ELEVEN (Active Control of Space Structures), Vols. 1 & 2, Draper, RADC TR-82-131.
26. ACOSS ELEVEN (Active Control of Space Structures), Draper, RADC TR-82-295.
27. ACOSS ELEVEN (Active Control of Space Structures), Draper, RADC TR-83-56.
28. ACOSS ELEVEN (Active Control of Space Structures), Vols. 1 & 2, Draper, RADC TR-83-158.
29. ACOSS TWELVE (Active Control of Space Structures), Lockheed, RADC TR-82-320.
30. ACOSS FOURTEEN (Active Control of Space Structures), TRW, RADC TR-83-51.
31. ACOSS FIFTEEN (Active Control of Space Structures), Control Dynamics Co., RADC TR-82-198.
32. ACOSS SIXTEEN (Active Control of Space Structures), Honeywell, RADC TR-82-225.
33. ACOSS SEVENTEEN (Active Control of Space Structures), Control Dynamics Co., work in progress.
34. Actively Controlled Structures Theory (U), Application of Design Method, Vol. II (of 2), Draper, RADC TR-79-268.
35. ACOSS TWO (Active Control of Space Structures) (U), Hughes, RADC TR-80-130.
36. Active Control of Space Structures (ACOSS) Model 2, C-5437, The Charles Stark Draper Laboratory, Inc., September 1981.
37. Modifications to ACOSS Model #2 Design, Technical Report, Data Base (Final), CSDL-R-1585, The Charles Stark Draper Laboratory, October 1982.
38. Preliminary Flight Control Avionic Requirements for Orbiter-attached Large Space Structures, CSDL-R-1531, The Charles Stark Draper Laboratory, Inc., January 1982.
39. An Investigation of Enabling Technologies for Large Precision Space Systems, Vol. 1, 2, and 3, CSDL-R-1499, The Charles Stark Draper Laboratory, Inc., November 1981.
40. Richard H. Travassos, "The MCP-100: A Turnkey System for Implementing Multivariable Flight Control Laws," National Aerospace and Electronics Conference (NAECON), May 1982.
41. MCP-100 Operations Manual (Draft), Integrated Systems Inc., Palo Alto, California, September 1982.
42. Deyst, J. J., et al., "Fault Detection Identification and Reconfiguration--An Emerging Discipline in the Development of Highly Reliable Space Systems," Meeting of the American Astronautical Society, October 20-23, 1980.
43. Marshall, M., and G. D. Low, "Final Report of the Autonomous Spacecraft Maintenance Study Group," JPL Publication 80-88, February 1, 1981.

Exact Nonlinear Control of Spacecraft Slewing Maneuverswith Internal Momentum Transfer*

by

Thomas A. W. Dwyer, III
 Department of Electrical Engineering
 Colorado State University
 Fort Collins, CO 80523

Abstract

The recent literature on spacecraft slewing maneuvers relies on two techniques for taking nonlinear effects into account: suboptimal torque commands are either generated by continuation techniques from open loop laws arising from Pontryagin's Maximum Principle, or else obtained by polynomial truncation of analytic feedback laws arising from Bellman's Optimality Principle. Correction for suboptimality and unmodelled disturbances must then be carried out based on a time-varying approximation of the error dynamics along the nominal state trajectory. In this paper it is shown how exact command generation and tracking can be obtained by standard linear methods, through the prior construction of nonlinear coordinate transformations together with nonlinear feedback, to transform the nonlinear equations of motion of a spacecraft controlled by internal reaction wheels into three decoupled double integrators, driven by acceleration commands. Maneuver specifications are then transformed into the equivalent linear representation thus obtained, and codified into linear optimal control or path planning problems with exact solutions, which are then transformed back. Moreover, correction for disturbances can also be carried out in the transformed linear representation, making gain scheduling unnecessary. Hardware and software implementation of the linearizing transformations is discussed, and corroborating simulation results presented.

Introduction

Control laws and control systems for sequential single axis spacecraft rotational maneuvers can be effectively designed with linear techniques, such as by Breakwell in [1], Melzer in [2], and with new techniques by Hefner in [3] and by Chun, Juang and Turner in [4] and [5]. The nonlinearity of the equations of rotational motion must be taken into account, however, to satisfy the increasingly stringent requirements of agile spacecraft undergoing fast multiaxial slews of large amplitude.

Such maneuvers are customarily formulated as nonlinear optimal control problems, and then approximately solved by essentially one of two approaches: either a suboptimal command is generated by relaxation or continuation methods from the coupled state and co-state equations derived from Pontryagin's Maximum Principle, such as by Junkins and Turner in [6] as well as Vadali and Junkins in [7] and [8], or else by polynomial truncations of optimal analytic feedback laws derived from Bellman's Optimality Principle, as done by the *Research supported in part by NSF Grant ECS-8304968 and by AFOSR Contract F4920-83-K-0032

author in [9] and [10] as well as by Carrington and Junkins in [11] and [12].

Such techniques have been found to be sufficiently accurate with few iterations for sufficiently slow maneuvers. However, implementable exact solutions, in the sense of guaranteeing zero terminal error with bounded controls in the absence of disturbances, have not been obtained by such means, except for the case of pure rigid detumbling with variable external torque controls treated by this author in [13].

Moreover, even when a sufficiently accurate nominal solution is obtained, the problem of correcting for unmodelled modes and disturbance during the maneuver leads to time-varying LQG problems, that have to be solved along the nominal trajectory, hence at best approximately implemented by gain-scheduling.

In contrast, the program begun by this author in [14] for the case of external torque actuators, and continued here with internal reaction wheel actuators, provides exact nominal solutions, practically implementable in software, or with hardware summers, scalars and integrators, by a proper choice of attitude and rate variables, followed by the application of two analytical artifices: appropriate invertible nonlinear coordinate transformations, coupled with nonlinear feedback, are first found for each system (not each maneuver), so that an equivalent linear model of the system equations is obtained, as advocated by Hunt, Su and Meyer in [15]. The transformed maneuver specifications are then formulated as linear optimal control problems, whence torque commands are obtained by means of the inverse transformations.

Besides providing an exact nominal solution, often in closed form, this approach also permits the design of a single linear regulator for the correction of the effects of unmodelled modes and disturbances, producing incremental corrections to the transformed command in response to the transformed error states. The full power of recently developed methods for linear regulation and tracking, such as in [3], [4], and [5], can thus be applied to general nonlinear maneuvers. The application of such linear methods to vibration and noise suppression during nonlinear slews will be reported in greater detail elsewhere, based upon the nominal command generation algorithms developed in [14] and in the present paper. Appended simulation results illustrate the effectiveness of the proposed command generation method, in comparison with direct suboptimal nonlinear control.

Spacecraft and Reaction Wheel Dynamics

The spacecraft model considered by Vadali and Junkins in [7] will be employed here. The model consists of a rigid main body equipped with three reaction wheels, mounted coaxially with the yaw, pitch and roll axes originating from the spacecraft's center of mass, as shown in Figure 1.

Some notation is in order: \underline{I}^0 will denote the matrix of products of inertia of the system (main body principal moments, transverse wheel moments and axial wheel moments), while \underline{I}^A will represent the diagonal matrix of axial wheel moments alone. By $\underline{\omega}$ will be meant the column matrix of components of inertial angular velocity of the spacecraft main body, resolved along the yaw, pitch and roll axes, while $\underline{\Omega}$ will denote the column matrix of axial angular velocities of each reaction wheel. Finally, \underline{H} will stand for the column matrix of components of the total angular momentum of the system, likewise resolved along the principal spacecraft axes.

As is shown in [7], the total spacecraft angular momentum is given by

$$\underline{H} = \underline{I}^0 \underline{\omega} + \underline{I}^A \underline{\Omega} \quad (1)$$

in terms of the spacecraft and wheel inertias and angular velocities. (A more general expression is given in [8] and [12], which permits more than three reaction wheels. However, the three wheel example will be retained here for simplicity.)

In the absence of external torques, conservation of angular momentum applied to eq. (1) yields

$$\underline{I}^0 \dot{\underline{\omega}} + \underline{I}^A \dot{\underline{\Omega}} + \underline{\omega} \times \underline{H} = \underline{0} \quad (2)$$

where a dot denotes a time derivative and \times a cross product, the latter arising because of the rotation of the body-fixed reference frame. (More generally, the right-hand side of the eq. (2) stands for the net external torque with respect to the spacecraft center of mass, also resolved along body axes.)

The rate of change of angular momentum about the center of mass of each reaction wheel likewise equals the corresponding wheel motor torques τ_i , which are shown in [7] to be jointly given by

$$\underline{I}^A (\dot{\underline{\Omega}} + \underline{\omega}) = \underline{\tau} \quad (3)$$

There is no cross product term because each component of eq. (3) corresponds to a pure spin. (Again a more general expression holds for other wheel configurations, as is given in [7] and [12].)

Insertion into eq. (2) of the expression for $\underline{I}^A \dot{\underline{\Omega}}$ obtained from eq. (3) finally yields the evolution equation for $\underline{\omega}$ in terms of the wheel torques $\underline{\tau}$ and the total angular momentum \underline{H} :

$$[\underline{I}^0 - \underline{I}^A] \dot{\underline{\omega}} = \underline{H} \times \underline{\omega} - \underline{\tau} \quad (4)$$

It is in general necessary to propagate the total angular momentum \underline{H} (or equivalently the wheel angular velocities $\underline{\Omega}$ hidden therein) to complete the dynamic model. However, in the absence of external torques it is possible, as in [7], to represent the angular momentum \underline{H} in terms of the column matrix \underline{H}^I of its (necessarily constant) inertial components, through the time-varying matrix \underline{C} that transforms the underlying inertial reference frame into the principal spacecraft axes, as will be shown next.

Kinematic Representation of the Angular Momentum

If the instantaneous spacecraft orientation is represented by a virtual rotation of ϕ radians about a unit vector \underline{e} then the change of basis matrix \underline{C} from inertial to body reference can as usual be parametrized by the symmetric Euler quaternion

$$\underline{\beta} = \text{col}(\beta_0, \underline{\beta}') \quad (5)$$

where $\beta_0 = \cos(\frac{1}{2}\phi)$ and $\underline{\beta}' = \sin(\frac{1}{2}\phi)\underline{e}$, as in [6] ('col' denotes a column matrix): indeed, the change of basis transformation is then given by

$$\underline{C} = \underline{C}(\underline{\beta}) = [2\underline{\beta}'\underline{\beta}'^T + (\beta_0^2 - \underline{\beta}'^T\underline{\beta}')\underline{I} - 2\underline{\beta}_0\underline{\beta}'\times] \quad (6)$$

where \underline{I} is the 3x3 identity matrix, T denotes transposition and $\underline{\beta}'\times$ is the matrix representation of the cross product operation, as is given in [7] but expressed here in coordinate-free form.

The inertial angular momentum \underline{H}^I can then be measured at the start of a maneuver by

$$\underline{H}^I = \underline{C}(\underline{\beta}(0))^{-1} \{ \underline{I}^0 \underline{\omega}(0) + \underline{I}^A \underline{\Omega}(0) \} \quad (7)$$

where the components of the initial angular velocity $\underline{\omega}(0)$ are measured by yaw, pitch and roll gyros, while the initial angular velocities $\Omega_i(0)$ of the wheels can be given by tachometers coaxially mounted with the wheel motors, with $\underline{I}^A \underline{\Omega}(0)$ encoding the initial orientation. Once \underline{H}^I is determined, the angular momentum in body-fixed coordinates is given by

$$\underline{H} = \underline{H}(\underline{\beta}(t)) = \underline{C}(\underline{\beta}(t)) \underline{H}^I \quad (8)$$

(A simplified representation is used in [7], that requires the pre-selection of a preferential inertial reference frame, but it will be seen below that in the approach being advocated here the choice of inertial reference frame is determined instead by maneuver-dependent requirements.)

To complete the equations of motion, the evolution of the kinematic parameter $\underline{\beta}$ must be taken into account, as is discussed next.

Spacecraft Attitude Kinematics

The evolution of the attitude quaternion can be represented in terms of quaternion algebra, as shown in [10], but is here decomposed into the evolution of its scalar part β_0 and that of its vector

part $\underline{\beta}'$, to yield as in [14]:

$$\dot{\underline{\beta}}_0 = -\frac{1}{2}\underline{\omega}^T \underline{\beta}' \quad (9a)$$

$$\dot{\underline{\beta}}' = \frac{1}{2}(\underline{\beta}_0 \underline{\omega} + \underline{\gamma} \times \underline{\beta}') \quad (9b)$$

In view of the identity

$$\underline{\beta}_0^2 + \underline{\beta}'^T \underline{\beta}' = 1 \quad (10)$$

that follows from the definition of $\underline{\beta}$ in eq. (5), the scalar part (9a) of the kinematic equations may be omitted, provided the spacecraft maneuver (or the choice of inertial frame of reference) is constrained to avoid having $\underline{\beta}_0 = 0$ (or equivalently $\underline{\beta}'^T \underline{\beta}' = 1$): that is, provided the instantaneous spacecraft orientation is always represented by a virtual rotation such that $-\pi < \phi < \pi$. One may then let

$$\underline{\gamma} = \underline{\beta}' \text{ and } \gamma_0 = \underline{\beta}_0 \text{ if } \underline{\beta}_0 > 0,$$

$$\underline{\gamma} = -\underline{\beta}' \text{ and } \gamma_0 = -\underline{\beta}_0 \text{ if } \underline{\beta}_0 < 0,$$

whence it follows that

$$\gamma_0 = \sqrt{1 - \underline{\gamma}^T \underline{\gamma}} \quad (11)$$

Any orientation is equally indexed by $\underline{\beta}$ or $-\underline{\beta}$ (cf. [14]), so that in effect $\underline{\gamma} = \underline{\beta}'$ for that attitude quaternion for which $\underline{\beta}_0 > 0$.

Reduced Equations of Motion

Given that

$$\underline{\underline{C}}(\underline{\beta})^{-1} = \underline{\underline{C}}(\underline{\beta}^*) \quad (12)$$

where $\underline{\beta}^* = \text{col}(\underline{\beta}_0, -\underline{\beta}')$ is the inverse of $\underline{\beta}$ in quaternion algebra (cf. [10]), the total angular momentum in inertial coordinates, \underline{H}^I , can be measured in terms of the initial reduced attitude parameter $\underline{\gamma}(0)$ by the formula

$$\underline{H}^I = \underline{\underline{C}}(-\underline{\gamma}(0))\{\underline{I}_0^0 \underline{\omega}(0) + \underline{I}_0^A \underline{\Omega}(0)\} \quad (13)$$

where the change of bases is re-expressed as

$$\underline{\underline{C}} = \underline{\underline{C}}(\underline{\gamma}) = [2\underline{\gamma}\underline{\gamma}^T + (\underline{\gamma}_0^2 - \underline{\gamma}^T \underline{\gamma})\underline{I} - 2\underline{\gamma}_0 \underline{\gamma} \times] \quad (14)$$

The angular momentum in body-fixed coordinates, \underline{H} , is then also given by

$$\underline{H} = \underline{H}(\underline{\gamma}(t)) = \underline{\underline{C}}(\underline{\gamma}(t))\underline{H}^I \quad (15)$$

The reduced equations of motion are then found from eqs. (9b) and (4) to be

$$\dot{\underline{\gamma}} = \underline{\underline{F}}(\underline{\gamma})\underline{\omega} \quad (16a)$$

$$\dot{\underline{J}}\underline{\omega} = \underline{H}(\underline{\gamma})\underline{x}\underline{\omega} - \underline{\tau} \quad (16b)$$

where $\underline{J} = \underline{I}^0 - \underline{I}^A$ and

$$\underline{\underline{F}}(\underline{\gamma}) = \frac{1}{2}[\underline{\gamma}_0 \underline{I} + \underline{\gamma} \times] \quad (17)$$

Nonlinear Optimal Control Formulation

The customary way of formulating an optimal maneuver, say for the terminal reorientation to coincide with the inertial axes, is to pose the optimal control problem of minimizing the performance index

$$\begin{aligned} & \frac{1}{2} p_1 \underline{\beta}'^T(t_f) \underline{\beta}'(t_f) + \frac{1}{2} p_2 \underline{\omega}^T(t_f) \underline{\omega}(t_f) \\ & + \frac{1}{2} \int_0^t \{q_1 \underline{\beta}'^T(t) \underline{\beta}'(t) + q_2 \underline{\omega}^T(t) \underline{\omega}(t) + \\ & r \underline{\tau}^T(t) \underline{\tau}(t)\} dt \end{aligned} \quad (18)$$

subject to the dynamic and kinematic equations (4) and (9). Zero terminal error in finite time can be obtained only when it is possible to let $p_1, p_2 \rightarrow \infty$.

In the work of Vadali and Junkins reported in [7] and [8], an open loop approach is followed, with the state equations (4) and (9) and corresponding co-state equations iteratively solved as a two-point boundary value problem by relaxation or continuation methods.

In the approach taken by Carrington and Junkins in [12], a closed loop point of view is taken, with the optimal nonlinear feedback law represented by a linear term followed by progressively more nonlinear corrections. This can be done recursively by linear processes, as shown by this author in [10] and demonstrated numerically in the above mentioned ref. [12].

In all these instances, only approximations to the optimal torque profile can be obtained, since solutions cannot be given in closed form. (It should be noted that the full attitude quaternion $\underline{\beta}$ is propagated in these references, but only its vector part $\underline{\beta}'$ is penalized, as was found in particular necessary to obtain convergence of the Riccati equation that generates the linear feedback term.)

Equivalent Linear Formulation

The approach followed in [14] as well as in the present paper exploits the fact that the reduced equations of motion (16) can be exactly transformed into an equivalent linear system (in fact into three decoupled double integrators), by appropriate change of coordinates together with appropriate nonlinear feedback: the new state vector is defined by

$$\underline{x} = \begin{bmatrix} \underline{x}_1 \\ \underline{x}_2 \end{bmatrix} = \begin{bmatrix} \underline{\gamma} \\ \underline{\gamma} \end{bmatrix} = \begin{bmatrix} \underline{\gamma} \\ \underline{\underline{F}}(\underline{\gamma})\underline{\omega} \end{bmatrix} \quad (19)$$

(cf. eqs. (16), (17)), and the new input is given by

$$\underline{u} = \ddot{\gamma} = \underline{\Gamma}(\gamma) \underline{\Gamma}^{-1} \{ \underline{H}(\gamma) \times \underline{\omega} - \underline{\tau} \} - \frac{1}{4} \underline{\omega}^T \underline{\omega} \gamma \quad (20)$$

as is shown in Appendix A of this paper. The transformed equations of motion thus become

$$\dot{\underline{x}}_1 = \underline{x}_2 \quad (21a)$$

$$\dot{\underline{x}}_2 = \underline{u} \quad (21b)$$

The attitude and angular rate variables can be recovered from the formulas

$$\gamma = \underline{x}_1 \quad (22a)$$

$$\underline{\omega} = 2(\underline{x}_0 \underline{x}_2 + \underline{x}_0^{-1} \underline{x}_1 \underline{x}_1^T \underline{x}_2 - \underline{x}_1 \times \underline{x}_2) \quad (22b)$$

where

$$\underline{x}_0 = \sqrt{1 - \underline{x}_1^T \underline{x}_1} \quad (23)$$

as is also shown in Appendix A. The torque $\underline{\tau}$ can then be recovered from the transformed input \underline{u} according to the fundamental inversion formula

$$\begin{aligned} \underline{\tau} = & -2\underline{J}[\gamma_0 \underline{I} + \gamma_0^{-1} \underline{\gamma} \underline{\gamma}^T - \underline{\gamma} \underline{x}] \underline{u} - \\ & - \frac{1}{2} \gamma_0^{-1} \underline{\omega}^T \underline{\omega} \underline{J} \underline{\gamma} + \underline{H}(\gamma) \times \underline{\omega} \end{aligned} \quad (24)$$

likewise derived in Appendix A.

Given the transformations (19) through (24), various maneuvers can be performed exactly, among which model (path) following and terminal control will be discussed below.

Path Following

By path following is meant following a desired attitude trajectory $\gamma^*(t)$. The optimal torque command is then found by substitution of the nominal attitudes, rates and accelerations

$$\gamma = \gamma^* \quad (25a)$$

$$\underline{\omega} = 2\{\gamma_0^* \dot{\gamma}^* + (\gamma_0^*)^{-1} \gamma^* \dot{\gamma}^{*T} \dot{\gamma}^* - \gamma^* \times \dot{\gamma}^*\} \quad (25b)$$

$$\underline{u} = \ddot{\gamma}^* \quad (25c)$$

into eq. (24): cf. eqs. (20), (22).

Care must be exercised in choosing the attitude trajectory $\gamma^*(t)$ so that $\gamma_0^*(t) > 0$ throughout, for otherwise the torque $\underline{\tau}_0$ becomes unbounded. Since usually only the initial and terminal attitudes or possibly discrete intermediate attitudes are specified, $\gamma^*(t)$ can be shaped accordingly. This is similar to 'path planning' for robot manipulators: cf. [16].

Terminal Control

By terminal control is meant determining a bounded command profile for reaching a desired terminal orientation. For an infinite horizon one is reduced to a regulator problem. In these cases the advantage of linearity in the transformed state equations (21) is lost if the transformed performance index is not quadratic. Therefore the angular velocity and torque penalties in the performance index (18) are replaced here by penalties on the parametric velocity $\dot{\gamma}$ and acceleration $\ddot{\gamma}$, so that eq. (18) becomes

$$\begin{aligned} & \frac{1}{2} p_1 \gamma(t_f)^T \gamma(t_f) + \frac{1}{2} p_2 \dot{\gamma}(t_f)^T \dot{\gamma}(t_f) + \\ & + \frac{1}{2} \int_0^t \{ q_1 \dot{\gamma}(t)^T \dot{\gamma}(t) + q_2 \ddot{\gamma}(t)^T \ddot{\gamma}(t) + r \dot{\gamma}(t)^T \dot{\gamma}(t) \} dt \end{aligned} \quad (26)$$

which is equivalent to

$$\begin{aligned} & \frac{1}{2} \underline{x}(t_f)^T \underline{P} \underline{x}(t_f) + \\ & + \frac{1}{2} \int \{ \underline{x}(t)^T \underline{Q} \underline{x}(t) + \underline{u}(t)^T \underline{R} \underline{u}(t) \} dt \end{aligned} \quad (26^*)$$

where $\underline{P} = \text{diag}(p_1 \underline{I}, p_2 \underline{I})$,

$\underline{Q} = \text{diag}(q_1 \underline{I}, q_2 \underline{I})$ and $\underline{R} = r \underline{I}$,

with $p_1, p_2, q_1, q_2 \geq 0$ and $r > 0$.

This latter performance index is to be minimized subject to the transformed state equations (21), with the weight q_1 chosen sufficiently large so that $\underline{x}_1(t)^T \underline{x}_1(t) < 1$ for $0 \leq t \leq t_f$ (for positive $\underline{x}_0 = \gamma_0$), with q_2 allowed to be zero.

Another approach, followed in [14] for the case of attitude control with external torques, is to set $q_1 = q_2 = 0$, whence solutions in closed form with $p_1, p_2 \rightarrow \infty$ can be obtained, as shown in Appendix B, and then to determine the locus of initial conditions for which one has

$$\max \quad \underline{x}_1(t)^T \underline{x}_1(t) < 1$$

This in turn reduces to evaluating $\underline{x}_1(t)$ at (at most two) real roots of $(d/dt) \underline{x}_1(t)^T \underline{x}_1(t)$ for $0 < t < t_f$, as is discussed more fully in Appendix C of the present paper. It turns out that $\gamma_0(t)$ remains positive with $q_1 = q_2 = 0$ for maneuvers where the initial angular rates are not too large, and in particular for the important case of rest-to-rest

maneuvers. The optimal transformed state and input trajectories obtained for $q_1 = q_2 = 0$ and after letting $p_1, p_2 \rightarrow \infty$ are shown in Appendix B to be given in terms of (t/t_f) by

$$\begin{aligned} \underline{x}_1(t) = \underline{\gamma}(t) = & 2\{1-(t/t_f)\}^2\{\frac{1}{2} + (t/t_f)\}\underline{\gamma}(0) + \\ & + \{1-(t/t_f)\}^2(t/t_f)t_f \dot{\underline{\gamma}}(0) \end{aligned} \quad (27)$$

$$\begin{aligned} \underline{x}_2(t) = \dot{\underline{\gamma}}(t) = & -(6/t_f)\{1-(t/t_f)\}(t/t_f)\underline{\gamma}(0) + \\ & + 3\{1-(t/t_f)\}\{\frac{1}{3} - (t/t_f)\}\dot{\underline{\gamma}}(0) \end{aligned} \quad (28)$$

$$\begin{aligned} \underline{u}(t) = \ddot{\underline{\gamma}}(t) = & (12/t_f^2)\{(t/t_f) - \frac{1}{2}\}\underline{\gamma}(0) + \\ & + (6/t_f)\{(t/t_f) - \frac{2}{3}\}\dot{\underline{\gamma}}(0) \end{aligned} \quad (29)$$

Command Generation

On-board command generation for exact terminal control can be carried out simply by exciting three integrators with step inputs with amplitudes given by

$$(6/t_f^2)\{(2/t_f)\underline{\gamma}_i(0) + \dot{\underline{\gamma}}_i(0)\}$$

and with integrator initial conditions given by

$$-(2/t_f)\{(3/t_f)\underline{\gamma}_i(0) + 2\dot{\underline{\gamma}}_i(0)\}$$

for each channel, as follows from differentiating eq. (29), which is seen to consist of ramp inputs.

The input voltages to the electric motors driving the reaction wheels can then be generated by passing the ramp signals $u_i(t)$ through a memoryless interface, with nonlinear characteristics given by the inversion formula (24) (under the presumption that the motor torques are proportional to their input voltages).

The nonlinear interface can be 'hard wired' off-line, either with dedicated integrated circuits or with microprocessors, inasmuch as the transformations can be implemented with summers, scalars and multipliers alone: indeed, $\gamma_o = |\beta_o|$ can be synthesized from $\underline{\gamma} = \pm \underline{\beta}'$, but it can also be measured by the same attitude determination sensors and processors that detect the other Euler attitude parameters. Alternatively, the inversion formula (24) can be coded as a fast nonrecursive subroutine within the autopilot (command generation) software.

Correction for Disturbances

Disturbances are generally introduced in the hardware implementation, such as the effects of parameter variations, e.g., oscillations in value of inertia matrices due to flexible modes, or else distortions within the wheel motor dynamics. The

actual attitude and rate variables will thus not coincide in general with their nominal values.

The latter can be generated in the transformed coordinates $\underline{x}_1, \underline{x}_2$, simply by integrating the nominal command \underline{u} once to obtain \underline{x}_2 and twice for \underline{x}_1 . Those values can then be compared on-line with the transformed measured states, via interfaces with nonlinear characteristics given by eq. (19).

A time-invariant linear regulator can then be designed to produce a correction signal $\Delta \underline{u}$, to be added to the nominal command before insertion thereof into the interface implementing eq. (24), to excite the wheel actuators.

The complete control system architecture is similar to the one designed in [14] for the case of control with external torque commands, except for the need to set the initial angular momentum $\underline{H}(\underline{\gamma}(0))$ in the command generation loops.

Discussion and Conclusions

It has been shown that the equations of motion for a spacecraft driven by internal reaction wheels can be globally linearized in three steps, as is reviewed below.

In the first step, the absence of a net external torque was shown to permit the elimination of the wheel dynamics, which can be expressed in terms of the Euler attitude parameters and the angular velocity of the body-fixed reference frame.

As a second step, the restriction of permissible maneuvers to those that avoid the orientations represented by virtual $\pm 180^\circ$ rotations (with respect to the otherwise freely chosen inertial reference frame), permitted the reduction of the four-dimensional Euler attitude quaternion equations to three-dimensional 'reduced' Euler parameter equations.

In the third and most important step, the reduced state equations were transformed into decoupled double integrators, by redefining the new state to consist of the reduced attitude parameter $\underline{\gamma}$ and its first time derivative $\dot{\underline{\gamma}}$, and the new input to be the second time derivative $\ddot{\underline{\gamma}}$.

Given the reduced, then globally linearized state equations, command generation tasks such as planning and following a prescribed attitude trajectory, as well as terminal control with bounded accelerations, were then formulated as analytically solvable linear problems, with state inequality constraints that can therefore be analytically tested.

The present slew control scheme is more directly implementable than the similar design proposed in [14] for the case of external torque commands, inasmuch as reaction wheel torques can be precisely varied with electromechanical actuators, whereas the usual hydrazine jets used for external torque control are not easily throttled to follow other than bang-bang commands.

It should be pointed out that if variable external torques are available then exact prior detumbling can also be carried out by linear means,

as has been shown by the author in [13]. In any case, bang-bang control with external torques can be used to bring the angular velocity down to levels that do not excite the feedback singularity, which can be mapped out off line as described in Appendix C of the present paper. One is then reduced to a rest-to-rest maneuver, that can be performed exactly without ever exciting the feedback singularity.

References

1. J. A. Breakwell, 'Optimal Feedback Slewing of Flexible Spacecraft,' AIAA J. of Guidance and Control, Vol. 4, No. 5, Sept.-Oct. 1981, pp. 472-479.
2. S. M. Melzer, 'A Terminal Controller for the Pointing of a Flexible Spacecraft,' The Aerospace Corporation, ATM79 (4901-03)-08 (Dec. 1978).
3. R. D. Hefner, 'Robust Controller Design Using Frequency Domain Constraints: Alternative Problem Formulations,' 4th VPI and SU/AIAA Symposium on Dynamics and Control of Large Structures, (Blacksburg, VA, June 6-8, 1983).
4. J. D. Turner and H. M. Chun, 'Optimal Feedback Control of a Flexible Spacecraft During a Large-Angle Rotational Maneuver,' AIAA Paper No. 82-1589-Cp, AIAA Guidance and Control Conference, (San Diego, CA, Aug. 9-12, 1982).
5. J. N. Juang, J. D. Turner and H. M. Chun, 'Optimal Terminal Controllers for Maneuvering Flexible Spacecraft,' 4th VPI and SU/AIAA Symposium on Dynamics and Control of Large Structures, (Blacksburg, VA., June 6-8, 1983).
6. J. L. Junkins and J. D. Turner, 'Optimal Continuous Torque Attitude Maneuvers,' J. of Guidance and Control, Vol. 3, No. 3, 1978, pp. 210-217.
7. S. R. Vadali and J. L. Junkins, 'Spacecraft Large Angle Rotational Maneuvers with Optimal Momentum Transfer,' AIAA Paper No. 82-1469, AIAA/AS Astrodynamics Conference, (San Diego, CA, Aug. 9-11, 1982).
8. S. R. Vadali and J. L. Junkins, 'Optimal Open Loop and Stable Feedback Control of Rigid Spacecraft Attitude Maneuvers,' AAS Paper No. 83-373, AAS/AIAA Astrodynamics Specialist Conference, (Lake Placid, NY, Aug. 22-25, 1983).
9. T. A. W. Dwyer, III, 'A Nonlinear Cauchy-Kovalevskaya Theorem and the Control of Analytic Dynamical Systems,' 4th International Symposium on the Mathematical Theory of Networks and Systems, (Santa Monica, CA, Aug. 5-7, 1981), Vol. 4, pp. 72-79.
10. T. A. W. Dwyer, III and R. P. Sena, 'Control of Spacecraft Slewing Maneuvers,' 21st IEEE Conference on Decision and Control, (Orlando, FL., Dec. 8-10, 1982), Vol. 3, pp. 1142-1144.
11. C. K. Carrington and J. L. Junkins, 'Nonlinear Feedback Control of Spacecraft Slew

Maneuvers,' AAS Paper No. 83-002, Rocky Mountain Guidance and Control Conference, (Key-stone, CO., Feb. 5-9, 1983).

12. C. K. Carrington and J. L. Junkins, 'Optimal Nonlinear Feedback Control for Spacecraft Attitude Maneuvers,' AIAA Paper No. 83-2230-CP, AIAA Guidance and Control Conference, (Gatlinburg, TN., Aug. 15-17, 1983).
13. T. A. W. Dwyer, III, 'The Control of Angular Momentum for Asymmetric Rigid Bodies,' IEEE Transactions on Automatic Control, Vol. AC-27, June 1982, pp. 686-688.
14. T. A. W. Dwyer, III, 'Design of an Exact Nonlinear Model Follower for the Control of Large-Angle Rotational Maneuvers,' 22nd IEEE Conference on Decision and Control, (San Antonio, TX., Dec. 14-16, 1983), also to appear in the IEEE Transactions on Automatic Control.
15. L. R. Hunt, R. Su and G. Meyer, 'Global Transformations of Nonlinear Systems,' IEEE Transactions on Automatic Control, Vol. AC-28, No. 1, (Jan. 1983) pp. 24-31.
16. J. Y. S. Luh, M. W. Walker and R. P. C. Paul, 'Optimum Path Planning for Mechanical Manipulators,' ASME Transactions: J. of Dynamics Systems, Measurement and Control, Vol. 103, No. 2, June 1981, pp. 142-151.

Appendix A: Derivation of the Linearizing Transformations

The following formulas will be needed:

$$\Gamma(\chi)^{-1} = 2[\gamma_0 I + \gamma_0^{-1} \chi \chi^T - \chi x] \quad (A1)$$

$$(\partial/\partial \omega) \Gamma(\chi) \omega = \Gamma(\chi) = \frac{1}{2}[\gamma_0 I + \chi x] \quad (A2)$$

$$(\partial/\partial \chi) \gamma_0 = (\partial/\partial \chi) (1 - \chi^T \chi)^{1/2} = -\gamma_0^{-1} \chi^T \quad (A3)$$

$$\begin{aligned} (\partial/\partial \chi) \Gamma(\chi) \omega &= (\partial/\partial \chi) \frac{1}{2}(\omega \gamma_0 + \chi x \omega) = \\ &= -\frac{1}{2}[\gamma_0^{-1} \omega \chi^T + \omega x] \end{aligned} \quad (A4)$$

$$\chi^T \Gamma(\chi) \omega = \frac{1}{2}\{\gamma_0 \chi^T \omega + \chi^T (\chi x \omega)\} = \frac{1}{2} \gamma_0 \chi^T \omega \quad (A5)$$

$$\begin{aligned} \omega x \Gamma(\chi) \omega &= \frac{1}{2} \omega x (\chi x \omega) = \\ &= \frac{1}{2} (\omega^T \omega \chi - \omega \omega^T \chi) \end{aligned} \quad (A6)$$

$$\begin{aligned} \Gamma(\chi)^{-1} \chi &= 2(\gamma_0 \chi + \gamma_0^{-1} \chi \chi^T \chi - \chi x \chi) = \\ &= 2\{\gamma_0 \chi + \gamma_0^{-1} (1 - \gamma_0^2) \chi\} = (2/\gamma_0) \chi \end{aligned} \quad (A7)$$

Eq. (22b) for \underline{u} follows from eqs. (19) and (A1).

Eq. (20) for \underline{u} follows from the insertion of eqs. (A2), (A4), (A5) and (A6), together with eqs. (16a) for $\underline{\gamma}$ and (16b) for \underline{u} , into the chain rule formula below:

$$\underline{u} = \ddot{\underline{\gamma}} = (d/dt)\dot{\underline{\gamma}} = \{(\partial/\partial \underline{\gamma}) \dot{\underline{\gamma}}\} \dot{\underline{\gamma}} + \{(\partial/\partial \underline{u}) \dot{\underline{\gamma}}\} \dot{\underline{u}} \quad (\text{A8})$$

Finally, eq. (20) yields

$$\begin{aligned} \underline{\tau} &= -J \dot{\underline{\gamma}}^{-1} (\underline{u} + \frac{1}{4} \underline{\omega}^T \underline{\omega}) + H(\underline{\gamma}) \underline{x} \underline{u} = \\ &= -J \dot{\underline{\gamma}}^{-1} \underline{u} - \frac{1}{4} \underline{\omega}^T \underline{\omega} J \dot{\underline{\gamma}}^{-1} \underline{\gamma} + H(\underline{\gamma}) \underline{x} \underline{u} \end{aligned} \quad (\text{A9})$$

whence eq. (24) for $\underline{\tau}$ follows from the insertion above of eq. (A7).

Appendix B: Derivation of the Optimal Control Solution

The minimizing control with $q_1 = q_2 = 0$ but finite p_1 and p_2 is given by the standard feedback law

$$\underline{u}(t) = -(1/r) [0 \quad I] P(t_f - t) \underline{x}(t) \quad (\text{B1})$$

where $P(\tau)$ is the positive definite solution of the matrix differential Riccati equation

$$\begin{aligned} \dot{P}(\tau) &= P(\tau) \begin{bmatrix} 0 & I \\ 0 & 0 \end{bmatrix} + \begin{bmatrix} 0 & 0 \\ I & 0 \end{bmatrix} P(\tau) - \\ &- P(\tau) \begin{bmatrix} 0 \\ I \end{bmatrix} (1/r) [0 \quad I] P(\tau) \end{aligned} \quad (\text{B2a})$$

in terms of the time-to-go $\tau = t_f - t$, initialized by

$$P(0) = \begin{bmatrix} p_1 I & 0 \\ 0 & p_2 I \end{bmatrix} \quad (\text{B2b})$$

The absence of a mean state penalty makes it doubly advantageous to propagate instead the inverse matrix

$$\Pi(\tau) = P(\tau)^{-1} \quad (\text{B3})$$

The evolution equation for $\Pi(\tau)$ is obtained by pre- and post-multiplying eq. (B2) by $\Pi(\tau)$ and changing sign, to yield

$$-\dot{\Pi}(\tau) = \begin{bmatrix} 0 & I \\ 0 & 0 \end{bmatrix} \Pi(\tau) + \Pi(\tau) \begin{bmatrix} 0 & 0 \\ I & 0 \end{bmatrix} - (1/r) \begin{bmatrix} 0 & 0 \\ 0 & I \end{bmatrix} \quad (\text{B4a})$$

initialized by

$$\Pi(0) = \begin{bmatrix} (1/p_1) I & 0 \\ 0 & (1/p_2) I \end{bmatrix} \quad (\text{B4b})$$

The double advantage is that eq. (B4) is a Lyapunov equation, hence linear, and moreover the terminal penalties p_i appear inverted, hence may be allowed to diverge before solving the equation. (The latter would still be true even for $q_i \neq 0$, although then eq. (B4) would become another Riccati equation.) By partitioning

$$\Pi = \Pi_{ij}, \quad i, j = 1, 2, \quad \text{with } \Pi_{12} = \Pi_{21},$$

eq. (B4) is reduced to the system

$$-\dot{\Pi}_{22}(\tau) = -(1/r) I, \quad \Pi_{22}(0) = 0 \quad (\text{B5a})$$

$$-\dot{\Pi}_{12}(\tau) = \Pi_{22}(\tau), \quad \Pi_{12}(0) = 0 \quad (\text{B5b})$$

$$-\dot{\Pi}_{11}(\tau) = 2\Pi_{12}(\tau), \quad \Pi_{11}(0) = 0 \quad (\text{B5c})$$

after letting $(1/p_i) \rightarrow 0$, $i = 1, 2$. Eqs. (B5) can be solved sequentially, to yield

$$\Pi(\tau) = \frac{1}{r} \begin{bmatrix} \frac{1}{3} \tau^3 I & -\frac{1}{2} \tau^2 I \\ -\frac{1}{2} \tau^2 I & \tau I \end{bmatrix} \quad (\text{B6})$$

which by inversion yields

$$P(\tau) = (2r/\tau^3) \begin{bmatrix} 6I & 3\tau I \\ 3\tau I & 2\tau^2 I \end{bmatrix} \quad (\text{B7})$$

(as stated without proof in [14]).

Insertion of eq. (B7) into eq. (B1) yields the optimal feedback law

$$\underline{u}(t) = -\{6/(t_f - t)^2\} \underline{x}_1(t) - \{4/(t_f - t)\} \underline{x}_2(t) \quad (\text{B8})$$

which when inserted in the double integrator eqs. (21) yields the time-varying linear vector equation

$$(t_f - t)^2 \ddot{\underline{x}}_1(t) + 4(t_f - t) \dot{\underline{x}}_1(t) + 6\underline{x}_1(t) = 0 \quad (\text{B9})$$

(also stated without proof in [14]), which has a regular singular point at $t = t_f$. However, eq. (B9) is fortunately of 'Euler type', with real roots for its indicial equation, leading to a simple closed-form solution of the form

$$\underline{x}_1(t) = (t_f - t)^3 \underline{p} + (t_f - t)^2 \underline{q} \quad (\text{B10})$$

whence

$$\underline{x}_2(t) = -3(t_f - t)^2 \underline{p} - 2(t_f - t) \underline{q} \quad (B11)$$

and

$$\underline{u}(t) = 6(t_f - t) \underline{p} + 2 \underline{q} \quad (B12)$$

The vector coefficients \underline{p} and \underline{q} are obtained from eqs. (B10) and (B11) with $t = 0$, in terms of the initial data $\underline{\gamma}(0)$ and $\underline{\chi}(0) = [\underline{\gamma}(0)]^{-1} \underline{u}(0)$, as found in [14], to finally yield eqs. (27), (28), and (29).

Appendix C: Singularity Avoidance

Since one has

$$\underline{x}_1(0)^T \underline{x}_1(0) = \underline{\gamma}(0)^T \underline{\chi}(0) < 1$$

by hypothesis, as well as $\underline{x}_1(t_f) = \underline{0}$ by inspection of eqs. (27) or (B10), it follows that the constraint $\gamma_0(t) > 0$ will be violated during the maneuver (by virtue of eq. (11)), if and only if it is violated at an interior local minimum of $\underline{x}_1(t)^T \underline{x}_1(t)$. It is enough therefore to examine the extrema of the normalized quadratic

$$3 \underline{p}^T \underline{p} s^2 + 5 \underline{p}^T \underline{q} s + 2 \underline{q}^T \underline{q} = 0 \quad (C1)$$

for $0 < s < 1$, where $s = (t_f - t)/t_f$, as follows from examining the formula

$$\begin{aligned} (d/dt) \{ \underline{x}_1(t)^T \underline{x}_1(t) \} &= \\ &= -(t_f - t)^3 \{ 3(t_f - t)^2 \underline{p}^T \underline{p} + 5(t_f - t) \underline{p}^T \underline{q} + 2 \underline{q}^T \underline{q} \} \end{aligned} \quad (C2)$$

that is easily derived from eq. (B10).

The feedback singularity will occur if and only if it occurs at $t_j = (1 - s_j)t_f$ for $j=1,2$, where the s_j are the roots of the quadratic (C1). Hence it is enough to test the norm of $\underline{x}_1(t)$ at two points at most, that is,

$$\underline{x}_1(t_j)^T \underline{x}_1(t_j) < 1, \quad j=1,2. \quad (C3)$$

In particular, the constraints (C3) will be vacuously satisfied if the roots of (C1) lie outside the open interval (0,1), as is the case for rest-to-rest maneuvers (as seen in [14]). The constraints are also vacuously satisfied if the roots of (C1) are complex, which occurs if and only if the condition

$$\cos^2(\underline{p}, \underline{q}) < 24/25 \quad (C4)$$

is verified.

If the tests (C3) and (C4) fail, such as for very high initial tumbling rates, then the commands defined by eq. (29) cannot be used. In this case either a prior detumbling command can be used, as derived exactly in [13] for the case of external torques, or one must choose a sufficiently large mean state penalty q_1 on \underline{x}_1 in the performance index (26*): in this case $\underline{p}(\tau)$ of eqs. (B1) and (B2) must be recalculated, and the locus of \underline{q}_1 for which $\gamma_0(t)$ remains positive determined therefrom.

Appendix D: Simulation Results

For the sake of comparison, the spacecraft with three identical orthogonal reaction wheels considered by Vadali and Junkins in [7] was selected for simulation, as well as the same maneuver time and initial conditions, as given below.

The spacecraft products of inertia were therefore chosen to be $I_{11}^0 = 87.212$, $I_{22}^0 = 86.067$, $I_{33}^0 = 114.562$, $I_{ij}^0 = -0.2237$ for $i \neq j$, and the common axial moments of inertia of the reaction wheels, all in $\text{kg} \cdot \text{m}^2$, were $I_i^A = 0.05$, $i=1,2,3$.

The initial Euler parameters were chosen as in [7] to correspond to a virtual rotation of $\phi = 100^\circ$ about the axis $\underline{e} = (1/\sqrt{3}) \text{col}(1,1,1)$,

$$\gamma_i(0) = \beta_i(0) = 0.44227597, \quad i = 1,2,3$$

$$\gamma_0(0) = \beta_0(0) = 0.64278761.$$

Again following [7], the initial angular velocity components in body axes in radians per second were chosen to be:

$$\omega_1(0) = 0.01$$

$$\omega_2(0) = 0.005$$

$$\omega_3(0) = 0.001$$

The reaction wheels were supposed to be initially at rest:

$$\Omega_i(0) = 0.0, \quad i = 1,2,3$$

It follows from eqs. (13) and (14) that the inertial components of the total angular momentum in $\text{kg} \cdot \text{m}^2/\text{sec}$ become:

$$H_1^I = 0.22030$$

$$H_2^I = 1.90914$$

$$H_3^I = 0.28042$$

It also follows from eqs. (16a) and (17) that

$$\dot{\gamma}_1(0) = 0.0023294$$

$$\dot{\gamma}_2(0) = 0.0035972$$

$$\gamma_3(0) = -0.0007843$$

The final time was also chosen as in [7] to be $t_f = 100.0$ seconds.

Figure 2 shows the simulated evolution of the Euler parameter $\beta_0(t) = \gamma_0(t)$, which is seen to have been driven exactly to its zero target at the end of the maneuver, as expected.

Figures 3a, b, c show the simulated evolution of the body components $\omega_i(t)$ of angular velocity in radians per second, which are also seen to have been driven exactly to their zero target.

Figures 4a, b, c show the simulated evolution of the torque components $\tau_i(t)$, which are seen to have remained bounded throughout the maneuver.

It should be noted finally that the axial angular velocity histories $\Omega_i(t)$ of the reaction wheels can be synthesized if desired from the torque component histories $\tau_i(t)$ and the spacecraft angular velocity component histories $\omega_i(t)$ by integration of eq. (3), which yields

$$\begin{aligned} \Omega_i(t) &= \Omega_i(0) + \omega_i(0)t - \\ &- \omega_i(t) + (1/I_i^A) \int_0^t \tau_i(s) ds \end{aligned} \quad (D1)$$

for $i = 1, 2, 3$ and $0 \leq t \leq t_f$. Since, as can be seen from figures 4a, b, c, the torque components cross over from positive to negative approximately half way during the terminal control maneuver, so that the integrals in eq. (D1) can be expected to be small for $t = t_f$. Since moreover $\omega_i(t_f) = 0$ and $\Omega_i(0) = 0$ by design, it follows that the final reaction wheel angular velocities $\Omega_i(t_f)$ should be comparable to the initial spacecraft angular velocity components $\omega_i(0)$ (with more integrated torque contributions the smaller the wheel inertias I_i^A). This behavior is consistent with the 'momentum transfer' character of the maneuver.

Acknowledgement

The computer simulations were carried out by Mr. Ning Chen with the aid of the DISSPLA software program at Colorado State University.

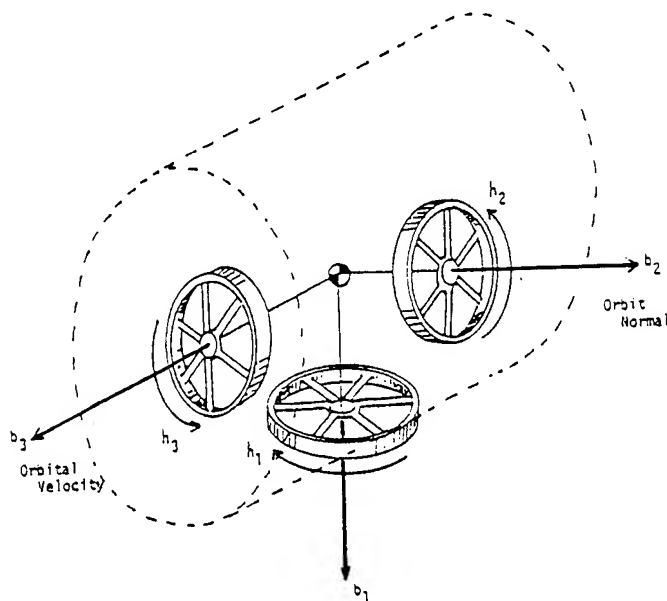


Figure 1. Dynamics of a Four Body Configuration

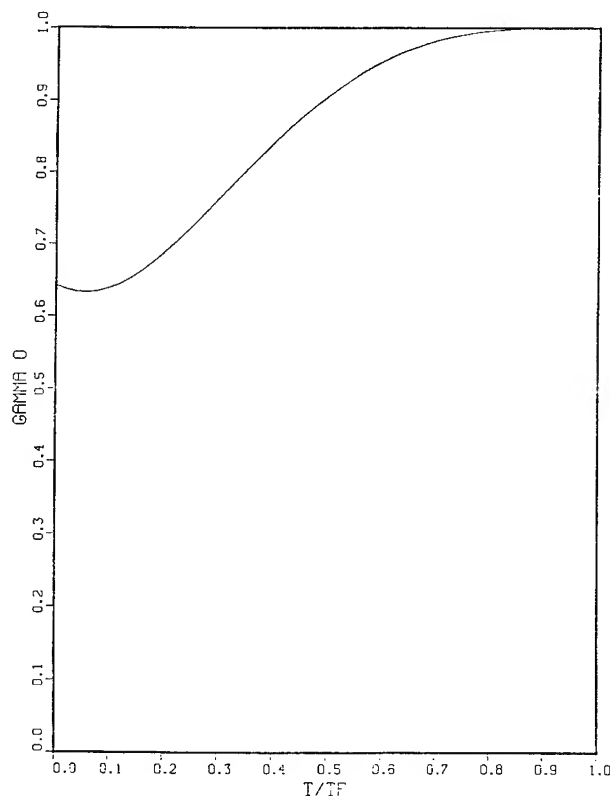


Figure 2. Attitude parameter $\gamma_0 = \cos(\phi/2)$

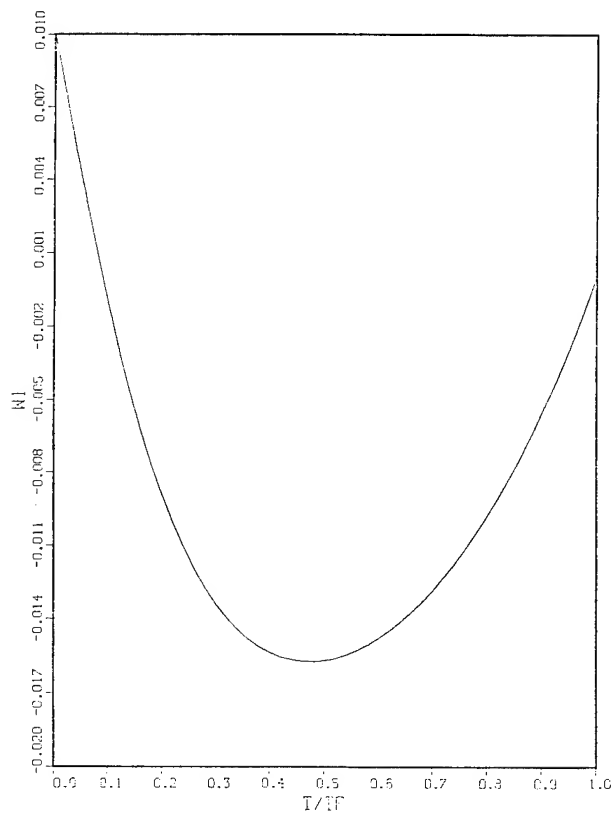


Figure 3a. Angular velocity ω_1 in radians/second

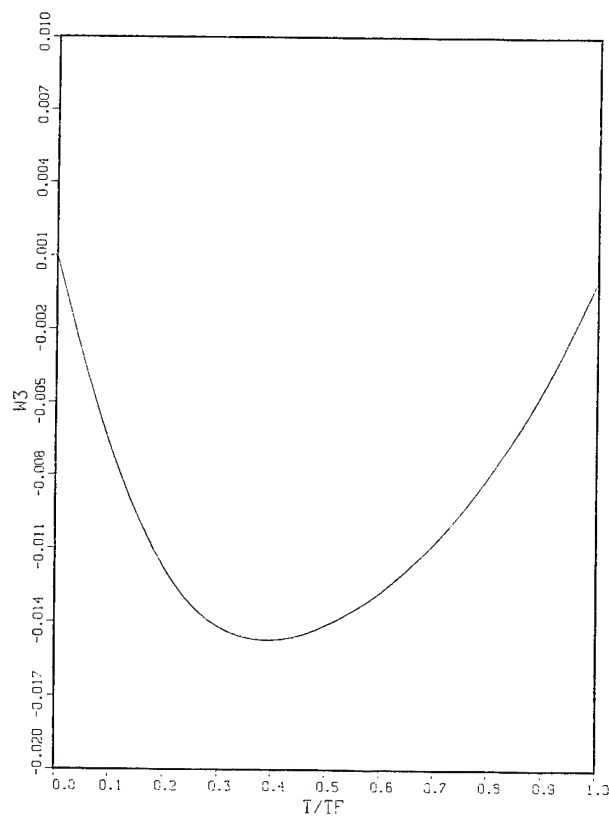


Figure 3c. Angular velocity ω_3 in radians/second

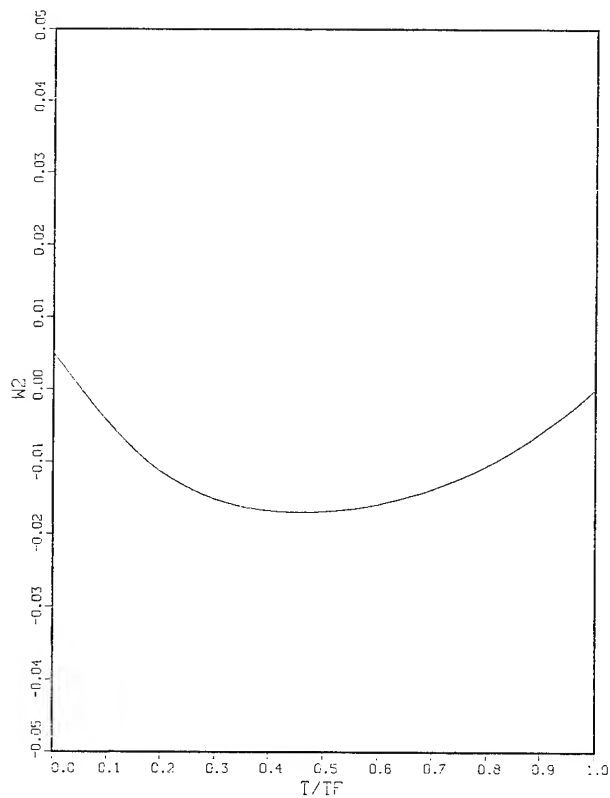


Figure 3b. Angular velocity ω_2 in radians/second

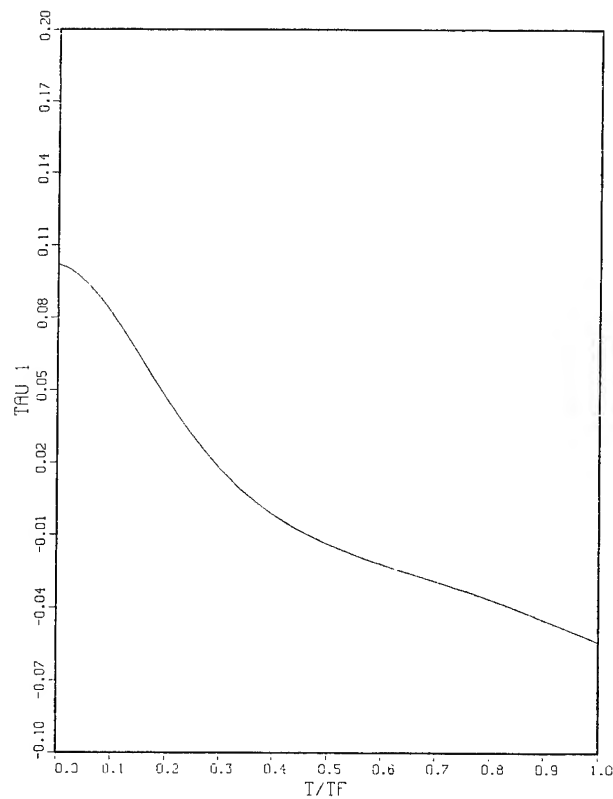


Figure 4a. Torque τ_1 in Newton.meters

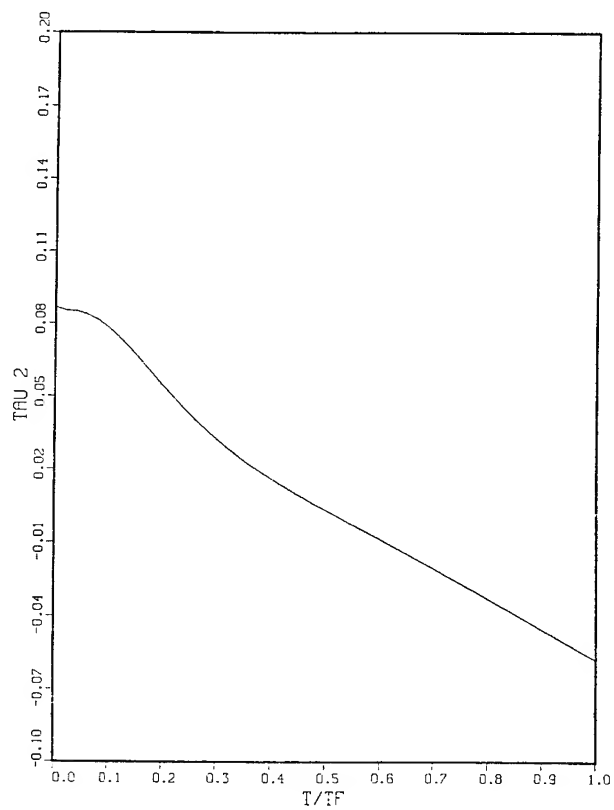


Figure 4b. Torque τ_2 in Newton.meters

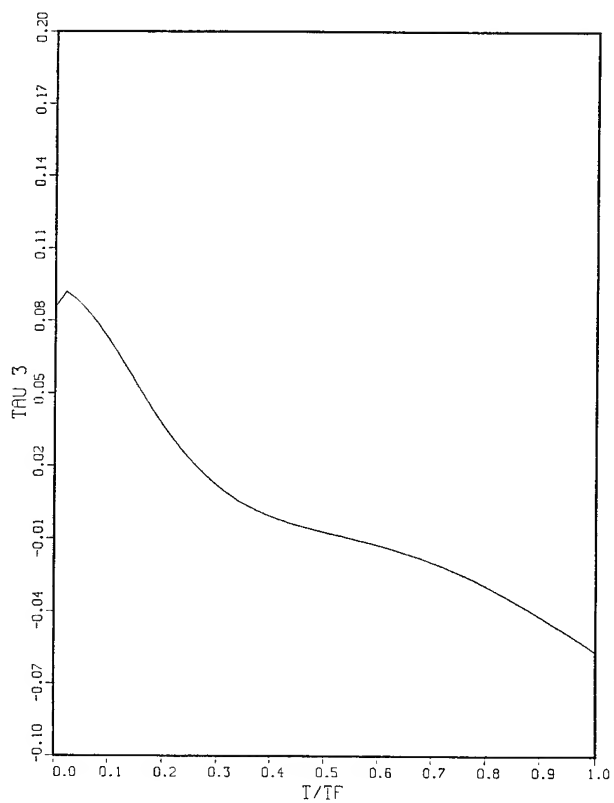


Figure 4c. Torque τ_3 in Newton.meters

S. R. Vadali*
 Iowa State University
 Ames, Iowa

Abstract

The large-angle maneuver problem with reaction wheels and on-off thrusters is addressed. On-off thrusters are used for the maneuver in the large, and the final attitude acquisition is performed by reaction wheels. Nonideal thruster operations are considered and analyzed.

I. Introduction

Reaction wheels and thrusters are the most common spacecraft attitude control devices. Thrusters can be used for large-angle maneuvers with short maneuver times at the expense of nozzle and fuel weights. Because of their discontinuous nature of operation they are unsuitable for precise attitude acquisition, as inertia and hysteresis effects cause chattering and limit cycling. Reaction wheels, on the other hand, can achieve and maintain precise attitudes.

Feedback control laws for large-angle maneuvers have been obtained for reaction wheel and continuous external torque systems using optimal control theory^{1,2} and Liapunov's second method.³ In this paper, the large-angle maneuver problem with reaction wheels and on-off thrusters is addressed. On-off thrusters are used for controlling the maneuver in the large and reaction wheels for the final attitude acquisition. Control laws are selected to provide ease of transfer between the two modes of control. Nonideal thruster operations are considered and analyzed for chattering conditions.

II. Spacecraft Dynamics and Kinematics

A rigid spacecraft with three identical reaction wheels (configured to lie along each of the principal axes of inertia) and thrusters is considered as a model. In terms of the angular velocities of the spacecraft (w_1, w_2, w_3) and the wheels ($\Omega_1, \Omega_2, \Omega_3$), the equations of motion are⁴

$$\begin{aligned}
 (I_1 - J)\dot{w}_1 &= (I_2 - I_3)w_2w_3 - J\Omega_3w_2 \\
 &\quad + J\Omega_2w_3 - U_1 + L_1 \\
 (I_2 - J)\dot{w}_2 &= (I_3 - I_1)w_3w_1 - J\Omega_1w_3 \\
 &\quad + J\Omega_3w_1 - U_2 + L_2 \\
 (I_3 - J)\dot{w}_3 &= (I_1 - I_2)w_1w_2 - J\Omega_2w_1 \\
 &\quad + J\Omega_1w_2 - U_3 + L_3 \\
 J\dot{\Omega}_i &= U_i - J\dot{w}_i, \quad i = 1, 2, 3
 \end{aligned} \quad (1)$$

where

I_1, I_2, I_3 = spacecraft principal moments of inertia

J = wheel axial moment of inertia

U_1, U_2, U_3 = wheel motor torques

L_1, L_2, L_3 = external torques.

The external torques along each axis are provided in the present context by on-off thrusters. For the spacecraft attitude description, Euler parameters are used.⁴ In terms of the four Euler parameters ($\beta_0, \beta_1, \beta_2, \beta_3$), the attitude motion is given by

$$\dot{\beta} = \frac{1}{2} [G(w)] \beta \quad (2)$$

where

$$[G(w)] = \begin{bmatrix} 0 & -w_1 & -w_2 & -w_3 \\ w_1 & 0 & w_3 & -w_2 \\ w_2 & -w_3 & 0 & w_1 \\ w_3 & w_2 & -w_1 & 0 \end{bmatrix}$$

It is well known that the Euler parameters are constrained by the relation

$$\beta^T \beta = 1. \quad (3)$$

III. Maneuvers With Reaction Wheels

Several stable feedback control laws for reaction wheel systems have been developed³ through Liapunov's second method. In essence, a positive definite function in the angular velocity and attitude errors is selected as a Liapunov function and its time derivative is guaranteed to be negative semidefinite by proper selection of the control laws.

Without loss of generality the final orientation is assumed to be $\beta_f = [1, 0, 0, 0]$. The final angular velocity state for a slewing maneuver is $\frac{w_f}{i_s} = 0$. One choice for the Liapunov function (V) is

$$\begin{aligned}
 V &= (\beta_0 - 1)^2 + \sum_{i=1}^3 [\beta_i^2 \\
 &\quad + \frac{1}{2}(I_i - J)w_i^2].
 \end{aligned} \quad (4)$$

With no thruster action ($L_i = 0$),

* Assistant Professor, Aerospace Engineering

$$\dot{V} = \sum_{i=1}^3 (\beta_i \omega_i - \omega_i U_i) \quad (5)$$

which leads to the following control laws

$$U_i = \beta_i + K_{1i} \omega_i + K_{2i} \omega_i \omega_i + K_{3i} \omega_i^3 + \dots, \quad i = 1, 2, 3. \quad (6)$$

with

$$K_{ji} \geq 0 \quad \begin{matrix} j = 1, 2, \dots \\ i = 1, 2, 3. \end{matrix}$$

It should be noted that the structure of the control laws given in equation (4) is not unique, and there exists a singularity for a rest-to-rest maneuver involving a 360° reorientation. For such a maneuver, the initial conditions are

$$\beta(0) = [-1, 0, 0, 0]^T, \quad \omega(0) = 0$$

and a different control law can be obtained by including terms such as $(\beta_0 - 1)\beta_i$ in the Liapunov function.

When both reaction wheels and on-off thrusters are to be used simultaneously, \dot{V} in equation (5) is given by

$$\dot{V} = \sum_{i=1}^3 (\beta_i \omega_i - \omega_i U_i + \omega_i L_i) \quad (7)$$

Then, for asymptotic stability of the closed-loop system, the control laws may be selected as

$$\left. \begin{aligned} U_i &= \beta_i + K_{1i} \omega_i + \dots \\ L_i &= -L_0 \operatorname{sgn}[\omega_i] \end{aligned} \right\} i = 1, 2, 3 \quad (8)$$

where

$$L_0 = L_i, \quad i = 1, 2, 3.$$

Since the wheel speeds (Ω_i) do not appear in V , the presence of constant external torques may lead to excessive momentum buildup and wheel saturation at the end of the maneuver. If Ω_i are included, a suitable control law may not be easily obtained. Moreover, using reaction wheels and thrusters simultaneously may not be practical for slewing maneuvers of tumbling spacecraft with short maneuver times. For this purpose it may be advantageous to use thrusters for the maneuver in the large and reaction wheels for high precision terminal control. In the small range, the assumption of linearity may be used to select the gains K_{ji} . For fast response times, the gains may be determined through the critical damping condition.

IV. Maneuvers With Thrusters

In this section, large-angle maneuvers with on-off thrusters are considered. Minimum time and

fuel optimal control problems can be easily formulated and necessary conditions for optimality derived by using optimal control theory. Generally, the thrusters are either required to switch between their upper and lower bounds, or remain off for a finite duration, depending on the signs of switching functions. The switching functions in turn are functions of the co-state variables. Moreover, for feedback control, the switching function should be expressible in terms of the state variables. For continuous external torque systems, it is possible to expand the co-state variables as a series in the state variables, with coefficients multiplying the linear, quadratic, cubic terms, and so on. The coefficients can then be selected such that as higher-order terms are included in the series, the approximate solution to the optimal co-state vector converges to the actual solution. One drawback of such a scheme is the need for an algebraic manipulator. The discontinuous thruster operations make this process more complicated, even though the sgn function can be expressed in terms of the hyperbolic tangent function, which in turn has a series representation with poor convergence properties.

In this paper, the feasibility of using the control laws developed for the reaction wheel systems as switching functions (with proper modifications) is examined. If this can be done with minimal modifications and provide acceptable performance, switching between the two modes of control can be achieved with ease.

As a preliminary study, two control laws are chosen as candidates:

$$\text{Control law I: } L_i = -\operatorname{sgn}[\beta_i + K_{1i} \omega_i] \quad (9)$$

$$\text{Control law II: } L_i = -\operatorname{sgn}[\beta_i + K_{2i} \omega_i \omega_i] \quad (10)$$

The second control law is reminiscent of that of the minimum time single-axis maneuver, with $K_{2i} = (I_i - J)/4L_0$, as β_i in the small are equivalent to half the angular displacements. The above control laws are now used to simulate a large-angle maneuver. The boundary conditions are given in Table 1. K_{1i} and K_{2i} are selected such that $K_{1i} = K_{2i} = (I_i - J)/4L_0$.

Table 1. Boundary conditions.

State	Initial Conditions	Final Conditions
β_0	0.6428	1
β_1	0.4423	0
β_2	0.4423	0
β_3	0.4423	0
ω_1	1.0 r/s	0
ω_2	0.5 r/s	0
ω_3	0.1 r/s	0

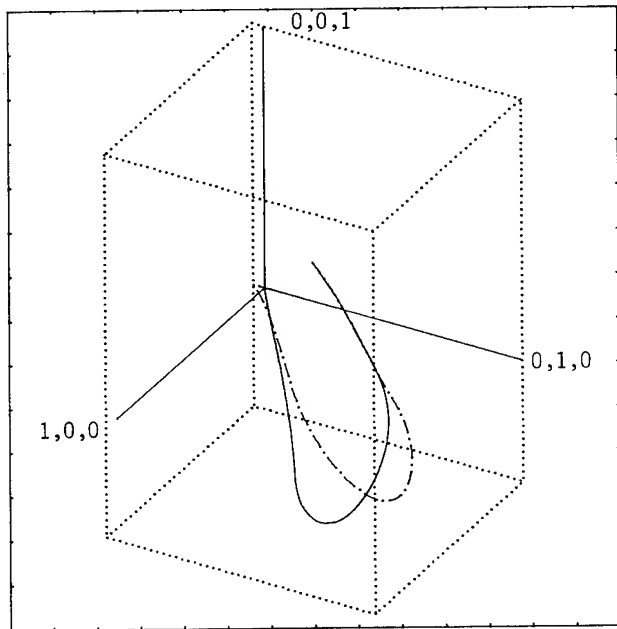


Fig. 1. Euler parameters ($\beta_1, \beta_2, \beta_3$)

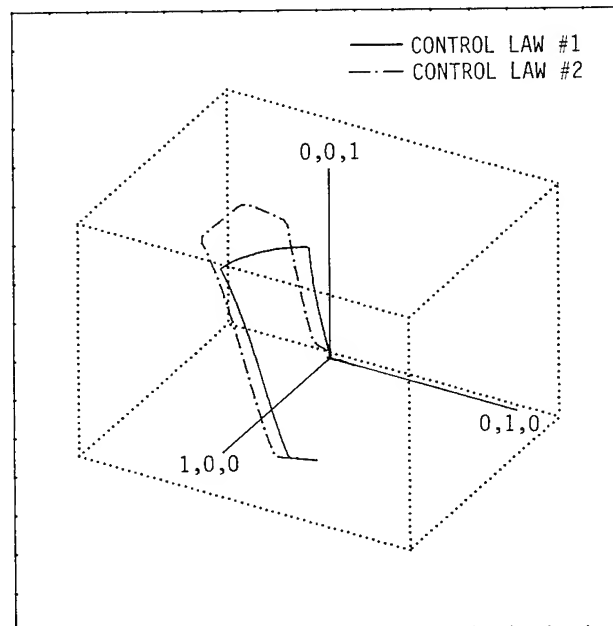


Fig. 2. Angular velocities ($\omega_1, \omega_2, \omega_3$)

I_1, I_2, I_3 are 86, 85, and 113 Kg m^2 , respectively, and $J = 0.05 \text{ Kg m}^2$. The magnitude of the torque due to each thruster is 20 Nm. Figures 1 and 2 show the Euler parameter and angular velocities respectively. For each maneuver the following performance index is evaluated:

$$J = \frac{1}{2} \int_0^{T_f} \left\{ 1 + \left[2(1 - \beta_0) + \sum_{i=1}^3 \omega_i^2 \right] \right\} dt \quad (11)$$

Note that $(1 - \beta_0)^2 + \sum \beta_i^2 = 2(1 - \beta_0)$, due to the Euler parameter constraint of equation 3. The final time and the value of the performance index are given in Table 2.

Table 2

Control Law #	J	T_f (sec)
1	15.43	16.8
2	11.86	10.32

It can be seen that the second control law allows the maneuver to be performed faster, with slightly lower state deviations, when compared with the first. In order to compare these maneuver times with that of an equivalent single axis maneuver of a spacecraft with $I_1 = 100 \text{ Kg m}^2$, $\omega(0) = 1 \text{ r/s}$, and the angular displacement $\theta(0) = \pi/2$, the maneuver time is computed by the following equation:

$$T'_f = \frac{I_1}{L_0} \omega(0) \text{sgn}[\xi(0)] + 2 \frac{I_1}{L_0} \theta(0) \text{sgn}[\xi(0)] + \frac{1}{2} \left[\frac{I_1}{L_0} \omega(0) \right]^2 \quad (12)$$

where

$$\xi = \theta + \frac{1}{2} \frac{I_1}{L_0} \omega |\omega|$$

For the above example, $T'_f = 14.02 \text{ sec}$, and it is comparable with the maneuver times for the two control laws.

Up to this point, only ideal switching has been considered. In practice, because of inertia and hysteresis effects, delays are present in the switching operations. These nonideal effects cause the controls to chatter. In order to investigate the nonideal behaviour of the above control laws, one must use the concept of Fillipov solutions^{5,6} to study the sliding motion, which is an idealization of the chatter phenomena in the vicinity of the switching surfaces. Specifically, the answers to questions such as "In what region of the phase plane does sliding occur?" and "Is the sliding motion stable?" are needed.

V. Nonideal Thrusting

The analysis of sliding modes is done by the "equivalent control method"⁶ in which the actual control is replaced by an equivalent control which idealizes the chattering motion (sliding) in the vicinity of the switching surfaces. The equivalent control for the n^{th} order system

$$\dot{\underline{x}} = \underline{f}(\underline{x}) + \underline{B} \underline{L}, \quad (13)$$

$$\underline{L}_i = -\operatorname{sgn}[S_i], \quad i = 1, 2, \dots, m,$$

$$\underline{S} = [S_1, S_2, \dots, S_m]^T$$

is given by

$$\underline{L}_{eq} = (\underline{GB})^{-1} \underline{G} \underline{f} \quad (14)$$

where

$$\underline{G} = \partial \underline{S} / \partial \underline{x} \text{ is an } m \times n \text{ matrix.}$$

If (\underline{GB}) is a diagonal matrix, then the sufficient conditions for sliding modes to exist are

$$\lim_{S_i \rightarrow 0^-} \dot{S}_i > 0 \quad (15)$$

and

$$\lim_{S_i \rightarrow 0^+} \dot{S}_i < 0. \quad (16)$$

The properties of the system (13) under sliding conditions are obtained by replacing \underline{L} in equation (13) by \underline{L}_{eq} from equation (14). The two control laws chosen previously are now studied for sliding conditions.

Control Law 1

$$S_i = \beta_i + \frac{I_i - J}{4L_0} \omega_i \quad i = 1, 2, 3. \quad (17)$$

It can be shown from equations (15) and (16) that sliding conditions may exist if the following conditions are satisfied on the switching curves

$$\begin{aligned} & \left| [\beta_0 \omega_1 - \beta_3 \omega_2 + \beta_2 \omega_3] / 2 \right. \\ & \quad \left. + \frac{1}{4L_0} [(I_2 - I_3) \omega_2 \omega_3] \right| < \frac{1}{4} \\ & \left| [\beta_3 \omega_1 + \beta_0 \omega_2 - \beta_1 \omega_3] / 2 \right. \\ & \quad \left. + \frac{1}{4L_0} [(I_3 - I_1) \omega_3 \omega_1] \right| < \frac{1}{4} \\ & \left| [-\beta_2 \omega_1 + \beta_1 \omega_2 + \beta_0 \omega_3] / 2 \right. \\ & \quad \left. + \frac{1}{4L_0} [(I_1 - I_2) \omega_1 \omega_2] \right| < \frac{1}{4} \quad (18) \end{aligned}$$

For sufficiently small states, these conditions may be satisfied. On the switching curves ($S_i = 0$)

$$\beta_i = -\frac{I_i - J}{4L_0} \omega_i \quad i = 1, 2, 3 \quad (19)$$

Hence the dimension of the state space can be reduced to 4. In order to examine the stability of the system, consider the Liapunov function

$$V = (\beta_0 - 1)^2 + \sum_{i=1}^3 \beta_i^2 \quad (20)$$

It can be shown that

$$\dot{V} = \sum_{i=1}^3 \beta_i \omega_i \quad (21)$$

Equations (19) and (21) show that \dot{V} is a negative definite function. Hence the sliding motion is stable.

Similar analysis for the second control law reveals that it too has stable sliding properties, and the time derivative of the Liapunov function of equation (20) yields

$$\dot{V} = - \sum_{i=1}^3 \frac{I_i - J}{4L_0} \omega_i^2 |w_i| \quad i = 1, 2, 3 \quad (22)$$

VI. Conclusions

The large-angle maneuver problem of spacecraft with reaction wheels and on-off thrusters is treated. The feedback controls for reaction wheels are obtained by the use of Liapunov theory. The switching functions for the thrusters are the same as the reaction wheel controls. Simulations indicate that these controls, even though not optimal in any sense, perform satisfactorily. Moreover, since the same functions are used for both modes of controls, switching from thruster mode to reaction wheel mode can be accomplished easily.

For nonideal thrusting, stability in the small has been verified through Filipov solutions to the sliding modes. Since chattering phenomena may not be ideal for fragile spacecraft, it may be necessary to switch from thrusters to reaction wheels when the sliding conditions are satisfied. These studies are currently in progress.

VII. References

1. Carrington, C. K. and Junkins, J. L., "Optimal Nonlinear Feedback Control for Spacecraft Attitude Maneuvers," Paper No. 83-2230-CP, AIAA Guidance and Control Conference, Gatlinburg, Tennessee, Aug. 1983.
2. Dwyer, T. A. W., "Design of an Exact Nonlinear Model Follower for the Control of Large Angle Rotational Maneuvers," Proc. 22nd IEEE Conference on Decision and Control, San Antonio, Texas, Dec. 14-16, 1983.
3. Vadali, S. R. and Junkins, J. L., "Optimal Openloop and Stable Feedback Control of Rigid Spacecraft Attitude Maneuvers," Paper No. 83-373, AAS/AIAA Astrodynamics Specialist Conference, Lake Placid, New York, Aug. 1983.

4. Vadali, S. R. and Junkins, J. L., "Spacecraft Large Angle Rotational Maneuvers with Optimal Momentum Transfer," The Journal of Astronautical Sciences, Vol. XXXI, No. 2, pp. 217-235, April-June, 1983.
5. Ryan, E. P., Optimal Relay and Saturating Control System Synthesis, Peter Peregrinus, Stevenage, U.K., 1982.
6. Utkin, V. I., "Variable Structure Systems with Sliding Modes," IEEE Transactions on Automatic Control, pp. 212-222, April 1977.

Bong Wie* and Peter M. Barba**

Ford Aerospace & Communications Corporation
Palo Alto, CaliforniaAbstract

This paper presents the stability and control analysis for large angle feedback reorientation maneuvers using reaction jets. Strapdown inertial reference system provides spacecraft attitude changes in terms of quaternions. Reaction jets with pulse-width pulse-frequency modulation provide proportional control torques. The use of quaternions as attitude errors for large angle feedback control is investigated. Closed-loop stability analysis for the 3-axis maneuvers is performed using the Liapunov's stability theorem. Unique characteristics of the quaternion feedback are discussed for single-axis motion using a phase-plane plot. The practical feasibility of a 3-axis large angle feedback maneuver is demonstrated by digital simulations.

Introduction

In many future spacecraft missions, large angle reorientation/slew maneuvers will be required. Conventional single-axis small angle feedback controls may not be adequate for the 3-axis large angle maneuvers. Many open-loop schemes (for example, see [1, 2]) have been proposed for large angle maneuvers. The purely open-loop maneuvers do not require any measurement for feedback, thus, there is no possibility of the closed-loop instability. However, in practice, they are sensitive to the spacecraft parameter uncertainties and to the unexpected disturbances. In general, combination of feedforward/feedback controls are desirable.

In an earlier work, Mortensen [3, 4] suggested the use of Cayley-Rodriguez parameters and quaternions as attitude errors for large angle feedback control. He extended the conventional linear regulator concept to the case of 3-axis large angle motion. Hrastar [5] applied Mortensen's control logic to the large angle slew maneuver of an Orbiting Astronomical Observatory (OAO) spacecraft. Recently, similar feedback control logic was compared with the model-reference adaptive slew maneuver about the Euler axis [6].

In most of the slew maneuver studies, reaction wheels have been extensively used for torquing devices. The use of on-off reaction jets for slew maneuvers is also often required. The so-called "bang-off-bang" may be the most common maneuver profile using the on-off reaction jets. Rapid slew maneuver about the Euler axis using reaction jets has been investigated by D'Amaro and Stubbs [7].

Index Category: Spacecraft Dynamics and Control

* Engineering Specialist, Systems Analysis Dept.,
Member AIAA

** Principal Engineer, Systems Analysis Dept.,
Member AIAA

In general, it is necessary to know the spacecraft attitude at all times for feedback controls. The large angle orientation can be represented by direction cosine matrix, Euler angles, or by quaternions. Quaternions [8, 9], also called Euler parameters, allow the description of the spacecraft orientation in all possible attitudes. Quaternions have no inherent geometrical singularity as do Euler angles; there are no singularities in the kinematical differential equations as do Cayley-Rodriguez parameters; and successive rotations follow the quaternion multiplication rules. Moreover, quaternions are well-suited for onboard real time computation since only products and no trigonometric relations exist in the quaternion equations. Thus, spacecraft orientation is now commonly described in terms of quaternions (e.g., HEAO, space shuttle, and Galileo [10]).

This paper presents the stability and control analysis of 3-axis large angle feedback maneuvers for a spacecraft which has an onboard microprocessor and strapdown inertial reference system. The rate integrating gyros operate in a pulse rebalance loop to provide incremental angle changes to the quaternion integration algorithm. The spacecraft has also earth and sun sensors, but not star sensor. Nearly proportional control torques are provided by pulse-width pulse-frequency modulated reaction jets. The use of quaternions as attitude errors for large angle feedback control will be investigated. Characteristics of quaternion feedback will be discussed using phase-plane plot for single-axis motion. Closed-loop stability analysis of quaternion feedback will be performed by using Liapunov's stability theorem. The practical feasibility of the large angle feedback maneuver will be demonstrated by digital simulations.

Reorientation Maneuver Requirements

Future spacecraft systems may use an integrated high efficiency bi-propellant propulsion system for both apogee and perigee maneuvers thereby reducing space shuttle launch costs. The orbital maneuvers will then be performed in the 3-axis stabilized mode in order to control a spacecraft with high liquid mass-fraction.

One of the unique characteristics of this system is the non-spinning deployment from the space shuttle. Many current satellites, which are 3-axis stabilized in orbit, are spin-stabilized during orbit injection. Thus, they are deployed from the space shuttle as spin-stabilized. However, if the spacecraft is 3-axis stabilized by using gimbaled main engine during perigee maneuver, then it may be beneficial to have non-spinning deployment from the shuttle. Reaction jets with 5-lb thrust level are being considered for 3-axis attitude control of the spacecraft shown in Fig. 1.

Imperfect deployment could induce an initial tip-off rotational rate which may induce large angle tumbling motion, if it is not actively controlled. However, the reaction jets should be disabled until the spacecraft is separated from the space shuttle by 200 ft, due to the shuttle safety requirement. The coast period without an active attitude control is about 200 sec since the expected deployment rate is 1 ft/sec for the spacecraft considered in this paper. During this period, the spacecraft will coast with large attitude drift due to an initial deployment tip-off rate of 0.5 deg/sec in its transverse axes (negligible in longitudinal axis). The strapdown inertial reference system must track the spacecraft's attitude drift during this coast period. After being separated from the space shuttle by 200 ft, the reaction jets are enabled to reorient the spacecraft to its desired attitude. Thus, the spacecraft may require a large angle reorientation maneuver up to 180 degrees.

The perigee orbit injection maneuver requires a total velocity pointing error of ± 3 deg (3 sigma). Part of the pointing error is due to the attitude determination error which includes the bias and scale factor errors of the gyros and also the computational error of the strapdown attitude algorithm. The reorientation pointing requirement is allocated as ± 0.5 deg (3 sigma) which is mainly due to attitude determination errors. A functional block diagram for the attitude determination and control system is shown in Fig. 2.

Attitude Determination and Control

Consider the general case of a rigid spacecraft rotating under the influence of body-fixed torquing devices. The Euler equations of motion about the principal axes of inertia are:

$$I_1 \dot{\omega}_1 + (I_3 - I_2) \omega_2 \omega_3 = T_1 \quad (1a)$$

$$I_2 \dot{\omega}_2 + (I_1 - I_3) \omega_1 \omega_3 = T_2 \quad (1b)$$

$$I_3 \dot{\omega}_3 + (I_2 - I_1) \omega_1 \omega_2 = T_3 \quad (1c)$$

where $(\omega_1, \omega_2, \omega_3)$, (I_1, I_2, I_3) , and (T_1, T_2, T_3) are the spacecraft angular rates, the moments of inertia, and the control torques about the principal axes, respectively.

Euler's rotational theorem states that the rigid body attitude can be changed from any given orientation to any other orientation by rotating the body about an axis, called the Euler-axis, that is fixed to the rigid body and stationary in inertial space. The quaternion then defines the spacecraft attitude as an Euler-axis rotation from an inertial reference frame. The four elements of quaternions are defined as:

$$Q_1 = C_1 \sin(\phi/2) \quad (2a)$$

$$Q_2 = C_2 \sin(\phi/2) \quad (2b)$$

$$Q_3 = C_3 \sin(\phi/2) \quad (2c)$$

$$Q_4 = \cos(\phi/2) \quad (2d)$$

where ϕ is the magnitude of the Euler-axis rotation and (C_1, C_2, C_3) are the direction cosines of the Euler axis relative to the inertial reference frame.

The kinematical differential equations for the quaternion are:

$$2\dot{Q}_1 = \omega_1 Q_4 - \omega_2 Q_3 + \omega_3 Q_2 \quad (3a)$$

$$2\dot{Q}_2 = \omega_1 Q_3 + \omega_2 Q_4 - \omega_3 Q_1 \quad (3b)$$

$$2\dot{Q}_3 = -\omega_1 Q_2 + \omega_2 Q_1 + \omega_3 Q_4 \quad (3c)$$

$$2\dot{Q}_4 = -\omega_1 Q_1 - \omega_2 Q_2 - \omega_3 Q_3 \quad (3d)$$

with the constraint equation of quaternion unit norm

$$Q_1^2 + Q_2^2 + Q_3^2 + Q_4^2 = 1$$

The initial condition of Q_1 in Eq. (3) defines the initial spacecraft attitude w.r.t. the inertial reference frame. For example, initial quaternions of $(0, 0, 0, 1)$ define that the spacecraft is initially aligned with the inertial reference frame.

For small attitude changes from the inertial reference frame ($Q_1 = Q_2 = Q_3 \approx 0, Q_4 \approx 1$), we have $2\dot{Q}_1 = \omega_1$, $2\dot{Q}_2 = \omega_2$, and $2\dot{Q}_3 = \omega_3$ from Eq. (3). Thus, the following approximations hold for small angles: $\theta_1 = 2Q_1$, $\theta_2 = 2Q_2$, and $\theta_3 = 2Q_3$ where $(\theta_1, \theta_2, \theta_3)$ are the conventional Euler angles. For a simple rotation about the fixed Euler-axis, we also have the relations: $\omega_1 = C_1 \dot{\phi}$, $\omega_2 = C_2 \dot{\phi}$, and $\omega_3 = C_3 \dot{\phi}$ where C_1, C_2 , and C_3 are constant direction cosines of the Euler-axis w.r.t. the inertial reference frame.

The quaternion kinematical differential equations are linear with time-varying coefficients for known body rates. They have repeated eigenvalues at

$$\pm j \sqrt{\omega_1^2 + \omega_2^2 + \omega_3^2} / 2.$$

In other words, the quaternion equations are neutrally stable for any value of angular rate input. This property may cause some difficulty in the numerical integration of the quaternion equations. All explicit numerical methods which are suitable for real-time computation have stability boundaries that do not include the imaginary axis except the origin. Therefore, any truncation or roundoff errors introduced in the computation will, in general, not die out. The strapdown attitude algorithm to be implemented in the onboard microprocessor will be discussed later.

The quaternion feedback control laws to be considered in this paper are:

Control Law #1

$$T_1 = -T_c [Kq_1 + K_1 \omega_1] \quad (4a)$$

$$T_2 = -T_c [Kq_2 + K_2 \omega_2] \quad (4b)$$

$$T_3 = -T_c [Kq_3 + K_3 \omega_3] \quad (4c)$$

Control Law #2

$$T_1 = -T_c [Kq_1/q_4^3 + K_1\omega_1] \quad (5a)$$

$$T_2 = -T_c [Kq_2/q_4^3 + K_2\omega_2] \quad (5b)$$

$$T_3 = -T_c [Kq_3/q_4^3 + K_3\omega_3] \quad (5c)$$

Control Law #3

$$T_1 = -T_c [\text{sgn}(q_4) Kq_1 + K_1\omega_1] \quad (6a)$$

$$T_2 = -T_c [\text{sgn}(q_4) Kq_2 + K_2\omega_2] \quad (6b)$$

$$T_3 = -T_c [\text{sgn}(q_4) Kq_3 + K_3\omega_3] \quad (6c)$$

where

$$\begin{bmatrix} q_1 \\ q_2 \\ q_3 \\ q_4 \end{bmatrix} = \begin{bmatrix} \bar{q}_4 & \bar{q}_3 & -\bar{q}_2 & -\bar{q}_1 \\ -\bar{q}_3 & \bar{q}_4 & \bar{q}_1 & -\bar{q}_2 \\ \bar{q}_2 & -\bar{q}_1 & \bar{q}_4 & -\bar{q}_3 \\ \bar{q}_1 & \bar{q}_2 & \bar{q}_3 & \bar{q}_4 \end{bmatrix} \begin{bmatrix} Q_1 \\ Q_2 \\ Q_3 \\ Q_4 \end{bmatrix} \quad (7)$$

where q_i is the control error quaternion, Q_i is the commanded attitude quaternion w.r.t. the inertial reference frame, \bar{Q}_i is the currently estimated spacecraft quaternion w.r.t. the inertial reference frame, and T_c is the control torque level of reaction jets; K and K_i are positive control gains.

Eq. (7) is the result of successive quaternion rotations using the quaternion multiplication and inversion rules. The control error quaternion, q_i , is simply the current spacecraft attitude quaternion w.r.t. the commanded attitude. For a special case of attitude regulation w.r.t. the inertial reference frame, the commanded quaternion is $(0, 0, 0, 1)$. Then, the currently estimated spacecraft quaternion simply becomes the control error quaternion. Also for an inertially-fixed commanded attitude quaternion, Q_i becomes the control error quaternion with re-initialization using Eq. (7).

The three control laws presented above are analogous to a conventional feedback control law in that the control torque is a function of position and rate. The first is linear feedback of state variables, while the second and third are nonlinear feedback control. The pulse-width pulse-frequency modulator was considered as a linear device in the above equations. The theoretical background of such assumption will be discussed later.

A Special Case of Single-Axis Large Angle Rotation

Some physical insight of the quaternion feedback control laws can be obtained by considering a single-axis large angle rotation. The closed-loop equations with the control laws #1, 2, and 3 can then be written as:

Control Law #1:

$$I\ddot{\phi} + T_c K_R \dot{\phi} + T_c K \sin(\phi/2) = 0 \quad (8a)$$

Control Law #2:

$$I\ddot{\phi} + T_c K_R \dot{\phi} + T_c K \sin(\phi/2)/\cos^3(\phi/2) = 0 \quad (8b)$$

Control Law #3:

$$I\ddot{\phi} + T_c K_R \dot{\phi} + T_c K \text{sgn}[\cos(\phi/2)] \sin(\phi/2) = 0 \quad (8c)$$

where ϕ is the single-axis attitude error, and attitude control about the origin is considered here.

We notice that the closed-loop equations have linear viscous damping and nonlinear "spring" terms. Eq. (8a) is similar to the nonlinear equation of a simple pendulum with viscous damping. Thus, the closed-loop behavior of the control law #1 is very much similar to the nonlinear behavior of a simple pendulum with large angle motion [17, 18].

A typical phase-plane plot of Eq. (8a) is shown in Fig. (3). Every trajectory, other than the separatrices going into the saddle points, ultimately approaches one of the stable equilibrium points. The number of full rotations before reaching the equilibrium point depends on the initial magnitude of rate. As to be expected, the greater the initial rate, the greater the number of full rotation before reaching the stable equilibrium point.

The separatrices come into the saddle points at $\phi = \pm 2\pi, \pm 6\pi, \dots$, whereupon the spacecraft has the choice of rotating either in the same direction or backward. Such saddle points in Fig. (3) correspond to the upside down position of a simple pendulum problem (but with $\phi = 180$ deg). The stable equilibrium points are $\phi = 0, \pm 4\pi, \dots$ as can be seen from Eq. (8a). For the control law #1, the saddle points correspond to $Q_4 = -1$; the stable equilibrium points correspond to $Q_4 = 1$. It is important to note that both the saddle and stable points in Fig. 3 correspond to the physically identical orientation.

Similar phase-plane plots for Eqs. (8b) and (8c) can also be constructed, which have saddle points at $\phi = \pm\pi, \pm 3\pi, \dots$ and stable equilibrium points at $\phi = 0, \pm 2\pi, \pm 4\pi, \dots$. Simple phase-plane interpretation discussed here may be useful to gaining physical insight into 3-axis large angle motion.

Liapunov Nonlinear Stability Analysis

Closed-loop stability is the major concern in any feedback control system design. If the system is linear and time-invariant, many stability criteria are available. If the system is nonlinear, such stability criteria do not apply. For small angles, the system with the control laws discussed previously become the classical single-axis position and rate feedback, which is well-known to be closed-loop stable. For single-axis large angle motion, the stability can be easily studied using phase-plane plot, as discussed before. However, for 3-axis large angle motion, it is not obvious whether such control laws can provide global

closed-loop stability or not.

The Liapunov second method (also known as the Liapunov direct method) to be used in this paper may be the most general method for the determination of stability of nonlinear systems. By using the Liapunov second method, we can determine the stability of a system without solving the state equations. Only inertially-fixed commanded attitude quaternion is considered here.

First, consider the control law #1. After substituting Eqs. (4) and (7) into the Euler equations, multiply each equation by ω_1 , ω_2 , and ω_3 , respectively. After multiplying each equation of Eq. (3) by $T_c K(Q_1 - \bar{Q}_1)$, $T_c K(Q_2 - \bar{Q}_2)$, $T_c K(Q_3 - \bar{Q}_3)$, and $T_c K(Q_4 - \bar{Q}_4)$ respectively, add these equations to the previously modified Euler equations. We then have

$$\dot{V} = \sum_{i=1}^3 I_i \dot{\omega}_i \omega_i + 2T_c K \sum_{i=1}^4 \dot{Q}_i (Q_i - \bar{Q}_i) = -T_c \sum_{i=1}^3 K_i \omega_i^2 < 0 \quad (9)$$

A positive definite Liapunov function, V , can then be found as

$$V = 1/2 \sum_{i=1}^3 I_i \omega_i^2 + T_c K \sum_{i=1}^4 (Q_i - \bar{Q}_i)^2 > 0 \quad (10)$$

Thus, the closed-loop system with the control law #1 is asymptotically stable in the large, since $\dot{V} < 0$, $\lim_{t \rightarrow \infty} V(x) = 0$ and $\lim_{t \rightarrow \infty} V(x) \rightarrow \infty$, where x is the state vector. The stable equilibrium point with this control law is: $\omega_1 = \omega_2 = \omega_3 = 0$ and $Q_i = \bar{Q}_i$ ($i = 1, 2, 3, 4$). Thus, this control law reorients the spacecraft to the desired attitude from an arbitrary initial orientation.

Similarly, for the control law #2, substitute Eqs. (5) and (7) into the Euler equations, then multiply each equation by $2\omega_1$, $2\omega_2$, and $2\omega_3$ respectively. Multiply each equation of Eq. (3) by $-T_c K(Q_i + 2Q_i/q_4)$, $i = 1, 2, 3, 4$. Add these equations to the previously modified Euler equations, we then have

$$\begin{aligned} \dot{V} &= 2 \sum_{i=1}^3 I_i \dot{\omega}_i \omega_i - 2T_c K \sum_{i=1}^4 \dot{Q}_i (Q_i + \bar{Q}_i) + 2T_c K(1-2q_4^{-3}) \dot{q}_4 \\ &= -2T_c \sum_{i=1}^3 K_i \omega_i^2 < 0 \end{aligned} \quad (11)$$

A positive definite Liapunov function, V , can then be found as

$$\begin{aligned} V &= \sum_{i=1}^3 I_i \omega_i^2 - T_c K \sum_{i=1}^4 (Q_i + \bar{Q}_i)^2 + 2T_c K(q_4 + q_4^{-2}) \\ &= \sum_{i=1}^3 I_i \omega_i^2 + 2T_c K(-1 + q_4^{-2}) > 0 \quad (\text{since } |q_4| \leq 1) \end{aligned} \quad (12)$$

Thus, the closed-loop system with the control law #2 is also asymptotically stable in the large, since $\dot{V} < 0$, $\lim_{t \rightarrow \infty} V(x) = 0$, $\lim_{t \rightarrow \infty} V(x) \rightarrow \infty$.

Note that there exist two asymptotically stable equilibrium points with the second control law:

$Q_i = +\bar{Q}_i$, $i = 1, 2, 3, 4$. The equilibrium point with $Q_i = -\bar{Q}_i$ is physically the same orientation with $Q_i = \bar{Q}_i$. For an initial error of $q_4 < 0$, the second control law becomes positive position feedback; it provides a shorter path and least action to reach the desired equilibrium point.

For small angles, the three control laws provide the same linear performance. However, for large angles, they provide significantly different performances. The q_4 becomes zero as the Euler rotation angle, ϕ , becomes 180 degrees. Thus, the second control law can result in a nearly infinite control signal for certain initial orientations. The first control law, however, never results in such a situation since the magnitude of q_i ($i = 1, 2, 3$) is never greater than one. For an initial orientation with $q_4 < 0$, however, the second control law provides more efficient reorientation maneuvers as discussed before.

The 3rd control law provides an efficient reorientation maneuver for an arbitrary initial orientation without the possibility of an infinite control signal. Feedforward time-varying slew command can also be generated to achieve smooth and time- and/or fuel-optimal maneuvers. In this paper, we consider feedback reorientation maneuvers with simple step attitude change command; time-varying slew command [7, 16, 20] is not considered.

In the previous stability analysis, the position gain has been restricted to be the same in each axis. Such a restriction resulted in an easy determination of the Liapunov function. It doesn't mean that the control laws discussed before become unstable without such constraint. Asymptotic stability in the large has not yet been proven when different position gain is used in each axis. Although we can't conclude anything about global stability from the stability of linearized system, it is known that when a linearized system is asymptotically stable the nonlinear system from which it is derived is also asymptotically stable [17].

Consider the control law #1 with different position gain in each axis. When the closed-loop system is linearized near the equilibrium point, the result is three uncoupled linear second-order systems. These are easily proven asymptotically stable by conventional methods. Thus, the original nonlinear system is also asymptotically stable with different position gain in each axis.

For a special case of 3-axis large angle motion but with small angular rate, the global stability of the control laws (#1, 2, 3) with different position gain in each axis can also be easily proved by Liapunov stability theorem.

PWPF Modulator

The Pulse-Width Pulse-Frequency (PWPF) modulator has been assumed as a linear device in the previous analysis. In this section, the theoretical background of such assumption will be briefly discussed. The PWPF modulator shown in Fig. 4a produces a pulse command sequence to the thruster valve by adjusting the pulse width and pulse frequency. In the linear range, the average torque produced equals the demanded torque input. The pulse width is very short and the pulse frequency is usually fast compared to the spacecraft rigid body dynamics.

The static characteristics of the modulator are good enough for rigid spacecraft attitude control, while the dynamic characteristics of the modulator are needed for flexible spacecraft attitude control, e.g., see Wie and Plescia [15].

With a constant input, the PWPF modulator drives the thruster valve with an on-off pulse sequence having a nearly linear duty cycle with input amplitude. The duty cycle or modulation factor is defined as the average output of the modulator. The static characteristics of the continuous-time modulator for a constant input E are as follows:

$$\text{Minimum Pulse Width} \cong T_m h / K_m U_m \quad (14a)$$

$$\text{Internal Deadband} \quad E_d = U_{on} / K_m \quad (14b)$$

$$\text{Saturation Level} \quad E_s = U_m + U_{off} / K_m \quad (14c)$$

where $h \triangleq U_{on} - U_{off}$ = hysteresis width.

The U_{on} , U_{off} , K_m , and T_m are the design parameters of the modulator. A typical plot of the duty cycle which is nearly linear over the range above deadband and below saturation is shown in Fig. 4b.

A discrete-time PWPF modulator for microprocessor implementation is also shown in Fig. 4c. The modulator gets an input signal every T sec and causes pulse command updates every $T/4$ sec. Equation (13a) derived for a continuous-time modulator becomes invalid for a discrete-time modulator. An equality relation for the discrete-time modulator with $T/4$ sec minimum pulse width can be obtained as

$$h < K_m U_m T / 4 T_m < 2 U_{on} \quad (15)$$

where T is the microprocessor sampling period.

The modulator provides an effective loop gain reduction at lower frequency and additional phase lag at higher frequency. The phase lag of the modulator decreases as the time constant T_m decreases. Detailed describing function analysis of the modulator can be found from Ref. [15].

Quaternion Integration for Strapdown Inertial Reference

There are a number of numerical methods available for solving the quaternion equations. Methods which can be applied to the strapdown attitude algorithms include Taylor series expansion [5, 16], rotation vector concept [10-12], Runge-Kutta algorithms, and state transition matrix [13]. Of these methods, the Taylor series expansion lends itself well to the use of an incremental angle output from the digital rate integrating gyros.

The strapdown attitude algorithm using the 4th-order Taylor series expansion, which requires only the current information from the gyros can be written as [16]:

$$\begin{aligned} Q_1(t+T) = & Q_1(t) + R_1(t) - D^2 Q_1(t) \\ & \text{1st} \quad \text{2nd} \\ & - D^2 R_1(t)/3 + D^4 Q_1(t)/6 \\ & \text{3rd} \quad \text{4th-order} \end{aligned} \quad (16)$$

$$\text{where } D^2 = (\Delta\theta_1)^2 + (\Delta\theta_2)^2 + (\Delta\theta_3)^2$$

$$R_1 = 1/2 [\Delta\theta_1 Q_4 - \Delta\theta_2 Q_3 + \Delta\theta_3 Q_2]$$

$$R_2 = 1/2 [\Delta\theta_1 Q_3 + \Delta\theta_2 Q_4 - \Delta\theta_3 Q_1]$$

$$R_3 = 1/2 [-\Delta\theta_1 Q_2 + \Delta\theta_2 Q_1 + \Delta\theta_3 Q_4]$$

$$R_4 = 1/2 [-\Delta\theta_1 Q_1 - \Delta\theta_2 Q_3 - \Delta\theta_3 Q_4]$$

and $\Delta\theta_1$, $\Delta\theta_2$, and $\Delta\theta_3$ are the incremental angle outputs from the gyros over the quaternion integration time step, T . The body rates to be used for feedback controls are simply $\Delta\theta_i/T$.

Different strapdown attitude algorithms can also be found from Refs. [10-12]. Such algorithms require the previous samples of the gyro outputs as well as the current outputs. For any algorithms there exist computational errors due to Taylor series truncation and microprocessor finite word length. Another type of error also exists known as degradation of quaternion unit norm length. However, this error can be eliminated by normalization of the quaternion update equation. Trade-off between algorithms complexity vs. algorithm truncation and roundoff errors is generally required.

Digital Simulation

A digital simulation was used to verify the practical feasibility of large angle feedback maneuvers. The spacecraft inertias are given in Fig. 1. The control torque level of reaction jets is assumed as 20 N-m in each axis, with negligible cross-axis coupling. The gyro has quantization of 0.9 arcsec/pulse, residual drift rate of 0.1 deg/hr, and scale factor error of 0.5%. It was assumed that only drift bias is estimated and calibrated in the shuttle before deployment. Thus, the scale factor error of 0.5% is relatively large and considered as the worst case. The 32-bit onboard microprocessor has 64 msec cycle time and 48 msec process delay.

The attitude determination error was defined as the difference between the true spacecraft attitude and the attitude computed from the strapdown inertial reference system using the gyros. Thus, the attitude errors consist of errors due to residual drift rate and scale factor error, and strapdown attitude update computational error. Because of a relatively fast sampling period of 64 msec, the pointing error is dominated by the gyro sensor error not by computational error. Thus, attitude update algorithm with the first-order Taylor was good enough for preliminary analysis and simulations. The true spacecraft attitude was computed by means of a 4th-order Runge-Kutta routine with integration time step of 16 msec in double precision.

The results of a typical simulation using the control law #1 are shown in Fig. 5 through 8. The desired attitude quaternion is assumed as (0, 0, 0, 1). The initial body rates are: $\omega_1 = \omega_2 = 0.53$ deg/sec and $\omega_3 = 0.053$ deg/sec. The control loop with $K = 0.5$ and $K_i = 200$ is enabled at $t = 200$ sec. Thus, for the reorientation maneuver, the initial orientation is: $Q_1 = 0.685$, $Q_2 = 0.695$, $Q_3 = 0.153$, and $Q_4 = 0.153$ with Euler rotation angle of 162 deg.

The spacecraft quaternions shown in Fig. 5 approach the desired value in a well-behaved manner. Figure 6 shows the time histories of the

body rates and the Euler rotation angles. Note that the Euler rotation angle decreases in an exponential manner. Figure 7 shows the time histories of the jet-firings. The periods of acceleration and deceleration, and attitude hold are evident. The jet firings are acceptable in practical sense, although the maneuver was not "optimal" like an ideal "bang-off-bang". Total jet firing time was 50 sec during the 300-sec reorientation and 500-sec attitude hold mode. Figure 7 also shows some measure of spacecraft attitude determination error, which meets the pointing requirement of 0.5 deg after reorientation maneuver. The attitude determination error increases as the spacecraft attitude drifts due to the scale factor error. Once the control loop is closed (at $t = 200$ sec), the pointing error decreases with an offset error. The offset error is due to the different path between the coast and the reorientation. The attitude error increases very slowly as time goes on due to the gyro drift bias.

The attitude-hold mode with $K = 100$ and $K_1 = 200$, which is automatically initiated at the end of the maneuver, maintains the attitude of the spacecraft inside the control loop deadband as shown in Fig. 8. The effective deadband angle was chosen as 0.1 degrees.

Conclusions

The stability and control analysis for large angle feedback reorientation maneuvers with strapdown inertial reference system have been presented. The control logic was a simple extension of the conventional feedback control to the 3-axis large angle coupled motion. Some physical interpretation of quaternion feedback was given using a phase-plane plot. Liapunov's stability theorem was used to determine the global stability of the closed-loop system. The maneuver discussed in this paper was not necessarily optimal in the theoretical sense of minimum time and/or fuel. However, the closed-loop system approached the desired attitude in a well-behaved manner. Dominant pointing error source was shown to be the effect of the gyro scale factor because of the nature of large-angle maneuvers.

References

1. Barba, P.M. and J.N. Aubrun, "Satellite Attitude Acquisition by Momentum Transfer," AIAA J. Vol. 14, No. 10, Oct., 1976.
2. Vadali, S.R. and J.L. Junkins, "Spacecraft Large Angle Rotational Maneuvers with Optimal Momentum Transfer," J. Astronautical Sciences, Vol. XXXI, No. 2, April-June, 1983.
3. Mortensen, R.E., "On Systems for Automatic Control of the Rotation of a Rigid Body," Electronics Research Lab., University of Calif. Berkeley, Rpt. No. 62-23, Nov. 27, 1963. (Also see J. Applied Mechanics, March 1965, pp. 228-230.)
4. Mortensen, R.E. "A Globally Stable Linear Attitude Regulator," International Journal of Control, Vol. 8, No. 3, pp. 297-302, 1968.
5. Hrstar, J., "Attitude Control of a Spacecraft with a Strapdown Inertial Reference System and Onboard Computer," NASA TN D-5959, Sept. 1970.
6. Bosch, P.P.J van den, et al., "An Adaptive Attitude Control System for Large Angle Slew Maneuvers," IFAC Automatic Control in Space, Netherland, 1982.
7. D'Amario, L.A. and G.S. Stubbs, "A New Single-Axis Autopilot for Rapid Spacecraft Attitude Maneuvers," J. Guidance and Control, Vol. 2, No. 4, July-Aug., 1979.
8. Margulies, G., "On Real Four-Parameter Representations of Satellite Attitude Motions," Mathematical Analysis Dept., Report No. 52, Philco Western Lab., Sept. 1963.
9. Kane, T.R., P.W. Likins, and D.A. Levinson, Spacecraft Dynamics, McGraw-Hill Book Company, 1983.
10. Wong, E.C. and W.G. Breckenridge, "Inertial Attitude Determination for a Dual-Spin Planetary Spacecraft," J. Guidance, Control and Dynamics, Vol. 6, No. 6, Nov.-Dec. 1983.
11. Miller, R.B., "A New Strapdown Attitude Algorithm," J. Guidance, Control and Dynamics, Vol. 6, No. 4, July-Aug. 1983.
12. McKern, R. and H. Musoff, "Strapdown Attitude Algorithms from a Geometric Viewpoint," J. Guidance and Control, Vol. 4, No. 6, Nov-Dec, 1981.
13. Mayo, R.A., "Relative Quaternion State Transition Relation," J. Guidance and Control, Vol. 2, No. 1, Jan.-Feb. 1979.
14. Bryson, A.E., Jr., Stabilization and Control of Flight Vehicles, Class Notes, Aero/Astro Dept., Stanford University, Stanford, CA., 1983.
15. Wie, B. and C.T. Plescia, "Attitude Stabilization of Flexible Spacecraft During Stationkeeping Maneuvers," AIAA Guidance and Control Conf., No. 83-2226, Gatlinburg, TN., Aug. 1983. (To be published in J. Guidance, Control and Dynamics).
16. Cunningham, D.C. et al., "System Design of the Annular Suspension and Pointing System (ASPS)," AIAA G & C Conf., No. 78-1311, Palo Alto, CA., 1978.
17. Struble, R.A., Nonlinear Differential Equations, McGraw-Hill Book Company, 1962. pp. 131-136.
18. Cannon, R.H., Dynamics of Physical Systems, McGraw-Hill Book Company, 1967. pp 355-370.
19. Ickes, B.P., "A New Method for Performing Control System Attitude Computation Using Quaternions," AIAA Journal, Vol. 8, No. 1, January 1970.
20. Breckenridge, W.G. and G.K. Man, "Quaternions for Galileo Scan Platform Control," AAS/AIAA Astrodynamics Specialist Conference Paper No. 83-321, Lake Placid, New York, Aug. 22-25, 1983.
21. Floyd, M.A. et al., "Implementation of a Minimum Time and Fuel On/Off Thruster Control System for Flexible Spacecraft," AAS/AIAA Astrodynamics Specialist Conference Paper No. 83-376, Lake Placid, New York, Aug. 22-25, 1983.

SPACECRAFT DEPLOYMENT FROM SPACE SHUTTLE

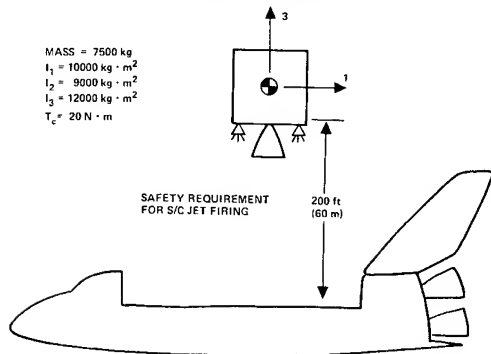


Figure 1.

ATTITUDE DETERMINATION AND CONTROL

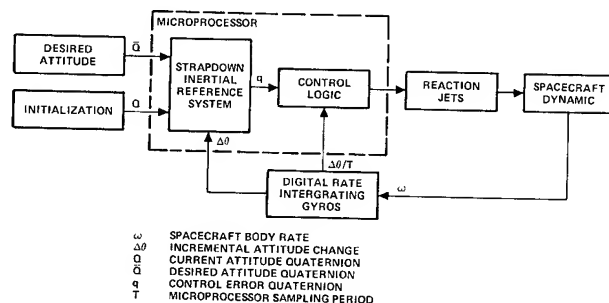


Figure 2.

PHASE-PLANE PLOT FOR SINGLE-AXIS ROTATION

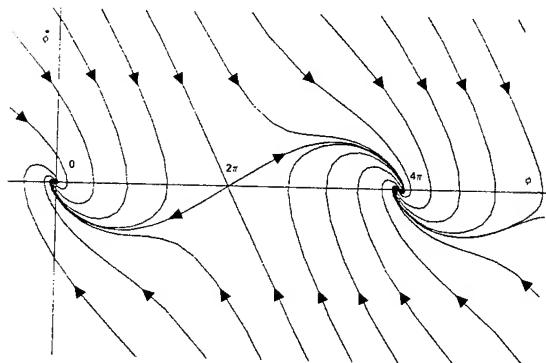


Figure 3.

PWPF MODULATOR

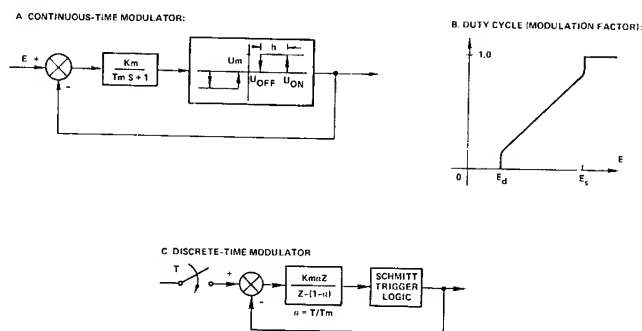


Figure 4.

DIGITAL SIMULATION RESULTS (QUATERNIONS)

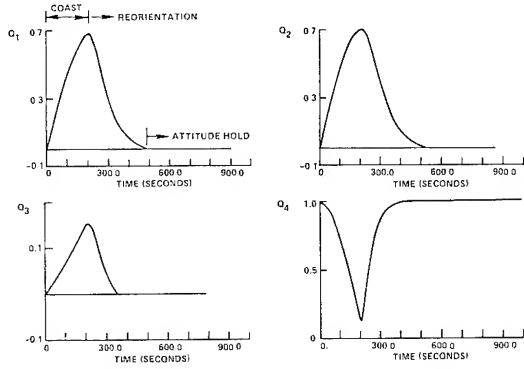


Figure 5.

DIGITAL SIMULATION RESULTS (BODY RATES AND EIGEN ANGLE)

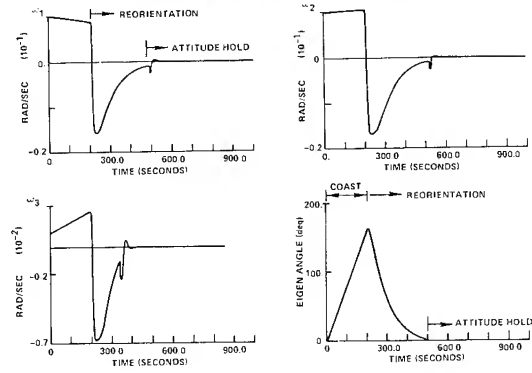


Figure 6.

DIGITAL SIMULATION RESULTS (THRUSTER ACTIVITY AND ATTITUDE ERROR)

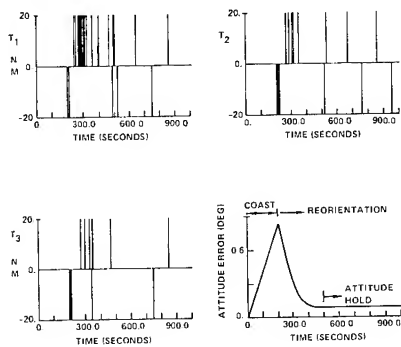


Figure 7.

DIGITAL SIMULATION RESULTS (STEADY-STATE LIMIT CYCLE)

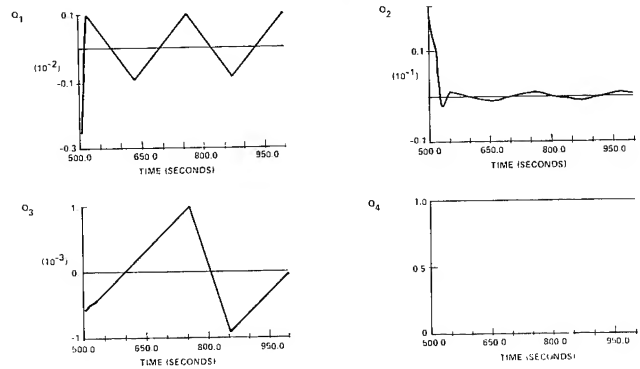


Figure 8.

D. C. Hyland*

Harris Corporation, GASD, Melbourne, FL 32902

Abstract

Several suboptimal approaches to reduced-order controller design are compared with the new optimal projection formulation of the quadratically optimal fixed-form compensator problem. The substantial similarities and significant differences among the various design techniques are highlighted by placing the design equations of all methods within a common notation. Basically, all methods characterize the reduced-order controller by a projection on the full state space. The suboptimal methods construct this projection on the basis of balancing considerations while the optimal projection equations define it as a consequence of optimality conditions. Issues relating to relative computational simplicity and design reliability are explored by applying two of the methods to the same example problem.

1. Introduction

The design of reduced-order dynamic controllers for high-order systems is of considerable importance for applications involving large spacecraft and flexible flight systems and extensive research has recently been devoted to this area. This paper reviews and compares, both theoretically and computationally, several current approaches to reduced-order controller design.

One procedure for addressing this problem is to first apply some suitable model reduction algorithm to reduce the plant model to the dimension desired for the controller and then obtain an LQG controller which is optimal for the reduced model. A second, and perhaps more satisfactory approach is to predicate the control design upon a higher order model and then to reduce the dimension of the controller. Of course, this technique presupposes that some form of model reduction is still employed to reduce the originally very high order plant model to a "Riccati-solvable" dimension.

Because they all reflect the latter "controller reduction" philosophy and exhibit significant similarities, we confine attention here to the following methods:

- 1) Balanced Controller Reduction Algorithm (BCRA)
--This is the internal balancing model reduction approach of Moore¹ applied to the controller reduction problem.
- 2) Balanced Controller Reduction Algorithm - Modified (BCRAM)
--A modification of BCRA by Yousuff and Skelton.²
- 3) Component Cost Algorithm (CCA)
--An application of Component Cost Analysis to this problem by Yousuff and Skelton.³

4) Optimal Projection Conditions (OPC)

--These design equations are actually the necessary stationarity conditions for quadratically optimal, fixed-order compensator design in the form originally derived in Reference 4. Subsequently, the derivation was significantly improved and strengthened by Hyland and Bernstein.⁵

5) Approximate Optimal Projection Conditions -- nth iterate (AOPC_n)

--This denotes the iterative algorithm, terminated at the nth iterate, for solution of the OPC as described in Reference 6. Under benign conditions, this algorithm is locally convergent so that AOPC_n becomes equivalent to OPC as $n \rightarrow \infty$.

A basic distinction among the above methods should be noted: (1) - (3) are admittedly suboptimal approaches based, essentially, upon balancing considerations while formulation (4) and its computational implementation (5) arise from consideration of quadratically optimal, fixed-order compensator design.

Of course, the stationary conditions for fixed-form compensation have been written down (see [7-12], for example). However, full exploitation of the stationary conditions has no doubt been retarded by their extreme complexity. What is lacking, to quote the insightful remarks of [11], "is a deeper understanding of the structural coherence of these equations." The contribution of References [4] and [5] was to show how the originally very complex stationary conditions can be reduced, without loss of generality, to much simpler and more tractable forms. The resulting equations preserve the simple form of LQG relations for the gains in terms of covariance and cost matrices, which, in turn, are determined by a coupled system of two modified Riccati equations and two modified Lyapunov equations. This coupling, by means of a projection (idempotent matrix) whose rank is precisely equal to the order of the compensator, represents a graphic portrayal of the demise of the classical separation principle.

The compensator form which naturally emerges from this formulation is fully defined by the gains and by the projection matrix, whose row and column spaces are, respectively, the observation and control subspaces of the compensator. In fact, the stationary conditions are of such a form that they determine this "optimal projection" together with the gains.

It must be emphasized that the emergence of such a compensator projection does not represent an a priori assumption regarding the controller structure but rather is a consequence of the first-order necessary conditions.

* Leader, Control Systems Analysis and Synthesis Group, Member, AIAA.

The highly structured character of the optimal projection conditions not only gives rise to direct numerical solution procedures (as has been illustrated in [6]) but also sheds light on the various suboptimal techniques. One aim of this paper is to elucidate the fundamental connections existing between the fixed-order compensator optimality conditions and the balancing approaches of methods 1-3.

Note that since method 4 above constitutes the optimality conditions for fixed-order compensation, it theoretically represents the "best" controller-order reduction scheme--i.e. it gives the minimum (zero) degree of suboptimality and can thus serve as a standard of comparison. On the other hand, solution of OPC via the iterative algorithm of method 5 entails more computational effort than methods 1-3. Thus, the second major goal of this paper is to examine the tradeoffs between the greater computational simplicity of methods such as 1-3 versus the possibilities of improved performance and design reliability offered by method 5.

The plan of the paper is as follows. After presenting the general problem formulation, we establish a common notation and display the basic equations of all methods side by side (see Table 1 below). This permits the various design approaches to be compared quite directly and introduces considerable efficiency in the discussion. After addressing several important theoretical issues, we finally apply a selection of the methods to a single numerical example which involves a 20 state reduced-order version (see Reference [13]) of the CSDL ACROSS Model No. 2. The theoretical and numerical results allow several conclusions to be drawn regarding the comparative efficiency and suboptimality of the several design methods. In particular, it is shown that with modest increase in computational effort the optimal projection approach produces stable and optimal designs in cases where in some suboptimal methods fail to yield stable designs.

2. Problem Statement - Setting Up a Common Notation

The problem addressed concerns the linear, finite-dimensional, time-invariant system:

$$\left. \begin{aligned} \dot{x} &= Ax + Bu + w_1; \quad x \in \mathbb{R}^N \\ y &= Cx + w_2; \quad y \in \mathbb{R}^P \end{aligned} \right\} \quad (1)$$

where x is the plant state, A is the plant dynamics matrix and B and C are control input and sensor output maps, respectively. w_1 is a white disturbance noise with intensity matrix $V_1 \geq 0$ and w_2 is observation noise with nonsingular intensity $V_2 > 0$.

The problem addressed by all the methods listed above is to design a constant gain dynamic compensator of the form:

$$\left. \begin{aligned} u &= -Kq, \quad u \in \mathbb{R}^l \\ \dot{q} &= A_c q + Fy, \quad q \in \mathbb{R}^{N_c} \\ N_c &< N \end{aligned} \right\} \quad (2)$$

such that the quadratic, steady-state performance index:

$$\left. \begin{aligned} J_s &\triangleq \lim_{t_1 \rightarrow \infty} J / |t_1 - t_0| \\ J &\triangleq \int_{t_0}^{t_1} dt \quad E[x^T R_1 x + u^T R_2 u] \\ R_1 &\geq 0, \quad R_2 > 0 \end{aligned} \right\} \quad (3)$$

is either minimized (subject to the structural constraints implicit in (2)) or at least, rendered as small as is practicable. The challenging aspect of the problem is that in accordance with practical implementation constraints associated with the limitations of on-line software, N_c (the dimension of the compensator) is chosen in advance to be some number which is less than the plant dimension.

Within the above problem formulation, it is now possible to distill all methods considered here into a common notation. Although reasonably obvious, the assertions made below beginning with equation (4) and concluding with equation (16) and Table 1 are substantiated for methods 1-3 in the Appendix. No additional confirmation is required for the optimal projection equations since the following ideas were explicitly stated for OPC in [4] and [5].

First, it can be shown that all design methods considered establish a projection of rank N_c :

$$\tau \in \mathbb{R}^{N \times N}, \quad \tau^2 = \tau, \quad \text{rank}(\tau) = N_c \quad (4)$$

which characterizes the observation and control subspaces encompassed by the compensator. Moreover, a factorization of τ is always employed (at least implicitly) which has the form:

$$\tau = g \Gamma g^T \quad (5.a)$$

where Γ and g are full-rank, $N_c \times N$ matrices satisfying:

$$\Gamma g^T = g \Gamma^T = I_{N_c} \quad (5.b)$$

Note that if τ is a projection, then Γ and g satisfying (5.b) always exist such that (5.a) holds.

Secondly, it can be shown that methods 1-5 all produce matrices K , F , A_c of the form:

$$\left. \begin{aligned} K &= \hat{K} g^T \\ F &= \Gamma \hat{F} \\ A_c &= \Gamma(A - \hat{F}C - B\hat{K})g^T \end{aligned} \right\} \quad (6)$$

where

$$\left. \begin{aligned} \hat{K} &= R_2^{-1} B^T P \\ \hat{F} &= Q C^T V_2^{-1} \end{aligned} \right\} \quad (7)$$

and where P and Q are both symmetric and positive semi-definite, $N \times N$ matrices.

In summary, all methods yield the closed-loop system equations:

$$\left. \begin{aligned} \dot{x} &= Ax - B\hat{K}g^Tq + w_1 \\ \dot{q} &= \Gamma(A - \hat{F}C - B\hat{K})g^Tq + \Gamma\hat{F}(Cx = w_2) \end{aligned} \right\} (8)$$

with \hat{K} and \hat{F} given by (7). In other words, the reduced-order compensator takes the form of a full-order compensator projected down to an N_C - dimensional subspace. The fact that (4) - (8) hold for the various suboptimal design methods was recently recognized in [14].

Thus, the principal distinction among the design methods rests in the manner in which P , Q and τ (or equivalently Γ and g) are constructed. To elucidate this matter, we first introduce the lemma (see [15]):

Lemma. Suppose $M_1 \in \mathbb{R}^{N \times N}$ and $M_2 \in \mathbb{R}^{N \times N}$ are positive semi-definite. Then the product $M \triangleq M_1 M_2$ is semi-simple (i.e. all Jordan blocks are of order unity) with real, non-negative eigenvalues.

For convenience, let us also set up some additional notation relating to semi-simple matrices. If $M \in \mathbb{R}^{N \times N}$ is semi-simple, then, for some non-singular ϕ :

$$M = \phi \lambda \phi^{-1} \quad (9)$$

where λ is the diagonal matrix of eigenvalues of M .

Now, letting u_K denote the K^{th} column of ϕ and v_K^T the K^{th} row of ϕ^{-1} , (9) may be expressed as:

$$M = \sum_{k=1}^N \lambda_K u_K v_K^T \quad (10.a)$$

where the sets of vectors $\{u_i\}$, $\{v_i\}$ are mutually biorthonormal--i.e.:

$$v_K^T u_j = \begin{cases} 1 & ; K = j \\ 0 & ; K \neq j \end{cases} \quad (10.b)$$

and where we adopt the convention that the λ_K 's are arranged in order of decreasing magnitude:

$$|\lambda_1| \geq |\lambda_2| \geq \dots \geq |\lambda_{N-1}| \geq |\lambda_N| \quad (10.c)$$

(10.a) is clearly analogous to the standard result for the spectral decomposition of a normal matrix. For this reason, we may term the quantify:

$$\pi_K[M] \triangleq u_K v_K^T \quad (11)$$

the eigen-projection of M associated with the K^{th} eigenvalue (under convention (10.c)). In view of (10.b), the $\pi_K[M]$ form a set of unit rank, mutually disjoint projections:

$$\left. \begin{aligned} (\pi_K[M])^2 &= \pi_K[M] \\ \pi_K[M] \pi_j[M] &= 0 \text{ if } K \neq j \end{aligned} \right\} (12)$$

and M is written:

$$M = \sum_{K=1}^N \lambda_K \pi_K[M] \quad (13)$$

with convention (10.c).

This notation together with:

$$\Sigma \triangleq BR_2^{-1}B^T, \quad \bar{\Sigma} \triangleq C^T V_2^{-1}C \quad (14)$$

$$\begin{aligned} A_P &\triangleq A - \Sigma P, \quad A_Q \triangleq A - Q \bar{\Sigma}, \quad \hat{A}_C \triangleq A - \Sigma P - Q \bar{\Sigma} \\ \hat{p} &\triangleq P \Sigma P, \quad \hat{q} \triangleq Q \bar{\Sigma} Q \end{aligned} \quad (15)$$

$$\tau_1 \triangleq I_N - \tau \quad (16)$$

allows us to state the basic design equations rather succinctly. Table 1 lists the equations determining P , Q and τ for BCRA, BCRAM, CCA, AOPC₁ and OPC, where P , Q , \hat{P} and \hat{Q} are required to be positive semi-definite. In view of the above Lemma, $\hat{Q}\hat{P}$ and $\hat{Q}\hat{P}$ are all semi-simple with real, non-negative eigenvalues. Thus all the methods displayed construct the projection τ as the sum of N_C (disjoint) eigenprojections associated with the N_C largest eigenvalues of a semi-simple matrix. Not shown in Table 1 is the computational algorithm, AOPC_n for solution of the optimal projection equations. This algorithm proceeds as follows:

AOPC_n

- 1) To start, set $\tau_0 = I_N$
- 2) Using the previous iterate, τ_{K-1} , for τ , solve the OPC equations for P , Q , \hat{P} and \hat{Q} .
- 3) Determine the eigenvalues and eigenvectors of $\hat{Q}\hat{P}$ and form the eigenprojections $\pi_K[\hat{Q}\hat{P}]$; $K = 1, \dots, N$.
(In general there will be $\tilde{N} > N_C$ non-zero eigenvalues. If there are exactly N_C non-zero eigenvalues at this point, then the OPC's are satisfied identically.)
- 4) Set τ_K equal to the sum of eigenprojections corresponding to the N_C largest eigenvalues of $\hat{Q}\hat{P}$.
- 5) Terminate if either (a) $K = n$ or (b) ratio of the $(N_C + 1)^{\text{th}}$ to the N_C^{th} eigenvalues of $\hat{Q}\hat{P}$ falls below some preassigned convergence tolerance, $\epsilon \ll 1$ (in which case the optimal projection conditions are satisfied to an acceptable approximation). Otherwise, increment K and return to Step 2.

In the following discussion, we shall constantly refer to Table 1 using the equation designations indicated--i.e. the first OPC equation will be referred to as Equation (OPC-a), etc.

Table 1

CCA	BCRA	BCRAM & AOPC ₁	OPC
$0 = PA + A^T P - \hat{P} + R_1$	$0 = PA + A^T P - \hat{P} + R_1$	$0 = PA + A^T P - \hat{P} + R_1$	$0 = PA + A^T P - \hat{P} + \tau_1^T \hat{P} \tau_1 + R_1$ (a)
$0 = QA^T + AQ - \hat{Q} + V_1$	$0 = QA^T + AQ - \hat{Q} + V_1$	$0 = QA^T + AQ - \hat{Q} + V_1$	$0 = QA^T + AQ - \hat{Q} + \tau_1 \hat{Q} \tau_1^T + V_1$ (b)
$0 = \hat{Q} \hat{A}_p^T + A_p \hat{Q} + \hat{Q}$	$0 = \hat{Q} \hat{A}_C^T + \hat{A}_C \hat{Q} + \hat{Q}$	$0 = \hat{Q} \hat{A}_p^T + A_p \hat{Q} + \hat{Q}$	$0 = \hat{Q} \hat{A}_p^T + A_p \hat{Q} + \hat{Q} - \tau_1 \hat{Q} \tau_1^T$ (c)
— — — — —	$0 = \hat{P} \hat{A}_C^T + \hat{A}_C^T \hat{P} + \hat{P}$	$0 = \hat{P} \hat{A}_Q + A_Q^T \hat{P} + \hat{P}$	$0 = \hat{P} \hat{A}_Q + A_Q^T \hat{P} + \hat{P} - \tau_1^T \hat{P} \tau_1$ (d)
$\tau = \sum_{k=1}^{N_c} \pi_k [\hat{Q} \hat{P}]$	$\tau = \sum_{k=1}^{N_c} \pi_k [\hat{Q} \hat{P}]$	$\tau = \sum_{k=1}^{N_c} \pi_k [\hat{Q} \hat{P}]$	$\tau = \sum_{k=1}^{N_c} \pi_k [\hat{Q} \hat{P}]$ (e)

3. Theoretical Comparisons

The above description of AOPC_n together with Table 1 summarizes all the design methods very succinctly. The similarities among the methods are evident. First, as already noted, all methods construct the compensator projection from the eigenprojections associated with the N_c largest eigenvalues of a product of two non-negative definite matrices. This provides additional motivation for the use of the term "optimal projection" in connection with the formulation of [4,5] since, there, the projection is determined via optimality not balancing considerations.

Secondly, all methods compute the cost matrices Q and P as solutions to Riccati equations or modified Riccati equations. Furthermore, BCRA, BCRAM and OPC construct τ from the product $\hat{Q}\hat{P}$ where \hat{Q} and \hat{P} are either controllability and observability grammians for the compensator (as in the case of BCRA) or are closely analogous quantities. The fact that CCA lacks a Lyapunov equation for \hat{P} entails less of a distinction than might first be thought since the term \hat{P} (=PSP) appearing in (CCA-e) is essentially the nonhomogeneous, driving term in the Lyapunov equations determining \hat{P} in the other methods. Thus, the eigenvalues of $\hat{Q}\hat{P}$ (termed the "component costs" in [3]) assign a relative weighting to the eigenprojections in a manner analogous to the other methods.

In connection with equations (a) and (b) of the various methods, it was stated in [14] that the optimal projection design is simply the projection of an LQG controller. Equations (7) and (8) show that this would indeed be so if P and Q in (7) were determined as solutions to the LQG Riccati equations (as in CCA, BCRA and BCRAM). However, in contrast to the suboptimal approaches, the OPC equations for P and Q are modified Riccati equations containing additional terms involving the projection. Thus, except under very special circumstances, the optimal fixed-order compensator is generally not a projection of an LQG design.

Indeed, the one striking distinction is that in OPC, the equations determining P , Q , \hat{P} and \hat{Q} involve the compensator projection explicitly. In essence, the terms $\tau_1^T \hat{P} \tau_1$ and $\tau_1 \hat{Q} \tau_1^T$ (which are lacking in the suboptimal approaches) serve to couple the "model reduction" portion of the problem (equations (OPC-c) and (OPC-d)) with the gain computation portion ((OPC-a) and (OPC-b)). An

indirect result of this feature is that only OPC fully accounts for the fact that the loop is being closed by an N_c - order compensator. In fact, as mentioned previously, OPC constitutes the first-order necessary conditions for the optimization problem--the optimal fixed-order controller design must entail satisfaction of the optimal projection equations. Also, under mild geometric restrictions, solution of the optimal projection equations guarantees closed-loop stability. In view of these properties, OPC can serve as a theoretical standard of comparison for all the other (suboptimal) methods.

Judging from the appearance of the design equations, BCRAM is the one suboptimal method most similar to OPC. In fact, as indicated in Table 1, BCRAM and AOPC₁ are identical. Basically, the BCRAM equations are the optimal projection equations with the coupling terms in τ_1 omitted, and numerical evidence presented in [2] suggests that BCRAM gives improved performance over BCRA (from which BCRAM was originally derived as a modification).

Note that the coupling terms $\tau_1^T \hat{P} \tau_1$ and $\tau_1 \hat{Q} \tau_1^T$ in OPC necessitate an iterative solution algorithm such as AOPC_n while CCA, BCRA and BCRAM compute the compensator projection in only one step. Nevertheless, the suboptimal methods cannot subsequently improve τ if it happens to result in an unsuitable design (with poor performance or instability). AOPC_n, in contrast, offers the mechanism for progressive refinement of the design to achieve a controller which is as nearly optimal as desired.

A further issue of general importance is whether or not the various methods can produce a minimal order optimal compensator. In other words, there may exist a compensator of order $M < N$ which yields the same performance as a full-order ($N_c = N$) compensator. It is highly desirable that the selected design method be capable of producing such a design when it exists. It turns out that all methods considered here meet this requirement. This is substantiated for BCRA, BCRAM in [1] and [2] respectively.

The capability of OPC to yield minimal order compensators follows generally from their status as optimality conditions. More specifically, however, if the LQG compensator has unobservable or uncontrollable poles, then the associated subspaces appear in the null space of $\hat{Q}\hat{P}$. This connection between unobservable/uncontrollable poles and the rank of $\hat{Q}\hat{P}$ was explored in [5]. Thus, if a minimal

realization of order M exists, then $\text{rank} [\hat{Q}\hat{P}] = M$ and setting $N_c = M$ in OPC gives the desired reduced order compensator.

To illustrate the point, consider the example given in [2]. In our notation, the defining matrices are:

$$A = \begin{bmatrix} 0 & -1 \\ 1 & 0 \end{bmatrix}, \quad B = \begin{bmatrix} 1 \\ 0 \end{bmatrix}, \quad C = [1, -1] \quad (17)$$

$$V_1 = \begin{bmatrix} 1 & -1 \\ -1 & 16 \end{bmatrix}, \quad V_2 = 1 \quad (18)$$

$$R_1 = \begin{bmatrix} 4 & 0 \\ 0 & 0 \end{bmatrix}, \quad R_2 = 1 \quad (19)$$

The second-order, LQG compensator is:

$$\left. \begin{aligned} \begin{pmatrix} \dot{q}_1 \\ \dot{q}_2 \end{pmatrix} &= \begin{bmatrix} -3 & 0 \\ 5 & -4 \end{bmatrix} \begin{pmatrix} q_1 \\ q_2 \end{pmatrix} + \begin{pmatrix} 1 \\ -4 \end{pmatrix} y \\ u &= -[2, 0]q \end{aligned} \right\} \quad (20)$$

It is clear from inspection of (20) that the minimal (unity order) compensator is obtained by deleting q_2 to get:

$$\left. \begin{aligned} \dot{q} &= -3q + y \\ u &= -2q \end{aligned} \right\} \quad (21)$$

At the same time, it is easily verified that the optimal projection equations yield the solution:

$$\left. \begin{aligned} P &= \begin{bmatrix} 2 & 0 \\ 0 & 2 \end{bmatrix}, \quad Q = \begin{bmatrix} 1 & 0 \\ 0 & \beta \end{bmatrix} \\ \beta &= 17/4 + 16/17 \\ \hat{P} &= \begin{bmatrix} 2 & 0 \\ 0 & 0 \end{bmatrix}, \quad \hat{Q} = \frac{17}{4} \begin{bmatrix} 1 & \alpha \\ \alpha & \alpha^2 \end{bmatrix} \\ \alpha &= -32/17 \end{aligned} \right\} \quad (22)$$

$$\text{and } \tau = \begin{bmatrix} 1 & 0 \\ \alpha & 0 \end{bmatrix} \quad (23)$$

$$\text{or } \Gamma = [1, 0], \quad g = [1, \alpha] \quad (24)$$

Using these results with (6) and (7) shows that $K = 2$, $F = 1$ and $A_c = -3$. Thus, OPC yields the minimal order compensator, (21). When one applies the iterative solution scheme, AOPC_n, it is found that the correct projection and the desired values of K , F and A_c are produced on the first iteration. Further iterations beyond AOPC₁ yield no change in τ , K , F and A_c . Incidentally this also illustrates how both AOPC₁ and BCRAM yield the minimal order compensator.

At this point, it should be mentioned that the new "LQG - balancing" method of Verriest [16, 17] and Jonckheere and Silverman [18] will not always yield a minimal order compensator when it exists

(and the property was, in fact, never claimed by the authors). In view of this distinction, and because the LQG - balancing method has been evaluated and compared extensively in [2] and [3], it is not given detailed consideration in the present paper.

4. Numerical Comparison Using A Common Example Problem

Finally, we explore issues relating to practical design efficiency by applying two of the methods considered here to the same example problem. We considered pointing and shape control of the "Solar Optical Telescope" spacecraft example discussed in [3]. The original 44 mode model was reduced to 10 modes (8 elastic and 2 rigid-body modes) by a Modal Cost Analysis in [13]. In the notation used here, the matrices defining this 20-state problem are:

$$\left. \begin{aligned} A &= \begin{bmatrix} 0 & I_{10} \\ -\omega^2 & -2\xi\omega \end{bmatrix} \\ \xi &= 0.001 \\ \omega &= \text{diag} [\omega_k] \\ &k=1, \dots, 20 \end{aligned} \right\} \quad (25)$$

$$B = \begin{bmatrix} 0 \\ \beta \end{bmatrix}, \quad C = [P, 0] \quad (26)$$

$$\left. \begin{aligned} V_1 &= 10^{-4} \begin{bmatrix} 0 \\ \beta \end{bmatrix} [0 \ \beta^T] \\ V_2 &= 10^{-15} I_3 \end{aligned} \right\} \quad (27)$$

$$\left. \begin{aligned} R_1 &= \begin{bmatrix} p^T \\ 0 \end{bmatrix} \begin{bmatrix} 1 & 0 & 0 \\ 0 & 10 & 0 \\ 0 & 0 & 10^{-3} \end{bmatrix} [P, 0] \quad \text{a.} \\ R_2 &= \rho I_8 \quad \text{b.} \end{aligned} \right\} \quad (28)$$

where the modal frequencies, $(\omega_k, k = 1, \dots, 10)$ and matrices β and P are given in Table 1 and 2, respectively, of [3]. In (28.b), ρ is a positive scalar used to adjust the relative weighting of the state and control input penalties of the performance index. Clearly, overall controller authority, actuator mean-square force levels and compensator bandwidth are all inversely proportional to ρ .

Here, we discuss numerical results for $\rho \in [0.01, 100.0]$ and for N_c in the range from 20 to 4 for design methods CCA and AOPC_n. The approach adopted for design comparison is to plot "regulation cost" ($E[x^T R_1 x]$) as a function of "control cost" ($E[u^T u]$) (obtained by varying ρ) for each value of N_c and for each of the design methods.

Results for these tradeoff curves are shown in Fig. 1. The very bottom-most curve represents the full-order (20 states) LQG design. Since this is the best obtainable when there is no restriction on compensator order, the problem is to obtain a lower order design whose tradeoff curve is as close to the LQG results as possible.

The thin black lines in Figure 1 show the $N_c=10, 6$, and 4 designs obtained via Component Cost Analysis, where N_c denotes the compensator dimension. These results were obtained in [3] using the

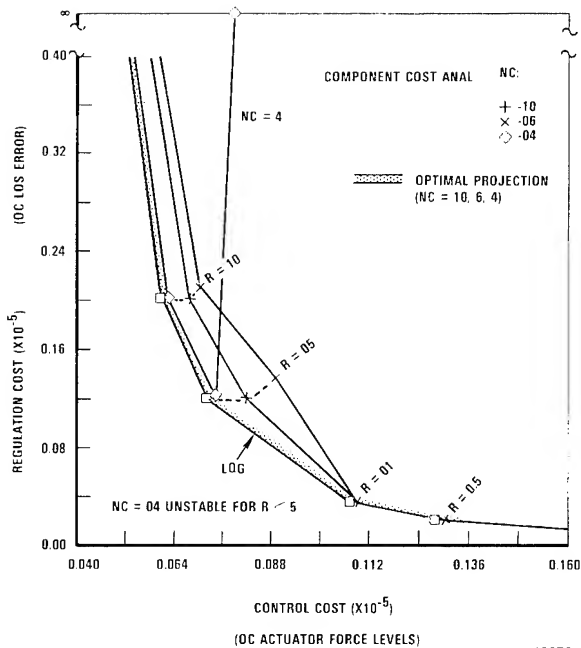


Fig. 1 Performance Tradeoff Curves For Component Cost Analysis and Optimal Projection

full design algorithm described in Appendix A, [3] - including the refinements of steps III.a through III.e. Note that the 10th and 6th order compensator designs are quite good, but when compensator order is sufficiently low ($N_C=4$) and controller bandwidth sufficiently large ($\rho < 5.0$), the method fails to yield stable designs. This difficulty is characteristic of suboptimal techniques, and in fairness, it should be noted that other suboptimal design methods (such as the LQG balanced design method proposed by Verriest [16, 17]) fail to give stable designs for compensator orders below 10.

In contrast, the width of the grey line in Figure 1 encompasses all the optimal projection results for compensators of order 10, 6, and 4. To provide a more detailed picture of the optimal projection results, Figure 2 shows the percent of total performance increase relative to the full-order, LQG designs (the quantity $(100 \times (J_S(N_C) - J_S(20)) / J_S(20))$) as a function of $1/\rho$ (proportional to controller bandwidth and to actuator force levels) for the various compensator orders considered.

Even for the 4th order design, the optimal projection performance is only ~5 percent higher than the optimal full-order design. Furthermore, the performance index for the optimal projection designs increases monotonically with decreasing controller order - as it should. Such is not necessarily the case for suboptimal design methods.

The OPC results were actually obtained via the iterative algorithm AOPC_n outlined in Section 2 (and described in more detail in [6]). In all cases except $N_C = 4$, $\rho = 0.5$, adequate convergence in performance was obtained in four iterations. For the case $N_C = 4$, $\rho = 0.5$, four iterations produced an unstable closed-loop system. This is apparently due to inadequate convergence in this case, since four additional iterations sufficed to give the results indicated in Fig's 1-2.

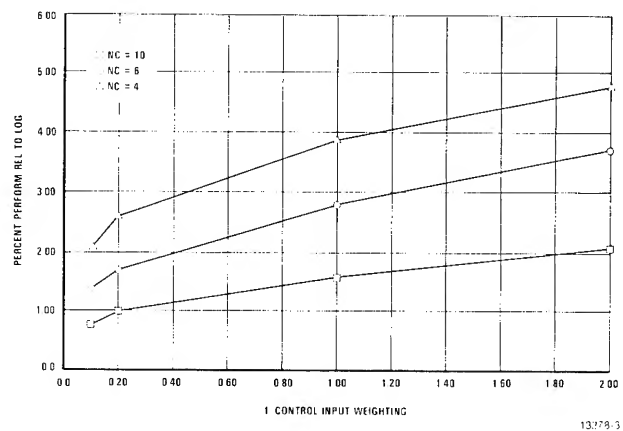


Fig. 2 Optimal Projection Results for S.O.T. Example - Percent Performance Increase Over LQG Design

Note from Table 1 that one iteration of AOPC_n requires only slightly more computation than CCA since CCA involves solution of only one Lyapunov equation and lacks an analogous equation for \hat{P} . Thus, it may be estimated that the OPC results given here required roughly 4 to 8 times the computational effort of CCA. This increased computational burden for OPC is offset, in the higher bandwidth cases, by the reliable production of very low-order but excellent performance designs.

5. Conclusions

In the preceding, we have established a common theoretical framework within which various "balancing" approaches (BCRA, BCRAM and CCA) to controller order reduction may be compared directly with a new formulation (OPC) of the quadratically optimal fixed-order compensation problem. The optimal and suboptimal approaches were found to be highly analogous, each technique characterizing the reduced-order compensator by a projection of rank equal to the desired compensator dimension. The major distinction among the methods is that in OPC, the projection arises as a consequence of optimality conditions, while in the suboptimal methods it is constructed on the basis of other considerations. The ramifications of this distinction were explored by comparing performance results obtained via CCA and OPC for the same example problem.

The above comparisons lead to the following conclusions:

- 1) In all cases considered, the total performance index for OPC is less than for CCA. Even in the case $N_C = 4$, the OPC regulation vs. control cost plot is very close to that of the full-order ($N_C = 20$) design.
- 2) The performance index for OPC increases monotonically with decreasing controller order. Such is not generally the case for

suboptimal design methods.

- 3) Various suboptimal methods (including CCA) fail to produce stable designs when the compensator order and control input weighting parameter, ρ , are both sufficiently small. Contrasting results with OPC solutions, we see that this effect is often an artifact of the suboptimal character of the design methods and does not necessarily imply non-existence of stabilizing compensator designs for small N_C .
- 4) The computational effort associated with the use of CCA, BCRA or BCRAM is roughly equal to the effort of one iteration of the AOPC_n algorithm used for solution of the optimal projection conditions. On the other hand, excellent results for OPC were obtained in 4 - 8 iterations. Thus, while it is significantly more reliable in producing satisfactory designs, OPC does necessitate an increase in computational burden.

The above remarks would seem to motivate continued exploration of the optimal projection approach and additional efforts to increase its computational efficiency. It is also possible that the optimal projection equations may provide the insight needed to devise improved suboptimal (and non-iterative) design techniques.

APPENDIX

Here we verify the statements made in Section 2. from equation (4) through (16) and Table 1 for the design methods BCRA, BCRAM and CCA.

BCRA

Here, consider the internal balancing approach to model reduction as applied to a full-order LQG compensator:

$$\left. \begin{aligned} \dot{q} &= A_C q + F y \\ u &= -K q \end{aligned} \right\} \quad (A.1)$$

where A_C , K and F are given by (6) and (7) with $g = \Gamma = I_N$ and P and Q satisfying the LQG Riccati equations. Considering $V_{-1/2} y$ as the system input and $R_{-1/2} u$ as the output, and assuming, in this discussion that A_C is asymptotically stable, the controllability and observability Grammians are determined as unique positive semidefinite solutions to (see Ref. [1], p. 21 and make allowance for notation and input, output definitions).

$$\left. \begin{aligned} 0 &= A_C W_C^2 + W_C^2 A_C^T + F V_{-1/2} F^T \\ 0 &= A_C^T W_0^2 + W_0^2 A_C + K^T R_{-1/2} K \end{aligned} \right\} \quad (A.2)$$

Having obtained these quantities, it is clear from the discussion of [1], p. 24, or from the Lemma in the main text of this paper that there exists a transformation with matrix P such that W_C and W_0 can both be reduced to the diagonal matrix of 2nd order modes, (Σ^2 in Moore's notation). Referring to the expressions given for W_C and W_0 under coordinate transformation given in [1], p. 23, we have

$$\left. \begin{aligned} W_C^2(P) &= P^{-1} \Sigma^2 P^{-1T}, \\ W_0^2(P) &= P^T \Sigma^2 P \end{aligned} \right\} \quad (A.3)$$

Obviously, (A.3) indicates that P^{-1} is the right eigenvector matrix and Σ^2 , the eigenvalues of $W_C^2 W_0^2$. Thus, employing the notation introduced in section 2:

$$W_C^2 W_0^2 = \sum_{k=1}^N \sum_K^4 \pi_K [W_C^2 W_0^2] \quad (A.4)$$

where the π_K are formed directly from the columns and rows of P^{-1} and P , respectively. As recommended in the Internal Dominance section of [1], one forms a reduced-order model of (A.1) by deleting, in the internally balanced basis, all states associated with the $N - N_C$ smallest second order modes. Setting:

$$\left. \begin{aligned} \Gamma &= 1^{st} N_C \text{ rows of } P \\ g^T &= 1^{st} N_C \text{ columns of } P^{-1} \end{aligned} \right\} \quad (A.5)$$

this is tantamount to defining a reduced order model of (A.1) via (6) and (7). Thus, (6) and (7) are verified for BCRA.

Now Γ and g as obtained above are obviously one factorization of the projection:

$$\begin{aligned} \tau &= g^T \Gamma \\ &= P^{-1} \begin{bmatrix} I_{N_C} & 0 \\ 0 & 0 \end{bmatrix} P \\ &= \sum_{k=1}^{N_C} \pi_K [W_C^2 W_0^2] \end{aligned} \quad (A.6)$$

However, any factorization of τ can be related to a given one by a similarity transformation of the reduced order system. Since the second-order modes and the compensator performance are invariant under such transformations, the particular factorization is immaterial. Thus the internal balancing approach to controller reduction is mathematically equivalent to defining a controller of the form (6) and (7) by (1) computing P and Q via LQG Riccati equations (BCRA-a and BCRA-b of Table 1) (2) determining $\hat{Q} \equiv W_C^2$ and $\hat{P} \equiv W_0^2$ from equations (A.2) (setting $\hat{Q} \equiv W_C^2$, $\hat{P} \equiv W_0^2$, $F = Q C^T V_{-1/2}^{-1}$, $K = R_{-1/2}^{-1} B^T P$ and $\hat{A}_C = A - \Sigma P - Q \Sigma$, equations (A.2) become BCRA-c and BCRA-d), (3) forming the compensator projection via (A.6) or, equivalently, (BCRA-e), and then effecting any suitable factorization in accordance with (5.a, b). This verifies (4) through (16) and Table 1 for BCRA.

BCRAM

This design method is a modification of BCRA proposed in [2] to circumvent difficulties in the application of BCRA when A_C is not asymptotically stable. Referring to equations (2.7.a) and (2.7.b) of [2], the only change from BCRA is that in (BCRA-c), \hat{A}_C is replaced by $A - BK = A - \Sigma P$ and in (BCRA-d), \hat{A}_C is replaced by $A - FC = A - Q \Sigma$. Note that since P and Q are LQG Riccati equation solutions, $A - \Sigma P$ and $A - Q \Sigma$ are asymptotically stable so that the method has a wider field of application.

In view of the preceding discussion, of BCRA, the simple changes noted suffice to substantiate (4) through (16) and Table 1 for BCRAM.

CCA

For simplicity, we consider only the basic Component Cost Analysis approach (termed the Cost-Decoupled Controller Design Algorithm) given in [3], omitting the special procedures described after Theorem 1 of Section III, Ref. [3] for identifying "nearly" unobservable states by use of a set of cost decoupled coordinates closely associated with a generalized Hessenburg representation. This means, that we confine attention to the algorithm in Appendix A of [3] without the computational refinements of steps III and IV.

Referring now to Appendix A, Ref. [3], the Cost-Decoupled design algorithm starts in steps Ia-Ib by computing the full-order, LQG compensator design. Allowing for differences in notation, the expressions (A.3b) - (A.3d) of Ref. [3] are identical to (6) and (7) with $\Gamma = g = I_N$. Similarly (A.3e) and (A.3f) of Ref. [3] are our equations (CCA-a) and (CCA-b) in Table 1.

Next consider step I.C. The quantities \hat{X} , BG and FV^T in [3] correspond to \hat{Q} , $-\Sigma P$ and $Q\bar{\Sigma}Q$ in our notation. Thus, equation (A.4) of Ref. [3] is equivalent to our (CCA-c) for determination of \hat{Q} . Noting that $G^T R G$ of [3] corresponds to the quantity $P\Sigma P$, steps I.d through II.a define a transformation matrix T_1 :

$$T_1 = \Theta_x \Theta_u \quad (A.7)$$

where Θ_x is the square root of \hat{Q} :

$$\hat{Q} = \Theta_x \Theta_x^T \quad (A.8)$$

and Θ_u is the orthonormal modal matrix of $\Theta_x P \Sigma P \Theta_x$:

$$\left. \begin{aligned} \Theta_u^T \Theta_x^T P \Sigma P \Theta_x \Theta_u &= \text{diag. } \{v_k\} \\ v_1 &\geq v_2 \geq \dots \geq v_N \geq 0 \end{aligned} \right\} \quad (A.9)$$

where the v_k 's are the nonnegative "component costs".

Some simple manipulation of (A.7) - (A.9) shows that T_1 is defined such that:

$$\left. \begin{aligned} (\hat{Q} P \Sigma P) T_1 &= T_1 \text{diag } \{v_k\} \\ T_1^{-1} \hat{Q} T_1^{-1T} &= I_N \\ T_1^T P \Sigma P T_1 &= \text{diag } \{v_k\} \end{aligned} \right\} \quad (A.10)$$

-i.e. T_1 is a right eigenvector matrix of the product $\hat{Q}(P\Sigma P)$ yielding a state transformation which simultaneously diagonalizes the factors \hat{Q} and $P\Sigma P$.

Step III basically effects a refinement of T_1 to isolate weakly observable components of the state. For convenience in the exposition we omit this here to obtain a statement of the "basic" CCA algorithm. Thus, set $T = T_1$ in Step IV and proceed to Step V. Equations (A.13e) and (A.13f) of [3] read:

$$\left. \begin{aligned} [T_R, T_T] &\triangleq T_1 ; T_R \in \mathbb{R}^{N \times N_C} \\ \begin{bmatrix} L_R \\ L_T \end{bmatrix} &\triangleq T_1^{-1} ; L_R \in \mathbb{R}^{N_C \times N} \end{aligned} \right\} \quad (A.11)$$

Clearly $T_R L_R$ defines a rank N_C projection on \mathbb{R}^N which, in view of (A.10), is the sum of the eigenprojections of $\hat{Q} P \Sigma P$ associated with the N_C largest eigenvectors. This verifies (CCA-e) of Table 1. Also, comparing $\tau = T_R L_R$ with (5.a), it is seen that T_R and L_R correspond to g^T and Γ , respectively. Thus, allowing for notational changes, equations (A.13b - A.13d) of [3] read:

$$\left. \begin{aligned} A_C &= \Gamma(A - Q\bar{\Sigma} - \Sigma P)g^T \\ F &= \Gamma Q C^T V_2^{-1} \\ K &= R_2^{-1} B^T P \end{aligned} \right\} \quad (A.12)$$

where P and Q are solutions to (CCA-a) and (CCA-b). (A-12) are obviously equivalent to (6) and (7).

REFERENCES

1. B.D. Moore; "Principal Component Analysis in Linear Systems; Controllability, Observability and Model Reduction", IEEE Trans. Automat. Contr., Vol. AC-26, pp. 17-32, 1981.
2. A. Yousuff and R. E. Skelton, "A Note on Balanced Controller Reduction", IEEE Trans. Automat. Contr., 1983 - to appear.
3. A. Yousuff and R. E. Skelton, "Controller Reduction by Component Cost Analysis", IEEE Trans. Automat. Contr., 1984 - to appear.
4. D. C. Hyland, "Optimality Conditions for Fixed-Order Dynamic Compensation of Flexible Spacecraft with Uncertain Parameters", AIAA 20th Aerospace Sciences Mtg., Orlando, Florida, January, 1982.
5. D. C. Hyland and D. S. Bernstein, "Explicit Optimality Conditions for Fixed-Order Dynamic Compensation," IEEE 22nd CDC, San Antonio, Texas, Dec. 14-16, 1983.
6. D. C. Hyland, "The Optimal Projection Approach to Fixed-Order Compensation: Numerical Methods and Illustrative Results", AIAA 21st Aerospace Sciences Mtg., Reno, Nevada, Jan. 9183.
7. C. J. Wenk and C. H. Knapp, "Parameter Optimization in Linear Systems with Arbitrarily Constrained Controller Structure", IEEE Transactions on Automatic Control, Vol. AC-25, pp. 496-500, 1980.
8. W. S. Levine, T. L. Johnson and M. Athans, "Optimal Limited State Variable Feedback Controllers for Linear Systems", IEEE Transactions on Automatic control, Vol. AC-16, pp. 785-793, 1971.
9. T. L. Johnson and M. Athans, "On the Design of Optimal Constrained Dynamic Compensators for Linear Constant Systems", IEEE Transactions on Automatic Control, Vol. 15, pp. 658-660, 1970.

10. R. B. Asher and J. C. Durrett, "Linear Discrete Stochastic Control with a Reduced-Order Dynamic Compensator" IEEE Transactions on Automatic Control, Vol. AC-21, pp. 626-627, 1976.
11. W. J. Naeije and O. H. Bosgra, "The Design of Dynamic Compensators for Linear Multivariable Systems", 1977 IFAC, Fredricksburg, Canada, pp. 205-212.
12. S. Basuthakur and C. H. Knapp, "Optimal Constant Controllers for Stochastic Linear Systems", IEEE Transactions on Automatic Control, Vol. AC-20, pp. 664-666, 1975.
13. R. E. Skelton, P. C. Hughes, "Modal Cost Analysis for Linear Matrix Second-Order Systems", J. Dyn. Syst. Meas. and Control, Vol. 102, Sept. 1980, pp. 151-180.
14. A. Yousuff, R. E. Skelton, "A Projection Approach to Controller Reduction", Proc. IEEE 22nd CDC, San Antonio, Texas, Dec., 1983.
15. C. R. Rao and S. H. Mitra, Generalized Inverse of Matrices and Its Application, John Wiley & Sons, Inc., New York, 1971, p. 123, Theorem 6.2.5.
16. E. I. Verriest, "Low Sensitivity Design and Optimal Order Reduction for the LQG Problem", Proc. 24th Symp. Circuits and Systems, pp. 365-369, June 1981.
17. E. I. Verriest, "Suboptimal LQG-design and Balanced Realizations", Proc. 20th IEEE CDC, pp. 686-687, Dec. 1981.
18. E. A. Jonckheere, L. M. Silverman, "A New Set of Invariants for Linear Systems - Application to Approximation", International Symposium Math. Th. Networks and Syst., Santa Monica, CA, 1981.

Robert A. Calico, Jr.*
David V. Tnyfault**

Abstract

The design of a stable multiple controller control system is presented in this paper. Sufficient conditions are given for both the total decoupling of the multiple controllers and for coupled but stable operation of the multiple controllers. The satisfaction of these conditions is shown to lead to requirements on the minimum numbers of sensors and actuators. The control of a thirty three mode model of the CSDL II spacecraft using direct output feedback is presented. Three separate controllers are used to successfully actively control twenty six modes leaving seven residual modes uncontrolled but stable.

Introduction

The modelling of flexible large space structures as discrete dynamical systems leads to extremely large order systems. These discrete models are normally obtained using finite element modal analysis. The spacecraft state is therefore typically represented by its rigid body orientation angles and their rates plus the modal amplitudes and modal rates. The large system order precludes the active control of the entire model state vector and hence the controller is designed about a reduced order model. The size of the reduced order model is in large part determined by considerations of either on board computer speed or the ability to accurately determine controller gains. This size limitation on the reduced order control model is a serious constraint. Satisfying stringent performance criteria may be impossible with a low order model. The reduced order model must be chosen and controlled in such a manner that the entire system remains stable and meets performance specifications as it is well established (1) that the uncontrolled modes affect system performance and can cause instability due to control and observation spillover.

Techniques for reducing or eliminating spillover effects have been developed by several authors. Sesak (2) developed a modal suppression technique which was later extended by Coradetti (3), which could be used to either reduce or eliminate control and observation spillover. Meirovitch and Oz (4) developed the technique of independent modal space control which eliminated spillover by designing separate controllers for each mode. The independent modal control however requires that the number of actuators and sensors at least equal the number of modes controlled. Calico and Miller (5) extended the work of references (2) and (3) to develop a decentralized control scheme using multiple controllers. Conditions were developed for the preservation of stability using an arbitrary number of controllers. The multiple controller technique of reference (5) provides a means by which large numbers of spacecraft modes might be actively con-

trolled. Specifically, each of several controllers may control as many modes as a single controller and hence the number of modes actively controlled is increased p -fold where p is the number of separate controllers. The technique represents a computational decoupling and is independent of the particular gain selection technique chosen. In fact, different control schemes may be used for each of the several independent controllers. The number of actuators and sensors required by the multiple controller scheme depends upon the modal groupings but it is less than the number of modes controlled.

Calico and Aldridge (6) extended the work of reference (5) to multiple controllers using direct output feedback. Reference (6) demonstrated that the conditions of decoupled direct output feedback control were the same as those for optimal full state feedback and successfully implemented a suboptimal direct output feedback controller for a twelve mode model of the CSDL II (7) spacecraft.

This paper applies the techniques of reference (6) to a thirty three mode model of the CSDL II spacecraft. It also extends the work of reference (6) by considering the effects of control weightings on the several controllers. The results for the three controller direct output feedback system are shown. Excellent control results are shown for the system.

Problem Formulation

The equation of motion for a large space structure acted upon by n_a point actuators can be written in terms of modal variables as:

$$\ddot{\bar{\eta}} + [\omega^2] \bar{\eta} + [2\zeta\omega] \dot{\bar{\eta}} = [\phi^T D_a] \ddot{u} \quad (1)$$

where $\bar{\eta}$ is an n vector of modal amplitudes, \ddot{u} an m control vector, $[\omega^2]$ an $n \times n$ diagonal matrix of modal frequencies squared, $[2\zeta\omega]$ a diagonal damping matrix, ϕ an $n \times n$ modal matrix and D_a a matrix describing actuator locations and orientations.

Defining a $2n$ state vector \bar{x} of modal amplitudes and velocities equations (1) are written in first order form as:

$$\dot{\bar{x}} = A\bar{x} + B\ddot{u} \quad (2)$$

The matrices A and B are given by:

$$A = \begin{bmatrix} 0 & I \\ -[\omega^2] & -[2\zeta\omega] \end{bmatrix}; \quad B = \begin{bmatrix} 0 \\ \phi^T D_a \end{bmatrix} \quad (3)$$

* Professor, Aerospace Engineering
Member, AIAA

** Graduate Student, Capt, USAF
Member, AIAA

This paper is declared a work of the U.S.
Government and therefore is in the public domain.

Associated with the system (2) is the output \bar{y} given by:

$$\bar{y} = C\bar{x} \quad (4)$$

In the case where n_s sensors measure amplitude and velocity at discrete locations, C takes the form:

$$C = [D_{sp}\phi, D_{sv}\phi] \quad (5)$$

where D_{sp} and D_{sv} describe the sensor locations and orientations. In the event that colocated actuators and position sensors are used $D_{sp} = D_a^T$. The satellite model available to the control designer is therefore that given in expressions (1) through (5).

Multiple Decoupled Controllers

The state vector \bar{x} is of order $2n$ and represents the entire spacecraft structural model plus the spacecrafts rigid body motion. The controller is typically based on a much smaller number of modes, N_c . If we assume that multiple controllers are present, each controlling n_i modes, the state vector \bar{x} is conveniently represented by:

$$\bar{x} = \{\bar{x}_1^T, \bar{x}_2^T, \dots, \bar{x}_N^T, \bar{x}_r^T\}^T = \{\bar{x}_c^T, \bar{x}_r^T\}^T \quad (6)$$

where the \bar{x}_i represent vectors of dimension n_i of states controlled by the i 'th controller and \bar{x}_r is an n_r -vector of residual states.

The controlled state, \bar{x}_c is that portion of the state which must be controlled in order to insure satisfactory system performance. The determination as to which modes must be actively controlled is an important question, especially when only a small number of modes may be controlled. Various authors (8), (9) have considered this problem and suggested selection criteria. In this paper control model selection is not addressed and the selection made is purely based on frequency. However, the techniques developed can be used with any choice of control model.

Using the representation of equation (6), we may now express our state equations in the following form:

$$\dot{\bar{x}}_i = A_i\bar{x}_i + B_i\bar{u} \quad i = 1, \dots, N \quad (7a)$$

and

$$\dot{\bar{x}}_r = A_r\bar{x}_r + B_r\bar{u} \quad (7b)$$

In addition, the output equation has the form:

$$\bar{y} = \sum_{i=1}^N C_i\bar{x}_i + C_r\bar{x}_r \quad (8)$$

where in the above equations,

$$A_i = \begin{bmatrix} 0 & I \\ -\omega_i^2 & -2\zeta\omega_i \end{bmatrix}; B_i = \begin{bmatrix} 0 \\ \phi^T D_{a_i} \end{bmatrix}, \quad i = 1, 2, \dots, N, r \quad (9a)$$

$$C_i = [D_{sp_i}\phi, D_{sv_i}\phi], \quad i = 1, 2, \dots, N, r \quad (9b)$$

In each case the systems described by (A_i, B_i, C_i) are completely controllable and observable.

The non-zero partitions of the matrices B_i have dimensions $n_i \times n_a$ and the partitions of the C_i are of dimension $n_s \times n_i$ where n_a and n_s are the numbers of actuators and number of sensors.

Control for N individual system of the form:

$$\begin{aligned} \dot{\bar{x}}_i &= A_i\bar{x}_i + B_i\bar{u} \\ \bar{y} &= C\bar{x} \end{aligned} \quad i = 1, \dots, N \quad (10)$$

is now considered. It is important to note that the control \bar{u} is the same control for each of the N systems and hence couples them. In addition, the output \bar{y} includes not just the modes of the i 'th system but all of the original system modes. Hence using these outputs directly will couple the N separate controllers. The coupling due to \bar{u} is referred to as controller spillover and that due to \bar{y} as observation spillover. Our interest is in designing the N separate controllers such that the system stability is not affected by the spillover effects. To this end, we consider the conditions first for the removal of all spillover and then only those necessary to preserve stability.

The spillover terms may be eliminated from the controlled states in the following manner. We define new control variables \bar{v}_i and new outputs \bar{w}_i by the relationships:

$$\bar{u} = \sum_{i=1}^N T_i\bar{v}_i \quad (11)$$

$$\bar{w}_i = \Gamma_i\bar{y} \quad (12)$$

The matrices T_i and Γ_i will be chosen to eliminate spillover effects. Substituting for \bar{u} in (7a) and using \bar{y} from (8) and ignoring residual modes, in (12) we obtain:

$$\dot{\bar{x}}_i = A_i\bar{x}_i + B_i \left(\sum_{j=1}^N T_j\bar{v}_j \right) \quad (13a)$$

$$\bar{w}_i = \Gamma_i \left(\sum_{j=1}^N C_j\bar{x}_j \right) \quad (13b)$$

If all spillover is to be removed, we require that:

$$B_i T_j = 0, \quad B_i T_i = 0 \quad (14)$$

$$i, j = 1, \dots, N$$

$$\Gamma_i C_j = 0, \quad \Gamma_i C_i = 0$$

Taking into account these relationships the state equations for the N systems may be written in the form

$$\dot{\bar{x}}_i = A_i \bar{x}_i + B_i \bar{v}_i \quad (15)$$

and the N output relationships as

$$\bar{w}_i = C_i^* \bar{x}_i \quad (16)$$

where $B_i^* = B_i T_i$ and $C_i^* = \Gamma_i C_i$. Since the conditions (14) have been satisfied in (15) and (16), no coupling exists between the individual controllers and N independent control systems can be designed for the N systems which when operated simultaneously would not interact. The systems (A_i, B_i^*, C_i^*) can be shown to be completely controllable and observable as long as the systems (A_i, B_i, C_i) are completely observable and controllable. Less restrictive conditions⁽⁵⁾ exist which allow for coupled but stable operation of the N controllers. These conditions are given by

$$B_i T_j = 0 \quad i = 1, \dots, N-1 \quad (17)$$

$$j = i + 1, \dots, N$$

$$\Gamma_i C_j = 0$$

In reference [5] full state feedback control using full state observers was implemented based on the equations (15), (16) and (17) for a simple system. The results of that study showed that the N controllers were coupled but that the coupling did not affect system stability. The eigenvalues of the entire system are merely the sum of the eigenvalues of the N individual controllers. In the foregoing, the residual modes have been ignored. Spillover between the modes contained in the controlled state \bar{x}_i and the residual states still exists. This is of course true for any reduced order controller. The ability to control a large number of modes can be used to provide frequency separation between heavily controlled modes and the residual modes. The effectiveness of this technique will be demonstrated in what follows.

Direct Output Feedback

The case of direct output feedback can best be understood by considering the relationships (13):

$$\dot{\bar{x}}_i = A_i \bar{x}_i + B_i \left(\sum_{j=1}^N T_j \bar{v}_j \right)$$

$$\bar{w}_i = \Gamma_i \left(\sum_{j=1}^N C_j \bar{x}_j \right)$$

Using direct output feedback, the control \bar{v}_j is given by:

$$\bar{v}_j = K_j^* \bar{w}_j \quad (18)$$

where \bar{w}_j is the output for the j'th system. Substituting the results of (18) into our state equations yields the closed loop state equation in the form:

$$\dot{\bar{x}}_i = A_i \bar{x}_i + B_i \sum_{j=1}^N T_j (K_j^* \Gamma_j \sum_{k=1}^N C_k \bar{x}_k) \quad (19)$$

If all spillover is eliminated (19) becomes:

$$\dot{\bar{x}}_i = A_i \bar{x}_i + B_i T_i K_i^* \Gamma_i C_i \bar{x}_i \quad (20)$$

Where the T_i and Γ_i satisfy (14) and K_i^* is the gain matrix for the i'th controller. If only enough spillover is eliminated to ensure stability, only the conditions (17) must be satisfied.

The closed loop state equations then have the form:

$$\dot{\bar{x}}_i = A_i \bar{x}_i + B_i \sum_{j=1}^N T_j (K_j^* \Gamma_j \sum_{k=1}^N C_k \bar{x}_k) \quad i=1, \dots, N \quad (21)$$

In the equations (21) the conditions (17) are assumed to be satisfied. Careful inspection of (21) shows that the systems eigenvalues are the sum of the eigenvalues of those of the individual A_{icl} given by:

$$A_{icl} = A_i + B_i K_i^* \Gamma_i C_i \quad i=1, \dots, N \quad (22)$$

where B_i^*, K_i^* , and C_i^* have previously been defined. Hence, direct output feedback control can be designed which totally decouples the N separate controllers or with less restrictive criteria the responses are coupled but stability is assured. Before moving to an example, a few words concerning the requirements for sensors and actuators are in order.

First, consider the conditions given by expressions (17). In order to satisfy these expressions, the columns of T_N must be orthogonal to the rows of B_1 thru B_{N-1} . That is, the columns of T_N must be in the span of the null space of the matrix B_{1N} , where:

$$B_{1N} = \begin{bmatrix} B_1 \\ \vdots \\ B_{N-1} \end{bmatrix} \quad (23)$$

Assuming that B_{1N} is of full rank, the null space of B_{1N} has dimension:

$$P_{1N} = (n_a - \sum_{i=1}^{N-1} n_i) \quad (24)$$

Hence, for the matrix T_N to exist, the number

of actuators n_a must be greater than the total number of modes controlled by the first $N-1$ controllers. That is:

$$n_a > \sum_{i=1}^{N-1} n_i \quad (25)$$

From expressions (11), we note that the dimensions of the control \bar{v}_N for the N 'th controller is of dimension P_{1N} . That is, the dimensions of \bar{v}_N equals the dimension of the null space of B_{1N} . Without the transformation T_N , the control of \bar{u} is of course of dimension n_a . This loss in control dimension is the price paid for the decoupling.

It is easily shown that the other conditions involving T_1 thru T_{N-1} can be met if inequality (25) is satisfied. Similarly, determining the Γ_i which satisfy expressions (17) requires that the number of sensors be such that:

$$n_s > \sum_{i=2}^N n_i \quad (26)$$

In a manner analogous to the control terms of the dimensions of the outputs of the individual system w_i are in general less than the dimension of \bar{y} . This is due to the dimensions of the matrices Γ_i .

The Model

The CSDL II spacecraft model was used in this study. Specifically, revision 3, as described in reference (7) of the CSDL II model was used. The model is shown in figure 1 and the modal characteristics may be derived from reference (7).

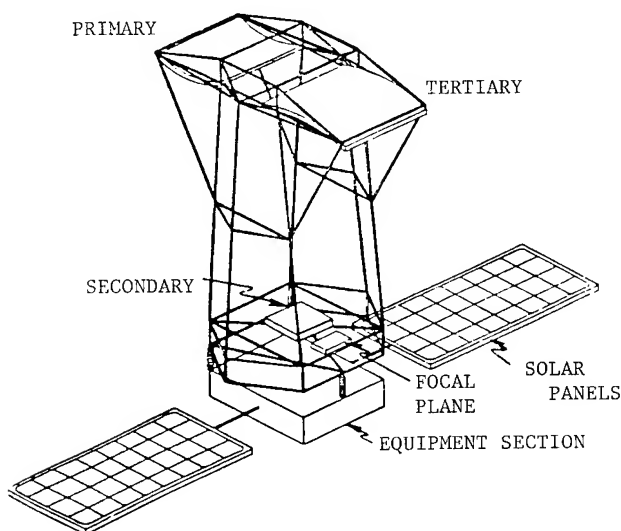


Figure 1

The specific control task undertaken in this study was the control of the line-of-sight and focus for the optical system. The calculation of the line-of-sight parameters LOS_x and LOS_y as well as the focus parameter F_z involved 21 modal displacement. So that each of these modal displacements could be controlled and measured, it was assured that 21 position or velocity sensors and 21 colocated force actuators existed and were aligned with the appropriate modal displacement.

Controller Design

Direct output feedback will be used to provide control gains for the N separate systems. That is each of the control vectors \bar{v}_i will be determined from

$$\bar{v}_i = K_i^* \bar{w}_i \quad (27)$$

The gain matrices K_i^* will be computed using a suboptimal approach first suggested by Kosut⁽¹⁰⁾. This technique first determines a set of optimal gains for a full state LQG controller and the K_i^* are based on these. That is, denoting the LQG gains by G_i^* , the controls \bar{v}_i are given by

$$\bar{v}_i = G_i^* \bar{x}_i \quad (28)$$

Substituting the output relationship into (27) and comparing the result with (28) yields

$$\bar{v}_i = K_i^* C_i^* \bar{x}_i = G_i^* \bar{x}_i \quad (29)$$

In order for the output feedback to provide the same control gains as the LQG controller we have

$$K_i^* C_i^* = G_i^* \quad (30)$$

In general the C_i^* are not square matrices and equation (30) cannot be solved exactly. An appropriate solution is however available in the form

$$K_i^* = G_i^* (C_i^*)^+ \quad (31)$$

where $(C_i^*)^+$ represents the psuedo-inverse of C_i^* .

This approach to the calculation of K_i^* has the advantage of being straightforward and simple. Unfortunately, no assurance of stability for such a controller exists and the stability of each of the N separate systems must be checked. If the systems are not stable either changes to the LQG weightings or modal regrouping among the several controllers is necessary until a stable solution is found. Once N stable controllers direct output feedback controllers have been found, the stability of the entire controlled system is however assured.

Example

The control of a thirty three mode model of the CSDL II spacecraft was accomplished using three independent controllers. The thirty three modes represented the rigid body rotations of the spacecraft plus the first thirty structural modes. Table 1 shows the frequencies associated with the spacecraft modes. The rigid body modes were assumed to

be undamped and one percent of critical damping was assumed for each structural mode. For the three controller case the conditions⁽¹⁷⁾, which must be met to insure stable operation reduce to

$$B_1 T_3 = B_2 T_3 = B_1 T_2 = 0 \quad (32)$$

$$\Gamma_1 C_2 = \Gamma_1 C_3 = \Gamma_2 C_3 = 0$$

The matrices T_1 and Γ_3 may be chosen as identities.

From considering the conditions (32) we note that the columns of T_3 must lie in the null space of B_{12} and those of T_2 in the null space of B_1 . Since the dimension of the control vectors \bar{v}_3 and \bar{v}_2 equals the column dimension of T_3 and T_2 respectively, the vector \bar{v}_3 is of smaller dimension than \bar{v}_2 and both are of smaller dimension than \bar{u} .

The dimension of \bar{v}_1 is equal to that of \bar{u} . Roughly speaking, we have the most control over system one and the least control over system three. A similar situation exists with respect to output but in reverse order. We are best able to observe system three and least able to observe system one.

This information can be used in determining modal groupings for the various controllers. As an example if we consider a case where equal numbers of sensors and actuators are available, the modes identified as most critical to performance might be put in controller two as a compromise between controllability and observability. On the other hand, if many more sensors are available than actuators, the loss in observability might be negated and the most critical modes could be assigned to controller one, the next most critical to controller two and the least critical to controller three.

Table 1
Modal Frequencies

Mode	Freq. rad/sec	Mode	Freq. rad/sec
1	0.0	18	6.11
2	0.0	19	7.28
3	0.0	20	9.75
4	.72	21	11.14
5	.92	22	14.14
6	.94	23	14.16
7	1.10	24	21.57
8	2.86	25	21.69
9	3.50	26	24.86
10	3.75	27	25.05
11	3.86	28	25.46
12	4.00	29	27.26
13	4.03	30	41.23
14	5.12	31	50.67
15	5.13	32	53.11
16	5.17	33	55.63
17	5.75		

The modal assignments for the three controllers were:

Controller 1: 1,2,3,4,6,7,8,10
 Controller 2: 5,9,11,12,13,14,15,16,17
 Controller 3: 18,19,20,21,23,25,26,27,28
 Residuals: 22,24,29,30,31,32,33

In order to determine the gain K_i^* we must first calculate the LQG gains G_i^* . For each system a cost functional of the form

$$J_i = \int_0^\infty (\bar{x}_i^T Q_i \bar{x}_i + \bar{v}_i^T R_i \bar{v}_i) dt$$

was minimized. The control weighting matrices were all chosen to be identity matrices of the proper size and the state weighting matrices were chosen to be diagonal matrices. The weights on the rigid body states 1, 2, 3 were chosen to be 2 and those for the structural modes represented by states 4 - 17 were chosen as 50,000. The weights on all the modes in controller three were 50.

This choice of weights was made in order to demonstrate the ability to provide varying amounts of control to the various controllers. The reason for this choice lies in trying to provide control for the lower seventeen modes and then a "dead zone" between the heavily controlled modes and the residual modes. The purpose for the "dead zone" is to provide a frequency separation between the residuals and those modes heavily controlled.

The LQG gains were determined and the direct output gains calculated assuming that the twenty one sensors were all rate sensors. The resulting system eigenvalues are shown in Table 2.

Table 2
Controlled System Eigenvalues

Mode	Ideal Value	Actual Value
1	0.0,0.0	0.0,0.0
2	0.0,-4.06	0.0,-4.04
3	-.10+ .04i	-.10+ .04i
4	-.11+ .25i	-.11+ .25i
5	-.21,-6.77	-.21,-6.63
6	-.03+ .86i	-.03+ .86i
7	-.26+ 2.38i	-.27+ 2.38i
8	-.14+ 3.58i	-.14+ 3.59i
9	-.50+ 3.73i	-.48+ 3.75i
10	-5.32,-7.70	-5.39,-7.68
11	-3.07+ 2.67i	-3.04+ 2.64i
12	-.90+ 4.02i	-.91+ 3.92i
13	-2.74+ 3.31i	-2.67+ 3.32i
14	-1.98+ 3.89i	-2.21+ 3.98i
15	-2.01+ 4.14i	-1.99+ 4.26i
16	-.39+ 4.86i	-.39+ 4.86i
17	-1.28+ 4.83i	-1.22+ 4.82i
18	-.06+ 7.10i	-.06+ 6.11i
19	-.07+ 7.28i	-.07+ 7.28i
20	-.10+ 9.75i	-.10+ 9.75i
21	-.11+ 11.14i	-.11+ 11.14i
22	-.14+ 14.14i	-.25+ 14.14i
23	-.14+ 14.16i	-.14+ 14.16i
24	-.22+ 21.57i	-.40+ 21.51i
25	-.22+ 21.69i	-.22+ 21.69i
26	-.25+ 24.86i	-.25+ 24.86i
27	-.25+ 25.05i	-.25+ 25.05i
28	-.26+ 25.46i	-.26+ 25.46i
29	-.27+ 27.26i	-2.07+ 26.93i
30	-.41+ 41.23i	-.57+ 41.04i
31	-.51+ 50.67i	-.58+ 50.66i
32	-.53+ 53.11i	-.35+ 53.19i
33	-.55+ 55.63i	-.55+ 55.65i

The column labeled Ideal Value in Table 2 gives the eigenvalues associated with a particular mode as obtained by the individual separate controllers.

For the residual modes the ideal values are their open loop values. The actual eigenvalues shown are system eigenvalues obtained when running the three controllers simultaneously. The movement of the eigenvalues is due to the coupling between the residual modes and the controlled modes. From Table 2 we see that in general the modes move very little due to the coupling. The residual modes do move some and in particular mode 29 has a significant shift in its real part. In the case at hand it becomes more stable. This much movement is however not desirable as it could easily have been in the destabilizing direction. This mode should probably be included as a controlled mode. It should be noted that the level of control over the first seventeen modes is quite high and could be reduced by lowering the state weightings on the LQG solutions for controllers one and two. A lower level of control over these modes would result in corresponding less motion of the residual modes. Finally a comment about the zero frequency rigid body modes is appropriate. These zero frequency roots are due to the exclusive use of rate sensors by the direct output feedback controller. By including some position sensors these modes may be controlled.

Conclusions

The feasibility of decoupled direct output feedback control has been demonstrated on the CSDLII spacecraft. The ability to actively control a large number of modes has been demonstrated. This ability to control a large number of modes actively greatly reduces the reliance on model order reduction schemes in controlling large space structures. The decoupling technique was also shown to be successful in creating a dead zone in the control by placing a very lightly controlled set of modes between the residual modes and the more heavily controlled modes.

References

- [1] Balas, M.J., "Active Control of Flexible Systems", J. Optimization Theory and Applications, Vol. 25, No. 3, July 1978, pp 415-436.
- [2] Sesak, J.R., "Control of Large Space Structures Via Singular Perturbation Optimal Control", presented at AIAA Conference on Large Space Platforms, Los Angeles, CA, Sep 27-29, 1978.
- [3] Coradetti, T., "Orthogonal Subspace Reduction of Optimal Regulator Order", Proc AIAA Guidance and Control Conference, Boulder, CO., August 6-8, 1979.
- [4] Meirovitch, L. and Öz, H., "Modal Control of Distributed Gyroscopic Systems", AIAA Astrodynamics Conference, Palo Alto, CA., Paper No. 78-1421, August 7-9, 1978.
- [5] Calico, R.A. and Miller, W.T., "Decentralized Control For a Flexible Spacecraft", AIAA/AS Astrodynamics Conference, San Diego, CA., Paper No. 82-1404, August 1983.
- [6] Calico, R.A. and Aldridge, E., "Stable Multiple Controller Control of the CSDL II Spacecraft Model", AIAA Guidance and Control Conf. AIAA Paper 83-2290, Gatlinburg, TN., Aug 15-17, 1983.

- [7] Henderson, T., "Modification to Acoos Model #2 Design", RADC-TR-83-56 (Final Technical Report), March 1983.
- [8] Hughes, P.C. and Skelton, R.E., "Modal Truncation for Flexible Spacecraft", J. of Guidance and Control, Vol. 4, No. 3, May-June 1981.
- [9] Skelton, R.E., "Observability Measures and Performance Sensitivity in the Model Reduction Problem", International J. of Control, Vol. 29, No. 4, 1979.
- [10] Kosut, R.L., "Suboptimal Control of Linear Time-Invariant Systems Subject to Control Structure Constraints", IEEE Trans. Automatic Control, Vol. AC-15, October 1970, pp. 557 - 563.

Dennis S. Bernstein**
Lincoln Laboratory/M.I.T.
Lexington, Mass. 02173

David C. Hyland†
Harris Corporation
Melbourne, Fla. 32901

Abstract

One of the major difficulties in designing implementable active controllers for distributed parameter systems such as flexible space structures is that such systems are inherently infinite dimensional while controller dimension is severely constrained by on-line computing capability. Suboptimal approaches to this problem usually either seek a distributed parameter control law or design a low-order dynamic controller for an approximate high-order finite-element model. This paper presents a more direct approach by deriving explicit optimality conditions for finite-dimensional steady-state fixed-order dynamic compensation of infinite-dimensional systems. In contrast to the pair of operator Riccati equations for the "full-order" LQG case, the optimal fixed-order dynamic compensator is characterized by *four* operator equations (two modified Riccati equations and two modified Lyapunov equations) coupled by a projection whose rank is precisely equal to the order of the compensator and which determines the optimal compensator gains. The coupling represents a graphic portrayal of the demise of the classical separation principle for the reduced-order controller case. The results obtained apply to a semigroup formulation in Hilbert space and thus are applicable to control problems involving a broad range of specific partial and hereditary differential equations.

1. Introduction

Numerous techniques have been proposed for the problem of designing an optimal finite-dimensional fixed-order dynamic compensator for an infinite-dimensional system. Generally speaking, most of these methods can be divided into two main categories. The first category, largely associated with the engineering literature, consists of methods that first replace the infinite-dimensional system with a discretized and truncated model and then seek a relatively low-order controller based upon the approximate model. A survey of design techniques proposed for this latter step can be found in Ref. 2; see also Ref. 3. Methods of the second category, associated with the mathematical literature, initially seek a control law for the infinite-dimensional system of a correspondingly infinite-dimensional nature.^{1,9,10} Practical implementation in this case requires subsequent approximation by a finite-dimensional controller.¹¹

A more direct approach^{18,23} is to both retain the infinite-dimensional model and fix the order of the finite-dimensional compensator. Although this idea is conceptually the most appealing, progress in this direction has undoubtedly been impeded by

the lack of optimality conditions such as are available for the infinite-dimensional controller case, i.e., the operator Riccati equations. The purpose of this paper is to make significant progress in filling this gap by presenting new, explicit conditions for characterizing the optimal finite-dimensional fixed-order dynamic compensator for an infinite-dimensional system. In contrast to the pair of operator Riccati equations for the LQG case, the optimal steady-state fixed-order dynamic compensator is characterized by four coupled operator equations (two modified Riccati equations and two modified Lyapunov equations). This coupling, by means of a projection (idempotent) operator whose rank is precisely equal to the order of the compensator, represents a graphic portrayal of the demise of the classical separation principle for the finite-dimensional reduced-order controller case. The optimal gains and compensator dynamics matrix are determined by the solutions of the modified Riccati and Lyapunov equations and by a factorization of the product of the solutions of the pair of modified Lyapunov equations. Considerable insight into the compensator structure is obtained since the projection operator determines control and observation subspaces. Because of the use of a projection in the form of a state-truncation operation in related model-reduction schemes,²¹ these equations have been termed the "optimal projection equations".¹⁷ In this regard it is briefly pointed out in this paper that the mathematical steps involved in characterizing the projection are analogous to the model-reduction method of Ref. 21. An in-depth investigation into this topic is reserved for Ref. 17.

It should be stressed that an important problem which is beyond the scope of the present paper is stabilizability, i.e., the existence of a dynamic compensator of a given order such that the closed-loop system is stable. Our approach is to assume that the set of stabilizing compensators is nonempty and then characterize the optimal compensator should it exist. We note that stabilizing compensators do exist for the class of problems considered in Refs. 4, 8 and 27.

It is important to point out that the results of this paper can be immediately adapted to finite-dimensional systems. One need only specialize the Hilbert space characterizing the dynamical system to a finite-dimensional Euclidean space. Then all "dense domain" considerations can be ignored, adjoints can be interpreted as transposes and other obvious simplifications can be invoked. The only mathematical aspect requiring attention is the treatment of white noise which, for convenient handling of the infinite-dimensional case, is interpreted according to Ref. 1. For the finite-dimensional case, however, the standard classical notions suffice and the results go through with virtually no modifications. The finite-dimensional case has been discussed in Refs. 14-16. Proofs of the results in the present paper can be found in Refs. 5 and 6.

* This work was sponsored by the Dept. of the Air Force. The U.S. Government assumes no responsibility for the information presented.

** Technical Staff, Control Systems Engineering Group

† Member, AIAA

Copyright © American Institute of Aeronautics and Astronautics, Inc., 1984. All rights reserved.

2. Preliminaries and Problem Statement

Let H and H' denote real separable Hilbert spaces with inner product $\langle \cdot, \cdot \rangle$ and let $B(H, H')$, $B_1(H, H')$ and $B_2(H, H')$ denote, respectively, the spaces of bounded, trace class and Hilbert-Schmidt operators from H into H' . 1, 13, 19, 25 If $H = H'$ then write $B(H) \triangleq B(H, H)$, etc. The adjoint of $L \in B(H, H')$ is $L^* \in B(H', H)$ and $\rho(L)$ denotes the rank of L . $L \in B(H)$ is nonnegative definite if $L = L^*$ and $\langle Lx, x \rangle \geq 0$, $x \in H$. With respect to fixed orthonormal bases in Euclidean spaces we identify $\mathbb{R}^{m \times n} = B(\mathbb{R}^n, \mathbb{R}^m)$. The transposes of $x_i \in \mathbb{R}^n$ and 1 . $M \in \mathbb{R}^{m \times n}$ are denoted by x_i^T and M^T and $M^{-1} \triangleq (M^T)^{-1}$. I_n is the $n \times n$ identity matrix and I_H is the identity operator on H .

We consider the following steady-state fixed-order dynamic-compensation problem. Given the control system

$$\dot{x}(t) = Ax(t) + Bu(t) + H_1 w(t)$$

$$y(t) = Cx(t) + H_2 w(t),$$

design a fixed-order dynamic compensator

$$\dot{x}_c(t) = A_c x_c(t) + B_c y(t),$$

$$u(t) = C_c x_c(t)$$

to minimize the performance criterion

$$J(A_c, B_c, C_c) \triangleq \lim_{T \rightarrow \infty} \mathbb{E}[\langle R_1 x(t), x(t) \rangle + u(t)^T R_2 u(t)].$$

The following data are assumed. The state x is an element of a real separable Hilbert space H and the state differential equation is interpreted in the weak sense (see, e.g., Ref. 1, pp. 229, 317). The closed, densely defined operator $A: D(A) \subset H \rightarrow H$ generates a strongly continuous semigroup e^{At} , $t \geq 0$. The control $u \in \mathbb{R}^m$, $B \in B(\mathbb{R}^m, H)$ and the operator $R_1 \in B_1(H)$ and the matrix $R_2 \in \mathbb{R}^{m \times m}$ are nonnegative definite and positive definite, respectively. $w(\cdot)$ is a "standard white noise process" in $L_2((0, \infty), H')$ (see Ref. 1, p. 314), where H' is a real separable Hilbert space, $H_1 \in B_2(H', H)$, $H_2 \in B(H, \mathbb{R}^k)$ and " \mathbb{E} " denotes expectation. We assume that $H_1 H_2^* = 0$, i.e., the disturbance and measurement noises are independent, and that $V_2 \triangleq H_2 H_2^*$ is positive definite, i.e., all measurements are noisy. Note that $V_1 \triangleq H_1 H_1^*$ is trace class. The observation $y \in \mathbb{R}^k$ and $C \in B(H, \mathbb{R}^k)$. The dimension of the compensator state x_c is of fixed order n and the optimization is performed over the matrices A_c , B_c and C_c . Under these and the following assumptions, J is independent of $x(0)$ and $q(0)$.

In order to guarantee the existence of $J(A_c, B_c, C_c)$ we confine (A_c, B_c, C_c) to the set of stabilizing compensators

$$A \triangleq \{(A_c, B_c, C_c): e^{At} \text{ is exponentially stable}\},$$

where

$$\tilde{A} \triangleq \begin{bmatrix} A & BC_c \\ B_c C & A_c \end{bmatrix}$$

is a closed, densely defined operator on $D(\tilde{A}) \triangleq D(A) \times \mathbb{R}^n \subset \tilde{H}$ and $\tilde{H} \triangleq H \oplus \mathbb{R}^n$ is a real separable Hilbert space with inner product

$\langle \tilde{x}_1, \tilde{x}_2 \rangle = \langle x_1, x_2 \rangle + x_1^T C_c^T x_2 + \tilde{x}_1^T \tilde{A} \tilde{x}_2$. Since the value of J is independent of the internal realization of the compensator, we can further restrict (A_c, B_c, C_c) to

$$A_+ \triangleq \{(A_c, B_c, C_c) \in A: (A_c, B_c) \text{ is controllable and } (C_c, A_c) \text{ is observable}\}.$$

3. Characterization of the Optimal Projection and Symmetrized Equations

In order to state our main result we require a factorization lemma (Lemma 3.3) concerning the product of two finite-rank nonnegative-definite operators. Since the existence of such a factorization is crucial to Theorem 3.1, we first discuss simultaneous diagonalization of pairs of matrices and then generalize to the case of finite-rank operators. It should be noted that since H is a real Hilbert space we restrict our attention to matrices with real entries.

Let $U \in \mathbb{R}^{n \times n}$. We shall say U is positive (resp., nonnegative) diagonal if U is diagonal with positive (resp., nonnegative) diagonal elements. U is semi-simple (Ref. 24, p. 13), or nondefective (Ref. 22, p. 375), if U has n linearly independent eigenvectors (i.e., U has a diagonal Jordan canonical form over the complex field). Call U real (resp., positive, nonnegative) semisimple if U is semisimple with real (resp., positive, nonnegative) eigenvalues. Note that U is real (resp., positive, nonnegative) semisimple if and only if there exists $n \times n$ invertible Φ such that $\Phi U \Phi^{-1}$ is diagonal (resp., positive diagonal, nonnegative diagonal).

The following terminology concerns simultaneous diagonalization.²⁴ Let $n \times n$ U, V be symmetric matrices. Then U and V are cogrediently diagonalizable if there exists $n \times n$ invertible Φ such that both $\Phi U \Phi^T$ and $\Phi V \Phi^T$ are diagonal. U and V are contragrediently diagonalizable if there exists $n \times n$ invertible Φ such that both $\Phi U \Phi^T$ and $\Phi^{-T} V \Phi^{-1}$ are diagonal. Since these two situations coincide when Φ is orthogonal, we shall say in this case that U and V are orthogonally diagonalizable.

The following lemma gives sufficient conditions under which symmetric U, V are cogrediently and contragrediently diagonalizable. Although this result goes beyond our needs, it serves the useful purpose of bringing together related results from the literature and hence places in perspective the results we actually require (see Ref. 22, p. 428 and Ref. 24, pp. 122-123).

Lemma 3.1. Suppose that $U, V \in \mathbb{R}^{n \times n}$ are symmetric. Then if either i) one of U and V is positive definite or ii) both U and V are nonnegative definite, then U and V are cogrediently and contragrediently diagonalizable.

Corollary 3.1. Suppose $U, V \in \mathbb{R}^{n \times n}$ are nonnegative definite. Then UV is nonnegative semisimple.

In generalizing the preceding results to the case in which U and V are finite-rank selfadjoint operators on H , we shall make use of the (infinite-) matrix representation of an operator with respect to an orthonormal basis. Note that all matrix representations given here will consist of real entries since the Hilbert spaces are real. Also, recall that every selfadjoint operator has a diagonal matrix representation with respect to some orthonormal basis.

Since orthogonal transformations correspond to a change in orthonormal basis, let us say, in analogy to the matrix case, that $U, V \in B(H)$ are orthogonally diagonalizable if there exists an orthonormal basis for H with respect to which both U and V have diagonal matrix representations (Ref. 12, p. 181). Also in analogy to the finite-dimensional case, call $U \in B(H)$ semisimple (resp., real semisimple, nonnegative semisimple) if there exists invertible $L \in B(H)$ such that LUL^{-1} is normal (resp., selfadjoint, nonnegative definite). This implies that LUL^{-1} has a complete set of orthonormal eigenvectors and, in the real-semisimple or nonnegative-semisimple cases, has real or nonnegative eigenvalues. Furthermore, we shall say that self-adjoint $\hat{Q}, \hat{P} \in B(H)$ are contragrediently diagonalizable if there exists invertible $L \in B(H)$ such that $L\hat{Q}L^*$ and $L^{-*}\hat{P}L^{-1}$ are orthogonally diagonalizable. Cogredient diagonalization is not needed and hence will not be discussed in the sequel. The next result is based upon Lemma 3.1 and upon Theorem 2.1, p. 240 of Ref. 12.

Lemma 3.2. Suppose $\hat{Q}, \hat{P} \in B(H)$ have finite rank and are nonnegative definite. Then \hat{Q} and \hat{P} are contragrediently diagonalizable.

We now have the following generalization of Corollary 3.1.

Corollary 3.2. Suppose $\hat{Q}, \hat{P} \in B(H)$ have finite rank and are nonnegative definite. Then $\hat{Q}\hat{P}$ is nonnegative semisimple.

The next result is a straightforward consequence of Corollary 3.2.

Lemma 3.3. Suppose $\hat{Q}, \hat{P} \in B(H)$ have finite rank, are nonnegative definite, and $\rho(\hat{Q}\hat{P}) = n_c$. Then there exist $G, \Gamma \in B(H, \mathbb{R}^{n_c})$ and $n_c \times n_c$ positive-semisimple M such that

$$\hat{Q}\hat{P} = G^*M\Gamma, \quad (3.1)$$

$$\Gamma G^* = I_{n_c}. \quad (3.2)$$

We shall refer to $G, \Gamma \in B(H, \mathbb{R}^{n_c})$ and $n_c \times n_c$ positive-semisimple M satisfying (3.1) and (3.2) as a (G, M, Γ) -factorization of $\hat{Q}\hat{P}$. Also, define the notation

$$\tau_{\perp} \triangleq I_H - \tau$$

and

$$\Sigma \triangleq BR_2^{-1}B^*, \quad \bar{\Sigma} \triangleq C^*V_2^{-1}C.$$

Main Theorem. Suppose $(A, B_c, C) \in A_+$ solves the steady-state fixed-order dynamic-compensation problem. Then there exist nonnegative-definite $Q, P, \hat{Q}, \hat{P} \in B_1(H)$ such that A_c, B_c and C_c are given by

$$A_c = \Gamma(A - Q\bar{\Sigma} - \Sigma P)G^*, \quad (3.3)$$

$$B_c = \Gamma Q C^* V_2^{-1}, \quad (3.4)$$

$$C_c = -R_2^{-1} B^* P G^*, \quad (3.5)$$

for some (G, M, Γ) -factorization of $\hat{Q}\hat{P}$, and such that with $\tau \triangleq G^*\Gamma$ the following conditions are satisfied:

$$\rho(\hat{Q}) = \rho(\hat{P}) = \rho(\hat{Q}\hat{P}) = n_c, \quad (3.6)$$

$$Q: D(A^*) \rightarrow D(A), \quad P: D(A) \rightarrow D(A^*), \quad (3.7)$$

$$\hat{Q}: H \rightarrow D(A), \quad \hat{P}: H \rightarrow D(A^*), \quad (3.8)$$

$$0 = A Q + Q A^* + V_1 - Q \bar{\Sigma} Q + \tau_{\perp} Q \bar{\Sigma} Q \tau_{\perp}^*, \quad (3.9)$$

$$0 = A^* P + P A + R_1 - P \bar{\Sigma} P + \tau_{\perp}^* P \bar{\Sigma} P \tau_{\perp}, \quad (3.10)$$

$$0 = (A - \Sigma P) \hat{Q} + \hat{Q} (A - \Sigma P)^* + Q \bar{\Sigma} Q - \tau_{\perp} Q \bar{\Sigma} Q \tau_{\perp}^*, \quad (3.11)$$

$$0 = (A - Q \bar{\Sigma})^* \hat{P} + \hat{P} (A - Q \bar{\Sigma}) + P \bar{\Sigma} P - \tau_{\perp}^* P \bar{\Sigma} P \tau_{\perp}. \quad (3.12)$$

Remark 3.1. When H is finite dimensional and $n = \dim H$ (i.e., the full-order case), the (G, M, Γ) -factorization of $\hat{Q}\hat{P}$ is given by $G = \Gamma = I_H$ and $M = \hat{Q}\hat{P}$. Since $\tau = I_H$, and thus $\tau_{\perp} = 0$, (3.9) and (3.10) yield the familiar Riccati equations.

Remark 3.2. Replacing x by Sx , where S is invertible, yields the "equivalent" compensator $(SA S^{-1}, SB, C S^{-1})$. Since $J(A, B, C) = J(SA S^{-1}, SB, C S^{-1})$, one would expect the Main Theorem to apply also to $(SA S^{-1}, SB, C S^{-1})$. This is indeed the case since transformation of the compensator state basis corresponds to the alternative factorization

$$\hat{Q}\hat{P} = (S^{-T}G)^T(SMS^{-1})(S\Gamma).$$

Next we give an alternative characterization of the optimal projection τ by demonstrating how it can be expressed in terms of the Drazin pseudo-inverse of $\hat{Q}\hat{P}$. Since $\hat{Q}\hat{P}$ has finite rank, its Drazin inverse exists (see Theorem 6, p. 108 of Ref. 20). Since $(\hat{Q}\hat{P})^{\#} = G^*M^{-1}\Gamma$, and hence $\rho(\hat{Q}\hat{P})^{\#} = \rho(\hat{Q}\hat{P})$, the "index" of $\hat{Q}\hat{P}$ is 1. In this case the Drazin inverse is traditionally called the group inverse and is denoted by $(\hat{Q}\hat{P})^{\#}$ (see, e.g., Ref. 7, p. 124, or Ref. 26).

Proposition 3.1. Let \hat{Q}, \hat{P} and τ be as in Theorem 3.1. Then

$$\tau = \hat{Q}\hat{P}(\hat{Q}\hat{P})^{\#}.$$

Proof. It is easy to verify that the conditions characterizing the Drazin inverse²⁰ for the case that $\hat{Q}\hat{P}$ has index 1 are satisfied by $G^*M^{-1}\Gamma$. Hence $(\hat{Q}\hat{P})^{\#} = G^*M^{-1}\Gamma$ and (3.2) yields the desired result. \square

The next result is useful in making connections with Ref. 21.

Proposition 3.2. Suppose $\hat{Q}, \hat{P} \in B(H)$ and

$G, \Gamma \in B(H, \mathbb{R}^{n_c})$ and $n_c \times n_c$ real-semisimple M satisfy (3.1) and (3.2). Then there exists invertible $L \in B(H)$ and an orthonormal basis for H with respect to which

$$\hat{Q}\hat{P} = L^{-1} \begin{bmatrix} \Lambda & 0 \\ 0 & 0 \end{bmatrix} L, \quad (3.13)$$

$$G^*\Gamma = L^{-1} \begin{bmatrix} I_{n_c} & 0 \\ 0 & 0 \end{bmatrix} L, \quad (3.14)$$

where $\Lambda \triangleq \text{diag}(\lambda_1, \dots, \lambda_{n_c})$ and $\lambda_1, \dots, \lambda_{n_c}$ are the eigenvalues of M .

We can now point out some interesting similarities between the technique used to obtain τ from $\hat{Q}\hat{P}$ and certain methods appearing in the model-reduction literature. In Ref. 21, for example, the positive-definite controllability and observability gramians,

$$W_c \triangleq \int_0^\infty e^{At} B B^T e^{A^T t} dt, \quad W_o \triangleq \int_0^\infty e^{A^T t} C^T C e^{At} dt,$$

are contragrediently diagonalized, i.e., Φ is chosen so that $\Phi^{-1} W_c \Phi^{-T}$ and $\Phi^T W_o \Phi$ are both positive diagonal. If Φ is chosen so that these matrices are also equal, the resulting model is said to be "internally balanced". The magnitudes of the diagonal components are then used as a guide for determining a suitable reduced-order model. Specifically, the order of the reduced model is chosen to be the number of "large" eigenvalues in the product of the Gramians and the reduced model is obtained by applying the projection

$$\begin{bmatrix} I_n & 0 \\ 0 & 0 \end{bmatrix}$$

in the transformed ("balanced") basis. Note that Proposition 3.2 shows that our "optimal" projection τ is indeed of this form in the basis with respect to which $\hat{Q}\hat{P}$ is diagonal (and which may very well be different from the balanced coordinates). Hence one would suspect that \hat{Q} and \hat{P} are somehow analogous to W_c and W_o . Indeed, since the order of the reduced model is chosen such that (3.6) is, in a sense, approximately satisfied, it is not surprising that in the optimal model-reduction problem, W_c and W_o can be shown¹⁷ to be approximations to \hat{Q} and \hat{P} .

Since Theorem 3.1 applies to closed-loop dynamic compensation with quadratic optimization, further comparison with the model-reduction literature is not feasible. It is important to point out, however, that because of the demise of the separation principle as graphically portrayed by the presence of τ in all four equations (3.8)-(3.12), it should not be expected that either an LQG design for a reduced-order model or a reduced-order LQG controller would correspond to an optimal fixed-order dynamic compensator as characterized by Theorem 3.1.

References

1. A.V. Balakrishnan, Applied Functional Analysis, Springer-Verlag, New York, 1981.
2. M.J. Balas, Trends in large space structure control theory: fondest hopes, wildest dreams, IEEE Trans. on Auto. Contr., AC-24(1982), pp. 522-535.
3. M.J. Balas, Toward a more practical control theory for distributed parameter systems, in Control and Dynamic Systems: Advances in Theory and Applications, Vol. 19, C.T. Leondes, ed., Academic Press, New York, 1982.
4. M.J. Balas, The structure of discrete-time finite-dimensional control of distributed parameter systems, preprint.

5. D.S. Bernstein, Explicit optimality conditions for fixed-order dynamic compensation of infinite-dimensional systems, submitted for publication.
6. D.S. Bernstein and D.C. Hyland, "The optimal projection equations for fixed-order dynamic compensation of infinite-dimensional systems", submitted for publication.
7. S.L. Campbell and C.D. Meyer, Jr., Generalized inverses of linear transformations, Pitman, London, 1979.
8. R.F. Curtain, Compensators for infinite-dimensional linear systems, J. Franklin Inst., 315 (1983), pp. 331-346.
9. R.F. Curtain and A.J. Pritchard, Infinite-dimensional linear systems theory, Springer-Verlag, New York, 1978.
10. J.S. Gibson, The Riccati integral equations for optimal control problems on Hilbert spaces, SIAM J. on Contr. and Optim., 17(1979), pp. 537-565.
11. J.S. Gibson, An analysis of optimal modal regulation: convergence and stability, SIAM J. on Contr. and Optim., 19(1981), pp. 686-707.
12. I. Gohberg and S. Goldberg, Basic operator theory, Birkhauser, Boston, 1981.
13. I. Gohberg and M.G. Krein, Introduction to the theory of linear nonselfadjoint operators, Translations of Mathematical Monographs, Vol. 18, American Mathematical Society, Providence, R.I., 1966.
14. D.C. Hyland, Optimality conditions for fixed-order dynamic compensation of flexible spacecraft with uncertain parameters, AIAA 20th Aerospace Sciences Mtg., Orlando, FL, January 1982.
15. D.C. Hyland, The optimal projection approach to fixed-order compensation: numerical methods and illustrative results, AIAA 21st Aerospace Sciences Mtg., Reno, NV, January 1983.
16. D.C. Hyland and D.S. Bernstein, Explicit optimality conditions for fixed-order dynamic compensation, Proc. 22nd IEEE Conf. on Decision and Control, San Antonio, TX, December 1983.
17. D.C. Hyland and D.S. Bernstein, "The optimal projection approach to model reduction and the relationship between the methods of Wilson and Moore", in preparation.
18. T.L. Johnson, Optimization of low-order compensators for infinite-dimensional systems, Proc. 9th IFIP Symp. on Optimization Techniques, Warsaw, Poland, September 1979.
19. T. Kato, Perturbation theory for linear operators, Springer-Verlag, New York, 1966.
20. D.C. Lay, Spectral properties of generalized inverses of linear operators, SIAM J. on Appl. Math., 29(1975), pp. 103-109.
21. B.C. Moore, "Principle component analysis in linear systems: controllability, observability and

model reduction", IEEE Trans. on Auto. Contr., AC-26(1981), pp. 17-32.

22. B. Noble and J.W. Daniel, Applied linear algebra, Second Edition, Prentice-Hall, Englewood Cliffs, N.J., 1977.

23. R.K. Pearson, Optimal fixed-form compensators for large space structures, in ACOSS SIX (Active Control of Space Structures), RADC-TR-81-289, Final Tech. Report, RADC, Griffiss AFB, New York, 1981.

24. C.R. Rao and S.K. Mitra, Generalized inverse of matrices and its applications, John Wiley and Sons, New York, 1971.

25. J.R. Ringrose, Compact non-self-adjoint operators, Van Nostrand Reinhold Co., London, 1971.

26. P. Robert, On the group-inverse of a linear transformation, J. Math. Anal. Appl., 22(1968), pp. 658-669.

27. J.M. Schumacher, A direct approach to compensator design for distributed parameter systems, SIAM J. on Contr. and Optim, 21(1983), pp. 823-836.

Raphael T. Haftka*
Zoran N. Martinovic**
William L. Hallauer Jr.***

Department of Aerospace and Ocean Engineering
Virginia Polytechnic Institute and State University

Abstract

A procedure for checking whether small changes in a structure have the potential for significant enhancements of its vibration control system is described. The first step in the procedure consists of the calculation of the sensitivity of the required strength of the control system to small changes in structural parameters. The second step consists of the optimization of the structural parameters to produce maximal reduction in required control system strength with minimal change in the structure. The procedure has been demonstrated for a flexible beam supported by four cables and controlled by a rate feedback single-colocated force-actuator velocity-sensor pair. Large changes in control strength requirement were obtained with small structural modifications. Analytical predictions of such effects have also been validated experimentally.

Nomenclature

$[C]$	damping matrix ($n \times n$)
C_f	actuator force per unit current
C_v	sensor voltage per unit velocity
c	viscous damping coefficient, control strength
$e(t)$	excitation signal
F	force generated by control system, defined in Eq. (23)
G	control gain
g_b	limits on the damping ratio or real parts of eigenvalues defined in Eqs. (21) and (22)
g_{hj}	j th constraint on the magnitude of change of the design variable
h_i	thickness of the i th beam element
i	structural design variable number, or electrical current
j	$(-1)^{1/2}$
K	power amplifier transduction constant
$[K]$	stiffness matrix ($n \times n$)
$[K^*]$	$(2n \times 2n)$ matrix defined in Eq. (5)
L	subscript denoting a lower limit on r th eigen-pair damping ratio
$[M]$	mass matrix ($n \times n$)
$[M^*]$	$(2n \times 2n)$ matrix defined in Eq. (4)
m_i	i th lumped mass

n	number of system degrees of freedom
r	mode number
$\{q(t)\}$	state vector ($2n \times 1$)
$\{q_0\}_r$	r th eigenvector ($2n \times 1$)
U	subscript denoting upper limit on real part of r th eigenvalue
$\{u\}$	displacement vector ($n \times 1$)
t	time
$\{x\}$	design variable vector
ω_r	imaginary part of r th eigenvalue defined in Eq. (8)
ω_{or}	r th frequency defined in Eq. (10)
σ_r	real part of r th eigenvalue defined in Eq. (8)
λ_r	r th pair of eigenvalues defined in Eq. (8)
τ	time constant defined in Eq. (18)
ζ_r	damping ratio of r th eigenvalue defined in Eq. (10)
ℓ	number of controlled modes

Introduction

Large space structures will face difficult problems of vibration control. Because of the requirement for low weight, such structures will probably lack the stiffness and damping required for adequate passive control of vibrations. Therefore, a great deal of work is currently in progress on designing active vibration control systems for such structures (see Ref.1, for some recent work).

Most active control studies assume that the structural configuration is determined from other considerations and that the control system has to be designed for a specified structure. Recently, however, there has been some interest in simultaneous design of the structure and the control system so as to produce a truly optimum configuration (e.g. Ref.2). Before one embarks on such an ambitious undertaking, it is important to determine that there is indeed a synergistic effect in designing a structure and its control system simultaneously. The purpose of the present paper is to investigate the possibility of such a synergistic effect.

The method used to assess the potential synergistic effect is determination of whether small structural modifications can produce large reductions in the control strength required to achieve a desired level of active damping. If this is indeed the case, then the synergistic effect is established and there is justification to attempt simultaneous structure-control system design of

* Professor, Member AIAA
** Graduate Research Assistant, Member AIAA
*** Associate Professor, Member AIAA

large space structures.

Two methods are proposed for assessing the potential of small structural modifications for reducing significantly the control requirements. The first method is the calculation of the sensitivity of the control requirements with respect to structural parameters. The second method is the optimization of structural parameters towards the goal of reducing control requirements, subject to a constraint limiting variations in the structural parameters to small values.

The two methods are demonstrated for a flexible beam supported by four cables and controlled by a rate feedback single-colocated force-actuator velocity-sensor pair. Small changes in the structure consist of adding small masses and making small changes in the thickness. The synergistic potential is predicted from a finite element model of the system and then validated by a laboratory experiment.

Calculation of Eigenvalues and their Derivatives

The structure-control system equations of motion for a structure with n degrees of freedom (DOF) and rate feedback control produced by pairs of colocated velocity sensors and actuators is

$$[M]\{\ddot{u}\} + [C]\{\dot{u}\} + [K]\{u\} = \{0\}. \quad (1)$$

For a single sensor-actuator pair, the damping matrix $[C]$ has only one nonzero entry, equal to c , at the diagonal position corresponding to the controlled DOF.

In state vector form Eq. (1) becomes

$$[M^*]\{\dot{q}\} + [K^*]\{q\} = \{0\}, \quad (2)$$

where

$$\{q\}^T = [\{\dot{u}\}^T \{u\}^T] \quad (3)$$

is the state vector ($2n \times 1$), and

$$[M^*] = \begin{bmatrix} [0] & [M] \\ [M] & [C] \end{bmatrix} \quad (4)$$

$$[K^*] = \begin{bmatrix} -[M] & [0] \\ [0] & [K] \end{bmatrix} \quad (5)$$

Assuming a solution of Eq. (2) of the form,

$$\{q(t)\} = e^{\lambda t} \{q_0\} \quad (6)$$

the associated eigenvalue problem becomes

$$(\lambda[M^*] + [K^*])\{q_0\} = \{0\} \quad (7)$$

The solution of Eq. (7) yields n complex conjugate eigenvalue pairs,

$$\lambda_r = \sigma_r \pm j\omega_r, \quad r = 1, 2, \dots, n. \quad (8)$$

The damping factor of the r th mode is

$$\zeta_r = -\sigma_r / (\sigma_r^2 + \omega_r^2)^{1/2} \quad (9)$$

The real and imaginary parts of λ_r may be

written in terms of a nominal frequency ω_{or} and ζ_r as

$$\begin{aligned} \sigma_r &= -\zeta_r \omega_{or} \\ \omega_r &= \omega_{or} (1 - \zeta_r^2)^{1/2} \end{aligned} \quad (10)$$

For the design of the structure and control system we require the derivatives of the eigenvalues λ_r with respect to design parameters x_i . These derivatives may be calculated by finite differences but this can become quite expensive. Therefore, analytical derivatives have been derived and employed.

Differentiating Eq. (7) with respect to a design variable x_i for the r th eigen-pair, one obtains:

$$\begin{aligned} (\lambda_r[M^*] + [K^*]) \partial\{q_0\}_r / \partial x_i + \partial\lambda_r / \partial x_i [M^*]\{q_0\}_r \\ + \lambda_r \partial[M^*] / \partial x_i \{q_0\}_r + \partial[K^*] / \partial x_i \{q_0\}_r = \{0\} \end{aligned} \quad (11)$$

After premultiplying Eq. (11) by the transpose of the r th eigenvector, and re-arranging of terms, one obtains:

$$\frac{\partial\lambda_r}{\partial x_i} = \frac{\{q_0\}_r^T (\lambda_r \partial[M^*] / \partial x_i + \partial[K^*] / \partial x_i) \{q_0\}_r}{\{q_0\}_r^T [M^*] \{q_0\}_r} \quad (12)$$

Equation (12) can be expressed also in the following form,

$$\partial\lambda_r / \partial x_i = \partial\sigma_r / \partial x_i + j \partial\omega_r / \partial x_i \quad (13)$$

The derivative of the damping ratio for the r th mode is obtained by differentiating Eq. (9) with respect to the design variable x_i ,

$$\frac{\partial\zeta_r}{\partial x_i} = \frac{\omega_r (\sigma_r \partial\omega_r / \partial x_i - \partial\sigma_r / \partial x_i \omega_r)}{(\sigma_r^2 + \omega_r^2)^{3/2}} \quad (14)$$

One of the design parameters x_i is the amount of damping c supplied by the colocated velocity sensor and actuator. The effect of a small change in a structural design variable x_i on the required value of c depends on the required performance of the system. Assume, for example, that we require a minimum level of ζ_r

$$\zeta_r \geq \zeta_{Lr} \quad (15)$$

where ζ_{Lr} is the specified minimum. If the requirement of the Eq. (15) is critical, then for our nominal structure $\zeta_r = \zeta_{Lr}$, and a change in a structural parameter x_i can be useful only if it tends to increase ζ_r . The possible reduction in c due to a change in variable x_i can be obtained by assuming that both change simultaneously

$$d\zeta_r = (\partial\zeta_r / \partial c)dc + (\partial\zeta_r / \partial x_i)dx_i \quad (16)$$

and setting $d\zeta_r = 0$ to obtain

$$dc/dx_i = -(\partial\zeta_r/\partial x_i) / (\partial\zeta_r/\partial c) \quad (17)$$

If the requirement of Eq.(15) is critical for several modes, then Eq.(17) has to be evaluated for each critical mode and the lowest value of dc/dx_i represents the actual possible gain.

Design Method

An initial structure is selected first, and a simple control system is designed for it. The control system design has to satisfy some prescribed minimum levels of active damping. This is classical control system design based on an invariant structure.

Next, a set of structural design variables is selected and an optimization procedure is employed to calculate the values of the structural variables which minimize the control strength required. Changes in the structural variables are constrained to a small percentage of their values for the initial structure, and the same prescribed minimum levels of active damping are imposed on control system design as before. This is simultaneous structure-control system design.

The synergistic effect is considered to be established if the percentage reduction in the control strength is much larger than the percent changes in structural variables.

Two quantities are used here as measures of modal control effectiveness or level of damping in the system. One is the damping factor ζ_r , and the other is the real part of eigenvalue σ_r as defined in Eq. (8). Note that the real part of an eigenvalue σ is related to the time τ required for the amplitude of vibration to be reduced by the factor of $1/e$ as

$$\tau = -1/\sigma \quad (18)$$

Optimization Procedure

The selection of the structural parameter vector $\{x\}$ was accomplished by solving the following minimization problem:

minimize c

such that

$$g_b(\lambda_r) \geq 0 \quad r=1,2,\dots,l \quad (19)$$

and

$$g_{hj}(x) \geq 0 \quad (20)$$

where $g_b(\lambda_r)$ represents a lower limit on the damping ratio ζ_r of the form,

$$g_b(\lambda_r) = \zeta_r - \zeta_{Lr} \quad (21)$$

or an upper limit on the real part

$$g_b(\lambda_r) = \sigma_{Ur} - \sigma_r \quad (22)$$

and $g_{hj}(x)$ represents constraints on the magnitude of change of the design variables.

The NEWSUMT optimization program (Ref.3) has been used to solve the optimization problem. NEWSUMT employs an extended interior penalty function formulation using Newton's method with approximate second derivatives for each unconstrained minimization.

Finite Element Model

The theory developed above has been applied for several numerical cases based on an existing small laboratory structure, which consists of a vertical beam and cables in tension suspending the beam, Figure 1. The structure is represented by a uniform steel beam 2.03 m long with rectangular cross section (51 mm x 3.2 mm). The beam is attached to floor and ceiling by four 2.3 mm diameter steel cables as shown on Figure 1. Beam finite elements of equal length with displacements and rotations as structural DOFs are used to model the beam. A string-in-tension finite element represents each cable. The model includes differential stiffness matrices accounting for tension in beam elements. The tension used at the top of the beam is 362 N and it is proportionally reduced down the beam due to the effect of gravity. Small lumped masses representing control system coils and cable clamps are added to the model.

Inherent passive structural damping is not included in the analysis because it is small in comparison with the active damping imposed by the controller. Active damping is effected by a rate feedback control involving a single force actuator collocated with a velocity sensor. The instantaneous control force is directly proportional, but opposite in sign, to the instantaneous velocity. This is equivalent to the attachment of a viscous dashpot to the structural DOF of the sensor, with the ratio of controlling force to sensed velocity being the viscous damping coefficient c . Therefore, c is defined to be the measure of control strength. The control sensor and actuator are located at the bottom of the beam, as shown on Figure 2 for an eight-element model.

Preliminary studies were done on three analytical models with the beam being modeled by four, eight, and sixteen equal finite elements respectively. The results showed that the eight element model was sufficiently accurate for further analysis.

Results and Discussion

All results were obtained for the beam structure modeled by eight beam finite elements and having 18 DOF. The uniform-thickness beam without any additional masses is called the baseline design.

First, the control system was designed for the baseline design. The requirements imposed on the control system for the first five modes were $0.9 \geq \zeta_r \geq 0.03$, $r = 1,2,3,4,5$. This requirement was satisfied with $c = 0.2204$ N-sec/cm. For this value of c , ζ_5 was equal to 0.03 and first four damping ratios were above this value.

Next, the effect of adding small masses at the nine nodes of the finite element model was investigated. The sensitivity of the control strength c with respect to the masses dc/dm_i ($i = 1$ thru 9) was obtained for the baseline design for ζ_5 constant (see Table 1). The results show that dc/dm_8 is the largest negative derivative and predict that the control requirement c would be reduced by 88.5% relative to the baseline value by adding 10% of the baseline beam mass at node 8 which is 25.4 cm above the beam bottom (see Figure 2).

Next, the optimization was performed with actual additional lumped masses at each of the nine beam nodes defined as the structure design variables. The total added mass was constrained not to exceed 10% of the baseline beam mass and the same requirements were imposed on the control system as for the baseline design. The optimization concentrated the entire 10% added mass at node 8 and reduced the required damping strength c to 0.1264 N-sec/cm, a 42.6% reduction relative to the baseline value. The only critical damping constraint was the lower limit on ζ_5 . The difference between the linear prediction of 88.5% reduction in c and the actual value of 42.6% is due to the rapid changes in dc/dm_i as mass is added. The values of dc/dm_i for the final design are also given in Table 1 and show that the potential for further improvements in c are much reduced.

Table 1: Control strength sensitivity to added masses, dc/dm_i (sec⁻¹)

Lumped mass	Baseline design	Optimal design
1	-24.23	-10.82
2	8.18	3.13
3	-22.71	-9.06
4	5.17	0.15
5	0.73	2.77
6	-36.04	-18.47
7	42.75	18.50
8	-77.39	-18.32
9	155.21	72.17

The sensitivity of the fifth eigenvalue decay rate ζ_5 (the most critical constraint) was plotted as a function of the position of the added mass (see Fig.3) for the beam modeled with 16 finite elements. It is clear from the figure why all the added mass is lumped at the single node and that there are also several local extrema. Figure 3 also indicated that there is very little difference between 8 and 16 element models.

The 42.6% reduction in required control strength by 10% mass addition is a clear synergistic effect. However, it was considered to be less attractive than achieving a similar result by a redistribution of mass in the structure by changing the beam thicknesses. Therefore, the next design

study was performed with the thickness of the beam elements h_i being design variables, and constrained to vary no more than 10% from their original baseline value. The demands on the control system were the same as in the previous case.

First, the potential for improvement was assessed by calculating dc/dh_i for the baseline design. The results in Table 2 show that the maximum derivative is for element 8 and that for this element a 10% decrease in thickness ($\Delta h = -0.32$ mm) is expected to reduce c by 9.4%. Next, an optimization was performed resulting in a thickness distribution shown in Figure 4, and the required damping strength c was reduced to 0.1625 N-sec/cm or by 26.3%, with a 2.5% increase in weight over the baseline design. Again, the constraint on the damping ratio of the fifth mode ζ_5 was active, indicating, therefore, that the structure is controlled by controlling the fifth mode of vibration.

The sensitivity of control c with respect to thickness (dc/dh_i , $i = 1$ thru 8) for the optimal design is also given in Table 2. The results showed in both cases that dc/dh_2 was small compared to the other sensitivity derivatives. Therefore, the thickness of the second element of the optimal design was reduced to its lower limit. This new design has no increase in mass relative to the baseline design, and it requires $c = 0.1637$ N-sec/cm or 25.7% less than baseline design.

Table 2: Control strength sensitivity to changes in element thicknesses, dc/dh_i (N-sec/cm²)

Element	Baseline design	Optimal design
1	-0.1356	-0.0630
2	0.0138	-0.0251
3	0.2139	0.1517
4	-0.2371	-0.0987
5	0.3217	0.2340
6	-0.2461	-0.2392
7	-0.2182	-0.2062
8	0.6510	0.5934

Next, the effect of the design requirement on the damping was investigated for the 10% added mass design. The demands on the level of damping in the system were varied from 0.035 to 0.010, and the same design procedure applied as before for the different limits on minimum value of damping ratios. The results are shown in Table 3.

In all cases the optimization procedure lumped the total added mass 25.4 cm above the beam bottom (node 8) and the fifth mode damping ratio was the only active behavior constraint.

Instead of imposing constraints on damping ratios, i.e. on the number of cycles required for decay of vibration, one can possibly impose constraints on the time τ_r of vibration decay by

Table 3: Effect of design requirements on the reduction in control strength afforded by 10% mass increase, constraints imposed on ζ_r

Required lower limit on damping ratio	Control strength c (N-sec/cm)		Percentage reduction in control strength
	Baseline design	Design with 10% added mass	
0.010	0.0658	0.0413	37.2
0.015	0.1002	0.0620	38.1
0.020	0.1364	0.0830	39.1
0.025	0.1756	0.1044	40.5
0.030	0.2205	0.1264	42.6

Table 4: Effect of design requirements on the reduction in control strength afforded by mass increase, constraints imposed on σ_r

Required upper limit on real part of eigenvalues (sec ⁻¹)	Time decay (sec)	Control Strength c (N-sec/cm)		Percentage reduction in control strength
		Baseline design	Design with added mass	
-0.7175	1.39	0.0520	0.0510	1.9
-1.4350	0.69	0.1033	0.1010	2.2
-2.1525	0.46	0.1532	0.1492	2.6

constraining the real parts of eigenvalues σ_r . Three designs obtained by imposing constraints on σ_r are shown in Table 4.

In all these designs the upper limit on σ_1 was the active constraint, which means that the first mode is controlling the design. These results indicate that small changes in design variables affect control gain very little and that the synergistic effect is nonexistent since the first mode is less sensitive to structural changes than the fifth one.

Experimental Apparatus and Procedure

An experiment was conducted to determine how well the theory predicts reality. The cases tested in the experimental study were the baseline beam-cable design and the design which was optimized by means of an added mass for $0.9 \geq \zeta_r \geq 0.03$. Frequency response functions were measured on the beam-cable laboratory structure, and values of ζ_r and ω_{or} were inferred from the data for comparison with theoretical predictions.

The basic experimental apparatus and procedures have been described at length in Ref.4. That description is summarized here, and some new aspects of apparatus and procedure relevant to this paper are described. Figure 5 is a photograph of the lower portion of the beam showing the mass added around node 8 and the control sensor and actuator.

The added mass consisted of several small magnets with collective weight equal to 10% of the weight of the beam. The magnets were held firmly to the steel beam by their own magnetic field. The added mass was distributed around, rather than concentrated at, node 8, and the distribution clearly also added some rotational inertia to the beam. The consequences of the added mass being distributed rather than concentrated were considered to be negligible for the lowest five structural vibration modes, so the distribution was not included in the theoretical model. The small additional beam and cable tension produced by the weight of the magnets also was considered negligible and was not accounted for theoretically.

Figure 6 represents the structure and the control and instrumentation systems. The velocity sensor and force actuator consisted of structure-borne conducting coils interacting with concentrated, radial magnetic fields produced by stationary, noncontacting magnetic field structures (Ref.4).

The analog controller circuit indicated on Figure 6 consisted simply of a few integrated circuit operational amplifiers, and some resistors and a potentiometer to produce gain G (Ref.4). In addition to producing the gain, the circuit served as a high impedance buffer, which helped to minimize current flow in the velocity-sensing coil.

The power amplifier indicated on Figure 6 was designed to produce controlled current output rather than the more standard controlled voltage

output (Ref. 5). This was necessary to establish a constant transduction of controller output voltage into actuator force, eliminating the effect of voltage induced by motion of the actuator coil. The transduction constant was calibrated as $K = 0.25$ ampere/volt.

The data acquisition and analysis system indicated on Figure 6 was developed by Synergistic Technology, Inc. of Cupertino, California. It provided excitation signal $e(t)$, as well as acquiring response and excitation signals and performing all data analysis. The excitation signal was added to the control feedback signal as input into the force-producing coil. Thus, that coil served the dual function of control actuator and exciter.

The relationship of the control system to the theoretical viscous damping constant c can be developed with use of the notation given on Figure 6. From elementary electromechanics theory, the voltage generated by the velocity-sensing coil moving with velocity \dot{u} is $C_v \dot{u}$, and the force generated by the force-producing coil carrying current i is $C_f i$. C_v and C_f are

constants (for u within the linear range) measured on the apparatus of Figure 5 to be 2.4 volts/m per sec and 2.4 N/ampere, respectively. Thus, from Figure 6 the force generated is

$$F = C_f K (-G C_v \dot{u} + e). \quad (23)$$

Hence the viscous damping constant is

$$c = G K C_f C_v. \quad (24)$$

With the desired value of c given, control gain G is calculated from this equation.

Velocity-to-force (\dot{u}/F) frequency response functions (FRF) were measured. Random excitation $e(t)$ was used. To achieve a good signal-to-noise ratio, the general excitation level was set as high as possible consistent with maintaining linear behavior of the velocity-sensing and force-producing coils. The linear range was approximately $|u| < 2$ mm. Fast Fourier transforms of the response and excitation signals were calculated, and the former was divided by the latter to produce an FRF. The frequency resolution was 0.0781 Hz. In all cases, the FRF calculated from a single excitation period without data windowing was reasonably smooth and reproducible, so neither averaging nor windowing were used. FRF's relating velocity output at node 9 to force input at node 8 also were measured (see the shaker in Figure 5), but the data are not included in this paper.

Table 5: Experimental and theoretical damping and frequency values

Structural vibration mode, r	Baseline Design				10% Added Mass Design			
	ζ_r		$\omega_{or}/2\pi$ (Hz)		ζ_r		$\omega_{or}/2\pi$ (Hz)	
	Experiment	Theory	Experiment	Theory	Experiment	Theory	Experiment	Theory
1	0.177	0.200	2.5	2.5	0.116	0.125	2.2	2.2
2	0.270	0.314	5.6	5.5	0.116	0.121	5.1	5.0
3	0.169	0.156	8.9	8.8	0.080	0.071	9.2	9.3
4	0.061	0.064	15.2	15.3	0.046	0.049	15.5	15.6
5	0.025	0.030	23.9	24.9	0.025	0.030	23.4	24.2

Experimental Results and Comparison with Theory

Representative FRF magnitudes are plotted on Figure 7. The solid curves are the experimentally measured data for the baseline and 10%-added-mass designs, and the dashed curves are curve fits to the experimental data. The curve fitting was based on a five-mode theoretical model, and it was performed by the standard software of the data acquisition and analysis system. The curve fits are clearly very good. The only significant deviation is at frequencies above that of the fifth mode, and this had a negligible effect on the calculated values of modal damping and frequency. The high frequency deviation was due to the absence of a sixth mode in the curve fit theoretical model.

The curve fit analysis calculated for each complex structural mode a damping ratio ζ_r , a frequency ω_{or} , and a complex amplitude value. The former two are relevant to this study and are listed in Table 5, along with the theoretically predicted values.

Experimental and theoretical frequency values agree very well. The differences shown for mode 5 are probably due to the relatively low order of the structure finite element model, which gives an undamped natural frequency of mode 5 about 1 Hz too high.

There is good quantitative agreement between experimental and theoretical damping ratios. The differences may be explained in part by the omission of inherent passive damping from the theoretical model. Inherent damping of the lightly damped beam-cable structure has proven difficult to measure accurately. It has been determined, however, that the inherent damping ratios are on the order of 0.001 for modes 1 and 2 (cable deformation modes in which the beam moves primarily as a rigid body), 0.01 for mode 3 (free-free beam first bending mode), and 0.005 for modes 4 and 5 (free-free beam higher bending modes). The higher inherent damping in mode 3 may explain why this is the only mode, for both designs, for which experimental damping exceeds theoretical damping.

Comparison of theoretical and experimental damping values suggests strongly that the control system produced a damping constant c which was lower than expected, or that some calibration factor or factors were incorrect. However, several independent checks of both the control system and

the data acquisition system failed to confirm these suspicions. So the small but consistent discrepancies in damping values remain unexplained, and the search for an explanation continues at this writing.

The search has produced one significant observation. Formerly, the centerline of the sensor-actuator pair of coils was positioned about 1 cm above the beam's bottom edge (node 9), and the value of ζ_5 measured for both designs was about 0.020. But the vicinity of the bottom edge is a region of very steep gradient in the normal mode shape of the fifth undamped structure mode, as shown on Figure 8. So this positioning error was important relative to the active damping provided to that mode. Repositioning the centerline of the coils downward by only 1 cm produced the 25% increase in ζ_5 shown in Table 5.

The reader might note on Figure 7 the significant difference in fifth mode peak magnitude between the baseline and added mass designs, even though both have the same value of ζ_5 . This is explained by Figure 8, which shows that the added mass design has substantially greater modal displacement at the beam's bottom edge than does the baseline design.

Concluding Remarks

A procedure for checking whether small changes in a structure have the potential for significant enhancements of its vibration control system was developed. The first step in the procedure consists of the calculation of the sensitivity of the required strength of the control system to small changes in structural parameters. The second step consists of the optimization of the structural parameters to produce maximal reduction in required control system strength with minimal change in the structure.

A flexible beam structure supported by four cables and controlled by a rate feedback single-colocated force-actuator velocity-sensor pair was used to demonstrate the procedure. Analytical calculations were performed and predicted that substantial reduction in control strength requirement can be achieved with minimal changes in the structure. These theoretical predictions were validated experimentally with good agreement between theory and test.

Acknowledgement

The research reported in this paper was supported in part by NASA Grant NAG-1-224. The experimental equipment was purchased with the aid of NSF Grant CME-8014059. The help of Mr. George Schamel in running the experiments and preparing the manuscript is gratefully acknowledged.

References

1. NASA Scientific and Technical Information Branch, "Technology for Large Space Systems - A Bibliography with Index", NASA SP-7046(09), July 1983.

2. Hale, A. L., and Lisowsky, R. J., "Optimal Simultaneous Structural and Control Design of Maneuvering Flexible Spacecraft", presented at the Fourth VPI & SU/AIAA Symposium on Dynamics and Control of Large Structures, June 6-8, 1983.

3. Miura, H., and Schmit, L. A., "NEWSUMT - A Fortran Program for Inequality Constrained Function Minimization - Users Guide", NASA Contractor Report 159070, June 1979.

4. Hallauer, W. L. Jr., Skidmore, G. R., and Mesquita, L. C., "Experimental-Theoretical Study of Active Vibration Control," Proc. of the 1st International Modal Analysis Conf., pp. 39-45, 1982.

5. Skidmore, G. R., "A Study of Modal-Space Control of a Beam-Cable Structure: Experiment and Theory," M. S. thesis, Virginia Polytechnic Inst. and State Univ., 1983.

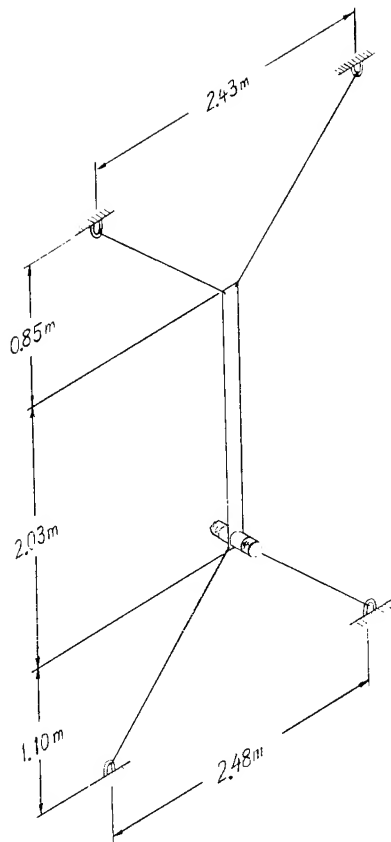


Figure 1. Beam-cable structure

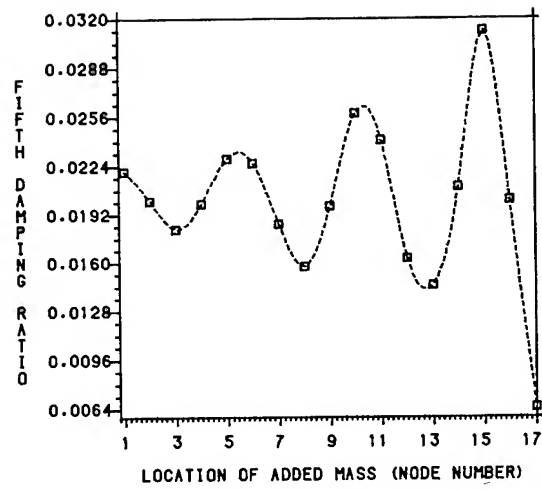


Figure 3. Fifth damping ratio ζ_5 as a function of the position of 10% added mass for 16-finite-element model

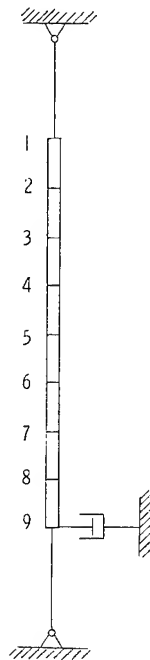


Figure 2. Finite element model

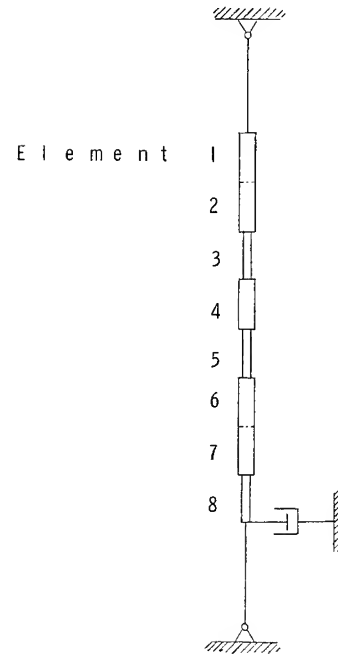


Figure 4. Optimal thickness distribution

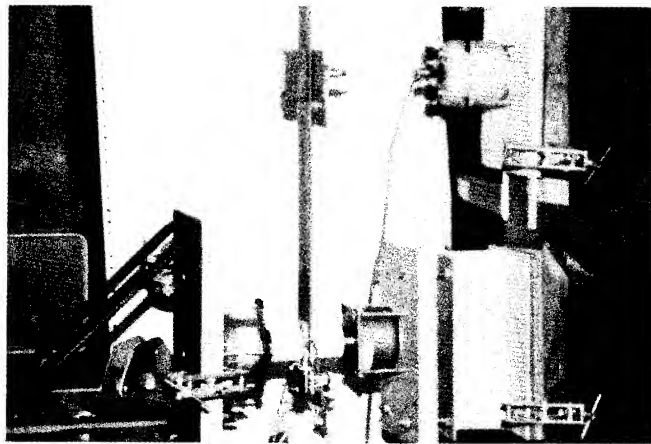


Figure 5. Lower portion of beam, including added mass, velocity sensor, and force actuator

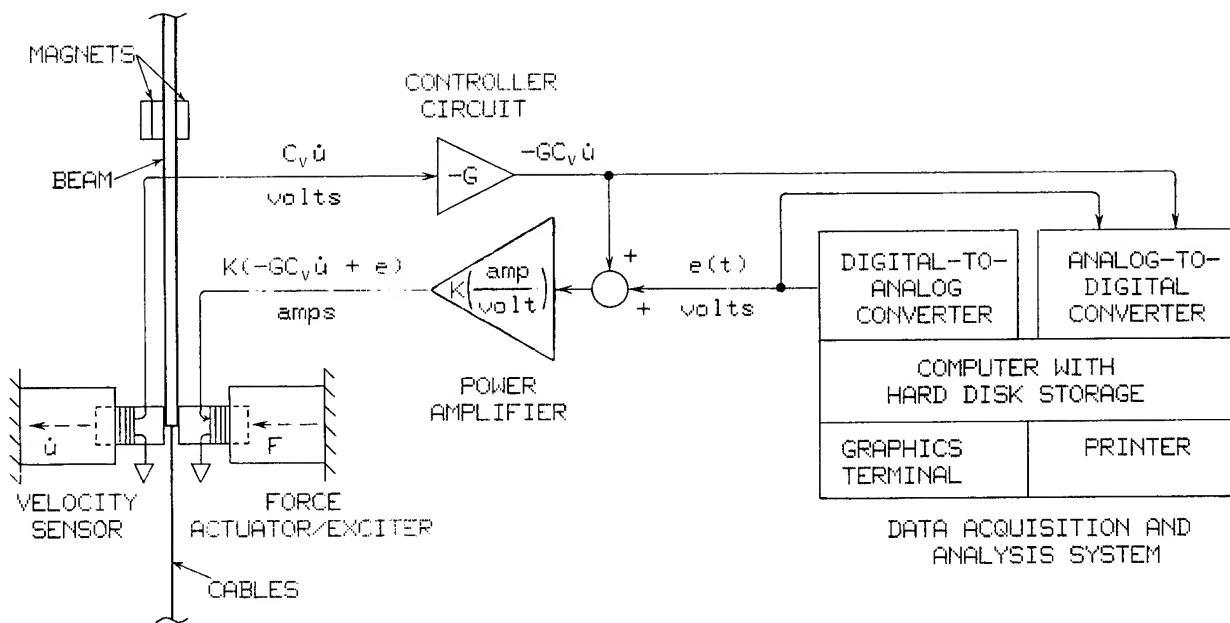


Figure 6. Schematic diagram of experimental apparatus

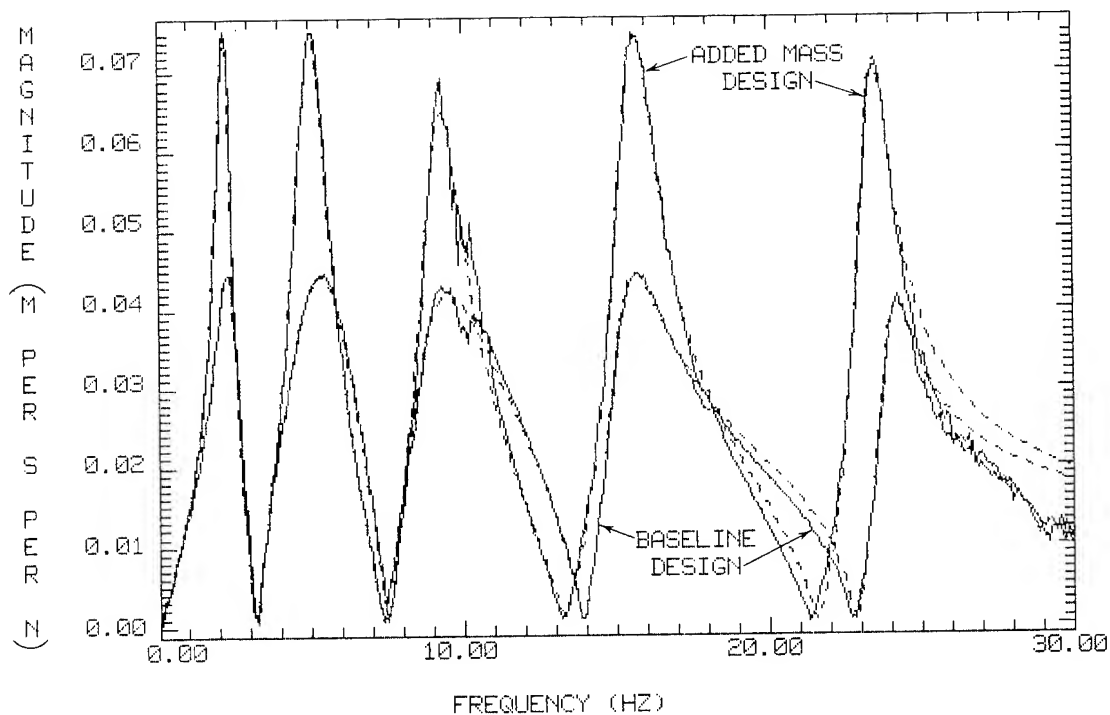


Figure 7. Experimental driving-point frequency response magnitudes for beam's bottom edge. Solid curves are experimental data, dashed curves are theoretical fits to the data.

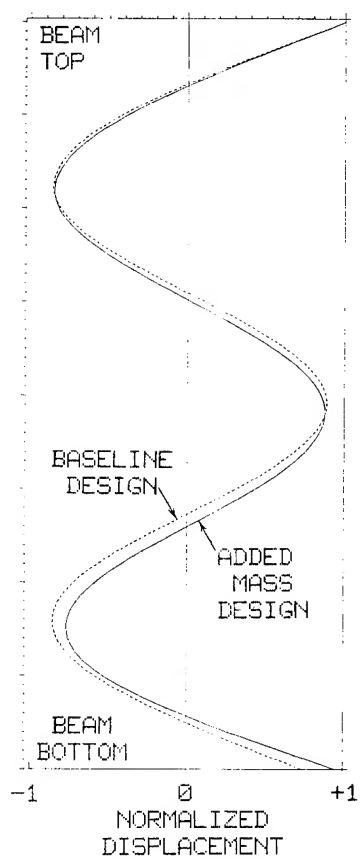


Figure 8. Calculated fifth mode shape of the beam

OPTIMAL DESIGN FOR SINGLE AXIS ROTATIONAL MANEUVERS OF A FLEXIBLE STRUCTURE

Ronald J. Lisowski*, and Arthur L. Hale**

Department of Aeronautical and Astronautical Engineering
University of Illinois at Urbana-Champaign
Urbana, Illinois

Abstract

An optimization problem for rotational maneuvers of a flexible structure is considered. Both structural parameters and active control torques are to be determined so that a specific cost functional is minimized. Obtaining a numerical solution to the problem is shown to be practical if reduced-order structural models are employed. The time and frequency nature of the problem is discussed, and numerical examples are presented for a single axis slew maneuver of a symmetric four boom structure.

1. Introduction

As in our earlier papers^{1,2}, this paper explicitly addresses optimally designing a flexible structure as well as its active control system. The discussion is restricted to maneuvers from an initial state to a final state in a finite time interval. An active control that accomplishes the desired maneuver is optimal if it minimizes a given quadratic cost functional. If, in addition, a set of structural parameters (constant in time) can be varied to further minimize the cost functional, a parameter optimization problem combined with the optimal control problem results. The optimization problem with specified terminal times is well posed so that a solution for both the control and the parameters exists. This is in direct contrast to parameter optimization for optimal free vibration regulation, where the problem is singular.

The combined optimization problem must be solved numerically^{1,2}. First, the necessary conditions for an optimum are divided into 1) those for the optimal control with given structural parameters, and 2) those for the optimal parameters. The former necessary conditions, in conjunction with the specified initial and final states, constitute a two-point boundary value problem in time. Because the latter conditions are nonlinear, they

must be solved iteratively. The iterative solution requires that a separate optimal control problem be solved at each iteration. Assuming that the equations of motion are linear, i.e., already linearized, solving each linear optimal control problem is tantamount to calculating the transition matrix between the terminal times for the coupled system of state and costate equations. Using the transition matrix, initial values of the costates can be determined for the specified initial and final states. Finally, the trajectory of the state-costate system must be calculated inside the time interval. From the trajectory, the cost itself and the residuals in the necessary conditions for the parameters are computed.

While the above numerical solution procedure is applicable to actual complex structures, it is computationally expensive when a structure's mathematical model has many degrees of freedom. Moreover, a real limitation exists on the size of the two-point boundary value problem that can be solved accurately, the upper limit being approximately one hundred state variables. Because the finite element model of a complex structure often has thousands of degrees of freedom, it is not a practical mathematical model for direct use in the optimization. The purpose of this paper is to investigate the viability of using reduced-order models, obtained from the finite element model, for parameter optimization purposes.

A candidate reduced-order model is one containing only the lower modes of free vibration of a structure. For maneuvers, one expects that only the lower natural modes contribute substantially to the response and, hence, to the control cost. This is ensured if the higher modes are not significantly excited. However, the higher modes are excited by rapid changes in the control, such as the terminal jump discontinuities that result from using a cost functional

* Graduate Research Assistant. Member AIAA.

** Assistant Professor, appointed jointly to the Civil Engineering Department. Member AIAA.

depending quadratically on the control. A "smooth" control that contains no discontinuities, on the other hand, will never excite the higher modes significantly. One way to obtain a "smooth" control is to penalize time derivatives of the control and to specify the initial and final values of the control to be zero³. The smooth control is optimal for a modified cost functional containing the control derivative penalties. The presence of control derivative penalties affects the structural optimization, and a secondary purpose of this paper is to consider the viability of using reduced-order models for parameter optimization in the presence of these penalties.

Section 2 below presents the parameter optimization problem with penalties on control derivatives and gives the necessary conditions for an optimum. Section 3 discusses an idealized structure with four booms appended to a rigid hub. The idealized structure has served as the basis for many illustrative examples in the literature, e.g., Refs. 2-4, and it is used again in this paper. Finally, Section 4 presents several numerical examples that illustrate the practical aspects of solving the combined structural and control optimal design problem. Optimal designs that are obtained with and without the inclusion of control derivative penalties are compared.

2. Optimal Control of Parametric Structures

Problem Statement

Because the emphasis is on maneuvering a flexible non-gyroscopic structure, the formulation commences with a general second order in time partial differential equation governing the structure's motion, namely,

$$\rho(\xi, x) \ddot{u}(x, t) + L_{\xi} u(x, t) = f(x, t) \quad (1)$$

Equation (1) must be satisfied at all points $x \in \Omega$ of the domain Ω and times t in the open interval $(0, t_f)$, where $u(x, t)$ is the distributed displacement, $\rho(\xi, x)$ is the structure's mass distribution, L_{ξ} is a self-adjoint linear differential operator of even order $2p$, and $f(x, t)$ is a control force distributed over the domain Ω . In addition, $u(x, t)$ must satisfy the following boundary conditions in space and time

$$B_i[u(x, t)] = 0, \quad i=0, 1, \dots, p-1, \quad x \in \delta\Omega, \quad t \geq 0 \quad (2)$$

$$u(x, 0) = u_0(x), \quad \dot{u}(x, 0) = v_0(x),$$

$$x \in \Omega + \delta\Omega \quad (3a, b)$$

$$u(x, t_f) = u_f(x), \quad \dot{u}(x, t_f) = v_f(x),$$

$$x \in \Omega + \delta\Omega \quad (3c, d)$$

where $\delta\Omega$ is the smooth boundary of Ω . In Eq. (2), the boundary operators B_i involve derivatives of order $\leq 2p-1$ and they form a normal covering on $\delta\Omega$. Both geometric and natural boundary conditions are included in Eq.(2). Moreover, the initial and final conditions of Eqs.(3) define the desired maneuver.

For structures of most concern here an analytical solution of Eq.(1) is impossible to obtain. To solve Eq.(1) numerically an appropriate spatial discretization must be introduced. To this end, using the Rayleigh-Ritz method, $u(x, t)$ is represented by the finite sum

$$u(x, t) = \sum_{k=1}^N U_k(t) \phi_k(x) \quad (4)$$

where the $\phi_k(x)$ are called admissible functions. For the functions $\phi_k(x)$ to be admissible, they need satisfy only the geometric boundary conditions embedded in Eq.(2) and be p times differentiable⁵. The functions $\phi_k(x)$ can be chosen as assumed modes, or they can be obtained by the finite element method. Substituting Eq.(4) into Eq.(1), multiplying by ϕ_{ℓ} , and integrating over Ω yields

$$M(\xi) \ddot{U}(t) + K(\xi) U(t) = G F(t) \quad (5)$$

where

$$M_{k\ell}(\xi) = \int_{\Omega} \rho(x) \phi_k(x) \phi_{\ell}(x) dx \quad (6a)$$

$$K_{k\ell}(\xi) = \int_{\Omega} L^{1/2}(\phi_k) L^{1/2}(\phi_{\ell}) dx \quad (6b)$$

$$(GF)_{\ell} = \int_{\Omega} f(x, t) \phi_{\ell}(x) dx \quad (6c)$$

Note that appropriate integrations by parts are necessary to obtain Eq.(6b). The discrete Eqs.(5) are subject to the discrete initial and final conditions obtained by discretizing Eqs.(3),

$$U(0) = U_0, \quad \dot{U}(0) = V_0 \quad (7a, b)$$

$$U(t_f) = U_f, \quad \dot{U}(t_f) = V_f \quad (7c, d)$$

In Eqs.(6) the mass and stiffness matrices actually depend on the distributed design parameter $\xi(x)$ which is a function of x , i.e., both ρ and the linear operator $L(\cdot)$ actually depend on $\xi(x)$. For a simple beam, for example, one could consider $\rho(x) = \rho_0 \xi(x)$ where ξ

is a function to be designed. However, corresponding to the spatial discretization of $u(x, t)$, a spatial discretization of $\xi(x)$ is also desired. To this end, $\xi(x)$ is represented as the sum

$$\xi(x) = \sum_{i=1}^{N_d} \psi_i(x) \xi_i = \underline{\psi}^T(x) \underline{\xi} \quad (8)$$

where the $\psi_i(x)$ are known functions. Therefore, the symmetric $N \times N$ dimensional mass and stiffness matrices $M(\underline{\xi})$ and $K(\underline{\xi})$, respectively, depend on the N_d -dimensional vector of discrete structural parameters $\underline{\xi}$. Because $\xi(x)$ often represents a physical parameter, such as a physical dimension, which cannot be negative, the discrete parameters ξ_i are constrained. For simplicity, herein the functions $\psi_i(x)$ will be assumed to be chosen in such a way that the individual explicit constraints

$$\xi_i > 0, \quad i=1, 2, \dots, N_d \quad (9)$$

are sufficient. One such choice of the functions $\psi_i(x)$ is a set of piecewise constant positive functions with local support in the domain Ω . Finally, the $N \times N_c$ input matrix G ($N_c < N$) reflects the spatial distribution of actuators that apply N_c generalized control forces \underline{F} . Note that if $\underline{\xi}$ is considered known, Eqs.(5) are linear.

One possible generic optimization problem, and the one of Refs. 1 and 2, seeks a control vector $\underline{F}(t)$ and a set of structural parameters $\underline{\xi}$ that minimize the cost functional

$$J(\underline{F}, \underline{\xi}) = \alpha P(\underline{\xi}) + \frac{1}{2} \int_0^t \{ \underline{F}^T R \underline{F} + \underline{U}^T Q_0 \underline{U} + \dot{\underline{U}}^T Q_1 \dot{\underline{U}} \} dt \quad (10)$$

where R is an $N_c \times N_c$ and Q_1, Q_0 are $N \times N$ symmetric weighting matrices, R is positive definite, Q_1, Q_0 are positive semidefinite, $P(\underline{\xi})$ represents a non-negative cost depending on the structural parameters only, and α is a non-negative real number. The minimization is, of course, subject to the differential equation constraints (5) and the inequality constraints (9). For simplicity, other explicit constraints such as bounds on displacements, on velocities, or on controls are not considered.

To eliminate jump discontinuities in the controls, however, terminal conditions on the control and its derivatives must be specified. Specifically, the control and one or more of its time derivatives should be zero at the terminal times. Because J is a quadratic function of \underline{F} , attempting to

constrain the control results in an ill posed problem from the calculus of variations standpoint. However, a well posed problem can be obtained by introducing penalties on derivatives of the control into the cost functional³. The presence of control derivative penalties introduces a differential equation in time for the control vector \underline{F} . Thus, as a generalization of the previous optimization problem, the present effort is to find a control $\underline{F}(t)$ and a set of structural design parameters $\underline{\xi}$ that minimize the new cost functional

$$J_p(\underline{F}, \underline{\xi}) = \alpha P(\underline{\xi}) + \frac{1}{2} \int_0^t \{ \sum_{i=0}^{N_p} \underline{F}^{(i)T} R_{ii} \underline{F}^{(i)} + \underline{U}^T Q_0 \underline{U} + \dot{\underline{U}}^T Q_1 \dot{\underline{U}} \} dt \quad (11)$$

where $\underline{F}^{(i)}$ is the i th derivative of \underline{F} with respect to time and R_{ii} ($i=1, \dots, N_p$) is the $N_c \times N_c$ corresponding symmetric positive semidefinite weighting matrix. Note that only the $R_{N_p N_p}$ weighting matrix must be positive definite.

Necessary Conditions

Necessary conditions for an extremal control-parameter pair are obtained using the calculus of variations⁶ to minimize Eq.(11) subject to the dynamic constraints (5) and the inequality constraints (9). Because $\underline{\xi}$ and $P(\underline{\xi})$ are not time dependent, the necessary conditions are separated into: 1) those for the optimal control of a structure with given parameters $\underline{\xi}$, and 2) those for the optimal structural parameters.

Using the same notation as in Ref. 2, the cost functional is augmented by introducing the N -dimensional vector of auxiliary coordinates $\underline{v} = \dot{\underline{U}}$ and the N -dimensional vectors \underline{w} and \underline{u}^* of Lagrange multipliers and adjoint displacements, respectively, to yield

$$J_{ap}(\underline{F}, \underline{\xi}) = \alpha P(\underline{\xi}) + \frac{1}{2} \int_0^t \{ \sum_{i=0}^{N_p} \underline{F}^{(i)T} R_{ii} \underline{F}^{(i)} + \underline{U}^T Q_0 \underline{U} + \underline{v}^T Q_1 \underline{v} \} dt + \int_0^t \{ \underline{w}^T S(\underline{v} - \dot{\underline{U}}) + \underline{u}^{*T} [M(\underline{\xi}) \dot{\underline{v}} + K(\underline{\xi}) \underline{U} - G \underline{F}] \} dt \quad (12)$$

The matrix S is any positive definite symmetric matrix.

Optimal Control With Given Parameters

With the initial time $t=0$ and the final time $t=t_f$ fixed, and with ξ specified, taking the first variation of J_{ap} yields the $4N+N_c$ necessary conditions for an optimal control

$$\sum_{i=0}^{N_p} (-1)^i R_{ii} \ddot{F}^{(2i)} = G^T \underline{U}^* \quad (13a)$$

$$-M(\xi) \ddot{\underline{U}}^* + S \underline{W} + Q_1 \underline{V} = \underline{0} \quad (13b)$$

$$S \dot{\underline{W}} + K(\xi) \underline{U}^* + Q_0 \underline{U} = \underline{0} \quad (13c)$$

$$S \dot{\underline{U}} - S \underline{V} = \underline{0} \quad (13d)$$

$$M(\xi) \dot{\underline{V}} + K(\xi) \underline{U} = G \underline{F} \quad (13e)$$

Because the vectors $\{\underline{U}^T, \underline{V}^T\}^T$ and $\{\underline{W}^T, \underline{U}^T\}^T$ are commonly referred to as the state and costate vectors, respectively, Eqs.(13b)-(13e) are the usual coupled state-costate equations. However, Eq.(13a) is a $2N_p$ -th order differential equation in the derivatives of the control vector which is coupled to the adjoint displacements. Upon defining $2N_p-1$ auxiliary coordinates, Eq.(13a) can be replaced by a system of $2N_p$ first order equations, so that Eqs.(13) are a system of $4N+2N_p N_c$ coupled equations. The system of Eqs.(13) must satisfy the boundary conditions

$$\underline{U}(0) = \underline{U}_0, \quad \underline{V}(0) = \underline{V}_0, \quad (13f)$$

$$\underline{U}(t_f) = \underline{U}_f, \quad \underline{V}(t_f) = \underline{V}_f, \quad (13g)$$

$$\underline{F}^{(i)}(0) = \underline{0}, \quad \underline{F}^{(i)}(t_f) = \underline{0}, \quad i=0,1,\dots,N_p-1 \quad (13h)$$

Necessary Conditions for Optimal Parameters

In addition to Eqs.(13a-h), it is necessary for the structural parameters to satisfy

$$\sum_{i=1}^{N_d} \delta \xi_i \left\{ \alpha \frac{\partial P}{\partial \xi_i} + \int_0^{t_f} \underline{U}^{*T} \left[\frac{\partial M}{\partial \xi_i} \dot{\underline{V}} + \frac{\partial K}{\partial \xi_i} \underline{U} \right] dt \right\} = 0 \quad (14)$$

where $\delta \xi_i$ is the variation of ξ_i . When an optimal parameter is on the boundary of the admissible parameters, $\xi_i=0$ must be used. In the neighborhood of extrema not on the boundary, the coefficient of each $\delta \xi_i$ must vanish, yielding the following N_d necessary conditions to be

satisfied along with Eqs.(13a-h).

$$\alpha \frac{\partial P}{\partial \xi_i} + \int_0^{t_f} \underline{U}^{*T} \left[\frac{\partial M}{\partial \xi_i} \dot{\underline{V}} + \frac{\partial K}{\partial \xi_i} \underline{U} \right] dt = 0, \quad i=1,2,\dots,N_d \quad (15)$$

Numerical Solution for an Optimum

The necessary conditions (13) and (15) are a hybrid system of coupled nonlinear equations which must be solved numerically. The iterative method used in the numerical examples of this paper is nearly identical to that presented in the Appendix of Ref. 2. The only differences are the inclusion of the control derivative penalties and the terminal boundary conditions (13h) on the control and its derivatives, and the consideration of a reduced-order model as discussed below.

Reduced-Order Problem

For complex structures, the dimension N of the equations of motion (5) can be large. A direct approach to the solution of the necessary conditions involves solving a linear optimal control problem, i.e., a two-point boundary value problem in time, at every iteration in the algorithm for updating the structural parameters. Solving the two-point boundary value problem accurately is possible only for relatively low dimension systems (e.g., $N < 100$). Even ignoring the accuracy limitation, the entire solution process would be prohibitively expensive for large dimension systems. Therefore, a method of reducing the number of degrees of freedom is necessary.

Before actually reducing the number of degrees of freedom, let us transform Eqs.(13) by choosing N orthogonal vectors as a new basis for each of the vectors \underline{U} , \underline{V} , \underline{W} , and \underline{U}^* . One apparent choice of vectors is the set of N real eigenvectors associated with the force-free response of Eq.(5). Although the eigenvectors depend on the mass and stiffness matrices, i.e., on the structural parameters ξ , the solution of Eqs.(13) and (15) is not changed provided all N eigenvectors are used. The time dependent coefficient of each eigenvector is referred to as a modal coordinate. In terms of the matrix $E(\xi)$ of eigenvectors, the transformation equations are

$$\underline{U} = E \underline{u} \quad (16a)$$

$$\underline{V} = E \underline{v} \quad (16b)$$

$$\underline{W} = E \underline{w} \quad (16c)$$

$$\underline{U}^* = E \underline{u}^* \quad (16d)$$

The matrix $E(\xi)$ is normalized so that $E^T M E = I$ and $E^T K E = \Delta(\xi)$ where $\Delta(\xi)$ is the diagonal matrix of eigenvalues. Introducing Eqs.(16) into Eqs.(13) and Eq.(15), premultiplying appropriate equations by E^T and choosing $S=M$, the necessary conditions in terms of \underline{u} , \underline{v} , \underline{w} , and \underline{u}^* are

$$\sum_{i=0}^N (-1)^i R_{ii} \underline{F}^{(2i)} = G^T E \underline{u}^* \quad (17a)$$

$$\dot{\underline{u}}^* + \underline{w} + E^T Q_1 E \underline{v} = \underline{0} \quad (17b)$$

$$\dot{\underline{w}} + \Delta(\xi) \underline{u}^* + E^T Q_0 E \underline{u} = \underline{0} \quad (17c)$$

$$\dot{\underline{u}} - \underline{v} = \underline{0} \quad (17d)$$

$$\dot{\underline{v}} + \Delta(\xi) \underline{u} = E^T G \underline{F} \quad (17e)$$

$$\alpha \frac{\partial P}{\partial \xi_i} + \int_0^{t_f} \underline{u}^{*T} \left[E^T \frac{\partial M}{\partial \xi_i} E \dot{\underline{v}} + E^T \frac{\partial K}{\partial \xi_i} E \underline{u} \right] dt = 0, \quad i=1,2,\dots,N_d \quad (17f)$$

Note that in solving Eqs.(17) iteratively, the transformation matrix $E(\xi)$ must be updated when the parameters ξ are updated. However, no derivatives of the eigenvalues or the eigenvectors with respect to the parameters are present.

Having transformed the necessary conditions to modal coordinates, a reduced-order model can be obtained by using only the eigenvectors associated with the $N_c < N$ smallest eigenvalues so that $E(\xi)$ is only $N \times N_c$ dimensional. The necessary conditions (17) are $4N_c + 2N_c + N_d$ coupled equations that approximate the original necessary conditions, and they can be written as a system of $4N_c + 2N_c + N_d$ equations. The solution of Eqs.(17) approximates the optimal control and parameters for the original problem. Of course, the initial and final conditions of Eqs. (13f) and (13g) are also only approximately satisfied. How well the approximate solution represents the actual solution depends on the participation of those modes that have been ignored (the residual modes). If the optimal control determined from Eqs.(17) excites the residual modes appreciably, the reduced order design of the parameters is invalid. However, the inclusion of control derivative penalties yields a smooth optimal control so that the level of excitation of the higher modes is small, thus possibly lending credence to the solution for the

parameters.

Since $4N_c + 2N_c + N_d$ first order equations must be solved, as N_c is increased by two, N_c can be decreased by one for the same computational effort. In practice, values of N_c of one and two cause a rapid rolloff of the high frequency content of the optimal control. Thus, if a small number N_c of eigenvectors is sufficient when $N_d > 0$, numerical solution of the combined problem is less costly.

Finite Time vs. Bandwidth

Only the always zero signal is both time-limited and band-limited. The optimal control and the corresponding response of \underline{U} and \underline{V} (either exact or approximate) are solutions to a two-point boundary value problem in time. Hence, the control is always time-limited. Often, the terminal conditions \underline{U}_f and \underline{V}_f are specified so that all elastic deformations are desired to be quiescent at the final time, i.e., the response of the flexible body modes is desired to be time-limited also. However, because the optimal control is time-limited, it always has an infinite bandwidth (taking the Fourier transform one integrates over $-\infty < t < \infty$). If a number of modes are neglected when solving the two-point boundary value problem, the calculated control will excite these modes and they will always have some excitation at times greater than t_f , i.e., their response is not time-limited. What is needed next is the notion that, if the response is small for $t > t_f$, say less than ϵ , then the response is essentially time-limited. Intuitively, if the control were band-limited with no frequency content greater than the highest modeled mode, the response of the residual modes would be nearly zero, and the total response would be essentially time-limited. However, the control always has infinite bandwidth and the companion concept of an essentially band-limited control is needed. The effect of including penalties on the derivatives of the control is to add a low pass prefilter of a sort to the control, with the filter parameters depending on the entries in each R_{ii} matrix. These entries are, in a sense, design parameters which allow a particular "essential" bandwidth for the prefilter to be specified. The number of control derivatives penalized affects the order of the prefilter which, in turn, determines its rolloff properties. The structural optimization yields the best physical design for a particular time-limited maneuver and a particular "essential" bandwidth of the optimal control.

3. Single Axis Slew Maneuvers of a Symmetric Flexible Structure

An idealized four boom structure (Fig. 1) is used to illustrate the design process. The booms are of length L and are fixed to a rigid hub with radius r and moment of inertia I_h about the axis of rotation. They are capable of bending displacements in the plane of rotation, which are assumed to be the same for each boom and to be antisymmetric. As in Ref. 2, the mass per unit length $\rho(x, \xi)$ and the bending stiffness $EI(x, \xi)$ depend explicitly on ξ . A control torque $f_1(t)$ acts on the rigid hub and additional idealized control torques $f_2(t) \dots f_{N_c}(t)$ can be applied on each boom at distances x_2, \dots, x_{N_c} , respectively, from the center of rotation.

Equations of Motion

Linearized equations of motion governing the single axis rotation and antisymmetric in-plane elastic deformations of the structure are derived in Refs. 3 and 4. The equations are valid for small elastic deformations about a trivial equilibrium and have the form of Eq.(5). Herein, a dimensionless form of the equations of motion is helpful. The characteristic constants used in normalizing the equations are the characteristic length of each boom, L , a characteristic mass per unit length, ρ_a , and the maneuver time, t_f . The dimensionless parameters are

$$\tilde{\rho}_o = \frac{\rho_o}{\rho_a}, \quad \tilde{EI}_o = t_f^2 \frac{EI}{\rho_a L^3},$$

$$\tilde{r} = \frac{r}{L}, \quad \tilde{I}_h = \frac{I_h}{\rho_a L^3},$$

and $\tilde{x} = (x-r)/L$, $\tilde{t} = t/t_f$ are the dimensionless length along each boom and the dimensionless time, respectively.

The bending displacement for each boom is spatially discretized using a finite element representation for a cantilever beam, i.e., the elastic deformations are represented as the sum of N_μ interpolation functions $\phi_i(x-r)$ ($r \leq x \leq r+L$) multiplying the time dependent generalized coordinates $\mu_i(t)$ ($i=1, \dots, N_\mu$). The interpolation functions are standard Hermite cubics. A total of N_d finite elements are used, and each element in the discretization requires four separate interpolation functions corresponding to the displacement and rotation, respectively, of each end, or node, of the element. Denoting the angle of the hub by $\theta(t)$, and letting $\phi_i(x) = \phi_i/L$, the dimensionless generalized coordinate vector $\underline{U}(t)$ in Eq.(5) is

$\underline{U} = \{\theta, \mu_1, \dots, \mu_{N_c}\}^T$ where μ_i are alternately dimensionless displacements and rotations for the N_d finite elements. The vector \underline{U} has $N=2N_d+1$ entries. The dimensionless coefficient matrices have the partitioned forms

$$M(\underline{\xi}) = \begin{bmatrix} I(\underline{\xi}) & \underline{M}_{\theta\mu}^T(\underline{\xi}) \\ \underline{M}_{\theta\mu}(\underline{\xi}) & \underline{M}_{\mu\mu}(\underline{\xi}) \end{bmatrix} \quad (18a)$$

$$K(\underline{\xi}) = \begin{bmatrix} 0 & \underline{0}^T \\ \underline{0} & \underline{K}_{\mu\mu}(\underline{\xi}) \end{bmatrix} \quad (18b)$$

$$G = \begin{bmatrix} 1 & 4 & \dots & 4 \\ 0 & 4 \underline{g}_2 & \dots & 4 \underline{g}_{N_c} \\ \vdots & & & \\ 0 & & & \end{bmatrix} \quad (18c)$$

The entries in the vectors \underline{g}_i are all zero except for the entry corresponding to the rotational coordinate of the node at which the i th control torque is applied, in which case the entry is one. The dimensionless moment of inertia of the undeformed structure about the axis of rotation is

$$I(\underline{\xi}) = \tilde{I}_h + 4 \int_0^1 \tilde{\rho}(\tilde{x}, \underline{\xi}) \tilde{x}^2 d\tilde{x}, \quad (19a)$$

the i th entry of $\underline{M}_{\theta\mu}(\underline{\xi})$ is

$$\underline{M}_{\theta\mu_i}(\underline{\xi}) = 4 \int_0^1 \tilde{\rho}(\tilde{x}, \underline{\xi}) \tilde{\phi}_i(\tilde{x}) \tilde{x} d\tilde{x}, \quad i=1, \dots, N_\mu, \quad (19b)$$

and the ij th entries of $\underline{M}_{\mu\mu}(\underline{\xi})$ and $\underline{K}_{\mu\mu}(\underline{\xi})$ are

$$\underline{M}_{\mu\mu_{ij}}(\underline{\xi}) = 4 \int_0^1 \tilde{\rho}(\tilde{x}, \underline{\xi}) \tilde{\phi}_i(\tilde{x}) \tilde{\phi}_j(\tilde{x}) d\tilde{x}, \quad i, j=1, \dots, N_\mu, \quad (19c)$$

$$\underline{K}_{\mu\mu_{ij}}(\underline{\xi}) = 4 \int_0^1 \tilde{EI}(\tilde{x}, \underline{\xi}) \tilde{\phi}_i''(\tilde{x}) \tilde{\phi}_j''(\tilde{x}) d\tilde{x}, \quad i, j=1, \dots, N_\mu, \quad (19d)$$

where the notation \sim denotes dimensionless quantities.

The explicit dependence of $\tilde{\rho}(\tilde{x}, \underline{\xi})$ and $\tilde{EI}(\tilde{x}, \underline{\xi})$ on the N_d entries of $\underline{\xi}$ remains to be considered. It is

convenient to take all elements of each boom to be of uniform length and to have rectangular cross sections of uniform height with piecewise constant dimensionless width $\tilde{w}(x, \xi)$. The piecewise constant widths are the structural parameters ξ_i to be designed (Fig. 2). Each boom is solid and made of the same homogeneous material as the others. The dimensionless width, $\tilde{w}(x, \xi)$ is, of course, non-negative. Moreover, it is essential in order to meet some mission requirement that each boom has at least a small uniform nondimensional mass per unit length, $\tilde{\rho}_0$, and negligible stiffness. Thus,

$$\tilde{\rho}(\tilde{x}, \xi) = \tilde{\rho}_0 + \tilde{w}(\tilde{x}, \xi) \quad (20a)$$

$$\tilde{EI}(\tilde{x}, \xi) = \tilde{EI}_0 \tilde{w}^3(\tilde{x}, \xi) \quad (20b)$$

where \tilde{EI}_0 depends on the specific material and \tilde{w} is the dimensionless width of the added structure.

The nature of the interpolation functions ϕ_i makes the evaluation of the integrals in Eqs. (19) a task that is generalized for any element. Thus, the global matrices are assembled from local mass and stiffness matrices⁵. An assembly process is also needed for the evaluation of Eq.(17f).

4. Numerical Examples

The following numerical examples use the specific dimensionless quantities

$$\tilde{\rho}_0 = 10^{-8}, \quad \tilde{r} = .075, \quad \tilde{I}_h = .1,$$

$$\tilde{EI}_0 = 1000.0$$

Moreover, they consider

$$\alpha = 0, \quad R_{ii} = R_i[I], \quad Q_0 = [0], \quad Q_1 = [0]$$

where $[I]$ is the identity matrix.

For the purpose of demonstrating the concepts, each boom is first modeled by four finite elements of equal length, constant thickness, and variable width. Thus, the design parameters are ξ_1 , ξ_2 , ξ_3 , and ξ_4 , where ξ_1 is the root width and ξ_4 is the tip width. There are a total of nine eigenvectors representing the rigid body mode and eight bending modes. Unless otherwise stated, only the lowest four modes are retained in a reduced-order model for determining the optimal parameters ($N=4$). Using the hub torque only, the structure is slewed from $\underline{u}(0)=\underline{v}(0)=0$ to $\underline{v}(1)=\underline{0}$, and $\underline{u}(1)=\{1, 0, \dots, 0\}^T$, i.e., $\theta(1)=1$. For each resultant set of design

parameters, the control determined from the reduced-order model is applied to the full-order structural model to obtain time histories of the control, rigid body displacement and velocity, and tip deflection and velocity. The magnitude spectrum of the control provides additional insight into the frequencies of the structure that are excited.

Maneuver Without Control Derivative Penalties ($N_d=4, N_\mu=4, N_p=0$)

Table 1 presents the optimal parameters for the maneuver with the control penalized using $R_0=1$ and no penalties on the control derivatives. A non-optimal set of constant parameters, each of which is the average value of the optimal parameters, is also included. The natural frequencies corresponding to the eigenvalues used in the reduced-order model are listed along with the natural frequencies corresponding to the residual modes. The table also presents the final values for the residual mode displacements and velocities for both cases. Note that all quantities are actually dimensionless.

Time histories in dimensionless physical coordinates resulting from the full-order simulation are shown in Fig. 3 and Fig. 4 for the optimal and non-optimal parameter sets, respectively. Fig. 5 presents the magnitude spectrum of the control with the optimal parameter case in solid lines and the non-optimal parameter case in dashed lines.

It is evident from the figures that the optimal control for the structure with optimal parameters is lower in magnitude and "quieter" than the optimal control for the structure with non-optimal parameters. The content of the former at frequencies of about 2 Hz and higher is almost two orders of magnitude (40 db) lower than that of the latter. The maximum tip deflections and velocities are also much lower for the optimal structure.

The results tabulated in Table 1 indicate that the final values for the first few residual modes in the simulation are smaller for the optimal structure. This comparison is roughly by equivalent frequency since most of the natural frequencies of the non-optimal structure are higher than those of the optimal structure. While the final displacements of the residual modes are small for both structures, final velocities are on the order of 10^{-3} .

Maneuver With Two Control Derivative Penalties ($N_d=4, N_\mu=4, N_p=2$)

The optimal parameters for the maneuver with the second derivative of the control penalized using $R_0=R_1=0, R_2=1$

are presented in Table 2. As before, a non-optimal set of parameters is included for comparison. The same information on natural frequencies and residual modes is presented as in the previous section. Fig. 6 and Fig. 7 present the time histories from the full-order simulation for both sets of parameters. Fig. 8 shows the magnitude spectrum for both sets, overlaid as before.

As expected, the control magnitude at the higher frequencies is greatly attenuated, on the order of -40 db down from the no derivative penalty control at about 5 Hz and greater. Additionally, the spectrum of the optimal control of the optimal structure is still about 30 db lower than that of the non-optimal structure. Again, the maximum tip deflection and velocity are lower for the maneuver of the optimal structure.

From Table 2 it is evident that the final displacements and, in particular, velocities of the residual modes are very nearly quiescent for both structures. When compared roughly by equivalent frequencies, those for the optimal structure are actually slightly better than those for the non-optimal structure.

Effects of Varying N_d and N_u

Table 3 presents the optimal parameters determined for the structure when slewed with a control calculated without control derivative penalties using various numbers of modes N_u in the model. For the configuration with four elements it is evident that the optimal structural parameters calculated using $N_u=4$ are not significantly different to the fourth decimal place from those using higher numbers of modes. In fact, the parameters using $N_u=4$ compare as well with those calculated using all nine modes in the model. Table 4 presents similar results using a control calculated with the second derivative of the control penalized. Again, the parameters do not change significantly to the fourth decimal place for $N_u > 4$.

For comparison with the four parameter results, Table 5 presents the optimal parameters, frequencies and residual response using two modes, $N_u=2$, for a case of only two design parameters. Each boom is now considered to be modeled by four finite elements but with $\xi_1=\xi_2$ and $\xi_3=\xi_4$, i.e., $N_d=2$ although $N=9$. In this case, all of the modes are more accurate than for $N=5$, so that a more definite statement concerning optimization using a reduced-order model can be made. Results with no control derivative penalties, $N_p=0$, and two penalties, $N_p=2$, are given in Table 5. Note that the final values for the residual mode displacements and

velocities are much less when $N_p=2$ than when $N_p=0$.

All of the above results tend to support the hypothesis that the optimal parameters can be determined with a reasonable level of confidence using a considerably reduced order model. Such a reduction in degrees of freedom offers significant savings in computational effort.

Additional Observations

A comparison of the control spectrum with the natural frequencies of the reduced-order model was made. The natural frequency of each mode included in the model falls at a minimum of the spectrum (within the frequency discretization level). This does not occur, of course, with the residual modes. It occurs for both the optimal and non-optimal structures and is due to the nature of the optimal control. If all of the modes were included in the model, each corresponding frequency would lie at a minimum of the control spectrum, i.e., the control is tuned to the structure over the time interval. Note that the spectrum is in terms of cycles per dimensionless unit of time. Since the present concern is to use fewer modes in the model, the obvious tradeoff involves deciding at which frequencies the maxima of the spectrum are sufficiently low to allow modes with higher frequencies to be ignored. Clearly, employing control derivative penalties lowers this frequency threshold. As these results indicate, optimizing the structure for the maneuver offers additional improvement.

5. Concluding Remarks

The unified problem of synthesizing a control and structural configuration for a maneuver can be made practical by using reduced-order structural models. Incorporating control derivative penalties to smooth the optimal control allows the designer to have greater confidence in the validity of the reduced-order model. For simplicity, only open loop maneuvers between specified states in a specified time interval have been considered. The ideas are applicable to other types of control system design problems where, for instance, the final state is unspecified but penalized in the cost functional or the controls and states are required to be within certain bounds, to name a few.

Numerical examples for a rest-to-rest rotational maneuver of a structure with four flexible booms have been presented. Results indicate that the control effort for an optimally designed structure is less than that for a non-optimal structure of the same mass. The

control, while certainly not band-limited, is more attenuated at high frequencies for the optimal structure, and much more attenuated if control derivatives are penalized. Finally, for the example considered, a reduce-order model of a dimension equal to the number of design parameters is all that is necessary.

6. References

1. A. L. Hale and R. J. Lisowski, "Optimal Simultaneous Structural and Control Design of Maneuvering Flexible Spacecraft," presented at the Fourth VPI&SU/AIAA Symposium on Dynamics and Control of Large Structures, Blacksburg, Virginia, June 6-8, 1983.
2. A. L. Hale, R. J. Lisowski and W. E. Dahl, "Optimizing Both the Structure and the Control of Maneuvering Flexible Spacecraft," AAS/AIAA Astrodynamics Conference, Lake Placid, New York, August 22-24, 1983.
3. J. D. Turner and H. M. Chun, "Optimal Distributed Control of a Flexible Spacecraft Using Control Rate Penalties in the Controller Design," presented as Paper No. 82-1438 at the Guidance and Control Conference, San Diego, California, August 9-12, 1982.
4. J. D. Turner and J. L. Junkins, "Optimal Large Angle Single-Axis Rotational Maneuvers of Flexible Spacecraft," Journal of Guidance and Control, Vol. 3, No. 6, 1980, pp. 578-585.
5. L. Meirovitch, Computational Methods in Structural Dynamics, Sijthoff and Noordhoff, 1980.
6. G. Leitmann, The Calculus of Variations and Optimal Control, Plenum Press, New York, 1981.
7. D. Slepian, "Some Comments on Fourier Analysis, Uncertainty and Modeling," SIAM Review, Vol. 25, No. 3, 1983, pp. 379-393.

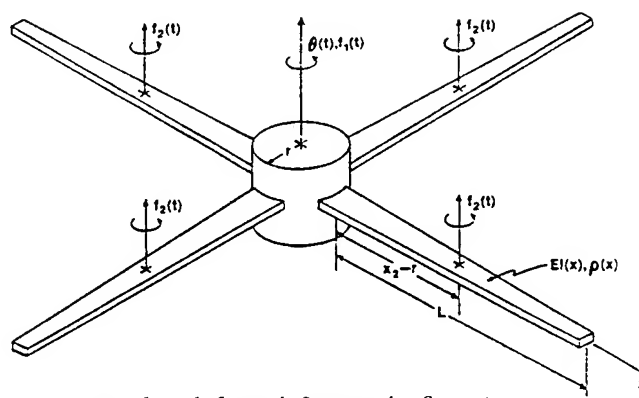


Fig. 1 Undeformed Symmetric Structure

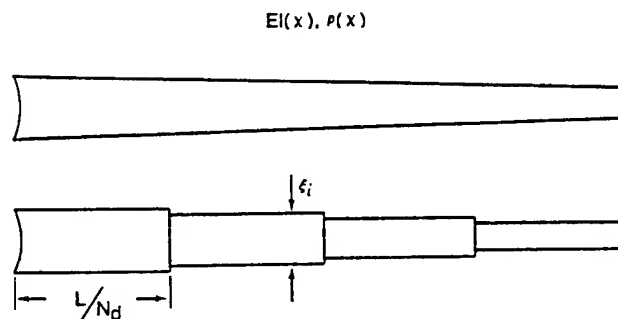


Fig. 2 Finite Element Model of Flexible Boom

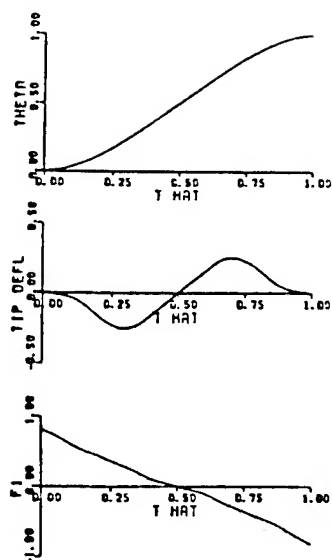


Fig. 3 Time Histories for the Optimal Structure
($N_d=4$ $N_u=4$ $N_p=0$)

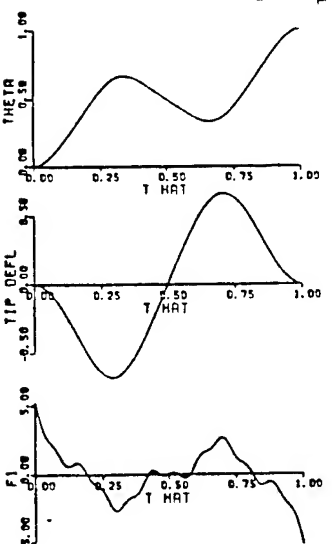
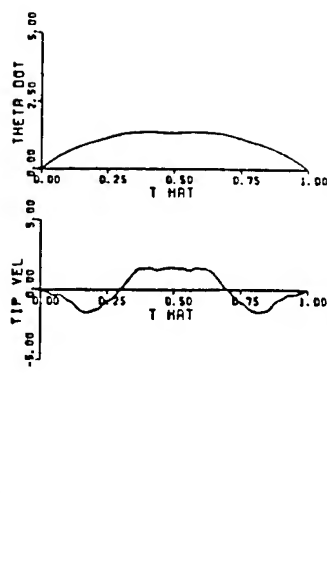


Fig. 4 Time Histories for the Non-Optimal Structure
($N_d=4$ $N_u=4$ $N_p=0$)

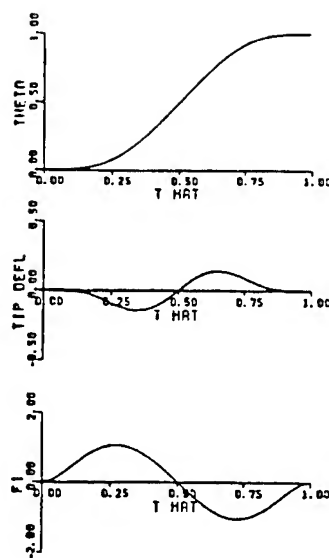


Fig. 6 Time Histories for the Optimal Structure
($N_d=4$ $N_u=4$ $N_p=2$)

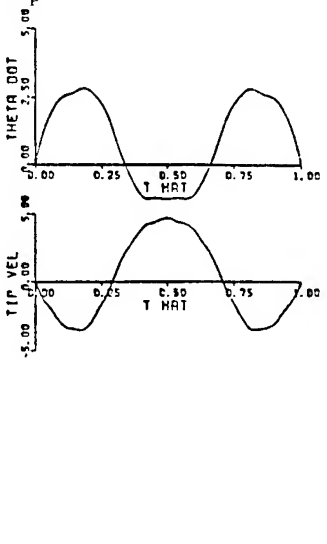


Fig. 7 Time Histories for the Non-Optimal Structure
($N_d=4$ $N_u=4$ $N_p=2$)

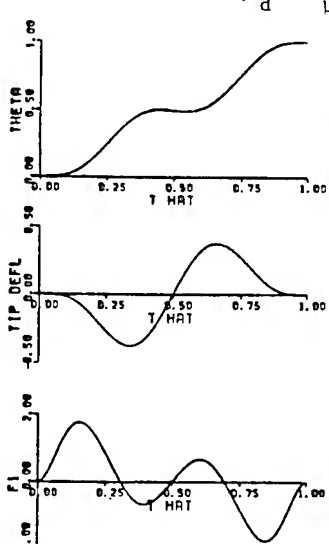


Fig. 8 Magnitude Spectra of Optimal Controls
($N_d=4$ $N_u=4$ $N_p=2$)

Table 1 Parameters, Frequencies, and Residual Response ($N_d=4$, $N_\mu=4$, $N_p=0$)

OPTIMAL PARAMETERS				NON-OPTIMAL PARAMETERS		
$\xi_1-\xi_4$.07533, .04065, .01837, .00723			.03539		
MODELED NATURAL FREQUENCIES (HZ)	0, 1.396, 3.434, 7.508			0, .778, 3.972, 11.097		
RESIDUAL MODE	NATURAL FREQUENCY (HZ)	FINAL DISPLACEMENT	FINAL VELOCITY	NATURAL FREQUENCY	FINAL DISPLACEMENT	FINAL VELOCITY
5	17.354	$.9 \times 10^{-5}$	$-.2 \times 10^{-2}$	21.864	$.5 \times 10^{-4}$	$.3 \times 10^{-2}$
6	23.558	$.6 \times 10^{-6}$	$.5 \times 10^{-3}$	40.650	$-.3 \times 10^{-5}$	$-.1 \times 10^{-2}$
7	40.627	$-.4 \times 10^{-6}$	$-.2 \times 10^{-3}$	65.279	$.1 \times 10^{-5}$	$-.6 \times 10^{-3}$
8	72.831	$-.7 \times 10^{-6}$	$-.2 \times 10^{-4}$	103.480	$-.2 \times 10^{-8}$	$.2 \times 10^{-4}$
9	141.034	$-.2 \times 10^{-6}$	$.2 \times 10^{-4}$	169.779	$-.4 \times 10^{-7}$	$.4 \times 10^{-4}$

Table 2 Parameters, Frequencies, and Residual Response ($N_d=4$, $N_\mu=4$, $N_p=2$)

OPTIMAL PARAMETERS				NON-OPTIMAL PARAMETERS		
$\xi_1-\xi_4$.12738, .05918, .02888, .01101			.05661		
MODELED NATURAL FREQUENCIES (HZ)	0, 2.197, 5.358, 12.432			0, 1.363, 6.394, 17.768		
RESIDUAL MODE	NATURAL FREQUENCY (HZ)	FINAL DISPLACEMENT	FINAL VELOCITY	NATURAL FREQUENCY	FINAL DISPLACEMENT	FINAL VELOCITY
5	27.377	$-.2 \times 10^{-7}$	$.7 \times 10^{-5}$	34.982	$-.7 \times 10^{-7}$	$-.9 \times 10^{-6}$
6	36.480	$-.2 \times 10^{-10}$	$.7 \times 10^{-7}$	65.028	$.4 \times 10^{-8}$	$-.1 \times 10^{-6}$
7	62.753	$.8 \times 10^{-9}$	$.3 \times 10^{-6}$	104.418	$-.3 \times 10^{-10}$	$.6 \times 10^{-7}$
8	112.076	$.1 \times 10^{-9}$	$-.2 \times 10^{-7}$	165.517	$.2 \times 10^{-12}$	$.4 \times 10^{-8}$
9	228.693	$.3 \times 10^{-11}$	$.7 \times 10^{-8}$	271.553	$.4 \times 10^{-13}$	$.4 \times 10^{-9}$

Table 3 Optimal Parameters for Various Reduced Order Models ($N_d=4$, $N_p=0$)

PARAMETER	$N_\mu = 2$	$N_\mu = 3$	$N_\mu = 4$	$N_\mu = 5$	$N_\mu = 6$	$N_\mu = 9$
1	.067553	.079908	.075331	.075554	.075720	.075780
2	.037145	.039533	.040646	.040875	.041025	.041019
3	.020166	.018555	.018373	.018391	.018377	.018409
4	.006601	.007156	.007232	.007222	.007173	.007166

Table 4 Optimal Parameters for Various Reduced Order Models ($N_d=4$, $N_p=2$)

PARAMETER	$N_\mu = 2$	$N_\mu = 3$	$N_\mu = 4$	$N_\mu = 5$	$N_\mu = 6$	$N_\mu = 7$
1	.101783	.120395	.127384	.127498	.127553	.127579
2	.056789	.060238	.059175	.058978	.059101	.059073
3	.031252	.028675	.028882	.028895	.028895	.028653
4	.010324	.011127	.011011	.011065	.011031	.010904

Table 5 Parameters, Frequencies, and Residual Response ($N_d=2$, $N_\mu=2$)

$N_p=0$				$N_p=2$		
$\xi_1-\xi_4$.06575, .02050			.09796, .03152		
MODELED NATURAL FREQUENCIES (HZ)	0, 1.370			0, 2.170		
RESIDUAL MODE	NATURAL FREQUENCY (HZ)	FINAL DISPLACEMENT	FINAL VELOCITY	NATURAL FREQUENCY (HZ)	FINAL DISPLACEMENT	FINAL VELOCITY
3	4.297	$-.9 \times 10^{-3}$	$.3 \times 10^{-1}$	6.623	$.3 \times 10^{-4}$	$.3 \times 10^{-2}$
4	10.192	$-.9 \times 10^{-4}$	$.4 \times 10^{-2}$	15.651	$.3 \times 10^{-6}$	$.5 \times 10^{-4}$
5	24.502	$.3 \times 10^{-8}$	$.7 \times 10^{-4}$	36.836	$-.3 \times 10^{-7}$	$-.3 \times 10^{-5}$
6	35.226	$-.3 \times 10^{-5}$	$.6 \times 10^{-3}$	53.838	$-.3 \times 10^{-8}$	$.5 \times 10^{-6}$
7	79.800	$.5 \times 10^{-6}$	$.2 \times 10^{-3}$	119.782	$-.7 \times 10^{-10}$	$-.4 \times 10^{-7}$
8	96.999	$.3 \times 10^{-6}$	$-.5 \times 10^{-6}$	147.930	$.3 \times 10^{-10}$	$.6 \times 10^{-8}$
9	190.500	$.3 \times 10^{-13}$	$-.2 \times 10^{-6}$	283.163	$.2 \times 10^{-11}$	$-.2 \times 10^{-8}$

D.T. Berry*, T.Y. Yang**, R.E. Skelton†
Purdue University
W. Lafayette, IN 47907

Abstract

Simple beam finite element analysis models for a flexible lattice beam with repetitive geometry are developed using the strain and kinetic energies formed by replacing the lattice with an equivalent continuum. This beam element has 6 degrees-of-freedom at each of its two nodes: three orthogonal displacements and three rotations. The performance of the simple finite element formulation in free vibration analysis is evaluated by comparison with free vibration results of a full or complex finite element model of the lattice formed by using truss bar elements. The accuracy of the frequencies predicted by the simple analysis models increases as the number of repeating cells in each half-wavelength increases. Modal Cost Analysis is performed on the modes obtained using both the simple analysis and complex models and the results are compared. Based on this information, model reduction decisions are influenced by the control objectives. The convergence of the modal costs is also illustrated. A set of reduced order controllers are designed based upon the resulting reduced order models. These controllers are used to control an evaluation model based on the full complex model. For low control energies, these controllers perform well when compared with the optimal controller based on the evaluation model itself. The example analysis shows that the simple finite element analysis models can be used with accuracy in the control law design process for lattice beams with low bandwidth controllers.

Introduction

The dynamics and control of lattice structures has attracted increasing attention recently due to their possible use in space applications. Structural and control design analyses of these lattices must be highly reliable since they cannot be tested full-scale in their operational environment prior to flight. Furthermore, simplified structural modeling techniques will be needed due to the size of these structures. For example, a full finite element analysis using truss bars of a structure containing large numbers of elements and nodes may be uneconomical especially during the initial design phases when the structure and associated systems are subject to change. At the same time, the structure's high flexibility requires a relatively large number of vehicle elastic modes to be accurately predicted. The controls analyst may also require accuracy in the structure's high frequency modes rather than just those of low frequency.

This paper describes techniques which result in simple structural analysis models that contain the dynamic information of the full complex model without the need for direct analysis on the complex model itself. Specifically, "simple finite element

analysis" models based upon an equivalent continuum of a given lattice beam are developed. To evaluate the accuracy of these finite element analysis models, natural frequencies and mode shapes are compared to a complete truss bar element model of the structure (the "complex model"). The accuracy of the simple analysis models is good especially when the half-wavelength of a mode spans many repeating cells. These simple analysis models will also be used as a basis for control law design after modal truncation using Modal Cost Analysis is performed. The resulting reduced order models will be called the "control design models." It will be shown that even the design model containing only one mode may yield a satisfactory control law design, depending on the control accuracy requirements.

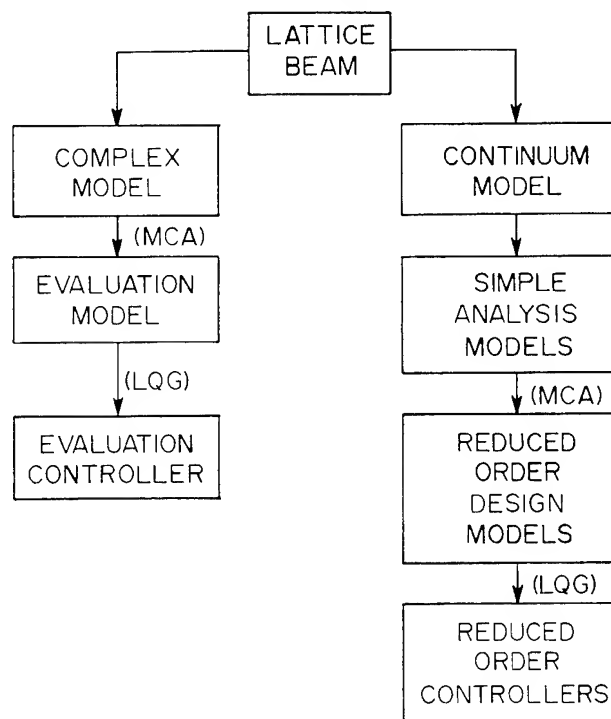


Fig. 1 Block diagram of the modeling process.

A graphic outline of the paper is shown in Fig. 1. A typical beam-like lattice structure is idealized as an equivalent continuum Timoshenko beam. The strain and kinetic energies of this continuum are used to formulate a 12 degree-of-freedom (d.o.f.) beam finite element. This element is used to produce a set of "simple finite element analysis models" of the lattice containing one to ten equal length elements. Free vibration analysis is performed on these simple analysis models and the results are compared with a full truss bar element model of the complete lattice grid. This full model will be referred to as the "complex model." The simple analysis models and the complex model are analyzed using Modal Cost Analysis (MCA) in order to judge the importance of the various modes in a given control problem. Modal truncation decisions are made at this point by retaining those modes

*Graduate Research Assistant, School of Aeronautics and Astronautics, Student Member, AIAA.

**Professor and Head, School of Aeronautics and Astronautics, Associate Fellow, AIAA.

†Professor, School of Aeronautics and Astronautics, Member, AIAA.

which have the largest modal cost. The resulting models are called the reduced order control "design models." Control laws are designed based on these control design models using Linear Quadratic Gaussian (LQG) control theory. These control laws are used to control an evaluation model constructed from the complex model. The evaluation of these control laws proceeds as shown in Fig. 2. The result of this analysis is the performance plot also shown in Fig. 2. It is essentially a plot of the magnitude of the control variable y (the output) vs. the magnitude of the control force u (the input). Using the performance plot, the usefulness and accuracy of the simple analysis models based on the equivalent continuum and used in control law design are evaluated.

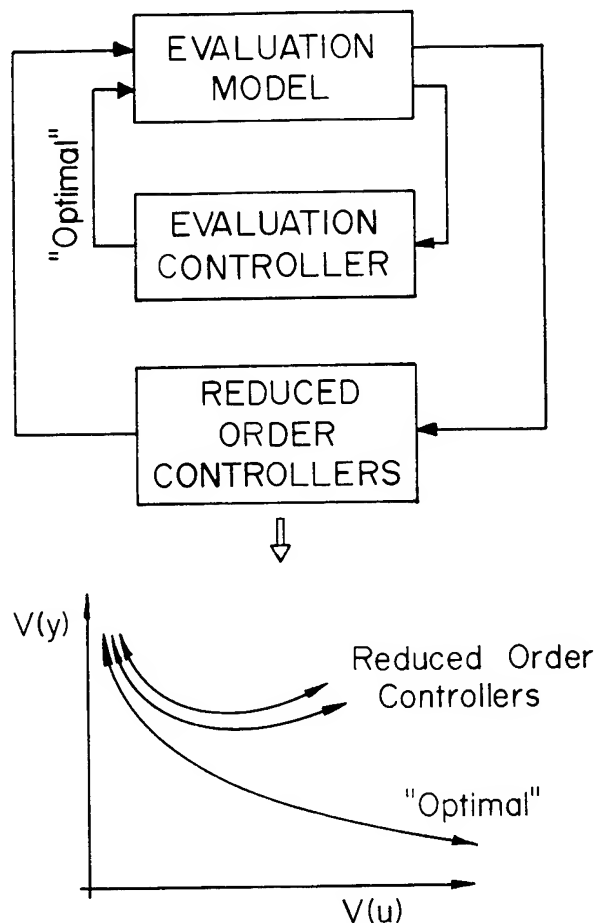
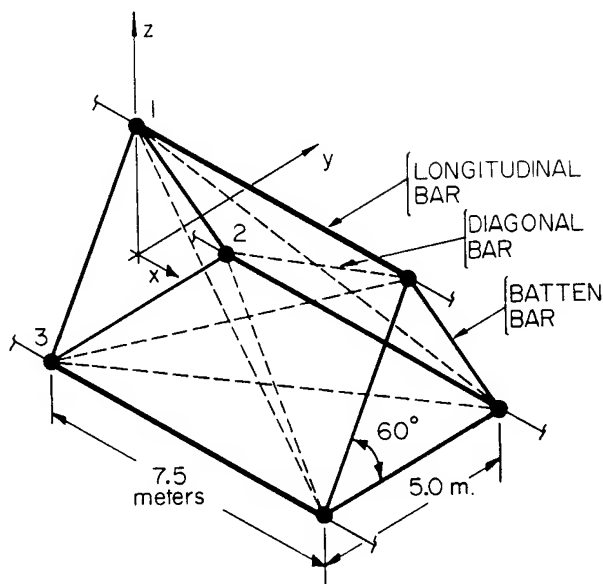


Fig. 2 Block diagram of the evaluation process.

Structural Modeling

The lattice beam model chosen for analysis is a 10 bay, simply supported beam with a repeating cell of the "single bay, double lace" type. The geometry of the cell is shown in Fig. 3. Three different types of bars are used in the lattice: longitudinal, diagonal and batten bars. The geometry and material characteristics of these bars are listed in Fig. 3. Overall length of the lattice beam is 75 meters. The lattice beam has 33 nodes and 123 bars. Although a lattice beam with more repeating cells could easily be modeled, it is shown later that the ten cell lattice has enough beam-like and non-beam-like behavior to illustrate the proposed method.

The complex model is produced by using axial truss bar elements of the type shown in Fig. 4.



BARS	$E (\frac{N}{m^2})$	$A (m^2)$	$\rho (\frac{kg}{m^3})$
LONGITUDINAL	71.7×10^9	$80. \times 10^{-6}$	2768.
DIAGONAL	71.7×10^9	$40. \times 10^{-6}$	2768.
BATTEN	71.7×10^9	$60. \times 10^{-6}$	2768.

Fig. 3 Repeating cell geometry: single bay, double lace lattice beam.

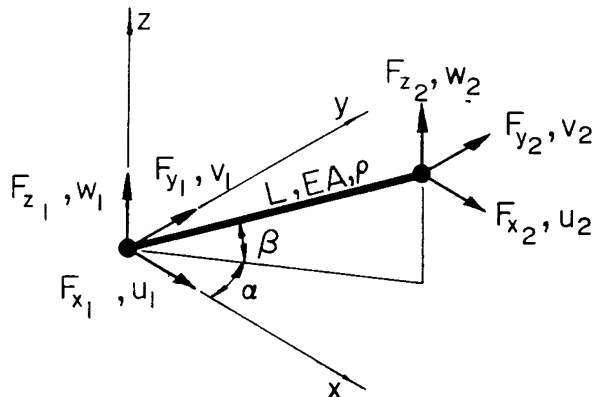


Fig. 4 Axial force bar element used in complex model.

The equations for a representative bar are

$$\frac{\rho A L}{6} \begin{bmatrix} 2 & & & & & \\ & 2 & & & & \\ & & 2 & & & \\ & 0 & 0 & 2 & & \\ 1 & 0 & 0 & 0 & 2 & \\ 0 & 1 & 0 & 0 & 0 & 2 \\ 0 & 0 & 1 & 0 & 0 & 0 & 2 \end{bmatrix} \begin{Bmatrix} \ddot{u}_1 \\ v_1 \\ \ddot{w}_1 \\ \ddot{u}_2 \\ \ddot{v}_2 \\ \ddot{w}_2 \end{Bmatrix}$$

$$+ \frac{EA}{L} \begin{bmatrix} S & -S \\ -S & S \end{bmatrix} \begin{Bmatrix} u_1 \\ v_1 \\ w_1 \\ u_2 \\ v_2 \\ w_2 \end{Bmatrix} = \begin{Bmatrix} F_{x_1} \\ F_{y_1} \\ F_{z_1} \\ F_{x_2} \\ F_{y_2} \\ F_{z_2} \end{Bmatrix} \quad (1)$$

$$\text{where } S = \begin{bmatrix} c_\beta^2 c_\alpha^2 & & \text{sym} \\ c_\beta^2 c_\alpha s_\alpha & c_\beta^2 s_\alpha^2 & \\ c_\beta s_\beta c_\alpha & c_\beta s_\beta s_\alpha & s_\beta^2 \end{bmatrix} \quad (1a)$$

$c_\alpha = \cos \alpha$, $c_\beta = \cos \beta$, $s_\alpha = \sin \alpha$, $s_\beta = \sin \beta$, and L = length of the truss bar element.

A consistent mass formulation has been used. Each bar in the lattice is modeled using one such element. The complex model has a total of 99 d.o.f.'s. The equations of motion for the assembled structure are of the following symbolic form

$$[M]\{\ddot{q}\} + [K]\{q\} = \{F\} \quad (2)$$

The simple finite element models are produced using the strain and kinetic energies of a Timoshenko beam continuum which is "equivalent" to the full lattice. Here, "equivalence" means that the lattice and the continuum contain equal kinetic and strain energies when both are subjected to the same displacement and velocity fields. The method used to produce the continuum model is presented in Reference 1. Briefly, the technique involves developing expressions for the strain and kinetic energies of a repeating lattice cell as functions of displacement and strain components along the centerline. These strain components are then expanded in a Taylor series about a suitably chosen origin. This expansion is, in effect, an assumption of a uniform state of strain across each repeating cell. This means that the half-wavelength of a structural mode must contain a reasonable number of repeating cells for that mode to be predicted accurately. The numerical coefficients on these displacement and strain components become the stiffness and mass coefficients of the equivalent continuum. They are calculated explicitly in Reference 1 for several lattice beam geometries, including the one used here. The strain energy has the form

$$U = \frac{1}{2} L \{\epsilon\}^T [C] \{\epsilon\} \quad (3)$$

where $\{\epsilon\}$ = beam-like strain components (6x1)

L = length of a repeating cell

and $[C]$ = stiffness coefficients of the equivalent continuum (6x6).

The kinetic energy is similarly represented as

$$T = \frac{1}{2} L \{\dot{u}\}^T [M] \{\dot{u}\} \quad (4)$$

where $\{u\}$ = beam-like displacement components (6x1)

L = length of a repeating cell

and $[M]$ = inertia coefficients of the equivalent continuum (6x6)

For the lattice beam shown in Fig. 3, the equivalent continuum is homogeneous and isotropic so the matrices $[C]$ and $[M]$ are diagonal and the stiffness

properties in the xy and xz planes are equal. The stiffness and mass properties of the equivalent continuum are as follows:

$$\begin{aligned} \text{Bending rigidity } EI &= 8.011 \times 10^7 \text{ N/m}^2 \\ \text{Axial rigidity } EA &= 2.528 \times 10^7 \text{ N} \\ \text{Shear rigidity } GA &= 2.203 \times 10^7 \text{ N} \\ \text{Torsional rigidity } GJ &= 9.178 \times 10^6 \text{ N/m}^2 \\ \text{Mass per unit length } \rho A &= 1.795 \text{ kg/m} \\ \text{Rotary inertia coefficient } \rho I &= 5.123 \text{ kg m}^2 \\ \text{Torsional inertia coefficient } \rho J &= 10.246 \text{ kg m}^2 \end{aligned} \quad (5)$$

Once the strain and kinetic energies of the continuum are known as functions of the constants listed in Eq. (5), finite element models are generated using a set of suitable displacement functions and Castigliano's theorem. As shown in Fig. 5, the simple finite element formulated is a 12 d.o.f. prismatic bar element with shear and rotary inertia effects included. The shear and rotary inertia are included in the same fashion as that by Archer². The matrix equations of motion for the beam finite element can be obtained by using Lagrange's equations.

$$\frac{d}{dt} \left(\frac{\partial T}{\partial \dot{q}_i} \right) + \frac{\partial V}{\partial q_i} = F_i \quad (6)$$

where T and U are the strain and kinetic energies of the continuum in terms of the beam element d.o.f.'s. These are obtained by using Eqs. 3 and 4 and the displacement functions for a Timoshenko beam². The resulting equations take the form

$$[M]\{\ddot{q}\} + [K]\{q\} = \{F\} \quad (7)$$

These are identical in form to the equations listed in Ref. 3 for a 12 d.o.f. homogeneous, isotropic Timoshenko beam.

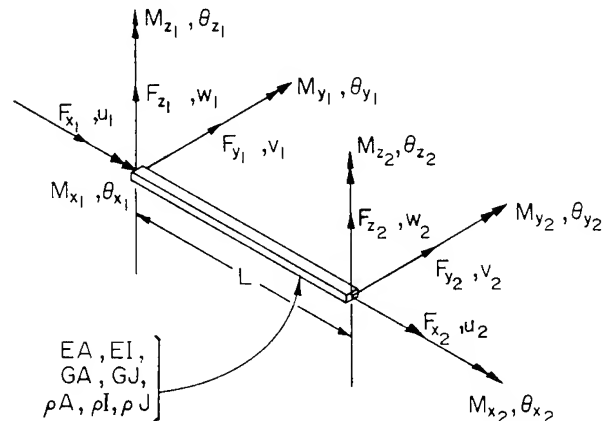


Fig. 5 Prismatic bar finite element used in simple analysis models.

Ten models with from one to ten equal length beam elements are constructed. The number of d.o.f.'s in each model varies from 12 in a one-element model to 66 in a 10-element model. If it is known beforehand that only, say, bending motions are observable in the output vector of interest, axial and torsional d.o.f.'s may be discarded leading to much smaller models. Modal Cost Analysis, the modal reduction technique used in this paper will do this automatically, however. The homogeneous, undamped equations of motion for the various models are of the form

$$[M]\{\ddot{q}\} + [K]\{q\} = \{0\} \quad (8)$$

Free Vibration Analysis

To evaluate the performance of the present formulation, free vibration analysis is performed on the simple analysis and complex models. Since the complex model does not have a node at its centerline, a multipoint constraint procedure is used. For example, if the average v displacement in the y -direction of the end cross-section (which contains nodes 1, 2, and 3 as shown in Fig. 3) is to be constrained, an equation of the form

$$v_1 + v_2 + v_3 = 0 \quad (9)$$

is written. This equation is used to express one of the displacements in terms of the others. The equations are substituted into the equations of motion for the lattice and the dependent d.o.f. is eliminated. Nine constraint equations of the form of Eq. (9) are needed to enforce the nine simply supported boundary conditions. The constrained complex model has 90 d.o.f.'s. The equations of motion for all of the models in free vibration are of the form

$$-\omega^2[M] + [K] \{\phi\} = \{0\} \quad (10)$$

Natural frequency results for the lattice beam example are shown in Table 1. Seven different models are used: 1) complex truss bar model, 2) five simple finite element analysis models with 1, 2, 3, 5, and 10 elements per model, and 3) an analytical solution of an equivalent homogeneous Timoshenko beam. These data show that frequencies of the simple models converge to the equivalent Timoshenko beam frequencies of the continuum as the number of simple finite elements increases.

Table 1: Natural Frequencies of the Simply Supported Lattice Beam Models

Mode Number	Mode	Number of Simple Finite Elements					Analytic Solution	Complex Model
		1	2	3	5	10		
1,2	1st Bending	12.98	11.71	11.67	11.66	11.65	11.65	11.44
4,5	2nd "	59.22	51.52	46.57	46.01	45.89	45.80	42.90
8,9	3rd "		127.8	114.5	102.0	100.8	100.4	88.37
11,12	4th "		232.4	208.3	179.9	174.2	172.4	142.4
15,16	5th "			369.2	306.4	264.1	258.9	201.1
21,22	6th "			507.4	425.9	369.4	357.0	261.2
24,25	7th "				608.5	489.8	464.4	318.6
26,27	8th "				849.9	625.2	579.2	367.8
29,30	9th "				1126.	772.6	699.8	401.6
3	1st Torsion	43.71	41.47	40.30	39.81	39.64	39.55	
7	2nd "	127.8	92.73	84.55	80.60	79.29	78.05	
10	3rd "			136.0	123.6	118.9	116.3	
13	4th "				190.5	169.1	158.6	152.2
14	5th "					218.6	198.2	185.2
17	6th "					272.0	237.9	214.5
19	7th "					327.8	277.5	238.9
20	8th "					381.0	317.2	257.3
23	9th "					421.6	356.8	268.8
6	1st Axial	86.67	80.63	79.50	78.92	78.68	78.60	78.05
18	2nd "		281.7	260.0	244.6	238.0	235.6	235.2
28	3rd "			471.7	433.3	403.2	393.0	395.3
31	4th "				649.8	578.1	550.2	559.2

Notes: 1) Units are radians per second.

2) Analytic solution is of an equivalent homogeneous Timoshenko beam (Ref. 4)

The rest of the data shows the comparison between the simple analysis models and the complex model of the lattice. It is noted that the complex model has approximately 31 beam-like modes. The term "beam-like" is used here to refer to bending, axial, and torsional behavior of the complex model.

The second torsional and second bending modes are plotted in Figs. 6 and 7. The 31 beam-like modes are those with the lowest frequencies. The highest 59 modes are, for the most part, non-beam-like modes which cannot be predicted by the simple models. Furthermore, the size of the complex models (90 d.o.f.'s) indicates that these upper 59 modes cannot be very accurate. They all have a frequency above 102 Hz while the beam-like modes all have frequencies below 89 Hz. Modes were identified strictly based upon their plotted shapes. While it is true that even the mode labeled as the first bending mode contains local non-beam-like effects (for example, distortion of the cross section in its own plane), these modes are characterized as "beam-like" and are compared to the modes of the simple analysis models. Fig. 7 shows the second bending mode for the complex model and the second bending mode for the simple analysis model containing five elements. Both modes have been normalized by their respective mass

MODE 7
FREQUENCY = 12.50 HZ

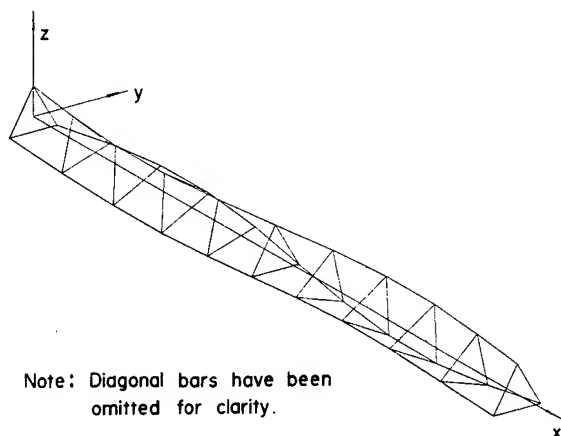


Fig. 6 Sample complex model torsional mode.

MODE 4
FREQUENCY = 6.83 HZ

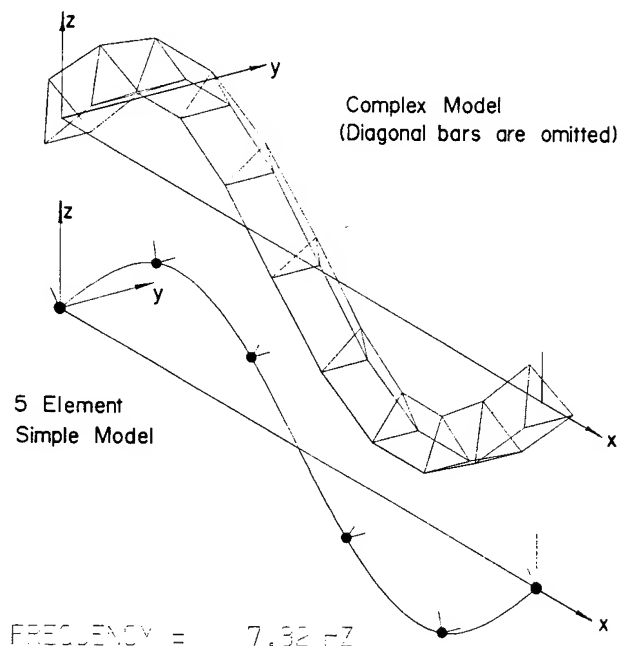


Fig. 7 Sample complex and simple model bending mode.

matrices. No unequal scaling was done for one mode relative to the other. The displacement functions used to generate the simple finite elements were used to interpolate values for the displacement between nodes. The rest of the beam-like modes have been plotted and match those of an equivalent simple analysis model. The 31 pairs of beam-like modes are given in Ref. 5.

Several comments can be made at this point about the comparison between the frequencies generated by the two models. First, low order bending, axial and torsional frequencies are predicted quite accurately. This accuracy decreases significantly for the higher modes, however. This is due to the fact that the half-wavelength of the higher modes span fewer repeating cells so the assumptions made in the development of the continuum are violated. For example, the half-wavelength of the n th mode spans $10/n$ repeating cells. Physically, the non-beam-like behavior of the lattice becomes dominant in the higher modes. This behavior cannot be predicted with a Timoshenko-type continuum beam model. The present example beam contains only ten repeating cells. However, the method is developed for handling lattice beams with considerably more cells. In fact, the simple models are developed specifically for use in the simultaneous structural and control optimization of structures with relatively large numbers of d.o.f.'s.

Modal Cost Analysis

The aim of this study is to develop reduced order controllers based on the simple finite element analysis models and to use these controllers to control an evaluation model based on the full complex model. Model reduction of the complex model to an evaluation model is needed due to the large size of the complex model. The issue of model reduction is, therefore, considered. Modal Cost Analysis is used to evaluate the importance and contribution of each mode in a given control problem.

Modal Cost Analysis is presented in detail in Refs. 6 and 7. It is a method which determines the importance of a particular mode to a given control problem. While the details are available in the above mentioned references, a brief description is given here. The total cost function is

$$V(y) = \lim_{t \rightarrow \infty} \frac{1}{t} E \left\{ \int_0^t ||y(\tau)||_Q^2 d\tau \right\} = \sum_{i=1}^n V_i(y) \quad (11)$$

where E is the expected value operator and $V_i(y)$ is the cost associated with the i th mode. $V_i(y)$ is defined by

$$V_i(y) = \lim_{t \rightarrow \infty} \frac{1}{t} E \left\{ \frac{\partial}{\partial x_i} \left[\int_0^t ||y(\tau)||_Q^2 d\tau \right] x_i \right\} \quad (12)$$

where x_i is the i th modal coordinate, and $v_i(y)$ are the modal costs.

$V_i(y)$ can be written in terms of modal data. Let the system be represented by the following matrix second order equations.

$$\begin{aligned} [M]\{\ddot{q}\} + [D]\{\dot{q}\} + [K]\{q\} &= [B]\{u\} + \{w\} \\ \{y\} &= [C]\{q\} + [C']\{\dot{q}\} \\ \{z\} &= [Z]\{q\} + [Z']\{\dot{q}\} + \{v\} \end{aligned} \quad (13)$$

The forcing term is a control input from noisy actuators. The measurement also includes noise. The

transformation to modal coordinates is made by using the modal matrix associated with the undamped, homogeneous system equations.

$$\{q\} = [\Phi]\{\eta\} \quad (14)$$

The modal matrix $[\Phi]$ is normalized with respect to the system mass matrix. After premultiplying by $[\Phi]^T$, the resulting equations are

$$\begin{aligned} \{\ddot{\eta}\} + [\Phi]^T[D][\Phi]\{\dot{\eta}\} + [\omega_i^2]\{\eta\} &= [\Phi]^T[B]\{u\} + \{v\} \\ \{y\} &= [C][\Phi]\{\eta\} + [C'][\Phi]\{\dot{\eta}\} \\ \{z\} &= [Z][\Phi]\{\eta\} + [Z'][\Phi]\{\dot{\eta}\} + \{v\} \end{aligned} \quad (15)$$

where $\{\eta\}$ is an $n \times 1$ vector. n is the number of modes in the model. Although damping must be included in the system equations, it is a highly uncertain parameter. It is assumed small for the present structure and has the form

$$[\Phi]^T[D][\Phi] = [2\zeta_i\omega_i] \quad (16)$$

and the modal damping ratio $\zeta_i = .005$ for all modes. Defining

$$\begin{aligned} [b_i^T] &= \text{ith row of } [\Phi]^T[B] \\ \{c_i\} &= \text{ith column of } [C][\Phi] \\ \{c_i'\} &= \text{ith column of } [C'][\Phi], \end{aligned} \quad (17)$$

it can be shown⁷ that for a system in the above form, the modal cost $V_i(y)$ associated with the mode x_i is given by

$$V_i(y) = \frac{1}{4\zeta_i\omega_i} \left[||c_i||_Q^2 + \omega_i^2 ||c_i'||_Q^2 \right] ||b_i||_W^2 \quad (18)$$

where the notation $||c_i||_Q^2 = \{c_i\}^T [Q] \{c_i\}$ is used.

$[Q]$ is a weighting matrix on the outputs and $[W]$ is the intensity of the actuator noise. Note that $V_i(y)$ are defined strictly in terms of modal data.

That is, $\{c_i\}$, $\{c_i'\}$, and $\{b_i\}$ are composed of the values of the i th mode shape at the input and output locations, respectively.

MCA is used to reduce the size of simple analysis models. The resulting models are called control design models. A set of reduced order controllers is then designed from these control design models. MCA will also be used to reduce the total set of complex model modes to an evaluation model which will be used to assess the performance of the reduced order controllers.

Results of Modal Cost Analysis

The results of the Modal Cost Analysis are now used to evaluate the importance of the modes of the complex model and of the simple analysis models in a particular control problem. The control problem analyzed is illustrated graphically in Fig. 8. A single force actuator is located at a distance of 7.5 meters from one end of the simply supported lattice beam. It is located at the top vertex of that particular triangular cross section and drives the z direction. The noise in the actuator is assumed to be uncorrelated Gaussian white noise with intensity $W = 1.0 \times 10^{-4} \text{ N}^2$. The sensor is located at the same point and measures the w displacement. Noise in the sensor is assumed to be

uncorrelated Gaussian white noise with intensity $V=1.0 \times 10^{-10} \text{ m}^2$. The control output variable is the w displacement at the top vertex of the midspan cross section. The sensor, actuator, and output for the simple analysis models are located at equivalent axial stations and measure the same displacements in the same directions. For this example, both $[Q]$ and $[R]$ equal 1.0 . These examples have been constructed so that only the lateral z direction bending modes will have significant modal costs.

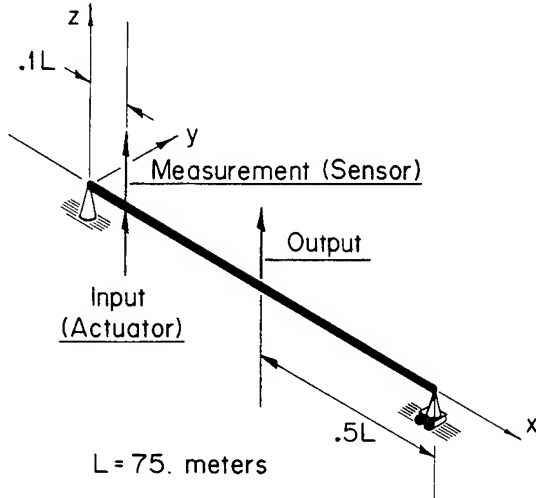


Fig. 8 Schematic of example control problem

Modal costs of the complex model modes and the simple analysis model modes generated with 2, 5, and 10 elements per model are shown in Figs. 9, 10, and 11, respectively. The modal cost data has been normalized so that the maximum modal cost has a value of 1.0 . Costs below 1.0×10^{-6} are set to this value. Several comments are in order about these figures. First, not every analysis model predicts every complex mode. As the number of elements in the analysis models increases, the number of modes predicted also increases. Second, the analysis model frequencies do not monotonically increase with mode number. They have been reordered to show the equivalence with the complex model modes. Third, only the odd bending modes have significant modal costs because the output location is at a node of the even-numbered modes. These modes are unobservable for this particular output location. Thus, these modes have no contribution to the cost function and can be dropped from any control design model. If a two mode model were needed, traditional modal truncation based on frequency would keep bending modes 1 and 2 which is no better than a one mode model of mode 1 since mode 2 has no effect on the output. Therefore, model reduction decisions cannot be divorced from the control objectives.

Figures 9, 10, and 11 show that, when compared with the complex model, the analysis models accurately predict the modal costs of the complex model for the lowest modes. The accuracy begins to decrease as the mode number increases. This is because the modal costs are inversely proportional to the cube of the natural frequency. For example, the complex model has a lower frequency in the third bending mode (mode 15) than the analysis models. This causes that mode of the complex model to have a higher modal cost than the equivalent mode of the analysis models. This higher modal cost indicates that the third bending mode is more impor-

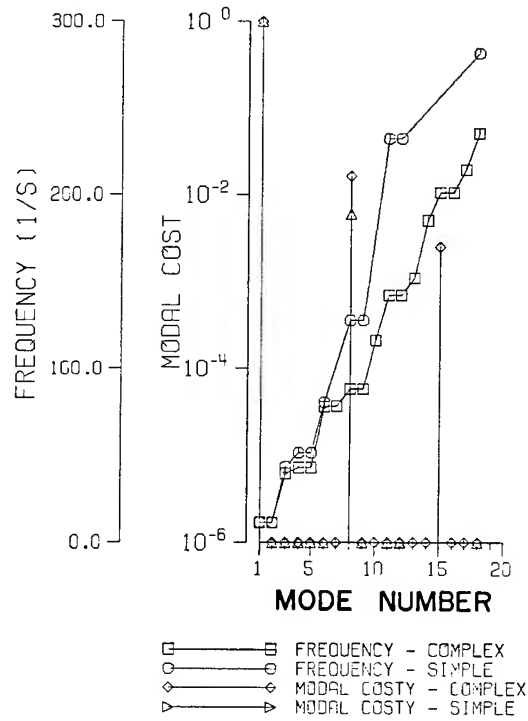


Fig. 9 Modal cost and frequency data for complex model and two element analysis model.

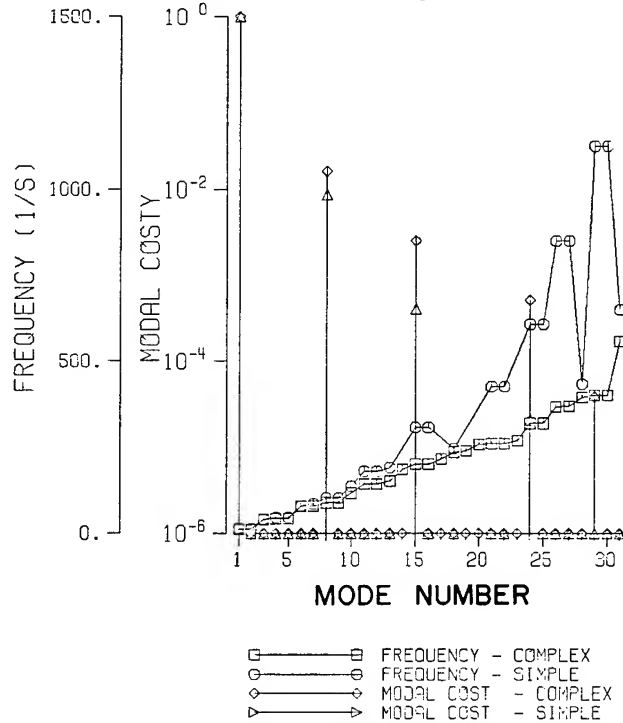


Fig. 10 Modal cost and frequency data for complex model and five element analysis model.

tant to the minimization of the cost function than the analysis models would predict. It is noted, however, that the trends of the modal cost data are accurately predicted by the analysis models. That is, modal truncation decisions based upon Modal Cost Analysis of an analysis model will at least preserve the relative importance of the modes of this analysis model to the overall control objective. It is also noted that as the number of elements in the analysis models increases, the accuracy of the modal

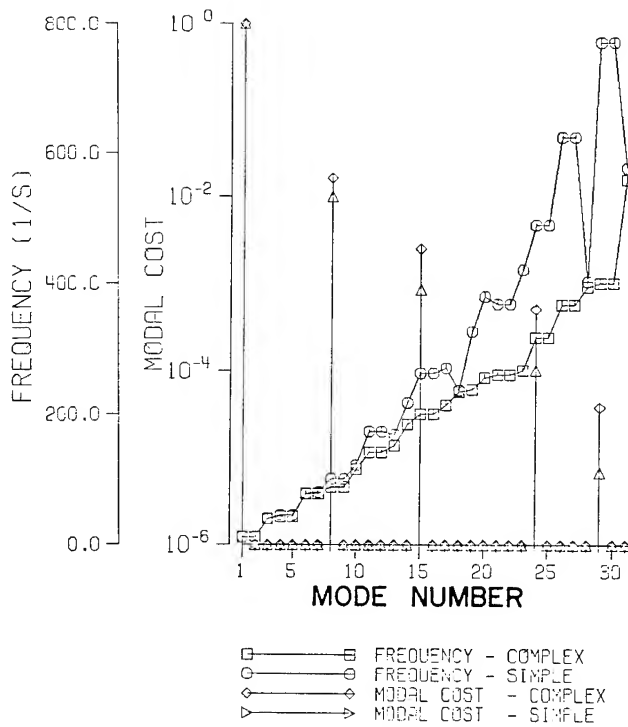


Fig. 11 Modal cost and frequency data for complex model and ten element analysis model.

costs converge, but that the error does not go to zero. This is to be expected since, although the frequencies of the analysis models converge, they converge to the frequency of the equivalent Timoshenko beam continuum and not to the frequency of the complex model (see Table 1). For example, the errors in the frequency of the second bending mode of the analysis models with one, two, three, and four elements with respect to the complex model is 38.0, 20.1, 8.5, and 7.6 percent, respectively. This is noted to show that the number of elements in the analysis model needed to converge to a particular frequency and modal cost can be estimated beforehand.

Model Reduction

Model reduction using Modal Cost Analysis is straightforward. For an n mode reduced order design model, the n modes with the highest modal cost are selected. Based on the information in Figures 9, 10, and 11, three reduced order design models are formed: 1) a 1 mode model containing the first bending mode of the two element analysis model, 2) a 2 mode model containing the first and third bending modes of the seven element analysis model, 3) a 4 mode model containing the first, third, fifth, and seventh bending modes of the ten element analysis model. Modal Cost Analysis is also used in the formation of an evaluation model. This reduced model is needed since the full complex model has too many modes to use as a basis for controller design and evaluation. The evaluation model is constructed from the first, third, fifth, seventh and ninth bending modes of the complex model.

A measure of how completely a reduced order model matches the total cost information of its parent model is given by the Cost Perturbation Index (CPI). The CPI is defined as

$$CPI = \frac{\sum_{i=1}^{\hat{n}} V_i(y)}{V(y)} \quad (19)$$

where $V(y)$ is the total modal cost and \hat{n} is the number of modes in the reduced order model. For a reduced model which contains all of the cost information of its parent, $CPI=1.0$. It is clear that those modes with the smallest $V_i(y)$ should be deleted. The reduced order design models and their associated cost perturbation indices are listed in Table 2.

Table 2: Reduced Order Design Models

Reduced Order Model Number	Reduced from which Model	Mode Numbers Retained	Cost Perturbation Index
Evaluation	Complex	1,8,15,24,29	.9997
1	1 Element Analysis	1	.9940
2	5 Element Analysis	1,8	.9996
3	10 Element Analysis	1,8,15,24	.9999

Reduced Order Controller Design

All of the reduced order design models are fully observable and controllable. A controller for each model is designed using Linear Quadratic Gaussian techniques.⁸ The equations of motion in state space form are

$$\dot{x}_R = [A_R]x_R + [B_R]u + \{w\}$$

$$y = [C_R]x_R$$

$$z = [Z_R]x_R + \{v\}$$

and

$$E(w(t)) = 0 \quad (20)$$

$$E(v(t)) = 0$$

$$E(w(\tau)w^T(t)) = [W]\delta(t-\tau)$$

$$E(v(\tau)v^T(t)) = [V]\delta(t-\tau)$$

$$E(w(t)x_R^T(0)) = 0$$

$$E(v(t)x_R^T(0)) = 0$$

$$E(v(t)w^T(\tau)) = 0$$

The cost function to be minimized is

$$V = \lim_{t \rightarrow \infty} \frac{1}{t} E \left\{ \int_0^t (||y(\tau)||_Q^2 + \sigma ||y(\tau)||_R^2) d\tau \right\} \quad (21)$$

The resulting controller is

$$\dot{x}_C = [A_C]x_C + [F]z$$

$$u = [G]x_C$$

$$[G] = -\frac{1}{\sigma} [R]^{-1} [B]^T [K] \quad (22)$$

$$[F] = [P][Z_R]^T [V]^{-1}$$

$$[A_C] = [A_R] + [B_R][G] - [F][Z_R]$$

where p and k satisfy the Riccati equations

$$[K][A_R] + [A_R]^T [K] - \frac{1}{\sigma} [K][B_R][R]^{-1}[B_R]^T [K]$$

$$\begin{aligned}
& + [C_R]^T [Q] [C_R] = [0] \\
& [P] [A_R]^T + [A_R] [P] - [P] [Z_R]^T [V]^{-1} [Z_R] [P] \\
& + [D_R] [W] [D_R]^T = [0]
\end{aligned} \quad (23)$$

This controller is optimal for the reduced order design model itself but will not perform optimally when used to drive the evaluation model. The evaluation model can be written

$$\begin{aligned}
\dot{\{x_E\}} &= [A_E] \{x_E\} + [B_E] \{u\} + \{w\} \\
\{y\} &= [C_E] \{x_E\} \\
\{z\} &= [Z_E] \{x_E\} + \{v\}
\end{aligned} \quad (24)$$

The entire closed loop system has the form

$$\begin{aligned}
\dot{\{x_a\}} &= [A_a] \{x_a\} + [B_a] \{w_a\} \\
\{y_a\} &= [C_a] \{x_a\}
\end{aligned} \quad (25)$$

where

$$\begin{aligned}
\{x_a\} &= \begin{Bmatrix} x_E \\ x_C \end{Bmatrix} \\
[A_a] &= \begin{bmatrix} A_E & B_E G \\ F Z_E & A_C \end{bmatrix} \{y_a\} = \begin{Bmatrix} y \\ u \end{Bmatrix} \quad [C_a] = \begin{bmatrix} C_E & 0 \\ 0 & G \end{bmatrix} \\
[D_a] &= \begin{bmatrix} B_E & 0 \\ 0 & F \end{bmatrix} \{w_a\} = \begin{Bmatrix} w \\ v \end{Bmatrix}
\end{aligned} \quad (25a)$$

The regulation cost $V(y)$ and control energy $V(u)$ are calculated as follows

$$V(y) = \lim_{t \rightarrow \infty} \frac{1}{t} E \left\{ \int_0^t \|y(\tau)\|_Q^2 d\tau \right\} = \text{tr} [C_E]^T [Q] [C_E] [X_{11}] \quad (26)$$

$$V(u) = \lim_{t \rightarrow \infty} \frac{1}{t} E \left\{ \int_0^t \|u(\tau)\|_R^2 d\tau \right\} = \text{tr} [G]^T [G] [X_{22}]$$

where x satisfies

$$\begin{aligned}
& [X] [A_a]^T + [A_a] [X] + [D_a] [W_a] [D_a]^T = \bar{0} \\
& [W_a] = \begin{bmatrix} W & 0 \\ 0 & V \end{bmatrix} \\
& [X] = \begin{bmatrix} X_{11} & X_{21}^T \\ X_{21} & X_{22} \end{bmatrix}
\end{aligned} \quad (27)$$

The evaluation process proceeds as follows. For a given reduced order design model, a set of reduced order controllers dependent upon the control weighting parameter σ is designed. These controllers are used to close the evaluation model loop and calculate a set of regulation cost vs. control energy values. Finally, a full order controller using the evaluation model itself as the control design model is designed. This serves as a comparison for the performance of the reduced order models. The resulting controller will be optimal while the controllers designed using the reduced order control design models will not be. The resulting performance plots of regulation cost vs. control energy will have the form shown in Fig. 2.

The plot has a limiting value for regulation cost. $V(y)(\sigma \rightarrow 0)$ is the lowest possible regulation cost value regardless of controller effort. This value is non-zero due to errors in reconstructing the state. Now, for the reduced order controllers, the regulation cost will decrease as $\sigma \rightarrow 0$, then increase. This is due to controllability of those higher modes which were not included in the control design model.

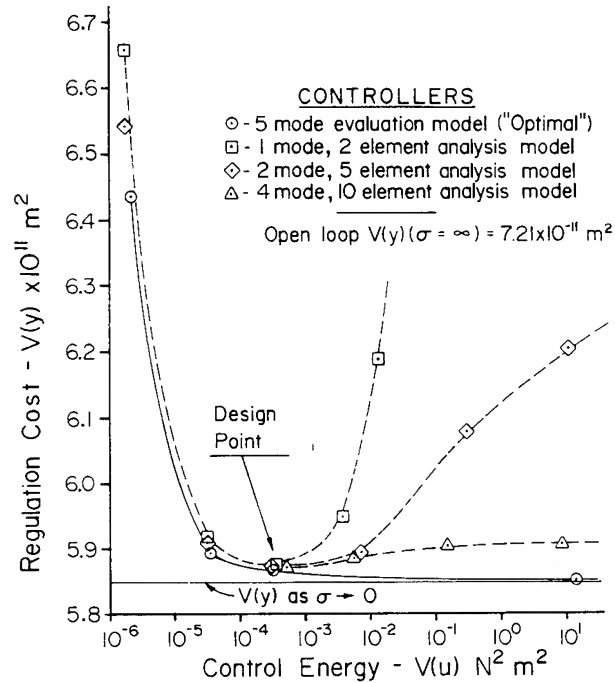


Fig. 12 Performance plot—3 reduced order controllers

A performance plot for the models in Table 2 has been calculated and is shown in Figure 12. As expected, all reduced order controllers are able to increase the performance of the system for low control effort. As control effort increases, however, system performance is degraded. The performance of all the reduced models, however, is exceptional. The 1 mode reduced order controller achieves a minimum regulation cost of $5.874e-11 \text{ m}^2$ before it begins to diverge from the optimal controller. When compared with the best theoretical system regulation cost of $5.8497e-11 \text{ m}^2$, this controller has an error in regulation cost of only .4 percent. The other two reduced order controllers perform better at higher control energies, but only slightly better at the "design point." Although in general the design point is a function of controller order, it is not in this case, since the first mode dominates the dynamic behavior of the lattice. It was also expected that for low values of σ , the controllability of the truncated modes would drive the system unstable as the control effort approaches infinity ($\sigma \rightarrow 0$). All of the closed loop systems were still stable, however, for σ as small as $\sigma = 1.e-25$.

Conclusions

A basic procedure for simple and efficient finite element modeling of flexible beam-like lattice structures with repetitive geometry has been developed. The formulation is based on the strain and kinetic energies of an equivalent continuum. The method is general and is not restricted to the par-

ticular lattice geometry studied here. Although the example studied contains ten repeating cells, the method is particularly suited to cases in which the number of repeating cells is considerably more than ten. The method will yield accurate results as long as there are a sufficient number of repeating cells per half-wavelength of a mode.

The present method can be extended in a straightforward manner to cases of plate- and shell-like lattice structures. These structures have been considered for such applications as large solar arrays for power generation and large curved antennas for communication purposes.

The present finite element analysis models allow the application of control theory to actual lattice structures in the form of the simple models. It has been common that the controls analyst has worked mostly with homogeneous isotropic finite element formulations or with large truss bar element models. The simple analysis models developed here present a modeling alternative. Using these models, free vibration analyses for beam-like lattice structures can be performed efficiently. The simplicity and efficiency of the simple models allows their application in preliminary control law design studies. The present formulation and procedures are also expected to be useful for studies on the optimization of sensor/actuator locations, the minimization of structural mass, etc.

Specifically, this study has used the simple finite element formulation in the control design process for a typical lattice beam. Modal truncation has been applied to these simple analysis models using Modal Cost Analysis, a standard model reduction technique. Other model reduction techniques and analysis methods may be similarly applied. The reduced order models resulting from modal truncation have been used in the control law design process. The example chosen has shown that the structural modeling problem and the control design problem are not separable since the model reduction process is influenced by the control objectives. This study has demonstrated a fundamental procedure for the integration of the structural modeling and control modeling problems which usually proceed separately.

Acknowledgements

This work was sponsored under Air Force Office of Scientific Research contract number AFOSR-83-0104 administered by Dr. Anthony Amos.

References

- ¹Noor, A.K., Anderson, M.S., Greene, W.H., "Continuum models for Beam- and Platelike Lattice Structures," *AIAA Journal*, Vol. 16, No. 12, December 1978, pp. 1219-1228.
- ²Archer, J.S., "Consistent Matrix Formulations for Structural Analysis Using Finite Element Techniques," *AIAA Journal*, Vol. 3, No. 10, October 1965, pp. 1910-1918.
- ³Przemienicki, J.S., *Theory of Matrix Structural Analysis*, McGraw Hill, New York, 1968.
- ⁴Blevins, R.D., *Formulas for Natural Frequencies and Mode Shape*, Van Nostrand Reinhold, New York, 1979.

⁵Berry, D.T., "Structural and Control Modeling of Large, Flexible Lattice Beams," M.S. Thesis, Purdue University, to be published.

⁶Skelton, R.E., Hughes, P.C., Hablani, H.B., "Order Reduction for Models of Space Structures Using Modal Cost Analysis," *Journal of Guidance, Control, and Dynamics*, Vol. 5, No. 4, July-August 1982, pp. 351-357.

⁷Skelton, R.E., Yousuff, A., Dornseif, M., "Case Studies of Model Reduction of Flexible Structures by Modal Cost Analysis," Report to Control Dynamics Co., Huntsville, Alabama, February 1983.

⁸Kwakernaak, H., Sivan, R., *Linear Optimal Control Systems*, Wiley and Sons, New York, 1982.

Vipperla B. Venkayya*†
Victoria A. Tischler*
Air Force Wright Aeronautical Laboratories
Wright-Patterson Air Force Base, Ohio

Introduction

Vibration Control is an important consideration in the design of dynamic systems on the ground, in the air and in space. The disturbances in ground and air vehicles are primarily caused by rough road (runway) profiles and air flow, such as gusts and power plants. Similarly in large space structures the disturbances are the result of slewing/pointing maneuvers, thermal transients, and mechanical machinery such as coolers, generators, etc. Control of the dynamic response is essential for maintaining the ride quality and performance requirements as well as for the safety of the structure.

The response of a structure is basically governed by three sets of parameters. The mass, damping and stiffness represent the structural parameters. The second set of parameters is due to the sources of external disturbances. These are generally external to the system and are considered as fixed inputs or their alteration is not within the realm of the structures/controllers designer. The third set represents the control system, assuming that the structure is actively controlled. Control of the dynamic response by modification of the structural parameters alone is considered as passive control. Passive control is most appealing both from the reliability and maintainability point of view if it can be achieved at all economically. Basically the stiffness and mass modifications result in frequency and mode changes, while the damping effects the dissipation energy of the system. The damping can be significantly altered by either viscoelastic coatings (or constrained layer damping) or by the provision of discrete dashpot mechanisms.

The objective of vibration control is to design the structure and its controls either to eliminate vibration completely or to reduce the mean square response of the system to a desired level within a reasonable span of time. In addition, it is important that this objective be achieved in some optimal way. For a structural designer the optimal design represents an adjustment of structural parameters to minimize the structural mass while improving the dynamic characteristics (such as changes in frequencies and mode shapes) to reduce the dynamic response. For a control designer, on the other hand, optimization represents sizing of the controllers in such a way that a specified performance index is minimized. If the locations and the number of actuators and sensors are predetermined and fixed, then the individual actuator inputs are the variables in the control optimization problem. Otherwise both the number and the locations of the actuators can also be variables in the optimal control design.

The interaction between the structures and controls designers has been very minimal in the past. The structural designer develops his designs based on strength and stiffness requirements derived from the peak maneuver loads expected during the operation of the flight vehicle. His primary concern is to design light weight (minimum mass) structures that satisfy the strength, stiffness and other performance requirements. In general the designer of active controls has little input in the evolution of the basic structural design. Similarly the structural analyst's participation in the control design is limited at best to providing information about the frequencies and mode shapes of the primary structure. This practice of compartmentalizing designs is promoted by the attitude that optimal controls can be designed for any structure and vice versa. This may be true to a great extent because many successful systems were designed in the past based on this philosophy. However, there has been strong indication in recent years that significant performance as well as cost improvements can be realized by optimizing the structure and the controls together. There is general agreement⁽¹⁾ that future research in large space structures dynamics and controls should develop algorithms to promote such an interdisciplinary approach to design. Recent advances in digital computers and computational algorithms provide ample opportunity for such development. Reference (2) contains a number of papers supporting this theme and also some ideas about how to formulate the combined optimization problem. However, there is also a realization that this combined optimization problem is not easily tractable for a number of reasons. For example, in structural optimization treatment of time response constraints can be quite involved, and the solution is, in general, not unique. Multiple minimums with the same or different merits can exist. The linear optimal control problem, on the other hand, is naturally a time response problem, and when the solution exists it is unique. The issues of how the relative minimums in structural optimization affect the control optimization problem are not clear and must be explored.

The object of this paper is to study the effects of modification of structural parameters on the dynamic response of flexible structures with and without active controls. The resulting automated analysis procedure is expected to be a precursor to the development of a sensitivity analysis in which the issues of both optimal structure and controls can be addressed. The problem will be treated as having dual objective functions. The optimization will be carried out independently, but the combined effect of structural optimization and controls on the dynamic response will be studied. The structural optimization will be posed as a problem of the minimization of structural mass with the constraint on the fundamental frequency. In the optimal control design a quadratic performance function involving the energy of the vibrating structure and the actuators will be minimized.

*Aerospace Engineers

†Member AIAA

Equations of Motion and Control Objectives

The second order differential equation that governs the forced vibration of a large space structure with active controls can be written as

$$\underline{m}(\underline{d})\ddot{\underline{r}}(t) + \underline{c}(\underline{d})\dot{\underline{r}}(t) + \underline{k}(\underline{d})\underline{r}(t) = \underline{F}_1(u, t) + \underline{F}_2(t) \quad (1)$$

The n coupled differential equations represent the mathematical model of a discretized (finite element model) large space structure. The $n \times 1$ vector $\underline{r}(t)$ represents the system response in the configuration space. The $n \times n$ mass (\underline{m}), damping (\underline{c}) and stiffness (\underline{k}) matrices are functions of the structural variables (\underline{d}). The number of structural variables can be as few as one or as many as a multiple of the number of finite elements in the structure. In addition the mass matrix generally consists of structural and non-structural components. Only the structural mass will be a function of the structural variables. In a finite element formulation the mass and stiffness matrices are symmetric and positive definite or at least semidefinite. The damping matrix will be assumed proportional to the stiffness and the mass matrices in this formulation

$$\underline{c}(\underline{d}) = \alpha \underline{k}(\underline{d}) + \beta \underline{m}(\underline{d}) \quad (2)$$

where α and β are proportionality constants.

The right side of equation (1) contains two parts. $\underline{F}_1(u, t)$ represents the control input. The function $\underline{F}_2(t)$ represents the external disturbances, which initiate or continue the vibration of the system. In this investigation only the vibration initiation will be considered (no forced motion, $\underline{F}_2(t) = 0$). In such a case the governing differential equation can be written as

$$\underline{m}(\underline{d})\ddot{\underline{r}}(t) + \underline{c}(\underline{d})\dot{\underline{r}}(t) + \underline{k}(\underline{d})\underline{r}(t) = \underline{b}\underline{u}(t) \quad (3)$$

It is assumed that the control system consists of a set of discrete actuators. The $m \times 1$ vector $\underline{u}(t)$ represents the input of the actuators, while \underline{b} is an $n \times m$ matrix that identifies the position and the relationship between the controllers and the actuators.

The state space representation of the governing differential equations for the open loop system is written as (3-8)

$$\dot{\underline{X}} = \underline{A}\underline{X} + \underline{B}\underline{u} \quad (4)$$

where the $2n \times 1$ vectors \underline{X} and $\dot{\underline{X}}$ are given by

$$\dot{\underline{X}} = \begin{bmatrix} \ddot{\underline{r}} \\ \dot{\underline{r}} \end{bmatrix}_{2n \times 1} \quad \underline{X} = \begin{bmatrix} \underline{r} \\ \dot{\underline{r}} \end{bmatrix}_{2n \times 1} \quad (5)$$

The open loop plant matrix \underline{A} and the control matrix \underline{B} are given by

$$\underline{A} = \begin{bmatrix} -\underline{m}^{-1}\underline{c} & -\underline{m}^{-1}\underline{k} \\ \underline{I} & \underline{0} \end{bmatrix}_{2n \times 2n} \quad \underline{B} = \begin{bmatrix} -\underline{m}^{-1}\underline{b} \\ \underline{0} \end{bmatrix}_{2n \times m} \quad (6)$$

The governing differential equations as given in equations (4) to (6) represent the full system formulation without modal reduction. The usual procedure to reduce the dimensionality of the system is by modal reduction which is obtained by substituting

$$\underline{r}(t) = \underline{\Phi}\underline{\eta}(t) \quad (7)$$

in equation (3). The $p \times 1$ vector $\underline{\eta}(t)$ represents the normal coordinates. The matrix $\underline{\Phi}$ is an $n \times p$ modal matrix which is a solution of the eigenvalue problem

$$\omega^2 \underline{m}\underline{\Phi} = \underline{k}\underline{\Phi} \quad (8)$$

The number of modes ($p \leq n$) required to represent the dynamic response depends on the type of disturbances and the number and locations of the actuators and sensors. ω^2 represents the eigenvalues of the system.

In the case of modal reduction the state vectors $\dot{\underline{X}}$ and \underline{X} in equation (4) are given by

$$\dot{\underline{X}} = \begin{bmatrix} \ddot{\underline{\eta}} \\ \dot{\underline{\eta}} \end{bmatrix}_{2p \times 1} \quad \underline{X} = \begin{bmatrix} \underline{\eta} \\ \dot{\underline{\eta}} \end{bmatrix}_{2p \times 1} \quad (9)$$

Now the plant and the control matrices of the open loop system are given by

$$\underline{A} = \begin{bmatrix} -2\zeta_1\omega_1 & -\omega_1^2 \\ \underline{I} & \underline{0} \end{bmatrix}_{2p \times 2p} \quad \underline{B} = \begin{bmatrix} \underline{\Phi}^T \underline{b} \\ \underline{0} \end{bmatrix}_{2p \times m} \quad (10)$$

The submatrices in \underline{A} are given by

$$[-2\zeta_1\omega_1] = \begin{bmatrix} 2\zeta_1\omega_1 & 0 & \dots & 0 \\ 0 & 2\zeta_2\omega_2 & \dots & 0 \\ \vdots & \vdots & \ddots & \vdots \\ 0 & 0 & \dots & 2\zeta_p\omega_p \end{bmatrix} \quad (11a)$$

$$[-\omega_1^2] = \begin{bmatrix} \omega_1^2 & 0 & \dots & 0 \\ 0 & \omega_2^2 & \dots & 0 \\ \vdots & \vdots & \ddots & \vdots \\ 0 & 0 & \dots & \omega_p^2 \end{bmatrix} \quad (11b)$$

The damping ratio ζ_1 is given by

$$\zeta_1 = \frac{\alpha}{2/\omega_1} + \frac{\beta}{2\omega_1} \quad (12)$$

The damping ratio, $\zeta_1 < 1$, which represents the underdamped case, is of interest to this discussion.

Returning to the open loop plant of the full system formulation

$$\dot{\underline{X}} = \underline{A}\underline{X} + \underline{B}\underline{u} \quad (13)$$

the output of the system can be represented by

$$\underline{y}_{s \times 1} = \underline{C}_{s \times 2n} \underline{X}_{2n \times 1} \quad (14)$$

Equation (14) includes both the velocity and the displacement sensors. $s=2n$ represents the case where there are enough sensors to measure the entire state. For most practical systems this would be an unrealistic assumption. $s < 2n$ represents a more realistic case.

The output as given by equation (14) represents the ideal state, while the actual observer state and the corresponding output will be represented by

$$\dot{\underline{\bar{X}}} = \underline{\bar{A}}\underline{\bar{X}} + \underline{\bar{B}}\underline{u} + \underline{\bar{L}}(\underline{y} - \underline{\bar{y}}) \quad (15)$$

where $\underline{\bar{y}}$ is given by

$$\underline{\bar{y}} = \underline{\bar{C}}\underline{\bar{X}} \quad (16)$$

and $\underline{\bar{L}}$ is a $2n \times s$ observer matrix. The elements of the observer matrix can be determined by an eigenvalue and eigenvector assignment (3).

As stated earlier the control variables are given by an $m \times 1$ vector \underline{u} which represents the inputs from the m actuators. To determine the optimal state feedback control law, modern control theory minimizes a quadratic performance index (PI) which is a function of the state and control vectors $\underline{X}(t)$ and $\underline{u}(t)$ and is given by

$$PI = \int_0^{\infty} (\underline{X}^t \underline{Q} \underline{X} + \underline{u}^t \underline{R} \underline{u}) dt \quad (17)$$

where \underline{Q} and \underline{R} are weighting matrices. Their selection can be somewhat arbitrary except that they must satisfy the requirements of positive definiteness. Matrix \underline{R} must be positive definite while \underline{Q} must at least be positive semidefinite. By adjusting these weighting matrices the control objectives such as amplitude of dynamic response, settling time (t_s) etc. can be altered. In addition, the weighting matrices can also be used as a means of imposing amplitude constraints on the control vector $\underline{u}(t)$. A brief discussion of how the matrices \underline{Q} and \underline{R} are selected for this investigation is given in the next section.

The result of the minimization of the quadratic performance index (while satisfying the state equation) is the optimal state feedback control law

$$\underline{u}^*(t) = -\underline{G}\underline{X}^*(t) \quad (18)$$

where $\underline{u}^*(t)$ is the optimal control input vector and $\underline{X}^*(t)$ is the corresponding state. The feedback matrix (control gain matrix) \underline{G} is given by

$$\underline{G} = \underline{R}^{-1} \underline{B}^t \underline{P} \quad (19)$$

where \underline{P} is a symmetric positive definite matrix known as the Riccati matrix and is obtained by the solution of the algebraic Riccati equation

$$\underline{A}^t \underline{P} - \underline{P} \underline{B} \underline{R}^{-1} \underline{B}^t \underline{P} + \underline{P} \underline{A} + \underline{Q} = 0 \quad (20)$$

Substitution of equation (18) in equation (13) gives the governing equations for the optimal closed loop system in the form

$$\dot{\underline{X}}^* = \underline{A}^* \underline{X}^* \quad (21)$$

where the closed loop plant matrix \underline{A}^* is given by

$$\underline{A}^* = \underline{A} - \underline{B} \underline{G} \quad (22)$$

Now the standard procedure for the solution of the optimal control problem for a given plant, control system and weighting matrices is as follows: The first step is to determine the controllability and observability of the system.

The condition of complete controllability is satisfied if

$$\text{RANK } \underline{M}_B = \text{RANK} [\underline{B} \quad \underline{A}\underline{B} \quad \dots \quad \underline{A}^{2n-1}\underline{B}] = 2n \quad (23)$$

where the matrices \underline{B} and \underline{A} are $2n \times m$ and $2n \times 2n$ dimensions respectively. Similarly complete observability is satisfied if

$$\text{RANK } \underline{M}_C = \text{RANK} [\underline{H} \quad \underline{A}^t \underline{H} \quad \dots \quad (\underline{A}^t)^{2n-1} \underline{H}] = 2n \quad (24)$$

where the factored matrix \underline{H} is given by

$$\underline{Q} = \underline{H} \underline{H}^t \quad (25)$$

For this investigation it was assumed that the sensors are located at the same place as the actuators and also that the true state is the observable state. The next step in the solution of the optimal control problem is to solve for the Riccati matrix \underline{P} from equation (20). The third step is to determine the control gain matrix \underline{G} by substituting the Riccati matrix, \underline{P} , in equation (19). The fourth step is to determine the state transition matrix from the solution of equation (21). From the state transition matrix and the initial state, the optimal state can be determined. Then the control input vector $\underline{u}^*(t)$ can be determined by equation (18). With this procedure, there is a facility to monitor the complete state, the control input, and the performance index PI. The weighting matrix \underline{R} will be selected in such a way that the second term in the performance index contains all the information about the power requirements of the individual actuators.

The Weighting Matrices \underline{Q} and \underline{R}

It is evident from the foregoing discussion that there are five important input matrices involved in the solution of the optimal control problem. The matrices \underline{A} and \underline{B} are unique to a given plant and control system. The matrix \underline{C} is also unique for the desired output. The weighting matrices, on the other hand, are not unique, and they can be selected to achieve certain desirable control objectives. However, the matrix \underline{R} must be positive definite,

and the Q matrix must be at least positive semi-definite. The weighting matrices selected for this investigation are as follows:

$$Q = \begin{bmatrix} \theta_m^2 & 1 & 0 \\ -\frac{m}{2} & \frac{1}{2} & 0 \\ 0 & 1 & \theta_k^2 \end{bmatrix}_{2n \times 2n} \quad (26)$$

and

$$R = \theta_R^t \theta_R^{-1} b \theta_R^{-1} b^t \theta_R^{-1}$$

where the quantities θ_m and θ_k are the scaling parameters that can be adjusted to achieve the desired control objectives. θ_R is an $m \times m$ diagonal matrix which will be used for similar scaling purposes on the matrix R . Some of the possible parameters that can be adjusted are the amplitude of the dynamic response, the settling time (t_s), etc. In addition, amplitude constraints on the control vector $u(t)$ can also be imposed.

In equation (26) k is assumed to be a nonsingular matrix. However, for a free-free structure k^{-1} does not exist, and the necessary modification is outlined in the sequel. The dimension of the singular matrix is $n \times n$ and its rank would be $n-l$, where l represents the number of rigid body degrees of freedom of the system. In such a case the weighting matrix R can be written symbolically as

$$R = \theta_R^t \begin{bmatrix} \bar{k}^{-1} & 0 \\ 0 & I \end{bmatrix}^{-1} \begin{bmatrix} \bar{b} \\ 0 \end{bmatrix} \theta_R \quad (27)$$

where \bar{k} is a nonsingular matrix of dimension $(n-l) \times (n-l)$. In other words \bar{k} is the original stiffness matrix with the rows and columns corresponding to the rigid body degrees of freedom removed. The $l \times l$ identity matrix takes the place of the rigid body degrees of freedom. It was assumed, for convenience, that the elastic and rigid body degrees of freedom are neatly partitioned as shown. However, in an actual structure these are generally interspersed, and they can be handled routinely without much difficulty. In the foregoing discussion it was tacitly assumed that a free-free structure will have two types of controllers, one set for controlling rigid body modes and the other for elastic modes. The interest of the present paper is only to address controllers with authority over the elastic modes.

In a modal formulation the R matrix remains the same as given by equation (26), but the Q matrix takes the following form:

$$Q = \begin{bmatrix} \theta_m^2 & 1 & 0 \\ -\frac{m}{2} & \frac{1}{2} & 0 \\ 0 & 1 & \theta_k^2 \omega_i^2 \end{bmatrix} \quad (28)$$

Now that the main aspects of the optimal control problem are outlined, a brief description of the structural optimization problem would be appropriate before presenting the results of this study.

Structural Optimization with Frequency Constraints

A cursory outline of the structural optimization problem is presented here. A more detailed description of the procedure used in this investigation is presented in references⁽⁹⁻¹¹⁾. The basic structural optimization problem is defined as follows

Minimize or maximize the objective function

$$W(\underline{d}) = W(d_1, d_2, \dots, d_q) \quad (29)$$

subject to the constraint conditions

$$D_i(\underline{d}) = D_i(d_1, d_2, \dots, d_q) \leq G_{i0} \quad (30)$$

$$i=1, 2, \dots, q$$

and

$$\underline{d}^{(L)} \leq \underline{d} \leq \underline{d}^{(U)} \quad (31)$$

where W is the structural mass and the constraints D_i are the fundamental frequencies in this discussion. However, the problem can also be posed as the maximization of the fundamental frequency with an equality constraint on the structural mass. The q variables, d_i , are the structural variables. The mass, stiffness and damping properties as well as the structural mass are functions of the structural variables. The vectors $\underline{d}^{(L)}$ and $\underline{d}^{(U)}$ are the (non-negative) lower and upper limits on the structural variables.

The Lagrangian formulation for constrained minimization can be written as

$$L(\underline{d}) = W(\underline{d}) + \sum_{i=1}^g \lambda_i \psi_i(\underline{d}) \quad (32)$$

where $L(\underline{d})$ is the Lagrangian function, and the λ 's are the Lagrangian multipliers corresponding to the g constraints. It is assumed that there are g constraints of the form

$$\psi_i(\underline{d}) = D_i(\underline{d}) - D_{i0} \leq 0 \quad (33)$$

Minimization of the Lagrangian $L(\underline{d})$ with respect to the structural variables, \underline{d} , and the Lagrangian multipliers λ^s gives the $q+g$ necessary conditions for optimality as follows:

$$\sum_{j=1}^g e_{ij} \lambda_j = 1 \quad i=1, 2, \dots, q \quad (34)$$

and

$$E \underline{\lambda} = \underline{D}_0 \quad (35)$$

where the quantity e_{ij} is given by

$$e_{ij} = \frac{\frac{\partial}{\partial d_i} [\psi_j(\underline{d})]}{\frac{\partial}{\partial d_i} [W(\underline{d})]} \quad (36)$$

and the matrix \bar{E} is given by

$$\bar{E} = \bar{e}^T \bar{d} \bar{e} \quad (37)$$

Based on the above optimality conditions an algorithm for the minimization of the structural mass with frequency constraints was derived⁽⁹⁾ and used for the structural modifications in this investigation.

Numerical Results and Discussion

The purpose of this numerical study is to highlight the effects of the changes in the parameters associated with the weighting matrices (Θ^S) and the structural variables (\bar{d}) on the dynamic response of an actively controlled structure. The dynamic response $\bar{X}(t)$, the actuator input $\bar{u}(t)$, the settling time t_s , and the performance index PI are a measure of the effectiveness of the control system. The object of vibration control is either to damp out the vibration completely or bring it to a predetermined level in a finite settling time t_s . Another practical limitation is on the actuator inputs. Actuator inputs can be limited because of their size and cost, particularly in large space structures. In the basic formulation of the optimal control problem (sections 2 and 3) none of these constraints were included. In the definition of the performance index both the actuator inputs and the time were assumed to be unbounded. However, by adjusting the scaling parameters in the weighting matrices (Θ^S), control objectives can be achieved with bounds on the actuator inputs and/or the settling time. The trade is between the actuator inputs and the settling time. Larger actuator inputs can reduce the settling time, or by increasing the settling time the demands on the actuators can be reduced. To study the effects of changes in the Θ^S on the control parameters, an equivalent damping parameter as defined by the logarithmic decrement will be monitored

$$\bar{\zeta} = \frac{1}{2\pi} \ln \left[\frac{y_p}{y_q} \right] \quad (38)$$

where $\bar{\zeta}$ is the equivalent damping parameter which includes the actual damping and the damping introduced by the control system. y_p and y_q are the amplitudes of the dynamic response in two consecutive cycles. For a given control system and a structure the variation of $\bar{\zeta}$ with the Θ^S can be monitored.

To test the effects of the parametric changes of the weighting matrices and the structural variables, the truss shown in figure 1 was selected for vibration control. The total length of the truss is 100" and it is divided into two equal bays. It is a cantilever truss with depth 36" at the base and 24" at the tip. The truss is fixed at the base and free everywhere else. It is assumed to move only in its plane, giving two degrees of freedom per node. Excluding the four degrees of freedom at the supports (base), the truss has 8 degrees of freedom in the configuration space (displacements) and 16 degrees of freedom in the state space (displacements and velocities). A non-structural mass of 1.29 lbs-sec²/in per node was assigned to all the nodes except the two at the base. The truss is made of aluminum with $E=10.0 \times 10^6$ psi and $\rho=0.1$

lbs/in³ (weight density).

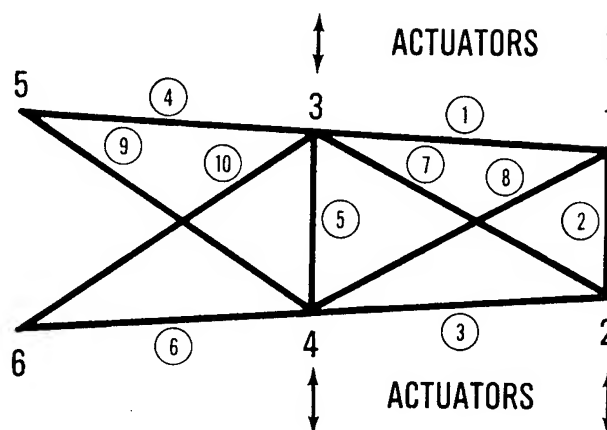


Fig. 1 Two Bay Truss with 4 Actuators

The feed back control system on the structure consists of four actuators located at nodes 1, 2, 3, and 4. The sensor locations are assumed to coincide with the actuators. The actuator forces are to be applied only in the transverse direction of the truss, in which case \bar{R} is a 4×4 matrix. Two primary truss designs are considered for this study. The first design which will be called the original structure, is a non-optimal structure with all the truss elements having the same cross-sectional area. The second one (called the optimal structure) is the same structure but its weight is minimized with the fundamental frequency constraint. Table 1 gives the details of the member cross-sectional areas and the natural frequencies for the two structures.

Table 1. Characteristics of Two Structures

EL./FREQ. NO.	Member Areas		Frequencies HZ	
	Orig Str	Opt Str	Orig Str	Opt Str
1	0.1	0.054	3.44	3.44
2	0.1	0.010	12.47	9.35
3	0.1	0.054	15.07	12.21
4	0.1	0.153	26.56	13.28
5	0.1	0.010	36.22	17.66
6	0.1	0.153	37.86	19.82
7	0.1	0.056	39.28	33.11
8	0.1	0.056	43.74	35.28
9	0.1	0.056		
10	0.1	0.056		
STR. WT LBS	4.88	3.44		

Table 2 gives the concentrated non-structural masses at the nodes for both the structures.

Table 2. Non-Structural Mass

Node No.	1	2	3	4
Mass*	1.29	1.29	1.29	1.29

*lbs-sec²
in.

As can be seen from the two tables, the structural mass is quite insignificant compared to the non-structural mass. The optimal and non-optimal structures have the same fundamental frequency, but the optimal structure is about 30% lighter. Even though there is a significant reduction in weight due to the optimization, it is accompanied by a movement of the higher frequencies to the lower frequency. In some dynamic response problems this may not be a desirable feature. In such cases multiple frequency constraints have to be imposed. For this particular study the closing in of the frequencies is not significant enough to present difficulties.

A list of the cases studied in this paper is given in table 3.

Table 3. Control Response Cases Studied

Case	Str.	Damping	Controls	$\frac{\theta_m}{\theta_{mo}} = \frac{\theta_K^*}{\theta_{Ko}}$	$\frac{\theta_R^*}{\theta_{Ro}}$
1	Orig	No	No	0	0
2	Orig	No	Yes	0.1	1.0
3	Orig	No	Yes	0.2	1.0
4	Orig	No	Yes	0.5	1.0
5	Orig	No	Yes	1.0	1.0
6	Orig	No	Yes	1.0	0.1
7	Orig	Yes	Yes	0.1	1.0
8	Orig	Yes	Yes	0.2	1.0
9	Opt	No	Yes	0.1	1.0
10	Opt	No	Yes	0.2	1.0
11	Opt	No	Yes	1.0	1.0
12	Opt	Yes	No	0	0
13	Opt	Yes	Yes	0.1	1.0

$$\frac{\theta_m}{\theta_{mo}} = \frac{\theta_K}{\theta_{Ko}} = \frac{\theta_R}{\theta_{Ro}} = \frac{1}{\sqrt{2}}$$

These cases include both the original and the optimal structure. In all cases the initial state was assumed to be a static displacement vector resulting from the application of a 1000 lbs force at each of the actuator locations and a zero velocity vector. The details of the initial state for both the structures are given in table 4.

Table 4. Details of the Initial State

	Original	Optimal
$\tilde{x}(0) =$	$\begin{bmatrix} 0 \\ 0 \\ 0 \\ 0 \\ 0 \\ 0 \\ 0 \\ 0 \\ 0 \\ -2.64 \\ 18.89 \\ 2.64 \\ 18.89 \\ -2.51 \\ 7.06 \\ 2.51 \\ 7.06 \end{bmatrix}$	$\begin{bmatrix} 0 \\ 0 \\ 0 \\ 0 \\ 0 \\ 0 \\ 0 \\ 0 \\ 0 \\ -2.33 \\ 18.98 \\ 2.33 \\ 18.98 \\ -1.44 \\ 7.96 \\ 1.44 \\ 7.96 \end{bmatrix}$

In cases 7, 8, 12, and 13, a passive damping of approximately 1.0% of the critical damping in the fundamental mode, was assumed in the structure.

In all cases studied the system is controllable and observable according to equations (23) and (24). The full system formulation (no modal reduction) was used in all cases. Tables of the open loop and closed loop eigenvalues are given (for cases 3 and 10 as examples) in tables 5 and 6 respectively.

Table 5. The Open Loop Eigenvalues (for Cases 3 and 10)

Original Structure		Optimized Structure	
Real Part	Imaginary Part	Real Part	Imaginary Part
0.	.275E+03	0.	.222E+03
0.	-.275E+03	0.	-.222E+03
0.	.247E+03	0.	.208E+03
0.	-.247E+03	0.	-.208E+03
0.	.238E+03	0.	.125E+03
0.	-.238E+03	0.	-.125E+03
0.	.227E+03	0.	.111E+03
0.	-.227E+03	0.	-.111E+03
0.	.167E+03	0.	.835E+02
0.	-.167E+03	0.	-.835E+02
0.	.947E+02	0.	.767E+02
0.	-.947E+02	0.	-.767E+02
0.	.784E+02	0.	.588E+02
0.	-.784E+02	0.	-.588E+02
0.	.216E+02	0.	.216E+02
0.	-.216E+02	0.	-.216E+02

Table 6. The Closed Loop Eigenvalues (for Cases 3 and 10)

Original Structure		Optimized Structure	
Real Part	Imaginary Part	Real Part	Imaginary Part
-.249E+02	.269E+03	-.158E+01	.222E+03
-.249E+02	-.269E+03	-.158E+01	-.222E+03
-.222E+02	.250E+03	-.636E+00	.208E+03
-.222E+02	-.250E+03	-.636E+00	-.208E+03
-.316E+02	.240E+03	-.279E+01	.125E+03
-.316E+02	-.240E+03	-.279E+01	-.125E+03
-.799E+00	.227E+03	-.102E+02	.111E+03
-.799E+00	-.227E+03	-.102E+02	-.111E+03
-.371E+01	.167E+03	-.116E+02	.834E+02
-.371E+01	-.167E+03	-.116E+02	-.834E+02
-.318E+01	.947E+02	-.793E+01	.769E+02
-.318E+01	-.947E+02	-.793E+01	-.769E+02
-.109E+02	.784E+02	-.818E+01	.588E+02
-.109E+02	-.784E+02	-.818E+01	-.588E+02
-.305E+01	.216E+02	-.305E+01	.216E+02
-.305E+01	-.216E+02	-.305E+01	-.216E+02

The number of iterations required for the Riccati solution in each case is given in table 7. The equivalent damping (as calculated from equation 38) resulting from the use of feedback controls is given in table 8 for the cases 1-5. In these cases only the multipliers of the Q matrix were assumed to vary while keeping the R matrix multipliers constant. As the value of the Q multipliers increases, the

equivalent damping increases. As the equivalent damping increases, the settling time decreases. However, the power requirements of the actuators (controllers) increase. The θ_R matrix is a diagonal matrix, and it is an identity matrix when there are no bounds on the input of the actuators. If some of the actuators have amplitude constraints (individual actuators) on their inputs, then the corresponding elements on the diagonal would be different from unity but nevertheless positive multipliers. A comprehensive description outlining the procedure for selecting these scalar multipliers will be included in a future study.

Table 7. Number of Iterations
for Riccati Solution

Case	2	3	4	5	6	7	8	9	10	11	13
Riccati Iterations	15	14	13	11	11	12	11	14	13	11	12

Table 8. Equivalent Damping

Case	1	2	3	4	5
$\frac{\theta_m}{\theta_{mo}} = \frac{\theta_K^*}{\theta_{Ko}}$	0.0	0.1	0.2	0.5	1.0
ζ_{EQ}	.00	.070	.141	.347	.687

$$\frac{\theta_R^*}{\theta_{Ro}} = 1$$

The tip displacement in the transverse direction is plotted against time for all thirteen cases (see figures 2a-14a). The actuator input at the tip is plotted against time for cases 2-5 and 9 (see figures 3b-6b and 10b). Due to symmetry, actuators 1 and 2 have the same input. Similarly the input of actuators 3 and 4 is the same. In the interest of saving space, plots of the third actuator input are given only for cases 2 and 3 (see figures 3c and 4d). The performance index is plotted against time for cases 1, 3, and 5 (see figures 2c, 4c, and 6c).

Summary and Conclusions

A brief outline of the optimal control and structural design problem is presented from a structural dynamicist's point of view. Selection of the weighting matrices in the definition of the performance index and their implication in control response is discussed in detail. By introducing simple scaling parameters, the weighting matrices were used effectively to achieve the desired control objectives. A number of case studies were made using a simple truss structure. A non-optimal and an optimal truss were used in this study with the same set of actuators. Modification of the structural parameters did not significantly alter the control design in this study. However, in the

presence of external disturbances (persistent) in addition to the initial conditions, the structural parameter changes are expected to have a more pronounced effect on the control systems design. This aspect of combined structural/control optimization will be the subject of our future study.

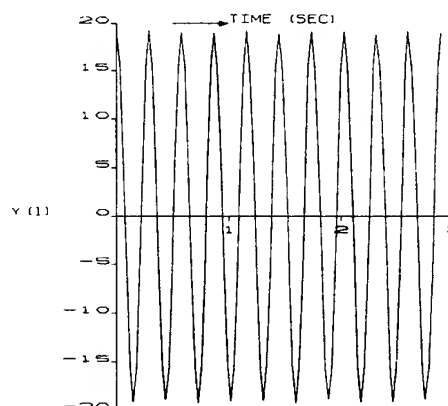


Fig. 2a Truss Tip Displacement in inches - Case 1

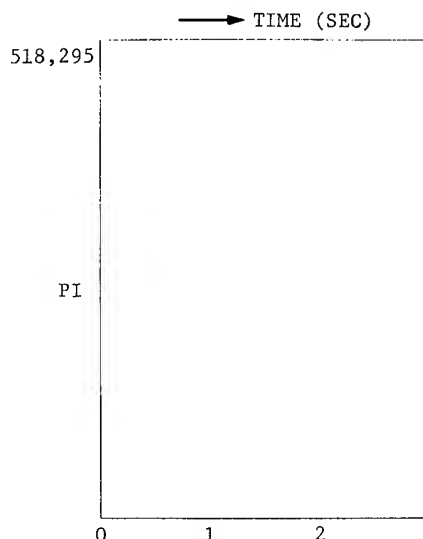


Fig. 2c Performance Index - Case 1

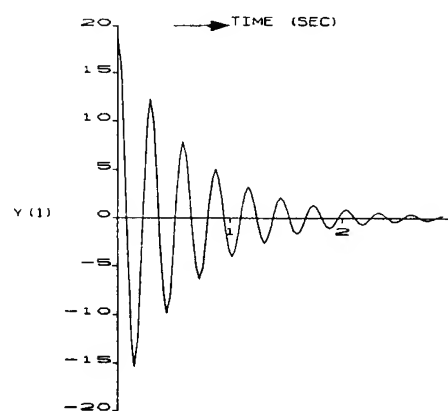


Fig. 3a Truss Tip Displacement in inches - Case 2

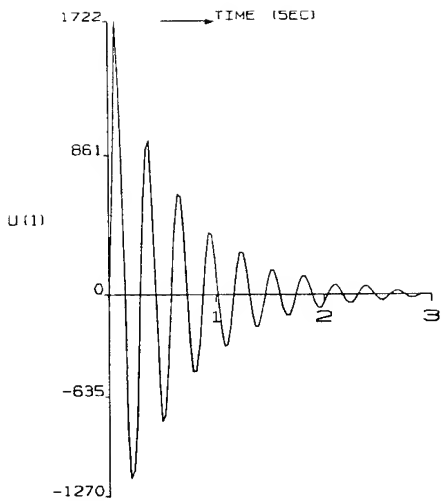


Fig. 3b Actuator Input at the Tip in lbs Force Case 2

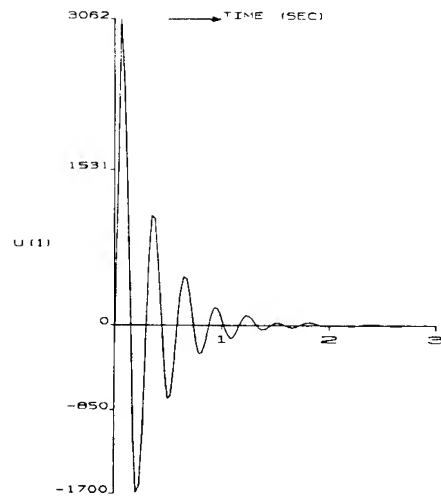


Fig. 4b Actuator Input at the Tip in lbs Force Case 3

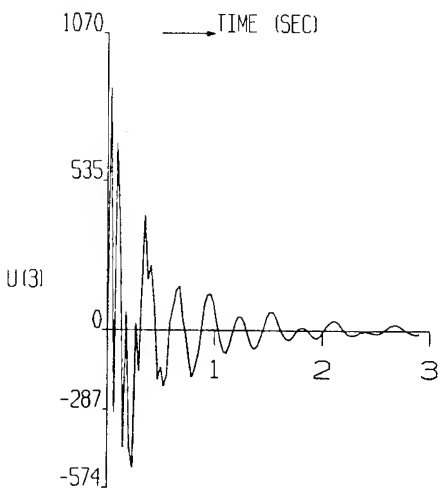


Fig. 3c Actuator Input at the Middle Node in lbs Force - Case 2

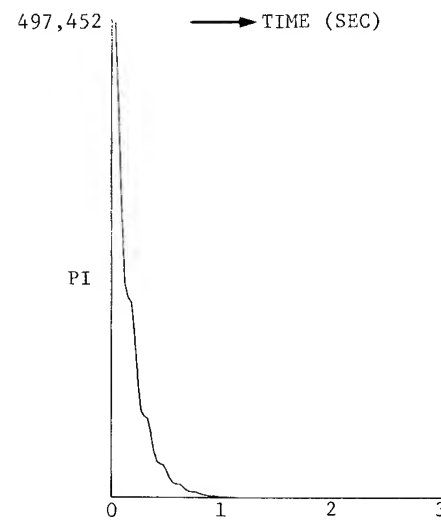


Fig. 4c Performance Index - Case 3

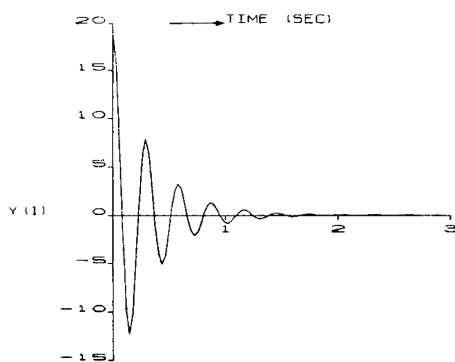


Fig. 4a Truss Tip Displacement in inches - Case 3

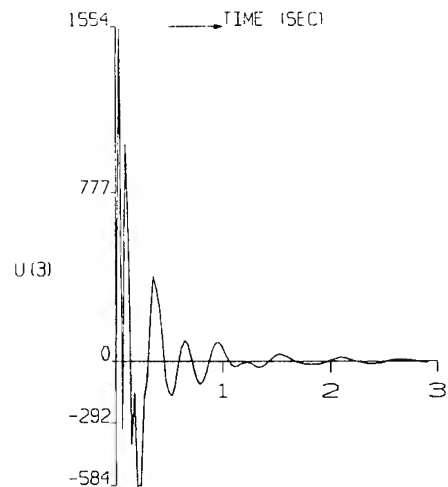


Fig. 4d Actuator Input at the Middle Node in lbs Force - Case 3

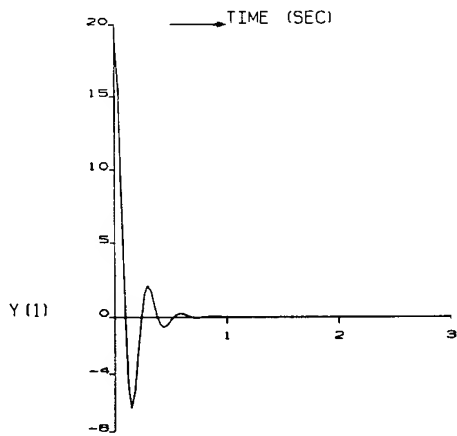


Fig. 5a Truss Tip Displacement in inches - Case 4

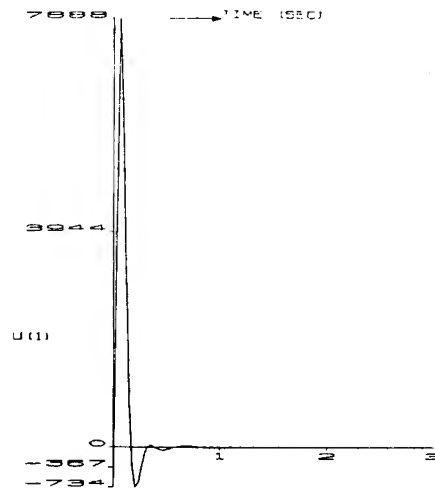


Fig. 6b Actuator Input at the Tip in in-lbs Force Case 5

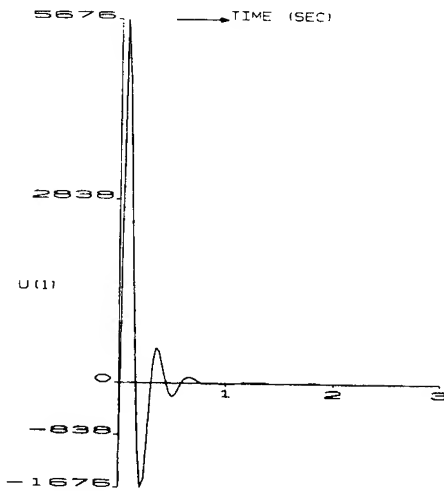


Fig. 5b Actuator Input at the Tip in lbs Force Case 4

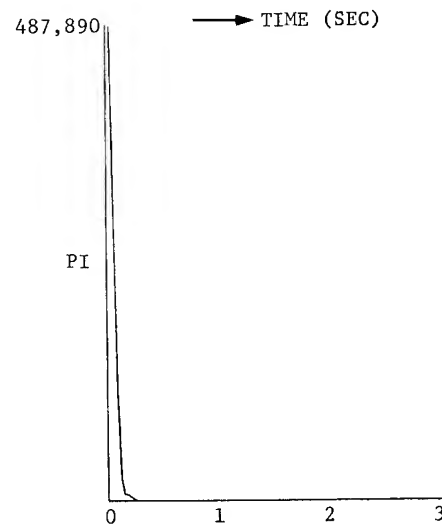


Fig. 6c Performance Index - Case 5

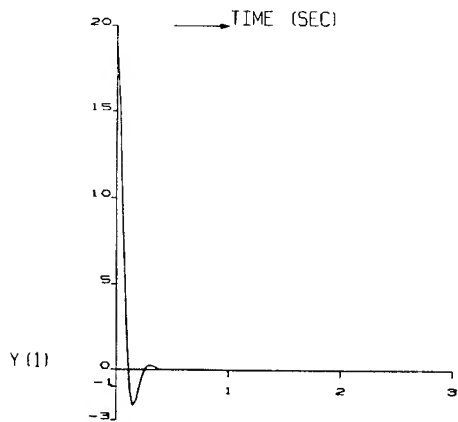


Fig. 6a Truss Tip Displacement in inches - Case 5

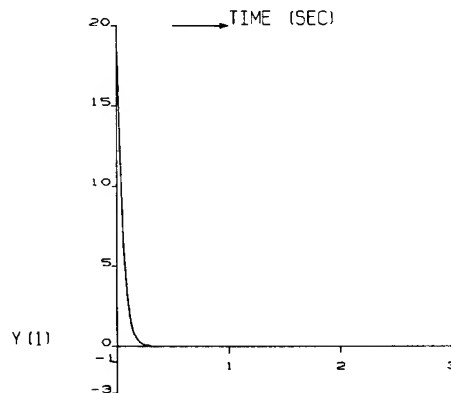


Fig. 7a Truss Tip Displacement in inches - Case 6

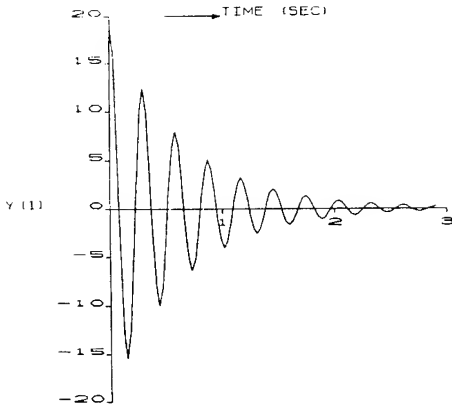


Fig. 8a Truss Tip Displacement in inches - Case 7

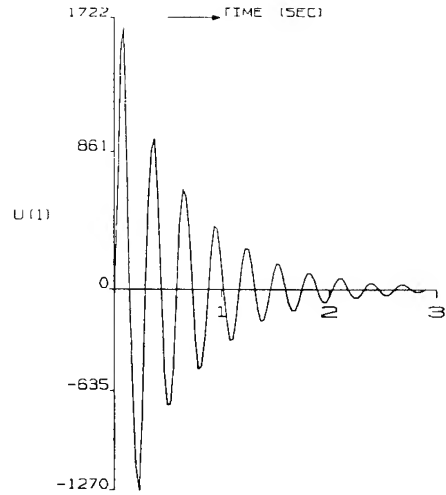


Fig. 10b Actuator Input at the Tip in lbs Force Case 9

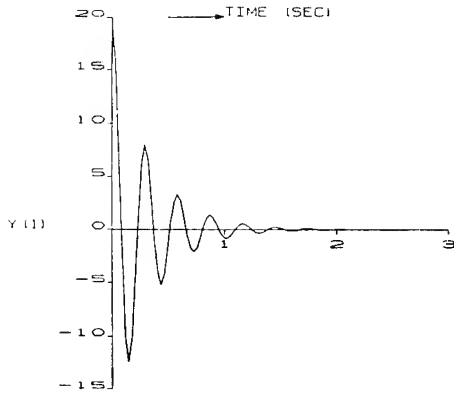


Fig. 9a Truss Tip Displacement in inches - Case 8

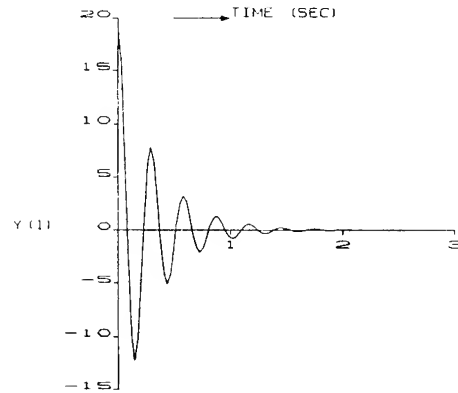


Fig. 11a Truss Tip Displacement in inches - Case 10

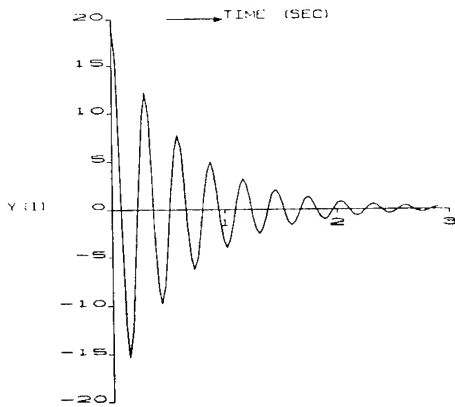


Fig. 10a Truss Tip Displacement in inches - Case 9

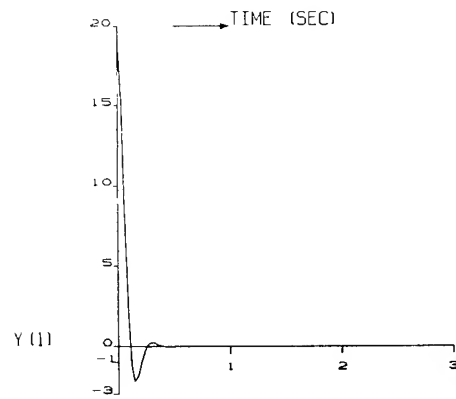


Fig. 12a Truss Tip Displacement in inches - Case 11

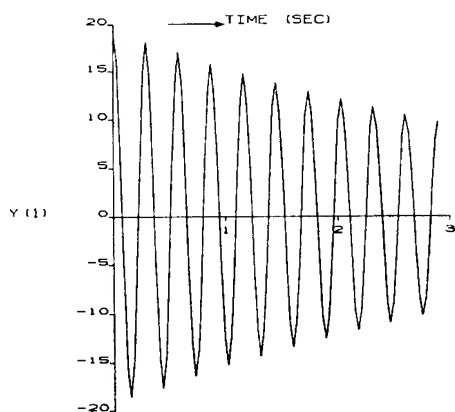


Fig. 13a Truss Tip Displacement in inches - Case 12

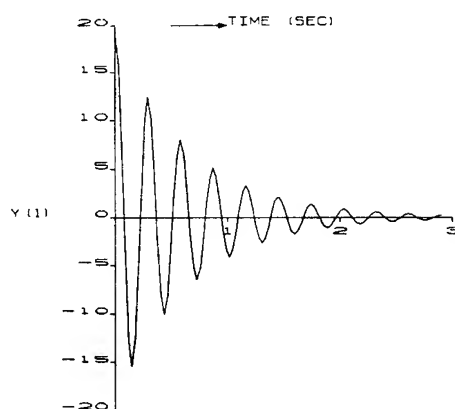


Fig. 14a Truss Tip Displacement in inches - Case 13

References

1. "Modeling, Analysis and Optimization Issues for Large Space Structures," Proceedings of a NASA, AFOSR Workshop held in Williamsburg, VA, May 13-14, 1982, Edited by L. D. Pinson, A. K. Amos, and V. B. Venkayya.
2. "Dynamics and Control of Large Structures," 4th VPI&SU/AIAA Symposium, Blacksburg, VA, June 6-8, 1983, Edited by L. Meirovitch.
3. J. J. D'Azzo, and C. H. Houpis, "Linear Control System Analysis and Design, Conventional and Modern," Second Edition, McGraw-Hill Book Company, New York, 1981.
4. M. Athans, and P. L. Falb, "Optimal Control - An Introduction to the Theory and its Applications," McGraw-Hill Book Company, New York, 1966.
5. N. R. Sandell and M. Athans, "Modern Control Theory - A Self Study Subject-Computer Manual," Center for Advanced Study, MIT.
6. L. Meirovitch, "Computational Methods in Structural Dynamics," Sijthoff & Noordhoff, Rockville, MD, 1980.

7. R. A. Calico and W. T. Miller, "Decentralized Control for a Flexible Spacecraft," Paper No AIAA-82-1404, AIAA/AAS Astrodynamics Conference, August 9-11, 1982, San Diego, California.
8. D. F. Miller and W. R. Wells, "Modal Control of Structural Systems," AFWAL-TR-84-(in preparation).
9. V. B. Venkayya and V. A. Tischler, "Optimization of Structures with Frequency Constraints," Conference Proceedings, Computer Methods for Nonlinear Solids and Structural Mechanics, ASME Applied Mechanics, Bioengineering and Fluids Engineering Conference, June 20-22, 1983, Houston, Texas, Edited by N. S. Atluri.
10. N. S. Khot, "Optimization of Structures with Multiple Frequency Constraints," to be published in Int. J. of Computers and Structures.
11. M. P. Kamat, V. B. Venkayya, and N. S. Khot, "Optimization with Frequency Constraints - Limitations," Journal of Sound and Vibration, 1983, 91(1), pp 147-154.

FREQUENCY DOMAIN ANALYSIS OF A PLATE WITH DISCRETE ELEMENTS ATTACHED*

Massood Omrani**

Daniel J. Inman***

Department of Mechanical and Aerospace Engineering
State University of New York at Buffalo
Buffalo, N.Y.

Abstract

In many applications in dynamics and control, discrete springs, dashpots and masses are added to distributed mass structures in an attempt to alter the structure's natural frequencies and response characteristics. This work examines the use of transforms to obtain a frequency domain analysis of distributed parameter model of a plate with various arrangements of attached discrete masses, springs and dashpots, and subject to point loads. The general equations of motion are given in distributed form. Then, following the method reported by Satter for beams, a transform of the solution is calculated and presented in closed form. This solution is then truncated and programmed. The program is then used to perform a numerical study on the plate deflection (response magnitude) at a specified point due to a unit impulse for various combinations and locations of the attached discrete elements. The numerical example is that of a simply supported stainless steel rectangular plate.

Introduction

Current interest in the active and passive control of flexible structures has been sparked by increased activity in the design of large space structures. The work presented here is an attempt to provide some insight into the effect of lumped dampers, masses and springs on the vibration of a plate. Previously, Satter¹ performed a similar study on the transverse vibrations of a beam using a Fourier Transform on the temporal variable in order to examine the deflection spectrum of the beam. The work presented here also uses the Fourier Transform and can be considered as an extension of Satter's work to a plate with lumped appendages.

The problem is formulated in general terms. First, a modal expansion of the deflection is performed. Then the Transform is used so Fourier that the temporal coefficients in the expansion can be solved for algebraically. This yields a closed form expression for the deflection of a plate subject to arbitrary point forces and corrected to lumped elements in the frequency domain. However, rather than inverting the transform, the response is studied in the frequency domain. This allows truncation of the problem to be performed as late in the analysis process as possible in keeping with the flexible nature of the structure. By appealing to control theory, it is shown that any optimal choice of discrete dampers based on the truncation will be

optimal for the fully distributed system.

The example studied is that of a rectangular plate with simply supported boundary conditions subjected to an impulsive load at a point. The plate is connected to several combinations of discrete springs and dampers.

Equation of Motion

Following the usual assumptions for the transverse vibrations of a plate of uniform thickness², the equation for the deflection of a plate attached to B springs, Q dampers, R point masses and J concentrated forces can be expressed as (see ref. 3 for a derivation)

$$\begin{aligned} & \left[\rho h + \sum_{r=1}^R M_r \delta(x-x_r) \delta(y-y_r) \right] w_{tt}(x,y,t) \\ & + \left[c + \sum_{q=1}^Q c_q \delta(x-x_q) \delta(y-y_q) \right] w_t(x,y,t) \\ & + \left[D \nabla^4 + \sum_{b=1}^B k_b \delta(x-x_b) \delta(y-y_b) \right] w(x,y,t) \\ & = \sum_{j=1}^J f_j(t) \delta(x-x_j) \delta(y-y_j) \end{aligned} \quad (1)$$

on the bounded simply connected domain, Ω , a region of the x-y plane. Here $w(x,y,t)$ is the deflection of the plate perpendicular to the x,y plane, ρ is the mass density, h is the plate thickness, M_r is the mass of the r^{th} point mass attached to the plate at the point (x_r, y_r) , δ is the usual dirac delta function, w_{tt} denotes the second partial derivative of w with respect to the time t , c is the damping coefficient for internal damping of the plate, c_q is the damping rate for the q^{th} discrete damper acting at the point (x_q, y_q) , D is constant consisting of the appropriate plate parameters, ∇^4 is the biharmonic operator, k_b is the stiffness coefficient of the b^{th} discrete spring attached at the point (x_b, y_b) and $f_j(t)$ is the j^{th} concentrated forcing function acting at the point (x_j, y_j) which represents an outside disturbance to the structure. In addition the deflection $w(x,y,t)$ must satisfy certain boundary and initial conditions.

If each of the terms involving delta functions is moved to the right hand side of equation (1), then the left hand side is the usual expression for the vibration of a thin plate⁴ with several point forcing functions. As such, it can easily be shown⁵ that the solution $w(x,y,t)$ can be expanded in the eigenfunctions associated with the operator ∇^4 , $\phi_{nm}(x,y)$, provided the boundary conditions are such that ∇^4 is self adjoint. In particular

* The work of the second author was sponsored in part by AFOSR grant #820242

** Graduate Student

***Assistant Professor, Member AIAA

$$w(x, y, t) = \sum_{n=1}^{\infty} \sum_{m=1}^{\infty} a_{nm}(t) \phi_{nm}(x, y) \quad (2)$$

where the coefficients $a_{nm}(t)$ are chosen to satisfy (1) and the initial conditions.

Since ∇^4 has a compact resolvent, the convergence in (2) is uniform and the set $\{\phi_{nm}(x, y)\}$ is a complete orthonormal set⁶. Taking the Fourier transform of (2) then yields

$$W(x, y, s) = \sum_{n=1}^{\infty} \sum_{m=1}^{\infty} A_{nm}(s) \phi_{nm}(x, y) \quad (3)$$

Where the capitals indicate a transformed variable and where s is the parameter in the transform. Equation (3) now represents the solution of (1) in the frequency domain. Analyzing the deflection in the frequency domain allows a more direct link to control theory as well as allowing the temporal coefficients $A_{nm}(s)$ to be calculated algebraically as shown in the next section.

Mathematical Analysis

The procedure for solving for each $A_{nm}(s)$, and thus $W(x, y, s)$, is to substitute (3) into (1) and use the orthogonality of the $\phi_{nm}(x, y)$. Rather than inverting $W(x, y, s)$ to get $w(x, y, t)$, analysis of the effect of the discrete appendages is carried out in the frequency domain. In order to solve for the magnitude of W the series in (3) must be truncated as must the various series used to calculate the $A_{nm}(s)$. The effect of various arrangements of the discrete elements is then studied using the truncated model. The validity in using this type of study for an optimal choice of discrete elements is derived from a control theory result⁷.

If the terms involving delta functions in equation (1) are treated as compact feedback controls and if the natural damping, C , is chosen such that the distributed system is underdamped⁸, then and optimal selection of the discrete elements based on the truncated model will converge to and optimal selection for the fully distributed model. In addition, stability is guaranteed (which is obvious in this case, since the controls are passive).

With the eventual truncation in mind, consider the substitution of (2) into (1). Multiplying the result by $\phi_{i1}(x)$ and integrating over Ω then yields

$$\begin{aligned} & \rho h \ddot{a}_{i1}(t) + \alpha C \dot{a}_{i1}(t) + D \lambda_{i1}^4 \beta a_{i1}(t) \\ & + \sum_{m=1}^{\infty} \sum_{n=1}^{\infty} \sum_{r=1}^R M_r \phi_{mn}(x_r, y_r) \phi_{i1}(x_r, y_r) \ddot{a}_{nm}(t) \\ & + \sum_{m=1}^{\infty} \sum_{n=1}^{\infty} \sum_{q=1}^Q C_q \phi_{mn}(x_q, y_q) \phi_{i1}(x_q, y_q) \dot{a}_{nm}(t) \\ & + \sum_{m=1}^{\infty} \sum_{n=1}^{\infty} \sum_{b=1}^B k_b \phi_{mn}(x_b, y_b) \phi_{i1}(x_b, y_b) a_{nm}(t) \end{aligned}$$

$$= \sum_{j=1}^J f_j(t) \phi_{i1}(x_j, y_j) \quad (4)$$

Here, λ_{i1}^4 denotes the eigenvalues of the ∇^4 operator and α and β are constants of orthogonality reflecting the geometry. Equation (4) follows from the orthogonality of the eigenfunctions and the use of the Dirac delta function integral. Taking the Fourier transform of (4) and solving the resulting expression for $A_{i1}(s)$ yields

$$\begin{aligned} A_{i1}(s) = & \left[s^2 \sum_{r=1}^R M_r \phi_{i1}(x_r, y_r) B_r - s \sum_{q=1}^Q C_q \phi_{i1}(x_q, y_q) B_q \right. \\ & \left. - \sum_{b=1}^B k_b \phi_{i1}(x_b, y_b) B_b + \sum_{j=1}^J F_j(s) \phi_{i1}(x_j, y_j) \right] / \Delta_{i1}(s) \end{aligned} \quad (5)$$

where $F_j(s)$ is the Fourier Transform of the applied force, where $j=\sqrt{-1}$ and where

$$\Delta_{i1}(s) = \alpha \rho h s^2 + \alpha C s + \beta D \lambda_{i1}^4 \quad (6)$$

$$B_r = \sum_{m=1}^{\infty} \sum_{n=1}^{\infty} \phi_{mn}(x_r, y_r) A_{mn}(s) \quad (7)$$

$$\bar{B}_q = \sum_{m=1}^{\infty} \sum_{n=1}^{\infty} \phi_{mn}(x_q, y_q) A_{mn}(s) \quad (8)$$

and

$$\bar{\bar{B}}_b = \sum_{m=1}^{\infty} \sum_{n=1}^{\infty} \phi_{mn}(x_b, y_b) A_{mn}(s) \quad (9)$$

Now the expression for $A_{i1}(s)$ in equation (5) can be written as $A_{mn}(s)$ and substituted into (7), (8) and (9) above. The resulting expressions can, after much algebraic manipulation, be solved for B_r , \bar{B}_q and $\bar{\bar{B}}_b$ independent of $A_{i1}(s)$. Once the independent expressions for B_r , \bar{B}_q and $\bar{\bar{B}}_b$ are found they can be placed in the right hand side of (5). The expression for $A_{mn}(s)$ along with the eigenfunction $\phi_{nm}(x, y)$ can then be used to expand the series in (3).

It should be noted, that while the coefficients B_r , \bar{B}_q and $\bar{\bar{B}}_b$ can be manipulated to eliminate the $A_{mn}(s)$ dependence, the expressions for these functions are not constants but rather depend on s . In addition, each element requires the evaluation of an infinite series to compute. Hence, equation (5) can not be simply inverted as a first glance may suggest. Thus the analysis of the response is carried out in the frequency domain and by using only a truncated portion of the series in (5), (7), (8) and (9).

The undamped natural frequencies of the plate may be obtained by solving equation (1) when the damping forces and forcing function are zero. A periodic solution will have the form

$$W(x, y, t) = \sum_{m=1}^{\infty} \sum_{n=1}^{\infty} \phi_{mn}(x, y) \cos \omega_{mn} t \quad (10)$$

By substituting (10) into (1) and after some manipulation the natural frequencies w_{mn} are found to be (see ref. 3)

$$w_{mn}^2 = \frac{D\beta\lambda_{mn}^4 + \sum_{b=1}^B k_b \phi_{mn}^2(x_b, y_b)}{\rho h a + \sum_{r=1}^R M_r \phi_{mn}^2(x_r, y_r)} \quad (11)$$

For a simply supported rectangular plate of dimensions

$$\phi_{mn} = \sin \frac{n\pi x}{a} \sin \frac{m\pi y}{b}$$

a by b the geometric factors α and β become

$$\alpha = \beta = \frac{ab}{4}$$

Then

$$\lambda_{mn}^4 = \left[\left(\frac{n\pi}{a} \right)^2 + \left(\frac{m\pi}{b} \right)^2 \right]^2 \quad (12)$$

can be substituted into (11) to yield the undamped natural frequencies.

The algebra involved in making the above calculations greatly simplifies if a small number of lumped elements are used. This is the case in the following example.

Example

The numerical study consisted of examining the vibrations of a simply supported rectangular plate of width a and length b. The plate is disturbed by a single pulse ($J=1$ in equation (4)), located at the point $x=.75a$, $y=.75b$. This location was chosen to avoid the nodal points of the first few modes. The material properties were chosen to coincide with those of a 10 ft by 12 ft stainless steel plate .2 ft thick. A five mode model of the plate was used, i.e., the first five terms of (3) were kept.

The first study consisted of moving a single damper ($Q=1$ in equation (1)) of fixed rate with no other attachments ($B=R=0$) along the length of the plate and the amplitude of $W(x,y,s)$ calculated at several positions. The result is the plot of figure 1 which clearly indicates that the dashpot should be placed at the center ($L/2=x$) for maximum reduction of amplitude

It should be noted that from equation (11), the natural frequencies of the plate are dependent on the lumped masses and the discrete springs constants. Equation (11) can be used to alter the natural frequency of the system when it is necessary to avoid resonance by adjusting the lumped masses and/or springs constants.

Passive control of distributed system with lumped appendages may be an effective way to control vibrations. Further examination of such systems in the frequency domain may be fruitful.

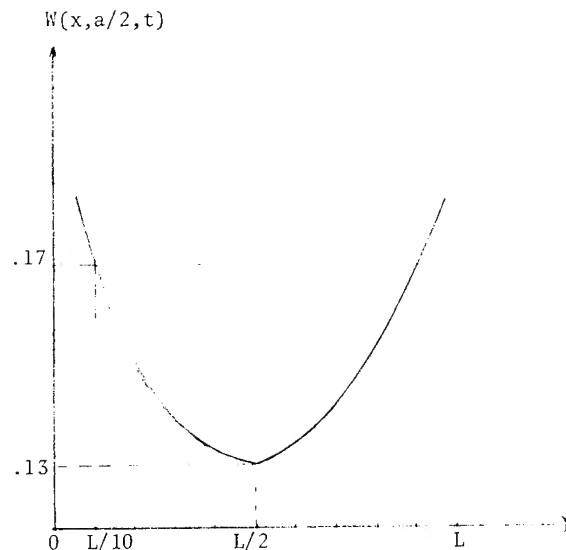


Fig. 1

References

- [1] Satter, M.A., "Vibration of Beams Carrying Discrete Dampers and Masses", ASME Journal of Mechanical Design, Vol. 101, pp.317-321, 1979.
- [2] Meirovitch, L., Analytical Methods in Vibrations, Macmillan Co., 1967, page 179.
- [3] Omrani, M., Vibration and Control of Beams and Plates Carrying Point Masses, Discrete Dampers Springs Due to Point Forces, M.S. project, State University of New York at Buffalo, Department of Mechanical and Aerospace Engineering, 1982, page 17.
- [4] Murthy, D.N.S., and Sherbourne, A.N., "Free Flexural Vibrations of Damped Plates", ASME Journal of Applied Mechanics, Vol. 39, pp.298-300, 1972.
- [5] Caughey, T.K., and O'Kelly, M.E.J., "Classical Normal Modes in Damped Linear Dynamic Systems", ASME Journal of Applied Mechanics, Vol. 32, pp.583-588, 1965.
- [6] Kato, T., Perturbation Theory for Linear Operators, Springer-Verlag, New York, 1966.
- [7] Gibson, J.S., "An Analysis of Optimal Modal Regulation: Convergence and Stability", SIAM Journal of Control and Optimization, Vol. 19, pp.686-706, 1981.
- [8] Inman, D.J., and Andry, A.N., Jr., "The Nature of the Temporal Solutions of Damped Distributed Systems with Classical Normal Modes", ASME Journal of Applied Mechanics, Vol. 49, pp.867-870, 1982.

S. B. Skaar* and L. Tang**
Dept. of Engineering Science and Mechanics
Iowa State University
Ames, IA 50011

Introduction

The most common approach used to achieve the feedback control of elastic, distributed parameter, dynamic systems requires the positioning of several sensors at various locations on an elastic region. Data from these sensors are used to estimate the amplitude of the first few modes of vibration at any instant. These amplitudes are then used in a finite-degree-of-freedom feedback control law designed to achieve a desired final distributed state of the system. Because the number of sensors is finite and because higher modes remain unmodeled, the resulting control histories are in error [1]. This error can be difficult to estimate.

The present approach adopts a different philosophy. Acceleration data is assumed to be available at a single location in the system at which the controlling force or torque acts (for example, the "rigid" hub of the torsion member of Fig. 1, or that of the satellite model of Fig. 2). This acceleration history is used to correct the motion at any current, mid-maneuver instant. Disturbances of several kinds acting on the hub would be permitted including mass loss, non-elastic deformation, extraneous torques, or small, unmodeled elastic regions. But the modeled elastic appendages must be regarded as undisturbed (directly) and perfectly modeled insofar as their response to the central "rigid" hub is concerned. The method allows for the specification of final velocities and positions of the hub region as well as a finite number of points on the modeled elastic appendages. It should be noted that while a distributed final state cannot be specified with the present method, it has been shown that the residual elastic and kinetic energy of a system in which only a few points are brought to a zero-displacement state of rest tends to be very low [2]. Moreover, the constraint of one additional appendage point incrementally reduces this residual energy dramatically.

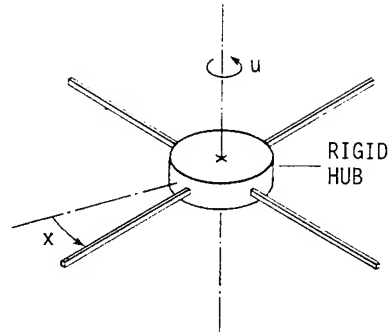
The Performance Index

The performance index treated here is given by

$$J = \int_{t_0}^{t_f} u^2(\lambda) d\lambda \quad (1)$$

*Asst. Prof., Engineering Science and Mechanics
Member, AIAA.

**Graduate student, Engineering Science and
Mechanics.



E = MODULUS OF ELASTICITY
 I = TRANSVERSE AREA MOMENT OF INERTIA
 ρ = MASS/LENGTH

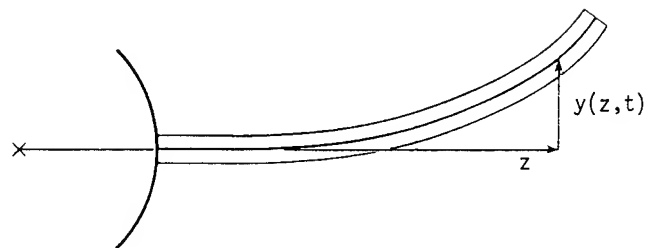
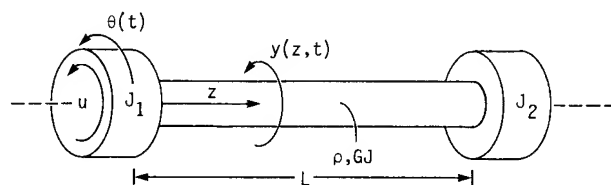


Fig. 1. The rigid hub/flexible appendage system (rotational motion).



ρ = axial mass moment of inertia/length of non-rigid shaft
 J_1 = axial mass moment of inertia of torqued mass (rigid)
 J_2 = axial mass moment of inertia of load at right end (rigid)
 $\theta(t)$ = angular position (absolute) of left end
 $y(z,t)$ = angular position relative to left end

Fig. 2. Rotational manipulator arm model.

where u is the controlling force or torque. This control is assumed to be continuously variable, and it acts on the hub as indicated in the configurations of Figs. 1 and 2. The performance index of Eq. (1) has been treated by other investigators in the context of satellite attitude control, although it is not the only index for which the approach described herein is applicable [3]. It has the disadvantage of tending to require non-zero control torques at the initial and final times of a maneuver. While this disadvantage can be eliminated through the addition of a u^2 term to the integrand of Eq. (1), the illustration of the method is most easily accomplished using the simpler performance criterion.

The Feedback Control Law

To illustrate the method, it is assumed that the hub of the model of Fig. 1 is to be brought to a prescribed final angular position θ_f and velocity $\dot{\theta}_f$ at time t_f . Likewise, the displacement and relative velocity of the opposite end ($y(L, t_f)$ and $\dot{y}(L, t_f)$ in Fig. 1) must be brought to zero at t_f . The system is assumed to be initially undeformed and in a state of rest.

Convolution integrals which describe the response of the torqued hub of Fig. 1 to an arbitrary input u can be found to have the form

$$\theta(t) = \int_0^t u(\lambda)g(t-\lambda)d\lambda \quad (2)$$

$$\dot{\theta}(t) = \int_0^t u(\lambda)\dot{g}(t-\lambda)d\lambda \quad (3)$$

where

$$g(t) = C_0 t + \sum_{i=1}^{\infty} C_i \sin \omega_i t \quad (4)$$

and

$$\dot{g}(t) = \frac{d}{dt} g(t) \quad (5)$$

A similar convolution integral form holds for the system of Fig. 2. The constants C_i and ω_i of Eq. (4) are shown in the next section to be derivable from the p.d.e. description of the system's response. It should be noted, however, that the practical usefulness of the method outlined here will depend upon the ability to recover these values experimentally for any actual linear elastic system.

Similarly, convolution integrals that describe the response of a displacement y located at any point or z along the shaft are available, such that

$$y(t) = \int_0^t u(\lambda)g_z(t-\lambda)d\lambda \quad (6)$$

$$\dot{y}(t) = \int_0^t u(\lambda)\dot{g}_z(t-\lambda)d\lambda \quad (7)$$

where, for the configuration of Fig. 1, g_z and \dot{g}_z are of the form given in Eqs. (4) and (5), respectively, with $C_0 = 0$ and the remaining C_i dependent upon the choice of the point location z .

Equation (1) may now be augmented using Eqs. (2), (3), (6), and (7) to have the form [4]

$$\begin{aligned} J = & \int_{t_0=0}^{t_f} \{u^2(\lambda) + K_1[u(\lambda)g(t_f-\lambda) - \theta_f/t_f] \\ & + K_2[u(\lambda)\dot{g}(t_f-\lambda) - \dot{\theta}_f/t_f] \\ & + K_3[u(\lambda)g_L(t_f-\lambda)] + K_4[u(\lambda)\dot{g}_L(t_f-\lambda)]\}d\lambda \\ = & \int_{t_0=0}^{t_f} F(u(\lambda))d\lambda \end{aligned} \quad (8)$$

where K_1, K_2, K_3 , and K_4 are Lagrange multipliers and where θ_f and $\dot{\theta}_f$ are desired final values of the hub's angular position and velocity.

Consider an intermediate time $0 < T < t_f$ during the maneuver. Eq. (8) may be rewritten

$$J = P(T) + \int_T^{t_f} F(u(\lambda))d\lambda \quad (9)$$

where

$$P(T) = \int_{t_0=0}^T F(u_a(\lambda))d\lambda \quad (10)$$

The function $u_a(t)$ is the actual "effective" torque history that has been applied to the hub prior to time T . As will be shown, this function can be recovered from the hub's accelerometer data.

The minimization of J in Eq. (9) for all time greater than or equal to T requires

$$\frac{d}{dt} \left(\frac{\partial F}{\partial \dot{u}} \right) = \frac{\partial F}{\partial u} \quad (11)$$

$$\begin{aligned} u(t) = & -\frac{1}{2} [K_1 g(t_f-t) + K_2 \dot{g}(t_f-t) \\ & + K_3 g_L(t_f-t) + K_4 \dot{g}_L(t_f-t)] \end{aligned} \quad (12)$$

Eq. (12) is of the form

$$u(t) = K_1 f_1(t) + K_2 f_2(t) + K_3 f_3(t) + K_4 f_4(t) \quad (13)$$

This is the form of the optimal control for all time $t \geq T$ regardless of disturbances to the hub prior to time T . The value of the multipliers K_i may be updated by substituting Eq. (13) into Eq. (2) evaluated at $t = t_f$, yielding

$$\begin{aligned} \theta_f = P_\theta(T) + \int_T^{t_f} [K_1 f_1(\lambda) + K_2 f_2(\lambda) + K_3 f_3(\lambda) \\ + K_4 f_4(\lambda)] g(t_f - \lambda) d\lambda \end{aligned} \quad (14)$$

where

$$P_\theta(T) = \int_0^T u_a(\lambda) g(t_f - \lambda) d\lambda \quad (15)$$

and where $u_a(\lambda)$ is determined from the hub's measured acceleration using

$$u_a(\lambda) = \int_0^\lambda \ddot{x}(\xi) \bar{g}(\lambda - \xi) d\xi \quad (16)$$

The function \bar{g} is the appropriate convolution integral kernel. The derivation of \bar{g} is shown below for the system of Fig. 1. Because \ddot{x} is the measured acceleration of the hub, Eq. (16) must be evaluated numerically.

The integral on the right side of Eq. (14) may be integrated analytically and rearranged to have the form

$$\begin{aligned} \theta_f - P_\theta(T) = K_1 g_{11}(T) + K_2 g_{12}(T) \\ + K_3 g_{13}(T) + K_4 g_{14}(T) \end{aligned} \quad (17)$$

A similar treatment using Eqs. (3), (6), and (7) would yield a matrix equation from which the multipliers K_j can be determined:

$$\begin{Bmatrix} \theta_f - P_\theta(T) \\ \dot{\theta}_f - P_{\dot{\theta}}(T) \\ -P_y(T) \\ -P_{\dot{y}}(T) \end{Bmatrix} = [g_{ij}(T)] \begin{Bmatrix} K_1 \\ K_2 \\ K_3 \\ K_4 \end{Bmatrix} \quad (18)$$

These values of the multipliers K_i would finally be substituted into Eq. (13) to produce the optimal feedback control.

The Convolution Integral

In Fig. 1, the moment of inertia J_2 of the rigid mass at the untorqued end of the shaft is, for simplicity, assumed to be zero. The equations and boundary conditions associated with that system are given by

$$\begin{aligned} J_T \frac{d^2 \theta}{dt^2} + \rho \int_0^L \frac{\partial^2 y}{\partial t^2} dz = u \\ GJ \frac{\partial^2 y}{\partial z^2} - \rho \left(\frac{\partial^2 y}{\partial t^2} + \frac{d^2 \theta}{dt^2} \right) = 0 \end{aligned} \quad (19)$$

$$y(0, t) = 0$$

$$\frac{\partial y}{\partial z}(L, t) = 0$$

where

- J_T is the total system mass moment of inertia about the z axis
- ρ is the mass moment of inertia per unit length of the shaft
- GJ is the shaft's torsional rigidity
- $y(z, t)$ is the angular deflection of a point along the appendage measured relative to the rotating rigid part
- L is the appendage length
- $u(t)$ is the control torque

A Laplace transformation of Eqs. (19) yields

$$\begin{aligned} J_T s^2 \Theta + \rho s^2 \int_0^L Y dz = U \\ GJ Y'' - \rho s^2 [Y + \Theta] = 0 \end{aligned} \quad (20)$$

$$Y(0) = 0$$

$$Y'(L) = 0$$

(Note that upper-case variable names represent the Laplace transform of each lower-case counterpart in the time domain.)

Eqs. (20) may be solved to have the form

$$\Theta = G(s) U \quad (21)$$

where

$$G(s) = [J_1 s^2 + \sqrt{GJ\rho} \tanh(\sqrt{\rho/GJ} L s)]^{-1} \quad (22)$$

Using the convolution theorem, it follows that

$$\theta(t) = \int_0^t u(\lambda) g(t-\lambda) d\lambda \quad (23)$$

where [4]

$$g(t) = L^{-1} \{G(s)\} = \frac{Kt}{c+b} + \sum_{n=1}^{\infty} \frac{2K \sin \omega_n t}{\omega_n [c+b/\cos^2(b\omega_n)]} \quad (24)$$

which is the form of Eq. (4), where, in this case,

$$\begin{aligned} K &= [GJ\rho]^{-1/2} \\ c &= M[GJ\rho]^{-1/2} \\ b &= L[\rho/GJ]^{1/2} \end{aligned} \quad (25)$$

The function \bar{g} used in Eq. (16) is derivable from Eq. (22) since, from Eq. (21),

$$\frac{U}{s^2 \theta} = 1/(s^2 G) \quad (26)$$

or

$$\bar{g} = L^{-1} \{1/s^2 G\} \quad (27)$$

Summary

A new approach to the use of feedback in the control of distributed parameter systems is outlined. The method is exact in the sense that it does not truncate the system model at a preset number of modes. It also allows for a direct interpretation of sensory data in that accelerations of actual points are required by the control law rather than modal amplitude estimates, which are based upon point measurements. The method also has disadvantages. Greatest of these is that, at the present time, no experimental method has been devised to find the response of points of interest on a distributed parameter system to a unit impulse of the actuator. Also, as presently formulated, the method will not work if appreciable disturbances act on the modeled appendages.

References

- [1] Meirovitch, L., Baruh, H., and Öz, H., "A Comparison of Control Techniques for Large Flexible Systems," Journal of Guidance, Control, and Dynamics, Vol. 6, No. 4, July-August 1983.
- [2] Skaar, S. B., "Closed Form Optimal Control Solutions for Continuous Linear Elastic Systems," accepted for publication in Journal of Astronautical Sciences.
- [3] Junkins, J. L., and Turner, J. D., "Optimal Continuous Torque Attitude Maneuvers," Paper 78-1400, AIAA/AAS Astrodynamics Conference, August, 1978.
- [4] Wylie, C. R., Advanced Engineering Mathematics, McGraw-Hill, New York, 1975.

CLOSED-FORM SOLUTIONS FOR A CLASS OF OPTIMAL QUADRATIC
REGULATOR PROBLEMS WITH TERMINAL CONSTRAINTS

Jer-Nan Juang⁺
NASA Langley Research Center
Hampton, VA 23665

James D. Turner⁺⁺ and Hon M. Chun⁺⁺⁺
The Charles Stark Draper Laboratory, Inc.
Cambridge, Massachusetts 02139

ABSTRACT

Closed-form solutions are derived for coupled Riccati-like matrix differential equations describing the solution of a class of optimal finite time quadratic regulator problems with terminal constraints. Analytical solutions are obtained for the feedback gains and the closed-loop response trajectory. A computational procedure is presented which introduces new variables for efficient computation of the terminal control law. Two examples are given to illustrate the validity and usefulness of the theory.

INTRODUCTION

Many engineering applications involve maneuvering a system between two quiescent or known moving states. These applications have motivated the research and development of a number of optimal maneuver strategies. Traditionally, the approach in treating the maneuver problem is typified by optimal control theory which leads to a system of coupled differential equations,¹⁻⁷ describing a two-point boundary value problem. The boundary conditions are usually divided with half specified at the initial time, and the rest at the final time. As a consequence, the most common tool for attacking this type of problem involves the use of numerical algorithms for solving two-point boundary problems. The main cost of this method is the computational burden, particularly in situations where high frequency modes are included in the system. In such cases, the simulation time may be substantially longer than the real time for control maneuvers, making real time control impossible.

For the problem of designing an optimal terminal controller⁸, some references⁷⁻¹⁰ exist and a fair amount of success has been obtained. The major drawback, as is common with penalized terminal states used in these papers, is numerical difficulties associated with handling a very large terminal weighting matrix. Furthermore, repeated simulation of a complex system over various terminal weighting matrix ranges can be very costly and sometimes not feasible.

This paper describes three new developments related to a class of optimal finite time quadratic regulator problems with terminal constraints. First, analytical solutions are presented for time varying gains given by three coupled Riccati-like matrix

differential equations for a terminal controller. Second, a closed form expression for the closed-loop system state trajectory is developed. Third, a set of new formulations is described for the computation of control laws. The new formulation leads to an alternate representation of the terminal control problem. Computation of the time varying gains is based on matrix transformations which reconstruct the three coupled nonlinear matrix differential equations into two uncoupled linear matrix differential equations and one algebraic matrix equation. It is not necessary to specify all the terminal states.

Examples including a first-order and a third-order system are used to demonstrate the validity of all the analytical solutions developed in this paper. In the second example, associated with the third-order system, the plant state is augmented to include the control, which enables the penalization of the control rate.

OPTIMAL TERMINAL CONTROLLER

The optimal terminal control problem is formulated by finding the control inputs $u(t)$ to minimize the typical cost function

$$J = \frac{1}{2} \int_{t_0}^{t_f} (x^T F Q F x + u^T R u) dt \quad (1)$$

for the system

$$\dot{x} = Ax + Bu, \text{ given } x(t_0) \quad (2)$$

with outputs

$$y = Fx \quad (3)$$

subject to the specified terminal constraints

$$x_i(t_f) = \bar{x}_i, \quad i = 1, \dots, q; \quad q \leq n \quad (4)$$

where x is the state vector, u is the control vector, A is the system dynamics matrix, B is the control influence matrix*, F is the measurement influence matrix, $Q = Q^T > 0$ is the output weighting matrix and $R = R^T > 0$ is the control weighting matrix. It is assumed that the $[A^T, F]$ pair is completely observable and $[A, B]$ stabilizable. Of particular interest is the fact that the performance index of Eq. (1) does not contain a terminal weight matrix,

⁺ Aerospace Engineer, member AIAA

⁺⁺ Dynamics Section Chief, member AIAA

⁺⁺⁺ Technical Staff, member AIAA

*For maneuvers where the state is augmented by the control and control-rate penalties, the matrices A and B are modified as shown in the reference [8].

which penalizes the final values of the state. Indeed, it is the principal intent of this paper to present a numerical technique which enforces the satisfaction of the constraints of Eq.(4), without incurring the numerical difficulties associated with a very large terminal weighting matrix approach for the problem.⁸

As shown in Ref.[1], the necessary conditions defining the optimal solution are given by the following coupled Riccati-like matrix differential equations

$$\dot{P} + PA + A^T P - PBR^{-1}B^T P + F^T Q F = 0 ; P(t_f) = 0 \quad (5)$$

$$\dot{S} + (A^T - PBR^{-1}B^T)S = 0 ; S^T(t_f) = (\partial\psi/\partial x)|_{t_f} \quad (6)$$

$$\dot{G} = S^T BR^{-1}B^T S ; G(t_f) = 0 \quad (7)$$

where $\psi^T = [\bar{x}_1, \bar{x}_2, \dots, \bar{x}_q]$ is the terminal constraints on the state vector and the optimal continuous feedback law is given by

$$u(t) = -C(t)x(t) - D(t)\psi \quad (8)$$

$$\text{and } C = R^{-1}B^T(P - SG^{-1}S^T) \quad (9)$$

$$D = R^{-1}B^T SG^{-1} \quad (10)$$

The control vector u will take the state vector from $x(t_0)$ at time t_0 to ψ at time t_f while minimizing the cost function of Eq.(1).

In order to compute $C(t)$ and $D(t)$ efficiently in Eqs.(9) and (10), closed form solutions for Eqs. (5)-(7) are presented, thus reducing the solution for the control problem to the direct computation of algebraic equations without numerical integration. The solution for Eq. (5) has been previously obtained in Refs. [7-9] and can be written as

$$P(t) = P_{SS} + Z^{-1}(t) \quad (11)$$

where P_{SS} is the positive definite solution for the algebraic Riccati equation

$$A^T P_{SS} + P_{SS} A - P_{SS} B R^{-1} B^T P_{SS} + F^T Q F = 0 \quad (12)$$

For a completely observable and stabilizable system², P_{SS} and $Z^{-1}(t)$ exist for $t_f \geq t \geq t_0$. The differential equation for $Z(t)$ is given by

$$\dot{Z} = \bar{A}Z + Z\bar{A}^T - BR^{-1}B^T ; Z(t_f) = -P_{SS}^{-1} \quad (13)$$

with the solution

$$Z(t) = Z_{SS} - e^{\bar{A}(t-t_f)}(Z_{SS} + P_{SS}^{-1})e^{\bar{A}^T(t-t_f)} \quad (14)$$

where $e^{(\cdot)}$ is the exponential matrix, $\bar{A} = A - BR^{-1}B^T P_{SS}$ is a stability matrix with eigenvalues having negative real parts and Z_{SS} satisfies the algebraic Lyapunov equation

$$\bar{A}Z_{SS} + Z_{SS}\bar{A}^T = BR^{-1}B^T \quad (15)$$

Obviously, there exists a continuous solution for the square matrix $Z(t)$.

The new solution for the rectangular time-varying matrix $S(t)$ in Eq. (6) follows on assuming the product form solution

$$S(t) = Z^{-1}(t)S_C(t) \quad (16)$$

Substitution of Eq. (16) into Eq. (6) with the aid of Eq. (13) leads to the following linear matrix differential equation for $S_C(t)$:

$$\dot{S}_C(t) - \bar{A}S_C(t) = 0 ; S_C(t_f) = -P_{SS}^{-1}S(t_f) \quad (17)$$

The solution for $S_C(t)$ is

$$S_C(t) = -e^{\bar{A}(t-t_f)}P_{SS}^{-1}S(t_f) \quad (18)$$

Now from Eq. (7), making use of Eqs.(6) and (13), the following solution for $G(t)$ is obtained:

$$G(t) = S^T(t)Z(t)S(t) + S^T(t_f)P_{SS}^{-1}S(t_f) \quad (19)$$

which can be easily verified by direct differentiation of Eq.(19). Note that⁴

$$G(t) < 0 \text{ for } t_f > t \geq t_0 \text{ since } \dot{G}(t) \geq 0 \text{ and } G(t_f) = 0.$$

CLOSED-FORM SOLUTION FOR THE STATE TRAJECTORY

Introducing the control input u into Eq.(2) yields the closed-loop system dynamics equation as follows

$$\dot{x} = [\bar{A} - BR^{-1}B^T Z_m^{-1}]x - BR^{-1}B^T S_m \psi \quad (20)$$

where, with the aid of the matrix inversion lemma¹,

$$Z_m(t) = [Z^{-1}(t) - S(t)G^{-1}(t)S^T(t)]^{-1} \quad (21-a)$$

$$= Z(t) + S_C(t)WS_C^T(t) ; W = [S^T(t_f)P_{SS}^{-1}S(t_f)]^{-1}$$

and

$$S_m(t) = S(t)G^{-1}(t) \quad (21-b)$$

It is obvious that $Z_m(t)$ exists for $t_f \geq t \geq t_0$ since $Z(t)$, $S_C(t)$ and W exist. Direct differentiation of Eq.(21) leads to

$$\dot{Z}_m = Z_m \bar{A}^T + \bar{A}Z_m - BR^{-1}B^T \quad (22)$$

To obtain the homogeneous solution x_h for Eq.(20), consider the following coordinate transformation for the variable $x_h(t)$

$$x_h(t) = Z_m(t)r(t) \quad (23)$$

where $r(t)$ is a vector function to be determined. Differentiating Eq.(23) in combination with Eq.(22), and inserting into Eq.(20) with $\psi = 0$, leads to

$$Z_m(\dot{r} + \bar{A}^T r) = 0 \quad (24)$$

Choose $r(t)$ to satisfy

$$\dot{r} + \bar{A}^T r = 0 \quad (25)$$

which possesses the solution

$$r = e^{-\bar{A}^T(t-t_0)}r_0 \quad (26)$$

where r_0 is an integration constant vector.

Let the dependent state vector x be

$$x(t) = \Phi(t)(r_0 + x_p(t)) \quad (27)$$

where

$$\Phi(t) = Z_m(t)e^{-\bar{A}^T(t-t_0)} \quad (28)$$

In view of Eqs.(20) and (22), it is easy to show that

$$\dot{\Phi}(t) = [\bar{A} - BR^{-1}B^T Z_m^{-1}(t)]\Phi(t) \quad (29)$$

Let Φ_1 be the inverse of Φ . Note that Φ is a nonsingular matrix for $t_f > t > t_0$. Pre and post multiplying Eq.(29) by Φ_1 lead to

$$\dot{\Phi}_1(t) = -\Phi_1(t)[\bar{A} - BR^{-1}B^T Z_m^{-1}(t)] \quad (30)$$

Substituting Eq.(27) into Eq.(20) with the aid of Eq.(29) yields

$$\dot{x}_p(t) = -\Phi_1(t)BR^{-1}B^T S_m(t)\psi \quad (31)$$

Now making use of Eq.(30) and the following formulation for S_m :

$$dS_m/dt = [-\bar{A}^T + Z_m^{-1}BR^{-1}B^T]S_m \quad (32)$$

Eq.(31) can be solved by

$$x_p(t) = [-\Phi_1(t)Z_m(t)S_m(t) + x_{p0}]\psi \quad (33)$$

where x_{p0} is an integration constant matrix to be determined by the initial condition. Eqs.(32) and (33) can be easily verified by direct differentiation. Combination of Eqs.(29) and (32) yields

$$d[\Phi^T(t)S_m(t)]/dt = 0 \quad (34)$$

$$\text{i.e. } \Phi^T(t)S_m(t) \equiv \text{constant}; t_f > t > t_0$$

Direct substitution of Eq.(33) into Eq.(27) and evaluation of the equation obtained at $t = t_0$ provides

$$x_p(t_0) = 0 \Rightarrow x_{p0} = S_m(t_0) \quad (35)$$

$$\text{and } x_h(t_0) = x(t_0) \Rightarrow r_0 = \Phi_1(t_0)x(t_0) \quad (36)$$

by noting that ψ is an arbitrary constant vector. The solution for the state vector x becomes

$$x(t) = \Phi(t)\Phi_1(t_0)x(t_0) + [\Phi(t)S_m(t_0) - Z_m(t)S_m(t)]\psi \quad (37)$$

For the special case where all the terminal states are specified (i.e. $q=n$), S is a nonsingular square matrix and algebraic manipulation leads to

$$S_m = -[Z + S_C P_{SS} S_C^T]^{-1} e^{\bar{A}^T(t-t_f)} \quad (38)$$

$$= [Z_{SS} e^{\bar{A}^T(t-t_f)} - e^{-\bar{A}^T(t-t_f)} Z_{SS}]^{-1}$$

and

$$Z_m^{-1} = Z^{-1} - SG^{-1}S^T = [Z + S_C P_{SS} S_C^T]^{-1} \quad (39)$$

$$= -[Z_{SS} e^{\bar{A}^T(t-t_f)} - e^{-\bar{A}^T(t-t_f)} Z_{SS}]^{-1} e^{-\bar{A}^T(t-t_f)}$$

It follows that

$$Z_m(t)S_m(t) = -e^{\bar{A}^T(t-t_f)} \quad (40)$$

For single degree of freedom S_m reduces to a hyperbolic function multiplied by a constant. Eq.(37) becomes

$$x(t) = \Phi(t)\Phi_1(t_0)x(t_0) + [e^{\bar{A}^T(t-t_f)} + \Phi(t)S_m(t_0)]\psi \quad (41)$$

It is immediately seen that, when $t = t_f$, $Z_m(t_f) = 0$ and $\Phi(t_f) = 0$ from Eqs.(39) and (28) and thus $x(t_f) = \psi$.

PRACTICAL COMPUTATION FOR THE SOLUTIONS

The above results allow solutions for a terminal controller with any given dimension (where by the dimension is meant the number of the states n and terminal constraints q). First, we obtain the solutions (14), (16), (18) and (19) at time t . Then Eqs.(11), (16) and (19) will determine gains C and D in Eqs. (9) and (10). The control $u(t)$ is thus calculated from Eq.(8) at any time t .

An alternative way to implement these solutions is introduced as follows. Examination of Eq.(22)

reveals that Z_m can be solved by

$$Z_m(t) = Z_{SS} + e^{\bar{A}^T(t-t_f)}[Z_m(t_f) - Z_{SS}]e^{\bar{A}^T(t-t_f)} \quad (42)$$

where Z_{SS} satisfies the algebraic equation (15) and $Z_m(t_f)$ is the terminal condition given by

$$Z_m(t_f) = -P_{SS}^{-1} + P_{SS}^{-1}S(t_f)[S^T(t_f)P_{SS}^{-1}S(t_f)]^{-1}S^T(t_f)P_{SS}^{-1} \quad (43)$$

which can be easily obtained from Eq.(21). For the case where all terminal states are specified (i.e. $q = n$ and $Z_m(t_f) = 0$) Eq.(43) obviously becomes Eq.(39). Eq.(34) suggests that S_m have the solution

$$S_m(t) = S(t)G^{-1}(t) = Z_m^{-1}(t)e^{\bar{A}^T(t-t_f)}Z_m(t_f)S_m(t_f) \quad (44)$$

Now combination of Eqs.(21-a) and (21-b) with some matrix manipulations leads to

$$Z_m(t)S_m(t) = S_C(t)W \quad (45)$$

which provides, with the aid of Eq.(18), the terminal condition

$$Z_m(t_f)S_m(t_f) = -P_{SS}^{-1}S(t_f)W \quad (46)$$

For $q = n$, Eq.(45) is replaced by Eq.(40). Eqs.(42) and (44) thus constitute the feedback control u as follows.

$$u(t) = -R^{-1}B^T[P_{SS} + Z_m^{-1}(t)]x(t) - R^{-1}B^T S_m(t)\psi \quad (47)$$

The solution for the state trajectory is given by Eq.(37). It is seen that this alternative procedure for the numerical implementation of the terminal controller eliminates the computation $G^{-1}(t)$. This considerably reduces the computational time and errors particularly when the size of matrix $G(t)$ is large.

Efficient methods for the computation of $\exp[\bar{A}(t-t_f)]$ and Z_m^{-1} are needed to reduce the computational burden on costs and numerical errors. For numerical simulations, the exponential matrix $\exp[\bar{A}(t-t_f)]$ is propagated forward in time using the relation

$$\exp[\bar{A}(t+\Delta t-t_f)] = \exp[\bar{A}(t-t_f)]\exp[\bar{A}\Delta t] \quad (48)$$

where $\exp[\bar{A}(t_0-t_f)]$ and $\exp[\bar{A}\Delta t]$ are computed only once, using a Padé series expansion approximation which is highly efficient and accurate [11]. When time proceeds, the matrix exponential at any other time will simply be the multiplication of the result at the previous time step.

The inverse of the time-dependent symmetric matrix $Z_m(t)$ becomes the most time consuming operation for the terminal controller. As far as computational speed is concerned, factorization methods developed in Ref. [12-13] are appropriate for this application.

ILLUSTRATIVE EXAMPLES

First order system:

As the first example, given the first-order system

$$\dot{x} = -x/a + u \quad (49)$$

determine a terminal controller that will drive the state x from its initial position x_0 to the terminal position ψ .

If x^2 is aimed to be kept below $x_m^2 = \text{constant}$, using u^2 below $u_m^2 = \text{constant}$, the following performance index is considered

$$2J = \int_{t_0}^{t_f} (Qx^2 + Ru^2) dt \quad (50)$$

where $Q = x_m^{-2}$ and $R = u_m^{-2}$, which is subjected to the terminal constraints

$$x(t_f) = \psi \quad (51)$$

The corresponding solution P_{SS} for the steady state Riccati equation (12) is

$$P_{SS} = R[-1/a + (Q/R + 1/a^2)^{1/2}] \quad (52)$$

Other related constants are given below

$$\bar{A} = -(Q/R + 1/a^2)^{1/2} \quad (53)$$

and

$$Z_{SS} = -[2R(Q/R + 1/a^2)^{1/2}]^{-1} \quad (54)$$

Then Eqs. (14) and (18) lead to

$$Z_m = Z + S_C P_{SS} S_C^T = -2Z_{SS} \sinh \bar{A}(t-t_f) e^{\bar{A}(t-t_f)} \quad (55)$$

which gives

$$\phi = 2Z_{SS} \sinh \bar{A}(t-t_f) e^{\bar{A}(t_0-t_f)} \quad (56)$$

Application of Eqs. (38) and (39) to Eq. (47) thus yields the control input u for Eq. (2) as follows

$$u = -R^{-1} \{ [P_{SS} e^{-\bar{A}(t-t_f)} / 2Z_{SS} \sinh \bar{A}(t-t_f)] x + [1/2Z_{SS} \sinh \bar{A}(t-t_f)] \psi \} \quad (57)$$

The value of x at any time t from Eq. (41) becomes

$$x(t) = x(t_0) \sinh \bar{A}(t-t_f) / \sinh \bar{A}(t_0-t_f) + \psi [\cosh \bar{A}(t-t_f) - \sinh \bar{A}(t-t_f) \coth \bar{A}(t_0-t_f)] \quad (58)$$

For $t = t_f$, the feedback gains C and D approach ∞ and the terminal state becomes ψ . Eq. (58) can also be obtained by direct integration of Eq. (20).

Suppose that $a = 10$, $Q = R = 1$. If $\psi = 0$, $x(t_0) = 1$ and $t_f = 5$, the control u and the state trajectory x are given in Figure 1. The final state $x(t_f)$ is zero.

For the second case, if $x(t_0) = 0$ and $\psi = 1$, Figure 2 shows the control u and the state history x for this case. The final state $x(t_f)$ is 1.

Third order system:

As the second example, consider the third-order system

$$\dot{u} = u_1 \quad (59)$$

$$\dot{\omega} = -\omega/a + b u/a \quad (60)$$

$$\dot{\phi} = \omega \quad (61)$$

where a and b are constants. Using quadratic synthesis, consider the minimization of the following performance index

$$2J = \int_{t_0}^{t_f} [(\phi/\phi_m)^2 + (u/u_m)^2 + (u_1/u_{1m})^2] dt \quad (62)$$

subject to the terminal constraints

$$\psi = x(t_f) = (u, \omega, \phi)_{t=t_f}^T \quad (63)$$

where ϕ_m , u_m and u_{1m} are constants representing weighting coefficients. The analytical solution P_{SS} of the Riccati equation (12) for this case can be found in Ref. [1], pp. 170. The solution Z_{SS} of the algebraic Lyapunov equation (15) can easily be obtained by straightforward manipulation in terms of elements in the matrix P_{SS} . Note that P_{SS} and Z_{SS} can be numerically computed [14-15].

For the rest-to-rest case, suppose that $a=100$, $b = \phi_m = u_m = u_{1m} = 1$, $u(t_0) = \omega(t_0) = u(t_f) = \omega(t_f) = \phi(t_f) = 0$, $\phi(t_0) = 1$ with $t_0 = 0$ and $t_f = 10$. This is a rest-to-rest maneuver because $\omega = \dot{\phi} = 0$ at $t = 0$ and $t = 10$. Figure 3 presents time histories of the states u , ω , and ϕ computed from Eq. (37) in

conjunction with Eqs. (42) and (44). The control input u_1 is also shown in Fig. (3) which shows the jump discontinuities at the initial time t_0 and final time t_f . However, the state u which is the integral of the control input u_1 , has a smooth curve. The state u is actually the control input for the state ω which may represent the spinning rate for a rigid body such as an aircraft undergoing a 1 radian rotation in 10 seconds subject to the air resistance with time constant a .

For the spin-up case, figure 4 presents a spin-up maneuver, in which the final angle ϕ is free to be determined by the controller, while $u(t_0)=\omega(t_0)=\phi(t_0)=u(t_f)=0$ and $\omega(t_f)=1$. This case is typical of the problem of increasing the rotation rate of a rigid satellite for on-orbit stabilization.

CONCLUDING REMARKS

The contribution of this paper is the closed-form solutions for the feedback control gains and the state trajectory with terminal constraints on state and time. In addition, a new way of implementing these solutions is developed. This is a particularly interesting result which leads to an alternate representation of the coupled differential matrix Riccati-like equations required to solve feedback gains of the terminal controller. Computational procedures have been considerably simplified to increase the computational speed. Results of example maneuvers are shown demonstrating the validity of the formulations developed in this paper.

References

1. Bryson, A. and Ho, Y. C., Applied Optimal Control, John Wiley & Sons, New York, 1975.
2. Kwakernaak, H. and Sivan, R., Linear Optimal Control Systems, John Wiley & Sons, Inc., New York, 1972.
3. Sage, A. P. and White, C. C., Optimum Systems Control, Prentice-Hall, Inc., Englewood Cliffs, New Jersey, 2nd Edition, 1977.
4. Schmitendorf, W. E. and Citron S. J., "On the Applicability of the Sweep Method to Optimal Control Problems," IEEE Trans. Automatic Control, Vol. AC-14, pp. 69-72, Feb., 1969.
5. Friedland, B., "On Solutions of the Riccati Equation in Optimization Problems," IEEE Trans. Automatic Control, Vol. AC-12, pp.303-304, June 1967.
6. Dreyfus, S. E., "Control Problems with Linear Dynamics, Quadratic Criterion, and Linear Terminal Constraints," IEEE Trans. Automatic Control, Vol. AC-12, pp. 323-324, June, 1967.
7. Brockett, R. W., Finite Dimensional Linear Systems, John Wiley and Sons, Inc., New York 1970.
8. Turner, J. D. and Chun, H. M., "Optimal Feedback Control of a Flexible Spacecraft During a Large-Angle Rotational Maneuver," Paper No.82-1589CP. Presented at the AIAA Guidance and Control Conference, San Diego, CA, 1982.
9. Potter, J. E. and Vander Velde, W. E., "Optimum Mixing of Gyroscope and Star Tracker Data," AIAA J. Spacecraft and Rockets, Vol. 5, No. 5, May 1968, pp. 536-540.
10. Breakwell, J. A., "Optimal Feedback Slewing of Flexible Spacecraft," AIAA J. Guidance and Control, Vol. 4, No. 5, Sept.-Oct. 1981, pp. 472-479.
11. Moler, C. and Van Loan, C., "Nineteen Dubious Ways to Compute the Exponential of a Matrix," SIAM Review, Vol. 20, No. 4, Oct. 1978, pp. 801-836.
12. Wilkinson, J. H., The Algebraic Eigenvalue Problem, Clarendon Press, Oxford University Press, London, 1965.
13. Bunch, J. R. and Parlett, B. N., "Direct Methods for Solving Symmetric Indefinite Systems of Linear Equations," SIAM J. Numer. Anal., 8(1971) pp. 639-655.
14. Armstrong, E. S., ORACLS - A Design System for Linear multivariable Control, Marcel Dekker, Inc. New York, 1980.
15. Kleinman, D. L., "On an Iterative Technique for Riccati Equation Computations," IEEE Trans. Autom. Control, Vol. AC-13, no. 1, Feb. 1968, pp. 114-115.

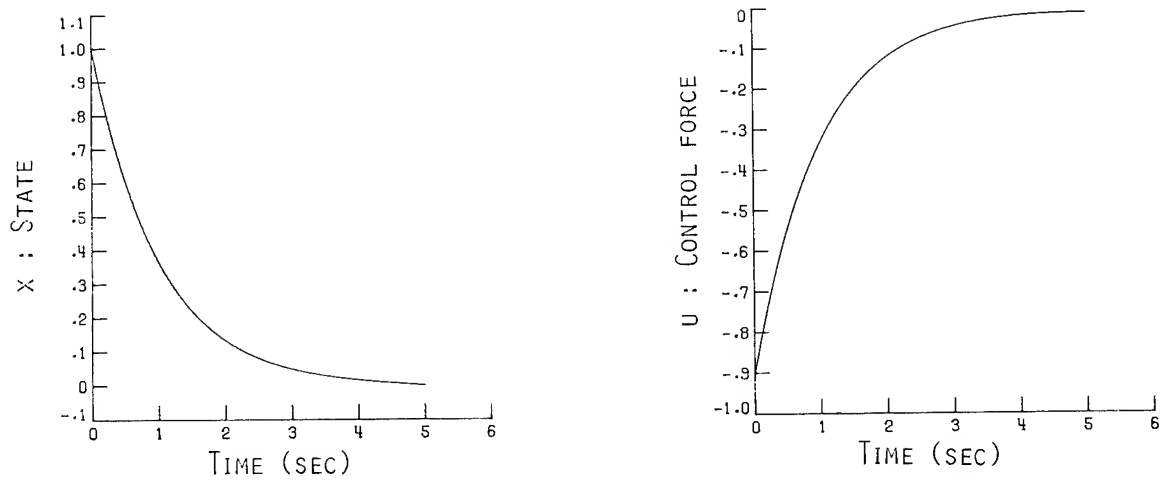


FIGURE 1 : INITIAL-POSITION-TO-ZERO STATE MANEUVER FOR A FIRST-ORDER SYSTEM

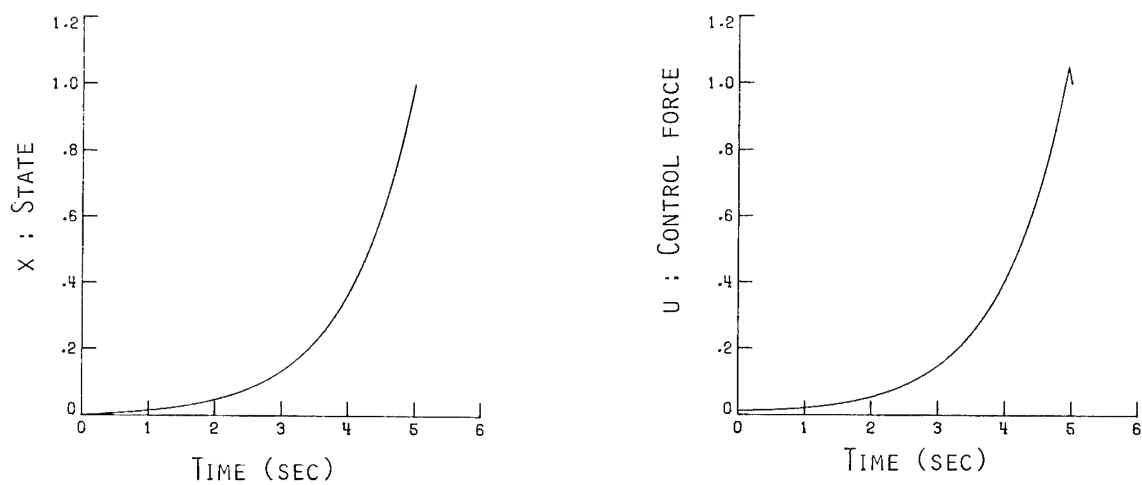


FIGURE 2 : ZERO-TO-PREScribed-POSITION STATE MANEUVER FOR A FIRST-ORDER SYSTEM

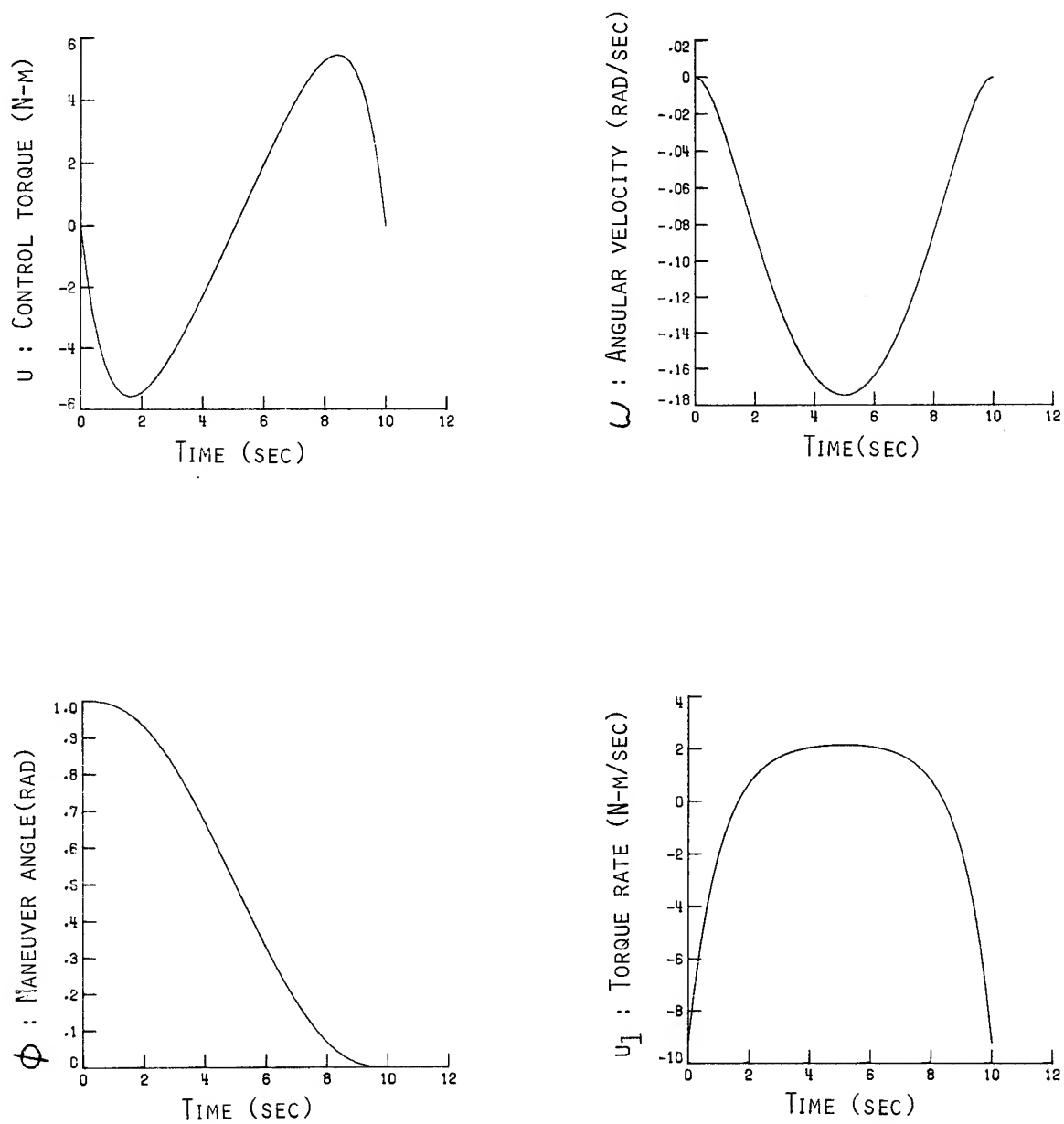


FIGURE 3 : REST-TO-REST MANEUVER

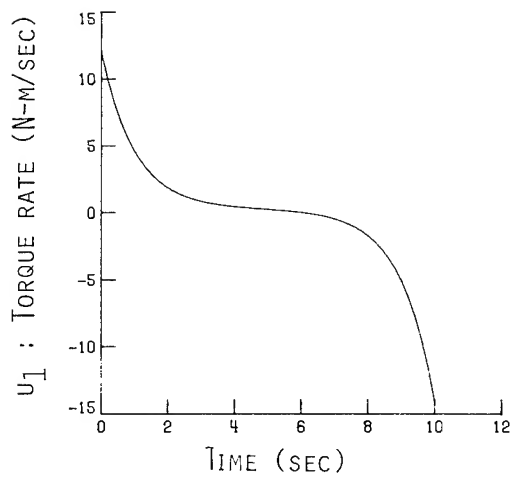
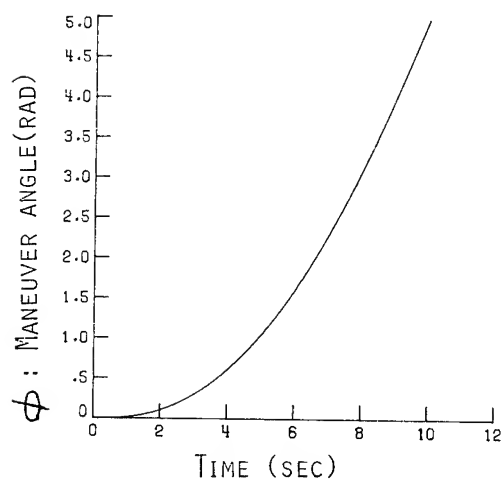
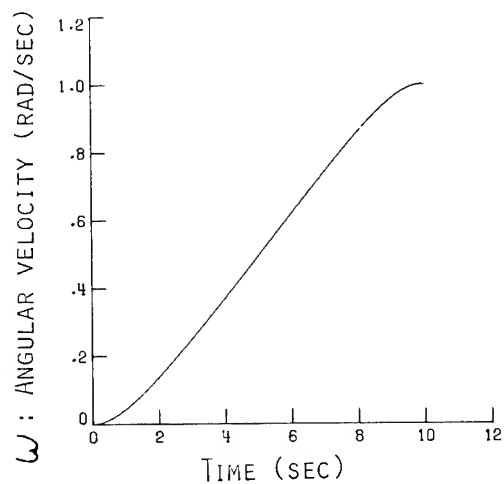
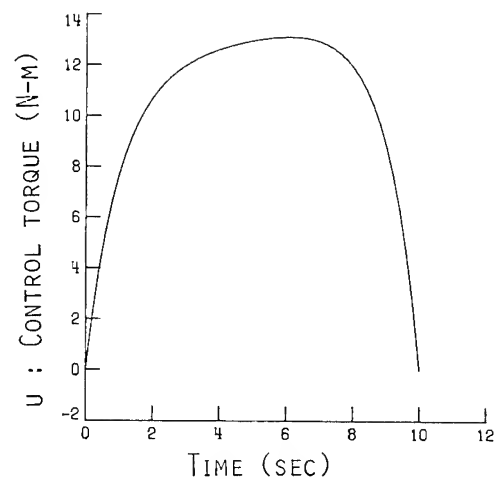


FIGURE 4 : FREE FINAL ANGLE SPIN-UP MANEUVER

L. Meirovitch¹ and G. Ryland²

Department of Engineering Science and Mechanics
Virginia Polytechnic Institute and State University
Blacksburg, Virginia 24061

Abstract

The response of linear damped gyroscopic systems can be obtained by means of techniques of linear systems theory, which involves the computation of the transition matrix. The response is in terms of complex quantities, which is likely to cause computational difficulties as the order of the system increases. In the absence of damping, it is possible to derive the response of a linear gyroscopic system with relative ease by working with real quantities alone. When damping is small, one can use a perturbation approach to produce the response by regarding the undamped gyroscopic system as the unperturbed system. In a previous paper, a perturbation analysis was used to derive the response of a gyroscopic system with small internal damping. This paper extends the approach to the case of external damping, which is characterized not only by symmetric coefficients multiplying velocities but also by skew symmetric coefficients multiplying displacements, where the latter terms are known as circulatory. A numerical example is presented.

1 INTRODUCTION

Certain space structures require mathematical models of relatively large order, so that the need exists for computationally efficient algorithms for the response of large-order systems. The equations of motion for such structures can be expected to include gyroscopic, damping and circulatory effects, in addition to the inertia and stiffness terms. The response of dynamical systems including all of these effects can be obtained by methods from linear systems theory. This involves the computation of the transition matrix and use of complex quantities (Ref. 1), which is likely to cause difficulties, especially for large-order systems.

The simplest case is, of course, that in which gyroscopic, damping and circulatory effects are absent. Even for gyroscopic systems,

Meirovitch (Refs. 2 and 3) has shown how the eigensolution and response can be obtained with relative ease when damping and circulatory effects are not present. Quite often, damping and circulatory forces are small, so that one may consider obtaining the eigensolution by a perturbation analysis, where the unperturbed system includes gyroscopic effects. In a previous paper (Ref. 4), a perturbation analysis was used to solve the eigenvalue problem of a gyroscopic system subject to small internal damping. This paper extends that work to include small external

damping forces, which contribute not only symmetric coefficients multiplying the generalized velocities, but also skew symmetric coefficients multiplying the generalized coordinates. These latter terms are often called circulatory (Refs. 5 and 6).

Perturbation analyses for the eigenvalue problem are well documented. Franklin (Ref. 7), Wilkinson (Ref. 8) and Lancaster (Ref. 9) present equivalent perturbation analyses based on the statement of the eigenvalue problem itself, which utilize the biorthogonality of the unperturbed eigenvectors. In contrast, the perturbation analysis presented here is based on the statement of biorthonormality of the perturbed eigenvectors. Such a basis is considered more appropriate because it is the biorthogonality of the eigenvectors that allows the decoupling of otherwise coupled equations of motion.

2 GENERAL PERTURBATION THEORY

Consider the algebraic eigenvalue problem

$$\lambda_i \underline{B} \underline{u}_i = \underline{A} \underline{u}_i, \quad i=1,2,\dots,n \quad (1a)$$

and its adjoint

$$\lambda_i \underline{B}^T \underline{v}_i = \underline{A}^T \underline{v}_i, \quad i=1,2,\dots,n \quad (1b)$$

where the $n \times n$ matrices \underline{A} and \underline{B} are assumed to possess no symmetries. The eigenvalues of both eigenvalue problems are the same, and for each eigenvalue λ_i there is a right eigenvector, \underline{u}_i , and a left eigenvector, \underline{v}_i . Upon normalization, the right and left eigenvectors satisfy the biorthonormality relations

$$\underline{v}_i^T \underline{B} \underline{u}_j = \Delta_{ij}, \quad \underline{v}_i^T \underline{A} \underline{u}_j = \lambda_i \Delta_{ij}, \quad i,j=1,2,\dots,n \quad (2a,b)$$

where Δ_{ij} is a modified Kronecker delta; it is zero when $i \neq j$ and either +1 or -1 when $i = j$.

The right and left eigenvectors \underline{u}_i and \underline{v}_i ($i=1,2,\dots,n$) can be used to construct the square matrices \underline{U} and \underline{V} as follows:

$$\underline{U} = [\underline{u}_1 \ \underline{u}_2 \ \dots \ \underline{u}_n], \quad \underline{V} = [\underline{v}_1 \ \underline{v}_2 \ \dots \ \underline{v}_n] \quad (3a,b)$$

Similarly, the eigenvalues and the modified Kronecker deltas can be arranged in the diagonal matrices

$$\Lambda = \text{diag}[\lambda_1 \ \lambda_2 \ \dots \ \lambda_n], \quad \Delta = \text{diag}[\Delta_{11} \ \Delta_{22} \ \dots \ \Delta_{nn}] \quad (3c,d)$$

Equations (2) can now be expressed as

* Supported in part by the AFOSR Research Grant 83-0017

¹University Distinguished Professor.

²Research Associate

$$V^T B U = \Delta, \quad V^T A U = \Lambda \Delta \quad (4a,b)$$

Let us consider the case in which matrices A and B can be written as

$$A = A_0 + A_1, \quad B = B_0 + B_1 \quad (5a,b)$$

where the norms of matrices A_1 and B_1 are significantly smaller than the norms of A_0 and B_0 , respectively. This difference in magnitude can be used to define an ordering scheme in which matrices A_0 and B_0 are $O(0)$ quantities, while A_1 and B_1 are $O(1)$ quantities. The scheme can be extended to higher orders, denoted as $O(2)$, $O(3)$, etc. Note that the modified Kronecker delta is an $O(0)$ quantity.

Substituting Eqs. (5) into Eqs. (4), we obtain

$$V^T (B_0 + B_1) U = \Delta, \quad V^T (A_0 + A_1) U = \Lambda \Delta \quad (6a,b)$$

Let us assume for the moment that $A_1 = B_1 = 0$.

Then Eqs. (6) reduce to

$$V_0^T B_0 U_0 = \Delta, \quad V_0^T A_0 U_0 = \Lambda_0 \Delta \quad (7a,b)$$

We refer to Eqs. (6) as the perturbed biorthonormality relations, and their solution, U, V and Λ , as the perturbed eigensolution. Similarly, Eqs. (7) are referred to as the unperturbed, or $O(0)$ biorthonormality relations, and their solution is the unperturbed, or $O(0)$ eigensolution.

Let us assume that the $O(0)$ eigensolution is available. Then, our objective is to develop a solution to the perturbed biorthonormality relations, based upon the known $O(0)$ eigensolution and matrices A_1 and B_1 . Furthermore, in generating this solution, we wish to avoid solving another eigenvalue problem. To this end, we consider transformation matrices E and Γ , which relate U and V to U_0 and V_0 , respectively, as follows:

$$U = U_0 E, \quad V = V_0 \Gamma \quad (8a,b)$$

Equations (8) can also be written as

$$u_i = U_{0i} \epsilon_i = \sum_{q=1}^n u_{0q} \epsilon_{qi}, \quad i=1,2,\dots,n \quad (9a)$$

$$v_i = V_{0i} \gamma_i = \sum_{p=1}^n v_{0p} \gamma_{pi}, \quad i=1,2,\dots,n \quad (9b)$$

where ϵ_i and γ_i are the i th columns of E and Γ , respectively, and where ϵ_{qi} and γ_{pi} are the (q,i) th and (p,i) th elements of E and Γ , respectively. Equations (8), and hence Eqs. (9), are valid because the u_{0p} and v_{0q} ($p,q = 1,2,\dots,n$) both span the space L^n , and u_i and v_i ($i=1,2,\dots,n$) are vectors in that space.

Substituting Eqs. (8) into Eqs. (6) and using Eqs. (7) we obtain

$$\Gamma^T (\Delta + \hat{B}) E = \Delta, \quad \Gamma^T (\Lambda_0 \Delta + \hat{A}) E = \Lambda \Delta \quad (10a,b)$$

where

$$\hat{A} = V_0^T A_1 U_0, \quad \hat{B} = V_0^T B_1 U_0 \quad (11a,b)$$

are $O(1)$ quantities. Because \hat{A} and \hat{B} are small, the matrices $(\Lambda_0 \Delta + \hat{A})$ and $(\Delta + \hat{B})$ are nearly diagonal. Then, it is reasonable to assume that the transformation matrices E and Γ , which diagonalize $(\Lambda_0 \Delta + \hat{A})$ and $(\Delta + \hat{B})$, represent near identity transformations. Hence, we consider the expansions

$$E = I + E_1 + E_2 + \dots, \quad (12a,b)$$

$$\Gamma = I + \Gamma_1 + \Gamma_2 + \dots$$

and

$$\Lambda = \Lambda_0 + \Lambda_1 + \Lambda_2 + \dots \quad (13)$$

where I is the identity matrix and where the subscripts indicate the order of magnitude. We assume that these expansions are convergent, which implies that any one term is one order of magnitude smaller than the preceding term. In writing the expansions of Eqs. (12) and (13), we assume that, as the perturbing matrices A_1 and B_1 tend to zero, we must have $E_1, E_2, \dots \rightarrow 0$, $\Gamma_1, \Gamma_2, \dots \rightarrow 0$ and $\Lambda_1, \Lambda_2, \dots \rightarrow 0$, or equivalently, $U \rightarrow U_0$, $V \rightarrow V_0$ and $\Lambda \rightarrow \Lambda_0$.

Substituting Eqs. (12) and (13) into Eqs. (10) and separating according to order, we obtain

$$O(0): \Delta = \Delta, \quad \Lambda_0 \Delta = \Lambda_0 \Delta \quad (14a,b)$$

$$O(1): \Delta E_1 + \Gamma_1^T \Delta = -\hat{B} \quad (14c)$$

$$\Lambda_0 \Delta E_1 + \Gamma_1^T \Lambda_0 \Delta = -\hat{A} + \Lambda_1 \Delta \quad (14d)$$

The $O(0)$ equations, Eqs. (14a,b), are satisfied identically, as anticipated.

Turning our attention to the $O(1)$ equations, let us equate homologous elements on both sides of these equations, so that

$$\Delta_{ii} \epsilon_{lij} + \gamma_{lji} \Delta_{jj} = -\hat{b}_{ij}, \quad i,j = 1,2,\dots,n \quad (15a)$$

$$\lambda_{0i} \Delta_{ii} \epsilon_{lij} + \gamma_{lji} \lambda_{0j} \Delta_{jj} = -\hat{a}_{ij} + \lambda_{1i} \Delta_{ij}, \quad i,j=1,2,\dots,n \quad (15b)$$

where ϵ_{lij} , γ_{lij} , \hat{b}_{ij} and \hat{a}_{ij} are the (i,j) elements of E_1 , Γ_1 , \hat{B} and \hat{A} , respectively. When $i = j$, Eqs. (15) become

$$\Delta_{ii}(\epsilon_{1ii} + \gamma_{1ii}) = -\hat{b}_{ii}, \quad i=1,2,\dots,n \quad (16a)$$

$$\lambda_{0i}\Delta_{ii}(\epsilon_{1ii} + \gamma_{1ii}) = -\hat{a}_{ii} + \lambda_{1i}\Delta_{ii}, \quad i=1,2,\dots,n \quad (16b)$$

Clearly, these equations indicate that $\lambda_{1i} = \Delta_{ii}(\hat{a}_{ii} - \lambda_{0i}\hat{b}_{ii})$ ($i=1,2,\dots,n$), but they provide no unique solution for ϵ_{1ii} and γ_{1ii} ($i=1,2,\dots,n$). To divide the weighting equally, let us take $\epsilon_{1ii} = \gamma_{1ii} = -\frac{1}{2}\Delta_{ii}\hat{b}_{ii}$ ($i=1,2,\dots,n$), which is consistent with the condition that E_1 and $\Gamma_1 \rightarrow 0$ as A_1 and $B_1 \rightarrow 0$. Alternatively, when $i \neq j$, $\Delta_{ij} = 0$, and Eqs. (15) can be solved independently for ϵ_{1ij} and γ_{1ij} . Hence, we have

$$\epsilon_{1ij} = -\Delta_{ii} \frac{\hat{a}_{ij} - \hat{b}_{ij}\lambda_{0j}}{\lambda_{0i} - \lambda_{0j}}, \quad i \neq j, \quad i,j=1,2,\dots,n \quad (17a)$$

$$\epsilon_{1ii} = \gamma_{1ii} = -\frac{1}{2}\Delta_{ii}\hat{b}_{ii}, \quad i=j=1,2,\dots,n \quad (17b)$$

$$\gamma_{1ij} = -\Delta_{ii} \frac{\hat{a}_{ji} - \lambda_{0j}\hat{b}_{ji}}{\lambda_{0i} - \lambda_{0j}}, \quad i \neq j, \quad i,j=1,2,\dots,n \quad (17c)$$

$$\lambda_{1i} = \Delta_{ii}(\hat{a}_{ii} - \lambda_{0i}\hat{b}_{ii}), \quad i=1,2,\dots,n \quad (18)$$

Determination of the perturbed eigensolution is now complete through $O(1)$. The analysis can be readily carried to higher orders. Indeed, using similar arguments, we obtain solutions to the $O(2)$ equations in the form

$$\epsilon_{2ij} = \frac{\Delta_{ii}}{\lambda_{0i} - \lambda_{0j}} \left\{ -(\lambda_{1i}\Delta_{ii}\epsilon_{1ij} + \gamma_{1ji}\lambda_{1j}\Delta_{jj}) + \sum_{p=1}^n [(\lambda_{0i} - \lambda_{0j})\Delta_{ii}\epsilon_{lip}\epsilon_{lpj}] + (\lambda_{0p} - \lambda_{0j})\gamma_{1pi}\Delta_{pp}\epsilon_{lpj} \right\}, \quad i \neq j, \quad i,j=1,2,\dots,n \quad (19a)$$

$$\epsilon_{2ii} = \gamma_{2ii} = \frac{1}{2}\Delta_{ii} \sum_{p=1}^n (\Delta_{ii}\epsilon_{lip}\epsilon_{lpi} + \gamma_{1pi}\Delta_{pp}\epsilon_{lpi} + \gamma_{1pi}\gamma_{1ip}\Delta_{ii}), \quad i = j, \quad i = 1,2,\dots,n \quad (19b)$$

$$\gamma_{2ij} = \frac{\Delta_{ii}}{\lambda_{0i} - \lambda_{0j}} \left\{ -(\lambda_{1j}\Delta_{jj}\epsilon_{1ji} + \gamma_{1ij}\lambda_{1i}\Delta_{ii}) \right\}$$

$$+ \sum_{p=1}^n [(\lambda_{0p} - \lambda_{0j})\gamma_{1pj}\Delta_{pp}\epsilon_{lpi} + (\lambda_{0i} - \lambda_{0j})\gamma_{1pj}\gamma_{1ip}\Delta_{ii}] \}, \quad i \neq j, \quad i,j=1,2,\dots,n \quad (19c)$$

$$\lambda_{2i} = \lambda_{1i}(\epsilon_{1ii} + \gamma_{1ii}) + \Delta_{ii} \sum_{p=1}^n (\lambda_{0i} - \lambda_{0p})\gamma_{1pi}\Delta_{pp}\epsilon_{lpi}, \quad i=1,2,\dots,n \quad (20)$$

where Eqs. (15) have been used to express \hat{a}_{ij} and \hat{b}_{ij} in terms of ϵ_{1ij} , γ_{1ij} , Δ_{ij} and λ_{1i} ($i,j=1,2,\dots,n$). The $O(3)$ equations yield the following eigenvalue perturbations:

$$\lambda_{3i} = \lambda_{1i}(\epsilon_{2ii} + \gamma_{2ii}) + \Delta_{ii} \sum_{p,q=1}^n \gamma_{1pi}(\hat{a}_{pq} - \lambda_{0i}\hat{b}_{pq})\epsilon_{lqi}, \quad i=1,2,\dots,n \quad (21)$$

Third-order eigenvector perturbations are deemed unnecessary.

We observe that the expressions for ϵ_{1ij} , ϵ_{2ij} , γ_{1ij} and γ_{2ij} involve division by $(\lambda_{0i} - \lambda_{0j})$ where $i \neq j$, $i,j=1,2,\dots,n$. Then, recalling the discussion regarding convergence, we conclude that the validity of the above results depends on the distinctness of the $O(0)$ eigenvalues, i.e. the quantity $(\lambda_{0i} - \lambda_{0j})$ ($i \neq j$, $i,j=1,2,\dots,n$) cannot be as small as $O(1)$.

One method of judging accuracy is to simply compare the magnitudes of successive terms in the expansions (12) and (13). A more pertinent measure of eigenvector accuracy is how well the \hat{A} expansions (12) diagonalize the matrices $(\Lambda_0\hat{A} + \hat{A})$ and $(\hat{A} + \hat{B})$. In the numerical example presented later, such a computation will be referred to as a "biorthonormality check".

3. GENERAL DAMPED, CIRCULATORY, GYROSCOPIC SYSTEMS

The linear equations of motion describing an n degree of freedom, damped, circulatory gyroscopic system can be written in the matrix form

$$\ddot{\mathbf{q}}(t) + (\mathbf{G} + \mathbf{C})\dot{\mathbf{q}}(t) + (\mathbf{K} + \mathbf{H})\mathbf{q}(t) = \mathbf{Q}(t) \quad (22)$$

where

M = real, symmetric, positive definite $n \times n$ mass matrix

G = real, skew symmetric $n \times n$ gyroscopic matrix

C = real, symmetric, positive semidefinite $n \times n$ damping matrix

K = real, symmetric $n \times n$ generalized stiffness matrix including elastic and centrifugal effects.

H = real, skew symmetric $n \times n$ circulatory matrix

$q(t)$ = $n \times 1$ column vector of generalized coordinates

$Q(t)$ = $n \times 1$ column vector of generalized forces

For details of the derivation of Eq. (22), the interested reader is referred to Meirovitch (Ref. 1). We note that, due to the presence of centrifugal effects in the generalized stiffness matrix, we cannot assume that K is positive definite. The eigenvalue problem corresponding to Eq. (22) and its adjoint are

$$\lambda_i^2 M q_i + \lambda_i (G + C) q_i + (K + H) q_i = 0, \quad i=1, 2, \dots, 2n \quad (23a)$$

$$\lambda_i^2 M p_i + \lambda_i (-G + C) p_i + (K - H) p_i = 0, \quad i=1, 2, \dots, 2n \quad (23b)$$

where λ_i ($i=1, 2, \dots, 2n$) is the i th eigenvalue and q_i and p_i ($i=1, 2, \dots, 2n$) are the i th right and left eigenvectors, respectively.

Now, because the coefficient matrices in Eqs. (23) are real, the coefficients in the characteristic polynomial are also real. Hence, complex eigenvalues must occur in conjugate pairs. Defining primed subscripts as $i' = i + n$ ($i=1, 2, \dots, n$) and $i' = i - n$ ($i = n + 1, n + 2, \dots, 2n$), the preceding statement can be written compactly as

$$\lambda_{i'} = \bar{\lambda}_i, \text{ when } \lambda_i = \text{complex} \quad (24a)$$

It follows that

$$q_{i'} = \bar{q}_i, \quad p_{i'} = \bar{p}_i, \text{ when } \lambda_i = \text{complex} \quad (24b)$$

An eigenvalue and the corresponding eigenvectors can also be real. We indicate this as

$$q_i, p_i = \text{real}, \text{ when } \lambda_i = \text{real} \quad (25)$$

There appear to be no relations analogous to Eqs. (24) for real eigenvalues. Due to the presence of matrices C and H , we do not anticipate purely imaginary eigenvalues.

It is convenient to express the equations of motion, Eq. (22), and the right and left eigenvalue problems, Eqs. (23), in the state form

$$M \ddot{x}(t) + K \dot{x}(t) = X(t) \quad (26)$$

$$\lambda_i M \dot{x}_i + K x_i = 0, \quad i=1, 2, \dots, 2n \quad (27a)$$

$$\lambda_i M^T \dot{y}_i + K^T y_i = 0, \quad i=1, 2, \dots, 2n \quad (27b)$$

where

$$x(t) = \begin{bmatrix} \dot{q}^T(t) \\ q^T(t) \end{bmatrix}^T, \quad X(t) = \begin{bmatrix} Q^T(t) \\ 0^T \end{bmatrix}^T \quad (28a,b)$$

$$x_i = \begin{bmatrix} \lambda_i q_i^T \\ q_i^T \end{bmatrix}^T, \quad y_i = \begin{bmatrix} -\lambda_i p_i^T \\ p_i^T \end{bmatrix}^T, \quad i=1, 2, \dots, 2n \quad (29a,b)$$

and

$$M^* = \begin{bmatrix} M & 0 \\ 0 & (K + H) \end{bmatrix} \quad (30a)$$

$$K^* = \begin{bmatrix} (G + C) & (K + H) \\ -(K + H) & 0 \end{bmatrix} \quad (30b)$$

Upon normalization, the right and left eigenvectors, x_i and y_i ($i=1, 2, \dots, 2n$) respectively, satisfy the biorthonormality relations

$$y_i^T M^* x_j = \Delta_{ij}, \quad y_i^T K^* x_j = -\lambda_i \Delta_{ij}, \quad i, j=1, 2, \dots, 2n \quad (31a,b)$$

To achieve a quasi-standard form, we consider the $2n \times 2n$ matrix

$$M_0^* = \begin{bmatrix} M & 0 \\ 0 & K \end{bmatrix} \quad (32)$$

and express it as

$$M_0^* = LDL^T \quad (33)$$

where L is a real lower triangular matrix and D is a real diagonal matrix with entries equal to either $+1$ or -1 . The determination of matrices L and D is accomplished by a procedure similar to the Cholesky decomposition (Ref. 1), where the matrix D has been inserted to accommodate minus signs.

Due to the partitioned nature of M_0^* , matrices L and D can also be written in partitioned form as follows:

$$L = \begin{bmatrix} L_1 & 0 \\ 0 & L_2 \end{bmatrix}, \quad D = \begin{bmatrix} D_1 & 0 \\ 0 & D_2 \end{bmatrix} \quad (34a,b)$$

where L_1 , L_2 , D_1 and D_2 are $n \times n$ matrices and where

$$M = L_1 D_1 L_1^T, \quad K = L_2 D_2 L_2^T \quad (34c,d)$$

Let us inspect Eq. (34c). Because the matrix M is positive definite, D_1 is in fact the identity matrix. However, because the positive

definiteness of matrix K cannot be assured, D_2 is not generally the identity matrix.

Next, let us rewrite Eq. (26) as

$$L^{-1}M^*L^{-T} \dot{\tilde{x}}(t) = -L^{-1}K^*L^{-T} \tilde{x}(t) + L^{-1}\tilde{x}(t) \quad (35)$$

Then, if we define

$$B = L^{-1}M^*L^{-T}, \quad A = -L^{-1}K^*L^{-T} \quad (36a,b)$$

$$\underline{u}(t) = L\tilde{x}(t), \quad \underline{U}(t) = L^{-1}\tilde{x}(t) \quad (37a,b)$$

Eq. (35) can be written compactly as

$$B\dot{\underline{u}}(t) = A\underline{u}(t) + \underline{U}(t) \quad (38)$$

The eigenvalue problems and biorthonormality relations corresponding to Eqs. (38) are

$$\lambda_i B \underline{u}_i = A \underline{u}_i, \quad \lambda_i B^T \underline{v}_i = A^T \underline{v}_i, \quad i=1,2,\dots,2n \quad (39a,b)$$

$$\underline{v}_i^T B \underline{u}_j = \Delta_{ij}, \quad \underline{v}_i^T A \underline{u}_j = \lambda_i \Delta_{ij}, \quad i,j=1,2,\dots,2n \quad (40a,b)$$

where

$$\underline{u}_i = L \underline{x}_i, \quad \underline{v}_i = L^T \underline{y}_i, \quad i=1,2,\dots,2n \quad (41a,b)$$

and where matrices A and B are as given by Eqs. (36). Relations analogous to Eqs. (24b) and (25) are

$$\underline{u}_i = \overline{\underline{u}_i}, \quad \underline{v}_i = \overline{\underline{v}_i}, \quad \text{when } \lambda_i = \text{complex} \quad (42a,b)$$

$$\underline{u}_i, \underline{v}_i = \text{real}, \quad \text{when } \lambda_i = \text{real} \quad (43a,b)$$

It is instructive to express matrices B and A in partitioned form. Furthermore, let us assume that the damping and circulatory effects are small, i.e., that the matrices C and H are small. Then substituting Eqs. (30) and (34) into Eqs. (36) and recalling Eqs. (5), we can write

$$B_0 = D = \begin{bmatrix} I & 0 \\ 0 & D_2 \end{bmatrix}, \quad B_1 = \begin{bmatrix} 0 & 0 \\ 0 & L_2^{-1} H L_2^{-T} \end{bmatrix} \quad (44a,b)$$

$$A_0 = \begin{bmatrix} -L_1^{-1} G L_1^{-T} & -L_1^{-1} L_2 D_2 \\ D_2 L_2^T L_1^{-T} & 0 \end{bmatrix} \quad (45a)$$

$$A_1 = \begin{bmatrix} -L_1^{-1} C L_1^{-T} & -L_1^{-1} H L_2^{-T} \\ L_2^{-1} H L_1^{-T} & 0 \end{bmatrix} \quad (45b)$$

which provides the motivation for considering a perturbation analysis. We note that the matrix B_0 is diagonal, B_1 and A_0 are skew symmetric and A_1 is symmetric. Furthermore, because the

product $L_1^{-1} L_2 D_2$ is lower triangular, the matrix A_0 is banded, with half-bandwidth n. Thus, if matrices C and H, and hence B_1 and A_1 are negligible, we obtain an eigenvalue problem characterized by a real diagonal matrix and a real skew symmetric matrix, the eigensolution of which can be generated with relative ease, as we shall see in the following section. Hence, the justification for using a perturbation analysis is evident.

4. UNPERTURBED GYROSCOPIC SYSTEMS

Consider the eigenvalue problem for an undamped gyroscopic system. Setting $C = H = 0$, we obtain $B = D$ and $A = A_0$, so that Eqs. (39) now appear as

$$\lambda_{0i} D \underline{u}_{0i} = A_0 \underline{u}_{0i}, \quad \lambda_{0i} D^T \underline{v}_{0i} = A_0^T \underline{v}_{0i}, \quad i=1,2,\dots,2n \quad (46a,b)$$

where the zero subscript has been inserted to indicate this special case. Equations (46) possess the same eigenvalues because the characteristic polynomials

$$F_{R0}(\lambda_0) \equiv |A_0 - \lambda_0 D| = 0, \quad (47a)$$

$$F_{L0}(\lambda_0) \equiv |A_0^T - \lambda_0 D| = 0 \quad (47b)$$

are the same. Now, because A_0 is skew symmetric, Eq. (47b) can be written as

$$F_{L0}(\lambda_0) = |A_0 + \lambda_0 D| = 0 \quad (48)$$

Comparing Eqs. (47a) and (48), we conclude that if λ_0 is an eigenvalue, then $-\lambda_0$ is also an eigenvalue. Hence, we have

$$\lambda_{0i} = -\lambda_{0i}, \quad i=1,2,\dots,2n \quad (49)$$

Let us rewrite Eq. (46b) in the form

$$\lambda_{0i} D^T \underline{v}_{0i} = A_0^T \underline{v}_{0i}, \quad i=1,2,\dots,2n \quad (50)$$

which can also be written as

$$\lambda_{0i} D^T \underline{v}_{0i} = A_0 \underline{v}_{0i}, \quad i=1,2,\dots,2n \quad (51)$$

Comparing Eqs. (46a) and (51), we conclude that

$$\underline{v}_{0i} = \underline{u}_{0i}, \quad i=1,2,\dots,2n \quad (52)$$

Because the system considered in this section is a special case of that in the previous section, the properties indicated in Eqs. (24a), (42) and (43) are certainly applicable here. Comparing Eqs. (24a) and (49), we conclude that if an unperturbed eigenvalue is complex, then it must be pure imaginary. Hence, we can state that any one of λ_{0i} ($i=1,2,\dots,2n$) is either real or imaginary. If an unperturbed eigenvalue is real, we can draw no additional conclusions regarding the corresponding eigenvectors beyond that reached from Eqs. (52). Alternatively, if an unperturbed eigenvalue is imaginary, Eqs. (42) and (52) indicate that

$$\underline{v}_{0i} = \overline{\underline{u}}_{0i}, \text{ when } \lambda_{0i} = \text{imaginary} \quad (53)$$

Equation (53) is a most convenient property. However, because it was derived from the statement of the eigenvalue problem, there is no guarantee that eigenvectors satisfying Eq. (53) can be normalized to +1. Indeed, let us inspect the product $\underline{v}_{0i}^T \underline{D} \underline{u}_{0i} = \overline{\underline{u}}_{0i}^T \underline{D} \underline{u}_{0i}$, where the corresponding eigenvalue λ_{0i} is imaginary. Because the diagonal matrix \underline{D} may contain -1 entries, the above product is merely real. Hence, to preserve Eq. (53), it may be necessary to allow -1 normalizations, as indicated by the modified Kronecker delta, Δ_{ij} , discussed earlier. Note that if the generalized stiffness matrix \underline{K} is positive definite, matrices \underline{D}_2 , and hence \underline{D} , are identity matrices, all of the unperturbed eigenvalues are imaginary and all of the eigenvectors enjoy a +1 normalization. We note that

$$\Delta_{i'i'} = \Delta_{ii} \quad , \quad i=1,2,\dots,2n \quad (54)$$

The solution of Eqs. (46) is generally complex, so that it is undesirable from a computational point of view. In the following, we reduce Eqs. (46) to a single eigenvalue problem involving a single real matrix and possessing a real eigensolution. We note that the procedure is a slight generalization of that presented by Meirovitch (Ref. 2), which was developed for a positive definite generalized stiffness matrix.

Recalling the skew symmetry of the matrix \underline{A}_0 , Eqs. (46) can be written as

$$\lambda_{0i} \underline{D} \underline{u}_{0i} = \underline{A}_0 \underline{u}_{0i} \quad , \quad -\lambda_{0i} \underline{D} \underline{v}_{0i} = \underline{A}_0 \underline{v}_{0i} \quad , \quad i=1,2,\dots,2n \quad (55a,b)$$

Premultiplication of Eqs. (55) by $-\underline{D} \underline{A}_0 \underline{D}$ yields

$$\begin{aligned} -\lambda_{0i} \underline{D} \underline{A}_0 \underline{D}^2 \underline{u}_{0i} &= -(\underline{D} \underline{A}_0)^2 \underline{u}_{0i}, \\ \lambda_{0i} \underline{D} \underline{A}_0 \underline{D}^2 \underline{v}_{0i} &= -(\underline{D} \underline{A}_0)^2 \underline{v}_{0i}, \end{aligned} \quad i=1,2,\dots,2n \quad (56a,b)$$

Because the matrix \underline{D} is equal to its inverse, we have $\underline{D}^2 = \underline{I}$. Then, using Eqs. (55), Eqs. (56) can be reduced to

$$\lambda_{0i}^2 \underline{u}_{0i} = \underline{C}_0 \underline{u}_{0i}, \quad \lambda_{0i}^2 \underline{v}_{0i} = \underline{C}_0 \underline{v}_{0i}, \quad i=1,2,\dots,2n \quad (57a,b)$$

where $\underline{C}_0 = (\underline{D} \underline{A}_0)^2$. Examining Eqs. (57), we observe that \underline{u}_{0i} and \underline{v}_{0i} ($i=1,2,\dots,2n$) satisfy the same eigenvalue problem, so that one need solve only one eigenvalue problem. The matrix \underline{C}_0 is real, and it has already been shown that λ_{0i}^2 ($i=1,2,\dots,2n$) is real, so that the eigenvectors are also real. The matrix \underline{C}_0 possesses no symmetries. Furthermore, each eigenvalue λ_{0i}^2 ($i=1,2,\dots,2n$) has multiplicity two, so that

the determination of orthogonal eigenvectors may cause difficulties.

Let us suppose that the n eigenvalues λ_{0i}^2 , each with multiplicity two, and the corresponding real orthogonal eigenvectors of the matrix \underline{C}_0 are available. Then, the question arises as to how these results should be interpreted. If an eigenvalue λ_{0i}^2 is positive, then $\lambda_{0i} = +\sqrt{\lambda_{0i}^2}$ and $\lambda_{0i}' = -\sqrt{\lambda_{0i}^2}$ and we can regard the corresponding eigenvectors as \underline{u}_{0i} and \underline{v}_{0i} . Equations (52) provide the eigenvectors \underline{u}_{0i} and \underline{v}_{0i} . Alternatively, if an eigenvalue λ_{0i}^2 is negative, then $\lambda_{0i} = +i\sqrt{-\lambda_{0i}^2}$ and $\lambda_{0i}' = -i\sqrt{-\lambda_{0i}^2}$ and, recalling Eq. (53), we can regard the corresponding pair of eigenvectors as the real and imaginary parts of \underline{u}_{0i} and \underline{v}_{0i} . Once again, Eq. (52) provides the eigenvectors \underline{u}_{0i} and \underline{v}_{0i} . We note that when the stiffness matrix \underline{K} is positive definite, matrix \underline{D} is the identity matrix and \underline{C}_0 is not only symmetric but also negative definite. Then the eigenvalues λ_{0i}^2 are all real and negative, leading to pure imaginary eigenvalues λ_{0i} ($i=1,2,\dots,2n$).

5. PERTURBED GYROSCOPIC SYSTEMS

In the present section, we first discuss some special properties arising from the various symmetries of the matrices \underline{B}_0 , \underline{B}_1 , \underline{A}_0 and \underline{A}_1 , as given by Eqs. (44) and (45). Then, we apply the perturbation theory to a whirling shaft with a lumped mass at its midspan.

Let us rewrite the expansions indicated by Eqs. (8) and (12) as

$$\begin{aligned} \underline{u}_i &= \underline{u}_{0i} + \underline{u}_{1i} + \underline{u}_{2i} + \dots, \\ \underline{v}_i &= \underline{v}_{0i} + \underline{v}_{1i} + \underline{v}_{2i} + \dots, \end{aligned} \quad i=1,2,\dots,2n \quad (58a,b)$$

Then, use of Eqs. (9) reveals that

$$\underline{u}_{1i} = \sum_{k=1}^{2n} \underline{u}_{0k} \epsilon_{1ki}, \quad \underline{u}_{2i} = \sum_{k=1}^{2n} \underline{u}_{0k} \epsilon_{2ki}, \quad i=1,2,\dots,2n \quad (59a,b)$$

$$\underline{v}_{1i} = \sum_{k=1}^{2n} \underline{v}_{0k} \gamma_{1ki}, \quad \underline{v}_{2i} = \sum_{k=1}^{2n} \underline{v}_{0k} \gamma_{2ki}, \quad i=1,2,\dots,2n \quad (59c,d)$$

From Eqs. (49) and (52) and the results of Sec. 2, it can be shown that

$$\lambda_{1i}' = \lambda_{1i}, \lambda_{2i}' = -\lambda_{2i}, \lambda_{3i}' = \lambda_{3i},$$

$$i=1,2,\dots,2n \quad (60a,b,c)$$

$$v_{1i}' = -u_{1i}, v_{2i}' = u_{2i}, i=1,2,\dots,2n \quad (60d,e)$$

Equations (60) can be used to reduce the computational effort. Additional effort-reducing properties can be derived from the fact that the λ_{0i} ($i=1,2,\dots,2n$) are either real or imaginary.

In particular, we can show that

$$\lambda_{1i}, \lambda_{2i}, \lambda_{3i} = \text{real}, \text{ when } \lambda_{0i} = \text{real} \quad (61a)$$

$$u_{1i}, u_{2i}, v_{1i}, v_{2i} = \text{real}, \text{ when } \lambda_{0i} = \text{real} \quad (61b)$$

and that

$$\lambda_{1i}, \lambda_{3i} = \text{real}, \lambda_{2i} = \text{imag},$$

$$\text{when } \lambda_{0i} = \text{imag} \quad (62a)$$

$$v_{1i} = -\bar{u}_{1i}, v_{2i} = \bar{u}_{2i}, \text{ when } \lambda_{0i} = \text{imag} \quad (62b)$$

Equations (61) indicate that the perturbed eigenvalues, summarized through $O(3)$, and the perturbed eigenvectors, summarized through $O(2)$, satisfy Eqs. (43). Equations (60) and (62) indicate the same satisfaction of Eqs. (24a) and (42).

The stability of a dynamical system is of prime importance, so that we focus attention on the real parts of the eigenvalues. The purpose of the present chapter is to investigate the effect of damping and/or circulatory forces on the undamped gyroscopic system. Because λ_{1i} ($i=1,2,\dots,2n$) is real, and because it is the largest eigenvalue perturbation, we wish to examine whether it tends to stabilize or destabilize the unperturbed system. It is advantageous to express λ_{1i} in terms of "original" variables as follows:

$$\lambda_{1i} = \Delta_{ii}(\lambda_{0i}^2 \hat{c}_{ii} + \lambda_{0i} \hat{h}_{ii}), \quad i=1,2,\dots,2n \quad (63a)$$

where

$$\hat{c}_{ii} = p_{0i}^T C q_{0i}, \quad \hat{h}_{ii} = p_{0i}^T H q_{0i}, \quad i=1,2,\dots,2n \quad (63b)$$

Let us suppose that λ_{0i} is imaginary. Then, $p_{0i} = \bar{q}_{0i}$ and it follows that $\lambda_{0i}^2 \hat{c}_{ii}$ is real because of the symmetry of the matrix C and nonpositive because of the positive semidefiniteness of the matrix C . Then, if $\Delta_{ii} = 1$, we observe that the dissipative effect of the matrix C causes the free response to attenuate. The quantity $\lambda_{0i} \hat{h}_{ii}$ is also real because of the skew symmetry of the matrix H . However, we can

make no statement regarding the sign of this quantity. Then, even if $\Delta_{ii} = 1$, the possibility exists that the inclusion of circulatory effects can lead to unstable solutions. This variety of instability is discussed by Huseyin (Ref. 5) and by Ziegler (Ref. 6) and is known as flutter.

Alternatively, let us assume that λ_{0i} is real. Then, p_{0i} and q_{0i} are real, but we cannot make any statements regarding the sign of \hat{c}_{ii} . In general, there are two ways that λ_{1i} can be negative, and two ways that it can be positive. They are as follows:

$$\text{Case i: } \Delta_{ii} = 1,$$

$$\lambda_{0i}^2 \hat{c}_{ii} + \lambda_{0i} \hat{h}_{ii} < 0 \Rightarrow \lambda_{1i} < 0 \quad (64a)$$

$$\text{Case ii: } \Delta_{ii} = 1,$$

$$\lambda_{0i}^2 \hat{c}_{ii} + \lambda_{0i} \hat{h}_{ii} > 0 \Rightarrow \lambda_{1i} > 0 \quad (64b)$$

$$\text{Case iii: } \Delta_{ii} = -1,$$

$$\lambda_{0i}^2 \hat{c}_{ii} + \lambda_{0i} \hat{h}_{ii} < 0 \Rightarrow \lambda_{1i} > 0 \quad (64c)$$

$$\text{Case iv: } \Delta_{ii} = -1,$$

$$\lambda_{0i}^2 \hat{c}_{ii} + \lambda_{0i} \hat{h}_{ii} > 0 \Rightarrow \lambda_{1i} < 0 \quad (64d)$$

Consider the small bending motions of a slender, rotating beam with a rigid disk at the midspan, as depicted in Fig. 1. Axes X and Y are inertial, and axes x and y are parallel to a set of axes embedded in the shaft and rotating with respect to X and Y at the constant angular rate $\dot{\theta} = \Omega$. Axes Z and z pass through the bearings. The disk has mass M and the shaft is uniform with mass per unit length m_0 and stiffnesses EI_x and EI_y about x and y , respectively. The ends are prevented from translating and they are mounted on springs that produce restoring bending moments proportional to the angular deflections, where the spring stiffnesses are K_1 at $Z = 0$ and K_2 at $Z = L$. Furthermore, we assume that there is uniformly distributed internal dissipation proportional to the local velocity, where the constant of proportionality is c . Similarly, we assume uniformly distributed external dissipation proportional to the absolute velocity, where the constant of proportionality is h . Note that the deflections $X(z,t)$, $Y(z,t)$ and $x(z,t)$, $y(z,t)$ are related according to

$$X(z,t) = x(z,t) \cos \theta - y(z,t) \sin \theta \quad (65a)$$

$$Y(z,t) = x(z,t) \sin \theta + y(z,t) \cos \theta \quad (65b)$$

where $\theta = \Omega t$.

The kinetic and potential energies and Rayleigh's dissipation function are

$$T(t) = \frac{1}{2} \int_0^L [m_0 + M\delta(z - L/2)] [\dot{x}^2(z, t) + \dot{y}^2(z, t)] dz \quad (66a)$$

$$V(t) = \frac{1}{2} \int_0^L \{EI_x [x''(z, t)]^2 + EI_y [y''(z, t)]^2\} dz + \frac{1}{2} K_1 \{[x'(0, t)]^2 + [y'(0, t)]^2\} + \frac{1}{2} K_2 \{[x'(L, t)]^2 + [y'(L, t)]^2\} \quad (66b)$$

$$F(t) = \frac{1}{2} \int_0^L \{c[\dot{x}^2(z, t) + \dot{y}^2(z, t)] + h[\dot{x}^2(z, t) + \dot{y}^2(z, t)]\} dz \quad (66c)$$

where the overdots and primes represent partial derivatives with respect to t and z , respectively. Application of Hamilton's principle (Ref. 10), yields the equations of motion and boundary conditions.

$$[m_0 + M\delta(z - L/2)] [\ddot{x}(z, t) - 2\Omega\dot{y}(z, t) - \Omega^2 x(z, t)] + (c+h)\dot{x}(z, t) + EI_x x^{iv}(z, t) - h\Omega y(z, t) = F_x(z, t) \quad (67a)$$

$$x(0, t) = 0, \quad EI_x x''(0, t) - K_1 x'(0, t) = 0 \quad (67b, c)$$

$$x(L, t) = 0, \quad EI_x x''(L, t) + K_2 x'(L, t) = 0 \quad (67d, e)$$

$$[m_0 + M\delta(z - L/2)] [\ddot{y}(z, t) + 2\Omega\dot{x}(z, t) - \Omega^2 y(z, t)] + (c+h)\dot{y}(z, t) + EI_y y^{iv}(z, t) + h\Omega x(z, t) = F_y(z, t) \quad (68a)$$

$$y(0, t) = 0, \quad EI_y y''(0, t) - K_1 y'(0, t) = 0 \quad (68b, c)$$

$$y(L, t) = 0, \quad EI_y y''(L, t) + K_2 y'(L, t) = 0 \quad (68d, e)$$

where F_x and F_y are the components of the nonconservative forces.

To discretize Eqs. (67a) and (68a) in space, we use Galerkin's method in conjunction with admissible functions, which requires that we integrate by parts and consider the natural boundary conditions. Admissible functions suitable for both the x and y components of motion are

$$\phi_j(z) = \sqrt{2} \sin \frac{j\pi}{L} z, \quad j=1, 2, \dots \quad (69)$$

Hence, let us take

$$x(z, t) = \sum_{m=1}^p \phi_j(z) q_j(t) \quad (70a)$$

$$y(z, t) = \sum_{j=p+1}^{2p} \phi_j(z) q_j(t) \quad (70b)$$

where $\phi_j(z) = \phi_{j+p}(z)$ ($j=1, 2, \dots, p$). Substituting Eqs. (69) and (70) into Eqs. (67a) and (68a), multiplying Eq. (67a) by $\phi_i(z)$ ($i=1, 2, \dots, p$) and Eq. (68a) by $\phi_i(z)$ ($i=p+1, p+2, \dots, 2p$) and integrating from $z = 0$ to $z = L$, we obtain a set of ordinary differential equations of motion, which can be written in the matrix form

$$\ddot{M}q(t) + (G + C)\dot{q}(t) + (K + H)q(t) = Q(t) \quad (71)$$

Equation (71) is identical to Eq. (22) if we take $2p = n$. The $n \times n$ coefficient matrices in Eq. (71) are partitioned into $p \times p$ submatrices

$$M = \begin{bmatrix} M_{11} & 0 \\ 0 & M_{22} \end{bmatrix} \quad (72a)$$

$$G = \begin{bmatrix} 0 & G_{12} \\ -G_{12} & 0 \end{bmatrix}, \quad C = \begin{bmatrix} C_{11} & 0 \\ 0 & C_{22} \end{bmatrix} \quad (72b, c)$$

$$K = \begin{bmatrix} K_{11} & 0 \\ 0 & K_{22} \end{bmatrix}, \quad H = \begin{bmatrix} 0 & H_{12} \\ -H_{12} & 0 \end{bmatrix} \quad (72d, e)$$

the elements of which are given as

$$[M_{11}]_{ij} = [M_{22}]_{ij} = m_0 L \delta_{ij} + 2M \sin \frac{i\pi}{2} \sin \frac{j\pi}{2}, \quad i, j=1, 2, \dots, p \quad (73a)$$

$$[G_{12}]_{ij} = -2\Omega [M_{11}]_{ij}, \quad i, j=1, 2, \dots, p \quad (73b)$$

$$[C_{11}]_{ij} = [C_{22}]_{ij} = (c + h) L \delta_{ij}, \quad i, j=1, 2, \dots, p \quad (73c)$$

$$[K_{11}]_{ij} = 2(K_1 + K_2 \cos i\pi \cos j\pi) \frac{i\pi}{L} \frac{j\pi}{L} + EI_x \left(\frac{i\pi}{L} \right)^2 \left(\frac{j\pi}{L} \right)^2 L \delta_{ij} - \Omega^2 [M_{11}]_{ij}, \quad i, j=1, 2, \dots, p \quad (73d)$$

$$[K_{22}]_{ij} = 2(K_1 + K_2 \cos i\pi \cos j\pi) \frac{i\pi}{L} \frac{j\pi}{L} + EI_y \left(\frac{i\pi}{L} \right)^2 \left(\frac{j\pi}{L} \right)^2 L \delta_{ij} - \Omega^2 [M_{11}]_{ij}, \quad i, j=1, 2, \dots, p \quad (73e)$$

$$[H_{12}]_{ij} = -h\Omega L \delta_{ij}, \quad i, j=1, 2, \dots, p \quad (73f)$$

The vector $Q(t)$ of nonconservative forces has the components

$$Q_j(t) = \begin{cases} \int_0^L \phi_j(z) F_x(z, t) dz, & j=1, 2, \dots, p \\ \int_0^L \phi_j(z) F_y(z, t) dz, & j=p+1, p+2, \dots, 2p \end{cases} \quad (74)$$

We consider three terms in each of Eqs. (70), $p = 3$, so that the submatrices M_{11} , M_{22} , G_{12} , C_{11} , C_{22} , K_{11} , K_{22} and H_{12} have dimensions 3×3 . Matrices M , G , C , K and H have dimensions 6×6 , so that the equations of motion and the eigenvalue problem have dimensions 12×12 when expressed in state form. Let us choose the numerical values

$$m_0 = 1 \text{ kg/m}, \quad M = 1 \text{ kg}, \quad L = 1 \text{ m} \quad (75a, b, c,)$$

$$EI_x = 4L^3/5\pi^2 \text{ Nm}^2, \quad EI_y = 9L^3/5\pi^2 \text{ Nm}^2 \quad (75d, e)$$

$$K_1 = K_2 = L^2/20 \text{ Nm}, \quad c = h = 1/4 \text{ Nsm}^{-1} \quad (75f, g)$$

$$\Omega = \sqrt{21.6} \pi \text{ rad s}^{-1} \quad (75h)$$

Following the developments of Secs. 3 and 4, we regard the matrices C and H as perturbations. In reducing the eigenvalue problem to quasistandard form, we find that

$$D_2 = \text{diag} [-1, -1, +1, -1, +1, +1] \quad (76)$$

indicating that K is sign-variable. Upon solving the unperturbed eigenvalue problem, we find that λ_{02} and λ_{08} are real and that the $O(0)$ eigenvectors indexed 1, 2, 7 and 8 satisfy -1 normalizations and the remaining eigenvectors satisfy +1 normalizations.

In the following tables, we list a few pertinent results from the perturbation analysis. In Table 1 we present the eigenvalues indexed 1 \rightarrow 6, 8, summarized through various orders, along with exact eigenvalues for comparison. The eigenvalues indexed 7, 9 \rightarrow 12 are the complex conjugates of those indexed 1, 3 \rightarrow 6, and hence are not included. We also note that λ_2 is real and positive, so that the system is unstable. We observe that λ_{12} and λ_{18} are negative. Then, because $\Delta_{22} = \Delta_{88} = -1$, these perturbations represent examples of Case iv, as in Eq. (64d). Alternatively, λ_{11} and λ_{17} are positive, and because $\Delta_{11} = \Delta_{77} = -1$, these perturbations are examples of Case iii, as in Eq. (64c). The remaining $O(1)$ eigenvalue perturbations are negative, and since the corresponding unperturbed eigenvectors satisfy +1 normalizations, they are examples of Case i, as in Eq. (64a). We conclude that the system is unstable due to one eigenvalue that is real and positive, and due to a pair of complex conjugate eigenvalues with positive real parts. In Table 2, we present the eigenvector u_2 summarized

through various orders, along with the exact eigenvector for comparison. We note that u_2 is real as discussed earlier. Another measure of eigenvector accuracy is available in the form of a biorthonormality check in which we inspect the products $Z^T(A_0 + A_1)W$ and $Z^T(B_0 + B_1)W$, where the columns of the matrices W and Z are the right and left eigenvectors summarized through various orders. In Table 3 we present the upper left 3×3 portion of the matrix $Z^T(B_0 + B_1)W$ as representative of the entire 12×12 matrix. Of the three generally complex numbers at each location in this table, the uppermost is the result of using unperturbed eigenvectors, while the second and third numbers were computed using the perturbed eigenvectors summarized through $O(1)$ and $O(2)$, respectively. It appears that the perturbation theory of Sec. 2 has produced reasonably accurate representations of the eigenvalues and eigenvectors.

6. DYNAMIC RESPONSE

Consider the set of linear ordinary differential equations of motion having the matrix form indicated by Eq. (38). The equation is

$$\dot{u}(t) = Au(t) + U(t) \quad (77)$$

where B and A are constant $2n \times 2n$ coefficient matrices, $u(t)$ is the $2n \times 1$ column vector of coordinates and $U(t)$ is the $2n \times 1$ column vector of excitations. To solve for the response $u(t)$, a modal analysis is often employed (Ref. 1). Such an analysis involves solving the eigenvalue problems

$$\lambda_i B u_i = A u_i, \quad \lambda_i B^T v_i = A^T v_i, \quad i=1, 2, \dots, 2n. \quad (78)$$

The eigenvectors are then used as the basis of a coordinate transformation whereby the biorthogonality property of the eigenvectors allows the equations of motion to be decoupled and then solved independently.

In practice, exact eigenvectors are rarely available. However, let us assume the availability of approximate eigenvectors $w_i \approx u_i$ and $z_i \approx v_i$ ($i=1, 2, \dots, 2n$), which can be arranged as the columns of the $2n \times 2n$ matrices W and Z , respectively. Then, we consider the linear transformation

$$u(t) = W\eta(t) \quad (79)$$

and substitute Eq. (79) into Eq. (77). Upon premultiplication by Z^T , we have

$$Z^T B W \dot{\eta}(t) = Z^T A W \eta(t) + Z^T U(t) \quad (80)$$

Because the vectors w_i and z_i are approximations

to the eigenvectors \underline{u}_i and \underline{v}_i ($i=1,2,\dots,2n$), respectively, it follows that the products $Z^T \underline{B} \underline{W}$ and $Z^T \underline{A} \underline{W}$ are nearly diagonal matrices. We approximate these matrix products as follows:

$$Z^T \underline{B} \underline{W} \approx \text{diag}(Z^T \underline{B} \underline{W}), \quad Z^T \underline{A} \underline{W} \approx \text{diag}(Z^T \underline{A} \underline{W}) \quad (81)$$

Then, Eq. (80) can be written in the approximately decoupled form

$$\dot{\underline{\eta}}(t) = \underline{R} \underline{\eta}(t) + \underline{N}(t) \quad (82)$$

where the elements of the diagonal matrix \underline{R} are given by

$$R_i = \frac{Z_i^T \underline{A} \underline{W}_i}{Z_i^T \underline{B} \underline{W}_i}, \quad i=1,2,\dots,2n \quad (83)$$

and where

$$\underline{N}(t) = [\text{diag}(Z^T \underline{B} \underline{W})]^{-1} Z^T \underline{U}(t) \quad (84)$$

The solution of Eq. (82) can be written in terms of a convolution integral as follows:

$$\underline{\eta}(t) = e^{\underline{R}t} \underline{\eta}(0) + \int_0^t e^{\underline{R}(t-\tau)} \underline{N}(\tau) d\tau \quad (85)$$

where the diagonal matrix $e^{\underline{R}t}$ has the form

$$e^{\underline{R}t} = \text{diag}[e^{R_1 t} \quad e^{R_2 t} \quad \dots \quad e^{R_{2n} t}] \quad (86)$$

and the diagonal matrix $e^{\underline{R}(t-\tau)}$ is constructed similarly. We note that the quantities $\underline{u}(t)$ and $\underline{U}(t)$ are related to $\underline{\eta}(t)$ and $\underline{N}(t)$, respectively, according to

$$\underline{u}(t) = \underline{W} \underline{\eta}(t) \Leftrightarrow \underline{\eta}(t) = [\text{diag}(Z^T \underline{B} \underline{W})]^{-1} Z^T \underline{B} \underline{u}(t) \quad (87a,b)$$

$$\underline{U}(t) = \underline{B} \underline{W} \underline{N}(t) \Leftrightarrow \underline{N}(t) = [\text{diag}(Z^T \underline{B} \underline{W})]^{-1} Z^T \underline{U}(t) \quad (87c,d)$$

We observe how the modal analysis, based upon approximations to the exact eigenvectors, allows a Rayleigh's quotient interpretation of the eigenvalues, as in Eqs. (83). The preceding developments are applicable to any modal analysis, irrespective of how the eigensolution has been determined.

Let us assume that the approximate eigenvectors \underline{w}_i and \underline{z}_i ($i=1,2,\dots,2n$) are the result of a perturbation analysis, and hence include the effects of the perturbation matrices \underline{A}_1 and \underline{B}_1 . In spite of the fact that response computations are relatively simple to perform, one may wish to express the perturbed response in terms of the unperturbed response and the perturbations \underline{A}_1 and \underline{B}_1 . Taking special forms for the excitation, Chen and Wada (Ref. 11) have done just that. However, to maintain the generality of Eq. (85), it appears that one cannot represent the perturbed response conveniently in

terms of the unperturbed response and matrices \underline{A}_1 and \underline{B}_1 .

Let us return to the example of Sec. 5 and compute the response of the system depicted in Fig. 1 to the forces

$$\begin{aligned} F_x(z,t) &= F_0 \delta(Z - L/2) \delta(t), \\ F_y &= 0, \quad F_0 = 1 \text{ Nm}^{-1} \text{ s}^{-1} \end{aligned} \quad (88)$$

The initial conditions are assumed to be zero. In place of the approximate eigenvectors \underline{w}_i and \underline{z}_i ($i=1,2,\dots,2n$), we use the eigenvectors from the example of Sec. 5, summarized through various orders, and compute the response according to Eqs. (82) - (87). The deflection of the center of the beam in inertial coordinates is plotted in Fig. 2 in the form of $Y(L/2,t)$ versus $X(L/2,t)$, with t as a parameter for $0 < t < 7\text{s}$. The curve labelled $O(0)$ was generated using the unperturbed eigenvectors. Similarly, the curve labeled $O(0) + O(1)$ was generated using eigenvectors summarized through $O(1)$. We note that within the accuracy of this plot, the curve generated using eigenvectors summarized through $O(2)$ is identical to the exact response. The instability should be evident.

7. CONCLUSION

The perturbation theory of Ref. 4 has been generalized to include -1 eigenvector normalizations and has been extended to gyroscopic systems with both internal and external damping. Moreover, the accuracy of the eigenvalue estimates used in the modal analysis has been enhanced by the use of Rayleigh's quotient. The theory is illustrated via a numerical example in which the response of a gyroscopic system with both internal and external damping is derived. The results are excellent.

8. REFERENCES

1. Meirovitch, L., Computational Methods in Structural Dynamics, Sijthoff-Noordhoff International Publishers, The Netherlands, 1980.
2. Meirovitch, L., "A New Method of Solution of the Eigenvalue Problem for Gyroscopic Systems", AIAA Journal, Vol. 12, No. 10, Oct. 1974, pp. 1337-1342.
3. Meirovitch, L., "A Modal Analysis for the Response of Linear Gyroscopic Systems", Journal of Applied Mechanics, Vol. 42, No. 2, June 1975, pp. 446-450.
4. Meirovitch, L. and Ryland, G., "Response of Slightly Damped Gyroscopic Systems", Journal of Sound and Vibration, Vol. 67, Nov. - Dec. 1979, pp. 1-19.
5. Huseyin, K., Vibrations and Stability of Multiple Parameter Systems, Sijthoff-Noordhoff International Publishers, The Netherlands, 1978.

6. Ziegler, H., Principles of Structural Stability, Blaisdell Publishing Co., Waltham, Mass., 1968.
7. Franklin, J. N., Matrix Theory, Prentice-Hall, Englewood Cliffs, N.J., 1968, Sec. 6.12.
8. Wilkinson, J. H., The Algebraic Eigenvalue Problem, Clarendon Press, Oxford, 1965, Secs. 2.5 - 2.7.
9. Lancaster, P., Lambda Matrices and Vibrating Systems, Pergamon press, Oxford, 1966.
10. Meirovitch, I., Analytical Methods in Vibrations, the Macmillan Co., New York, 1967.
11. Chen, J. C. and Wada, B. K., "Matrix Perturbation for Structural Dynamic Analysis", AIAA Journal, Vol. 15, No. 8, Aug. 1977, pp. 1095-1100.

TABLE 1 - Eigenvalue Summary, $c = h = 1/4$, $\Omega = \sqrt{21.6} \pi$

	0(0)	0(0) + 0(1)	0(0) + ... + 0(2)	0(0) + ... + 0(3)	Exact
λ_1	i12.394,400	0.189,662 +i12.394,400	0.189,662 +i12.379,192	0.187,768 +i12.379,192	0.187,815 +i12.379,469
λ_2	2.692,432	2.565,343	2.565,395	2.565,409	2.565,408
λ_3	i8.799,942	-0.158,855 +i8.799,942	-0.158,855 +i8.798,580	-0.158,846 +i8.798,580	-0.158,846 +i8.798,580
λ_4	i16.805,929	-0.352,790 +i16.805,929	-0.352,790 +i16.821,616	-0.350,904 +i16.821,616	-0.350,951 +i16.821,338
λ_5	i29.325,467	-0.372,910 +i29.325,467	-0.372,910 +i29,323,856	-0.372,924 +i29.323,856	-0.372,924 +i29.323,856
λ_6	i40.434,096	-0.278,016 +i40.434,096	-0.278,016 +i40.432,571	-0.278,018 +i40.432,571	-0.278,018 +i40.432,571
λ_8	-2.692,432	-2.819,522	-2.819,575	-2.819,561	-2.819,561

TABLE 2 - Eigenvector Summary u_2 , $c = h = 1/4$, $\Omega = \sqrt{21.6} \pi$

0(0)	0(0) + 0(1)	0(0) + ... + 0(2)	Exact
0.0	0.0	0.0	0.0
0.222,939	0.218,363	0.218,226	0.218,227
0.0	0.0	0.0	0.0
0.0	0.0	0.0	0.0
-0.203,329	-0.197,437	-0.197,476	-0.197,474
0.0	0.0	0.0	0.0
0.0	0.0	0.0	0.0
0.735,760	0.755,388	0.755,848	0.755,869
0.0	0.0	0.0	0.0
0.0	0.0	0.0	0.0
-0.671,043	-0.683,271	-0.683,963	-0.683,986
0.0	0.0	0.0	0.0

TABLE 3 - Summary $Z_1^T (B_0 + B_1)W$

Upper leftmost 3×3 portion, $c = h = 1/4$, $\Omega = \sqrt{21.6} \pi$

-1.0	- i0.021,920	0.0	+ i0.0	0.0	+ i0.003,096
-1.004,805	+ i0.000,064	0.0	+ i0.0	0.000,297	+ i0.0
-1.000,059	+ i0.001,044	0.0	+ i0.0	0.000,002	- i0.000,036
0.0	+ i0.0	-0.954,350	+ i0.0	0.0	+ i0.0
0.0	+ i0.0	-0.998,449	+ i0.0	0.0	+ i0.0
0.0	+ i0.0	-0.999,938	+ i0.0	0.0	+ i0.0
0.0	+ i0.003,096	0.0	+ i0.0	1.0	+ i0.006,705
0.000,297	+ i0.0	0.0	+ i0.0	1.000,030	+ i0.0
0.000,002	- i0.000,036	0.0	+ i0.0	1.0	+ i0.000,003

Fig. 1 - The Rotating Beam

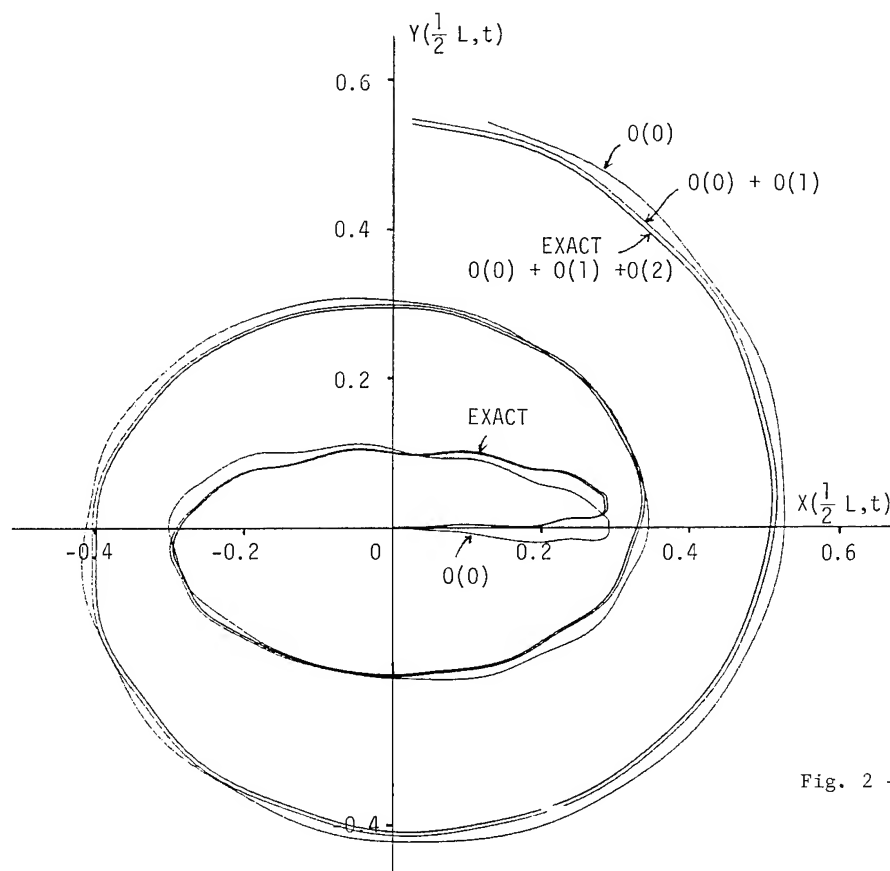
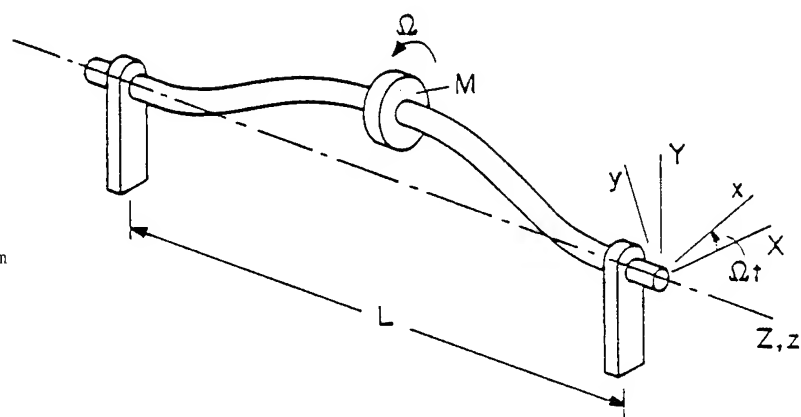


Fig. 2 - Dynamic Response

$c = h = 1/4$, $\Omega = \sqrt{21.6} \pi$

A GENERALIZED MULTIPLE-INPUT, MULTIPLE-OUTPUT
MODAL PARAMETER ESTIMATION ALGORITHM

Roy R. Craig, Jr.*
The University of Texas at Austin
Austin, TX 78712

Mark A. Blair**
Lockheed Missiles and Space Corp.
Sunnyvale, CA 94086

Abstract

A new method for experimental determination of the modal parameters of a structure is presented. The method allows for multiple input forces to be applied simultaneously, and for an arbitrary number of acceleration response measurements to be employed. These data are used to form the equations of motion for a damped linear elastic structure. The modal parameters are then obtained through an eigenvalue technique. In conjunction with the development of the equations, an extensive computer simulation study was performed. The results of the study show a marked improvement in the mode shape identification for closely-spaced modes as the number of applied forces is increased. Also demonstrated is the influence of noise on the method's ability to identify accurate modal parameters. Here again, an increase in the number of exciters leads to a significant improvement in the identified parameters.

Nomenclature

- [A/] = diagonal modal admittance matrix,
(n x n)
- $$[A/] = \frac{-w^2}{(w_r^2 - w^2) + i(2\xi_r w w_r)} \quad , r = 1, n$$
- [C_i] = damping matrix defined by Eq. 7
- [D] = force distribution matrix defined by Eq. 2
- {F(w)} = Fourier-transformed input force vector,
(n x 1)
- [H(w)] = complex frequency response function matrix, (n x n)
- $$[H(w)] = [\phi] [A/] [\phi]^T$$
- [K_i] = stiffness matrix defined by Eq. 7
- [M_i] = mass matrix defined by Eq. 7

- m = number of modes active in a given frequency range
- n = number of acceleration measurement stations
- { $\ddot{X}_i(w)$ } = acceleration at "independent" stations, (m x 1)
- { $\ddot{X}_d(w)$ } = acceleration at "dependent" stations, ((n-m) x 1)
- [T], [Y], [Z] = matrices defined by Eqs. 11 and 12
- w = circular frequency
- w_r = circular natural frequency of mode r
- [ϕ] = modal matrix, (n x n)
- ξ_r = damping ratio of mode r
- λ = eigenvalue defined by Eq. 17

Introduction

The need for modal testing (sometimes referred to as modal analysis) of structures is well-known and documented. The problem is that there is no foolproof and highly efficient method to extract modal coefficients from structural test data. Over the past forty years several different types of analysis have been developed and practiced with varying degrees of success. These analyses range from the time-honored Multi-Shaker Sine Dwell Test (1) and its recent variations (2), to the newer time-domain analyses: the Least-Squares Curve-Fitting Time-Domain Method (3) and the Ibrahim Time Domain Method (4-5). For several years, since the advent of digital computers and the development of the Fast Fourier Transform (FFT), considerable time has gone into developing frequency-domain analyses. Several methods have been developed which produce frequency response functions (FRFs) of a structure, using either single-point excitation (6) or multi-point excitation (7). There are also many algorithms which estimate the modal parameters from the FRFs (8-14).

* Professor, Aerospace Engineering and Engineering Mechanics
Associate Fellow, AIAA

** Senior Associate Engineer
Formerly Graduate Student, Aerospace Engineering
The University of Texas at Austin

With respect to the frequency-domain techniques, in particular, there are many problems associated with obtaining accurate estimates of the modal parameters. There are the problems of energy dissipation within the structure and the possibility of locating a shaker near a node line. Some of the curve-fitting techniques also involve excessive numerical manipulations, including transferring the FRFs back into the time domain.

Development of a New Multi-Shaker Algorithm

A technique to avoid problems associated with single-point testing is to apply forces at multiple locations. The method to be developed in this paper is an extension of the Simultaneous Frequency Domain (SFD) method described by Coppolino (13). Since the standard modal analysis methods are applicable to single-shaker testing only, this alternative approach involves a reformulation of the equations of motion to accommodate the use of multiple forces.

Development of Basic Algorithm

The Multi-Shaker Modal Analysis (MSMA) method presented here assumes that a linear structure can be accurately described over a limited frequency range by a finite number of degrees of freedom (DOF). This assumption yields the standard frequency-domain matrix equation relating the output accelerations at given points on the structure to the input forces

$$\{\ddot{X}(w)\} = [H(w)] \{F(w)\} \quad (1)$$

The force vector is rewritten in a form that includes only the DOF where forces are applied. A distribution matrix relates this new force vector, $\{f(w)\}$, to the original force vector, $\{F(w)\}$.

$$\{F(w)\} = [D] \{f(w)\} \quad (2)$$

For example, if a 4DOF system has exciters at points 1 and 3, the equation would be

$$\{F(w)\} = \begin{Bmatrix} f_1 \\ 0 \\ f_3 \\ 0 \end{Bmatrix} = \begin{bmatrix} 1 & 0 \\ 0 & 0 \\ 0 & 1 \\ 0 & 0 \end{bmatrix} \begin{Bmatrix} f_1 \\ f_3 \end{Bmatrix}$$

So, Eq. (1) is now

$$\{X(w)\} = [\phi] [A(w)] [\phi]^T [D] \{f(w)\} \quad (3)$$

It is assumed that there are n points where the responses are measured, and if it is assumed that the structure can be accurately described over the frequency range of interest by m DOF ($m < n$), then Eq. (3) can be partitioned into sets of 'independent' DOF and 'dependent' DOF equations. Thus,

$$\begin{Bmatrix} \ddot{X}_i(w) \\ \ddot{X}_d(w) \end{Bmatrix} = \quad (4)$$

$$\begin{bmatrix} [\phi_i] \\ [\phi_d] \end{bmatrix} [A(w)] \begin{bmatrix} [\phi_i]^T \\ [\phi_d]^T \end{bmatrix} \begin{bmatrix} [D_i] \\ [D_d] \end{bmatrix} \{f(w)\}$$

or

$$\begin{Bmatrix} \ddot{X}_i(w) \\ \ddot{X}_d(w) \end{Bmatrix} = \quad (5)$$

$$\begin{bmatrix} [I] \\ [\phi_d] [\phi_i]^{-1} \end{bmatrix} \begin{bmatrix} [\phi_i] & [A(w)] & [\phi_i]^T & [D_{id}] \end{bmatrix} \{f(w)\}$$

where

$$[D_{id}] = [D_i] + [\phi_i]^{-T} [\phi_d]^T [D_d]$$

From Eq. (5) a relationship between the independent and dependent DOF accelerations is

$$\{\ddot{X}_d(w)\} = [\phi_d] [\phi_i]^{-1} \{\ddot{X}_i(w)\} \quad (6a)$$

This equation will be employed later to determine the modal components of the dependent DOFs for the identified natural frequencies. The equation relating the independent accelerations to the forces is

$$\{\ddot{X}_i\} = [\phi_i] [A(w)] [\phi_i]^T [D_{id}] \{f(w)\} \quad (6b)$$

Pre-multiplying both sides of Eq. (6b) by $([\phi_i] [A(w)] [\phi_i]^T)^{-1}$ and expanding yields

$$\begin{aligned} ([\phi_i] [A(w)] [\phi_i]^T)^{-1} \{\ddot{X}_i\} &= [D_{id}] \{f(w)\} \\ [\phi_i]^{-T} [/(1/A(w))] [\phi_i]^{-1} \{\ddot{X}_i\} &= [D_{id}] \{f(w)\} \\ [\phi_i]^{-T} [/(1 - i2\xi_r (w_r/w) - (w_r/w)^2)] [\phi_i]^{-1} \{\ddot{X}_i\} \\ &= [D_{id}] \{f(w)\} \\ [\phi_i]^{-T} [\phi_i]^{-1} \{\ddot{X}_i\} \\ &+ [\phi_i]^{-T} [2\xi_r w_r/] [\phi_i]^{-1} (-i/w) \{\ddot{X}_i\} \\ &+ [\phi_i]^{-T} [w_r^2/] [\phi_i]^{-1} (-1/w^2) \{\ddot{X}_i\} \\ &= [D_{id}] \{f(w)\} \end{aligned}$$

or, in summary,

$$[M_i] \{\ddot{X}_i\} + [C_i] \{\dot{X}_i\} + [K_i] \{X_i\} = [D_{id}] \{f(w)\} \quad (7)$$

where

$$\begin{aligned} [M_i] &= [\phi_i]^{-T} [\phi_i]^{-1} \\ [C_i] &= [\phi_i]^{-T} [2\xi_r w_r/] [\phi_i]^{-1} \\ [K_i] &= [\phi_i]^{-T} [w_r^2/] [\phi_i]^{-1} \\ \{\dot{X}_i\} &= (-i/w) \{\ddot{X}_i\} \\ \{X_i\} &= (-1/w^2) \{\ddot{X}_i\} \end{aligned}$$

Least-squares averaging may be employed to estimate the matrices $[M_i]$, $[C_i]$, and $[K_i]$. Therefore, the accelerations, velocities, dis-

placements and forces in Eq. (7) are expanded into matrices, where each column corresponds to a discrete frequency point. That is,

$$[\ddot{X}_i] = [\ddot{X}_i(w_1) | \ddot{X}_i(w_2) | \dots | \ddot{X}_i(w_k)] \quad (8)$$

where, $k > m$. Multiplication of Eq. (7) by $[M_i]^{-1}$ yields

$$-[\ddot{X}_i] = \begin{bmatrix} [\tilde{C}_i] & [\tilde{K}_i] & [\tilde{D}_{id}] \end{bmatrix} \begin{bmatrix} [\dot{X}_i] \\ [X_i] \\ [f(w)] \end{bmatrix} \quad (9)$$

where,

$$[\tilde{C}_i] = [M_i]^{-1} [C_i] \quad (10a)$$

$$[\tilde{K}_i] = [M_i]^{-1} [K_i] \quad (10b)$$

$$[\tilde{D}_{id}] = -[M_i]^{-1} [D_{id}] \quad (10c)$$

Since $[\tilde{C}_i]$, $[\tilde{K}_i]$, and $[\tilde{D}_{id}]$ are real matrices, Eq. (9) can be rewritten for the real and imaginary parts of the responses and inputs.

$$-\begin{bmatrix} [\ddot{X}_{iRe}] & [\ddot{X}_{iIm}] \end{bmatrix} = \begin{bmatrix} [\tilde{C}_i] & [\tilde{K}_i] & [\tilde{D}_{id}] \end{bmatrix} \begin{bmatrix} [\dot{X}_{iRe}] & [\dot{X}_{iIm}] \\ [X_{iRe}] & [X_{iIm}] \\ [f_{Re}] & [f_{Im}] \end{bmatrix} \quad (11)$$

Since this equation is over-determined ($k > m$), a least-squares solution is used. Equation (11) may be rewritten symbolically

$$[Y] = [T] [Z] \quad (12)$$

The least-squares solution for $[T]$ is

$$[T] = [Y] [Z]^T [Z] [Z]^T^{-1} \quad (13)$$

The $[\tilde{C}_i]$ and $[\tilde{K}_i]$ that were solved for in Eq. (13) can now be used to determine the eigenvalues and eigenvectors for the system in the following manner. From Eq. (9) the free vibration equation

$$\ddot{X}_i + [\tilde{C}_i] \dot{X}_i + [\tilde{K}_i] X_i = 0 \quad (14)$$

may be written. Since the matrices $[\tilde{C}_i]$ and $[\tilde{K}_i]$ are constant, X_i and its derivatives in Eq. (14) may be written in the time domain, rather than in the frequency domain as originally expressed in Eq. (7). Thus, let

$$X_i = x e^{\lambda t} \quad (15a)$$

$$\dot{X}_i = \lambda X_i \quad (15b)$$

$$\ddot{X}_i = \lambda^2 X_i \quad (15c)$$

From Eq. (15b)

$$\lambda X_i - \dot{X}_i = 0 \quad (16d)$$

Thus, combining Eqs. (14) and (15) yields

$$\lambda \begin{bmatrix} \dot{X}_i \\ X_i \end{bmatrix} + \begin{bmatrix} [\tilde{C}_i] & [\tilde{K}_i] \\ [-I] & [0] \end{bmatrix} \begin{bmatrix} \dot{X}_i \\ X_i \end{bmatrix} = \begin{bmatrix} 0 \\ 0 \end{bmatrix} \quad (17)$$

which is a standard linear eigenvalue problem. The eigenvectors will produce mode shape components for the 'independent' DOFs only. To include the 'dependent' DOFs, Eq. (6a) is expanded to matrix form for the k frequency points and then manipulated, via the least-squares technique, to produce a relationship between the 'dependent' and 'independent' modal coefficients.

$$\begin{aligned} [\ddot{X}_d] &= [\phi_d] [\phi_i]^{-1} [\ddot{X}_i] \\ [\phi_d] &= [\ddot{X}_d] [\ddot{X}_i]^T [X_i] [X_i]^T^{-1} [\phi_i] \end{aligned} \quad (18)$$

Forcing Functions

As indicated by Eqs. (4) and (5), the forces may be applied at the dependent DOFs as well as the independent DOFs. This feature of the equations allows for forces to be applied where either accelerations could not be measured or where an accelerometer produced bad readings and was subsequently discarded. It also allows the user more freedom in determining which locations are to be identified as independent DOFs. If, after data acquisition is completed and a general analysis done, it is determined that a particular DOF is not important, its responses can be reduced out of further calculations, even though it was forced.

In addition to the freedom of location of forces, there is also a freedom in the type of forces which can be applied, subject to one constraint. From Eq. (13) it is seen that, if two forces are fully coherent, the inverse of the matrix will be singular. However, the restriction is not too severe. If two forcing functions are identical, only one forcing function needs to be included in the force array. The force distribution matrix will handle the duplication in the applied force spectra. Since, in reality, a structure will have a different input impedance at each location, similar signals into the shakers will produce different forces. The best way to avoid any potential problems, however, is to have a low coherence between forces. This can be achieved by using either of two forcing methods, independent random signals at each shaker or simultaneous sine sweeps with each shaker having a different phase shift.

Another type of excitation is a free-decay response. A minor reformulation of the equations is involved, with Eq. (11) being modified to the form

$$- \begin{bmatrix} \ddot{X}_{iRe} \\ \ddot{X}_{iIm} \end{bmatrix} = \begin{bmatrix} \ddot{X}_{iRe} & \ddot{X}_{iIm} \\ X_{iRe} & X_{iIm} \end{bmatrix} \begin{bmatrix} \tilde{C}_i \\ \tilde{K}_i \end{bmatrix} \quad (18)$$

This formulation eliminates the need for measurement of the forces, thus allowing free-decay responses to be employed. This can also be used in conjunction with the Randomdec method, where a free-decay response is generated from a structure that is being randomly excited.

Averaging

There are two possible methods to eliminate noise contamination in the eigenvalue results. Both methods involve a type of signal averaging. The first method involves averaging FRFs from several runs to form a single acceleration and force FRF spectrum at each location before insertion into Eq. (13).

There is one serious drawback to this method. With random excitations, excessive averaging can produce an FRF spectrum with a uniform value, effectively giving fewer independent columns in Eq. (13) with which to do a least-squares fit. For a swept-sine test, this averaging technique should suffice, since the FRF will not tend to become uniform, especially if the signal generator has a phase modulator.

The second method is to string the multiple runs together in the same manner as the individual frequencies were in Eq. (8). That is

$$\{\ddot{X}(w)\} = \{\ddot{X}_1(w)\} \mid \{\ddot{X}_2(w)\} \mid \dots \mid \{\ddot{X}_p(w)\}$$

This increases the number of columns, therefore the accuracy of the least-squares fit, but the required storage space for the matrices is also increased.

Pseudo-Degrees-of-Freedom

If the structure being tested has more modes in the frequency range of interest than there are measurement locations, there is a technique to increase the number of DOFs based on existing measurement DOFs. This method involves sampling extra sets of data and placing each new set into the equations as if they were new DOFs. With this approach is an alternate method in which the responses of the originally measured data are partitioned into subsets and correspondingly labeled as different sets of data. In this way the number of DOFs is increased without the need for more measurements. This, however, gives fewer columns of data for the least-squares process, since this procedure takes some of the columns in Eq. (8) and makes new rows out of them.

Mode Selection

Proper selection of the true modes of vibration from the eigensolution of Eq. (16) is just as important as any other part of the modal analysis. When the number of modes is overspecified, either through oversight or to compensate for noise contamination, a systematic method is needed to identify the spurious modes. Usually the spurious modes can be eliminated immediately by a quick examination of the eigenvalues. The damping values are often excessively high, low, or even negative. The natural frequencies might have values that are out of the measured frequency range. At other times, however, the spurious mode eigenvalues are within the range of tolerance. Then, an inspection of the eigenvectors is needed. One procedure involves the use of pseudo-DOFs. A comparison of the portion of the eigenvector representing the pseudo-DOFs with the portion of the eigenvector which corresponds to the independent DOFs from which the pseudo DOFs were produced can readily determine the validity of the mode. A favorable relationship would be one where there is a high correlation of eigenvector values at corresponding DOFs. Another method would be to analyze results of analyses from several data sets; modes that repeatedly show up would indicate valid modes.

Simulation Studies

To verify the validity and accuracy of the MSMA technique previously described, several computer simulations were conducted. The primary concerns evaluated in the tests were: (1) resolution of the modes in high noise, (2) identification of modes less than ξ_w apart, (3) accuracy of dependent DOFs, and (4) application of forces at dependent DOFs.

A computer program was designed such that the system natural frequencies, damping, and mode shapes, and a noise-to-signal ratio are input. The noise level is calibrated by using the root-mean-square of the response signal over the entire frequency range. Also input are the frequency range, number of independent DOFs and their corresponding locations, number of dependent DOFs and their locations, number of forced DOFs and their locations, and the method of excitation. The program creates the frequency responses for the accelerations and forces and then proceeds to manipulate them in accordance with the equations presented earlier.

The first series of tests was on System A having nine natural frequencies, seven of which were below 10 Hz. As noted in Table 1, two of the frequencies were selected less than ξ_w apart, so that the effects of closely-coupled modes could be observed. The noise-to-signal ratio was selected at 20% in conjunction with an applied random force signal. Changed during the test series was the number of forced DOFs: 1, 4, and 8 forces were used. As indicated in Table 2a, the mode shapes had magnitudes at each station of 1.0, except for one DOF in each mode whose magnitude was set at 0.01 to simulate a point close to a node line.

Mode	System A		System B	
	Freq. (Hz)	Damping	Freq. (Hz)	Damping
1	5.00	0.01	5.00	0.01
2	5.25	0.01	5.25	0.01
3	5.50	0.01	5.50	0.01
4	5.55	0.01	5.55	0.01
5	5.90	0.01	15.00	0.01
6	6.20	0.01	25.00	0.01
7	6.60	0.01		
8	15.00	0.01		
9	25.00	0.01		

Table 1. Natural Frequencies and Damping Factors for Simulated Parameter Identification Tests

DOF 1	2	3	4	5	6	7	8
MODE							
1	.01	1.00	1.00	1.00	1.00	1.00	1.00
2	1.00	.01	1.00	1.00	-1.00	-1.00	-1.00
3	1.00	1.00	-.01	-1.00	-1.00	-1.00	1.00
4	1.00	1.00	-1.00	-.01	1.00	1.00	-1.00
5	1.00	-1.00	-1.00	1.00	.01	-1.00	-1.00
6	1.00	-1.00	-1.00	1.00	-1.00	.01	1.00
7	1.00	-1.00	1.00	-1.00	-1.00	1.00	-.01
8	1.00	-1.00	1.00	-1.00	1.00	-1.00	1.00
9	1.00	1.00	1.00	1.00	1.00	1.00	1.00
No. of Forces		Force Locations					
1		1					
4		1-4					
8		1-8					

Table 2a. System A Mode Shapes (defined at 8 DOFs only); Forces and Locations

DOF 1	2	3	4	5	6	7	8
MODE							
1	.01	1.00	1.00	1.00	1.00	1.00	1.00
2	1.00	.01	1.00	1.00	-1.00	-1.00	-1.00
3	1.00	1.00	-.01	-1.00	-1.00	-1.00	1.00
4	1.00	1.00	-1.00	-.01	1.00	1.00	-1.00
5	1.00	-1.00	-1.00	1.00	.01	-1.00	-1.00
6	1.00	-1.00	-1.00	1.00	-1.00	.01	1.00
No. of Forces		Force Locations					
1		1					
5		1-5					
8		1-8					

Table 2b. System B Mode Shapes (defined at 8 DOFs only); Forces and Locations

A sampling run was first made using a single shaker to obtain an estimate of the number of modes in the 0-10 Hz range. A check of the FRFs showed that six modes were fairly apparent, so an estimate of eight modes (six for the observed ones and two more for any missed modes or any pseudo or spurious modes created by the noise) did not seem unreasonable.

Three runs were made for each of the forced-DOF conditions plus one additional run utilizing the averaging technique of placing several runs into one large array. The averaged analysis used three individual runs which differed from the previous three runs.

To check the accuracy of the results, an error analysis was used that looked at the percentage of error in the natural frequency, damping, and real part of the modal vector compared to the input system characteristics. To highlight the results, the errors for three modes were investigated. The first was the 5.9 Hz mode, which was relatively uncoupled. The other two modes were the coupled modes, 5.5 Hz and 5.55 Hz. Referring to the diagrams in Fig. 1, it can be seen that with 20% noise the natural frequency estimates are highly accurate, even for the closely-coupled modes. Also evident in the diagrams is the overall higher accuracy of the parameters corresponding to the 5.9 Hz mode compared to the 5.5 and 5.55 Hz modes. Although the errors for the damping and modal vectors are large for the 20% noise single-shaker case, the diagrams show a trend towards lower error levels as the number of shakers is increased. In fact, when eight shakers were employed, the error levels for the closely-coupled modes are seen to be comparable to the error level for the 5.9 Hz mode.

System A was also employed in a series of tests on the effect of noise level. The noise-to-signal ratio was changed from 0% to 10% and finally to 20%. To illustrate the effect of noise on the results and the effect of additional shakers, the identified modal parameters for the 5.0, 5.5, and 5.55 Hz modes are tabulated for the single-shaker and 8-shaker simulations (see Tables 3 and 4). An analysis of the tables shows, once again, a clear trend toward higher levels of accuracy at a given noise level for an increase in the number of shakers. A dramatic result from this set of runs was the absence of the 5.0 Hz mode from the single-shaker analysis when noise was present. As the number of shakers increased though, the 5.0 Hz mode appeared and then increased in accuracy. Overall, by a comparison of the tables, it is seen that the algorithm does not become unstable with increasing noise levels. On the contrary, good results are obtained even at relatively high noise levels when several shakers are used.

Undamped
Nat. Freq.= 5.0063 5.5000 5.5498

Damping
Factor = 0.0143 0.0100 0.0100

DOF	Modal Coeff.	Modal Coeff.	Modal Coeff.
Re(1)	0.00308	0.99605	-0.99496
Re(2)	0.99493	0.99698	-0.99296
Re(3)	0.99824	-0.00735	0.99870
Re(4)	0.99609	-0.99690	0.95447
Re(5)	0.99875	-0.99868	-0.99729
Re(6)	0.99814	-0.99871	-0.99735
Re(7)	1.00000	1.00000	1.00000
Re(8)	0.99931	0.99989	0.99973
Im _{max}	0.02780	0.00769	0.00062

Table 3a. Identified Modal Parameters for System A. No. Forces = 1, Noise Ratio = 0.0

Undamped
Nat. Freq.= 4.9966 5.5000 5.5499

Damping
Factor = 0.0099 0.0100 0.0100

DOF	Modal Coeff.	Modal Coeff.	Modal Coeff.
Re(1)	0.01429	1.00000	-0.99759
Re(2)	1.00000	0.99934	-0.99663
Re(3)	0.99818	-0.01186	0.99938
Re(4)	0.99943	-0.99939	0.00978
Re(5)	0.99744	-0.99812	-0.99870
Re(6)	0.99777	-0.99810	-0.99873
Re(7)	0.99667	0.99719	1.00000
Re(8)	0.99707	0.99726	0.99987
Im _{max}	0.00086	0.00228	0.00064

Table 4a. Identified Modal Parameters for System A. No. Forces = 8, Noise Ratio = 0.0

Undamped
Nat. Freq.= No 5 Hz mode 5.4982 5.5657

Damping
Factor = identi- fied 0.0092 0.0126

DOF	Modal Coeff.	Modal Coeff.	Modal Coeff.
Re(1)		1.00000	0.96980
Re(2)		0.96169	1.00000
Re(3)		-0.11159	-0.60195
Re(4)		-0.95309	-0.03063
Re(5)		-0.86633	0.66319
Re(6)		-0.87422	0.65522
Re(7)		0.85209	-0.57500
Re(8)		0.85267	-0.64153
Im _{max}		0.24759	0.29919

Table 3b. Identified Modal Parameters for System A. No. Forces = 1, Noise Ratio = 0.1

Undamped
Nat. Freq.= 4.9980 5.5058 5.5490

Damping
Factor = 0.0097 0.0103 0.0100

DOF	Modal Coeff.	Modal Coeff.	Modal Coeff.
Re(1)	0.02516	-0.98585	0.98362
Re(2)	0.98621	-0.99463	1.00000
Re(3)	1.00000	0.02763	-0.95197
Re(4)	0.98411	1.00000	-0.06453
Re(5)	0.97350	0.94609	0.87503
Re(6)	0.97147	0.95297	0.87421
Re(7)	0.97307	-0.98640	-0.88674
Re(8)	0.96948	-0.95976	-0.89013
Im _{max}	0.02016	0.0644	0.21813

Table 4b. Identified Modal Parameters for System A. No. Forces = 8, Noise Ratio = 0.1

Undamped
Nat. Freq.= No 5 Hz mode 5.5003 5.5879

Damping
Factor = identi- fied 0.0098 0.0110

DOF	Modal Coeff.	Modal Coeff.	Modal Coeff.
Re(1)		0.89703	-0.72131
Re(2)		1.00000	-0.56014
Re(3)		-0.26396	0.83339
Re(4)		-0.71778	-0.07690
Re(5)		-0.09235	-0.41497
Re(6)		-0.17339	-0.50867
Re(7)		0.55184	1.00000
Re(8)		0.51095	0.94717
Im _{max}		0.21516	0.06490

Table 3c. Identified Modal Parameters for System A. No. Forces = 1, Noise Ratio = 0.2

Undamped
Nat. Freq.= 5.0007 5.4918 5.5512

Damping
Factor = 0.0093 0.0079 0.0100

DOF	Modal Coeff.	Modal Coeff.	Modal Coeff.
Re(1)	0.00020	1.00000	-0.83500
Re(2)	0.99549	0.97812	-0.82366
Re(3)	0.98808	-0.00563	0.92143
Re(4)	0.99560	-0.94902	-0.06190
Re(5)	0.99595	-0.92819	-0.96699
Re(6)	0.98004	-0.95929	-0.96398
Re(7)	0.98590	0.96932	1.00000
Re(8)	1.00000	0.98243	0.96990
Im _{max}	0.05798	0.18716	0.18870

Table 4c. Identified Modal Parameters for System A. No. Forces = 8, Noise Ratio = 0.2

The second series of tests considered objectives (3) and (4). System B (see Table 1), an 8 DOF system with four modes in the 0-10 Hz range, was used. In this case the noise-to-signal ratio was also 20%, but the number of forces was set at 1, 5, and 8 (an initial sampling run indicated three, possibly four, modes present in the 0-10 Hz range, so five independent DOF were selected).

The previous series of tests was again performed, but since the only substantial errors occurred in the coupled modes, their parameters were the only ones analyzed. In this analysis, only the normalized independent modal vectors and a ratio of the normalized dependent to independent modal vectors were calculated (see Fig. 2).

Again a convergence toward higher accuracy is seen in these results as the number of applied forces is increased. An important feature of the results is that the accuracy of the dependent DOF, calculated from Eq. (17), follows closely the same trends as the independent DOFs. Also to be noted in the diagrams are the error levels for five shakers and for eight shakers. Although three shakers are exciting dependent DOFs in the eight-shaker case, the accuracy is either maintained or improved in almost every instance. Even if there happens to be a higher error indication for an increase in shakers, there is a definite lessening in the error spread.

Two more series of tests were run. The first was a set of runs identical to the first test case with the exception that the forcing functions were swept-sines instead of random excitation. The results of this set were basically identical to the random excitation set. The final series also used the same set-up as the first test, except that no noise was introduced and the test range was from 0-1024 Hz with 256 data points (a delta frequency of 4 Hz). The ninth mode corresponding to 25 Hz was also deleted. All modes were identified to extremely high accuracy (the error was less than one part per billion) in spite of the fact that there were seven natural frequencies between two of the data points!

Conclusions

The theory of a method used to determine an estimation of the modal parameters for a viscously-damped, linear structure has been developed. The MSMA method involves the application and measurement of several non-coherent forces. Verification of the method was demonstrated analytically through an extensive computer simulation study.

The computer simulation showed the MSMA method to be stable. With increasing amounts of noise the results did not diverge dramatically. Also, as the number of applied forces was increased, the results converged to the system values.

Several advantages of the MSMA method were demonstrated by the computer analysis. The first is the ability to locate a mode which has a node line in the vicinity of a shaker by applying several forces. The second is the small amount of user judgement and expertise involved. Basically, the only user judgement needed is a knowledge of the approximate number of modes in the analysis range, and that is usually supplied by a previous

finite element simulation or can be estimated by examination of a preliminary FRF. The third advantage is the relatively fast analysis time. With the small amount of user interaction, the analysis time is basically dependent upon computation speed and total amount of data processed.

Acknowledgments

This work was supported by NASA Contract NAS8-33980 with Marshall Space Flight Center. The interest and encouragement of the contract monitor, Mr. Larry Kiefling, are gratefully acknowledged.

References

- 1) Lewis, R.C. and Wrisley, D.L. "A System for the Excitation of Pure Natural Modes of Complex Structures," J. Aero. Sci., Vol. 17, n. 11, 1950, pp. 705-722.
- 2) Anderson, S.E., "Another Look at Sine-Dwell Mode Testing," AIAA/ASME/ASCE/AHS 22nd Structures, Structural Dynamics and Materials Conference, Part 2, April 1981, pp. 202-211.
- 3) Smith, W.R., "Least-Squares Time-Domain Method for Simultaneous Identification of Vibration Parameters from Multiple Free-Response Records," AIAA/ASME/ASCE/AHS 22nd Structures, Structural Dynamics and Materials Conference, Part 2, April 1981, pp. 194-201.
- 4) Ibrahim, S.R. and Mikulcik, E.C., "A Method for the Direct Identification of Vibration Parameters from Free Response," Shock and Vibration Bulletin, Bulletin 47, Part 4, Sept. 1977, pp. 183-198.
- 5) Pappa, R.S., "Close-Mode Identification Performance of the ITD Algorithm," AIAA/ASME/ASCE/AHS 24th Structures, Structural Dynamics and Materials Conference, Part 2, May 1983, pp. 193-205.
- 6) Richardson, M., "Modal Analysis Using Digital Test Systems," Seminar on Understanding Digital Control and Analysis in Vibration Test Systems, The Shock and Vibration Information Center, Washington, DC, May 1975, pp. 43-64.
- 7) Allemang, R.J., Investigation of Some Multiple Input/Output Frequency Response Function Experimental Modal Analysis Techniques, Ph.D. Dissertation, U. of Cincinnati, 1980.
- 8) Kennedy, C.C. and Pancu, C.D.P., "Use of Vectors in Vibration Measurement," J. Aero. Sci., V. 14, n. 11, Nov. 1947, pp. 603-625.
- 9) Craig, R.R. and Su, Y-W. T. "On Multiple Shaker Resonance Testing," AIAA Journal, V. 12, n. 7, 1974, pp. 924-931.
- 10) Richardson, M. and Kniskern, S., "Identifying Modes of Large Structures from Multiple Input and Response Measurements," SAE Paper No. 760875, Nov. 1976.

- 11) Brown, D.L., et al., "Parameter Estimation Techniques for Modal Analysis," Paper No. 790221, SAE Transactions, V. 88, Sect. 1, 1979, pp. 828-846.
- 12) Ensminger, R.R. and Turner, M.S., "Structural Parameter Identification from Measured Vibration Data," AIAA/ASME/ASCE/AHS 20th SDM Conference, April 1979, pp. 410-416.
- 13) Coppolino, R.N., "A Simultaneous Frequency Domain Technique for Estimation of Modal Parameters from Measured Data," SAE Paper No. 811046, Oct. 1981.
- 14) Vold, H., Kundrat, J., Rocklin, G.E., Russell, R., "A Multi-Input Modal Estimation Algorithm For Mini-Computers," SAE Paper No. 820194, 1982.

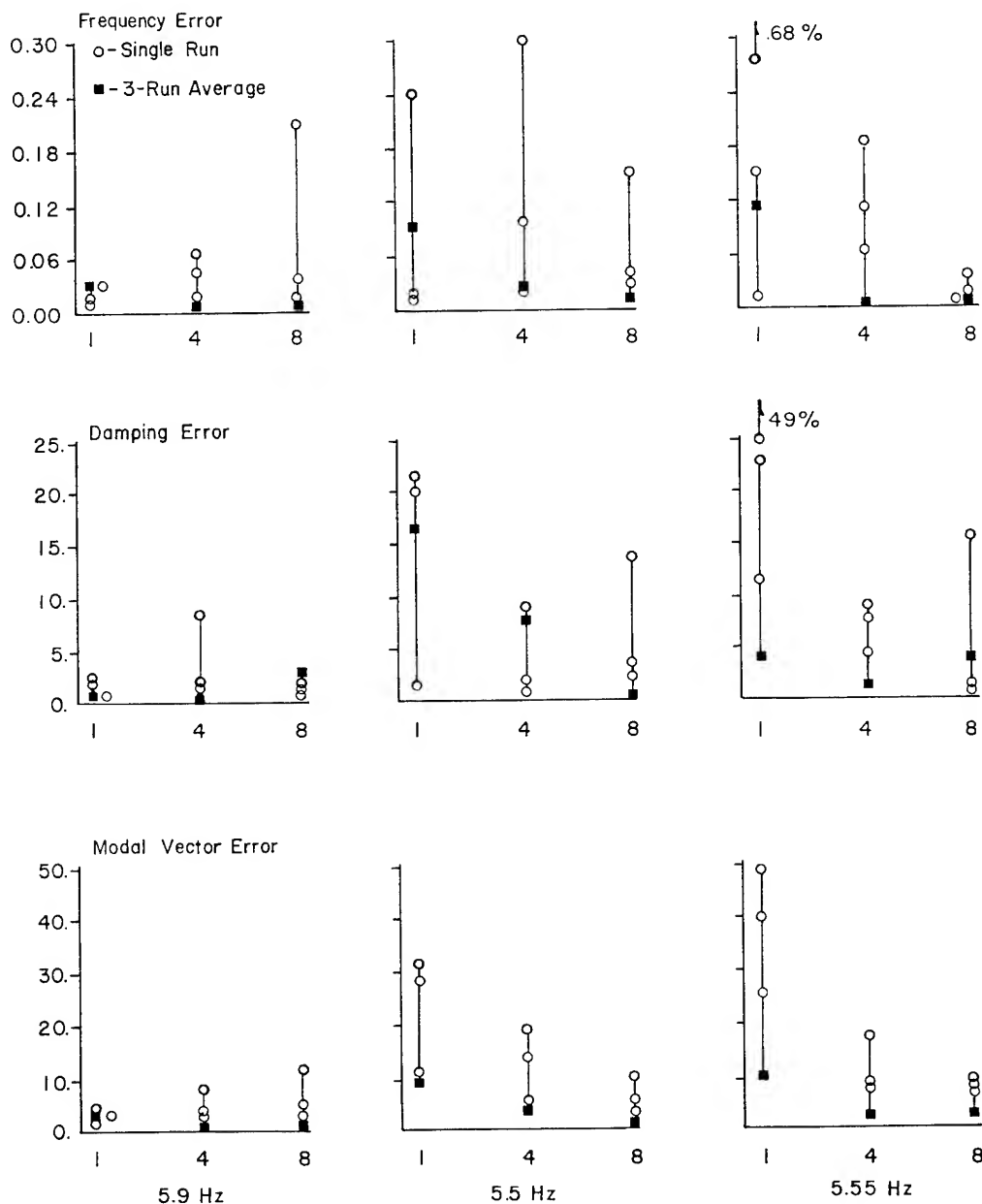


Figure 1. Error Comparisons for Test Series 1 (System A)
Noise/Signal = 0.2, Random Noise Excitation

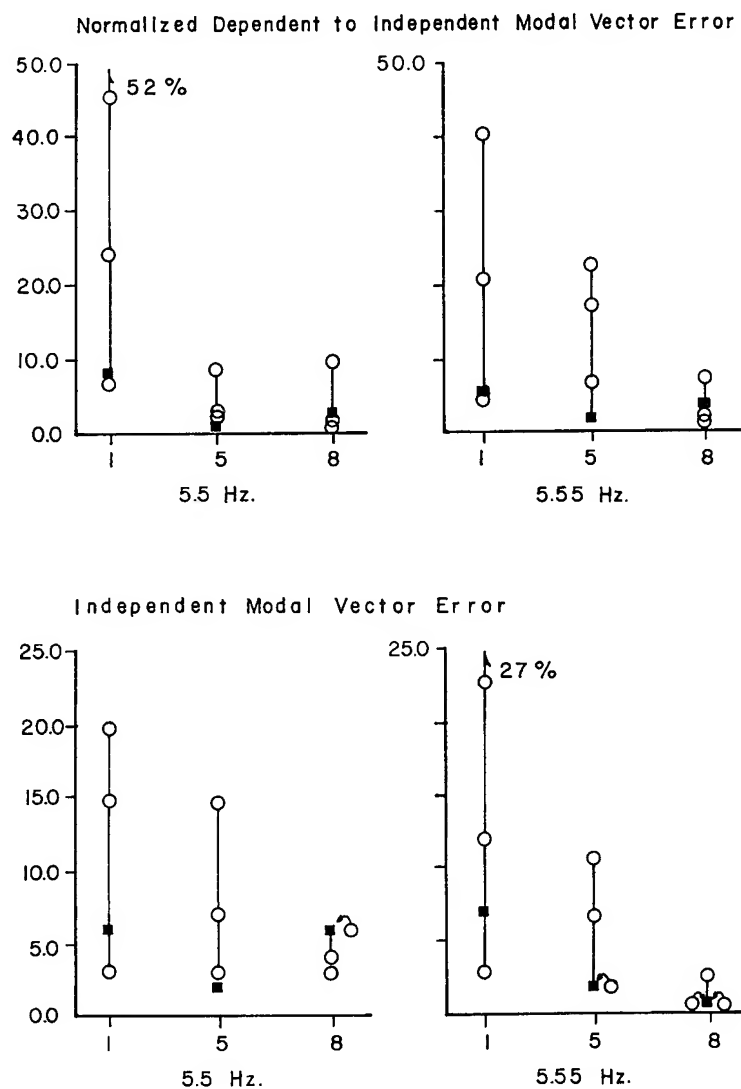


Figure 2. Error Comparisons for Test Series 2 (System B)
Noise/Signal = 0.2, Random Noise

Jay-Chung Chen*
Linda F. Peretti*
John A. Garba**

Applied Mechanics Technology Section
Jet Propulsion Laboratory
California Institute of Technology
Pasadena, California

Abstract

A structural parameter estimation procedure using the measured natural frequencies and kinetic energy distribution as observers is proposed. The theoretical derivation of the estimation procedure is described and its constraints and limitations are explained. This procedure is applied to a large complex spacecraft structural system to identify the inertia matrix using modal test results. The inertia matrix is chosen after the stiffness matrix has been updated by the static test results.

INTRODUCTION

For aerospace structural systems, where the responses and loads dictate the design and thus the size and weight of the structure, the accuracy of the analytical model is of major importance because of stringent weight constraints. A so-called test-verified analytical model is always required for the final verification loads analysis. The modal test, from which the natural frequencies, mode shapes, modal dampings and other modal characteristics are determined experimentally, is used to verify the analytical model. Frequently, analytical model predicted modal characteristics do not agree with the corresponding test measured values. If the disagreement is substantial, the analytical model must be modified or updated such that a better correlation between the test and analysis can be achieved. Thus, a new analytical model is identified by the test results.

Historically, the model modification and updating has been accomplished by a "trial and error" approach which was heavily dependent upon the individual's experience and intuition. With increasing complexity of the structural system, the model modification becomes difficult and systematic approaches are necessary. In recent years, a number of systematic procedures have been developed. References 1 to 10 are some of the typical examples.

In principle the procedure uses the differences between the test measured and analytically obtained eigenvectors and eigenvalues to identify or estimate those model parameters which effect these quantities. The parameters which effect the eigenvalues and eigenvectors are the stiffness and mass representations in the model. In other words, it is the objective of system identification procedure that stiffness and mass matrices, if finite element formulation is adapted, be modified based on the

modal test results. It is common that the measured modal characteristics, namely, the natural frequencies and mode shapes, are used in the identification procedure. However, mode shapes are vector quantities whose elements are the motions of individual degrees-of-freedom (DOF). For a large complex structural system, the amplitude of each DOF could be an order of magnitude different. In other words, for certain modes, some dominating DOF's would have very large modal displacement and other DOF's would have very little motion at all. Now, the identification procedure uses the differences between a test measured mode and a corresponding analytical mode. If the two modes are very close such that their dominating DOF's have the same amplitude and only the lesser important DOF's have different amplitude, the resulting difference between these two vectors will be dominated by those unimportant DOF's. This may lead to incorrect parameter identification. The quantities needed to represent the mode shape should be such that the important or dominating DOF's are more emphasized than those unimportant DOF's. In the present study, the kinetic energy distribution is chosen in place of the mode shape for identification procedure. The kinetic energy is defined as the quantity of modal displacement squared multiplied by the mass associated with that DOF. The idea is to make those DOF's with large mass and/or large amplitude modal displacement more important than others. Kinetic energy terms specifically eliminate the importance of those large local modal amplitudes associated with very small mass DOF's. Also, it is thought that kinetic energy may smooth out some of the instrumentation errors by weighting the measurements with the mass matrix.

The objective of the present study is to develop the estimation procedure by using the measured natural frequencies and kinetic energy distribution. The procedure will be demonstrated on a large complex spacecraft structural system.

Approach for Parameter Estimation

The approach used in the present study is to establish a method which will estimate the parameters of a finite element model capable of providing modal characteristics consistent with those measured in test. The procedure uses the values of parameters originally assigned to the model as a starting point from which the parameters are modified iteratively based on the differences between the analytical and test values. Therefore, the relationship between the measureables and the parameters must be established. The derivation of obtaining this relationship will be briefly described.

Consider a mathematically well-behaved function f of n variables (r_1, r_2, \dots, r_n), the relation-

* Member of Technical Staff, Member AIAA

** Supervisor, Structures & Dynamics Technology Group, Member AIAA

ship between the function f and the variable r_n 's can be written in the form of a Taylor series expansion:

$$\begin{aligned} f(r_1, r_2, \dots, r_n) &= f(\bar{r}_1, \bar{r}_2, \dots, \bar{r}_n) \\ &+ \sum_{i=1}^n \left(\frac{\partial f}{\partial r_i} \right)_{r_i = \bar{r}_i} (r_i - \bar{r}_i) \\ &+ \sum_{i=1}^n \left(\frac{\partial^2 f}{\partial r_i^2} \right)_{r_i = \bar{r}_i} (r_i - \bar{r}_i)^2 \\ &+ \dots \end{aligned} \quad (1)$$

For the small difference between r_i and \bar{r}_i , Eq. (1) can be approximated as:

$$\begin{aligned} f(r_1, r_2, \dots, r_n) &\cong f(\bar{r}_1, \bar{r}_2, \dots, \bar{r}_n) \\ &+ \sum_{i=1}^n \left(\frac{\partial f}{\partial r_i} \right)_{r_i = \bar{r}_i} (r_i - \bar{r}_i) \end{aligned} \quad (2)$$

If a number of functions are involved, Eq. (2) can be written in matrix form,

$$\{f(r)\} = \{f(\bar{r})\} + \left[\frac{\partial f(r)}{\partial r} \right]_{r = \bar{r}} \{r - \bar{r}\} \quad (3)$$

where

$$\{f(r)\} = \begin{Bmatrix} f_1(r_1, r_2, \dots, r_n) \\ f_2(r_1, r_2, \dots, r_n) \\ \vdots \\ f_m(r_1, r_2, \dots, r_n) \end{Bmatrix} \quad (4)$$

$$\{f(\bar{r})\} = \begin{Bmatrix} f_1(\bar{r}_1, \bar{r}_2, \dots, \bar{r}_n) \\ f_2(\bar{r}_1, \bar{r}_2, \dots, \bar{r}_n) \\ \vdots \\ f_m(\bar{r}_1, \bar{r}_2, \dots, \bar{r}_n) \end{Bmatrix} \quad (5)$$

$$\left[\frac{\partial f}{\partial r} \right]_{r = \bar{r}} = \begin{bmatrix} \frac{\partial f_1}{\partial r_1} \big|_{r_1 = \bar{r}_1} & \frac{\partial f_1}{\partial r_2} \big|_{r_2 = \bar{r}_2} & \dots & \frac{\partial f_1}{\partial r_n} \big|_{r_n = \bar{r}_n} \\ \frac{\partial f_2}{\partial r_1} \big|_{r_1 = \bar{r}_1} & \frac{\partial f_2}{\partial r_2} \big|_{r_2 = \bar{r}_2} & \dots & \frac{\partial f_2}{\partial r_n} \big|_{r_n = \bar{r}_n} \\ \vdots & \vdots & \ddots & \vdots \\ \frac{\partial f_m}{\partial r_1} \big|_{r_1 = \bar{r}_1} & \dots & \dots & \frac{\partial f_m}{\partial r_n} \big|_{r_n = \bar{r}_n} \end{bmatrix} \quad (6)$$

$$r - \bar{r} = \begin{Bmatrix} (r_1 - \bar{r}_1) \\ (r_2 - \bar{r}_2) \\ \vdots \\ (r_n - \bar{r}_n) \end{Bmatrix} \quad (7)$$

For a structural system under consideration, the parameters r_i 's representing the mass and stiffness properties of the system are to be identified and \bar{r}_i 's are the corresponding values used in the original analysis. Functions $f_i(r)$'s represent the test measured eigenvalues and kinetic energy distribution which are functions of the parameters r_i 's, and the $f_i(\bar{r})$'s are the corresponding eigenvalues and kinetic energies obtained from the original model where parameter values of $\bar{r}_1, \bar{r}_2, \dots, \bar{r}_n$ are used. Finally, the matrix $[\partial f / \partial r]_{r = \bar{r}}$ is referred to as the Jacobian matrix whose elements are the derivatives of the eigenvalues and kinetic energies with respect to the parameters and these derivatives are evaluated at $\bar{r}_1, \bar{r}_2, \dots, \bar{r}_n$.

Equation (3) can be simplified to read:

$$\{\Delta f\} = \left[\frac{\partial f(r)}{\partial r} \right] \{\Delta r\} \quad (8)$$

where

$$\begin{aligned} \{\Delta f\} &= \{f(r)\} - \{f(\bar{r})\} \quad \text{and} \\ \{\Delta r\} &= \{r - \bar{r}\} \end{aligned} \quad (9)$$

Equation (8) states that the differences between the test measured quantities and the corresponding analytically obtained quantities are linearly related to the changes of parameters. It must be noted that only in exceptional cases are the eigenvalues and eigenvectors of a structural system linear functions of the parameters which are, in this case, the mass and stiffness properties. However, Eq. (8) as well as Eq. (3) are valid, in an approximate sense, as long as the changes to the parameters are small. Therefore, this is a "priori" condition for most estimation problems.

In principle the parameter difference $\{\Delta r\}$ can be solved using Eq. (8) once the Jacobian matrix and the vector $\{\Delta f\}$ are available. However, this is true only if the matrix $[\partial f / \partial r]$ is nonsingular

and the vectors $\{\Delta f\}$ and $\{\Delta r\}$ have the same dimensions. Unfortunately the dimensions of the two vectors are usually not equal and other techniques must be used to estimate $\{\Delta r\}$. Sometimes these techniques are referred to as generalized matrix inversion (Refs. 11, 12 and 13). In the following, one proposed technique will be described and its mathematical insights with respect to certain imbedded optimal features will be explained.

Let

$$\left. \begin{aligned} \text{Dimension of } \{\Delta f\} &= n \text{ (no. of equations)} \\ \text{Dimension of } \{\Delta r\} &= m \text{ (no. of unknown)} \end{aligned} \right\} \quad (10)$$

Then

$$\text{Dimension of } \left[\frac{\partial f}{\partial r} \right] = n \times m \quad (11)$$

Case A: $n = m$

For the case where the measurement vector $\{\Delta f\}$ and the parameter vector $\{\Delta r\}$ in Eq. (8) are equal, the Jacobian matrix $[\partial f / \partial r]$ will be a square matrix by definition. Then the number of unknowns in Eq. (8) is equal to number of governing equations. Further, if each equation is linearly independent, a unique set of solution of the unknowns are assured. In other words, the inverse of the Jacobian matrix exists, and

$$\{\Delta r\} = \left[\frac{\partial f}{\partial r} \right]^{-1} \{\Delta f\} \quad (12)$$

Case B: $n > m$

For the case where the number of measurements is greater than the number of parameters, Eq. (8) contains more governing equations (n) than the unknowns (m). Mathematically, Eq. (8) is over-constrained and no solution exists. Therefore, one seeks an approximate solution instead. Let a residual vector $\{e\}$ be defined as

$$\{e\} = \{\Delta f\} - \left[\frac{\partial f}{\partial r} \right] \{\Delta r\} \quad (13)$$

The Euclidian norm of the residual vector is

$$\begin{aligned} Q &= \{e\}^T \{e\} \\ &= \left(\{\Delta f\} - \left[\frac{\partial f}{\partial r} \right] \{\Delta r\} \right)^T \left(\{\Delta f\} - \left[\frac{\partial f}{\partial r} \right] \{\Delta r\} \right) \end{aligned} \quad (14)$$

It is postulated that the best approximate solution will minimize the Euclidian norm of residual vector, i.e.,

$$\left\{ \frac{\partial Q}{\partial (\Delta r)_i} \right\} = 2 \left[\frac{\partial f}{\partial r} \right]^T \left(\left[\frac{\partial f}{\partial r} \right] \{\Delta r\} - \{\Delta f\} \right) = 0 \quad (15)$$

which gives

$$\{\Delta r\} = \left(\left[\frac{\partial f}{\partial r} \right]^T \left[\frac{\partial f}{\partial r} \right] \right)^{-1} \left[\frac{\partial f}{\partial r} \right]^T \{\Delta f\} \quad (16)$$

It should be noted that matrix $[\partial f / \partial r]$ is of $n \times m$ dimension and since $n > m$, without loss of generality, it can be assumed that $[\partial f / \partial r]$ has a full rank of m . In other words, $[\partial f / \partial r]$ contains m columns of vectors which are linearly independent. Therefore, $[\partial f / \partial r]^T [\partial f / \partial r]$ is also having full rank m which guarantees its positive definite and existence of its inverse, $([\partial f / \partial r]^T [\partial f / \partial r])^{-1}$.

Furthermore, from Eq. (15), the Hessian matrix can be obtained as

$$\left\{ \frac{\partial^2 Q}{\partial r^2} \right\} = 2 \left[\frac{\partial f}{\partial r} \right]^T \left[\frac{\partial f}{\partial r} \right] \quad (17)$$

and because it is positive definite, it implies that Q is indeed a minimum for the solution expressed by Eq. (16). This solution is also known as the least-square solution.

Case C: $n < m$

For the case where the number of measurements is less than the number of parameters, Eq. (18) contains more unknowns (m) than the governing equations (n). Mathematically, Eq. (8) is under constrained and there are infinite number of solutions which will satisfy Eq. (8). It is postulated that among these infinite number of solutions, the one whose norm is minimum will be the approximate solution. Therefore, this is a constrained minimization problem, where the minimization of $||\Delta r^2||$ is to be accomplished subject to Eq. (8). Let

$$\left. \begin{aligned} ||\Delta r^2|| &= \{\Delta r\}^T \{\Delta r\} \\ \text{and} \\ R &= \frac{1}{2} ||\Delta r^2|| + \{\lambda\}^T \left(\{\Delta f\} - \left[\frac{\partial f}{\partial r} \right] \{\Delta r\} \right) \end{aligned} \right\} \quad (18)$$

where $\{\lambda\}$ = an $n \times 1$ vector of Lagrange Multipliers the minimization procedure calls for

$$\left\{ \frac{\partial R}{\partial (\Delta r)_i} \right\} = \{\Delta r\} - \left[\frac{\partial f}{\partial r} \right]^T \{\lambda\} = 0 \quad (19)$$

$$\left\{ \frac{\partial R}{\partial \lambda_i} \right\} = \{\Delta f\} - \left[\frac{\partial f}{\partial r} \right] \{\Delta r\} = 0 \quad (20)$$

Multiplying $[\partial f / \partial r]$ to Eq. (19) and adding the resulting equation to Eq. (20), one obtains

$$\{\Delta f\} - \left[\frac{\partial f}{\partial r} \right] \left[\frac{\partial f}{\partial r} \right]^T \{\lambda\} = 0 \quad (21)$$

and

$$\{\lambda\} = \left(\left[\frac{\partial f}{\partial r} \right] \left[\frac{\partial f}{\partial r} \right]^T \right)^{-1} \{\Delta f\} \quad (22)$$

The existence of

$$\left(\left[\frac{\partial f}{\partial r} \right] \left[\frac{\partial f}{\partial r} \right]^T \right)^{-1}$$

is guaranteed by virtue of its full rank of n . Substituting Eq. (22) into Eq. (19), one obtains

$$\{\Delta r\} = \left[\frac{\partial f}{\partial r} \right]^T \left(\left[\frac{\partial f}{\partial r} \right] \left[\frac{\partial f}{\partial r} \right]^T \right)^{-1} \{\Delta f\} \quad (23)$$

Equations (12), (16) and (23) are to be used for estimating the parameter differences Δr if the number of measurements used in this procedure is equal to, greater than and less than the parameters to be identified, respectively. After the parameters are identified, the analytical model will be modified and new eigenvalues and eigenvectors will be computed. The entire procedure is repeated until a predetermined convergence between the test and analysis is achieved.

GALILEO SPACECRAFT

The Galileo is an interplanetary spacecraft whose mission is to conduct scientific exploration of the planet Jupiter. It is to be launched by the Space Shuttle and a modified Centaur Upper Stage in 1986. Figure 1 shows the Galileo spacecraft in its modal test configuration with its major components indicated. The total weight of the spacecraft is approximately 5300 lbs. A finite element model using NASTRAN code was constructed for performing the design loads analysis. Figure 2 shows the schematics of the model. This model consists of approximately 10,000 static degrees-of-freedom (DOF) and 1600 mass DOF. It is this loads analysis model which is required to be verified by the modal test.

Extensive pre-test analysis has been conducted prior to the modal test (Ref. 14) for the purpose of understanding the modal characteristics of the loads model. This was essential in the design of the modal test such as the instrumentation distribution and external excitation selection. After careful consideration, it was determined that 162 channels of accelerometer measurements as well as 118 channels of strain gage measurements were to be taken. The instrumentation distribution was such that all the important modal displacements and modal forces were measured with sufficient resolution. Since the number of DOF in the loads analysis model was a few orders of magnitude greater than the number of measurements to be made during test, a condensed model was constructed such that its DOF would be compatible with the measurements. This condensed

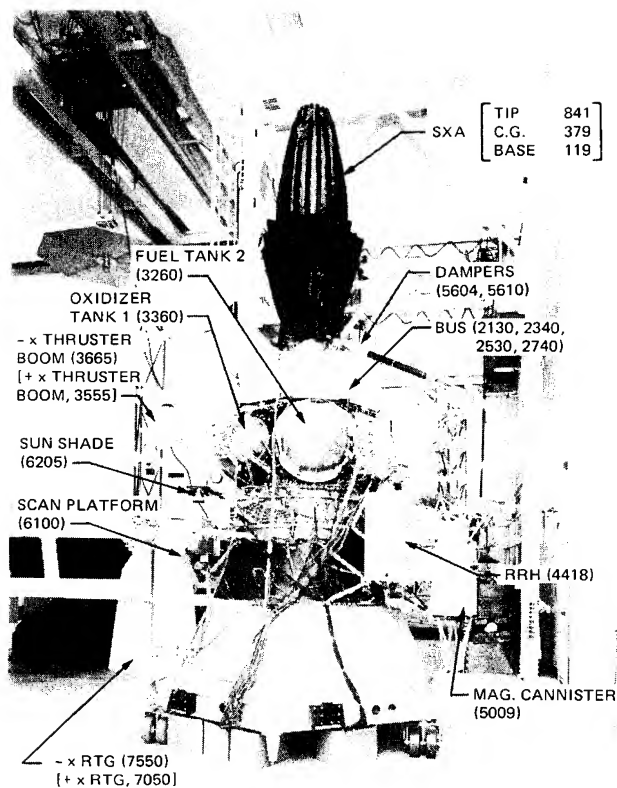


Fig. 1 Galileo Spacecraft in Modal Test Configuration.

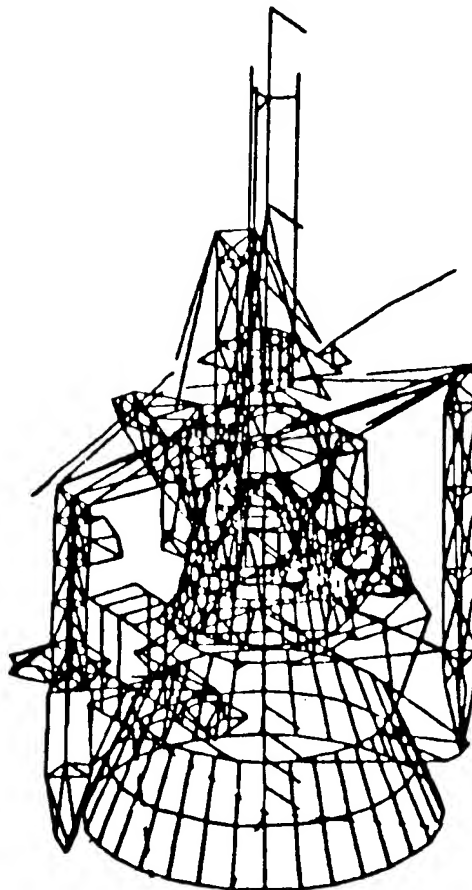


Fig. 2 Galileo NASTRAN Model.

model was called the Test-Analysis Model, TAM, which was obtained by Guyon reduction method to collapse the mass and stiffness matrices in the loads analysis model onto 162 DOF. The TAM was so adjusted that all the modal characteristics predicted by the loads model should be reproduced by TAM within the range of interest. The construction of TAM was an evolution process because of the changes and improvements of the model. Figure 3 shows the progress of each TAM up to December 1983. The basic model is the TAM6 which reflects some of

the hardware changes of the test article such as the weights of the components.

The modal test was performed by using various testing techniques and their results were reported and compared for evaluations of the methods, (Refs. 15 to 19). The modal test data chosen for the identification process were obtained from the multi-shaker sine dwell because of the relative high amplitude responses which are thought to be closer to reality in flight. Although 17 independent modes were obtained by the multi-shaker sine dwell method, only 9 of them will be used in the identification procedure. They are selected because of the large effective masses which are indications for the global modes. Table 1 lists the frequencies and descriptions of these test modes and those of TAM6. Tables 2 and 3 show the orthogonality and cross-orthogonality, respectively. The analytical mass matrix and modes are those of TAM6.

Subsequent to the modal test, a static test was performed. The results was used in improving the Galileo stiffness matrix. The model improvement and modification were reflected in the TAM7, TAM8 and TAM9. Table 1 also lists the frequencies of TAM9 comparing to the test and TAM6. Table 3 also shows the cross orthogonality between TAM9 and test modes. Figure 4 shows the kinetic energy comparison between the TAM6, TAM9 and the test. With respect to the test results, TAM9 shows certain improvement over TAM6, but discrepancies still exist.

In view of the corrections of stiffness based on the static test results, the parameters in the identification procedure are limited to the mass representation of the model. Table 4 lists the parameters and their original masses. These parameters are not individual elements in the mass matrices but rather are the lumped masses of several nodes within the major components. All together 51 test measured quantities are selected as the

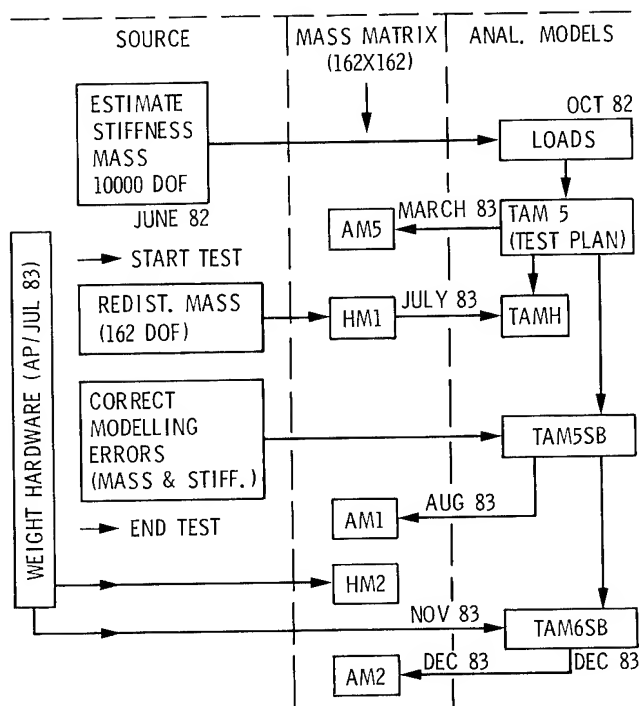


Fig. 3 Evolution of Test Analysis Models.

Table 1 Test and analysis modes comparison

Test		TAM6			TAM9			Description
Mode No.	Frequency (Hz)	Mode No.	Frequency (Hz)	% Error	Mode No.	Frequency (Hz)	% Error	
1	13.48	1	13.49	0.07	1	13.87	2.89	SXA in x
2	13.69	2	13.74	0.37	2	14.03	2.48	SXA in y
3	17.95	4	18.15	1.11	3	18.48	2.70	Core Bending y
4	18.15	5	18.83	3.75	4	18.89	4.08	SXA in x-y
5	18.59	3	16.44	11.57	5	19.56	5.22	Torsion
6	21.60	7	20.52	5.00	7	21.22	1.76	+RTG in z
7	23.58	9	22.97	2.59	8	23.04	2.29	+RTG in z
8	24.85	8	21.27	14.41	10	24.53	1.29	Torsion
14	37.59	17	33.77	10.16	18	37.44	0.40	Bouncing
Average				5.45	Average		2.57	

Table 2 Orthogonality for test modes

	1	2	3	4	5	6	7	8	14
1	1.00	0.49	0.02	-0.14	0.13	0.07	0.02	-0.03	-0.01
2		1.00	-0.14	-0.10	-0.02	0.06	-0.09	0.00	0.01
3			1.00	0.45	-0.02	-0.04	-0.04	-0.02	0.02
4				1.00	0.16	0.00	0.02	0.02	0.01
5					1.00	-0.02	-0.01	-0.07	-0.04
6						1.00	-0.01	0.02	-0.08
7							1.00	0.02	-0.01
8								1.00	-0.02
14									1.00

observations which include 9 frequencies and kinetic energies of each of the chosen test modes whose amplitudes exceed 5%. The sensitivity or Jacobian matrix, whose elements are the derivatives of the eigenvalues and kinetic energies with respect to the parameters, is constructed by making a small change of the specific parameter, ∂r_i , and then calculating the new eigenvalues and kinetic energies due to this change, δf_j , $j = 1, 2, \dots, 51$. Then in the limiting case, one obtains the derivatives as

$$\frac{\partial f_j}{\partial r_i} = \lim_{\delta r_i \rightarrow 0} \left(\frac{\delta f_j}{\delta r_i} \right) \quad (24)$$

Varying one parameter at a time and meanwhile keeping all other parameters unchanged, one column of the Jacobian matrix which consists of 51 elements can be constructed according to Eq. (24). Although a new eigen problem solution is required for each small change of parameters, a seemingly expensive procedure for large model, in practice, the same decomposed stiffness matrix can be used for each eigenproblem and using NASTRAN restart, the computation cost is very reasonable. After every parameter is disturbed, the entire Jacobian matrix is completed. Since the number of measurements used in the procedure (51) is greater than the number of parameters (10), Eq. (16) is used to calculate the changes in the parameters, (Case B). Table 4 also lists the results of the parameter identification. Based on the estimated new parameters, a new model was constructed and its eigenproblem is solved. It should be noted that one of the parameters, namely the Despun Box mass was identified as having an increment of 290% which is

physically impossible. Therefore, in the new model, a 20% limit was imposed on that parameter. The 20% was chosen because of the requirement of small changes as a priori condition. Table 5 shows the frequencies calculated from this new model and the comparisons with the test frequencies. In general, the new model is improved as compared with the previous model shown in Table 1. The average frequency error is reduced from 5.45% to 1.70%. Tables 6 and 7 show the new orthogonality and cross orthogonality similar to those of the previous model as shown in Tables 2 and 3, respectively. The orthogonality has been improved slightly, however the major large off-diagonal terms are still present. The improvement on the cross orthogonality is more evident, especially for the diagonal terms whose values are closer to unity comparing with previous models. The kinetic energy comparison is shown in Fig. 5 for the four selected modes. Except for the mode 6 which is a local RTG mode, all others show significant improvement.

WEIGHTED ESTIMATION

Equation (16) provides the estimation of parameters in the sense of least-square best fit. It should be noted that all the measurements are treated equally in the identification process. In other words, no consideration is made for the error differences between the instruments or the differences in the importance of different modes. However, in reality, the test measured quantities are different not only in their accuracies but also in the importance of each mode with respect to the loads analysis. These physical considerations seem to indicate that the measurements should be weighted in the identification procedure. This can be accomplished by performing the minimization pro-

Table 3 Cross orthogonality for test vs. TAM6 and TAM9

TAM	Test								
	1	2	3	4	5	6	7	8	14
1* (1)**	-0.87 (0.92)	-0.06 (0.15)	-0.15 (0.08)	0.20 (-0.18)	-0.16 (0.20)	-0.05 (0.03)	0.02 (-0.03)	0.01 (-0.01)	0.02 (-0.02)
2 (2)	-0.42 (0.34)	-0.97 (0.97)	0.30 (-0.23)	0.22 (-0.14)	-0.02 (0.01)	0.01 (-0.01)	0.03 (-0.01)	0.03 (-0.02)	0.02 (-0.02)
4 (3)	-0.06 (-0.07)	-0.17 (-0.11)	-0.88 (-0.85)	-0.66 (-0.77)	0.02 (0.05)	-0.03 (0)	-0.09 (0.01)	-0.03 (-0.02)	-0.02 (-0.02)
5 (4)	0.16 (-0.10)	0.05 (-0.01)	0.23 (0.44)	0.48 (-0.49)	-0.42 (0.06)	-0.01 (-0.13)	0.03 (-0.04)	0.03 (0.01)	0.02 (0)
3 (5)	-0.06 (0.05)	0.02 (0.04)	0.15 (0.03)	-0.45 (-0.24)	-0.85 (-0.91)	-0.07 (0.12)	0.02 (0.09)	0.02 (0.09)	0.02 (0.02)
7 (7)	0.02 (0.04)	0.10 (0.04)	-0.02 (0.03)	0.02 (-0.03)	-0.08 (0.12)	0.77 (0.90)	-0.24 (0.13)	-0.02 (-0.07)	0 (-0.02)
9 (8)	-0.01 (-0.01)	0.05 (0.06)	0.02 (0.04)	-0.02 (0)	-0.02 (-0.02)	0.07 (0.12)	-0.60 (-0.75)	0.12 (-0.01)	-0.01 (0.01)
8 (10)	-0.02 (-0.01)	0 (0.02)	-0.02 (-0.01)	0 (0.02)	-0.02 (0.01)	-0.02 (0.15)	0.09 (-0.13)	0.94 (0.73)	0.09 (0)
17 (18)	0 (0.01)	-0.02 (-0.01)	0.02 (0)	-0.01 (0)	0.01 (0)	0.05 (0.06)	0.01 (0.02)	-0.05 (0.03)	-0.78 (-0.70)

* Numbers without parentheses are for TAM6

** Numbers with parentheses are for TAM9

cedure on an extended vector norm which is defined as:

$$\bar{Q} = \{e\}^T [W] \{e\} \quad (25)$$

$$= \left(\left\{ \Delta f \right\} - \left[\frac{\partial f}{\partial r} \right] \left\{ \Delta r \right\} \right)^T [W] \left(\left\{ \Delta f \right\} - \left[\frac{\partial f}{\partial r} \right] \left\{ \Delta r \right\} \right)$$

where

$[W]$ = a positive definite compatible weighting matrix

$\{e\}$ = residual vector defined in Eq. (13).

The solution to the minimization procedure similar to Eq. (15) is as follows,

$$\left\{ \Delta r \right\} = \left(\left[\frac{\partial f}{\partial r} \right]^T [W] \left[\frac{\partial f}{\partial r} \right] \right)^{-1} \left[\frac{\partial f}{\partial r} \right] [W] \left\{ \Delta f \right\} \quad (26)$$

For the Galileo modal test, weighting matrix will be defined by the effective mass distribution for each mode. The larger the effective mass indicates the more participation for the mode in the loads analysis, therefore the more importance. Table 8 shows the effective mass in percentage of the total mass for the 9 test modes. The sum of the effective mass over the six directions is the weighting factor for each mode in the weighting matrix $[W]$. Each measurement in the same mode is assigned to a same weighting factor and no weighting correlations exist between the modes. Therefore the matrix $[W]$ is a diagonal matrix with 9 different numbers assigned to 9 corresponding modes.

The results of Eq. (26) are shown in Tables 4, 5, 6 and 7 and Fig. 5. In general, the weighted results show better improvement in frequency errors, cross-orthogonality and kinetic energy distribution. However, these improvements are not as significant as one would like them to be.

CONCLUDING REMARKS

A system identification procedure has been described and an application to a realistic complex

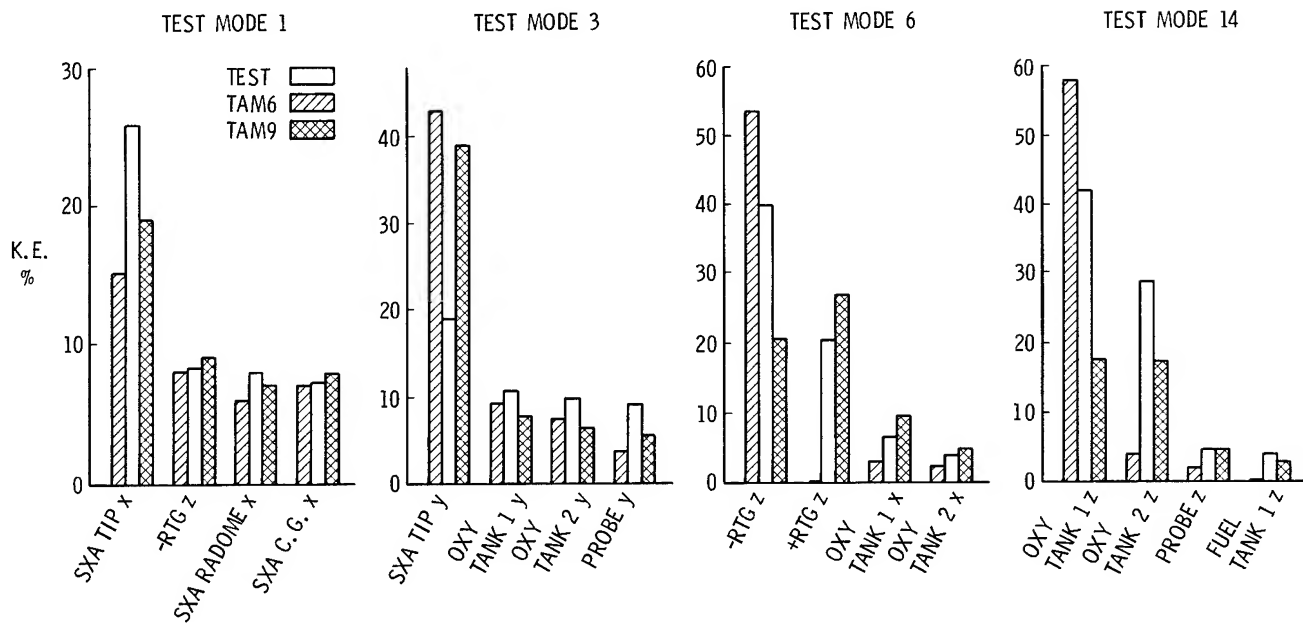


Fig. 4 Kinetic Energy Distribution for Analytical Models.

Table 4 Structural parameters

Parameter	Description	Original Weight (lbs)	Identified Model			
			Unweighted		Weighted	
			Identified Weight (lbs)	% Increment	Identified Weight (lbs)	% Increment
r_1	SXA	77.92	92.60	18.84	91.36	17.25
r_2	Bus	538.68	452.58	-15.98	342.01	-36.51
r_3	Despun Box	217.24	849.34*	290.97*	753.36*	246.79*
r_4	Science Boom	156.01	155.03	-0.63	163.85	5.03
r_5	Scan Platform	207.65	195.72	-5.74	195.92	-5.65
r_6	+X RTG	159.78	161.07	0.81	161.78	1.25
r_7	-X RTG	153.98	156.99	1.95	150.86	-2.03
r_8	Probe	640.41	662.92	3.52	647.81	1.15
r_9	RPM Mx, My	2315.98	2265.80	-2.17	2415.48	4.30
r_{10}	RPM Mz	2315.98	2392.06	3.29	2468.31	6.58

*The identified despun box mass is unrealistically high. They are limited arbitrarily to 20% increment in the identified model.

Table 5 Identified modes comparison

Test		Unweighted Model			Weighted Model			Description
Mode No.	Frequency (Hz)	Mode No.	Frequency (Hz)	% Error	Mode No.	Frequency (Hz)	% Error	
1	13.48	2	13.54	0.45	2	13.63	1.11	SXA in x
2	13.69	1	13.52	1.31	1	13.56	0.95	SXA in y
3	17.95	4	18.01	0.33	4	18.11	0.89	Core Bending y
4	18.15	3	17.85	1.65	3	17.99	0.88	SXA in x-y
5	18.59	5	19.48	4.79	5	19.10	2.74	Torsion
6	21.60	7	21.23	1.71	7	21.26	1.57	±RTG in z
7	23.58	8	22.92	2.80	8	22.93	2.76	+RTG in z
8	24.85	10	24.47	1.53	10	24.54	1.25	Torsion
14	37.59	18	37.33	0.69	18	37.13	1.22	Bouncing
Average				1.70	Average			1.49

Table 6 Test modes orthogonality with respect to identified model

	1	2	3	4	5	6	7	8	14
1	1.00	0.49 (0.49)	0.01 (0.01)	-0.06 (-0.06)	0.10 (0.09)	0.06 (0.06)	-0.02 (-0.02)	-0.03 (-0.03)	-0.01 (-0.01)
2		1.00	-0.06 (-0.06)	-0.01 (-0.01)	-0.03 (-0.03)	0.04 (0.04)	-0.07 (-0.07)	0.00 (0.00)	0.01 (0.01)
3			1.00	0.45 (0.44)	-0.02 (-0.03)	-0.05 (-0.05)	-0.04 (-0.04)	-0.02 (-0.02)	0.02 (0.02)
4				1.00	0.16 (0.18)	0.01 (0.01)	0.01 (0.01)	0.02 (0.02)	0.01 (0.01)
5					1.00	-0.03 (-0.02)	-0.01 (-0.01)	-0.06 (-0.05)	-0.04 (-0.03)
6						1.00	-0.01 (0.01)	0.02 (0.02)	-0.09 (-0.10)
7							1.00	0.02 (0.02)	0.00 (0.00)
8								1.00	-0.02 (-0.02)
14									1.00

Numbers without parentheses are for unweighted model.
Numbers with parentheses are for weighted model.

Table 7 Cross orthogonality for Test vs. identified model

Model	Test								
	1	2	3	4	5	6	7	8	14
2* (2)**	-0.94 (-0.98)	-0.71 (-0.40)	0.01 (0.00)	0.04 (0.05)	-0.11 (-0.11)	0.00 (-0.03)	0.01 (0.03)	0.01 (0.00)	0.02 (0.02)
1 (1)	0.29 (-0.10)	-0.68 (-0.90)	0.02 (0.02)	-0.07 (-0.06)	0.08 (0.04)	0.05 (0.04)	-0.02 (-0.02)	0.01 (0.01)	0.00 (0.01)
4 (4)	0.00 (0.01)	-0.02 (-0.01)	0.83 (0.74)	0.01 (-0.17)	0.18 (0.13)	-0.17 (-0.17)	-0.06 (-0.07)	0.02 (0.02)	0.00 (0.00)
3 (3)	-0.01 (0.00)	0.01 (-0.02)	-0.51 (0.63)	-0.91 (0.92)	0.18 (-0.09)	-0.10 (0.06)	0.00 (0.00)	-0.02 (0.01)	-0.02 (0.02)
5 (5)	0.03 (0.02)	0.04 (0.03)	0.12 (0.10)	-0.31 (-0.25)	-0.89 (-0.92)	0.11 (0.07)	0.08 (0.08)	0.07 (0.06)	0.02 (0.02)
7 (7)	0.05 (0.05)	0.04 (0.05)	0.05 (0.04)	-0.02 (-0.05)	0.14 (0.07)	0.88 (0.89)	0.12 (0.17)	-0.07 (-0.06)	-0.02 (-0.02)
8 (8)	-0.01 (0.02)	0.07 (-0.06)	0.04 (-0.04)	0.00 (-0.01)	-0.02 (0.02)	0.10 (-0.18)	-0.80 (0.68)	-0.01 (-0.02)	0.01 (-0.01)
10 (10)	0.00 (0.01)	0.03 (-0.03)	-0.01 (0.01)	0.02 (-0.01)	0.01 (0.01)	0.24 (-0.19)	-0.04 (0.15)	0.66 (-0.68)	0.00 (0.00)
18 (18)	-0.01 (0.00)	0.02 (0.02)	0.00 (0.00)	0.01 (0.01)	-0.01 (0.00)	-0.08 (-0.07)	-0.02 (-0.02)	-0.03 (-0.03)	0.91 (0.92)

*Numbers without parentheses are for unweighted model

**Numbers with parentheses are for weighted model

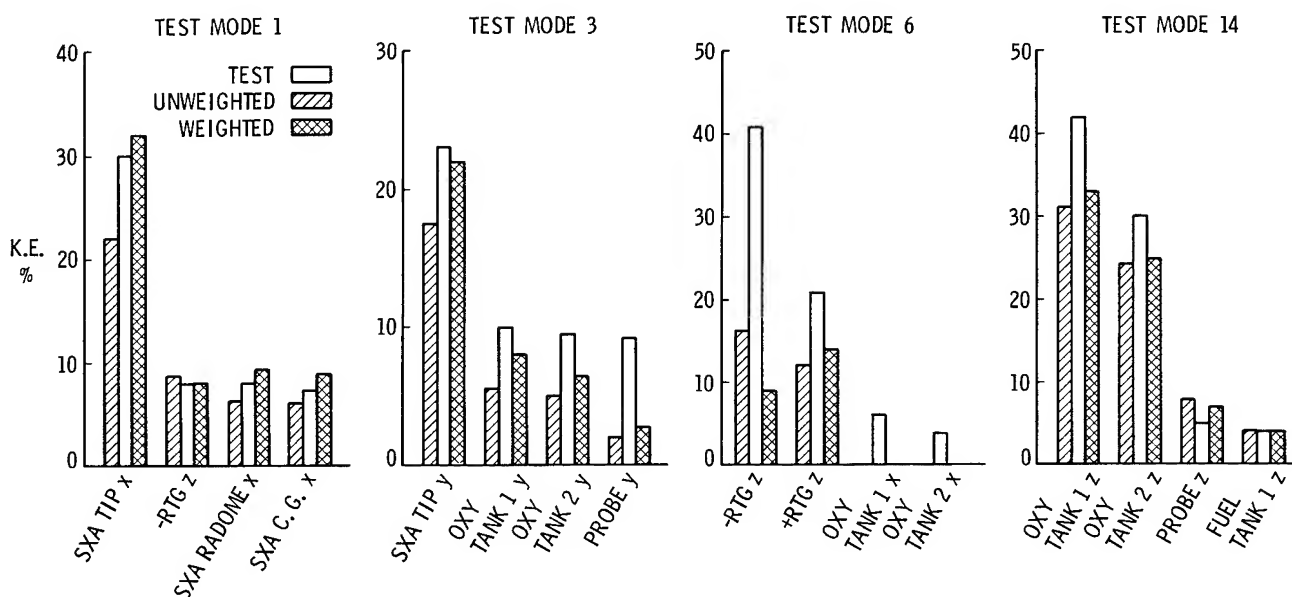


Fig. 5 Kinetic Energy Distribution for Identified Models.

Table 8 Effective mass of test modes

Mode	x	y	z	ϕ_x	ϕ_y	ϕ_z	Sum*
1	0.3695	0.0199	0	0.0356	0.5850	0	1.000
2	0.0231	0.2677	0	0.4011	0.0320	0	0.7239
3	0.0735	0.4456	0	0.3587	0.0550	0	0.9327
4	0.1737	0.2033	0	0.1790	0.1484	0.0548	0.7591
5	0	0	0	0	0.0285	0.2972	0.3257
6	0.2766	0.0103	0.0127	0	0.1346	0.0123	0.4465
7	0	0	0.1018	0.0089	0	0	0.1107
8	0.0133	0	0	0.0022	0	0.3581	0.3737
14	0	0	0.7511	0	0	0	0.7511

*Numbers are used in the Weighting Matrix.

spacecraft structure was performed. The usual modal displacements are replaced by the kinetic energy distributions as the measurement quantities in the procedure. Also, the concept of weighting the measurements in order to emphasize certain data was described. The results show that indeed the proposed approach produces a better model which predicts better modal characteristics than the original analytical model.

One shortcoming of the approach is that engineering judgement is still required for eliminating the physically impossible parameter changes. Also a more important aspect of the approach is the selection of parameters which is primarily based on individual's liking or intuition. A more systematic method of selection would be assigning a large number of parameters and calculating the sensitivity of modal characteristics with respect to these parameters. Only the ones with higher sensitivity are retained for the identification. However, sensitivity calculation is a very expensive process, therefore, it may not be a cost effective method for a large system which contains large numbers of parameters.

ACKNOWLEDGEMENT

The work described in this paper was carried out by the Jet Propulsion Laboratory, California Institute of Technology, under contract with the National Aeronautics and Space Administration.

REFERENCES

1. Rodden, W.P., "A Method for Deriving Structural Influence Coefficients from Ground Vibration Tests," *AIAA J.*, Vol. 5, No. 5, May 1967, pp. 991-1000.
2. Berman, A., and Flannelly, W.C., "Theory of Incomplete Models of Dynamic Structures," *AIAA Journal*, Vol. 9, No. 8, August 1971, pp. 1481-1487.
3. Pilkey, W.D. and Cohen, R. (editors), "System Identification of Vibrating Structures, Mathematical Models from Test Data," American Society of Mechanical Engineers, New York, NY, 1972.
4. Collins, J.D., Hart, G.C., Hasselman, T.K., and Kennedy, B., "Statistical Identification of Structures," *AIAA Journal*, Vol. 12, Feb. 1974, pp. 185-190.
5. Garba, J.A., and Wada, B.K., "Application of Perturbation Methods to Improve Analytical Model Correlation with Test Data," SAE paper 770959, presented at SAE Aerospace Meeting, Los Angeles, CA, Nov. 14-17, 1977.
6. Baruch, M., "Optimization Procedure to Correct Stiffness and Flexibility Matrices Using Vibration Tests," *AIAA J.*, Vol. 16, No. 11, Nov. 1978, pp. 1208-1210.
7. Chen, J.C., Garba, J.A., "Analytical Model Improvement Using Modal Test Results," *AIAA J.*, Vol. 18, No. 6, June 1980, pp. 684-690.
8. M.W. Dobbs, K.D. Blakely, and W.E. Gundy, "System Identification of Large-Scale Structures," SAE Technical Paper 811050, October 1981.
9. Berman, A., and Nagy, E.J., "Improvement of Large Dynamic Analytical Model Using Ground Vibration Test Data," AIAA Paper No. 82-0743, presented at the 23rd Structures, Structural Dynamics and Materials Conference, New Orleans, LA, May 10-12, 1982.
10. Chen, J.C., Kuo, C.P., and Garba, J.A., "Direct Structural Parameter Identification by Modal Test Results," AIAA Paper No. 83-0812, presented at the 24th Structures, Structural Dynamics and Materials Conference, Lake Tahoe, Nevada, May 2-4, 1983.

11. Penrose, R., "A Generalized Inverse for Matrices," Proceedings of the Cambridge Philosophical Society, Vol. 51, 1955, pp. 406-413.
12. Greville, T.N.E., "The Pseudoinverse of a Rectangular Singular Matrix and Its Application to the Solution of System Linear Equations," SIAM Review, Vol. 1, No. 1, Jan. 1959.
13. Shapiro, E.Y., and Decarli, H.E., "Generalized Inverse of a Matrix: The Minimization Approach," Technical Note, AIAA Journal, Vol. 14, No. 10, October 1976, pp. 1483-1484.
14. Chen, J.C. and Trubert, M., "Galileo Model Test and Pre-Test Analysis," Proceedings of the 2nd International Modal Analysis Conference, Feb. 6-9, 1984, Orlando, FL, pp. 796-802.
15. Trubert, M., "Assessment of Galileo Modal Test Results for Mathematical Model Verification," AIAA Paper No. 84-1066, presented at the AIAA Dynamics Specialists Conference, May 17-18, 1984, Palm Springs, CA.
16. Stroud, R.C., Pamidi, M.R. and Bausch, H.P., "Some Measurement and Analysis Methods Used on the Galileo Modal Survey," AIAA Paper No. 84-1067, presented at the AIAA Dynamic Specialists Conference, May 17-18, 1984, Palm Springs, CA.
17. Hunt, D.L. and Chen, J.C., "Application of Multi-Shaker Random Excitation and Polyreference Analysis Techniques to the Galileo Spacecraft Modal Tests," AIAA Paper No. 84-1069, presented at the AIAA Dynamic Specialists Conference, May 17-18, 1984, Palm Springs, CA.
18. Pappa, R.S., "ITD Analysis of Free-Decay Response From the Galileo Modal Test," AIAA Paper No. 84-1070, presented at the AIAA Dynamics Specialists Conference, May 17-18, 1984, Palm Springs, CA.
19. Chen, J.C., "Evaluations of Modal Testing Methods," AIAA Paper No. 84-1071, presented at the AIAA Dynamics Specialists Conference, May 17-18, 1984, Palm Springs, CA.

by

L. A. Bergman¹, A. L. Hale², and J. C. Goodding³
University of Illinois at Urbana-Champaign
Urbana, Illinois 61801Abstract

This paper utilizes the method of Poisson Moment Functionals (PMF) to identify the parameters of increasingly complex time invariant linear structures in a noisy environment. Two formulations are given. The first provides identification of the first order state equations of the structure from measurements of generalized displacements, velocities, and forces. The second provides identification of the second order differential equations of the structure from measurements of only the generalized displacements and forces. Both formulations identify the initial conditions of the system. Results of some parametric studies are given, and comparisons are made with a second order Auto Regressive Moving Average (ARMA) method.

1. Introduction

The method of Poisson Moment Functionals (PMF) leads to an effective time domain algorithm for linear system identification. The method was first explicitly introduced by Fairman and Shen [1,2] and Fairman [3], and was later refined in a series of papers by Saha and Prasada Rao [4-8] and Sivakumar and Prasada Rao [9]. The latter were primarily concerned with transfer function synthesis of systems of order $n/2$, and with identification of the state equations of n dimensional systems for the force-free case. In a recent note by Bergman and Hale [10], the method was extended to encompass the more general forced case of identification of the state equations for homogeneous initial conditions, making both the state and input matrices of the system available for further analysis [11].

Among the advantages of PMF, previously noted, are:

- (a) Identification is done in continuous time.
- (b) The method is somewhat naturally immune to zero-mean additive noise.

- (c) The PMF's of the process signals can be obtained online as the response of a Poisson filter chain.

In this paper, we first augment the operational matrices defined in [10] in order to accommodate and identify arbitrary initial values of the state variables. This additional flexibility, in conjunction with the now well known attributes of the PMF, provides an effective method for the on-line identification of linear systems. We also present a second formulation that is especially convenient for structural dynamic systems.

The first formulation is used to identify a single degree of freedom system and a three degree of freedom system in progressively noisier environments. Results are given for the fully determined (invertible) case. The results are compared with those obtained from a second order Auto Regressive Moving Average (ARMA) analysis of the data [11,12].

2. Poisson Moment Functionals

The PMF transform takes a signal $f(t)$ over the interval $[0, t_0]$ and converts it to a set of real numbers

$$f_k^o = f_k(t_0) = \int_0^{t_0} f(t) p_k(t_0 - t) dt$$

$$(k = 0, 1, 2, \dots) \quad (1)$$

where

$$p_k^t = p_k(t) = t^k \exp(-\lambda t) / k! \quad (2)$$

and

$$\lambda(\text{real}) > 0, \quad (3a)$$

$$f_{-1}(t_0) = f(t_0). \quad (3b)$$

¹Assistant Professor, Department of Theoretical and Applied Mechanics, 104 S. Wright St., Urbana, IL 61801.

²Assistant Professor, Department of Aeronautical and Astronautical Engineering, appointed jointly to the Department of Civil Engineering, 104 S. Matthews Ave., Urbana, IL 61801. Member AIAA.

³Research Assistant, Department of Theoretical and Applied Mechanics.

If $f(t)$ and $df(t)/dt$ are arbitrary at $t = 0$, and if $f_k^{(1)}(t_0)$ denotes the k th PMF of $df(t)/dt$, then it can be shown [5] that

$$f_k^{(1)}(t_0) = -\lambda f_k(t_0) + f_{k-1}(t_0)$$

$$- f(0) p_k(t_0),$$

$$(k = 0, 1, 2, \dots). \quad (4)$$

3. Linear System Identification by PMF When All of the States and Forces are Measured

This result can be applied directly to the first system that we wish to identify from potentially noisy response data, namely,

$$\dot{x}(t) = [A] x(t) + [B] u(t), \quad t > 0 \quad (5)$$

$$x(0) = x_0. \quad (6)$$

Here, $x(t)$ is an n -dimensional state vector comprised, normally, of generalized displacements and generalized velocities, and $u(t)$ is an m -dimensional input vector consisting of generalized forces.

Taking PMF's of the state vector $x(t)$, its derivative $\dot{x}(t)$, and the input vector $u(t)$ about a single time t_0 , and rearranging the state equations, we arrive at the formulation

$$[C] = [Y] [\Psi] [\Phi]^{-1} \quad (7)$$

where

$$[C] = [[A] [B] x_0], \quad \text{an } n \times (n+m+1) \text{ matrix}; \quad (8)$$

$$[Y] = [[I] [A]], \text{ an } n \times 2n \text{ matrix}; \quad (9)$$

$[I]$, the $n \times n$ identity matrix and

$$[A] = -\lambda [I]; \quad (10)$$

$$[\Psi] = \begin{bmatrix} x_{k-1} & x_k & \dots & x_{k+n+m-1} \\ x_k & x_{k+1} & \dots & x_{k+n+m} \end{bmatrix}, \quad (11)$$

a $2n \times (n+m+1)$ matrix;

$$\text{and } [\Phi] = \begin{bmatrix} x_k & x_{k+1} & \dots & x_{k+n+m} \\ u_k & u_{k+1} & \dots & u_{k+n+m} \\ p_k & p_{k+1} & \dots & p_{k+n+m} \end{bmatrix}, \quad (12)$$

an $(n+m+1) \times (n+m+1)$ matrix;

where the dependence of the PMF's of $x(t)$ and $u(t)$ on t_0 is not shown explicitly.

Alternately, it may be desirable to minimize the maximum order of the transformation by sampling at multiple instants of time (t_0, t_1, \dots). This may be advantageous as the dimension of the system grows large, because higher moments

can be very small due to the division by k factorial. In this case, the formulation becomes

$$[C] = [Y] [\hat{\Psi}] [\hat{\Phi}]^{-1}, \quad (13)$$

where $[C]$ and $[Y]$ are as defined previously;

$$[\hat{\Psi}] = \begin{bmatrix} t_1 & t_2 & \dots & t_{n+m+1} \\ x_{k-1} & x_{k-1} & \dots & x_{k-1} \\ t_1 & t_2 & \dots & t_{n+m+1} \\ x_k & x_k & \dots & x_k \end{bmatrix}, \quad (14)$$

a $2n \times (n+m+1)$ matrix;

$$[\hat{\Phi}] = \begin{bmatrix} t_1 & t_2 & \dots & t_{n+m+1} \\ x_k & x_k & \dots & x_k \\ t_1 & t_2 & \dots & t_{n+m+1} \\ u_k & u_k & \dots & u_k \\ t_1 & t_2 & \dots & t_{n+m+1} \\ p_k & p_k & \dots & p_k \end{bmatrix}, \quad (15)$$

an $(n+m+1) \times (n+m+1)$ matrix;

and where the superscript t_j denotes the appropriate PMF evaluated at time t_j .

When identification is sought in an environment wherein noise is present not only within the response process but also due to measurement error, it may sometimes be advantageous to utilize more data than required, resulting in "averaging" of the error. As we will use the multiple time formulation exclusively in the following work, the appropriate least square formulation for the multiple time case is given by

$$[C] = [Y] ([\hat{\Psi}][\hat{\Phi}]^T)([\hat{\Phi}][\hat{\Phi}]^T)^{-1} \quad (16)$$

where, now, the moments are computed at more than $n+m+1$ instants of time.

4. Linear System Identification When Only Generalized Displacements and Forces are Measured

In the previous identification procedure, an $n \times n$ state matrix $[A]$ and an $n \times m$ input matrix $[B]$ were identified from PMF's of all n state variables $x(t)$ and m inputs $u(t)$. For structural dynamic systems, the state variables are usually defined as $n/2$ generalized displacements and $n/2$ generalized velocities. Often, all n state variables are not conveniently measured; that is they are not readily available for input to a Poisson filter chain. This section considers direct identification from PMF's computed from the $n/2$ generalized displacements.

Let the state vector be given by $x(t) = [x_1^T x_2^T]^T$, where $x_1 = x_1(t)$ denotes the vector of generalized displacements, and $x_2 = x_2(t) = \dot{x}_1$ denotes the vector of generalized velocities. We seek to identify from potentially noisy data the second order system

$$\ddot{x}_1 + [\bar{c}] \dot{x}_1 + [\bar{k}] x_1 = [\bar{g}] u, \quad t > 0 \quad (17)$$

$$x_1(0) = a, \quad \dot{x}_2(0) = \dot{x}_1(0) = b. \quad (18a,b)$$

Here, the unknown coefficient matrices can be considered to be obtained by premultiplication by the inverse of an $n/2 \times n/2$ positive definite, symmetric mass matrix $[m]$ so that

$$[\bar{c}] = [m]^{-1}[c], \quad [\bar{k}] = [m]^{-1}[k],$$

$$[\bar{g}] = [m]^{-1}[g] \quad (19a,b,c)$$

where $[c]$, $[k]$, and $[g]$ are the usual damping, stiffness, and input matrices, respectively.

The first order equations of state associated with (17) are given by

$$\dot{x}_1 = x_2 \quad (20)$$

$$\dot{x}_2 = -[\bar{k}] x_1 - [\bar{c}] x_2 + [\bar{g}] u. \quad (21)$$

Now, taking PMF's of (20) and (21) about time t_j yields

$$x_{1,k-1}^j - \lambda x_{1,k}^j = x_{2,k}^j + a p_k^j = \bar{x}_{2,k}^j \quad (22)$$

$$x_{2,k-1}^j - \lambda x_{2,k}^j = -[\bar{k}] x_{1,k}^j - [\bar{c}] x_{2,k}^j + [\bar{g}] u_k^j + b p_k^j. \quad (23)$$

Because it is assumed that only PMF's of $x_1(t)$ are available, we have introduced $\bar{x}_{2,k}^j$ which can be calculated from (22) with knowledge of $x_{1,k-1}^j$ and $x_{1,k}^j$. Thus (23) can be rewritten as

$$\begin{aligned} \bar{x}_{2,k-1}^j - \lambda \bar{x}_{2,k}^j &= -[\bar{k}] x_{1,k}^j - [\bar{c}] \bar{x}_{2,k}^j \\ &+ [\bar{g}] u_k^j + \bar{b} p_k^j + a p_{k-1}^j \end{aligned} \quad (24)$$

where

$$\bar{b} = b + ([\bar{c}] - \lambda[I])a. \quad (25)$$

Thus, we have again arrived at the formulation of equation (13) for sampling at multiple instants of time,

$$[C] = [Y][\hat{\Psi}][\hat{\Phi}]^{-1}$$

where, now,

$$[C] = [-[k] \quad -[\bar{c}] \quad [\bar{g}] \quad a \quad \bar{b}] \quad (26)$$

an $n/2 \times (n+m+2)$ matrix;

$$[Y] = [[I] \quad [\Lambda]], \quad a \quad n/2 \times n \text{ matrix}; \quad (27)$$

$[I]$ = the $n/2 \times n/2$ identity matrix

$$\text{and } [\Lambda] = -\lambda[I]; \quad (28)$$

$$[\hat{\Psi}] = \begin{bmatrix} -t_1 & -t_2 & \cdots & -t_{n+m+2} \\ x_{2,k-1} & x_{2,k-1} & \cdots & x_2 \\ -t_1 & -t_2 & \cdots & -t_{n+m+2} \\ x_{2,k} & x_{2,k} & \cdots & x_{2,k} \end{bmatrix}, \quad (29)$$

an $n \times (n+m+2)$ matrix;

and

$$[\hat{\Phi}] = \begin{bmatrix} t_1 & t_2 & \cdots & t_{n+m+2} \\ x_{1,k} & x_{1,k} & \cdots & x_1 \\ -t_1 & -t_2 & \cdots & -t_{n+m+2} \\ x_{2,k} & x_{2,k} & \cdots & x_{2,k} \\ u_k & u_k & \cdots & u_k \\ p_{k-1} & p_{k-1} & \cdots & p_{k-1} \\ t_1 & t_2 & \cdots & t_{n+m+2} \\ p_k & p_k & \cdots & p_{k-1} \end{bmatrix}, \quad (30)$$

An $(n+m+2) \times (n+m+2)$ matrix.

Note that both $\bar{x}_{2,k-1}^j$ and $\bar{x}_{2,k}^j$ ($i = 1, 2, \dots, n+m+2$) are needed in (29,30), where they are obtained from $x_{1,k-2}^j$, $x_{1,k-1}^j$, and $x_{1,k}^j$ according to

$$\begin{bmatrix} [I] & [\Lambda] & [0] \\ [0] & [I] & [\Lambda] \end{bmatrix} \begin{Bmatrix} x_{1,k-2}^j \\ x_{1,k-1}^j \\ x_{1,k}^j \end{Bmatrix} = \begin{Bmatrix} -t_j \\ -t_j \\ -t_j \end{Bmatrix}, \quad (31)$$

($i = 1, 2, \dots, n+m+2$).

Finally, we note that although the initial displacement a is identified directly, the initial velocity b is not identified directly, but must be calculated from (25) when a and $[\bar{c}]$ are known.

5. Linear System Identification by a Second Order ARMA Method

The system that we wish to identify is again given by the state equations (20,21) represented by

$$\dot{x}(t) = [A] x(t) + [B] u(t). \quad (32)$$

As in [12] it is assumed that the exact input vector $u(i\Delta t)$ is available from measurements at the discrete times $t_i = i\Delta t$, where Δt is a suitably small time increment. Also, from a total

of n components of the state vector, only $n/2$ potentially noisy measurements, corresponding to the generalized displacements $\bar{x}_1(t)$, are available at the times t_i . That is,

$$\bar{z}(i) = [D] \bar{x}(i) + \text{noise}(i) \quad (33)$$

where $[D]$ is an $n/2 \times n$ output matrix given by

$$[D] = \begin{bmatrix} [I] & [0] \end{bmatrix}, \quad (34)$$

$[I]$ is the $n/2 \times n/2$ identity matrix, and (i) means $(t_i = i\Delta t)$.

Because the measurements are available at discrete times $t_i = i\Delta t$, the continuous time equation (32) is transformed to the corresponding discrete time form

$$\bar{x}(i+1) = [\bar{A}] \bar{x}(i) + [\bar{B}] u(i) \quad (35)$$

where

$$[\bar{A}] = \exp([A]\Delta t) \quad (36)$$

is the $n \times n$ state transition matrix of the identified model, and

$$[\bar{B}] = \begin{bmatrix} \Delta t \\ \int_0^{\Delta t} \exp([A]\tau) d\tau \end{bmatrix} [B]. \quad (37)$$

Equation (35) with $[\bar{B}]$ as in (37) is strictly valid only when $u(t)$ is constant and equal to $u(i)$ over the interval (t_i, t_{i+1}) . Furthermore, the identified model is obtained assuming that the structure is completely controllable and observable.

The discrete time equation (35) is now transformed into an observable canonical form. Because the system is observable, the matrix

$$[Q] = \begin{bmatrix} [D] \\ [D][A] \end{bmatrix} \quad (38)$$

is nonsingular. Defining $\bar{x}_c = [Q] \bar{x}$, the canonical form of (35) is

$$\bar{x}_c(i+1) = [\bar{A}_c] \bar{x}_c(i) + [\bar{B}_c] u(i) \quad (39)$$

where

$$\bar{x} = [Q]^{-1} \bar{x}_c, \quad (40)$$

$$[\bar{B}_c] = [Q] [\bar{B}], \quad (41)$$

and

$$[\bar{A}_c] = [Q] [\bar{A}] [Q]^{-1} = \begin{bmatrix} [0] & [I] \\ [F_2] & [F_1] \end{bmatrix}. \quad (42)$$

Then, the ARMA model

$$\begin{aligned} \bar{z}(i) &= [F_1] \bar{z}(i-1) + [F_2] \bar{z}(i-2) \\ &+ [G_1] u(i-1) + [G_2] u(i-2) \end{aligned} \quad (43)$$

is obtained, in which

$$\begin{bmatrix} [G_1] \\ [G_2] \end{bmatrix} = \begin{bmatrix} [I] & [0] \\ -[F_1] & [I] \end{bmatrix} [\bar{B}_c]. \quad (44)$$

Parameter identification methods, such as ordinary

least squares, are used to determine the ARMA model (43); i.e., to identify estimates of the matrices $[F_1]$, $[F_2]$, $[G_1]$, $[G_2]$. Then, the continuous time state equations must be determined from the ARMA model. As in [12], matrices $[A_c]$ and $[B_c]$ are evaluated from

$$[A_c] = \frac{1}{\Delta t} (\lambda n[\bar{A}_c]) \quad (45)$$

$$[B_c] = \left[\int_0^{\Delta t} \exp([A_c]\tau) d\tau \right]^{-1} [\bar{B}_c] \quad (46)$$

in which

$$\lambda n[\bar{A}_c] = \sum_{p=1}^{\infty} \frac{1}{p} (-1)^{p-1} ([\bar{A}_c] - [I])^p. \quad (47)$$

Forming the transformation matrix

$$[\bar{Q}] = \begin{bmatrix} [D] \\ [D][A_c] \end{bmatrix}, \quad (48)$$

the state matrices of the system are given by

$$[A] = [\bar{Q}] [A_c] [\bar{Q}]^{-1} \quad (49)$$

$$[B] = [\bar{Q}] [B_c]. \quad (50)$$

6. Discussion of Numerical Experiments

We have studied two systems. The first is a simple single degree of freedom (1DOF) oscillator governed by the equation of motion

$$\ddot{x}(t) + \dot{x}(t) + 10 x(t) = 5 u(t), \quad t > 0 \quad (51)$$

$$x(0) = 1, \quad \dot{x}(0) = 2. \quad (52)$$

The matrix to be identified by PMF, then, is

$$[C] = \begin{bmatrix} 0 & 1 & 0 & 1 \\ -10 & -1 & 5 & 2 \end{bmatrix} \quad (54)$$

which includes the system matrix in the first two columns, and the input vector and initial conditions in the third and fourth columns, respectively.

The second is a three degree of freedom (3DOF) system with equations of motion given by

$$[m]\ddot{x}(t) + [c]\dot{x}(t) + [k]x(t) = g u(t), \quad t > 0 \quad (55)$$

$$\ddot{x}(0) = 0, \quad \dot{x}(0) = 1, \quad (56)$$

where

$$[m] = [I], \quad \text{a } 3 \times 3 \text{ identity matrix;} \quad (57)$$

$$[c] = .10 [I], \quad (58)$$

$$[k] = \begin{bmatrix} 96 & -48 & 0 \\ -48 & 96 & -48 \\ 0 & -48 & 48 \end{bmatrix}, \quad \text{and} \quad (59)$$

$$g^T = \begin{bmatrix} 1 & 2 & 1 \end{bmatrix}. \quad (60)$$

The matrix to be identified by PMF is

$$[C] = \begin{bmatrix} 0 & 0 & 0 & 1 & 0 & 0 & 0 & 0 \\ 0 & 0 & 0 & 0 & 1 & 0 & 0 & 0 \\ 0 & 0 & 0 & 0 & 0 & 1 & 0 & 0 \\ -96 & 48 & 0 & -.10 & 0 & 0 & 1 & 1 \\ 48 & -96 & 48 & 0 & -.10 & 0 & 2 & 1 \\ 0 & 48 & -48 & 0 & 0 & -.10 & 1 & 1 \end{bmatrix} \quad (61)$$

The free vibration characteristics of both systems are given in Table 1 in which ϕ_i is the i^{th} normalized eigenvector. We note that the ARMA algorithm does not provide identification of the initial conditions, and thus the last column of (54) and (61) will be omitted in the comparison of the two methods.

The PMF algorithm was implemented on the Control Data Corp. Cyber 175 at the University of Illinois. The equations of motion were solved analytically assuming $u(t)$ to be $\sin 4\pi t$. The peak response of each state was determined, and provision was made for adding zero mean Gaussian noise as a percentage of peak response to each state as well as the input. Zero mean Gaussian noise was obtained by using IMSL routine GGUBF3 [14]. As the fully observable, fully determined, multiple time formulation was used exclusively in this analysis, PMF's were computed numerically at four equally spaced times for the 1DOF system and eight equally spaced times for the 3DOF system, the times being equally spaced over one second. Numerical integrations of the analytical data plus noise were performed using IMSL routine DCADRE [14] to simulate implementation of the analog Poisson filter chain. Finally, the identified matrix was determined using IMSL routine OFIMAS to solve the ordinary least squares problem given by equation (16), although a simple Gauss elimination routine would have sufficed as the systems studied were fully determined.

Numerical experiments were conducted on both systems, where the additive noise component of the process signals were assigned values of 0, 10, 50 and 100% of the peak noise-free values. In all cases, the maximum moment, given by the parameter k , was set equal to one; and the parameter λ was also set equal to one.

The ARMA algorithm was also implemented on the CYBER 175. Data was generated at equal time intervals from the known excitation, $\sin 4\pi t$, and analytical solutions for the system states. To the states was added a zero mean Gaussian noise component as a percent of peak, as in the PMF analysis. Two sets of data were generated and analyzed for each of the four noise levels described in the previous section and each of the two systems. These corresponded to time increments Δt of .04, and .01 seconds, respectively, over a full sample of 1.0 second. Again, IMSL routine OFIMAS was used to solve the ordinary least squares problem, yielding the unknown matrices $[F_1]$, $[F_2]$, $[G_1]$, and $[G_2]$, from which the continuous time state equations were reconstructed.

For both the PMF and ARMA methods, the identification error was defined by [13]

$$\text{ERROR} = \frac{\| [C]_{\text{exact}} - [C]_{\text{identified}} \|_F}{\| [C]_{\text{exact}} \|_F} \quad (62)$$

where $\| \cdot \|_F$ denotes the Frobenius matrix norm [13].

7. Results and Conclusions

The results of the PMF analyses are given in Table 2. Several conclusions can be drawn from the data. First and foremost is that identification is nearly perfect and is impervious to zero mean additive noise in the input and output signals, even at levels significantly greater than those tabulated. This was also found to be true for arbitrary $\lambda > 0$ and for a maximum value of $k > 1$, although as stated earlier, large k may lead to numerical difficulties. The second conclusion is that the ordinary least square formulation of equation (16) is not required in the presence of zero mean additive noise, as the data attests. Rather, the fully determined formulation of equation (13) provides adequate accuracy.

In similar studies performed by Saha and Prasada Rao (5) and Sivakumar and Prasada Rao (9), the presence of zero mean additive noise severely degraded the quality of the identification, leading to Kalman filtering of the process signals. This phenomenon, we now believe, is due to the use of Simpson's rule to perform the integrations necessary to compute the PMF's. As the moments can be defined as the response of a Poisson filter chain, the integrations are ideally performed in an analog medium. The use of digital multistep methods, such as Simpson's rule, produces sufficient propagative errors to render the method unattractive.

The results of the ARMA analysis are given in Table 3. It is apparent that the ordinary least squares solution, although biased, provides excellent identification in a noise free environment, even when sampled data is sparse. However, in the presence of zero mean additive noise, the identification error is significant, especially when compared with comparable PMF results. We expect that instrumental variable or maximum likelihood [12] estimation of the ARMA model would improve these results considerably, although with a comparable increase in computational complexity.

While the error of (62) as presented in Tables 2 and 3 is indicative, it is also demonstrative to present the actually identified matrices. We do this in Table 4 for only the 1DOF system and 10% noise. Here, the Frobenius error indicates the order of magnitude of the error in each matrix entry.

Finally, we would like to comment on the relative computational efficiency of the PMF and ARMA algorithms. Because the PMF's can be easily computed by analog means, when they are available to insert in the operational matrices at the start of the algorithm, identification requires only inversion of a $n+m+1$ dimensional matrix and simple matrix multiplication. On the other hand, ARMA requires a least squares solution of an $(n + 2m) \times (\text{no. of samples})$ matrix followed by transformation from discrete to continuous time. This fact, plus the inability to effectively accommodate zero mean additive noise without

additional computation, makes the PMF method of system identification for linear time invariant systems significantly more attractive than the ARMA method.

References

- [1] F. W. Fairman and D. W. C. Shen, "Parameter Identification For Linear Time Varying Dynamic Processes," Proceedings of the Institute of Electrical Engineers, vol. 117, pp. 2025-2029, Oct. 1970.
- [2] F. W. Fairman and D. W. C. Shen, "Parameter Identification For a Class of Distributed Systems," Proceedings of the Institute of Electrical Engineers, vol. 11, pp. 929-940, 1970.
- [3] F. W. Fairman, "Parameter Identification For a Class of Multivariable Non-linear Processes," International Journal of Systems Science, vol. 1(3), pp. 291-296, 1971.
- [4] D. C. Saha and G. Prasada Rao, "Time Domain Synthesis Via Poisson Moment Functionals," International Journal of Control, vol. 30(3), pp. 417-426, 1979.
- [5] D. C. Saha and G. Prasada Rao, "Identification of Lumped Linear Systems in the Presence of Unknown Initial Conditions Via Poisson Moment Functionals," International Journal of Control, vol. 31(4), pp. 637-644, 1980.
- [6] D. C. Saha and G. Prasada Rao, "Identification of Lumped Linear Time-Varying Parameter Systems Via Poisson Moment Functionals," International Journal of Control, vol. 32(4), pp. 709-721, 1980.
- [7] D. C. Saha and G. Prasada Rao, "Identification of Lumped Linear Systems in the Presence of Small Unknown Delays -- the Poisson Moment Functional Approach," International Journal of Control, vol. 33(5), pp. 945-951, 1981.
- [8] D. C. Saha and G. Prasada Rao, "A General Algorithm For Parameter Identification in Lumped Continuous Systems -- the Poisson Moment Functional Approach," IEEE Transactions in Automatic Control, vol. AC-27(1), pp. 223-225, Feb. 1982.
- [9] L. Sivakumar and G. Prasada Rao, "Parameter Identification in Lumped Linear Continuous Systems in a Noisy Environment Via Kalman-Filtered Poisson Moment Functionals," International Journal of Control, vol. 35(3), pp. 509-519, 1982.
- [10] L. A. Bergman and A. L. Hale, "Linear System Identification Via Poisson Moment Functionals," to appear in the AIAA Journal.

- [11] A. L. Hale and L. A. Bergman, "The Dynamic Synthesis of General Nonconservative Structures From Separately Identified Substructure Models," presented as AIAA Paper No. 83-0879 at the 24th AIAA Structures, Structural Dynamics, and Materials Conference, Lake Tahoe, NV, May 2-4, 1983.
- [12] M. Shinozuka, C.-B. Yun, and H. Imai, "Identification of Linear Structural Dynamic Systems," ASCE Journal of the Engineering Mechanics Division, vol. 108(6), pp. 1271-1390, 1982.
- [13] G. W. Stewart, Introduction to Matrix Computations, Academic Press, 1973.
- [14] IMSL, Inc., the IMSL Subroutine Library.

System	Mode	f, Hz	ζ	ϕ_i
1DOF	1	.503	.158	1.0
3DOF	1	.629	.0795	.328
				.591
				.737
	2	1.764	.0283	.737
				.328
				.591
	3	2.548	.0196	.591
				.737
				.328

Table 1

Free Vibration of the Example Systems

System	% Noise	Ident. Error
100F	0	7.49171396E-7
	10	7.49192418E-7
	50	7.49293580E-7
	100	7.49293580E-7
300F	0	1.89424238E-5
	10	2.10782882E-5
	50	2.09945823E-5
	100	1.87680145E-5

Table 2

PMF Identification Error as a Function of Zero Mean Additive Noise;
 $\lambda = 1$, $k = 1$; one second of data.

<u>System</u>	<u>% Noise</u>	<u>Ident. Error</u>	
		<u>No. or Records</u>	
		<u>25</u>	<u>100</u>
1DOF	0	8.68509727E-13	2.48952423E-10
	10	2.95502623E-03	1.23125340E-02
	50	1.46730854E-02	5.97148086E-02
	100	2.90896470E-02	1.14834761E-01
300F	0	5.97716927E-08	2.72252295E-07
	10	1.08191218E-01	4.68912816E-01
	50	4.33527720E-01	8.85997354E-01
	100	6.52983692E-01	9.52061891E-01

Table 3

ARMA Identification Error as a Function
of Zero Mean Additive Noise and Number
of Records; one second of data.

PMF

$$[A] = \begin{bmatrix} 2.446165E-08 & 1.000000E+00 \\ -1.000000E+01 & -1.000000E+00 \end{bmatrix},$$

$$[B] = \begin{bmatrix} 1.928472E-07 \\ 4.999991E+00 \end{bmatrix}$$

ARMA

$$[A] = \begin{bmatrix} 8.077936E-27 & 1.000000E+00 \\ -1.003216E+01 & -1.007923E+00 \end{bmatrix},$$

$$[B] = \begin{bmatrix} 9.925720E-02 \\ 4.790323E+00 \end{bmatrix}$$

Table 4

Identified Coefficient Matrices for 1DOF System
and 10% noise; $k = 1$, $\lambda = 1$ for PMF;
25 records for ARMA.

K.W. Lips* and F.R. Vigneron*
Department of Communications
Communications Research Centre
Ottawa, Canada

Abstract

The report demonstrates a method for calculation of system damping factors that is based on solving the 'general' eigenvalue problem for the motion equations, given component data as the base input information. The method exhibits no computational difficulties and is confirmed by comparison to approximate results based on the Method of Averaging. The method is applied to the Hermes spacecraft, a configuration which consists of a central rigid body, two flexible solar array substructures, a momentum wheel and a liquid mercury damping device. The synthesized modal damping values for the structural modes vary relative to those measured in orbit by factors ranging from zero to five.

Principal Symbols

d_1, d_2	offset of damper from system center of mass, Fig. 1(c)
$\{F\}$	forcing function applied to roll/yaw state vector, Eq. (6b)
h_0	momentum wheel bias vector
I_{ij}	system mass moment of inertia about xyz axes
IP, OOP	in-plane, out-of-plane
$M_\epsilon, K_\epsilon, C_\epsilon$	substructure mass, stiffness and damping matrix associated with coordinates $\epsilon=U, W$ and $\bar{\alpha}$; Eqs. (7)
O_i	base of array and origin of local array reference frame, Fig. 1(b)
Q_k	mode shape for kth 'constrained' mode
R_2, R_3	offset of O_i relative to undeformed spacecraft center of mass, Fig. 1(a)
$s(), c()$	sine (), cosine ()
$\{S_1\}, \{S_3\}$	integrals of assumed mode shape functions, combined as in Eqs. (7d)-(7f)
u_i, w_i, α_i	in-plane (x_i), out-of-plane (z_i) and twist
$U_i, W_i, \bar{\alpha}_i$	deformations and associated time dependent coordinates for ith array, Fig. 1(b)
x_i, y_i, z_i	local appendage coordinates with origin at O_i , Fig. 1(b)

ζ_k, ω_k	equivalent linear viscous damping ratio and frequency of kth 'unconstrained' mode
λ_k	kth eigenvalue, Eq. (8)
σ_k, ρ_k	equivalent linear viscous damping ratio and frequency of kth 'constrained' mode
$\{\psi\}, \{\phi\}, \{\Lambda\}$	set of shape functions assumed for in-plane, out-of-plane and twist deformations
ω_0	nominal orbital angular velocity of spacecraft center of mass
$\{\}, \{\}$	column matrix, square matrix

All damping factors are negative, but only magnitudes are presented. It is common to relax matrix notation using the symbol without an identifying bracket.

Introduction

It is generally recognized that improvement is needed in methods for forecasting the damping characteristics of spacecraft structures in orbit. The need for improvement stems from the current trend towards spacecraft that are so large and flexible that conventional laboratory measurement of structural properties of the completely-assembled spacecraft is not possible.

A method of synthesizing damping that is straightforward in principle is: (i) establish a mathematical model that includes damping for each substructure and main component, by ground test and/or analysis; (ii) mathematically assemble the sub-models into an overall structural model of the spacecraft; (iii) derive modal damping factors, modal frequencies and mode shapes from the overall model by eigenproblem analysis. The method is, of course, an extension of standard practice for calculating modal frequencies and mode shapes for situations where damping can be ignored. With damping included in the procedure, a number of practical difficulties are encountered. Tractable models of damping of the subparts are difficult to establish and are often unreliable. This is particularly true for material damping in members, for components with unrestrained fluids, and for connections between structures. Differences between gravitational, thermal and vacuum conditions in orbit and on the ground add complication and

* Research Scientist, Member AIAA

uncertainty to the process. Inadvertent omission of damping sources is a potential problem as well. Truncation of modes and off-diagonal damping matrix terms can also contribute errors. There are few documented case studies where damping factors synthesized by this type of method are compared to measured results, and hence the degree to which this type of method is successful, and the limitations, are not yet very well established. References 1-4 and associated cited works are among the recent contributions to damping synthesis.

In Reference 3, a method of the above-described type is applied using ground test data and compared with some of the flight results from the Hermes satellite*. In many cases, the in-orbit measured values are higher than the calculated ones by a factor of 2 or 3. Between 1976 and the end of the mission in 1980, a great deal more flight data was acquired from Hermes. This data confirms the original measurements reported in Reference 3 and establishes that the damping values are essentially constant with time. In addition, measurements for several more flexible modes are made⁵⁻⁷. Damping information on the nutational mode⁸, with momentum wheel spinning⁹ and despun⁹, is also obtained.

In this paper, the synthesis method outlined above is applied to a case study of in-orbit damping characteristics of the Hermes spacecraft in the 3-axis stabilized state. As well as damping, the system possesses gyroscopic stiffness. The extent to which damping in the solar array substructure and the liquid mercury damper can be related to damping in the overall spacecraft is investigated. Of particular interest is the source of damping for the nutational mode. Approximate functional relationships between component damping factors and damping of the nutational mode, based on the Method of Averaging, are used to validate the calculations associated with the eigenvalue analysis. Flight Derived modal data for the Hermes is updated, summarized and then compared with the synthesized results.

System Model

Configuration

The spacecraft consists of a central rigid body, two flexible solar arrays, a liquid mercury damper and a momentum wheel, configured as shown in Fig. 1. The reference frame (0xyz) is attached to the central rigid body, with 0 at the nominal system mass center (without deformation) of the total configuration. The arrays rotate about the 0y axis

* Also known as the Communications Technology Satellite (CTS).

together and nominally track the sun. The central body nominally tracks the earth. The angle between the arrays and the central body is denoted by γ , and its rate is maintained constant at one revolution per day by a drive and track mechanism. $(0_C, \underline{1}, \underline{2}, \underline{3})$ is an orthogonal orbiting reference frame with origin fixed at the instantaneous mass center O_C , $\underline{1}$ aligned along the tangent to the trajectory in the direction of motion, $\underline{2}$ parallel to the orbit normal and $\underline{3}$ pointing inward along the local vertical towards the center of the earth. The frame is thus rotating about the oz axis at the negative of the orbit rate $(-\omega_0)$.

Satellite attitude motion is defined by Eulerian rotations ϕ (roll), θ (pitch), ψ (yaw) of body-fixed frame (0, x, y, z) with respect to the orbit frame $(0_C, \underline{1}, \underline{2}, \underline{3})$. The central body rotates relative to inertial space with rates $(\omega_1, \omega_2, \omega_3)$, which in turn are related to pitch, roll and yaw rates, to linear order, by

$$\begin{aligned} \omega_1 &= \dot{\phi} - \omega_0 \psi; & \omega_2 &= \dot{\theta} - \omega_0; \\ \omega_3 &= \dot{\psi} + \omega_0 \phi. \end{aligned} \quad (1)$$

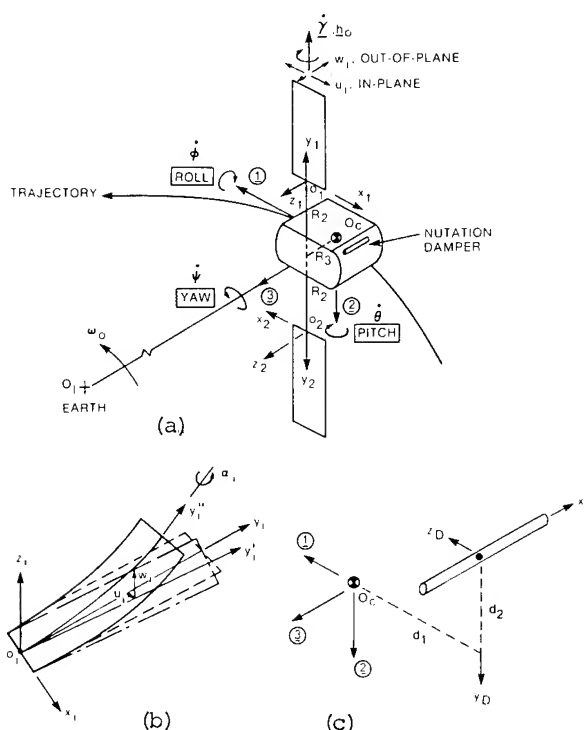


Fig. 1 Schematic for the Hermes class of spacecraft: (a) overall configuration; (b) array coordinates; (c) offset and coordinates of liquid mercury damper.

Component Models

Momentum Wheel The momentum wheel is assumed to spin at constant speed, relative to the central body, and to be aligned so that its angular momentum vector h_0 points in the negative Oy direction.

Liquid Mercury Damper The damper is a cylindrically-shaped tube partially filled with mercury and aligned parallel to the pre-deployment spin axis, as is depicted schematically in Fig. 1. Detailed modelling of in-orbit performance is not straight-forward, and further it is difficult to verify by ground test because of Earth gravity effects. Both geometric parameters (size, orientation and offset with respect to center of mass) and dynamic parameters (mass, natural frequency, energy dissipation rate, spin rate, gravitational field) play a role in determining the damper's performance.

Originally, the Hermes damper was designed for the specific purpose of damping out the nutation associated with the spin-stabilized phase (before deployment of the arrays and start up of the momentum wheel). It was tuned to provide a maximum damping effect at about a 0.40 Hz nutation. Flight data available for this phase indicates that the nutational mode had damping ratios ranging from 0.001 to 0.007.⁸

For the spacecraft in the 3-axis stabilized phase with arrays fully deployed the damper will be excited by roll/yaw nutation, pitch axis librations, and by symmetric and anti-symmetric array vibrations. Specifically, the spacecraft motion here consists of a combination of a slow rotation about pitch (once in 24 hours), a small low frequency nutation (0.2° at 2.77×10^{-3} Hz), and flexing of the various structural modes (at 0.15 Hz and higher). Relation of the damper's operation in this dynamic environment to earth-based test or spin phase operation is not entirely clear. In orbit, centrifugal and gravitational forces acting on the mercury are in equilibrium hence, surface tension effects can be expected to cause the mercury to form into a single slug. It is possible, for example, that the liquid mercury damper will function as a ball-in-tube type damper, resonant at all times with the rate of nutation. Due to the uncertainties and complexities associated with the fluid behaviour, the approach adopted herein is to model the damper as a single degree of freedom translational mass-spring-dashpot device located as in Fig. 1. The mass (m_D) is the actual mass of the mercury and is assumed to be a slug in equilibrium at $(-d_1, -d_2)$ in $(0xyz)$, and the dashpot and spring parameters (c_D and k_D) are selectable to

match desired damper energy dissipation and resonance characteristics. Although the c_D and k_D cannot be obtained with certainty for Hermes, by varying these parameters the range of possible influence of the damper on the spacecraft can be established. Such a representation is common in the literature.¹⁰ With the nutation damper fixed in space, the kinetic, potential and dissipation functions are, respectively:

$$\frac{1}{2}m_D\dot{x}_D^2; \quad \frac{1}{2}k_Dx_D^2; \quad \frac{1}{2}c_D\dot{x}_D^2. \quad (2)$$

Solar Array Substructures Each solar array substructure is described in the overall system model by specifying its fixed-base (constrained) modal data; namely, modal frequencies (Ω 's), shapes (Q 's) and damping factors (σ 's). The analytic structural model for determining modal frequency and mode shape assumes that deformations are discretized in the spirit of the Rayleigh-Ritz method and is described in detail in Ref. 11. The related computer software has been extended to calculate the modal integral coefficients required in the system dynamics. A comparison of these coefficients (Table 3 of Ref. 8) and the generalized mass data indicates that the fundamental mode is dominant, thus ensuring that truncation to the first few modes will be valid.

Unlike modal frequencies and shapes, damping factors cannot be obtained using analysis only. Neither can they be measured directly in ground test, due to the difference between gravitational effects on the ground and in-orbit. Consequently a combination of one-g test data and one-g to zero-g conversion analysis can be tried, such as that done prior to the launch of Hermes (Table 1).

Table 1 Modal frequency and damping factors for the fixed-base (constrained) Hermes array³ as determined using ground test and adjusted by analysis to $g=0$

MODE	FREQUENCY	DAMPING RATIO
<u>Out-of-plane</u>		
1	0.16	0.003* - 0.006**
2	0.51	0.008 - 0.012 ⁺
<u>In-plane</u>		
1	0.32	0.014 - 0.020
<u>Twist</u>		
1	0.15	0.090 - 0.160
2	0.50	0.013 - 0.022

* based on 'hysteretic' damping law

** based on 'viscous' damping law

+ constructed using Table 1 of Reference 3

Using the Model of Ref. 1, mode shapes and modal frequencies for the one-g state are obtained by solving the undamped eigenvalue problem. Experimentally measured modal frequencies and modal damping factors are also determined in ground tests. Then the analytical model and ground test results are brought into agreement by appropriate adjustments to the analytical model.⁶ In turn, this model is then used to calculate in-orbit modal frequencies and shapes by setting g equal to zero.^{3,6}

Based on the above formulation the kinetic, potential and linear viscous dissipation functions are, respectively, for the north (1) array:

$$\frac{1}{2} \dot{U}_1^T M_U \dot{U}_1 + \frac{1}{2} \dot{W}_1^T M_W \dot{W}_1 + \frac{1}{2} \dot{\alpha}_1^T J_{\alpha} \dot{\alpha}_1 ; \quad (3a)$$

$$\frac{1}{2} U_1^T K_U U_1 + \frac{1}{2} W_1^T K_W W_1 + \frac{1}{2} \alpha_1^T G_{\alpha} \alpha_1 ; \quad (3b)$$

$$\frac{1}{2} U_1^T C_U \dot{U}_1 + \frac{1}{2} W_1^T C_W \dot{W}_1 + \frac{1}{2} \alpha_1^T C_{\alpha} \dot{\alpha}_1 . \quad (3c)$$

It is convenient to transform to 'symmetric' and 'antisymmetric' coordinates. For example for the in-plane degrees of freedom:

$$U_S = \frac{1}{2}(U_1 - U_2); \quad U_a = \frac{1}{2}(U_1 + U_2) . \quad (4)$$

Equations of Motion

Second order equations governing the attitude motion (pitch, roll, yaw) and array vibrations for the Hermes type of configuration of Fig. 1(a), just described, are well documented.^{12, 13} In absence of a damper, symmetries inherent in the configuration serve to uncouple dynamics of pitch from roll/yaw. As well, symmetric array oscillations interact with pitch only and vice versa. Similarly roll/yaw degrees of freedom interact only with antisymmetric bending vibrations and vice versa. This paper extends the above representation to account for the liquid mercury damper. With the damper included, roll/yaw and pitch are, in general, coupled. If offset d_1 is nonzero and offset d_2 is zero, the damper couples to pitch but not roll/yaw, if d_1 is zero and d_2 is nonzero the damper couples to roll/yaw, but not to pitch. To aid in isolating the effect of the damper, this study is confined to these bounding cases. The complete second order system equations for this case are contained in Ref. 8.

Following the approach outlined in Ref. 14, which is similar to that of Ref. 15, the equations are transformed

to a first order set through introduction of a state vector made up of generalized displacement and generalized velocity. By choosing a suitable constraint between generalized velocity and displacement, system matrices are rendered symmetric, or skew symmetric. Algebraic manipulation is used to avoid use of complex numbers when generating response from the resulting eigenvalue problem and its adjoint. Once system eigenvalues and eigenvectors are known, response depends on the solution of coupled, real-valued, scalar, first order equations. For the roll/yaw dynamics, the state vector chosen is,

$$\{z\} = \{\omega_1 \quad \omega_3 \quad U_a^T W_a^T \dot{x}_D \quad U_a^T W_a^T x_D\}^T. \quad (5)$$

The transformed equations then take on the form:

$$[A] \{\dot{z}\} + [B] \{z\} = \{F\} ; \quad (6a)$$

where:

$$\{F\} = \{L_1 \quad L_3 \quad 0 \quad 0 \quad 0 \quad 0 \quad 0\}^T ; \quad (6b)$$

$$[A] = \begin{bmatrix} I_{11} & I_{13} & -2s_Y S_1^T & -2c_Y S_1^T & -m_D d_2 & 0 & 0 & 0 \\ I_{13} & I_{33} & -2c_Y S_1^T & 2s_Y S_1^T & 0 & 0 & 0 & 0 \\ -2s_Y S_1 & -2c_Y S_1 & 2M_U & 0 & 0 & 0 & 0 & 0 \\ -2c_Y S_3 & 2s_Y S_3 & 0 & 2M_W & 0 & 0 & 0 & 0 \\ -m_D d_2 & 0 & 0 & 0 & m_D & 0 & 0 & 0 \\ 0 & 0 & 0 & 0 & 0 & 2K_U & 0 & 0 \\ 0 & 0 & 0 & 0 & 0 & 0 & 2K_W & 0 \\ 0 & 0 & 0 & 0 & 0 & 0 & 0 & k_D \end{bmatrix} ; \quad (6c)$$

$$[B] = \begin{bmatrix} 0 & h_0 & 0 & 0 & 0 & 0 & 0 & 0 \\ -h_0 & 0 & 0 & 0 & 0 & 0 & 0 & 0 \\ 0 & 0 & 2C_U & 0 & 0 & 2K_U & 0 & 0 \\ 0 & 0 & 0 & 2C_W & 0 & 0 & 2K_W & 0 \\ 0 & 0 & 0 & 0 & c_D & 0 & 0 & k_D \\ 0 & 0 & -2K_U & 0 & 0 & 0 & 0 & 0 \\ 0 & 0 & 0 & -2K_W & 0 & 0 & 0 & 0 \\ 0 & 0 & 0 & 0 & -k_D & 0 & 0 & 0 \end{bmatrix} . \quad (6d)$$

Also,

$$M_U = \int \Psi \Psi^T dm; \quad M_W = \int \Phi \Phi^T dm; \quad (7a)$$

$$K_U = \Omega_U^2 M_U; \quad K_W = \Omega_W^2 M_W ; \quad (7b)$$

$$C_U = 2M_U \Omega_U \sigma_U; \quad C_W = 2M_W \Omega_W \sigma_W ; \quad (7c)$$

$$B_1 = \int Y \Psi dm; \quad B_3 = \int Y \Phi dm ; \quad (7d)$$

$$D_1 = \int \Psi dm; \quad D_3 = \int \Phi dm ; \quad (7e)$$

$$S_1 = B_1 + R_2 D_1; \quad S_2 = B_3 + R_2 D_3. \quad (7f)$$

The associated eigenvalue problem for

Eq. 6(a) is (taking $L_1 = L_3 = 0$) :

$$(\lambda_k [A] + [B]) \{X_k\} = \{0\} \quad (8)$$

The development for the symmetric pitch dynamics is analogous and the relevant equations are available in Ref. 8.

Based on this formulation, computer software is developed to solve for system natural modes, frequencies and damping factors for both the roll/yaw and the pitch dynamics. Results computed using the roll/yaw software are demonstrated for the Hermes satellite configuration of Fig. 1, in Table 2. A set of nominal input parameters are assigned which include the measured/computed modal characteristics for the constrained array, together with the spin-phase damper design characteristics ($m_D = 0.1145$ kg, $\omega_D = 0.40$ Hz, $\sigma_D \approx 0.004$)⁸. The frequencies calculated agree quite well with those published in Refs. 5, 7 and other works, thus validating the software. No numerical or computational problems are experienced with the method.

Table 2 Unconstrained modal frequency and damping ratio computed for Hermes spacecraft using Damped Natural Modes theory.

Mode Description	Mode Number, k	Frequency ω_k , Hz	Damping Ratio, ζ_k **
(a) Pitch Dynamics			
Out-of-plane, symmetric	1	0.149	0.0061
Out-of-plane, symmetric	2	0.506	0.0060
Out-of-plane, symmetric	3	0.957	0.0060
Out-of-plane, symmetric	4	2.489	0.0060
Out-of-plane, symmetric	5*	11.600	0.0060
In-plane, symmetric	1	0.324	0.0153
In-plane, symmetric	2	3.268	0.0150
In-plane, symmetric	3*	19.270	0.0150
Twist, symmetric	1	0.144	0.0909
Twist, symmetric	2	0.493	0.0909
Twist, symmetric	3*	0.925	0.0909
Damper	-	0.400	0.0040
(b) Roll/Yaw Dynamics			
Nutation	-	0.00277	4×10^{-8}
Damper	-	0.400	0.0043
Out-of-plane, Antisymmetric	1	0.444	0.0173
Out-of-plane, Antisymmetric	2	0.509	0.0066
Out-of-plane, Antisymmetric	3	0.970	0.0063
Out-of-plane, Antisymmetric	4	2.542	0.0060
Out-of-plane, Antisymmetric	5*	12.165	0.0060
In-plane, Antisymmetric	1	0.851	0.0393
In-plane, Antisymmetric	2	3.319	0.0155
In-plane, Antisymmetric	3*	19.300	0.0150

* Modes are not accurate, due to limitations of the Rayleigh-Ritz method used.

** Based on input damping ratios of 0.006 out-of-plane, 0.015 in-plane and 0.090 in twist for the constrained array substructure (Table 1) and a nominal value of 0.004 for the damper.

Update of Measured Hermes Data

Measurements of natural frequency and damping factor for the vibrational

modes of the Hermes satellite are reported in Refs. 3, 5, 7 and other unpublished internal reports. The in-orbit data is derived from residual oscillations associated with array deployment and slewing, and from specially-implemented excitation by the thrusters (SPEX). Damping factors are deduced from the decay envelope of free vibration (log decrement method) and from the sharpness given by the Fourier transform of the vibrational data.

To obtain a single and updated consistent set of in-orbit values, both published and unpublished data were reviewed. Table 3 summarizes the results. For most modes reported, the accelerometer data from which the results are deduced is of excellent quality, and the confidence level in the measurements is rated high. For the second out-of-plane antisymmetric mode, the accelerometer data is of lower quality and the confidence level is rated medium.

Table 3 Modal frequency and damping ratio as measured in-orbit on Hermes.

Mode Number	γ RAD	Description of Mode	ω_k (Hz)	ζ_k
Nutation		Roll/Yaw	0.00293	0.00015
1	0	Out-of-Plane, Symmetric	0.150	0.030-0.038
1	0	Out-of-Plane, Antisymmetric	0.440	0.015-0.022
2	0	Out-of-Plane, Antisymmetric	0.500	0.007-0.008
1	0	In-Plane, Symmetric	0.300	0.030-0.039
1	0	In-Plane, Antisymmetric	0.820	0.012-0.016
1	$\pi/2$	In-Plane, Antisymmetric	0.980	
2	0	In-Plane, Antisymmetric	0.890	
1	0	Twist, Symmetric	0.130	0.080-0.090
2	0	Twist, Symmetric	0.460	

Late in the mission, an in-orbit dynamics test was carried out to establish the characteristics of nutation in the 3-axis stabilized model. A nutation cone of one degree was initiated, the thrusters were inhibited, and the satellite was allowed to nutate without disturbance for 12 hours. Data from the tests are reproduced in Fig. 2. The nutation period and damping ratio are measured to be 341 seconds and 1.5×10^{-4} , respectively (entered in Table 3). Good agreement exists between the measured and calculated nutation frequencies.

Parametric Assessment of Component Damping Effect

There exists a degree of uncertainty as to what level of damping to use for the components once in orbit. Whereas damper mass and offsets are well known,

σ_D and Ω_D are not. Similarly, in the modal representation for the array, the exact level of damping associated with each mode and the effect of mode truncation are not known with confidence. By first isolating and then varying these parameters, their range of possible influence on the spacecraft can be determined. For the case of the damper this includes varying, not just damping, but frequency as well in order to simulate resonance with either the array vibration or nutation. A special case for the arrays involves determining the effect of critical damping in the constrained mode input. This knowledge of system sensitivity to inputs at the component level is helpful in understanding the flight-derived data.

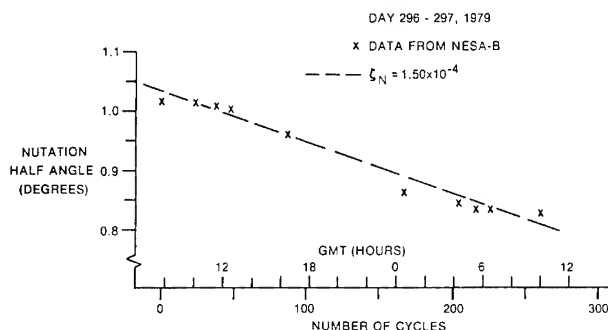


Fig. 2 Orbital data reflecting nutational decay of Hermes with arrays fully deployed.

Role of the Array Substructure

To establish the degree to which damping factors measured in orbit can be attributed to damping sources in the arrays, σ_D is set equal to zero and computer runs are made using, for damping input, those values as determined from the ground-based substructure test results of Table 1, along with variations as adopted in Table 4.

It is seen, from Table 4, that the inherent damping of the arrays has little influence on damping of the system nutation. Input modal damping parameters σ_k associated with the substructure are varied between 0.001 and 0.100. Over this range, when the damping occurs in-plane only, then a nutation damping of $\zeta_N = 5 \times 10^{-10}$ and 5×10^{-8} , respectively, results (i.e., ζ_N is proportional to σ_k , I_P). On the other hand, input damping associated with array out-of-plane motions only is seen to have an effect an order of magnitude greater which, however, is still not significant when compared with the measured level of $\zeta_N = 1.5 \times 10^{-4}$. The overall effect on ζ_N is no greater when in-plane, out-of-plane inputs are combined. Also, using input damping ratios consistent with typical ground-based array measurements still results in an insignificant effect on the nutation, that is $\zeta_N \approx 5 \times 10^{-8}$, in this case.

Table 4 also provides information about the relationship between damping ratio for unconstrained antisymmetric modes (ζ_k) and the input damping associated with the constrained arrays (σ_k). It is seen that when the substructure is damped in-plane only, then system damping is greatest in-plane as well. The same holds true for the out-of-plane degrees of freedom. Specifically, the magnitudes of damping calculated for these modes, referred to as the 2nd and 3rd system modes in-plane or out-of plane, are very close to the levels of damping input for the 2nd and 3rd modes of the substructure. However, damping computed for the 1st modes, in each category of motion, is significantly larger than the damping input for the fundamental mode of the array only. This is consistent with the nature of the dynamic interactions occurring for

Table 4 Contribution of array substructure to damping of system roll/yaw modes.

ARRAY SUBSTRUCTURE INPUT DAMPING						OUTPUT MODAL DAMPING								
IN-PLANE			OUT-OF-PLANE			NUTATION ζ_N	IN-PLANE			OUT-OF-PLANE			DAMPER ζ_D	
σ_1	σ_2	σ_3	σ_1	σ_2	σ_3		ζ_1	ζ_2	ζ_3	ζ_1	ζ_2	ζ_3		
0.001	0.001	0.001				5×10^{-10}	2.6×10^{-3}	1×10^{-3}	1×10^{-3}	1×10^{-6}	1×10^{-7}	6×10^{-7}	1×10^{-9}	
0.100	0.100	0.100				5×10^{-8}	2.7×10^{-4}	1.04×10^{-4}	1.01×10^{-4}	1×10^{-6}	9×10^{-6}	1×10^{-5}	1×10^{-7}	
			0.001	0.001	0.001	6×10^{-9}	2×10^{-6}	7×10^{-10}	4×10^{-13}	2.9×10^{-3}	1.1×10^{-3}	1.1×10^{-3}	4×10^{-6}	
			0.100	0.100	0.100	6×10^{-7}	1×10^{-4}	7×10^{-8}	4×10^{-11}	3.1×10^{-4}	1.04×10^{-4}	1.05×10^{-4}	4×10^{-5}	
0.100	0.100	0.100	0.100	0.100	0.100	6×10^{-7}	2.7×10^{-4}	1.04×10^{-4}	3.0×10^{-4}	1.1×10^{-4}	1.04×10^{-4}	1.06×10^{-4}	4×10^{-5}	
0.020	0.020	0.020				1×10^{-8}	5.2×10^{-2}	2.1×10^{-2}	2×10^{-2}	2×10^{-5}	2×10^{-6}	1×10^{-5}	2×10^{-8}	
0.020	0.020	0.020	0.006	0.006	0.006	5×10^{-8}	5.2×10^{-2}	2.1×10^{-2}	2×10^{-2}	1.7×10^{-2}	6.6×10^{-3}	6.6×10^{-3}	2×10^{-5}	
0.020	0.020	0.020	0.006	0.010		5×10^{-8}	5.2×10^{-2}	4×10^{-4}	6×10^{-6}	1.7×10^{-2}	1×10^{-2}	3×10^{-4}	2×10^{-4}	
0.020	0.020	0.020	0.006	0.010	1.0	5×10^{-8}	5.2×10^{-2}	4×10^{-4}	6×10^{-6}	1.9×10^{-2}	1×10^{-2}	3×10^{-4}	2×10^{-5}	
0.020	0.020	0.020				6×10^{-9}	5.2×10^{-2}	2.1×10^{-2}	2×10^{-2}	2×10^{-5}	2×10^{-6}	1×10^{-5}	5×10^{-9}	
1.0	1.0	1.0				3×10^{-7}	1	6×10^{-3}	3×10^{-4}	8×10^{-5}	4×10^{-6}	2×10^{-6}	2×10^{-7}	
	1.0	1.0				1×10^{-12}	4×10^{-4}	1	1×10^{-5}	4×10^{-9}	1×10^{-9}	2×10^{-7}	1×10^{-14}	
1.0	1.0	1.0				3×10^{-7}	1	0.98*	1	8×10^{-5}	4×10^{-6}	2×10^{-6}	2×10^{-7}	

* $(\omega_2)_{IP} = 0.58$ Hz for this case.

Note: (1) $m_D = 0.1145$ kg; $\sigma_D = 0$; $d_1 = 0$; $d_2 = -0.29$ m;
(2) blank entries are zero.

this class of spacecraft and is analogous to the differences in frequencies recorded between the system and subsystem data.⁸ Note too that the presence of a nonzero out-of-plane damping input gives rise to nonzero damping ratios for unconstrained in-plane modes and vice versa (i.e. if $\sigma_{k,IP} = 0.10$ or $\sigma_{k,OOP} = 0.10$, then $\zeta_{1,OOP} = 1 \times 10^{-4}$ or $\zeta_{1,IP} = 1 \times 10^{-4}$). In a similar parametric study carried out using software developed for the pitch dynamics, it is found that modal damping of the symmetric spacecraft modes remains very close to that input for a single constrained array (within 2%).

The techniques used for measuring damping, as explained earlier, depend on having an oscillatory response. It is possible that a critically damped or overdamped substructure mode could be missed in the test results or truncated. This issue is addressed for the roll/yaw dynamics in Table 4. For example a $\sigma_k = 1.0$ for the fundamental constrained in-plane mode, yields unconstrained damping ratios for the 1st, 2nd and 3rd in-plane modes which are critical, 0.006 and 0.0003, respectively. That is, the degree of intermodal coupling in damping is slight. This is found to be the case also if the higher modes are input with critical damping. A similar situation exists for the pitch dynamics. It is implied by such behaviour that the ζ 's of spacecraft modes measured in-orbit are not sensitive to the input σ 's of those higher order, and in most instances unmeasured, modes.

Role of the Liquid Mercury Damper

To isolate the effect of the damper, input damping associated with the array substructures is set equal to zero. The approach is to then vary Ω_D and σ_D over a wide range in order to ascertain the theoretical limits for the damper's effect on spacecraft damping in-orbit.

A parametric study using the roll/yaw software yields the following results. When damper input frequency (Ω_D) is away from the nutation frequency ($\omega_N = 0.00277$ Hz), the damping factor of the system nutation remains extremely small (10^{-12}), even if damping input associated with the damper itself becomes large (e.g., $\sigma_D = 0.5$). As Ω_D approaches ω_N , the influence of the damper although still small, nevertheless, increases noticeably (i.e. for $\Omega_D = 0.0015$ Hz and $\sigma_D = 0.006$, $\zeta_N = 5 \times 10^{-8}$). If the damper component frequency is set equal to the nutation rate, a resonant condition exists and the effect on level of nutation damping is dramatic, as shown

in Fig. 3 where $\Omega_D = \omega_N$ and $10^{-5} < \sigma_D < 1$. Over this range of input, ζ_N achieves a maximum value of 9×10^{-4} which is comparable to the flight-determined level of 1.5×10^{-4} .

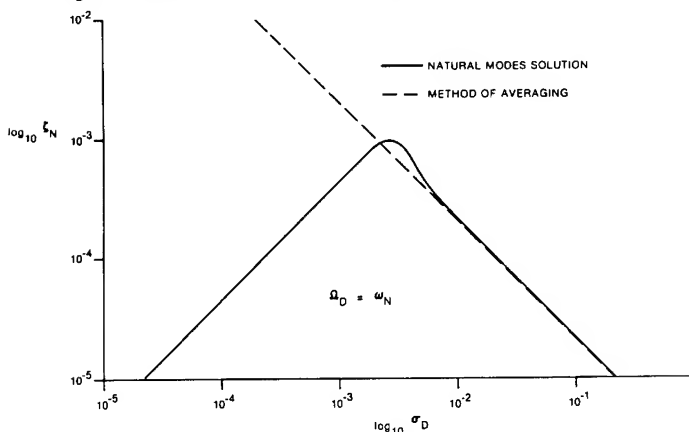


Fig. 3 Calculated nutation damping of Hermes for the case of a resonant damper.

The calculated nutation damping factors extend over at least eight orders of magnitude, thus raising concern about whether or not the software-generated data is reliable over such a wide range. For this reason, the following approximate formulas are derived by the Method of Averaging,⁸ and applied to check the software:

$$\zeta_N \approx \frac{1}{4} \left(\frac{m_D d^2}{I} \right) \left(\frac{1}{\zeta_D} \right) \text{ when } \omega_N = \omega_D; \quad (9a)$$

$$\zeta_N \approx \frac{1}{4} \left(\frac{m_D d^2}{I} \right) \left(\frac{\omega_N}{\omega_D} \right)^3 \zeta_D \text{ when } \omega_N \ll \omega_D. \quad (9b)$$

Results from the two methods are compared in Fig. 3 for the resonant case. It is seen that the Method of Averaging data yields excellent agreement with the software calculations over the range $0.001 \leq \sigma_D \leq 0.100$ and thus confirms operation of the software. Note, however, for the Method of Averaging to work the degree of interaction must be weak. The analysis of Ref. 8 (Appendix A) shows that this is not the case when the damper is very lightly damped. In particular, from Fig. 3, it is seen that the exact formulation is required when dealing with levels of damper input smaller than 10^{-3} . Away from resonance, the methods agree reasonably well. Using Eq. (9b), at $\omega_D = 0.020$ Hz and $\zeta_D = 0.005$, ζ_N becomes 3×10^{-11} and 10×10^{-11} when computed by Method of Averaging and the Natural Modes theory, respectively.

The functional relationships described by Eqs. (9) show, as well, that

damper effectiveness in increasing the ζ_N output is proportional to m_D and varies quadratically with the offset geometry d_2 . A similar set of relations applies to the effect of substructure damping input on ζ_N .

The effect of the damper on other system modes is small. With $\sigma_D = 0.5$ and damper frequencies either near or removed from the nutation resonance condition, the output damping ratios for the antisymmetric modes remain less than 10^{-6} . The only exception occurs for $\Omega_D = \omega_{1,00p} = 0.44$ Hz, where, if $\sigma_D = 0.1$, then $\zeta_{1,00p} = 2 \times 10^{-4}$, which is still considerably less than the measured value of 0.015-0.022. For the symmetric modes the greatest damper effect occurs with the damper tuned to be near resonance with the first twist mode. In this case a maximum damping ratio of only 10^{-5} is found for the fundamental twist mode over the input range $0.001 \leq \sigma_D \leq 0.100$, significantly less than the flight-measured value of 0.08 - 0.09.

In summary, it can be concluded that: (a) the liquid mercury damper could have contributed the damping of the nutational mode, but to do so the fluid would have had to be excited to resonance by the nutations; (b) the damper did not contribute significantly to the damping factors of either the symmetric or antisymmetric vibrational modes.

Correlation of Computed and Flight-Derived Modal Damping

In Table 5 damping factors measured in orbit are compared to corresponding ones synthesized from substructure component damping. The damper is not included in this comparison as its influence has already been discussed in detail in the parameter study where it is found that only when resonant with

the nutations can it be a significant factor.

For one set of calculations the input damping adopted is the nominal ground-test-derived damping of the constrained array. The substructure modelling assumes an equivalent linear viscous modal damping process. The results computed are contained in the first data column of Table 5 and originate in Table 2. When compared with the flight-measured information, it is seen that agreement is quite good for the first and second antisymmetric out-of-plane modes and for the fundamental symmetric twist modes. The nutation, the first out-of-plane symmetric as well as first in-plane symmetric and antisymmetric modes, however, do not correlate well.

A possible reason that agreement is poor in some cases is that the viscous model put forth for array damping is inadequate. An alternative is the hysteretic model for which damping coefficient, rather than being a constant, varies inversely with the frequency. Calculations carried out using a hysteretic model and the nominal ground-based array damping input give the results contained in the second data column of Table 5. Although both nutational damping and the damping for the first antisymmetric in-plane mode compare more favourably with the measured result, there is no consistent improvement in correlation achieved with this approach.

Another attempt is made to improve the calculated result by revising the input damping factors. Since input constrained modes are very similar to the flight-measured symmetric unconstrained modes (the spacecraft central body is heavy relative to the arrays and is essentially a fixed-base in orbit), it is logical to try, as the input σ 's, the

Table 5 Measured versus calculated damping factors

Mode Description	Calculated* ζ_k ; σ from Ground-Based Data ⁺		Calculated* ζ_k ; σ derived from in orbit symmetric modes ⁺⁺		Flight Measured ζ_k (Table 3)
	Viscous	Hysteretic	Viscous	Hysteretic	
Nutation	4×10^{-8}	2×10^{-6}	2×10^{-7}	1×10^{-5}	1.5×10^{-4}
1st Symmetric, Out-of-Plane	0.0061	0.0061	0.0305	0.0305	0.030-0.038
1st Symmetric, In-Plane	0.0153	0.0163	0.0305	0.0325	0.030-0.039
1st Symmetric, Twist	0.0909	0.0977	0.0806	0.0868	0.080-0.090
1st Antisymmetric, Out-of-Plane	0.0173	0.0059	0.0872	0.0297	0.015-0.022
2nd Antisymmetric, Out-of-Plane	0.0066	0.0067	0.0328	0.0335	0.007-0.008
1st Antisymmetric, In-Plane	0.0393	0.0153	0.0788	0.0308	0.012-0.016

* Damping from Array Substructure Only, $\sigma_D = 0$. + 0.015 in-plane, 0.006 out-of-plane and 0.090 in twist.

++ 0.030 in-plane, 0.030 out-of-plane and 0.080 in twist.

corresponding flight-measured symmetric ζ 's. The runs corresponding to this concept are listed in Table 5 as well, for both a viscous and a hysteretic model. As would be expected, the ζ 's for the symmetric modes match the flight data well. However the antisymmetric modal damping correlation is considerably poorer. Again the hysteretic model does not result in any consistent improvement over the viscous prediction.

Conclusions

A Natural Modes approach is used to synthesize the component and substructure damping of a spacecraft into the system level damping factors associated with the damped gyroscopic modes. The method is seen to be systematic and to have no computational instabilities. The functional relationships between component damping factors and the damping factor for the nutational mode, as derived by the Method of Averaging, confirm the functioning of the computer software developed for the eigenvalue analysis.

The performance of the method is demonstrated by applying it to the Hermes data. All synthesized modal frequencies agree with flight data, and thus are consistent with previously reported works based on models with no damping. Ignoring the special case for nutation, the synthesized modal damping factors are found to differ relative to those measured in-orbit by factors ranging from zero to five. Also excluding the nutation mode, the source of damping for the system level modes is the structural damping of the solar array. It is the liquid mercury damper, on the other hand, that likely contributed to damping of the nutational mode.

The agreement achieved between measured and synthesized damping factors is similar to that of the few earlier published works. Shortcomings in correlation could be due to inadequacies in the law chosen to model damping of the solar arrays, or possibly, to omission of a damping source (such as friction between the substructures).

References

1. Kana, D.D., and Huzar, S., "Synthesis of Shuttle Vehicle Damping Using Substructure Test Results," J. Spacecraft and Rockets, Vol. 10, Dec. 1973, pp 790-797.
2. Hasselman, T.K., "Damping Synthesis from Substructure Tests," AIAA Journal, Vol. 13, October 1976, pp. 1409-1418.
3. Vigneron, F.R., "Ground-Test Derived and Flight Values of Damping for a Flexible Spacecraft," ESA-SP-117, Proc. Symposium on Dynamics and Control of Non-Rigid Spacecraft, Frascati, Italy, May 24-26, 1977, pp. 325-333.
4. Santini, P., Castellani, A., and Nappi, A., "An Introduction to the Problem of Dynamic Structural Damping," AGARD Report #663, January 1978.
5. Vigneron, F.R., "Dynamics, Control and Structural Flexibility Results From the Hermes Mission," in Astronautics for Peace and Human Progress, Pergamon Press, 1979, pp. 397-411.
6. Vigneron, F.R., and Hughes, P.C., "Structural Dynamics Modelling for Hermes - Modelling and Measurement," Hermes (The Communication Technology Satellite) Its Performance and Applications, Proceedings of the Royal Society of Canada, 20th Symposium, 1977, IBSNO - 920064-12-4.
7. Garg, S.C., Hughes, P.C., Millar, R.A., and Vigneron, F.R., "Flight Results on Structural Dynamics from Hermes," J. Spacecraft & Rockets, Vol. 16, No. 2, March-April 1979, pp. 81-87.
8. Lips, K.W., and Vigneron, F.R., "Damping Synthesis for a Spacecraft Structure Using Substructure and Component Data," to be published as CRC Report No.1365, Department of Communications, Ottawa, Canada, 1983.
9. Vigneron, F.R., and Krag, W.E., "Optical Measurements and Attitude Motion of Hermes After Loss of Stabilization," AIAA-82-4256, J. of Guidance, Control, and Dynamics, Vol. 5, No. 5, Sept.-Oct. 1982, pp. 539-541.
10. Cochran, J.E., Jr., and Thompson, J.A., "Nutation Dampers vs. Precession Dampers for Asymmetric Spacecraft," J. Guidance and Control, Vol. 3, No. 1, January-February, 1980, pp. 22-28.
11. Vigneron, F.R., "A Structural Dynamics Model for Flexible Solar Arrays of the Communications Technology Satellite," CRC Report #1268, Department of Communications, Ottawa, Canada, April 1975.
12. Hughes, P.C., "Flexibility Considerations for the Pitch

Attitude Control of the
Communications Technology
Satellite," CASI Transactions,
Vol. 5, No. 1, March 1972.

13. Hughes, Peter C., "Attitude Dynamics of a Three-Axis Stabilized Satellite with a Large Flexible Solar Array," Journal of the Astronautical Sciences, Vol. XX, No. 3, Nov.-Dec. 1972, pp. 166-189.
14. Vigneron, F.R., "Natural Modes and Real Modal Variables for Flexible Spacecraft," CRC Report #1348, Department of Communications, Ottawa, Canada, November 1981.
15. Meirovitch, L., and Baruh, H., "Optimal Control of Damped Flexible Gyroscopic Systems," J. Guidance and Control, Vol. 4, No. 2, March-April 1981, pp. 157-163.

AN AUTOMATED TUNING AND DATA
COLLECTION SYSTEM FOR SINE DWELL
MODAL TESTING

David L. Hunt
SDRC, Inc.
San Diego, California

Jeff Matthews
SDRC, Inc.
Hitchin, England

Roger Williams
SDRC, Inc.
Hitchin, England

Abstract

A minicomputer-based system for performing normal mode testing has been developed which features digital control of the exciters and data acquisition for up to 128 channels. The digital control enables the tuning to be performed by the computer for precise definition and measurement of a normal mode, thereby reducing test time and improving data quality.

Introduction

The multipoint sine dwell (MPSD) method, traditionally used to perform modal survey tests of complex structures, has proven usefulness in accurately defining normal modes and quantifying structural nonlinearities. However, one of the main shortcomings of this method has been the requirement for manually tuning each mode. The process can be time-consuming and often requires an experienced test engineer. "Acceptable" tuning is usually left up to the judgment of that same engineer.

An automated process for tuning a mode to within specified limits has been developed and implemented. A closed-loop system allows the computer to adjust each exciter in both force level and phase so that acceptable tuning is performed rapidly. At that point, a short sine sweep is automatically performed. This enables modal coefficients to be computed using least squares methods rather than simply recording the amplitude at the tuned frequency.

This paper examines the approach used in the tuning and data collection, its implementation into software, and the hardware used to control the entire process.

Hardware

The hardware configuration is based upon a GenRad 2508 minicomputer-based analyzer. The system is augmented with four digital-to-analog (D/A) converters for exciter control as well as two 64-channel analog-to-digital (A/D) converters for data acquisition with a DR11B control card. See Figure 1.

The four D/A's permit closed-loop independent control of up to four exciters by the processor. A load cell measures the force at each input location and is monitored through the A/D section of

the system. The output to each amplifier is adjusted until the load cell measures the desired force input. Each exciter can be stepped up or down in level and phased relative to the other exciters. As a result, both normal modes and complex modes can be excited. The remaining 124 A/D channels are used to measure the response of the structure under test. Phase shifts induced by multiplexing are automatically accounted for through software.

The system uses a microprocessor to synthesize a sine wave that is periodic in the sample period. Sample rates are automatically set to accomplish this and thus avoid leakage. This also avoids the need to provide any windows which could induce small errors and increase data processing time.

Tuning

The tuning procedure attempts to excite a normal mode through minimization of the Indicator Function (IF). This function is defined as:

$$IF_k(\omega) = \sum_i \frac{|\text{Real } H_{ik}(\omega)| \cdot |H_{ik}(\omega)|}{|\sum_i H_{ik}(\omega)|^2}$$

where i = response measurement location
 k = input location
 H_{ik} = frequency response function between location i and k

The frequency response functions (frf's) come from sine sweep or random excitation "panorama" tests which give an initial preview of the structure's modes and natural frequencies. At resonance, the Indicator Function approaches a value of zero, as the real part of each frf becomes a minimum.

The first step in the tuning process is to set initial force patterns for the exciters. This data may come from a finite element prediction or an estimate based upon a previously conducted modal test performed with frequency-response-based methods used to determine mode shapes. A new technique for calculating force patterns from frequency response functions just introduced [1] may prove to be more accurate and effective than the traditional methods currently in use.

To obtain the minimum for the Indicator Function at resonance, the initial force pattern is adjusted in several ways. At any particular

frequency, each exciter force is adjusted up or down relative to one exciter which acts as reference. This process is repeated for the other exciter, until a minimum for the IF at that frequency is obtained. Phase adjustment may be specified as another variable, within user-supplied tolerances. The software then moves to a slightly different frequency and repeats the process. This continues until the optimum tuning is obtained over a discrete frequency range around resonance. The frequency at which the lowest minimum was achieved is the resonant frequency. Since the entire procedure is automatic, no operator interaction is required and the entire process can be completed within a few minutes. However, poor choice of input locations can lengthen the time it takes to find the optimum forcing pattern and result in exciting a mode that is not normal.

Data acquisition consists of performing a short tuned sweep around the resonance, holding the tuned force pattern constant throughout the sweep. This results in a "zoom" frf which is processed using single-degree-of-freedom (SDOF) techniques to compute the mode shape. During the sweep, time domain averaging is used to remove any random content in the measurement.

Software Implementation

The software automates many of the functions of the sine system in addition to the tuning procedure. These other functions include file utility, calibration, setup, data acquisition, data analysis, data validation, documentation, and interface to other software codes.

The setup section permits the operator to describe each of the 128 channels by location, type of measurement, and sensitivity. The calibration procedure includes the capability to perform a check on each transducer and update its true sensitivity.

In the data acquisition mode, several graphic displays aid in reporting the tuning procedure. The Indicator Function, referenced to any of the inputs, may be displayed and updated during the tuning. An Amplitude/Phase display may be selected which yields a qualitative measure of how normal is the mode being excited. See Figure 2. This display plots an amplitude and phase for each of the response channels along the abscissa. Responses are scaled so that the maximum amplitude (ordinate) value is one. Threshold scaling permits the user to see those channels whose response is greater than a specified percentage of the maximum. As a result, the operator quickly sees how many channels are within an acceptable range of quadrature response. A cursor allows him to then identify which channels are out of that range. For any individual channel, a display of the current and averaged time signal can be plotted to see if the response is sinusoidal or contaminated by noise, harmonic responses, etc.

After data acquisition, the SDOF fitting process is performed. This requires no operator intervention, although each individual curve fit can be displayed. Damping is also computed using half-power methods. The validation module permits the calculation of modal participation factor,

modal assurance criteria, synthesis, and orthogonality.

The utility, documentation, and interface modules provide the means to store and report setups and data and to provide the results to other software programs for subsequent processing and display.

Applications

A 64-channel version of the described system has been in operation for the past three years. It has been used successfully in the testing of various aerospace structures, including the Spacelab Pallet[2]. An upgrade of the system to 128 channels has recently been completed and it is currently scheduled for testing of the European Skynet Spacecraft and Solar Array and Eurostar Spacecraft.

Summary

A multichannel data acquisition system for normal mode testing has been developed which features independent digital control and tuning of up to four exciters. This advance automates the portion of a sine dwell test which is usually performed by hand subjectively, requiring skill, patience, and often good fortune to conduct successfully. Combined with other automated features, this unique system reduces the time required to perform normal mode testing while improving the quality of results through more precise mode definition. Its recent successful application aerospace structures suggests significant advantages for use in multipoint sinedwell tests.

References

1. Hunt, David L., "The Optimal Selection of Excitation Methods for Enhanced Modal Testing," AIAA Dynamics Specialists, 84-1068-CP, May 1984.
2. Gabri, B.S. and J.T. Matthews, "Normal Mode Testing Using Multiple Exciters Under Digital Control," SEECN 79, May 1979.

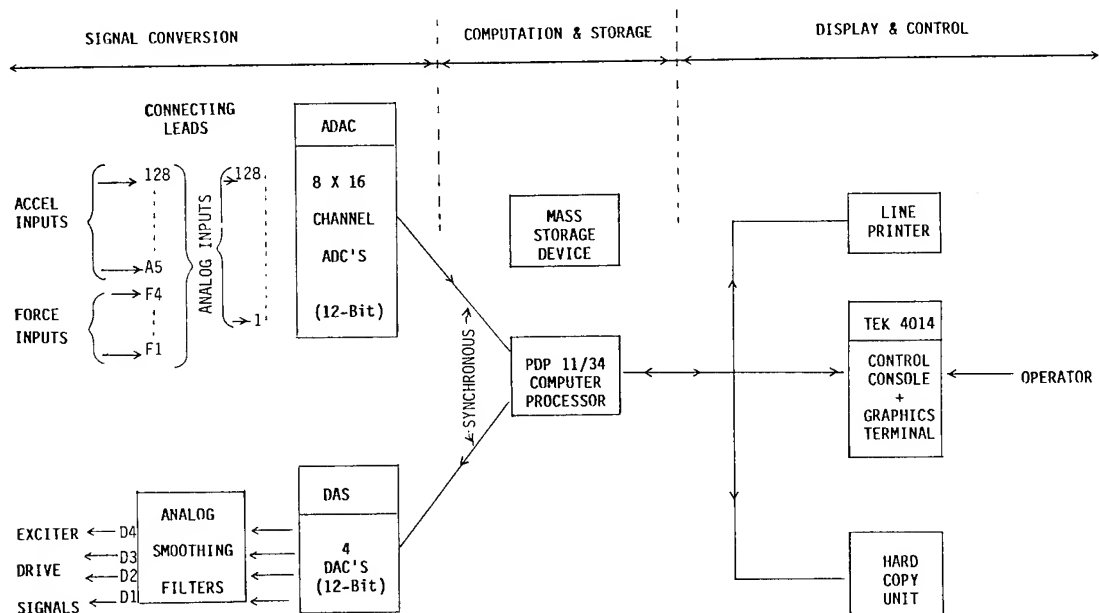


Figure 1. Diagram of automated tuning and data collection system for normal mode testing.

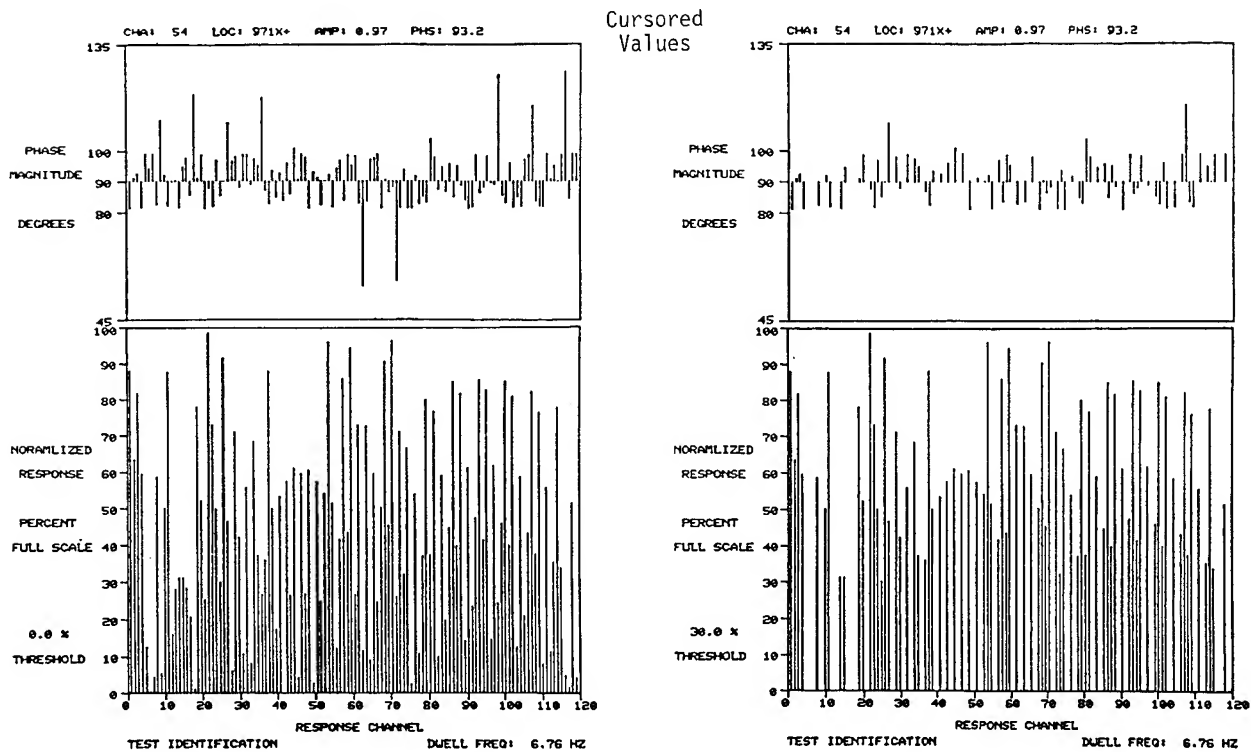


Figure 2. Amplitude/Phase plot for observing quality of tuned mode. Plot on left is for all 120 channels. Plot on right is for channels with response greater than 30% of maximum response.

A RAPID METHOD FOR OBTAINING FREQUENCY-RESPONSE
FUNCTIONS FROM MULTIPLE INPUT PHOTOGRAMMETRIC DATA

Marian L. Kroen* and John S. Tripp**
NASA Langley Research Center
Hampton, Virginia

Abstract

A new, rapid method for obtaining frequency-response functions from photogrammetric data is developed. This method has application to mode shape determination from remote displacement data such as measurements of deflections of large space structures or of wing surfaces in wind tunnel tests.

In this photogrammetric measurement technique the motion of each of several targets on a vibrating surface is recorded as a four-dimensional time series by a pair of remote digital cameras. Previously, three-dimensional frequency-response functions have been obtained from the camera data by means of a coordinate transformation algorithm, applied point-by-point in the time domain to each target position time record, followed by Fourier transformation. However, coordinate transformation of data records of sufficient length to ensure adequate statistical sampling requires excessive computation time. A new method has been developed which reverses the order of operations. Fourier transformation is performed in four-dimensional camera coordinates to obtain averaged cross and autopower spectra. Frequency-response functions in three-dimensional spatial coordinates are then obtained by means of the coordinate transformation algorithm. This method reduces the computation time by a factor proportional to the number of averages computed. The accuracy of three-dimensional frequency-response functions computed by this method is shown to be dependent on the component of deflection normal to the camera focal plane and also upon the geometry of the camera installation.

Nomenclature

A	projection matrix defined in (17A)
\bar{A}_j	jth row of matrix A
a	damping coefficient; power series coefficient; general scalar element
B	general matrix
b	power series coefficient
C	maximum perturbation magnitude (45A)

* Aerospace Technologist, Electro-Mechanical Instrumentation Branch, Instrument Research Division.

** Aerospace Technologist, Electro-Mechanical Instrumentation Branch, Instrument Research Division.

c	camera focal length; power series coefficient
D	functional mapping defined in (19A)
$D_z(t)$	diagonal matrix defined in (43A)
d	power series coefficient
E	expected value
$\bar{E}(\omega)$	error defined in (22A)
$\bar{E}_F(\omega)$	error defined in (39A)
$\bar{E}_K(\omega)$	error defined in (34A)
$\bar{e}_F(t)$	error defined in (38A)
$\bar{e}_K(t)$	error defined in (40A)
$F(\omega)$	general Fourier transform
$F\{f(t)\}$	Fourier transform of function $f(t)$
$f(t)$	general time function
$g(t)$	driving function
$H(\omega)$	frequency-response matrix
h_z	defined in (35A)
$\bar{h}_{\cdot j}(\omega)$	column of $H(\omega)$
$h_{ij}(\omega)$	element of $H(\omega)$
I	identity matrix
K	scale factor
M	rotation matrix defined in (4A)
M_k^3	row 3 matrix M_k
M_k^{12}	rows 1 and 2 of matrix M_k
M_z	composite matrix defined in (10A)
O	object
P_A	pseudo inverse of matrix A defined in (20A)
P_n	matrix of constants
$R_{UU}(\tau)$	autocovariance matrix
$R_{WU}(\tau)$	cross-covariance matrix
$S_{UU}(\omega)$	autospectral matrix

$S_{UU}(\omega)$	autospectral matrix	ω_d	damped natural frequency, rad/sec
$S_{WU}(\omega)$	cross-spectral matrix	Subscripts:	
$s_{gg}(\omega)$	autopower spectrum of $g(t)$	DFP	dual focal plane space
t	time in seconds	OBJ	object space
$\delta \bar{U}(t)$	input driving vector in OBJ space	P	principal point
\bar{u}, \bar{v}	general vectors	1	camera 1
$\delta \bar{u}(t)$	input driving vector in DFP space	2	camera 2
W	point in object space	Superscripts:	
$w_n(t)$	normalized magnitude of $\delta \bar{W}(t)$	\wedge	estimated value
$\delta \bar{W}(t)$	perturbation in object space	*	complex conjugate
\bar{w}	point in DFP space	Special Notation:	
$\delta \bar{w}(t)$	perturbation in DFP space	$\ \bar{v}\ $	norm of vector \bar{v} defined in (27A)
X, Y, Z	object space coordinates	$\ A\ $	norm of matrix A defined in (28A)
x, y, z_F	DFP space coordinates	<u>Introduction</u>	
Z	diagonal perturbation matrix defined in (15A)	<p>Remote measurement of displacement becomes necessary for many structural test conditions. For example, the mass of transducers may modify the dynamic characteristics of the structure being tested, a hostile test environment may restrict use of attached transducers, measurement of low frequency, low acceleration vibrations may preclude use of accelerometer devices, or measurement of large amplitudes may limit the use of proximity probes. Photogrammetric techniques offer an alternative in such conditions. A stereoscopic digital camera system can provide three-dimensional dynamic measurement of position of multiple targets for such applications as modal analysis or frequency-response estimation.</p> <p>Stereoscopic data are recorded for off-line analysis as a pair of two-dimensional sampled time functions for each target. Previously, each recorded stereoscopic pair was mapped into three-dimensional object space coordinates by means of the Direct Linear Transformation (DLT) algorithm.¹ Frequency-response functions were then obtained from averaged auto and cross-power spectra computed from the discrete Fourier transforms of the three-dimensional data. This sequence of operations requires excessive computation time for data records of sufficient length to ensure adequate statistical sampling.</p> <p>The method developed herein performs discrete Fourier (DF) transformation of the recorded data and computation of averaged auto and cross-power spectra in four-dimensional camera coordinates followed by Direct Linear (DL) coordinate transformation of the averaged spectra. This computational sequence reduces the number of points to be transformed for each recorded target position by a factor equal to the number of data blocks to be averaged. This produces a corresponding increase in computational speed, since DL transformation is slow compared to DF transformation.</p> <p>Since camera projection and DL transformation (inverse operations of one another) are nonlinear</p>	
$\delta Z(t)$	diagonal perturbation matrix defined in (16A)		
z	distance from object to principal point plane		
δz	perturbation parallel to z axis		
α, β	constants		
Γ_k	matrix defined in equations (30B), (33B), and (35B)		
γ_k	least angle between $\delta \bar{W}(t)$ and z_k axis		
γ_{kj}	element of Γ_k		
δ	perturbation symbol		
ϵ_m	maximum relative perturbation, defined in (47A)		
ϵ_{RMS}	relative RMS error defined in (53A)		
ϵ_z	maximum negative relative perturbation, defined in (50A)		
ζ	damping ratio, defined in (64A)		
θ, ϕ, ψ	orientation angles, Fig. 10		
Λ_k	matrix defined in (37B)		
$\lambda_{\cdot j}$	column j of matrix Λ_k		
σ	condition number of matrix A defined in (42A)		
ω	general frequency, rad/sec		

transformations, error is introduced by interchanging DL and DF transformation, which limits the applicability of the new method. An analysis given in Appendix A develops error bounds which enable the user to determine constraints on experimental geometry and excitation amplitudes necessary to maintain a given accuracy. Results of computer error studies are given which compare errors incurred by the new method for a typical geometric configuration and several deflection functions. Finally, experimental data are given which compare results computed by both methods.

Sources of Error

Error incurred by the DF-DL sequence of transformation is shown to be dependent on the ratio of the component of deflection normal to the focal plane (δz) to the target-to-principal point plane distance (z), as well as the geometry of the cameras.

The source of the error is now described briefly. The perspective projection of a solid object onto the camera focal plane, illustrated in Fig. 1, is foreshortened along the z axis of the camera. Fig. 2 shows the perspective projection on the focal plane of a point oscillating sinusoidally with time in the X-Y plane in space. The nonsinusoidal projected image is distorted because of the component of motion normal to the focal plane. DL transformation of the focal plane image of the time function back to object space (OBJ) coordinates eliminates the distortion. However, DF transformation of the distorted focal plane time function introduces harmonics not present in the original time function in OBJ coordinates. DL transformation of the distorted DF-transformed data to OBJ coordinates does not eliminate the unwanted harmonics, thus introducing error.

Motion normal to the camera focal planes must, therefore, be sufficiently limited in magnitude to limit error to an acceptable level. Motion parallel to the camera focal planes is not distorted and can be transformed without error by the DF-DL transformation sequence. Figure 3 shows the Fourier transforms of a sinusoidal time function in space for which the ratio $\delta z/z$ is 0.25 and of its distorted projection in the camera image plane. The latter transform contains a peak at a fundamental frequency and harmonics of the fundamental whose amplitudes are proportional to $(1/z)^n$ (where n is harmonic number) and which rapidly decrease to zero amplitude.

Error Analysis

The transformation equations from object space (OBJ) coordinates to dual focal plane (DFP) coordinates are derived in Appendix A. Let $\delta \vec{w}(t)$ denote a time varying perturbation of a target point in OBJ coordinates, and let $\delta \vec{w}(t)$ denote its projected image in DFP coordinates. Coordinate transformation from OBJ to DFP coordinates is given by Appendix equation (18A)

$$\delta \vec{w}(t) = [Z + \delta Z(t)]^{-1} A \delta \vec{w}(t) \quad (1)$$

where matrices Z , δZ , and A are defined in Appendix equations (15A), (16A), and (17A).

The inverse transformation from DFP coordinates to OBJ coordinates (computed via the DLT algorithm) is given by Appendix equation (19A)

$$\delta \vec{w}(t) = P_A [Z + \delta Z(t)] \delta \vec{w}(t) = D [\delta \vec{w}(t)] \quad (2)$$

where matrix P_A is defined in Appendix equation (20A). The error incurred by the DL-DF transformation sequence is

$$\bar{E}(\omega) = F(\delta \vec{w}(t)) - P_A (Z + \delta Z(t)) F(\delta \vec{w}(t)) \quad (3)$$

The relative RMS error defined as

$$\epsilon_{RMS} = \left(\int_{-\infty}^{\infty} \bar{E}(\omega)^2 d\omega \right)^{1/2} / \left(\int_{-\infty}^{\infty} [F(\delta \vec{w}(t))]^2 d\omega \right)^{1/2} \quad (4)$$

is shown in Appendix equation (53A) to be bounded by

$$\epsilon_{RMS} \leq \sigma \left(\frac{\epsilon_m}{1 - \epsilon_z} \right) \left(\int_{-\infty}^{\infty} w_n^4(t) dt \right)^{1/2} / \left(\int_{-\infty}^{\infty} w_n^2(t) dt \right)^{1/2} \quad (5)$$

where $\epsilon_m = \max |\delta z_k / z_k|$
 δz_k = perturbation component normal to the focal plane
 z_k = distance from target to principal point plane
 $\epsilon_z = |\max(0, \delta z_k / z_k)|$
 σ = condition number of matrix A defined in Appendix equation (42A)
 $w_n(t)$ = normalized magnitude of $\delta \vec{w}(t)$

Matrix A is determined by camera configuration and ϵ_m is determined by the direction and amplitude of $\delta \vec{w}(t)$. It is shown for the special case where $\delta \vec{w}(t)$ is a unidirectional, exponentially-damped sinusoid (Appendix equation (63A)), a typical perturbation function encountered in modal analysis, that ϵ_{RMS} is bounded by

$$\epsilon_{RMS} \leq 0.613 \sigma \frac{\epsilon_m}{1 - \epsilon_z} \quad (6)$$

Equations (5) and (6) show that ϵ_{RMS} varies directly with perturbation amplitude and inversely with target-to-principal-point plane distance and that components of motion parallel to both focal planes contribute no error.

Computer Error Studies

The relative RMS error, ϵ_{RMS} , incurred by DF-DL transformation of dynamic data, was computed numerically in a series of computer error studies as follows. The perturbation function $\delta\bar{W}(t)$ (in OBJ coordinates) is transformed into DFP coordinates by equation (1) for the geometry shown in Fig. 4. The resultant error $E(\omega)$ is obtained via equation (3) and relative RMS error, ϵ_{RMS} , given by (4) is obtained by numerical integration. These numerical results and the corresponding error bounds (maximum ϵ_{RMS}) obtained from inequalities (5) and (6) are summarized in Tables 1 through 3. The perturbation functions were damped sinusoids with damping coefficient a of 0.05 and damped natural frequency ω_d of 10 Hz.

Table 1 Perturbation in Y direction (damped sinusoid)

$$\delta\bar{W}(t) = C \begin{pmatrix} 0 \\ 1 \\ 0 \end{pmatrix} e^{-at} \sin \omega_d t$$

$\delta z/z$	Computed C (inches)	Maximum ϵ_{RMS} (%)	ϵ_{RMS} (%)
0.25	35.36	22.85	28.897
0.10	14.142	9.055	9.632
0.025	3.536	2.085	2.220
0.01	1.414	0.877	0.876

Table 2 Perturbation in Z direction parallel to focal plane (damped sinusoid)

$$\delta\bar{W}(t) = C \begin{pmatrix} 0 \\ 0 \\ 1 \end{pmatrix} e^{-at} \sin \omega_d t$$

$\delta z/z$	Computed C (inches)	Maximum ϵ_{RMS} (%)	ϵ_{RMS} (%)
0	35.35	0.097	0
0	14.142	0.119	0
0	3.536	0.097	0
0	1.414	0.115	0

Computed values of ϵ_{RMS} are nonzero due to computer round-off errors.

Table 3 Perturbation rotating in X-Y plane

$$\delta\bar{W}(t) = Ce^{-at} \begin{bmatrix} \begin{pmatrix} 1 \\ 0 \\ 0 \end{pmatrix} \sin \omega_d t + \begin{pmatrix} 0 \\ 1 \\ 0 \end{pmatrix} \cos \omega_d t \end{bmatrix}$$

$\delta z/z$	C (inches)	Computed ϵ_{RMS} (%)	Maximum ϵ_{RMS} (%)
0.25	35.36	17.750	28.897
0.10	14.142	6.360	9.632
0.025	3.536	1.515	2.220
0.01	1.414	0.603	0.876

Fourier transform $F[\delta\bar{W}(t)]$ is compared with DL transform $D(F[\delta\bar{W}(t)])$ for Tables 1 through 3 in Figs. 5 through 7 respectively. The good agreement shown in the figures is confirmed by the corresponding values of ϵ_{RMS} in the tables.

Experimental Results

Dynamic data were obtained using the experimental apparatus shown in Fig. 8. From this set of data, frequency-response functions estimated via DF-DL transformation were compared with those obtained via DL-DF transformation. The experimental and computational procedures are now described briefly.

A cantilevered steel beam was driven by band-limited random noise directed in the X direction. A stereoscopic digital camera system recorded the motion of five light-emitting-diode (LED) targets attached at selected stations along the length of the beam. Target 1 describes the motion of the driving function; targets 2 through 5 describe beam response at their respective stations. Stereoscopic data measurements were sampled at a rate of 312 samples per second in 100 blocks of 512 samples per block. Thus 51,200 samples were recorded for each of five targets for a total of 256,000 data values.

A non-least-squares estimate of element $h_{11}(\omega)$ of frequency-response matrix $H(\omega)$ (defined in Appendix equation (3B)) by DF-DL transformation was obtained by direct solution of Appendix equations (29B) and (31B) for an X-directed driving function. Thus

$$\hat{h}_{11}(\omega) = \gamma_{1k} D \left[\frac{\hat{S}_{wu}(\omega)}{\hat{S}_{uu_{kk}}(\omega)} \right] \quad (7)$$

where $\hat{S}_{wu}(\omega)$ is column k of cross-spectral matrix $\hat{S}_{wu}(\omega)$ (Appendix equation (21B)) $\hat{S}_{uu_{kk}}(\omega)$ is the k,k element of

autospectral matrix $\hat{S}_{uu}(\omega)$ (Appendix equation (20B))

and γ_{1k} is the 1,k element of matrix Γ_1 (Appendix equation (30B)).

Note in equation (7) that DF transformation, averaging, and spectral estimation precede DL transformation.

Frequency-response function $h_{11}(\omega)$ was computed via equation (7) for response targets 2 through 5. The elements of smoothed autospectral and cross-spectral matrices $\hat{S}_{uu}(\omega)$ and $\hat{S}_{wu}(\omega)$ used in (7) were estimated by means of Appendix equation (24B) and (25B) after DF transformation of the recorded data set. After averaging and cross-spectral estimation, only 512 values of 4-element vector $\bar{S}_{wu.k}(\omega)$ require

DL transformation, for response targets 2 through 5 for a total of 2048 transformations.

A corresponding estimate of $h_{11}(\omega)$ by DL-DF transformation was obtained as follows. The set of 256,000 recorded 4-element data vectors underwent DL coordinate transformation into 3-element vectors which were then Fourier transformed, after which smoothed autospectral and cross-spectral matrices $\hat{S}_{uu}(\omega)$ and $\hat{S}_{wu}(\omega)$ were estimated. Element $h_{11}(\omega)$ was then obtained by equating elements (1,1) of equation (3D). This procedure, requiring 256,000 DL transformations, required over 49 hours of computation on an in-house minicomputer, as compared to approximately 20 minutes for the former procedure.

Frequency-response functions obtained by both procedures for stations 2 through 5 are compared in Fig. 9. Agreement is good at lower frequencies. As frequency increases agreement worsens as decreasing signal amplitude approaches the limit of camera resolution.

Conclusions

A rapid computational procedure for reduction of stereoscopic dynamic data has been proposed. Its accuracy has been predicted by means of an analytical error analysis and by computer error studies. It was shown that error is roughly proportional to the component of motion normal to the camera focal plane divided by target-to-principal-point plane distance. Error is also magnified by the condition number of the stereoscopic projection matrix determined by camera-target geometry.

The proposed procedure was employed to estimate frequency-response functions using test data obtained from a simple vibration experiment. Comparison of these results with those obtained by the conventional procedure showed satisfactory agreement. Data reduction time for this case was reduced by a factor of 125.

Appendix A

Development of Projection Equations

It is desired to remotely sense the three-dimensional position of a vibrating object O as a function of time by means of a stereoscopic system, as shown in Fig. 4, which employs two cameras focused on O . The image of O , denoted by O' , appearing in each camera focal plane is modeled as a perspective projection. That is, each point W of O projects onto the point of intersection of the camera focal plane with the line passing from W through the camera principal point W_p . The camera principal point plane mentioned in the sequel is parallel to the focal plane and intersects W_p .

Define an object space (OBJ) coordinate system denoted by X, Y, Z . For each camera define a focal plane (FP) coordinate system, denoted by x, y, z_F , whose origin lies on the focal plane. Let the OBJ coordinates of object point W be

$$\bar{W} = (X \ Y \ Z)_{OBJ}^T \quad (1A)$$

Let \bar{W}_p denote the coordinates of the principal point in OBJ space

$$\bar{W}_p = (X_p \ Y_p \ Z_p)_{OBJ}^T \quad (2A)$$

Let $(x_p, y_p, c)_{FP}$ denote the FP coordinates of the principal point and let $(x, y, 0)_{FP}$ denote the FP coordinates of the projected image of W . Then the transformation from OBJ coordinates to FP coordinates is

$$\begin{pmatrix} x - x_p \\ y - y_p \\ -c \end{pmatrix}_{FP} = -\frac{c}{z} M \begin{pmatrix} X - X_p \\ Y - Y_p \\ Z - Z_p \end{pmatrix}_{OBJ} \quad (3A)$$

where c is the camera focal length, z is the distance from W to the principal point plane, and M is the rotational transformation matrix from OBJ orientation to FP orientation given by

$$M = \begin{bmatrix} \cos \phi \cos \theta & \sin \psi \sin \phi \cos \theta + \cos \psi \sin \theta \\ \cos \phi \sin \theta & \cos \psi \cos \theta - \sin \psi \sin \phi \sin \theta \\ \sin \phi & -\sin \psi \cos \phi \end{bmatrix}$$

$$\begin{bmatrix} \sin \psi \sin \theta - \cos \psi \sin \phi \cos \theta \\ \sin \psi \cos \theta + \cos \psi \sin \phi \sin \theta \\ \cos \psi \cos \phi \end{bmatrix} \quad (4A)$$

See figure 10 for angle definitions.

By means of both cameras, a subset of the three-dimensional object space is mapped into a four-dimensional dual focal plane (DFP) space. Let subscripts 1 and 2 in the sequel denote cameras 1 and 2. Let M_{12} denote the 2 by 3 matrix consisting of rows 1 and 2 of M , and let M_3 denote the third row of M . Also let

$$\bar{w} \triangleq (x_1, y_1, x_2, y_2)^T \quad (5A)$$

$$\bar{w}_1 \triangleq (x_1, y_1)^T \quad (6A)$$

$$\bar{w}_2 \triangleq (x_2, y_2)^T \quad (7A)$$

and

$$\bar{z} \triangleq (z_1, z_2)^T \quad (8A)$$

An expression for \bar{z} in terms of \bar{w} can be obtained as

$$\bar{z} \triangleq \begin{pmatrix} z_1 \\ z_2 \end{pmatrix} = M_z \begin{pmatrix} X \\ Y \\ Z \end{pmatrix} - \begin{bmatrix} 3 & 1 & 0 \\ M_1 & & \\ 0 & & 3 \\ & & M_2 \end{bmatrix} \begin{pmatrix} X_{p1} \\ Y_{p1} \\ Z_{p1} \\ X_{p2} \\ Y_{p2} \\ Z_{p2} \end{pmatrix} \quad (9A)$$

where

$$M_z = \begin{bmatrix} 3 & \\ M_1 & \\ 3 & \\ M_2 & \end{bmatrix} \quad (10A)$$

Through the use of (3A) it can be shown that \bar{w} is related to \bar{W} and \bar{z} by

$$\begin{pmatrix} \begin{pmatrix} x_1 - x_{p1} \\ y_1 - y_{p1} \end{pmatrix} z_1 \\ \begin{pmatrix} x_2 - x_{p2} \\ y_2 - y_{p2} \end{pmatrix} z_2 \end{pmatrix} = \begin{bmatrix} 12 & \\ -c_1 M_1 & \\ 12 & \\ -c_2 M_2 & \end{bmatrix} \begin{pmatrix} X \\ Y \\ Z \end{pmatrix} + \begin{bmatrix} c_1 M_1 & 1 & 0 \\ 0 & & c_2 M_2 \end{bmatrix} \begin{pmatrix} X_{p1} \\ Y_{p1} \\ Z_{p1} \\ X_{p2} \\ Y_{p2} \\ Z_{p2} \end{pmatrix} \quad (11A)$$

Let $\delta \bar{w} = (\delta X \ \delta Y \ \delta Z)^T$ be a perturbation in \bar{w} (see Fig. 4). From (9A) the corresponding perturbation $\delta \bar{z}$ is

$$\delta \bar{z} = \begin{bmatrix} 3 \\ M_1 \\ 3 \\ M_2 \end{bmatrix} \begin{pmatrix} \delta X \\ \delta Y \\ \delta Z \end{pmatrix} = M_z \delta \bar{w} \quad (12A)$$

From (11A) and (12A) the projection of $\delta \bar{w}$ onto DFP space, $\delta \bar{w}$, is given in terms of $\delta \bar{w}$ and $\delta \bar{z}$ as

$$\begin{bmatrix} \begin{bmatrix} 12 & \\ -c_1 M_1 & \end{bmatrix} \begin{pmatrix} x_1 - x_{p1} \\ y_1 - y_{p1} \end{pmatrix} \\ \begin{bmatrix} 12 & \\ -c_2 M_2 & \end{bmatrix} \begin{pmatrix} x_2 - x_{p2} \\ y_2 - y_{p2} \end{pmatrix} \end{bmatrix} - \begin{bmatrix} 3 \\ M_1 \\ 3 \\ M_2 \end{bmatrix} \begin{pmatrix} \delta X \\ \delta Y \\ \delta Z \end{pmatrix} = \begin{pmatrix} (z_1 + \delta z_1) \begin{pmatrix} \delta x_1 \\ \delta y_1 \end{pmatrix} \\ (z_2 + \delta z_2) \begin{pmatrix} \delta x_2 \\ \delta y_2 \end{pmatrix} \end{pmatrix} \quad (13A)$$

which may be written in matrix form as

$$A \delta \bar{w} = (Z + \delta Z) \delta \bar{w} \quad (14A)$$

where

$$Z = \begin{bmatrix} z_1 & 0 & 0 & 0 \\ 0 & z_1 & 0 & 0 \\ 0 & 0 & z_2 & 0 \\ 0 & 0 & 0 & z_2 \end{bmatrix} \quad (15A)$$

$$\delta Z = \begin{bmatrix} \delta z_1 & 0 & 0 & 0 \\ 0 & \delta z_1 & 0 & 0 \\ 0 & 0 & \delta z_2 & 0 \\ 0 & 0 & 0 & \delta z_2 \end{bmatrix} \quad (16A)$$

and

$$A = \begin{bmatrix} -c_1 M_1^{12} \\ -c_2 M_2^{12} \end{bmatrix} - \begin{bmatrix} x_1 - x_{p1} & 0 \\ y_1 - y_{p1} & 0 \\ 0 & x_2 - x_{p2} \\ 0 & y_2 - y_{p2} \end{bmatrix} \begin{bmatrix} M_1^3 \\ M_2^3 \end{bmatrix} \quad (17A)$$

From (14A) the projection equation for $\delta\bar{w}$ as a function of $\delta\bar{w}$ can be written as a mapping D^{-1} from OBJ space into DFP space as

$$\delta\bar{w} = (Z + \delta Z)^{-1} A \delta\bar{w} \triangleq D^{-1}(\delta\bar{w}) \quad (18A)$$

If A has full rank then an inverse mapping D is obtained as

$$\delta\bar{w} = P_A (Z + \delta Z) \delta\bar{w} \triangleq D(\delta\bar{w}) \quad (19A)$$

where

$$P_A = (A^T A)^{-1} A^T \quad (20A)$$

Over the column space of A matrix P_A is a two-sided inverse of A . Mappings D and D^{-1} are nonlinear transformations because of the dependency of (δZ) on $\delta\bar{w}$. Therefore, composition of Fourier transformation and mapping under D is noncommutative; that is

$$F(\delta\bar{w}(t)) = F(D(\delta\bar{w}(t))) \neq D(F(\delta\bar{w}(t))) \quad (21A)$$

where F denotes Fourier transformation and D is extended to a complex mapping by

$$D(\bar{u} + i\bar{v}) = D(\bar{u}) + iD(\bar{v})$$

(In the sequel the "(t)" notation will be suppressed in $F(\delta\bar{w}(t))$ and $F(\delta\bar{w}(t))$.) However, if the perturbation magnitudes are small, the error

$$\bar{E}(\omega) \triangleq D[F(\delta\bar{w})] - F(\delta\bar{w}) \quad (22A)$$

may be acceptably small. An expression for $\bar{E}(\omega)$ will now be obtained. The Fourier transform of $\delta\bar{w}(t)$ may be obtained as

$$F(\delta\bar{w}) = Z^{-1} \left(AF(\delta\bar{w}) - F(\delta Z(Z + \delta Z)^{-1} A \delta\bar{w}) \right) \quad (23A)$$

Substitute $F(\delta\bar{w})$ into (19A) for $\delta\bar{w}$, noting that since δZ is dependent on $\delta\bar{w}$ in (19A), it will now be dependent on $F(\delta\bar{w})$ (denoted by $\delta Z|_{F(\delta\bar{w})}$), giving

$$D(F(\delta\bar{w})) = P_A (Z + \delta Z|_{F(\delta\bar{w})}) F(\delta\bar{w}) \quad (24A)$$

Equations (23A) and (24A) are combined to yield

$$\begin{aligned} D(F(\delta\bar{w})) &= F(\delta\bar{w}) - P_A F(\delta Z(Z + \delta Z)^{-1} A \delta\bar{w}) \\ &+ P_A \delta Z|_{F(\delta\bar{w})} Z^{-1} \left(AF(\delta\bar{w}) - F(\delta Z(Z + \delta Z)^{-1} A \delta\bar{w}) \right) \end{aligned} \quad (25A)$$

The expression for $\bar{E}(\omega)$ is obtained from (25A) as

$$\begin{aligned} \bar{E}(\omega) &= P_A (I - \delta Z|_{F(\delta\bar{w})} Z^{-1}) F(\delta Z(Z + \delta Z)^{-1} A \delta\bar{w}) \\ &+ P_A \delta Z|_{F(\delta\bar{w})} Z^{-1} AF(\delta\bar{w}) \end{aligned} \quad (26A)$$

Determination of Error Bounds

Let $\|\bar{v}\|$ denote the Euclidean norm of n -element \bar{v} , where

$$\|\bar{v}\| \triangleq \left(\sum_{i=1}^n v_i^2 \right)^{1/2} \quad (27A)$$

and let $\|A\|$ denote the norm of a general m by n matrix A , where

$$\|A\| \triangleq \max_{x \neq 0} \frac{\|Ax\|}{\|x\|} \quad (28A)$$

It can be shown² that $\|A\|$ equals the largest singular value of A . It follows from (28A) that

$$\|A\bar{x}\| \leq \|A\| \cdot \|\bar{x}\| \quad (29A)$$

It can also be shown² that

$$\|AB\| \leq \|A\| \cdot \|B\| \quad (30A)$$

where A and B are conformable matrices. The vector triangle inequality,

$$\|\bar{x} + \bar{y}\| \leq \|\bar{x}\| + \|\bar{y}\| \quad (31A)$$

is true also for matrix norms² as

$$\|A + B\| \leq \|A\| + \|B\| \quad (32A)$$

ERRATA TO PAPER NO. 84-1060

Computer Error Studies

The relative RMS error, ϵ_{RMS} , incurred by DF-DL transformation of dynamic data, was computed numerically in a series of computer error studies as follows. The perturbation function $\delta\bar{W}(t)$ (in OBJ coordinates) is transformed into DFP coordinates by equation (1) for the geometry shown in Fig. 4. The resultant error $E(\omega)$ is obtained via equation (3) and relative RMS error, ϵ_{RMS} , given by (4) is obtained by numerical integration. These numerical results and the corresponding error bounds (maximum ϵ_{RMS}) obtained from inequalities (5) and (6) are summarized in Tables 1 through 3. The perturbation functions were damped sinusoids with damping coefficient a of 0.05 and damped natural frequency ω_d of 10 Hz.

Table 1 Perturbation in Y direction (damped sinusoid)

$$\delta\bar{W}(t) = C \begin{pmatrix} 0 \\ 1 \\ 0 \end{pmatrix} e^{-at} \sin \omega_d t$$

$\delta z/z$	C (inches)	Computed ϵ_{RMS} (%)	Maximum ϵ_{RMS} (%)
0.25	35.36	22.85	28.897
0.10	14.142	9.055	9.632
0.025	3.536	2.085	2.220
0.01	1.414	0.877	0.876

Table 2 Perturbation in Z direction parallel to focal plane (damped sinusoid)

$$\delta\bar{W}(t) = C \begin{pmatrix} 0 \\ 0 \\ 1 \end{pmatrix} e^{-at} \sin \omega_d t$$

$\delta z/z$	C (inches)	Computed ϵ_{RMS} (%)	Maximum ϵ_{RMS} (%)
0	35.35	0.097	0
0	14.142	0.115	0
0	3.536	0.097	0
0	1.414	0.115	0

Computed values of ϵ_{RMS} are nonzero due to computer round-off errors.

Table 3 Perturbation rotating in X-Y plane

$$\delta\bar{W}(t) = C e^{-at} \left[\begin{pmatrix} 1 \\ 0 \\ 0 \end{pmatrix} \sin \omega_d t + \begin{pmatrix} 0 \\ 1 \\ 0 \end{pmatrix} \cos \omega_d t \right]$$

$\delta z/z$	C (inches)	Computed ϵ_{RMS} (%)	Maximum ϵ_{RMS} (%)
0.25	35.36	17.750	28.897
0.10	14.142	6.360	9.632
0.025	3.536	1.515	2.220
0.01	1.414	0.603	0.876

Fourier transform $F[\delta\bar{W}(t)]$ is compared with DL transform $D(F[\delta\bar{W}(t)])$ for Tables 1 through 3 in Figs. 5 through 7 respectively. The good agreement shown in the figures is confirmed by the corresponding values of ϵ_{RMS} in the tables.

Experimental Results

Dynamic data were obtained using the experimental apparatus shown in Fig. 8. From this set of data, frequency-response functions estimated via DF-DL transformation were compared with those obtained via DL-DF transformation. The experimental and computational procedures are now described briefly.

A cantilevered steel beam was driven by band-limited random noise directed in the X direction. A stereoscopic digital camera system recorded the motion of five light-emitting-diode (LED) targets attached at selected stations along the length of the beam. Target 1 describes the motion of the driving function; targets 2 through 5 describe beam response at their respective stations. Stereoscopic data measurements were sampled at a rate of 312 samples per second in 100 blocks of 512 samples per block. Thus 51,200 samples were recorded for each of five targets for a total of 256,000 data values.

A non-least-squares estimate of element $h_{11}(\omega)$ of frequency-response matrix $H(\omega)$ (defined in Appendix equation (3B)) by DF-DL transformation was obtained by direct solution of Appendix equations (29B) and (31B) for an X-directed driving function. Thus

$$\hat{h}_{11}(\omega) = \gamma_{1k} D \left[\hat{S}_{wu.k}(\omega) / \hat{S}_{uu.kk}(\omega) \right] \quad (7)$$

where $\hat{S}_{wu.k}(\omega)$ is column k of cross-spectral matrix $\hat{S}_{wu}(\omega)$ (Appendix equation (21B)) $\hat{S}_{uu.kk}(\omega)$ is the k,k element of

In the sequel it is assumed realistically that the norms $\|\delta\bar{W}(t)\|$ and $\|F[\delta\bar{W}]\|$ are bounded and that the integral $\int_{-\infty}^{\infty} \|F(\delta\bar{W})\|^2 d\omega$ exists.

Take the norm of (26A) and apply inequalities (29A-32A) to obtain

$$\begin{aligned} \|\bar{E}(\omega)\| &\leq \|P_A\| \cdot \|I - Z^{-1} \delta Z\|_{F(\delta\bar{W})} \\ &\cdot \|F(\delta Z(Z + \delta Z)^{-1} A \delta\bar{W})\| \\ &+ \|P_A\| \cdot \|A\| \cdot \|Z^{-1} \delta Z\|_{F(\delta\bar{W})} \cdot \|F(\delta\bar{W})\| \quad (33A) \end{aligned}$$

Inequality (33A) shows that if $\|Z^{-1} \delta Z\|_{F(\delta\bar{W})}$ is made sufficiently small by scaling $F(\delta\bar{W})$, $\bar{E}(\omega)$ will be dominated by $P_A F(\delta Z(Z + \delta Z)^{-1} A \delta\bar{W})$. The effect of scaling $F(\delta\bar{W})$ in (33A) is now calculated. Replace $D(F(\delta\bar{W}))$ in (22A) by $KD[(1/K)F(\delta\bar{W})]$, where K is the scale factor. Equation (26A) is then rewritten as

$$\begin{aligned} \bar{E}_K(\omega) &\triangleq P_A \left(I - Z^{-1} \delta Z \right|_{(1/K)F(\delta\bar{W})} \left. F(\delta Z(Z + \delta Z)^{-1} A \delta\bar{W}) \right) \\ &+ P_A Z^{-1} \delta Z \left|_{(1/K)F(\delta\bar{W})} A F(\delta\bar{W}) \right) \quad (34A) \end{aligned}$$

Define

$$h_z \triangleq \frac{(z + \delta z)_{\max}}{z_{\min}} \|P_A\| \cdot \|F(\delta\bar{W})\|_{\max} \quad (35A)$$

It can be shown that $\|\bar{E}_K(\omega)\|$ is bounded by

$$\begin{aligned} \|\bar{E}_K(\omega)\| &\leq (1 + (1/K) h_z) \|P_A\| \cdot \|F(\delta Z(Z + \delta Z)^{-1} A \delta\bar{W})\| \\ &+ (1/K) h_z \|P_A\| \cdot \|A\| \cdot \|F(\delta\bar{W})\| \quad (36A) \end{aligned}$$

Through appropriate choice of scale factor K the norm $\|E_K(\omega)\|$ can be made arbitrarily close to

$$\|\bar{E}_F(\omega)\| \triangleq \|P_A\| \cdot \|F(\delta Z(Z + \delta Z)^{-1} A \delta\bar{W})\| \quad (37A)$$

where

$$\bar{e}_F(t) \triangleq \|P_A\| \delta Z(t) (Z + \delta Z(t))^{-1} A \delta\bar{W}(t) \quad (38A)$$

and

$$\bar{E}_F(\omega) \triangleq F(\bar{e}_F(t)) \quad (39A)$$

The Fourier transform in (37A) cannot be analytically evaluated even for simple time functions because of the inverse factor

$(Z + \delta Z(t))^{-1}$. This fact prevents determination of a useful bound. However, the integral of $\|\bar{E}_K(\omega)\|^2$ over ω can be bounded analytically as is now shown. Let

$$\bar{e}_K(t) = \left(1 + \frac{1}{K} h_z\right) \bar{e}_F(t) + \frac{1}{K} h_z \|P_A\| \cdot \|A\| \cdot \delta\bar{W}(t) \quad (40A)$$

Take the norm of (38A) and apply inequalities (29A) and (30A) to give

$$\|\bar{e}_F(t)\| \leq \sigma \|D_z(t)\| \cdot \|\delta\bar{W}(t)\| \quad (41A)$$

where

$$\sigma = \|P_A\| \cdot \|A\| \quad (42A)$$

and

$$D_z(t) \triangleq \delta Z(t) (Z + \delta Z(t))^{-1} \quad (43A)$$

Each element of $D_z(t)$ has the form

$$\frac{\delta z_k(t)/z_k}{1 + \delta z_k(t)/z_k} \text{ where } k = 1 \text{ or } 2. \text{ Let } \gamma_k \text{ be the}$$

smallest angle attained for any t between $\delta\bar{W}(t)$ and the z_k axis. From equation (12A) it follows that

$$|\delta z_k(t)/z_k| \leq \max_k (|\cos \gamma_k|/z_k) \|\delta\bar{W}(t)\| \quad (44A)$$

Let

$$C \triangleq \max_t \|\delta\bar{W}(t)\| \quad (45A)$$

$$w_F(t) = (1/C) \|\delta\bar{W}(t)\| \quad (46A)$$

and

$$\epsilon_M \triangleq C \max_k (|\cos \gamma_k|/z_k) = \max_{k,t} (\delta z_k(t)/z_k) \quad (47A)$$

Then from (44A-47A)

$$|\delta z_k(t)/z_k| \leq \epsilon_M w_F(t) \quad (48A)$$

It follows that $\|D_Z(t)\|$ is bounded by

$$\|D_Z(t)\| \leq \frac{\epsilon_M}{1 - \epsilon_Z} w_F(t) \quad (49A)$$

where

$$\epsilon_Z = \min_{k,t} (0, \delta z_k(t)/z_k) \quad (50A)$$

Therefore, from (41A), (46A), and (49A) $\|\bar{e}_F(t)\|$ is bounded by

$$\|\bar{e}_F(t)\| \leq \sigma \frac{\epsilon_M}{1 - \epsilon_Z} C w_F^2(t) \quad (51A)$$

To bound $\|\bar{e}_K(t)\|$ apply (46A) and (51A) to the norm of (40A) and simplify to obtain

$$\|\bar{e}_K(t)\| \leq (1 + \frac{1}{K} h_z) \sigma \frac{\epsilon_M}{1 - \epsilon_Z} C w_F^2(t) + \frac{1}{K} h_z \sigma C w_F(t) \quad (52A)$$

Define the relative RMS error as

$$\epsilon_{RMS} \triangleq \frac{\left(\int_{-\infty}^{\infty} \|\bar{e}_K(\omega)\|^2 d\omega \right)^{1/2} \left(\int_{-\infty}^{\infty} \|\bar{e}_K(t)\|^2 dt \right)^{1/2}}{\left(\int_{-\infty}^{\infty} \|F(\delta \bar{w})\|^2 d\omega \right)^{1/2} \left(\int_{-\infty}^{\infty} \|\delta \bar{w}(t)\|^2 dt \right)^{1/2}} \quad (53A)$$

which follows from Parseval's Theorem³. Evaluate the integral in the denominator of (53A), using (46A) to obtain

$$\int_{-\infty}^{\infty} \|\delta \bar{w}(t)\|^2 d\omega = C^2 \int_{-\infty}^{\infty} w_F^2(t) dt \quad (54A)$$

Integrate the square of (52A) and divide by (54A) to obtain the bound to ϵ_{RMS} as

$$\epsilon_{RMS}^2 \leq \sigma^2 \left[\left(1 + \frac{h_z}{K} \right)^2 \left(\frac{\epsilon_M}{1 - \epsilon_Z} \right)^2 \frac{\left(\int_{-\infty}^{\infty} w_F^4(t) dt \right)}{\left(\int_{-\infty}^{\infty} w_F^2(t) dt \right)} + \frac{h_z}{K} \left(2 \left[1 + \frac{h_z}{K} \right] \left[\frac{\epsilon_M}{1 - \epsilon_Z} \right] + \frac{h_z}{K} \right) \right] \quad (55A)$$

Since $0 \leq w_F(t) \leq 1$ it follows that

$$0 \leq w_F^4(t) \leq w_F^2(t) \quad (56A)$$

Therefore, the ratio of integrals in (55A) is bounded by unity.

Choose K sufficiently large so that the terms involving $\frac{h_z}{K}$ are negligible in (55A). Then ϵ_{RMS} is bounded by

$$\epsilon_{RMS} \leq \sigma \left(\frac{\epsilon_M}{1 - \epsilon_Z} \right) \frac{\left(\int_{-\infty}^{\infty} w_F^4(t) dt \right)^{1/2}}{\left(\int_{-\infty}^{\infty} w_F^2(t) dt \right)^{1/2}} \leq \sigma \left(\frac{\epsilon_M}{1 - \epsilon_Z} \right) \quad (57A)$$

where

$$w_F(t) = \|\delta \bar{w}(t)\| / \max_t \|\delta \bar{w}(t)\| \quad (58A)$$

$$\epsilon_M = \max_{k,t} (\delta z_k(t)/z_k) \quad (59A)$$

$$\epsilon_Z = \min_{k,t} (0, \delta z_k(t)/z_k) \quad (60A)$$

$$\sigma = \|P_A\| \cdot \|A\| \quad (61A)$$

Factor σ equals the ratio of the largest singular value of A to the smallest nonzero singular value of A , defined as the condition number of A . Matrix A tends to be poorly conditioned if cameras 1 and 2 are closely spaced with nearly parallel focal planes (angles ϕ_1 and ϕ_2 small in figure 4) or if they are nearly opposed (ϕ_1 and ϕ_2 close to $\pi/2$ in Fig. 4). Matrix A is well conditioned if the principal axes are coplanar and at right angles to each other (ϕ_1 and ϕ_2 equal to $\pi/4$ in figure 4).

Special Cases

Inequality (91) is evaluated analytically for the special case where $\delta \bar{w}(t)$ is a vector of fixed direction with varying magnitude. Let

$$\delta \bar{w}(t) = \bar{h} w_F(t) \quad (62A)$$

A typical perturbation function encountered in modal analysis is the exponentially damped sinusoid

$$w_F(t) = \begin{cases} e^{-at} \sin \omega_d t, & t \geq 0 \\ 0, & t < 0 \end{cases} \quad (63A)$$

Inequality (94) can be evaluated analytically for this case in terms of the damping ratio ζ where

$$\zeta = a (w_d^2 + a^2)^{1/2} \quad (64A) \quad \text{and}$$

$\approx a/w_d$ for $a \ll w_d$, to give

$$\epsilon_{\text{RMS}} < \sigma \frac{\epsilon_M}{1 - \epsilon_z} \left(\frac{3}{8(4\zeta^2 + 1)} \right)^{1/2} \quad (65A)$$

A similar computation can be performed for the exponentially damped cosine

$$f(t) = \begin{cases} e^{-at} \cos w_d t, & t > 0 \\ 0, & t < 0 \end{cases} \quad (66A)$$

to give

$$\epsilon_{\text{RMS}} < \sigma \left(\frac{\epsilon_M}{1 - \epsilon_z} \right) \left(\frac{16\zeta^4 + 28\zeta^2 + 3}{64\zeta^4 + 48\zeta^2 + 8} \right)^{1/2} \quad (67A)$$

In modal analysis of metal structures typical values of ζ seldom exceed 0.02, in which case inequalities (103) and (109) reduce to

$$\epsilon_{\text{RMS}} < 0.613\sigma \left(\frac{\epsilon_M}{1 - \epsilon_z} \right) \quad (68A)$$

Geometric Example

Figure 4 shows an example of typical geometry in which the object is located at the intersection of the normals to each focal plane, the y_1 and y_2 axes are parallel to the Z axis, and focal plane coordinates (x_1, z_{F1}) and (x_2, z_{F2}) are rotated from the XY coordinates by angles ϕ_1 and ϕ_2 , respectively. Rotation matrices M_1 and M_2 are then

$$M_k = \begin{bmatrix} \cos \phi_k & \sin \phi_k & 0 \\ 0 & 0 & 1 \\ \sin \phi_k & -\cos \phi_k & 0 \end{bmatrix} \quad (69A)$$

for $k = 1, 2$. Matrices A and M_z defined in (17A) and (10A) are constructed from M_1 and M_2 as

$$A = \begin{bmatrix} c_1 \cos \phi_1 & c_1 \sin \phi_1 & 0 \\ 0 & 0 & c_1 \\ c_2 \cos \phi_2 & -c_2 \sin \phi_2 & 0 \\ 0 & 0 & c_2 \end{bmatrix} \quad (70A)$$

$$M_z = \begin{bmatrix} \sin \phi_1 & -\cos \phi_1 & 0 \\ \sin \phi_2 & -\cos \phi_2 & 0 \end{bmatrix} \quad (71A)$$

If constants are chosen such that $\phi_2 = -\phi_1$, $z_1 = z_2$, $c_1 = c_2 = c$, $\psi_1 = \psi_2 = \pi/2$, and $\theta_1 = \theta_2 = 0$, then the norm $\|A\|$ is readily obtained as

$$\|A\| = \sqrt{2} c \quad (72A)$$

Matrix P_A is found to be

$$P_A = (A^T A)^{-1} A^T = \frac{1}{2c} \begin{bmatrix} \sec \phi & 0 & \sec \phi & 0 \\ \csc \phi & 0 & -\csc \phi & 0 \\ 0 & 1 & 0 & 1 \end{bmatrix} \quad (73A)$$

and the norm $\|P_A\|$ is obtained as

$$\|P_A\| = \frac{1}{\sqrt{2} c} \max (\sec \phi, \csc \phi) \quad (74A)$$

For this case

$$\sigma = \|P_A\| \cdot \|A\| = \max (\sec \phi, \csc \phi) \quad (75A)$$

Effects of Error on Modal Analysis

The effects on modal analysis caused by the computation of $F(\delta \bar{w}(t))$ by the approximation $KD[(1/K)F(\delta \bar{w}(t))]$ can be deduced by examination of error expression (26A), whose dominant part has been shown to be

$$\bar{E}_K(\omega) = P_A F(D_z(t) A \delta \bar{w}(t)) \quad (76A)$$

for suitably large K . The j^{th} element of $D_z(t) A \delta \bar{w}(t)$ is

$$\begin{aligned} e_{jj}(t) &\stackrel{\Delta}{=} d_{jj}(t) \bar{A}_j \cdot \delta \bar{w}(t) \\ &= \frac{\delta z_k(t)/z_k}{1 + \delta z_k(t)/z_k} \bar{A}_j \cdot \delta \bar{w}(t) \end{aligned} \quad (77A)$$

where \bar{A}_j is the j^{th} row of A and $k = 1$ or 2 . Recall from (12A) that

$$\delta z_k(t) = M_k^3 \delta \bar{w}(t) \quad (78A)$$

Expand $d_{jj}(t)$ into a power series

$$d_{jj}(t) = \sum_{n=1}^{\infty} \left(\frac{\delta z_k(t)}{z_k} \right)^n \quad (79A)$$

which is convergent for $\left| \frac{\delta z_k(t)}{z_k} \right| < 1$. For

simplicity, suppose that $\delta \bar{w}(t)$ contains only two damped cosinusoidal components at frequencies ω_1 and ω_2 . Then $\delta z(t)/z$ will be of the form

$$\frac{\delta z(t)}{z} = \alpha_1 e^{-a_1 t} \cos \omega_1 t + \alpha_2 e^{-a_2 t} \cos \omega_2 t \quad (80A)$$

A power series expansion for $e_{jj}(t)$ may be obtained as

$$e_{jj}(t) = \sum_{n=2}^{\infty} \sum_{m=0}^n b_{nm}(t) \cos^{n-m} \omega_1 t \cos^m \omega_2 t \quad (81A)$$

where the coefficients $b_{nm}(t)$ are weighted sums of products of powers of $e^{-a_1 t}$ and $e^{-a_2 t}$. The Fourier transform of (81A) can be written as

$$E_{jj}(\omega) = F(e_{jj}(t)) = \frac{1}{2} F \left[\sum_{n=2}^{\infty} \sum_{m=0}^n \left(b_{nm}(t) \cos^{(n-m)/2} \sum_{k=0}^{m/2} d_{n-m,k} \cos^k \omega_1 t \cos^{m-k} \omega_2 t \right) \right] \quad (82A)$$

where the d_{ij} are elements which sum to unity over m .

Equation (82A) shows that the error frequency spectrum contains peaks at harmonic frequencies (all integer multiples of ω_1 and ω_2) and at cross-modulated frequencies (sums and differences of all fundamental and harmonic frequencies). The amplitudes of the spectral peaks decrease rapidly with increasing frequency because the n^{th} harmonic is weighted by $(1/z)^n$ in the power series.

If the experimenter can identify true modes in $D(F(\delta \bar{w}(t)))$ and discard harmonic and cross-modulated error peaks, then error effects are relatively unimportant to modal analysis since the fundamental frequencies are not shifted.

However, estimated damping ratios may be somewhat in error due to distortion in the shapes of fundamental peaks.

Appendix B

Estimation of Frequency-Response Functions

The dynamics of three-dimensional structures, whose modal characteristics are to be identified, are modeled by a three-dimensional coupled system of N th order linear time-invariant differential equations in OBJ space. Let $\delta \bar{u}(t)$ be a three-element vector driving function and let $\delta \bar{w}(t)$ be a three-element vector response function at point \bar{w} . Then $\delta \bar{w}(t)$ and $\delta \bar{u}(t)$ are related by

$$\sum_{n=1}^N \frac{d^n}{dt^n} P_n \delta \bar{w}(t) + P_0 \delta \bar{w}(t) = \delta \bar{u}(t) \quad (1B)$$

where P_N, \dots, P_0 are three-by-three matrices of constants. Take the Fourier transform of (1B) to obtain

$$\left(\sum_{n=0}^N (i\omega)^n P_n \right) \delta \bar{w}(\omega) = \delta \bar{u}(\omega) \quad (2B)$$

By means of techniques of linear systems analysis⁴ equation (2B) may be solved for $\delta \bar{w}(\omega)$ as

$$\delta \bar{w}(\omega) = H(\omega) \delta \bar{u}(\omega) \quad (3B)$$

where $H(\omega)$, defined as the three-by-three frequency-response matrix, is the inverse of $\sum_{n=0}^N (i\omega)^n P_n$. It is desired to estimate $H(\omega)$ from observations in dual focal plane (DFP) space.

Let $\|Z^{-1} \delta Z\|$ be sufficiently small so that mappings D^{-1} and D defined in equation (18A) and (19A) are approximated well by

$$\delta \bar{w}(t) = D^{-1}(\delta \bar{w}(t)) \approx Z^{-1} A \delta \bar{w}(t) \quad (4B)$$

and

$$\delta \bar{w}(t) = D(\delta \bar{w}(t)) \approx P_A Z \delta \bar{w}(t) \quad (5B)$$

Although P_A is only a right inverse of A it is true that

$$Z^{-1} A P_A Z \delta \bar{w}(t) = \delta \bar{w}(t) \quad (6B)$$

whenever $\delta \bar{w}(t)$ is contained in the column space of $Z^{-1} A$, or equivalently, in the range of mapping D^{-1} . Since all $\delta \bar{w}(t)$ and $\delta \bar{u}(t)$ to be considered are contained in the range of D^{-1} , $P_A Z$ and $Z^{-1} A$ are hereafter treated as two-sided inverses of each other. Therefore, $\delta \bar{u}(t)$ and $\delta \bar{u}(t)$ are related by

$$\delta \bar{U}(t) \approx P_A Z \delta \bar{u}(t) \quad (7B)$$

$$\delta \bar{u}(t) \approx Z^{-1} A \delta \bar{U}(t) \quad (8B)$$

Let $\delta \bar{U}(t)$ be a zero-mean multivariate stochastic process which is stationary in the wide sense⁵. Then $\delta \bar{w}(t)$, $\delta \bar{u}(t)$, and $\delta \bar{v}(t)$ are also zero-mean, wide-sense stationary processes. The cross-covariance matrix between $\delta \bar{w}(t)$ and $\delta \bar{U}(t)$ is defined as

$$R_{WU}(\tau) = E(\delta \bar{w}(t) \delta \bar{U}^*(t - \tau)) \quad (9B)$$

and the autocovariance matrix of $\delta \bar{U}(t)$ is defined as

$$R_{UU}(\tau) = E(\delta \bar{U}(t) \delta \bar{U}^*(t - \tau)) \quad (10B)$$

where E denotes the expected value.

The cross-spectral matrix $S_{WU}(\omega)$ and the autospectral matrix $S_{UU}(\omega)$ are defined as

$$S_{WU}(\omega) = F(R_{WU}(\tau)) \quad (11B)$$

$$S_{UU}(\omega) = F(R_{UU}(\tau)) \quad (12B)$$

Similarly, define in DFP coordinates

$$S_{uu}(\omega) = F(E(\delta \bar{u}(t) \delta \bar{u}^*(t - \tau))) \quad (13B)$$

$$S_{wu}(\omega) = F(E(\delta \bar{w}(t) \delta \bar{u}^*(t - \tau))) \quad (14B)$$

It can be readily shown using (4B) and (5B) that

$$S_{UU}(\omega) = P_A Z S_{uu}(\omega) Z P_A^T \quad (15B)$$

$$S_{WU}(\omega) = P_A Z S_{wu}(\omega) Z P_A^T \quad (16B)$$

It is shown in Ref. (6) that if $\delta \bar{w}(\omega)$ and $\delta \bar{u}(\omega)$ are related by (3B) then $S_{WU}(\omega)$ and $S_{UU}(\omega)$ are related by

$$S_{WU}(\omega) = H(\omega) S_{UU}(\omega) \quad (17B)$$

Thus, if $S_{WU}(\omega)$ and $S_{UU}(\omega)$ are known, the solution of (17B) determines $H(\omega)$. If $\bar{w}(t)$ contains additive noise, it can be shown⁶ that the

solution of (17B) furnishes a minimum-mean-square-error estimate of $H(\omega)$.

Since experimental data are observed in DFP space, it is advantageous to computationally estimate $S_{uu}(\omega)$ and $S_{wu}(\omega)$, and to then estimate $H(\omega)$ using (15B)-(17B). Smoothed estimates of $S_{uu}(\omega)$ and $S_{wu}(\omega)$ are obtained as averaged conjugate outer products of the Fourier transforms of N observed data blocks of length T of $\delta \bar{w}(t)$ and $\delta \bar{u}(t)$. Thus, the Fourier transforms of the n th block are

$$\Delta \bar{w}_n(\omega) = \int_{(n-1)T}^{nT} \delta \bar{w}(t) e^{-i\omega t} dt \quad (18B)$$

$$\Delta \bar{u}_n(\omega) = \int_{(n-1)T}^{nT} \delta \bar{u}(t) e^{-i\omega t} dt \quad (19B)$$

and the smoothed estimated autospectral and cross-spectral matrices are

$$\hat{S}_{uu}(\omega) = \frac{1}{N} \sum_{n=1}^N \Delta \bar{u}_n(\omega) \Delta \bar{u}_n^* T(\omega) \quad (20B)$$

$$\hat{S}_{wu}(\omega) = \frac{1}{N} \sum_{n=1}^N \Delta \bar{w}_n(\omega) \Delta \bar{u}_n^* T(\omega) \quad (21B)$$

Smoothed estimates of $S_{UU}(\omega)$ and $S_{WU}(\omega)$ are obtained from $\hat{S}_{uu}(\omega)$ and $\hat{S}_{wu}(\omega)$ using transformations (15B) and (16B). Then $H(\omega)$ can be estimated using (21B), provided $\hat{S}_{UU}(\omega)$ is nonsingular, as

$$\hat{H}(\omega) = \hat{S}_{WU}(\omega) \hat{S}_{UU}^{-1}(\omega) \quad (22B)$$

Note that $\hat{S}_{UU}(\omega)$ is singular if $\bar{U}(t)$ is unidirectional (of the form $g(t) \bar{U}$) or planar (of the form $g_1(t) \bar{U}_1 + g_2(t) \bar{U}_2$). Even if $\hat{S}_{UU}(\omega)$ is nonsingular, computation of (22B) may be expensive since a three-by-three matrix must be inverted for each value of ω . These observations suggest that three unidirectional mutually orthogonal driving functions $\bar{U}(t)$ be applied in three independent measurements to estimate $H(\omega)$.

The observed driving function, $\delta \bar{u}(t)$, and the observed response function, $\delta \bar{w}(t)$, in DFP space are related through equations (1B), (5B), and (7B). Take Fourier transforms of $\delta \bar{w}(t)$ and $\delta \bar{u}(t)$ in equations (5B) and (7B) and premultiply (3B) by $Z^{-1} A$ to obtain

$$\delta \bar{w}(\omega) = Z^{-1} A H(\omega) P_A Z \delta \bar{u}(\omega) \quad (23B)$$

It follows⁶ from (23B) that $S_{wu}(\omega)$ and $S_{uu}(\omega)$ are related by

$$S_{wu}(\omega) = Z^{-1} A H(\omega) P_A Z S_{uu}(\omega) \quad (24B)$$

so that

$$P_A Z S_{wu}(\omega) = H(\omega) P_A Z S_{uu}(\omega) \quad (25B)$$

A method for estimation of a full nondiagonal $H(\omega)$ matrix is the following. Let scalar input $g(t)$ be applied in three independent tests to the X, Y, and Z components respectively of $\delta \bar{u}(t)$. From the observed input $\delta \bar{u}(t)$ and the observed response $\delta \bar{w}(t)$ in DFP space for each test one column of $H(\omega)$ can be estimated. Thus apply $g(t)$ in the X direction. Then input vector $\delta \bar{u}(t)$ is

$$\delta \bar{u}(t) = g(t) \begin{pmatrix} 1 \\ 0 \\ 0 \end{pmatrix} \quad (26B)$$

Expressed in DFP coordinates the input vector is

$$\delta \bar{u}(t) = g(t) Z^{-1} A \begin{pmatrix} 1 \\ 0 \\ 0 \end{pmatrix} \quad (27B)$$

Autospectral matrix $S_{uu}(\omega)$ is then

$$S_{uu}(\omega) = s_{gg}(\omega) Z^{-1} A \begin{bmatrix} 1 & 0 & 0 \\ 0 & 0 & 0 \\ 0 & 0 & 0 \end{bmatrix} A^T Z^{-1} \quad (28B)$$

where $s_{gg}(\omega)$ is the autopower spectrum of $g(t)$. Equation (28B) may be rewritten as

$$P_A Z S_{uu}(\omega) = s_{gg}(\omega) \Gamma_k \quad (29B)$$

where (for $k = 1$)

$$\Gamma_1 = \begin{bmatrix} \frac{a_{11}}{z_1} & \frac{a_{21}}{z_1} & \frac{a_{31}}{z_2} & \frac{a_{41}}{z_2} \\ 0 & 0 & 0 & 0 \\ 0 & 0 & 0 & 0 \end{bmatrix} \quad (30B)$$

and a_{ij} is the i - j th element of A . From equations (25B) and (30B) it follows that

$$P_A Z S_{wu}(\omega) = s_{gg}(\omega) H(\omega) \Gamma_k \quad (31B)$$

Autopower spectrum $s_{gg}(\omega)$ can be estimated from $\hat{S}_{uu}(\omega)$ using equation (29B). Column 1 of $H(\omega)$ is then estimated from the estimate $\hat{s}_{gg}(\omega)$ and cross-spectral matrix $\hat{S}_{wu}(\omega)$ using equation (31B). Columns 2 and 3 of $H(\omega)$ are estimated in a similar manner. Thus, apply $g(t)$ in the Y direction for $k = 2$ to give

$$\delta \bar{u}(t) = g(t) \begin{pmatrix} 0 \\ 1 \\ 0 \end{pmatrix} \quad (32B)$$

and

$$\Gamma_2 = \begin{bmatrix} 0 & 0 & 0 & 0 \\ \frac{a_{12}}{z_1} & \frac{a_{22}}{z_1} & \frac{a_{32}}{z_2} & \frac{a_{42}}{z_2} \\ 0 & 0 & 0 & 0 \end{bmatrix} \quad (33B)$$

Use equations (29B) and (31B) to estimate $s_{gg}(\omega)$ and column 2 of $H(\omega)$. Finally apply $g(t)$ in the Z direction for $k = 3$ to give

$$\delta \bar{u}(t) = g(t) \begin{pmatrix} 0 \\ 0 \\ 1 \end{pmatrix} \quad (34B)$$

and

$$\Gamma_3 = \begin{bmatrix} 0 & 0 & 0 & 0 \\ 0 & 0 & 0 & 0 \\ \frac{a_{13}}{z_1} & \frac{a_{23}}{z_1} & \frac{a_{33}}{z_2} & \frac{a_{43}}{z_2} \end{bmatrix} \quad (35B)$$

Use equations (29B) and (31B) as before to estimate $s_{gg}(\omega)$ and column 3 of $H(\omega)$.

Least Squares Estimation of Frequency-Response Matrix

A method is developed for least-squares estimation of $H(\omega)$ from equations (29B) and (31B). Since $S_{uu}(\omega)$ and $S_{wu}(\omega)$ are estimated in equations (20B) and (21B) and since measurements of

$\bar{u}(t)$ and $\bar{w}(t)$ are noisy, no values of $\hat{s}_{gg}(\omega)$ and $\hat{h}(\omega)$ exist in general which will satisfy equations (29B) and (31B) for estimated matrices $\hat{s}_{uu}(\omega)$ and $\hat{s}_{wu}(\omega)$. Thus, in general for every value of $\hat{s}_{gg}(\omega)$ in (29B)

$$\hat{s}_{uu}(\omega) \neq \hat{s}_{gg}(\omega) \Lambda_k \quad (36B)$$

where

$$\Lambda_k = Z^{-1} A \Gamma_k \quad (37B)$$

and for every $\hat{h}(\omega)$ in (31B)

$$P_A Z \hat{s}_{wu}(\omega) \neq \hat{s}_{gg}(\omega) \hat{h}(\omega) \Gamma_k \quad (38B)$$

Optimum estimates of $s_{gg}(\omega)$ and $H(\omega)$ can be determined by choosing $\hat{s}_{gg}(\omega)$ and $\hat{h}_k(\omega)$ such that the sum of the squares of the Euclidian distances between corresponding columns is minimized in inequalities (36B) and (38B). Thus, from (36B) define

$$\begin{aligned} \epsilon_u^2 &= \sum_{j=1}^4 \|\hat{s}_{uu,j}(\omega) - \hat{s}_{gg}(\omega) \bar{\lambda}_{.j}\|^2 \\ &= \sum_{j=1}^4 (\hat{s}_{uu,j}(\omega) - \hat{s}_{gg}(\omega) \bar{\lambda}_{.j})^T (\hat{s}_{uu,j}(\omega) - \hat{s}_{gg}(\omega) \bar{\lambda}_{.j}) \end{aligned} \quad (39B)$$

where

$\hat{s}_{uu,j}(\omega)$ is the j th column of $\hat{s}_{uu}(\omega)$ and $\bar{\lambda}_{.j}$ is the j th column of Λ_k .

To minimize ϵ_u^2 differentiate (39B) with respect to $\hat{s}_{gg}(\omega)$, set to zero, and solve for $\hat{s}_{gg}(\omega)$ to obtain

$$\hat{s}_{gg}(\omega) = \left(\sum_{j=1}^4 \bar{\lambda}_{.j}^T \hat{s}_{uu,j}(\omega) \right) / \left(\sum_{j=1}^4 \bar{\lambda}_{.j}^T \bar{\lambda}_{.j} \right) \quad (40B)$$

To estimate $\bar{h}_k(\omega)$ use (38B) to define

$$\epsilon_h^2 = \sum_{j=1}^4 \|\hat{\sigma}_{wu,j}(\omega) - \hat{s}_{gg}(\omega) \gamma_{kj} \hat{h}_k(\omega)\|^2 \quad (41B)$$

where $\hat{\sigma}_{wu,j}(\omega)$ is the j th column of

$P_A Z S_{wu}(\omega)$ and where $\hat{s}_{gg}(\omega)$ is given by (40B). Proceed as above to minimize ϵ_h and solve for $\hat{h}_k(\omega)$ to obtain

$$\bar{h}_k(\omega) = \left(\sum_{j=1}^4 \gamma_{kj} \hat{\sigma}_{wu,j}(\omega) \right) / \left(\hat{s}_{gg}(\omega) \sum_{j=1}^4 \gamma_{kj} \right) \quad (42B)$$

References

- ¹Abdel-Aziz, Y. I. and Karara, H. M., "Direct Linear Transformation from Comparator Coordinates into Object Space Coordinates in Close-Range Photogrammetry," proceedings of the ASP/UI Symposium on Close-Range Photogrammetry, Urbana, Illinois, January 1971.
- ²Forsythe, G. E. and Moler, C. B.: Computer Solution of Linear Algebraic Systems, Prentice-Hall, 1967.
- ³Papoulis, A.: The Fourier Integral and Its Applications, McGraw-Hill, 1962.
- ⁴Swisher, G. M.: Introduction to Linear Systems Analysis, Matrix Publishers, Inc., 1976.
- ⁵Papoulis, A.: Probability, Random Variables, and Stochastic Processes, McGraw-Hill, 1965.
- ⁶Jenkins, G. M. and Watts, D. G.: Spectral Analysis and Its Applications, Holden Day, Inc., 1968.

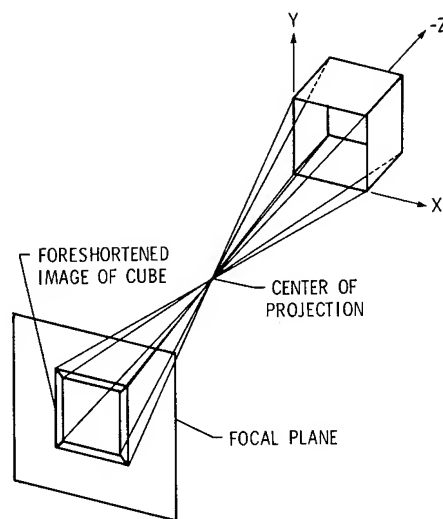


Fig. 1 Perspective projection of a cube.

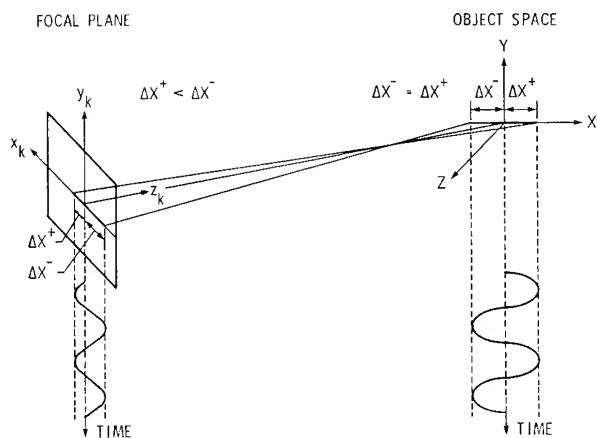


Fig. 2 Perspective distortion of a sinusoidal time function.

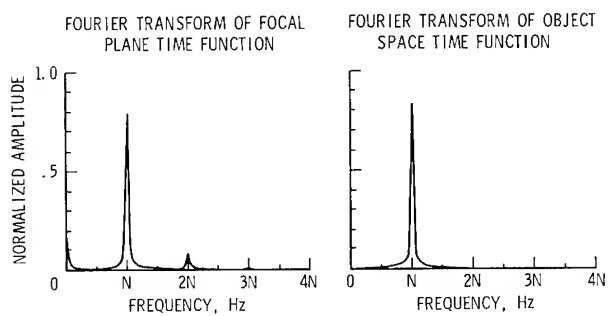


Fig. 3 Fourier transforms of distorted and nondistorted sinusoids.

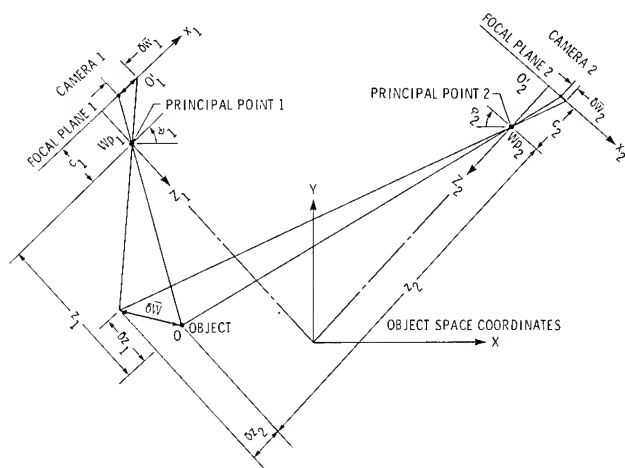
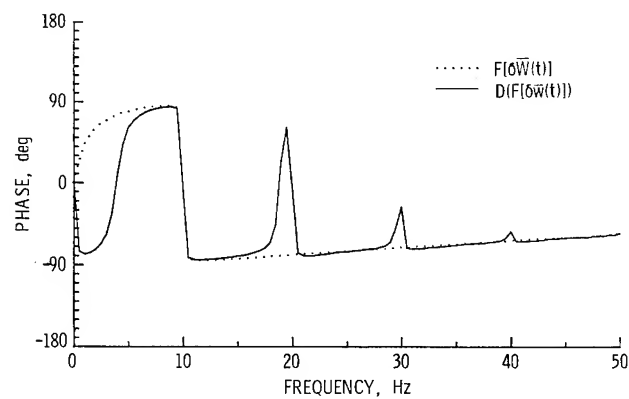
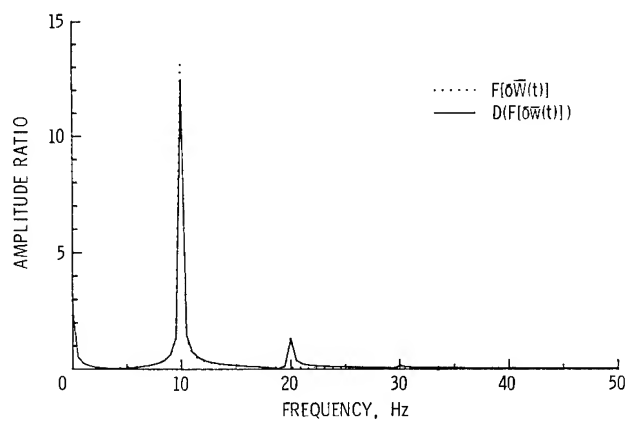
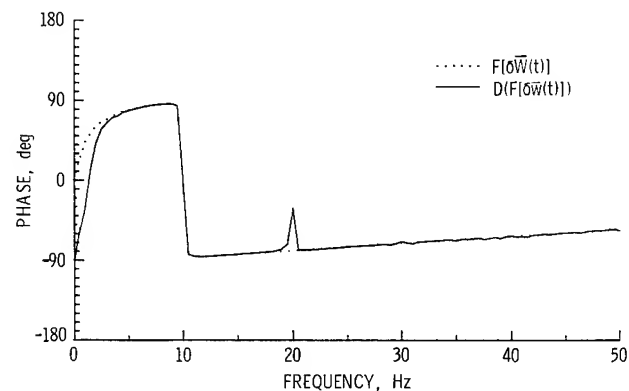
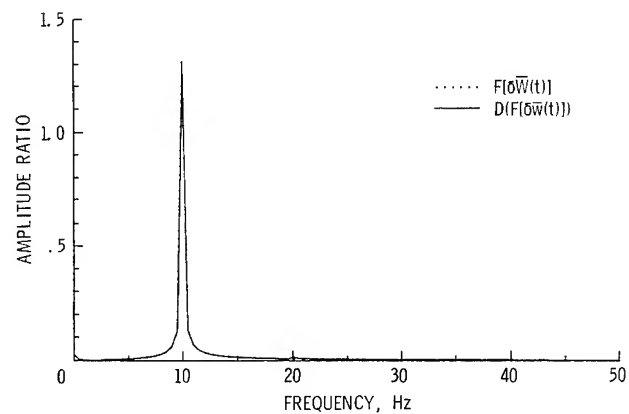


Fig. 4 Stereoscopic projection system showing perturbations and images.



a. $\delta z/z = 0.25$



b. $\delta z/z = 0.025$

Fig. 5 Comparison of calculated transforms (damped sinusoid in Y direction).

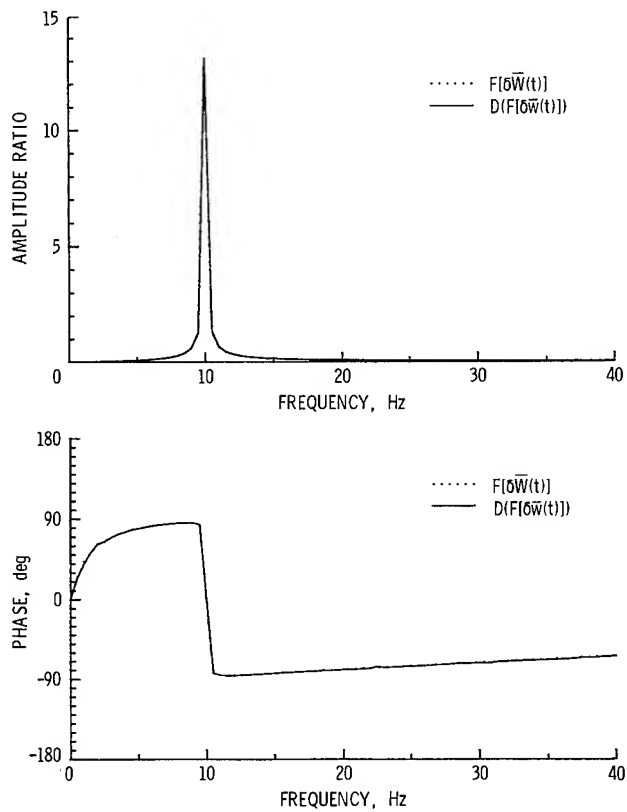
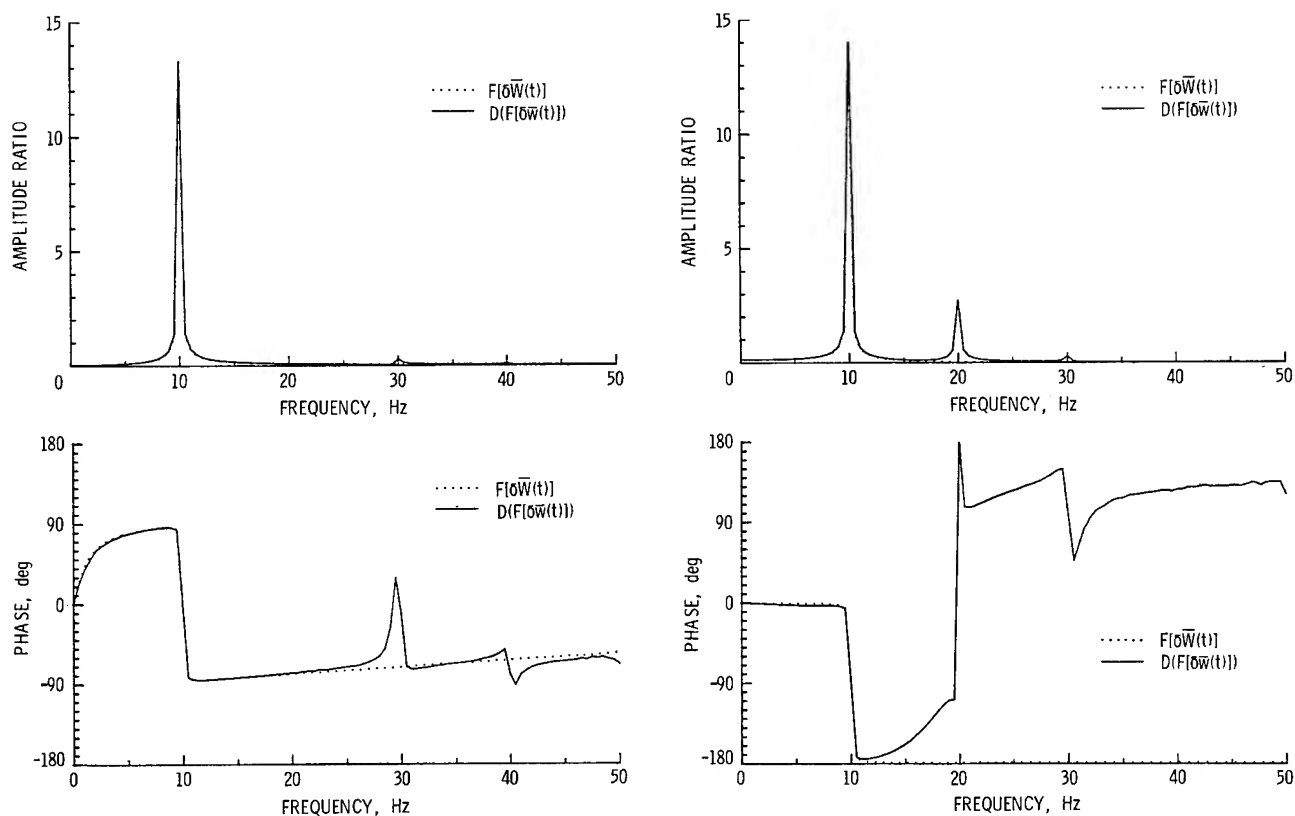


Fig. 6 Comparison of calculated transforms (damped sinusoid in Z direction).



a. X component

b. Y component

Fig. 7 Comparison of calculated transforms (sum of damped sinusoids in X and Y directions with $\delta z/z = 0.25$).

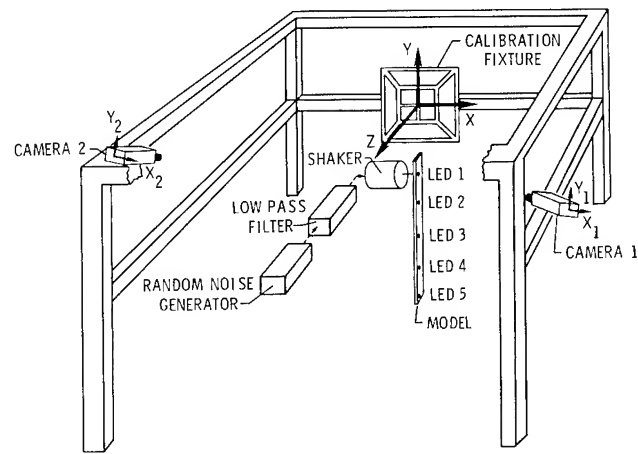


Fig. 8 Test apparatus.

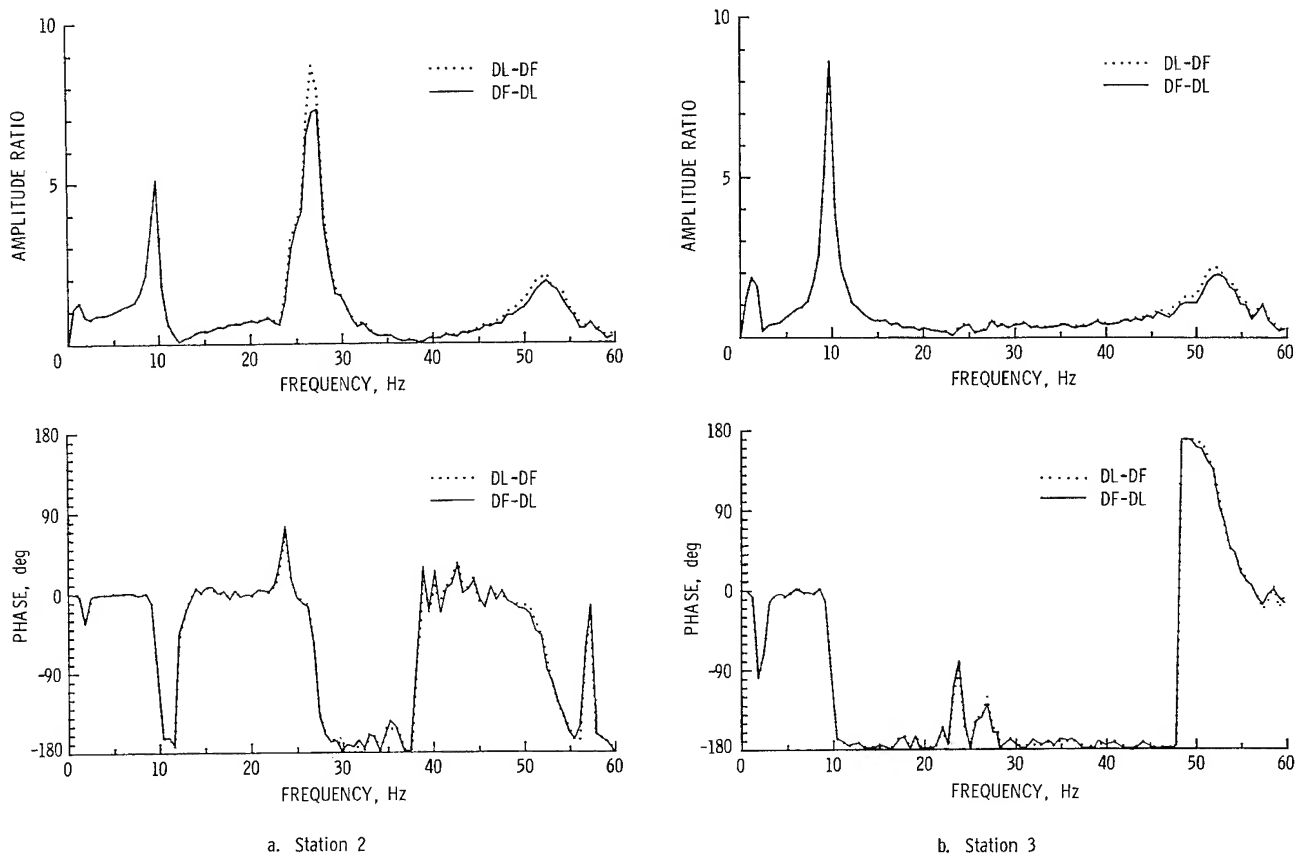
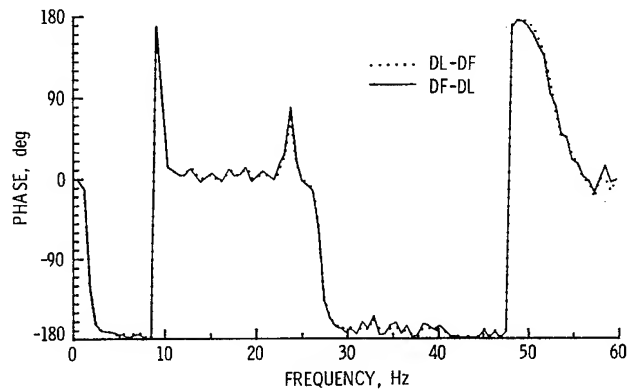
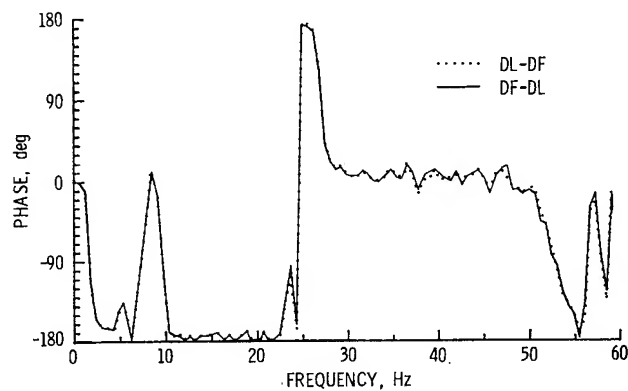
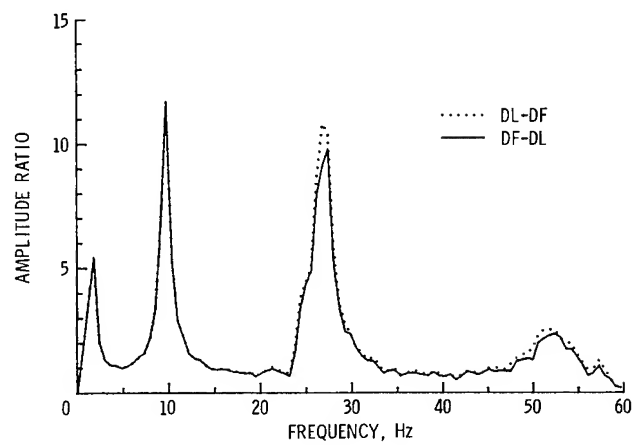
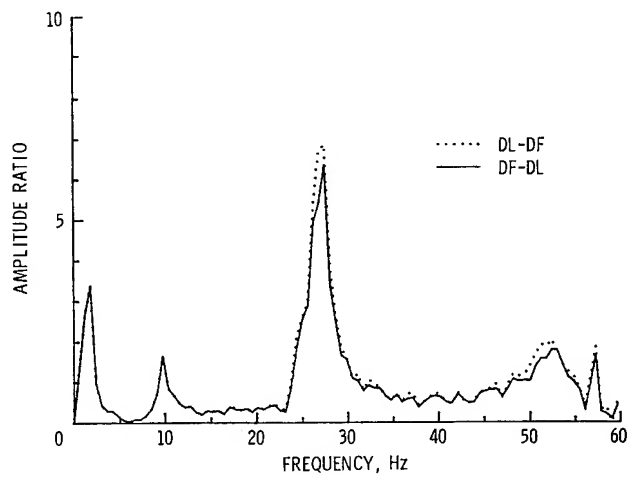


Fig. 9 Comparison of frequency-response functions from DF-DL and DL-DF transforms.



c. Station 4

d. Station 5

Fig. 9 Concluded

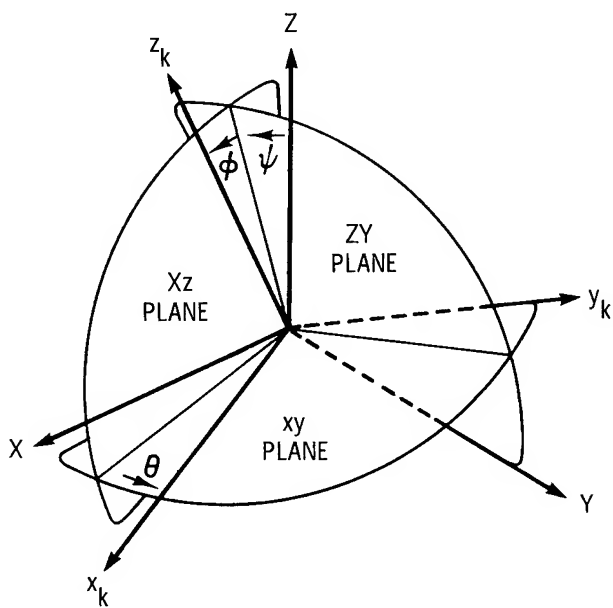


Fig. 10 Angles of exterior orientation.

Marc Trubert*
Jet Propulsion Laboratory
California Institute of Technology
4800 Oak Grove Drive
Pasadena, CA 91109

ABSTRACT

The modal test program for the Galileo Spacecraft was completed at the Jet Propulsion Laboratory in the summer of 1983. The multiple sine dwell method was used for the baseline test. The Galileo Spacecraft is a rather complex 2433 kg structure made of a central core on which seven major appendages representing 30% of the total mass are attached, resulting in a high modal density structure. The test revealed a strong non-linearity in several major modes. This non-linearity discovered in the course of the test necessitated running additional tests at the unusually high response levels of up to about 21g. The high levels of response were required to obtain a model verification valid at the level of loads for which the spacecraft was designed. Because of the high modal density and the non-linearity, correlation between the dynamic mathematical model and the test results becomes a difficult task. Significant changes in the pre-test analytical model are necessary to establish confidence in the upgraded analytical model used for the final load verification. This verification, using a test verified model, is required by NASA to fly the Galileo Spacecraft on the Shuttle/Centaur launch vehicle in 1986.

INTRODUCTION

The Galileo system modal test was performed at JPL with the spacecraft in the launch configuration cantilevered at the Centaur/Galileo interface on the JPL seismic block.

The objective of the test was to measure the basic structural dynamic characteristics of the spacecraft in the 0 to 45 Hz range in order to verify and/or upgrade the analytical model used for the Galileo structural loads analysis.

The traditional tuned sine-dwell method was the base line method.¹ In addition to generating the needed basic data, the sine-dwell method was also intended to provide comparative data for the newer, more advanced modal testing methods, that were implemented on Galileo in a parallel effort, in order to establish confidence in these new methods. The comparative results are presented in a separate publication.²

The test has clearly shown a definite non-linear effect in the Galileo structure. The discovery of this nonlinearity dictated a redirection of the test to obtain data at the highest possible response level, a departure from previous programs. The only available method to achieve this goal at the time of the test was the sine-dwell method, because of the

inherent capability of concentrating power in a single frequency.

During a large part of the test, the emphasis was then to obtain the maximum amount of pertinent data in such a way that investigating the effect of large amplitude on a small number of key modes became more important than identifying the largest possible number of modes.

The situation of the Galileo modal test is a reminder that a modal test is basically a structural test aimed at the investigation of the structure, and as such must show great flexibility in its implementation (hardware, software and procedures).

The presence of nonlinearities may have cast some doubts on the validity of the linear analytical approach to calculate loads. It is the belief of the author that the use of linear models must continue, because it is the only tractable analysis possible at the present time and it remains the most valuable tool. It is simply that the task of generating a meaningful worse case linear model has become much more difficult.

As a result of the test a significant upgrading of the test analytical model (TAM) appears necessary since a number of discrepancies exist between the measured data and the pre-test analytical prediction of the modes.

An enormous amount of data has been generated from the test and is available as a JPL report.¹ However, only a small portion of these data has practical value. The most valuable data subsets to be used to upgrade the pre-test mathematical model are:

- the natural frequencies
- the plots of local deformation of the core
- the energy plots
- the effective mass

HARDWARE

Test Article

The test article was the Galileo Development Test Model (DTM) shown in Fig. 1. Fig. 2 is a photograph of the DTM in the modal test tower during the test. Fig. 3 shows a schematic view of the structural arrangement and the coordinate system. Basically for the DTM all the load carrying members are actual flight-like structures, only the electronic subsystems and science instruments are mass mockups. The mass of the fluid (1036 kg) in the four propellant tanks was simulated by isopropyl alcohol and freon referee fluids. To prevent sloshing the tanks were 100% full. This was accomplished by using pressurized ullage bottles mounted away from

*Member of Technical Staff
Member AIAA

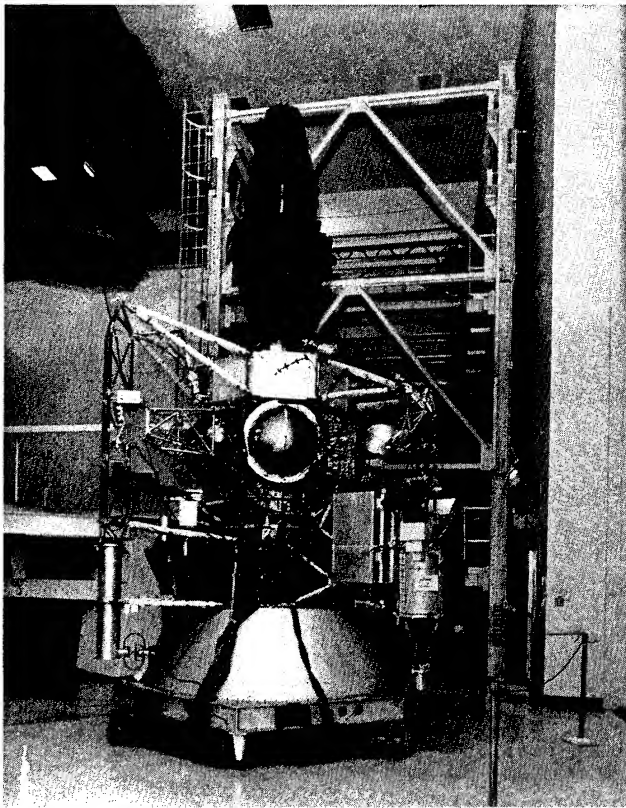


Fig. 1. Galileo DTM

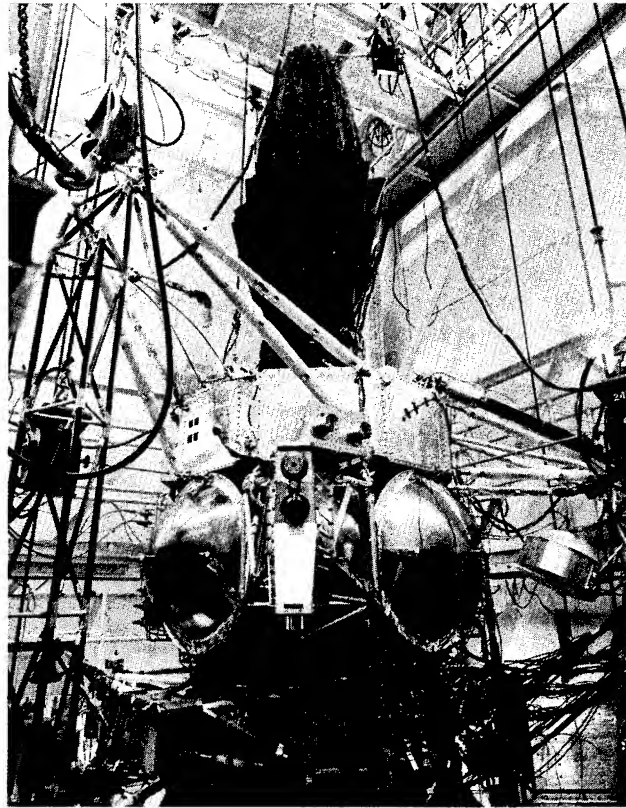


Fig. 2. Galileo DTM at Test Site.

and above the tanks. The total weight of the spacecraft under test was 2431 kg including test cables.

Galileo is a dual-spin spacecraft when in the cruise configuration. In the launch configuration the spun portion is temporarily locked to the despun portion in order to form one single continuous system and in addition, all the deployable appendages are in the stowed position. The entire stowed system is attached to the Centaur upper stage through a conical adapter. The system modal test was for this launch configuration with the spacecraft cantilevered on a seismic bloc at the Centaur/Galileo interface, i.e., the base of the conical adapter (Fig. 3).

Galileo Peculiar Structure

a) The Galileo spacecraft is a rather complex structure basically made of a central core on which 7 major appendages are attached, i.e.,

- One 50 kg deployable High-Gain Antenna (SXA) mounted on the top of the spacecraft bus and protruding 2.5 meters above it,
- Two deployable Radioisotope Thermoelectric Generators (RTG), 77 and 80 kg each, tucked on the +X and -X sides of the spacecraft,
- One 77 kg deployable Science Boom on the +Y side of the spacecraft,
- One 110 kg box of electronics (Despun Box) sandwiched between the core and the Science Boom,

- One 342 kg Probe placed inside the Galileo/Centaur adapter,
- One 96 kg Scan Platform on the -Y axis side of the spacecraft.

b) Five of these seven appendages have a very significant interaction with the motion of the core. For example, unlike previous JPL spacecraft, the lowest two natural frequencies are basically the High-Gain Antenna appendage modes, with slight core participation, instead of being mainly core modes as for previous spacecraft.

c) The Galileo structure has a high modal density as shown by the analysis which exhibits 31 modes of vibration between 13 and 45 Hz, representing an average of 1 mode per Hz.

d) In addition, several major modes have very close natural frequencies that are about 1% apart.

e) Several areas of the spacecraft, principally the High-Gain Antenna, the RTG's and possibly the Load Transfer Ring have an inherent frequency/amplitude non-linearity which because it is present in addition to the high modal density mentioned above creates large variations of modal coupling with amplitude.

f) As a consequence a rather stringent requirement must be imposed on the stability of the sine dwell driving frequency of the pilot oscillator, analog or digital. It is this high stability requirement, underestimated prior to the test, which made the use of a proposed computer driven sine oscillator impractical in its existing form at the time of test.

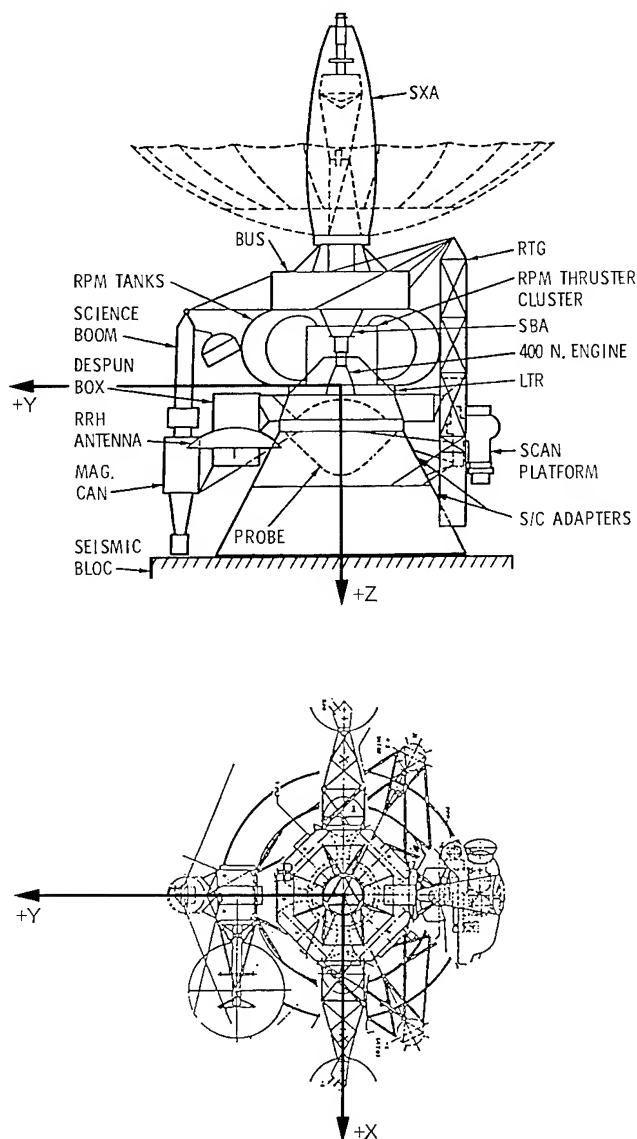


Fig. 3. Galileo Modal Test Configuration and Coordinate System

Nature of the Galileo Modal Test

The above observations result in the following consequences.

Since the spacecraft design loads correspond to large amplitudes, 10 to 50g range, the testing had to be performed at a level as high as possible, at least for the load inducing modes, in order to be representative of the actual flight levels.

The pre-test linear mathematical model was found to be very sensitive to inaccuracies in modelling. This resulted in poor correlation between pre-test analysis and test values.

The non-linearity of frequency versus amplitude for a number of major modes makes the analysis/test correlation a very challenging

task since basically one has to find a linear model that would fit, at best, a nonlinear structure for each range of response level.

The traditional orthogonality and effective mass assessments which are a combination of both analytical (mass matrix) and test results, loses a great deal of its significance for the in-test evaluation of the goodness of the experimental data. In this respect it is only after the mathematical model is refined and with appropriate linearization, that the orthogonality criteria can possibly be used as a final check of the goodness of the test and analysis combination as a whole.

Instrumentation

The general arrangement of the analog instrumentation is shown in Figure 4.

The 162 accelerometer locations were chosen according to the results of the pre-test analysis done on the Test Analytical Model (TAM) corresponding to the degrees of freedom with mass. These accelerometers were bonded on the spacecraft prior to the beginning of the test.

In addition to the 162 fixed accelerometers a roving accelerometer (rover) was used to further define the mode shapes of selected modes as discrepancies between test and analysis became apparent during the test. The roving accelerometer provided response measurements at 108 locations in addition to those of the 162 fixed accelerometers. The need for the rover exemplifies the nature of this type of modal test which must exhibit great flexibility for measuring response data at extra locations that are not known until the test is in progress.

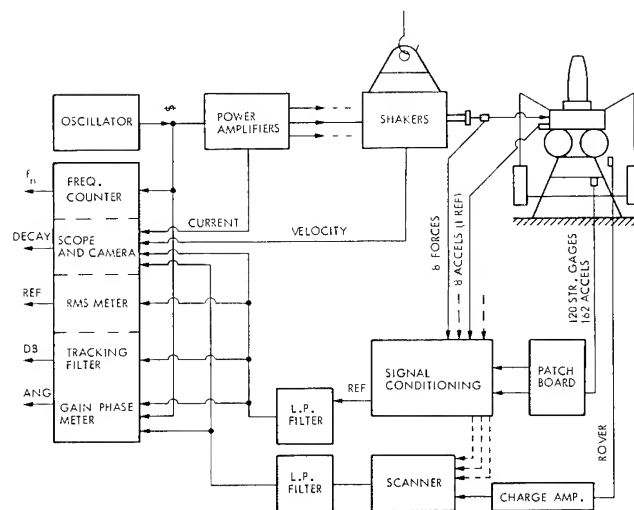


Fig. 4. Shaker/Instrumentation Analog Arrangement

The shaking equipment consisted of ten 15-lb Ling shakers and four 75-lb Unholtze Dickie shakers. The latter were used to excite the high level of responses which became necessary after the low level assessment. A various number of shakers were used simultaneously in various combinations and locations depending upon the mode to be excited. The number of simultaneously used shakers varied from a minimum of 2 to a maximum of 8.

As in previous JPL spacecraft modal tests, the shakers were supported in a pendulum fashion by adjustable hoists which provided a suspension frequency of a few Hz, well below the fundamental frequency of the spacecraft.

In order to measure the force applied to the structure a force gage was also placed in series between the spacecraft and the armature either before or after the fuse.¹ The gage allowed amplitude and phase measurement of the force delivered to the spacecraft by each shaker. To complement the force measurement, an accelerometer (shaker accelerometer) was also placed as close as possible to the point of attachment of the shaker, usually on the spacecraft, to form an "impedance head". The combination of the force gage and accelerometer measurements allowed the calculation of the generalized force applied by each shaker to the spacecraft.

NATURAL RESONANT FREQUENCIES AND NON-LINEARITIES

A number of 17 separate modes, i.e. natural frequencies, modes shapes, and dampings were measured, while the total number of actual measurements was 36 counting non-linearity runs and repeats.

For a number of more important modes the tuning was done at several response levels to investigate the effect of non-linearities. Some of the modes showed a very strong change of natural frequency with amplitude.

Table 1 shows a listing of the natural frequencies as measured and as calculated from TAM6SB, which is an update of the pre-test TAM after a number of inaccuracies of the original TAM were noted and corrected. TAM6SB is not an update from the test values; this is a future task to be performed. Fig. 5 shows the evolution of the TAM through the modal test program.

Figures 6 through 8 show typical non-linearity plots of the variation of natural frequencies with amplitude. Note that the level of the HGA response of Figure 6 is particularly high for a modal test. It was found necessary to run at such a high level since the HGA/core modes have a predominant contribution to the total loads. Although the 20g tip level is high for a modal test it is still only about 40% of the design load level which is about 50g. Additional non-linearity plots can be found in the report.¹

Data Acquisition

After the tuned-dwell condition above was achieved and held, the raw data was recorded during the dwell for each patchboard (Fig. 4), one channel at a time for all the shaker force gages, the shaker accelerometers, and the mode shape accelerometers of that particular patchboard.

The data consisted of amplitude ratio, in db, and phase measurement, in degrees, of each channel, both with respect to the reference accelerometer. The RMS voltage of the reference accelerometer, remaining approximately constant (low drift) throughout the taking of the data, was also recorded.

Each channel of the data, one at a time, and the reference accelerometer were simultaneously filtered, narrow band, by a dual channel tracking filter tuned at the pilot frequency (Fig. 4). A low pass filter was used simultaneously for each of the 2 channels before entering the tracking filter in order to eliminate any high frequency component that could have saturated the tracking filter. The two low pass filters were identical and set to the same cut-off frequency avoiding any phase shift between channels. The cut-off frequency was 40 to 80 Hz depending upon the mode being measured. Each channel was scanned one at a time with a manual scanner, the ratio and phase angle read from digital voltmeters, and manually logged on an input sheet for subsequent keying to a VAX computer for processing.

Generalized Force

Calling

$$FZ(J) = F(J) + i G(J) \quad \text{the physical force}$$

$$AZ(J) = X(J) + i Y(J) \quad \begin{array}{l} \text{the acceleration at} \\ \text{the point of applica-} \\ \text{tion of the force} \end{array}$$

The generalized force is defined by:

$$GFR(J) + i GFI(J) = \sum_{J=1}^{NS} FZ(J) * AZ(J) \quad (1)$$

where NS is the total number of shakers.

Then the real and imaginary parts and modulus of the generalized force are:

$$GFR(J) = \sum_{J=1}^{NS} F(J) * X(J) - G(J) * Y(J) \quad (2)$$

$$GFI(J) = \sum_{J=1}^{NS} F(J) * Y(J) + G(J) * X(J) \quad (3)$$

$$GFM = \sqrt{GFR^2 + GFI^2}$$

Table 1 Analysis/test frequency comparison and damping

TAM 6SB		Test					Description of Mode
Mode Number	Freq (Hz)	Mode Number	Freq (Hz)	Amplitude	Damping		
					Analog	Digital	
1	13.49	1	13.05 13.07 13.18 13.71 13.48 13.32	1.3 g SXA TIP 1.3 g SXA TIP 1.4 g SXA TIP 7.1 g SXA TIP 13.6 g SXA TIP 21.1 g SXA TIP	0.021 - - - 0.020 -	- 0.018 - - - -	HGA X
2	13.74	2	12.70 12.85 12.85 13.74 13.69 13.56	1.5 g SXA TIP 1.3 g SXA TIP 1.5 g SXA TIP 7.5 g SXA TIP 14.0 g SXA TIP 20.2 g SXA TIP	0.017 - - 0.024 0.023 -	0.016 0.018 - - - -	HGA Y
3	16.44	5	18.59	1.5 g MAG CAN	-	0.015	SCIENCE BOOM X
4	18.15	3	17.42 17.45 17.70 17.79 17.95	0.27 g BUS 0.27 g BUS 0.41 g BUS 0.38 g BUS 1.20 g BUS	- 0.013 0.011 - 0.020	0.012 - - - -	} CORE BENDING
5	18.83	4	17.66 17.72 18.15	0.22 g BUS 0.38 g BUS 1.02 g BUS	0.010 - -	0.013 - -	
6	20.42		22.22 23.08	0.46 g RTG 0.68 g RTG	0.010 -	- -	
7	20.52	6	21.60	2.8 g RTG	0.010	-	
8	21.27	8	24.85 25.25 25.27	0.67 g BUS 0.35 g BUS 0.31 g BUS	- - -	- - 0.011	TORSION
9	22.97	7	23.58	1.06 g RTG	-	0.017	RTG Z
11	26.59	10	25.73	1.00 g SC BOOM	-	0.013	SC. BOOM Z/PROBE Y
16	32.54		37.84	2.0 g MAG TIP	0.018	-	SC BOOM/RRH
17	33.77		37.52 37.59 37.78	1.0 g TANKS 0.88 g TANKS 0.72 g TANKS	- - -	- - 0.006	BOUNCE
19	36.25		42.27	2.7 g - THRUSTER	-	0.005	-X THRUSTER
20	37.08		41.35	2.5 g + THRUSTER	-	0.006	+X THRUSTER
21	38.48		28.16	0.04 rad/sec ²	0.014	-	SCAN PLATFORM
27	42.62		33.35	0.86 g SCAN	0.010	-	SCAN PLATFORM/PROBE X
28	43.68		33.83 40.50	0.30 g (LATERAL) 1.20 g	-	-	+ RTG LAT/PROBE X
31	45.80		29.91 37.42	0.45 g (LATERAL) 2.60 g	- -	0.011 -	-RTG LAT

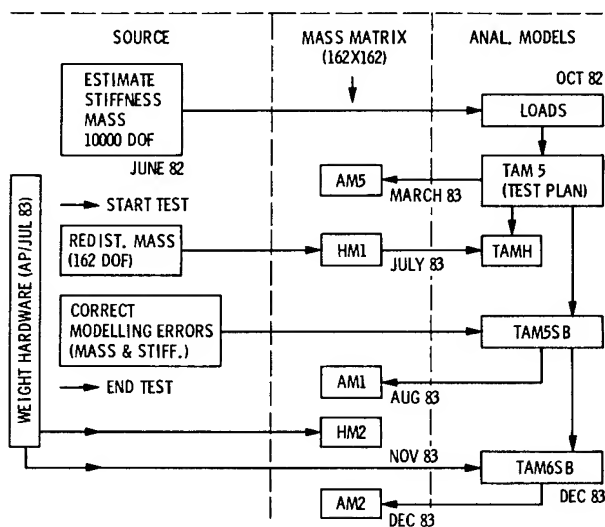


Fig. 5. Evolution of Analytical Models

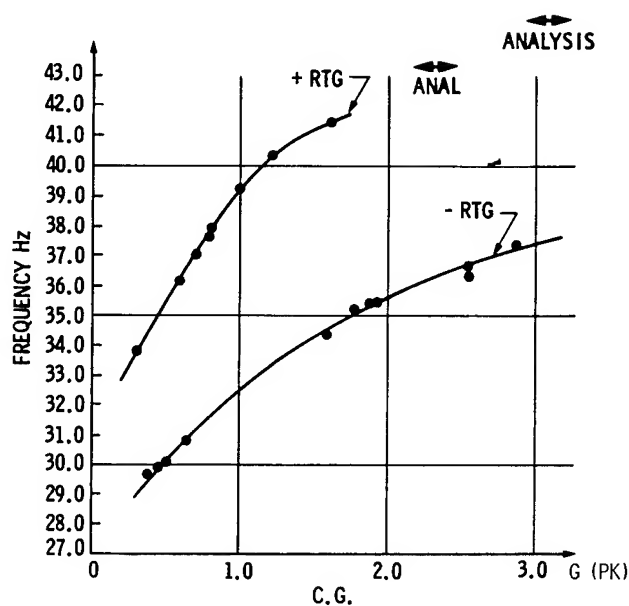


Fig. 8. RTG's (Tangential) Frequencies vs Amplitude

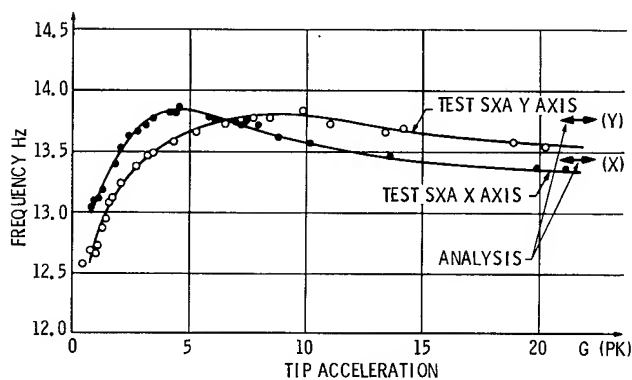


Fig. 6. High Gain Antenna Frequencies vs Amplitude

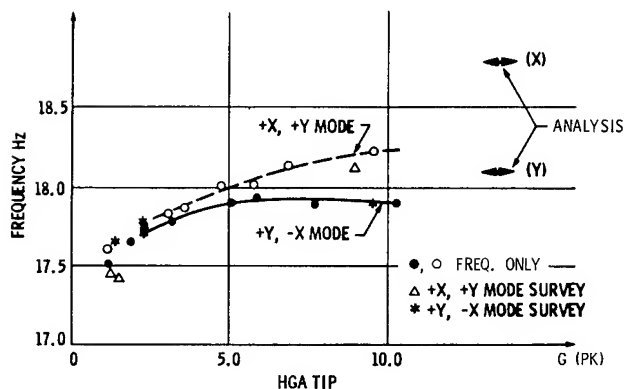


Fig. 7. Core Bending Frequencies vs Amplitude

Transformation Matrix

A transformation matrix $[T]$ (162 x 162) was constructed from the location and orientation of the accelerometers with respect to each node of the TAM. This matrix $[T]$ transforms the 162 translation acceleration readings $\{AR\}$ into the corresponding 162 responses $\{A\}$, translation and/or rotation, degrees of freedom of the TAM

$$\{A\} = [T]\{AR\} \quad (4)$$

Mode Shape Determination

Ideal Condition. For the sake of simplicity to understand the basic problem let us assume the ideal case of proportional damping, i.e., the damping matrix is a linear combination of the stiffness and mass matrices. Then, if only one mode n was harmonically excited at a frequency ω , the modal response $q_n(t)$ would follow the basic equation of a simple one-degree-of-freedom spring-mass system:

$$\ddot{q}_n + 2\xi_n \omega_n \dot{q}_n + \omega_n^2 q_n = f_n(t) = GFM e^{i\omega t} \quad (5)$$

where ω_n is the natural frequency

ξ_n is the modal damping,

$f_n(t) = GFM e^{i\omega t}$ is the generalized force.

The homogeneous solution of Eq. (5) is also a harmonic function

$$q_n(t) = Q_n e^{i(\omega t - \theta)} \quad (6)$$

$$\dot{q}_n(t) = i\omega Q_n e^{i(\omega t - \theta)} = \omega Q_n e^{i(\omega t - \theta + 90^\circ)} \quad (7)$$

$$\ddot{q}_n(t) = -\omega^2 Q_n e^{i(\omega t - \theta)} \quad (8)$$

where θ is the phase shift between the force and the response.

The acceleration response $A_{jn}(t)$ at any point J of the structure is

$$A_{jn}(t) = \phi_n(J) * (-\omega^2 Q_n e^{i(\omega t - \theta)}) \quad (9)$$

where $\phi_n(J)$ is the real mode shape of mode n and $J = 1, 2, \dots, \text{NDOF}$. The object is to obtain $\phi_n(J)$ from the time history $A_{jn}(t)$. Only the amplitude A_{jn} of $A_{jn}(t)$ needs to be measured. This amplitude is proportional to the mode shape $\phi_n(J)$.

The resonance condition is for $\omega = \omega_n$ for which (Fig. 9)

a) the modal velocity $\dot{q}_n(t)$ is in phase with the force $GFM e^{i\omega t}$, i.e., from Eq. (7) $\theta = 90^\circ$, and it follows that the modal acceleration $\ddot{q}_n(t)$ is 90° out of phase with the force,

b) from Eq. (9) the accelerations for the locations in J in the structure are all in phase with each other, i.e., will fall on a straight line perpendicular to the force vector in the complex plane.

Figure 10 shows an ideal plot of the acceleration vectors and force vector in the complex plane. The positions of the acceleration line and the force vector in the complex plane are arbitrary and depend upon the choice of the reference phase. If the reference is an acceleration, as done in the actual test reported here, then the acceleration line is on the real axis.

Actual Case. The ideal condition of Fig. 10 is only very approximately achieved in practice during a modal test because:

- the damping is not proportional
- there are inaccuracies in the measurements
- more than one mode is excited
- the structure is not linear
- ...

In particular, Item c) means that the response $A_{jn}(t)$ is not for mode n only but also contains the response of other modes with natural frequencies ω_o other than ω_n . The phase shift for these modes is not 90° as shown by point P on Fig. 9.

Consequently, a certain amount of scatter is expected to occur from the ideal condition of Figure 10. An example plot of the expected actual measured data is shown in Fig. 11.

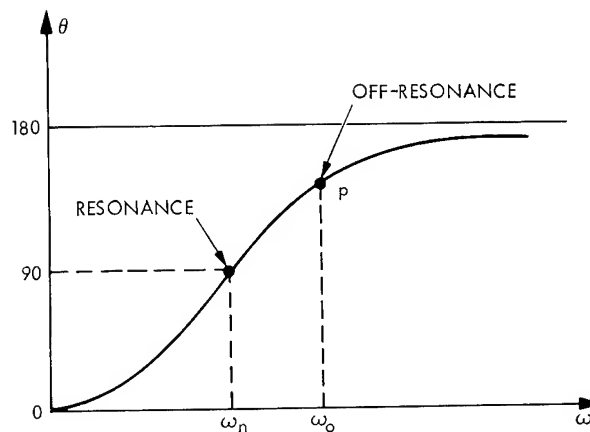


Fig. 9. Phase Shift vs Frequency for a Spring-Mass System

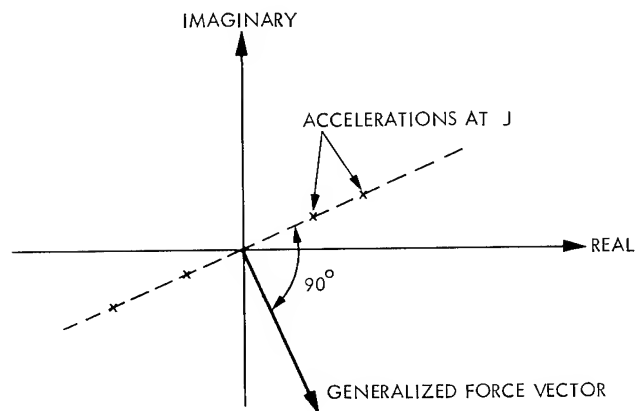


Fig. 10. Ideal Acceleration/Force Vectors for a Tuned Condition

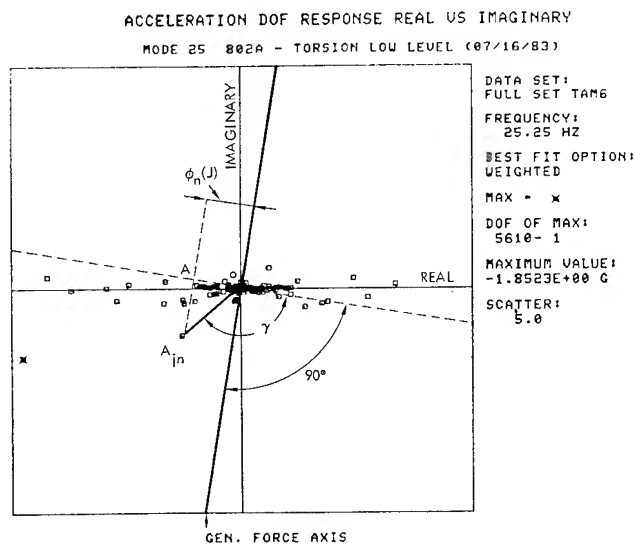


Fig. 11. Mode Shape Method 1

Condition of Resonance. The object is to make best use of the A_{jn} and force data, to obtain the best estimate of the real mode shape $\phi_n(J)$. Three methods have been experimented with:

a) Method 1. In this method each acceleration vector A_{jn} is simply projected on an axis (dashed line in Fig. 11) perpendicular to the force axis. The mode shape at point J is the segment OA.

$$\phi_n(J) = A_{jn} \cos \gamma \quad (10)$$

This method does not make use of any statistics on the data.

b) Method 2. In this method a best fit straight line (dotted line in Fig. 12) is passed through the scattered acceleration vectors A_{jn} . These vectors are then projected on this best fit straight line to give $\phi_n(J)$. This method ignores the position of the force vector data and in general the best fit straight line is not perpendicular to the force vector ($\beta \neq 90^\circ$). The best fit calculation can be made by weighing each point by its modal energy to give more emphasis on the points that are significant in a given mode.

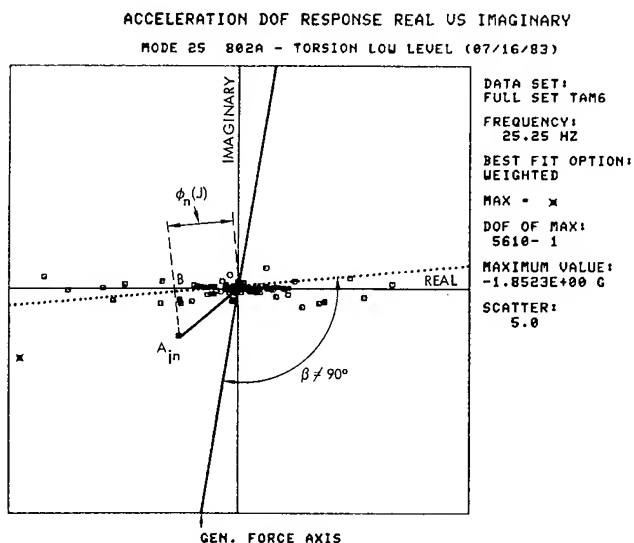


Fig. 12. Mode Shape Method 2

c) Method 3. Since methods 1 or 2, separately, do not make use of the statistics on the data, or all the data, a more elaborate approach is to combine the 2 methods to best fit the acceleration data in a manner compatible with the force data in a statistical fashion. A simple way to implement such a combination is

to define a reference line halfway between the dashed line and the dotted line. The difference between the two methods is minor in practice. Method 3, unweighted has been used.

Selected Mode Shape Plots

Plots for the HGA/Bus subsystems for the first "HGA Mode", nominally in y direction, is shown in Fig. 13 for different amplitudes from 1.39g to 13.9g at the tip. These curves are normalized to have a unity acceleration at the top of the bus. The plot clearly shows a variation of stiffness with amplitude in the HGA support can and struts at the interface between the HGA base and the top of the bus. This part of the structure becomes stiffer as the amplitude increases. Note that the plot for the motion of the can are for the rover data.

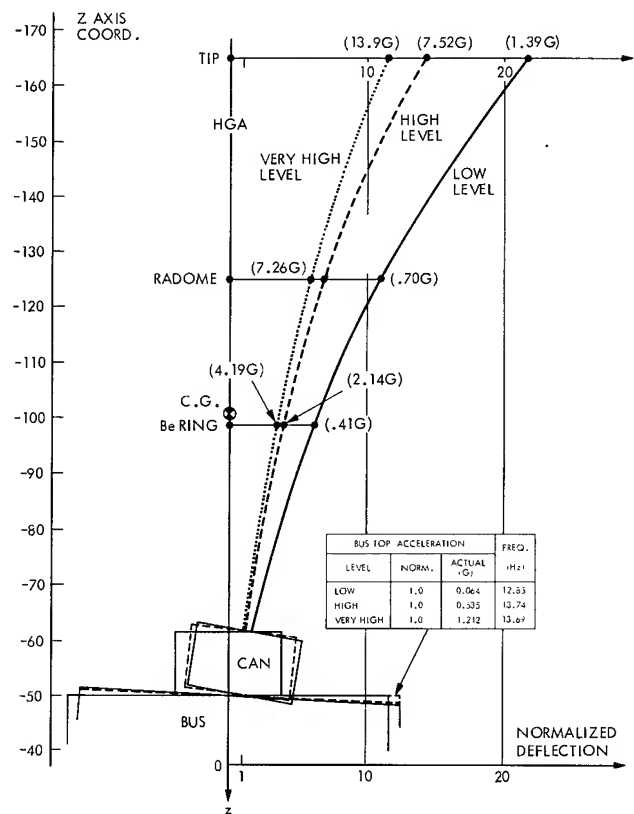


Fig. 13. Normalized HGA Y Axis Mode Variation with Amplitude

ROVER MODAL DATA

Background and Locations

During the course of the test it became apparent that a local definition of the core mode shapes was necessary to investigate further the discrepancies between the test results and the Test Analytical Model (TAM).

A total number of 108 additional degrees of freedom corresponding to 36 locations were chosen at 7 stations along the core structure to perform the additional measurements. Figure 14

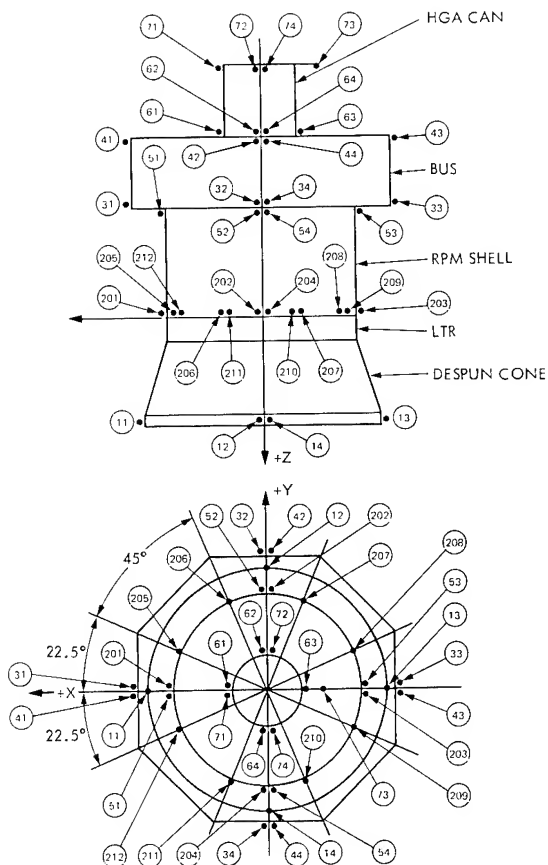


Fig. 14. Rover Locations on the Core Structure

shows the locations of the measurements, each with 3 degrees of freedom. Accelerometers were not bonded at these locations because of non-availability and/or lack of time. Instead, a single accelerometer, the "rover" was used as in the past JPL test programs. The rover was placed sequentially on all desired locations and orientations with double stick pressure sensitive tape, to measure the response with respect to the reference accelerometer. For simplicity no mass was allocated to these locations although it could have been done as a further step to refine the model. It follows that the rover measurements are for stiffness/displacement measurement only and have not been used for the global modal data reported later in this paper.

Rover Mode Shapes

A total of 6 modes were surveyed locally using the rover. As shown in the report¹ the rover data displayed less scatter than the fixed accelerometer data and consequently is considered as of a very good quality. Lateral displacements for the spacecraft core are shown on Fig. 15 for the first bending mode, the HGA Y axis mode. These plots are for the center of each cross-section at different stations along the core obtained from averaging the data measured at the periphery of the section. Low and high levels are compared showing the variation of the knee with amplitude at the HGA base.

Figs. 16 and 17 show the data for station 2 entire cross section at the Load Transfer Ring/

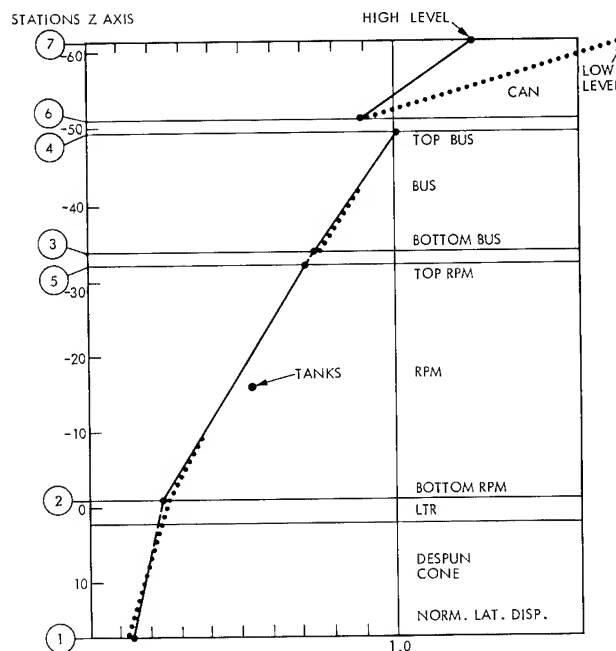


Fig. 15. Comparison HGA Y Axis High and Low Levels

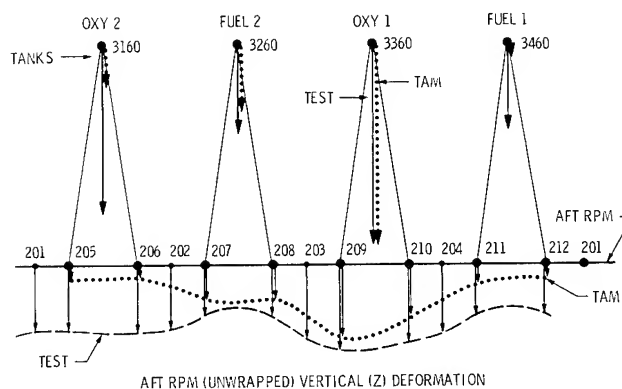


Fig. 16. Bounce High Level (1702A), Cross Section Station 2

Retro Propulsion Module interface for the bounce mode at 37.52 Hz.

GLOBAL MODAL DATA

Preamble

All the frequency and mode shape data above have been evaluated without the use of any mass distribution knowledge of the test article. To process the data in any further manner a mass matrix $[M]$ (162×162) corresponding to the degrees of freedom experimentally measured is needed. It is also noted that the post-processing of the modes assumes real modes with proportional damping and linearity of the test article.

Because of the uncertainty of the mass matrix, the non-proportional damping and the non-linearity of the test article, the post-processing to obtain orthogonality, modal

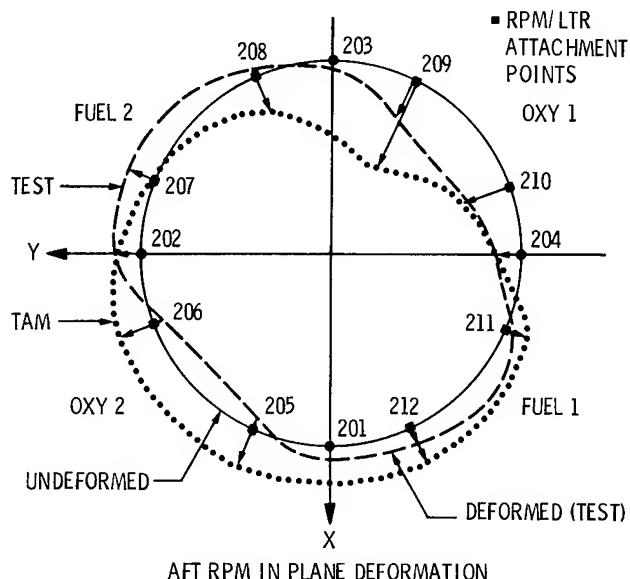


Fig. 17. Bounce High Level (1702A), In Plane Station 2

energy, modal effective mass, cross-orthogonality, etc., must be regarded only as an indication rather than a definite assessment of the goodness of the measured modes.

Post Processing Mass Matrix [M]

For the post processing one could consider using a mass matrix (AM2) analytically generated from the TAM. However, this matrix is obtained by a Guyan reduction of the original 10,000 degrees of freedom to the 162 degrees of freedom of the ASET and as such, contains to a certain degree, inaccuracies and errors coming from the original model. If the original model was perfect this mass matrix would be exact and could indeed be used. But since it is not, and the objective of the test is after all to update the model, a mass matrix [M] was constructed by engineering judgement distributing the mass according to the 162 degrees of freedom of the measured modes. This matrix is by no means perfect but it has at least a physical significance unlike the Guyan reduction mass matrix. This physical mass matrix is diagonal and referred to by HM2.

All the post-processing for the experimental modes used the physical mass matrix HM2. A number of runs were also made with the analytical mass matrix AM2. The difference was found to be minor.

Orthogonality

Call $\{\phi EX\}$ the matrix of the NE experimental modes for the $JM = 162$ degrees of freedom. Pre- and post-multiplying the mass matrix by the experimental modes gives the classical orthogonality matrix:

$$[ORTH] = \{\phi EX\}^T [M] \{\phi EX\} \quad (11)$$

Alternately each term of [ORTH] can be written:

$$\mu_{nl} = \{\phi EX\}_n^T [M] \{\phi EX\}_l = \begin{cases} 0 & l \neq n \\ 1 & l = n \end{cases} \quad (12)$$

i.e. ideally, [ORTH] is a diagonal matrix. For convenience the modes are normalized to have a unity value for the diagonal of [ORTH]. Assuming a perfect mass matrix [M], the presence of non-zero off-diagonal terms would indicate the deviation from the perfect modes.

Equation (11) was calculated for all the 36 measured modes including the several takes of a given mode either because of simple repeats or because of non-linearities. Then a subset of 17 distinct modes was extracted from the larger set on the basis of retaining the modes giving the smallest off-diagonal values.

Table 2 shows a listing of these modes with frequencies and Table 3 the corresponding orthogonality matrix.

Table 4 has been assembled to exemplify the inadequacy of using the orthogonality criteria, a quantity derived from linear theory, to assess the purity of experimental modes that are in reality non-linear. Table 4 shows a summary of the evolution of the orthogonality for the two HGA modes taken at different amplitude levels.

The unshaded area represents the orthogonality for each HGA mode X (or Y) with itself, showing the change of the mode as the amplitude varies. The shaded area shows the orthogonality between the two modes X and Y. The numbers vary from a perfect orthogonality of .00 to a large value of .50 depending upon the amplitude. This indicates that the classical orthogonality check is no longer a good criteria when non-linearity is present since the off-diagonal terms vary so widely with amplitude.

Note that the same tip amplitude for the two modes (X and Y) does not mean that the modes are "compatible" since the overall mode shape distribution is still different.

Modal Kinetic Energy

The orthogonality condition of Eq. (12) can be rewritten as:

$$\mu_{nl} = \sum_{I=1}^{JM} \phi EX(L, I) \sum_{J=1}^{JM} (M(I, J) * \phi EX(N, J)) \quad (13)$$

In this paper the term within the overall summation on I in Eq. (13) for $L = N$, is called the "modal kinetic energy" for each degree of freedom I. This represents the distribution of kinetic energy between all the degrees of freedom for a given mode N:

$$EN(N, I) = \phi EX(N, I) \sum_{J=1}^{JM} M(I, J) * \phi EX(N, J) \quad (14)$$

If the mass matrix $M(I, J)$ is diagonal then

$$EN(N, I) = M(I, I) * (\phi EX(N, I))^2$$

Table 2. Distinct Modes with Minimum Off-Diagonal Values

EXPERIMENTAL NATURAL FREQUENCIES IN HZ		
MODE	FREQUENCIES	MODE TITLE
1	13.48	105A - HGA BENDING X AXIS (VERY HIGH LEVEL) (07/27/83)
2	13.74	204A - HGA BENDING Y (HIGH LEVEL) (07/22/83)
3	17.72	502A - CORE BENDING (-X, +Y) (07/09/83)
4	18.15	503A - CORE BENDING (+X, +Y) (HIGH LEVEL) (07/26/83)
5	18.59	301A - SCIENCE BOOM (X) (07/05/83)
6	21.60	601A - RTG Z / RPM BUS X (06/30/83)
7	23.58	702A - RTG Z / PROBE Y / SC. BOOM Z (HIGH LEVEL) (07/05/83)
8	24.85	803A - TORSION (HIGH LEVEL) (07/18/83)
9	25.73	901A - SC. BOOM Z / PROBE Y / RTG Z (07/02/83)
10	28.16	2101A - SCAN PLATFORM (THETA X) (07/19/83)
11	29.91	3101A - -RTG (LATERAL) (LOW LEVEL) (07/13/83)
12	33.35	2601A - SCAN / PROBE X / SC BOOM (07/20/83)
13	33.83	2701A - +RTG (LATERAL) / PROBE X (LOW LEVEL) (07/13/83)
14	37.59	1702A - BOUNCE HIGH LEVEL (07/18/83)
15	37.84	1701A - RRH / SC BOOM / DESPUN (07/20/83)
16	41.35	2001A - +X THRUSTER (LATERAL) (07/08/83)
17	42.27	1801A - -X THRUSTER (LATERAL) / RPM TANKS (07/08/83)

Table 3. Minimum Orthogonality for Experimental Modes

	ORTHOGONALITY FOR EXPERIMENTAL MODES																
	1	2	3	4	5	6	7	8	9	10	11	12	13	14	15	16	17
1	1.00	0.00	0.19	-0.14	0.09	0.07	-0.02	-0.03	0.00	0.00	-0.01	-0.01	-0.02	0.01	-0.03	-0.02	-0.01
2	0.00	1.00	-0.23	-0.01	-0.06	-0.06	0.00	0.01	0.01	0.01	0.02	-0.01	0.01	0.01	0.00	0.00	0.00
3	0.19	-0.23	1.00	-0.10	0.06	-0.07	-0.02	-0.03	-0.03	-0.04	-0.02	-0.01	0.01	0.01	-0.10	0.00	0.00
4	-0.14	-0.01	-0.10	1.00	0.26	0.02	0.01	0.05	0.08	-0.02	0.01	0.04	-0.02	0.00	0.20	0.02	0.02
5	0.09	-0.06	0.06	0.26	1.00	0.00	0.00	-0.01	0.05	0.00	0.02	0.02	-0.01	-0.04	0.36	0.03	0.04
6	0.07	-0.06	-0.07	0.02	0.00	1.00	-0.03	0.03	0.00	0.02	0.01	-0.02	0.02	-0.07	0.06	-0.01	0.00
7	-0.02	0.00	-0.02	0.01	0.00	-0.03	1.00	0.03	-0.13	0.12	0.01	-0.01	0.07	-0.01	0.01	0.01	0.00
8	-0.03	0.01	-0.03	0.05	-0.01	0.03	0.03	1.00	0.19	0.00	0.04	0.05	-0.10	0.00	0.06	-0.03	0.00
9	0.00	0.01	-0.03	0.08	0.05	0.00	-0.13	0.19	1.00	-0.07	0.01	-0.01	-0.03	-0.03	0.06	-0.01	0.00
10	0.00	0.01	-0.04	-0.02	0.00	0.02	0.12	0.00	-0.07	1.00	-0.03	-0.11	0.00	0.05	0.01	-0.01	-0.01
11	-0.01	0.02	-0.02	0.01	0.02	0.01	0.01	0.04	0.01	-0.03	1.00	-0.17	-0.10	0.06	-0.12	-0.10	-0.05
12	-0.01	-0.01	-0.01	0.04	0.02	-0.02	-0.01	0.05	-0.01	-0.11	-0.17	1.00	-0.10	-0.08	-0.03	0.04	0.04
13	-0.02	0.01	0.01	-0.02	-0.01	0.02	0.07	-0.10	-0.03	0.00	-0.10	-0.10	1.00	0.02	0.09	0.09	0.03
14	0.01	0.01	0.01	0.00	-0.04	-0.07	-0.01	0.00	-0.03	0.05	0.06	-0.08	0.02	1.00	-0.01	0.00	0.02
15	-0.03	0.00	-0.10	0.20	0.36	0.06	0.01	0.06	0.06	0.01	-0.12	-0.03	0.09	-0.01	1.00	0.04	0.01
16	-0.02	0.00	0.00	0.02	0.03	-0.01	0.01	-0.03	-0.01	-0.01	-0.10	0.04	0.09	0.00	0.04	1.00	0.18
17	-0.01	0.00	0.00	0.02	0.04	0.00	0.00	0.00	0.00	-0.01	-0.05	0.04	0.03	0.02	0.01	0.18	1.00

ROOT MEAN SQUARE OFF-DIAGONAL = 0.071878

Note that for a given mode N the total energy for that mode obtained by adding the energy for all degrees of freedom is equal to the diagonal of the orthogonality matrix, equal to unity because of normalization

$$\sum_{I=1}^{JM} EN(N,I) = 1. \quad (15)$$

A pictorial representation of the energy distribution per mode for 2 major modes in a bar-graph form is shown in Figs. 18 through 20 where the entire spacecraft has been subdivided into 10 subsystems. The large bars represent the subsystems. The narrow bars within the large bars are the 6 degrees of freedom 1 through 6 for

each subsystem. These plots provide a convenient way to identify which parts of the spacecraft are participating in a given mode and to compare test with analysis. The data correspond to both the measured modes (left plots) and the corresponding analytic modes (right plots) of TAM6SB for comparison. A perfect match between analysis and test would make the bars of the right plot coincide with those of the left plot. These plots are used to assess the matching of the measured modes to the analytical modes and to effect the updating of the TAM.

For example Fig. 18 shows that the experimental HGA Y axis mode low level, is basically a "local" mode of the HGA while the corresponding analytic mode is more an overall mode with a predominant energy in the core (RPM and Bus). Fig. 19 for the highest level shows the improved match when the test amplitude is increased.

Table 4. Orthogonality Variation with Amplitude for HGA Modes (Physical Mass Matrix HM2)

TIP AMPL. G	HGA X					HGA Y				
	1.27	1.34	1.37	7.1	13.7	1.31	1.48	1.48	7.5	14.0
FREQ. Hz	13.05	13.07	13.18	13.71	13.48	12.85	12.85	12.70	13.74	13.69
1	1	0.99	0.92	-0.88	0.19	0.17	0.21	0.36	-0.14	
		1	0.99	0.93	-0.87	0.22	0.20	0.24	0.39	-0.11
			1	0.93	-0.87	0.23	0.21	0.25	0.41	-0.10
				1	-0.85	0.30	0.25	0.31	0.48	-0.01
					1	0.17	0.19	0.15	0.00	0.50
						1	0.99	0.99	0.96	0.90
							1	0.98	0.94	0.88
								1	0.96	0.89
									1	0.85
										1

Effective Mass

The calculation of the effective mass needs the introduction of the rigid body modes $[\phi R]$, a 162×6 matrix which is a geometrical property of the spacecraft reflecting the locations and orientations of the elements of the mass matrix.

The experimental rigid elastic coupling matrix $[MER]$ is defined by combining $[\phi R]$, $[M]$, and $[\phi EX]$ in a manner similar to Eq. (11)

$$[MER] = [\phi EX]^T [M] [\phi R] \quad (16)$$

or alternately, for a given mode N and a given interface degree of freedom K:

$$MER(K,N) = \sum_{I=1}^{JM} \phi R(K,I) \sum_{J=1}^{JM} M(I,J) * \phi EX(N,J) \quad (17)$$

The product:

$$MEFN(K,L,N) = MER(K,N) * MER(L,N) \quad (18)$$

is called the "modal effective mass matrix" for mode N. Only the diagonal $K = L$ of this matrix is retained here. The effective mass and effective inertia for each interface degree of freedom K are:

$$MEFN(K,N) = MER(K,N)**2 \quad (19)$$

$K = 1,3$ for the mass

$K = 4,6$ for the inertia.

Table 5 gives the values of effective masses and inertias for 17 distinct modes with the highest amplitude.

A summation of the effective masses for the distinct modes gives the mass accounted by taking all these distinct modes.

$$MEF(K) = \sum_{N=1}^{ND} MEFN(K,N) \quad (20)$$

where ND is the number of distinct modes.

Ideally, if all the distinct modes were accounted for and the structure was linear, $MEF(K)$ would be equal to the physical mass and inertia of the spacecraft with respect to the interface. Therefore, $MEF(K)$ is considered a measure of how many significant modes have been surveyed.

Table 5 also shows the total effective mass for the 17 distinct modes measured. The fact that degree of freedom 4 has a ratio greater than unity is one more indication that the system is non-linear.

Fig. 21 shows the variation of the effective mass with amplitude for the first bending mode, HGA Y axis.

Cross-Orthogonality

The cross-orthogonality matrix is a convenient way to relate the experimental modes with the analytic modes calculated from the mathematical model. The evaluation of this matrix requires the use of an even more detailed part of the analysis than the quantities calculated before. In a manner similar to Eq. (11) it is defined as the triple product of the experimental modes, the mass matrix and the analytic modes.

$$[CROSS] = [\phi EX]^T [M] [\phi A] \quad (21)$$

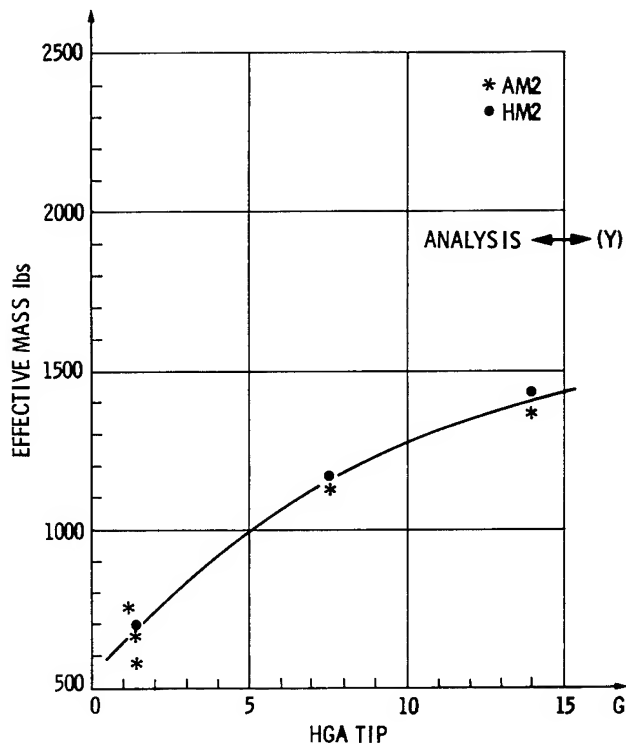


Fig. 21. Variation of Effective Mass with Amplitude HGA Y Axis Mode

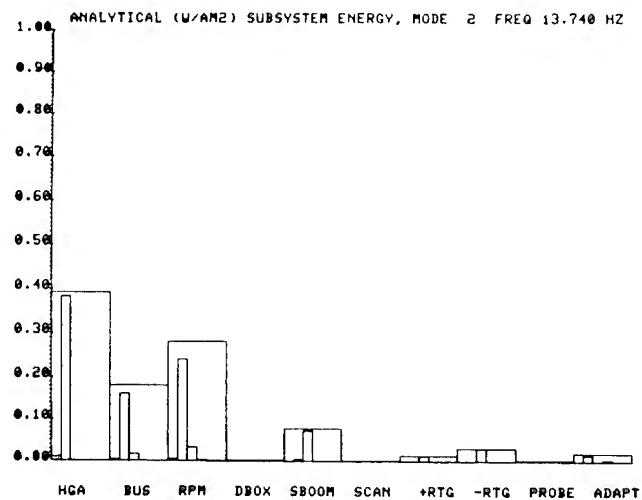
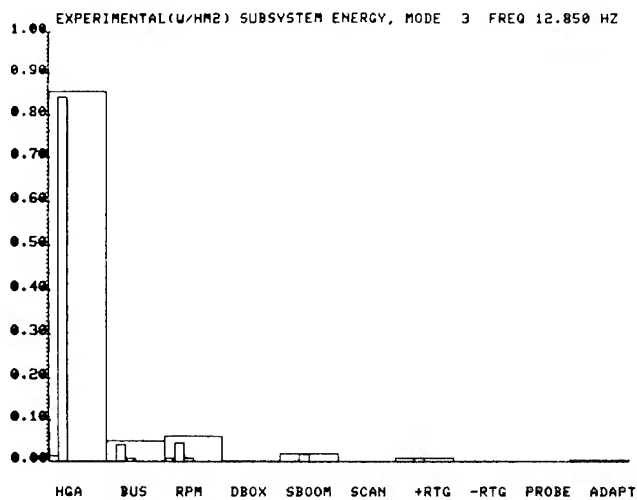


Fig. 18. Experimental/Analytical Energy HGA Y Low Level

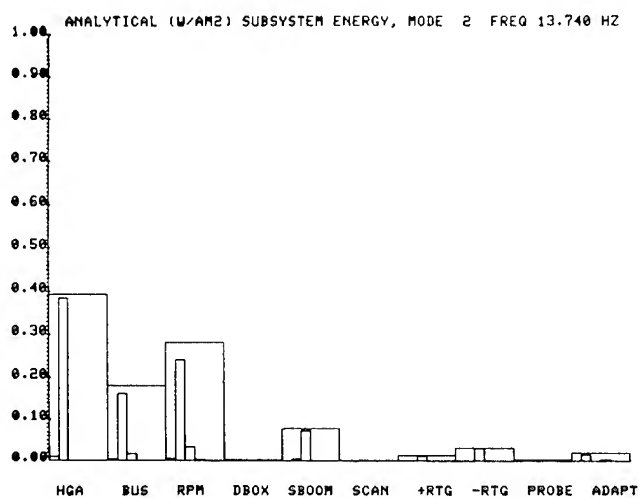
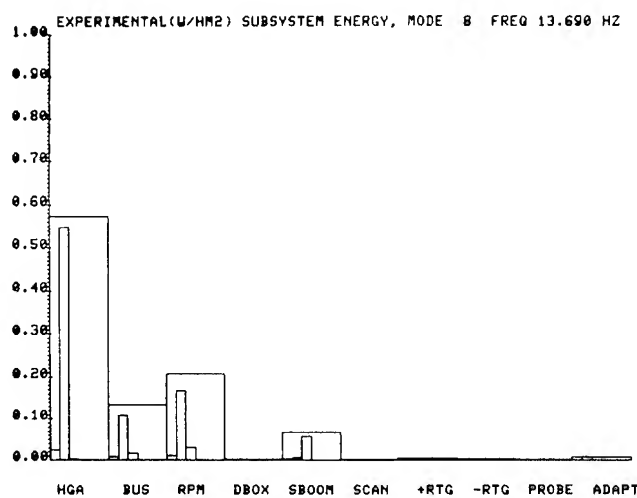


Fig. 19. Experimental/Analytical Energy HGA Y Axis Very High Level

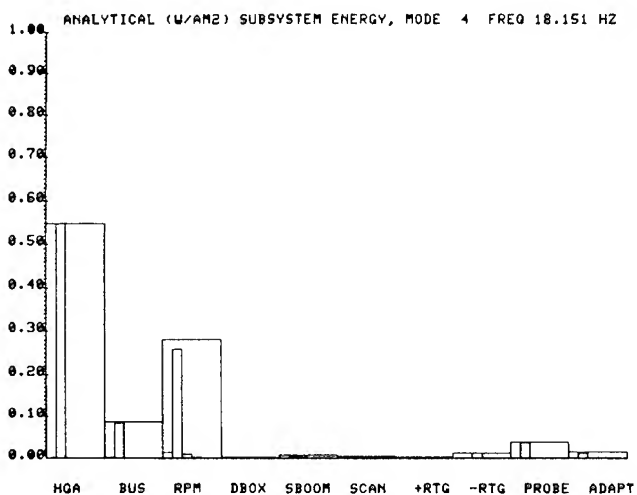
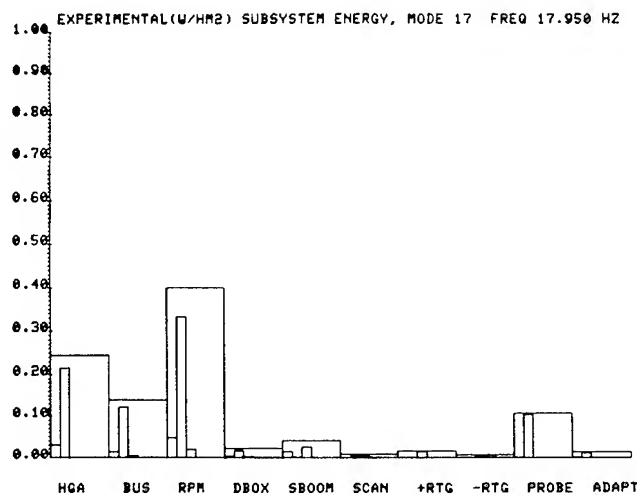


Fig. 20. Experimental/Analytical Energy Core Y

Table 5. Effective Mass Distribution for 17 Measured Modes (HM2) (Highest Level)

EFFECTIVE MASS FOR EXPERIMENTAL MODES

MODES	FREQUENCIES	EFFECTIVE MASS IN LBS AND LBS-IN**2					
		1	2	3	4	5	6
1	13.48	1.294169E+03	9.428874E+01	1.528331E+00	1.985377E+06	2.269471E+07	4.750404E+02
2	13.69	8.560544E+01	1.273283E+03	1.770821E+00	2.208836E+07	1.321083E+06	6.974691E+02
3	17.95	2.788294E+02	2.238784E+03	4.448385E+00	1.978371E+07	2.135910E+06	2.084778E+04
4	18.15	6.174972E+02	9.001788E+02	3.332483E-04	8.812015E+06	5.416022E+06	3.120396E+05
5	18.59	1.999606E+00	3.617139E+00	4.164540E-01	1.390936E+04	6.626640E+05	1.507882E+06
6	21.60	1.027250E+03	5.667891E+01	4.823038E+01	1.840742E+05	5.400304E+06	7.602895E+04
7	23.58	5.502610E+00	1.492428E+01	3.716206E+02	3.900225E+05	6.388154E+02	9.085202E+01
8	24.85	6.074694E+01	6.924258E+00	6.224400E+00	1.147144E+05	1.690983E+05	1.487903E+06
9	25.73	6.663065E+00	2.367858E+01	4.614418E+02	1.265469E+05	1.265728E+04	1.434090E+05
10	28.16	3.132791E-01	2.367781E+01	3.265210E+01	2.027531E+03	2.037730E+03	1.727185E+03
11	29.91	6.584089E+01	6.447977E+01	3.141757E-01	4.251607E+04	7.658515E+04	5.290181E+05
12	33.35	1.251094E+01	5.695358E+00	4.997353E+00	1.316421E+03	1.114421E+04	1.646350E+04
13	33.83	1.290803E+02	5.496418E+01	7.641978E+00	3.031649E+04	3.195983E+05	6.915161E+05
14	37.59	7.559170E+00	1.322208E+01	2.703479E+03	6.020285E+04	4.419889E+04	1.361486E+03
15	37.84	8.379469E+00	4.562767E+01	7.390891E+00	1.090363E+05	8.655936E+03	8.216824E+04
16	41.35	1.592499E+00	7.724789E+00	1.994816E+01	4.911862E+03	4.506135E+03	4.750427E+03
17	42.27	9.697754E-01	6.503032E-01	7.122403E+01	4.548206E+03	8.121013E+02	1.593597E+03

TOTAL EFFECTIVE MASS FOR EXPERIMENTAL MODES (LB)

	1	2	3	4	5	6
1	3.604510E+03	7.164973E+02	4.114638E+02	1.036572E+05	-3.512743E+05	-4.759186E+03
2	7.164973E+02	4.828400E+03	2.080269E+02	4.960190E+05	-1.006939E+05	-3.020357E+03
3	4.114638E+02	2.080269E+02	3.743330E+03	1.755587E+04	-3.589415E+04	5.156248E+03
4	1.036572E+05	4.960190E+05	1.755587E+04	5.375360E+07	-1.353284E+07	-5.381751E+05
5	-3.512743E+05	-1.006939E+05	-3.589415E+04	-1.353284E+07	3.830062E+07	-2.159737E+05
6	-4.759186E+03	-3.020357E+03	5.156248E+03	-5.381751E+05	-2.159737E+05	4.877972E+06

RATIO OF TOTAL EFFECTIVE MASS AND INERTIA TO INTERFACE MASS AND INERTIAS

	1	2	3	4	5	6
	0.673	0.901	0.698	1.170	0.847	0.724

All the 36 experimental modes are considered when using Eq. (21). The matrix [CROSS] is a 40 x 36 matrix. The maximum value in the *i*th row of [CROSS] identifies the column, i.e., the experimental mode that is, on the average, the closest to the analytical mode. This method has been used to retain a single mode out of the several takes of the same mode.

CONCLUSION

The modal test program of Galileo has exhibited a number of unexpected findings due to the complexity of the spacecraft structure which required redirection of the test as it progressed.

The results show a definite need to upgrade the actual Galileo Analytic Model to be used for the pre-flight verification loads analysis.

The unexpected findings are an indication that flexibility must remain the primary concern of the modal test planners. The modal test of a complex spacecraft such as the Galileo is an exploratory test, which main objective is not just to verify an a priori mathematical model but

to uncover the unexpected, if it is there, and to provide basic data to modify, upgrade or recast the analytical model as needed.

In the same line of thoughts it is the belief of this author that all the modal testing methods, old and new, will have their place and should all be made available to the test team for use at any time of the test.

ACKNOWLEDGEMENT

The research described in this paper was performed by the Jet Propulsion Laboratory, California Institute of Technology, under contract with the National Aeronautics and Space Administration.

REFERENCES

1. Marc Trubert "Galileo System Modal Test" Jet Propulsion Laboratory JPL D-950 January 31, 1984.
2. J.C. Chen "Evaluation of Modal Testing Methods" Paper 84-1071-CP, AIAA Dynamics Specialist Conference, May 17-18, 1984, Palm Springs, California.

by

Richard C. Stroud and M. R. Pamidi
Synergistic Technology Incorporated
Cupertino, California

and

H. Peter Bausch
Wyle Laboratories
Norco, CaliforniaABSTRACT

This paper describes the support provided by Synergistic Technology Incorporated and Wyle Laboratories for the Galileo Spacecraft Modal Survey performed at the Jet Propulsion Laboratory in Pasadena, California during June and July 1983. The objectives of the modal survey, the technical approach, as well as hardware and software features are discussed.

The spacecraft was subjected to an extensive modal testing program to identify significant modes and verify the analytical model. Target modes were selected on the basis of a pretest finite-element analysis of the spacecraft. A variety of excitation functions and analytical techniques were used. However, the primary test method was the classical tuned-multiexciter sinusoidal dwell. Special software was developed to expedite use of this technique. Additional excitations included fast sinusoidal sweeps (chirps), random vibration, plus single-exciter and multiexciter sinusoidal sweeps. Frequency response functions were computed in realtime using the Sine Wave Integration Fourier Transform (SWIFT) technique during the sinusoidal sweeps. Most of the command generation, data-acquisition, and data analysis tasks were performed with Wyle Modal Analysis and Test System (MATS).

Modal analyses were performed by curve-fitting in the frequency domain. Modal properties (i.e., the natural frequencies, modal damping and mode shapes) were determined for all pertinent modes in the 5- to 45-Hertz frequency range. Most of the target modes were identified and characterized.

INTRODUCTIONThe Galileo Mission

Figure 1 is a line drawing of the Galileo Spacecraft in its Cruise Configuration. The Galileo/Centaur will be placed in an Earth orbit by the Space Shuttle. The Centaur will deliver the Spacecraft to Jupiter. The

Shuttle/Centaur launch is scheduled for May 1986. Eight months later, in January 1987, there will be a midcourse maneuver to change from the Earth-orbit plane to the Jupiter-orbit plane and to increase velocity. As the Spacecraft approaches Jupiter, it will separate into two parts: One, a probe that will enter Jupiter's atmosphere, deploy parachutes, and will descend, sending signals until it is destroyed. The rest of the Spacecraft will go into orbit around Jupiter. It will receive signals from the probe as it descends. It will observe Jupiter and then, using some very sophisticated orbital maneuvers, will encounter and observe several of Jupiter's Moons.

A variety of sensors deployed on long booms may be seen in Figure 1. The High-Gain Antenna (at the top of the Figure) is for Earth communication. The item at the bottom of Figure 2 is the probe that will enter Jupiter's atmosphere.

The Spacecraft is spin stabilized. The entire structure spins about an axis passing through the axes of the Probe and the High-Gain Antenna. However, there is an inertially stable platform, the so-called "De-Spun Box", that supports the Scan Platform and the Relay Antenna which receives signals from the Probe. Notice there are no solar arrays. There is not sufficient solar energy near Jupiter to power the Spacecraft. Alternate power sources are required.

The Galileo Spacecraft Modal Survey

The primary reason for the Galileo Spacecraft Modal Survey (GSMS) was to establish credibility of the analytical model. This is, of course, the motivation for a great majority of modal surveys. NASA's analysis requirements stated, "Loads and deformations shall be based on a test-verified payload structural-dynamic math model and NASA-supplied test-verified STS (Space Transportation System) math models and forcing functions". NASA requirements further stated, "A modal-survey test

shall be run to verify the analytical mode shapes, resonant frequencies, and modal damping used in loads analysis". A second reason for the modal survey was to provide information needed for the design of the Spacecraft's control system.

In June and July 1983, Jet Propulsion Laboratory (JPL) conducted the GSMS in Pasadena, California. JPL dictated that the modal survey would be performed using the classical tuned-dwell method. In addition, through the generosity and cooperation of JPL and several researchers, a research activity was conducted wherein nearly every known excitation, data-acquisition, and analysis method was applied to the Galileo Spacecraft.

Excitation methods included tuned-multiexciter sinusoidal dwell, single-exciter sinusoidal sweeps, tuned-multiexciter sinusoidal sweeps [1], chirps (fast sinusoidal sweeps) [2], single-exciter random, and multiexciter random [3]. Data-acquisition methods included acquisition of response histories for subsequent analysis and realtime acquisition of response spectra using the SWIFT algorithm. Analysis techniques included direct measurement of modal properties by tuned-dwell methods, frequency-domain curvefitting, time-domain analysis [4], polyreference analysis [5,6], and simultaneous frequency domain analysis [7].

JPL contracted Wyle Laboratories to perform data acquisition and analysis for the modal survey. Wyle, in turn, subcontracted STI to prepare for and perform several phases of the Modal Survey. JPL contracted STI separately to coordinate and participate in the research aspects of the GSMS.

DATA ACQUISITION

Following is a description of the software, hardware, and instrumentation used in the GSMS tests. Additional details may be found in a paper by Bausch and Stroud [8].

Data acquisition was accomplished using Wyle's Modal Analysis and Test System (MATS). A block diagram of MATS is shown in Figure 2. MATS was assembled by STI and is a special version of STI-11/23. The processor has 256K bytes of memory and operates under DEC's RSX-11M operating system, providing multiple terminals and multiple tasks. Supported by an 80-Megabyte disk drive and a small array processor, MATS offers 64 channels of data acquisition and two command channels. For multiexciter sinusoidal excitation, one command channel drove a eight-channel Shaker Control System. This Control System accepts a sine wave and outputs eight sine waves with the same frequency but having variable gain and polarity.

Instrumentation consisted of 162 accelerometers, connected to patch boards via charge amplifiers, and 120 strain gages connected to patch boards via bridge completion/amplifier units. In addition, there were eight load-cell/accelerometer pairs for measuring applied forces and drive-point responses. Figure 3 shows a schematic of the data system.

Since there were nearly 300 instruments and MATS has only 64 channels of acquisition, multiple acquisitions were required. This was accomplished by tuning a mode, acquiring data for 64 channels, then, without changing the excitation, switching patch boards until all channels were recorded.

DISCUSSION

Tuned-Dwell Software

The tuned-multiexciter sinusoidal dwell is the classical method of modal testing first developed by Lewis and Wrisley [9] in 1950. The method involves manual variation of excitation frequency and forces to accentuate the response of a single mode while suppressing all others. Mode shapes are determined from direct measurements of tuned response. Damping is estimated from analysis of decay data. Because tuned-dwell technology evolved before digital methods were introduced, it is based on analog techniques.

In order to expedite the modal-tuning process, STI developed an interactive program called "DWEELL" which is intended to implement the tuned-dwell procedure on a modern data-acquisition and analysis system. DWEELL permits the Operator to simultaneously observe all or selected responses and their changes as frequency and forces are adjusted. An example of a typical plot available to the Operator during the tuning process is shown in Figure 4.

Once a mode has been satisfactorily tuned, DWEELL will automatically acquire response measurements, record resonant frequency and mode shape in a VAMP modal-analysis file, terminate excitation and acquire decay measurements, and allow interactive measurement of modal damping.

Tuned Sweep

It has been shown [10] that tuned-dwell testing can produce undetectable errors. The tuned-sweep procedure described in Reference [1] is intended to use the best features of both the tuned-response and signal-analysis approaches to modal testing.

The tuned-sweep process is to approximately tune a mode, perform a narrowband sweep about the suspected resonance, and

use frequency-domain analysis to estimate modal parameters.

Several tuned sweeps were performed as part of the GSMS research effort.

Single-Exciter Multifrequency Excitation

A widely used modal-testing method is often referred to as the single-point random method. This technique involves exciting the structure at a single point with a broadband input, computing frequency response functions, and determining modal properties by curvefitting analytical expressions to those measured functions. Although the popular name for this approach implies the use of random excitation, other forms of broadband excitation can be used. Random, chirp, and sinusoidal sweep excitations were used on GSMS to provide frequency response functions.

Random vibration is probably the most popular form of excitation. It produces less noise than transient excitation and yields good results with ensemble averaging.

Chirp is a fast sinusoidal sweep during which the structure does not reach steady-state response. It produces the cleanest spectra and requires fewer ensemble averages than other forms of multifrequency excitation.

The discrete sweep (a sequence of dwells) lends itself to "on-the-fly" spectrum calculations (and substantial time savings) in either single-exciter or multiexciter testing. Reference [10] shows that, for more than a few channels, sinusoidal-sweep testing using the SWIFT realtime algorithm is the fastest means of obtaining frequency response functions. SWIFT (Sine Wave Integration Fourier Transform) is a computer-controlled discrete sine sweep that performs on-the-fly Fourier calculations for all measurements. Sinewave testing provides very clean spectral measurements.

ANALYSIS PROCEDURE

For the GSMS, frequency response functions were obtained by the SWIFT and by FFT processing of responses to random and chirp excitations.

The transfer functions derived from the SWIFT, chirp, and random tests were used to estimate modal parameters. Analysis of these measurements was performed with STI VAMP by means of frequency-domain curvefitting. Figure 5 is a typical example of such a curvefit; two analytical modes (represented by solid lines) have been fitted to the measurements (represented by the dotted lines).

The SWIFT data were also analyzed by a technique known as the simultaneous fre-

quency domain (SFD) method. Developed by Coppolino [7], this method is based on the concept that the total response of a structure can be represented by a subset of generalized functions. The SFD method states that all frequency response functions can be represented as a linear combination of a few functions which are themselves linear combinations of all the FRFs. A linear transformation between the complete and reduced sets is established. Reduced damping and stiffness matrices are then established by least-squares fit to the reduced set of functions. Next, the frequency, damping, and reduced mode shapes are found by eigensolution of the reduced matrices. Finally, the total mode shapes are found by linear transformation.

DISCUSSION OF RESULTS

Table 1 is a summary of results obtained using SWIFT excitation and frequency-domain curvefitting. This approach identified 27 modes ranging from the first mode of the stowed high-gain antenna at approximately 12.5 Hz to a thruster mode at almost 45 Hz. Damping ranged from 0.5% for several modes to over 3% for the damper mode. Of the 21 target modes, 16 were characterized. Agreement between predicted and measured resonant frequencies were generally good; i.e., within 10%.

Table 2 compares the results of SWIFT, chirp, and random testing. Analysis of the chirp and random data had an advantage in that they used the SWIFT analysis as an initial estimate. In spite of that advantage, it was not possible to identify several of the modes in the chirp and random data. The missing modes can generally be described as "weak". In most instances, they were concentrated in the deployable appendages of the spacecraft which probably were not adequately excited by the broadband excitation, at least at the levels used. Where modes were found, the agreement between analyses was good. The agreement was particularly good for chirp and random results.

Table 3 compares the results of frequency-domain curvefitting and the simultaneous frequency-domain method as applied to the SWIFT data. Three separate analyses were performed with the SFD method, i. e. for each of the X, Y, and Z SWIFT sweeps. The agreement is very good; particularly between curvefit results and SFD analysis for the corresponding excitation. For example, the first mode in curvefit analysis was done on the y-excitation data and compares well with the SFD y excitation analysis. That quality extends through all the modes. The SFD analysis found 6 modes that were not characterized by curvefit analysis.

CONCLUDING REMARKS

The development of modal testing/analysis technology can be divided into three eras. Through the 1960's, the technique did not directly involve the use of a computer. The 1970's was the era of the "digital revolution" and saw the emergence of several methods based on the use of dedicated minicomputers for data acquisition and interactive analysis. In the 1980's, the trend seems to be towards data acquisition with minicomputers but more ambitious and less interactive analysis on mainframe computers or, at least, minicomputers. Techniques from each of these eras were successfully applied on the GSMS.

REFERENCES

1. Stroud, R. C., Smith, S. and Hama, G. A., "MODALAB: A New System for Structural Dynamic Testing", Shock and Vibration Bulletin, No. 46, Part 5, pp: 153-175, August 1976.
2. Stroud, R. C., Bonner, C. J. and Chambers, G. J., "Modal-Testing Options in Spacecraft Development", SAE Paper No. 781043, SAE Transactions, Vol. 78, 1978.
3. Allemang, R. J., "Investigation of Some Multiple Input/Output Frequency Response Function Experimental Modal Analysis Techniques", Ph.D. Dissertation, University of Cincinnati, 1980.
4. Ibrahim, S. R. and Mikulcik, E. C., "A Method for the Direct Identification of Vibration Parameters from the Free Response", The Shock and Vibration Bulletin, Bulletin 47, September 1977, pp: 183-198.
5. Hunt, D. and Peterson, E., "Multishaker Broadband Excitation for Experimental Modal Analysis", SAE Aerospace Congress and Exposition, October, 1983.
6. Vold, H. and Rocklin, G. E., "The Numeric Implementation of a Multi-Input Modal Estimation Method for Minicomputers", International Modal Analysis Conference, pp: 542-548 1982.
7. Coppolino, R. N., "A Simultaneous Frequency Domain Technique for Estimation of Modal Parameters from Measured Data", Paper No. 811046, SAE Aerospace Congress and Exposition, October, 1981.
8. Bausch, H. P. and Stroud, R. C., "Data Acquisition and Analysis for the Galileo Spacecraft Modal Survey", International Modal Analysis Conference, pp: 803-808, 1984.

9. Lewis, R. C. and Wrisley, D. L., "A System for the Excitation of Pure Natural Modes of Complex Structures", Journal of Aeronautical Sciences, Vol. 17, No. 11, pp: 705-722 1950.

10. Hama, G. A., Smith, S. and Stroud, R. C., "An Evaluation of Excitation and Analysis Methods for Modal Testing", Paper No. 760872, SAE Aerospace Engineering and Manufacturing Meeting, November-December, 1976.

11. Wilson, S., Chen, J. and Trubert, M., "Galileo Modal Test Plan and Test Procedures", Wyle Test Procedure No. 14586-04, May, 1983.

Table 1
Galileo Spacecraft Modal Survey
Swift Tests
Description of Analytical Modes and Comparison with Test Results

GEM	Natural Frequency (Hz)/ Critical Damping	Description of Mode	Excitation Direction	Target Mode	Predicted Frequency (Hz)
1	12.54 / .0116	SXA Tip	Y	2	13.45
2	13.78 / .0209	SXA Tip	X	1	13.22
3	17.40 / .0112	Core Bending	X	5	18.90
4	17.62 / .0134	Core Bending	Y	4	18.13
5	18.22 / .0070	SXA & + X Thrust	Z		
6	18.59 / .0172	SXA			
7	18.93 / .0103	Science Boom	X	3	16.81
8	19.31 / .0085	RRH	Z		
9	22.04 / .0077	RTG	X	9	23.46
10	22.23 / .0072	RTG	Z	6	20.45
11	22.35 / .0070	RTG	Z	7	20.77
12	25.30 / .0117	+X Thruster & Damper	Y	8	21.48
13	26.22 / .0235	Damper, SB, & Mas Can.	Y		
14	26.83 / .0168	Damper, SB,	Y	12	29.92
15	27.61 / .0100	SB, RRH, & Probe	X		
16	28.37 / .0059	RRH, SB, & Probe	X		
17	29.48 / .0330	Damper	X	17	32.59
18	33.02 / .0117	Probe	X	16	32.28
19	33.40 / .0109	Thrusters & SXA	Y	14	32.11
20	33.63 / .0069	Probe & +X Thruster	Z		
21	33.70 / .0078	Mas Can. & Sci. Room	Y		
22	33.98 / .0066	Mas Can. & DHS	Y		
23	38.17 / .0055	Bounce Mode	Y		
24	39.70 / .0063	RRH	Y	19	35.86
25	41.01 / .0108	RRH & Mas Can.	Y		
26	42.99 / .0096	Thrusters & RRH	Y	20	36.30
27	44.82 / .0055	Thrusters & RRH	Y	21	36.84

LEGEND: GEM - Galileo Experimental Modes
RRH - Radio Relay Hardware
RTG - Radioisotope Thermal-Electrical Generator
SB - Science Boom
SXA - S-X Band Antenna

Table 2
Galileo Spacecraft Modal Survey
Swift Tests
Comparison of Frequency-Domain and Simultaneous Frequency-Domain Analysis

GEM	FREQUENCY-DOMAIN CURVEFIT		Excitation	SIMULTANEOUS FREQUENCY-DOMAIN ANALYSIS		
	Natural Frequency (Hz)	Damping Ratio		X-Excitation	Y-Excitation	Z-Excitation
1	12.54	.0116	Y	12.64 / .0132	12.52 / .0106	
2	13.78	.0209	Y	13.78 / .0237	13.76 / .0339	13.92 / .0108
3	17.40	.0112	X	17.47 / .0117		
4	17.62	.0134	Y		17.62 / .0106	
5	18.22	.0070	Z	18.34 / .0239	18.37 / .0365	18.29 / .0040
6	18.59	.0172	Z	18.61 / .0212	18.74 / .0313	18.67 / .0233
7	18.93	.0103	X	19.07 / .0128	18.93 / .0109	
8	19.31	.0085	Z			19.45 / .0222
9	22.04	.0077	X	22.05 / .0071	22.03 / .0114	
10	22.23	.0072	Z			22.27 / .0091
11	22.35	.0070	Z			22.52 / .0136
12	25.30	.0117	Y	24.57 / .0106	24.59 / .0092	
13	26.22	.0235	Y	25.41 / .0141	25.37 / .0099	25.29 / .0137
14	26.83	.0168	Y		26.86 / .0121	26.23 / .0092
15	27.61	.0100	X	27.62 / .0097	27.08 / .0223	
16	28.37	.0059	X	28.42 / .0081	28.13 / .0065	28.24 / .0114
17	29.48	.0330	X	29.43 / .0390	29.47 / .0412	28.81 / .0066
18	33.02	.0093	X	33.04 / .0093		33.02 / .0092
19	33.40	.0109	Y		33.35 / .0095	
20	33.63	.0069	Z			33.69 / .0049
21	33.75	.0078	Y	33.76 / .0065		
22	33.98	.0066	Y		33.99 / .0045	
23	38.17	.0055	Y	37.05 / .0090	37.21 / .0071	
24	39.70	.0063	Y	38.22 / .0050	38.14 / .0048	
25	41.01	.0108	X	39.74 / .0063	39.75 / .0064	
				41.22 / .0078	41.11 / .0082	
					41.63 / .0063	
				42.04 / .0056		
26	42.99	.0096	Y		42.98 / .0044	
27	44.82	.0055	Y	44.69 / .0030	44.86 / .0040	
					44.93 / .0028	

Table 3
Galileo Spacecraft Modal Survey
Swift, Chirp, and Random Tests
Comparison of Analytical and Test Results

GEM	Swift	Natural Frequency (Hz) / Damping Ratio			Random	Excitation Direction	Target Mode	Predicted Frequency (Hz)
		Up	Chirp	Ensemble Average				
1	12.54 / .0116	12.59 / .0222	12.62 / .0343	12.66 / .0222	Y		2	13.45
2	13.78 / .0209	13.87 / .0199	13.97 / .0019	13.86 / .0193	Y		1	13.22
3	17.40 / .0112	17.90 / .0132	17.91 / .0139	18.14 / .0110	X		5	18.90
4	17.62 / .0134	17.98 / .0165	17.81 / .0175	17.95 / .0153	Y		4	18.13
5	18.22 / .0070	18.54 / .0129	18.60 / .0138	18.54 / .0155	Z			
6	18.59 / .0172	18.59 / .0151	18.60 / .0147	18.62 / .0147	Z			
7	18.93 / .0103	19.24 / .0161	19.35 / .0100	19.34 / .0089	X		3	16.81
8	19.31 / .0085	19.34 / .0094	19.62 / .0098	19.31 / .0071	Z			
9	22.04 / .0077	21.98 / .0063	21.98 / .0059	22.08 / .0046	X		9	23.46
10	22.23 / .0072	22.24 / .0067	22.26 / .0063	22.21 / .0095	Z		6	20.45
11	22.35 / .0072	22.60 / .0063	22.61 / .0076	22.48 / .0119	Y		7	20.77
12	25.30 / .0117	25.71 / .0098	25.68 / .0108	25.74 / .0088	Y		8	21.48
13	26.22 / .0235	25.53 / .0232			Y			
14	26.83 / .0168	25.75 / .0073			Y		12	29.92
15	27.61 / .0100			27.63 / .0178	X			
16	28.37 / .0059	28.56 / .0053	28.60 / .0055	28.51 / .0077	X			
17	29.48 / .0330				X		17	32.59
18	33.02 / .0117	33.21 / .0091		33.13 / .0071	X		16	32.28
19	33.40 / .0109	33.78 / .0072		33.79 / .0072	Y		14	32.11
20	33.63 / .0069	33.74 / .0067		33.67 / .0078	Z			
21	33.75 / .0078	33.90 / .0068	33.70 / .0085	33.79 / .0070	Y			
22	33.98 / .0066		33.90 / .0080		Y			
23	38.17 / .0055	38.09 / .0057	38.09 / .0056	37.94 / .0059	Z			
24	39.70 / .0063				Y		19	35.86
25	41.01 / .0108				X			
26	42.99 / .0096				Y		20	36.30
27	44.82 / .0055	44.70 / .0126		44.34 / .0094	Y		21	36.84

LEGEND: GEM - Galileo Experimental Modes

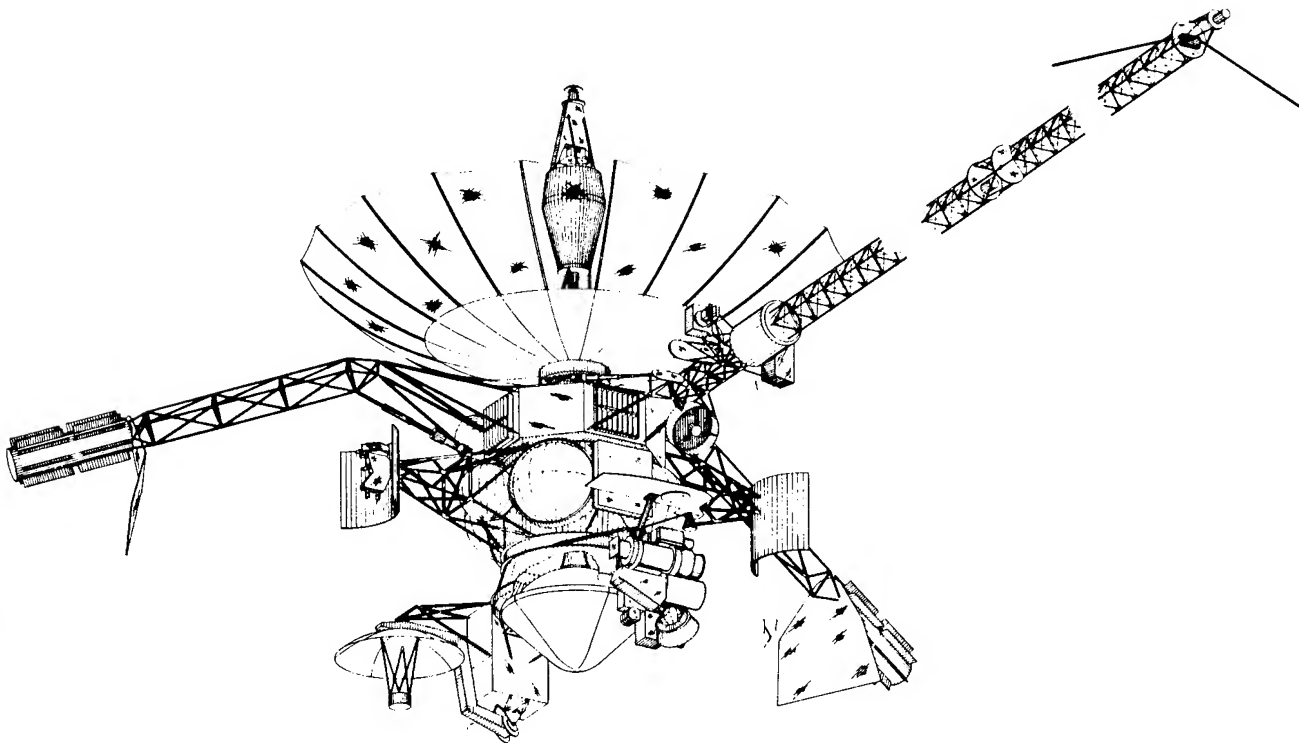


Figure 1. Galileo Spacecraft Cruise Configuration

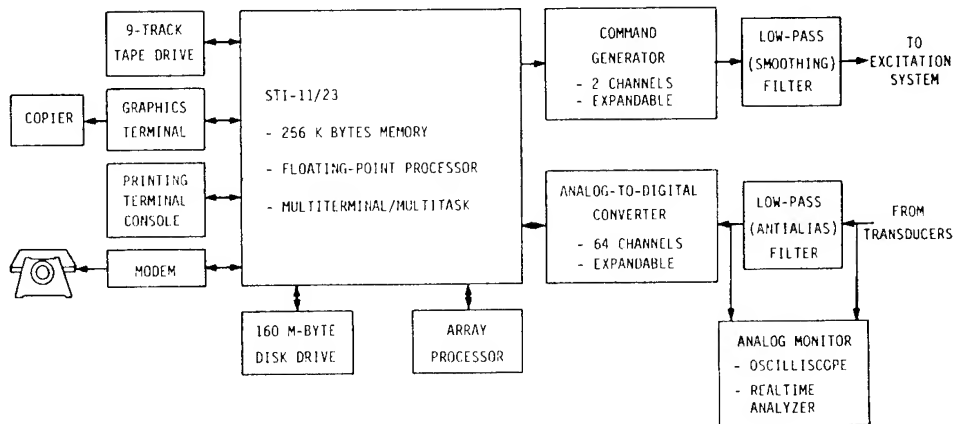


Figure 2. Wyle Modal Analysis and Test System Functional Diagram

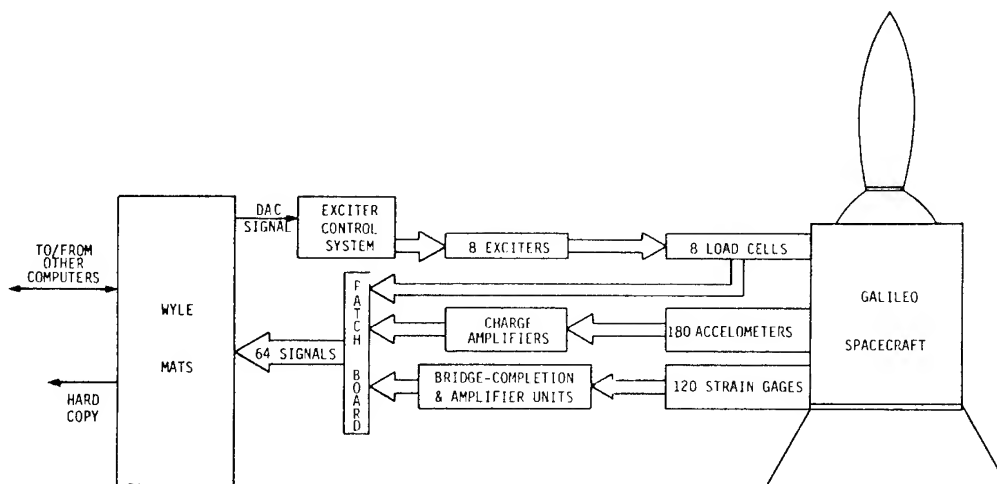


Figure 3. Galileo Spacecraft Modal Survey Data System

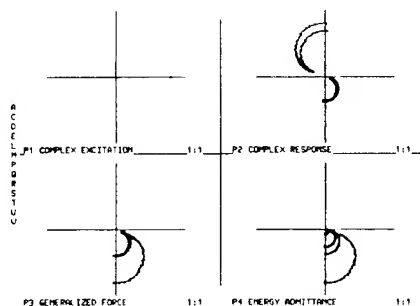


Figure 4. Tuned-Dwell Composite Plot

GALILEO SPACECRAFT MODAL SURVEY, CHIRP TESTS
Z-DIRECTION, G3221,31045.C03 & G3222,41045.C02
COPY (Y/N):

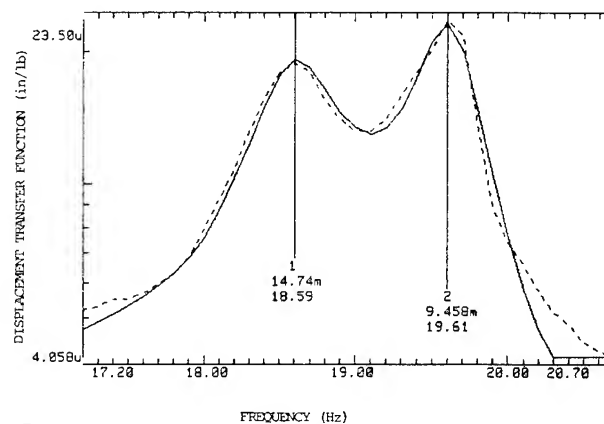


Figure 5. VAMP Frequency-Domain Analysis

David L. Hunt
SDRC, Inc.
San Diego, California

Håvard Vold
SDRC, Inc.
Milford, Ohio

Edward L. Peterson
SDRC, Inc.
Milford, Ohio

Roger Williams
SDRC, Inc.
Hitchin, England

Abstract

The choice of excitation method is critical to the successful performance of a modal test. The method selected determines the type of data that can be obtained as well as how much time the test will require. Newly developed methods offer significant benefits, as evidenced by research applied to the Galileo spacecraft modal test. Knowledge of the advantages and disadvantages of the various methods can help the test engineer make the optimal selection.

Introduction

Over the past two years, many advances have been made in modal testing and analysis methods along with the introduction of powerful hardware systems and software packages. Dynamicists and test engineers now have various options for performing experimental modal analysis of a structure, including which excitation method to use to define the structure's modes of vibration. A few years ago the excitation choices were limited to impact (transient), single-point random, or the traditional multipoint sine dwell. The complexity of the test article and the accuracy and detail required in the results usually dictated which of those methods would be used. Now, with numerous techniques to choose from (for example, multiple input random, multiple input step-sine) which are capable of meeting the technical objectives of a modal survey, the testing engineer must consider other factors when selecting an excitation method(s).

The new methods, combined with hardware and software advances, offer significant benefits for performing experimental modal surveys in a much shorter time with equal or improved accuracy of results. This translates into cost savings due to a shorter test, efficiency in analysis of the results and correlation activities, and, overall, a favorable impact on the program schedule. For these reasons, engineers and managers cannot afford to ignore these new methods.

This paper presents an overview of all excitation methods and their associated strengths and limitations. A new technique for determining initial force patterns for normal mode excitation is described. Guidance is given for utilizing the techniques so that a successful test can be performed in the shortest time. A description of

this methodology as applied in theory to a recently performed modal survey of an aerospace structure, the Galileo spacecraft, yields a perspective on the benefits of this new approach.

Overview of Excitation Methods

The various excitation methods can be classified by the general technique employed by each. The two main methods are modal tuning and frequency response. Modal tuning methods attempt to excite and isolate one particular mode through sinusoidal excitation. Frequency response methods attempt to excite modes occurring in a finite frequency band and measure frequency response functions (frf's). Analysis of the frf's is performed to compute parameters associated with each of the excited modes of interest. Within each of the two main methods, modal tuning and frequency response, various techniques produce the excitation in a manner that will permit measurement of the desired data. Most of the methods are conducive to both single and multiple inputs. (See Appendix A for a discussion on calculating frf's from multiple input data.) These methods, which are summarized in Table 1, form the basis for further discussion.

Table 1. Classification of Excitation Methods.

Frequency Response		Modal Tuning
- random	} single or multiple input	- sine dwell
- random-transient		- tuned sweep
- step sine		
- sine sweep	} single input only	
- chirp		
- transient		
- step relaxation		

Understanding the strengths and limitations of each method is essential in determining when and how to apply the method to a particular modal survey program. Previous experience with a particular method usually enhances the degree of success of a test. However, none of the methods are so sophisticated that they cannot be learned with the help of someone who's had more practice. A good way to begin is to use a new method as a research tool on a test in addition to a more familiar technique. Table 2 highlights the

inherent strengths and weaknesses of the methods when applied by an experienced test engineer.

Table 2. Strengths and Weaknesses of Various Excitation Methods.

<u>Excitation Method</u>	<u>Strengths</u>	<u>Weaknesses</u>
Frequency response	Generally fast test time	Requires postprocessing
Random	Easy after initial set-up for single input case	Low force level only; damping <.01% may not be accurately determined due to leakage
Random transient	No leakage	Low force level only; more complicated input
Step sine	Variable force level; does not require FFT; can employ multiple inputs	Slower than random methods
Sine sweep	Variable force level	Slower than random methods; not implemented for multiple inputs
Chirp	No leakage	Requires special hardware to form input signal
Transient	Easy; quick to set up	Not conducive to complex structures and/or damping >.04%
Step - relaxation	Provides excitation in 0-2 Hz range	Slow, requires special fixturing
Modal tuning	Good definition of the mode; requires little or no post-processing; variable force level	Generally slow; requires information for placing, tuning inputs
Sine dwell	Forces a normal mode	Requires precise tuning to isolate a mode; long test time for more than a few modes
Tuned sweep	Can use curve-fitting to yield a more accurate mode estimate	Requires post-processing; may not give good isolation for the mode

Many modal test applications are adequately performed using single-input methods such as transient or random. In these cases the structures are either uncomplicated (e.g., beamlike or plate-

like, low damping) or detailed results are not required. The rest of this paper assumes that the test is to be performed on a complicated structure for which highly accurate results are required. For these applications, a single input location will not excite all modes of interest. Multiple input locations are required, whether used singly or in groups.

Table 2 indicates that the main deficiencies with the various methods relate to time, inadequacy in using high force levels, postprocessing, and special hardware requirements. Hardware requirements will not be considered in this paper, but those wishing to use techniques involving special hardware should not reject the technique solely on that basis. With the implementation of powerful modal estimation techniques such as poly-reference [1], the postprocessing consideration is becoming less of a factor. Whenever high force levels of excitation are required, a sinusoidal method will be needed to satisfy that requirement. Often, this is for the purpose of investigating the linearity of the test article by determining how the modal parameters change as a function of force level. However, the choice of a sinusoidal method for fulfilling that objective does not mean that it must also be used to perform parts of the test relating to other objectives. A combination of methods may be appropriate. When all considerations have been addressed, the logical choice is the method(s) which satisfy the test objectives and require the least time and cost to perform.

Selection of Excitation Methods

An understanding of the test article, modal data requirements, and the information in Table 2 provide the basis for selecting the excitation method. If modal tuning methods are to be employed, frequency response methods should still be used first to characterize the modal parameters and select modal tuning input locations and forcing patterns. A finite element model is generally not satisfactory for this purpose because a very accurate understanding of the modes in the frequency vicinity of the mode of interest is required to allow adequate isolation of the desired mode.

The steps in the frequency response test are selection of input locations, data acquisition, modal parameter estimation, and verification. The last two subjects are well covered elsewhere in the literature [2]. The method of excitation for final data acquisition may not be selected until exciter locations have been determined. The primary basis for selection of exciter locations is adequate definition of all modes of interest. Exciter locations can be chosen in various ways. One way is to first select a small set of response points which represent all important structural components. Frf's between these points and each

candidate input location are measured using transient or random excitation (a hammer is faster than using an exciter but may not provide sufficient energy). This set of data will yield (1) the frequencies of the modes of interest, (2) which components respond at which modes, and (3) which input locations excite the modes. From this information, a set of input locations is derived which will determine all modes of interest.

Armed with a more thorough understanding of the test article and a set of input locations, the test engineer can now choose the excitation method. Data acquisition is then performed using multiple input techniques, if possible, at the selected input locations. Modal parameter estimation and verification are performed. If modal tuning methods are required, the modal data obtained from the frequency response test can be used to determine input locations and initial forcing pattern estimates. One newly developed method which offers advantages for automating this process is described here.

Initial Force Patterns for Normal Mode Excitation

Assume that a frequency response matrix $H(\omega)$ has been obtained by multiple input methods such as multipoint random or stepped sine excitation. The structural response is steady-state for a purely real force vector $F(\omega)$ and is given by

$$X(\omega) = H(\omega)F(\omega) \quad (1)$$

or dropping the frequency from the notation

$$X = HF \quad (2)$$

Expanding into real and imaginary components, equation 2 becomes,

$$X_r + iX_i = H_r F + iH_i F \quad (3)$$

If a normal mode can be excited at a particular frequency, a force vector F must be found such that the real part X_r of the response vector is as small as possible compared to the total response. We define the norm of the real response by

$$||X_r||^2 = X_r^T M X_r \quad (4)$$

where M is a mass matrix, either from a finite element model or a rough estimate of local mass distribution. Likewise, the norm of the total response is given by

$$||X_r + iX_i||^2 = X_r^T M X_r + X_i^T M X_i \quad (5)$$

The minimization problem is given by

$$\min_{||F||=1} \frac{||X_r||^2}{||X_r + iX_i||^2} = \lambda \quad (6)$$

which after some algebra becomes

$$\min_{||F||=1} \frac{F^T A F}{F^T (A+B) F} = \lambda \quad (7)$$

where $A = H_r^T M H_r$, and

$$B = H_i^T M H_i$$

Noting the similarity of equation 7 to a Rayleigh quotient, it can be shown that the solution to equation 7 is found by finding the smallest eigenvalue λ_{\min} and corresponding eigenvector F_{\min} of

$$A F = (A+B) F \lambda \quad (8)$$

Plotting the smallest eigenvalue times a function of frequency gives a multivariate mode indicator function that clearly shows at which frequencies a normal mode exists that can be excited from the current set of exciter locations. Repeating the procedure for the second smallest eigenvalue reveals which frequencies, if any, are repeated modes. In those cases, the associated force eigenvector will be orthogonal to the first one, so that both modes can be tuned individually at the same frequency. Consequently, all eigenvalues of equation 8 should be plotted as functions of frequency to show the multiplicity of normal modes.

Methodology Applied to Galileo Spacecraft Modal Survey

A modal test was performed in the summer of 1983 on the Galileo spacecraft[3,4]. The purpose of this test was to validate a finite element model and to study the linearity of the spacecraft as a function of response level. The primary method used to excite the structure was sine dwell. This choice was based, at the time, on prior experience testing other spacecraft. However, many of the other methods listed in Table 1 were applied as research tools for comparison with the results from the sine dwell test[5]. Most of the methods yielded very similar results, indicating their validity in defining modal parameters for a complex aerospace structure[6]. A close look at the way the Galileo test was performed, compared with how it could have been performed using the methodology presented here, reveals the benefits of the new approach.

The Galileo modal survey required eight weeks. This period was divided into three main tasks for the modal tuning effort:

- (1) Check and debug all instrumentation - 2 weeks
- (2) Define modes using low level sine dwell - 3 1/2 weeks

- (3) Investigate modal response to high level sine dwell - 2 1/2 weeks

The research methods were applied towards the end of the eight-week period during the evening shift.

Optimal selection of excitation methods would have significantly reduced the total time required for the test as well as yielded more complete results. Task 2, low level definition of modes, would be performed using random or random transient (depending upon leakage considerations). Multiple-input random was one of the methods utilized in the research portion of the test. A comparison, shown in Table 3, indicates a dramatic difference between the results achieved with each of these two methods.

Table 3. Comparison of Methods Used in the Galileo Modal Survey.

Method	Number of Modes Identified	Data Collection Time	Data Analysis Time
Multiple Input Random	26	2 days	2 days
Low Level Sine Dwell	14	3 1/2 weeks	----

Using multiple input random, almost twice as many modes were defined in a fraction of the time, as compared to the sine dwell. An orthogonality check indicated that the dominant modes from the random test were more orthogonal than those from the sine test. See Reference 4.

Task 3, the high level sine excitation for linearity investigation, required 2 1/2 weeks to complete. Shaker positioning for exciting normal modes had been defined by the low level sine testing (Task 2). In this new approach, the positioning would be determined by the method described earlier. The 2-1/2-week period required for this task might be shortened if more effective shaker locations were computed than those deduced through the traditional approach.

An alternative for Task 3 would be step sine excitation using multiple inputs. As compared to random multiple input, step sine yields variable force level, enabling the structure to be excited at a level limited only by exciter capability. This approach could significantly reduce the 2-1/2-week period, in a manner similar to that shown for the lower level testing comparison in Table 3. This study suggests that a test of the Galileo spacecraft could be successfully performed now in five--perhaps three--weeks with an increase in the amount of valuable modal data obtained.

Summary

Many excitation techniques now exist which are suitable for performing modal surveys of complicated structures. Optimal selection of the excitation method, or methods, for a particular test offers significant advantages for reducing the time and cost associated with the modal test program. This selection procedure requires a thorough understanding of each method and its strengths and limitations relative to the test

objectives. Successful application of the methods also requires personnel having direct experience with each of the selected methods.

Insight and experience gained on the Galileo spacecraft modal survey suggest that a traditional sine dwell test can be replaced by a test involving various frf-based methods. As a result, test time can be reduced by up to 50% with a significant increase in the experimental modal definition.

Appendix

Simultaneous Multipoint Frequency Response Function Acquisition and Estimation

For a linear structure at the frequency ω , the relationship between the vectors of measured forces, $F_i(\omega)$, and responses, $X_i(\omega)$, are given by the matrix equation,

$$X_i(\omega) = H(\omega) F_i(\omega) \quad (1)$$

where $H(\omega)$ is the matrix of frequency response functions. By measuring at least as many linearly independent force vectors, $F_i(\omega)$ and corresponding response vectors, $X_i(\omega)$ as there are force inputs to the structure, one can rewrite equation 1 as the overdetermined system.

$$X(\omega) = H(\omega) F(\omega) \quad (2)$$

where

$$X(\omega) = [X_1(\omega), \dots, X_i(\omega), \dots, X_n(\omega)], \text{ and} \quad (3)$$

$$F(\omega) = [F_1(\omega), \dots, F_i(\omega), \dots, F_n(\omega)] \quad (4)$$

Traditionally, equation (2) has been solved for $H(\omega)$ by solving the least squares normal equations

$$G_{XF}(\omega) = H(\omega) G_{FF}(\omega) \quad (5)$$

where $G_{XF}(\omega) = X(\omega) F^T(\omega)$ is the matrix of cross spectra between forces and responses and $G_{FF}(\omega) = F(\omega) F^T(\omega)$ is the auto spectral matrix of the force channels. $F^T(\omega)$ is the transposition of the complex conjugate of $F(\omega)$.

To solve equation 5, $G_{FF}(\omega)$ must be non-singular, a condition that for random broadband excitation is met by using individual, incoherent noise sources for the exciter systems. For multipoint stepped sine excitation, linearly independent force vectors can be obtained by changing exciter phase patterns between measurements. An advantage of the multipoint stepped sine frequency response function acquisition is that data is obtained with the identical force levels and boundary conditions that would apply to a tuned sine dwell test using the same testing system.

References

1. Vold, H., G.T. Rocklin, "The Numerical Implementation of a Multi-input Modal Estimation Method for Mini-Computers," International Modal Analysis Conference, November, 1982.
2. Crowley, J.R., D.L. Hunt, G.T. Rocklin, H. Vold, "The Practical Use of the Polyreference Modal Parameter Estimation Method," International Modal Analysis Conference, February, 1984.

3. Garba, J.A., B.K. Wada, J.C. Chen, "Summary of the Galileo Spacecraft Modal Test Activities," AIAA Dynamics Specialists Conference, Paper No. 84-1072-CP, May, 1984.
4. Hunt, D.L. and J.C. Chen, "Application of Multi-Shaker Random Excitation and Poly-reference Analysis Techniques to the Galileo Spacecraft Modal Test," AIAA Dynamics Specialists Conference, Paper No. 84-1069-CP, May, 1984.
5. Coppolino, R., D.L. Hunt, S.R. Ibrahim, and R.C. Stroud "Advanced Methods Used on the Galileo Spacecraft Modal Survey," International Modal Analysis Conference, February, 1984.
6. Chen, J.C., "Evaluations of Modal Testing Methods," AIAA Dynamics Specialists Conference, Paper No. 84-1071-CP, May, 1984.

APPLICATION OF MULTIPLE INPUT RANDOM AND POLYREFERENCE ANALYSIS TECHNIQUES TO THE GALILEO SPACECRAFT MODAL TEST

J. C. Chen
Jet Propulsion Laboratory
Pasadena, California

D. L. Hunt
SDRC, Inc.
San Diego, California

Abstract

An experimental modal analysis of the Galileo spacecraft was required to verify a finite element model used in loads analysis. Multiple input random and polyreference analysis techniques were applied in this program to demonstrate their effectiveness in determining the modal characteristics of a complex space structure. The methods were successful in determining an accurate set of modal data from two days of data acquisition. A complete set of results was available within 24 hours of test completion. Final analysis shows the modes from the multiple input random tests to be more complete and orthogonal than those obtained from classical sine dwell methods.

Introduction

Two modal surveys were performed on the Galileo spacecraft using the multiple input random method. Frequency response functions were calculated from the measured force and acceleration data and used to determine modal parameters using the polyreference analysis method. Results were compared to an analytic model as well as to test results obtained using classical tuned sine dwell techniques. This paper describes the methods used to perform the multiple input random testing and parameter estimation and presents the results in both stand-alone and comparative fashion.

Multiple Input Random

Multiple input random [1] uses a multiple set of shakers to excite and define all modes of interest **simultaneously**. Frequency response functions (frf's) are calculated between each response measurement and each of the individual force inputs. A consistent data set is obtained because the structure is unlikely to change during a single test; thus boundary conditions are constant, and the distribution of internal forces throughout the structure remains consistent. A structure's dynamic characteristics (hence, modal parameters) can change significantly, even for seemingly linear structures, whenever one or more of those conditions are violated. Some typical situations are:

1. Change in structure and/or its environment (temperature, etc.). High level excitation, for example, can loosen bolts and rivet areas.

2. Changes in boundary conditions. Every time a different shaker setup is used (for example, different shaker position(s) or different number of shakers) boundary conditions change. This can result in different structural response and shifts in mode frequency and damping.
3. Inconsistent distribution of internal forces. Each time a shaker configuration is altered, the structure is excited in a different fashion. This is true especially for sine-dwell testing but also if separate single-shaker random tests are performed. Bolted and/or sliding joints, fittings, and other nonhomogeneous structural areas respond differently depending upon the distribution of the internal forces.

Multiple input random not only overcomes these potential inconsistencies but also excites the structure with forces similar to real environments; that is, random input at multiple locations. This yields the best linear modal representation of even a highly nonlinear structure. Sine-dwell testing can then characterize nonlinearity as changes in frequency and damping as a function of input force level. [2] The choice of number and locations of exciters is based upon candidate positions (there are usually restrictions on where exciters can be attached) and engineering experience and judgement.

Multiple input methods have been shown to be most effective when the exciters are not aligned with any principal axes or towards the structural center of gravity. [3] In this situation, the force inputs are evenly distributed and all modes are excited rather uniformly (that is, no particular modes are emphasized). This results in frf's in which all dominant modes have similar amplitudes. The parameter estimation algorithms work better with data of this type. This distributed input method also reduces the chances of computational problems that can occur when the majority of one response is from one exciter. In this case, the frf's computed between that response and the other shakers may suffer due to lack of analyzer dynamic range.

Multiple input random is an extension of the concepts involved in single input random

excitation. Both methods determine frf's between measurements of the output(s) and input(s). For the multiple input case, matrix procedures are required to compute n frf's from each response due to n inputs. To accomplish this, the inputs must not be correlated. The use of separate random waveform generators satisfies this need. The n frf's determined in the multiple input case are inherently more consistent than if measured one at a time, as in the single input case. A reduction in data acquisition time by up to a factor of n is another benefit of multiple input methods.

Polyreference Modal Parameter Estimation

Polyreference [4] estimates modal parameters from frequency response functions. The technique is actually a time-domain curve-fitting approach using the impulse response functions--the inverse Fourier-transformed frequency response functions. An overview of the technique reveals the advantages of this type of approach.

Normally, not all modes of a structure can be excited sufficiently from a single exciter position. One reason for this is that the exciter may be positioned at a node for a particular mode in the frequency range of interest. Also, sufficient energy may not be present to excite modes whose primary motion is orthogonal to the exciter direction. Therefore, to accurately model a mechanical system, it is often necessary to analyze data from a number of different exciter locations.

The polyreference method uses frequency response data from multiple exciter (reference) locations in a global least-squares fashion. These data may be obtained from several single-exciter tests, such as single-point random, or from a multiple-exciter test, such as multiple input random. Simultaneous analysis of the data can yield a consistent modal model while minimizing the analyst's effort. Most other curve-fitting algorithms fail to use data from more than one exciter location consistently and thus force the analyst to choose between several estimates of the same modal quantities.

The accuracy and consistency of results obtained using polyreference depend upon the accuracy and consistency of the measured data. Polyreference has demonstrated the ability to define closely spaced modes, including repeated roots for symmetric structures, and it handles high modal damping (>10% critical) [5]. As such, it is best applied to data acquired under multiple input conditions where data consistency is highest.

Technical Approach for Galileo

A modal survey of the Galileo spacecraft was required to verify a mathematical model used in loads analysis. The methods described in this paper were applied as a research tool

for determining their effectiveness in performing an experimental modal analysis. Specific objectives were:

- (1) Demonstrate the validity of these techniques on a complex space structure. Define the modal characteristics in the 10 Hz to 40 Hz range.
- (2) Perform the data acquisition in two days or less.
- (3) Provide initial results (frequency, damping, mode shapes) in one day or less.
- (4) Assist in comparing the results to those obtained using other techniques as well as those obtained from the Test Analysis Model (TAM). [6]

The approach used to fulfill those objectives included:

- Using the JPL excitation and measurement system. [7]
- Performing and controlling the data acquisition using a GenRad 2508 16-channel structure analysis system.
- Performing the on-site polyreference analysis using JPL computers.

The on-site program was performed in five days. Two days were devoted to equipment setup and checkout. The third and fourth days consisted of data collection and analysis (fourth day only). Data review and equipment removal comprised the fifth day.

Data Acquisition and Analysis

A photo of the test configuration is shown in Figure 1. Two complete modal surveys were performed, one using three exciters and one using four exciters. Random signals, used to drive the power amplifiers, were obtained from separate noise generators. Thirty 1024-point data blocks were measured by sampling at 150 Hz, with an antialiasing filter setting of 60 Hz. This resulted in a Δf of 0.15 Hz. Data acquisition for 162 response channels required approximately three hours to complete for each survey. For each of the two tests, frf's were calculated between every response point (162 + number of shakers) and every input point (exciter). Reciprocity between exciter locations was excellent. See Figure 2. Polyreference analysis of the frf's was performed in the 10 Hz to 47 Hz range (256 spectral lines) which contained all modes of interest.

Test Results and Comparisons

Analysis of the multiple input random data identified two sets of modal parameters (frequency, damping, stiffness, mode shape): 21 modes for the three-shaker test and 27 for

the four-shaker test. Orthogonality and effective mass results were computed with the analytic model (TAM). Multiple input random results were compared to the TAM model by frequency, mode shape, and effective mass. Additionally, a comparison was made to the results obtained from a sine dwell modal survey, performed prior to the random tests. A summary of these results and comparisons follows.

Table 1 presents a summary of the multiple input test results. For each of the two surveys (three-shaker and four-shaker) each mode is identified by frequency, damping, effective mass participation (by percentage of total) and major structural participation. Modal quantities shown in bold represent global modes which possess 10% or greater effective mass in any one of six directions.

Figure 3 plots comparisons between measured frf's and synthesized frf's. The synthesis function is computed from the experimental modal parameters. [8] The comparison indicates the degree of accuracy of those modal quantities calculated with polyreference.

Table 2 compares the three-shaker random modes to the four-shaker random modes using modal assurance criterion (MAC) [9]. The MAC value indicates the degree of independence between mode shape estimates. A value of 1.0 indicates the modes are identical. Values close to 0.0 signify independent (different) modes. All MAC values were above 0.6; many are above .9, indicating the modal estimates are nearly identical. Note, however, the structure responded differently for the two tests based upon a shift in frequency for modes 1 and 3, possibly due to a change in the antenna support stiffness. The antenna is a significant component in these two modes; its structural connection to the spacecraft suggests possible nonlinear behavior.

A sine dwell modal test of the Galileo spacecraft identified 14 modes. This test was performed in a six-week period immediately preceding the multiple input random survey. Modal assurance between TAM model modes and the corresponding test results, including the sine test, are shown in Table 3. In general, the four-shaker modes are closer in agreement to the model modes than are those of either the three-shaker or sine dwell shapes. A MAC comparison between the four-shaker test and sine test for the 14 corresponding modes is shown in Table 4. Most modes show good correlation, although some modes are different between the two tests, based on the MAC values.

Orthogonality results for the three-shaker and four-shaker "global" modes are shown in Table 5. The four shaker data yields the best orthogonality; only one off-diagonal term exceeds 10%. Orthogonality for the global sine modes is shown in Table 6. Many of

the sine dwell mode shapes are not very orthogonal, based upon the number of off-diagonal terms exceeding 10%.

Summary

Multiple input random excitation and polyreference analysis methods were successfully applied to the Galileo spacecraft modal survey program. All modal data was collected in two days. The analysis of this data identified all 14 modes derived from six weeks of sine dwell testing and defined 15 additional local modes which further characterized Galileo structural dynamics. Accuracy and completeness of the modal data were verified through synthesis, modal assurance criterion, effective mass, and orthogonality checks. These results demonstrate that the methods can be applied to complex aerospace structures with high modal density, offering an alternative to traditional sine dwell and single point methods.

References

1. Hunt, D., E. Peterson, "Multiple Input Broadband Excitation for Experimental Modal Analysis," SAE Aerospace Congress and Exposition, October, 1983.
2. Hunt, D., E. Peterson, H. Vold, R. Williams, "Optional Selection of Excitation Methods for Enhanced Modal Testing," AIAA SDM, May 1984.
3. Nessler, G.L., J.R. Crowley, A.J. Wolfer, H. Vold, "Application of Multi-Point Random Excitation and Polyreference Analysis to a Centrifugal Blower," International Modal Analysis Conference, 1984.
4. Crowley, J., D. Hunt, T. Rocklin, "Practical Use of the Polyreference Modal Parameter Estimation Method," International Modal Analysis Conference, 1984.
5. Leuridan, J., J. Kundrat, "Advanced Matrix Methods for Experimental Modal Analysis - Multimatrix Method for Direct Parameter Extraction," International Modal Analysis Conference, 1982, pp. 192-200.
6. Chen, J., and M. Trubert, "Galileo Modal Test and Pre-test Analysis," International Modal Analysis Conference, 1984.
7. Bausch, P., R.C. Stroud, "Galileo Data Acquisition and Test Control System Implementation," International Modal Analysis Conference, 1984.
8. User Manual for MODAL-PLUS, SDRC, 1982.
9. Allemang, R.A., D.L. Brown, "A Correlation Coefficient for Modal Vector Analysis," International Modal Analysis Conference, November 1982.

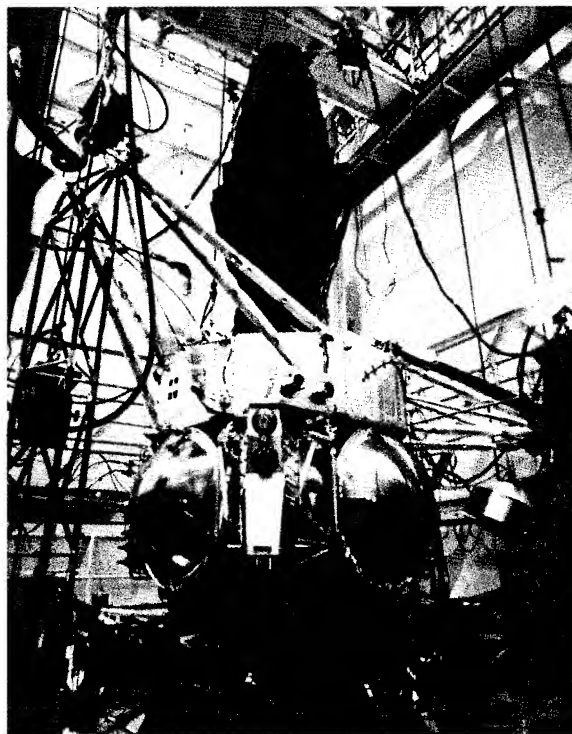
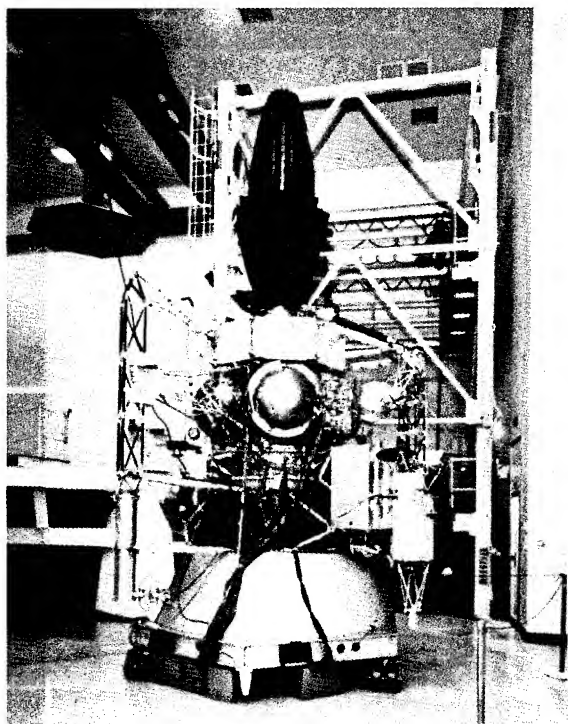


Figure 1. Galileo spacecraft in test configuration for modal survey prior to installation in test bed (left), mounted to concrete seismic mass (right).

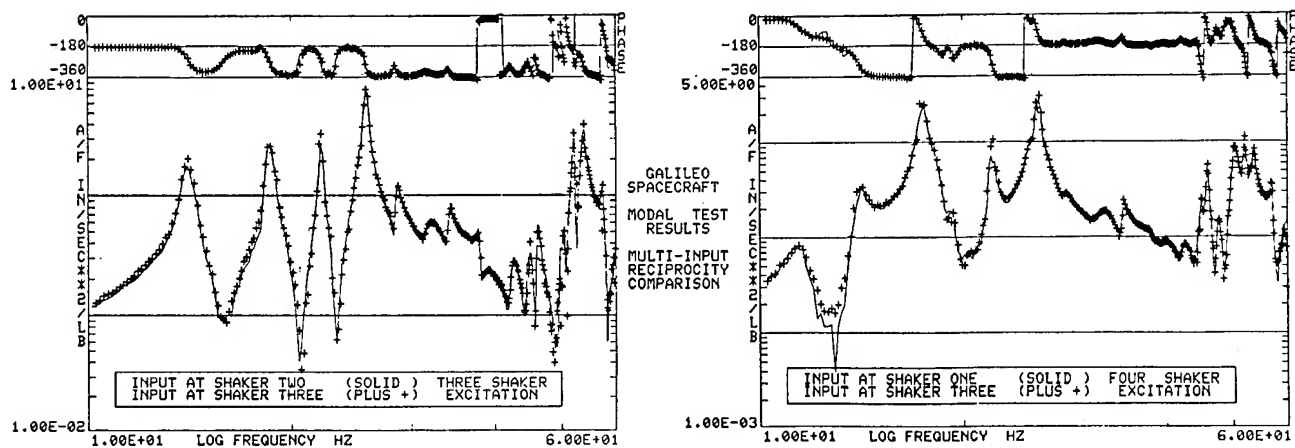


Figure 2. Reciprocity for three input test (left) and four input test (right) is excellent.

Table 1

MODAL PARAMETER RESULTS FOR MULTIPLE INPUT RANDOM TESTS

THREE INPUT SURVEY									FOUR INPUT SURVEY									MODE DESCRIPTION
EFFECTIVE MASS %									EFFECTIVE MASS %									
MODE	FREQ	DAMP	X	Y	Z	Ox	Oy	Oz	MODE	FREQ	DAMP	X	Y	Z	Ox	Oy	Oz	
1	13.73	.021	0	14	0	32	1	0	1	11.46	.030	1	5	0	15	2	0	High Gain Antenna Y
2	14.10	.017	25	0	0	1	53	0	2	14.02	.017	23	0	0	1	48	0	High Gain Antenna X
3	18.32	.011	1	32	0	34	0	0	3	17.44	.009	2	42	0	52	2	0	Core Bending Y
4	18.62	.013	23	0	0	0	22	4	4	18.54	.018	19	1	0	1	17	5	Core Bending X
5	19.45	.008	0	0	0	0	0	19	5	19.33	.009	0	0	0	0	1	19	Science Boom X
6	22.19	.006	24	2	0	1	15	2	6	22.06	.005	21	3	0	1	14	1	± RTG Z out of phase
-	NI								7	22.22	.026	0	5	1	8	0	0	± RTG Z out of phase, Sci Boom Z
7	22.81	.007	6	9	2	2	4	1	8	22.52	.009	4	15	2	5	2	1	± RTG Z in phase, Sci Boom Z o/p
8	25.33	.011	0	3	13	1	0	1	9	25.19	.010	0	2	13	0	0	2	± RTG Z in phase, Sci Boom Z i/p
9	25.80	.006	1	0	1	0	0	24	10	25.80	.007	1	1	2	1	1	22	Core Twist about Z
10	26.64	.023	2	4	0	1	2	0	11	26.36	.020	0	3	0	0	0	0	Damper Y
11	27.89	.021	0	0	2	0	0	1	12	27.84	.020	1	0	4	0	0	2	Damper +Y, RRH - Y
12	28.16	.006	0	0	0	0	0	0	-	NI								Sunshade Z
13	28.58	.007	0	0	0	0	0	1	13	28.29	.011	0	0	0	0	0	1	RRH Y
-	NI								14	30.50	.035	1	0	6	1	1	0	Scan Platform Z
14	31.92	.028	1	0	1	0	3	9	15	31.84	.029	0	1	0	0	0	7	Damper X
15	33.46	.012	14	0	1	0	5	0	16	33.42	.015	13	0	1	0	4	0	Core 2nd Bending X, ± RTG +Y
-	NI								17	33.76	.011	4	1	0	0	1	5	Core 2nd Bending X, ± RTG -Y
16	34.32	.008	4	0	0	0	2	3	18	34.50	.007	1	0	0	0	0	2	Science Boom X, Z
17	37.98	.006	0	0	45	0	0	0	19	37.91	.006	0	0	46	0	0	0	Core +Z, Appendages -Z
-	NI								20	39.14	.046	0	0	10	0	0	1	± Thruster Y in phase
18	39.88	.006	0	0	0	0	0	0	-	NI								RRH Y
-	NI								21	39.77	.012	0	6	0	5	0	3	Science Boom Y, ± Thruster Y o/p
-	NI								22	41.73	.018	0	0	1	0	0	1	+ Thruster Y
19	42.57	.014	0	2	0	0	0	1	23	42.35	.028	0	2	0	1	0	0	± Thruster Y o/p RRH, Sci Boom Y
-	NI								24	42.36	.007	0	1	0	1	0	0	- Thruster Y
-	NI								25	44.61	.006	0	2	0	1	0	1	± Thruster Y in phase, RRH Y o/p
20	45.14	.005	0	0	1	0	0	0	26	44.98	.005	0	0	1	0	0	0	± Thruster Y out of phase
21	46.05	.007	0	1	0	1	0	0	27	46.00	.004	0	1	0	1	0	0	± Thruster Y in phase
102 68 67 75 108 66									91 90 86 95 93 72									

102 68 67 75 108 66

91 90 86 95 93 72

Global modes are shown in bold

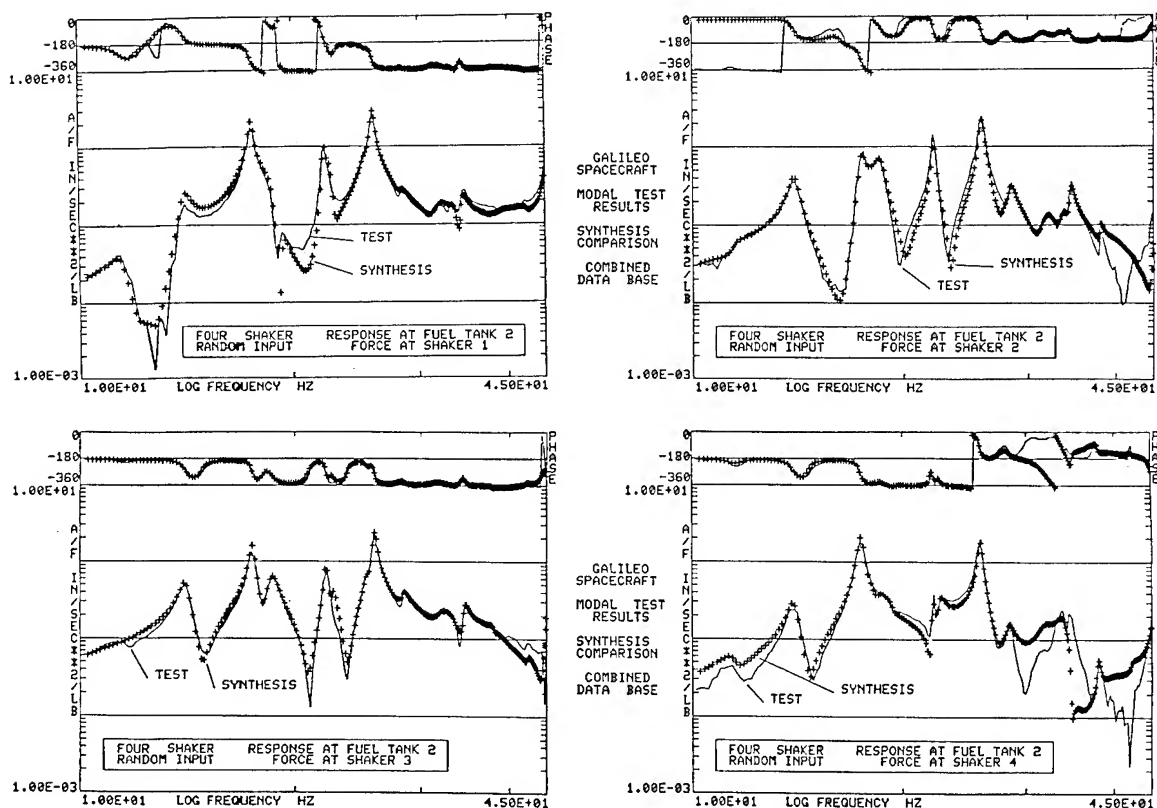


Figure 3. Modal data base accuracy is indicated by the close agreement between measured and synthesized frf's.

Table 2

Modal assurance criterion between modes from three and four
input random tests

3 INPUT MODE NO.	3 INPUT FREQ.	4 INPUT MODE NO.	4 INPUT FREQ.	MAC VALUE
1	13.73	1	11.46	0.97
2	14.10	2	14.02	0.97
3	18.32	3	17.44	0.77
4	18.62	4	18.54	0.94
5	19.45	5	19.33	0.99
6	22.19	6	22.06	0.62
7	22.81	8	22.52	0.56
8	25.33	9	25.19	0.99
9	25.80	10	25.80	0.96
10	26.64	11	26.36	0.98
11	27.89	12	27.84	0.73
13	28.58	13	28.29	0.96
14	31.92	15	31.84	0.99
15	33.46	16	33.42	0.86
16	34.32	18	34.50	0.99
17	37.98	19	37.91	0.95
19	42.57	23	42.35	0.77
20	45.15	26	44.98	0.80
21	46.05	27	46.00	0.96

Table 3

Modal assurance criterion between modes from TAM model
and test results

4-INPUT MODE NO.	MODEL FREQ.	3 INPUT FREQ.	MAC VALUE	4 INPUT FREQ.	MAC VALUE	SINE DWELL FREQ.	MAC VALUE
1	11.08	13.73	0.93	11.46	0.86	12.70	0.90
2	11.20	14.10	0.92	14.02	0.85	13.11	0.98
3	15.08	18.32	0.68	17.44	0.49	17.76	0.26
4	14.94	18.62	0.75	18.54	0.58	17.40	0.27
5	16.36	19.45	0.80	19.33	0.81	18.60	0.83
6	20.04	22.19	0.61	22.06	0.48	21.67	0.42
8	20.37	22.81	0.22	22.52	0.59	23.10	0.29
9	23.53	25.33	0.34	25.19	0.39	23.66	0.05
10	21.02	25.80	0.46	25.80	0.42	25.46	0.42
13	26.41	28.58	0.37	28.29	0.43	29.70	0.04
19	32.78	37.98	0.63	37.91	0.63	37.92	0.59

Table 4

Modal assurance criterion between modes from sine dwell and
four input random tests

SINE DWELL MODE NO.	SINE DWELL FREQ.	4 INPUT MODE NO.	4 INPUT FREQ.	MAC VALUE
1	12.70	1	11.46	0.99
2	13.11	2	14.02	0.85
3	17.76	3	17.44	0.80
4	17.40	4	18.54	0.69
5	18.60	5	19.33	0.95
6	21.67	6	22.06	0.65
7	23.10	8	22.52	0.56
8	23.66	9	25.19	0.54
9	25.46	10	25.80	0.87
10	26.12	12	27.84	0.64
11	29.70	13	28.29	0.09
12	37.92	19	37.91	0.93
13	42.20	22	41.73	0.34
14	42.53	24	42.36	0.10

TABLE 5

Orthogonality results for global modes

1	2	3	4	5	6	7	8	9	15	17	Mode no.
1.00	-0.03	<u>-0.22</u>	0.03	-0.05	-0.02	0.01	-0.05	-0.01	0.01	-0.01	1
	1.00	0.01	-0.03	-0.04	0.04	-0.04	0.01	-0.02	0.04	0.01	2
		1.00	-0.07	-0.04	0.02	-0.01	0.02	-0.01	0.02	-0.03	3
			1.00	0.01	0.05	-0.07	0.04	-0.04	0.04	-0.02	4
				1.00	0.00	0.00	-0.07	0.03	-0.01	0.03	5
					1.00	<u>-0.25</u>	-0.07	-0.03	<u>0.15</u>	-0.01	6
						1.00	0.07	0.07	-0.04	0.00	7
							1.00	0.04	-0.03	0.00	8
								1.00	-0.07	0.03	9
									1.00	-0.03	15
										1.00	17

Three input random survey

1	2	3	4	5	6	8	9	10	16	19	Mode no.
1.00	0.02	<u>-0.16</u>	0.04	-0.03	-0.04	0.04	-0.04	-0.02	0.00	-0.01	1
	1.00	0.02	-0.04	0.04	-0.04	0.00	-0.02	-0.02	0.00	-0.03	2
		1.00	0.01	-0.03	-0.02	0.01	0.01	0.00	0.01	-0.01	3
			1.00	0.05	-0.05	0.01	-0.07	-0.02	0.00	0.01	4
				1.00	0.05	0.02	-0.01	-0.02	-0.02	0.03	5
					1.00	-0.03	-0.02	0.02	0.09	0.01	6
						1.00	0.07	-0.04	-0.04	0.00	8
							1.00	-0.05	0.00	0.00	9
								1.00	0.09	-0.03	10
									1.00	0.01	16
										1.00	19

Four input random survey

TABLE 6

Orthogonality results for global modes

1	2	3	4	5	6	9	12	Mode No.
1.00	<u>0.32</u>	<u>0.20</u>	-0.04	0.00	0.03	-0.01	-0.01	1
	1.00	<u>0.10</u>	0.04	0.05	<u>0.15</u>	-0.02	-0.01	2
		1.00	<u>-0.19</u>	<u>0.16</u>	<u>-0.17</u>	0.01	0.02	3
			1.00	<u>0.15</u>	<u>-0.20</u>	0.01	-0.02	4
				1.00	<u>-0.22</u>	0.04	0.02	5
					1.00	-0.08	-0.02	6
						1.00	0.02	9
							1.00	12

Sine dwell survey

Jay-Chung Chen*
 Applied Mechanics Technology Section
 Jet Propulsion Laboratory
 California Institute of Technology
 Pasadena, California

Abstract

Modal tests are playing an increasingly important role in structural dynamics efforts which are in need of analytical model verification or trouble shootings. In the meantime, the existing modal testing methods are undergoing great changes as well as new methods are being created. Although devoted advocates of each method can be found to argue the relative advantages and disadvantages, the general superiority, if any, of one or the other is not yet evident.

The Galileo spacecraft, a realistic, complex structural system, will be used as a test article for performing modal tests by various methods. The results will be used to evaluate the relative merits of the various modal testing methods.

Introduction

Modal testing plays a significant role in the spacecraft development activity in which the experimentally determined natural frequencies, mode shapes and other modal parameters are used to verify the analytical model for design purpose. Although the traditional modal test method was first proposed in 1950 (Ref. 1), this so-called "multi-shaker sine dwell" method is still used extensively in the aerospace industry. However, with the advent of the computers and mini-computers, the so-called "frequency response function" method becomes popular. It would have been beneficial, had some detailed comparisons of these two approaches been made. So far most of the comparisons were made on relatively simple structures such as a beam or a plate. Only limited actual testing comparisons were performed on realistic complex structures, (Refs. 2 and 3). In the summer of 1983, the Galileo spacecraft modal test provided an opportunity to evaluate these modal testing methods. The results of the evaluation are the subject of the present report.

Basically all modal testings can be classified as forced vibration test in which external forces are applied and responses are measured. A linear elastic structure behaves as selected bandpass filters as far as input and output relation is concerned. In other words, the structure will amplify the output at certain frequencies and suppress it at others. By properly arranging the inputs, i.e., the external forces, certain desirable type of responses may be obtained. The multi-shaker sine dwell method is to concentrate the input at a discrete frequency and force the responses into a particular shape which is similar to one of its normal modes. The eigenvalues and eigenvectors, i.e., the natural frequencies and the mode shapes, are measured directly and no further data processing is necessary. Also since the structure is responding in steady state, no high

speed data acquisition and analysis capability is required once the mode is tuned. On the other hand, the "Frequency Response Function" methods make sure that the inputs contain all the frequencies of interest. The responses filtered by the structural characteristics will carry informations which are functions of modal parameters. In other words, all the modes of interest are excited simultaneously. From the measured time history, the eigenvalues and eigenvectors are extracted. Therefore, it is necessary that high speed data acquisition and analysis systems are available to process the data. It became clear why the multi-shaker sine dwell method was the only modal testing technique more than 30 years ago and the frequency response function methods were not possible until the microprocessor technology became matured. A detailed description of the development of testing methods with extensive bibliography can be found in Ref. 4.

These drastically different testing methods have advantages and disadvantages of each and, as such, have their own ardent devotees. The objective of the present study is not to evaluate the ease or difficulty in implementing these testing techniques since no matter which method was chosen, the success of the test is still quite heavily dependent on the experiences, or luck to a certain degree, of the test engineer who performs the test. Of course, the complexity of the test article is the foremost important factor in determining the qualities of the test results. Therefore, the present evaluation will be focused on two aspects of the modal test. One is the theory on which the testing method was based. The inherent difficulties of satisfying the theoretical assumptions will be examined for the different testing techniques.

The second aspect is to evaluate the results of the modal testing of the same test article in terms of the qualities of the results. Although identical test article and instrumentation were used in the applications of these different testing methods, different test personnel was put in charge for implementing the different methods. Since each plays leading role in the modal testing community in their chosen method, the quality of the testing itself will be assured, hopefully.

Theoretical Background

In the evaluation of modal testing methods, the differences in the theoretical approach are obviously of prime concern. As mentioned before, the following brief theoretical description is for the purpose of examining the inherent constraints of the modal testing methods.

The equations of motion for an n-DOF (degrees-of-freedom) linear damped system under external excitation can be written as:

$$[M]\{\ddot{x}\} + [C]\{\dot{x}\} + [K]\{x\} = \{F(t)\} \quad (1)$$

*Member of Technical Staff, member AIAA.

Released to AIAA to publish in all forms.

where $[M]$, $[C]$ and $[K]$ are the mass, damping and stiffness matrices of the structure, respectively, and $\{F(t)\}$ is the external forcing function vector. The system represented by Eq. (1) is said to possess classical normal modes if and only if it can be reduced to a set of n uncoupled second order systems. A necessary and sufficient condition for the existence of classical normal modes is that matrices

$$[M]^{-1}[C] \text{ and } [M]^{-1}[K]$$

commute (Ref. 5).

$$[M]^{-1}[C][M]^{-1}[K] = [M]^{-1}[K][M]^{-1}[C] \quad (2)$$

For the type of spacecraft structural system, although the damping is usually unknown, its values are small and assumed to be proportional to the mass and stiffness matrices,

$$[C] = \alpha[M] + \beta[K] \quad (3)$$

where α and β are arbitrary proportional constants. It is also defined, obviously, as the proportional damping. The existence of the classical normal modes assures the following orthogonality conditions

$$\left. \begin{aligned} [\phi]^T [M] [\phi] &= [I] = \text{unity matrix} \\ [\phi]^T [C] [\phi] &= [2\gamma_n \omega_n] \\ [\phi]^T [K] [\phi] &= [\omega_n^2] \end{aligned} \right\} \quad (4)$$

where

$$\left. \begin{aligned} [\phi] &= \text{normal mode or eigenvector matrix} \\ [2\gamma_n] &= \text{percentage of critical damping} \\ [\omega_n^2] &= \text{eigenvalues.} \end{aligned} \right\} \quad (5)$$

Now, applying the modal transformation

$$\{x\} = [\phi]\{q\} \quad (6)$$

The governing equation, Eq. (1) can be written as

$$\begin{aligned} \{\ddot{q}_n\} + [2\gamma_n \omega_n] \{\dot{q}_n\} + [\omega_n^2] \{q_n\} \\ = [\phi]^T F(t) \end{aligned} \quad (7)$$

Once the external forces $\{F(t)\}$ is defined, the motion of the system may be obtained by Eqs. (6) and (7).

1. Multi-Shaker Sine Dwell Method

For the case of multi-shaker sine dwell method, the external forces are sinusoidal with frequency Ω , therefore,

$$\{F(t)\} = \{f\} \sin \Omega t \quad (8)$$

where $\{f\}$ represents the amplitudes of the forces distributed on the system and Ω is the frequency of these forces. The generalized forces in Eq. (7) will be defined as

$$[\phi]^T \{F(t)\} = [\phi]^T \{f\} \sin \Omega t = \{g_n\} \sin \Omega t \quad (9)$$

The acceleration responses measured by the accelerometers during test can be obtained from Eq. (6) and (7) as

$$\begin{aligned} \{\ddot{x}\} &= \left(\sum_{i=1}^{i=n} a_i \cdot g_i \{ \psi_i \} \right) \sin \Omega t \\ &+ \left(\sum_{i=1}^{i=n} b_i g_i \{ \phi_i \} \right) \cos \Omega t \end{aligned} \quad (10)$$

where

$$\left. \begin{aligned} a_i &= \frac{1 - \left(\frac{\Omega}{\omega_i} \right)^2}{\left[1 - \left(\frac{\Omega}{\omega_i} \right)^2 \right]^2 + 4\gamma_i^2 \left(\frac{\Omega}{\omega_i} \right)^2} \\ b_i &= \frac{2\gamma_i \left(\frac{\Omega}{\omega_i} \right)}{\left[1 - \left(\frac{\Omega}{\omega_i} \right)^2 \right]^2 + 4\gamma_i^2 \left(\frac{\Omega}{\omega_i} \right)^2} \\ g_i &= \phi_i^T \{f\} \\ \phi_i &= i^{\text{th}} \text{ normal mode, a subset of } [\phi] \end{aligned} \right\} \quad (11)$$

The first part and second part of the right hand side of Eq. (10) are also known as CO (coincidence) and QUAD (quadrature) responses because of their in-phase and 90° out-of-phase nature with respect to the input forces.

As outlined originally by Lewis and Wrisley (Ref. 1), that a number of shakers could be "tuned" to "exactly" balance the dissipative forces in a structure at a certain frequency. The external forces will be assumed as

$$\{f\} = [C]\{x\} \quad (12)$$

and the response of the structure will be that, let's say, the j th mode. Hence

$$\{x\} = \{ \phi_j \} \quad (13)$$

and the Shaker forces will become, according to Eq. (12)

$$\{f\} = [C] \{ \phi_j \} \quad (14)$$

Substituting Eq. (14) into the generalized forces in Eq. (11) and using Eqs. (3) and (4), one obtains

$$\left. \begin{aligned} g_i &= 0 & \text{for } i \neq j \\ g_j &\neq 0 \end{aligned} \right\} \quad (15)$$

Next, the forcing function frequency will be "tuned" to be that of the j th resonance frequency, i.e.,

$$\Omega = \omega_j \quad (16)$$

The a_i 's and b_i 's can be obtained as

$$\left. \begin{aligned} a_i &= \frac{- \left[1 - \left(\frac{\omega_j}{\omega_i} \right)^2 \right]}{\left[1 - \left(\frac{\omega_j}{\omega_i} \right)^2 \right]^2 + 4\gamma_i^2 \left(\frac{\omega_j}{\omega_i} \right)^2} & \text{for } i \neq j \\ b_i &= \frac{2\gamma_i \left(\frac{\omega_j}{\omega_i} \right)}{\left[1 - \left(\frac{\omega_j}{\omega_i} \right)^2 \right]^2 + 4\gamma_i^2 \left(\frac{\omega_j}{\omega_i} \right)^2} & \omega_i \neq \omega_j \\ a_j &= 0, \quad b_j = \frac{1}{2\gamma_j} \end{aligned} \right\} \quad (17)$$

The acceleration responses, Eq. (10), becomes

$$\{\ddot{x}\} = \frac{1}{2\gamma_j} g_j \cdot \{\phi_j\} \cos \Omega t \quad (18)$$

Under this perfect condition, the response will be 90° from the input forces and its spatial distribution will be exactly that of the i th mode.

However, in practice, things are far from ideal. First, in general only very limited number of shakers will be available because of physical constraints, therefore, Eq. (12) can not be satisfied. In other words, it is impossible to balance out the dissipative forces since one can not install shakers at all the DOF. Secondly, the j th mode shape can not be known as an a priori condition, only an estimated one based on pre-test analysis or engineering judgment is available. Therefore, Eq. (13) is also not satisfied. At the best, the force distribution as expressed in Eq. (14) is an approximation,

$$\{f\} \cong [C] \{\phi_j\} \quad (19)$$

and according to Eq. (11)

$$\left. \begin{aligned} g_i &\neq 0 & \text{for } i = 1, 2, \dots, n \\ g_j &\gg g_i & \text{for } i \neq j \end{aligned} \right\} \quad (20)$$

During the test, the frequency is easier to "tune" to one of the resonance frequencies since both the 90° phase angle and maximum amplitude criteria can be used. The resonance condition, Eq. (16), or a very close one can be achieved.

Therefore Eq. (17) implies that for an "almost tuned" j th mode, the following are valid.

$$\left. \begin{aligned} b_j &\gg b_i & \text{for } i \neq j \\ |a_i| &< 1.0 & \text{for all } i \end{aligned} \right\} \quad (21)$$

With these considerations, the acceleration response, Eq. (10), will be

$$\{\ddot{x}\} = b_j g_j \{\phi_j\} \cos \Omega t + \text{Contamination} \quad (22)$$

where

$$\text{Contamination} = \sum_{i=1}^{i=n} \left[(a_i g_i \cdot \sin \Omega t + b_i g_i \cos \Omega t) \{\phi_i\} \right] \quad (23)$$

(for $i \neq j$)

Based on Eqs. (20) and (21), the first term of the right hand side is much greater than the contamination terms. This assumes that the response measurements are indeed similar to the j th mode.

For the case of very close modal frequencies, or close mode shapes, the inequalities in Eqs. (20) and (21) are weakened. This will emphasize the contamination terms and pollutes the measurements. It is evident that the key issue of the multi-shaker sine dwell is the shaker force appropriation which has generated many studies (Refs. 6 to 9). However, none has been accepted as industry standard.

In summary, the inherent constraints of the multi-shaker sine dwell method are inability of tuning the "pure" mode except in very limited cases and the difficulty in separating the close modes.

2. Frequency Response Function Method

The solution of Eq. (1) in the form of Laplace transformation can be written as

$$\{x(s)\} = [\phi] \left[S^2 + 2\gamma\omega_n S + \omega_n^2 \right]^{-1} [\phi]^T \{F(s)\} \quad (24)$$

where $x(s)$ and $F(s)$ are the Laplace transforms of $x(t)$ and $F(t)$ respectively. Furthermore if one substitutes the Laplace variable S by $i\Omega$, the acceleration responses of the system can be obtained

$$\{\ddot{x}(i\Omega)\} = [\phi] \left[(a_i + ib_i) \right] [\phi]^T \{F(i\Omega)\} \quad (25)$$

where a_i and b_i are defined in Eq. (11) and the frequency response function (frf) is defined as

$$\left[(\text{frf})_{ij} \right] = [\phi] \left[(a_i + ib_i) \right] [\phi]^T \quad (26)$$

Eq. (26) contains all the information related to the modal parameters, namely, mode shapes, fre-

quencies and damping. The idea is to develop a curve-fitting procedure for Eq. (26) to determine all the modal parameters.

If a single shaker is used during test, the element in one column of the $[(frf)_{ij}]$ matrix can be readily obtained by dividing the measured responses by the input forces, the concept of transfer function. It can be shown that only a single column or a single row of the $[(frf)_{ij}]$ matrix is needed for determining all the modal parameters.

If multiple shakers are used, in principle, multiple rows or columns of the frequency response function matrix can be obtained. There are algorithms that utilize as much of the redundant information within these frequency response functions as possible. A primary example is the Poly Reference approach.

If the responses are measured after the external forces have been terminated, an equivalent time domain formulation similar to that of Eq. (25) can be written for the free decay response. Ibrahim Time Domain approach extracts the modal parameters from this free decay information.

The brief description given above for the frequency response function method of modal testing indicated that the approach is based on sound theory and seemingly no constraint is apparent in its modal parameter extraction concept. Although one may question the accuracy of the curve-fitting procedure, the concept is valid, nevertheless. However, one of the most important aspects of this approach has yet to be discussed. This concerns how the measured time domain data is transformed into the frequency domain data for modal parameter extraction process. The Fourier transform has served as the bridge between the time domain and frequency domain functions. The basis is a Fourier transform pair for continuous signals defined as follows.

$$\left. \begin{aligned} X(f) &= \int_{-\infty}^{\infty} x(t) e^{-i2\pi ft} dt \\ x(t) &= \int_{-\infty}^{\infty} X(f) e^{i2\pi ft} df \end{aligned} \right\} \quad (27)$$

The upper case $X(f)$ represents the frequency domain function; and the lower case $x(t)$ is the time domain function. Their relationship is governed by Eq. (27). However, when the measured time domain data are sampled and analyzed, it is the finite, discrete version of the Fourier transform, or the Fourier series expansion, that must be used. The analogous discrete Fourier transform pair are as follows:

$$\left. \begin{aligned} X(\omega_j) &= \frac{1}{N} \sum_{k=0}^{N-1} x(t_k) e^{-2\pi i \frac{k}{N}} \\ x(t_k) &= \sum_{j=0}^{N-1} X(\omega_j) e^{i2\pi i \frac{k}{N}} \end{aligned} \right\} \quad (28)$$

$$j = 0, 1, 2, \dots, N-1; k = 0, 1, 2, \dots, N-1.$$

Although most of the properties of the continuous Fourier transform are retained, several differences result from the constraint that the discrete Fourier transform must operate on the time domain data defined over finite intervals. The so-called Cooley-Tukey fast Fourier transform (FFT) algorithm is simply an efficient method for computing the discrete Fourier transform. The FFT can be used in place of the continuous Fourier transform only to the extent that the discrete Fourier transform could be before, but with a substantial reduction in computer time. Some of the inherent constraints of the discrete Fourier transform will be briefly described in the following.

The ideal condition for a time domain function is to be sampled exactly at the peaks and zeros. Problems will appear if the deviations from the ideal case occur. One of the problems is the "aliasing" which is caused by the high frequency components of a time function impersonating low frequencies if the sampling rate is too low. The cure to this problem involves sampling the signal at a rate at least twice as high as the highest frequency present. If the signal has been passed through a low-pass filter, a sampling rate can be chosen so that the components above the Nyquist frequency are negligible.

Another problem is the "leakage" which is inherent in the Fourier analysis of any finite record of data. Neglecting everything before and after the data period is equivalent to multiplying the signal by a rectangular window in time domain and performing a convolution in the frequency domain. The results are a series of spurious peaks will appear because of this abrupt ending of the signal in time domain. These "leakages" in the frequency domain seriously affect the accuracy of the curve-fitting procedure. The usual approach to reduce the leakage is applying a data window to the time domain function, which has lower spurious peaks in the frequency domain than that of the rectangular data window. One of the most commonly used data window is the Hanning window.

In summary, the inherent constraints of the frequency response function modal test method are the leakage and aliasing problems. However, the effects of these problems can be reduced by applying anti-aliasing filters, increasing sampling rate and proper choice of time domain functions and windows.

Galileo Spacecraft Modal Test

The Galileo is an interplanetary spacecraft whose mission is to conduct scientific exploration of the planet Jupiter. It is to be launched by the Space Shuttle and a modified Centaur Upper Stage in 1986. Fig. 1 shows the Galileo spacecraft in its modal test configuration with its major components indicated. The total weight of the spacecraft is approximately 5300 lbs. A finite element model using NASTRAN code was constructed for performing the design loads analysis. This model consists of approximately 10,000 static

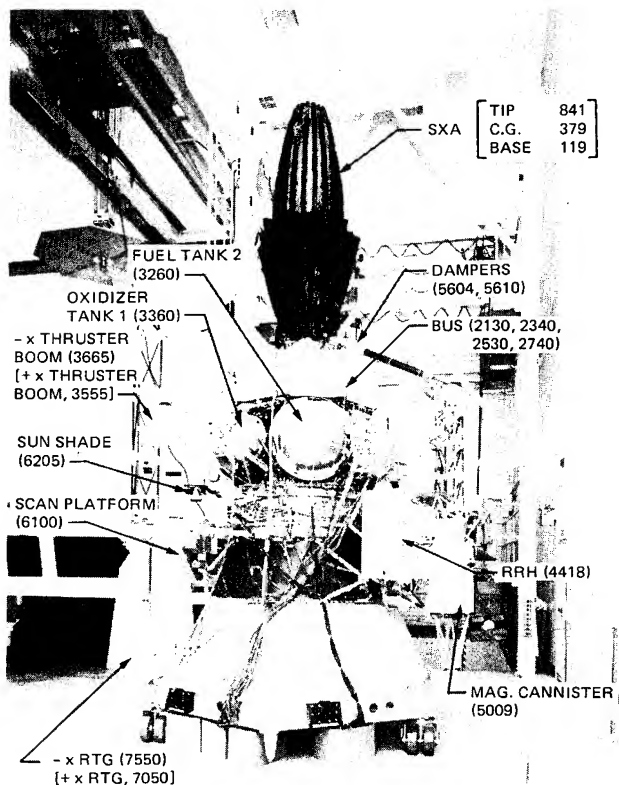


Fig. 1. Galileo Spacecraft in Model Test Configuration

degrees-of-freedom (DOF) and 1600 mass DOF. It is this loads analysis model which is required to be verified by the modal test.

Extensive pre-test analysis has been conducted prior to the modal test (Ref. 10) for the purpose of understanding the modal characteristics of the loads model. This was essential in the design of the modal test such as the instrumentation distribution and external excitation selection. After careful consideration, it was determined that 162 channels of accelerometer measurements as well as 118 channels of strain gage measurements were to be taken. The instrumentation distribution was such that all the important modal displacements and modal forces were measured with sufficient resolution. Since the number of DOF in the loads analysis model was few orders of magnitude greater than the number of measurements to be made during test, a condensed model was constructed such that its DOF would be compatible with the measurements. This condensed model was called the Test-Analysis Model, TAM, which was obtained by Guyon reduction method to collapse the mass and stiffness matrices in the loads analysis model onto 162 DOF. The TAM was so adjusted that all the modal characteristics predicted by the loads model should be reproduced by TAM within the range of interest. Table 1 shows the TAM prediction of the modes.

The modal test was performed by various testing methods and their detailed descriptions and results can be found in Refs. 11 to 14. Table 2 summarizes the methods used and the participants associated with the methods. These participants have all been involved in

Table 1 TAM prediction

Mode no.	Frequency (Hz)	Description
1	11.08	SXA in Y
2	11.20	SXA in X
3	14.94	Global Bending in X
4	15.08	Global Bending in Y
5	16.36	1st Global Torsion
6	20.04	RTG Walking Mode
7	20.37	Appendages in Z
8	21.03	2nd Global Torsion
9	23.53	Science Boom in Z
10	24.87	Sun Shade in Z
11	25.33	Probe in Y
12	26.41	EDP in Y
13	30.67	Thruster Booms in Y, Out of Phase
14	31.77	Thruster Booms in Y, In Phase
15	32.21	RRH in Y
16	32.78	Global Bounce Mode Z
17	33.03	RRH in Y
18	34.81	400 N. Engine in Y
19	35.35	Science Boom in X-Y
20	35.51	400 N. Engine in Y

modal testings for number of years especially for using their chosen methods. It is their professional dedication which assures high quality of the test results. Fig. 2 shows typical response function for various methods. As expected, they are very similar.

Results Comparisons

Table 3 lists the frequencies of the normal modes obtained by the methods listed in Table 2 with the exceptions of Tuned Sweep and ITD method. Incomplete channels of data were taken for the Tuned Sweep method and the results of the ITD method were not available to this author at the time. However they can be found in Ref. 14. The correlation of the modes obtained by the various methods is carried out by examining not only the frequencies but also the mode shapes, cross-orthogonality between modes from different methods, effective mass and kinetic energy distribution. As pointed out in the pre-test analysis, (Ref. 10), that vibration modes are not equal in the degrees of importance with respect to the loads analysis in the design process. Some modes contribute to the dynamic loads more heavily than others and these important modes are usually the target modes to be verified in a modal test. The modes which are important for the Galileo spacecraft loads analysis have been identified as global modes and all of them have been test verified by all the methods as shown in Table 3. Furthermore, the frequencies of these modes are consistent regardless which method was used. The two exceptions are that the first mode obtained by the 4-shaker random method is noticeably lower than the rest of them and the single point random method failed to obtain the fifth mode. As for the rest of the non-global modes (local modes), the following observations can be made:

1. Except for mode 30, in general the frequencies are in good agreement for all modes.

Table 2 Summary of Galileo modal test methods

No.	Methods	No. of shakers	Input function	Participant/organ.	Remark
1	Sine dwell	Up to 8	Sine	Trubert/JPL ¹	Required by Galileo Project
2	Multi-shaker random	3	Random	Hunt/SDRC ²	Uncorrelated signals for the shakers
3	Multi-shaker random	4	Random	Hunt/SDRC	Uncorrelated signals for the shakers
4	Single-point random	1	Random	Stroud/STI ³	
5	CHIRP	1	Fast sine sweep	Stroud/STI	
6	SWIFT	1	Discrete sine sweep	Stroud/STI	frf's are obtained between the frequency changes
7	Tuned sweep	1	Discrete sine sweep	Stroud/STI	Sweep within narrow frequency band
8	SFD ⁴	1	Random	Coppolino/MSC, ⁵ Stroud/STI	Used same frf's as no. 4
9	ITD	1	Random decay	Pappa/LaRC ⁶ Stroud/STI	New modal parameter extraction algorithm

1. Jet Propulsion Laboratory
2. Structural Dynamics Research Corporation
3. Synergistic Technology Incorporated
4. Simultaneous Frequency Domain (Ref. 15)
5. MacNeal-Schwendler Corporation
6. NASA Langley Research Center

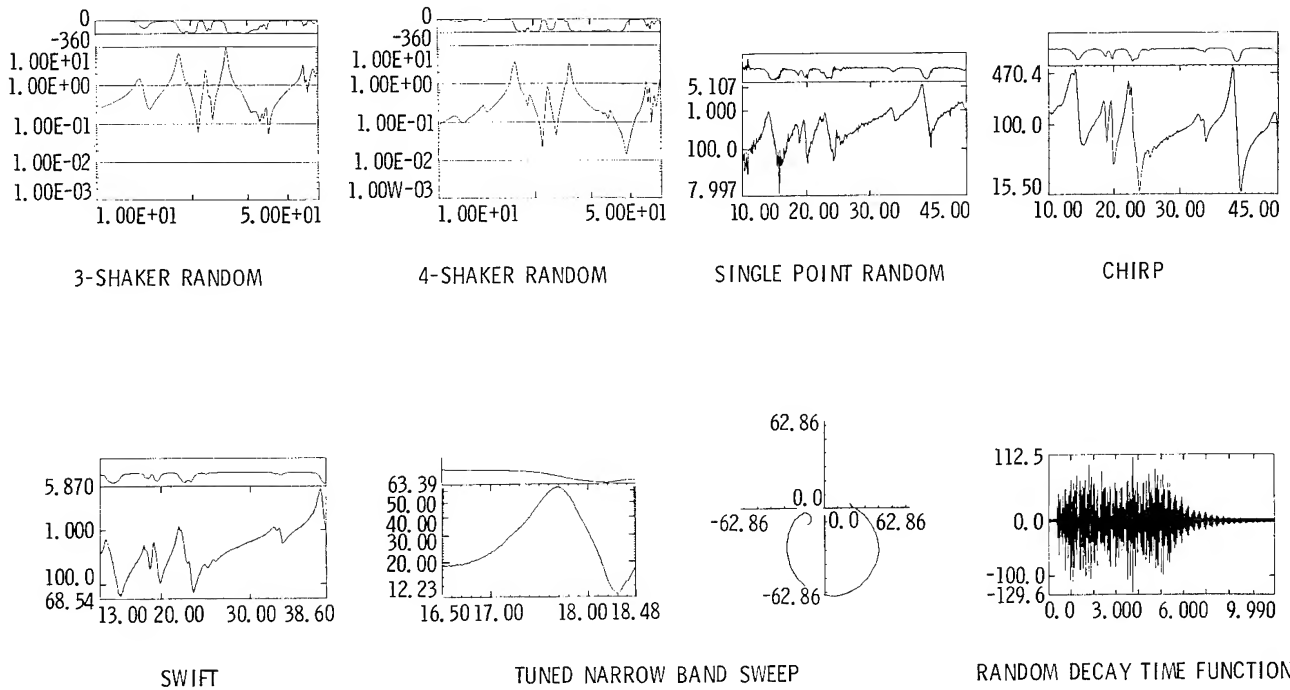


Fig. 2. Response Functions of Modal Test

Table 3 Frequency comparison for various test methods

No.	TAM	Sine dwell	4-Shaker random	3-Shaker random	SWIFT	CHIRP	Single-pt. random	SFD	Description
1	*11.08	12.70	11.46	13.73	12.54	12.59	12.66	12.52	SXA in Y
2	*11.20	13.11	14.02	14.10	13.78	13.86	13.88	13.76	SXA in X
3	*14.94	17.41	18.54	18.62	17.40	17.95	18.14	17.47	Global Bending in X
4	*15.08	17.76	17.44	18.32	17.62	17.97	17.93	17.62	Global Bending in Y
5	*16.36	18.59	19.33	19.45	18.93	19.30	-	18.93	1st Global Torsion
6	-	-	-	-	18.22	18.54	18.54	18.37	SXA and + X Thruster in Y
7	-	-	-	-	18.59	18.59	18.62	18.74	SXA in X
8	-	-	-	-	19.31	19.34	19.31	19.45	RRH in Y
9	-	-	22.22	-	22.04	21.98	22.08	22.03	RTG in Z
10	*20.04	21.67	22.06	22.19	22.23	22.24	22.21	22.27	RTG Walking Mode
11	20.37	23.10	22.52	22.81	22.35	22.62	22.48	22.52	Appendages in Z
12	*21.03	25.46	25.80	25.80	25.30	25.71	25.74	25.37	2nd Goba1 Torsion
13	*23.53	23.66	25.19	25.33	27.61	-	27.63	27.62	Science Boom in Z
14	-	-	-	-	-	-	-	24.57	-
15	24.87	-	-	28.16	-	-	-	-	Sun Shade in Z
16	25.33	-	26.36	26.64	-	-	-	-	Probe in Y
17	26.41	-	-	-	26.83	25.75	-	26.86	EDP in Y
18	-	-	-	-	-	-	-	27.08	-
19	-	-	-	-	-	-	-	28.81	-
20	30.67	29.71	33.42	33.46	-	-	-	-	Thruster Boom in Y O/P
21	-	26.12	30.50	-	28.37	28.56	28.51	28.13	Damper in Y
22	31.77	42.20	39.14	-	-	-	-	-	Thruster Boom in Y I/P
23	-	-	31.84	31.92	29.48	-	-	29.47	Damper in X
24	-	-	-	-	33.02	33.21	33.13	33.04	Probe in X
25	-	-	-	-	33.63	33.74	33.64	33.69	Probe and + Thruster in X
26	-	-	-	-	33.98	-	-	33.99	Mag. Can. and DDS in X
27	-	-	33.76	-	33.40	33.80	-	33.35	Thruster in X
28	32.21	-	27.84	27.89	26.22	25.53	-	26.23	RRH in Y
29	*32.78	37.92	37.91	37.98	38.17	38.09	37.94	38.14	Global Z Mode
30	33.03	-	28.29	28.58	39.70	-	-	39.75	RRH in Y
31	34.81	-	42.35	42.57	-	-	-	-	400 N Engine in Y
32	35.35	-	34.50	34.32	33.75	33.85	33.79	33.76	Science Boom in X-Z
33	35.51	-	41.73	-	-	-	-	-	400 N. Engine in Y
34	-	-	-	-	-	-	-	37.05	-
35	-	-	39.77	-	-	-	-	-	Science Boom in Y
36	-	-	-	39.88	41.01	-	-	41.11	RRH and Mag. Can. in Y
37	-	-	-	-	-	-	-	41.63	-
38	-	-	-	-	-	-	-	42.04	-
39	-	-	42.36	-	-	-	-	-	Thruster in Y
40	-	-	44.61	-	-	-	-	-	Thrusters in Y I/P
41	-	42.53	44.98	45.14	42.99	-	-	42.98	Scan Platform in X
42	-	-	46.00	46.05	44.82	44.70	44.34	44.86	Thrusters and RRH in Y
43	-	-	-	-	-	-	-	44.93	-
No. of Mode		14	27	21	27	21	18	34	

*Denote the global modes

2. Mode 15, an analytical predicted local mode was test obtained by the 3-shaker random method only. The 4-shaker random method as well as all others failed to obtain this mode.

3. Modes 16, 17, 20, 22, 33, all predicted by the analysis, are test obtained by only some of the methods.

4. Modes 28, 30, 31, 32, 33, all predicted by the analysis, are test obtained only by the frequency response function methods.

5. Modes 6, 7, 8, 23, 24, 25, and 26 are test obtained by only the single shaker methods. Neither the multi-shaker random methods, nor the analysis succeeded in identifying them.

6. In general, the frequency response function methods identifies more modes than the sine dwell method.

7. Several modes identified by the SFD method only are suspicious.

For detailed comparisons, the sine dwell method and 4-shaker random method will be chosen to represent the force appropriation and the frequency response function approaches of the testing techniques, respectively. Tables 4 and 5 show the effective mass of the modes from the two methods in percentage. The effective mass usually is considered as a criterion for completeness of the test. Their comparisons indicate that effective mass for 4-shaker random method is only 10 ~ 20% higher

Table 4. Effective Mass for Sine Dwell Modes

MODE	FREQUENCY	x	y	z	θ_x	θ_y	θ_z
201	12.70	0.3	8.7	0.0	23.1	0.9	0.0
101	13.11	13.3	0.3	0.0	0.6	33.5	0.0
501	17.76	9.6	26.5	0.1	31.5	10.9	0.2
404	17.40	13.8	19.1	0.0	25.2	18.3	0.4
301	18.60	0.0	0.0	0.0	0.0	1.9	20.2
601	21.67	42.4	0.3	0.1	0.3	39.6	2.4
*2050	23.10	0.0	2.6	4.0	1.2	0.4	0.1
* 702	23.66	0.0	0.6	6.7	1.1	0.0	0.0
803	25.16	0.8	0.0	0.2	0.0	0.3	23.2
* 902	26.12	0.1	0.1	5.7	0.2	0.0	4.3
*2902	29.71	1.0	0.8	0.0	0.1	0.1	6.5
1503	37.92	0.2	0.2	45.8	0.0	0.2	0.1
*2002	42.20	0.1	0.0	0.4	0.0	0.0	0.0
*1801	42.53	0.0	0.0	1.2	0.0	0.0	0.1
		81.6	59.3	64.1	83.3	106.2	57.5

*Denote for local modes

than that of the sine dwell method, although almost twice as many modes was obtained by the 4-shaker random method. This clearly demonstrates that the sine dwell method has obtained all the major modes despite only 50% fewer modes were tested.

Next, the orthogonality of the test modes are examined as it is a measurement of "cleanness" of the modes, especially the global modes. Tables 6 and 7 show the orthogonality of the modes obtained by the sine dwell method and 4-shaker random method, respectively. Off-diagonal terms greater than 0.10 are boxed and the results show clearly that modes from 4-shaker random test are much more orthogonal than those from the sine dwell test. In fact, if only the global modes are considered, the orthogonality of the sine dwell modes is not very good at all. Of course the errors could also be due to incorrect mass matrix used in the orthogonality check. The cross-orthogonality between the modes obtained by the two method is shown in Table 8. The more similar of the modes, the coupling terms will be closer to unity, 1.00. On the other hand, the small coupling terms indicate the modes are orthogonal. Correlation between the modes is identified by boxing the coupling terms. For certain modes with close similarity of shapes with more than one mode from the other group, the identification is made by other consideration such as the closeness of the frequencies and characteristics of the modes.

Table 9 shows the mode shape comparison for the first mode. The modal amplitude is listed in the order of its amplitude with the

Table 5. Effective Mass for Multi-Shaker Random Modes

MODE	FREQUENCY	x	y	z	θ_x	θ_y	θ_z
1	11.46	0.7	4.8	0.0	14.8	1.5	0.0
2	14.02	22.7	0.2	0.4	0.7	48.0	0.0
3	17.44	1.8	41.6	0.3	52.1	1.7	0.0
4	18.54	18.6	0.5	0.2	0.6	17.2	4.7
5	19.33	0.0	0.2	0.0	0.1	0.6	19.4
6	22.06	21.3	2.9	0.3	1.3	14.2	1.3
7	22.52	3.6	14.8	1.5	5.4	1.5	0.9
8	25.19	0.0	1.7	12.5	0.1	0.0	1.6
9	25.80	1.3	0.8	1.9	0.8	0.6	22.0
*10	26.36	0.0	3.3	0.0	0.4	0.0	0.3
*11	27.84	0.1	0.1	3.8	0.0	0.1	1.7
*12	28.29	0.3	0.4	0.0	0.1	0.0	0.7
*13	30.50	0.7	0.0	5.7	0.9	0.9	0.0
*14	31.84	0.2	0.5	0.1	0.2	0.1	7.1
15	33.42	13.3	0.0	0.9	0.1	3.8	0.2
*16	33.76	3.8	0.7	0.1	0.1	1.2	4.6
*17	34.50	0.8	0.2	0.0	0.0	0.2	2.2
18	37.91	0.1	0.2	45.6	0.1	0.1	0.0
*19	39.14	0.2	0.0	9.8	0.2	0.2	1.0
*20	39.77	0.2	6.3	0.2	4.9	0.1	2.7
*21	41.73	0.0	0.0	1.1	0.0	0.0	0.6
*22	42.35	0.0	1.5	0.0	0.6	0.1	0.0
*23	42.36	0.1	0.7	0.1	0.8	0.0	0.0
*24	44.61	0.2	2.1	0.0	1.2	0.2	0.6
*25	44.98	0.2	0.4	1.0	0.4	0.1	0.0
*26	46.00	0.0	0.9	0.0	1.0	0.1	0.2
		90.4	84.5	85.6	87.2	92.5	72.0

*Denote for local mode

maximum normalized to unity. It is obvious that the first mode is the antenna bending in y direct since its larger motion in that direction. The RSS 1 is the square root of the sum of the differences of TAM and test modal amplitude squared and the RSS 2 is the similar value between the two test obtained modes. It is interesting to note that differences between the TAM and test modes are greater than the differences between the two test modes. Table 10 shows the mode shape comparison of the RTG walking mode. The predicted TAM value indicates that the two RTG are moving symmetrically although in opposite

Table 6. Orthogonality of Sine Dwell Modes

MODE	201	101	501	404	301	601	2050	702	803	902	2902	1503	2002	1801
201	1.00	.32	.20	-.04	0	.03	-.02	-.02	-.01	0	.01	-.01	.01	-.01
101		1.00	.10	.04	.05	.15	.08	-.01	-.02	0	0	-.01	0	.01
501			1.00	-.19	.16	-.17	-.04	-.01	.01	0	-.01	.02	.01	0
404				1.00	.15	-.20	-.16	.04	.01	.02	0	-.02	-.01	-.03
301					1.00	-.22	-.13	.02	.04	-.05	.01	.02	.03	.02
601						1.00	-.26	-.06	-.08	.08	0	-.02	-.02	-.01
2050							1.00	.80	.01	-.07	-.01	-.05	0	.02
702								1.00	.08	-.19	-.02	-.01	-.01	0
803									1.00	.12	0	.02	.03	.01
902										1.00	0	0	.02	.02
2902											1.00	-.09	-.05	-.05
1503												1.00	0	-.02
2002													1.00	.20
1801														1.00

*Shaded numbers are local modes.

Table 7. Orthogonality of Multi-Shaker Random Modes

MODE	1	2	3	4	5	6	7	8	9	10	11	12	13	14	15	16	17	18	19	20	21	22	23	24	25
1	1.00	.02	-.16	.04	-.03	-.04	.04	-.04	-.02	-.01	.02	0	-.07	.02	0	.01	.01	-.01	-.01	-.02	-.05	0	.05	.06	.03
2		1.00	.02	-.04	.04	-.04	0	-.02	-.02	0	-.01	0	-.03	.05	0	-.01	-.01	.03	.02	-.01	.02	0	-.02	.02	0
3			1.00	.01	-.03	-.02	.01	.01	0	-.01	-.03	.02	-.07	-.02	.01	.01	.01	-.01	-.01	-.22	.05	-.06	.08	.06	.01
4				1.00	.05	-.04	.01	-.07	-.02	-.02	.04	.10	-.06	-.15	0	-.02	.01	.01	.02	-.06	.02	.01	-.06	-.01	-.02
5					1.00	.05	.02	-.01	-.02	.02	.12	.17	0	.08	-.02	-.02	.01	.03	-.01	-.16	.03	.02	.01	-.05	-.02
6						1.00	-.03	-.02	.02	-.07	.04	.06	.07	.02	.09	.09	-.02	.01	-.03	-.09	.03	-.03	.07	-.03	-.03
7							1.00	.07	-.04	-.14	-.02	-.04	.04	-.01	-.04	-.05	0	0	.02	-.03	-.01	0	.01	.03	.03
8								1.00	-.04	.25	-.23	0	-.02	.01	0	-.01	.04	0	-.01	.01	0	0	.02	0	.01
9									1.00	.03	-.13	-.10	-.03	.44	.09	.09	-.07	-.03	-.05	-.10	0	-.01	.05	.08	.01
10										1.00	.33	-.08	-.36	-.03	-.04	.01	-.04	-.01	-.03	-.06	-.03	0	.02	.02	.01
11											1.00	.40	-.25	.07	-.04	.02	0	-.03	-.01	.07	.01	-.09	.05	0	-.04
12												1.00	.05	.05	.03	.03	.03	.01	-.03	-.09	.08	.19	.09	-.06	-.10
13													1.00	-.05	0	.20	-.02	.07	-.18	.03	.14	-.04	.04	-.14	-.11
14														1.00	.34	.33	.22	.11	-.10	-.05	.01	-.01	.10	.05	-.11
15															1.00	.50	-.09	.01	-.15	-.13	.18	-.05	.15	-.19	-.13
16																1.00	-.06	0	-.18	-.14	.14	.01	.12	-.13	-.11
17																	1.00	0	.06	.07	-.04	-.04	-.02	.03	-.02
18																		1.00	.46	.06	.12	-.01	0	-.02	-.02
19																			1.00	.01	-.08	-.06	-.14	-.15	.10
20																				1.00	-.37	.45	-.34	.29	.07
21																					1.00	-.59	-.23	-.54	-.01
22																						1.00	-.30	.17	.03
23																							1.00	-.14	-.07
24																								1.00	.27
25																									1.00

* SHADED NUMBERS ARE LOCAL MODES

direction. However, both test modes indicate that one RTG amplitude is much higher than the others. Table 11 and Table 12 show the kinetic energy distribution for the corresponding modes shown in Table 9 and 10. For the first mode, more than 90% of the kinetic energy is y direction and among them more than 70% is concentrated at the SXA. This mode is described as the SXA antenna bending

in y direction. From Table 12 the kinetic energy for the RTG walking mode indicates that contrary to the TAM results, the energies of the two RTG's are indeed different. Careful examination of the test article shows physical differences in mass mockups. The kinetic energy distribution is a very useful tool in the understanding of detailed modal characteristics.

Table 8. Cross Orthogonality Between Sine Dwell and Multi-Shaker Random Modes

MODE	1	2	3	4	5	6	7	8	9	10	11	12	13	14	15	16	17	18	19	20	21	22	25
201	1.00	-.02	-.06	.06	-.04	.01	.02	-.04	.02	0	.03	.01	-.07	.05	.01	.01	.03	0	-.02	-.06	-.01	-.03	.07
101	.39	1.00	-.06	-.26	.13	.01	-.01	-.03	-.02	0	0	-.01	-.03	.04	-.01	-.02	-.01	0	-.01	-.04	.02	-.02	.02
501	.33	-.08	-1.00	-.35	.10	.08	-.01	0	-.02	.06	.07	-.04	.08	-.03	0	0	-.02	0	.01	.22	-.05	.07	-.07
404	-.12	-.13	.63	-1.00	.25	.01	-.01	.10	.08	-.01	-.06	-.01	.03	-.12	0	.02	.03	-.02	-.01	-.13	0	-.06	.13
301	0	-.03	.09	.08	1.00	.06	.01	-.01	-.02	.02	.07	.08	.01	.07	0	-.01	.02	.03	-.01	-.14	.01	.05	-.01
601	.09	.27	.10	.22	-.22	-1.00	.31	.09	-.10	-.04	-.07	.02	-.04	-.06	-.09	-.10	-.03	-.02	.02	.02	.05	-.03	-.06
2050	-.06	.25	.03	.18	-.22	1.00	-.87	-.84	-.18	.57	.10	-.06	-.20	-.07	-.10	-.07	-.01	-.10	.06	-.11	-.03	0	.03
702	-.05	0	.04	-.04	.04	.24	.53	1.00	-.10	.70	.27	-.05	-.31	.02	-.11	-.10	.03	0	.02	-.06	-.06	0	.02
803	-.05	-.04	-.04	0	.06	.06	-.03	.12	1.00	.15	-.12	-.09	-.04	.35	.05	.07	-.29	.01	-.08	-.13	.01	-.02	.05
902	.01	-.03	-.05	-.06	-.08	.01	.03	.43	.13	-.62	-1.00	.03	.42	-.07	.11	.08	0	-.02	.06	.03	.03	-.01	
2902	.07	.02	.04	.05	.11	.06	-.05	-.06	.02	0	.25	.34	-.38	-.30	-.99	-.65	-.23	-.24	1.00	-.11	-.03	-.72	.27
1503	-.02	-.03	-.03	0	.02	.02	.01	-.01	-.02	-.03	-.04	.01	.09	.09	-.02	-.02	-.01	1.00	-.45	.05	.12	-.02	-.01
2002	.06	.01	.01	.03	.03	0	-.01	-.05	.07	.03	-.03	-.11	.02	.08	.11	.12	-.12	.03	1.00	.33	-.98	.68	.18
1801	-.01	.06	.03	.09	.02	-.02	-.02	0	.03	0	-.05	0.06	.23	.25	-.04	0	.03	-.04	.36	.65	-.47	.71	1.00

NOTE: SHADED NUMBERS INDICATE QUESTIONABLE COUPLING.

Table 9. Mode Shape Comparison

	TAM 1 (11.08 HZ)	SD 201 (12.70 HZ)	MSR 1 (11.46 HZ)
SXA TIP IN Y	1.00 (1)	1.00 (1)	1.00 (1)
SXA BASE RING IN Y	0.49 (2)	0.47 (2)	0.49 (2)
SXA C.G. IN Y	0.25 (3)	0.30 (3)	0.30 (3)
SXA TIP IN X	0.10 (4)	-0.22 (4)	-0.27 (4)
EDP IN Z	0.08 (5)	0.06 (7)	0.06 (7)
MAG. CANISTER IN Z	0.08 (6)	0.05 (8)	0.06 (9)
SCIENCE BOOM HINGE IN Z	0.08 (7)	0.07 (6)	0.09 (6)
PLS IN Z	0.08 (8)	0.04	0.03
MAG. CANISTER IN Z	0.07 (9)	0.05 (9)	0.05 (10)
MAG. CANISTER I/F IN Z	0.07 (10)	0.05	0.05
RSS 1		0.330	0.384
RSS 2			0.059

Table 11. Kinetic Energy Distribution

	TAM 1 (11.08 HZ)			SD 201 (12.70 HZ)			MSR 1 (11.46 HZ)		
	X	Y	Z	X	Y	Z	X	Y	Z
SXA TIP	0.7	73.5	0	3.5	75.2	0	5.5	76.5	0.3
BUS	0	1.6	0.2	0	0.9	0.2	0.2	0.1	0
BUS	0	2.5	0.3	0.1	1.2	0.4	0.1	0.2	0.1
OXIDIZER 2	0	1.8	0.3	0	1.3	0.1	0.1	0.4	0
OXIDIZER 1	0	1.8	0.3	0.1	1.0	0.1	0.4	0.6	0
	0.9	93.9	4.7	4.1	92.9	2.8	7.0	90.5	2.1

Table 10. Mode Shape Comparison

	TAM 6 (20.04 HZ)	SD 601 (21.67 HZ)	MSR 6 (22.06 HZ)
+X RTG IN Z	1.00 (1)	0.69 (4)	0.35 (5)
-X RTG IN Z	-0.97 (2)	-0.94 (2)	-1.00 (1)
RRH IN Y	-0.32 (3)	-0.66 (5)	-0.65 (2)
SXA TIP IN X	-0.26 (4)	-0.11	0.15
MAG. CANISTER IN X	0.23 (5)	-0.37	0.26 (7)
MAG. CANISTER I/F IN X	0.20 (6)	1.00 (1)	0.28 (6)
EPD IN X	0.17 (7)	0.66 (6)	0.21
-X THRUSTER IN Z	0.16 (8)	-0.21	0.17
BUS IN X	-0.16 (9)	-0.56 (9)	-0.16
BUS IN X	-0.16 (10)	0.62 (7)	-0.18
RSS 1		1.66	0.84
RSS 2			1.59

Table 12. Kinetic Energy Distribution

	TAM 6 (20.04 HZ)			SD 601 (21.67 HZ)			MSR 6 (22.06 HZ)		
	X	Y	Z	X	Y	Z	X	Y	Z
OXIDIZER 2	4.2	0.1	0	7.3	0.2	0.1	4.3	0.7	0.1
FUEL 2	1.5	0.2	0	4.1	0.8	0	2.0	0.3	0
OXIDIZER 1	4.9	0	0	13.7	0.8	0	7.7	0.2	0.1
FUEL 1	2.2	0.1	0	5.0	0.6	0	4.4	0.4	0.1
+X RTG	0	0	39.2	0.2	0	7.8	0	0	6.2
-X RTG	0	0	36.7	0.4	0	14.5	0	0	50.5
	19.5	1.3	77.9	65.5	6.2	25.7	30.8	8.1	59.6

Finally, the test measured damping values are plotted as shown in Fig. 3. It is totally uncorrelated with the frequency. Fig. 3 contains only the sine dwell and multi-shaker random tests, however data from other test results are equally scattered.

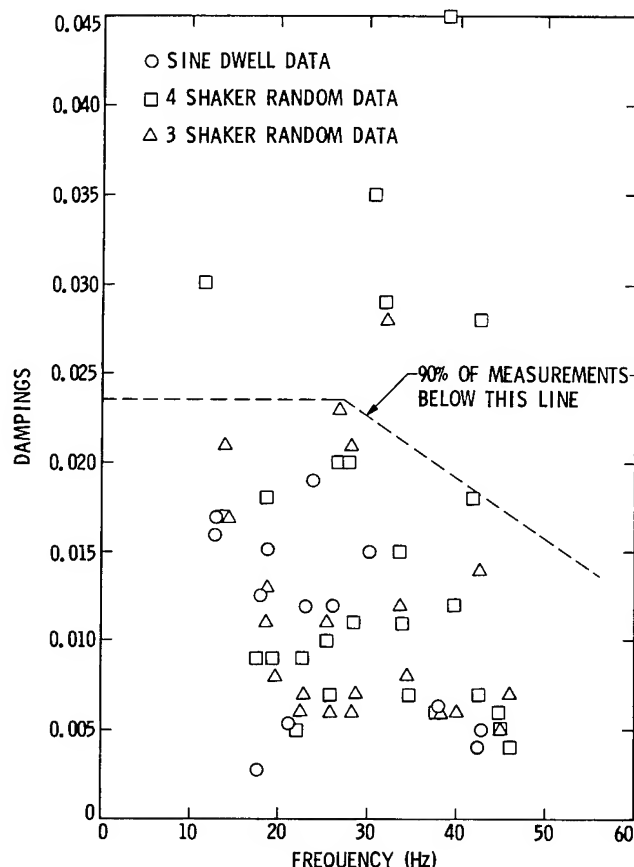


Fig. 3. Modal Dampings

Evaluation of Testing Methods

It must be emphasized here that conclusions from the present experiences are valid for the specific type of structural system that we tested, namely, the large, complex spacecraft. The basic objective for the modal test is to verify the analytical model for the design process. It tends to involve large number of measurements and extensive test/analysis correlation. Of course it is recognized that there are many other objectives for doing modal testings on a variety of systems and each has its own particular requirement and constraints. These individual conditions may ultimately determine the selection of testing method. Nevertheless, based on the present experiences, the evaluations are as follows:

1. All methods are able to extract the major modes of importance.
2. The modal parameters obtained by different methods are generally consistent.
3. Frequency response function methods

extract more modes than that of the multi-shaker sine dwell method.

4. Sine dwell method is able to make large amplitude response to investigate the non-linear effects.

5. Sine dwell method excites the test article in "pure" mode which is suitable for investigating the pathological behavior of the structures.

6. Actual testing time for the frequency response function methods is only a small fraction of that of the sine dwell method.

7. Data processing for the frequency response function method can be made almost real time. The data from multi-shaker random tests were processed immediately by a VAX 11/780 computer and reports for modal parameters are available within 24 hours.

8. Multi-shaker random tests simplify the test by not repeating the test for other shaker configurations as required by the single shaker tests.

9. Input energy distribution among modes is more even for the multi-shaker random test than that of the single shaker tests.

10. The operational simplicity of the single shaker tests is quite remarkable. This is definitely an advantage for those who lack extensive modal testing experiences.

11. SWIFT method seems to perform better among the single shaker tests.

12. Damping data is very inconsistent, in fact, it is quite chaotic.

Concluding Remarks

In addition to the evaluation of various modal testing methods, the objective of the present study also includes the attempts to rank these methods according to their capabilities. However, it has failed because of the fact that each method has its own unique merit that others cannot provide. The selection of proper modal testing method should be determined by the requirements, constraints and the nature of the test article.

It should be reassuring that the age old sine dwell method still possesses certain capabilities that other modern frequency response methods can provide. Perhaps, this is the reason why the method which was developed in the 1950's is still popular among aerospace industry. On the other hand, the modern modal test methods by data processing demonstrate their powerful capabilities and tremendous operational ease. It is this author's belief that these frequency response function methods will be matured further and become the standard practice.

Acknowledgements

The work described in this paper was carried out by the Jet Propulsion Laboratory, California Institute of Technology, under Contract with the National Aeronautics and Space Administration.

References

1. Lewis, R. C., and Wrisley, D. L., "A System for the Excitation of Pure Natural Modes of Complex Structures," *Journal of Aeronautical Sciences*, Vol. 17, No. 11, 1950, pp. 705-722.
2. Leppert, E. L., Lee, S. H., Day, F. D., Chapman, C. P., and Wada, B. K., "Comparison of Modal Test Results: Multi-Point Sine Versus Single Point Random," SAE Paper No. 760879, San Diego, CA, November 29 - December 2, 1976.
3. Hanks, B., Ibrahim, S. R., Miserentino, R., Lee, R., and Wada, B. K., "Comparison of Modal Test Method on the Voyager Payload," SAE Paper No. 781044, San Diego, CA, November 1978.
4. Allemang, R. J., "Experimental Modal Analysis," ASME Bounded Volume AMD-Vol. 59, Modal Testing and Model Refinement, pp. 1-29, presented by the Winter Annual Meeting of ASME, Boston, Mass., Nov. 13-18, 1983.
5. T. K. Caughey and M. E. J. O'Kelly, "Classical Normal Modes in Damped Linear Systems", *Jour. Appl. Mech.*, vol. 32, *Trans. ASME*, vol. 87, Series E, pp. 583-588.
6. Asher, G. W., "A Method of Normal Mode Excitation Utilizing Admittance Measurements," *Proceedings, National Specialists' Meeting, IAS; Dynamics and Aeroelasticity*, Nov. 1958, pp. 69-76.
7. Ibáñez, P., "Force Appropriation by Extended Asher's Method," SAE paper 760873, Engineering and Manufacturing Meeting, San Diego, 1976.
8. Morosow, G., and Ayre, R. S., "Force Appropriation for Modal Vibration Testing Using Incomplete Excitation," *Shock and Vibration Bulletin*, Vol. 48, Part 1, 1978, pp. 39-48.
9. Anderson, J. E., "Another Look at Sine-Dwell Mode Testing," AIAA paper No. 81-0532, *Proceedings of AIAA/ASME/ASCE/AHS 22nd Structures, Structural Dynamics and Materials Conference*, Atlanta, Georgia, April 9-10, 1981, pp. 202-212.
10. Chen, J. C., and Trubert, M., "Galileo Model Test and Pre-Test Analysis," *Proceedings of the 2nd International Modal Analysis Conference*, Feb. 6-9, 1984, Orlando, FL, pp. 796-802.
11. Trubert, M., "Assessment of Galileo Modal Test Results for Mathematical Model Verification," AIAA Paper No. 84-1066, presented at the AIAA Dynamics Specialists Conference, May 17-18, 1984, Palm Springs, CA.
12. Stroud, R. C., Pamidi, M. R., and Bausch, H. P., "Some Measurement and Analysis Methods Used on the Galileo Modal Survey," AIAA Paper No. 84-1067, presented at the AIAA Dynamic Specialists Conference, May 17-18, 1984, Palm Springs, CA.
13. Hunt, D. L., and Chen, J. C., "Application of Multi-Shaker Random Excitation and Polyreference Analysis Techniques to the Galileo Spacecraft Modal Tests," AIAA Paper No. 84-1069, presented at the AIAA Dynamic Specialists Conference, May 17-18, 1984, Palm Springs, CA.
14. Pappa, R. S., "ITD Analysis of Free-Decay Response From the Galileo Modal Test," AIAA Paper No. 84-1070, presented at the AIAA Dynamics Specialists Conference, May 17-18, 1984, Palm Springs, CA.
15. Coppolino, R. N., "A Simultaneous Frequency Domain Technique for Estimation of Modal Parameters from Measured Data," SAE paper 811046, presented at Aerospace Congress and Exposition, Anaheim, Calif., Oct. 5-8, 1981.

DYNAMIC CHARACTERIZATION AND MICROPROCESSOR CONTROL OF THE NASA/UVA PROOF MASS ACTUATOR

David C. Zimmerman, Graduate Research Assistant
 Daniel J. Inman, Assistant Professor*
 Department of Mechanical and Aerospace Engineering
 State University of New York at Buffalo

Garnett C. Horner, Aerospace Technologist*
 NASA Langley Research Center

Abstract

A microprocessor controlled, lightweight, reaction type force actuator system has been developed and tested. The dynamic characteristics of the system were determined using digital Fourier analysis. Finally, the actuator system was demonstrated by controlling the vibrations of a cantilevered beam.

Introduction

A current area of research concerns itself with the study of large, flexible space structures. The theory behind large space structures, and in particular how to control their vibrations, has grown greatly in the past decade. However, the experimental testing and verification of these structural control problems has lagged behind.

One apparent need that must be met to carry out meaningful control experiments is the development of hardware to implement these control laws. This work reports on the development of a small, lightweight, self-contained force actuator system that may be used to implement a wide range of control laws. The actuator system is not attached to ground, allowing it to be placed nearly anywhere on the test structure.

A description of the NASA-UVA Proof Mass Actuator (PMA) system follows. The dynamic characteristics of the actuator were determined and guidelines are suggested for when actuator dynamics may be neglected in the derivation of the control law. Finally, the actuator system was used to add active control to control the vibrations of a cantilevered beam.

Description of the PMA Systems

The PMA system is comprised of the PMA, its collocated sensors, various amplifiers, and a dedicated microprocessor controller.

The PMA is an electro-magnetic reaction type force actuator with a stroke length of $\pm 1/2$ inch. The PMA has two collocated sensors. The accelerometer measures the structures local acceleration. The Linear Variable Displacement Transducer (LVDT) measures the position of the actuators' proof mass with respect to the structure.

A current-controlled amplifier is used to drive the actuator's coil. The other amplifier

used is in the signal conditioning circuitry for the accelerometer.

A dedicated microprocessor is used to provide the PMA with localized digital control. Digital control was selected because of the many advantages it has over analog control. For the intended uses of the PMA system, a major advantage of digital control is that the control laws may be easily changed by just changing the digital control program stored in memory, in comparison to the hardware changes that would be needed in an analog control device. Also, digital control programs can be easily tested using software simulation techniques.

A typical digital control system is shown in figure 1. The inputs to the digital controller, R_1 to R_n , are typically a reference signal which the plant is to follow and state variable information that is being fed back. The digital controller is comprised of the sample and holds, the A/D and D/A converters, and the digital computer. The digital computer normally includes a central processing unit, memory, and input-output (I/O) ports.

In keeping with the spirit of trying to reduce the size of the PMA system, the microprocessor included in the PMA system is the Intel 2920 Analog Signal Processor^[1]. The 2920 is a single chip "microcomputer" which was designed especially to process real time signals. It has onboard program (EPROM) and scratchpad (RAM) memory, A/D, D/A, and I/O circuitry, and a digital processor. It is a complete digital control system on a single chip. Using this microprocessor greatly reduces the part count, and thus the size, of the digital controller.

The tradeoff in using the 2920 as the digital controller is that the system now has a fixed amount of memory and I/O ports, and the 2920 itself has a small instruction set. However, considering the intended applications of the PMA system, these limitations are acceptable. It should be noted that if needed, 2920's may be cascaded to increase the amount of memory and the number of I/O ports of the controller.

The PMA system is shown in figure 2. The typical 2920 program samples and converts to digital words one or more of the input signals, performs some arithmetic operations on the words, and then outputs one or more signals.

The program executes in an endless loop (no internal program jumps allowed). If an input is sampled once during a program, the sample rate of the controller is the time it takes the 2920 to

* Member AIAA

pass through the program loop once. Typical sample rates are on the order of 70-110 μ sec. Shannons sampling theorem^[2] is obviously satisfied for the intended control applications of the system.

Dynamic Testing

Many researchers have developed various control laws to reduce the vibrations of large, flexible structures. These control laws have generally been based solely on the dynamic properties of the structure to be controlled. The importance of actuator (and sensor) dynamics has just recently received attention in the literature. Caughey and Goh^[3] have shown that actuator dynamics, if not properly treated, may cause an otherwise stable system to become unstable. Kosut and Salzwedel^[4] have developed control laws ignoring actuator dynamics, but the effects of actuator dynamics on the control are then evaluated.

The dynamic characteristics of the PMA system were determined so that they may be included in future control work. The dynamic testing was also used to determine the physical limitations of the PMA and will help in gaining insight on how to build better actuators in the future.

The dynamic characteristics of the PMA were determined experimentally using digital Fourier analysis techniques. The experimental set-up is shown in figure 3.

The PMA is excited by a broadband random voltage signal with a Gaussian distribution. A fraction of the relative position of the proof mass is fed back. This feedback creates an electronic pseudo-spring in that a force that is proportional to the proof masses' displacement from the midpoint of the coil is applied to the proof mass. This pseudo-spring is present to stop the proof mass from hitting the stops of the PMA shell.

A block diagram description is shown in figure 4. It should be noted that the inductance effects of the coil were found to be negligible. The closed loop transfer function of this model can be expressed as:

$$\frac{F}{V}(S) = \frac{k_1 ms^2}{ms^2 + k_1 ds + k_1 k_2} \quad (1)$$

where:

- F - force output of actuator
- V - input voltage to amplifier
- S - Laplace operator
- k_1 - gain of amplifier and actuator
- m - mass of proof mass
- $1/(ms^2)$ - synthesizes position of proof mass
- k_2 - gain of LVDT feedback
- ds - back emf effects due to relative motion of proof mass with respect to coil

Three separate tests were performed to determine the constants in the model. A different value of the feedback spring constant, k_2 , was

used in each test and the RMS voltage input was adjusted so that the full stroke length of the PMA was utilized. It should be noted that the friction present in the actuator is negligible when the full stroke length is utilized. However, if the full stroke length is not utilized, the effect of friction is noticeable. Instead of trying to model the friction, the approach taken here was to test at full stroke length and to try to reduce the friction in the future. It will also become evident later that the low frequency characteristics of the system are improved when the full stroke length is utilized.

The mass of the proof mass, m , was determined to be 0.0159 lbf-sec²/ft.

The measured frequency response functions are shown in figure 5¹. The value of k_1 can be determined by noting that the magnitude of the frequency response function, determined by substituting $s=jw$ in equation (1), tends toward k_1 as w tends toward infinity, i.e.,

$$\lim_{w \rightarrow \infty} \left| \frac{F}{V}(jw) \right| = k_1$$

k_1 was determined to be 0.617 lbf/volt.

In order to determine the back emf constant d , which effectively adds damping to the PMA system, we must first express the system transfer function in standard time constant form:

$$\frac{F}{V}(S) = \frac{\left(\frac{m}{k_2}\right)s^2}{1 + 2\xi\left(\frac{s}{w_n}\right) + \left(\frac{s}{w_n}\right)^2} \quad (2)$$

where

$$w_n = \sqrt{\frac{k_1 k_2}{m}} \quad (3)$$

$$\xi = \frac{d}{2} \sqrt{\frac{k_1}{k_2 m}} \quad (4)$$

Figure 5c gives the Bode magnitude plot of the three tests where the numerator dynamics of the transfer function have been removed digitally and the gain set to unity. These plots are just the frequency response function of a plant consisting of a pair of complex conjugate poles, i.e. :

$$W(S) = \frac{1}{1 + 2\xi\left(\frac{s}{w_n}\right) + \left(\frac{s}{w_n}\right)^2} \quad (5)$$

The damping rate was determined by noting that the magnitude of $W(jw_n)$ is:

$$|W(jw_n)| = \frac{1}{2\xi} \quad (6)$$

The natural frequency, w_n , was taken to be the frequency at which the phase was equal to ninety degrees. The back emf constant was deter-

¹ Magnitude plots should be multiplied by 10 to reflect the change made in the gain of the current-controlled amplifier.

mined by minimizing the squared errors between the experimentally observed damping rate and that predicted by equation 4, i.e.

$$\min_{d} \sum_{i=1}^3 \left((\xi_{\text{exp}})_i - \frac{d}{2} \frac{k_1}{(k_2)_i m} \right)^2 \quad (7)$$

From this minimization, the constant d was determined to be 3.865 volt-sec/ft.

We have now determined all the unknown quantities in equation 1. We can see that the PMA system actually acts like a high pass filter. Since the voltage input to the system cannot exceed one volt, the maximum force output of the actuator is 0.617 lbf.

There is some operational frequency, w_{op} , above which the frequency response function is flat and the phase difference is approximately zero. If the frequency content of the voltage signal has no component lower than w_{op} , the force out will directly follow the input voltage. Practically speaking, this means that above w_{op} , the PMA system can be made to behave like the ideal force actuator many researchers have assumed available in their theoretical optimal control work. Since large, flexible structures generally have low natural frequencies, we obviously would like to make w_{op} as low as possible.

The only system parameter which one can easily change is the feedback spring rate constant k_2 . By inspection, one can see that lowering k_2 raises the amount of system damping present and lowers the breakpoint frequency w_n . Both of these factors tend to lower w_{op} . Although both of the above factors affect the phase plot, the two effects seem to cancel each other out.

Therefore, to lower w_{op} , one can minimize k_2 subject to the constraint that the pseudo-spring must be stiff enough to stop the proof mass from hitting its stops during an experiment.

Experimental Study

The purpose for developing the PMA system was to have a self-contained device capable of implementing various control laws to control the vibrations of flexible structures. To demonstrate the working PMA system, a relatively simple structural control problem was formulated.

In this experiment, the PMA system was used to control the vibrations of a cantilevered beam. The control law is based on rate feedback, which essentially adds damping to the structure.

The actuator was placed near the end of the beam. The rate feedback law is implemented by digitally integrating the structures acceleration and multiplying it by some damping constant. Likewise, the pseudo-spring is created by digitizing the LVDT signal and multiplying it by a stiffness constant. It was determined that the minimum stiffness constant needed to stop the proof mass from hitting its stops during the

experiment was 0.2688 lbf/in. It was chosen arbitrarily that the damping constant would be 1.78×10^{-2} lbf-sec/in. The vibrational characteristics of the beam were then determined using experimental modal analysis.

To serve as a comparison, a NASTRAN model of the experiment was formulated, as shown in figure 6. The effects of the PMA system were modeled as idealized discrete elements. The rate feedback law is equivalent to having the beam connected to ground through a viscous damper. The pseudo-spring-proof mass, which is inherent in the PMA system, is the same as having an untuned vibration absorber attached to the beam. Finally, the mass of the PMA shell and the sensors are modeled as a lumped mass attached to the beam.

The natural frequencies of the controlled and uncontrolled beam are shown in figure 7. Case B is actually the structure to which the PMA provides active control. The observed damped natural frequencies of the system in case C do not differ greatly from those predicted by NASTRAN².

The mode shapes of the actively controlled beam are depicted in figure 8. The mode shapes have been normalized to a unit largest component and the complex portion of the mode ignored. Once again, the experimental results are quite close to those predicted by NASTRAN.

The damping ratios, ξ , are given in table 1. It can be seen that the observed damping rates are higher than those predicted by theory. The additional damping is probably due to a combination of structural and air damping. There is also some error associated with the assumption that the controlled structure is proportionally damped, which it obviously is not.

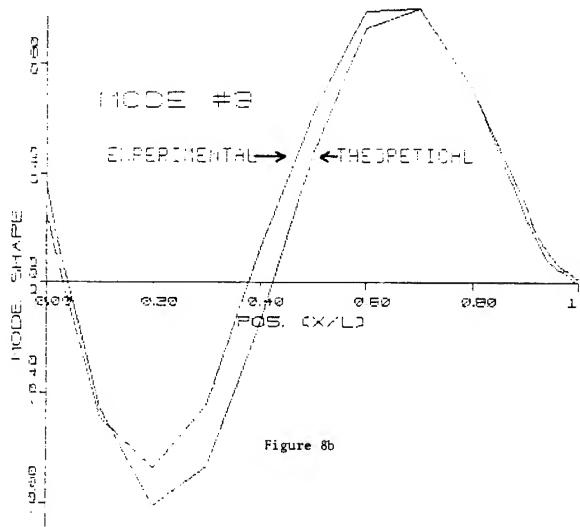
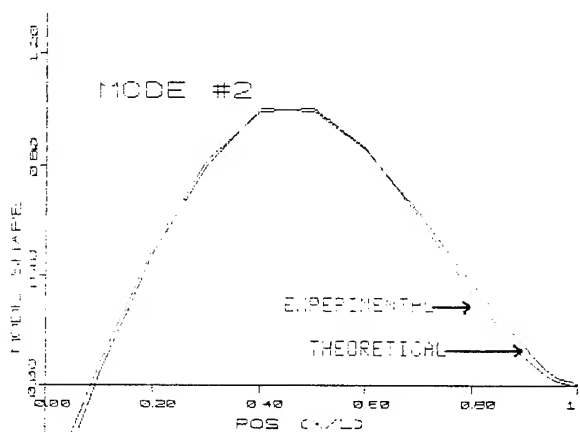
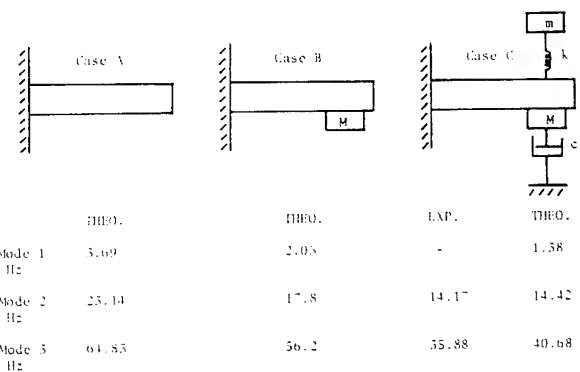
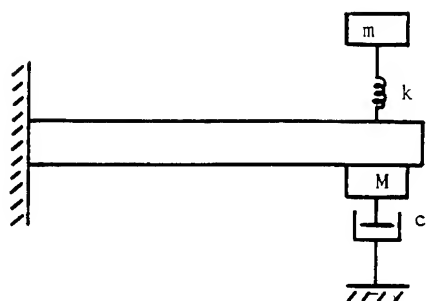
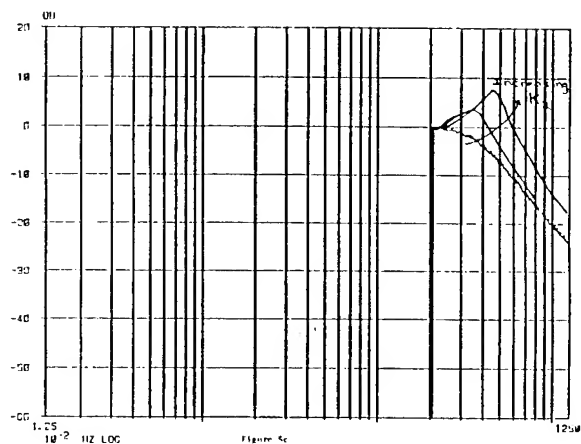
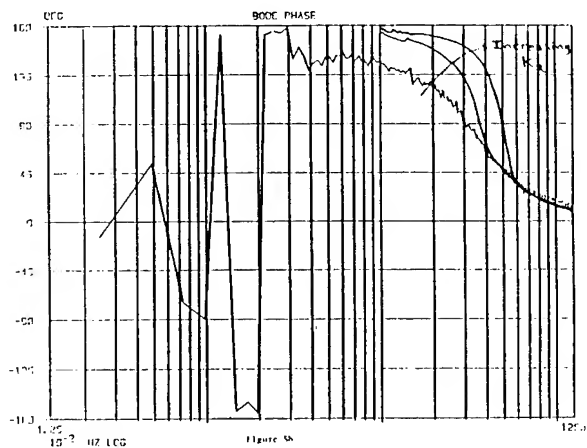
Summary

A self-contained, actuator-sensor-controller system has been developed and tested. The digital control system is small enough to allow it to be attached to the actuator, is capable of implementing numerous control laws, and allows for future expansion. The actuator itself is not attached to ground so that it can be placed nearly anywhere on the test structure.

A linear, time invariant model of the system has been developed. The model shows how the system parameters affect the PMA's frequency response. This knowledge is useful in practice and may also serve as a guide for future actuator designs.

Finally, the PMA system was demonstrated on a cantilevered beam. The experiment showed that the system was able to implement the desired rate feedback control law.

² Mode 1 characteristics not determined experimentally due to frequency response of response accelerometer used.



Acknowledgements

This work was supported by the National Aeronautics and Space Administration and the Graduate Student Researchers Program, grant number NGT 33183801. The research was conducted at the NASA Langley Research Centers Structural Dynamics Branch.

References

- [1] 2920 Analog Signal Processor Design Handbook, Intel Corporation, 1980.
- [2] Kuo, B.C., Digital Control Systems, 1980, Holt, Rinehart and Winston, Inc.
- [3] Caughey, T.K. and Goh, C.J., "Vibration Suppression in Large Space Structures", Proceeding of the Workshop on Applications of Distributed System Theory to the Control of Large Space Structures, 1983, pp.119-142.
- [4] Kosut, R.L. and Salzwedel, H., "Stability and Robustness of Control Systems for Large Space Structures", Proceedings of the Third VPI and SU/AIAA Symposium on the Dynamics and Control of Large Flexible Spacecraft, 1981, pp.343-364.

Mode	Experimental	Theoretical
1	--	0.121
2	0.00742	0.00253
3	0.00349	0.00001

Table 1

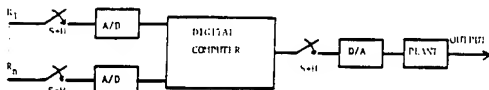


Figure 1

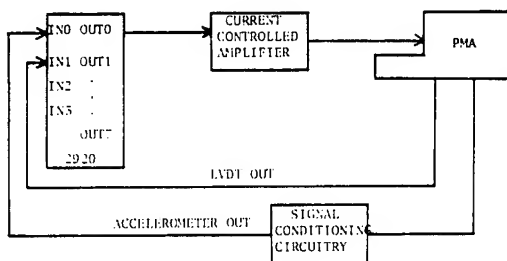


Figure 2

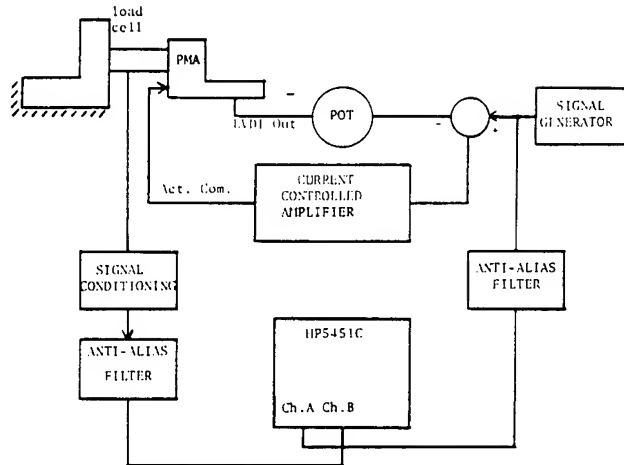


Figure 3

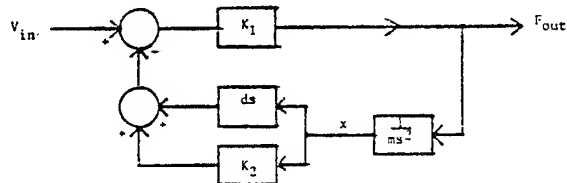


Figure 4

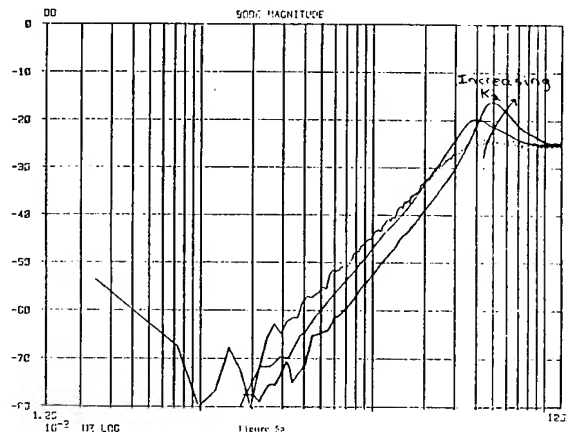


Figure 5

TRANSONIC CALCULATION OF AIRFOIL STABILITY
AND RESPONSE WITH ACTIVE CONTROLS

J. T. Batina*
NASA Langley Research Center
Hampton, Virginia

T. Y. Yang**
Purdue University
West Lafayette, Indiana

Abstract

Transonic aeroelastic stability and response analyses are performed for the MBB A-3 supercritical airfoil. Three degrees of freedom are considered: plunge, pitch, and aileron pitch. The objective of this study is to gain insight into the control of airfoil stability and response in transonic flow. Stability analyses are performed using a Padé aeroelastic model based on the use of the LTRAN2-NLR transonic small-disturbance finite-difference computer code. Response analyses are performed by coupling the structural equations of motion to the unsteady aerodynamic forces of LTRAN2-NLR. The focus of the present effort is on transonic time-marching transient response solutions using modal identification to determine stability. Frequency and damping of these modes are directly compared in the complex s-plane with Padé model eigenvalues. Transonic stability and response characteristics of 2-D airfoils are discussed and comparisons are made. Application of the Padé aeroelastic model and time-marching analyses to flutter suppression using active controls is demonstrated.

Nomenclature

a_h	nondimensional elastic axis location, positive aft of midchord
b	airfoil semi-chord
c_β	nondimensional aileron hinge line location
$[C]$	nondimensional damping matrix
$\{G\}$	control distribution vector
h	plunging d.o.f., positive downward from elastic axis
K_D, K_V, K_A	displacement, velocity, and acceleration control gains, respectively
$[K]$	nondimensional stiffness matrix
m	mass of the airfoil per unit span
M	free stream Mach number
$[M]$	nondimensional mass matrix
p	nondimensional sensor location, positive aft of midchord
$\{p\}$	aerodynamic load vector
r_α, r_β	radii of gyration of airfoil about elastic axis and of aileron about hinge axis, respectively
s	$\sigma + i\omega$, Laplace transform variable
t, \bar{t}	time; $\omega_\alpha t$, nondimensional time

U, U^*	free stream velocity; $U/b\omega_\alpha$, nondimensional flight speed
x_α, x_β	nondimensional distances from elastic axis to airfoil mass center and hinge line to aileron mass center, respectively
$\{X\}, \{Z\}$	displacement and state vectors, respectively
α	airfoil pitching d.o.f., positive leading edge up
β	aileron pitching d.o.f., positive trailing edge down
β_c	control surface command
ζ_β	control surface viscous damping ratio
μ	$m/\pi\rho b^2$, airfoil mass ratio
ξ	h/b , nondimensional plunging d.o.f., positive downward from elastic axis
ξ_s	nondimensional sensor plunging displacement, positive downward from sensor location
ρ	free stream air density
$\omega_h, \omega_\alpha, \omega_\beta$	uncoupled natural frequencies of plunging, pitching about elastic axis, and aileron pitching about hinge axis, respectively

Introduction

Aeroelastic time-response characteristics of airfoils and wings in transonic flow have recently attracted considerable research interest.¹⁻⁶ In the time-response analysis the structural equations of motion are coupled to transonic aerodynamic codes using a numerical integration procedure to calculate transient responses.

Time-marching transient solutions of plunging and pitching airfoils were analyzed by Edwards, et al.,⁷ using a complex exponential modal identification technique. Transonic flutter boundaries versus Mach number and angle of attack were determined for the NACA 64A010 and MBB A-3 airfoils. A state-space aeroelastic model employing Padé approximants for the unsteady airloads demonstrated the accuracy of the time-marching technique for the linearized case. Subsequently, Bland and Edwards⁸ demonstrated that such locally linear procedures may be used with airloads derived from a transonic small-disturbance code.

Batina⁹ studied transonic aeroelastic stability and response behavior of two conventional airfoils, NACA 64A006 and NACA 64A010, and one supercritical airfoil, MBB A-3. In the present study, further results are presented for

*Aerospace Engineer, Unsteady Aerodynamics Branch, Member AIAA.

**Professor and Head, School of Aeronautics and Astronautics, Associate Fellow AIAA.

the MBB A-3 airfoil. Three degrees of freedom (d.o.f.) are considered: plunge, pitch, and aileron pitch. Response analyses are performed by simultaneously integrating the structural equations of motion along with the unsteady aerodynamic forces of transonic code LTRAN2-NLR.¹⁰ A modal identification technique similar to that of Bennett and Desmarais¹¹ is applied to the time-marching response curves to identify the aeroelastic modes. Estimated frequency and damping of these modes are plotted in a "root-locus" type format in the complex s-plane. Stability analyses are performed using a state-space aeroelastic model, termed the Padé model, formulated using Padé approximants of the unsteady aerodynamic forces. These forces are described by an interpolating function determined by a least squares curve-fit of LTRAN2-NLR harmonic transonic aerodynamic data. The Padé model is written as a set of linear, first-order, constant coefficient, differential equations. These equations are solved in the Laplace domain yielding eigenvalues compared in the complex s-plane with time-marching modal estimates. The objective of the stability analysis is to investigate the applicability of locally linear aeroelastic modeling to airfoils in transonic flow. Representative Padé model stability results for the NACA 64A010 airfoil were reported in Ref. 12. (The Padé model may alternatively be solved in the time domain with appropriate initial conditions yielding the aeroelastic displacement time-histories.¹³)

Open-loop stability and response analyses are performed to determine the behavior of the aeroelastic modes as a function of flight speed. Time-marching response calculations are performed at three different flight speeds to investigate subcritical, critical, and supercritical flutter conditions. Frequency and damping of the aeroelastic modes identified from these transient responses are compared with Padé model results.

Closed-loop stability and response analyses are performed to investigate application of the Padé aeroelastic model and time-marching analyses to flutter suppression using active controls. The control law is intentionally simple for illustrative purposes. Aeroelastic effects due to simple, constant gain, feedback control laws utilizing displacement, velocity, or acceleration sensing are studied using a variety of control gains.

The objective of this study is to gain insight into the control of airfoil stability and response in transonic flow. The focus of the present effort is on time-marching transient response solutions with aeroelastic modal identification. The calculations presented here reveal some interesting aeroelastic behavior discovered when augmenting the aeroelastic system with active controls. Transonic aeroelastic stability and response characteristics of 2-D airfoils are discussed and comparisons are made.

Time-Marching Response Analysis

Response analyses are performed by simultaneously integrating the structural equa-

tions of motion along with the unsteady aerodynamic forces of the transonic code LTRAN2-NLR. The equations of motion for a typical airfoil section oscillating with three d.o.f.'s can be written as^{9,12-14}

$$[M]\{\ddot{X}\} + [C]\{\dot{X}\} + [K]\{X\} = \{p\} + \{G\}\beta_c \quad (1)$$

where $\{X\} = [\xi \ \alpha \ \beta]^T$ is the displacement vector containing plunge displacement ξ , pitching rotation α , and aileron pitching rotation β . The dot denotes differentiation with respect to nondimensional time $\omega_{\alpha}t$.

For closed-loop study, a simple, constant gain, feedback control law has been assumed of the form

$$\beta_c = K_D \dot{\xi}_s + K_V \dot{\xi}_s + K_A \ddot{\xi}_s \quad (2)$$

where K_D , K_V , and K_A are the displacement, velocity, and acceleration control gains, respectively; ξ_s is the sensor measured plunging motion. A single sensor was placed along the airfoil chord to obtain a measure of airfoil plunge and pitch motions from

$$\xi_s = [H_J]\{X\} \quad (3)$$

where $[H_J] = [1 \ (p-a_h) \ 0]$ and p is the sensor location aft of midchord.

The control system consists of a single sensor located near the control surface hinge line at 70% chord ($p = 0.4$), the control law, Eq. (2), and a trailing edge control surface of 25% chord. With this system, control surface aerodynamic forces are utilized to alleviate flutter instability. Details of the control system and equations may be found in Ref. 12.

By expressing the control law Eq. (2) in terms of the airfoil motion, the aeroelastic equations of motion may be written in general form for time-integration as

$$[M^*]\{\ddot{X}\} + [C^*]\{\dot{X}\} + [K^*]\{X\} = \{p\} \quad (4)$$

$$\text{where } [M^*] = [M] - K_A\{G\}[H_J] \quad (5a)$$

$$[C^*] = [C] - K_V\{G\}[H_J] \quad (5b)$$

$$[K^*] = [K] - K_D\{G\}[H_J] \quad (5c)$$

Details of the time-marching response solution procedures were given in Ref. 13.

A modal identification technique is used to determine the damping, frequency, amplitude, and phase of the aeroelastic modes from the time-marching displacement response histories. A method similar to that of Bennett and Desmarais¹¹ was used to least-squares curve-fit the time responses by complex exponential functions in the form

$$x(\bar{t}) = a_0 + \sum_{j=1}^m e^{\left(\frac{\sigma}{\omega_{\alpha}}\right)_j \bar{t}} \left[a_j \cos \left(\frac{\omega}{\omega_{\alpha}}\right)_j \bar{t} + b_j \sin \left(\frac{\omega}{\omega_{\alpha}}\right)_j \bar{t} \right] \quad (6)$$

The damping and frequency of the complex modes thus obtained

$$\left(\frac{\sigma}{\omega}\right)_j + i \left(\frac{\omega}{\omega_\alpha}\right)_j = \left(\frac{s}{\omega_\alpha}\right)_j \quad (7)$$

are estimates of the aeroelastic eigenvalues and may then be directly compared in the complex s-plane with those computed by the Padé model.

As an example, Fig. 1 shows a typical response analysis of the MBB A-3 airfoil at $M = 0.765$ and $c_{\ell} = 0.58$. The LTRAN2-NLR time-marching pitching response α and the modal curve fit using Eq. (6) are shown in the top part of the figure. Only the data used for curve fitting (144 points) is shown. In the lower part of the figure are the two component aeroelastic modes, identified from the modal fit.

Padé Model Stability Analysis

Stability analyses are performed using a linear eigenvalue analysis of the Padé model. This model was formulated by curve-fitting the unsteady aerodynamic forces by a Padé approximating function.^{9,12} These approximating functions are then expressed as linear differential equations which, when coupled to the structural equations of motion, lead to the first-order matrix equation

$$\{\dot{Z}\} = \frac{s}{\omega_\alpha} \{Z\} = [A]\{Z\} + \{B\}\beta_c \quad (8)$$

where $\{Z\}$ is the state vector containing displacement, velocity, and augmented states; s/ω_α is the complex eigenvalue. By expressing the control law Eq. (2) in terms of the state-vector $\{Z\}$, Eq. (8) is easily solved using standard eigenvalue solution techniques. Details of the Padé model formulation are given in Ref. 12.

Results and Discussion

Transonic aeroelastic stability and response analyses were reported in Ref. 9 for three airfoil configurations: NACA 64A006, NACA 64A010, and MBB A-3. All three airfoils are among those proposed by AGARD for aeroelastic applications of transonic unsteady aerodynamics.¹⁵ Aeroelastic behavior of the MBB A-3 airfoil was studied at the design Mach number $M = 0.765$ and at (1) zero mean angle of attack $\alpha = 0^\circ$; and (2) the design steady lift coefficient $c_{\ell} = 0.58$. The mean angle of attack necessary to match $c_{\ell} = 0.58$ using LTRAN2-NLR is $\alpha = 0.86^\circ$. In this report, representative time-marching response histories and s-plane stability root-loci for the MBB A-3 airfoil at $M = 0.765$ and $c_{\ell} = 0.58$ are presented. Aeroelastic parameter values selected are the same as those used in Refs. 12 and 13 and are listed in Table 1.

Table 1. Aeroelastic parameter values for stability and response analyses.

$\omega_h/\omega_\alpha = 0.3$	$x_\alpha = 0.2$
$\omega_\beta/\omega_\alpha = 1.5$	$r_\alpha = 0.5$
$\mu = 50.0$	$x_\beta = 0.008$
$a_h = -0.2$	$r_\beta = 0.06$
$c_\beta = 0.5$	$\zeta_\beta = 0.0$

Steady pressure solutions are required as aerodynamic initial conditions for unsteady calculations. As an example, the MBB A-3 steady pressure distribution computed using LTRAN2-NLR at $M = 0.765$ and $c_{\ell} = 0.58$ is shown in Fig. 2 along with the airfoil contour. This steady pressure data compares well with the experimental results of Bucciantini et al.¹⁶ There is a relatively weak shock wave on the airfoil upper surface near 55% to 60% chord. Steady pressure distributions for all of the cases considered indicate shock locations in the range of 50% to 65% chord and shock strengths that are well within the range of applicability of transonic small-disturbance theory.⁹

Open-Loop

Open-loop stability and response analyses are performed to determine the behavior of the aeroelastic modes as a function of flight speed. These calculations were first performed using the Padé aeroelastic model with results plotted in a flight speed root-locus format. As an example, open-loop root-loci as a function of flight speed are presented in Fig. 3 for the MBB A-3 airfoil. With increasing flight speed, the torsion branch moves to the left in the stable left-half of the complex s-plane. The aileron branch is also stable throughout, moving up and to the left as flight speed is increased. The bending dominated root-locus becomes the flutter mode at a nondimensional flutter speed of $U_F^* = 2.370$. In addition, the Padé model also predicts the divergence speed, where an aerodynamic lag root moves onto the positive real axis, as $U_D^* = 3.320$. This divergence phenomenon is similar to that reported by Edwards,¹⁴ where static divergence of a typical section in incompressible flow occurred due to the emergence of a real positive root from the complex s-plane origin. In Ref. 14, this root appeared in addition to the original structural poles and was also predicted using a Padé model. Table 2 compares the flutter and divergence speeds with those computed using linear aerodynamic theory. Flutter speeds from a p-k method flutter analysis are also tabulated for further comparison. These p-k method calculations were performed to assess the accuracy of the Padé model flutter solution. Padé model flutter speeds compare well with the p-k method values.

Table 2. Summary of open-loop flutter and divergence speeds for the MBB A-3 airfoil at $M = 0.765$.

AIRFOIL	FLUTTER METHOD	FLUTTER SPEED U_F^*	DIVERGENCE SPEED U_D^*	$\frac{U_D}{U_F}$
MBB A-3 $c_L = 0.58$	Padé	2.370	3.320	1.401
	p-k	2.403		
LINEAR THEORY	Padé	2.711	3.611	1.332
	p-k	2.729		

Time-marching transient responses were then obtained at three different flight speeds to investigate subcritical, critical, and supercritical flutter conditions. These calculations were performed independent of the Padé approximation, primarily for verification purposes. Transient response histories are shown in Fig. 4 for three values of flight speed near the flutter speed. A one-percent semi-chord plunge displacement was used as initial condition. Time-responses for $U/U_F = 1.0$ in Fig. 4 are nearly neutrally stable corresponding to the flutter condition. The flutter speed used for time-marching analyses was the p-k method value. Aeroelastic transients for $U/U_F = 0.844$ and $U/U_F = 1.156$ in Fig. 4 show converging (subcritical) and diverging (supercritical) oscillatory behavior, respectively.

Damping and frequency estimates of the aeroelastic modes were determined from the time-response histories of Fig. 4. These estimates are compared with Padé model eigenvalues for the bending and torsion modes in Fig. 5. In general, the Padé results compare well with the time-marching modal frequency and damping values. Agreement for the lower frequency bending mode is, in general, better than that for the higher frequency torsion mode. Frequency and damping estimates for the aileron mode are much less accurate than those for bending and torsion. The above discrepancies are attributed to: (1) the Padé model is less accurate at the higher damping ratios involved; (2) the structural integration is performed with fewer time-steps per cycle of the higher frequency modes; and (3) since the aileron mode has much more damping in comparison with bending and torsion, its contribution to the responses dies out quickly leaving very little information for modal curve-fitting.

Closed-Loop

The Padé aeroelastic model was used to study the effects of active feedback control on the aeroelastic modes at the flight speed equal to the open-loop flutter value. These calculations were performed primarily to determine the range and sign of the control gains required to stabilize the flutter mode. Padé stability calculations were also performed at the same Mach numbers using linear subsonic aerodynamic theory for comparison with transonic Padé model results. Effects due to displacement, velocity,

and acceleration feedback were further assessed using time-marching response analyses for comparison with Padé results. Finally, an example is presented illustrating the effectiveness of velocity feedback upon flutter suppression at speeds above and below the open-loop flutter speed.

Effects of Active Control on Flutter Mode.—Closed-loop analyses are first performed at the flight speed equal to the open-loop flutter value, to determine the behavior of the aeroelastic modes as a function of control gain. Effects of active control on the bending dominated flutter mode are of primary interest. Control gain root-loci computed using the Padé model for displacement, velocity, and acceleration control laws are shown in the left, center, and right of Fig. 6, respectively. Corresponding root-loci computed using linear subsonic theory are given in Fig. 7. In each case there are three open-loop aeroelastic roots or "poles" corresponding to the three structural d.o.f.'s. The two poles in the stable left-half of the complex s-plane correspond to the torsion and aileron modes; the pole that lies on the imaginary axis is the bending dominated flutter mode. These aeroelastic roots move toward "zeros" of the aeroelastic transfer function as the control gains K_D , K_V , or K_A are monotonically increased or decreased. Solid-line root-loci indicate the sign of the control gain that stabilizes the flutter mode whereas the dashed-line loci indicate the opposite effect. Comparison of LTRAN2-NLR results of Fig. 6 with the linear theory results of Fig. 7 indicates that frequency and damping values are significantly different for transonic and subsonic cases, although the overall root-locus trends are similar. This lack of agreement between linear theory results and LTRAN2-NLR root-loci illustrates the importance of including transonic effects in aeroelastic stability calculations.

Displacement feedback with negative control gains easily stabilized the flutter mode as shown in Figs. 6 and 7. Negative displacement feedback, however, results in static divergence of the same nature found in the open-loop cases. For the MBB A-3 airfoil at $M = 0.765$ and $c_L = 0.58$, this occurs for $K_D \leq -0.5$. Divergence root locations are shown in Figs. 6 and 7 for $K_D = -1.0$. Also, positive displacement feedback destabilized the flutter mode.

Velocity feedback with positive control gains stabilized the bending dominated flutter pole and increased the damping of the torsion mode. The transonic results of Fig. 6 indicate that there is more damping in bending and aileron modes, and much less in torsion than predicted by linear subsonic theory in Fig. 7. Also, negative velocity feedback destabilized the flutter mode.

Acceleration feedback with positive control gains stabilized the flutter pole and decreased damping and frequency of the torsion mode. Also, negative acceleration feedback destabilized the flutter mode.

Effects Due to Displacement Feedback. - Aeroelastic effects due to displacement feedback, ξ_s , were further studied by obtaining time-marching transient responses for $K_D = -1.0$ and detailed Padé stability results for the range of displacement gains $-1.0 \leq K_D \leq 0.0$. These calculations were performed primarily to investigate the divergence phenomenon predicted by a positive real aerodynamic lag root in the Padé model. The three d.o.f. time-histories computed using LTRAN2-NLR at $U/U_F = 1.0$ and $K_D = -1.0$ are given in Fig. 8. These responses show that flutter has been suppressed and that the aeroelastic displacements are indeed divergent. Comparisons of time-marching frequency and damping estimates with Padé eigenvalues are shown in Fig. 9. Good agreement is found in predicting this aeroelastic divergence. In addition, negative displacement feedback increased the damping in bending and decreased the torsion mode frequency. The lower frequency bending mode damping and frequency values for $K_D = -1.0$ compare well; results from the time-marching modal fits for the higher frequency torsion and aileron modes were not reliably determined.

Padé stability calculations were then performed for the range of gains $-1.0 \leq K_D \leq 0.0$ to reveal the effects of negative displacement feedback on flutter and divergence speeds. These more detailed results are shown in Fig. 10 for the MBB A-3 airfoil. Negative displacement feedback slowly increases the flutter speed and first rapidly increases the divergence speed. For gains K_D between approximately -0.2 and -0.5 , divergence is eliminated. In this region, the aerodynamic lag root previously causing divergence no longer crosses through the origin. For $K_D \leq -0.5$, divergence reappears as the critical mode of instability at speeds much lower than flutter. The flutter speed is increased approximately 14% for $K_D = -0.5$.

Effects Due to Velocity Feedback. - Aeroelastic effects due to velocity feedback, ξ_s , were further investigated by obtaining transient responses for successively increased velocity feedback. These calculations are first performed at the flight speed $U^* = U_F^*$. Values selected for the control gains were $K_V = 3.0, 6.0$, and 9.0 , the same gains shown by the triangles in the center portion of Fig. 6. LTRAN2-NLR response results are shown in Fig. 11. These response histories show that as K_V is increased the dominant motion is consistently more damped and of higher frequency. Also, positive velocity feedback significantly increased the nonrational part¹⁴ of the plunge displacement responses. Here, the ξ -transients oscillate about an asymptotically decaying rather than a zero mean value.

Damping and frequency of the aeroelastic modes determined from the LTRAN2-NLR displacement transients are plotted in Fig. 12 along with Padé model results. The flutter mode damping and frequency are both successively increased for values of $K_V = 3.0, 6.0$, and 9.0 . The torsion mode damping is significantly

increased with little effect upon the torsion mode frequency. Comparison of Padé eigenvalues with time-marching modal estimates shows general agreement. Discrepancies between the two sets of results are attributed to the same reasons as in the open-loop case. Also, the torsion mode for $K_V = 6.0$ and 9.0 could not be identified from the time-marching transients because of the large increase in damping.

Velocity feedback with positive control gains suppressed flutter for the range of flight speeds investigated. Some sensitivity with respect to mean angle of attack has been observed though in calculations using velocity feedback.¹² For the MBB A-3 airfoil at $M = 0.765$ and zero mean angle of attack, the flutter speed was increased by only 11% for the gain $K_V = 9.0$. Additional calculations also showed that velocity feedback does not affect the divergence speed. Therefore for the $C_L = 0.58$ case, the aeroelastic instability becomes that of static divergence. Since the control law with velocity feedback was found to be generally the most effective in raising flutter speeds,¹² more detailed calculations were performed. These results are described in a following section entitled "Illustrative Example."

Effects Due to Acceleration Feedback. - Aeroelastic effects due to acceleration feedback, ξ_s , were further investigated by obtaining transient responses for successively increased acceleration feedback. These calculations are performed at the flight speed $U^* = U_F^*$. Values selected for the control gains were $K_A = 6.0, 12.0$, and 18.0 , the same gains shown by the triangles in the right portion of Fig. 6. LTRAN2-NLR response results are shown in Fig. 13. These response histories show that as K_A is increased the dominant motion is consistently more damped and of lower frequency. Also, a higher frequency transient becomes more visible in the α and β responses for the larger values of K_A . This is due to the decreased damping of the torsion mode as shown in the frequency and damping comparisons of Fig. 14. Positive acceleration feedback increased damping in bending, decreased damping in torsion, and lowered the frequencies of both modes. Comparison of Padé eigenvalues with time-marching modal estimates shows general agreement. Results for the lower frequency bending mode are in better agreement than results for the higher frequency torsion mode.

Acceleration feedback with positive control gains raised the flutter speed approximately 25% for the maximum gain studied, $K_A = 18.0$. Additional calculations showed that acceleration feedback does not affect the divergence speed.

Illustrative Example. - Additional aeroelastic analyses were performed at speeds above and below the open-loop flutter speed using the velocity feedback control law since this control law was found to be generally the most effective.¹² These results are presented to further illustrate application of the Padé

and time-marching methods. Padé flight speed root-loci are shown in Fig. 15 for values of the velocity gain $K_V = 3.0, 6.0$, and 9.0 . Positive velocity feedback significantly increased the damping of the torsion root-locus and decreased the damping of the aileron mode. The bending root-locus for $K_V = 3.0$ reflects an increase in flutter speed of approximately 29% ($U_F^* = 3.050$), while for $K_V = 6.0$ and 9.0 flutter has been eliminated. Since velocity feedback does not affect the divergence speed, the aeroelastic instability becomes that of static divergence at the uncontrolled divergence speed $U_D^* = 3.320$. This divergence speed is approximately 40% greater than the open-loop flutter speed as shown in Table 2.

Time marching response calculations were then performed for $U/U_F = 1.266$ using LTRAN2-NLR to complement and verify the Padé model results. These response histories shown in Fig. 16, correspond to the $U^* = 3.0$ diamond-symbol eigensolutions of Fig. 15. These aeroelastic transients are bending dominated and converging for all three values of the control gain K_V . As K_V is increased, the responses become more stable indicating a monotonic increase in bending mode damping, at approximately the same frequency. Again, positive velocity feedback significantly increased the nonrational part of the plunge displacement responses.

Effects of velocity feedback on bending and torsion modes at $U/U_F = 1.266$ are shown in Fig. 17. Because of the large damping increase in torsion due to K_V and the relatively high frequency of the aileron mode, only the bending mode was determined from the aeroelastic transients of Fig. 16. Comparison of the two sets of bending root-locus results in Fig. 17 shows very good agreement. Positive velocity feedback increased bending mode damping at approximately the same frequency.

Finally, open and closed-loop flight speed root-loci are shown in Fig. 18 for both bending and torsion modes. The velocity feedback gain used to generate the closed-loop results is $K_V = 9.0$, the same value used in the right portion of Fig. 15. Padé model and time-marching solutions for the bending mode compare well. The control gain $K_V = 9.0$ increased the torsion mode damping for the range of flight speeds $0.844 \leq U/U_F \leq 1.266$, such that the results do not permit comparison between Padé and time-marching solutions. Fig. 18 illustrates again that positive velocity feedback has eliminated the flutter instability for the MBB A-3 airfoil at $M = 0.765$ and $c_L = 0.58$.

Conclusions

Transonic aeroelastic stability and response calculations have been performed for 2-D airfoils using the LTRAN2-NLR transonic small-disturbance code. Representative results are presented here for the MBB A-3 airfoil at the design condition $M = 0.765$ and $c_L = 0.58$. Emphasis is placed on time-marching transient response solutions with modal identification for

comparison with Padé model eigenvalues. Extension of the time-marching transient response analysis to a three degree of freedom aeroelastic system including active controls is demonstrated. Accurate frequency and damping estimates were obtained using a complex exponential least squares curve-fit of the aeroelastic responses. Good agreement was found between s-plane eigenvalues calculated using the Padé aeroelastic model and time-marching modal estimates. Therefore, locally linear aeroelastic modeling was found to be applicable to 2-D airfoils in small-disturbance transonic flow, for cases that are within the range of validity of the transonic codes. The importance of including transonic effects in aeroelastic stability calculations was illustrated by the differences between root-loci calculated using linear subsonic theory and LTRAN2-NLR. Although the overall root-locus trends are similar, frequency and damping values are significantly different for transonic and subsonic cases.

Effects due to simple, constant gain, control laws utilizing displacement, velocity, or acceleration sensing were studied. Displacement feedback with negative control gains suppressed flutter but caused airfoil responses to diverge. Comparison of Padé eigenvalues with time-marching frequency and damping estimates showed good agreement in predicting this aeroelastic divergence. In addition, negative displacement feedback increased the damping in bending, and decreased the torsion mode frequency. Detailed Padé stability calculations revealed the effects of negative displacement feedback on flutter and divergence speeds. Velocity feedback with positive control gains suppressed flutter. Padé stability results compared well with time-marching frequency and damping values. In general, positive velocity feedback increased damping in both bending and torsion modes, and significantly increased the nonrational part of the plunge displacement responses. Here, the plunge transients oscillated about an asymptotically decaying rather than a zero mean value. Acceleration feedback with positive control gains also increased flutter speeds. Again, Padé results compared well with time-marching modal estimates. In general, positive acceleration feedback increased damping in bending, decreased damping in torsion, and lowered the frequencies of both modes.

References

- ¹Ballhaus, W. F. and Goorjian, P. M., "Computation of Unsteady Transonic Flows by the Indicial Method," *AIAA Journal*, Vol. 16, Feb. 1978, pp. 117-124.
- ²Rizzetta, D. P., "Time-Dependent Responses of a Two-Dimensional Airfoil in Transonic Flow," *AIAA Journal*, Vol. 17, Jan. 1979, pp. 26-32.
- ³Guruswamy, P. and Yang, T. Y., "Aeroelastic Time Response Analysis of Thin Airfoil by Transonic Code LTRAN2," *Journal of Computers and Fluids*, Vol. 9, Dec. 1981, pp. 409-425, (Also AFFDL-TR-79-3077, June 1979).

⁴Borland, C. J. and Rizzetta, D. P., "Nonlinear Transonic Flutter Analysis," AIAA Journal, Vol. 20, Nov. 1982, pp. 1606-1615.

⁵Yang, T. Y. and Chen, C. H., "Transonic Flutter and Response Analyses of Two Three-Degree-of-Freedom Airfoils," Journal of Aircraft, Vol. 19, Oct 1982, pp. 875-884, (Also AFWAL-TR-81-3103, Aug. 1981).

⁶Yang, T. Y. and Batina, J. T., "Transonic Time-Response Analysis of Three D.O.F. Conventional and Supercritical Airfoils," Journal of Aircraft, Vol. 20, Aug. 1983, pp. 703-710.

⁷Edwards, J. W., Bennett, R. M., Whitlow, W., Jr. and Seidel, D. A., "Time-Marching Transonic Flutter Solutions Including Angle-of-Attack Effects," Journal of Aircraft, Vol. 20, Nov. 1983, pp. 899-906.

⁸Bland, S. R. and Edwards, J. W., "Airfoil Shape and Thickness Effects on Transonic Airloads and Flutter," AIAA Paper No. 83-0959, presented at the AIAA/ASME/ASCE/AHS 24th Structures, Structural Dynamics and Materials Conference, Lake Tahoe, NV, May 2-4, 1983, also Journal of Aircraft, Vol. 21, March 1984, pp. 209-217.

⁹Batina, J. T., "Transonic Aeroelastic Stability and Response of Conventional and Supercritical Airfoils Including Active Controls," Ph.D. Thesis, Purdue University, West Lafayette, December 1983.

¹⁰Houwink, R. and van der Vooren, J., "Results of an Improved Version of LTRAN2 for Computing Unsteady Airloads on Airfoils Oscillating in Transonic Flow," AIAA Paper 79-1553, AIAA 12th Fluid and Plasma Dynamics Conference, Williamsburg, VA., July 23-25, 1979.

¹¹Bennett, R. M. and Desmarais, R. N., "Curve Fitting of Aeroelastic Transient Response Data with Exponential Functions in Flutter Testing Techniques," NASA SP-415, 1975, pp. 43-58.

¹²Batina, J. T. and Yang, T. Y., "Application of Transonic Codes to Aeroelastic Modeling of Airfoils Including Active Controls," accepted for publication in Journal of Aircraft.

¹³Batina, J. T. and Yang, T. Y., "Transonic Time-Responses of the MBB A-3 Supercritical Airfoil Including Active Controls," submitted for review to Journal of Aircraft.

¹⁴Edwards, J. W., "Unsteady Aerodynamic Modeling and Active Aeroelastic Control," SUDAAR 504, Stanford University, Feb. 1977.

¹⁵Bland, S. R., "AGARD Two-Dimensional Aeroelastic Configurations," AGARD-AR-156, August 1979.

¹⁶Bucciantini, G., Oggiano, M. S., and Onorato, M., "Supercritical Airfoil MBB A-3, Surface Pressure Distributions, Wake and Condition Measurements," AGARD-AR-138, May 1979, pp. A8-1 to A8-25.

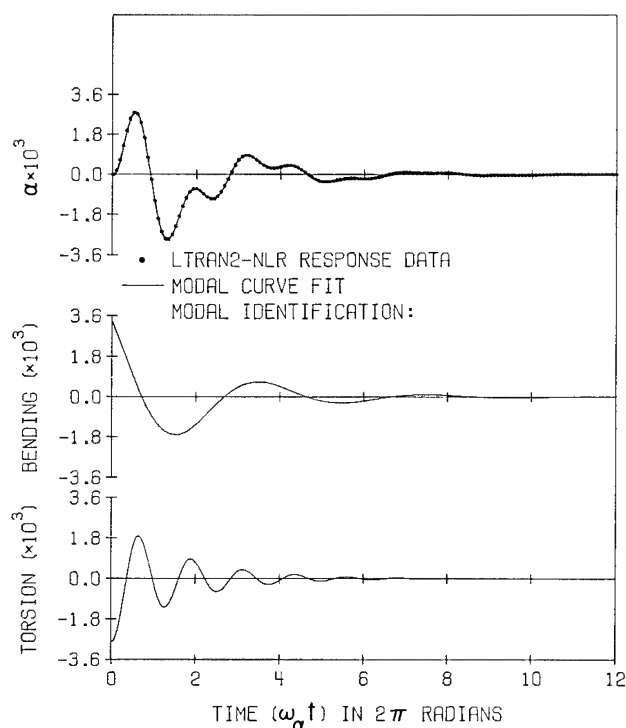


Fig. 1 Modal curve fit of aeroelastic time-marching pitching response of the MBB A-3 airfoil at the open-loop flutter speed $U/U_F = 1.0$, $K_A = 18.0$, $M = 0.765$, and $c_L = 0.58$.

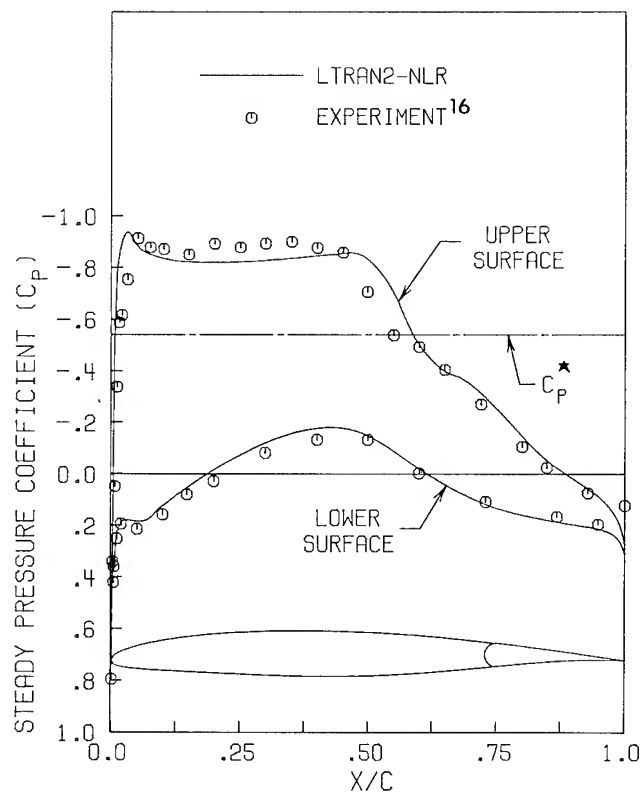


Fig. 2 Steady pressure distributions for the MBB A-3 airfoil at $M = 0.765$ and $c_L = 0.58$.

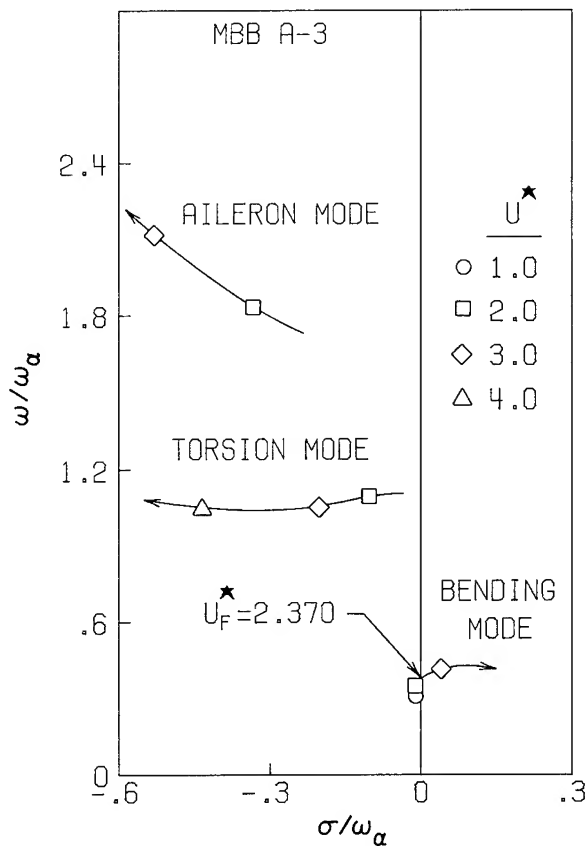


Fig. 3 MBB A-3 open-loop flight speed root-loci at $M = 0.765$ and $c_l = 0.58$.

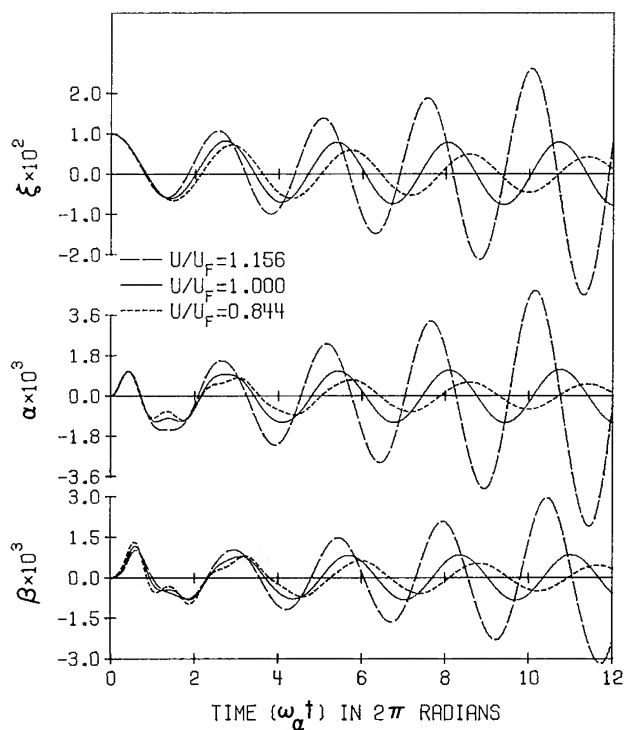


Fig. 4 Effect of flight speed on MBB A-3 open-loop time-marching displacement responses at $M = 0.765$ and $c_l = 0.58$.

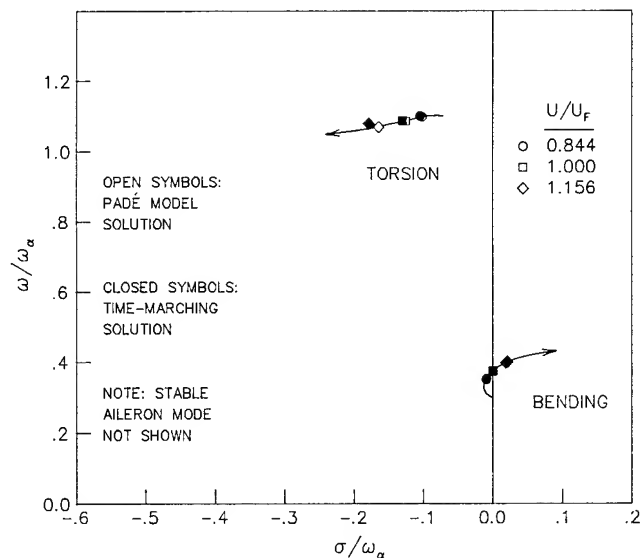


Fig. 5 MBB A-3 flight speed root-loci for bending and torsion modes at $M = 0.765$ and $c_l = 0.58$.

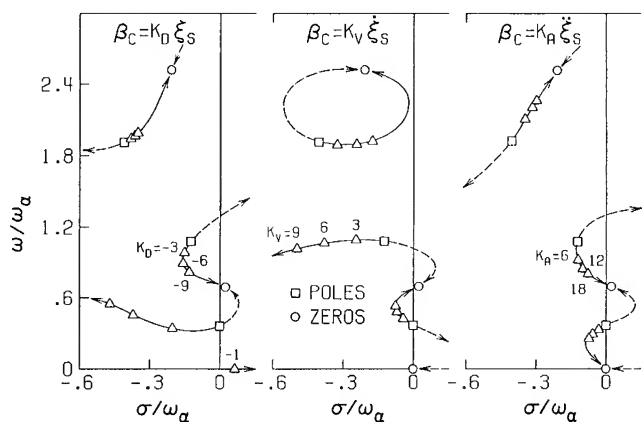


Fig. 6 MBB A-3 control gain root-loci at the open-loop flutter speed ($U^* = U_F^*$), $M = 0.765$ and $c_l = 0.58$.

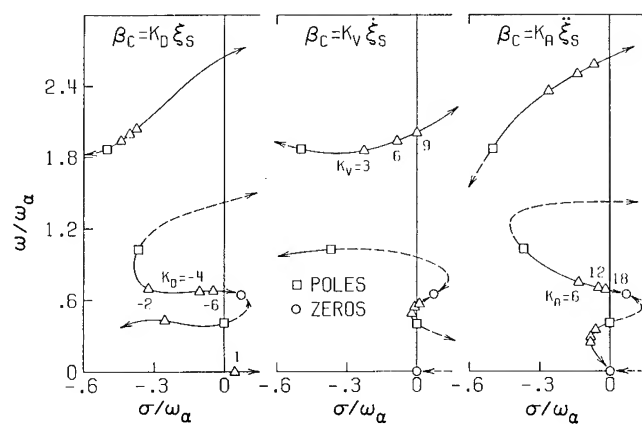


Fig. 7 Control gain root-loci at the open-loop flutter speed ($U^* = U_F^*$) computed using linear subsonic aerodynamic theory at $M = 0.765$.

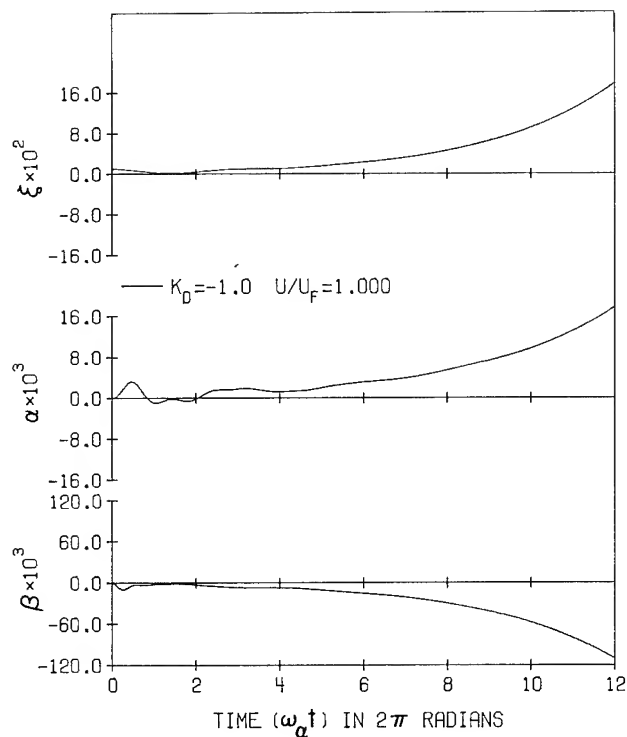


Fig. 8 Effect of displacement feedback on MBB A-3 time-marching displacement responses at the open-loop flutter speed $U/U_F = 1.0$, $M = 0.765$ and $c_\ell = 0.58$.

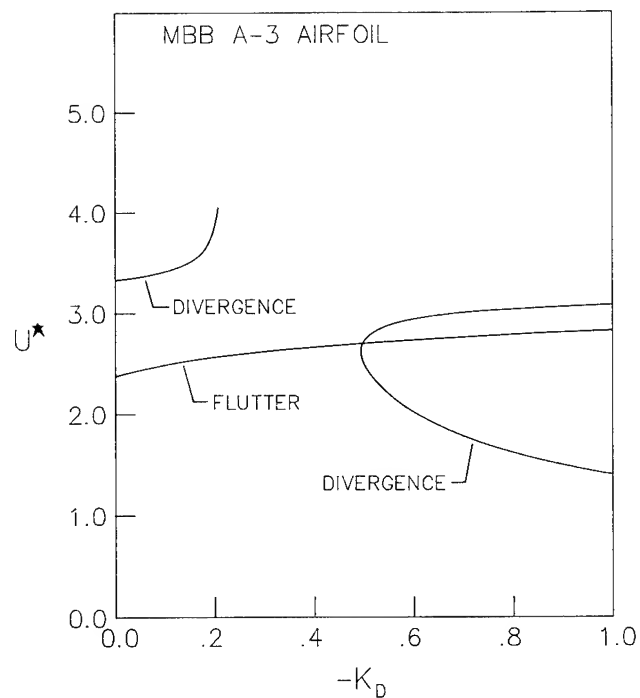


Fig. 10 Effect of negative displacement feedback on MBB A-3 flutter and divergence speeds at $M = 0.765$ and $c_\ell = 0.58$.

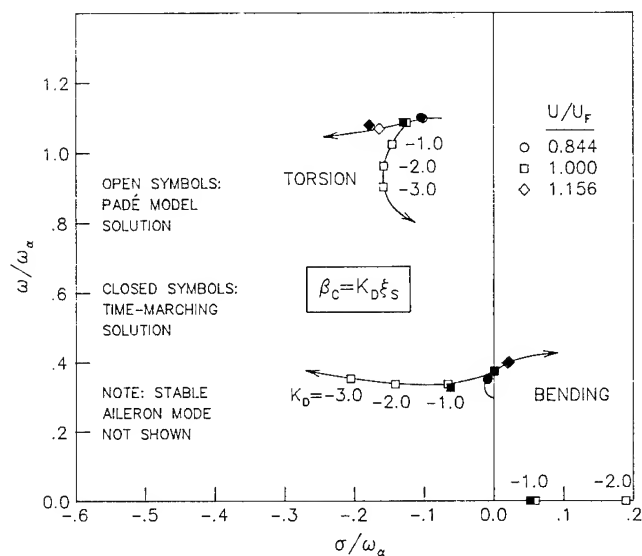


Fig. 9 Effect of displacement feedback on MBB A-3 bending and torsion modes at the open-loop flutter speed $U/U_F = 1.0$, $M = 0.765$, and $c_\ell = 0.58$.

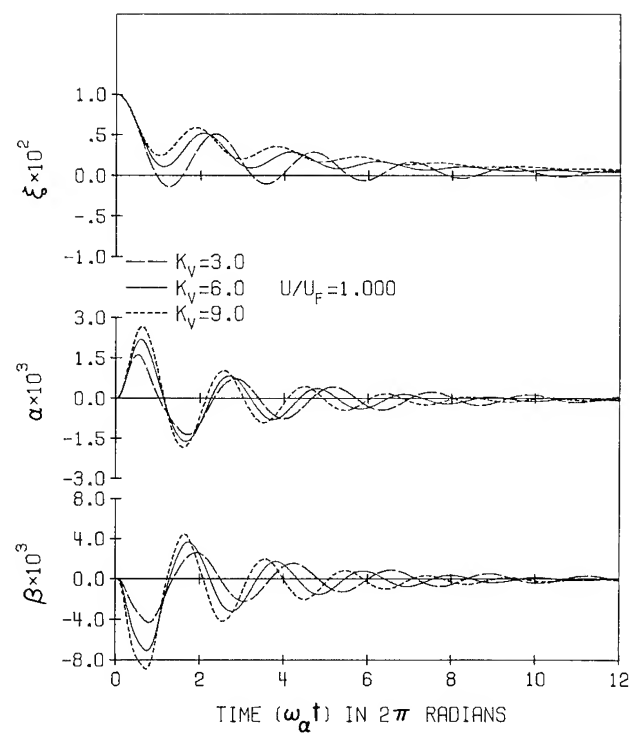


Fig. 11 Effect of velocity feedback on MBB A-3 time-marching displacement responses at the open-loop flutter speed $U/U_F = 1.0$, $M = 0.765$ and $c_\ell = 0.58$.

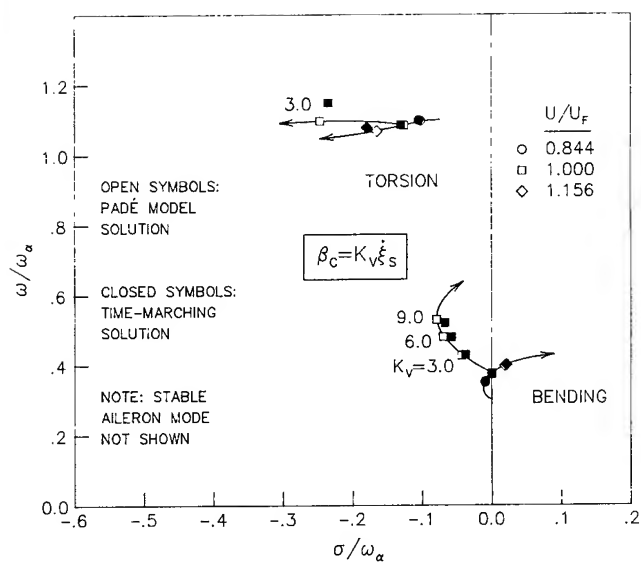


Fig. 12 Effect of velocity feedback on MBB A-3 bending and torsion modes at the open-loop flutter speed $U/U_F = 1.0$, $M = 0.765$ and $c_\ell = 0.58$.

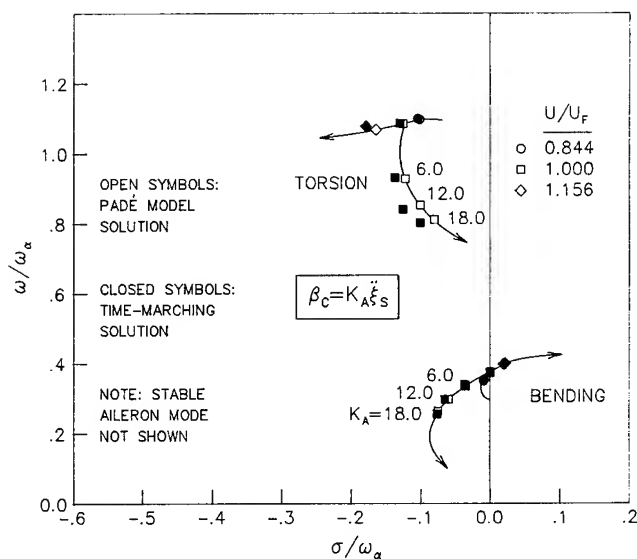


Fig. 14 Effect of acceleration feedback on MBB A-3 bending and torsion modes at the open-loop flutter speed $U/U_F = 1.0$, $M = 0.765$ and $c_\ell = 0.58$.

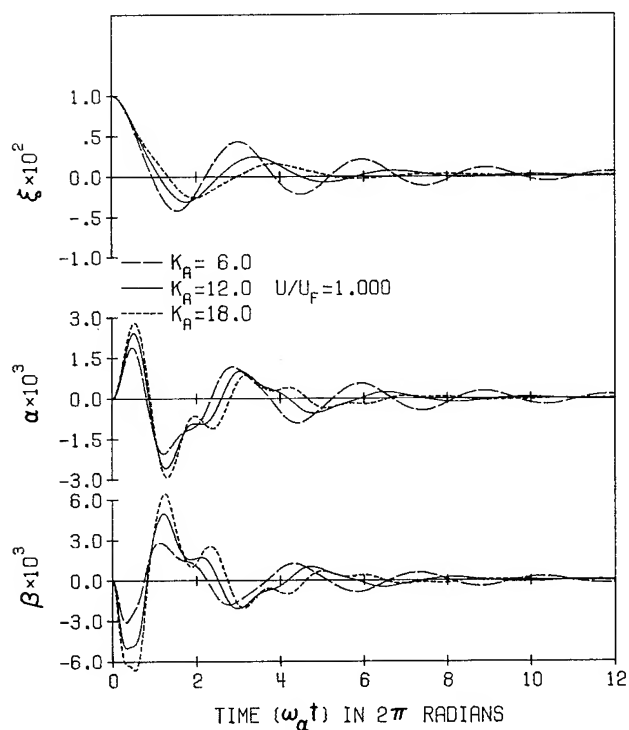


Fig. 13 Effect of acceleration feedback on MBB A-3 time-marching displacement responses at the open-loop flutter speed $U/U_F = 1.0$, $M = 0.765$ and $c_\ell = 0.58$.

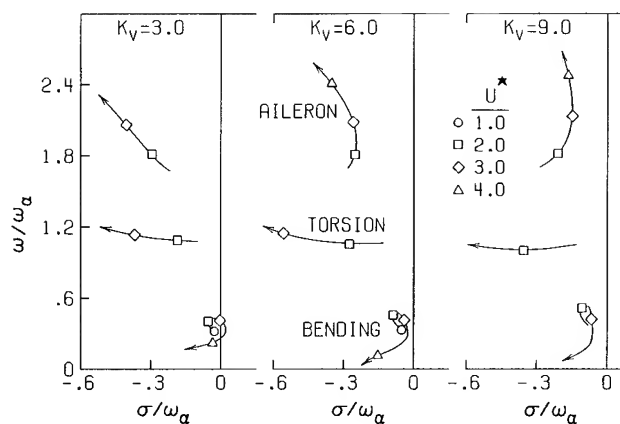


Fig. 15 MBB A-3 velocity feedback, flight speed root-loci at $M = 0.765$ and $c_\ell = 0.58$.

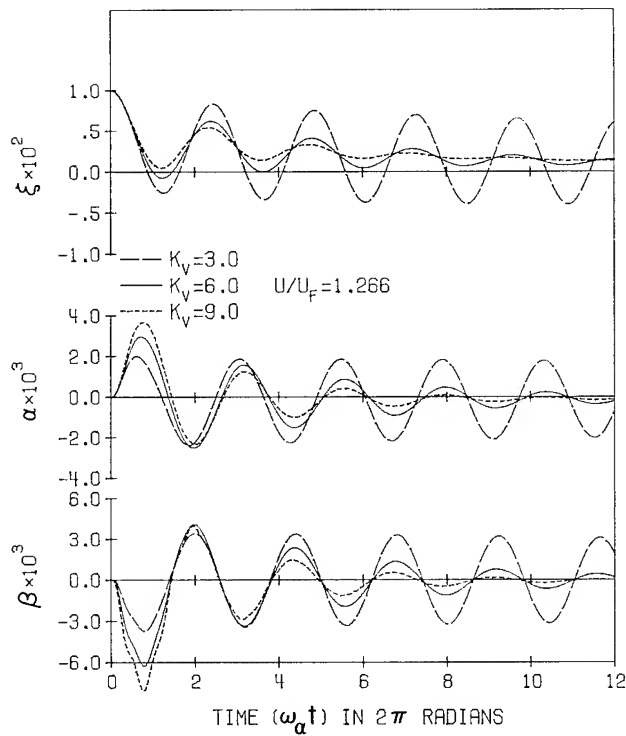


Fig. 16 Effect of velocity feedback on MBB A-3 time-marching displacement responses at $U/U_F = 1.266$, $M = 0.765$ and $c_{\ell} = 0.58$.

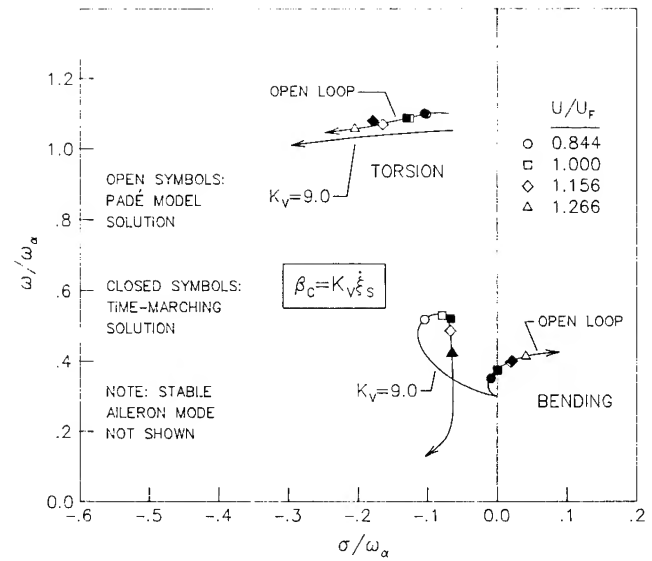


Fig. 18 MBB A-3 open and closed ($K_V = 9.0$) loop flight speed root-loci for bending and torsion modes at $M = 0.765$ and $c_{\ell} = 0.58$.

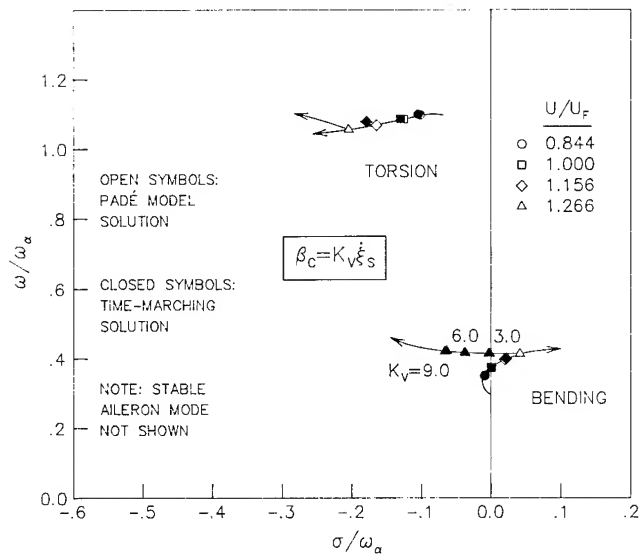


Fig. 17 Effect of velocity feedback on MBB A-3 bending and torsion modes at $U/U_F = 1.266$, $M = 0.765$ and $c_{\ell} = 0.58$.

Brian J. Landsberger*
6520 Test Group, Range Squadron
Edwards Air Force Base, CA 93523

John Dugundji**
Department of Aeronautics and Astronautics
Massachusetts Institute of Technology
Cambridge, MA 02139

Abstract

An analytical and experimental investigation was made of the aeroelastic deflection, divergence, and flutter behavior of both straight and 30° forward swept rectangular, graphite/epoxy, cantilevered plate type wings, with various amounts of bending-torsion stiffness coupling. The analytical investigation used a Rayleigh-Ritz formulation together with incompressible 3-dimensional Weissinger L-Method aerodynamics for the divergence, and incompressible 2-dimensional unsteady strip theory for the flutter. Rough attempts were also made to obtain the steady airload deflections of the wing including the nonlinear stall behavior. Experiments on 13 wing configurations showed divergence and bending-torsion flutter at low angles of attack, and torsion stall flutter and bending stall flutter at higher angles of attack. Good agreement with theory was found for the divergence and bending-torsion flutter cases at low angles of attack, and for the nonlinear steady wing deflections at high angles of attack. The +15° ply configuration was efficient in relieving the adverse divergence effect of the forward swept wing.

1. Introduction

The use of composite materials in aircraft structures had added another design dimension to the aircraft designer. These composite materials are useful not only for their high strength to weight ratio, but also because they give the designer the ability to vary the force deflection behavior by varying the layup scheme, and thus have made some previously impractical design options attractive. In particular, forward swept wings have gained renewed interest because their major drawback, low wing divergence speeds, can be significantly improved by using tailored composite material in wing construction. A good general discussion of this is given by Hertz, Shirk, Ricketts, and Weisshaar.¹ Other detailed studies of forward swept wings are given in References 2 through 8. The later studies begin to explore the effects of rigid body pitch modes on these forward swept wings.

The present paper is a continuation of previous work by Hollowell and Dugundji,⁹ who explored the divergence and flutter behavior of a series of stiffness coupled, graphite/epoxy, unswept cantilever plate wings. Using that work as a foundation, the present paper extends the range by investigating some new ply layup patterns and by investigating the 30 degree forward sweep case as well. As before, both the low angle of attack (linear) and the high angle of attack (nonlinear) aeroelastic properties of cantilever wings are explored. All static deflection, divergence, and flutter data are carefully documented and as such they extend the experimental base for aeroelastic tailoring with composites. The present paper is based on an M.S. thesis by the first author.¹⁰ More extensive details of the analysis and experiment can be found there.

2. Theory

For all tests, the flat plate wing was mounted vertically in the wind tunnel. The corresponding swept wing geometry is shown in Figure 1, with the z axis pointing into the paper along with positive deflection w, and positive lift L. The positive fiber ply direction θ_F used for this investigation is also shown. All static and dynamic analyses were done using the Rayleigh-Ritz method with five modes to describe the vertical deflection w, namely,

$$w = \sum_{i=1}^5 \gamma_i(\bar{x}, \bar{y}) q_i(t) \quad (1)$$

where

$$\gamma_i = \phi_i(\bar{x}) \psi_i(\bar{y}) \quad (2)$$

and $\phi_i(\bar{x})$ and $\psi_i(\bar{y})$ are single dimension modes in the \bar{x} and \bar{y} directions respectively, given by

*Major, USAF, Chief, Test Mission Control Branch.

**Professor of Aeronautics and Astronautics.
Member of AIAA.

$$\begin{aligned}
\phi_1(\bar{x}) &= 1^{\text{st}} \text{ cantil. beam mode, } \psi_1(\bar{y})=1 \\
\phi_2(\bar{x}) &= 2^{\text{nd}} \text{ cantil. beam mode, } \psi_2(\bar{y})=1 \\
\phi_3(\bar{x}) &= \sin(\pi\bar{x}/2\bar{\ell}), \quad \psi_3(\bar{y})=\bar{y}/\bar{c} \\
\phi_4(\bar{x}) &= \sin(3\pi\bar{x}/2\bar{\ell}), \quad \psi_4(\bar{y})=\bar{y}/\bar{c} \\
\phi_5(\bar{x}) &= \frac{\bar{x}}{\bar{\ell}} (1 - \frac{\bar{x}}{\bar{\ell}}), \quad \psi_5(\bar{y})=[4(\frac{\bar{y}}{\bar{c}})^2 - \frac{1}{3}]
\end{aligned} \quad (3)$$

These modes represent first bending (1B), second bending (2B), first torsion (1T), and second torsion (2T), and first chordwise bending (1C), respectively, and are the same modes used in the previous analysis by Hollowell and Dugundji.⁹

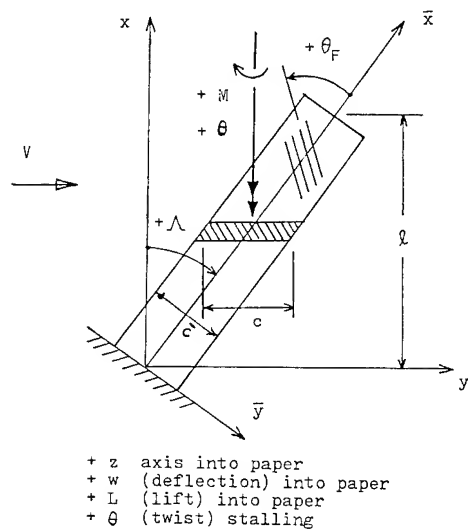


Fig. 1 Swept Wing Coordinate System

The strain energy U for a symmetric anisotropic laminate plate is¹¹

$$\begin{aligned}
U &= \frac{1}{2} \int_0^{\bar{\ell}} \int_{-\frac{\bar{c}}{2}}^{\frac{\bar{c}}{2}} [D_{11}(w, \bar{x}\bar{x})^2 + 2D_{12}w, \bar{x}\bar{x}w, \bar{y}\bar{y} \\
&+ D_{22}(w, \bar{y}\bar{y})^2 + 4D_{16}w, \bar{x}\bar{x}w, \bar{x}\bar{y} + 4D_{26}w, \bar{y}\bar{y}w, \bar{x}\bar{y} \\
&+ 4D_{66}(w, \bar{x}\bar{y})^2] d\bar{y}d\bar{x} \quad (4)
\end{aligned}$$

where a comma denotes partial differentiation, and the D_{ij} 's are the appropriate bending stiffnesses for the laminate. The kinetic energy T for the plate is

$$T = \frac{1}{2} \int_0^{\bar{\ell}} \int_{-\frac{\bar{c}}{2}}^{\frac{\bar{c}}{2}} m \dot{w}^2 d\bar{y}d\bar{x} \quad (5)$$

where $(\dot{}) = d/dt$, $m = \rho_G t_G$ is the mass per unit area, ρ_G the density of graphite/epoxy, and t_G the total plate thickness. The change in external work δW_e can be expressed as

$$\delta W_e = \int_0^{\bar{\ell}} \int_{-\frac{\bar{c}}{2}}^{\frac{\bar{c}}{2}} \Delta p_z \delta w d\bar{y}d\bar{x} \quad (6)$$

where Δp_z is the distributed lateral load per unit area. Finally, placing all the previous terms into Lagrange's equations, results in the five equations of motion,

$$[M] \ddot{q} + [K] q = Q \quad (7)$$

where $[K]$ and $[M]$ are the appropriate stiffness and mass matrices resulting from strain and kinetic energies, while Q is the generalized force whose elements are given by

$$Q_i = \iint \gamma_i \Delta p_z d\bar{x}d\bar{y} \quad (8)$$

The elements of the $[K]$ and $[M]$ matrices are given in Reference 9 (earlier version) and 10.

The structural deflection and twist behavior of the wing tip for a given applied tip load P can be obtained from Equation (7) by neglecting the inertia terms $[M]\ddot{q}$ and setting the generalized forces $Q_1 = P \gamma_1(\bar{\ell})$, $Q_2 = -P \gamma_2(\bar{\ell})$, $Q_3 = Q_4 = Q_5 = 0$. Solving Equation (7) for q and placing into Equation (1) gives the desired deflections and twists. Similarly, the deflection behavior due to an applied tip twisting moment M_t can be obtained by setting $Q_1 = Q_2 = Q_5 = 0$, $Q_3 = M_t/\bar{c}$, $Q_4 = -M_t/\bar{c}$ in Equation (7).

Steady Airload Deflections and Divergence

The steady deflections of a wing in an air-stream is obtained by combining the structural deflection characteristics of the wing together with the aerodynamic loads developed on the wing. Conventional linear theory for the structure and the aerodynamics will be assumed here. Later, the effects of aerodynamic nonlinearity will be examined.

The swept wing geometry is shown in Figure 1, with the z axis pointing into the paper, along with positive deflection w and positive lift L . The angle of attack θ of a wing section parallel to the on-coming flow, due to the elastic deformation of the wing $w(x,y)$, can be expressed as

$$\theta = -\frac{\partial w}{\partial y} = -\frac{\partial w}{\partial y} \cos \Lambda - \frac{\partial w}{\partial x} \sin \Lambda \quad (9)$$

Placing the assumed deflection pattern Equation (1) into the above, one can express the elastic angle of attack θ at a number of spanwise stations x_i in matrix form as

$$\underline{\theta} = [S] \underline{q} \quad (10)$$

$$S_{ij} = -\frac{\partial \gamma_j}{\partial \bar{y}} (\bar{x}_i, \bar{y}_i) \cos \Lambda - \frac{\partial \gamma_j}{\partial \bar{x}} (\bar{x}_i, \bar{y}_i) \sin \Lambda$$

where the elements S_{ij} are evaluated at the 3/4 chord of each spanwise section. The total angle of attack α of each section is given as

$$\alpha = \alpha_0 + \theta \quad (11)$$

where α_0 represents the root angle of attack of the wing.

The aerodynamic lift on each section of the wing can be expressed as,

$$L = q c C_{\ell} \Delta x \quad (12)$$

where q is the dynamic pressure, c the chord, C_{ℓ} the local lift coefficient, and Δx the width of the section. To relate the lift to the local angle of attack, 3-dimensional Weissinger L-Method theory for a finite swept wing in incompressible flow is used. This is presented by De Young and Harper¹² as

$$\alpha_i = \sum_{j=1}^4 \frac{a_{ij}}{4\ell} (cC_{\ell})_j \quad (13)$$

where ℓ is the semispan (see Figure 1) and a_{ij} are nondimensional coefficients tabulated in Reference 12 for different configurations at the Multhopp stations $x/\ell = .924, .707, .383$, and 0. In matrix form, Equations (12) and (13) become

$$\underline{L} = q [\bar{W}] \underline{cC_{\ell}} \quad (14)$$

$$\underline{\alpha} = [A] \underline{cC_{\ell}} \quad (15)$$

where $[\bar{W}]$ is an appropriate section width diagonal matrix weighted for the Multhopp station distribution. Inverting Equation (15) and placing into (14) gives the lift distribution L resulting from a given angle of attack distribution α . The corresponding generalized force matrix \tilde{Q} which causes deformation of the wing Equation (1), can be obtained by considering the lift loads as point loads acting at the 1/4 chord of the wing. Using Equation (8), this gives

$$\underline{\tilde{Q}} = [R] \underline{L} \quad (16)$$

where the elements $R_{ij} = \gamma_i (\bar{x}_j, \bar{y}_j)$ are evaluated at the 1/4 chord of each section.

The steady airload deflections of the wing in an airstream are obtained by neglecting the inertia terms $[M] \ddot{q}$ in Equation (7) and combining with Equations (10), (11), (14), (15), (16) to give

$$\left(\frac{1}{q}[I] - [D]\right) \underline{\theta} = [D] \underline{l} \alpha_0 \quad (17)$$

where the matrix $[D]$ is defined as

$$[D] = [S][K]^{-1}[R][\bar{W}][A]^{-1} \quad (18)$$

In the above, $[I]$ is a square unity matrix, \underline{l} is a column of 1's, and α_0 is the root angle of attack. Solution of Equation (17) gives the elastic twist distribution θ , which is then added to α_0 to give the total α as indicated by Equation (11). The total lift loads L corresponding to this α are then found from Equations (14) and the inverted (15).

Divergence, for this linear problem, occurs when the determinant of the left-hand-side of Equation (17) equals zero. This gives rise to the standard real eigenvalue problem,

$$[D] \underline{\theta} = \frac{1}{q} \underline{\theta} \quad (19)$$

The largest positive eigenvalue $1/q$ gives the lowest value of q for divergence. For some configurations, the largest eigenvalue is negative, thereby indicating no divergence possible for that wing.

Flutter Analysis

The flutter analysis was done using the familiar V-g method.¹³ A structural damping coefficient g , is introduced into the equations of motion Equations (7), to represent the amount of damping that must be added to the structure to attain neutral stability (flutter) at the given velocity. Negative values of g indicate the structure is stable, while positive values indicate instability. Flutter occurs when g is equal to the actual damping in the structure.

Assuming harmonic motion $q = q e^{i\omega t}$, the equations of motion Equations (7) become

$$([K] - \omega^2[M])q e^{i\omega t} = \underline{Q} \quad (20)$$

where the generalized force Q is defined by Equation (8) and comes from the aerodynamic loadings. For the aerodynamics, 2-dimensional, incompressible, unsteady strip theory is used with sections taken parallel to the flow as shown in Figure 1. To obtain Q , it is convenient to express the change in external work δW_e of Equation (6) as

$$\delta W_e = \int_0^{\ell} (L\delta h + M\delta\theta + N\delta\zeta) dx = \sum_{i=1}^5 Q_i \delta q_i \quad (21)$$

where the section forces and deflections here are taken at the midchord, and all twists θ and moments M are taken about an axis parallel to the x axis. The section forces and moments are defined as

$$\begin{aligned} L &= \int \Delta p \, dy \\ M &= - \int (y - y_c) \Delta p \, dy \\ N &= \int \psi_5 \Delta p \, dy \end{aligned} \quad (22)$$

while the section deflection, twist and camber change are expressed using Equations (1), (2), (3) and (9) as

$$\begin{aligned} h &= \phi_1 q_1 + \phi_2 q_2 \\ \theta &= -\frac{1}{c} (\phi_3 q_3 + \phi_4 q_4) \cos \Lambda \\ &\quad - \left(\frac{d\phi_1}{dx} q_1 + \frac{d\phi_2}{dx} q_2 \right) \sin \Lambda \\ \zeta &= \phi_5 q_5 \end{aligned} \quad (23)$$

Using 2-dimensional, incompressible unsteady aerodynamic theory and including camber effects as adapted from Spielberg¹⁴ and described in Reference 9, the aerodynamic forces can be expressed as,

$$\begin{aligned} L &= \pi \rho \omega^2 b^3 \cos \Lambda (L_{AB}^h + L_B^{\theta} + L_C^{\zeta}) e^{i\omega t} \\ M &= \pi \rho \omega^2 b^4 \cos \Lambda (M_{AB}^h + M_B^{\theta} + M_{CB}^{\zeta}) e^{i\omega t} \\ N &= \pi \rho \omega^2 b^3 \cos \Lambda (N_{AB}^h + N_B^{\theta} + N_{CB}^{\zeta}) e^{i\omega t} \end{aligned} \quad (24)$$

where $b = c/2$ represents the semichord, ρ is the air density, and the $\cos \Lambda$ factor accounts for the sweep. Placing Equations (23) into (21) and matching coefficients of δq_j gives the five generalized forces Q_j . Then substituting Equations (24) and (23) into these relations gives the generalized force matrix \underline{Q} in the final form,

$$\underline{Q} = \pi \rho \omega^2 b^3 [\underline{A}] \underline{q} e^{i\omega t} \quad (25)$$

where the elements A_{ij} of the 5×5 aerodynamic matrix $[\underline{A}]$ involve the sweep angle Λ , certain definite integrals of ϕ_i and $d\phi_i/dx$, and the aerodynamic functions L_A, M_A, \dots which are complex functions of reduced frequency, $k = \omega b/V$. Expressions for A_{ij} are given by Landsberger.¹⁰

Combining the aerodynamic forces Equations (25) with the structural representation Equation (20), introducing structural damping by multiplying the stiffness matrix $[\underline{K}]$ by $(1 + ig)$,

and rearranging, gives rise to the complex eigenvalue problem,

$$[\underline{B}] \underline{q} = \underline{Z} [\underline{K}] \underline{q} \quad (26)$$

where,

$$[\underline{B}] = [\underline{M}] + \pi \rho b^3 [\underline{A}], \quad \underline{Z} = \frac{(1 + ig)}{\omega^2} \quad (27)$$

For given values of reduced frequency, $k = \omega b/V$, the complex coefficients A_{ij} are evaluated, and together with M_{ij} and K_{ij} are placed into Equation (26) which is solved for the five complex eigenvalues \underline{Z} . From these eigenvalues and from k , the ω , g , and V are determined. Plots of g and ω versus V then characterize the flutter stability and frequencies of the wing. The ω values at $V \approx 0$ represent the natural frequencies with air mass effects present. The natural frequencies in a vacuum are also obtained from Equation (26) by using a small value of air density and a large value of k .

Nonlinear Steady Airload Deflections

Because the flat plate wings were flexible and could deflect to large bending and twisting angles without failure, the wings would stall out when the linear calculated divergence speed was approached or even exceeded. Accordingly, an attempt was made to calculate the nonlinear steady airload deflections and twist behavior by using rough approximations to the nonlinear lift and drag characteristics. Only the straight wing case, $\Lambda = 0^\circ$, was attempted

Figure 2 shows the measured lift and drag coefficients on a flat plate wing as given by Riegels.¹⁵ Also, an aft center of pressure movement was noticed from about 25% c at $\alpha = 5^\circ$ to 40% c at 20° . These force coefficient data were first resolved in the direction normal to the chord, and then fitted by a simple power series in α . Then the pressure was distributed over the surface in the chordwise direction in a manner roughly resembling linear theory, but

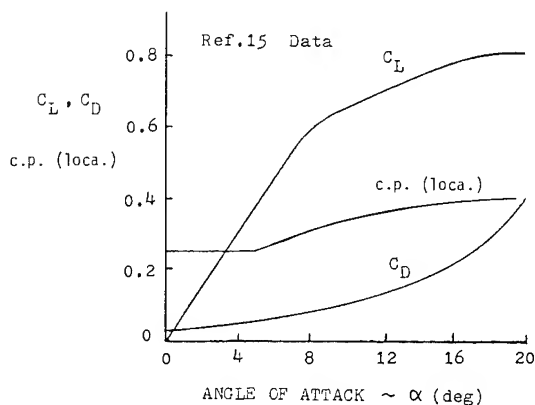


Fig. 2 Lift and Drag Coefficients for Flat Plate

including the aft center of pressure movement. Finally, a spanwise tip correction was added to insure the pressures fall to zero at the tips. The resulting approximation used is given below for the pressure coefficient c_p .

$$c_p = (A_4 \alpha^4 + A_3 \alpha^3 + A_2 \alpha^2 + A_1 \alpha) \times (1.11) [1 - (x/l)^9] \{ (3.5 - 5.7\alpha) [1.5 - (y/c)^{2.5}] + 1.63 \alpha \} + 3.5 \alpha^3 \quad (28)$$

For further details and motivations, see Landsberger.¹⁰ The angle of attack α to be used in the above can be approximated as,

$$\alpha(x) \equiv \alpha_0 + \frac{q_3}{c} \sin \frac{\pi x}{l/2} \quad (29)$$

since the vast majority of the twist θ is from the first torsion mode, Equations (1) and (9).

To obtain a solution for the steady deflections and twist, a numerical iteration process is used. First, to start, the rigid angle of attack α_0 is placed in Equation (28) and the pressure coefficient c_p is evaluated at a number of chordwise and spanwise points on the wing. The pressures, $\Delta p_z = q c_p$, are then placed into Equations (8) to obtain the generalized forces Q_i by numerical integration of the pressure distribution. Placing the Q_i into Equation (7) without the mass term $[M]\ddot{q}$, allows one to solve for the deflections q . Placing q into Equation (29) then gives a new $\alpha(x)$ distribution to start the process over again. For low air speeds, three iterations were sufficient for convergence. At the higher speeds of this investigation, up to seven iterations were used.

Experiment

Experimental aeroelastic tests were conducted on a series of 13 flat plate wings with different ply configurations at 0° and 30° sweep. The 0° sweep configurations complemented some earlier studies by Hollowell and Dugundji⁹, while the 30° forward sweep configurations ($\Lambda = -30^\circ$) were new.

The wing models for the tests were similar to those used in Reference 9, and the properties are described more fully there. Basically, each model had an effective length of 305 mm (12 in.) and a chord of 76 mm (3 in.), giving the wings a length to chord ratio $l/c = 4$. The models were all made up of 6 plies of Hercules AS1/3501-6 graphite/epoxy with 7 different ply layouts, namely, $[0_2/90]_s$, $[+15_2/0]_s$, $[+15/0]_s$, $[+30_2/0]_s$, $[+30/0]_s$, $[+45_2/0]_s$, $[+45/0]_s$. By reversing the direction of flow, another 6 configurations were obtained, $[-15_2/0]_s$, $[-15/0]_s$, ... to give a total of 13 configurations. These spanned a good range of bending-torsion stiffness coupling.

Structural deflection tests were conducted on the wings by placing them in a stiff jig frame and subjecting them to force and moment couples applied near the tip, and carefully monitoring the resulting tip deflection and twist.

All wind tunnel tests were performed in the M.I.T. Acoustic Wind Tunnel. This tunnel has continuous flow with a 1.5×2.3 m (5×7.5 ft.) free-jet test section 2.3 m (7.5 ft.) long, located inside a large anechoic chamber, and can be varied continuously up to approximately 30 m/s (98.4 ft/sec). The model was mounted vertically on a turntable which could readily be rotated to change the angle of attack. See Figure 3. Additionally a large, heavy, swivel clamp joint at the wing root could be rotated to change the angle of sweep. For the present tests, only the unswept ($\Lambda = -30^\circ$) positions were investigated.

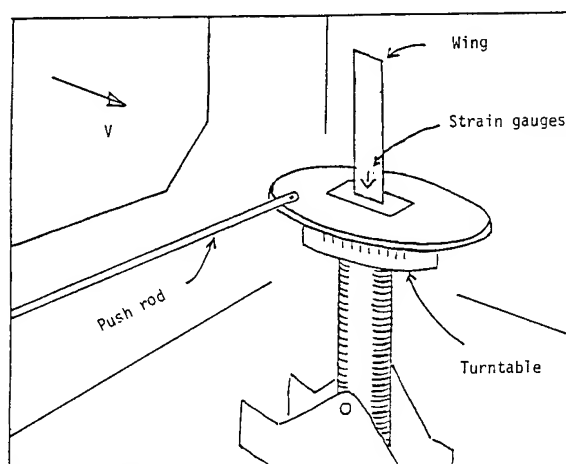


Fig. 3 Test Set-up in Wind Tunnel

The wind tunnel tests were carefully monitored by video movies, photographs, and strain gages in an attempt to obtain the static deflections and angles under airloads as well as the flutter vibration amplitudes and frequencies. An overhead mirror was mounted above the test wings, and by proper angles, one could look down upon the wing tip and view it against a grid painted on the turntable base. Subsequent analysis of video movies taken under floodlight and strobe light conditions (to slow down the motion), allowed one to obtain tip deflections and twists under both steady airloads and during flutter. The movies were taken both looking down upon the wing and also looking directly at the wing.

Before each wind tunnel test, the natural vibration frequency of a wing was checked. With the wing mounted for the wind tunnel test, a simple initial deflection in twist and in bending was given to the wing and then quickly released. The resulting oscillations picked up by the strain gages were recorded on a strip chart, and gave a good estimate of the bending and torsion frequencies of the wing.

For the wind tunnel tests, the wings were set at zero angle of attack and the tunnel was run up to a given airspeed. The angle of attack was then varied to check for possible flutter conditions. If flutter was found, the strain gage signals were recorded and the frequency additionally checked with a strobe light. After finishing tests at that airspeed, the angle of attack was reduced, the airspeed increased by 1 m/s, and the test procedure was repeated. This allowed the flutter boundary curve of flutter speed versus root angle of attack to be mapped out for a wing. After the flutter boundary curve was defined, certain points were selected for further examination. For these tests, more complete records were taken including video movies and photographs in order to check the flutter amplitudes, frequencies and average static positions of the wing. Additionally, on the unswept wings ($\Lambda = 0^\circ$), tests were run at several fixed airspeeds to observe the variation of steady wing tip deflection and twist with root angle of attack under steady airload conditions.

4. Results

The present studies explored the nonlinear as well as the linear aspects of flutter and divergence. The models were sufficiently flexible so that when they actually fluttered or diverged, they were not destroyed, but rather went into steady-state limit cycles which were limited by the nonlinear airforces (stalling).

The structural deflection and twist characteristics of a typical wing under given applied forces and moments is given in Figure 4. Since the wings were 30.5 cm length, the deflections are over large ranges. The linear 5 mode Rayleigh-Ritz analysis gave good correlation for small amplitudes, including the bending-torsion stiffness coupling. Occasional buckling occurred for the low angle, lightly coupled layups due to slight camber imperfection effects resulting from ply layup inaccuracies.

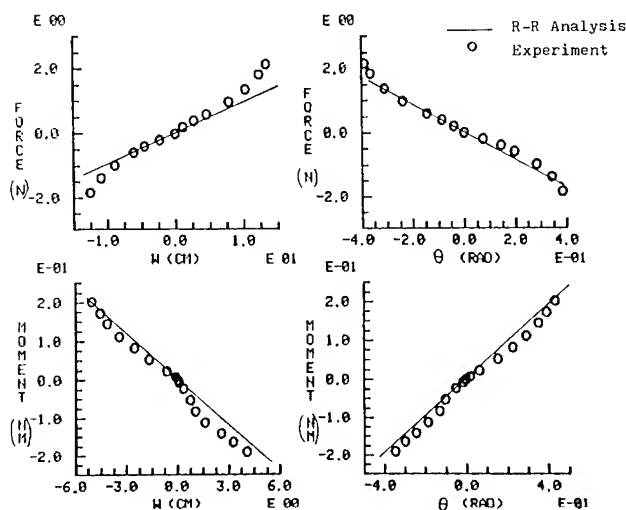


Fig. 4 Structural Deflections of $[+30_2/0]_S$ Wing

The natural frequencies of the wings are given in Table 1. These were found from the initial deflection tests prior to the wind tunnel runs, and agreed reasonably well with the theoretical calculations and with previous values given by Reference 9, and by Jensen, Crawley, and Dugundji.¹⁶ Occasionally, the third mode could not be picked out by the transient decay.

Table 1 Natural Frequencies of Wings

WING	First Bending		First Torsion		Second Bending	
	Theo. (hz)	Exp. (hz)	Theo. (hz)	Exp. (hz)	Theo. (hz)	Exp. (hz)
[0 ₂ /90] _s	10.8	10.5	39	44	67	****
[+15 ₂ /0] _s	8.5	9.2	48	48	58	66
[±15/0] _s	9.9	10.0	50	52	63	77
[+30 ₂ /0] _s	6.0	7.1	60	60	41	44
[±30/0] _s	7.8	8.0	65	68	50	****
[+45 ₂ /0] _s	4.6	6.2	55	48	31	32
[±45/0] _s	5.7	6.0	69	76	37	36

The flutter and divergence characteristics of these wings are presented in Figures 5 and 6 for the unswept and the forward swept wings respectively. These plots of flutter speed versus root angle of attack give the nonlinear (high angle of attack) behavior as well as the linear (low angle of attack) behavior. The frequency (Hz) of the resulting oscillations is also indicated on the graphs in order to show the change in flutter modes. As in Reference 9, four different type of aeroelastic phenomena are observed; bending-torsion flutter ($\omega_h < \omega < \omega_a$) and divergence at low tip angles of attack, and torsion stall flutter ($\omega \approx \omega_a$) and bending stall flutter ($\omega \approx \omega_h$) at high tip angles of attack. The sharp drop in torsion stall flutter speed versus root angle of attack was also reported by Rainey¹⁷ for isotropic wings, and probably results from the tip section going in and out of stall. Further studies of stall flutter were also conducted by Dugundji and Aravamudan¹⁸ and Dugundji and Chopra¹⁹ on 2-dimensional sections. The bending stall flutter is not very familiar, and was reported earlier in Reference 9. The divergence condition was noted when the angle of attack could not be set small enough to keep the wing from flipping over to either one side or the other. Generally, a bending stall oscillation at the low bending frequency would then begin for these flexible wings.

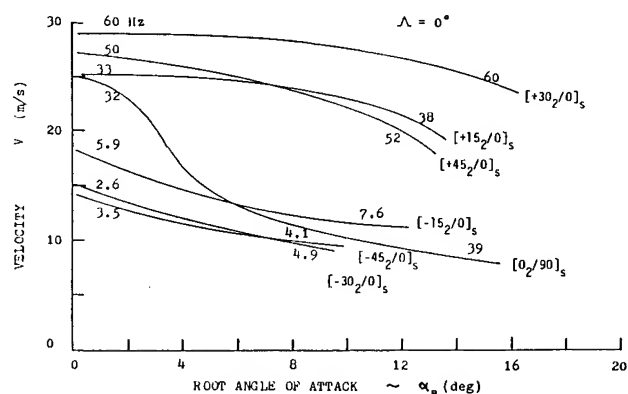


Fig. 5 Flutter and Divergence Boundaries ($\Lambda = 0^\circ$)

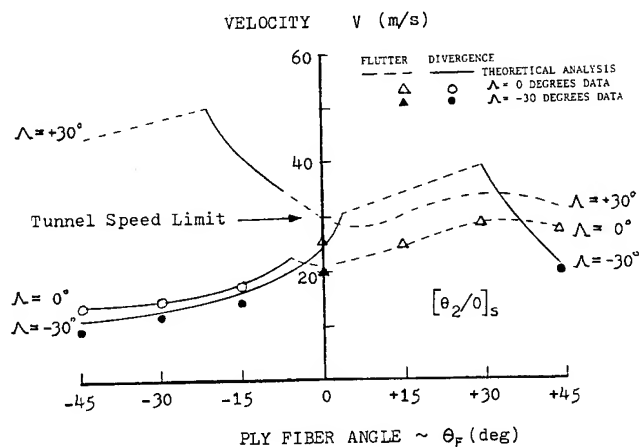


Fig. 7 Flutter and Divergence at Low Angles α_0

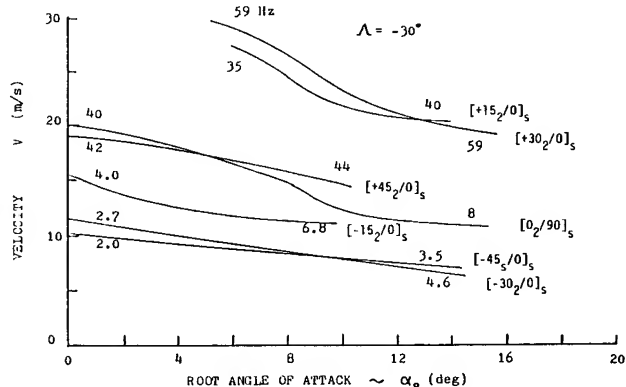


Fig. 6 Flutter and Divergence Boundaries ($\Lambda = -30^\circ$)

The linear flutter and divergence characteristics of the wings at low root angles of attack are shown in Figure 7 for the $[+0_2/0]_s$ family of wings. Similar, but less dramatic results, were obtained from the $[\pm 0_2/0]_s$ family. Figure 7 represents a crossplot from the data of Figure 5 and 6 at $\alpha_0 = 0$. For negative ply angles θ_F and forward sweep ($\Lambda = -30^\circ$), divergence dominates the aeroelastic behavior. Going to positive ply angles increases the divergence speed of the forward swept wing, and a higher flutter speed now limits the flight speed. However, too much positive ply angle ($+45^\circ$) results in a low divergence speed again since the bending stiffness becomes too low, and the coupling cannot overcome the geometric divergence tendency. A positive ply angle layup $[+15_2/0]_s$ seemed to be about optimum here, both from Figure 7 and from Figures 5 and 6. The linear 5 mode flutter and divergence analyses gave good correlation with these experimental results, particularly for the divergence, where 3-dimensional aerodynamic theory was used. It should be noted that the experimental trends shown in Figure 7 are also similar to the theoretical trends shown in Figure 7 of Hertz, Shirk, Ricketts, and Weisshaar.¹

The nonlinear steady airload deflections and twists of the wing tip are shown in Figures 8 and 9 for two contrasting wings, $[+30_2/0]_s$ and $[-30_2/0]_s$ with no sweep ($\Lambda = 0^\circ$). These were obtained from visual inspection of the resulting video movies and photos of the test, and show a highly nonlinear relation with root angle of attack, particularly for the $[-30_2/0]_s$ wing which diverges at 15 m/s. The contrasting character of the two wings, were one twists negatively to offset the root angle of attack change while the other twists positively to bring the tip rapidly to the stall condition, is readily apparent. The analytical calculations using the rough nonlinear theory including stall effects described earlier, give a reasonable correlation with theory.

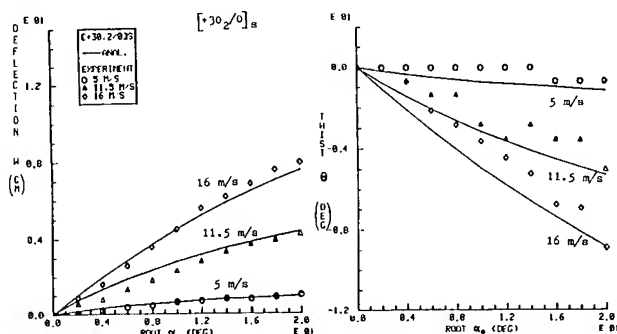


Fig. 8 Steady Airload Deflections of $[+30_2/0]_s$

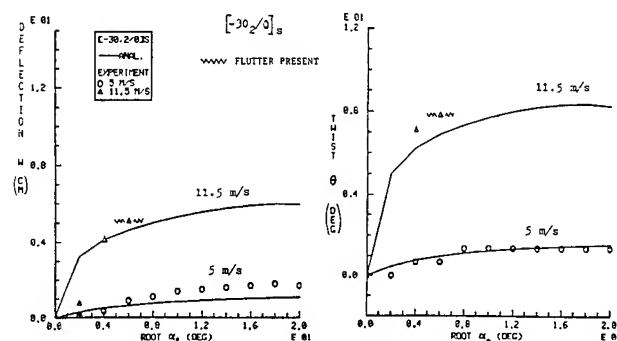


Fig. 9 Steady Airload Deflections of $[-30_2/0]_s$

The amplitudes, frequencies, and average static positions of the resulting flutter oscillations for the different wings are shown in Tables 2 and 3. These were measured visually from the video movies and photos, and give some interpretation to the nonlinear flutter behavior indicated in Figures 5 and 6. In particular, the character of the flutter, whether of a bending or a torsional nature, and the associated frequency, is apparent.

Table 2 Flutter Data, Unswept Wing ($\Lambda=0^\circ$)

WING	V (m/s)	α_c (deg)	w_{avg} (cm)	Δw (cm)	θ_{avg} (deg)	$\Delta\theta$ (deg)	ω (hz)
[02/90]s	26	1	0.5	0.7	1.0	10.3	33
	13	10	2.4	0	3.5	9.8	40
[+152/0]s	25	1	0.2	0.2	0.7	8.1	32
	24	10	5.1	0.2	-4.0	19.3	37
[\pm 15/0]s	28	3	4.0	0.8	-0.7	8.5	37
	16	10	3.8	0	0.4	5.0	49
[\mp 15/0]s	21	1	4.3	0.5	4.8	14	43
	10	10	2.2	0.1	2.8	7.0	43
[-152/0]s	18	1	4.7	9.4	10.1	17.4	5.8
	13	10	3.3	11.7	7.9	28.4	7.6
[+302/0]s	29	0	-0.6	1.7	2.4	12	60
	28	12	7.9	4.0	-4.8	35	61
[\pm 30/0]s	27	10	11.7	1.2	-3.7	12	46
[\mp 30/0]s	24	1	13.5	1.3	13.5	8.8	40
	15	10	8.4	0.2	5.6	6.7	52
[-302/0]s	15	1	5.1	17.2	3.9	16	2.6
	8	10	3.0	4.5	4.9	5.8	4.9
[+452/0]s	27	1	2.1	3.6	2.2	23	25
	23	10	9.9	2.7	-2.7	20	26
[\pm 45/0]s	25	8	13.1	0.4	-2.4	3.2	44
	18	10	10.8	0.6	-4.2	6.8	49
[\mp 45/0]s	22	1	16.0	0.9	9.0	1.5	40
	14	10	12.2	0.1	6.3	6.3	55
[-452/0]s	14	1	10.9	12	10	14	3.5
	9	10	5.2	10.3	5.2	9.1	4.2

Table 3 Flutter Data, Forward Sweep ($\Lambda=-30^\circ$)

WING	V (m/s)	α_c (deg)	w_{avg} (cm)	Δw (cm)	θ_{avg} (deg)	$\Delta\theta$ (deg)	ω (hz)
[02/90]s	20	1	8.8	0	6.1	1.5	40
	18	10	8.3	11.0	1.5	3.0	8
[+152/0]s	21	10	12.2	1.1	-10.7	16.7	40
[\pm 15/0]s	25	1	7.8	0	-1.6	27	44
	18	10	8	0	-0.4	14.3	50
[\mp 15/0]s	19	1	6.2	11.9	4.8	9.5	4.7
	15	10	5.2	12.8	4.7	9.3	7.5
[-152/0]s	15	1	3.2	15	8.3	23.4	4.0
	12	10	3.9	12.9	7.7	18.1	6.8
[+302/0]s	21	10	14.5	0.8	-18	12	59
[\pm 30/0]s	22	1	19.8	0.7	-6	44	33
	20	10	21.5	1	-7	42	31
[\mp 30/0]s	17	1	6.9	19.7	4.0	12	3
	13	10	7.5	9.5	2.5	5	5.6
[-30/0]s	11	1	4.1	18.1	7.0	22	2.7
	8	10	3.7	10.9	3.5	17	4.6
[+452/0]s	20	1	16.9	0.2	6.9	25	42
	15	10	16.9	0.7	14.5	19.1	44
[\pm 45/0]s	20	1	19.5	3.0	-10.5	11	5.7
	14	10	12.9	6.3	3.5	21	4.8
[\mp 45/0]s	14	2	9.5	19	5.5	11	2.8
	11	10	9	14	1.5	1	4.3
[-452/0]s	10	1	7.1	8.6	8.4	14.7	2
	8	10	6.9	11.6	7.5	15	3.5

5. Conclusions

An analytical and experimental investigation was made of the aeroelastic deflection, divergence, and flutter behavior of unswept and 30° swept forward graphite/epoxy cantilevered plate wings, with various amounts of bending-torsion stiffness coupling, in incompressible flow. The present work complements an earlier investigation by Hollowell and Dugundji⁹ on unswept wings. Both the low angle of attack (linear) and the high angle of attack (nonlinear) properties were explored. The investigation extends the experimental base for aeroelastic tailoring with composites.

Structural deflection tests on the 6 ply composite plate type wings, revealed reasonable linear bending and twisting behavior up to large deflections. The bending-twist couplings were well predicted by Rayleigh-Ritz analysis. Occasional buckling occurred for low angle, lightly coupled layups due to ply layup inaccuracies.

The divergence and flutter investigation showed the large variation in aeroelastic properties possible by changes in ply layups. Four different types of aeroelastic phenomena were observed; bending-torsion flutter and divergence at low tip angles of attack (linear range), and torsion stall flutter and bending stall flutter at high tip angles of attack (nonlinear range).

The flutter and divergence characteristics at low angles of attack were well predicted by linear theory. A 5 mode Rayleigh-Ritz analysis gave good correlation with experiment for divergence using 3-dimensional aerodynamics, and gave reasonable correlation with experiment for flutter using 2-dimensional, velocity parallel, unsteady aerodynamics. The effects of ply orientation were well predicted. A positive ply angle layup $[+15_2/0]_S$ seemed to have efficient bending-torsion coupling to overcome the adverse geometric divergence effect of the 30° forward swept wing.

Nonlinear steady airload deflections and twists of the wing tips were obtained, and gave good indication how the wings were behaving aeroelastically. Analytical calculations using rough nonlinear theory including stalling effects gave reasonable correlation with experiment.

The amplitudes, frequencies, and average static position of selected flutter points were measured and recorded. This helped identify the severity and character of the flutter modes encountered. The nonlinear flutter tests gave additional insight into the stall behavior of flexible wings, which had been pointed out earlier by Rainey.¹⁷

Acknowledgements

The authors wish to acknowledge the assistance of Robert Dare in the experiments and data reduction. Also, they wish to acknowledge the support of the United States Air Force and the Air Force Office of Scientific Research under Grant AFOSR 82-0071, Dr. Anthony Amos, technical monitor.

References

1. Hertz, T.J., Shirk, M.H., Ricketts, R.H. and Weisshaar, T.A., "On the Track of Practical Forward Swept Wings", *Astronautics and Aeronautics*, Vol. 20, No. 1, January 1982, pp. 40-53.
2. Krone, N.J., "Divergence Elimination with Advanced Composites," AIAA Paper No. 75-1009, August 1975.
3. Sherrer, V.C., Hertz, T.J., and Shirk, M.H., "Wind Tunnel Demonstration of the Aeroelastic Tailoring Applied to Forward Swept Wings", *Journal of Aircraft*, Vol. 18, No. 11, November 1981, pp. 976-983.
4. Blair, M., and Weisshaar, T., "Swept Composite Wing Aeroelastic Divergence Experiments", *Journal of Aircraft*, Vol. 19, No. 11, November 1982, pp. 1019-1024.
5. Weisshaar, T.A., Zeiler, T.A., Hertz, T.J., and Shirk, M.H., "Flutter of Forward Swept Wings", Proceedings of 23rd AIAA/ASME/ASCE/AHS Structures, Structural Dynamics and Materials Conference, New Orleans, LA, May 10-12, 1982, Part 2, pp. 111-121.
6. Miller, G.D., Wykes, J.H., Brosnan, M.J., "Rigid Body-Structural Mode Coupling on a Forward Swept Wing Aircraft", Proceedings of 23rd AIAA/ASME/ASCE/AHS Structures, Structural Dynamics, and Materials Conference, New Orleans, LA, May 10-12, 1982, Part 2, pp. 201-208.
7. Weisshaar, T.A., and Foist, B.L., "Vibration and Flutter of Advanced Composite Lifting Surfaces", Proceedings of 24th AIAA/ASME/ASCE/AHS Structures, Structural Dynamics, and Materials Conference, Lake Tahoe, NV, May 2-4, 1983, Part 2, pp. 498-508.
8. Noll, T.E., Eastep, F.E., Calico, R.A., "Active Flutter Suppression of Aeroelastic Instabilities on a Forward Swept Wing", Proceedings of 24th AIAA/ASME/ASCE/AHS Structures, Structural Dynamics, and Materials Conference, Lake Tahoe, NV, May 2-4, 1983, Part 2, pp. 577-588.
9. Hollowell, S.J., and Dugundji, J., "Aeroelastic Flutter and Divergence of Stiffness Coupled, Graphite/Epoxy Cantilevered Plates", *Journal of Aircraft*, Vol. 21, No. 1, January 1984, pp. 69-76. See also earlier version in 23rd AIAA/ASME/ASCE/AHS Structures, Structural Dynamics and Materials Conference, New Orleans, LA, May 10-12, 1982, Part 2, pp. 416-426.
10. Landsberger, B.J., "Aeroelastic Properties of Straight and Forward Swept Graphite/Epoxy Wings", M.I.T. Department of Aeronautics and Astronautics, M.S. Thesis, February 1983.
11. Ashton, J.E., and Whitney, J.M., *Theory of Laminated Plates*, Technomic Publishing Co., Stamford, CT, 1970.

12. DeYoung, J., and Harper, C.W., "Theoretical Symmetrical Span Loading at Subsonic Speeds", NACA Report 921, 1948.
13. Bisplinghoff, R.L., Ashley, H., and Halfman, R.L., Aeroelasticity, Addison-Wesley Publishing Co., Reading, Ma. 1955.
14. Spielberg, I.N., "The Two-Dimensional Incompressible Aerodynamic Coefficients for Oscillatory Changes in Airfoil Camber", Journal of the Aeronautical Sciences, Readers Forum, Vol. 20, No. 6, June 1953, pp. 432-434.
15. Riegels, F.W., Aerfoil Sections, Butterworths Publishing House, 1961.
16. Jensen, D.W., Crawley, E.F., and Dugundji, J., "Vibrations of Cantilevered Graphite/Epoxy Plates with Bending-Torsion Coupling", Journal of Reinforced Plastics and Composites, Vol. 1, July 1982, pp. 254-269.
17. Rainey, G.A., "Preliminary Study of Some Factors which Affect the Stall-Flutter Characteristics of Thin Wings", NACA TN-3622, March 1956.
18. Dugundji, J. and Aravamudan, K., "Stall Flutter and Nonlinear Divergence of a Two-Dimensional Flat Plate Wing", M.I.T. Aeroelastic and Structures Research Laboratory, ASRL-TR-159-6, Air Force Office of Scientific Research, AFOSR TR 74-1734, July 1974.
19. Dugundji, J. and Chopra, I., "Further Studies of Stall Flutter and Nonlinear Divergence of Two-Dimensional Wings", M.I.T. Aeroelastic and Structures Research Laboratory, ASRL TR 180 -1, NASA CR-144924, August 1975.

V. UTILIZATION OF ATFs AS AN ANALYSIS TOOL

With the derivation of the ATF completed, it is now possible to apply equation (14) to the task of finding the best possible exciter locations, or at least evaluating what modes may or may not be excited by a particular exciter location.

To accomplish this it is necessary to solve equation (14) for all possible combinations of exciter and response locations within the frequency range of interest for the modal test. For example, if a full size analytical model were reduced to "n" dofs, then normally "n" response and "n" exciter locations are available for analysis, with $2 * n^2$ ATFs possible (magnitude & phase).

In some cases this number can be reduced by physical constraints, such as the physical inability to actually position an exciter "stinger" at the proper location and orientation. Obviously, if it is impossible to drive the structure at a particular location, there is no need to compute the $2 * n$ ATFs for that location other than for academic interest.

Even with some reduction in the number of ATFs to be computed and inspected, the task might at first appear formidable. Indeed, to evaluate and compare possibly many thousands of ATFs might seem an overwhelming task. However, with the aid of a computer, the job can be reduced to a manageable size both for the creation of the ATFs and for their eventual analysis as will be discussed later.

Creating a computer algorithm to obtain the ATFs is not a very difficult task, but it can consume considerable computer time based on the number of ATFs generated as well as the frequency range and interval. For purposes here, the initial work should be to create a program to:

1. solve for the ATFs as a function of frequency
2. store the accumulated data in some form which can be easily later utilized for selection.

VI. QUALIFYING ATF PEAKS AS TRUE RESONANT RESPONSES

Once the accumulated data from above is available for further analysis, the next step in exciter location selection involves establishing the criteria that will determine which peak magnitudes and associated phase angles of an ATF "qualify" as true resonant responses to the given target frequencies. In other words, it is the contention of this paper that not all peaks meet the requirements of resonance for a given target frequency near them, both from the standpoint of not actually being related and also from not satisfying the additional requirements of resonance.

To be a true resonant peak, representing an acceleration at the response point for a force at the exciter point for some target frequency, the following requirements are made:

1. The magnitude of the ATF must have passed thru an inflection point (maximum).
2. The frequency of this peak must be within some defined bandwidth on either side of a target frequency.
3. The associated phase angle must have passed thru the $\pm \pi/2$ point at which the forcing frequency equals the undamped natural frequency within the same bandwidth.

It might be argued at this point that it is sufficient to satisfy requirements 1 and 2, but it is felt that adding the extra requirement practically guarantees a "true" resonant response rather than just a "good" response. Analytical data obtained for an actual test has confirmed that, in some cases, peaks appearing to be resonant responses did not actually have a resonant phase shift associated with them. They came quite close in some cases, but didn't qualify (See Figures 1 & 2). This might well be an indication that the mode shape at this particular response dof is not very pure and should probably not be used for exciter selection purposes. In any case, if required, the criteria of phase angle shift can always be relaxed or deleted by the analyst.

In selecting both the frequency interval for ATF generation, and the bandwidth for resonant peak selection, some factors to keep in mind are:

1. system damping, (which will affect the amount by which a target frequency differs from its equivalent center frequency peak on the ATF),
2. closeness of the target frequencies to each other, (which will affect the necessary frequency interval for ATF computation).

At this time, no definitive rules or algorithms have been developed to automate the selection of a frequency interval and bandwidth. Good engineering judgement and common sense are needed. If the target frequencies are well spaced and damping is small, it is reasonable to increase the frequency interval for ATF computation as well as decrease the selection bandwidth for peak qualification.

VII. EXCITER LOCATION SELECTION

With the technique of peak selection established, it is necessary to devise some means to store the qualified acceleration level peaks so that final selection of driver locations can be readily accomplished.

SELECTION AND EVALUATION OF OPTIMUM EXCITER
LOCATIONS FOR MODAL TESTING VIA AUTOMATED
ACCELERATION TRANSFER FUNCTION ANALYSIS

84-0996

David N. Kopec*

Pasquale Girolamo**

ABSTRACT

Modal testing to extract system natural frequencies and mode shapes has always been a somewhat trial and error proposition, with initial exciter locations being determined by a combination of experience, intuition, accessibility, some analytical analysis, and luck. If the initial exciter selections failed to separate the required responses, a "shotgun" approach was usually employed until either test time expired or all desired modes and frequencies were finally found.

However, there is a relatively convenient and easily applied method, utilizing acceleration transfer function data, that will provide the modal test analyst with a pre-test selection of exciter locations that will adequately drive the test structure to obtain the desired mode shapes and frequencies of the system.

In addition, each analytically selected exciter location can be compared or rated against the other possible selections to determine how well it excites a given mode shape.

Further, since acceleration transfer functions can be directly related to expected test accelerometer output, it is possible to provide the test conductor with a set of abort channel accelerometer locations and magnitudes based on the maximum desired test levels.

The method itself involves creation of a three-dimensional summary matrix of "qualified" peak acceleration levels, based on selection criteria presented. This matrix is then "viewed" from various axes to provide two dimensional summary arrays that simplify exciter selection.

The topics discussed in the paper are applicable to virtually any type of modal test, and can be implemented on a computer.

II. NOMENCLATURE AND DEFINITIONS

$[\phi]$ = system modes matrix

$[M]$ = system mass matrix

$[K]$ = system stiffness matrix

$\{\delta\}_R$ = selector vector for desired response dof

$\{\delta\}_F$ = selector vector for desired exciter dof

ω = circular system frequency
(target frequency)

Ω = driver frequency

ζ = modal damping coefficient

X/F_0 = output acceleration magnitude for a
1 lb. input exciter force, i.e.
transfer function magnitude/phase

ATF(s) = Acceleration Transfer Function(s)

dof = degree of freedom

(i) = ith response degree of freedom

(j) = jth target frequency

(k) = kth exciter degree of freedom

F_0 = peak magnitude of a sinusoidal force

$F(t)$ = time dependent exciter force

...
 x, \dot{x}, \ddot{x} = discrete displacement, velocity,
and acceleration

...
 q, \dot{q}, \ddot{q} = modal displacement, velocity, and
acceleration

C = discrete damping

s = Laplace Operator

* Staff Engineer, Analytical Mechanics Section

** Senior Engineer, Analytical Mechanics Section
Member AIAA

Figure 1

Typical Acceleration Transfer Function
(3rd Mode Excitation w/o 2nd Mode Excitation)

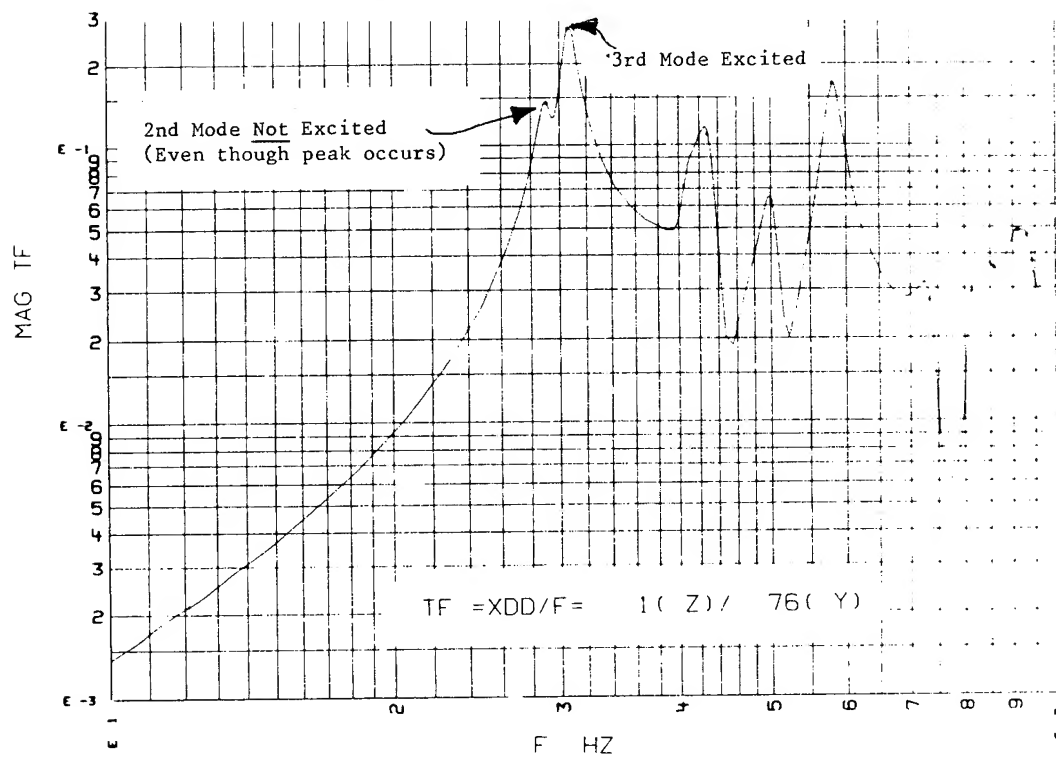
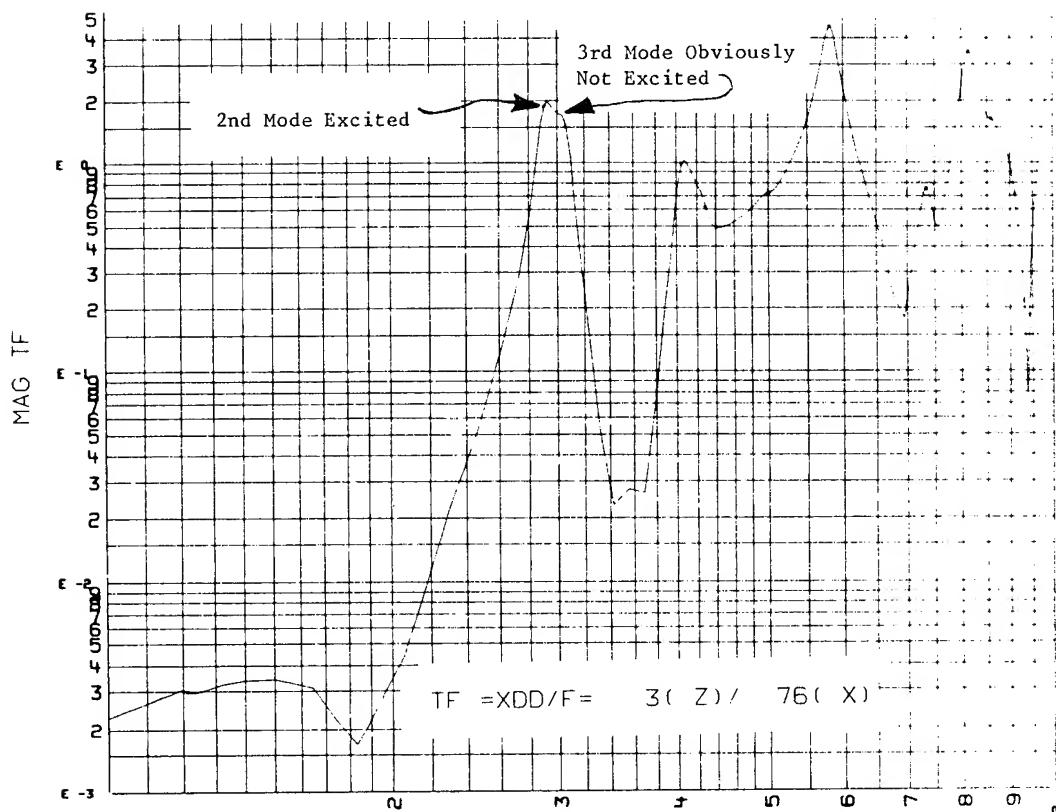


Figure 2

Typical Acceleration Transfer Function
(2nd Mode Excitation w/o 3rd Mode Excitation)



Since there are three basic variables involved (exciter locations, response locations, and target frequencies), it would seem appropriate to store the acceleration magnitudes of qualified peaks in a three (3) dimensional array, with each axis representing one of the variables. This concept, illustrated in Figure (3), has the advantage of simple computer implementation along with the ability to have "slices" of the matrix easily viewed from various axes. The real importance of this matrix can be better understood when it is realized that all the necessary information from the entire set of ATFs (normally several thousand) has been distilled into this one block of data in easily accessible form.

With the data available in this form it is simply a matter of the analyst determining which type of information (or view) is desired. The three possible views of the matrix that can be used are summarized in Table (1), with two of the three views illustrated by Figure (3); and typical output from an actual computer run displayed in Tables 2 & 3.

MATRIX VIEW

Target freq(j)

Exciter dof(k)

Response dof(i)

OUTPUT(2 dimensional array of peak magnitudes*)

(n) exciter dofs

(n) : see :
response : TABLE 2 :
dofs : :

(m) target freqs.

(n) : see :
response : TABLE 3 :
dofs : :

(m) target freqs.

(n) : not :
exciter : illustrated :
dofs : :

TABLE (1)

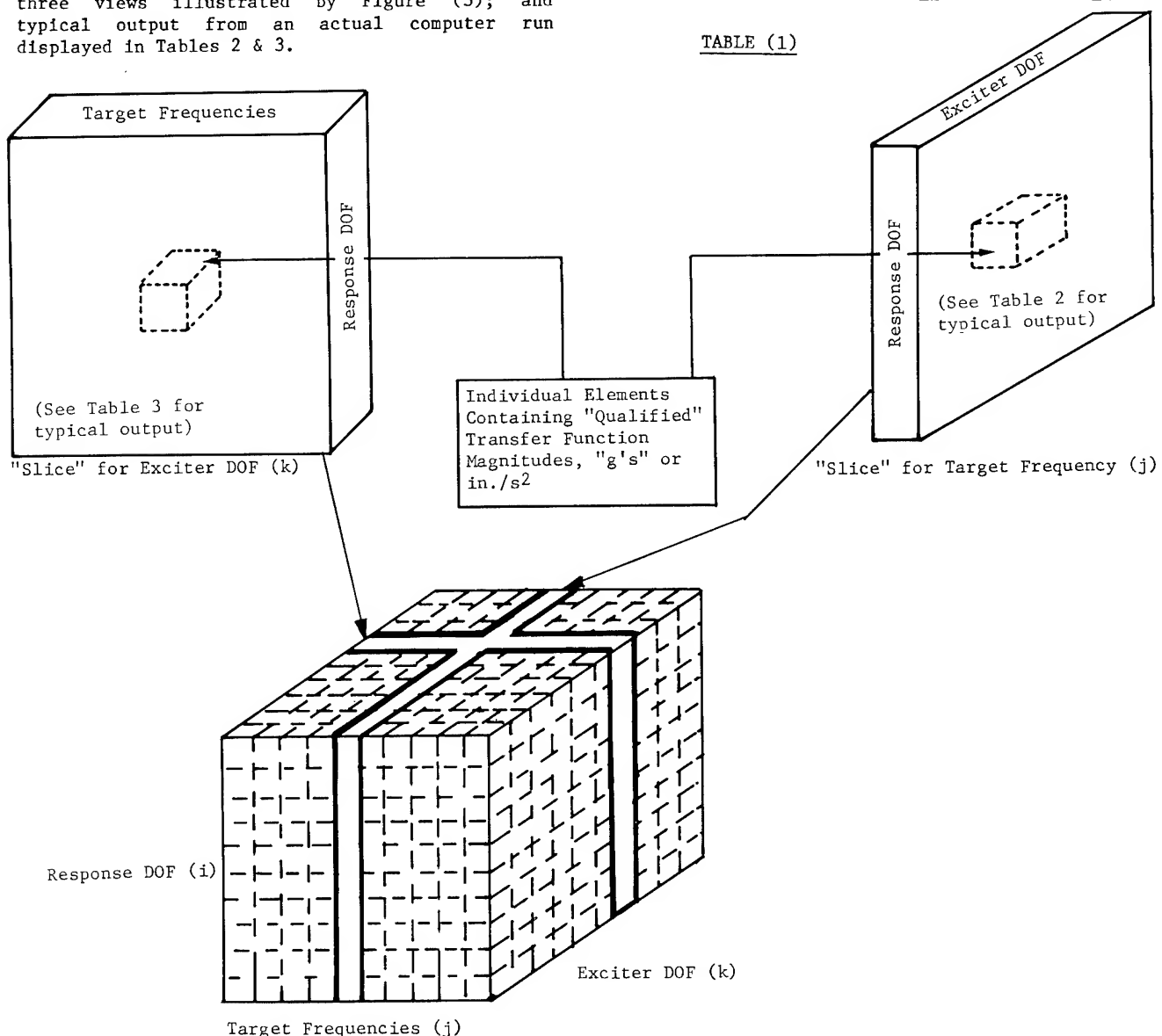


Figure 3 Three-Dimensional Summary Matrix of Transfer Function Magnitudes

TABLE (2)

Partial View of a Typical 3-D Summary Matrix*
for
a given Target Frequency

MODE # 2(= 29.35 HZ.)

FORCE COND. =	1(Z)	3(Z)	5(Z)	7(Z)	9(Z)	12(Z)	13(Z)	19(Z)	20(Z)	21(Z)	27(Z)	30(Z)	76(X)	76(Y)	76(Z)
RESPONSE PT.															
1(Z)	0.00	0.01	0.04	0.00	0.00	0.06	0.01	0.01	0.05	0.09	0.02	0.06	0.10	0.13	0.05
3(Z)	0.01	0.21	0.92	0.03	0.03	1.10	0.32	0.29	0.91	1.59	0.31	1.01	1.75	2.23	0.92
5(Z)	0.04	0.92	3.37	0.17	0.12	4.98	1.44	1.34	4.18	7.30	1.40	4.57	8.41	9.87	4.21
7(Z)	0.00	0.03	0.17	0.01	0.00	0.21	0.06	0.07	0.15	0.29	0.07	0.21	0.39	0.47	0.15
9(Z)	0.00	0.03	0.12	0.00	0.00	0.13	0.07	0.11	0.11	0.20	0.07	0.19	0.33	0.47	0.11
12(Z)	0.06	1.10	4.98	0.21	0.13	6.06	1.45	1.23	4.87	8.86	1.79	5.75	10.83	12.53	4.90
13(Z)	0.01	0.32	1.44	0.06	0.07	1.45	0.36	0.31	1.13	2.10	0.45	1.43	2.60	3.12	1.14
19(Z)	0.01	0.29	1.34	0.07	0.11	1.23	0.31	0.49	0.98	1.71	0.41	1.24	2.26	2.89	0.99
20(Z)	0.05	0.91	4.18	0.15	0.11	4.87	1.13	0.98	3.76	7.00	1.46	4.61	8.61	10.24	3.79
21(Z)	0.09	1.59	7.30	0.29	0.20	8.86	2.10	1.71	7.00	12.80	2.60	8.30	15.56	18.30	7.05
27(Z)	0.02	0.31	1.40	0.07	0.07	1.79	0.45	0.41	1.46	2.60	0.50	1.63	3.12	3.55	1.47
30(Z)	0.06	1.01	4.57	0.21	0.19	5.75	1.43	1.24	4.61	8.30	1.63	5.24	9.95	11.54	4.65
76(X)	0.10	1.75	8.41	0.39	0.33	10.83	2.60	2.26	8.61	15.56	3.12	9.95	17.95	22.46	8.68
76(Y)	0.13	2.23	9.87	0.47	0.47	12.53	3.12	2.89	10.24	18.30	3.55	11.54	22.46	24.63	10.33
76(Z)	0.05	0.92	4.21	0.15	0.11	4.90	1.14	0.99	3.79	7.05	1.47	4.65	8.68	10.33	3.82
120(X)	0.08	1.37	6.60	0.31	0.24	8.61	2.03	1.73	6.81	12.37	2.50	7.96	14.25	18.08	6.86
120(Y)	0.09	1.53	6.70	0.33	0.29	8.73	2.10	1.88	7.09	12.80	2.51	8.15	15.98	17.40	7.16
120(Z)	0.04	0.82	3.74	0.12	0.10	4.20	0.99	0.84	3.26	6.06	1.26	4.00	7.64	8.73	3.28
123(X)	0.03	0.58	2.90	0.12	0.10	3.62	0.86	0.72	2.84	5.17	1.05	3.33	5.93	7.62	2.86
123(Y)	0.04	0.62	2.84	0.13	0.05	3.45	0.79	0.67	2.75	5.02	0.98	3.17	6.45	6.83	2.77
123(Z)	0.04	0.94	4.00	0.14	0.11	4.73	1.17	0.89	3.70	6.80	1.39	4.42	8.46	9.60	3.72
132(X)	0.14	3.12	12.34	0.51	0.55	17.23	4.49	3.61	13.89	25.14	5.08	16.34	30.25	35.45	14.00
132(Y)	0.14	5.41	13.19	0.52	0.34	20.50	4.30	3.72	18.05	27.82	4.32	14.69	29.24	29.46	18.19
132(Z)	0.05	1.20	4.43	0.19	0.16	6.26	1.82	1.62	5.19	9.11	1.76	5.72	10.63	12.27	5.23
135(X)	0.13	2.58	11.72	0.49	0.51	15.38	3.43	2.93	12.29	22.90	4.88	15.53	28.36	34.17	12.39
135(Y)	0.13	2.83	12.00	0.44	0.30	13.80	4.09	4.05	11.84	20.42	3.85	12.73	23.98	26.51	11.95
135(Z)	0.00	0.12	0.25	0.01	0.00	0.28	0.26	0.25	0.36	0.41	0.11	0.28	0.46	0.85	0.36
143(X)	0.06	1.30	6.28	0.24	0.24	8.26	1.85	1.64	6.36	11.93	2.55	7.99	14.26	18.35	6.41
143(Y)	0.04	1.01	5.25	0.13	0.00	4.46	1.75	1.94	3.89	6.20	1.11	3.44	6.46	7.56	3.92
143(Z)	0.01	0.17	0.78	0.03	0.04	1.03	0.24	0.19	0.80	1.50	0.32	1.01	1.93	2.25	0.80
155(X)	0.02	0.58	1.45	0.08	0.06	2.40	0.11	0.22	2.18	3.52	0.57	1.97	4.19	3.85	2.20
155(Y)	0.03	0.63	2.34	0.12	0.07	3.53	1.11	1.11	3.00	5.10	0.95	3.10	5.42	6.86	3.02
155(Z)	0.03	0.58	2.20	0.10	0.08	3.15	0.91	0.84	2.63	4.60	0.89	2.89	5.26	6.26	2.66
150(X)	0.04	0.67	2.92	0.15	0.08	4.27	0.90	0.94	3.24	6.10	1.32	4.10	6.85	9.89	3.26
150(Y)	0.00	0.17	0.00	0.00	0.00	0.52	0.52	0.87	0.60	0.91	0.38	1.10	2.52	2.38	0.60
150(Z)	0.00	0.00	0.19	0.00	0.00	0.03	0.00	0.00	0.00	0.07	0.08	0.22	0.40	0.55	0.00
158(Z)	0.33	6.22	27.94	1.19	0.92	34.54	8.65	7.15	27.70	50.17	10.17	32.78	61.72	71.80	27.95

TABLE (3)

Partial View of a Typical 3-D Summary Matrix*
for
a given Exciter DOF

FORCING POINT = 76(X)

F(NATURAL)S = 12.14 29.35 34.95 40.88 44.86 50.40

RESPONSE PT.	Good Response	No Response
1(Z)	0.10	0.10
3(Z)	2.89	1.75
5(Z)	1.59	8.41
7(Z)	0.46	0.39
9(Z)	0.50	0.33
12(Z)	0.03	10.83
13(Z)	6.37	2.60
19(Z)	7.32	2.26
20(Z)	3.35	8.61
21(Z)	0.74	15.56
27(Z)	1.97	3.12
30(Z)	4.69	9.95
76(X)	8.47	17.95
76(Y)	15.93	22.46
76(Z)	3.38	8.68
120(X)	7.18	14.25
120(Y)	14.08	15.98
120(Z)	4.18	7.64
123(X)	1.71	5.93
123(Y)	7.12	6.45
123(Z)	4.07	8.46
132(X)	3.32	30.25
132(Y)	49.77	29.24
132(Z)	3.97	10.63
135(X)	1.19	28.36
135(Y)	28.91	23.98
135(Z)	3.24	0.46
143(X)	3.91	14.26
143(Y)	20.54	6.46
143(Z)	0.71	1.93
155(X)	0.20	4.19
155(Y)	2.93	5.42
155(Z)	2.24	5.26
150(X)	6.85	6.85
150(Y)	10.98	2.52
150(Z)	2.57	0.40
158(Z)	9.00	61.72

Notes:

* units = in/sec² (output) / 1 lbf (input)

** For this particular exciter DOF, there are many response DOFs with non-zero values indicating qualified resonant peaks. This exciter is thus identified as a good exciter for target frequency #2 (and for several others).

*** Target frequency #3 will definitely not be excited by this particular exciter DOF.

Similar data is available, but not presented, which illustrates that target frequency #3 is excited while #2 is not (for the same exciter node, but in a different orientation). See Figures (2) and (3).

The entire three dimensional summary matrix can be further summarized by obtaining maximums across all target frequencies for a given exciter dof and a given response dof. Table 4 presents this summary-of-a-summary for all combinations of exciter and response dofs. Carrying the summary process to its conclusion, a single vector of "max-max" values (last line) can be extracted. Each element represents the largest response (abort maximum) at a given exciter location.

Table 4

Partial Abort Maximum Summary															
ABORT MAXIMUMS															
FORCE COND. =	1(Z)	3(Z)	5(Z)	7(Z)	9(Z)	12(Z)	13(Z)	19(Z)	20(Z)	21(Z)	27(Z)	30(Z)	76(X)	76(Y)	76(Z)
RESPONSE PT.															
1(Z)	0.00	0.03	0.13	0.01	0.02	0.11	0.16	0.29	0.27	0.24	0.02	0.08	0.14	0.19	0.27
3(Z)	0.03	1.03	3.03	0.16	0.18	1.10	2.25	2.58	1.20	1.59	0.68	1.62	6.04	5.56	1.21
5(Z)	0.13	3.03	25.27	1.21	1.08	4.98	4.85	7.93	7.21	9.88	3.18	8.67	15.83	9.87	7.40
7(Z)	0.01	0.16	1.21	0.07	0.08	0.65	0.73	1.35	1.26	1.18	0.17	0.49	0.76	0.87	1.30
9(Z)	0.02	0.18	1.08	0.08	0.35	0.94	1.35	2.40	2.19	2.00	0.31	0.78	1.07	2.22	2.25
12(Z)	0.11	1.10	4.98	0.65	0.94	7.02	8.04	14.50	13.05	12.19	1.79	5.75	10.83	12.53	13.42
13(Z)	0.16	2.25	4.85	0.73	1.35	8.04	11.48	20.54	18.67	16.94	1.50	5.26	6.37	12.22	19.20
19(Z)	0.29	2.58	7.93	1.35	2.40	14.50	20.54	36.55	33.27	30.22	2.15	9.38	7.32	14.04	34.21
20(Z)	0.27	1.20	7.21	1.26	2.19	13.05	18.67	33.27	30.15	27.22	1.75	8.37	8.61	10.24	31.00
21(Z)	0.24	1.59	9.88	1.18	2.00	12.19	16.94	30.22	27.22	24.40	2.60	8.30	15.56	18.30	28.00
27(Z)	0.02	0.68	3.18	0.17	0.31	1.79	1.50	2.15	1.75	2.60	0.50	1.63	3.12	3.76	1.77
30(Z)	0.08	1.62	8.67	0.49	0.78	5.75	5.26	9.38	8.37	8.30	1.63	5.24	9.95	11.54	8.61
76(X)	0.14	6.04	15.83	0.76	1.07	10.83	6.37	7.32	8.61	15.56	3.12	9.95	48.84	33.35	8.68
76(Y)	0.19	5.56	9.87	0.87	2.22	12.53	12.22	14.04	10.24	18.30	3.76	11.54	33.35	30.51	10.33
76(Z)	0.27	1.21	7.40	1.30	2.25	13.42	19.20	34.21	31.00	28.00	1.77	8.61	8.68	10.33	31.87
120(X)	0.12	5.25	12.69	0.62	0.96	8.61	5.41	6.27	6.81	12.37	2.50	7.96	42.60	28.57	6.92
120(Y)	0.17	4.93	7.44	0.77	0.88	8.73	10.83	12.44	7.09	12.80	3.32	8.15	32.02	27.00	7.16
120(Z)	0.26	1.48	11.31	1.26	2.10	12.50	17.90	31.75	28.81	26.06	2.09	7.89	7.64	8.73	29.62
123(X)	0.07	2.79	2.90	0.16	0.51	3.62	1.26	3.23	3.62	5.17	1.05	3.33	22.88	15.08	3.79
123(Y)	0.11	2.50	13.68	0.66	0.90	5.25	7.59	13.36	12.01	10.76	1.68	3.99	12.87	13.67	12.36
123(Z)	0.27	1.45	7.48	1.35	2.26	13.47	19.34	34.41	31.20	28.20	2.20	8.58	8.46	9.60	32.08
132(X)	0.37	3.12	19.87	1.15	6.44	17.23	5.12	11.88	13.89	25.14	5.97	16.34	30.25	42.31	14.00
132(Y)	0.59	17.55	16.01	2.74	3.03	20.50	38.51	44.19	20.56	27.82	11.71	27.74	49.77	95.19	20.72
132(Z)	0.08	1.98	16.51	0.79	1.42	6.26	4.24	6.84	5.64	9.11	1.76	5.72	10.63	12.27	5.74
135(X)	0.32	3.22	17.35	1.02	5.56	15.38	7.21	12.63	12.29	22.90	4.99	15.53	28.36	35.04	12.39
135(Y)	0.34	10.23	12.00	1.59	1.76	13.80	22.46	25.74	16.30	20.42	6.81	16.13	33.03	55.34	16.74
135(Z)	0.04	1.14	2.48	0.18	0.42	1.83	2.51	4.03	3.71	3.41	0.76	1.86	3.30	6.20	3.81
143(X)	0.21	4.51	37.23	1.78	3.36	8.26	7.82	14.63	13.30	12.04	3.17	7.99	35.04	24.10	13.67
143(Y)	0.28	7.28	54.52	2.59	3.94	7.53	15.96	18.31	16.67	15.21	4.85	11.47	48.68	39.44	17.13
143(Z)	0.09	2.18	18.00	0.86	0.78	2.47	3.38	6.29	5.65	5.04	0.70	2.29	11.35	6.29	5.81
155(X)	0.09	3.22	9.64	0.92	0.93	2.40	8.01	3.79	4.42	5.18	3.33	9.14	26.95	16.62	4.62
155(Y)	0.15	3.54	29.25	1.40	1.04	6.52	7.59	14.98	13.66	12.42	2.96	8.11	18.57	10.25	14.04
155(Z)	0.07	1.75	14.54	0.70	0.64	3.15	4.19	5.02	6.32	5.70	1.48	4.05	9.13	6.26	6.49
150(X)	0.12	5.07	21.35	1.03	1.24	4.27	5.20	6.79	6.35	7.41	1.59	5.00	41.37	26.35	6.64
150(Y)	0.21	5.19	11.39	0.63	3.62	3.48	8.55	9.80	6.76	7.74	3.24	8.39	42.85	28.43	7.06
150(Z)	0.04	0.91	1.90	0.19	0.61	1.87	2.68	4.84	4.38	3.94	0.61	1.46	2.57	4.93	4.50
158(Z)	1.20	6.60	39.20	5.76	9.85	64.14	83.77	148.10	133.86	107.85	16.93	44.85	81.61	133.72	137.56
202(X)	0.03	1.22	6.52	0.34	0.43	1.40	2.90	4.59	3.66	2.70	1.20	3.25	10.23	6.31	3.71
202(Y)	0.10	2.09	17.60	0.93	0.89	4.86	7.91	12.70	10.94	9.88	3.25	3.71	9.22	11.42	11.26
202(Z)	0.16	1.97	8.92	1.20	1.38	12.96	12.88	24.43	23.32	22.38	3.22	10.33	19.47	22.58	24.04
221(Z)	1.69	14.14	92.92	13.36	14.83	146.29	139.41	268.38	257.04	247.55	9.61	68.59	49.83	75.07	265.20
228(X)	0.59	4.99	50.43	4.81	5.31	43.73	49.20	91.11	84.80	78.98	8.11	20.21	17.18	9.49	87.28
228(Y)	0.46	6.61	62.92	3.89	4.22	29.55	38.77	69.59	63.23	57.14	11.02	27.49	13.64	12.63	64.93
228(Z)	1.51	13.11	81.85	11.89	13.19	131.30	124.16	239.44	229.68	221.59	14.73	63.33	69.72	116.96	236.99
260(Z)	0.93	15.04	91.89	5.33	7.57	47.84	64.74	116.42	106.33	97.03	18.36	36.33	126.24	78.46	109.39
262(Z)	1.15	20.36	160.61	8.71	9.28	59.94	81.36	141.90	130.67	120.67	30.94	47.81	38.45	44.71	134.45
264(Z)	0.67	17.02	132.80	6.90	6.80	8.37	59.99	93.46	73.72	53.19	25.91	70.54	101.59	62.24	74.73
266(Z)	0.99	24.23	200.63	10.34	10.05	25.19	88.34	138.34	108.19	76.74	38.52	105.39	43.24	50.97	109.65
.
.
.
320(Y)	0.24	7.15	44.42	2.12	1.75	9.81	15.71	18.00	8.42	14.75	4.76	11.27	31.93	38.66	8.50
320(Z)	0.13	2.97	24.62	1.17	0.89	3.31	2.93	3.24	2.92	2.61	0.80	3.14	15.47	8.57	3.00
338(X)	0.28	2.03	14.42	0.85	4.68	12.27	6.61	11.85	10.75	18.15	4.26	12.28	22.31	30.46	11.04
338(Y)	0.46	12.71	89.66	4.27	3.25	17.54	19.82	22.69	18.00	26.67	5.99	17.55	102.99	64.76	18.74
338(Z)	0.63	14.77	122.27	5.82	4.45	16.65	15.81	29.65	26.73	23.92	4.01	15.61	76.91	42.63	27.48
343(X)	0.34	3.52	18.18	1.07	5.83	17.04	7.62	13.31	13.63	25.39	5.40	17.21	31.42	37.83	13.75
343(Y)	0.48	14.32	27.70	2.23	2.47	18.39	31.44	36.06	19.84	26.38	9.55	22.61	40.56	77.58	20.38
343(Z)	0.08	2.31	2.44	0.36	0.40	2.66	5.07	5.81	4.28	3.88	1.54	3.65	6.54	12.51	4.40
351(X)	0.31	3.77	16.91	0.98	5.24	15.39	9.55	15.38	13.95	23.21	5.09	16.13	29.21	35.75	14.32
351(Y)	0.28	9.50	22.01	1.53	3.51	18.29	25.50	34.06	31.00	28.18	5.05	13.65	53.30	41.06	31.83
351(Z)	0.08	1.07	8.97	0.41	1.27	4.24	5.66	10.09	9.10	8.16	1.57	4.40	7.37	9.03	9.35
354(X)	0.30	4.57	16.68	0.96	5.04	15.48	12.16	17.17	15.59	23.51	5.25	16.59	30.74	36.91	16.00
354(Y)	0.37	13.70	31.45	2.10	4.80	26.33	37.21	45.42	41.31	37.51	7.59	17.20	67.22	61.22	42.41
354(Z)	0.12	1.94	15.87	0.75	1.81	5.88	8.12	14.54	13.11	11.75	2.20	6.19	10.26	12.82	13.47
MAX-MAX	1.69	24.23	200.63	13.36	14.83	146.29	139.41	268.38	257.04	247.55	38.52	105.39	126.24	133.72	265.20

VIII. FINAL THOUGHTS AND SUMMARY

This paper has presented detailed methodology for determination of the "best" exciter locations to extract target modes and frequencies plus actual abort channel acceleration levels and their magnitudes for a modal test of a structure.

The techniques discussed included utilization of acceleration transfer functions, selection criteria for resonant peaks of the transfer functions, and methods to utilize and inspect the data thus generated. Significant attention was focused on the selection criteria as well as means of determining the final exciter locations to be used in the test.

The methods discussed are general enough that they can, and should be, adapted to the user's specific situation. This entire paper should be considered as one more analytical tool for assistance in modal testing. It should be used in conjunction with any other available tools or techniques available.

IX. ACKNOWLEDGEMENT

The authors wish to thank Mr. J. R. Baratono for again making available the necessary time to write and assemble the text, and Mr. L.J. Demchak for technical assistance and support.

III. INTRODUCTION AND BACKGROUND

Modal testing has always been (and still is) a somewhat inexact discipline for the dynamics engineer. Some of the analytical questions and decisions that confront the test engineer before any tests are:

- 1) Do I have a good full sized analytical structural model representative of the physical structure?
- 2) Can I get a reduced analytical test model that is still representative of the full system?
- 3) How large should the reduced model be?
- 4) Which modes and frequencies do I want to extract from the test?
- 5) Where will the structure be forced to properly generate resonant responses for the modes/frequencies desired?

Usually the first four concerns are reasonably well answered by conventional wisdom and analytical orthogonality/cross-orthogonality checks, but the fifth question does not always have a clear-cut answer using existing conventional tools such as mode shape plots, etc. It is the purpose of this paper to address this last, and perhaps most difficult, question by providing an analytical approach to solve it.

IV. DERIVATION OF ACCELERATION TRANSFER FUNCTION

Assuming that an accurate analytically reduced model is available, and that accelerometers can be fastened at all the reduced dofs, it is now appropriate to direct efforts toward creating ATFs as the next step in determining "ideal" exciter locations.

Acceleration transfer functions are preferred in the analysis of exciter location selection since accelerometers are normally used as response read-out devices and thus can be directly related to the ATFs.

Presented, as a review, is a brief derivation of the acceleration transfer function for a damped system with harmonic excitation.

The equation of motion for a forced system with damping is:

$$[M]\ddot{x}(t) + [C]\dot{x}(t) + [K]x(t) = F(t) \quad (1)$$

This equation is transformed to the modal domain by:

$$\begin{aligned} x(t) &= [\phi] q(t) \\ \dot{x}(t) &= [\phi] \dot{q}(t) \\ \ddot{x}(t) &= [\phi] \ddot{q}(t) \end{aligned} \quad (2)$$

Substitutions (2) into (1), and premultiplying by $[\phi]^T$, (1) becomes:

$$[\phi]^T [M] [\phi] \ddot{q}(t) + [\phi]^T [C] [\phi] \dot{q}(t) + [\phi]^T [K] [\phi] q(t) = [\phi]^T F(t) \quad (3)$$

Utilizing mass normalized mode shapes,

$$[\phi]^T [M] [\phi] = [I] \quad (4)$$

$$[\phi]^T [K] [\phi] = [w^2] \quad (5)$$

$$[\phi]^T [C] [\phi] = [2\zeta w] \quad (6)$$

Substituting (4), (5), and (6) into (3):

$$\ddot{q}(t) + [2\zeta w] \dot{q}(t) + [w^2] q(t) = [\phi]^T F(t) \quad (7)$$

Applying the Laplace transform,

$$\begin{aligned} q(t) &= Q(s) \\ \dot{q}(t) &= sQ(s) \\ \ddot{q}(t) &= s^2 Q(s) \end{aligned} \quad (8)$$

to (7) yields:

$$(s^2 + [2\zeta w]s + [w^2])Q(s) = [\phi]^T F(s) \quad (9)$$

Since the relationship between $x(t)$ and $\ddot{x}(t)$ is S^2 , ie:

$$\ddot{Q}(s) = s^2 \bar{Q}(s) \quad (10)$$

Utilizing (10), (9) can be expressed as:

$$\frac{\ddot{Q}(s)}{F(s)} = \frac{-s^2}{s^2 + [2\zeta w]s + [w^2]} [\phi]^T \quad (11)$$

Substituting $s = i\Omega$ into (11), the absolute acceleration transfer function, in the modal domain, becomes:

$$\left| \frac{\ddot{Q}}{F_0} \right| = \frac{\Omega^2}{[w^2] + [2\zeta w i \Omega] - \Omega^2} [\phi]^T \quad (12)$$

By use of relationship (z), (12) becomes:

$$\left| \frac{\ddot{X}}{F_0} \right| = [\phi] \frac{\Omega^2}{[w^2] + [2\zeta w i \Omega] - \Omega^2} [\phi]^T \quad (13)$$

Equation (13) is the basic equation for the acceleration transfer function in the time domain.

In practice, two selector vectors can now be used to operate on the modes matrices to extract a scalar ATF representing a given input exciter location (δ_F) and a given response location (δ_R). In addition, a given maximum excitation force can be selected (such as +/- 1 lb.) and rationed to determine actual abort levels. The final form of equation (13) used is:

$$\left| \frac{\ddot{X}}{F_0} \right| = \left\{ \delta \right\}_R [\phi] \frac{\Omega^2}{[w^2] + [2\zeta w i \Omega] - \Omega^2} [\phi]^T \left\{ \delta \right\}_F \quad (14)$$

M.El-Baraka *

P.S.Krishnaprasad **

Electrical Engineering Department
University of Maryland
College Park, MD 20742

Abstract: In this paper, we use differential geometric methods to understand the dynamics and control of certain multibody systems. Specifically, we treat rigid spacecraft with rotors and announce a basic stability theorem for the dual-spin maneuver. We then show how to decouple the effect of disturbance torques from spacecraft attitude variables.

Our stability arguments based on Lie-Poisson structures involve general principles that are applicable to more complex multibody systems than those considered here. The techniques for decoupling disturbance torques that we use here also admit applications to more complex multibody systems including elastic elements.

1. Introduction

There has been a tremendous resurgence of interest in the subject of analytical mechanics in recent years. This has been partly due to the systematic infusion of a rich variety of geometric ideas and techniques into the foundations of the subject. Recent discoveries of new integrable classes of systems (both finite and infinite dimensional), phenomena related to 'chaos' and recent developments in stability and critical point theory of mechanical systems have relied heavily on geometric and algebraic ideas. Along side these developments, there has been a steady effort on the part of control theorists to understand problems of control and estimation of nonlinear systems using geometric tools.

In this paper, we aim to show certain geometric methods and ideas in action, - in solving concrete problems related to attitude control of spacecraft. We focus on the simplest class of multibody spacecraft, namely rigid spacecraft carrying symmetric rotors. There is a Hamiltonian structure underlying this class of dynamical systems even when the rotors are driven. A complete understanding of this fact would necessitate an excursion into the recent developments in Hamiltonian systems with inputs and outputs due to Brockett, Takens, Willems and Van-der-Schaft (see [1], [16], [19], [17]). Instead we outline a treatment based on Lie-Poisson structures and announce a basic stability theorem for dual-spin spacecraft. Details of the proof are to be found in [9], [10].

We then proceed to solve the problem of decoupling a spacecraft with momentum wheels from

internal disturbance torques. This is achieved by designing appropriate nonlinear feedback laws for the driving torques on the wheels. To keep the paper self-contained an exposition of the abstract disturbance decoupling theory is also given.

2. Dynamics of Rigid Spacecraft with Rotors

The equations of motion for a rigid spacecraft carrying multiple symmetric rotors may be obtained by systematic application of Newton's laws. In the notation of Wittenburg [20], these are,

$$J\dot{\omega} + \sum_{i=1}^m h_i^o + \omega \times \left[J\omega + \sum_{i=1}^m h_i + \sum_{i=m+1}^m h_i \right] = M - \sum_{i=m+1}^m h_i, \quad (2.1a)$$

$$u_i \cdot (J_i^r \dot{\omega} + h_i^o) = M_i^r, \quad i=1,2,\dots,m, \quad (2.1b)$$

where, we assume that of a total of $(m+n)$ rotors each indexed by i the first m are subject to known

axial torque components M_i^r and the remaining n have known angular momenta $h_i(t)$ with respect to the body of the spacecraft. In the scalar equations (2.1.b), u_i denotes a unit vector along the axis of the i th rotor, and $(\cdot)^o$ denotes differentiation with respect to a spacecraft frame.

J_i^r = moment of inertia of i th rotor about its spin axis and J = moment of inertia of spacecraft with all rotors locked. ω is the spacecraft body angular velocity and h_i is the angular momentum of the i th rotor relative to the spacecraft. M denotes the resultant of external torques.

Suppose now that one is interested in understanding the dual-spin maneuver. Here the intuition is the following: if the spacecraft contains a driven rotor spinning at a sufficiently high constant relative angular velocity, then in the presence of a suitable additional damping mechanism, the spacecraft body angular velocity eventually converges to an (unique) equilibrium spin. Although many attempts have been made in analyzing the dual-spin turn, our stability theorem below appears to be the first rigorous verification of the above intuition for a model linear damping mechanism based on rotors.

We assume that the spacecraft has two sets of three symmetric rotors each; one set free-spinning with linear damping and one set driven at constant relative angular velocities. The equations of motion (2.1.a-b) now take the form,

Partial support for this work was provided by the National Science Foundation under Grants ECS-81-18138 and ECS-82-19123 and by the Department of Energy under Contract DEAC01-80-RA50420-A001, and the Govt. of Morocco.

Released to AIAA to publish in all forms.

$$\begin{aligned}\dot{h}_v &= S(J^{-1}h_v) [h_v + h_d + h_w] - \gamma h_v + \delta h_d \\ \dot{h}_d &= \gamma h_v - \delta h_d \\ \dot{h}_w &= 0,\end{aligned}\quad (2.2)$$

where, $h_d = J_a^d (\omega_a + \omega_a^d)$ is the 3-vector of angular momenta of the damping rotors with respect to

inertial space; $h_w = J_a^w \omega_a^w$ is the 3-vector of angular momenta of the driven rotors relative to the spacecraft; $h_v = J\omega_a$ and ω_a = spacecraft angular

velocity vector; J_a^v = moment of inertia of spacecraft with all rotors locked and

$J = J_a^v - J_a^d$; $\gamma = \alpha J^{-1}$, $\delta = \alpha J_a^{d-1}$ and α = diagonal matrix of positive damping coefficients of the free-spinning wheels. Among the main results in [9], [10] we mention:

- (1) as $\alpha \rightarrow 0$, the system (2.2) tends to a Hamiltonian system;
- (2) the Hamiltonian structure in (1) is not canonical but is a Lie-Poisson structure;
- (3) if $\alpha > 0$, then for h_w sufficiently large, we have proved an asymptotic stability theorem.

The details are to be found in [9]. We enlarge upon items 1 and 2 above.

Let \mathfrak{g} be a finite dimensional Lie algebra with bracket $[\cdot, \cdot]$. Let \mathfrak{g}^* be the dual space of \mathfrak{g} . The space $F(\mathfrak{g}^*)$ of smooth real-valued functions on \mathfrak{g}^* carries a Poisson structure (bracket) as follows:

$$\begin{aligned}\{ \cdot, \cdot \} : F(\mathfrak{g}^*) \times F(\mathfrak{g}^*) &\rightarrow F(\mathfrak{g}^*) \\ (\phi, \psi) &\rightarrow \{ \phi, \psi \} \\ \{ \phi, \psi \} (f) &= \langle f, [\frac{\delta \phi}{\delta f}, \frac{\delta \psi}{\delta f}] \rangle,\end{aligned}$$

Where $f \in \mathfrak{g}^*$, $\langle \cdot, \cdot \rangle$ denotes the natural pairing between \mathfrak{g}^* and \mathfrak{g} , and $\frac{\delta \phi}{\delta f}$, $\frac{\delta \psi}{\delta f}$ denote Lie algebra gradients ([4], [5], [11], [12], [18]). Given H (a Hamiltonian) in $F(\mathfrak{g}^*)$, the vector field X_H is defined by setting

$$X_H(\phi) = \{ H, \phi \}.$$

If x denotes a global coordinate system on \mathfrak{g}^* then the differential equation,

$$\frac{dx}{dt} = X_H(x)$$

is known as the Lie-Poisson equation associated to \mathfrak{g}^* , H and the chosen basis. The vector fields X_H leave invariant the coadjoint orbits in \mathfrak{g}^* (see [9]).

In [9] we showed that the system (2.2) with $\alpha = 0$ (and hence $\gamma = \delta = 0$) is in Lie-Poisson form, with

$$\mathfrak{g} = \mathfrak{so}(3) \oplus \mathbb{R}^3 \oplus \mathbb{R}^3$$

$$\begin{aligned}H &= \frac{1}{2} \langle h_v, J^{-1} h_v \rangle + \\ &\frac{1}{2} \langle h_d, J_a^{d-1} h_d \rangle\end{aligned}$$

The coadjoint orbits are spheres and are invariant (~~and~~ total body angular momentum is conserved). The Hamiltonian $H = T - Q - W$, where T = total kinetic energy of spacecraft, Q = total energy supplied through driven rotors, W = kinetic energy of driven rotors (maintained constant).

If $\alpha > 0$, we showed in [9] that for a range of values of h_w (given by the perfectness conditions of [10]), the system (2.2) is asymptotically stable in the large (i.e all trajectories converge to one of the equilibrium points). The Lyapunov function used to establish this is $V = H + W$. The key observation here is that W is an element in the center the Poisson bracket algebra $F(\mathfrak{g}^*)$. The addition of such an element (called a Casimir element) to the Hamiltonian gives us a Lyapunov function. This is not accidental and is part of a rather general picture see ([4], [11]).

We have

Theorem: Assume that h_w is large enough for the perfectness conditions of ([9] [10]) to hold. Then almost all trajectories of (2.2) converge to the unique global minimum of V on the momentum variety,

$$\|h_v + h_d + h_w\|^2 = \mu^2 = \text{constant}$$

3. Disturbance Decoupling in Spacecraft

Spacecraft control system designers must design attitude control systems that shield or decouple the attitude variables from a variety of disturbance effects. These include,

- (a) external forces and torques due to gravity gradient, solar pressure on panels, aerodynamic drag at low altitudes, magnetic field interactions etc.;
- (b) internal forces and torques due to crew motion, internal reconfiguration (e.g. space shuttle manipulator motions), fuel sloshing etc.

When accurate models of such disturbances are available, it is possible to design specific compensation schemes. For a recent survey of the literature and an overview of techniques, see [15].

In this paper, we show how to design nonlinear feedback control laws for momentum wheels which can decouple a part of the attitude dynamics (more precisely, a row of the direction cosine matrix) from internal disturbance torques. This is a long exercise in Lie bracket calculations and solution of first order partial differential equations. The only previous effort of this nature (that we are aware of) is in [14]. In that paper the authors treat the (simpler) problem of decoupling (from external

disturbances), rigid body dynamics using reaction jets.

Eliminating the rotor dynamics from (2.1) and relabeling certain variables we get the following basic model,

$$\begin{aligned}\dot{A} &= S(\omega)A \\ \dot{\omega} &= J^{-1}S(\omega)Ah + g_1 u_1 \\ &\quad + g_2 u_2 + pw\end{aligned}$$

where A = direction cosine matrix, ω = body angular velocity vector, $g_1 = (1, 0, 0)^T$, $g_2 = (0, 1, 0)^T$

and $p = (0, 0, 1)$; $J = J_a^V - J_a^W$, h = conserved angular momentum vector.

The normalized momentum wheel torques are denoted as $u_1(t)$ and $u_2(t)$ and $w(t)$ is an (internal) disturbance torque.

Our aim is to design a feedback law, of the form $u_1 = f_1(\omega, A)$ and $u_2 = f_2(\omega, A)$ such that the last row of the attitude matrix A is unaffected by the disturbance $w(\cdot)$.

In section 4 below, we outline the general geometric framework for disturbance decoupling. The basic ideas appeared in linear system theory during the period 1969-1975 and a comprehensive exposition may be found in [22] (see also [21]). Nonlinear decoupling methods are of recent origin and the basic results are in [3], [6].

Our solution to the disturbance decoupling problem for spacecraft using momentum wheels is given in section 5. Since repeated use of differential geometric notation is made in the following pages we note here:

(i) given $f(x)$ and $g(x)$, two smooth n -vector functions viewed as local coordinate representation of two vectorfields in R^n , the Lie bracket $[f, g]$ has the local coordinate representation

$$[f, g] := \left(\frac{\partial g}{\partial x} \right) f - \left(\frac{\partial f}{\partial x} \right) g$$

(ii) The Lie derivative of a smooth function $\alpha(x)$ along a vector field $X = \sum_{i=1}^n f_i \frac{\partial}{\partial x_i}$ is given by

$$X\alpha = \sum_{i=1}^n f_i \frac{\partial \alpha}{\partial x_i}$$

4. Disturbance Decoupling (an outline):

An analytic nonlinear control system on a manifold M (= phase space) may be represented in local coordinates in the form

$$\begin{aligned}\dot{x} &= f(x) + G(x)u \\ y &= h(x),\end{aligned}\tag{4.1}$$

where $G(x) = [g_1(x), \dots, g_m(x)]$, f , g_i are analytic vector fields and h is an analytic output map.

By a (smooth) distribution Δ on M we mean a (smooth) choice of a subspace $\Delta_x \subset TM_x$ of the tangent space at each point $x \in M$.

A distribution Δ is invariant under the dynamics Σ if

$$\begin{aligned}[f, \Delta] &\subset \Delta \\ [g_i, \Delta] &\subset \Delta \quad i=1, 2, \dots, m\end{aligned}\tag{4.2}$$

Have $[\cdot, \cdot]$ denotes Lie bracketting.

The involutive closure $\bar{\Delta}$ of a distribution Δ is the smallest distribution containing Δ and satisfying,

$$[\Delta, \bar{\Delta}] \subset \bar{\Delta}\tag{4.3}$$

Fact: If Δ is invariant under Σ then so is $\bar{\Delta}$.

Let Δ be an involutive (i.e. $\bar{\Delta} = \Delta$), invariant distribution of constant rank k for the system Σ . We obtain a reduction theorem for Σ as follows:

Let (x_1, x_2) be local coordinates such that $x_1 \in R^{n-k}$ and $x_2 \in R^k$ respectively.

and

$$\Delta_x = \text{span} \left\{ \frac{\partial}{\partial x_2} \right\}$$

In these coordinates the system Σ becomes

$$\begin{aligned}\dot{x}_1 &= f_1(x_1, x_2) + G_1(x_1, x_2)u \\ \dot{x}_2 &= f_2(x_1, x_2) + G_2(x_1, x_2)u \\ y &= h(x_1, x_2).\end{aligned}\tag{4.4}$$

But since Δ is invariant,

$$\left[f, \frac{\partial}{\partial x_2} \right] \in \text{span} \left\{ \frac{\partial}{\partial x_2} \right\}.$$

This implies $\frac{\partial f_1}{\partial x_2} = 0$

Similarly $\frac{\partial G_1}{\partial x_2} = 0$

Thus f_1 , G_1 are functions of x_1 alone and we obtain

$$\Sigma_p : \dot{x}_1 = f_1(x_1) + G_1(x_1)u\tag{4.5}$$

a subsystem of Σ .

For the purposes of disturbance decoupling we need a modified notion of invariance.

Let $\alpha(x) \Delta$ ($\alpha_1(x), \dots, \alpha_m(x)$) denote a smooth R^m -valued function of x and let $\beta(x) \Delta$ $[\beta_{ij}(x)]_{m \times m}$ denote a smooth $m \times m$ matrix valued (invertible) function of x . We interpret $\alpha(x)$ as defining a nonlinear feedback and $\beta(x)$ as defining a change of coordinates in the input space which depends nonlinearly on x .

For the purposes of disturbance decoupling we need a modified notion of invariance.

Let $\alpha(x) \Delta (\alpha_1(x), \dots, \alpha_m(x))$ denote a smooth \mathbb{R}^m -valued function of x and let $\beta(x) \Delta [\beta_{ij}(x)]_{m \times m}$ denote a smooth $m \times m$ matrix valued (invertible) function of x . We interpret $\alpha(x)$ as defining a nonlinear feedback and $\beta(x)$ as defining a change of coordinates in the input space which depends nonlinearly on x .

Let $(G\beta)_i$ denote the i th column of the matrix $G\beta$ and let $f+G\alpha$ denote the closed loop drift vectorfield.

We say that a distribution Δ is (f, G) invariant if there exist $\alpha(x)$ and $\beta(x)$ such that

$$\begin{aligned} [f + G\alpha, \Delta] &\subset \Delta \\ [(G\beta)_i, \Delta] &\subset \Delta \end{aligned} \quad 4.6$$

In other words there is a nonlinear feedback law α and a nonlinear change of coordinates β in input space such that Δ is invariant under the new dynamics

$$\tilde{f} = f + G\alpha$$

$$\tilde{G} = G\beta$$

Often it is difficult to establish (f, G) invariance. But there is a related concept:

A distribution Δ is locally (f, G) invariant if

$$[f, \Delta](x) \subset \Delta(x) + \text{span} \{g_i(x)\}_{i=1}^m$$

$$[(G\beta)_i, \Delta](x) \subset \Delta(x) + \text{span} \{g_i(x)\}_{i=1}^m.$$

Lemma: [7] Suppose Δ is locally (f, G) invariant and $\bar{\Delta}$ is its involutive closure and the

dimensions of $\bar{\Delta}(x)$, $\text{span} \{g_i(x)\}_{i=1}^m$ and $\bar{\Delta}(x) \cap \text{span} \{g_i(x)\}_{i=1}^m$ are constant. Then locally around each $x \in M$ there exists an $\alpha(x)$ and an invertible $\beta(x)$ satisfying (4.6).

The concept of (f, G) invariance plays a crucial role in the disturbance decoupling problem.

We outline the main ideas behind disturbance decoupling. Consider a system

$$\begin{aligned} \dot{x} &= f(x) + G(x)u + P(x)w \\ \sum_d : \quad y &= h(x) \end{aligned}$$

Here the vector $u \in \mathbb{R}^m$ is a control and the vector $w \in \mathbb{R}^p$ is a (time-dependent) disturbance. One says that the system Σ_d is disturbance decoupled if the output y is independent of the disturbance w . Now a given system Σ_d may not have this property. So one can try to modify the system using feedback $\alpha(x)$ and input change of coordinates $\beta(x)$ such that the modified system is disturbance decoupled. This is the essential idea. Now it is possible to achieve local disturbance decoupling, by testing the conditions of the following theorem.

Theorem: For analytic control systems the state feedback disturbance decoupling problem is solvable locally (with β invertible) iff there exists a distribution Δ such that

Δ is (f, G) invariant

$$\text{image}(P(x)) \subset \Delta_x \subset \text{Ker}(dh(x)) //$$

This theorem together with the previous lemma provides a very useful tool for control synthesis to achieve disturbance decoupling.

The above theorem is due to Hirschorn [3] and independently Isidori, Krener, Gori-Georgi and Monaco [6]. Other variations due to Van der Schaft & Nijmeier are also known. See ([13]–[14])

5 Disturbance decoupling using momentum wheels:

In this section we show using the general theory outlined in section 4, that it is possible to design nonlinear feedback laws for 2 momentum wheels to decouple a part of the spacecraft attitude variable from internal disturbance torques.

5.1 Equations in local coordinates

We know from section 3 that the equations of motion are:

$$\begin{aligned} \dot{A} &= S(\omega)A \\ \dot{\omega} &= J^{-1}S(\omega)A h(0) + J^{-1}z \end{aligned} \quad (5.1.1)$$

Denoting the attitude matrix as

$$A = \begin{bmatrix} r_1 & s_1 & t_1 \\ r_2 & s_2 & t_2 \\ r_3 & s_3 & t_3 \end{bmatrix}$$

we can rewrite (5.1.1) as

$$\begin{aligned} \dot{r}_1 &= \omega_3 r_2 - \omega_2 r_3 \\ \dot{r}_2 &= -\omega_3 r_1 + \omega_1 r_3 \\ \dot{r}_3 &= \omega_2 r_1 - \omega_1 r_2 \\ \dot{s}_1 &= \omega_3 s_2 - \omega_2 s_3 \\ \dot{s}_2 &= -\omega_3 s_1 + \omega_1 s_3 \\ \dot{s}_3 &= \omega_2 s_1 - \omega_1 s_2 \\ \dot{t}_1 &= \omega_3 t_2 - \omega_2 t_3 \\ \dot{t}_2 &= -\omega_3 t_1 + \omega_1 t_3 \\ \dot{t}_3 &= \omega_2 t_1 - \omega_1 t_2 \\ \dot{\omega}_1 &= \omega_3 \Omega_2^1 - \omega_2 \Omega_3^1 + u_1 \\ \dot{\omega}_2 &= \omega_1 \Omega_3^2 - \omega_3 \Omega_1^2 + u_2 \\ \dot{\omega}_3 &= \omega_2 \Omega_1^3 - \omega_1 \Omega_2^3 + d \end{aligned} \quad (5.1.2)$$

$$y = \begin{bmatrix} r_3 \\ s_3 \\ t_3 \end{bmatrix}$$

Where

$$\begin{aligned} \Omega_2^1 &= \ell_1 r_2 + \ell_2 s_2 + \ell_3 t_2 \\ \Omega_3^1 &= \ell_1 r_3 + \ell_2 s_3 + \ell_3 t_3 \\ \Omega_3^2 &= \ell_4 r_3 + \ell_5 s_3 + \ell_6 t_3 \\ \Omega_1^2 &= \ell_4 r_1 + \ell_5 s_1 + \ell_6 t_1 \\ \Omega_1^3 &= \ell_7 r_1 + \ell_8 s_1 + \ell_9 t_1 \\ \Omega_2^3 &= \ell_7 r_2 + \ell_8 s_2 + \ell_9 t_2 \\ \Omega_1^1 &= \ell_1 r_1 + \ell_2 s_1 + \ell_3 t_1 \\ \Omega_2^2 &= \ell_4 r_2 + \ell_5 s_2 + \ell_6 t_2 \\ \Omega_3^3 &= \ell_7 r_3 + \ell_8 s_3 + \ell_9 t_3 \end{aligned} \quad (5.1.3)$$

Here (ℓ_1, ℓ_2, ℓ_3) is the normalized vector of total body angular momentum $h(0)$ (which remains invariant under internal disturbance torques).

5.2 Existence of an (f, G) invariant distribution

We have:

$$y = \begin{bmatrix} r_3 \\ s_3 \\ t_3 \end{bmatrix}; \quad p = e_{12}; \quad G = [e_{10}, e_{11}]$$

where $\{e_1, \dots, e_{12}\}$ denotes the standard basis in R^{12} .

We are looking for a distribution Δ such that:

$$p \in \Delta \subset \text{Ker } dy = R^{12} / \text{Span } \{e_3, e_6, e_9\}$$

and Δ is locally (f, G) invariant:

$$[f, \Delta] \subset \Delta + \text{Span } \{g_1, g_2\}$$

$$[g_1, \Delta] \subset \Delta + \text{Span } \{g_1, g_2\}$$

H. Nijmeijer and van der Schaft [13] give an algorithm for computing the maximal (f, G) invariant distribution contained in a given distribution (Ker dy here); the same algorithm is given in a dual form by A. Isidori et al. in [6]. This algorithm requires us to solve systems of PDE's in a $12 \times 12 + 12 = 156$ dimensional space! We therefore have to take an alternative approach.

Consider the following distribution:

$$\Delta = \text{Span } \{p = e_{12} = X_1, X_2 =$$

$$\begin{bmatrix} r_2 \\ -r_1 \\ 0 \\ s_2 \\ -s_1 \\ 0 \\ t_2 \\ -t_1 \\ 0 \\ \omega_2 \\ -\omega_1 \\ 0 \end{bmatrix} \}$$

Clearly $p \in \Delta$ and $\Delta \subset \text{Ker } dy$.

Now let us check that Δ is locally (f, G) invariant.

In all the following computations of Lie brackets, we need to compute

$$\frac{\partial f}{\partial x}$$

which is given by:

$$\begin{bmatrix} 0 & \omega_3 & -\omega_2 & 0 & 0 & 0 & 0 & 0 & 0 & 0 & -r_3 & r_2 \\ -\omega_3 & 0 & \omega_1 & 0 & 0 & 0 & 0 & 0 & 0 & r_3 & 0 & -r_1 \\ \omega_2 & -\omega_1 & 0 & 0 & 0 & 0 & 0 & 0 & 0 & -r_2 & r_1 & 0 \\ 0 & 0 & 0 & 0 & \omega_3 & -\omega_2 & 0 & 0 & 0 & 0 & -s_3 & s_2 \\ 0 & 0 & 0 & -\omega_3 & 0 & \omega_1 & 0 & 0 & 0 & s_3 & 0 & -s_1 \\ 0 & 0 & 0 & \omega_2 & -\omega_1 & 0 & 0 & 0 & 0 & -s_2 & s_1 & 0 \\ 0 & 0 & 0 & 0 & 0 & 0 & 0 & \omega_3 & -\omega_2 & 0 & -t_3 & t_2 \\ 0 & 0 & 0 & 0 & 0 & 0 & -\omega_3 & 0 & \omega_1 & t_3 & 0 & -t_1 \\ 0 & 0 & 0 & 0 & 0 & 0 & \omega_2 & -\omega_1 & 0 & -t_2 & t_1 & 0 \\ 0 & \ell_1 \omega_3 & -\ell_1 \omega_2 & 0 & \ell_2 \omega_3 & -\ell_2 \omega_2 & 0 & \ell_3 \omega_3 & -\ell_3 \omega_2 & 0 & -\eta_3^1 & \eta_2^1 \\ -\ell_4 \omega_3 & 0 & \ell_4 \omega_1 & -\ell_5 \omega_3 & 0 & \ell_5 \omega_1 & -\ell_6 \omega_3 & 0 & \ell_6 \omega_1 & \eta_3^2 & 0 & -\eta_1^2 \\ \ell_7 \omega_2 & -\ell_7 \omega_1 & 0 & \ell_8 \omega_2 & -\ell_8 \omega_1 & 0 & \ell_9 \omega_2 & -\ell_9 \omega_1 & 0 & -\eta_2^3 & \eta_1^3 & 0 \end{bmatrix}$$

$$\Delta = \text{Span} \{X_1, X_2\}$$

$$\begin{aligned} [f, \Delta] &\subset \Delta + \text{Span} \{g_1, g_2\} \Leftrightarrow [f, X_1] \in \Delta + \\ &\quad \text{Span} \{g_1, g_2\} \\ &\quad (5.2.1) \\ [f, X_2] &\in \Delta + \\ &\quad \text{Span} \{g_1, g_2\} \\ &\quad (5.2.2) \end{aligned}$$

$$[f, X_1] = \frac{\partial X_1}{\partial x} f - \frac{\partial f}{\partial x} X_1 = \frac{\partial f}{\partial x} X_1 =$$

$$= \begin{bmatrix} -r_2 \\ +r_1 \\ 0 \\ -s_2 \\ s_1 \\ 0 \\ -t_2 \\ t_1 \\ 0 \\ -\Omega_2^1 \\ \Omega_1^2 \\ 0 \end{bmatrix}$$

$$\begin{aligned} \text{Therefore } [f, X_1] &= -X_2 + (\omega_2 - \Omega_2^1) g_1 \\ &\quad + (\Omega_1^2 - \omega_1) g_2 \end{aligned}$$

$$\text{where } g_1 = e_{10} \text{ and } g_2 = e_{11}$$

$$\text{Hence } [f, X_1] \in \Delta + \text{Span} \{g_1, g_2\}$$

$$\text{Now, } [f, X_2] = \frac{\partial X_2}{\partial x} f - \frac{\partial f}{\partial x} X_2 \quad (5.2.3)$$

$$\frac{\partial X_2}{\partial x} = \begin{bmatrix} 1 & 2 & 3 & 4 & 5 & 6 & 7 & 8 & 9 & 10 & 11 & 12 \\ 1 & 0 & 1 & 0 & 0 & 0 & 0 & 0 & 0 & 0 & 0 & 0 \\ 2 & -1 & 0 & 0 & 0 & 0 & 0 & 0 & 0 & 0 & 0 & 0 \\ 3 & 0 & 0 & 0 & 0 & 0 & 0 & 0 & 0 & 0 & 0 & 0 \\ 4 & 0 & 0 & 0 & 0 & 1 & 0 & 0 & 0 & 0 & 0 & 0 \\ 5 & 0 & 0 & 0 & -1 & 0 & 0 & 0 & 0 & 0 & 0 & 0 \\ 6 & 0 & 0 & 0 & 0 & 0 & 0 & 0 & 0 & 0 & 0 & 0 \\ 7 & 0 & 0 & 0 & 0 & 0 & 0 & 0 & -1 & 0 & 0 & 0 \\ 8 & 0 & 0 & 0 & 0 & 0 & 0 & -1 & 0 & 0 & 0 & 0 \\ 9 & 0 & 0 & 0 & 0 & 0 & 0 & 0 & 0 & 0 & 0 & 0 \\ 10 & 0 & 0 & 0 & 0 & 0 & 0 & 0 & 0 & 0 & 1 & 0 \\ 11 & 0 & 0 & 0 & 0 & 0 & 0 & 0 & 0 & 0 & -1 & 0 \\ 12 & 0 & 0 & 0 & 0 & 0 & 0 & 0 & 0 & 0 & 0 & 0 \end{bmatrix}$$

Hence:

$$\begin{aligned} [f, X_2] &= (\omega_1 \Omega_3^2 - \omega_3 \Omega_1^2 + \omega_3 \Omega_1^1 - \Omega_3^1 \omega_1) g_1 + \\ &\quad (\omega_2 \Omega_3^1 - \omega_3 \Omega_2^1 - \omega_2 \Omega_3^2 + \omega_3 \Omega_2^2) g_2 \\ &\in \Delta + \text{span} \{g_1, g_2\} \end{aligned} \quad (5.2.4)$$

Next we have to check that, for each $x \in M$, the statespace, the vectors, $[g_1, X_1](x)$, $[g_2, X_2](x)$, $[g_1, X_2](x)$ and $[g_2, X_1](x)$ all belong to $\text{span} \{g_1, g_2\}$. This can be verified by direct calculation that,

$$[g_1, X_1] = [g_2, X_1] = 0;$$

and

$$[g_1, X_2] = -e_{11};$$

$$[g_2, X_2] = e_{10}.$$

This completes the verification that Δ is locally (f, G) invariant. It can be further explicitly verified [2], that.

(a). Δ is involutive and of rank 2.

(b). $\dim(\text{span} \{g_1, g_2\}) = 2 = \text{constant}$ on $TSO(3)$ the tangent bundle of $SO(3) = \text{attitude} \times \text{angular velocity space}$.

(c). $\dim(\Delta \cap \text{span} \{g_1, g_2\})$

$$= 0 = \text{also constant}.$$

Thus the hypotheses of the lemma of section 4 are satisfied. Hence there exists a feedback law $\alpha(x)$ and a nonlinear change of coordinates in the input space $\beta(x)$ such that Δ is (f, G) invariant i.e.,

$$[f + G\alpha, \Delta] \subset \Delta \quad (5.2.5)$$

$$[(G\beta)_i, \Delta] \subset \Delta$$

$$i=1, 2$$

This implies, from the theorem of section 4, that the disturbance decoupling problem is solvable. In the next section we explicitly compute $\alpha(\cdot)$ and $\beta(\cdot)$.

5.3 Construction of decoupling feedback laws

Summarizing what we already have:

$$\Delta = \text{Span} \{X_1, X_2\}$$

$$[f, X_1] = -X_2 + (\omega_2 - \Omega_2^1) g_1 + (\Omega_1^2 - \omega_1) g_2 \quad (5.3.1)$$

$$\begin{aligned} [f, X_2] &= (\omega_1 \Omega_3^2 - \omega_3 \Omega_1^2 + \omega_3 \Omega_1^1 - \Omega_3^1 \omega_1) g_1 \\ &\quad + (\omega_2 \Omega_3^1 - \omega_3 \Omega_2^1 + \omega_3 \Omega_2^2 - \Omega_3^2 \omega_2) g_2 \end{aligned} \quad (5.3.2)$$

$$[g_1, X_1] = [g_2, X_1] = 0 \quad (5.3.3)$$

$$[g_1, X_2] = -g_2 \quad [g_2, X_2] = g_1 \quad (5.3.4)$$

$$[X_1, X_2] = 0 \quad (5.3.5)$$

We want to find $\alpha(x) = \begin{bmatrix} \alpha_1(x) \\ \alpha_2(x) \end{bmatrix}$ and $\beta(x) = \begin{bmatrix} \lambda(x) & \mu(x) \\ \nu(x) & \sigma(x) \end{bmatrix}$

such that Δ is invariant under the new dynamics:

$$\tilde{f} = f + G \alpha$$

$$\text{and } \tilde{G} = G \beta$$

$$G = [g_1, g_2] = [e_{10} \ e_{11}]$$

$$G \alpha = [e_{10} \ e_{11}] \begin{bmatrix} \alpha_1 \\ \alpha_2 \end{bmatrix} = \alpha_1 e_{10} + \alpha_2 e_{11}$$

$$\text{Therefore } \tilde{f} + G \alpha = f + \alpha_1 e_{10} + \alpha_2 e_{11} \quad (5.3.6)$$

and we should have

$$[f + \alpha_1 e_{10} + \alpha_2 e_{11}, \Delta] \in \Delta,$$

or equivalently

$$[f + \alpha_1 e_{10} + \alpha_2 e_{11}, X_1] \in \Delta, \quad (5.3.7)$$

$$[f + \alpha_1 e_{10} + \alpha_2 e_{11}, X_2] \in \Delta. \quad (5.3.8)$$

$$(5.3.7) \Leftrightarrow [f + \alpha_1 e_{10} + \alpha_2 e_{11}, X_1] =$$

$$[f, X_1] - X_1(\alpha_1)g_1 - X_1(\alpha_2)g_2 \in \Delta \quad (5.3.9)$$

$$X_1(\alpha_1) = \frac{\partial \alpha_1}{\partial \omega_3} \quad (5.3.10)$$

$$X_1(\alpha_2) = \frac{\partial \alpha_2}{\partial \omega_3}.$$

Using equations (5.3.1), (5.3.9) and (5.3.10) we get:

$$\frac{\partial \alpha_1}{\partial \omega_3} = \omega_2 - \Omega_2^1 \quad (I)$$

$$-\frac{\partial \alpha_2}{\partial \omega_3} = \omega_1 - \Omega_1^2 \quad (II)$$

$$(5.3.8) \Leftrightarrow [f + \alpha_1 g_1 + \alpha_2 g_2, X_2] =$$

$$[f, X_2] - (\alpha_1 + X_2(\alpha_2))g_2$$

$$- (\alpha_2 - X_2(\alpha_1))g_2 \in \Delta \quad (11)$$

From (5.3.11) and (5.3.2) we get

$$\omega_3(\Omega_3^2 - \Omega_3^1) - \omega_3(\Omega_1^2 - \Omega_1^1) + \alpha_2 - X_2(\alpha_1) = 0 \quad (III)$$

$$\omega_3(\Omega_2^2 - \Omega_2^1) - \omega_2(\Omega_3^2 - \Omega_3^1) + \alpha_1 - X_2(\alpha_2) = 0 \quad (IV)$$

where $X_2(\alpha)$ is given by:

$$X_2(\alpha) = r_2 \frac{\partial \alpha}{\partial r_1} - r_1 \frac{\partial \alpha}{\partial r_2} + s_2 \frac{\partial \alpha}{\partial s_1} - s_1 \frac{\partial \alpha}{\partial s_2} +$$

$$t_2 \frac{\partial \alpha}{\partial s_2} - t_1 \frac{\partial \alpha}{\partial t_2} + \omega_2 \frac{\partial \alpha}{\partial \omega_1} - \omega_1 \frac{\partial \alpha}{\partial \omega_2}. \quad (5.3.12)$$

Therefore we seek to solve the system of PDE's (I)-(IV); which can be written as follows:

$$\frac{\partial \alpha_1}{\partial \omega_3} = \omega_2 - \Omega_2^1 \quad (I)$$

$$\frac{\partial \alpha_2}{\partial \omega_3} = -\omega_1 + \Omega_1^2 \quad (II)$$

$$X_2(\alpha_1) - \alpha_2 = \omega_1(\Omega_3^2 - \Omega_3^1) - \omega_3(\Omega_1^2 - \Omega_1^1) \quad (III)$$

$$X_2(\alpha_2) - \alpha_1 = \omega_3(\Omega_2^2 - \Omega_2^1) - \omega_2(\Omega_3^2 - \Omega_3^1) \quad (IV)$$

From (5.1.3) we get,

$$\Omega_3^2 - \Omega_3^1 = (\ell_4 - \ell_1)r_3 + (\ell_5 - \ell_2)s_3 + (\ell_6 - \ell_3)t_3 \quad (5.3.13)$$

$$\Omega_1^2 - \Omega_1^1 = (\ell_4 - \ell_1)r_1 + (\ell_5 - \ell_2)s_1 + (\ell_6 - \ell_3)t_1 \quad (5.3.14)$$

Similarly

$$\Omega_2^2 - \Omega_2^1 = (\ell_4 - \ell_1)r_2 + (\ell_5 - \ell_2)s_2 + (\ell_6 - \ell_3)t_2 \quad (5.3.15)$$

$$\Omega_3^2 - \Omega_3^1 = (\ell_4 - \ell_1)r_3 + (\ell_5 - \ell_2)s_3 + (\ell_6 - \ell_3)t_3 \quad (5.3.16)$$

From (5.3.13), (5.3.14) and (III) we get:

$$X_2(\alpha_1) - \alpha_2 = (\ell_4 - \ell_1) \dot{r}_2 + (\ell_5 - \ell_2) \dot{s}_2 + (\ell_6 - \ell_3) \dot{t}_2 \quad (5.3.17)$$

From (5.3.15), (5.3.16) and (IV) we get:

$$X_2(\alpha_2) - \alpha_1 = (\ell_4 - \ell_1) \dot{r}_1 + (\ell_5 - \ell_2) \dot{s}_1 + (\ell_6 - \ell_3) \dot{t}_1 \quad (5.3.18)$$

Now, let us make the following change of variables:

$$\alpha_1 = (\omega_2 - \ell_1 r_2 - \ell_2 s_2 - \ell_3 t_2) \omega_3 + A_1(r_1, r_2, \dots, \omega_2) \quad (5.3.19)$$

$$\alpha_2 = (-\omega_1 + \ell_4 r_1 + \ell_5 s_1 + \ell_6 t_1) \omega_3 + A_2(r_1, r_2, \dots, \omega_2) \quad (5.3.20)$$

Define the new variables:

$$\sigma_1 = \ell_4 - \ell_1 \quad \sigma_2 = \ell_5 - \ell_2 \quad \sigma_3 = \ell_6 - \ell_3 \quad (5.3.21)$$

After further manipulations, we get the following system:

$$X_2(A_1) - A_2 = \sigma_1 \omega_1 r_3 + \sigma_2 \omega_1 s_3 + \sigma_3 \omega_1 t_3 \quad (V)$$

$$X_2(A_2) + A_1 = -\sigma_1 \omega_2 r_3 - \sigma_2 \omega_2 s_3 + \sigma_3 \omega_2 t_3 \quad (VI)$$

One can check that:

$$A_1 = -\sigma_1 \omega_2 r_3 - \sigma_2 \omega_2 s_3 - \sigma_3 \omega_2 t_3 \quad (22)$$

$$A_2 = 0 \quad (23)$$

is a solution to the system (V), (VI).

This leads to the following expressions for α_1 and α_2 :

$$\alpha_1 = \omega_2 \omega_3 - \ell_1 r_2 \omega_3 - \ell_2 s_2 \omega_3 - \ell_3 t_2 \omega_3 - \sigma_1 \omega_2 r_3 - \sigma_2 \omega_2 s_3 - \sigma_3 \omega_2 t_3 \quad (5.3.24)$$

$$\alpha_2 = -\omega_1 \omega_3 + \ell_4 r_1 \omega_3 + \ell_5 s_1 \omega_3 + \ell_6 t_1 \omega_3 \quad (5.3.25)$$

Furthermore α_1 and α_2 satisfy equations (I) and (II):

From (5.3.24) we have

$$\frac{\partial \alpha_1}{\partial \omega_3} = \omega_2 - (\ell_1 r_2 + \ell_2 s_2 + \ell_3 t_2) = \omega_2 - \Omega_2^1$$

From (5.3.25) we have

$$\frac{\partial \alpha_2}{\partial \omega_3} = -\omega_1 + (\ell_4 r_1 + \ell_5 s_1 + \ell_6 t_1) = -\omega_1 + \Omega_1^2$$

Now, let us compute β which satisfies:

$$[(G\beta)_i, \Delta] \in \Delta, \quad i=1,2, \quad (5.3.26)$$

$$G\beta = \begin{bmatrix} e_{10} & e_{11} \end{bmatrix} \begin{bmatrix} \lambda & \mu \\ v & \sigma \end{bmatrix} = \begin{bmatrix} \lambda e_{10} + \mu e_{11}, \\ \nu e_{10} + \sigma e_{11} \end{bmatrix} \quad (5.3.27)$$

$$\text{Therefore } [\lambda e_{10} + \nu e_{11}, \Delta] \in \Delta \quad (5.3.28)$$

$$[\mu e_{10} + \sigma e_{11}, \Delta] \in \Delta \quad (5.3.29)$$

the pairs (λ, ν) and (μ, σ) play a symmetric role and therefore will satisfy the same system of partial differential equations.

$$(5.3.28) \Rightarrow [\lambda e_{10} + \nu e_{11}, X_1] \in \Delta$$

$$\text{but } [\lambda e_{10} + \nu e_{11}, X_1] = -X_1(\lambda) e_{10} - X_1(\nu) e_{11}$$

$$\text{Hence } X_1(\lambda) = 0 \quad (5.3.30)$$

$$X_1(\nu) = 0 \quad (5.3.31)$$

$$(5.3.28) \Rightarrow [\lambda e_{10} + \nu e_{11}, X_2] = (\nu - X_2(\lambda)) e_{10} - (\lambda + X_2(\nu)) e_{11} \in \Delta$$

$$\text{Therefore } X_2(\lambda) - \nu = 0 \quad (5.3.32)$$

$$X_2(\nu) - \lambda = 0 \quad (5.3.33)$$

(μ, σ) satisfy the same system of equations (5.3.30)-(5.3.33). We note that (r_1, r_2) , (s_1, s_2) and (t_1, t_2) are all solutions to the system of PDE's (5.3.30)-(5.3.33).

Now, we summarize our results in the following theorem.

Theorem : Consider the momentum wheels attitude control system of equation 5.1.1. The feedback law:

$$\begin{aligned} u_1 &= (\omega_2 \omega_3 - \ell_1 r_2 \omega_3 - \ell_2 s_2 \omega_3 - \ell_3 t_2 \omega_3 - \sigma_1 \omega_2 r_3 - \\ &\quad \sigma_2 \omega_2 s_3 - \sigma_3 \omega_2 t_3) + r_1 v_1 + s_1 v_2 \\ u_2 &= (-\omega_1 \omega_3 + \ell_4 r_1 \omega_3 + \ell_5 s_1 \omega_3 + \ell_6 t_1 \omega_3) + \\ &\quad r_2 v_1 + s_2 v_2 \end{aligned}$$

decouples the last row (r_3, s_3, t_3) of the attitude matrix from a disturbance acting on an internal disturbance torque acting along the ω_3 axis.

6. Final Remarks:

We have shown how differential geometric methods contribute to the solution of two types of problems arising in multibody spacecraft - spin stabilization and disturbance decoupling. The tools used here are expected to play an essential role in rigorous analytical investigations of more complex multibody spacecraft and related control synthesis questions.

References

1. R.W. Brockett (1977), Control theory and analytical mechanics, in C. Martin and R. Hermann eds, Proc. The 1976 Ames Research Center (NASA) Conference on Geometric Control Theory, in series Lie Groups: History, Frontiers and Application vol. VII, Math Sci. Press, Boston.
2. M. El-Baraka (1983), Nonlinear Invertibility and Disturbance Decoupling of Attitude Control Systems, M.S. Thesis, Department of Electrical Engineering, University of Maryland, College Park (also Technical Research Report SRR 83-8).

3. R.M. Hirschorn (1981), (A,B) - Invariant distributions and disturbance decoupling of nonlinear systems, SIAM J. Control and Optimization, vol. 19, no.1, 1-19.
4. D. Holm, J.E. Marsden and T. Ratiu and A. Weinstein (1984), Stability of rigid body motion using the energy-Casimir method, Technical Report PAM-200/SRBM Center for Pure and Applied Mathematics, University of California, Berkeley (also to appear in J.E. Marsden ed, Fluids and Plasmas : Geometry and Dynamics, proc AMS-SIAM-IMS Summer Research Conference Boulder, Colorado, July 17-23, 1983).
5. P. Holmes and J.E. Marsden (1983), Horseshoes and Arnold diffusion for Hamiltonian systems on Lie groups, Indiana Univ. Math. J., vol. 32, 273-310.
6. A. Isidori, A.J. Krener, C. Gori-Giorgi and S. Monaco (1981), Nonlinear decoupling via feedback: a differential geometric approach, IEEE Trans. Aut. Control, vol. AC-26, no.2, 331-345.
7. A. Isidori, A.J. Krener, C. Gori-Giorgi and S. Monaco (1981), Locally (f,g) invariant distributions, Systems and Control Letters, vol.1, no.1, 12-15.
8. A.J. Krener (1979), A heuristic view of nonlinear decoupling, Proc. 13th Asilomar Conference on Circuits, Systems and Computers.
9. P.S. Krishnaprasad (1983), Lie-Poisson structures, dual-spin spacecraft and asymptotic stability, Journal of Nonlinear Analysis : Theory Methods and Applications (to appear), also Technical Research Report SRR 83-39, Department of Electrical Engineering, University of Maryland, College Park.
10. P.S. Krishnaprasad and C.A. Berenstein (1984), On the equilibria of rigid spacecraft with rotors, Systems and Control Letters, vol. IV, no. 3, (in press).
11. J.E. Marsden and A. Weinstein (1983), Coadjoint orbits, vortices and Clebsch variables for incompressible fluids, Physica 7D, 305-323.
12. J.E. Marsden, T. Ratiu and A. Weinstein (1984) Reduction and Hamiltonian structures on duals of semidirect product Lie algebras, Technical Report PAM - 205/RHSD, Center for Pure and Applied Mathematics, University of California, Berkeley. (also to appear in J.E. Marsden ed : Fluids and Plasmas : Geometry and Dynamics, Proc. AMS-SIAM-IMS Summer Research Conference, Boulder Colorado, July 17-23, 1983).
13. H. Nijmeijer and A.J. Van der Schaft (1982), Controlled invariance for nonlinear systems, IEEE Trans Aut. Contr., vol. AC-27, 904-914.
14. H. Nijmeijer and A.J. van der Schaft (1982), Controlled invariance for nonlinear systems : two worked examples, Mathematisch Centrum Rapport BW 156/82, Amsterdam, The Netherlands.
15. S.K. Shrivastava and V.J. Modi (1983), Satellite attitude dynamics and control in the presence of environmental torques - a brief survey, J. Guidance and Control, vol. 6, no. 6, 461-471.
16. F. Takens (1976), Variational and conservative systems - I, Rapport ZW-7603 Math. Inst. Groningen, The Netherlands.
17. A.J. Van-der-Schaft (1983), System-Theoretic Models for the Analysis of Physical Systems, Ph.D. Thesis, Math. Institute Tracts, Groningen, The Netherlands.
18. A. Weinstein (1983), The local structure of Poisson manifolds, J. Diff. Geom. (to appear).
19. J.C. Willems (1979), System-theoretic models for the analysis of physical systems, Ricerca di Automatica, vol. 10, no. 2, 71-106.
20. Jens Wittenburg (1977), Dynamics of Systems of Rigid Bodies, B.G. Teubner, Stuttgart.
21. W.M. Wonham (1979), Geometric state-space theory in linear multivariable control : a status report, Automatica, vol. 15, 5-13.
22. W.M. Wonham (1979), Linear Multivariable Control : A Geometric Approach, 2nd edition, Springer-Verlag, New York.

(*) M. El-Baraka is a graduate student in Electrical Engineering at the University of Maryland.

(**) P.S.Krishnaprasad is Associate Professor of Electrical Engineering at the University of Maryland.

Correspondence concerning this paper should be addressed to Prof.P.S.Krishnaprasad.

CONVECTED TRANSIENT ANALYSIS FOR LARGE
SPACE STRUCTURES MANEUVER AND DEPLOYMENT

Jerrold Housner *
NASA Langley Research Center
Hampton Virginia 23665

Abstract

An application of convected finite element transient analysis to maneuver and deployment of flexible multi-member trusses and frames for application to large space structures is presented. The use of convected analysis within the finite element framework permits accurate treatment of both large elastic deformations and large rigid body rotations, while permitting the utilization of a vast storehouse of existing computational finite element technology. A consistent mass (rather than a lumped mass) formulation of the equations of motion is developed so that exact rotational inertial properties are retained in the analysis. This is critical for space structures which undergo unlimited rotations. A shortcoming of consistent mass formulations for rotating elastic systems is that they lead to inertial terms which depend upon elastic motion and thus require up-dating. It is shown that this shortcoming may be avoided by making appropriate approximations with little loss in accuracy. The analysis is used to study maneuver of slender booms, deployment of axisymmetric hoops composed of flexible members and deployment of planar unfolding multi-flexible-member structures. It is found that multi-member structures can possess natural deployment patterns such as a sequential (member-by-member) pattern. Such patterns may be highly desirable features of deployment design and their achievement without the use of complex control mechanisms could represent considerable cost savings.

Nomenclature

$a_{i,1}, a_{i,2}$	coefficients of i^{th} beam element flexural shape function	(F)	vector of external forces
$A_{i,11}, A_{i,12}, A_{i,21}, A_{i,22}$	integrals of flexural shape function as given in Appendix B	(\hat{G}_i)	vector of nonlinear inertial terms for the i^{th} finite element.
[B]	connectivity matrix, eq. (20)	(G)	total vector of nonlinear inertial terms
[C]	constraint matrix, eq. (22)	$(\hat{G}_i(j))$	components of (\hat{G}_i) ; $(\hat{G}_i) = \sum_{j=1}^4 (\hat{G}_i(j))$
[D]	damping matrix	$g_i(j)_{,mn}$	entries of $(\hat{G}_i(j))$ as given in Appendix B; $1 \leq m \leq 6$; $1 \leq n \leq 6$
(\hat{d}_i)	vector of displacement degrees-of-freedom for i^{th} finite element	h_i	bending displacement of i^{th} finite element beyond the i^{th} convected coordinate, eq. (13)
(d)	full vector of displacement degrees-of-freedom, see eq. (20)	$H_{i,j}$	integrals of the flexural shape function; $1 \leq i \leq N$; $1 \leq j \leq 5$, see Appendix B
(\hat{f}_i)	vector of generalized forces for i^{th} finite element, see Appendix A	k	rotational spring constant at joints of deployable structures
(f)	full vector of generalized forces	$[K_S]$	spring constant matrix, see eq. (30)
		L_i	length of i^{th} finite element
		m_i	mass of i^{th} finite element
		$m_i(j)_{,rs}$	entries of $[M_i(j)]$; $1 \leq r \leq N$; $1 \leq s \leq N$, see Appendix A
		[M]	assembled mass matrix
		$[\hat{M}_i]$	mass matrix for i^{th} finite element
		$[\hat{M}_i(j)]$	components of mass matrix; $[\hat{M}_i] = \sum_{j=1}^3 [\hat{M}_i(j)]$
		N	total number of members
		N_D	total number of independent degrees of freedom
		r, R	local radius of hoop member during deployment at its center and either end, respectively
		R_h	fully deployed hoop radius
		\bar{s}	local dimensionless coordinate along convected beam finite element; $0 \leq s \leq 1$

* Aerospace Engineer, Member AIAA

$[T_i]$	convected coordinate transformation matrix for i th finite element	bility and large angle rotation, flexible and rotational responses are uncoupled and a linear solution is possible.
u, v	local displacement of beam element parallel to x and y axis respectively	This situation can occur when the following conditions are satisfied:
x, y	global cartesian coordinate system	(i) the structural modes (including rigid body modes) do not change with time
α_i	angle formed by i th undeformed finite element and x axis	(ii) the contributions of the external forces in each modal shape (including rigid shape) do not depend on the structure's rotated position
$\Gamma_{i,11}, \Gamma_{i,12}, \Gamma_{i,21}, \Gamma_{i,22}$	integrals of flexural shape functions, see Appendix A	(iii) the structural deformations are small
δ	variational operator	(iv) the nonlinear centrifugal and Coriolis forces are negligible.
$\epsilon_{m,i}$	mean axial strain of straight line joining end points of i th finite element	
$\epsilon_{0,i}$	mean axial strain of i th deformed finite element	
$\eta_{i,1}, \eta_{i,2}$	end point displacements of i th finite element parallel to x axis	
θ_i	angle formed by straight line joining the end points of i th finite element and the x axis	
$\xi_{i,1}, \xi_{i,2}$	end point displacements of i th finite element parallel to y axis	
$\phi_{i,1}, \phi_{i,2}$	rotations of i th finite element end points	
ψ	angle formed by hoop member and vertical axis, see figure 7	

Introduction

Recently, interest has grown in establishing permanently manned space stations. Space stations may be composed of multi-body interconnected structural components some of which are thin shells (habitation and work modules), panels (solar arrays and radiators) or booms (space booms, towers and robotic manipulator arms). These components or the entire space station may, from time to time, be maneuvered or, as in the case of robotic arms, manipulated through large rotations. Such maneuvers result in dynamic loads on the various space station components. It is likely that to obtain structural component loads for preliminary design, maneuvers of large beam-frame models will be analyzed.

In addition, many station components may be sent aloft packaged and then deployed in orbit. Deployment concepts often involve large rotations of flexible truss-type members. Since deployment experiments are both difficult and expensive to perform either on the ground or in orbit, dynamic analyses will be relied upon to validate performance of proposed deployment concepts.

In any of the three application areas, maneuver, manipulation or deployment, dynamics of interconnected flexible components undergoing large rotations is involved. In some cases involving flexi-

When only some of these conditions are met, it may still be accurate to perform a quasi-linear analysis in which the modes and/or external force contributions in the modal shapes are updated periodically in the course of the analysis. However, there exists a large class of problems in which the nonlinear coupling between flexibility and large angle rotation must be accounted for.

In space structures problems requiring a nonlinear analysis, the strains in the structural components are small even though rotations and hence displacements are large. To avoid the computations associated with accurate strain measures for large motions, it is desirable to separate the rigid body rotations from the structural deformations. This separation may be accomplished by using an updated or convected coordinate system.

Over the past decade, convected coordinates have been successfully used in conjunction with finite element models in performing transient response analyses using explicit time integration algorithms. (For example, see references 1-4). Thus, convected transient analysis techniques offer a viable approach for analyzing maneuver, manipulation and deployment. Two additional benefits to this approach are the utilization of a vast storehouse of finite element computational technology and the capability of the convected analysis within the finite element framework to account for both large elastic deformations and large rigid body rotations.

Even though convected transient analysis has seen considerable use, its application to fundamental configurations which are likely to arise in space stations and their components has not received much attention. Previous developments in convected frame analysis have been limited to structures containing large concentrated masses, such as automobiles where the engine, transmission, differential, etc, may be treated as lumped masses. A lumped mass formulation has considerable numerical advantages over a consistent mass formulation. However, many flexible components of large space systems do not lend themselves to an accurate lumped mass treatment. (See reference 5.) For example, large space booms and antenna structures have uniform or slowly varying distributed mass. Lumping the distributed mass leads to overestimating the rotational inertia and thus underestimating

its rigid body rotational rate. In addition, the coupling between rigid body motion and structural deformation due to nonlinear centrifugal and Coriolis forces or large structural deformations may be inaccurately represented in a lumped mass formulation. Thus a consistent mass formulation is desirable.

The purpose of this paper is to present the development and application of a consistent mass finite element formulation for convected transient analysis of two-dimensional beam-frame configurations for use in space. The computational consequences of a consistent mass formulation are discussed with emphasis on reducing computations through appropriate approximations. The analysis is applied to rotational maneuver and translation of long slender booms, deployment of an unfolding multi-flexible-member axisymmetric hoop and deployment of a planar unfolding multi-flexible-member structure.

Convected Analysis

The purpose in using a convected analysis is to separate rigid body rotations from structural deformations for in each finite element. The need for this separation arises since any truncated form of the physical strain measure in a fixed coordinate system is inaccurate for large rotations. Separation may be accomplished by setting up a collection of convected coordinate systems which follow the rotation of each finite element. The convected analysis used herein deviates from that of references 1 thru 3 in that the development of the inertial terms uses a consistent mass formulation rather than a lumped mass formulation. The consistent formulation is important when rigid body rotations must be accurately accounted for. To illustrate this consider the rotation of a single rigid beam member. Figure 1 illustrates the error from the exact rotational inertia associated with a lumped mass or diagonal mass matrix formulation. This simple illustration demonstrates that when a lumped mass formulation is used, five rigid finite elements are required to approximate the exact rotational inertia to within eight percent. On the other hand, a consistent mass formulation requires only one rigid finite element for the exact value.

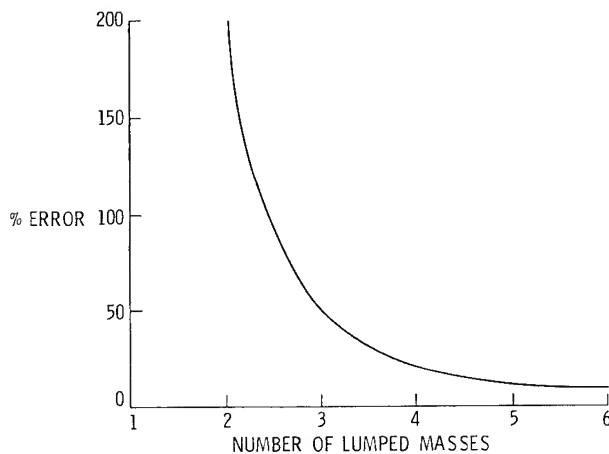


Figure 1. Percent Error in Centroidal Rotational Inertia For Lumped Mass Modeling of Beam Member [Error=(Approx. value)/(Exact value) - 1]

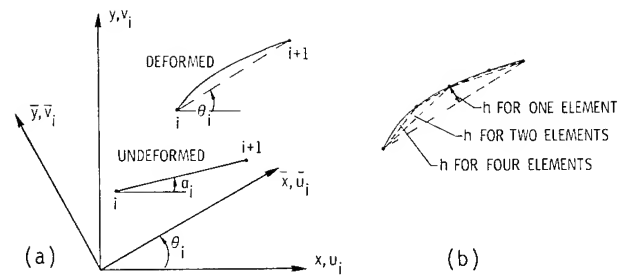


Figure 2. Finite Element Deformation and Convected Coordinate System

(a) Rotation of Convected Axes

(b) One, Two and Four Finite Element Modeling of a Single Beam Member

Coordinate system

Consider the deformed beam finite element shown in figure 2a. The convected motion of the element is defined by the straight line which joins the ends of the element. Deviation from this line constitutes the deformation of the element. A convected coordinate system, local to each element is thus defined which rotates with the element, but does not translate with it. (The convected coordinate system could be defined to translate with the element, but this is not necessary.) The convected system in general differs for each element. Coordinates in the global stationary coordinate system are related to those in the i^{th} convected system by

$$\begin{pmatrix} x_i \\ y_i \end{pmatrix} = [T_i] \begin{pmatrix} \bar{x}_i \\ \bar{y}_i \end{pmatrix} \quad (1)$$

where barred and unbarred quantities denote measurements in the convected and stationary coordinate systems respectively and

$$[T_i] = \begin{bmatrix} \cos\theta_i & -\sin\theta_i \\ \sin\theta_i & \cos\theta_i \end{bmatrix} \quad (2)$$

The convection angle θ_i for the i^{th} element is defined by

$$\tan\theta_i = (L_{i,y} + \Delta\xi_i)/(L_{i,x} + \Delta\eta_i) \quad (3)$$

where $L_{i,x}$ and $L_{i,y}$ are the projected lengths of the i^{th} undeformed element on the x and y axes respectively and

$$\Delta\eta_i = \eta_{i,2} - \eta_{i,1}$$

$$\Delta\xi_i = \xi_{i,1} - \xi_{i,2}$$

in which $\eta_{i,1}$, $\eta_{i,2}$, $\xi_{i,1}$ and $\xi_{i,2}$, are the values of grid point displacements at the ends of the i^{th} element and parallel to the x and y axes as shown in figure 2a.

The displacements in the convected system at any point on the i^{th} element transform as

$$\begin{pmatrix} u_i \\ v_i \end{pmatrix} = [T_i] \begin{pmatrix} \bar{u}_i \\ \bar{v}_i \end{pmatrix} \quad (4)$$

However, the velocities transform as

$$\begin{pmatrix} \dot{u}_i \\ \dot{v}_i \end{pmatrix} = [T_i] \begin{pmatrix} \dot{\bar{u}}_i \\ \dot{\bar{v}}_i \end{pmatrix} + [T_i][I^*] \begin{pmatrix} \dot{\bar{u}}_i \\ \dot{\bar{v}}_i \end{pmatrix} \dot{\theta}_i \quad (5a)$$

where,

$$[I^*] = \begin{bmatrix} 0 & -1 \\ 1 & 0 \end{bmatrix}$$

and the accelerations transform as,

$$\begin{pmatrix} \ddot{u}_i \\ \ddot{v}_i \end{pmatrix} = [T_i] \begin{pmatrix} \ddot{\bar{u}}_i \\ \ddot{\bar{v}}_i \end{pmatrix} - 2[I^*] \begin{pmatrix} \dot{\bar{u}}_i \\ \dot{\bar{v}}_i \end{pmatrix} \dot{\theta}_i - [I^* \ddot{\theta}_i + I(\dot{\theta}_i)^2] \begin{pmatrix} \bar{u}_i \\ \bar{v}_i \end{pmatrix} \quad (5b)$$

In equation (5b) the second and fourth terms on the right hand side are recognized as the Coriolis and centrifugal contributions, respectively, to the absolute acceleration vector. Converse relationships for equations (5a) and (5b) may readily be derived.

Rotation and Strain Rates

The rotational rate of the straight line joining the end points of the i^{th} finite element may be found by differentiating eq. (3) with respect to time and the mean axial strain rate may be found by differentiating with respect to time the relation

$$\epsilon_{i,m} = \sqrt{(L_{i,x} + \Delta\eta_i)^2 + (L_{i,y} + \Delta\xi_i)^2} - 1 \quad (6)$$

The result is

$$\begin{pmatrix} \dot{\epsilon}_{i,m} \\ (1 + \epsilon_{i,m}) \dot{\theta}_i \end{pmatrix} = (1/L_i)[T_i]^T \begin{pmatrix} \dot{\Delta\eta}_i \\ \dot{\Delta\xi}_i \end{pmatrix} \quad (7)$$

For small strains, $\epsilon_{i,m}$ on the left hand side of eq. (7) may be neglected compared to unity.

Finite Element Displacements

The finite element displacements may be approximated in the convected system as,

$$u_i(\bar{s}) = \eta_{i,1} + \bar{s}\Delta\eta_i \quad (8a)$$

$$v_i(\bar{s}) = \xi_{i,1} + \bar{s}\Delta\xi_i + h_i(\bar{s}) \quad (8b)$$

where, h_i is the flexural displacement and

$$h_i(0) = h_i(1) = 0$$

and

$$0 \leq \bar{s} \leq 1$$

The local strain at the neutral axis of the i^{th} element may be found from by adding on to $\epsilon_{i,m}$, the usual first-order neutral axis strain due to flexure to yield,

$$\epsilon_{i,0} = \epsilon_{i,m} + (1/2L_i^2)(h_i')^2 \quad (9)$$

and the axial strain at any point through the thickness of the element is,

$$\epsilon_i = \epsilon_{i,0} - (z/L_i^2)v_i''$$

where z is a thickness coordinate measured from the neutral axis.

Virtual Work

The virtual work contribution from the internal forces of the i^{th} element is given by,

$$\delta U_i = L_i \int_0^1 (P_i \delta \epsilon_{i,0} - (M_i/L_i^2) \delta v_i'') d\bar{s} \quad (10)$$

where P_i is the average axial load over the length of the i^{th} element and M is the bending moment in the i^{th} element given by,

$$M_i = -(EI)_i v_i''/L_i^2$$

From eqs. (7) and (9),

$$\delta \epsilon_{i,0} = (\delta \Delta\eta_i \cos \theta_i + \delta \Delta\xi_i \sin \theta_i) / L_i + h_i' \delta h_i' / L_i^2 \quad (11)$$

Substituting eqs. (11) and (8b) into eq. (10) gives,

$$\begin{aligned} \delta U_i = & P_i (\delta \Delta\eta_i \cos \theta_i + \delta \Delta\xi_i \sin \theta_i) + (1/L_i^2) \int_0^1 M_i \delta h_i' d\bar{s} \\ & + (1/L_i) \int_0^1 P_i h_i' \delta h_i' d\bar{s} \end{aligned} \quad (12)$$

Herein the flexural displacement is defined as,

$$\begin{aligned} h_i(s) = & a_{i,1}(s)\phi_{i,1} + a_{i,2}(s)\phi_{i,2} \\ & - [a_{i,1}(s) + a_{i,2}(s)](\theta_i - \alpha_i) \end{aligned} \quad (13)$$

where $\phi_{i,1}$ and $\phi_{i,2}$ are rotations of nodes 1 and 2 at the ends of the i^{th} element. Substituting into eq. (12) yields,

$$\delta U_i = (\hat{f}_i)(\delta \hat{d}_i) \quad (14)$$

where

$$(\hat{d}_i) = (\eta_{i,1}, \xi_{i,1}, \phi_{i,1}, \eta_{i,2}, \xi_{i,2}, \phi_{i,2})^T$$

and the expressions for entries of the internal force vector (f_i) are given in Appendix A.

For a consistent mass formulation, the contribution of the i^{th} element to the total virtual work done by the inertial forces is expressed as,

$$\delta W_i = m_i \int_0^1 (\delta u_i, \delta v_i)(\dot{u}_i, \dot{v}_i)^T d\bar{s} \quad (15)$$

where m_i is the uniform mass of the i^{th} element and the expressions for δu_i and δv_i may be found by substituting the variations of eqs. (8a) and (8b) into eq. (5) to yield

$$\begin{pmatrix} \delta u_i \\ \delta v_i \end{pmatrix} = \begin{pmatrix} \delta \eta_{i,1} + \bar{s} \delta \Delta\eta_i \\ \delta \xi_{i,1} + \bar{s} \delta \Delta\xi_i \end{pmatrix} + \begin{pmatrix} -h_i \delta \theta_i \cos \theta_i - \delta h_i \sin \theta_i \\ -h_i \delta \theta_i \sin \theta_i + \delta h_i \cos \theta_i \end{pmatrix} \quad (16a)$$

The expressions for \ddot{u}_i and \ddot{v}_i are found by differentiating eqs. (8a) and (8b) and substituting into eq. (6) to yield,

$$\begin{pmatrix} \ddot{u}_i \\ \ddot{v}_i \end{pmatrix} = \begin{pmatrix} \ddot{\eta}_{i,1} + s \ddot{\Delta\eta}_i \\ \ddot{\xi}_{i,1} + s \ddot{\Delta\xi}_i \end{pmatrix} + \begin{pmatrix} -\ddot{h}_i \sin \theta_i - 2\dot{\theta}_i \dot{h}_i \cos \theta_i - h_i \ddot{\theta}_i^2 \sin \theta_i - \dot{\theta}_i \dot{h}_i \cos \theta_i \\ \ddot{h}_i \cos \theta_i - 2\dot{\theta}_i \dot{h}_i \sin \theta_i - h_i \ddot{\theta}_i^2 \cos \theta_i - \dot{\theta}_i \dot{h}_i \sin \theta_i \end{pmatrix} \quad (16b)$$

In each of equations (16a) and (16b) the first column vector on the right hand side arises from the rigid body motion of the finite element while the second term arises from the flexural deformations of the element. Coriolis and centrifugal terms are explicit in the the second term of eq. (16b) and implicit in the first term. The implicit effect may be observed by transforming the first term of eq. (16b) to convected coordinates via eq. (6) and then evaluating the result at the element end points.

When the product of eqs. (16a) and (16b) is taken to produce the integrand of eq. (18) and the indicated integration is performed, rigid body rotation and flexural deformation terms are coupled. The result for the i^{th} element may be expressed as

$$\delta W_i = m_i(\delta \hat{d}_i)[\hat{M}_i](\ddot{\hat{d}}_i) + m_i(\delta \hat{d}_i)^T(\hat{G}_i) \quad (17)$$

where $[\hat{M}_i]$ is the mass matrix of the i^{th} finite element, and (\hat{G}_i) is a vector of nonlinear kinematic terms.

The mass matrix contains terms due to rigid body motion and the predominant inertial coupling between rigid body motion and flexural deformation. The treatment of the mass matrix is simplified by observing that it may be separated into three distinct parts, namely,

$$[\hat{M}_i] = \sum_{j=1}^3 [\hat{M}_i(j)]$$

The entries of $[\hat{M}_i(j)]$ are given in Appendix B. Entries of $[\hat{M}_i(1)]$ are independent of i and arise from rigid body motions and stretching of the i^{th} finite element while those of $[\hat{M}_i(2)]$ and $[\hat{M}_i(3)]$ arise from flexural motions of the i^{th} finite element. The entries of both $[\hat{M}_i(2)]$ and $[\hat{M}_i(3)]$ depend on the convected rotation θ_i and hence would generally require up-dating during the analysis. Furthermore, those entries requiring up-dating contain h_i .

As the size of the finite element is reduced, the value of h_i decreases as is noted in figure 2b and then the entries of $[\hat{M}_i(3)]$ also decrease. Thus for a sufficiently fine finite element grid, the contribution of $[\hat{M}_i(3)]$ to the total virtual work becomes negligible and if retained would require few up-dates during the analysis. Furthermore, if an element is rigid, then from eq. (13),

$$\phi_{i,1} = \phi_{i,2} = \theta_i \quad (18)$$

It may then be shown that the contributions of $(\delta \hat{d}_i)[\hat{M}_i(2)](\ddot{\hat{d}}_i)$ to the virtual work of the inertial forces vanishes for a rigid element and furthermore for a stiff element, approaches zero as h approaches zero. It follows, that for relatively stiff elements, few up-dates of $[\hat{M}_i(2)]$ will be required. For the cases considered herein, it was found that even for booms with slenderness ratios up to 1000, $[\hat{M}_i(2)]$ still required few up-dates and $[\hat{M}_i(3)]$ could be entirely neglected when two finite elements were used per half-wave of beam member deformation.

Similarly the vector (\hat{G}_i) may be separated as,

$$(\hat{G}_i) = \sum_{j=1}^4 (\hat{G}_i(j))$$

whose entries are given in Appendix B. These vectors arise from coupling between element flexure and nonlinear centrifugal and Coriolis effects. All five vectors vanish as h_i approaches zero. Furthermore, for small h_i , $(\hat{G}_i(1))$, $(\hat{G}_i(2))$ and $(\hat{G}_i(3))$ behave as h_i , while $(\hat{G}_i(4))$ behaves as h_i^2 . (This does not imply that all centrifugal and Coriolis effects vanish as h_i approaches zero, for these effects are implicit in the piecewise representation of the entire member).

As a consequence of the foregoing discussion, it is clear that many terms in the governing equations will be quite small in many applications and either be negligible or require few up-dates.

Equations of Motion and Constraint

The equations of motion may be derived from the principle of virtual work using eqs. (14) and (17)

$$\sum_{i=1}^N (\delta \hat{d}_i)^T \{m_i[\hat{M}_i](\ddot{\hat{d}}_i) + m_i(\hat{G}_i) + (\hat{f}_i)\} = \delta W_e \quad (19)$$

where δW_e is the virtual work of applied external forces and N is the total number of beam members. Lumped masses are accommodated by appropriate additions to the diagonal entries of $[\hat{M}_i]$. Equation (19) yields the equations of motion if the entries of $(\delta \hat{d}_i)$ are independent. However, they are not independent since members are connected together and since multi-point constraints or other constraints may exist. An independent set of displacements can be formed by utilizing the constraints on the system.

Connectivity Constraints

Connectivity relations may be expressed by the matrix equation,

$$((\hat{d}_i)(\hat{d}_2)_j, \dots, (\hat{d}_N))^T = [B](d) \quad (20)$$

where (d) is a vector of N_D degrees of freedom. The connectivity matrix $[B]$ will usually contain many zeros and ones. Rather than substitute eq. (20) into eq. (19), connectivity is usually accounted for in finite element computer implementation when the mass matrix and internal force vectors are assembled. This is accomplished by appropriate superposition of entries in (\hat{G}_i) , (\hat{f}_i) and $[\hat{M}_i]$ as directed by the connectivity array and computer storage addresses. Thus after assembly, eq. (19) effectively takes on the form,

$$(\delta d)^T \{[M](d) + (G) + (f)\} = (\delta d)^T (F) \quad (21)$$

where (F) is a vector of external forces.

Linear Multi-point Constraints

For N_C (less than N_D) multi-point constraints one has,

$$[C_{DD}; C_{DI}] \begin{pmatrix} d_D \\ - \\ d_I \end{pmatrix} = 0$$

where the constraint matrix and displacement vector (d) have been partitioned into dependent and independent sets. The selected set of dependent degrees-of-freedom be expressed in terms of the independent set of degrees-of-freedom as

$$(d_D) = [C](d_I)$$

where,

$$[C] = -[C_{DD}]^{-1}[C_{DI}] \quad (22)$$

Eq. (22) could be substituted into a partitioned form of eqs. (21). However, in some applications, the multi-point constraints can change many times during the course of analysis. This can be due to lock-up of certain members in a deployment analysis, contact conditions as in assembly, docking and berthing or articulation of structural components. In such cases it may be more computationally efficient to eliminate the jth dependent degree-of-freedom by multiplying the jth row of [M], (G), (f) and (F) by c_{jk} (where c_{jk} is an entry of the constraint matrix), and adding the result to all the other rows of [M], (G), (f) and (F) respectively, for all k and j in the ranges $1 < k \leq N_D$ and $1 < j \leq N_C$. This effectively eliminates (δd_D) . A similar procedure is followed for the columns of [M] thereby effectively eliminating (d_D).

Constraints Due to Rigid Members

Axial rigidity

The ith member is defined as axially rigid if the neutral axis strain, its variation and its derivatives vanish. Then from eqs (11),

$$\delta n_{i,1} = \delta n_{i,2} + \delta \Delta \xi_i \tan \theta_i \quad (23a)$$

$$\dot{n}_{i,1} = \dot{n}_{i,2} + \Delta \dot{\xi}_i \tan \theta_i \quad (23b)$$

where, for simplicity, the first-order nonlinear term of eq. (11) caused by local finite element flexure has been dropped. Differentiation with respect to time of eq. (23b) yields,

$$\ddot{n}_{i,1} = \ddot{n}_{i,2} + \Delta \ddot{\xi}_i \tan \theta_i + \Delta \dot{\xi}_i \dot{\theta}_i \sec^2 \theta_i \quad (23c)$$

and from eqs. (7) and (23b)

$$\dot{\theta}_i = \Delta \dot{\xi}_i / (L_i \cos \theta_i)$$

Equations (23a) and (23c) may be used to eliminate $\delta n_{i,1}$ and $\dot{n}_{i,1}$ in eq. (21) by appropriate manipulation of the rows of (G), (f) and (F), and the rows and columns of [M]. The nonlinear term in eq. (23c) cannot be dropped as it is not a negligible term. It may be handled through appropriate augmentation of the internal force vector (f).

Flexural rigidity

If the ith member is flexurally rigid then, from eq. (18),

$$\delta \phi_{i,1} = \delta \phi_{i,2}$$

$$\dot{\phi}_{i,1} = \dot{\phi}_{i,2}$$

and from the second of eqs. (7),

$$\delta \xi_{i,1} = \delta \xi_{i,2} - \delta \Delta n_i \tan \theta_i - L_i \delta \phi_{i,2} / \cos \theta_i \quad (24a)$$

$$\dot{\xi}_{i,1} = \dot{\xi}_{i,2} - \Delta \dot{n}_i \tan \theta_i - L_i \dot{\phi}_{i,2} / \cos \theta_i \quad (24b)$$

Differentiation of eq. (24b) with respect to time yields,

$$\ddot{\xi}_{i,1} = \ddot{\xi}_{i,2} - \Delta \ddot{n}_i \tan \theta_i - L_i \ddot{\phi}_{i,2} / \cos \theta_i - \dot{\xi}_{i,2} \dot{\theta}_i L_i \cos \theta_i \quad (24c)$$

Eqs. (24a) and (24c) may be used to eliminate $\delta \phi_{i,1}$, $\dot{\phi}_{i,1}$, $\delta \xi_{i,1}$, $\dot{\xi}_{i,1}$ in eq. (21) by appropriate manipulation of the rows of (G), (f), and (F) and the rows and columns of [M]. The nonlinear term in eqs. (24c) cannot be dropped as it is not negligible. It may be handled through appropriate augmentation of the internal force vector (f).

Numerical Solution of Equations of Motion

Equation (24) may be solved numerically by selecting from any of a wide choice of time integration algorithms. (See for example the survey article of reference 6.) An explicit algorithm is chosen here because it can readily accommodate a host of nonlinearities, damping mechanisms and control actuators. In particular a modified central difference algorithm is selected. This leads to the following recursive procedure,

$$\begin{aligned} (\ddot{d}(t)) &= -\{[M] + (1/2)\Delta t[D]\}^{-1}\{(f(d(t))) \\ &+ (G(d(t), \dot{d}_p(t), \ddot{d}_p(t)) + [D](\dot{d}(t-\Delta t)) - (F)) \\ (\dot{d}(t)) &= (\dot{d}(t-\Delta t)) + (1/2)\Delta t(\ddot{d}(t) + \ddot{d}(t-\Delta t)) \\ (d(t)) &= (d(t-\Delta t)) + \Delta t(\dot{d}(t)) \end{aligned} \quad (25)$$

where (\dot{d}_p) and (\ddot{d}_p) are velocity and acceleration predictors which are used only in conjunction with terms on the order of the flexure of a finite element. The predictors are chosen herein as,

$$\dot{d}_p(t) = \dot{d}(t-\Delta t) + \Delta t \ddot{d}(t-\Delta t) \quad (26)$$

$$\ddot{d}_p(t) = \ddot{d}(t-\Delta t) \quad (27)$$

and [D] is a linear viscous damping matrix.

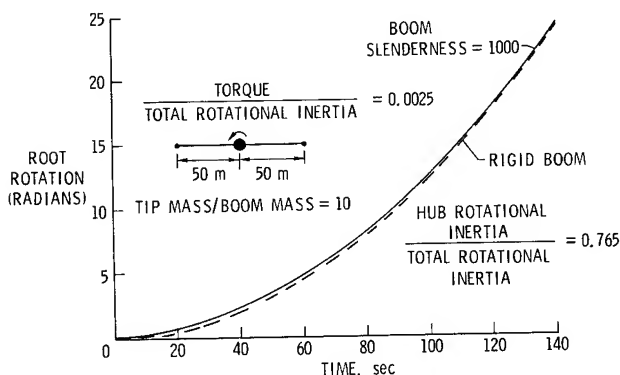


Figure 3. Hub Rotation Due To Applied Torque Step Load

Applications

The convected transient analysis presented herein is applicable to multi-body flexible truss and frame problems which may involve maneuver through large angles, translation through space or deployment. In this section the following problems are considered: slewing maneuver of a long slender boom, translation of two slender beams hinged together, deployment of an axisymmetric multi-flexible-member hoop and deployment of a planar multi-flexible member unfolding structure. In each application cubic flexural shape functions are chosen.

Slewing Maneuver

Figure 3 displays the time varying response of a slender boom with a rigid central hub subject to an applied torque. The hub rotation for a connected flexible boom with slenderness ratio 1000 is compared with that of a connected rigid boom. The hub rotation with a connected flexible boom is always equal to or greater than that of a connected rigid boom. This occurs because the inertial mass accelerated by the applied torque is the sum of the hub inertial mass plus the inertial mass of the boom from the hub out to the flexural wave front and the latter mass is less than or equal to the total boom inertial mass. Hence, the variation of the hub motion with connected rigid and flexible booms depends on the relative rotational inertial masses of the hub and boom as well as boom slenderness ratio. For the case displayed in figure 3, the inertial mass of the hub is considerably greater than that of the boom. Hence the deviation between the rigid and flexible responses is small.

As shown in figure 4, the tip motions of the flexible and rigid booms are quite different from that of the hub. Specifically, the tip motion with the flexible boom lags that with the rigid boom. This may be understood by considering the time delay caused by flexural wave propagation along the boom. As might be expected, the difference between rigid and flexible boom tip motion is relatively large compared to the differences at the hub. Thus boom flexibility can greatly influence pointing without significantly influencing hub rotation. Finally, in figure 5, the axial load experienced by the flexible and rigid booms is compared. Axial loads are due to centrifugal

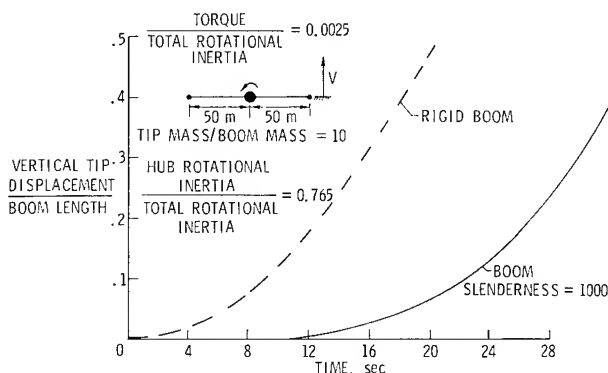


Figure 4. Boom Tip Displacement Due To Applied Torque Step Load

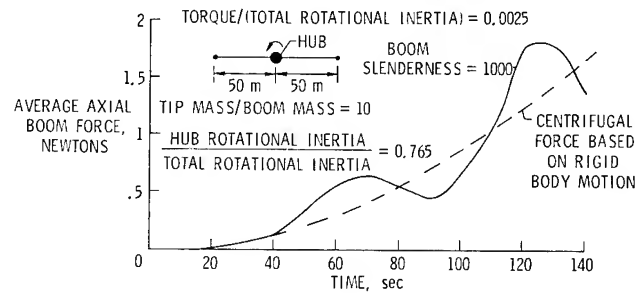


Figure 5. Axial Load Due To Applied Torque Step Load

force. The flexible boom axial load is seen to oscillate about the rigid value with increasing amplitude and frequency as the boom gains angular velocity.

Translation of two hinged flexible beams by a constant-direction step load

Figures 6a and 6b display the calculated motion of two identical beams hinged together at their ends and subject to constant-direction step load at one end. The problem is kinematically nonlinear because the torque caused by the constant-directional load and the load components in the beam modes vary with the kinematics. Displacements are shown in figure 6a for a flexible beam and the trajectory of the load application point is shown in figure 6b for both a flexible and a rigid beam. Examination of the trajectories of the load application point indicate that flexure has little effect on trajectory during the early phase of motion, but becomes more important as the motion proceeds.

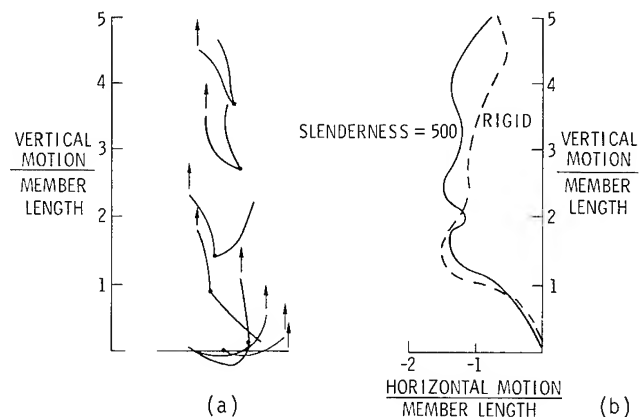


Figure 6. Large Distortion and Motion of Two Pin-Connected Beams Subject to a Vertical Tip Step Load

(a) Member Deformations

(b) Load Point Trajectory

Hoop Deployment

The hoop investigated here is similar in some respects to that of the Hoop/Column Antenna concept of reference 7. In the present study the complex control linkage between adjacent members of the hoop in reference 7 is replaced by

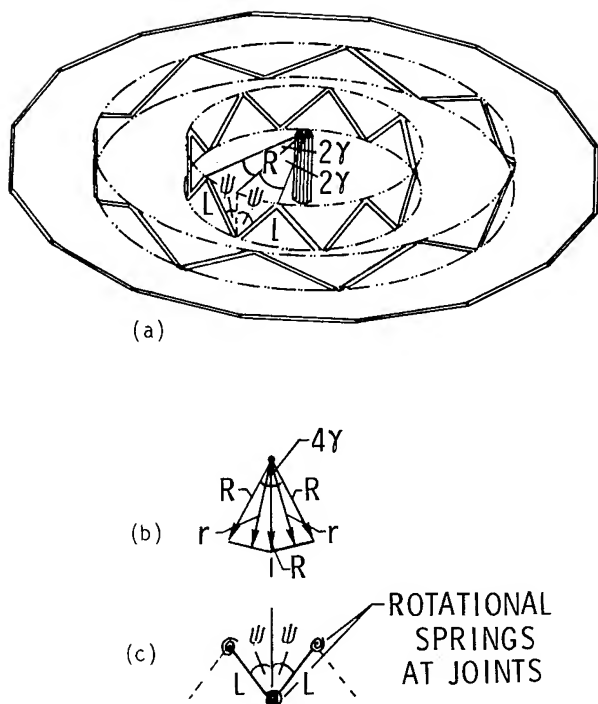


Figure 7. Hoop Deployment (N=16)
 (a) Deployment Sequence
 (b) Top View of Two Adjacent Members
 (c) Front View of Two Adjacent Members

simple linear rotational springs at each joint which drive the deployment as shown in figures 7a and b. The hoop is assumed to be composed of N, (an even integer), identical flexible beam members of length L. The members are assumed to be connected through universal joints which do not transmit any moments. At any time during deployment, the members project on the horizontal plane as an N sided polygon with the joints between adjacent members lying on a circle of radius R. As deployment proceeds, R increases to a fully deployed hoop values of R_h .

Due to the symmetry of the hoop, only one member of the hoop, say the i^{th} member, needs to be analyzed provided the effects of the other members on it are accounted for. The effect of the other members on the i^{th} member can be systematically derived by establishing the virtual work of all the members in terms of the motions of the i^{th} member. Effectively, the other members constrain the motion of the i^{th} member and it is shown herein that this constraint may be modeled as an additional mass matrix superimposed on the mass matrix of the i^{th} member.

As shown in figure 7b, the i^{th} member lies in a plane normal to and translating parallel to the local radius r. Thus its virtual work has a contribution from the motion of the member in the plane and a contribution from the motion of the plane, namely,

$$\delta W_i = \delta W_i^{(1)} + \delta W_i^{(2)}$$

The first term is associated with member motion in the plane and has already been established in eq. (17). It remains to establish the second term. The second term is derived from the geometric relationship between the translations of the plane and motions of the i^{th} member in the plane. For the purpose of deriving this geometric relationship, the members are assumed to behave rigidly. However, this assumption is relaxed later in performing the dynamic deployment analysis.

The angle 2γ which is formed by the radii of two adjacent joints depends on the number of hoop members as

$$\gamma = \pi/N$$

The value of α remains constant during deployment, but as R increases during the deployment process, the angle ψ formed by the member and the vertical axis varies since,

$$R \sin \gamma = (L/2) \sin \psi \quad (27)$$

When fully deployed ψ is $\pi/2$ and

$$R_h = L/(2 \sin \gamma) \quad (28)$$

Since,

$$\sin \psi = (\eta_b - \eta_a)/L$$

where η_a and η_b are horizontal displacements of the hoop member ends in a plane normal to r, eq. (27) yields,

$$R \sin \gamma = (1/2)(\eta_b - \eta_a) \quad (29)$$

The contribution to the virtual work due to radial motion is,

$$\delta W_i^{(2)} = m \ddot{r} \delta r$$

Noting that

$$r = R \cos \gamma$$

and substituting from eq. (29) gives

$$\delta W_i^{(2)} = (m/4)(\ddot{\eta}_b - \ddot{\eta}_a)(\delta \eta_b - \delta \eta_a) \cot^2 \gamma$$

The principle of virtual work applied to the entire hoop may be expressed as,

$$N \delta W_i^{(1)} + N(\delta d)^T [M_h](d) + 2N(\delta d)^T [K_s](d) = 0 \quad (30)$$

where,

$$(d) = (\eta_{i,1}, \xi_{i,1}, \phi_{i,1}, \eta_{i,2}, \xi_{i,2}, \phi_{i,2}, \dots, \eta_{p,2}, \xi_{p,2}, \phi_{p,2})^T$$

and p is the number of finite elements employed to model the i^{th} hoop member. The nonzero entries of $[M_h]$ are,

$$(m_h)_{1,1} = (m_h)_{q,q} = (m/4) \cot^2 \gamma$$

$$(m_h)_{1,q} = (m_h)_{q,1} = -(m/4) \cot^2 \gamma$$

The nonzero entries of $[K_S]$ are

$$(k_s)_{1,3} = (k_s)_{6p,6p} = k$$

where k is the rotational spring constant at each joint. Dividing eq. (30) by N reveals that the equation of motion for axisymmetric deployment is identical to that for a single hoop member whose mass matrix is incremented by $[M_h]$ and which has grounded rotational springs at each end with a spring constant equal to twice the nominal spring constant value.

As an example application, consider a twenty member hoop ($N=20$). Figure 8 displays the predicted motion of two adjacent flexible hoop members during the deployment process. Each member has a slenderness ratio of 1000. Hoop member deformation is shown at one quarter, one-half and near fully deployed. During deployment, each member deforms into a two half-wave pattern which is consistent with the symmetry of the hoop. In figure 9, the time for the hoop to reach full deployment is examined over a range of N values. Two cases are displayed. In one case the individual hoop member length is fixed so that as N increases, the fully deployed hoop radius and total hoop weight also increase, while in the other case, the fully deployed hoop radius is fixed so that as N increases, the individual member lengths and mass decrease, however the total hoop weight remains essentially unchanged.

In each case results are shown for hoops containing all rigid or all flexible members and flexibility is seen to have little affect on deployment time.

The trends for the two cases are different and, where they cross, the hoop geometries are identical. The trend for each case may be approximately established in closed form by considering only the influence of the diagonal entries of the added mass matrix $[M_h]$ on a rigid member. Such a consideration reveals that for the fixed length case the deployment time varies linearly with N while for the fixed radius case it varies inversely with the square root of N . The deployment analysis confirms these trends.

TOP VIEWS

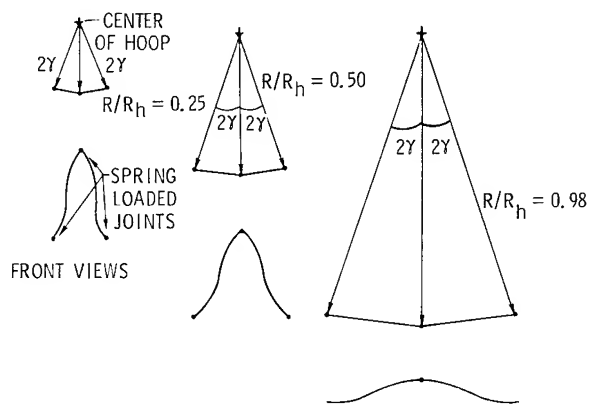


Figure 8. Top and Front Views of Two Adjacent Hoop Members During Deployment of Twenty Member Hoop, $k=2.82 \text{ m.N/radian}$

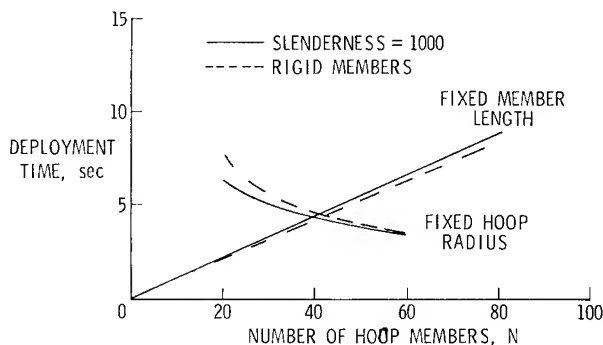


Figure 9. Deployment Times For Hoops Composed of Various Numbers of Members

Multi-member Unfolding Deployment

An accordion-like flexible beam deployable structure having N pin-connected members is shown in figure 10. When fully deployed the structure is a continuous flexible boom. Thus, when the angle between two adjacent members reaches 180 degrees, the joint is assumed locked and thereafter is a rigid joint. The deployment of the structure is driven by rotational springs located at each joint. All springs are identical, initially compressed and fully relaxed when the joint they are located at locks-up. Considerable insight into unfolding deployable structures is gained by examination of this generic structure.

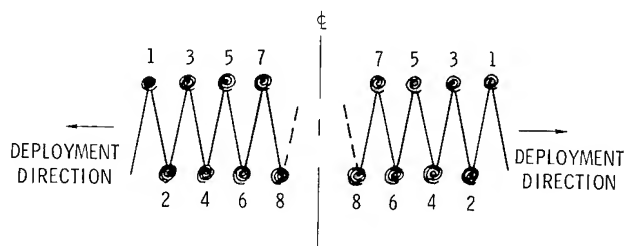


Figure 10. Geometric Configuration of Planar Unfolding Structure Showing Rotational Joint Springs and Joint Numbering Pattern. (Not An Actual Deployment)

Even Number of Members ($N=2,4,6,\dots$)

$N=2$ - Figure 11 displays the calculated deployment sequence of a two-member structure in a cumulative superimposed fashion where each member was modeled with two finite elements. Member deformations have not been scaled-up, but are consistent with the drawn member length and little flexure of the members prior to lock-up is visible. Following lock-up considerable member flexure occurs and the deployed boom vibrates in essentially a first symmetric free-free mode shape.

$N=4$ - Figure 12 displays the deployment of a four member structure in the same fashion as that used in figure 11. Prior to lock-up, members appear to exhibit more flexure than in the single-member case. Since the outer members accelerate less mass, the outer joints lock-up first shortly followed by the inner joint. Following lock-up,

the deployed boom vibrates with essentially a second symmetric free-free mode shape. However, the post-lock-up shape depends upon member stiffness. Though not shown, stiffer members can yield a first symmetric free-free vibration shape.

$N=6,8,10,\dots$ When the structure has six or more members, the time difference between the lock-up of the joints becomes greater than that exhibited in the two-member case. Lock-up begins at the outer most joints and proceeds towards the center of the structure as shown, for example, in the progressive deployment states of the sixteen-member structure of figure 13. Also, lock-up times for some of the joints in various multi-member configurations are provided in the Table.

Joints are numbered beginning at the outermost joint and progressing towards the center so that, independent of the number of members, the outermost joint is always joint number one. Note that the lock-up time for joint 1 is independent of the number of members and that other joint lock-up times also become independent of the number of members as the number of members increases. In general, lock-up times for all but the innermost joints are independent of the number of members. The result is that the structural joints lock-up sequentially even though all members and springs are identical. Again the reason for this is traced to the quantity of mass the various members must accelerate.

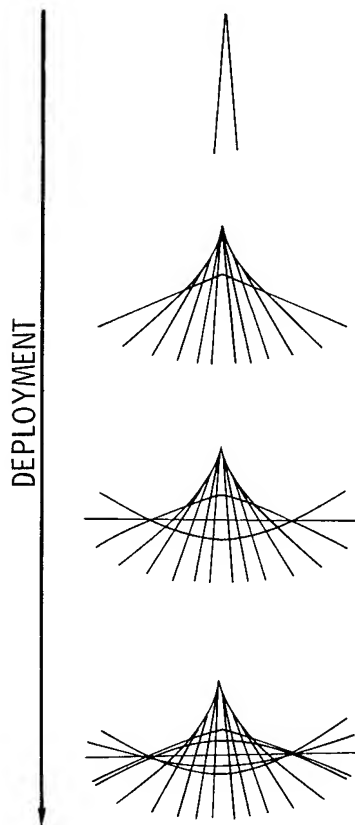


Figure 11. Deployment Sequence of Two-Flexible-Member Unfolding Structure

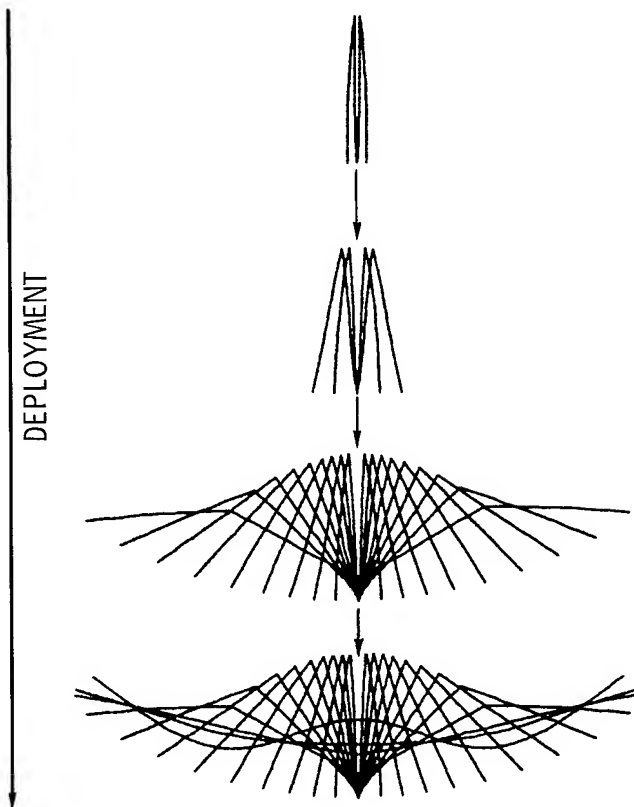


Figure 12. Deployment Sequence of Four-Flexible-Member Unfolding Structure

This basically sequential pattern is considered a desirable quality for deployable space structures. (See references 8 and 9.) For the multi-member structure considered here, sequential deployment appears to occur naturally; that is, without the aid of external mechanisms, controls or dampers. It is anticipated that multi-member deployment configurations other than the one considered here will also exhibit natural deployment patterns, though they may not be of the sequential type. If this is the case, it would allow the designer to select member and spring properties to achieve a preferred deployment pattern without the expensive addition of controlled or passive mechanisms to enforce a prescribed pattern.

Odd Number of Members ($N=3,5,7,\dots$)

For the unfolding type structures considered here the deployment pattern for an odd number of members differs from that of an even number of members. For example, consider the five member structure of figure 14. Due to the odd number of members, the deployment pattern tends to appear rotated counter-clockwise. Actually, the two outer members are rotating clockwise while the three inner members are rotating counter-clockwise. The result is that the pattern satisfies the conservation of angular momentum. As in the case of an even number of members, the deployment pattern tends to become sequential as the number of members in the structure increases. However, the pattern will be distorted somewhat due to the conservation of angular momentum. This distortion should decrease as the number of members increases.

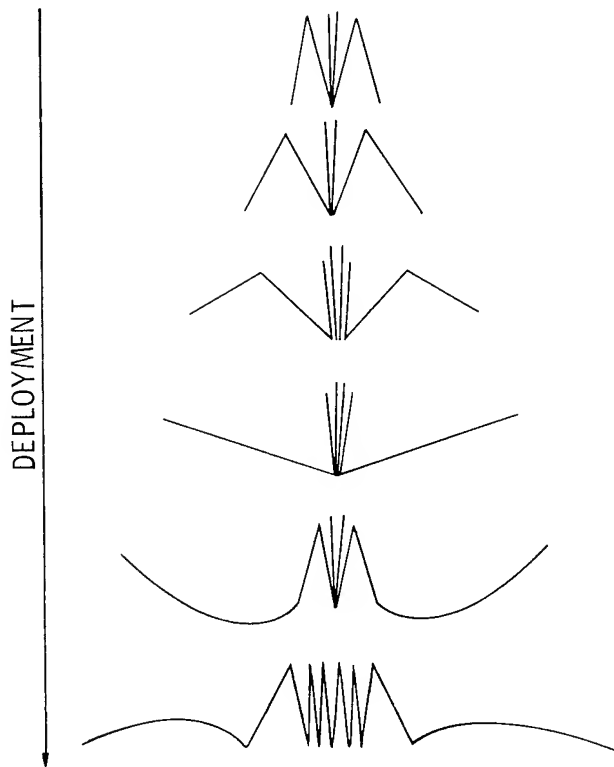


Figure 13. Deployment Sequence of Sixteen-Flexible-Member Unfolding Structure

Concluding Remarks

The application of convected finite element transient analysis to maneuver and deployment of two-dimensional truss and frame space structures has been presented. This approach permits the utilization of a vast storehouse of finite element computational technology and, within the finite element framework, the convected analysis accounts for both large rotations and large elastic deformations.

A consistent mass (rather than a lumped mass) formulation of the equations of motion has been incorporated so that exact rotational inertial properties are retained in the analysis which is critical for space structures which can undergo large rotations. Within the convected analysis framework, a consistent mass approach has been shown to allow the resulting inertial terms to be ordered in relative magnitude and many of the terms which require frequent updating may often be safely neglected when the finite element grid is a relatively fine one. For the problems considered herein, little or no updating was required even for booms with slenderness ratios of 1000 when two finite elements were used per halfwave of deformation. Thus, frequent up-dating, a major shortcoming of the consistent mass approach in a convected coordinate system can be avoided.

Results of the convected analysis have been presented for maneuvering of slender booms through large rotations, translation of two hinged beams, deployment of an unfolding multi-flexible-member axisymmetric hoop and deployment of a planar unfolding multi-flexible-member structure. For a symmetrical arrangement of booms extended from a

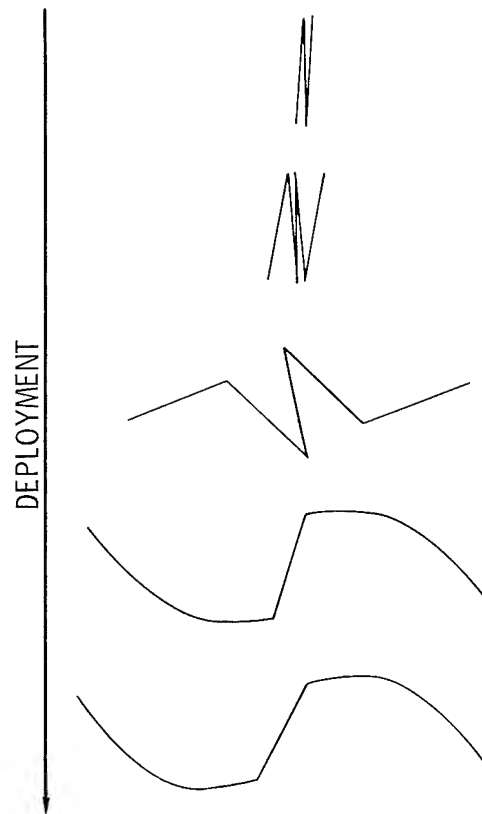


Figure 14. Deployment Sequence of Five-Flexible-Member Unfolding Structure

central hub and subject to a torque, flexibility influences boom tip deflection and hence pointing, but has little influence on hub rotation.

Deployment of an axisymmetric multi-flexible-member hoop may be analyzed by considering only one hoop member when an appropriate derived mass matrix is superimposed on the member mass matrix. Applying this procedure some aspects of hoop deployment have been studied. It has been found that hoop deployment time is essentially independent of member flexibility and that flexible members deform in a two-half-wave pattern.

Furthermore, planar unfolding deployment of a multi-flexible-member structure has indicated that these structures may possess natural deployment patterns which are very desirable in practice. The structure considered herein displays a natural sequential deployment pattern without the use of any control mechanisms which are usually quite complicated and expensive.

Number of Members	Joint Number				
	1	2	3	4	5
4	1.448	1.468			
8	1.453	2.308	2.792	2.814	
12	1.452	2.330	2.856	3.631	3.930
16	1.454	2.401	2.861	3.680	4.643
20	1.461	2.476	2.877	3.816	-

Table. Joint Lock-Up Times In Seconds For An Even Number Of Deploying Members

REFERENCES

1. Belytschko, T. and Hsieh, B.J.: Nonlinear Transient Finite Element Analysis With Convected Coordinates. International Journal for Numerical Methods in Engineering. Vol. 7, 1973, pp. 255-272.
2. Belytschko, T.; Welch, R.E.; and Bruce, R.W.: Large Displacement Nonlinear Transient Analysis by Finite Elements. Proceedings of International Conference on Vehicle Structural Mechanics. SAE, Warrendale Pa., 1974, pp. 188-197.
3. Belytschko, T. and Schwew, L.: Large Displacement Transient Analysis of Space Frames. International Journal for Numerical Methods in Engineering. Vol 11, 1977, pp. 65-84.
4. Housner, J.M. and Knight, N. F., Jr.: On the Dynamic Collapse of a Column Impacting a Rigid Surface. AIAA Journal, Aug. 1983, Vol. 20, pp. 1187-1195.
5. Laurenson, R.M.: Influence of Mass Representation on the Modal Analysis of Rotating Flexible Structures. Proceedings of the 24 th AIAA SDM, Lake Tahoe NV, May 1983, Paper No. 83-0915.
6. Park, K.C.: Time Integration of Structural Dynamics Equations: A Survey. ASME Pressure Vessels and Piping: Design Technology. 1982 edition, pp.277-291.
7. Sullivan, M. R.: LSST (Hoop/Column) Maypole Antenna Development Program. NASA CR 3558, Parts 1 and 2, June 1982.
8. Hedgepeth, J.M.: Sequential Deployment of Truss Structures. Large Space Systems Technology - 1981, NASA CP 2215, Part 1, pp 179-192, Nov. 1981.
9. Schwartzberg, F.R.; Coyner, J.V., Jr.; and Tobey, W.H.: Development and Application of Space-Deployable Box Truss Structures. Presented at 32nd Congress of the International Astronautical Federation, U. of Rome, Rome Italy, Sept. 6-12, 1981.

Appendix A

This appendix contains entries of the vector (\hat{f}_i) .

$$f_{i,1} = -P_i c - (T_{i,1} + T_{i,2})s/L_i + P_i(\gamma_{i,1} + \gamma_{i,2})s$$

$$f_{i,2} = -P_i s + (T_{i,1} + T_{i,2})c/L_i - P_i(\gamma_{i,1} + \gamma_{i,2})c$$

$$f_{i,3} = T_{i,1} + P_i \gamma_{i,1}$$

$$f_{i,4} = -f_{i,1}$$

$$f_{i,5} = -f_{i,2}$$

$$f_{i,6} = T_{i,2} + P_i \gamma_{i,2}$$

where,

$$T_{i,1} = -(EI)_i h''(0)$$

$$T_{i,2} = (EI)_i h''(1)$$

$$\gamma_{i,1} = (\Gamma_{i,11} + \Gamma_{i,21})\phi_{i,1} + (\Gamma_{i,12} + \Gamma_{i,22})\phi_{i,2}$$

$$- (\Gamma_{i,11} + \Gamma_{i,12} + \Gamma_{i,21} + \Gamma_{i,22})(\theta_i - \alpha_i)$$

$$\Gamma_{i,11} = \int_0^1 a_{i,1} a_{i,1}'' d\bar{s}; \quad \Gamma_{i,12} = \int_0^1 a_{i,1} a_{i,2}'' d\bar{s}$$

$$\Gamma_{i,21} = \int_0^1 a_{i,2} a_{i,1}'' d\bar{s}; \quad \Gamma_{i,22} = \int_0^1 a_{i,2} a_{i,2}'' d\bar{s}$$

$$c = \cos \theta_i$$

$$s = \sin \theta_i$$

Appendix B

This appendix contains entire of the matrices $[M_{ij}^{(k)}]$; $j=1,2,3$ and the vectors $(G_i^{(k)})$; $k=1,2,3,4$.

$$m_{11}^{(1)} = m_{22}^{(1)} = m_{44}^{(1)} = m_{55}^{(1)} = 1/3$$

$$m_{14}^{(1)} = m_{25}^{(1)} = 1/6$$

$$m_{i,11}^{(2)} = [2(e_{i,1} - e_{i,s}) + e_{i,2}]s^2$$

$$m_{i,12}^{(2)} = -[2(e_{i,1} - e_{i,s}) + e_{i,2}]sc$$

$$m_{i,13}^{(2)} = (A_{i,1s} - A_{i,1} - A_{i,12} - A_{i,11})s$$

$$m_{i,14}^{(2)} = (2e_{i,s} - e_{i,1} - e_{i,2})s^2$$

$$m_{i,15}^{(2)} = -(2e_{i,s} - e_{i,1} - e_{i,2})sc$$

$$m_{i,16}^{(2)} = (A_{i,2s} - A_{i,2} - A_{i,12} - A_{i,22})s$$

$$m_{i,22}^{(2)} = (2e_{i,1} - 2e_{i,s} + e_{i,2})c^2$$

$$m_{i,23}^{(2)} = (A_{i,1} - A_{i,1s} + A_{i,11} + A_{i,12})c$$

$$m_{i,24}^{(2)} = (e_{i,1} + 2e_{i,2} - 2e_{i,s})sc$$

$$m_{i,25}^{(2)} = (2e_{i,s} - e_{i,1} - e_{i,2})c^2$$

$$m_{i,26}^{(2)} = (A_{i,2} - A_{i,2s} + A_{i,12} + A_{i,22})c$$

$$m_{i,33}^{(2)} = A_{i,11}$$

$$m_{i,34}^{(2)} = (A_{i,11} + A_{i,12} - A_{i,1s})s$$

$$m_{i,35}^{(2)} = (A_{i,1s} - A_{i,11} - A_{i,12})c$$

$$m_{i,36}^{(2)} = A_{i,12}$$

$$m_{i,44}^{(2)} = (e_{i,2} - 2e_{i,s})s^2$$

$$m_{i,45}^{(2)} = -(e_{i,2} - 2e_{i,s})cs$$

$$m_{i,46}^{(2)} = (A_{i,12} + A_{i,22} - A_{i,2s})s$$

$$m_{i,55}^{(2)} = (e_{i,2} - 2e_{i,s})c^2$$

$$m_{i,56}^{(2)} = (A_{i,2s} - A_{i,12} - A_{i,22})c$$

$$m_{i,66}^{(2)} = A_{i,22}$$

$$m_{i,11}^{(3)} = 2(H_{i,s} - H_{i,1})sc + H_{i,2}s^2$$

$$m_{i,12}^{(3)} = (H_{i,1} - H_{i,s})(c^2 - s^2) - H_{i,2}sc$$

$$m_{i,14}^{(3)} = (H_{i,1} - 2H_{i,s})sc - H_{i,2}s^2$$

$$m_{i,15}^{(3)} = H_{i,s}(c^2 - s^2) - H_{i,1}c^2 + H_{i,2}sc$$

$$m_{i,22}^{(3)} = 2(H_{i,1} - H_{i,s})sc - H_{i,2}sc$$

$$m_{i,24}^{(3)} = H_{i,1}s^2 + H_{i,s}(c^2 - s^2) + H_{i,2}sc$$

$$m_{i,25}^{(3)} = 2H_{i,s}sc - H_{i,2}c^2$$

$$m_{i,44}^{(3)} = 2H_{i,s}sc + H_{i,3}s^2$$

$$m_{i,45}^{(3)} = -H_{i,s}(c^2 - s^2) - H_{i,3}sc$$

$$m_{i,55}^{(3)} = -2H_{i,s}sc$$

where

$$e_{i,1} = A_{i,1} + A_{i,2}$$

$$e_{i,2} = A_{i,11} + 2A_{i,12} + A_{i,22}$$

$$e_{i,s} = A_{i,1s} + A_{i,2s}$$

$$A_{i,1} = \frac{1}{L_i} \int_0^1 a_{i,1} d\bar{s}; \quad A_{i,2} = \frac{1}{L_i} \int_0^1 a_{i,2} d\bar{s}$$

$$A_{i,11} = \frac{1}{L_i^2} \int_0^1 a_{i,1}^2 d\bar{s}; \quad A_{i,12} = \frac{1}{L_i^2} \int_0^1 a_{i,1} a_{i,2} d\bar{s};$$

$$A_{i,11} = \frac{1}{L_i^2} \int_0^1 a_{i,2}^2 d\bar{s}$$

$$A_{i,1s} = \frac{1}{L_i} \int_0^1 \bar{s} a_{i,1} d\bar{s}; \quad A_{i,2s} = \frac{1}{L_i} \int_0^1 \bar{s} a_{i,2} d\bar{s}$$

$$H_{i,1} = A_{i,1}\phi_{i,1} + A_{i,2}\phi_{i,2} - (A_{i,1} + A_{i,2})(\theta_i - \alpha_i)$$

$$H_{i,s} = A_{i,1s}\phi_{i,1} + A_{i,2s}\phi_{i,2} - (A_{i,1s} + A_{i,2s})(\theta_i - \alpha_i)$$

$$H_{i,2} = A_{i,11}\phi_{i,1}^2 + A_{i,22}\phi_{i,2}^2 + (A_{i,11} + 2A_{i,12} + A_{i,22})(\theta_i - \alpha_i)^2 + 2A_{i,12}\phi_{i,1}\phi_{i,2} - 2(A_{i,11} + A_{i,12})(\theta_i - \alpha_i)\phi_{i,1} - 2(A_{i,12} + A_{i,22})\phi_{i,2}(\theta_i - \alpha_i)$$

$$g_{i,1}^{(1)} = (e_{i,1} + e_{i,2} - e_{i,s})s\dot{\theta}_i\dot{\epsilon}_{m,i}$$

$$g_{i,2}^{(1)} = -(e_{i,1} + e_{i,2} - e_{i,s})c\dot{\theta}_i\dot{\epsilon}_{m,i}$$

$$g_{i,3}^{(1)} = -(A_{i,11} + A_{i,12})\dot{\theta}_i\dot{\epsilon}_{m,i}$$

$$g_{i,4}^{(1)} = (e_{i,s} - e_{i,2})s\dot{\theta}_i\dot{\epsilon}_{m,i}$$

$$g_{i,5}^{(1)} = -(e_{i,s} - e_{i,2})c\dot{\theta}_i\dot{\epsilon}_{m,i}$$

$$g_{i,6}^{(1)} = -(A_{i,12} + A_{i,22})\dot{\theta}_i\dot{\epsilon}_{m,i}$$

$$g_{i,1}^{(2)} = [2c\dot{H}_{i,3} + H_{i,3}(s\dot{\theta}_i - c\dot{\epsilon}_{m,i}) + sH_{i,2}\dot{\epsilon}_{m,i}]\dot{\theta}_i$$

$$g_{i,2}^{(2)} = -[2s\dot{H}_{i,3} + H_{i,3}(c\dot{\theta}_i + s\dot{\epsilon}_{m,i}) + cH_{i,2}\dot{\epsilon}_{m,i}]\dot{\theta}_i$$

$$g_{i,3}^{(2)} = g_{i,6}^{(2)} = 0$$

$$g_{i,4}^{(2)} = [-2c\dot{H}_{i,s} + H_{i,s}(s\dot{\theta}_i - c\dot{\epsilon}_{m,i}) - sH_{i,2}\dot{\epsilon}_{m,i}]\dot{\theta}_i$$

$$g_{i,5}^{(2)} = [c\dot{H}_{i,2}\dot{\epsilon}_{m,i} - 2s\dot{H}_{i,s} + H_{i,s}(c\dot{\theta}_i + s\dot{\epsilon}_{m,i})]\dot{\theta}_i$$

where

$$H_{i,3} = H_{i,1} - H_{i,2}$$

$$c = \cos \theta_i; \quad s = \sin \theta_i$$

$$g_{i,1}^{(3)} = s(H_{i,s}\dot{\epsilon}_{m,i}^* - H_{i,1}\ddot{\eta}_{i,1}^{**}) + (sH_{i,2} - cH_{i,3})\dot{\theta}_i^* + [H_{i,4}\phi_{i,1} + H_{i,5}\phi_{i,2} - (H_{i,4} + H_{i,5})(\theta_i - \alpha_i)]s\dot{\theta}_i^*$$

$$g_{i,2}^{(3)} = c(H_{i,s}\dot{\epsilon}_{m,i}^* + H_{i,1}\ddot{\eta}_{i,1}^{**}) - (sH_{i,3} + cH_{i,2})\dot{\theta}_i^* - [H_{i,4}\phi_{i,1} + H_{i,5}\phi_{i,2} - (H_{i,4} + H_{i,5})(\theta_i - \alpha_i)]c\dot{\theta}_i^*$$

$$g_{i,3}^{(3)} = g_{i,6}^{(3)} = 0$$

$$g_{i,4}^{(3)} = s(H_{i,s} \dot{\xi}_{m,i}^* + H_{i,1} \ddot{\eta}_{i,1}^{**}) - (cH_{i,s} + sH_{i,2}) \dot{\theta}_i^* \\ - [H_{i,4} \phi_{i,1} + H_{i,5} \phi_{i,2} \\ - (H_{i,4} + H_{i,5})(\theta_i - \alpha_i)] s \dot{\theta}_i^*$$

$$g_{i,5}^{(3)} = -c(H_{i,s} \dot{\xi}_{m,i}^* + H_{i,1} \ddot{\eta}_{i,1}^{**}) + (cH_{i,2} - sH_{i,s}) \dot{\theta}_i^* \\ + [H_{i,4} \phi_{i,1} + H_{i,5} \phi_{i,2} \\ - (H_{i,4} + H_{i,5})(\theta_i - \alpha_i)] c \dot{\theta}_i^*$$

where,

$$H_{i,4} = A_{i,11} \phi_{i,1} + A_{i,12} \phi_{i,2} - (A_{i,11} + A_{i,12})(\theta_i - \alpha_i)$$

$$H_{i,5} = A_{i,21} \phi_{i,1} + A_{i,22} \phi_{i,2} - (A_{i,21} + A_{i,22})(\theta_i - \alpha_i)$$

and where (*) denotes time differentiation with convected terms omitted, i.e.,

$$\dot{\xi}_{m,i}^* = (c \Delta \ddot{\eta}_i + s \Delta \ddot{\xi}_i) / L_i$$

$$\dot{\theta}_i^* = (c \Delta \ddot{\xi}_i - s \Delta \ddot{\eta}_i) / L_i$$

$$\ddot{\eta}_{i,1}^{**} = (c \ddot{\eta}_{i,1} + s \ddot{\xi}_{i,1}) / L_i$$

$$g_{i,1}^{(4)} = s \dot{\theta}_i \{ 2(H_{i,4} \dot{\phi}_{i,1} + H_{i,5} \dot{\phi}_{i,2}) - (H_{i,4} + H_{i,5}) \dot{\theta}_i \\ + [H_{i,4} \phi_{i,1} + H_{i,5} \phi_{i,2} \\ - (H_{i,4} + H_{i,5})(\theta_i - \alpha_i)] \dot{\xi}_{m,i} \}$$

$$g_{i,2}^{(4)} = -c \dot{\theta}_i \{ 2(H_{i,4} \dot{\phi}_{i,1} + H_{i,5} \dot{\phi}_{i,2}) - (H_{i,4} + H_{i,5}) \dot{\theta}_i \\ + [H_{i,4} \phi_{i,1} + H_{i,5} \phi_{i,2} \\ - (H_{i,4} + H_{i,5})(\theta_i - \alpha_i)] \dot{\xi}_{m,i} \}$$

$$g_{i,3}^{(4)} = -H_{i,4} \dot{\theta}_i^2$$

$$g_{i,4}^{(4)} = -g_{i,1}^{(4)}$$

$$g_{i,5}^{(4)} = -g_{i,2}^{(4)}$$

$$g_{i,6}^{(4)} = -H_{i,5} \dot{\theta}_i^2$$

GALILEO SPACECRAFT MODAL IDENTIFICATION USING
AN EIGENSYSTEM REALIZATION ALGORITHM

Richard S. Pappa* and Jer-Nan Juang*
NASA Langley Research Center
Hampton, VA 23665

Abstract

A modal parameter identification technique referred to as the Eigensystem Realization Algorithm (ERA) was applied to free-response measurements from the Galileo spacecraft modal survey test. The data were recorded following single-point random excitation of the structure. This work is one phase in a research project coordinated by the Jet Propulsion Laboratory to compare the performance of various contemporary identification techniques using Galileo data. Principal emphasis is placed on estimating the accuracy of the ERA-identified modal parameters. Various accuracy indicators, such as Modal Amplitude Coherence and Modal Phase Collinearity, are discussed. More than 20 modes of the spacecraft were identified, demonstrating the ability of the ERA method to determine the dynamics of such complex structures using only a few seconds of test data.

Introduction

The Galileo spacecraft is an interplanetary vehicle to be launched in 1986 for a detailed investigation of the planet Jupiter and its moons. It consists of a planetary orbiter and an atmospheric entry probe that will be deployed towards the planet. Improved instrumentation, combined with satellite flybys more than 20 times closer than achieved by Voyager, promises exceptional data on the chemical composition and structure of the Jovian system.

In the design of the spacecraft, finite-element analytical models of the structure are used to assess dynamic launch loads and interaction effects with the attitude control system. As a final check of the accuracy of these models, modal survey tests^{1,2} were conducted on a completely assembled twin of the flight vehicle--the so-called Development Test Model (DTM). These tests were performed at the Jet Propulsion Laboratory (JPL) in the summer of 1983. The DTM is a replica of the flight unit except that all electronics and scientific instruments are replaced by rigid mass simulations. It was built to mission specifications and will later be refurbished to become the backup flight vehicle.

The primary objective of the modal survey test is to confirm that the important natural frequencies, mode shapes, and modal damping of the structure agree adequately with those of the analytical model. Damping is an assumed quantity in the analysis, of course, prior to receiving actual test data. Because of high modal density, nonlinearities, and the large number of measurements that are made, however, the experimental results for such complex structures are not easily obtained. For several decades, the standard method in the

aerospace industry for modal survey tests has been the multi-shaker, sine-dwell approach. In recent years, however, several alternate methods using other types of excitation and data analysis have evolved³⁻⁶. These newer techniques, while offering significant reductions in test time and complexity over the traditional method, are not yet universally accepted⁷.

Based on past successful experience, the classical multi-shaker, sine-dwell approach was selected as the principal modal identification method for the Galileo test⁸. In addition, as a research project, several other methods were also used during testing of the DTM in launch configuration^{2,9,10}. These newer techniques were applied by researchers outside JPL who had experience with the methods. This paper discusses the results of one of these independent research analyses of Galileo test data, using a recently implemented modal identification technique referred to as the Eigensystem Realization Algorithm (ERA)¹¹. A future comparison of all results from the project will hopefully provide an improved understanding of the various approaches.

Recent emphasis on interaction of control systems with the dynamics of large flexible space structures has resulted in increased interdisciplinary research in these areas. The ERA method was developed under this interdisciplinary activity. It is an extended version of the Ho-Kalman algorithm¹², based on system realization theory established in the controls and process modeling fields^{13,14}. A summary of the ERA technique is provided in the Appendix of this paper. More detailed explanation is contained in Ref. 11, including its relationship to other successful time-domain identification methods, such as that discussed in Refs. 4, 15, 16, and 17.

In the next two sections of the paper, the test configuration and the test and data acquisition procedures that were used are described briefly. The following section contains a summary of the ERA results, with emphasis placed throughout on estimating the accuracy of the identified modal parameters.

Test Configuration

Several views of the Galileo spacecraft are shown in Figs. 1 and 2. The data for this research were obtained during modal survey tests of the spacecraft in launch configuration, as shown in Fig. 2. All appendages, including the S-X band antenna (SXA) at the top of the vehicle, were locked in their stowed positions. The structure was cantilevered from its base by bolting the bottom edge of the conical spacecraft adapter ring to a massive seismic block. The adapter ring is

*Aerospace Engineer, Structural Dynamics Branch, Structures and Dynamics Division. Member AIAA.

the interface between Galileo and a Centaur upper stage that will provide the interplanetary boost.

Completely assembled, the test article mass was about 2400 kgs. Approximately 40 percent of the total was concentrated in the Retro Propulsion Module (RPM), and approximately 35 percent in seven major appendages. All four RPM fuel tanks were filled, using alcohol and freon substitute liquids, and held under low pressurization. For dynamic excitation, several electrodynamic shakers of about 110 N capacity, hung on soft suspensions from overhead cranes, could be attached at various points. Response measurements were made with 162 accelerometers distributed over the test article.

The finite-element model of the structure in this configuration predicted 45 modes of vibration below 50 Hz, with the lowest frequency at about 13 Hz. However, as discussed in Ref. 1, many of the modes are of lesser importance based on their predicted contribution to the dynamic launch loads. In fact, only about 15 of the modes are major contributors. The presence of the others, however, interspersed in frequency with the important ones, results in high modal density and makes accurate parameter identification more difficult.

Complete details of the test configuration, the analytical model predictions, and the method used to estimate the relative importance of the modes can be found in Refs. 1, 2, and 8.

Test and Data Acquisition Procedures

All results presented in this paper were obtained from two sets of free-response measurements recorded following single-point random excitation of the structure. The first data set was obtained using single-shaker, lateral excitation--in the global x direction--and the second set with single-shaker, vertical excitation--in the global z direction. These tests are referred to as simply the "x direction" and "z direction" tests. For both tests, no special effort was made to select the position for the shaker. Each position was chosen using only the knowledge that many modes were excited from the location in previous tests. Other than the point and direction of excitation, all characteristics of the test, data acquisition, and data reduction processes were exactly the same for both data sets.

The random excitation signal, bandlimited to the interval from 10 to 45 Hz, was generated digitally with the same test system which was also used to record the accelerometer response signals. Approximately five seconds of data were recorded following the end of the excitation signal. The responses were digitized at a rate of 102.4 samples per second, resulting in about 500 free-response points in each test.

Two minor compromises of a practical nature were necessary during data acquisition. The first occurred because the number of signals being recorded in the test was several times larger than the number that could be digitized simultaneously by the recording system. For the data analysis, however, all free-response measurements in each test should correspond to exactly the same initial state of the structure. Because the 162 accel-

ometer signals were distributed across four recording groups, the excitation sequence was repeated four different times for each test (after allowing all previous motion to damp out). Since the excitation sequence was generated digitally, it could be repeated precisely each time. However, though a common response signal appearing in each of the four groups was found to have been repeated closely each time, the repetition was not exact. The four data groups were then later combined, with the accelerometer signals rearranged using a global numbering scheme established for the test.

The second compromise necessary during testing was the use of relatively low instrumentation amplifier gains. The data for this work (and for the others in the research project to compare modern identification techniques) were recorded off-hours on the same days that were also being used for multi-shaker, sine-dwell tests during normal working hours. To avoid possible mistakes in resetting the large number of instrumentation channels, project rules stipulated that the channel gains not be varied. The gains at which the amplifiers were set were based on acceleration levels encountered during the multi-shaker, sine-dwell testing. However, the typical dynamic response levels in those tests were significantly higher than in single-shaker random tests, where the maximum force capacity of the shaker was distributed over a 35 Hz bandwidth. Thus, in general, the free-response data used in this work were smaller, and therefore of lower signal-to-noise ratio, than if variable gain settings had been available.

Identification Results

Because of the large number of measurements made in this test, it is difficult to summarize all the results quantitatively. This is particularly true for the identified mode shapes, which consist of 162 complex-valued components each. Since the main purpose of this paper is not to describe the structural dynamic characteristics of Galileo, but rather to discuss the identification performance achieved with the ERA method in this application, the following approach is taken:

1. An overview of the ERA results is made in Fig. 3 by a comparison of ERA-identified natural frequencies with those obtained by two other experimental techniques and with those predicted by the pre-test NASTRAN model.
2. Typical examples of information obtained in the ERA analysis are shown in Figs. 4 through 6, and are discussed in individual subsections of the paper. The examples selected for Figs. 3 through 6 represent four fundamental types of information obtained in each ERA analysis: eigenvalues (natural frequencies and modal damping), mode shapes, modal amplitudes, and data reconstructions.
3. An overall summary of the results is then made in Tables I and II, in which the identified natural frequencies and modal damping factors are listed alongside a set of parameters used as indicators of the identification accuracy that was achieved.

Since the ERA-identified mode shapes are in good agreement with the shape descriptions provided elsewhere (in Table 2 of Ref. 9, for example), the descriptions are not repeated in this paper.

Natural Frequencies

In Fig. 3, the natural frequencies identified by ERA analysis for both x- and z-direction tests are compared with one another and with the results obtained by two other experimental techniques and by pre-test NASTRAN analysis. A line spectrum format was chosen to permit rapid visual comparison.

For the ERA results, shown in parts (e) and (f), the individual spectral lines are of variable height to also indicate a measure of confidence with which each mode was identified. The parameter chosen for this purpose, referred to as the Modal Amplitude Coherence, is defined later when typical modal amplitude results are discussed. It provides a good indication of how strongly the mode was identified in the data analysis, relative to the instrumentation noise floor. The other spectral lines in the figure, in parts (a) through (d), are all of equal height since no confidence information appeared in the literature from which the results were extracted^{1,9}.

The meaning of the expression "+ shift ERA analysis" used in the (e) and (f) subcaptions is explained in Step 4 of the Appendix. Its significance will also be discussed further in the Summary of Results section.

Several conclusions can be drawn from the results in Fig. 3:

1. The pre-test NASTRAN analysis predicted more modes than were identified by any of the experimental methods.
2. The multi-shaker, sine-dwell test identified about half the number of modes obtained by the other methods (which was by choice, since only the principal loads-inducing modes predicted by analysis were sought^{1,8}).
3. Somewhat different frequencies were obtained among the ERA and Polyreference⁶ analyses. Two explanations are possible. Since the data were (unfortunately) recorded on four different days during the test program, a change in structural characteristics cannot be discounted. A more likely explanation, however, is the influence of known nonlinearities⁸, causing frequency shifts between different excitation conditions.
4. A large drop in the frequency of the lowest mode (a first bending mode of the S-X band antenna) in the 4-shaker Polyreference test was not apparent in the other experimental results. As discussed in Ref. 10, one possible explanation is that high-level sine testing directed at this mode, which occurred in the time period between the 3- and 4-shaker Polyreference tests, caused a significant structural change. Though the z-direction ERA test was also performed after this point in time, the lowest two modes were found in this data to remain near 14 Hz. Since the mode at 13.8 Hz in the z-direction ERA test was only very weakly excited, however, the

differences are not conclusive.

5. The frequency of the lowest two modes was about 13 Hz in the NASTRAN and multi-shaker, sine-dwell results, but about 14 Hz in the other results. This may be explained by the nonlinearity of these modes. The results in Fig. 3 of Ref. 8, however, suggest that the ERA-identified frequencies, which were obtained with about 0.1 g antenna-tip acceleration, should be lower than the sine-dwell results.

Mode Shapes

Because of the difficulty in visualizing three-dimensional mode shapes of such distributed structures--using sketches of the deformed shape, for example--typical results are presented, rather, as x-y plots of relative amplitude and phase of the motion versus measurement point number. Though this format provides no information on the physical shape of the deformation pattern, it is generally more useful for comparing results from different tests and for studying the degree of identification scatter. Further information on the location and direction of each of the 162 response sensors would add little to the discussion of ERA identification performance. Additionally, as mentioned earlier, the physical shapes of the ERA-identified modes are in good agreement with the descriptions provided in Ref. 9.

Three typical ERA-identified mode shapes are shown in Fig. 4. (Note that a negative amplitude is assigned to those components with phase angle closer to 180° than to 0°. This was done to permit easier noting of the relative phasing of the motion.) Using the results in Fig. 4 and observations from other data not shown, the following conclusions can be drawn:

1. The local behavior of many of the Galileo modes--exemplified by the antenna mode shown in Fig. 4(a) in which only about five measurements show motion--makes it more difficult to accurately identify all 162 components of the mode shapes because of the low response levels. (This situation is certainly true for other identification techniques as well.)
2. A good measure of the effects of noise on the mode shape accuracy is often indicated by the amount of scatter in the identified modal phase angles from the ideal 0°-180° normal-mode behavior. Of course, true complex-mode behavior needs to be differentiated from identification scatter due to noise and nonlinearity. The best remedy is to compare the results for the same mode obtained in several different tests.
3. How closely the modal phase angle results for each mode cluster near 0° and 180° can be well summarized by a parameter referred to as the Modal Phase Collinearity¹¹. Calculated using principal component analysis, it indicates the extent to which the information in each complex-valued mode shape is representable as a real-valued vector. It ranges from a value of zero for no collinearity to 100 percent for perfect collinearity.
4. Based on studies with simulated data, the

accuracy of mode shapes showing clustering of the identified phase angles near 0° and 180° , such as in Figs. 4(a) and (b), can generally be accepted with little questioning. Those modes with significant phase angle scatter, such as in Fig. 4(c), however, should not be used without further confirmation.

5. Most mode shape components whose identified phase angles are displaced from the 0° and 180° lines are those with the smallest amplitudes. This characteristic is consistently observed in the result shown in Fig. 4(b). Small modal amplitude results for these components, however, usually indicate accurately that the response amplitude is, in fact, very small. This information is all that can be expected from a measurement standpoint, and is all that is required in many instances.

Modal Amplitudes

Another important indicator of ERA identification accuracy is the purity of the individual modal amplitude time histories. For each identified eigenvalue, a modal amplitude time sequence is obtained. This data provides a direct indication of the strength with which the mode was identified in the analysis. For strongly identified modes, the modal amplitude history is a pure, exponentially decaying sinusoid of the corresponding frequency and damping, which decays smoothly over the entire analysis interval. For weakly identified modes, the modal amplitude history is distorted. In particular, the history is a sequence of noise for any eigenvalue not corresponding to a structural mode.

Typical examples of modal amplitude results from the Galileo analysis are shown in Fig. 5. These data were selected to illustrate the variation in the purity of the modal amplitude histories for a mode which was strongly excited in only one of the two ERA tests. The figure will also be used to clarify the definition of Modal Amplitude Coherence, mentioned earlier.

Note that although these ERA-identified modal amplitudes are similar in form to traditional decay plots obtained following sine-dwell modal tuning, they are the result of digital processing of random response data.

The mode shown in Fig. 5, at approximately 38 Hz, is the fundamental z-direction "bounce mode" of the structure. As would be expected, the modal amplitude plots illustrate that the mode was more strongly excited in the z-direction test than in the x-direction test. This conclusion is made by comparing the purity and amplitude of the time history shown in Fig. 5(a) with that in 5(b). To better see how well the exponential decay persists at small amplitudes, the right-hand plots in Fig. 5 show the data from the left-hand side on a logarithmic scale. In this form, exponential decay corresponds to a linearly decreasing envelope. As a reference, the waveform in Fig. 5(c) is included to show how closely the test results correspond to pure exponential decay. This plot was calculated by extrapolating the initial value of the time history in Fig. 5(a) to later points in time using the identified frequency and damping

for the mode.

Because the purity of the modal amplitude time history is a good indicator of identification accuracy, a means of automatically assessing the level of purity is used. This is done by calculating the coherence between each modal amplitude history, such as in Fig. 5(a), and an ideal one, such as in 5(c). The parameter, referred to as Modal Amplitude Coherence¹¹, is the square of the correlation coefficient between the two time sequences. This parameter is used later in Tables I and II to highlight those modes judged of higher accuracy in each ERA analysis.

Data Reconstruction

The final aspect of the ERA method available for assessing identification accuracy is the process of data reconstruction. This procedure consists of comparing the original free-response time histories (and their frequency spectra) with ones calculated using the set of identified modal parameters. If the ERA modal decomposition process is performed accurately, the reconstruction results will closely match the original data.

Figure 6 shows a typical such comparison from the Galileo data analysis. The two time histories are compared at the top of the figure, and their Fourier transforms (FFT), in both amplitude and phase, in the lower plots. The reconstruction result, the smoother of the two lines in the FFT plots, is seen to closely follow the original data in both amplitude and phase. The increase in amplitude of the test data below 2 Hz is due to residual motion of the shaker on its soft suspension. These response characteristics, well below the first flexural mode of the spacecraft, do not affect the modal results and were not retained in the identified parameter set.

Summary of Results

A summary of the identification results for the x- and z-direction tests is provided in Tables I and II, respectively.

The three damping results in these tables correspond to three variations in the realization of the state matrix (see Step 4 of the Appendix). Because the best approach among the three is still a subject of current research, all three results are shown for completeness.

Based on analysis of simulated data, the presence of noise causes the identified damping values to be somewhat too high in positive time shift analyses, and somewhat too low in negative time shift analyses. The degree to which the results are displaced from their true value is related to how closely the signal strength of the particular mode is to the measurement noise floor. When data are analyzed by both methods, then, the results should straddle the true damping value. Additionally, the amount of separation between the two estimates provides a good indication of the degree to which noise affected the results.

The third column of damping results in Tables I and II, labeled "Avg. A Matrix," are those

obtained using a variation in the calculation of the state matrix which offers lower damping bias than either of the other two approaches. Because the performance characteristics of this approach are still under study, though, its use cannot yet be recommended over the others. The damping bias is reduced in this approach by using a state matrix formed as the linear combination of those used for positive and negative time shift analyses.

One characteristic of the negative time shift and Avg. A Matrix analyses is that they provide somewhat less indication of the weakly excited modes than does the standard positive time shift analysis. This characteristic caused several of the weakly identified modes in the positive time shift analysis not to appear in either or both of the other two analyses.

The columns on the right half of Tables I and II contain several accuracy indicators that were used in this research. Perhaps they can be combined into a single parameter when the characteristics of the ERA method are more thoroughly understood. Doing so at this point in the development of the method, however, was judged unwise.

As mentioned earlier, the best single accuracy indicator now available is the Modal Amplitude Coherence. Its value from the positive time shift analyses is used in Tables I and II to rate the identified modes at various degrees of confidence. The rating scale--using either two asterisks, one asterisk, or a plus sign--is noted in the key beneath the tables. A brief description of the information in each of the three columns on the far right of the tables is also contained in the keys. The significance of Modal Phase Collinearity was discussed previously in the Mode Shapes section of the paper. The data in the other two columns provide a good indication of the strength of the modal response signals relative to the instrumentation noise floor. These results are provided as additional general indicators of the identification accuracy that was achieved.

Concluding Remarks

The Eigensystem Realization Algorithm (ERA) is an application of system realization theory to structural dynamics data analysis. The approach permits well-established theory for dynamic systems analysis developed in the controls field to be used in improving modal survey test results. Further exchanges of this type between structural dynamics and controls disciplines are needed to correctly assess the adequacy of current technology for on-orbit system identification and control of large flexible space structures.

In the analysis of the Galileo data, approximately 30 modes of the spacecraft were identified with ERA using two sets of free-response measurements. These data, about five seconds in length, were recorded following single-shaker random excitation of the structure. Less than ten minutes of CPU time on a CDC mainframe computer were required for the analysis. Though general agreement was found between the ERA results and those obtained by other experimental techniques, a closer comparison is difficult in view of the measured nonlinearities of the structure, since each technique, in

general, acquired data under a different set of excitation conditions.

Principal emphasis in this application was on estimating the accuracy of the ERA-identified modal parameters. Based on the results of other analyses of simulated data, the parameters referred to as Modal Amplitude Coherence and Modal Phase Collinearity are good indicators of the identification accuracy that is achieved. Using these indicators, more than half of the modes from the Galileo analysis are judged to be of high accuracy. Additional research is needed, however, to correctly assess the degree of accuracy achieved by those modes showing significant identification scatter. The effects of structural nonlinearities on the results also need further attention.

References

- ¹Chen, J. C., and Trubert, M.: Galileo Modal Test and Pre-Test Analysis. Proc. of the 2nd International Modal Analysis Conference. Orlando, FL, February 1984.
- ²Garba, J. A., Wada, B. K., and Chen, J. C.: Summary of Galileo Spacecraft Modal Test Activities. AIAA Dynamics Specialists Conference. AIAA Paper 84-1072, May 1984.
- ³Stroud, R. C., Smith, S., and Hamma, G.: MODALAB--A New System for Structural Dynamics Testing. Shock and Vibration Bulletin. No. 46, Part 5, August 1976, pp. 153-175.
- ⁴Ibrahim, S. R., and Mikulcik, E. C.: A Method for the Direct Identification of Vibration Parameters from the Free Response. Shock and Vibration Bulletin. No. 47, Part 4, September 1977, pp. 183-198.
- ⁵Brown, D. L., Allemang, R. J., Zimmerman, R., and Mergeay, M.: Parameter Estimation Techniques for Modal Analysis. SAE Paper 790221. February 1979.
- ⁶Vold, H., and Russell, R.: Advanced Analysis Methods Improve Modal Test Results. Sound and Vibration. March 1983, pp. 36-40.
- ⁷Anderson, J. E.: Another Look at Sine-Dwell Mode Testing. AIAA Paper 81-0532, April 1981.
- ⁸Trubert, M.: Galileo Modal Tests/Multiple Sine Dwell. Proc. of the 2nd International Modal Analysis Conference. Orlando, FL, February 1984.
- ⁹Chen, J. C.: Comparison of Various Modal Test Analysis Results. Proc. of the 2nd International Modal Analysis Conference. Orlando, FL, February 1984.
- ¹⁰Stroud, R. C., Coppolino, R. N., Hunt, D. L., and Ibrahim, S. R.: Advanced Methods Used on the Galileo Spacecraft Modal Survey. Proc. of the 2nd International Modal Analysis Conference. Orlando, FL, February 1984.
- ¹¹Juang, J. N., and Pappa, R. S.: An Eigensystem Realization Algorithm (ERA) for Modal Parameter Identification. JPL Workshop on Identification and Control of Flexible Space Structures. June 1984.

- ¹²Ho, B. L., and Kalman, R. E.: Effective Construction of Linear State-Variable Models From Input/Output Data. Proc. 3rd Allerton Conference on Circuit and System Theory. October 1965, pp. 449-459.
- ¹³Kailath, T.: Linear Systems. Prentice-Hall, Inc., Englewood Cliffs, NJ, 1980.
- ¹⁴Seinfeld, J. H., and Lapidus, L.: Mathematical Methods in Chemical Engineering. Vol. 3: Process Modeling, Estimation, and Identification. Prentice-Hall, Inc., Englewood Cliffs, NJ, 1974.
- ¹⁵Hanks, B. R., Miserentino, R., Ibrahim, S. R., Lee, S. H., and Wada, B. K.: Comparison of Modal Test Methods on the Voyager Payload. Transactions of the ASME, Vol. 87, 1978.
- ¹⁶Ibrahim, S. R., and Pappa, R. S.: Large Modal Survey Testing Using the Ibrahim Time Domain Identification Technique. J. Spacecraft and Rockets. Vol. 19, No. 5, Sept-Oct. 1982, pp. 459-465.
- ¹⁷Ibrahim, S. R.: Time Domain Parameter Identification and Modeling of Structures. Proc. of the American Control Conference. San Francisco, CA, June 1983.
- ¹⁸Klema, V. C., and Laub, A.J.: The Singular Value Decomposition: Its Computation and Some Applications. IEEE Trans. on Automatic Control. Vol. AC-25, No. 2, April 1980, pp. 164-176.

TABLE I. ERA IDENTIFICATION RESULTS FOR X-DIRECTION, RANDOM EXCITATION TEST.

MODE NO.	Identified FREQ. HZ	Identified DAMPING FACTOR, %			----- ACCURACY INDICATORS -----			
		+ Shift	- Shift	Avg. A Matrix†	Modal Amplitude Coherence, %	MPC, ¹ %	Max. ² I.A.	No. ³ >.01g
					+ Shift	+	+	+
1	13.613**	3.301	2.239	2.257	98.6**	99.0	.104	6
2	14.153**	1.645	1.337	1.442	99.8**	94.2	.063	5
3	18.369**	1.409	1.456	1.464	99.7**	98.7	.270	59
4	18.680**	1.086	.942	.965	99.7**	79.8	.068	17
5	19.516**	.659	.640	.633	96.5**	99.1	.090	23
6	22.040	8.311			50.7	43.1	.009	0
7	22.047**	.777	.363	.583	98.8**	97.7	.122	58
8	22.132**	.356	.107	.240	97.5**	99.3	.088	45
9	22.640*	1.282	.449	.633	93.1*	86.6	.018	4
10	25.126**	1.515	1.246	1.443	99.8**	89.8	.239	27
11	25.751+	5.569			80.2+	56.2	.043	15
12	25.871**	.806	.528	.957	98.6**	99.4	.279	67
13	28.517**	.835	.708	.721	97.7**	98.0	.121	10
14	29.659*	1.723		.179	91.7*	61.2	.010	1
15	30.940**	3.003	1.547	1.950	98.2**	77.1	.059	5
16	32.828	6.668			67.9	52.8	.015	2
17	33.288*	2.894		.344	93.4*	44.0	.012	4
18	33.613**	1.326	.309	.148	98.1**	59.8	.024	3
19	34.402**	1.057	.902	.915	98.2**	98.4	.047	15
20	36.890*	1.633		.411	93.3*	73.1	.020	2
21	37.631	5.957			50.0	76.2	.041	2
22	38.019*	.575			94.1*	44.9	.008	0
23	39.551	4.048			75.5	99.2	.240	5
24	41.021*	2.038			92.4*	89.8	.123	17
25	42.169	3.737			65.2	89.1	.022	6
26	42.273*	1.124	-.012	.404	92.9*	68.5	.011	3
27	43.758*	1.614	.712	.908	94.2*	57.7	.019	3
28	44.892**	.394	.398	.441	99.4**	99.1	.513	24
29	45.173	4.188			79.6	67.0	.021	6
30	45.174	.835			78.5	78.7	.041	3
31	47.191+	2.126		.192	84.3+	50.8	.008	0
32	48.311*	1.214			94.4*	78.3	.034	5
33	48.414	3.300			59.2	57.0	.014	3
34	50.385+	1.143	.130	.221	89.5+	40.2	.027	3

**95% < MAC < 100%

*90% < MAC < 95%

+80% < MAC < 90%

†Best damping estimate

¹Modal Phase Collinearity--indicates extent of modal phase angle clustering near 0° and 180°.²Maximum initial response amplitude in g's among the 162 identified components. (The measurement noise floor was approximately .002 g.)³No. of mode shape components of 162 with initial response amplitude > .01 g. Indicator of local or global response.

TABLE 11. ERA IDENTIFICATION RESULTS FOR Z-DIRECTION, RANDOM EXCITATION TEST.

MODE NO.	Identified FREQ. HZ	Identified DAMPING FACTOR, %			----- ACCURACY INDICATORS -----			
		DAMPING FACTOR, %			Modal Amplitude Coherence, %	MPC, ¹ %	Max. ² L.A. >.01g	No. ³ >.01g
		+	-	Avg. A				
	Shift	Shift	Shift	Matrix†	+ Shift	+	+	+
1	13.819*	4.003	.777	1.701	93.3*	57.7	.004	37
2	14.075**	1.613	1.318	1.482	99.7**	95.4	.132	51
3	18.415**	1.608	1.028	1.342	98.6**	83.3	.078	48
4	18.555	4.584			67.3	66.6	.056	24
5	19.341**	.713	.685	.702	98.9**	98.6	.205	40
6	20.246	.521			58.9	32.0	.007	0
7	22.128**	.299	.272	.282	99.3**	97.7	.155	66
8	22.583**	.567	.496	.484	95.1**	98.4	.202	46
9	25.251**	.811	.814	.876	99.7**	96.0	.619	62
10	25.932**	.469	.389	.325	99.4**	93.3	.063	36
11	26.653**	1.691	.736	.837	97.5**	94.6	.287	21
12	28.016+	2.651	.568	.720	88.2+	71.0	.151	25
13	30.699	3.638			63.4	49.5	.062	13
14	33.208**	1.007	.908	.941	99.6**	55.7	.677	66
15	33.802**	.773	.619	.680	98.9**	41.4	.321	45
16	34.973**	.772	.695	.729	98.2**	98.5	.260	32
17	37.328*	2.342	.912	1.369	91.8*	74.6	.370	28
18	38.037**	.513	.486	.493	99.8**	93.1	.277	79
19	39.437+	3.656	.627	.900	86.7+	95.5	2.894	44
20	40.325+	4.390			82.0+	95.8	3.667	59
21	41.886	4.505			55.9	71.7	.366	18
22	43.359	5.530			54.1	81.8	.259	26
23	44.917+	1.466			89.1+	73.0	.142	24
24	45.099**	.611	.341	.308	96.0**	87.2	.175	17
25	46.188	3.592			63.9	37.2	.134	18
26	47.314	6.523			50.8	45.3	.109	29

**95% < MAC < 100%

*90% < MAC < 95%

+80% < MAC < 90%

†Best damping estimate

¹Modal Phase Collinearity--indicates extent of modal phase angle clustering near 0° and 180°.²Maximum initial response amplitude in g's among the 162 identified components. (The measurement noise floor was approximately .002 g.)³No. of mode shape components of 162 with initial response amplitude > .01 g. Indicator of local or global response.

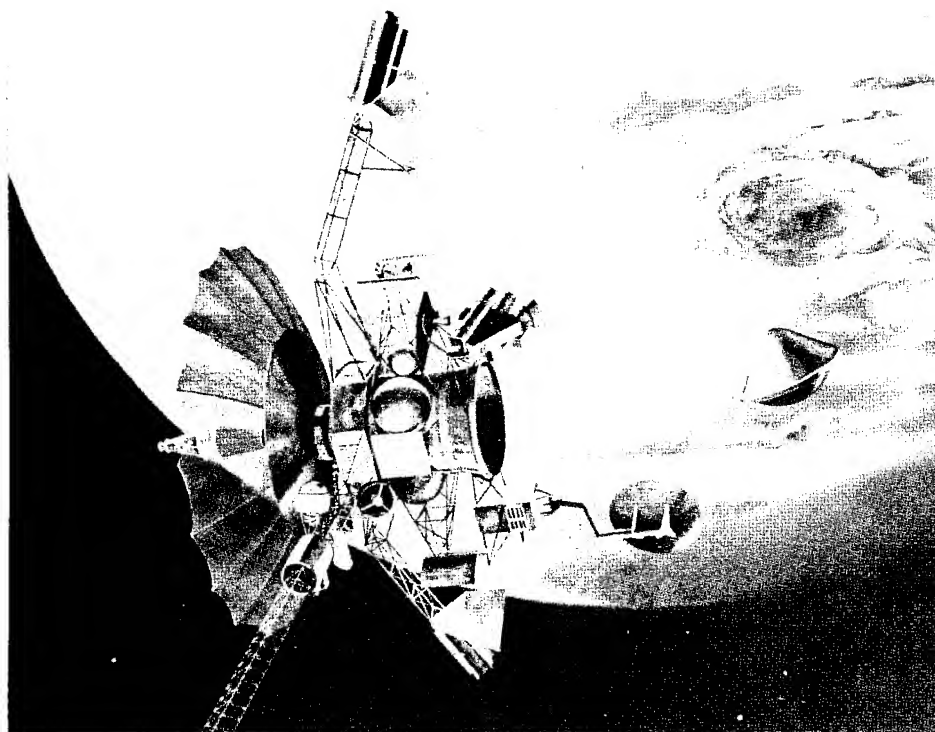
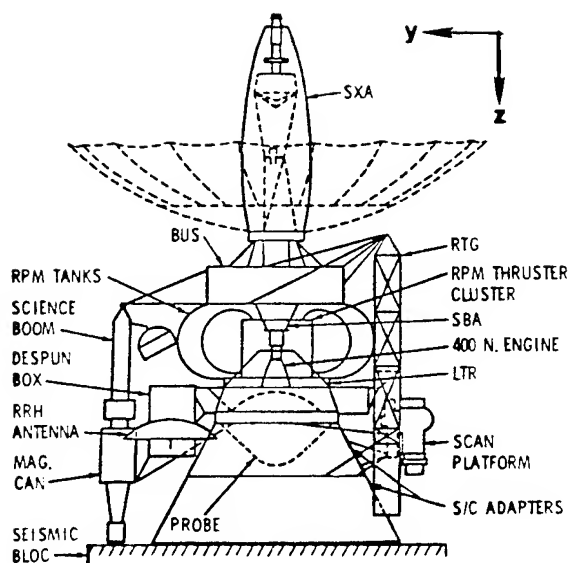
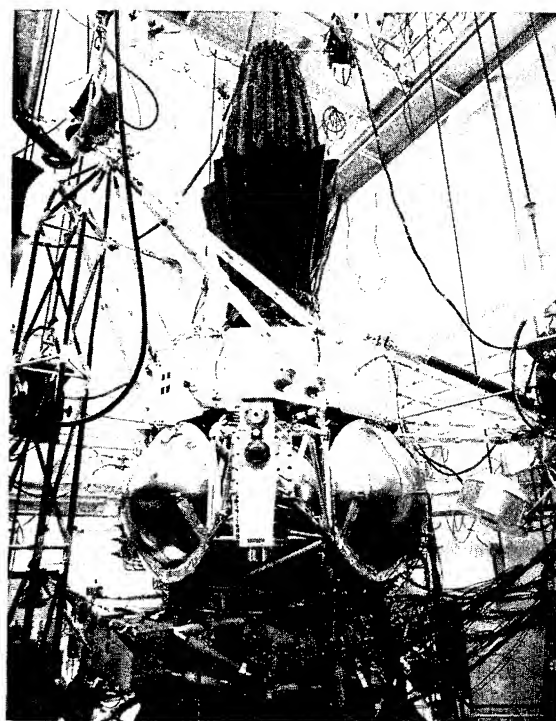


Fig. 1 The Galileo mission to Jupiter.



(a) Major structural components
(antenna stowed during tests)



(b) The Development Test Model (DTM) in
test cell, with shakers attached

Fig. 2 Modal survey test configuration.

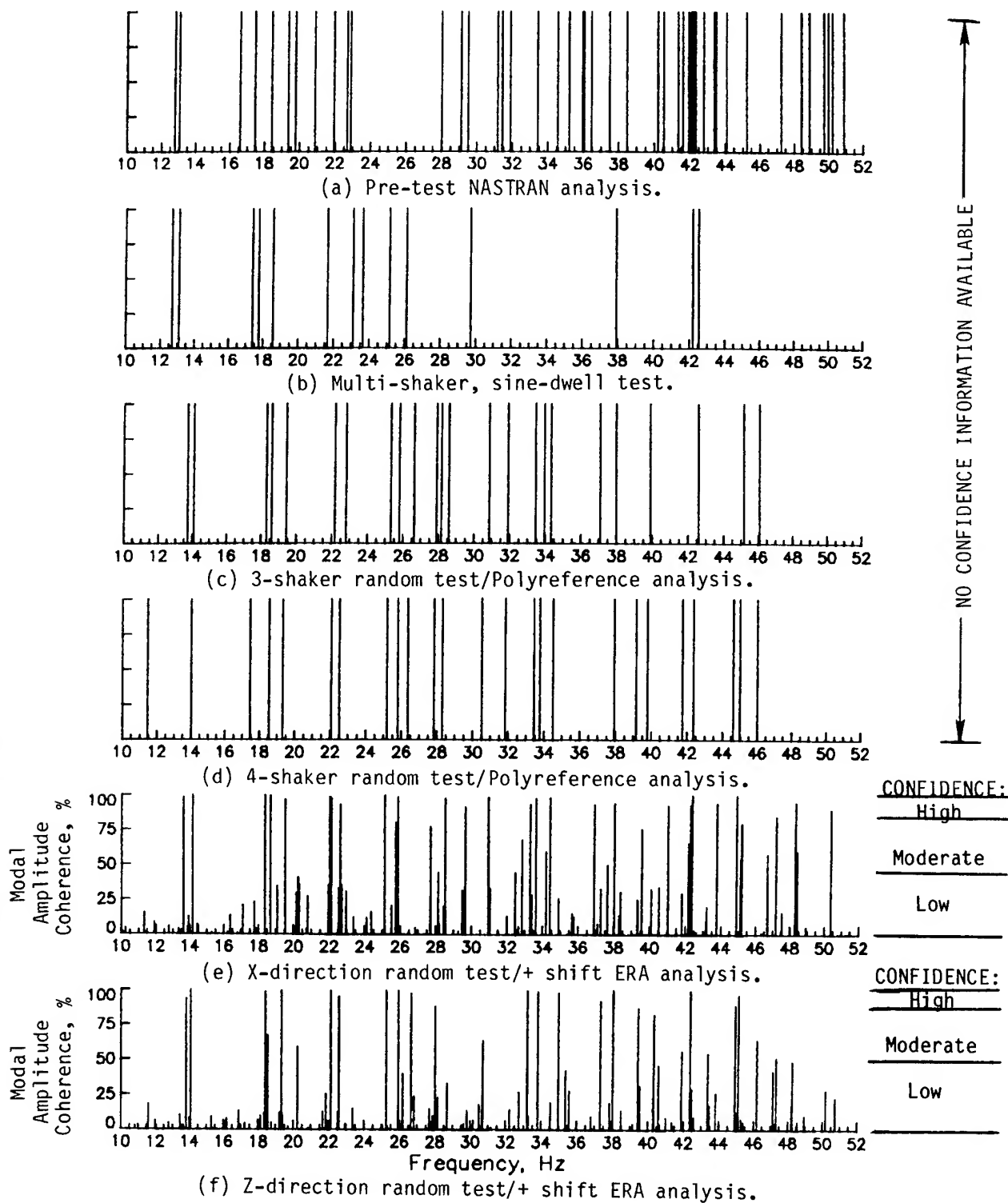
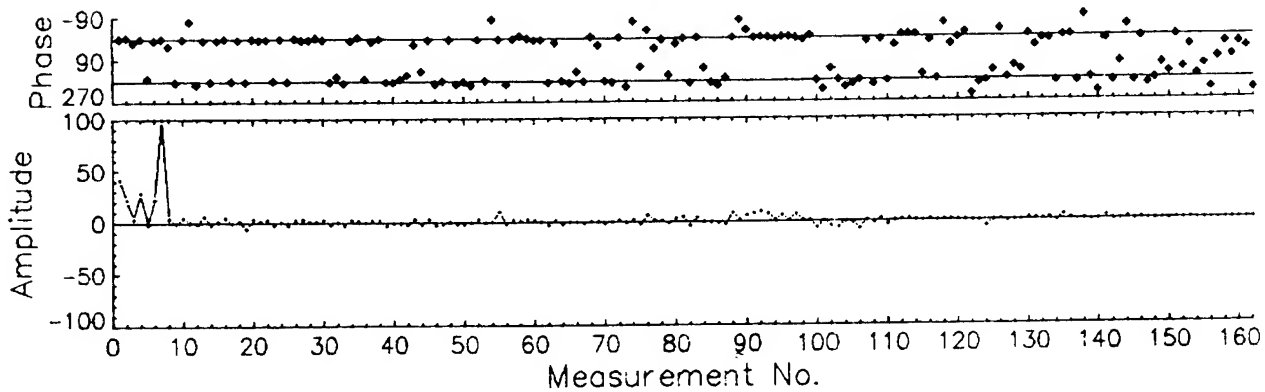


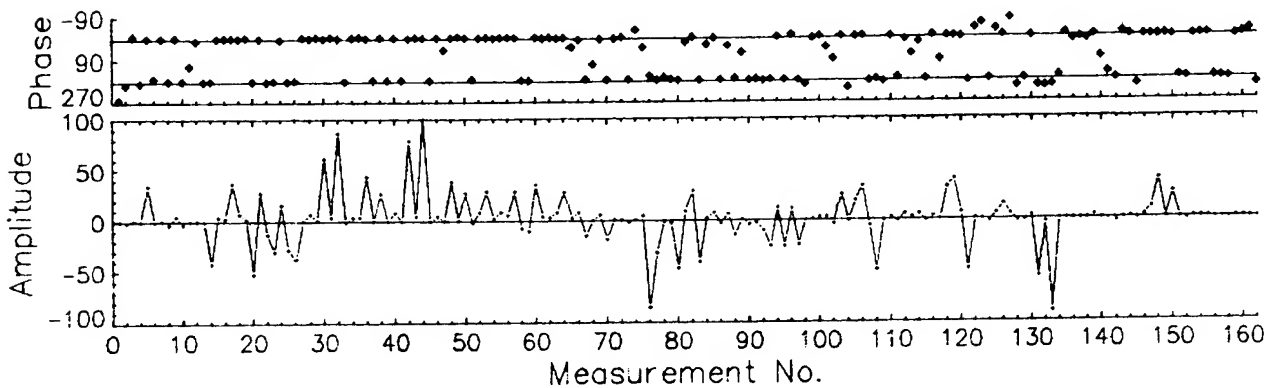
Fig. 3 Comparison of ERA-identified frequencies with NASTRAN and with other experimental results.

Frequency = 13.613 Hz Damping = 3.301%
 Modal Amplitude Coherence = 98.6% Modal Phase Colinearity = 99.0%



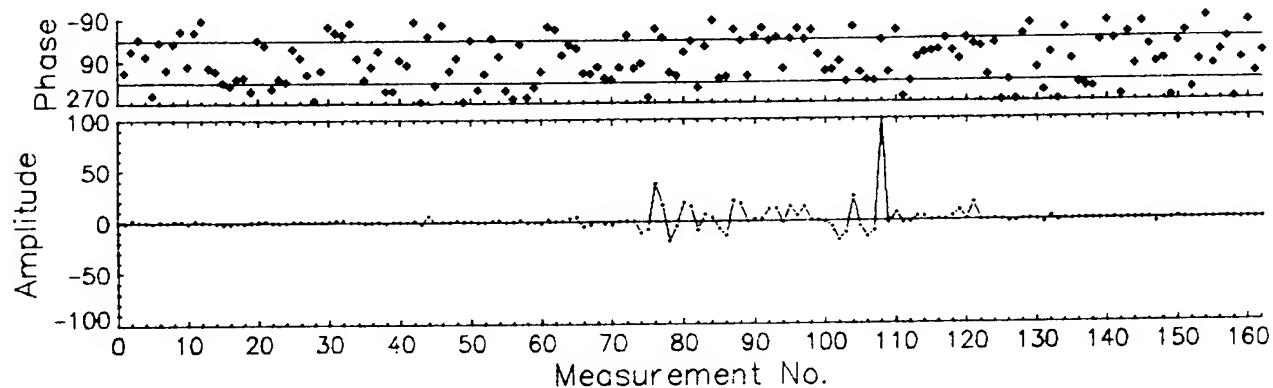
(a) 13.613 Hz antenna bending mode from x-direction random test.

Frequency = 38.037 Hz Damping = .513%
 Modal Amplitude Coherence = 99.8% Modal Phase Colinearity = 93.1%



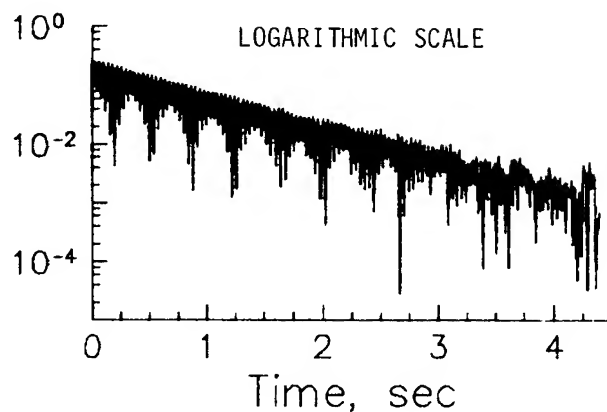
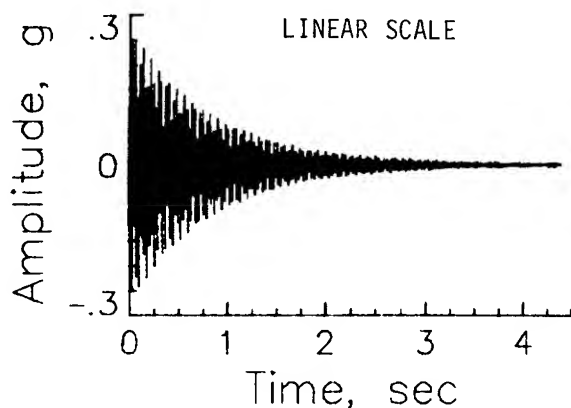
(b) 38.037 Hz "bounce" mode from z-direction random test.

Frequency = 28.016 Hz Damping = 2.651%
 Modal Amplitude Coherence = 88.2% Modal Phase Colinearity = 71.0%

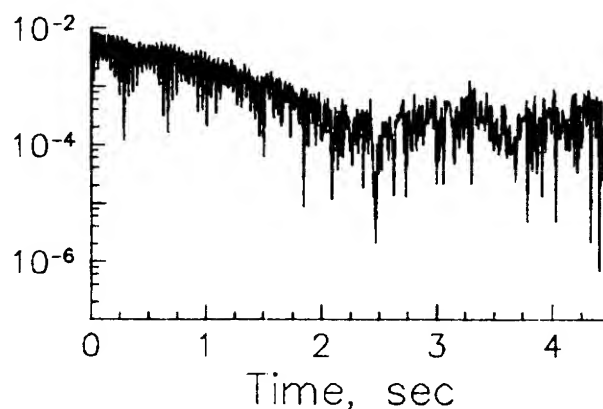
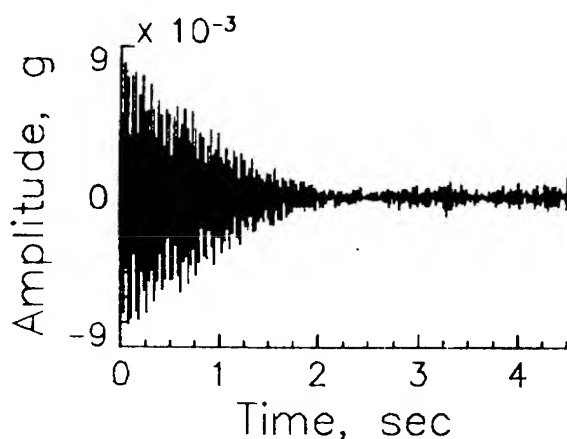


(c) 28.016 Hz mode from z-direction random test. Predominantly science boom and RRH antenna motion.

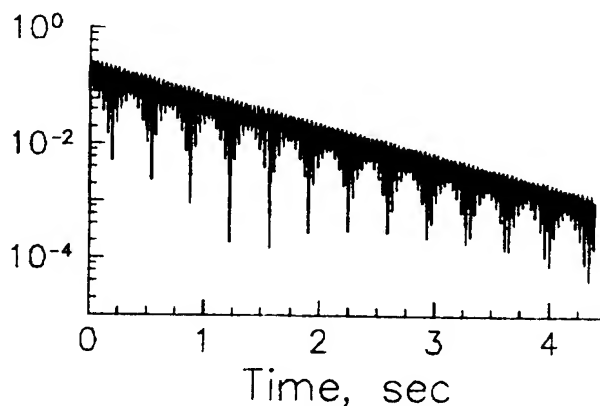
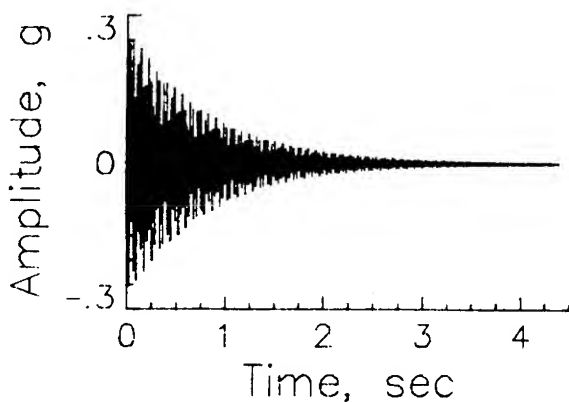
Fig. 4 Example ERA-identified mode shapes, illustrating various degrees of phase angle scatter. All three results are from + time shift analyses.



(a) 38.037 Hz modal amplitude from z-direction, random excitation test.
Modal Amplitude Coherence = 99.8%.



(b) 38.019 Hz modal amplitude from x-direction, random excitation test.
Modal Amplitude Coherence = 94.1%.



(c) Extrapolated-in-time modal amplitude using initial value in (a) and the identified eigenvalue.

Fig. 5 Example modal amplitude results. This mode near 38 Hz is the fundamental z-direction "bounce mode" of the structure. Comparison of (a) and (b) shows that the mode was more strongly excited in the z-direction test, as expected.

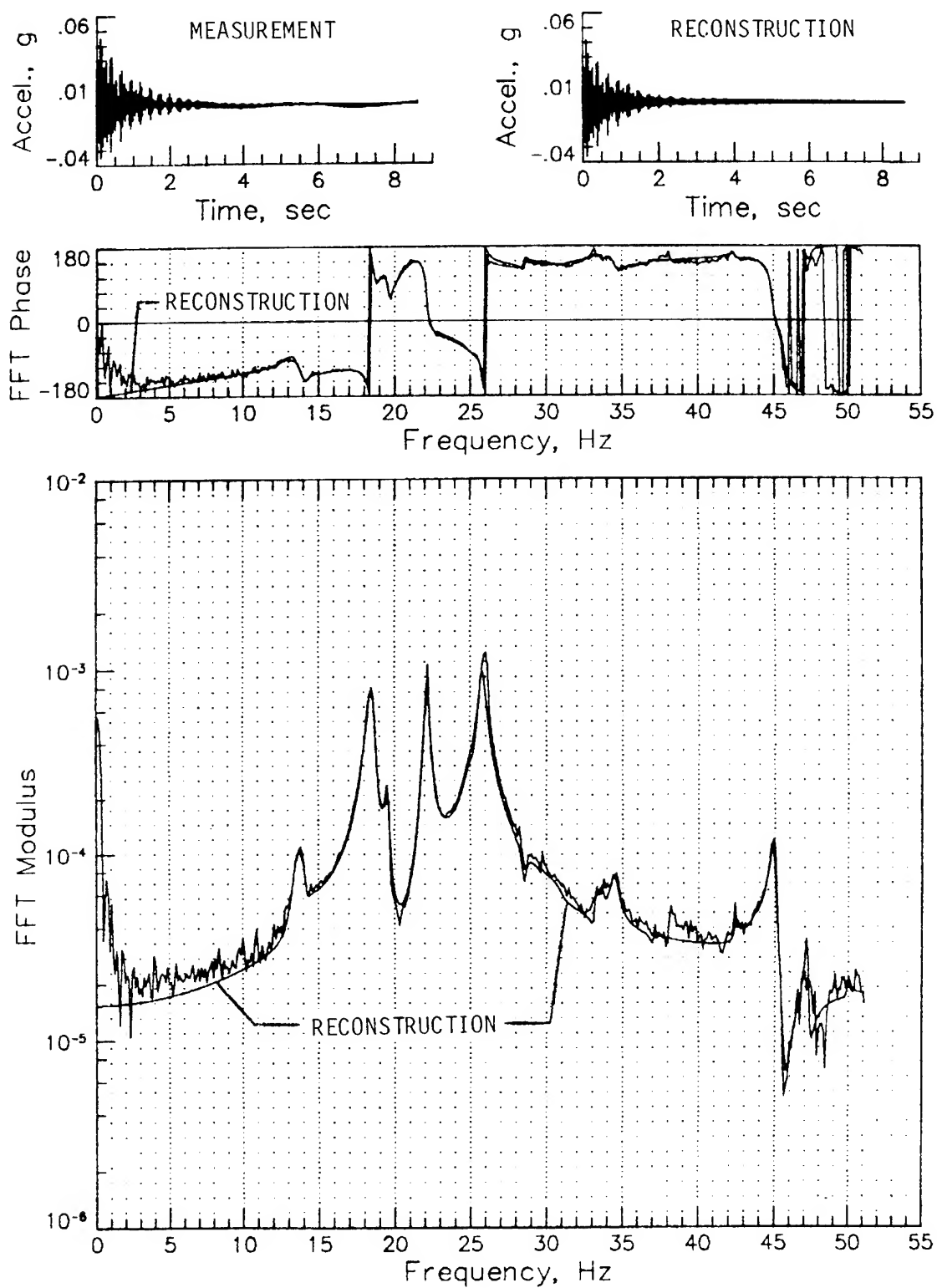


Fig. 6 Example comparison of a measurement from x-direction, random decay test with a 22-mode reconstruction. The reconstruction used Avg. A Matrix results and extrapolated-in-time modal amplitude histories.

$$H_{rs}(0) = PDQ^T, \quad (4)$$

This section summarizes the ERA identification technique; complete details are contained in Ref. 11.

The approach is based on the construction of a minimum-order, linear, state-variable representation, or realization, of the dynamic system under study using measurements of its free response. Because only a finite number of modes can ever be excited in a test, even though structures are, in general, infinite-dimensional dynamic systems, a finite-dimensional realization can always be used to represent the behavior over the bandwidth of excitation. A realization consists of the triple $[A, B, C]$, where A is an $n \times n$ state matrix, B is an $n \times m$ input matrix, and C is a $p \times n$ output matrix, for which the discrete-time, state-variable description of a finite-dimensional, constant dynamic system,

$$\begin{aligned} x(k+1) &= Ax(k) + Bu(k) \\ y(k) &= Cx(k), \end{aligned} \quad (1)$$

holds for all sets of input and output data. In Eqs. (1), $x(k)$ is an n -dimensional state vector, $u(k)$ is an m -dimensional input vector, $y(k)$ is a p -dimensional output vector, and k is an integer time index. A minimum realization is one for which n , the order of the state matrix A , is a minimum. This is a deterministic formulation, treating process and measurement noise implicitly in Eqs. (1).

The impulse response of the system of equations (1) is

$$Y(k) = CA^k - 1B, \quad (2)$$

where Y is a $p \times m$ matrix, and the free-response from an arbitrary set of m initial conditions is

$$Y(k) = CA^k [x_1(0), x_2(0), \dots, x_m(0)]. \quad (3)$$

(In the arbitrary initial conditions case, $A[x_1(0), x_2(0), \dots, x_m(0)]$ is synonymous with B in the determination of $Y(k)$.) All information about the linear dynamics of the system is contained in the triple $[A, B, C]$ and is extracted by appropriate algebraic calculations.

In particular, the following steps--also summarized in flowchart form in Fig. A1--are used for modal parameter identification by the ERA method:

1. Construct a block-Hankel matrix¹¹, $H_{rs}(0)$, using measurements of $Y(k)$. Repeated roots of multiplicity i are identifiable if data for at least i different initial conditions are used simultaneously in constructing $H_{rs}(0)$. There are no restrictions on the number of response measurements that can be processed in a single analysis, regardless of the order of the system.
2. Decompose $H_{rs}(0)$ using singular value decomposition¹⁸ as

where P is an isometric matrix of left singular vectors, Q is an orthogonal matrix of right singular vectors, and D is a diagonal matrix of the singular values. There are no restrictions on the rank deficiency of $H_{rs}(0)$.

3. Determine n , the order of the system (over the bandwidth of excitation). When the data noise level is sufficiently low, the correct order equals the number of singular values above a jump in magnitude that occurs when they are arranged by decreasing magnitude. In these cases, the order will be determined automatically. When the data noise level is too high, judgment must be applied. The best choice for n in these cases is still a subject of current research.
4. Construct a minimum-order realization using a second block-Hankel matrix, $H_{rs}(k)$, consisting of data k samples away in time from corresponding elements of $H_{rs}(0)$, as the triple

$$[P_d^{\#} H_{rs}(k) Q, Q^T E_m, E_p^T P_d], \quad (5)$$

where $P_d = PD$, $P_d^{\#} = D^{-1}P^T$, $E_m^T = [I_m, 0_m, 0_m, \dots]$, and $E_p^T = [I_p, 0_p, 0_p, \dots]$. The calculation of the state matrix using Eq. (5) is referred to as the "+ time shift method." Two other variations, both still under study as tools to better deal with a (usually small) damping bias that occurs with noisy data, are:

$$[P_d^{\#} H_{rs}(-k) Q]^{-1}, \quad (6)$$

referred to as the "- time shift method," and

$$\{P_d^{\#} H_{rs}(k) Q + [P_d^{\#} H_{rs}(-k) Q]^{-1}\}/2, \quad (7)$$

referred to as the "Avg. A matrix method."

5. Find the eigenvalues z and eigenvectors ψ of the realized state matrix, A .
6. The modal damping rates and damped natural frequencies are simply the real and imaginary parts, respectively, of the state matrix eigenvalues, after transformation from the z - to the s -plane using the relationship

$$s = (1/k\Delta t) \ln z, \quad (8)$$

where Δt is the data sampling interval.

7. Modal amplitude time histories are the rows of the matrix product

$$\psi^{-1} Q^T \quad (9)$$

A modal amplitude history is obtained for each set of initial conditions used in the analysis.

8. The desired mode shapes, or modal displacements, are the columns of the matrix product

$$E_p^T P_d \psi \quad (10)$$

9. The degree to which the modes were excited by the selected initial conditions--the degree of controllability¹³--can be assessed by the purity of the modal amplitude time histories determined in Step 7. One method to quickly estimate the purity is to calculate the correlation coefficient (or its square, the coherence) between the identified modal amplitude history and an ideal one formed by extrapolating the initial value of the history to later points in time using the identified eigenvalue.
10. If the purity of the modal amplitude history is high, the degree to which the mode was sensed by the selected measurements--the degree of observability¹³--can then be assessed by studying the mode shape results determined in Step 8; for example, by checking the deviation from 0-180° behavior among the identified mode shape components (when approximate normal-mode behavior is a reasonable assumption).
11. The accuracy of the complete modal decomposition process can be examined by comparing a reconstruction of $Y(k)$ formed by

$$Y(k) = CA^{k-1}B \quad (11)$$

with the original free-response data, using various numbers of the identified modes, for example.

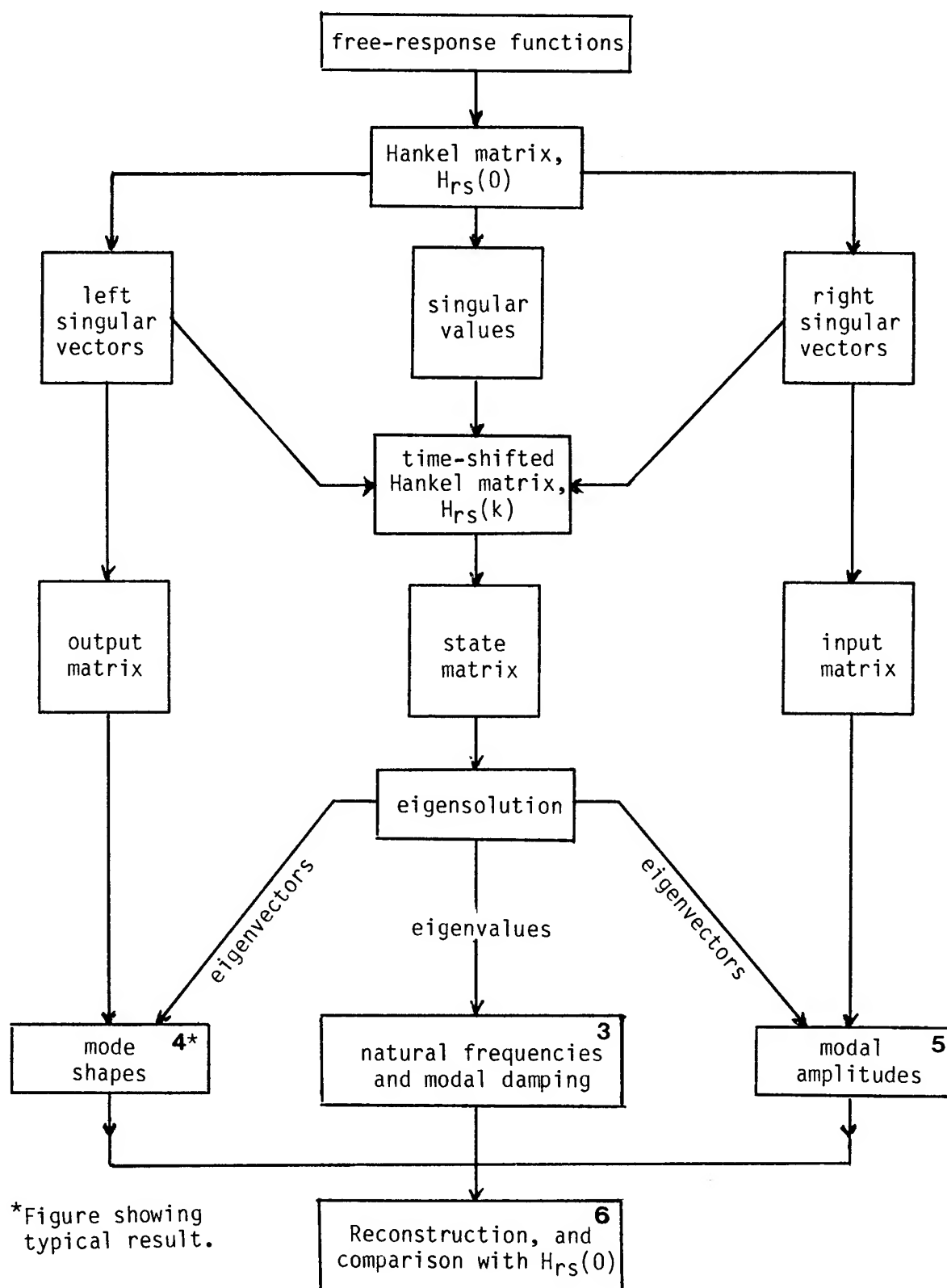


Fig. A1 Flowchart of ERA.